HIGHLIGHTS FROM TERMIS EU 2019

EDITED BY: Dimitrios I. Zeugolis and Maria Chatzinikolaidou
PUBLISHED IN: Frontiers in Bioengineering and Biotechnology

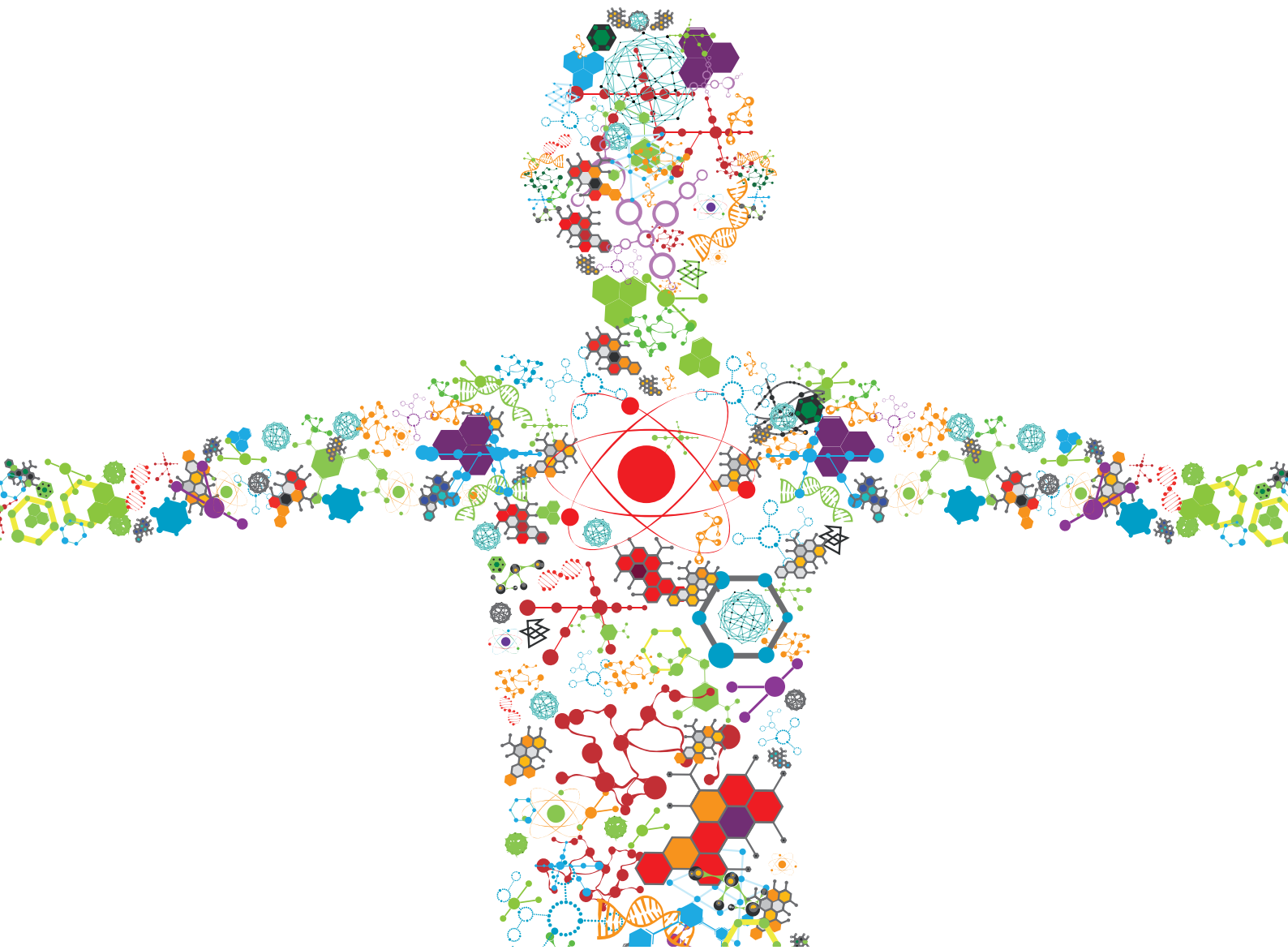

frontiers Research Topics

frontiers

ISSN 1664-8714
ISBN 978-2-88966-309-5
DOI 10.3389/978-2-88966-309-5

About Frontiers

Frontiers is more than just an open-access publisher of scholarly articles: it is a pioneering approach to the world of academia, radically improving the way scholarly research is managed. The grand vision of Frontiers is a world where all people have an equal opportunity to seek, share and generate knowledge. Frontiers provides immediate and permanent online open access to all its publications, but this alone is not enough to realize our grand goals.

Frontiers Journal Series

The Frontiers Journal Series is a multi-tier and interdisciplinary set of open-access, online journals, promising a paradigm shift from the current review, selection and dissemination processes in academic publishing. All Frontiers journals are driven by researchers for researchers; therefore, they constitute a service to the scholarly community. At the same time, the Frontiers Journal Series operates on a revolutionary invention, the tiered publishing system, initially addressing specific communities of scholars, and gradually climbing up to broader public understanding, thus serving the interests of the lay society, too.

Dedication to Quality

Each Frontiers article is a landmark of the highest quality, thanks to genuinely collaborative interactions between authors and review editors, who include some of the world's best academicians. Research must be certified by peers before entering a stream of knowledge that may eventually reach the public - and shape society; therefore, Frontiers only applies the most rigorous and unbiased reviews.
Frontiers revolutionizes research publishing by freely delivering the most outstanding research, evaluated with no bias from both the academic and social point of view. By applying the most advanced information technologies, Frontiers is catapulting scholarly publishing into a new generation.

What are Frontiers Research Topics?

Frontiers Research Topics are very popular trademarks of the Frontiers Journals Series: they are collections of at least ten articles, all centered on a particular subject. With their unique mix of varied contributions from Original Research to Review Articles, Frontiers Research Topics unify the most influential researchers, the latest key findings and historical advances in a hot research area! Find out more on how to host your own Frontiers Research Topic or contribute to one as an author by contacting the Frontiers Editorial Office: researchtopics@frontiersin.org

HIGHLIGHTS FROM TERMIS EU 2019

Topic Editors:
Dimitrios I. Zeugolis, National University of Ireland Galway, Ireland
Maria Chatzinikolaidou, University of Crete, Greece

Citation: Zeugolis, D. I., Chatzinikolaidou, M., eds. (2021). Highlights from TERMIS EU 2019. Lausanne: Frontiers Media SA. doi: 10.3389/978-2-88966-309-5

Table of Contents

frontiers in Bioengineering and Biotechnology

EDITORIAL
published: 04 November 2020
doi: 10.3389/fbioe.2020.604661

Editorial: Highlights From TERMIS EU 2019

Maria Chatzinikolaidou[1,2]* *and Dimitrios I. Zeugolis*[3,4,5]*

[1] Department of Materials Science and Technology, University of Crete, Crete, Greece, [2] Institute of Electronic Structure and Laser, Foundation for Research and Technology-Hellas, Crete, Greece, [3] Regenerative, Modular & Developmental Engineering Laboratory, National University of Ireland Galway, Galway, Ireland, [4] Science Foundation Ireland, Centre for Research in Medical Devices, National University of Ireland Galway, Galway, Ireland, [5] Regenerative, Modular & Developmental Engineering Laboratory, Faculty of Biomedical Sciences, Università della Svizzera Italiana, Lugano, Switzerland

Keywords: tissue engineering, regenerative medicine, cell therapies, functional biomaterials, preclinical models

Editorial on the Research Topic

Highlights From TERMIS EU 2019

Tissue Engineering and Regenerative Medicine International Society (TERMIS) is the most prominent organization in the field of tissue engineering and regenerative medicine globally. TERMIS promotes education, research, innovation, clinical translation, and social responsibility within the field of tissue engineering and regenerative medicine through regular meetings, training courses, scientific and lay publications, outreach activities, and other forms of communication. TERMIS provides an international forum for informed discussion on the challenges and achievements of tissue engineering therapies.

This special issue is associated with the TERMIS EU Chapter 2019 meeting at Rhodes, Greece, 27-31 May. The theme of the meeting was "*Tissue Engineering Therapies: From concept to clinical translation and commercialisation.*" This special issue covers all aspects of tissue engineering and regenerative medicine, including computational models for the cost efficient production of cell-based tissue engineered products (Mehrian et al.); development of media [e.g., sodium hyaluronate supplemented culture media for chondrogenic differentiation (Monaco et al.)] and tools [e.g., non-invasive techniques to measure oxygen gradients in cell culture (Peniche Silva et al.), processes to generate and culture three dimensional cell spheroids in a microfluidic set-up (Lopa et al.), cell-derived matrices to control cell phenotype (Penolazzi et al.)] for more accurate cell culture and for effectively monitoring the fate of implantable devices [e.g., multiparametric optical bioimaging (Elagin et al.)]; the potential of large animal models in regenerative medicine (Ribitsch et al.); and clinical indication specific discussion [e.g., inflammation and bone repair (Goodman et al.), electrospun scaffolds for cartilage engineering (Yilmaz and Zeugolis)].

Advancements in chemistry and engineering have made numerous new materials available and nano/micro fabrication technologies have potential in modern tissue engineering and regenerative medicine. With this in mind, this special issue discusses a range of natural and synthetic systems [e.g., fibrin-agarose hydrogels (Campos et al.), gellan gum hydrogels (Gomes et al.), elastin-like recombinamer hydrogels (Ibáñez-Fonseca et al.), poly(ethylene terephthalate) electrospun scaffolds decorated with poly(lactic acid-co-glycolic acid) (PLGA) or poly(glycolic acid) (PGA) electrosprayed nanoparticles (McCormick et al.), tripolyphosphate crosslinked chitosan/gelatin biocomposite inks (Fischetti et al.), inorganic calcium phosphate, chitosan, and hyaluronic acid scaffolds (Rammal et al.), polycaprolactone-polypyrrole printed conductive biomaterials (Vijayavenkataraman et al.)] for a diverse range of clinical targets, as well as advances in stimuli responsive materials as controlled delivery vehicles (Laurano and Boffito; Boffito et al.).

Edited and reviewed by:
Ranieri Cancedda, Independent Researcher, Genova, Italy

***Correspondence:**
Maria Chatzinikolaidou
mchatzin@materials.uoc.gr
Dimitrios I. Zeugolis
dimitrios.zeugolis@usi.ch

Specialty section:
This article was submitted to Tissue Engineering and Regenerative Medicine, a section of the journal Frontiers in Bioengineering and Biotechnology

Received: *10 September 2020*
Accepted: *21 September 2020*
Published: *04 November 2020*

Citation:
Chatzinikolaidou M and Zeugolis DI (2020) Editorial: Highlights From TERMIS EU 2019. Front. Bioeng. Biotechnol. 8:604661. doi: 10.3389/fbioe.2020.604661

Considering that cells are the basic building blocks of tissues (both healthy and diseased), contemporary tissue engineering and regenerative medicine exploits the power of cells for the development of implantable devices that will revolutionize healthcare due to their therapeutic and reparative capabilities (e.g., hybrid bioprinting of chondrogenically induced human mesenchymal stem cell spheroids with a photocrosslinkable methacrylamide-modified gelatin printed medium (De Moor et al.), cornea cells with a plastic compressed nanostructured fibrin-agarose biomaterial (Garzón et al.), vascular endothelial growth factor (VEGF)-transduced bone marrow stem cells with a hydroxyapatite scaffold (Largo et al.), human pluripotent stem cell-smooth muscle cell-endothelial cell vascular organoids embedded in collagen/fibrinogen/fibronectin matrices (Markou et al.), but also for the development of organ on chip models to study cell functions [e.g., osteoblast maturation toward osteocytes and matrix mineralisation (Nasello et al.), aged tendon organoids (Yan et al.)] and of *in vitro* pathophysiology models for drug screening purposes [e.g., skin (Schmidt et al.; Zurina et al.), tumor (Gupta et al.), intervertebral degenerative disc (Li et al.) models].

Tissue engineering and regenerative medicine have the potential to provide effective treatments for uncurable injuries and diseases, potentially enabling the development of *in vitro* models for the study of disease progression and to assess the potential of novel therapies. This collection of manuscripts captures the state-of-play in this field, indicating that the development of effective therapies is underway.

AUTHOR CONTRIBUTIONS

All authors listed have made a substantial, direct and intellectual contribution to the work, and approved it for publication.

FUNDING

This work received funding from the European Union's Horizon 2020 research and innovation programme, grant agreement no. 814410; the Hellenic Foundation for Research and Innovation (HFRI) under the First Call to support Faculty members and Researchers, grant no. HFRI-FM17-1999; the European Union's Horizon 2020 research and innovation programme under the Marie Skłodowska-Curie, grant agreement no. 676338; European Research Council (ERC) under the European Union's Horizon 2020 research and innovation programme, grant agreement no. 866126; Science Foundation Ireland, Career Development Award, grant agreement no. 15/CDA/3629; and Science Foundation Ireland/European Regional Development Fund, grant agreement no. 13/RC/2073.

Conflict of Interest: The authors declare that the research was conducted in the absence of any commercial or financial relationships that could be construed as a potential conflict of interest.

frontiers in Bioengineering and Biotechnology

REVIEW
published: 19 September 2019
doi: 10.3389/fbioe.2019.00230

Inflammation and Bone Repair: From Particle Disease to Tissue Regeneration

Stuart B. Goodman[1,2,3]*, *Jukka Pajarinen*[3], *Zhenyu Yao*[4] and *Tzuhua Lin*[4]

[1] Department of Orthopaedic Surgery, Stanford University School of Medicine, Redwood City, CA, United States, [2] Department of Bioengineering, Stanford University, Stanford, CA, United States, [3] Department of Medicine, Clinicum, University of Helsinki and Helsinki University Hospital, Helsinki, Finland, [4] Orthopaedic Research Laboratories, Stanford University, Stanford, CA, United States

When presented with an adverse stimulus, organisms evoke an immediate, pre-programmed, non-specific innate immune response. The purpose of this reaction is to maintain the organism's biological integrity and function, mitigate or eradicate the injurious source, and re-establish tissue homeostasis. The initial stage of this protective reaction is acute inflammation, which normally reduces or terminates the offending stimulus. As the inflammatory reaction recedes, the stage of tissue repair and regeneration follows. If the above sequence of events is perturbed, reconstitution of normal biological form and function will not be achieved. Dysregulation of these activities may result in incomplete healing, fibrosis, or chronic inflammation. Our laboratory has studied the reaction to wear particles from joint replacements as a paradigm for understanding the biological pathways of acute and chronic inflammation, and potential translational treatments to reconstitute lost bone. As inflammation is the cornerstone for healing in all anatomical locations, the concepts developed have relevance to tissue engineering and regenerative medicine in all organ systems. To accomplish our goal, we developed novel *in vitro* and *in vivo* models (including the murine femoral continuous intramedullary particle infusion model), translational strategies including modulation of macrophage chemotaxis and polarization, and methods to interfere with key transcription factors NFκB and MyD88. We purposefully modified MSCs to facilitate bone healing in inflammatory scenarios: by preconditioning the MSCs, and by genetically modifying MSCs to first sense NFκB activation and then overexpress the anti-inflammatory pro-regenerative cytokine IL-4. These advancements provide significant translational opportunities to enhance healing in bone and other organs.

Keywords: inflammation, bone healing, bone repair, wear particle disease, osteogenesis

OPEN ACCESS

Edited by:
Dimitrios I. Zeugolis, National University of Ireland Galway, Ireland

Reviewed by:
Marnie Marie Saunders, University of Akron, United States
Marco Tatullo, Tecnologica S.r.l., Italy
Hajime Sasaki, University of Michigan, United States
Qin Shi, First Affiliated Hospital of Soochow University, China

***Correspondence:**
Stuart B. Goodman
goodbone@stanford.edu

Specialty section:
This article was submitted to Tissue Engineering and Regenerative Medicine, a section of the journal Frontiers in Bioengineering and Biotechnology

Received: *28 July 2019*
Accepted: *06 September 2019*
Published: *19 September 2019*

Citation:
Goodman SB, Pajarinen J, Yao Z and Lin T (2019) Inflammation and Bone Repair: From Particle Disease to Tissue Regeneration. Front. Bioeng. Biotechnol. 7:230. doi: 10.3389/fbioe.2019.00230

INTRODUCTION

When exposed to trauma, infection, thermal or chemical injury, or other adverse stimuli, all organisms including humans evoke an immediate, programmed, non-antigen specific immune response to preserve the organism's integrity and re-establish homeostasis (Medzhitov, 2008). This reaction is governed by cells of the innate immune system and defines the acute inflammatory

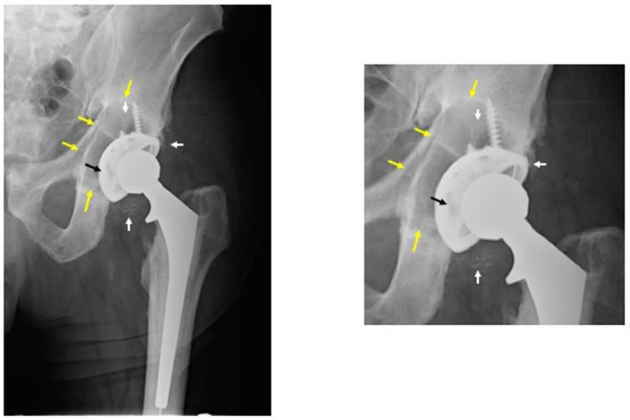

FIGURE 1 | Periprosthetic osteolysis post total hip replacement (THR). The left radiograph shows a hybrid THR with a cemented stem and a cementless cup with screws. The components are well fixed, however, there is polyethylene wear and the metallic cup has fractured adjacent to the screw holes (note: two of the screw holes are larger than they should be and confluent instead of separate—black arrow). The small white radio-dense particles represent metallic debris from the cup (white arrows). There is a large radiolucent black area of bone destruction (osteolysis) (yellow arrows) surrounding the acetabular component. The radiograph on the right is a magnified view of the acetabular area.

response (Mosser and Edwards, 2008; Chen and Nuñez, 2010). Acute inflammation is the first stage of healing of all tissues, and normally results in repair and regeneration of the damaged structures (Mantovani et al., 2013). If the sequence of events comprising tissue healing is interrupted or dysregulated, the typical healing of host tissue becomes impaired (Gerstenfeld et al., 2003). Furthermore, if the injurious stimulus is not quickly mitigated, either the organism as a whole will succumb (if the injury or resulting response is overwhelming), or the local tissues may progress to a state of chronic inflammation, in which ongoing injury and attempts at repair persist. Thus, the end result of an adverse stimulus may vary from complete restoration of anatomical form and function at one end of the spectrum, to subsequent death at the other extreme; injuries often result in intermediate outcomes including partial tissue regeneration, fibrosis, and/or chronic inflammation.

With regards to bone and soft tissues, the response to injury is no different than for other organs. When bone is subjected to trauma or an adverse stimulus, the resident cells release numerous cytokines, chemokines, and other substances that initiate local vasodilatation and efflux of inflammatory cells from the circulation; a pro-inflammatory cascade of events is launched to terminate the adverse event and initiate the regenerative process (Marsell and Einhorn, 2011; Karnes et al., 2015). Although, numerous cells are directly involved in these ongoing activities, local macrophages, as well as circulating surveillance monocyte/macrophages orchestrate the ensuing series of biological events (Fujiwara and Kobayashi, 2005; Medzhitov, 2008; Nich et al., 2013; Sinder et al., 2015; Kaur et al., 2017). Specialized cellular systems have evolved including pattern recognition receptors (PRRs) to identify chemical motifs from bacteria and infectious agents (so called pathogen-associated molecular patterns or PAMPs) and byproducts of cell death and tissue injury (damage-associated molecular patterns or DAMPS) (Kawai and Akira, 2010). When PRRs are ligated, a system of effector mechanisms including Toll Like Receptors (TLRs), Nucleotide-binding Oligomerization Domain (NOD) and leucine-rich repeat-containing receptors (NLRs), Retinoic acid inducible gene (RIG) receptors, and others transmit these signals through intermediate molecules to upregulate the formation and release of pro-inflammatory substances (Akira and Takeda, 2004; Medzhitov, 2008). These include cytokines e.g., tumor necrosis factor alpha (TNFα), Interleukin 1 beta (IL-1β), IL-6, IL-8, and others, chemokines including macrophage chemotactic protein 1 (MCP-1), macrophage inhibitory protein 1 (MIP-1), reactive oxygen intermediates (such as inducible nitric oxide synthetase or iNOS), and growth factors (such as vascular endothelial growth factor or VEGF, transforming growth factor beta or TGFβ etc.). These cells and substances eradicate invading microbes, limit the injurious stimulus, and recruit more cells to participate in the biological confrontation, and begin the resolution and reparative phases (Medzhitov, 2008; Mosser and Edwards, 2008; Mantovani et al., 2013).

This paper will summarize the important biological processes of inflammation as they relate to bone healing and emphasize the critical intercellular communications that participate in repair of bone subjected to adverse stimuli. *In vitro* and *in vivo* research performed in our laboratory and by others that facilitates bone repair in inflammatory conditions will be highlighted.

THE BIOLOGICAL REACTION TO WEAR PARTICLES FROM JOINT REPLACEMENTS: A PARADIGM FOR ACUTE AND CHRONIC INFLAMMATION

Traditionally, most joint replacements have used a bearing couple composed of ultra-high molecular weight polyethylene (UHMWPE), and a metallic or ceramic counter surface. This bearing couple has recently been improved, with the development of enhanced crosslinking of the polyethylene and embedded anti-oxidants, and by reducing the surface asperities and polishing of the countersurface. However, for the first 40 years of joint replacement surgery, the biological reaction to wear particles, and the resultant sterile inflammation and bone loss (known as periprosthetic osteolysis) were the predominant reasons for revision (redo) surgery (Jacobs et al., 2001; Purdue et al., 2007; Gallo et al., 2013) (**Figure 1**). This subject has been studied extensively by our group and others; numerous *in vitro* and *in vivo* models have been developed to simulate the events of wear particle-induced inflammation.

In general, wear particles stimulate a non-specific macrophage dominated inflammatory reaction characteristic of the innate immune system, in a background fibrovascular stroma (Goodman et al., 1998; Goodman, 2007). The characteristics of the wear particles are important to this reaction: smaller

(0.3 to <5–10 μm) irregularly shaped particles of polymers appear to be more inciting of an inflammatory response, compared to ceramic or metallic particles, however this point is controversial (Goodman, 1994; Kaufman et al., 2008; Goodman et al., 2009). Particles ∼1 μm or less are the most prominent and reactive ones (Campbell et al., 1995). In addition, to the above particle characteristics, the surface area, surface energy and overall number and volume of particles are key factors in the resultant histological reaction (Shanbhag et al., 1994; González et al., 1996; Green et al., 1998, 2000). Certain metallic particles and byproducts can stimulate both the innate and adaptive immune systems, the latter occurring when the metallic moiety and attached protein function as a hapten (Haynes et al., 1993; Hallab et al., 2001; Caicedo et al., 2008). Indeed, all particles are bound to serum proteins such as albumin, alpha-1-antitrypsin, apolipoprotein, and others, and activate specific cell surface receptors to engage the inflammatory cascade (Nakashima et al., 1999; Sun et al., 2003). These complexes are recognized by cell surface receptors, or if small enough, phagocytosed altogether (Nakashima et al., 1999; Purdue et al., 2007). Although, numerous biological pathways in macrophages, fibroblasts and other cells are involved in these events, the key molecules involved in particle-associated inflammation include the adapter protein Myeloid Differentiation primary response gene 88 (MyD88), and the transcription factor nuclear factor kappa-light-chain-enhancer of activated B cells (NFκB) (Nakashima et al., 1999; Clohisy et al., 2004; Ren et al., 2004; Baumann et al., 2005; Pearl et al., 2011). Activation of MyD88 and NFκB lead to the transcription of numerous pro-inflammatory substances and upregulation of the innate and (to a lesser degree with respect to wear particle disease) the adaptive immune systems (Pearl et al., 2011; Landgraeber et al., 2014; Nich et al., 2016). In bone and the surrounding tissues, this results in an influx of primarily monocyte/macrophages, but also mast cells, polymorphonuclear leukocytes, T lymphocytes, osteoclasts and other cells are present (Hallab and Jacobs, 2017). The resulting pro-inflammatory environment leads to increased bone destruction by cells of the monocyte/macrophage/osteoclast lineage and suppressed bone formation by cells of the mesenchymal stem cell (MSC)/osteoblast lineage (Kadoya et al., 1996; Vermes et al., 2000; Jacobs et al., 2001). With regards to osteoclastogenesis, the Receptor Activator of Nuclear Factor-kappa B Ligand (RANKL)-RANK- osteoprotegerin (OPG) axis becomes dysregulated, leading to increased osteoclast formation and activation (Haynes et al., 2001). Furthermore, soluble and particulate cobalt-chrome molybdenum alloy (and other particle types) are capable of activating the intracellular inflammasome pathway which increases the secretion of IL-1 and other pro-inflammatory cytokines (Caicedo et al., 2008). As more wear particles are continuously produced with use of the artificial implant, the acute inflammatory reaction becomes chronic, with progressive synovitis and bone destruction. In addition, the presence of endotoxin on the particles and other bacterial byproducts can sustain and exacerbate the inflammatory reaction (Bi et al., 2001).

IN VITRO AND *IN VIVO* MODELS OF PARTICLE-INDUCED INFLAMMATION SUGGEST POTENTIAL AVENUES FOR TREATMENT

In general, our tact has been to develop *in vitro* models for proof-of-principle testing of new concepts and biologics, and then expand and validate these hypotheses using *in vivo* models that simulate the biological events of wear particle disease as closely as possible. One appreciates the associated temporal compression of such models compared to a disease in humans that usually takes many years to develop. Moreover, in investigating the resultant inflammatory bone loss associated with wear particles, one also recognizes the suppressive effects of particles on MSC-osteoblast lineage cells (Wang et al., 2002; Chiu et al., 2006, 2009; Goodman et al., 2006; Ramachandran et al., 2006; Atkins et al., 2009; Pajarinen et al., 2017a). This realization has led to novel methods not only to mitigate bone destruction, but to enhance bone formation, subjects very relevant to the broader topics of tissue engineering and repair of bone. It is also recognized that the pro-inflammatory effects associated with wear particles are not the only factors leading to dysregulated bone biology around joint replacements; other factors include the presence of bacterial ligands, mechanical forces, fluid pressure, and immune reactions especially to metal byproducts etc. (Aspenberg and Herbertsson, 1996; Aspenberg and Van der Vis, 1998; Bi et al., 2002; Cho et al., 2002; Choi et al., 2005; Caicedo et al., 2008; Greenfield and Bechtold, 2008).

Numerous studies have established that wear particles both upregulate the inflammatory cascade and suppress the pathways that facilitate bone formation (Jacobs et al., 2001; Goodman, 2007; Purdue et al., 2007; Goodman and Ma, 2010). *In vivo* models of particle induced osteolysis have the difficulty of simulating a complex series of biological events in a short period of time, in a cost-effective and practical manner. Nonetheless, both small and large animal models have demonstrated some of the important pathogenetic mechanisms leading to particle-associated osteolysis (Lind et al., 1998; Cordova et al., 2014; Moran et al., 2017).

Originally, our laboratory used simpler models encompassing a single bolus of different particles alone, or with more basic implants resurfacing only one side of a joint, or in bone harvest chambers in rabbits; we also implanted particles around a solid intramedullary rod in mice (Goodman et al., 1993; Goodman, 1994; Sacomen et al., 1998; Epstein et al., 2005b; Zilber et al., 2008). While these models provided important information regarding the acute inflammatory reaction to particles (which perhaps was more relevant to the bedding in phase of wear and osseointegration of implants), there were several deficiencies. First, particles are continuously produced from bearing surfaces in human joint replacements and a single bolus of particles does not simulate this scenario. Second, the cellular processes reflective of more chronic particle exposure and the longer-term attempts at re-establishment of tissue homeostasis could not be investigated. Third, some of the models, such as the calvarial

model (using a flat bone) were anatomically and physiologically dissimilar from the clinical situation in which human implants are placed in long bones that have a different anatomical and biomechanical structure, and blood supply. Furthermore, the calvarial model does not usually use an implant to simulate a prosthesis. Fourth, the rabbit models were expensive and proved difficult to use with cutting-edge technologies such as genetic manipulation of cells, advanced imaging techniques etc. Nevertheless, single bolus models are still relevant, as they have demonstrated that wear particles of different materials stimulated a macrophage dominated foreign body inflammatory reaction that increased bone destruction and diminished bone formation. The key pro-inflammatory cytokines (TNFα, IL-1β, IL-6, and others) and chemokines (MCP-1, etc.) associated with this reaction were identified (Trindade et al., 1999; Epstein et al., 2005a,b). Using these models, we investigated potential treatments for osteolysis, such as the effects of oral non-steroidal anti-inflammatory medications, an oral p38 mitogen-activated protein kinase (MAPK) inhibitor, and locally placed growth factor (e.g., Transforming Growth Factor beta) (Goodman et al., 1999; Kumagai et al., 2008). However, these substances also adversely affected bone formation, and the timing of delivery and optimal dosage were difficult to establish *in vivo*.

As a result, more representative models of continuous particle delivery over a more extended time period in small rodents were developed by our laboratory. These models were less costly, simulated the clinical scenario more closely, and could take advantage of newer genetic and imaging technologies. Thus, we developed the murine femoral continuous intramedullary particle infusion model, in which a diffusion pump implanted in the subcutaneous paraspinal region was connected via tubing to a hollow titanium rod placed in the intramedullary canal of the distal third of the femur (**Figure 2**). Particles and potential therapeutic agents could be loaded into the pump and continuously delivered into bone via the hollow rod over ∼28 days. The model was validated first *ex vivo*, prior to its use in live animals (Ortiz et al., 2008a,b). Using histomorphometry, immunohistochemistry, and microCT analysis, we then reported that continuous infusion of clinically relevant polyethylene particles produced a chronic inflammatory macrophage dominated reaction and decreased local bone volume, compared to infusion of the carrier alone (Patterson et al., 2008). Recently we demonstrated that extending the particle delivery time up to 56 days leads to further evolution of chronic inflammation, with continued macrophage activation and bone loss, similar to the progressive clinical scenario (Pajarinen et al., 2017b). We also extended this model to study systemic macrophage trafficking by injecting genetically altered reporter macrophages into the tail vein immediately after surgery, and repeatedly tracked the migration of these cells throughout the body non-destructively via bioluminescence (Ren et al., 2010). To follow systemic trafficking of reporter MSCs, we needed to develop another technique, using left ventricular cardiac cell injection in the beating heart, because the much larger MSCs delivered through the tail vein would sequester in the pulmonary microvasculature, rather than pass through the lungs into the arterial system (Fritton et al., 2012). From these experiments we learned the following: (a) infusion of the chemokine MCP-1 or polyethylene particles via the osmotic pump induces systemic recruitment of reporter macrophages to the local area which results in osteolysis. This macrophage reporter cell trafficking and bone loss could be mitigated by interrupting the MCP-1-CCR2 chemokine-receptor axis using an MCP-1 receptor antagonist or reporter cells from knockout mice that do not possess the CCR2 receptor ($CCR2^{-}$ cells) (Gibon et al., 2012a); (b) luciferase expressing reporter MC3T3 pre-osteoblasts injected into the left ventricle migrated systemically to the area of particle infusion in the distal femur and were associated with increased bone mineral density and markers of bone turnover locally. These effects could be mitigated by injection of an inhibitor of the C-C chemokine receptor CCR1, which interferes with both leukocyte and MSC chemotaxis (Fritton et al., 2012; Gibon et al., 2012b). The above interventions revealed the local and systemic pathways associated with particle-associated inflammation and suggested potential mechanistic interventions for treatment.

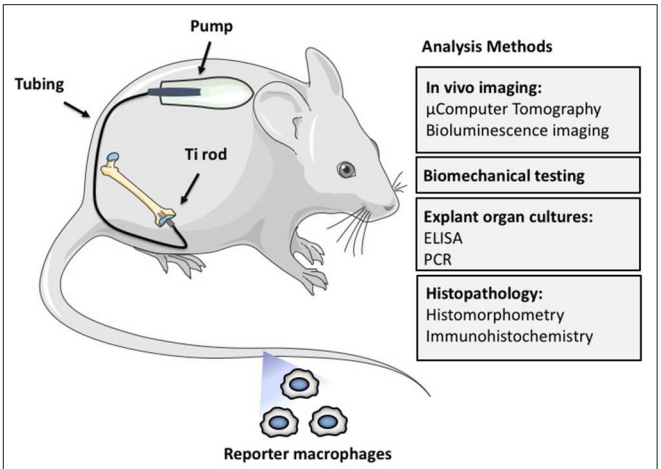

FIGURE 2 | The murine femoral continuous intramedullary particle infusion model. First, the osmotic pump is loaded with biomaterial wear debris and then implanted in the subcutaneous tissue at the dorsum of the mouse. The pump is then connected via subcutaneous tubing to a hollow titanium rod that has been press fit into the intramedullary canal of the distal femur. This arrangement facilitates continuous delivery of biomaterial wear debris to the intramedullary space for 28 days, resulting in continued low grade inflammation and bone loss. The particle delivery can be further extended by changing the pump in a minor surgery. The resulting bone loss at the distal femur can be quantified by imaging techniques such as μCT, biomechanical testing of the peri-implant bone, and histomorphometry. The chronic inflammatory reaction can be quantified by analysis of femoral explant cultures and various histopathological techniques including identification of specific cell populations and their activation states by immunohistochemistry. Finally, systemic homing of macrophages and other cells to the area of inflammation can be quantified by utilizing luciferase labeled reporter macrophages that are injected into the circulation via the tail vein. Adding biologics to the pump with the particles allows the study of potential therapeutic effects of different locally infused treatments.

More recently, we have engaged 3 strategies to decrease particle associated bone destruction using our murine models (**Figure 3**). First, we have coated the distal femoral intramedullary rod with a mutant MCP-1 (MCP-1 is also

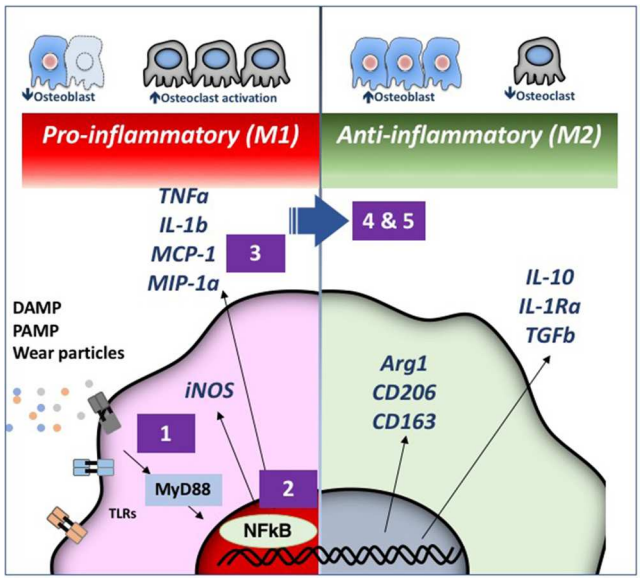

FIGURE 3 | Strategies for immunomodulation to mitigate periprosthetic osteolysis induced by wear particles. Wear particles and adherent pathogen-associated molecular patterns (PAMPs) and byproducts of cell death and tissue injury (damage-associated molecular patterns or DAMPS) can be recognized by Toll-like Receptors (TLRs) and other receptors on macrophages, which then activate downstream pathways including the key transcription factor Nuclear Factor-kappa B (NFκB). The induced pro-inflammatory responses driven by NFκB activation include the expression of inducible nitric oxide synthetase (iNOS) and cytokines/chemokines including Tumor Necrosis Factor alpha (TNFα), Interleukin 1 beta (IL-1b), Macrophage Chemotactic Protein 1 (MCP-1), Macrophage Inhibitory Protein 1 alpha (MIP-1α), and others. These events may lead to periprosthetic osteolysis due to reduced osteoblast and increased osteoclast activity. We have demonstrated that the particle-induced osteolysis can be mitigated by inhibiting (1) the TLR pathway; (2) NFκB activation; or (3) macrophage migration using a mutant MCP-1 called 7ND recombinant protein. Alternatively, pro-inflammatory macrophages (M1, **Left**) can be polarized by (4) Interleukin 4 (IL-4) treatment or (5) genetically modified or preconditioned mesenchymal stem cells (MSCs) (see **Figure 4** for details) into an anti-inflammatory, pro-tissue repair macrophage (M2) phenotype (**Right**). M2 macrophages are identified by their expression of Arginase 1 (Arg1) and the surface markers CD206 and CD163. M2 macrophages produce Interleukin 10 (IL-10), IL-1 receptor antagonist (IL-1ra), and Transforming Growth Factor beta (TGFβ). Myeloid Differentiation primary response 88 (MyD88) is a universal adapter protein that is downstream of nearly all TLRs (except TLR3), and leads to activation of NFκB.

referred to as CCL2) protein called 7ND recombinant protein via a layer-by-layer (LBL) technique to function as a drug eluting device to decrease macrophage trafficking locally (Keeney et al., 2013). Using microCT, immunohistochemical staining, and bioluminescence imaging, local delivery of 7ND protein via the LBL coating decreased systemic reporter macrophage recruitment to the particle infusion area, decreased the number of osteoclasts locally, and mitigated wear particle-induced bone loss in the distal femur (Nabeshima et al., 2017).

Our second strategy was to interfere with the master transcription factor NFκB, which regulates the expression of pro-inflammatory cytokines and chemokines of the innate immune system, and if persistently activated, leads to decreased bone formation and increased bone destruction. We have accomplished this downregulation of NFκB via local infusion of an NFκB decoy oligodeoxynucleotide (ODN), a synthesized duplex DNA that suppresses NFκB activity through competitive binding. We have confirmed the effectiveness of this strategy in *in vitro* studies, and *in vivo*, using the murine calvarial model and the femoral intramedullary particle infusion model (Lin et al., 2014, 2017a; Sato et al., 2015).

Our third strategy is to polarize local macrophages temporally, from an initial pro-inflammatory phenotype (also called M1) to an anti-inflammatory pro-regenerative (M2) phenotype. We accomplished this by exposing the M1 macrophages to interleukin-4, an anti-inflammatory cytokine. *In vitro* studies were first performed in co-culture of undifferentiated macrophages (M0), M1, or M2 together with pre-osteoblasts to determine the optimum time and concentration of cells and IL-4 to optimize bone formation. Polarizing M0 or M1 macrophages to M2 macrophages by the addition of IL-4 optimized matrix mineralization at 3 weeks, and osteocalcin and alkaline phosphatase expression, if the IL-4 was added after ∼72 h (Loi et al., 2016b; Córdova et al., 2017). Adding IL-4 earlier or continuously was less optimal. This finding substantiated the belief that a given period of inflammation and osteoprogenitor priming was necessary for optimizing bone formation (Gerstenfeld et al., 2003). After further *in vitro* validation, we subsequently showed that local delivery of IL-4 protein decreased the inflammatory response to particles, and increased net bone formation using the calvarial and the femoral intramedullary particle infusion models (Nich et al., 2013; Pajarinen et al., 2015, 2017b; Sato et al., 2016).

Thus, 3 local potentially translational strategies for modulation of the innate immune system in response to particle challenge were shown to mitigate the adverse inflammatory response and augment bone formation. Although, wear particle disease involves both local, and to some degree, systemic activation of innate immune processes, our group has focused on developing treatment options that are applied locally, directly to the site of the particle induced inflammation; this approach concentrates on altering the biological sequelae of particle disease directly at the source of the problem thereby limiting potential systemic toxicity of the treatments. These potential treatments might have a role in the early stages of osteolysis, when the prosthesis is still salvageable. This biologically based approach supplements ongoing innovations in material science and tribology of joint replacements.

MODULATION OF INFLAMMATION: RELEVANCE TO TISSUE ENGINEERING AND BONE HEALING

As stated previously, inflammation is the first stage of healing for all tissues. Interestingly, aging is associated with a state of ongoing low grade inflammation ("inflammaging"), and dysregulated macrophage polarization in response to potentially injurious stimuli (Mahbub et al., 2012; Gibon et al., 2016).

In other words, with aging, an injury does not always result in a measured coordinated inflammatory reaction with subsequent resolution and repair, but may develop into a chronic inflammatory state with ongoing tissue destruction. Furthermore, aging is associated with a general decrease in the response of both the adaptive and innate immune systems to adverse stimuli (Frasca and Blomberg, 2015). These facts may explain the delayed and/or insufficient healing in the elderly when subjected to traumatic injuries or other adverse stimuli including communicable diseases.

The immune system and the musculoskeletal systems are intimately co-dependent (Loi et al., 2016a). Crosstalk between macrophages and other hematopoietic cells, and MSC lineage cells is important to hematopoiesis, immunomodulation, and the resolution of inflammation, as well as the healing and repair of musculoskeletal tissues (Maggini et al., 2010; Mountziaris et al., 2011; Guihard et al., 2012; Mantovani et al., 2013; Wu et al., 2013; Vi et al., 2015; Loi et al., 2016b). We and others have shown that continuous crosstalk between macrophages and MSC lineage cells are critical to bone healing (Mountziaris et al., 2011; Omar et al., 2011; Vi et al., 2015; Loi et al., 2016b). In addition, with aging, osteogenesis by MSC lineage cells is depressed; these effects have been shown by our group to be associated with ongoing upregulated NFκB activity by aged MSCs (Lin T. H. et al., 2017). Thus, one potential approach to facilitating bone healing in the elderly might be local/regional modulation of NFκB activity in macrophages, directly or indirectly. This approach has been alluded to above.

Two additional approaches to immunomodulation by altering MSCs to improve bone healing in inflammatory clinical scenarios have been explored by our group (**Figure 4**). These approaches are potentially relevant to bone repair in the young and aged alike.

The first approach includes preconditioning the MSCs prior to their use, mimicking the inflammatory environment to which the MSCs are exposed when they first enter the area of tissue damage and regeneration. Other laboratories have demonstrated that preconditioning of MSCs by exposing them to inflammatory cytokines including interferon gamma (INFγ) and TNFα synergistically enhances their immunomodulatory properties by suppressing the activation of T cells (Ren et al., 2008; François et al., 2012). We developed a novel method of preconditioning of MSCs for bone healing applications, using a combination of lipopolysaccharide (LPS- a constituent found in the cell wall of gram negative bacteria) together with TNFα (Lin et al., 2017b). When these preconditioned MSCs (pMSCS) were co-cultured with macrophages, the macrophages polarized from an M1 to an M2 phenotype and were associated with increased osteogenic differentiation of the MSCs, and greater alkaline phosphatase expression and matrix mineralization. Given the fact that inflammation is often part of recalcitrant bone infections, non-union of fractures, periprosthetic osteolysis, osteonecrosis, and other diseases of bone, preconditioning of MSCs may have a direct translational application in the healing of acute and chronic bone defects. Furthermore, the preconditioning protocol developed in our laboratory may prove useful for immunomodulation of other systemic inflammatory disorders such as sepsis, rejection of solid organ transplants etc. in which MSCs are infused.

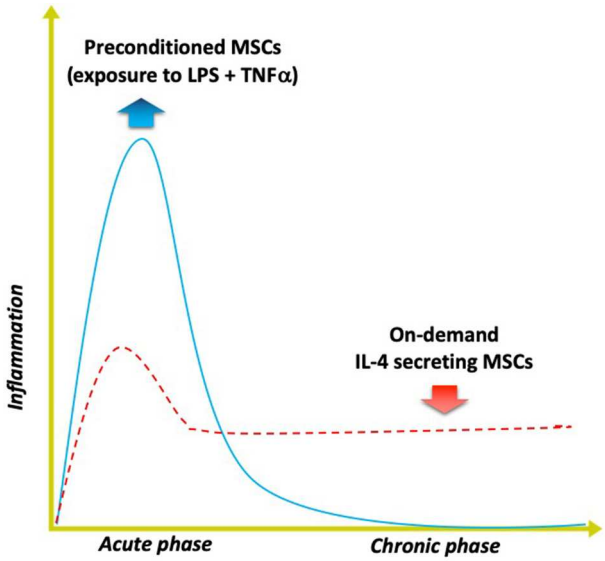

FIGURE 4 | Modulating inflammation with specialized MSCs to enhance bone formation. Optimal bone regeneration is mediated by a transient acute inflammatory reaction (for several days), followed by the resolution of inflammation and the tissue repair phase (blue solid line). Impairment or dysregulation of the acute inflammatory phase may lead to unresolved chronic inflammation and subsequent delayed bone healing (red dashed line). The strategy of using MSCs preconditioned by exposure to both lipopolysaccharide (LPS) plus TNFα *ex vivo* mimics the acute phase response and enhances the MSCs' osteogenic and immunomodulating abilities. Alternatively, genetically modified MSCs that first sense NFkB activation then over-express IL-4 secretion ("on demand") can respond to unresolved chronic inflammation by modulating the local conditions into the desired anti-inflammatory, tissue repair environment for improved bone healing.

The second approach encompasses genetic modification of MSCs to over-express the immune-modulating pro-regenerative cytokine IL-4. We have developed 2 constructs to accomplish this goal. In one construct, overexpression of IL-4 by MSCs is continuous; in the other construct, IL-4 is only overexpressed by MSCs when NFκB activity is first sensed as upregulated (Lin et al., 2017c). In the latter construct, when NFκB activity diminishes, the excess production of IL-4 is stopped. Thus, when an inflammatory stimulus is encountered, these genetically modified MSCs (GM-MSCs) can secrete increased amounts of IL-4, subsequently polarizing M1 macrophages (in the vicinity) to an M2 phenotype. Because acute traumatic conditions or adverse stimuli require an initial pro-inflammatory environment to precondition or license the local MSCs for bone healing or other immunomodulatory functions, the IL-4 secreting MSCs would be most useful several days after acute injury, or in chronic inflammatory conditions. The advantage of the NFκB sensing IL-4 overexpressing MSCs is that the delivery of IL-4 could be temporally and spatially tailored to an ever changing inflammatory and immune environment, i.e., be context dependent.

DISCUSSION

Acute and chronic inflammation are biological processes within the immune system that are integral to the sustenance of life for all organisms. In humans, the innate and adaptive immune systems are highly developed. The former (innate immunity) responds to injury or adverse stimuli in a pre-determined, non-specific manner that is generally dependent on the interaction of cells with chemical motifs that comprise the adverse stimulus. The latter (adaptive immunity) is dependent on the interaction of specific receptors on cells (antigen presenting cells as well as T and B lymphocytes) with a more specific antigenic stimulus. Previously it was thought that only the adaptive immune system had the potential for memory of a previously encountered stimulus challenge; it is now recognized that the innate immune system has a mechanism that "remembers" previous interactions (Italiani and Boraschi, 2017). With subsequent challenges by the same or similar stimuli, monocytes/macrophages can increase ("trained immunity") or decrease ("tolerance") the production of cytokines, chemokines, and other substances to effectively deal with a potentially injurious event (Dobrovolskaia and Vogel, 2002). This non-specific innate immune memory can last for months and allows monocytes/macrophages to modulate their functional state according to the persistence of the adverse stimulus. This innate immune memory optimizes survival of the organism by facilitating a relatively speedy and enhanced reaction to potentially harmful stimuli, but also allows a measured defensive response that does not consume the organism (Medzhitov et al., 2012). We are currently exploring these concepts, but much work remains in this paradigm-changing research. For example, it may be possible to create implants that release specific substances based on local contextual cues (e.g., the presence of bacterial ligands or excessive amounts of wear debris); these released substances would then precondition local MSCs or other cells to undertake specific immunomodulatory activities.

How are the above concepts related to wear particle disease? Wear particles are continuously produced by orthopedic implants with repeated usage. In general, debris from commonly used polymers, ceramics and metals in orthopedics provoke an innate immune response; in some cases, protein-metallic byproducts can also act as haptens, thereby stimulating the adaptive immune system as well. Thus, the biological reaction to wear particles from orthopedic implants can function as a paradigm for exploring the mechanisms associated both with acute and chronic inflammation and activation of the immune system using relevant *in vitro* and *in vivo* models. Once these biological processes are elucidated, it may be possible to (a) optimize the composition and design of biomaterials and implants, and (b) modulate tissue-implant responses to facilitate integration of the device or otherwise improve its function *in vivo* in the short and long terms. For joint replacements specifically, these concepts can be translated from bench to beside. For example, implants could be coated with biological substances to facilitate and even expedite initial osseointegration and promote early physiological loading, thus providing pathways for earlier return to function. Methods to mitigate infection, one of the leading causes of implant failure, need to be addressed. This might be accomplished using newer fabrication (for example 3D printing) and coating techniques; alternatively, the periprosthetic environment could be manipulated immunologically to minimize bacterial colonization and expansion. The techniques above to enhance osseointegration and prevent infection could be combined with novel methods to interrogate and sense the periprosthetic environment and then release specific diagnostic and therapeutic agents on demand. These and other interventions would require extensive *in vitro* and *in vivo* testing using relevant animal models. Many of the immune modulating interventions discussed above have only been delivered in the short term. Longer term studies outlining strategies for resolving inflammation at an appropriate time point, without local or systemic adverse effects are needed. Furthermore, novel strategies are needed to address continuous particle production and chronic inflammation over many decades, and potential methods to facilitate particle clearance. Indeed, continuous long-term immunomodulation may have deleterious effects to the host. Thus, solutions will undoubtedly entail better methods of diagnosis of particle-associated inflammation including potential biomarkers that are more sensitive than conventional radiographs, computed tomography, or MRI. In this way, biological interventions could be delivered intermittently at timepoints of higher particle loads and inflammatory responses.

An understanding of the constant interactions among cells of the monocyte-macrophage-osteoclast lineage and the MSC-osteoblast lineage also is critical to tissue engineering of bone. Indeed, the processes of inflammation and bone and soft tissue healing are so intertwined, that impairment of one process impacts the other (Guihard et al., 2012; Mantovani et al., 2013; Loi et al., 2016a,b). Thus, there are significant opportunities for modulating inflammation to obtain a desired outcome for bone healing and regeneration (Mountziaris et al., 2011).

By studying wear particle disease and related pathologies of bone, our group and others have begun to understand the cellular and molecular processes associated with inflammation and activation of the innate immune system and in particular, their role in the formation and destruction of bone. This understanding has led to the design of innovative *in vitro* and *in vivo* models to simulate the activities of the innate immune system and develop potential local treatments to mitigate injurious stimuli and facilitate bone maintenance and repair. As the crosstalk between the innate immune system and MSCs is so critical to bone and soft tissue modeling, investigating ways to optimize their communications has been a continued focus of our current investigations.

On a broader level, innate immune processes and interaction with MSCs are part of a much larger domain. Innate immune cells and MSCs play a major role in the regulation and repair of all cells in the body. Thus, concepts such as modulation of local and systemic cell trafficking, NFκB activity and macrophage polarization provide potential biological strategies for improved clinical outcomes in a variety of diseases that affect virtually every organ system in the body. Thus, from our initial intentions of developing concepts and methods to

better understand wear particle disease, our research goals have broadened significantly in order to elucidate and design novel systems for tissue engineering and regenerative medicine. It is hoped that continued research will not only improve the outcome of current and future joint replacements, but provide tangible, evidence-based translational strategies for improving the healing and repair of other organ systems in the body.

AUTHOR CONTRIBUTIONS

All authors contributed to the initial concepts, experimental design and methodology, analysis of results and writing of the present manuscript.

ACKNOWLEDGMENTS

The authors gratefully acknowledge the work of many undergraduate, graduate, postdoctoral, and medical students, as well as numerous other collaborators who contributed their time, effort, and resources in support of the experiments carried out in our laboratory. The authors also acknowledge the generous support of the National Institute of Arthritis and Musculoskeletal and Skin Diseases of the National Institute of Health, Grant No. R01AR055650, R01AR063717, R01AR073145, R01AR072613 and the Ellenburg Chair in Surgery, and the Stanford University Medical Scholars Research Grant.

REFERENCES

Akira, S., and Takeda, K. (2004). Toll-like receptor signalling. *Nat. Rev. Immunol.* 4, 499–511. doi: 10.1038/nri1391

Aspenberg, P., and Herbertsson, P. (1996). Periprosthetic bone resorption. Particles versus movement. *J. Bone Joint Surg.* 78, 641–646. doi: 10.1302/0301-620X.78B4.0780641

Aspenberg, P., and Van der Vis, H. (1998). Migration, particles, and fluid pressure. A discussion of causes of prosthetic loosening. *Clin. Orthop. Relat. Res.* 352, 75–80. doi: 10.1097/00003086-199807000-00010

Atkins, G. J., Welldon, K. J., Holding, C. A., Haynes, D. R., Howie, D. W., and Findlay, D. M. (2009). The induction of a catabolic phenotype in human primary osteoblasts and osteocytes by polyethylene particles. *Biomaterials* 30, 3672–3681. doi: 10.1016/j.biomaterials.2009.03.035

Baumann, B., Seufert, J., Jakob, F., Nöth, U., Rolf, O., Eulert, J., et al. (2005). Activation of NF-kappaB signalling and TNFalpha-expression in THP-1 macrophages by TiAlV- and polyethylene-wear particles. *J. Orthop. Res.* 23, 1241–1248. doi: 10.1016/j.orthres.2005.02.017.11002 30602

Bi, Y., Collier, T. O., Goldberg, V. M., Anderson, J. M., and Greenfield, E. M. (2002). Adherent endotoxin mediates biological responses of titanium particles without stimulating their phagocytosis. *J. Orthop. Res.* 20, 696–703. doi: 10.1016/S0736-0266(01)00176-0

Bi, Y., Seabold, J. M., Kaar, S. G., Ragab, A. A., Goldberg, V. M., Anderson, J. M., et al. (2001). Adherent endotoxin on orthopedic wear particles stimulates cytokine production and osteoclast differentiation. *J. Bone Miner. Res.* 16, 2082–2091. doi: 10.1359/jbmr.2001.16.11.2082

Caicedo, M. S., Desai, R., McAllister, K., Reddy, A., Jacobs, J. J., and Hallab, N. J. (2008). Soluble and particulate Co-Cr-Mo alloy implant metals activate the inflammasome danger signaling pathway in human macrophages: a novel mechanism for implant debris reactivity. *J. Orthop. Res.* 27, 847–854.doi: 10.1002/jor.20826

Campbell, P., Ma, S., Yeom, B., McKellop, H., Schmalzried, T. P., and Amstutz, H. C. (1995). Isolation of predominantly submicron-sized UHMWPE wear particles from periprosthetic tissues. *J. Biomed. Mater. Res. A* 29, 127–131. doi: 10.1002/jbm.820290118

Chen, G. Y., and Nuñez, G. (2010). Sterile inflammation: sensing and reacting to damage. *Nat. Rev. Immunol.* 10, 826–837. doi: 10.1038/nri2873

Chiu, R., Ma, T., Smith, R. L., and Goodman, S. B. (2006). Polymethylmethacrylate particles inhibit osteoblastic differentiation of bone marrow osteoprogenitor cells. *J. Biomed. Mater. Res. A* 77, 850–856. doi: 10.1002/jbm.a.30697

Chiu, R., Ma, T., Smith, R. L., and Goodman, S. B. (2009). Ultrahigh molecular weight polyethylene wear debris inhibits osteoprogenitor proliferation and differentiation *in vitro*. *J. Biomed. Mater. Res. A* 89, 242–247. doi: 10.1002/jbm.a.32001

Cho, D. R., Shanbhag, A. S., Hong, C. Y., Baran, G. R., and Goldring, S. R. (2002). The role of adsorbed endotoxin in particle-induced stimulation of cytokine release. *J. Orthop. Res.* 20, 704–713. doi: 10.1016/S0736-0266(01)00179-6

Choi, M. G., Koh, H. S., Kluess, D., O'Connor, D., Mathur, A., Truskey, G. A., et al. (2005). Effects of titanium particle size on osteoblast functions *in vitro* and *in vivo*. *Proc. Natl. Acad. Sci. U.S.A.* 102, 4578–4583. doi: 10.1073/pnas.0500693102

Clohisy, J. C., Hirayama, T., Frazier, E., Han, S. K., and Abu-Amer, Y. (2004). NF-kB signaling blockade abolishes implant particle-induced osteoclastogenesis. *J. Orthop. Res.* 22, 13–20. doi: 10.1016/S0736-0266(03)00156-6

Córdova, L. A., Loi, F., Lin, T. H., Gibon, E., Pajarinen, J., Nabeshima, A., et al. (2017). CCL2, CCL5, and IGF-1 participate in the immunomodulation of osteogenesis during M1/M2 transition *in vitro*. *J. Biomed. Mater. Res. A* 105, 3069–3076. doi: 10.1002/jbm.a.36166

Cordova, L. A., Stresing, V., Gobin, B., Rosset, P., Passuti, N., Gouin, F., et al. (2014). Orthopaedic implant failure: aseptic implant loosening–the contribution and future challenges of mouse models in translational research. *Clin. Sci.* 127, 277–293. doi: 10.1042/CS20130338

Dobrovolskaia, M. A., and Vogel, S. N. (2002). Toll receptors, CD14, and macrophage activation and deactivation by LPS. *Microbes Infect.* 4, 903–914. doi: 10.1016/S1286-4579(02)01613-1

Epstein, N. J., Bragg, W. E., Ma, T., Spanogle, J., Smith, R. L., and Goodman, S. B. (2005a). UHMWPE wear debris upregulates mononuclear cell proinflammatory gene expression in a novel murine model of intramedullary particle disease. *Acta Orthop.* 76, 412–420. doi: 10.1080/17453670510041321

Epstein, N. J., Warme, B. A., Spanogle, J., Ma, T., Bragg, B., Smith, R. L., et al. (2005b). Interleukin-1 modulates periprosthetic tissue formation in an intramedullary model of particle-induced inflammation. *J. Orthop. Res.* 23, 501–510. doi: 10.1016/j.orthres.2004.10.004

François, M., Romieu-Mourez, R., Li, M., and Galipeau, J. (2012). Human MSC suppression correlates with cytokine induction of indoleamine 2,3-dioxygenase and bystander M2 macrophage differentiation. *Mol. Ther.* 20, 187–195. doi: 10.1038/mt.2011.189

Frasca, D., and Blomberg, B. B. (2015). Inflammaging decreases adaptive and innate immune responses in mice and humans. *Biogerontology* 17, 7–19. doi: 10.1007/s10522-015-9578-8

Fritton, K., Ren, P. G., Gibon, E., Rao, A. J., Ma, T., Biswal, S., et al. (2012). Exogenous MC3T3 preosteoblasts migrate systemically and mitigate the adverse effects of wear particles. *Tissue Eng. Part A* 18, 2559–2567. doi: 10.1089/ten.tea.2012.0086

Fujiwara, N., and Kobayashi, K. (2005). Macrophages in inflammation. *Curr. Drug Targets* 4, 281–286. doi: 10.2174/1568010054022024

Gallo, J., Goodman, S. B., Konttinen, Y. T., and Raska, M. (2013). Particle disease: biologic mechanisms of periprosthetic osteolysis in total hip arthroplasty. *Innate Immun.* 19, 213–224. doi: 10.1177/1753425912451779

Gerstenfeld, L. C., Cho, T. J., Kon, T., Aizawa, T., Tsay, A., Fitch, J., et al. (2003). Impaired fracture healing in the absence of TNF-alpha signaling: the role of TNF-alpha in endochondral cartilage resorption. *J. Bone Miner. Res.* 18, 1584–1592. doi: 10.1359/jbmr.2003.18.9.1584

Gibon, E., Loi, F., Córdova, L. A., Pajarinen, J., Lin, T., Lu, L., et al. (2016). Aging affects bone marrow macrophage polarization: relevance to bone healing. *Regen. Eng. Transl. Med.* 2, 98–104. doi: 10.1007/s40883-016-0016-5

Gibon, E., Ma, T., Ren, P. G., Fritton, K., Biswal, S., Yao, Z., et al. (2012a). Selective inhibition of the MCP-1-CCR2 ligand-receptor axis decreases systemic trafficking of macrophages in the presence of UHMWPE particles. *J. Orthop. Res.* 30, 547–553. doi: 10.1002/jor.21548

Gibon, E., Yao, Z., Rao, A. J., Zwingenberger, S., Batke, B., Valladares, R., et al. (2012b). Effect of a CCR1 receptor antagonist on systemic trafficking of MSCs and polyethylene particle-associated bone loss. *Biomaterials* 33, 3632–3638. doi: 10.1016/j.biomaterials.2012.02.003

González, O., Smith, R. L., and Goodman, S. B. (1996). Effect of size, concentration, surface area, and volume of polymethylmethacrylate particles on human macrophages *in vitro*. *J. Biomed. Mater. Res. A* 30, 463–473. doi: 10.1002/(SICI)1097-4636(199604)30:4<463::AID-JBM4>3.0.CO;2-N

Goodman, S. B. (1994). The effects of micromotion and particulate materials on tissue differentiation. Bone chamber studies in rabbits. *Acta Orthop. Scand.* 258, 1–43. doi: 10.3109/17453679409155227

Goodman, S. B. (2007). Wear particles, periprosthetic osteolysis and the immune system. *Biomaterials* 28, 5044–5048. doi: 10.1016/j.biomaterials.2007.06.035

Goodman, S. B., Gómez Barrena, E., Takagi, M., and Konttinen, Y. T. (2009). Biocompatibility of total joint replacements: a review. *J. Biomed. Mater. Res. A* 90, 603–618. doi: 10.1002/jbm.a.32063

Goodman, S. B., Huie, P., Song, Y., Schurman, D., Maloney, W., Woolson, S., et al. (1998). Cellular profile and cytokine production at prosthetic interfaces. Study of tissues retrieved from revised hip and knee replacements. *J. Bone Joint Surg.* 80, 531–539. doi: 10.1302/0301-620X.80B3.0800531

Goodman, S. B., and Ma, T. (2010). Cellular chemotaxis induced by wear particles from joint replacements. *Biomaterials* 31, 5045–5050. doi: 10.1016/j.biomaterials.2010.03.046

Goodman, S. B., Ma, T., Chiu, R., Ramachandran, R., and Smith, R. L. (2006). Effects of orthopaedic wear particles on osteoprogenitor cells. *Biomaterials* 27, 6096–6101. doi: 10.1016/j.biomaterials.2006.08.023

Goodman, S. B., Magee, F. P., and Fornasier, V. L. (1993). Radiological and histological study of aseptic loosening using a cemented tibial hemiarthroplasty in the rabbit knee. *Biomaterials* 14, 522–528. doi: 10.1016/0142-9612(93)90241-S

Goodman, S. B., Song, Y., Chun, L., Regula, D., and Aspenberg, P. (1999). Effects of TGFbeta on bone ingrowth in the presence of polyethylene particles. *J. Bone Joint Surg.* 81, 1069–1075. doi: 10.1302/0301-620X.81B6.0811069

Green, T. R., Fisher, J., Matthews, J. B., Stone, M. H., and Ingham, E. (2000). Effect of size and dose on bone resorption activity of macrophages by *in vitro* clinically relevant ultra high molecular weight polyethylene particles. *J. Biomed. Mater. Res. A* 53, 490–497. doi: 10.1002/1097-4636(200009)53:5and<490::AID-JBM7and>3.0.CO;2-7

Green, T. R., Fisher, J., Stone, M., Wroblewski, B. M., and Ingham, E. (1998). Polyethylene particles of a 'critical size' are necessary for the induction of cytokines by macrophages *in vitro*. *Biomaterials* 19, 2297–2302. doi: 10.1016/S0142-9612(98)00140-9

Greenfield, E. M., and Bechtold, J. (2008). What other biologic and mechanical factors might contribute to osteolysis? *J. Am. Acad. Orthop. Surg.*16 (Suppl. 1), S56–62. doi: 10.5435/00124635-200800001-00012

Guihard, P., Danger, Y., Brounais, B., David, E., Brion, R., Delecrin, J., et al. (2012). Induction of osteogenesis in mesenchymal stem cells by activated monocytes/macrophages depends on oncostatin M signaling. *Stem Cells* 30, 762–772. doi: 10.1002/stem.1040

Hallab, N. J., and Jacobs, J. J. (2017). Chemokines associated with pathologic responses to orthopedic implant debris. *Front. Endocrinol.* 8:5. doi: 10.3389/fendo.2017.00005

Hallab, N. J., Mikecz, K., Vermes, C., Skipor, A., and Jacobs, J. J. (2001). Differential lymphocyte reactivity to serum-derived metal-protein complexes produced from cobalt-based and titanium-based implant alloy degradation. *J. Biomed. Mater. Res. A* 56, 427–436. doi: 10.1002/1097-4636(20010905)56:3<427::AID-JBM1112>3.0.CO;2-E

Haynes, D. R., Crotti, T. N., Potter, A. E., Loric, M., Atkins, G. J., Howie, D. W., et al. (2001). The osteoclastogenic molecules RANKL and RANK are associated with periprosthetic osteolysis. *J. Bone Joint Surg.* 83, 902–911. doi: 10.1302/0301-620X.83B6.0830902

Haynes, D. R., Rogers, S. D., Hay, S., Pearcy, M. J., and Howie, D. W. (1993). The differences in toxicity and release of bone-resorbing mediators induced by titanium and cobalt-chromium-alloy wear particles. *J. Bone Joint Surg.* 75, 825–834. doi: 10.2106/00004623-199306000-00004

Italiani, P., and Boraschi, D. (2017). Induction of innate immune memory by engineered nanoparticles: a hypothesis that may become true. *Front. Immunol.* 8:734. doi: 10.3389/fimmu.2017.00734

Jacobs, J. J., Roebuck, K. A., Archibeck, M., Hallab, N. J., and Glant, T. T. (2001). Osteolysis: basic science. *Clin. Orthop. Relat. Res.* 393, 71–7. doi: 10.1097/00003086-200112000-00008

Kadoya, Y., Revell, P. A., Al-Saffar, N., Kobayashi, A., Scott, G., and Freeman, M. A. (1996). Bone formation and bone resorption in failed total joint arthroplasties: histomorphometric analysis with histochemical and immunohistochemical technique. *J. Orthop. Res.* 14, 473–482. doi: 10.1002/jor.1100140318

Karnes, J. M., Daffner, S. D., and Watkins, C. M. (2015). Multiple roles of tumor necrosis factor-alpha in fracture healing. *Bone* 78, 87–93. doi: 10.1016/j.bone.2015.05.001

Kaufman, A. M., Alabre, C. I., Rubash, H. E., and Shanbhag, A. S. (2008). Human macrophage response to UHMWPE, TiAlV, CoCr, and alumina particles: analysis of multiple cytokines using protein arrays. *J. Biomed. Mater. Res. A* 84, 464–474. doi: 10.1002/jbm.a.31467

Kaur, S., Raggatt, L. J., Batoon, L., Hume, D. A., Levesque, J. P., and Pettit, A. R. (2017). Role of bone marrow macrophages in controlling homeostasis and repair in bone and bone marrow niches. *Semin. Cell Dev. Biol.* 61, 12–21. doi: 10.1016/j.semcdb.2016.08.009

Kawai, T., and Akira, S. (2010). The role of pattern-recognition receptors in innate immunity: update on Toll-like receptors. *Nat. Immunol.* 11, 373–384. doi: 10.1038/ni.1863

Keeney, M., Waters, H., Barcay, K., Jiang, X., Yao, Z., Pajarinen, J., et al. (2013). Mutant MCP-1 protein delivery from layer-by-layer coatings on orthopedic implants to modulate inflammatory response. *Biomaterials* 34, 10287–10295. doi: 10.1016/j.biomaterials.2013.09.028

Kumagai, K., Vasanji, A., Drazba, J. A., Butler, R. S., and Muschler, G. F. (2008). Circulating cells with osteogenic potential are physiologically mobilized into the fracture healing site in the parabiotic mice model. *J. Orthop. Res.* 26, 165–175. doi: 10.1002/jor.20477

Landgraeber, S., Jäger, M., Jacobs, J. J., and Hallab, N. J. (2014). The pathology of orthopedic implant failure is mediated by innate immune system cytokines. *Mediat. Inflamm.* 2014:185150. doi: 10.1155/2014/185150

Lin, T., Pajarinen, J., Nabeshima, A., Córdova, L. A., Loi, F., Gibon, E., et al. (2017a). Orthopaedic wear particle-induced bone loss and exogenous macrophage infiltration is mitigated by local infusion of NF-kappaB decoy oligodeoxynucleotide. *J. Biomed. Mater. Res. A* 105, 3169–3175. doi: 10.1002/jbm.a.36169

Lin, T., Pajarinen, J., Nabeshima, A., Lu, L., Nathan, K., Jämsen, E., et al. (2017b). Preconditioning of murine mesenchymal stem cells synergistically enhanced immunomodulation and osteogenesis. *Stem Cell Res. Ther.* 8:277. doi: 10.1186/s13287-017-0730-z

Lin, T., Pajarinen, J., Nabeshima, A., Lu, L., Nathan, K., Yao, Z., et al. (2017c). Establishment of NF-kappaB sensing and interleukin-4 secreting mesenchymal stromal cells as an "on-demand" drug delivery system to modulate inflammation. *Cytotherapy* 19, 1025–1034. doi: 10.1016/j.jcyt.2017.06.008

Lin, T. H., Gibon, E., Loi, F., Pajarinen, J., Córdova, L. A., Nabeshima, A., et al. (2017). Decreased osteogenesis in mesenchymal stem cells derived from the aged mouse is associated with enhanced NF-kappaB activity. *J. Orthop. Res.* 35, 281–288. doi: 10.1002/jor.23270

Lin, T. H., Yao, Z., Sato, T., Keeney, M., Li, C., Pajarinen, J., et al. (2014). Suppression of wear-particle-induced pro-inflammatory cytokine and chemokine production in macrophages via NF-kappaB decoy oligodeoxynucleotide: a preliminary report. *Acta Biomater.* 10, 3747–3755. doi: 10.1016/j.actbio.2014.04.034

Lind, M. S., Song, Y., Goodman, S. B. (1998). "Animal models for investigation of biomaterial debris," in *Animal Models in Orthopedic Research*, eds Y. H. An and R. J. Freidman (Boca Raton: CRC Press), 427–441.

Loi, F., Córdova, L. A., Pajarinen, J., Lin, T. H., Yao, Z., and Goodman, S. B. (2016a). Inflammation, fracture and bone repair. *Bone* 86, 119–130. doi: 10.1016/j.bone.2016.02.020

Loi, F., Córdova, L. A., Zhang, R., Pajarinen, J., Lin, T. H., Goodman, S. B., et al. (2016b). The effects of immunomodulation by macrophage subsets on osteogenesis *in vitro*. *Stem Cell Res. Ther.* 7:15. doi: 10.1186/s13287-016-0276-5

Maggini, J., Mirkin, G., Bognanni, I., Holmberg, J., Piazzón, I. M., Nepomnaschy, I., et al. (2010). Mouse bone marrow-derived mesenchymal stromal cells turn activated macrophages into a regulatory-like profile. *PLoS ONE*. 5:e9252. doi: 10.1371/journal.pone.0009252

Mahbub, S., Deburghgraeve, C. R., and Kovacs, E. J. (2012). Advanced age impairs macrophage polarization. *J. Interferon Cytokine Res*. 32, 18–26. doi: 10.1089/jir.2011.0058

Mantovani, A., Biswas, S. K., Galdiero, M. R., Sica, A., and Locati, M. (2013). Macrophage plasticity and polarization in tissue repair and remodelling. *J. Pathol*. 229, 176–185. doi: 10.1002/path.4133

Marsell, R., and Einhorn, T. A. (2011). The biology of fracture healing. *Injury* 42, 551–555. doi: 10.1016/j.injury.2011.03.031

Medzhitov, R. (2008). Origin and physiological roles of inflammation. *Nature* 454, 428–435. doi: 10.1038/nature07201

Medzhitov, R., Schneider, D. S., and Soares, M. P. (2012). Disease tolerance as a defense strategy. *Science* 335, 936–941. doi: 10.1126/science.1214935

Moran, M. M., Wilson, B. M., Ross, R. D., Virdi, A. S., and Sumner, D. R. (2017). Arthrotomy-based preclinical models of particle-induced osteolysis: a systematic review. *J. Orthop. Res.* 35, 2595–2605. doi: 10.1002/jor.23619

Mosser, D. M., and Edwards, J. P. (2008). Exploring the full spectrum of macrophage activation. *Nat. Rev. Immunol.* 8, 958–969. doi: 10.1038/nri2448

Mountziaris, P. M., Spicer, P. P., Kasper, F. K., and Mikos, A. G. (2011). Harnessing and modulating inflammation in strategies for bone regeneration. *Tissue Eng. Part B Rev*. 17, 393–402. doi: 10.1089/ten.teb.2011.0182

Nabeshima, A., Pajarinen, J., Lin, T. H., Jiang, X., Gibon, E., Córdova, L. A., et al. (2017). Mutant CCL2 protein coating mitigates wear particle-induced bone loss in a murine continuous polyethylene infusion model. *Biomaterials* 117, 1–9. doi: 10.1016/j.biomaterials.2016.11.039

Nakashima, Y., Sun, D. H., Trindade, M. C., Maloney, W. J., Goodman, S. B., Schurman, D. J., et al. (1999). Signaling pathways for tumor necrosis factor-alpha and interleukin-6 expression in human macrophages exposed to titanium-alloy particulate debris *in vitro*. *J. Bone Joint Surg.* 81, 603–615. doi: 10.2106/00004623-199905000-00002

Nich, C., Takakubo, Y., Pajarinen, J., Ainola, M., Salem, A., Sillat, T., et al. (2013). Macrophages-key cells in the response to wear debris from joint replacements. *J. Biomed. Mater. Res. A* 101, 3033–3045. doi: 10.1002/jbm.a.34599

Nich, C., Takakubo, Y., Pajarinen, J., Gallo, J., Konttinen, Y. T., Takagi, M., et al. (2016). The role of macrophages in the biological reaction to wear debris from artificial joints. *J. Long Term Eff. Med. Implants* 26, 303–309. doi: 10.1615/JLongTermEffMedImplants.2017011287

Omar, O. M., Granéli, C., Ekström, K., Karlsson, C., Johansson, A., Lausmaa, J., et al. (2011). The stimulation of an osteogenic response by classical monocyte activation. *Biomaterials* 32, 8190–8204. doi: 10.1016/j.biomaterials.2011.07.055

Ortiz, S. G., Ma, T., Epstein, N. J., Smith, R. L., and Goodman, S. B. (2008a). Validation and quantification of an *in vitro* model of continuous infusion of submicron-sized particles. *J. Biomed. Mater. Res. B Appl. Biomater*. 84, 328–333. doi: 10.1002/jbm.b.30875

Ortiz, S. G., Ma, T., Regula, D., Smith, R. L., and Goodman, S. B. (2008b). Continuous intramedullary polymer particle infusion using a murine femoral explant model. *J. Biomed. Mater. Res. B Appl. Biomater*. 87, 440–446. doi: 10.1002/jbm.b.31122

Pajarinen, J., Lin, T. H., Nabeshima, A., Jämsen, E., Lu, L., Nathan, K., et al. (2017a). Mesenchymal stem cells in the aseptic loosening of total joint replacements. *J. Biomed. Mater. Res. A* 105, 1195–1207. doi: 10.1002/jbm.a.35978

Pajarinen, J., Nabeshima, A., Lin, T. H., Sato, T., Gibon, E., Jämsen, E., et al. (2017b). Murine model of progressive orthopedic wear particle-induced chronic inflammation and osteolysis. *Tissue Eng. Part C Methods* 23, 1003–1011. doi: 10.1089/ten.tec.2017.0166

Pajarinen, J., Tamaki, Y., Antonios, J. K., Lin, T. H., Sato, T., Yao, Z., et al. (2015). Modulation of mouse macrophage polarization *in vitro* using IL-4 delivery by osmotic pumps. *J. Biomed. Mater. Res. A* 103, 1339–1345. doi: 10.1002/jbm.a.35278

Patterson, T. E., Kumagai, K., Griffith, L., and Muschler, G. F. (2008). Cellular strategies for enhancement of fracture repair. *J. Bone Joint Surg.* 90 (Suppl. 1), 111–119. doi: 10.2106/JBJS.G.01572

Pearl, J. I., Ma, T., Irani, A. R., Huang, Z., Robinson, W. H., Smith, R. L., et al. (2011). Role of the Toll-like receptor pathway in the recognition of orthopedic implant wear-debris particles. *Biomaterials* 32, 5535–5542. doi: 10.1016/j.biomaterials.2011.04.046

Purdue, P. E., Koulouvaris, P., Potter, H. G., Nestor, B. J., and Sculco, T. P. (2007). The cellular and molecular biology of periprosthetic osteolysis. *Clin. Orthop. Relat. Res.* 454, 251–261. doi: 10.1097/01.blo.0000238813.95035.1b

Ramachandran, R., Goodman, S. B., and Smith, R. L. (2006). The effects of titanium and polymethylmethacrylate particles on osteoblast phenotypic stability. *J. Biomed. Mater. Res. A* 77, 512–517. doi: 10.1002/jbm.a.30649

Ren, G., Zhang, L., Zhao, X., Xu, G., Zhang, Y., Roberts, A. I., et al. (2008). Mesenchymal stem cell-mediated immunosuppression occurs via concerted action of chemokines and nitric oxide. *Cell Stem Cell* 2, 141–150. doi: 10.1016/j.stem.2007.11.014

Ren, P. G., Huang, Z., Ma, T., Biswal, S., Smith, R. L., and Goodman, S. B. (2010). Surveillance of systemic trafficking of macrophages induced by UHMWPE particles in nude mice by noninvasive imaging. *J. Biomed. Mater. Res. A* 94, 706–711. doi: 10.1002/jbm.a.32744

Ren, W., Li, X. H., Chen, B. D., and Wooley, P. H. (2004). Erythromycin inhibits wear debris-induced osteoclastogenesis by modulation of murine macrophage NF-kappaB activity. *J. Orthop. Res.* 22, 21–29. doi: 10.1016/S0736-0266(03)00130-X

Sacomen, D., Smith, R. L., Song, Y., Fornasier, V., and Goodman, S. B. (1998). Effects of polyethylene particles on tissue surrounding knee arthroplasties in rabbits. *J. Biomed. Mater. Res. A* 43, 123–130. doi: 10.1002/(sici)1097-4636(199822)43:2<123::aid-jbm6>3.0.co;2-q

Sato, T., Pajarinen, J., Behn, A., Jiang, X., Lin, T. H., Loi, F., et al. (2016). The effect of local IL-4 delivery or CCL2 blockade on implant fixation and bone structural properties in a mouse model of wear particle induced osteolysis. *J. Biomed. Mater. Res. A* 104, 2255–2262. doi: 10.1002/jbm.a.35759

Sato, T., Pajarinen, J., Lin, T. H., Tamaki, Y., Loi, F., Egashira, K., et al. (2015). NF-kappaB decoy oligodeoxynucleotide inhibits wear particle-induced inflammation in a murine calvarial model. *J. Biomed. Mater. Res. A* 103, 3872–3878. doi: 10.1002/jbm.a.35532

Shanbhag, A. S., Jacobs, J. J., Black, J., Galante, J. O., and Glant, T. T. (1994). Macrophage/particle interactions: effect of size, composition and surface area. *J. Biomed. Mater. Res. A* 28, 81–90. doi: 10.1002/jbm.820280111

Sinder, B. P., Pettit, A. R., and McCauley, L. K. (2015). Macrophages: their emerging roles in bone. *J. Bone Miner. Res.* 30, 2140–2149. doi: 10.1002/jbmr.2735

Sun, D. H., Trindade, M. C., Nakashima, Y., Maloney, W. J., Goodman, S. B., Schurman, D. J., et al. (2003). Human serum opsonization of orthopedic biomaterial particles: protein-binding and monocyte/macrophage activation *in vitro*. *J. Biomed. Mater. Res. A* 65, 290–298. doi: 10.1002/jbm.a.10477

Trindade, M. C., Song, Y., Aspenberg, P., Smith, R. L., and Goodman, S. B. (1999). Proinflammatory mediator release in response to particle challenge: studies using the bone harvest chamber. *J. Biomed. Mater. Res. A* 48, 434–439. doi: 10.1002/(SICI)1097-4636(1999)48:4<434::AID-JBM6>3.0.CO;2-Y

Vermes, C., Roebuck, K. A., Chandrasekaran, R., Dobai, J. G., Jacobs, J. J., and Glant, T. T. (2000). Particulate wear debris activates protein tyrosine kinases and nuclear factor kappaB, which down-regulates type I collagen synthesis in human osteoblasts. *J. Bone Miner. Res.* 15, 1756–1765. doi: 10.1359/jbmr.2000.15.9.1756

Vi, L., Baht, G. S., Whetstone, H., Ng, A., Wei, Q., Poon, R., et al. (2015). Macrophages promote osteoblastic differentiation *in-vivo*: implications in fracture repair and bone homeostasis. *J. Bone Miner. Res.* 30, 1090–1102. doi: 10.1002/jbmr.2422

Wang, M. L., Nesti, L. J., Tuli, R., Lazatin, J., Danielson, K. G., Sharkey, P. F., et al. (2002). Titanium particles suppress expression of osteoblastic phenotype in human mesenchymal stem cells. *J. Orthop. Res.* 20, 1175–1184. doi: 10.1016/S0736-0266(02)00076-1

Wu, A. C., Raggatt, L. J., Alexander, K. A., and Pettit, A. R. (2013). Unraveling macrophage contributions to bone repair. *Bonekey Rep.* 2:373. doi: 10.1038/bonekey.2013.107

Zilber, S., Epstein, N. J., Lee, S. W., Larsen, M., Ma, T., Smith, R. L., et al. (2008). Mouse femoral intramedullary injection model: technique and microCT scan validation. *J. Biomed. Mater. Res. B Appl. Biomater.* 84, 286–290. doi: 10.1002/jbm.b.30872

Conflict of Interest: The authors declare that the research was conducted in the absence of any commercial or financial relationships that could be construed as a potential conflict of interest.

frontiers in Bioengineering and Biotechnology

ORIGINAL RESEARCH
published: 09 October 2019
doi: 10.3389/fbioe.2019.00256

Osteoinductive Material to Fine-Tune Paracrine Crosstalk of Mesenchymal Stem Cells With Endothelial Cells and Osteoblasts

*Hassan Rammal[1,2], Laura Entz[1], Marie Dubus[1,2], Aurélie Moniot[1], Nicolae B. Bercu[3], Johan Sergheraert[1,2,4], Sophie C. Gangloff[1,5], Cédric Mauprivez[1,2,4] and Halima Kerdjoudj[1,2]**

[1] EA 4691, Biomatériaux et Inflammation en Site Osseux (BIOS), SFR CAP Santé (FED4231), Université de Reims Champagne Ardenne, Reims, France, [2] UFR d'Odontologie, Université de Reims Champagne Ardenne, Reims, France, [3] EA 4682, Laboratoire de Recherche en Nanoscience (LRN), Université de Reims Champagne-Ardenne, Reims, France, [4] Pôle Médecine bucco-dentaire, Hôpital Maison Blanche, Centre Hospitalier Universitaire de Reims, Reims, France, [5] UFR de Pharmacie, Université de Reims Champagne Ardenne, Reims, France

OPEN ACCESS

Edited by:
Maria Chatzinikolaidou, University of Crete, Greece

Reviewed by:
Roberta Tasso, University of Genoa, Italy
Anna Lange-Consiglio, University of Milan, Italy

***Correspondence:**
Halima Kerdjoudj
halima.kerdjoudj@univ-reims.fr

Specialty section:
This article was submitted to Tissue Engineering and Regenerative Medicine, a section of the journal Frontiers in Bioengineering and Biotechnology

Received: *01 July 2019*
Accepted: *23 September 2019*
Published: *09 October 2019*

Citation:
Rammal H, Entz L, Dubus M, Moniot A, Bercu NB, Sergheraert J, Gangloff SC, Mauprivez C and Kerdjoudj H (2019) Osteoinductive Material to Fine-Tune Paracrine Crosstalk of Mesenchymal Stem Cells With Endothelial Cells and Osteoblasts. Front. Bioeng. Biotechnol. 7:256. doi: 10.3389/fbioe.2019.00256

While stem cell/biomaterial studies provide solid evidences that biomaterial intrinsic cues deeply affect cell fate, current strategies tend to neglect their effects on mesenchymal stem cells (MSCs) secretory activities and resulting cell-crosstalks. The present study aims to investigate the impact of bone-mimetic material (B-MM), with intrinsic osteoinductive property, on MSCs mediator secretions; and to explore underlying effects on cells involved in bone regeneration. Human MSCs were cultured, on B-MM, made from inorganic calcium phosphate supplemented with chitosan and hyaluronic acid biopolymers. Collected MSCs culture media were assessed for mediators release quantification and used further to stimulate endothelial cells (ECs) and alveolar bone derived osteoblasts (OBs). Without osteogenic supplements, MSCs committed into bone lineage forming thus 3D bone-*like* nodules after 21 days. Despite a weak percentage of cell commitment, our data elucidate new aspects of osteoinductive material effect on MSCs functions through the regulation of the secretion of mediators involved in bone regeneration and subsequently the MSCs/ECs indirect crosstalk with osteogenesis-boosting effect. Using MSCs culture media, we demonstrate a large potential of osteoinductive materials and MSCs in bone regenerative medicine. Such strategies could help to address some insights in cell-free therapies using MSCs derived media.

Keywords: mesenchymal stem cells, paracrine activities, cell crosstalk, osteoinductive material, culture media

INTRODUCTION

During the last decade, mesenchymal stem cells (MSCs) have been proven effective for bone regeneration as evidenced through *in vitro, in vivo* animal experiments and clinical trials (Asatrian et al., 2015; Jin and Lee, 2018). Scientific investigations have tried to understand the MSCs biological mechanism of action in skeletal tissue repair and to decipher their potential in cell therapy and regenerative medicine. Early MSCs studies in bone regenerative medicine were focused on their great potential to differentiate into multiple tissue types and supported the idea that MSCs have the

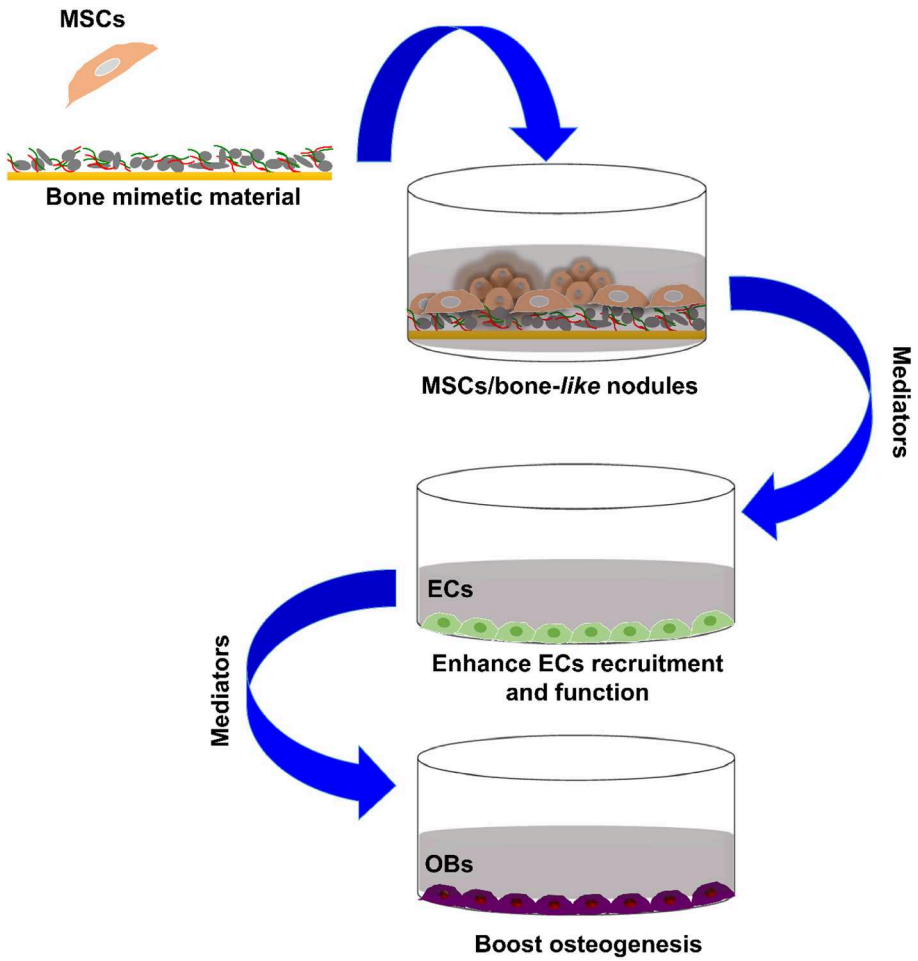

GRAPHICAL ABSTRACT | Bone forming cells paracrine crosstalk.

capacity for tri-lineage differentiation into, osteoblasts (OBs), chondrocytes or adipocytes. Such optimism suggested that upon implanting, MSCs would colonize and differentiate at the bone lesion site along the osteoblastic lineage and thus replace damaged resident OBs (Bruder et al., 1994, 1998; Golchin and Farahany, 2019).

Bone tissue engineering has emerged as an interdisciplinary strategy combining biomaterials, MSCs and/or biologically active molecules, aiming to reconstruct injured or lost bone (Place et al., 2009). Along with the direct relationship between osteoblastic lineage and bone formation, major developments were focused on osteoinductive materials able to induce MSCs osteoblastic differentiation, without chemical exogenous stimuli. Materials mimicking physicochemical and mechanical properties of bone extracellular matrix are developed to guide MSCs fate (Gao et al., 2017; Li et al., 2017; Zhang et al., 2018a). Indeed, MSCs sense physical and mechanical signals from their microenvironment and simultaneously convert them into environmental signals that regulate their behavior. We have recently developed a versatile osteoinductive coating made of organic chitosan/hyaluronic acid biopolymers and inorganic calcium phosphate, with a compositional analogy to human mineral bone and offers interesting properties for bone regenerative medicine, as it provides a suitable framework for MSCs osteogenic commitment (Rammal et al., 2017a).

MSCs are a heterogeneous population that contains a very low yield of cells able to differentiate into osteoblastic lineage. Once injected into a damaged tissue, MSCs showed a relatively poor rate of cell engraftment and engrafted ones are rather to be short-lived (Wang et al., 2014). Taken together, the current research seems to argue that MSCs differentiation contributes minimally to tissue regeneration while paracrine activities play a more predominant role. MSCs secrete cytokines, chemokines and growth factors to orchestrate tissue repair (i.e., by promoting angiogenesis and tissue regeneration and inhibiting fibrosis, apoptosis and inflammation) (Glenn and Whartenby, 2014; Wang et al., 2014; Haumer et al., 2018; Najar et al., 2018). Furthermore, an increase in bone resistance to fracture along with an increase in bone mineral density were reported following MSCs-based therapy for osteoporosis (Aghebati-Maleki et al.,

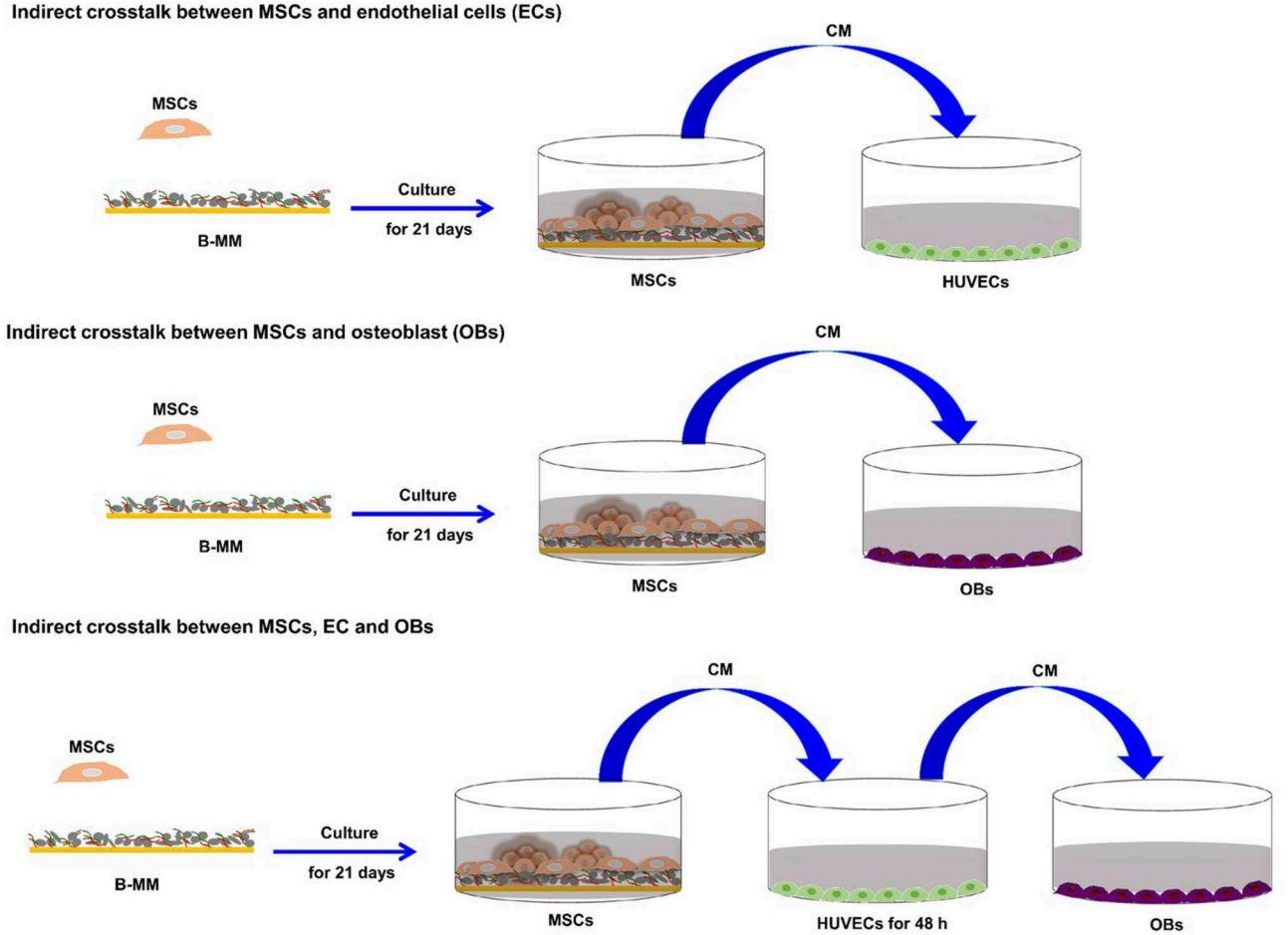

FIGURE 1 | Representative schema of the study experimental design.

2018; Saito et al., 2018). Local administrations of allogenic MSCs into the bone marrow cavity of irradiation-induced osteoporotic mice or of ovariectomy-induced osteoporotic rats were found to be effective against osteoporosis progression, to enhance bone apposition, and to promote freshly osteoid formation. Using MSCs to treat osteoporosis is already in clinical trials and no outcomes have been described (ClinicalTrials.gov identifier: NCT02566655; NCT01532076).

In light of these data, the present study investigates the capacity of bone-mimetic material (B-MM) to promote pro-regenerative secretome from MSCs especially on the production of either angiogenic or osteogenic factors (**Figure 1**). Our results provide, herein, evidences that the indirect crosstalk between MSCs and various cell types involved in bone regeneration, namely endothelial cells (ECs) and OBs, might be finely regulated by B-MM.

MATERIALS AND METHODS

Experimental Design

To investigate the effect of bone-mimetic material (B-MM) on MSCs differentiation and secretome, Wharton's jelly derived MSCs were cultured for 21 days on both B-MM and glass. The study of the crosstalk between MSCs and EC or OBs was performed using MSCs culture media collected between 19th and 21st day of culture (**Figure 1**).

Bone-Mimetic Material

Material

Calcium chloride hydrate ($CaCl_2$, $2H_20$: 0.32 M) and chitosan (low molecular weight: 0.3 mg/mL) were dissolved in NaCl (0.15 M)/HCl (2 mM) buffer pH 4 (A solution). Sodium dihydrogen phosphate hydrate (NaH_2PO_4: 0.19 M) and hyaluronic acid (molecular weight of 200 kDa: 0.3 mg/mL) were prepared in NaCl (0.15 M) buffer pH 10 (B solution). Both salt solutions were prepared in ultrapure water (Millipore®). Coverslips of 14 mm diameter were provided from Thermo Scientific. Each experiment was preceded by a cleaning step of the glass coverslips with sodium dodecyl sulfate (100 mM) for 15 min at 100°C. After an intensive ultrapure water (Millipore®) rinse, coverslips were brought in contact with HCl (100 mM) for 15 min at 100°C and finally rinsed with ultrapure water and kept at 4°C.

Substrate Build-Up

An automated spraying device was used for bone-mimetic material (B-MM) build-up. This device is constituted of four identical Airbrushes VL (Paasche®, USA) nozzles. Each nozzle is pressurized by in-house compressed air line under a pressure of 1 bar and connected to solenoid valves. The spraying of the different solutions, following a chosen deposition sequence, is obtained by a succession of closings and openings of the valves controlled by homemade software. Three nozzles allow spraying of the A solution, the B solution and of the rinsing solution. The fourth nozzle, free of solution, is used for the drying step. The cleaned coverslip is mounted vertically on a mobile holder. For homogenous B-MM build-up, the holder was rotated at 150 rpm. Both A and B solutions were sprayed simultaneously, on coverslip, for 2 s followed by a rinsing step of 2 s with ultrapure water and a drying step of 2 s under compressed air. These steps were repeated 50 times and polymer concentrations were adjusted after calculation of flows during spraying in order to keep a charge ratio hyaluronic acid/chitosan constant and equal to 0.7 to optimize the complex formation (Cado et al., 2012).

Cell Culture

Human specimen (umbilical cord, mandibular bone specimen, and venous blood) harvestings were approved ethically and methodologically by our local Research Institution and were conducted with informed patients (written consent) in accordance with the usual ethical legal regulations (Article R 1243-57). All procedures were done in accordance with our authorization and registration number DC-2014-2262 given by the National "Cellule de Bioéthique."

Wharton's Jelly Mesenchymal Stem Cells (MSCs)

MSCs were enzymatically isolated from fresh human umbilical cords obtained after full-term births (Mechiche Alami et al., 2014). MSCs were amplified at a density of 3×10^3 cell/cm^2 in α-MEM culture medium supplemented with 10% decomplemented fetal bovine serum (FBS), 1% Penicillin/Streptomycin/Amphotericin B and 1% Glutamax® (*v/v*, Gibco) and maintained in a humidified atmosphere of 5% CO_2 at 37°C with a medium change every 2 days. At the fourth passage, MSCs were seeded in 24 well plates at 24×10^3 cells/cm^2 on UV-decontaminated B-MM or UV-decontaminated glass coverslip. MSCs were cultured for 21 days with a culture medium change every 2 days. Between 19th and 21st day of culture, MSCs culture media (MSCs-CM) were collected, centrifuged at 300 g and stored at −80°C. For a better comprehension, culture media from MSCs cultured on B-MM and glass were designated as CM_{B-MM} and CM_g, respectively. Effective MSCs commitment into osteoblastic lineage was checked on cross sections of embedded paraffin samples according to previously published procedure (Mechiche Alami et al., 2017). Alizarin red staining was performed on consecutive tissue sections and images were taken using scanner iScan Coreo AU (Roche®, Ventana). For immunohistochemistry, after deparaffinization, 4 µm sections were incubated with the Cell Conditioner 1 (EDTA, pH 8.4) for 64 min, followed by preprimary peroxidase inhibition and incubation with the primary rabbit polyclonal antibody targeting osteocalcin (at a 1/100 dilution, Calbiochem) at 37°C overnight. Then, the staining reaction was performed using the UltraView Universal DAB v3 Kit (Ventana Medical System). Images were taken using scanner iScan Coreo AU.

Human Umbilical Cord Vein Endothelial Cells (HUVECs)

HUVECs were enzymatically isolated from fresh human umbilical cords veins obtained after full-term births following Jaffe et al., method (Rammal et al., 2017b). HUVECs were amplified at a density of 10^4 cell/cm^2 in endothelial basal medium (EBM)-2 supplemented with 20% decomplemented FBS, 1% Penicillin/Streptomycin/Amphotericin B and 1% Glutamax® (*v/v*, Gibco) and maintained in a humidified atmosphere of 5% CO_2 at 37°C with a medium change every 2 days. At the second passage, HUVECs were cultured in 12 well plates at 10^4 cells/cm^2 in the presence of diluted CM_{B-MM}, and CM_g (1:1 in EBM-2) for 48 h. HUVECs stimulated with recombinant human Tumor Necrosis Factor α (TNF α, R&D Systems) at 10 ng/mL for 48 h were used as inflammatory positive control. After 48 h, culture media were collected, centrifuged at 300 g and stored at −80°C. For a better comprehension, culture media of CM_{B-MM} and CM_g stimulated HUVECs were designated as EC-CM_{B-MM} and EC-CM_g, respectively.

Human Mandibular Pre-osteoblasts (OBs)

Human mandibular bone specimens without any clinical or radiographic evidence of pathology were obtained from young patients (aged 13–33 years) undergoing windows teeth extraction oral surgery. After extensive (four to five times) washing steps, bone specimens were scraped to remove attached soft tissue and periosteum, broken into small pieces and predigested for 1 h with trypsin-EDTA (0.5%, *v/v*)/B collagenase (1 mg/mL) in a serum-free Dulbecco's Modified Eagle medium (DMEM). Fragments were then placed into 25 cm^2 tissue culture flask and maintained in a humidified atmosphere of 5% CO_2 at 37°C, allowing thus OBs migration and proliferation in the presence of DMEM supplemented with 20% FBS and 1% Penicillin/Streptomycin (*v/v*, Gibco). OBs were then amplified at a density of 10^4 cell/cm^2 in 10% FBS supplemented DMEM with a medium change twice/week and used at the third passage in our experimental study design. At the third passage, OBs were cultured in 24 well plates at 10^4 cells/cm^2 in the presence of diluted CM_{B-MM}, CM_g, EC-CM_{B-MM}, and EC-CM_g (1:1 in DMEM) for 7 days. OB maintained in basal and osteogenic media (i.e., DMEM supplemented with 10 mM β-glycerophosphate, 250 µM L-ascorbic acid 2-phosphate and 5 nM dexamethasone) were used as controls.

Co-culture of Human Neutrophils With HUVECs

Neutrophils were purified from human whole blood collected on EDTA (BD Vacutainer® K2E, Franklin Lakes, USA) using the Polymorphprep™ protocol. Contaminating red blood cells were removed by a hypotonic shock. Resulting neutrophils were resuspended in complete RPMI 1640 media supplemented with 1% Penicillin/Streptomycin and 2.5% heat-inactivated

autologous human serum and represented >97% of the cells. The PMNs were at least 95% viable. One million of neutrophils was finally brought in contact with un-stimulated and stimulated HUVECs (i.e., incubated for 48 h with CM_{B-MM} and CM_g).

ELISA Cytokines, Chemokines, and Growth Factors Release

Secreted levels, in MSCs culture media (CM_{B-MM} and CM_g), of IL-1β, IL-6, IL-8, IL-10, transforming growth factor (TGF-β), osteoprotegerin (OPG), Prostaglandin E_2 (PGE_2), receptor activator of nuclear factor kappa-B ligand (RANKL), hepatocyte growth factor (HGF), vascular endothelial growth factor (VEGF), fibroblast growth factor (b-FGF), and bone morphogenic protein-2 (BMP-2) were assessed. ELISA MAX™ Deluxe kit for human IL-6, IL-8, IL-10, and b-FGF (BioLegend), DuoSet ELISA Kit for human IL-1β, TGF-β, Osteoprotegerin/TNFRSF11B, TRANCE/RANKL/TNFSF11, HGF, VEGF, and BMP-2 (R&D Systems, France) and PGE-2 ELISA Kit (Cayman Chemical) were used. Absorbance was measured according to the manufacturers' instructions.

Transwell Migration Assay

HUVECs were seeded on the top of a cell culture insert membrane (Millicell® Hanging Cell Culture Inserts) at the density of 2×10^3 cells/well. MSCs culture media (CM_{B-MM} and CM_g) were deposited in the bottom of a 24 well plastic culture plate. After 48 h of incubation at 37°C in 5% CO_2, non-migrating HUVECs were removed from the top of the membrane and migrated cells at the bottom of the insert membrane were fixed with methanol then stained with crystal violet. Migrated cells were finally imaged using EVOS® digital microscope and counted. EBM-2 and α-MEM ± 10% FBS were used as controls.

PCR Gene Expression Analysis

For CM_{B-MM} and CM_g stimulated HUVECs and OBs as well as EC-CM_{B-MM} and EC-CM_g stimulated OBs (**Figure 1**, study experimental design), total RNA was isolated and purified using MasterPure™ RNA Purification Kit (Epicenter® Biotechnologies) in accordance with the manufacturer protocol. RNA purity was assessed by measuring the absorbance ratio at 260/280 nm (Nanodrop 2000C, ThermoScientific), which was comprised between 1.8 and 2. Total RNAs (500 ng) were reverse transcribed into cDNA using a High Capacity cDNA Reverse Transcription kit (Applied Biosystems) following manufacturer instructions. Ten nanograms of reverse transcription product were amplified by qRT-PCR on a StepOnePlus™ system (Applied Biosystems). Using this approach, the transcriptional levels of *RPS18* (internal control), *TNFα*, *IL-6*, *IL-8*, *SELE*, *ICAM1,* and *BMP-2* mRNA in stimulated HUVECs and the transcriptional levels of *HPRT-1* (internal control), *COL1A1,* and *BGLAP* mRNA in stimulated OBs were determined using Power SYBR® Green PCR Master MIX (Applied Biosystems) and TaqMan® Fast Advanced Master Mix (Applied Biosystems) for *ALPL* and *Runx2* mRNA. After a first denaturation step at 95°C for 10 min, qRT-PCR reactions were performed according to a thermal profile that corresponds to 40 cycles of denaturation at 95°C for 15 s, annealing and extension at 60°C for 1 min. Data analysis was performed with the StepOne™ Software v2.3 (Applied Biosystems).

Scanning Electron Microscopy With a Field Emission Gun (FEG-SEM)

Neutrophils adhered to stimulated HUVECs (i.e., incubated for 48 h with CM_{B-MM} and CM_g) were fixed with 2.5% (w/v) glutaraldehyde (Sigma Aldrich) at room temperature for 1 h. Samples were dehydrated in graded ethanol solutions from 50 to 100% and desiccated in hexamethyldisilazane (Sigma Aldrich) for 10 min. After air-drying at room temperature, samples were sputtered with a thin gold–palladium film under a JEOL ion sputter JFC 1100 and viewed using FEG-SEM (JEOL JSM-7900F). Images were acquired from secondary electrons at primary beam energy between 5 to 20 kV.

Mitochondrial Activity

WST-1 cell proliferation assay (Roche Diagnostics) was performed on human mandibular osteoblasts (OBs) cultured in MSC (CM_{B-MM} and CM_g) and stimulated HUVECs (EC-CM_{B-MM} and EC-CM_g) culture media for 2, 4, and 7 days. Absorbance was measured at 440 nm using a FLUOstar Omega microplate reader (BMG Labtech) against a background control as blank. A wavelength of 750 nm was used as the correction wavelength. Mitochondrial activity, an indicator of cell viability, was calculated as the absorbance ratio between stimulated and basal culture medium (considered as 100% of viable osteoblasts).

Statistical Analysis

All MSCs experiments were performed with six independent umbilical cords. HUVECs, OBs, and neutrophils, were performed with three independent donors. ELISA and PCR results are presented as box plot chart with median using GraphPad® Prism 5 software. Multivariate statistical analysis was performed by XL Stat software. Metabolic activity results are presented as histograms with mean ± standard error of the mean. All statistical analysis were performed using GraphPad® Prism 5 software. For Mann Whitney test, a value of $p < 0.05$ was accepted as statistically significant p (rejection level of the null-hypothesis of equal medians).

RESULTS AND DISCUSSION

We recently reported that intrinsic features of bone-mimetic material (B-MM) made from inorganic calcium phosphate supplemented with chitosan and hyaluronic acid biopolymers influences MSCs fate through mechanobiological pathway, inducing the expression of bone specific proteins (up to 1 week) (Rammal et al., 2017a). Bone develops through a tightly regulated process leading to a hierarchically ordered three-dimensional structure described in the literature as

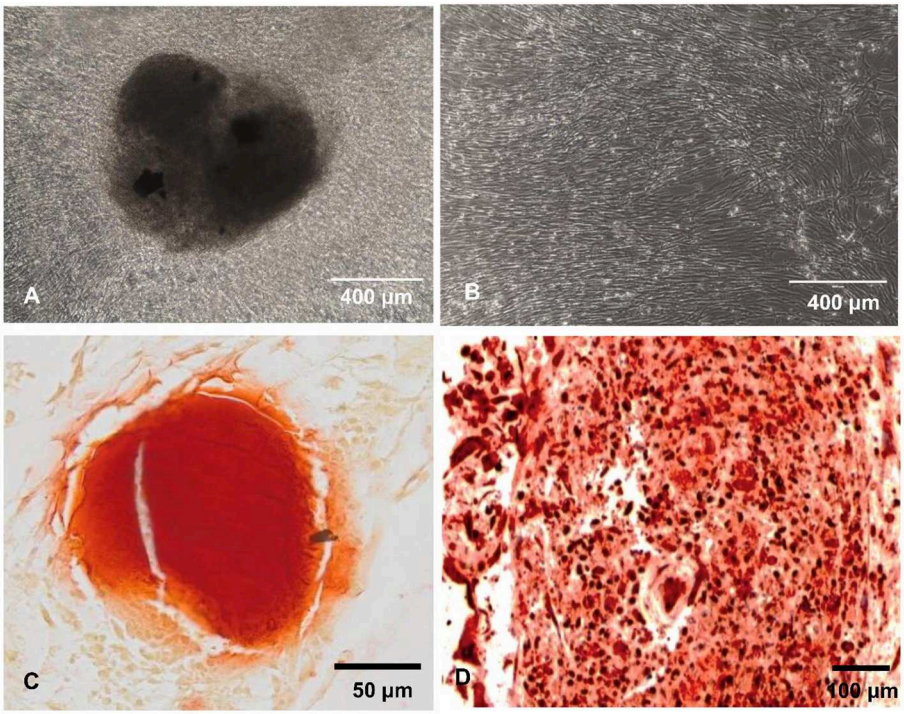

FIGURE 2 | MSCs behavior. **(A,B)** Representative optical images showing MSCs accretions on bone-mimetic material **(A)** and cellular layer on glass **(B)** (scale bar 400 µm). **(C)** Red alizarin histological staining and **(D)** osteocalcin immunohistochemistry (scale bars 50 and 100 µm, respectively), demonstrating the bone-*like* nodule formation on B-MM.

bone nodule (Mechiche Alami et al., 2016). Starting from day 14, MSCs cultured on B-MM formed 3D nodules in some distinct region (about 8% of the cultured area), whereas on control glass coverslip, no major morphological changes and no nodules were observed Histological and immunohistochemical analysis of paraffin-embedded nodules evidenced the presence of mineralized matrix positive to red alizarin and cells positive to osteocalcin (**Figure 2** and **Figure S1**). A deeper characterization of these bone-*like* nodules would require multiscale investigations (Gentleman et al., 2009) that are out of scoop of the present study. The nodule density of around 9 ± 2 nodules in the cultured area suggests a low commitment of MSCs into osteoprogenitor cells. These observations are consistent with other studies highlighting a very low yield of MSCs able to differentiate into osteoblastic lineage (Jin and Lee, 2018; Golchin and Farahany, 2019). Along their capacity to differentiate into desired phenotype, MSCs contribute to tissue regeneration through the secretion of soluble and insoluble mediators (Glenn and Whartenby, 2014; Wang et al., 2014; Haumer et al., 2018; Najar et al., 2018). Focusing our investigations on the secretion of soluble mediators required for bone regeneration, the paracrine activity of MSCs cultured on B-MM was analyzed and compared to glass (**Figure 3A**, experimental design). ELISA results showed that MSCs cultured on B-MM decreased significantly the secretion of IL-1β, IL-6, and IL-8 pro-inflammatory mediators ($\approx$ 5-, 4-, and 2-fold vs. glass, $p < 0.01$, $p = 0.007$ and $p < 0.04$, respectively, Mann Whitney test) but increased significantly PGE-2 production ($\approx$ 1.37-fold vs. glass, $p < 0.01$, Mann Whitney test) (**Figure 3B**). TNF-α and RANKL were below the detection limit while the constitutive production of OPG was found to be not sensitive to culture substrate (**Figure 3B**). These mediators have great potential in bone repair and homeostasis (Raisz, 1999; Kon et al., 2001; Marsell and Einhorn, 2011; Sugimoto et al., 2016; Lin et al., 2018), but at high level, IL-1β, IL-6, IL-8, TNF-α, and soluble RANKL could be involved in osteoclast activation, bone destruction and ineffective regeneration (Mountziaris and Mikos, 2008). MSCs secrete various soluble growth factors to promote bone formation (TGF-β, VEGF and BMPs) and vascularization (HGF, b-FGF, VEGF) (Gerber et al., 1999; Tang et al., 2009; Chim et al., 2013; Crane et al., 2016). While the secretion of TGF-β and HGF was unchanged, the production of VEGF and b-FGF was significantly increased on B-MM ($\approx$ 4.5- and 36-fold vs. glass, $p < 0.001$, Mann Whitney test). Surprisingly BMP-2 was not detected in MSCs supernatants (**Figure 3B**). Bone extracellular matrix (ECM) may not only sequester and store soluble BMPs but also expose them to OBs receptors; explaining away the lack of soluble BMP-2 detection in culture media (Chim et al., 2013). Despite its inability to induce MSCs osteogenic commitment, TGF-β promotes the recruitment and proliferation of osteoprogenitors during bone healing process (Chim et al., 2013). VEGF and b-FGF are known to promote ECs migration and tissue vascularization and indirectly OBs migration, proliferation, and differentiation (Gerber et al., 1999; Tang et al., 2009; Chim et al., 2013). Taken together, these results

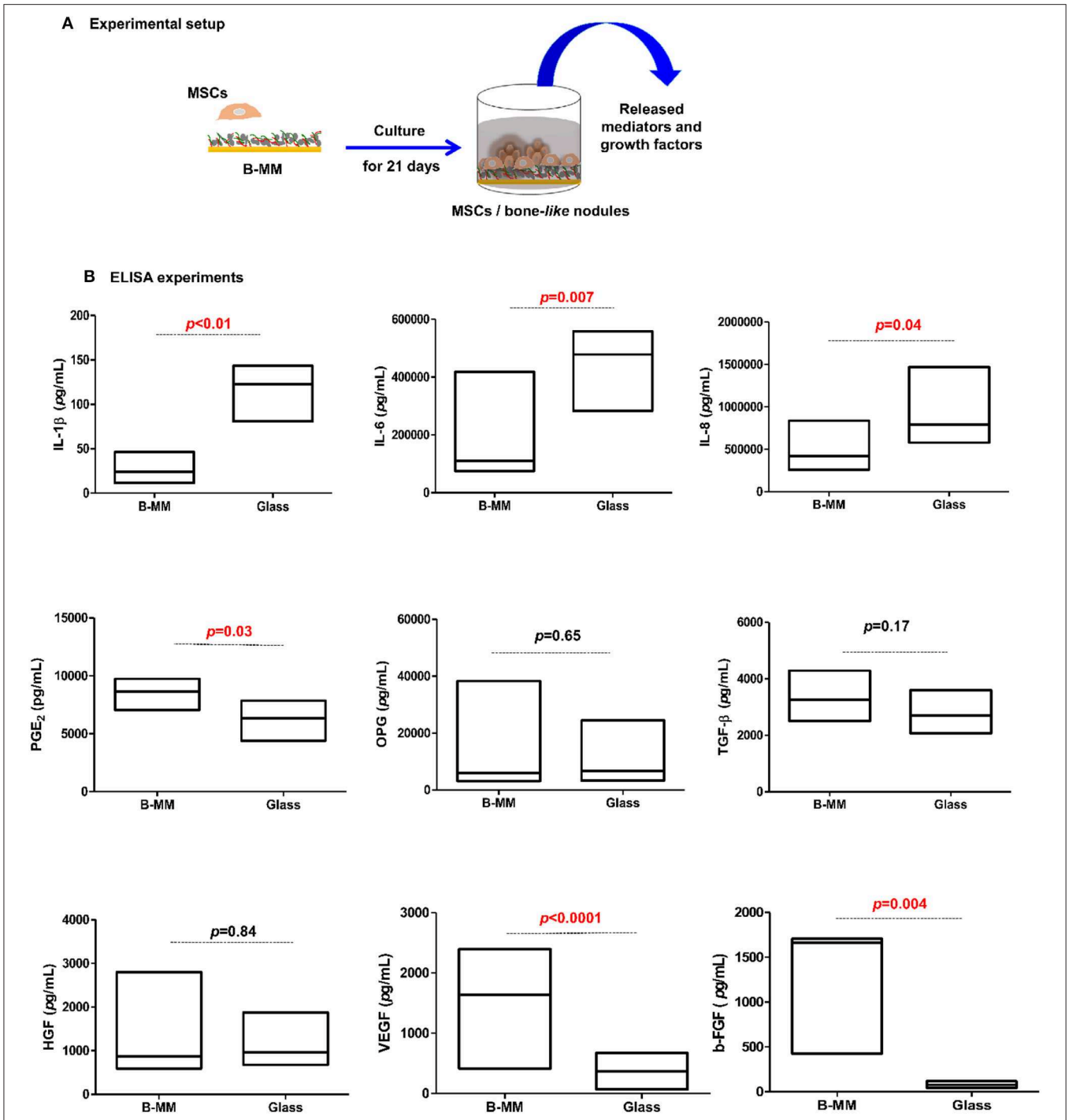

FIGURE 3 | Cytokines, chemokines, and growth factors production. **(A)** Experimental setup and **(B)** Released IL-1β, IL-6, IL-8, PGE-2, OPG, TGF-β, HGF, VEGF, and b-FGF quantified by ELISA, indicating a down production of inflammatory mediators and up release of angiogenic mediators by MSCs cultured on bone-mimetic material (B-MM) compared to glass ($n = 6$, Mann Whitney test). TNF-α, IL-10, soluble RANKL, and BMP-2 were not detected in MSCs media.

suggest that the paracrine activities of MSCs cultured on B-MM seems to be imbalanced in favor of vasculogenesis rather than osteogenesis. This conclusion was supported by principal component analysis (Wu et al., 2016) that showed data variance superior to 60% (**Figure 4A**). It appears that b-FGF, VEGF, HGF, TGF-β, OPG as well as PGE-2 are closer to MSCs on B-MM whereas IL-1β, IL-6, and IL-8 are closer to MSCs on glass. Discrimination of secretory activity was not affected by donor

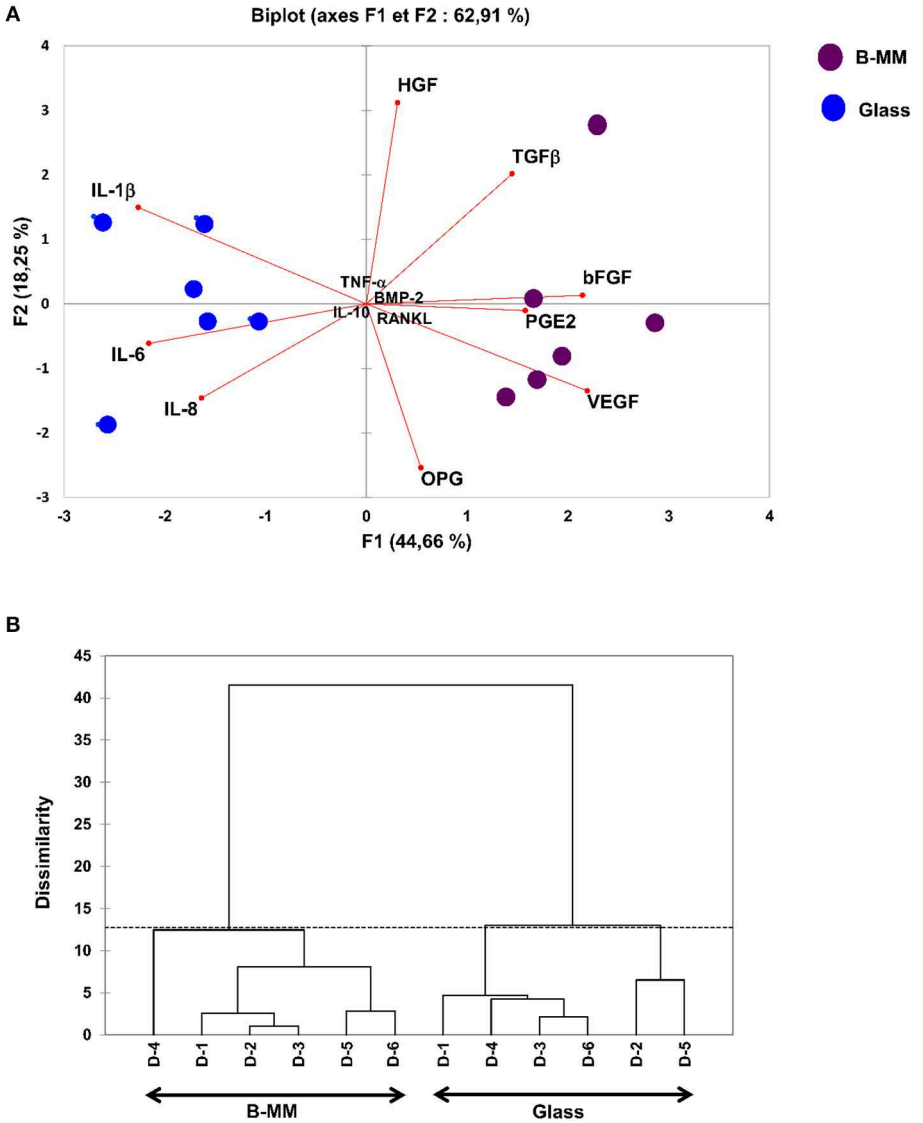

FIGURE 4 | Multivariate statistical analysis. **(A)** Principal Component Analysis (PCA) plots and **(B)** Dendrogram, indicating, despite donor (D) variability, a clear separation between the averages of secreted mediators by MSCs cultured on bone-mimetic material (B-MM) and on glass.

variability but resulting differences were due to MSCs behavior once on B-MM or glass substrate (**Figure 4B**).

Indirect MSCs/Endothelial Cells (ECs) Crosstalk

The crosstalk between MSCs/OBs/ECs is essential for bone formation and remodeling as well as around implanted graft during bone repair (Helmy et al., 2012). Above results suggest that MSCs cultured on B-MM could have a great potential in boosting ECs migration and proliferation (Gerber et al., 1999; Mountziaris and Mikos, 2008). To evaluate the effect of MSCs cultured on B-MM on ECs migration, transwell chemotaxis assay was performed. MSCs culture media (MSCs-CM) harvested between 19th and 21st day of culture and primary HUVECs were used (**Figure 5A**, experimental design). For better comprehension, we designated culture media from MSCs cultured on B-MM and on glass by CM_{B-MM} and CM_g, respectively. CM_{B-MM} enhanced significantly HUVECs recruitment with about 50% of migrated HUVECs whereas CM_g recruited only 2% (**Figure 5B**), confirming the superior chemotactic activity of MSCs on B-MM compared to glass.

Upon bone graft implantation, recruited leukocytes secrete an array of pro-inflammatory cytokines and growth factors, orchestrating the graft integration into host bone tissue (Luu et al., 2013). ECs through the expression of adhesion molecules and the release of inflammatory cytokines, constitute the main regulators of leukocyte recruitment (Ucuzian and Greisler, 2007; McGettrick et al., 2012). In contrast to differentiated MSCs, naïve cells, mainly through IL-6 and TGF-β release, are

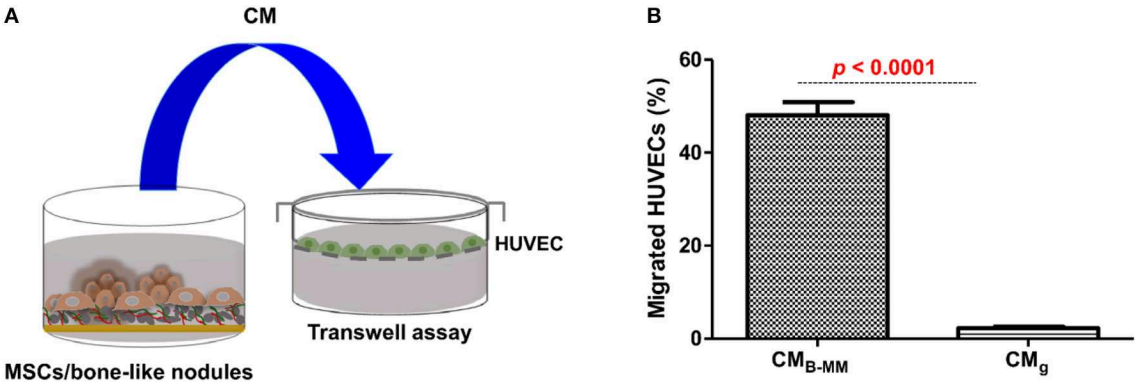

FIGURE 5 | Endothelial cell recruitment. **(A)** Experimental design and **(B)** Transwell chemotaxis assay, showing a significant increase in endothelial cell migration in presence of MSCs culture media (MSCs-CM) in presence of bone-mimetic material (B-MM) compared to glass (for MSCs and HUVECs, $n = 6$ and 3, respectively, Mann Whitney test).

known to regulate leukocyte diapedesis (Ucuzian and Greisler, 2007). Although B-MM slightly increased TGF-β release, above cited results indicated a significant decrease in IL-6 production (**Figure 3B**), suggesting a potential indirect effect on leukocyte recruitment. Thus, a second set of experiments was conducted to investigate the latter hypothesis. HUVECs were incubated with CM_{B-MM} and CM_g for 48 h and qRT-PCR experiments were conducted to assess HUVECs inflammatory phenotype through gene regulation of *TNFA*, *IL6, IL8*, *SELE,* and *ICAM1* (**Figure 6A**, experimental design). Note that once stimulated, ECs kept their characteristic cobblestone morphology (**Figure 6B**). Compared to un-stimulated HUVECs (i.e., cultured in endothelial basal medium), qRT-PCR results revealed an up-regulation of all studied genes in CM_{B-MM} and CM_g stimulated HUVECs (at least an up-regulation of $2^{-\Delta\Delta CT}$), signature of inflammatory phenotype. Regardless ECs inflammatory phenotype and compared to TNF-α stimulus (positive inflammatory control), MSCs-CM had a lower inflammatory impact on *ICAM1, SELE,* and *TNFA,* but up-regulated both *IL6* and *IL8*. Interestingly, although no differences were observed for *TNFA, IL6, IL8,* and *SELE,* we noticed a significant over-expression of *ICAM1* in presence of CM_{B-MM} (1.5-fold vs. CM_g, $p < 0.02$, Mann Whitney test, **Figure 6C**).

ICAM-1, constitutively expressed at low levels on ECs, can be up-regulated in response to pro-inflammatory stimuli, mediating neutrophil diapedesis (Anderson et al., 2008). Thus, adhesion of neutrophils to CM_{B-MM} and CM_g stimulated HUVECs was followed. Whatever the studied condition, the cobblestone monolayer integrity was altered when neutrophils were added. SEM revealed that neutrophils, in close similarity with TNF-α stimulated HUVECs condition, exhibited membrane ruffling and vesicles, indicative of neutrophil activation in contact with CM_{B-MM} stimulated HUVECs; whereas in contact with CM_g stimulated HUVECs, neutrophils, as for un-stimulated HUVECs condition, were rounded and appeared less activated (**Figure 6D** and **Figure S2**). Furthermore, a higher magnification of activated neutrophils in close contact to the apical part of HUVECs showed elongated neutrophils with long protrusions embracing HUVECs and forming adhesion points (**Figure 6D**, arrows). These observations corroborate previous studies, indicating that spreading can be signature of transmigrating neutrophils (Anderson et al., 2008; Schaefer et al., 2014).

Adding ECs to bone engineered constructs increases vascularization within and surrounding implanted constructs and boosts bone formation (Gerber et al., 1999; Von Wedel-Parlow et al., 2011). In response to VEGF, ECs produce BMP-2 that stimulates OBs differentiation, promoting fracture healing (Zhang et al., 2018b). Regarding the significant increase in VEGF release by MSCs cultured on B-MM vs. glass (**Figure 3B**); the expression of BMP-2 by HUVECs was followed. Despite a significant *BMP2* up-regulation in CM_{B-MM} stimulated HUVECs ($\approx 5^{-\Delta\Delta CT}$, **Figure 6C**), released BMP-2 was not detected in the culture supernatant, suggesting that BMP-2 production is under the detection threshold of the kit or is accumulated within the cell cytoplasm. These results are consistent with other observations demonstrating that ECs require direct contact with bone marrow derived MSCs for the effective production of BMP-2 (Kaigler et al., 2005).

Do MSCs Cultured on B-MM Promote Indirectly Pre-osteoblasts Differentiation?

As shown above, IL-1β, IL-6, IL-8, and VEGF secretion levels from MSCs cultured on B-MM were significantly modulated compared to glass (**Figure 3B**). These soluble factors are reported to mediate, in dose-dependent manner, pre-osteoblasts proliferation and differentiation (Mountziaris and Mikos, 2008). In the following, proliferation kinetic of human alveolar bone derived OBs cultured in presence of CM_{B-MM} and CM_g was firstly investigated (**Figure 7A**, experimental design). When cultured in CM_{B-MM}, the proliferation of OBs was significantly promoted compared to OBs cultured in osteogenic media (**Figure S3**). Moreover, we noticed a significant increase in MSCs-CM stimulated OBs proliferation from day 2 to 4 with a slow proliferation rate for CM_g ($p < 0.0001$, Mann

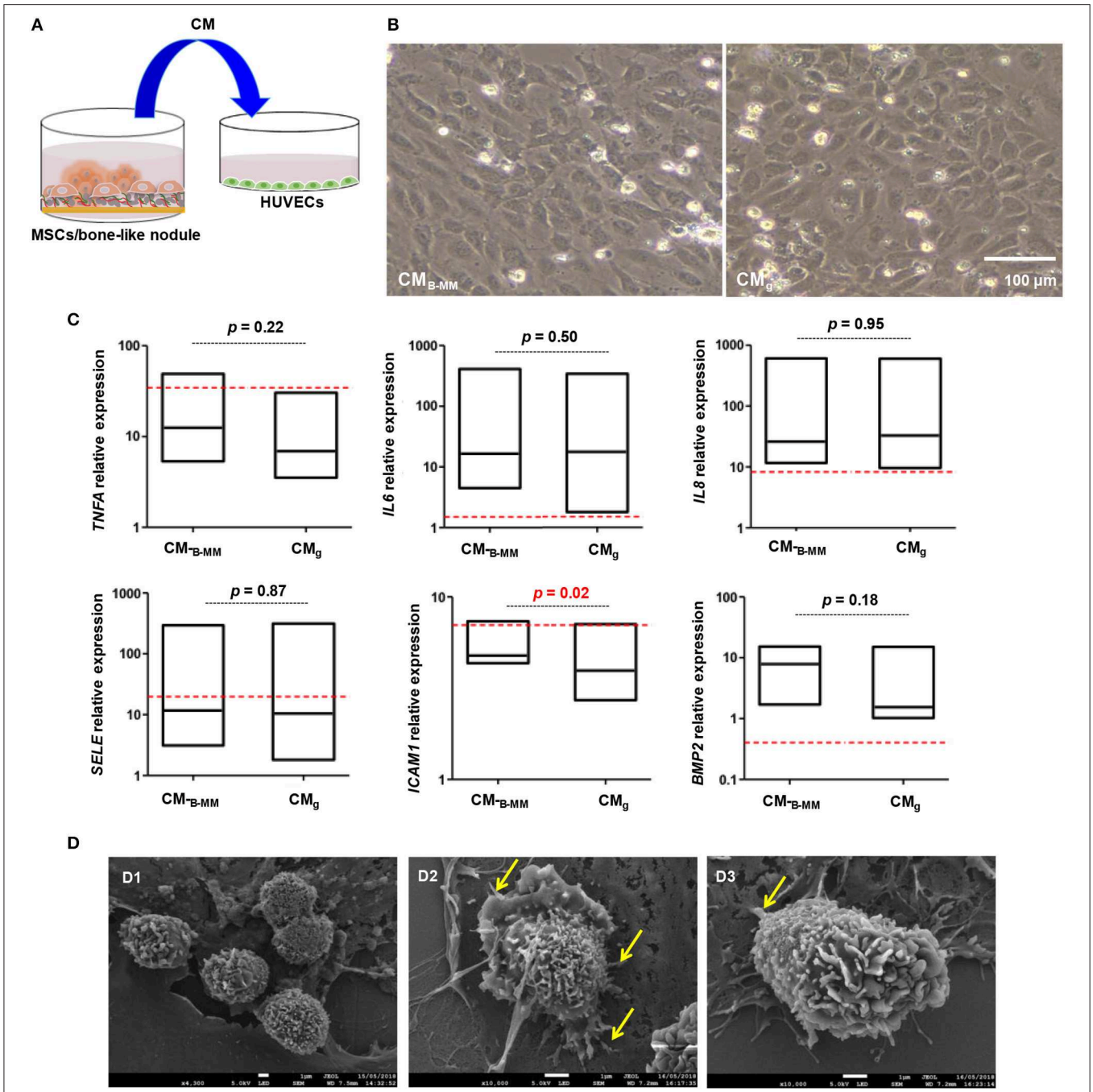

FIGURE 6 | Endothelial cell inflammatory phenotype. **(A)** Experimental design and **(B)** representative optical images of stimulated HUVECs by MSCs culture media (MSCs-CM_{B-MM} and MSCs-CM_g, scale bar = 100 µm), highlighting a cobblestone morphology. **(C)** Gene expression of *ICAM1*, *SELE*, *TNFA*, *IL6*, *IL8*, and *BMP2* quantified by qRT-PCR (red bars indicate TNF-α stimulated endothelial cells positive control) (for MSCs and HUVECs, $n = 6$ and 3, respectively, Mann Whitney test), showing a significant over-expression of *ICAM1* in presence of CM_{B-MM}. **(D)** Endothelial cell/neutrophil interaction imaged by scanning electron microscopy (Yellow arrows indicating neutrophil protrusion, scale bars = 1 µm), showing spread neutrophils with a transmigrating aspect in presence of CM_{B-MM}.

Whitney test). Whatever the stimulus, a plateau appeared from day 4 to 7 (**Figure 7B**). No significant difference in OBs morphology was noticed among the studied conditions (**Figure 7C**), suggesting that MSCs-CM stimuli did not affect the cell cytoskeleton. Differentiation of OBs cultured in presence of MSCs-CM was secondly investigated. During the early stage of bone formation, the gene expression of Runx-2 and ECM proteins including COL-I is concomitant with OBs proliferation

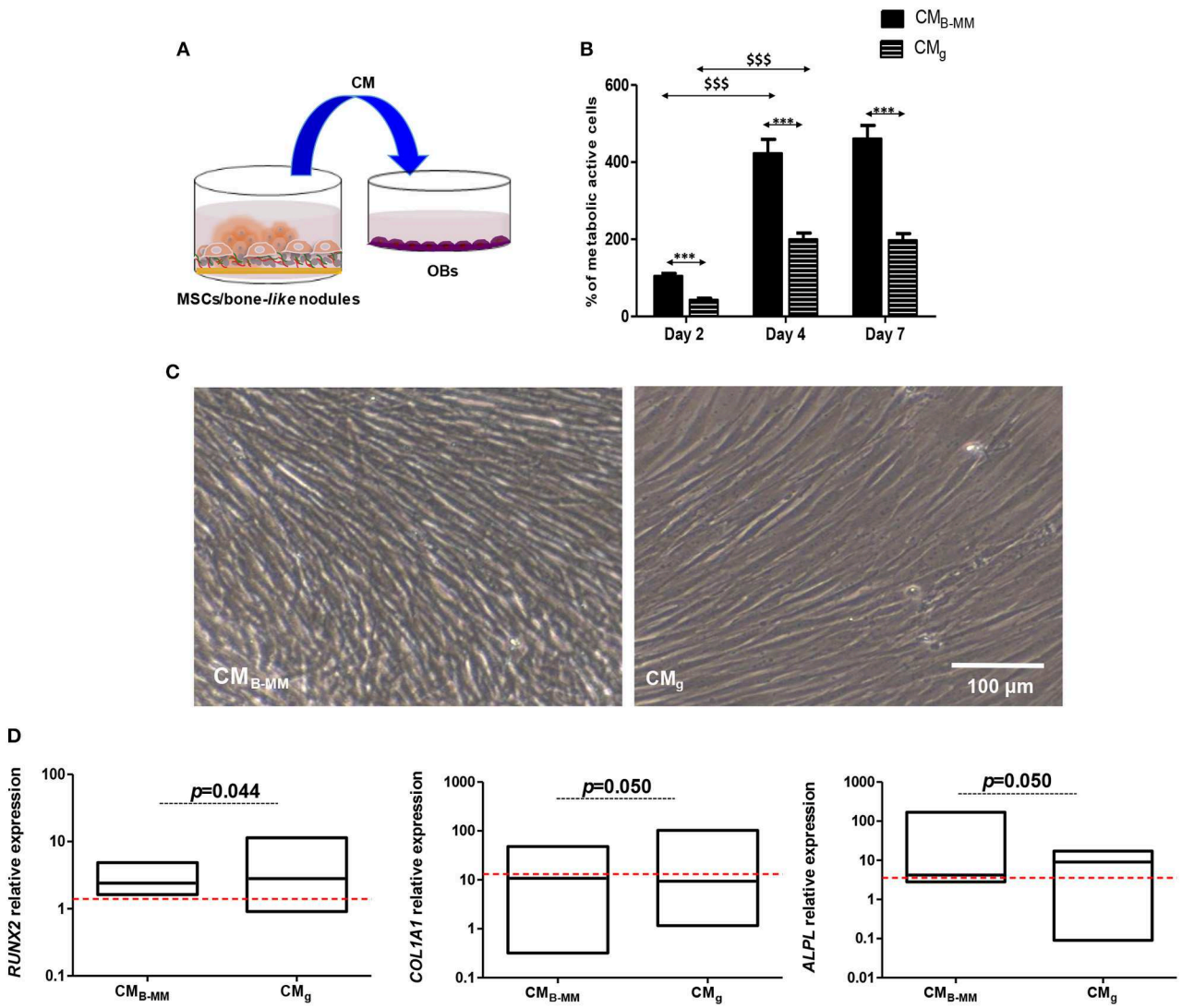

FIGURE 7 | Indirect MSCs/pre-osteoblasts crosstalk. **(A)** Experimental design and **(B)** pre-osteoblast (OBs) proliferation in presence of MSCs culture media (MSCs-CM). Results normalized to un-stimulated OBs, showing a significant increase in OB proliferation in presence of MSCs-CM cultured on bone-mimetic material compared to inert glass (*CM_{B-MM} vs. CM_g and $^{\$}$D4 and D7 vs. D2, for MSCs and OBs, $n = 6$ and 3, respectively, Mann Whitney test). **(C)** Optical images of stimulated OBs after 7 days of culture in MSCs-CM_{B-MM} and MSCs-CM_g, indicating fibroblastic cell morphology (Scale bars = 100 µm). **(D)** Gene expression of *RUNX2, COL1A1,* and *ALPL* quantified by qRT-PCR (red bars indicates OBs cultured in presence of osteogenic media), indicating the absence of an effective osteoblastic differentiation in the studied conditions (for MSCs and OBs, $n = 6$ and 3, respectively, Mann Whitney test). *** or $$$ means $p < 0.0001$. * is media dependent for the same kinetic time point and the $ is kinetic time point dependent for the same media.

whereas the non-proliferative and immature OBs up-regulate certain genes such as alkaline phosphatase (*ALPL*), a specific enzyme involved in the mineralization process. The late stage of bone formation corresponds to matrix mineralization, which is characterized by an up-regulation of non-collagenous proteins such as osteocalcin (*BGLAP*) (Mechiche Alami et al., 2017). While MSCs-CM stimulated the OBs proliferation, we failed to observe their effective differentiation (**Figure 7D**). Indeed, as for OBs cultured in osteogenic media, qRT-PCR experiments showed that both MSCs-CM up-regulate the expression levels of *RUNX2*, *COL1A1*, and *ALPL* over the time, however no statistically significance was distinguished between the studied conditions. Furthermore, no boosting effect of OBs differentiation was observed as *BGLAP*, late bone specific marker, was not detected.

Do MSC-CM Stimulated HUVECs Boosts Pre-osteoblasts Differentiation?

The intimate association between ECs and OBs suggests that ECs are to be prime sources for bone development (Gerber et al., 1999). In this part of the study, we assessed the effect of stimulated HUVEC supernatant (ECs-CM) on OBs (**Figure 8A**). As noticed above, we had a significant increase in OBs proliferation from day 2 to 4 with plateau from day 4 to 7

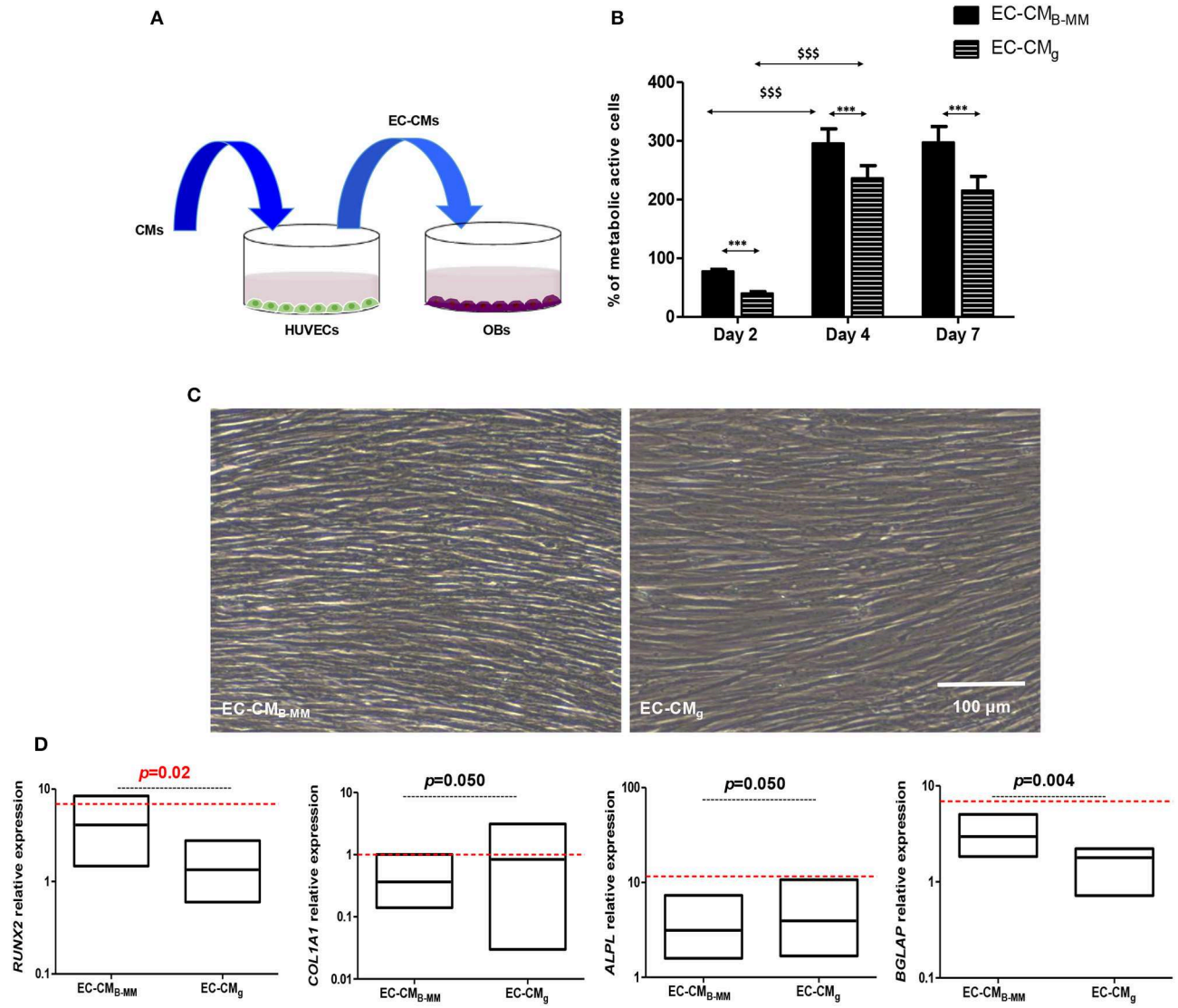

FIGURE 8 | Indirect MSCs/HUVECs/pre-osteoblasts crosstalk. **(A)** Experimental design and **(B)** pre-osteoblast (OBs) proliferation in presence of endothelial cell-culture media (ECs-CM). Results normalized to un-stimulated OBs, showing a significant increase in OBs proliferation in presence of EC-CM (HUVECs stimulated with CM of MSCs cultured on bone-mimetic material and glass, *EC-CM_{B-MM} vs. EC-CM_g and $^{\$}$D4 and D7 vs. D2, for MSCs and OBs, $n = 6$ and 3, respectively, Mann Whitney test). **(C)** Optical images of stimulated OBs after 7 days of culture in EC-CM_{B-MM} and EC-CM_g, indicating fibroblastic cell morphology (Scale bars = 100 µm). **(D)** Gene expression of *RUNX2*, *COL1A1*, *ALPL,* and *BGLAP* quantified by q-RT-PCR (red bars indicates OBs cultured in presence of osteoinductive medium), suggesting an acceleration of the osteoblastic differentiation in presence with EC-CM_{B-MM} (for MSCs and OBs, $n = 6$ and 3, respectively, Mann Whitney test). *** or $$$ means $p < 0.0001$. * is media dependent for the same kinetic time point and the $ is kinetic time point dependent for the same media.

without changes in cell morphology (**Figures 8B,C**). However, proliferation rate of OBs seemed slower in presence of ECs-CM compared to MSCs-CM (≈ 300 vs. 450% after 4 days of culture). Investigating the OBs differentiation in presence of ECs-CM, qRT-PCR experiments showed a down regulation of *COL1A1* and *ALPL* concomitantly to an up-regulation of *RUNX2* and *BGLAP* after 7 days (**Figure 8D**). Thus, despite the absence of BMP-2 release by HUVECs, compared to CM_g, CM_{B-MM} stimulated ECs up-regulated significantly *RUNX2* and *BGLAP* in OBs, suggesting a potential acceleration of OB differentiation.

CONCLUSION AND PERSPECTIVES

Herein we show that MSCs cultured on osteoinductive B-MM formed bone-*like* nodules. These nodules, arising from MSCs fibroblastic layers, occupied only 8% of cultured area. Despite the small fraction of committed osteoprogenitors, B-MM decreased the production of IL-1β, IL-6, and IL-8 inflammatory mediators and increased the release of b-FGF, VEGF angiogenic growth factors. Compared to CM_g, CM_{B-MM} enhanced endothelial cell migration and neutrophil diapedesis via *ICAM1* up-regulation. Regarding osteogenesic capacities,

both CM_{B-MM} and CM_g failed to boost pre-osteoblast differentiation. Interestingly, EC-CM_{B-MM} up-regulated BGLAP expression, suggesting an acceleration of pre-osteoblast maturation. Our results showed that BMP-2 seemed not responsible for ECs osteogenic property, suggesting the implication of other mediators. A deeper characterization (i.e., microarray analysis) of collected media is required to highlight the implication of other factors. MSCs and ECs are known to release therapeutic microvesicles that can act in a paracrine manner on tissue healing (Kaigler et al., 2005; Behera and Tyagi, 2018). Thus, it will be interesting to investigate the potential contribution of B-MM on microvesicles production and features.

DATA AVAILABILITY STATEMENT

All data generated or analyzed during this study are included in this published article (and its **Supplementary Information Files**). If not, they are available from the corresponding author on reasonable request.

ETHICS STATEMENT

The studies involving human participants were reviewed and approved by our local Research Institution and were conducted with informed patients (written consent) in accordance with the usual ethical legal regulations (Article R 1243-57). All procedures were done in accordance with our authorization and registration number DC-2014-2262 given by the National Cellule de Bioéthique. The patients/participants provided their written informed consent to participate in this study.

AUTHOR CONTRIBUTIONS

HR, LE, MD, NB, AM, and JS: participated in experiments designing and performance. HR: materials conception and cell culture. LE: qRT-PCR. MD: ELISA experiments. NB: scanning electron microscopy. JS: technical support. AM: neutrophils co-culture assay. HR, CM, SG, and HK: participated in study design and manuscript writing. All authors reviewed the results and approved the final version of the manuscript.

FUNDING

This work was partially supported by Interreg V France-Wallonie-Vlaanderen program-TEXTOS program and Geules Cassées foundation (61-2017).

ACKNOWLEDGMENTS

Authors are grateful to the staff of Reims Maternity Hospital for providing umbilical cords and to the staff of oral surgery department of Reims hospital for providing bone explants and blood samples. Authors also thank N. Bouland and C. Fichel for histology technical support, and Prof. P. Schaaf, Dr. J. Hemmerlé, and Dr. F. Boulmedais from INSERM U1121 and ICS (Strasbourg University, France) for SSCI setup.

SUPPLEMENTARY MATERIAL

The Supplementary Material for this article can be found online at: https://www.frontiersin.org/articles/10.3389/fbioe.2019.00256/full#supplementary-material

REFERENCES

Aghebati-Maleki, L., Dolati, S., Zandi, R., Fotouhi, A., Ahmadi, M., Aghebati, A., et al. (2018). Prospect of mesenchymal stem cells in therapy of osteoporosis: a review. *J. Cell. Physiol.* 29, 1–9. doi: 10.1002/jcp.27833

Anderson, J. M., Rodriguez, A., and Chang, D. T. (2008). Foreign body reaction to biomaterials. *Semin. Immunol.* 20, 86–100. doi: 10.1016/j.smim.2007.11.004

Asatrian, G., Pham, D., Hardy, W. R., James, A. W., and Peault, B. (2015). Stem cell technology for bone regeneration: current status and potential applications. *Stem Cells Cloning Adv. Appl.* 8, 39–48. doi: 10.2147/SCCAA.S48423

Behera, J., and Tyagi, N. (2018). Exosomes: mediators of bone diseases, protection, and therapeutics potential. *Oncoscience* 5, 181–195. doi: 10.18632/oncoscience.421

Bruder, S. P., Fink, D. J., and Caplan, A. I. (1994). Mesenchymal stem cells in bone development, bone repair, and skeletal regeneration therapy. *J. Cell. Biochem.* 56, 283–294. doi: 10.1002/jcb.240560303

Bruder, S. P., Jaiswal, N., Ricalton, N. S., Mosca, J. D., Kraus, K. H., and Kadiyala, S. (1998). Mesenchymal stem cells in osteobiology and applied bone regeneration. *Clin. Orthop. Relat. Res.* 335, S247–S256. doi: 10.1097/00003086-199810001-00025

Cado, G., Kerdjoudj, H., Chassepot, A., Lefort, M., Benmlih, K., Hemmerlé, J., et al. (2012). Polysaccharide films built by simultaneous or alternate spray: a rapid way to engineer biomaterial surfaces. *Langmuir* 28, 8470–8478. doi: 10.1021/la300563s

Chim, S. M., Tickner, J., Chow, S. T., Kuek, V., Guo, B., Zhang, G., et al. (2013). Angiogenic factors in bone local environment. *Cytokine Growth Factor Rev.* 24, 297–310. doi: 10.1016/j.cytogfr.2013.03.008

Crane, J. L., Xian, L., and Cao, X. (2016). Role of TGF-β signaling in coupling bone remodeling. *Methods Mol. Biol.* 1344, 287–300. doi: 10.1007/978-1-4939-2966-5_18

Gao, C., Peng, S., Feng, P., and Shuai, C. (2017). Bone biomaterials and interactions with stem cells. *Bone Res.* 5:17059. doi: 10.1038/boneres.2017.59

Gentleman, E., Swain, R. J., Evans, N. D., Boonrungsiman, S., Jell, G., Ball, M. D., et al. (2009). Comparative materials differences revealed in engineered bone as a function of cell-specific differentiation. *Nat. Mater.* 8, 763–770. doi: 10.1038/nmat2505

Gerber, H. P., Vu, T. H., Ryan, A. M., Kowalski, J., Werb, Z., and Ferrara, N. (1999). VEGF couples hypertrophic cartilage remodeling, ossification and angiogenesis during endochondral bone formation. *Nat. Med.* 5, 623–628. doi: 10.1038/9467

Glenn, J. D., and Whartenby, K. A. (2014). Mesenchymal stem cells: Emerging mechanisms of immunomodulation and therapy. *World J. Stem Cells.* 6, 526–539. doi: 10.4252/wjsc.v6.i5.526

Golchin, A., and Farahany, T. Z. (2019). Biological products: cellular therapy and FDA approved products. *Stem Cell Rev.* 15: 166–175. doi: 10.1007/s12015-018-9866-1

Haumer, A., Bourgine, P. E., Occhetta, P., Born, G., Tasso, R., and Martin, I. (2018). Delivery of cellular factors to regulate bone healing. *Adv. Drug Deliv. Rev.* 129, 285–294. doi: 10.1016/j.addr.2018.01.010

Helmy, A., Antoniades, C. A., Guilfoyle, M. R., Carpenter, K. L. H., and Hutchinson, P. J. (2012). Principal component analysis of the cytokine and chemokine response to human traumatic brain injury. *PLoS ONE* 7:e39677. doi: 10.1371/journal.pone.0039677

Jin, Y. Z., and Lee, J. H. (2018). Mesenchymal stem cell therapy for bone regeneration. *Clin. Orthop. Surg.* 10, 271–278. doi: 10.4055/cios.2018.10.3.271

Kaigler, D., Krebsbach, P. H., West, E. R., Horger, K., Huang, Y. C., and Mooney, D. J. (2005). Endothelial cell modulation of bone marrow stromal cell osteogenic potential. *FASEB J.* 19, 665–667. doi: 10.1096/fj.04-2529fje

Kon, T., Cho, T. J., Aizawa, T., Yamazaki, M., Nooh, N., Graves, D., et al. (2001). Expression of osteoprotegerin, receptor activator of NF-κB ligand (Osteoprotegerin Ligand) and related proinflammatory cytokines during fracture healing. *J. Bone Miner. Res.* 16, 1004–1014. doi: 10.1359/jbmr.2001.16.6.1004

Li, Y., Xiao, Y., and Liu, C. (2017). The horizon of materiobiology: a perspective on material-guided cell behaviors and tissue Engineering. *Chem. Rev.* 117, 4376–4421. doi: 10.1021/acs.chemrev.6b00654

Lin, D., Chai, Y., Ma, Y., Duan, B., Yuan, Y., and Liu, C. (2018). Rapid initiation of guided bone regeneration driven by spatiotemporal delivery of IL-8 and BMP-2 from hierarchical MBG-based scaffold. *Biomaterials* 17, 1–16. doi: 10.1016/j.biomaterials.2018.05.011

Luu, N. T., McGettrick, H. M., Buckley, C. D., Newsome, P. N., Rainger, G. E., Frampton, J., et al. (2013). Crosstalk between mesenchymal stem cells and endothelial cells leads to downregulation of cytokine-induced leukocyte recruitment. *Stem Cells* 31, 2690–2702. doi: 10.1002/stem.1511

Marsell, R., and Einhorn, T. A. (2011). The biology of fracture healing. *Injury* 42, 551–555. doi: 10.1016/j.injury.2011.03.031

McGettrick, H. M., Butler, L. M., Buckley, C. D., Rainger, G. E., and Nash, G. B. (2012). Tissue stroma as a regulator of leukocyte recruitment in inflammation. *J. Leukoc. Biol.* 91, 385–400. doi: 10.1189/jlb.0911458

Mechiche Alami, S., Gangloff, S. C., Laurent-Maquin, D., Wang, Y., and Kerdjoudj, H. (2016). Concise review: *in vitro* formation of bone-like nodules sheds light on the application of stem cells for bone regeneration. *Stem Cells Transl. Med.* 5, 1587–1593. doi: 10.5966/sctm.2015-0413

Mechiche Alami, S., Rammal, H., Boulagnon-Rombi, C., Velard, F., Lazar, F., Drevet, R., et al. (2017). Harnessing Wharton's jelly stem cell differentiation into bone-like nodule on calcium phosphate substrate without osteoinductive factors. *Acta Biomater.* 49, 575–589. doi: 10.1016/j.actbio.2016.11.042

Mechiche Alami, S., Velard, F., Draux, F., Siu Paredes, F., Josse, J., Lemaire, F., et al. (2014). Gene screening of Wharton's jelly derived stem cells. *Biomed. Mater. Eng.* 24, 53–61. doi: 10.3233/BME-140974

Mountziaris, P. M., and Mikos, A. G. (2008). Modulation of the inflammatory response for enhanced bone tissue regeneration. *Tissue Eng. Part B Rev.* 14, 179–186. doi: 10.1089/ten.teb.2008.0038

Najar, M., Krayem, M., Merimi, M., Burny, A., Meuleman, N., Bron, D., et al. (2018). Insights into inflammatory priming of mesenchymal stromal cells: functional biological impacts. *Inflamm. Res.* 67, 467–477. doi: 10.1007/s00011-018-1131-1

Place, E. S., Evans, N. D., and Stevens, M. M. (2009). Complexity in biomaterials for tissue engineering. *Nat. Mater.* 8, 457–470. doi: 10.1038/nmat2441

Raisz, L. G. (1999). Prostaglandins and bone: physiology and pathophysiology. *Osteoarthritis Cartilage* 7, 419–421. doi: 10.1053/joca.1998.0230

Rammal, H., Dubus, M., Aubert, L., Reffuveille, F., Laurent-Maquin, D., Terryn, C., et al. (2017a). Bioinspired nanofeatured substrates: suitable environment for bone regeneration. *ACS Appl. Mater. Interfaces.* 9, 12791–12801. doi: 10.1021/acsami.7b01665

Rammal, H., Harmouch, C., Maerten, C., Gaucher, C., Boulmedais, F., Schaaf, P., et al. (2017b). Upregulation of endothelial gene markers in Wharton's jelly mesenchymal stem cells cultured on polyelectrolyte multilayers. *J. Biomed. Mater. Res. A.* 105, 292–300. doi: 10.1002/jbm.a.35868

Saito, A., Nagaishi, K., Iba, K., Mizue, Y., Chikenji, T., Otani, M., et al. (2018). Umbilical cord extracts improve osteoporotic abnormalities of bone marrow-derived mesenchymal stem cells and promote their therapeutic effects on ovariectomised rats. *Sci. Rep.* 8:1161. doi: 10.1038/s41598-018-19516-6

Schaefer, A., Te Riet, J., Ritz, K., Hoogenboezem, M., Anthony, E. C., Mul, F. P., et al. (2014). Actin-binding proteins differentially regulate endothelial cell stiffness, ICAM-1 function and neutrophil transmigration. *J. Cell Sci.* 127, 4470–4482. doi: 10.1242/jcs.154708

Sugimoto, M. A., Sousa, L. P., Pinho, V., Perretti, M., and Teixeira, M. M. (2016). Resolution of inflammation: what controls its onset? *Front. Immunol.* 7:160. doi: 10.3389/fimmu.2016.00160

Tang, Y., Wu, X., Lei, W., Pang, L., Wan, C., Shi, Z., et al. (2009). TGF-beta1-induced migration of bone mesenchymal stem cells couples bone resorption with formation. *Nat. Med.* 15, 757–765. doi: 10.1038/nm.1979

Ucuzian, A. A., and Greisler, H. P. (2007). *In vitro* models of angiogenesis. *World J. Surg.* 31, 654–663. doi: 10.1007/s00268-006-0763-4

Von Wedel-Parlow, M., Schrot, S., Lemmen, J., Treeratanapiboon, L., Wegener, J., and Galla, H. J. (2011). Neutrophils cross the BBB primarily on transcellular pathways: an *in vitro* study. *Brain Res.* 1367, 62–76. doi: 10.1016/j.brainres.2010.09.076

Wang, Y., Chen, X., Cao, W., and Shi, Y. (2014). Plasticity of mesenchymal stem cells in immunomodulation: pathological and therapeutic implications. *Nat. Immunol.* 15, 1009–1016. doi: 10.1038/ni.3002

Wu, M., Chen, G., and Li, Y. (2016). TGF-β and BMP signaling in osteoblast, skeletal development, and bone formation, homeostasis and disease. *Bone Res.* 4:16009. doi: 10.1038/boneres.2016.9

Zhang, K., Wang, S., Zhou, C., Cheng, L., Gao, X., Xie, X., et al. (2018a). Advanced smart biomaterials and constructs for hard tissue engineering and regeneration. *Bone Res.* 6:31. doi: 10.1038/s41413-018-0032-9

Zhang, Y., Yang, W., Devit, A., and Van den Beucken, J. J. J. P. (2018b). Efficiency of coculture with angiogenic cells or physiological BMP-2 administration on improving osteogenic differentiation and bone formation of MSCs. *J. Biomed. Mater. Res. A* 9999, 1–11. doi: 10.1002/jbm.a.36581

Conflict of Interest: The authors declare that the research was conducted in the absence of any commercial or financial relationships that could be construed as a potential conflict of interest.

frontiers in Bioengineering and Biotechnology

ORIGINAL RESEARCH
published: 16 October 2019
doi: 10.3389/fbioe.2019.00266

3D-Printed PCL/PPy Conductive Scaffolds as Three-Dimensional Porous Nerve Guide Conduits (NGCs) for Peripheral Nerve Injury Repair

Sanjairaj Vijayavenkataraman[1,2,3]*, *Sathya Kannan*[4], *Tong Cao*[4], *Jerry Y. H. Fuh*[1], *Gopu Sriram*[4] *and Wen Feng Lu*[1]*

[1] Department of Mechanical Engineering, National University of Singapore, Singapore, Singapore, [2] Division of Engineering, New York University Abu Dhabi, Abu Dhabi, United Arab Emirates, [3] Department of Mechanical Engineering, Tandon School of Engineering, New York University, New York, NY, United States, [4] Faculty of Dentistry, National University of Singapore, Singapore, Singapore

OPEN ACCESS

Edited by:
Maria Chatzinikolaidou, University of Crete, Greece

Reviewed by:
ZuFu Lu, University of Sydney, Australia
Pavel Makarevich, Lomonosov Moscow State University, Russia

***Correspondence:**
Sanjairaj Vijayavenkataraman
vs89@nyu.edu
Wen Feng Lu
mpelwf@nus.edu.sg

Specialty section:
This article was submitted to Tissue Engineering and Regenerative Medicine, a section of the journal Frontiers in Bioengineering and Biotechnology

Received: *19 July 2019*
Accepted: *27 September 2019*
Published: *16 October 2019*

Citation:
Vijayavenkataraman S, Kannan S, Cao T, Fuh JYH, Sriram G and Lu WF (2019) 3D-Printed PCL/PPy Conductive Scaffolds as Three-Dimensional Porous Nerve Guide Conduits (NGCs) for Peripheral Nerve Injury Repair. Front. Bioeng. Biotechnol. 7:266. doi: 10.3389/fbioe.2019.00266

Conductivity is a desirable property of an ideal nerve guide conduit (NGC) that is being considered for peripheral nerve regeneration. Most of the conductive polymers reported in use for fabrication of tissue engineering scaffolds such as polypyrrole (PPy), polyaniline, polythiophene, and poly(3,4-ethylenedioxythiophene) are non-biodegradable and possess weak mechanical properties to be fabricated into 3D structures. In this study, a biodegradable and conductive block copolymer of PPy and Polycaprolactone (PPy-b-PCL) was used to fabricate 3D porous NGCs using a novel electrohydrodynamic jet 3D printing process which offers superior control over fiber diameter, pore size, porosity, and fiber alignment. PCL/PPy scaffolds with three different concentrations of PPy-b-PCL (0.5, 1, and 2% v/v) were fabricated as a mesh (pore size 125 ± 15 μm) and the effect of incorporation of PPy-b-PCL on mechanical properties, biodegradability, and conductivity of the NGCs were studied. The mechanical properties of the scaffolds decreased with the addition of PPy-b-PCL which aided the ability to fabricate softer scaffolds that are closer to the properties of the native human peripheral nerve. With increasing concentrations of PPy-b-PCL, the scaffolds displayed a marked increase in conductivity (ranging from 0.28 to 1.15 mS/cm depending on concentration of PPy). Human embryonic stem cell-derived neural crest stem cells (hESC-NCSCs) were used to investigate the impact of PPy-b-PCL based conductive scaffolds on the growth and differentiation to peripheral neuronal cells. The hESC-NCSCs were able to attach and differentiate to peripheral neurons on PCL and PCL/PPy scaffolds, in particular the PCL/PPy (1% v/v) scaffolds supported higher growth of neural cells and a stronger maturation of hESC-NCSCs to peripheral neuronal cells. Overall, these results suggest that PPy-based conductive scaffolds have potential clinical value as cell-free or cell-laden NGCs for peripheral neuronal regeneration.

Keywords: EHD-jet 3D printing, nerve guide conduit, tissue engineering scaffolds, conductive scaffolds, stem cells, peripheral nerve injury

INTRODUCTION

Scaffolds play an integral role in tissue engineering and regeneration by providing the structural support and mechanical cues for the adhesion, growth, proliferation, and differentiation of cells (O'brien, 2011; Vijayavenkataraman et al., 2017). Biocompatibility, biodegradability, porous, and biomimetic architecture are some of the essential properties of tissue engineering scaffolds (Zhang et al., 2019). In addition to these basic requirements, conductivity is a highly desirable property (Balint et al., 2014). Normal biological functions such as wound healing, muscle contraction, and nerve signaling are significantly influenced and controlled by the bioelectricity present in the human body (Ghasemi-Mobarakeh et al., 2011). Hence, providing a conductive scaffold would help in enhanced tissue regeneration by providing a connecting link for the normal bioelectric flow in the body. In addition, the cellular activities such as cell migration, DNA synthesis and protein secretion could be modulated by external electrical stimulation (Rouabhia et al., 2013; Wang et al., 2017).

Nerve Guide Conduits (NGCs) are being pursued as alternate method of treatment for peripheral nerve injuries (PNI), to overcome the shortcomings of autografts (Vijayavenkataraman et al., 2018). Conductivity plays a critical role in neuronal tissue regeneration (Ghasemi-Mobarakeh et al., 2011). Hence, in neural tissue engineering and neuronal regeneration treatment of neurodegenerative diseases such as Parkinson's disease, there is an emphasis on using conductive substrates and scaffolds to enhance the electrical conduction through the tissue engineering scaffolds to increase cell differentiation and tissue regeneration (Sirivisoot et al., 2014). The most commonly used conductive polymers in tissue engineering are polypyrrole (PPy), polyaniline (PANI), polythiophene (PTh), and poly(3,4-ethylenedioxythiophene) (PEDOT) (Balint et al., 2014). Most of the biological studies involving conductive polymers are performed on 2D substrates (Jakubiec et al., 1998; Gumus et al., 2010; Ghasemi-Mobarakeh et al., 2011). However, it is a well-known and well-established fact that the three-dimensional (3D) microenvironment mimics the natural tissue conditions in the body more closely than traditional monolayer cultures (Cukierman et al., 2001; Pampaloni et al., 2007). Conductive polymers possess weak mechanical properties and poor processability to be fabricated into 3D scaffolds (Lee, 2013). Conductive polymers can be mixed or copolymerized along with other polymers such as polycaprolactone (PCL) to enhance the mechanical and rheological properties and thereby its processability into 3D scaffolds.

There are previous works reported on conductive electrospun scaffolds for tissue engineering of neural, cardiac, and skeletal muscles, where a conducting polymer is mixed with other electrospinnable polymers are fabricated into nanofibrous scaffolds. Some of these works include electrospinning of PPy-Polyethylene Oxide (PEO) (Chronakis et al., 2006), PANI-gelatin (Li et al., 2006), PANI-Polycaprolactone (PCL) (Chen et al., 2013), PANI-PCL-gelatin (Ghasemi-Mobarakeh et al., 2009), and PPy-Poly(lactic acid) (PLA) (Zong et al., 2005). In these studies, the conductive scaffolds were found beneficial to the neural cell proliferation, growth, and differentiation, however, there are a few limitations. Firstly, the conductive polymers that were used are non-biodegradable. Biodegradability is an important prerequisite of any tissue engineering scaffold. Secondly, the limitations of the electrospinning process in terms of less control over the micro- and macro-architecture of the scaffolds (Jaworek and Krupa, 1999). The pore size, porosity, and fiber direction cannot be controlled precisely in the electrospinning process.

To overcome the above limitations, in this work, we used a novel 3D printing process called electrohydrodynamic jet (EHD-jet) 3D printing is used to print PCL-based scaffolds (Liu et al., 2017; Wu et al., 2017), which offers a superior control over pore size, porosity, fiber diameter, and alignment. Furthermore, to enable conductive properties to the scaffolds, PCL was mixed with a conductive block copolymer of PPy and PCL (PPy-b-PCL) (shown in **Figure 1**). Three different concentrations of PPy-b-PCL (0.5, 1, and 2% v/v) are mixed with PCL (70% w/v) in glacial acetic acid and fabricated into 3D porous scaffolds. To mimic the tubular nature of NGCs, the sheets of 3D printed scaffolds were rolled into tubular conduits and heat-sealed, and the material, mechanical and biodegradation properties are characterized. As a proof-of-concept for the application of these PCL/PPy-based conductive scaffolds as NGCs for peripheral nerve regeneration, *in vitro* neural differentiation studies were carried out using human embryonic stem cells -derived neural crest stem cells (hESC-NCSCs).

EXPERIMENTAL SECTION

Materials

Polycaprolactone (PCL) pellets (80 kDa), Polypyrrole-block-poly(caprolactone) (PPy-b-PCL) and glacial acetic acid (>99.7% pure) were purchased from Sigma-Aldrich Pte Ltd., Singapore.

Preparation of PCL and PCL/PPy Solution and Scaffold Fabrication

A concentration of 70% (w/v) PCL in acetic acid is was prepared by ultra-sonication at 60°C and 40 kHz for 3 h. For PCL/PPy solution, three different concentrations of PPy-b-PCL (0.5, 1 and 2% v/v) were mixed with acetic acid, PCL pellets (70% w/v) were then added into the PPy-b-PCL/acetic acid solution and was ultra-sonicated at the same conditions. The solutions prepared are then fabricated into 3D scaffolds using an in-house built EHD-jet 3D printing system, the specifications of the system were published in our previous works (Vijayavenkataraman et al., 2018).

Material Characterization

Scanning Electron Microscope, Raman Spectroscopy, and Wettability

Scaffolds were imaged using a scanning electron microscope (JEOL JSM-5500) and an image analysis software (ImageJ, National Institute of Health, Bethesda, MD) was used to calculate the average pore size and fiber diameter. Horiba Jobin Yvon Modular Raman Spectrometer at a laser excitation wavelength of 514 nm (Stellar Pro Argon-ion laser) was used to record the Raman spectra. VAC Optima Surface Analysis

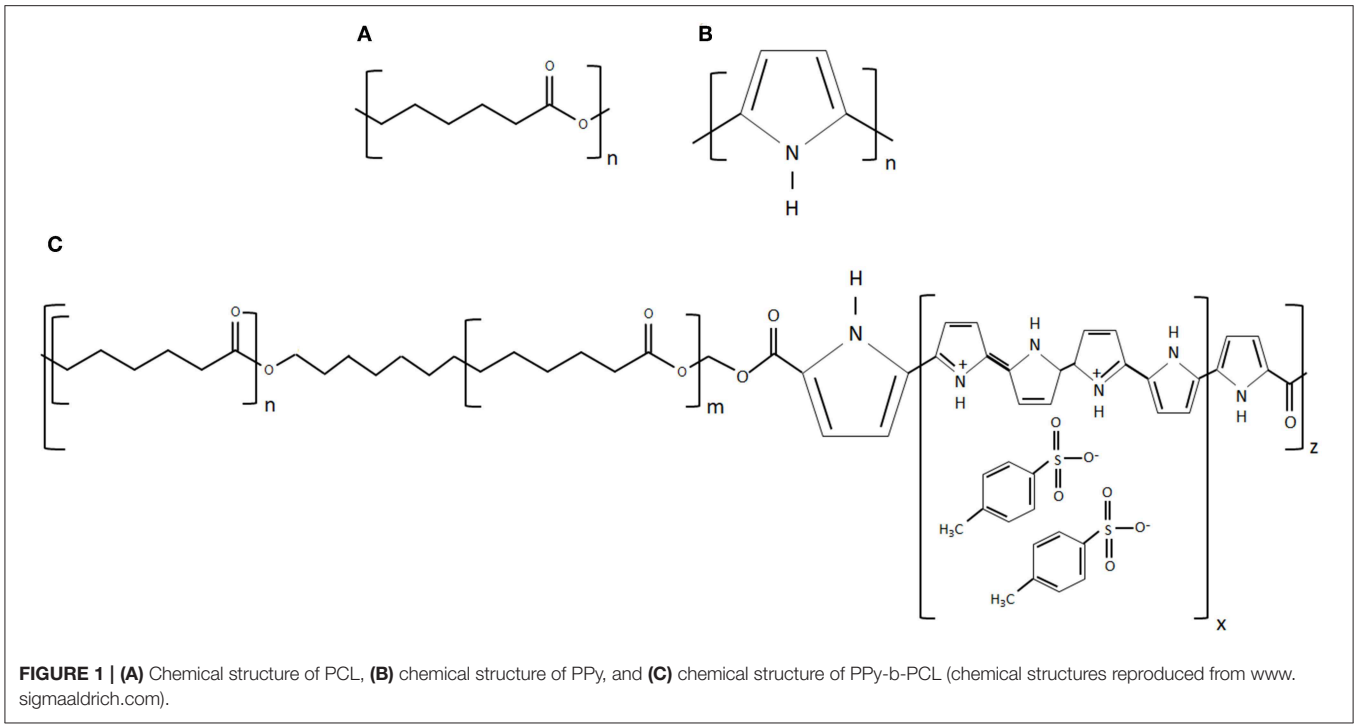

FIGURE 1 | (A) Chemical structure of PCL, **(B)** chemical structure of PPy, and **(C)** chemical structure of PPy-b-PCL (chemical structures reproduced from www.sigmaaldrich.com).

System (AST Products, Billerica, MA) was used to measure the contact angle.

Differential Scanning Calorimetry (DSC), Thermo-Gravimetric Analysis (TGA), and Differential Thermal Analysis (DTA)

DSC and TGA of scaffolds (∼1 mg each) was performed using a differential scanning calorimeter (Perkin-Elmer Diamond DSC) and a thermogravimetric analyzer (Perkin Elmer Pyris 1), respectively, at a heating rate of 10°C/min (Argon atmosphere).

Conductivity

A conductivity meter (SevenCompactTM pH/Ion meter S220, Mettler-Toledo Singapore Pte Ltd., Singapore) was used to measure the conductivity of PCL/PPy-b-PCL solutions.

Mechanical Testing

Mechanical properties of tubular NGCs and rectangular scaffold samples (in degradation studies) were obtained from tensile testing (Instron 3345, USA, 100 N load cell) at 10 mm/min strain rate.

Degradation Studies

The scaffold samples (30 mm long and 5 mm wide) with the initial weight (W_i) were submerged in 10 mL of 0.5 M NaOH solution at a pH of 13.36 and maintained at 37°C in an incubator with shaker to mimic the physiological conditions. One set ($n = 3$) of samples was removed at each time point, dried at room temperature for 48 h, which are then weighed (W_{dry}) and tested for their mechanical properties (refer section Mechanical Testing). Gravimetric analysis was performed to determine the weight loss at each time point using Equation (1).

$$\text{Weight loss}\ (\%) = (W_i - W_{dry})/W_i \times 100\%. \quad (1)$$

Neural Crest Stem Cell *in vitro* Studies

Cell Culture

hESC-NCSCs were used for the cell culture studies. The detailed protocols for obtaining NCSCs from hESCs and differentiation of NCSCs to peripheral neurons are published previously (Zhu et al., 2017). PCL/PPy scaffolds were cut in shape to fit the 24-well plate. The scaffolds were soaked in 70% ethanol for 30 min, and then rinsed twice with phosphate buffered saline (PBS), and DMEM/F12 (Life Technologies). To aid cell attachment (as the scaffolds are relatively hydrophobic), they were coated with Matrigel (BD Biosciences) (10 μg/ml) in DMEM/F12 for 2 h prior to cell seeding at a density of 25,000 cells per cm^2, and were placed in ultralow attachment cell culture plates. Culture media consisted of neurobasal media (Life Technologies) supplemented with 1× non-essential amino acids, 1× GlutaMAX™ (Sigma), 1× N2, 1× B27 (Life Technologies), 20 ng/ml EGF (Sigma), 20 ng/ml bFGF, 10 ng/ml nerve growth factor-β, and 25 μM Y27632 (Miltenyi Biotec) for differentiation of hESC-derived NCSCs to peripheral neurons. Media changes were performed once every 3 days for 2 weeks, after which the differentiated peripheral neurons were analyzed for protein expression by immunocytochemistry.

Cell Proliferation Assay

Cell proliferation was investigated by performing MTS assay (CellTiter 96 AQueous One Solution Cell Proliferation Assay, Promega) at 3 and 7 days. Cells were seeded as mentioned

above onto the PCL/PCLPPy scaffolds placed within ultralow attachment 24-well plates. Cells were washed with 1× PBS and incubated with CellTiter 96® AQueous One Solution in DMEM for 1 h at 37°C. After incubation the supernatant was removed to a 96-well plate and the absorbance was measured at 490 nm with Infinite 200 microplate reader (Tecan). Negative control included CellTiter 96 AQueous One Solution in DMEM without cells.

RT-PCR

The RNA from cultured cells were isolated using MN NucleoSpin RNA kit (Macherey-Nagel, Germany) according to the manufacturer's instructions. Nanodrop ND-1000 spectrophotometer (Nanodrop technologies, Wilmington, DE) was used to quantify the extracted RNA. 1 μg of mRNA was reverse transcribed into cDNA using iScript™ cDNA Synthesis Kit (BioRad) in the MyCycler™ Thermal Cycler System (BioRad). Real-time PCR was performed in triplicates with 500 ng cDNA template per reaction using iTaq™ Universal SYBR Green Supermix (BioRad) and CFX Connect™ Real-Time System (BioRad) as per manufacturer's instructions. The sequences of the forward and reverse primers of genes analyzed are provided in **Supplementary Table 1**. The target gene expression was normalized to GAPDH as the internal control, and results were expressed as fold change relative to cells grown on control PCL scaffolds.

Immunocytochemistry and Image Analysis

Cells were fixed with 4% paraformaldehyde (Sigma) for 30 min at room temperature. Fixed cells were permeabilized using 0.1% TritonX-100/PBS (Sigma) for 10 min, washed thrice with 0.05% Tween-20/PBS (Sigma), and blocked with 2% bovine serum albumin/5% goat serum for 60 min to prevent non-specific binding. Subsequently, the cells were labeled with β3 tubulin [1:200, Santa Cruz sc-58888, monoclonal (Clone TuJ-1)] and neurofilament heavy (NF-H) (1:600, Abcam ab8135, polyclonal) primary antibodies at 4°C overnight. After washing, the cells were fluorescently labeled using appropriate secondary antibodies Alexa Flour 488 and Alexa Flour 594 (Life Technologies) for 60 min, then counterstained with 4′,6-diamidino-2-phenylindole (DAPI, Sigma). Images were taken with Olympus FV1000 confocal microscope. Imaris software was used to quantify the protein markers β3 tubulin and NF-H. From the immunostained 3D z-stack images, mean fluorescent intensity values of β3 tubulin (green channel) and NF-H (red channel) were measured, from which the fluorescence was normalized to β3 tubulin expression to obtain the normalized fluorescence intensity. Then, total volume of expression for these two proteins were calculated; data was normalized to the total cell numbers (based on counting DAPI stained nuclei) present in each region of interest to get the level of expression of the two proteins. Detailed information provided in supplementary information (**Supplementary Figure 1** and **Supplementary Materials**).

Statistical Analysis

Experiments were run in triplicates and all measurements were expressed as mean ± SD. One-way ANOVA test and Independent 2-sample *t*-test were used to determine the differences between the mean values of the experimental groups Differences (statistically significant at $p < 0.05$).

RESULTS

Impact of PCL-b-PPy on Scaffold Surface Characteristics

Figures 2A–H shows the SEM images of PCL (**Figures 2A,B**), PCL/PPy 0.5% (**Figures 2C,D**), PCL/PPy 1% (**Figures 2E,F**),

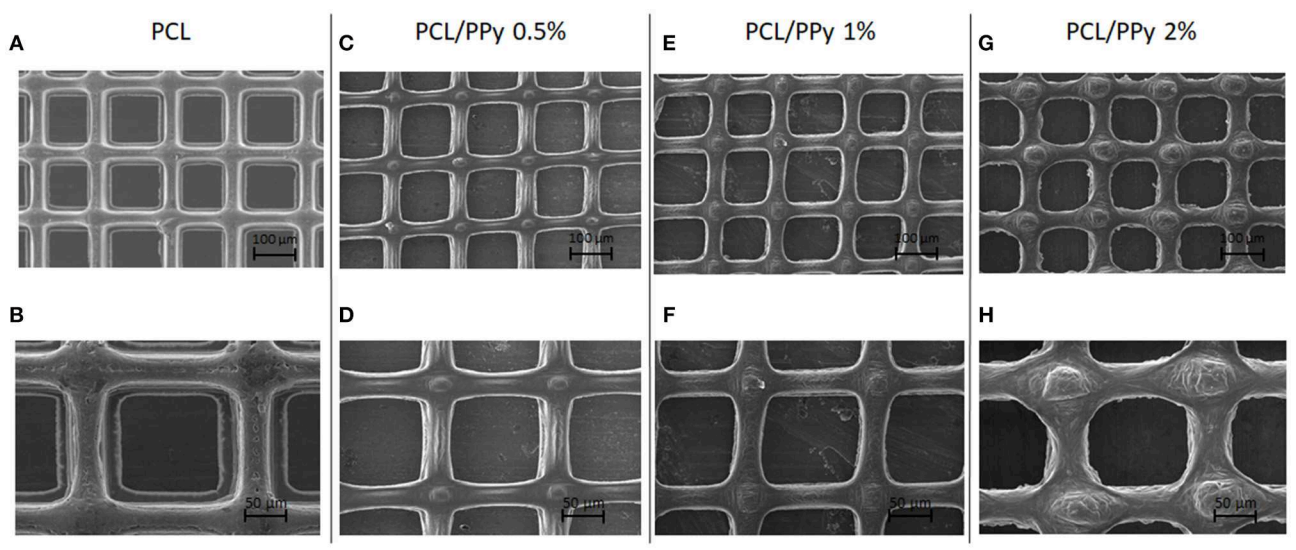

FIGURE 2 | SEM images of EHD-jet 3D-printed scaffolds for nerve guide conduits (NGCs) (input voltage = 2.4 kV, stage speed = 75 mm/min, flow rate = 10 μl/min, nozzle-to-substrate distance = 2 mm) **(A,B)** PCL scaffolds, **(C,D)** PCL/PPy 0.5%, **(E,F)** PCL/PPy 1%, and **(G,H)** PCL/PPy 2% at different magnifications.

and PCL/PPy 2% (**Figures 2G,H**) scaffolds. The average fiber diameters measured are 30 ± 10 μm (PCL), 33 ± 8 μm (PCL/PPy 0.5%), 38 ± 7 μm (PCL/PPy 1%), and 44 ± 5 μm (PCL/PPy 2%), with an average pore size of 125 ± 15 μm. The addition of PPy-b-PCL changes the scaffold surface texture, with rigid fibers and sharp edges in PCL scaffolds and blunt fibers and rounded edges in PCL/PPy scaffolds (more rounded with increasing PPy-b-PCL) as visible in PCL/PPy 2% in **Figures 2G,H**.

Impact of PCL-b-PPy on Material Composition of PCL Scaffolds

The Raman spectrum of the EHD-jetted scaffolds is shown in **Figure 3**, the band positions and assignments (Vigmond et al., 1995; Chen et al., 2003) are tabulated in **Table 1**. The characteristic peaks of PCL (1,725, 2,916, 1,116, 916 cm^{-1}) are present in both as-received PCL pellets and EHD-jetted scaffolds suggesting that the EHD-jetting process did not alter the material composition of PCL. The characteristic peaks of PPy, namely C-H in-plane deformation at 1,080 cm^{-1}, C-H ring stretching at 1,320 cm^{-1}, and C=C symmetrical stretching at 1,596 cm^{-1} are present in the PCL/PPy scaffolds but are not present in as-received PCL pellets and PCL scaffolds, confirming the presence of PPy in the PCL/PPy scaffolds. In summary, the spectrum suggests that there are no major changes in the material composition due to the fabrication process.

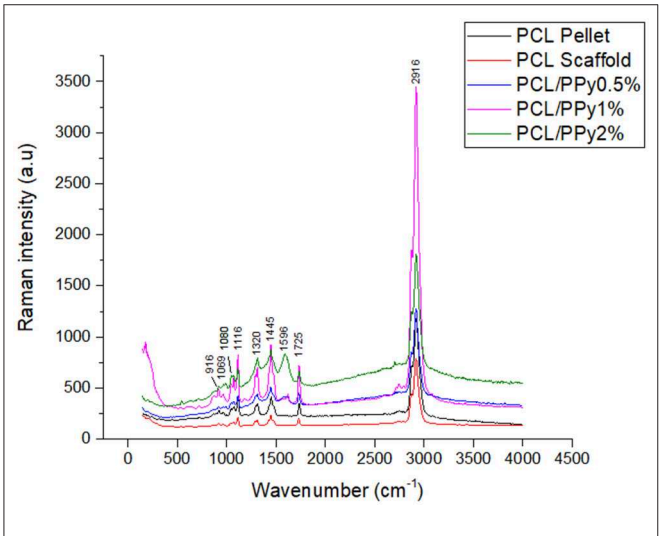

FIGURE 3 | Raman spectra of as-received PCL pellets, and EHD-jetted scaffolds.

TABLE 1 | Raman bands [cm^{-1}] and their assignments for EHD-jetted PCL/PPy Scaffolds (Vigmond et al., 1995; Chen et al., 2003).

Raman bands (cm^{-1})		Assignments
916	PCL	ν(C–COO); crystalline
1,069	PCL	ν(COC); crystalline
1,080	PPy	C-H in-plane deformation
1,116	PCL	ν(COC); crystalline
1,320	PPy	C-H ring stretching
1,445	PCL	$\delta(CH_2)$; crystalline
1,596	PPy	C=C symmetrical stretching
1,725	PCL/PPy	ν(C=O); crystalline
2,916	PCL	Antisymmetric C–H stretching $\nu(CH_2)_{asym}$

Addition of PCL-b-PPy Has Minimal Impact on Hydrophilicity of PCL Scaffolds

The wettability of EHD-jetted scaffolds are measured to be 71.7 ± 4.1° (PCL), 73.7 ± 3.1° (PCL/PPy 0.5%), 74.7 ± 3.9° (PCL/PPy 1%), and 76.6 ± 1.7° (PCL/PPy 2%) as shown in **Figure 4A**. There was no significant changes in the wettability of the scaffolds with the addition of PPy-b-PCL, with only a slight increase of water contact angle due to the hydrophobicity of PPy.

Inclusion of PCL-b-PPy Dramatically Increases the Conductivity of PCL Scaffolds

Conductivity measurements were recorded as 0.09 ± 0.005 μS/cm (PCL) (insignificant, mainly due to acetic acid), 0.28 ± 0.02 mS/cm (PCL/PPy 0.5%), 1.02 ± 0.03 mS/cm (PCL/PPy 1%), and 1.15 ± 0.03 mS/cm (PCL/PPy 2%). There is significant increase in the conductivity with increasing concentration of PPy-b-PCL, as shown in the **Figure 4B**.

Impact of PCL-b-PPy on Thermal Properties of PCL Scaffolds

DSC thermograms, representing the thermal properties of END-jetted scaffolds are shown in **Figure 5A**. The melting point of PCL scaffolds was within 57–64°C range, implied by the endothermic peak observed at 61.28°C (Acharya et al., 2012). The endothermic peak shifted to lower temperatures with addition of PPy-b-PCL (60.01°C for PCL/PPy 0.5%, 58.45°C PCL/PPy 1%, and 56.95°C PCL/PPy 2% scaffolds), indicating PPy-b-PCL presence, which agrees with the previous studies (Lu et al., 2010). Also, it is known from the literature that the endothermic peak (50°C) of pure PPy increased in intensity when grafted with PCL (Mecerreyes et al., 2002). TGA and DTA curves were shown in **Figures 5B,C**, respectively. The onset decomposition temperatures of PCL scaffold is around 300°C (as shown in **Figure 5B**), which is in agreement with the earlier studies (Liu et al., 2013). The onset decomposition temperature of PCL/PPy 0.5%, PCL/PPy 1%, and PCL/PPy 2% scaffolds were greater than that of the PCL scaffold (between 350 and 450°C), indicating the presence of PPy-b-PCL (Ramaprasad et al., 2017). A two-step decomposition process could be observed in all the scaffolds. The first decomposition step for PCL occurs between 50 and 300°C (Arunraj et al., 2013) and for PCL/PPy scaffolds between 50 and 350°C (Najar and Majid, 2014; Ramaprasad et al., 2017). The first step of decomposition is attributed to residual water loss. The second decomposition step for PCL occurs between 300 and 450°C (Arunraj et al., 2013) and for PCL/PPy scaffolds between 350 and 500°C (Najar and Majid, 2014; Ramaprasad et al., 2017). The second step of decomposition is due to the breakdown of the polymer chain, mainly the polysaccharide structure of the molecule (Arunraj et al., 2013). DTA curves

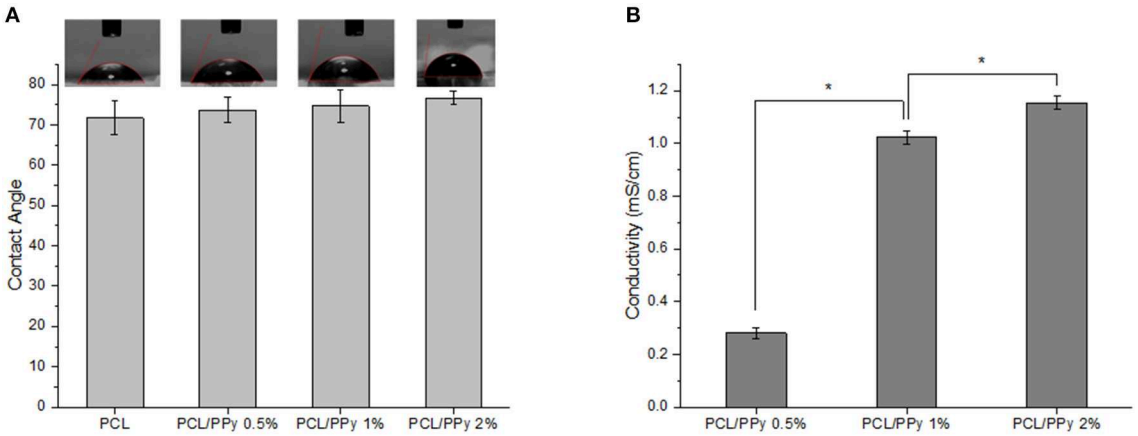

FIGURE 4 | Hydrophilicity and conductivity properties of PCL and PCL/PPy scaffolds **(A)** water contact angle, and **(B)** conductivity of 3D-printed scaffolds ($n = 3$; $^*p < 0.05$).

(**Figure 5C**) shows smaller endothermic peaks between 50 and 350°C, and exothermic peaks between 350 and 450°C, indicating absorbed water loss and continuous polymer chain decomposition, respectively (Liu et al., 2013; Ramaprasad et al., 2017). The DSC and TGA curves of PCL/PPy scaffolds follows the same characteristics as that of pure PCL scaffolds, suggesting that the thermal properties was not significantly altered with PPy-b-PCL addition. PPy-b-PCL renders the conductive property to the scaffolds. Since PCL is a widely used biomaterial and used for *in vivo* experiments already, PCL/PPy scaffolds is also inferred to be safer as the properties are very similar to PCL scaffolds. The DSC and TGA curves also suggest the biodegradability of the EHD-jetted PCL/PPy scaffolds.

Incorporation of PCL-b-PPy Aids Fabrication of Softer Scaffolds Suitable for Neural Applications

The stress-strain curves and the mechanical properties of NGCs are shown in **Figures 6A–F**, respectively. A significant reduction of Young's modulus of the NGC structure was observed between PCL (204 ± 6.7 MPa) and PCL/PPy scaffolds (35 ± 5.6 MPa with PCL/PPy 2%). However, between PCL/PPy 0.5%, PCL/PPy 1%, and PCL/PPy 2%, there is not much difference, with the range of Young's modulus between 51 ± 4.55 MPa (PCL/PPy 0.5%) and 35 ± 5.6 MPa (PCL/PPy 2%). Similar trend is observed with the yield strength and ultimate strength. This demonstrated decrease in the mechanical properties with the addition of PPy-b-PCL is indeed a desired effect as softer scaffolds aid in better neural cell differentiation (Vijayavenkataraman et al., 2017).

Incorporation of PCL-b-PPy Improves Degradation Properties of PCL Scaffolds

The weight loss behavior and representative stress-strain curves (on Days 0 and 14) of the 3D-printed scaffolds are shown in **Figures 7A–C**, respectively.

The scaffold degradation rate increased with increasing PPy-b-PCL concentration (**Figure 7A**), with 55.8% weight loss in PCL/PPy 2% scaffolds against 37.28% in PCL scaffolds at day 14. The pH values of the immersed medium decreased from an initial pH of 13.36–13, for all the four different scaffold types. **Figures 7B,C** shows that all the scaffolds exhibited a typical polymeric stress-strain curve, but for the PCL/PPy 2% scaffolds, all of them lost most of their mechanical strength, corroborating to the weight loss trend.

The mechanical properties evaluated during the scaffold degradation studies are shown in **Table 2**. Better mechanical properties were observed with the rolled NGC structure shown in **Figure 6** than that of the as-printed scaffolds in the degradation study (**Table 2**), the aim of which was to assess the influence of PPy-b-PCL addition on degradation more accurately. From the degradation studies, it can be deduced that the mechanical properties decrease as the weight decreases and attains a minimum after 3 days. From day 7, the scaffolds start disintegrating and the mechanical properties couldn't be determined, the stress-strain curves don't represent the characteristic stress-strain curve of typical polymers.

PCL/PPy (1%) Scaffolds Support Proliferation and Stronger Maturation of NCSCs to Peripheral Neurons

Cell culture on all scaffolds were performed to test if they supported proliferation and differentiation of neural lineage cell types. Here we observed the attachment of hESC-NCSCs to matrigel-coated scaffolds within the first 24 h of cell seeding. To assess the effect of PPy on cell proliferation, MTS assay was performed. Results showed significantly higher proliferation of hESC-NCSCs in all scaffolds containing PPy at days 3 and 7 when compared to pure PCL scaffolds (**Figure 8A**). Addition of PPy 0.5% showed the highest cell proliferation at both time points. Besides, there was a significantly higher proliferation of the hESC-NCSCs between days 3 and 7 in all the scaffolds demonstrating cyo-compatibility over long-term culture. Therefore, putting the results together addition of PPy to

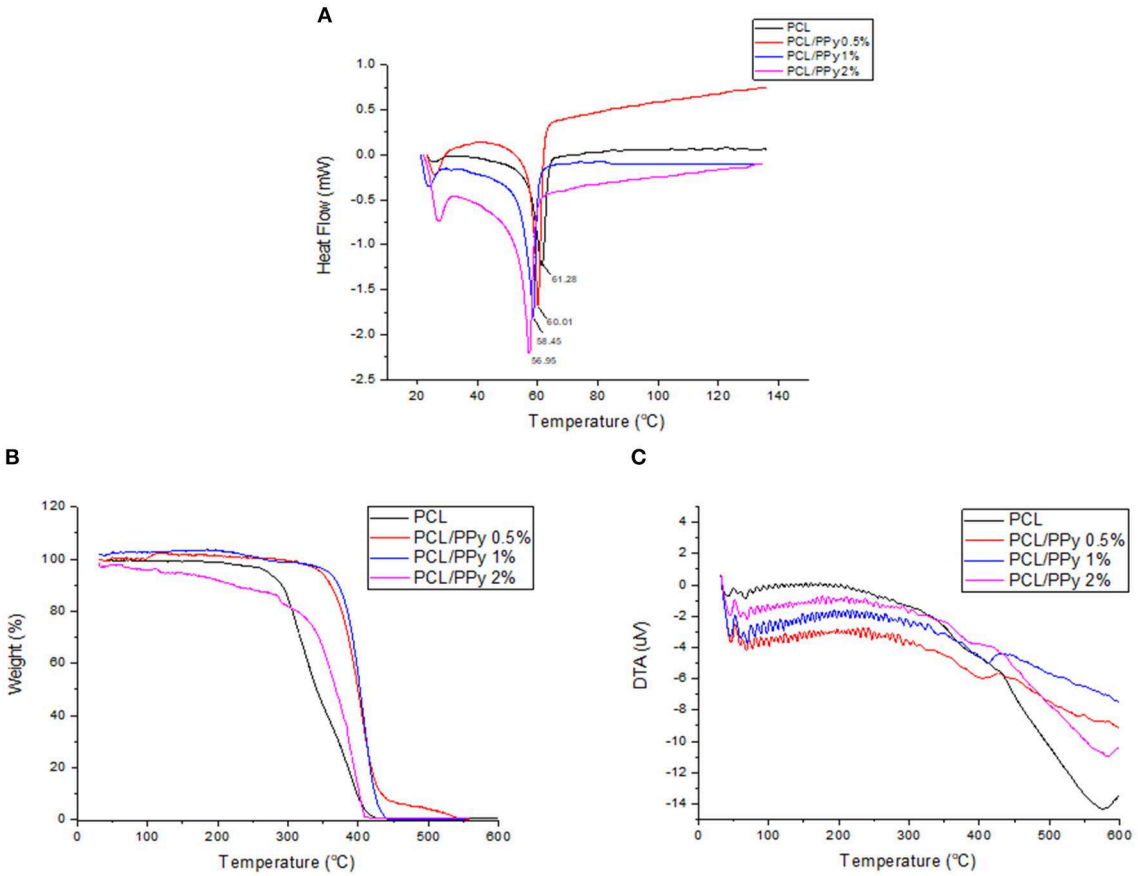

FIGURE 5 | Thermal degradation of PCL and PCL/PPy scaffolds: **(A)** DSC Thermogram, **(B)** TGA curves, and **(C)** DTA curves of EHD-jetted scaffolds.

PCL scaffolds significantly increased the proliferation of hESC-NCSCs over the 7-day culture period.

Impact of PCL/PPy on the differentiation of hESC-NCSCs was assessed by RT-PCR and immunocytochemistry. Gene expression analysis by RT-PCR showed significant downregulation of transcripts for NCSC marker (*HNK1*) in the cells grown on all PCL/PPy scaffolds compared to PCL scaffolds (**Figure 8B**). Secondly, there was not much difference in the expression of *TUBB3* (β3 tubulin, a pan-neuronal marker), except between PCL/PPy1% and PCL/PPy2% (**Figure 8C**). Down-regulation of *HNK1* expression suggest that PCL/PPy aids differentiation of NCSCs, while the lack of difference in *TUBB3* expression among the different scaffolds suggest that the scaffolds aid growth of neural-lineage cells in general. This was further confirmed by the analysis of β3 tubulin by immunocytochemistry (**Figures 9A,B**). Assessment of volumetric fluorescence intensity of β3 tubulin staining showed no significant difference among the different scaffolds suggesting all the scaffold types offer a similar support to neural-lineage cell types (**Figure 9C**).

To specifically assess the differentiation of hESC-NCSCs to peripheral neurons, the expression of transcripts for *PRPH* (Peripherin, a peripheral neuron-specific marker) and *NEFH* (neurofilament-heavy subunit, NF-H; a peripheral neuron maturation marker) was assessed by RT-PCR. The results showed a trend toward higher expression of *PRPH* in PCL/PPy scaffolds, though not statistically significant except PCL/PPY1% scaffold. Additionally, the expression of *NEFH* transcripts, was significantly higher in cells differentiated on all PCL/PPy scaffolds when compared to pure PCL scaffolds (**Figures 8B,C**). These results suggest that PCL/PPy scaffolds potentially aid the differentiation of hESC-NCSCs toward peripheral neurons and in particular support their maturation. This was further confirmed by semi-quantitative assessment of the expression of the protein NF-H by immunocytochemistry (detailed methods for the semi-quantitative assessment are provided in the **Supplementary Information**). Normalized fluorescence intensity of NF-H (normalized to respective β3 tubulin) shows a significantly higher intensity of signals in the PCL/PPy (1 and 2%) scaffolds (**Figure 9B**). Secondly, assessment of volumetric fluorescence intensity of NF-H staining showed significantly higher intensity of signals in the PCL/PPy1% scaffolds. Collectively, these results indicate higher amounts of NF-H expressing mature peripheral neurons in PCL/PPy scaffolds (in particular PCL/PPy1%), Hence, the PCL/PPy scaffolds support differentiation and stronger maturation of peripheral neurons.

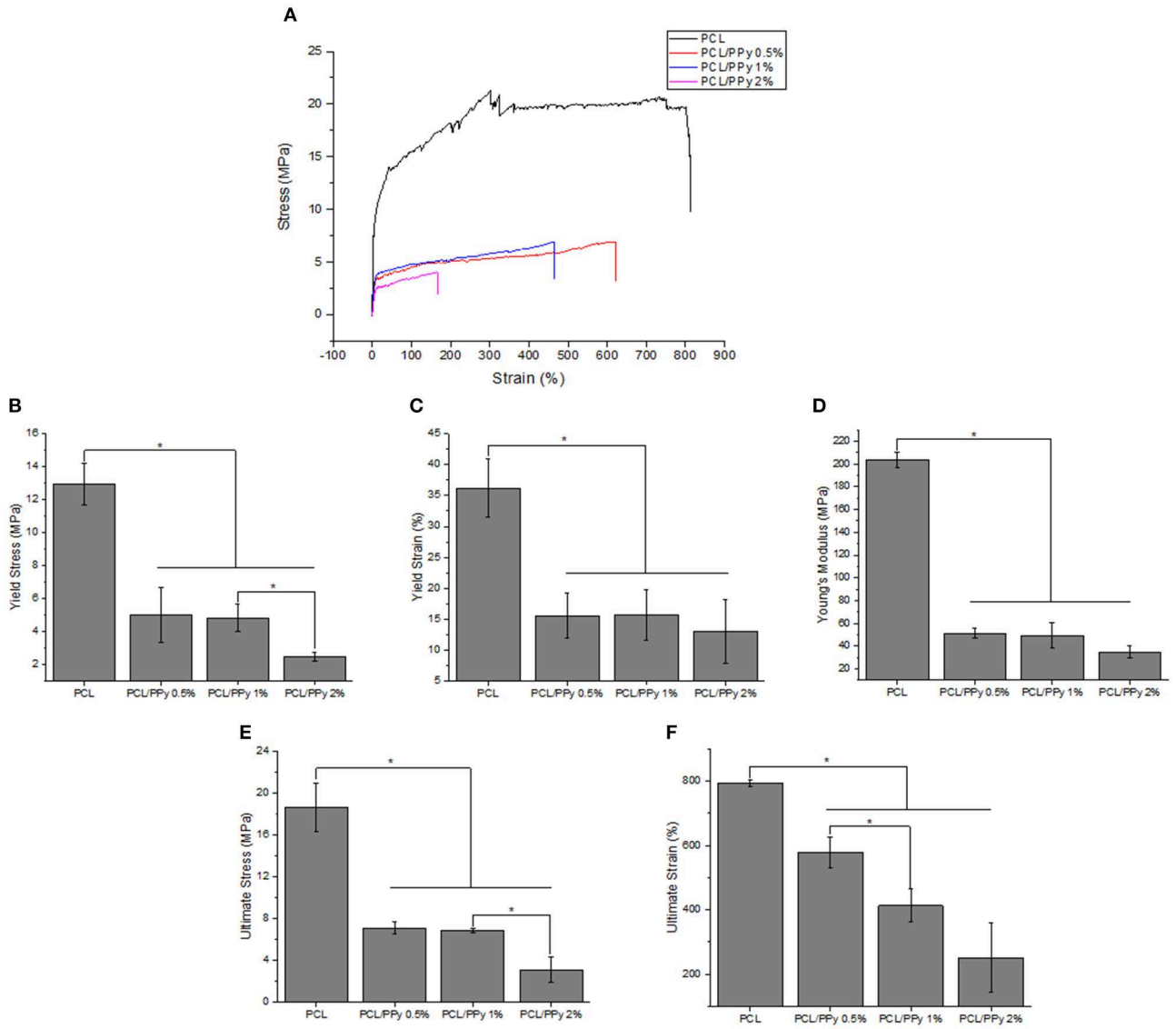

FIGURE 6 | Mechanical properties of PCL and PCL/PPy NGCs: **(A)** representative stress-strain curves **(B)** Young's modulus, **(C)** yield stress, **(D)** yield strain, **(E)** ultimate stress, and **(F)** ultimate strain ($n = 3$, $^*p < 0.05$).

DISCUSSION

Conductivity is a desired property of NGCs which would aid in enhanced electrical conduction thereby increasing the cell differentiation and tissue regeneration (Sirivisoot et al., 2014). Though there are previous reports on electrospinning of conductive nanofibrous scaffolds (Prabhakaran et al., 2011; Sharma et al., 2012), they suffer from 2-fold limitation namely non-biodegradability and inability to control the scaffold morphology precisely. In this study, biodegradable PCL/PPy composites EHD-jetted into 3D porous NGCs (Vijayavenkataraman et al., 2019a,b). The effect of PPy-b-PCL concentration (0.5, 1, and 2%) on the mechanical properties of the NGCs are studied, with pure PCL scaffolds as the control. Our results demonstrated decrease in the mechanical properties with the addition of PPy-b-PCL, which is indeed a desired effect as softer scaffolds aid in better neural cell differentiation (Vijayavenkataraman et al., 2017). Accelerated *in vitro* degradation studies in 0.5 M NaOH solution at a pH of 13.6 demonstrated the degradability of PCL/PPy scaffolds. The degradation rate of PCL/PPy scaffolds are higher compared to the pure PCL scaffolds; the mechanical properties deteriorated with time and loses most of its mechanical strength after day 10.

NGCs fabricated from PCL and PPy-b-PCL has many advantages. Previous studies on conductive scaffolds use non-biodegradable conductive polymers such as PPy, PANI or PEDOT. In this study, a block copolymer of PPy and PCL (PPy-b-PCL) was used which is biocompatible and

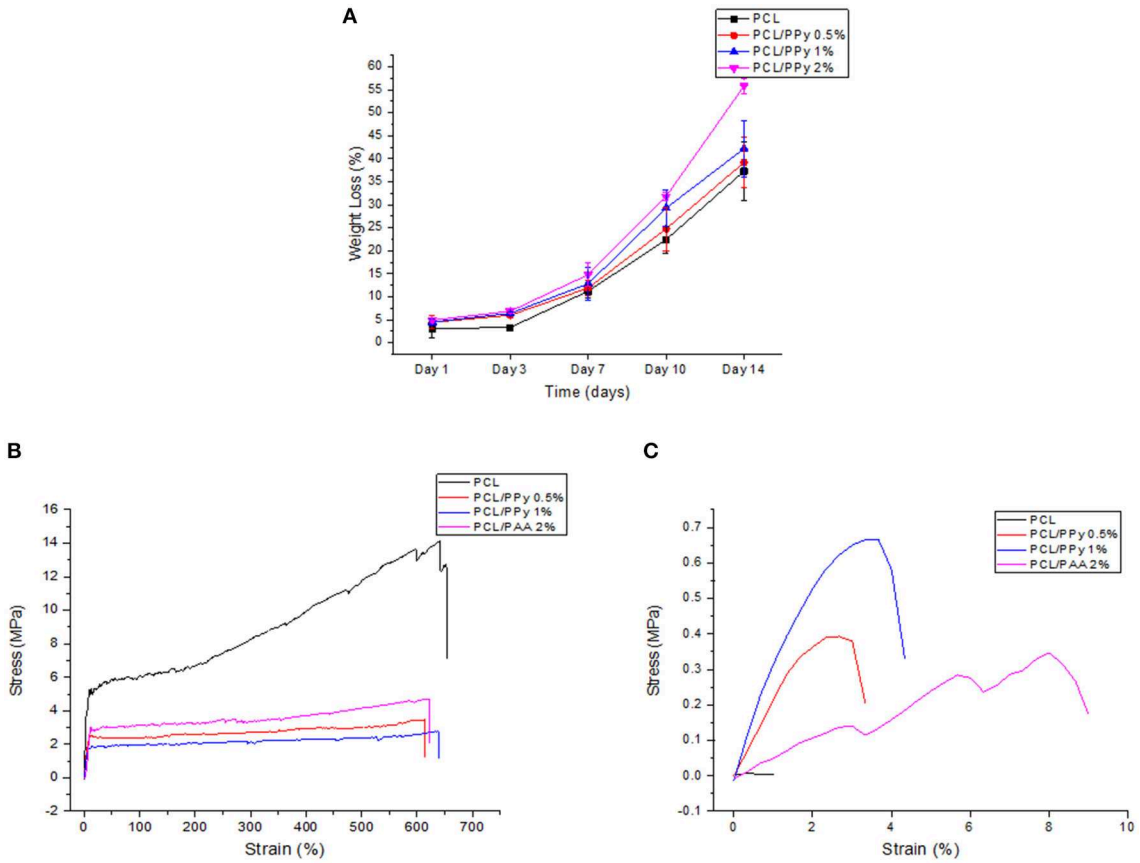

FIGURE 7 | Accelerated degradation studies on PCL and PCL/PPy scaffolds: **(A)** percentage of weight loss as a function of degradation time, **(B)** representative stress-strain curves at day 0, and **(C)** day 14.

biodegradable at the same time (Boutry et al., 2013). PCL is an FDA approved polymer, easy to print and better mechanical stability (Middleton and Tipton, 2000). Ideally, NGCs must provide good structural, mechanical, and conductive support for they act as templates for axonal regeneration (Lackington et al., 2017). PCL provides the structural support and mechanical cues while PPy-b-PCL provides conductive properties that can be exploited for neuronal regeneration.

In this study, we used EHD-jet 3D printing process to print PCL and PCL/PPy (0.5, 1, and 2%) scaffolds, with 125 ± 15 μm pores. In another study of ours using PCL scaffolds with five different pore sizes (ranging from 125 to 550 μm) and *in vitro* neural differentiation of PC12 cells, a pore size of 125 ± 15 μm best supported neural differentiation (Vijayavenkataraman et al., 2018). The sheets of scaffolds were rolled to form NGCs, mimicking the native peripheral nerve dimensions (1.2 mm diameter, ∼200 um wall thickness, 1–3 cm long), porosity > 60% (Chiono and Tonda-Turo, 2015) and with aligned fibers that serve as a directional cue for directing the growth and alignment of neurons. The fibers are directionally aligned and the pore size are precisely controlled in the EHD-jet 3D printing unlike the electrospinning process. Addition of PPy-b-PCL has only a minor influence on the scaffold surface morphology. The PCL/PPy scaffold surface is non-uniform and wavy in nature, which could be attributed to the viscosity changes due to addition of PPy-b-PCL. Raman spectra (**Figure 3**) of PCL/PPy scaffolds suggest that there are no major changes in the material composition due to the fabrication process. The wettability of PCL/PPy scaffolds does not differ significantly from that of pure PCL scaffolds (**Figure 4A**), while the conductivity increases significantly with addition of PPy-b-PCL (**Figure 4B**). The DSC and TGA curves indirectly demonstrates the biodegradability of the EHD-jetted PCL/PPy scaffolds and the thermograms of PCL/PPy scaffolds are characteristically similar to that of pure PCL scaffolds.

The NGC mechanical properties decrease with the addition of PPy-b-PCL, with insignificant difference PCL/PPy 0.5% and PCL/PPy 1% scaffold mechanical properties. The yield strength of the NGC decreases from 12.95 ± 1.26 MPa of that of pure PCL scaffolds to 5.02 ± 1.68 MPa (PCL/PPy 0.5%) and 4.82 ± 0.84 MPa (PCL/PPy 1%), which is closer to the properties of the native human peripheral nerve (∼6.5 MPa) (Dumont and Born, 2005; Nectow et al., 2011). PCL/PPy 2% scaffolds are much weaker than the other scaffolds, which might be due to the viscosity changes due to higher concentration of PPy-b-PCL. NGCs made

TABLE 2 | Mechanical properties of PCL, PCL/PPy 0.5%, PCL/PPy 1%, and PCL/PPy 2% scaffolds at various degradation time points (X denotes indeterminable values).

Mechanical property	Scaffold type	Day 0	Day 1	Day 3	Day 7	Day 10	Day 14
Yield strength	PCL	4.57 ± 0.3	1.2 ± 0.3	1.01 ± 0.5	X	X	X
	PCL/PPy 0.5%	2.38 ± 0.1	1.47 ± 0.02	1.13 ± 0.03	0.57 ± 0.04	X	X
	PCL/PPy 1%	2.19 ± 1.6	3.31 ± 0.6	1.11 ± 0.2	0.82 ± 0.01	0.61 ± 0.02	X
	PCL/PPy 2%	3.05 ± 0.8	1.85 ± 0.8	1.7 ± 0.5	1.21 ± 0.1	0.42 ± 0.1	0.14 ± 0.02
Yield strain	PCL	27.45 ± 2.5	7.17 ± 2.6	4.05 ± 1.6	X	X	X
	PCL/PPy 0.5%	15 ± 2.4	10.56 ± 1.5	8.17 ± 3.5	2.51 ± 0.2	X	X
	PCL/PPy 1%	16.23 ± 2.8	5.89 ± 1.3	2.84 ± 0.7	1.23 ± 0.5	0.58 ± 0.3	X
	PCL/PPy 2%	11.34 ± 0.9	6.34 ± 1.9	5.78 ± 1.5	4.23 ± 0.5	3.21 ± 0.3	3 ± 0.2
Young's modulus	PCL	96.73 ± 4.4	58.63 ± 6.2	42.37 ± 7.5	X	X	X
	PCL/PPy 0.5%	42.97 ± 3.4	28.39 ± 5.7	19.27 ± 3.4	22.53 ± 1.5	X	X
	PCL/PPy 1%	41.12 ± 8.4	29.21 ± 3.2	17.89 ± 5.1	11.95 ± 2.5	2.53 ± 1.1	X
	PCL/PPy 2%	21.08 ± 3.9	20.24 ± 4.4	12.67 ± 2.3	9.42 ± 1.3	5.23 ± 1.8	5.58 ± 2
Ultimate strength	PCL	13.46 ± 1.6	1.68 ± 0.4	1.24 ± 0.9	X	X	X
	PCL/PPy 0.5%	4.4 ± 0.9	3.41 ± 0.2	1.2 ± 0.4	0.73 ± 0.2	X	X
	PCL/PPy 1%	3.26 ± 1.9	3.36 ± 0.5	1.3 ± 0.2	1.43 ± 0.4	0.93 ± 0.3	X
	PCL/PPy 2%	3.15 ± 1.4	2.38 ± 1.5	1.31 ± 0.3	0.85 ± 0.05	0.49 ± 0.02	0.35 ± 0.03
Ultimate strain	PCL	652.19 ± 45	281.75 ± 34	35.75 ± 6.5	X	X	X
	PCL/PPy 0.5%	607.91 ± 11	138.37 ± 22	17 ± 9.9	5.17 ± 1.2	X	X
	PCL/PPy 1%	569.43 ± 26	227.46 ± 13	19.25 ± 12	5.67 ± 0.8	4.23 ± 0.1	X
	PCL/PPy 2%	610.39 ± 12	208.17 ± 8	16.15 ± 6	10.56 ± 5	8.18 ± 0.5	8 ± 0.05

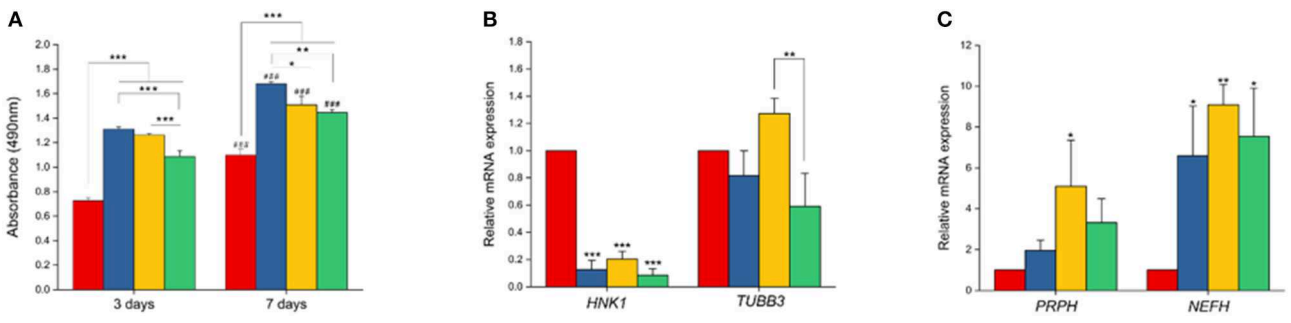

FIGURE 8 | Cell proliferation and gene expression analysis. **(A)** MTS assay. Proliferation of NCSCs were tested at two different time points (3 and 7 days). **(B,C)** Gene expression levels of *HNK1*, *TUBB3*, *PRPH*, and *NEFH* by RT-PCR ($n = 3$ for all experiments). $^{*}p < 0.05$, $^{**}p < 0.01$, $^{***}p < 0.001$. $^{\#\#\#}$in **(A)** refers to statistical significance ($p < 0.001$) when compared to first time-point (day-3) using independent Student *t*-test.

of PCL/PPy thus could withstand the biological stresses when implanted inside the body.

The degradability of the PCL/PPy scaffolds were assessed by accelerated *in vitro* degradation studies using 0.5 M NaOH solution. Degradation studies, if carried out in physiological conditions, might take several months for evaluating the degradation profiles of slow degrading polymers such as PCL. In such cases, accelerated degradation studies are carried out to simulate similar degradation profiles within a short period of time (Lam et al., 2008). Degradation rate of PCL/PPy scaffolds are higher compared to the pure PCL scaffolds, while the scaffolds with the highest PPy-b-PCL concentration having a greater weight loss (**Figure 7**). Although the stress-strain curves of all the scaffolds follow a characteristic stress-strain curve of polymers at the start of the study, the behavior is lost with the passage of time as the scaffolds degrade and disintegrate. Mechanical testing results at different degradation time points (**Table 2**), indicates that the scaffolds start losing their mechanical integrity rapidly starting day 7 and the scaffold begins to disintegrate. It is to be noted that even with such harsh environment, the scaffolds withstand the stress till day 7, having appreciable mechanical properties. Given that the physiological conditions are much milder than the testing conditions, the NGCs could maintain their mechanical integrity much longer than 7 days in *in vivo* conditions.

As a proof-of-concept, in this study we are primarily interested to understand the impact of the conductive scaffolds on promoting peripheral neuronal growth. In our previous study using PCL scaffolds (Vijayavenkataraman et al., 2018), we had used PC12 cells cultured under neural differentiation

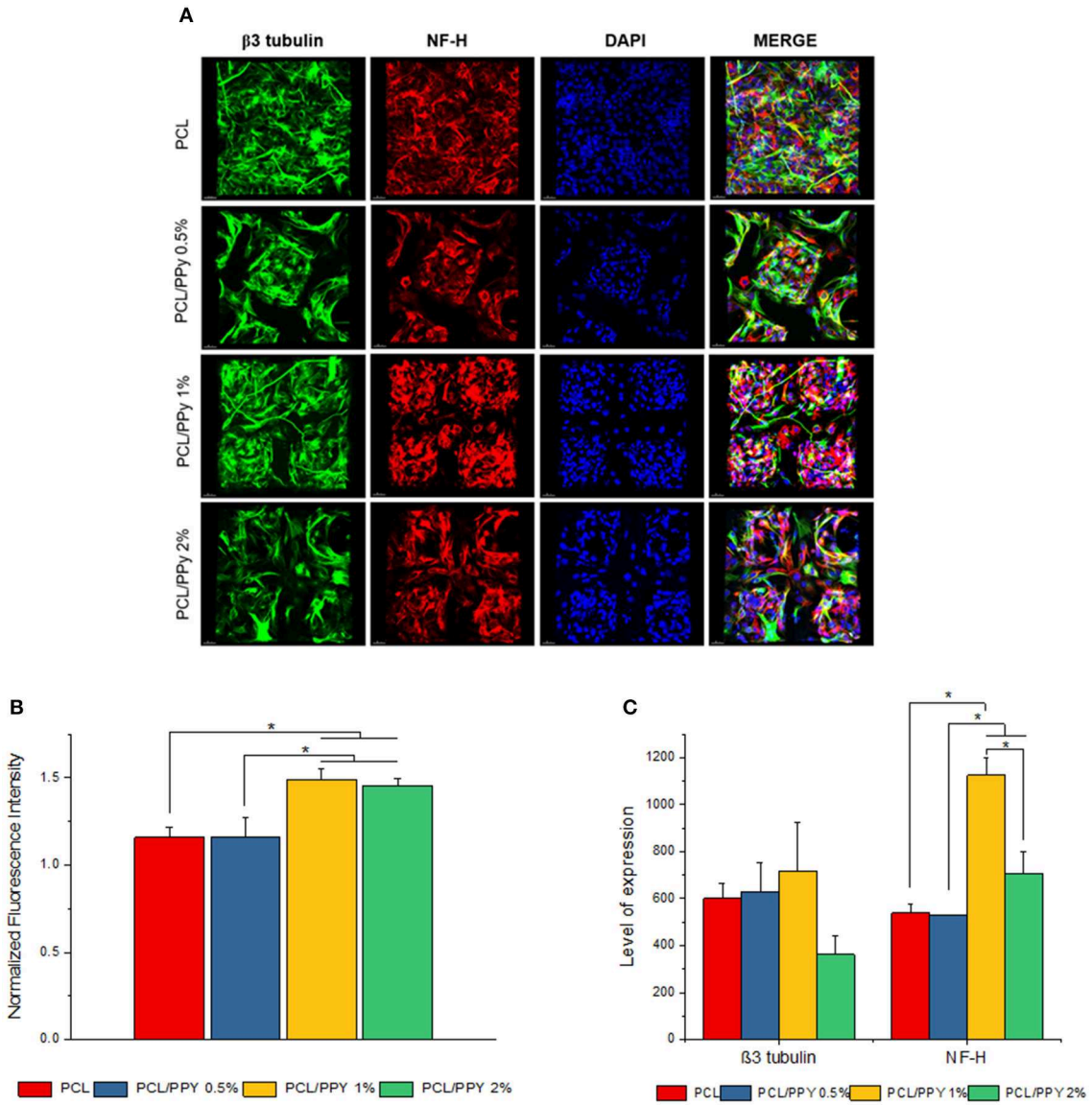

FIGURE 9 | Expression of pan-neuronal marker (β3 tubulin) and peripheral neuron marker (NF-H) by immunocytochemistry. **(A)** 3D projection of the confocal z-stack images of hESC-NCSCs differentiated into peripheral neurons on PCL and PCL/PPy (0.5, 1, and 2%) scaffolds at day 14. Scale bar 30 μm. **(B)** Normalized fluorescence intensity of cells calculated from mean fluorescence intensity of NF-H (red channel) normalized to mean fluorescence intensity of β3 tubulin (green channel). **(C)** Volumetric fluorescence intensity of β3 tubulin and NF-H calculated from volume of expression relative to cell numbers ($n = 3$ for all experiments). *$p < 0.05$.

conditions as representative of neural cells. However, the PC12 cells is a cell line derived from a tumor (pheochromocytoma) of the rat adrenal medulla which means these cells are not physiologically normal, though neural crest-derived they are not neural cells *per se* and lastly, they are of animal origin. PC12 cells and neuronal cells derived from rat dorsal root ganglia are often used as representative of peripheral neuronal cells as it is not possible to culture human-derived peripheral neuronal cells. We had earlier reported a methodology to derive peripheral neurons using hESCs-derived NCSCs as source of cells (Zhu et al., 2017). The peripheral neuronal cells differentiated from hESC-NCSCs have the advantage of being human-derived, representative of peripheral neurons and are physiologically normal (not tumor-derived). Hence, in this study, we used hESC-NCSCs to investigate the impact of PPy-b-PCL based conductive scaffolds on the growth and differentiation to peripheral neuronal cells. The results demonstrate that the hESC-NCSCs were able to grow on PCL and PCL/PPy scaffolds, in particular the PCL/PPy (1 and 2%) scaffolds supported higher growth of neural cells as demonstrated by the higher proliferation, and higher normalized fluorescence intensity. β3 tubulin is a pan-neuronal marker expressed among all neuronal lineages. NF-H is a subunit

of neurofilament proteins that is expressed within peripheral neurons and in particular, is more strongly expressed in mature peripheral neurons (Yuan et al., 2017). Hence, the expression of NF-H is indicative of maturation status of neurons. Hence, the PCL/PPy scaffolds (in particular, PCL-PPy 1%) supported stronger maturation of hESC-NCSCs to peripheral neuronal cells as demonstrated by higher expression of *PRPH* and *NEFH* transcripts and higher volumetric fluorescence intensity of NF-H staining. Overall, these results suggest that PCL/PPy 1% based conductive scaffolds better supports and enhances the differentiation and maturation of hESC-NCSCs to peripheral neurons and hence, have potential clinical value as cell-free or cell-laden NGCs for peripheral neuronal regeneration.

The use of scaffold materials that conduct electricity have been shown to be advantageous for the growth of neurons as these cells have an inherent capacity to be excited by electricity (Mammadov et al., 2013). Previous studies on electrospun poly-L-lactic acid with carbon nanotubes have shown that increased electrical conductivity promotes overall neural differentiation of mouse embryonic stem cells (Mammadov et al., 2013). In another work, poly(L-lactide-co-ε-caprolactone) was combined with a conductive polymer, polyaniline to create a scaffold material that supported the growth of neurites in PC-12 cell lines (Bhang et al., 2012). In our study, addition of PPy to PCL increased electrical conductive properties of the scaffold material progressively from 0.28 ± 0.02 mS/cm in PCL/PPy 0.5%, to 1.15 ± 0.03 mS/cm in PCL/PPy 2%. The culture and differentiation of hESC-NCSCs on various PCL/PPy scaffolds showed that peripheral neural lineage cell types preferred PCL/PPy 1% which had a conductive property of 1.02 ± 0.03 mS/cm. Though, as to why the differentiation was better with PCL/PPy1% and not with PCL/PPy2% which has higher conductance, requires further speculation. Though the PCL/PPy scaffolds have conductive properties, electrical stimulus is not provided in this study. So, future studies on the impact of electrical stimulus and conductive scaffolds on the growth, maturation and alignment of peripheral neuronal cells will provide more insights on the regenerative potential of the PCL/PPy-based conductive NGCs. Further, future studies in animal models of peripheral neuron damage would help to validate the regenerative potential of these conductive polymer-based NGCs.

CONCLUSION

Conductive and biodegradable PCL/PPy scaffolds with three different concentrations of PPy-b-PCL (0.5, 1, and 2% v/v) fabricated using EHD-jet 3D Printing method were evaluated for their potential as NGCs for peripheral nerve regeneration. Inclusion of PPy-b-PCL into PCL-based scaffolds aids the fabrication of softer scaffolds with conductive properties, mechanical properties similar to native human peripheral nerve (∼6.5 MPa), improved degradation profiles and ability of aid growth and differentiation of peripheral neuronal cells *in vitro*. Overall, our results suggest that PCL/PPy scaffolds may be a promising material for guidance conduits in nerve tissue regeneration. The use of neural stem cells on electro-conductive scaffolds produces a symbiotic combination that may have high potential in future for the treatment of neurodegenerative disorders.

DATA AVAILABILITY STATEMENT

All datasets generated for this study are included in the manuscript/**Supplementary Files**.

AUTHOR CONTRIBUTIONS

SV conceived and designed the experiments, analyzed the data, and wrote the paper. SV and SK performed the experiments. SV and GS reviewed and edited the paper. SV, GS, TC, JF, and WL worked on funding acquisition. GS, TC, JF, and WL supervised the whole work.

FUNDING

This research was funded by Agency for Science, Technology, and Research (A*STAR) Advanced Manufacturing and Engineering (AME) Research Grant (R-265-000-630-305 and R-221-000-122-305). SV and SK are supported by President's Graduate Fellowship (National University of Singapore and Ministry of Education, Singapore).

ACKNOWLEDGMENTS

The authors would like to acknowledge Lee Shu Ying from Confocal Microscopy Unit, Yong Loo Lin School of Medicine, National University of Singapore for her help in confocal microscopy and image analysis.

SUPPLEMENTARY MATERIAL

The Supplementary Material for this article can be found online at: https://www.frontiersin.org/articles/10.3389/fbioe.2019.00266/full#supplementary-material

REFERENCES

Acharya, G., Lee, C. H., and Lee, Y. (2012). Optimization of cardiovascular stent against restenosis: factorial design-based statistical analysis of polymer coating conditions. *PLoS ONE* 7:e43100. doi: 10.1371/journal.pone.0043100

Arunraj, T., Rejinold, N. S., Kumar, N. A., and Jayakumar, R. (2013). Doxorubicin-chitin-poly (caprolactone) composite nanogel for drug delivery. *Int. J. Biol. Macromol.* 62, 35–43. doi: 10.1016/j.ijbiomac.2013.08.013

Balint, R., Cassidy, N. J., and Cartmell, S. H. (2014). Conductive polymers: towards a smart biomaterial for tissue engineering. *Acta Biomater.* 10, 2341–2353. doi: 10.1016/j.actbio.2014.02.015

Bhang, S. H., Jeong, S. I., Lee, T. J., Jun, I., Lee, Y. B., Kim, B. S., et al. (2012). Electroactive electrospun polyaniline/poly[(L-lactide)-co-(epsilon-caprolactone)] fibers for control of neural cell function. *Macromol. Biosci.* 12, 402–411. doi: 10.1002/mabi.201100333

Boutry, C. M., Gerber-Hörler, I., and Hierold, C. (2013). Electrically conducting biodegradable polymer composites (polylactide-polypyrrole and polycaprolactone-polypyrrole) for passive resonant circuits. *Polym. Eng. Sci.* 53, 1196–1208. doi: 10.1002/pen.23373

Chen, F., Zhang, J., Wang, F., and Shi, G. (2003). Raman spectroscopic studies on the structural changes of electrosynthesized polypyrrole films during heating and cooling processes. *J. Appl. Polym. Sci.* 89, 3390–3395. doi: 10.1002/app.12606

Chen, M.-C., Sun, Y.-C., and Chen, Y.-H. (2013). Electrically conductive nanofibers with highly oriented structures and their potential application in skeletal muscle tissue engineering. *Acta Biomater.* 9, 5562–5572. doi: 10.1016/j.actbio.2012.10.024

Chiono, V., and Tonda-Turo, C. (2015). Trends in the design of nerve guidance channels in peripheral nerve tissue engineering. *Prog. Neurobiol.* 131, 87–104. doi: 10.1016/j.pneurobio.2015.06.001

Chronakis, I. S., Grapenson, S., and Jakob, A. (2006). Conductive polypyrrole nanofibers via electrospinning: electrical and morphological properties. *Polymer* 47, 1597–1603. doi: 10.1016/j.polymer.2006.01.032

Cukierman, E., Pankov, R., Stevens, D. R., and Yamada, K. M. (2001). Taking cell-matrix adhesions to the third dimension. *Science* 294, 1708–1712. doi: 10.1126/science.1064829

Dumont, C. E., and Born, W. (2005). Stimulation of neurite outgrowth in a human nerve scaffold designed for peripheral nerve reconstruction. *J. Biomed. Mater. Res. Part B Appl. Biomater.* 73, 194–202. doi: 10.1002/jbm.b.30202

Ghasemi-Mobarakeh, L., Prabhakaran, M. P., Morshed, M., Nasr-Esfahani, M. H., Baharvand, H., Kiani, S., et al. (2011). Application of conductive polymers, scaffolds and electrical stimulation for nerve tissue engineering. *J. Tissue Eng. Regen. Med.* 5, e17–35. doi: 10.1002/term.383

Ghasemi-Mobarakeh, L., Prabhakaran, M. P., Morshed, M., Nasr-Esfahani, M. H., and Ramakrishna, S. (2009). Electrical stimulation of nerve cells using conductive nanofibrous scaffolds for nerve tissue engineering. *Tissue Eng. Part A* 15, 3605–3619. doi: 10.1089/ten.tea.2008.0689

Gumus, A., Califano, J. P., Wan, A. M., Huynh, J., Reinhart-King, C. A., and Malliaras, G. G. (2010). Control of cell migration using a conducting polymer device. *Soft Matter* 6, 5138–5142. doi: 10.1039/b923064e

Jakubiec, B., Marois, Y., Zhang, Z., Roy, R., Sigot-Luizard, M. F., Dugre, F. J., et al. (1998). *In vitro* cellular response to polypyrrole-coated woven polyester fabrics: potential benefits of electrical conductivity. *J. Biomed. Mater. Res. Part A* 41, 519–526. doi: 10.1002/(SICI)1097-4636(19980915)41:4<519::AID-JBM2>3.0.CO;2-F

Jaworek, A., and Krupa, A. (1999). Classification of the modes of EHD spraying. *J. Aerosol. Sci.* 30, 873–893. doi: 10.1016/S0021-8502(98)00787-3

Lackington, W. A., Ryan, A. J., and O'Brien, F. J. (2017). Advances in nerve guidance conduit-based therapeutics for peripheral nerve repair. *ACS Biomater. Sci. Eng.* 3, 1221–1235. doi: 10.1021/acsbiomaterials.6b00500

Lam, C. X., Savalani, M. M., Teoh, S.-H., and Hutmacher, D. W. (2008). Dynamics of *in vitro* polymer degradation of polycaprolactone-based scaffolds: accelerated versus simulated physiological conditions. *Biomed. Mater.* 3:034108. doi: 10.1088/1748-6041/3/3/034108

Lee, J. Y. (2013). Electrically conducting polymer-based nanofibrous scaffolds for tissue engineering applications. *Polym. Rev.* 53, 443–459. doi: 10.1080/15583724.2013.806544

Li, M., Guo, Y., Wei, Y., MacDiarmid, A. G., and Lelkes, P. I. (2006). Electrospinning polyaniline-contained gelatin nanofibers for tissue engineering applications. *Biomaterials* 27, 2705–2715. doi: 10.1016/j.biomaterials.2005.11.037

Liu, C., Lv, K., Huang, B., Hou, C., and Wang, G. (2013). Synthesis and characterization of graft copolymers poly (ethylene oxide)-g-[poly (ethylene oxide)-b-poly (ε-caprolactone)] with double crystallizable side chains. *RSC Adv.* 3, 17945–17953. doi: 10.1039/c3ra43024c

Liu, H., Vijayavenkataraman, S., Wang, D., Jing, L., Sun, J., and He, K. (2017). Influence of electrohydrodynamic jetting parameters on the morphology of PCL scaffolds. *Int. J. Bioprint.* 3, 72–82. doi: 10.18063/IJB.2017.01.009

Lu, X., Qiu, Z., Wan, Y., Hu, Z., and Zhao, Y. (2010). Preparation and characterization of conducting polycaprolactone/chitosan/polypyrrole composites. *Compos. Part A Appl. Sci. Manuf.* 41, 1516–1523. doi: 10.1016/j.compositesa.2010.06.014

Mammadov, B., Sever, M., Guler, M. O., and Tekinay, A. B. (2013). Neural differentiation on synthetic scaffold materials. *Biomater. Sci.* 1, 1119–1137. doi: 10.1039/c3bm60150a

Mecerreyes, D., Stevens, R., Nguyen, C., Pomposo, J., Bengoetxea, M., and Grande, H. (2002). Synthesis and characterization of polypyrrole-graft-poly (ε-caprolactone) copolymers: new electrically conductive nanocomposites. *Synth. Met.* 126, 173–178. doi: 10.1016/S0379-6779(01)00503-3

Middleton, J. C., and Tipton, A. J. (2000). Synthetic biodegradable polymers as orthopedic devices. *Biomaterials* 21, 2335–2346. doi: 10.1016/S0142-9612(00)00101-0

Najar, M. H., and Majid, K. (2014). Nanocomposite of polypyrrole with the nanophotoadduct of sodium pentacyanonitrosylferrate (II) dihydrate and EDTA: a potential candidate for capacitor and a sensor for HF radio wave detection. *Synth. Met.* 198, 76–83. doi: 10.1016/j.synthmet.2014.09.015

Nectow, A. R., Marra, K. G., and Kaplan, D. L. (2011). Biomaterials for the development of peripheral nerve guidance conduits. *Tissue Eng. Part B Rev.* 18, 40–50. doi: 10.1089/ten.teb.2011.0240

O'brien, F. J. (2011). Biomaterials & scaffolds for tissue engineering. *Mater. Today* 14, 88–95. doi: 10.1016/S1369-7021(11)70058-X

Pampaloni, F., Reynaud, E. G., and Stelzer, E. H. (2007). The third dimension bridges the gap between cell culture and live tissue. *Nat Rev Mol Cell Biol.* 8:839. doi: 10.1038/nrm2236

Prabhakaran, M. P., Ghasemi-Mobarakeh, L., Jin, G., and Ramakrishna, S. (2011). Electrospun conducting polymer nanofibers and electrical stimulation of nerve stem cells. *J. Biosci. Bioeng.* 112, 501–507. doi: 10.1016/j.jbiosc.2011.07.010

Ramaprasad, A., Latha, D., and Rao, V. (2017). Synthesis and characterization of polypyrrole grafted chitin. *J. Phys. Chem. Solids* 104, 169–174. doi: 10.1016/j.jpcs.2017.01.017

Rouabhia, M., Park, H., Meng, S., Derbali, H., and Zhang, Z. (2013). Electrical stimulation promotes wound healing by enhancing dermal fibroblast activity and promoting myofibroblast transdifferentiation. *PLoS ONE* 8:e71660. doi: 10.1371/journal.pone.0071660

Sharma, Y., Tiwari, A., Hattori, S., Terada, D., Sharma, A. K., Ramalingam, M., et al. (2012). Fabrication of conducting electrospun nanofibers scaffold for three-dimensional cells culture. *Int. J. Biol. Macromol.* 51, 627–631. doi: 10.1016/j.ijbiomac.2012.06.014

Sirivisoot, S., Pareta, R., and Harrison, B. S. (2014). Protocol and cell responses in three-dimensional conductive collagen gel scaffolds with conductive polymer nanofibres for tissue regeneration. *Interface Focus* 4:20130050. doi: 10.1098/rsfs.2013.0050

Vigmond, S. J., Ghaemmaghami, V., and Thompson, M. (1995). Raman and resonance-Raman spectra of polypyrrole with application to sensor–gas probe interactions. *Can. J. Chem.* 73, 1711–1718. doi: 10.1139/v95-209

Vijayavenkataraman, S., Shuo, Z., Fuh, J. Y., and Lu, W. F. (2017). Design of three-dimensional scaffolds with tunable matrix stiffness for directing stem cell lineage specification: an in silico study. *Bioengineering* 4:66. doi: 10.3390/bioengineering4030066

Vijayavenkataraman, S., Thaharah, S., Zhang, S., Lu, W. F., and Fuh, J. Y. H. (2019a). Electrohydrodynamic jet 3D-printed PCL/PAA conductive scaffolds with tunable biodegradability as nerve guide conduits (NGCs) for peripheral nerve injury repair. *Mater. Des.* 162, 171–184. doi: 10.1016/j.matdes.2018.11.044

Vijayavenkataraman, S., Thaharah, S., Zhang, S., Lu, W. F., and Fuh, J. Y. H. (2019b). 3D-printed PCL/rGO conductive scaffolds for peripheral nerve injury repair. *Artif. Organs* 43, 515–523. doi: 10.1111/aor.13360

Vijayavenkataraman, S., Zhang, S., Thaharah, S., Sriram, G., Lu, W., and Fuh, J. (2018). Electrohydrodynamic jet 3D printed nerve guide conduits (NGCs) for peripheral nerve injury repair. *Polymers* 10:753. doi: 10.3390/polym10070753

Wang, Y., Rouabhia, M., Lavertu, D., and Zhang, Z. (2017). Pulsed electrical stimulation modulates fibroblasts' behaviour through the Smad signalling pathway. *J. Tissue Eng. Regen. Med.* 11, 1110–1121. doi: 10.1002/term.2014

Wu, Y., Wu, B., Vijayavenkataraman, S., San Wong, Y., and Fuh, J. Y. H. (2017). Crimped fiber with controllable patterns fabricated via electrohydrodynamic jet printing. *Mater. Des.* 131, 384–393. doi: 10.1016/j.matdes.2017.06.027

Yuan, A., Rao, M. V., Veeranna, and Nixon, R. A. (2017). Neurofilaments and neurofilament proteins in health and disease. *Cold Spring Harb. Perspect. Biol.* 9:a018309. doi: 10.1101/cshperspect.a018309

Zhang, S., Vijayavenkataraman, S., Chong, G. L., Fuh, J. Y. H., and Lu, W. F. (2019). Computational design and optimization of nerve guidance conduits for improved mechanical properties and permeability. *J. Biomech. Eng.* 141:051007. doi: 10.1115/1.4043036

Zhu, Q., Li, M., Yan, C., Lu, Q., Wei, S., Gao, R., et al. (2017). Directed differentiation of human embryonic stem cells to neural crest stem cells, functional peripheral neurons, and corneal Keratocytes. *Biotechnol. J.* 12:1700067. doi: 10.1002/biot.201700067

Zong, X., Bien, H., Chung, C.-Y., Yin, L., Fang, D., Hsiao, B. S., et al. (2005). Electrospun fine-textured scaffolds for heart tissue constructs. *Biomaterials* 26, 5330–5338. doi: 10.1016/j.biomaterials.2005.01.052

Conflict of Interest: The authors declare that the research was conducted in the absence of any commercial or financial relationships that could be construed as a potential conflict of interest.

frontiers in Bioengineering and Biotechnology

REVIEW
published: 18 February 2020
doi: 10.3389/fbioe.2020.00077

Electrospun Polymers in Cartilage Engineering—State of Play

Elif Nur Yilmaz[1,2] *and Dimitrios I. Zeugolis*[1,2]*

[1] Regenerative, Modular & Developmental Engineering Laboratory, National University of Ireland Galway, Galway, Ireland,
[2] Science Foundation Ireland, Centre for Research in Medical Devices, National University of Ireland Galway, Galway, Ireland

Articular cartilage defects remain a clinical challenge. Articular cartilage defects progress to osteoarthritis, which negatively (e.g., remarkable pain, decreased mobility, distress) affects millions of people worldwide and is associated with excessive healthcare costs. Surgical procedures and cell-based therapies have failed to deliver a functional therapy. To this end, tissue engineering therapies provide a promise to deliver a functional cartilage substitute. Among the various scaffold fabrication technologies available, electrospinning is continuously gaining pace, as it can produce nano- to micro- fibrous scaffolds that imitate architectural features of native extracellular matrix supramolecular assemblies and can deliver variable cell populations and bioactive molecules. Herein, we comprehensively review advancements and shortfalls of various electrospun scaffolds in cartilage engineering.

Keywords: electrospinning, fibrous scaffolds, cartilage engineering, functionalised scaffolds, *in vivo* models

OPEN ACCESS

Edited by:
Lorenzo Moroni,
Maastricht University, Netherlands

Reviewed by:
Fang Yang,
Radboud University Nijmegen Medical Centre, Netherlands
Rui Cruz Pereira,
Fondazione Istituto Italiano di Technologia, Italy

***Correspondence:**
Dimitrios I. Zeugolis
dimitrios.zeugolis@nuigalway.ie

Specialty section:
This article was submitted to Tissue Engineering and Regenerative Medicine, a section of the journal Frontiers in Bioengineering and Biotechnology

Received: *11 November 2019*
Accepted: *29 January 2020*
Published: *18 February 2020*

Citation:
Yilmaz EN and Zeugolis DI (2020) Electrospun Polymers in Cartilage Engineering—State of Play. Front. Bioeng. Biotechnol. 8:77. doi: 10.3389/fbioe.2020.00077

INTRODUCTION

Adult articular cartilage is a relatively thin (2–4 mm), aneural, avascular, and alymphatic tissue that acts as cushion against physiological loads at joints. Once injured, it loses much of its carrying capacity, causing a susceptible environment for wearing and tearing between the joints (Correa and Lietman, 2017; Zhang et al., 2019). It has been reported that 60–66% of routine knee arthroscopies caused by articular cartilage defects. The breakdown molecules following injury cause an inflammation in the joints. This inflammation increases the level of synovial cytokines, alters the resident cell phenotypes and induces matrix-degrading enzymes. Thus, it causes a more conducive environment for tissue degradation, which finally ends up with osteoarthritis (OA) (Homandberg et al., 1993; Homandberg and Hui, 1996; Cecil et al., 2005; Kurz et al., 2005; Goldring et al., 2011; Camp et al., 2014). Conjecturally, up to 240 million people around the world suffer from OA. The observed symptoms (e.g., pain, stiffness, joint instability, and pain-related psychological distress) start approximately at the age of 55 and have devastating consequences in the quality of life of the patients (Hunter et al., 2008; Van Spil et al., 2019). In 2013, OA was the second most expensive health condition treated at US hospitals with $16.5 billion expenditure (Torio and Moore, 2013). Women have a higher age-related prevalence of arthritis than men, 10% men and 13% in women suffer from aged-related OA (aged 60 years or older) (Zhang and Jordan, 2010). This prevalence is projected to increase due to increasing aging population and obesity (Sun et al., 2015).

There are numerous treatments for articular cartilage defects, including extensive surgical interventions (e.g., osteotomy, distraction of joints), therapeutic interventions without active biologics (e.g., lavage, arthroscopy, debridement, shaving, laser chondroplasty, abrasion chondroplasty, pridie drilling, microfracture, and spongialization), therapeutic interventions with active biologics (e.g., perichondrial/periosteal grafts, osteochondral transplantation, allogenic

osteochondral, and chondral grafting) and tissue engineering (a still elusive combination of scaffolds, cells, biologics). Cartilage engineering constitute the ultimate frontier, as all other interventions are nothing more than relieving the pain or delaying tissue degradation (Hunziker, 2002; Musumeci et al., 2014). Various scaffold fabrication technologies have been assessed over the years for cartilage engineering with variable degree of efficiency (Cheng et al., 2019; Li et al., 2019). Among them, electrospinning has emerged as a promising technique, due to its high versatility (e.g., ability to produce functionalised nanofibrous scaffolds with a variety of orientations, sizes, and mechanical properties) (Garg and Bowlin, 2011; Casanellas et al., 2018; Casanova et al., 2018; Li et al., 2018; Liu et al., 2018). Herein, we briefly describe the cellular and extracellular composition and architecture of cartilage, along with key modulators of chondrogenesis, and we comprehensively review advancements and shortfalls of electrospun scaffolds in cartilage engineering.

CARTILAGE

Cartilage Cellular Composition and Key Signaling Molecules in Chondrogenesis

Cartilage is a hypocellular tissue, with only 4% of its wet weight consisting of a highly differentiated cell population, called chondrocytes (Matzat et al., 2013). The morphology of chondrocytes varies in shape in each zone (see section Cartilage extracellular matrix composition and architecture). Chondrocytes together with the pericellular matrix (a basket-like network of fine fibrils of elaborate structure composed of laminin, fibronectin, biglycan, decorin, fibromodulin, matrilin 3, and cartilage oligo matrix protein) and the capsule (composed of collagen type VI, collagen type IX, and proteoglycans) surrounding the pericellular matrix form the chondron, which reduces the mechanical, osmotic and physicochemical changes induced by dynamic loading, maintain tissue homoeostasis and contribute to tissue regeneration (Muir, 1995; Alexopoulos et al., 2003; Youn et al., 2006; Vonk et al., 2014; Wilusz et al., 2014; Decker et al., 2015; Li and Xu, 2015). Alterations in the composition of the pericellular matrix is associated with OA (Wadhwa et al., 2005a,b; Hu et al., 2006; van der Weyden et al., 2006; Alexopoulos et al., 2009). Chondrocytes are responsible for synthesis of the articular cartilage extracellular matrix (ECM) (Bhosale and Richardson, 2008; Demoor et al., 2014) and its remodeling through secreted enzymes (e.g., matrix metalloproteinases, hyaluronidases, aggrecanases) (Buttle et al., 1997; Shlopov et al., 1997; Flannery et al., 1998; Demoor et al., 2014).

Chondrocytes are originated from mesenchymal stem cells (MSCs), found in the bone marrow of mature individuals. Condensation of MSCs and chondroprogenitor cell differentiation initiate cartilage formation. Expression of collagen type I and type II results in the onset of chondrogenesis (Archer and Francis-West, 2003; Demoor et al., 2014). Pre-chondrocytes start expressing cartilage-specific transcription factors (e.g., Sox9, Sox5, Sox6) and then they become mature chondrocytes by producing an ECM that has a great amount of proteoglycans (e.g., aggrecan) and collagens (e.g., collagen types II, IX, and XI) (Bi et al., 1999; Ikeda et al., 2004; Demoor et al., 2014). As the chondrocytes proliferate, they express collagen type VI and matrilin 1 under the control of the parathyroid hormone-related peptide/Indian hedgehog. Indian hedgehog is a secreted factor in hypertrophic chondrocytes, which is regulated by the activation of the cyclins. The cyclins regulate chondrocyte proliferation via formation of complexes with cyclin-dependent kinases. By secreting the cartilaginous matrix, MSCs differentiate to chondrocytes and they continue to divide during chondrogenesis. At the final step of their development, they become hypertrophic and secrete calcification proteins in the calcified zone (Temenoff and Mikos, 2000; Zelzer et al., 2001; Goldring, 2012).

Various transcription factors are crucial in chondrogenesis (**Figure 1**). Sox9, which is a master chondrogenic transcription factor during the chondrogenic differentiation, upregulates the transcriptional activity of collagen type II gene through interacting with the first intron-specific enhancer. Sox9 is crucial for articular cartilage formation and the hypertrophic maturation of chondrocytes. In the absence of Sox9, Sox5, and Sox6 induce the transcriptional activity of collagen type II gene, albeit slightly. These three members of the Sox family also regulate the gene expression of collagen type IX, collagen type XI and aggrecan (Lefebvre and Smits, 2005; Wuelling and Vortkamp, 2011; Demoor et al., 2014). Runx2 and Runx3 are expressed in pre-hypertrophic and hypertrophic chondrocytes. Deletion of Runx2 and Runx3 delays chondrocyte maturation. Hypertrophic chondrocytes cannot be formed when lacking these two transcription factors (Yoshida et al., 2004). c-Maf is a basic leucine zipper transcriptional activator and allows hypertrophic and terminal chondrocytes to terminally differentiate (MacLean et al., 2003; Lefebvre and Smits, 2005).

Growth factors also play key roles in chondrogenesis. Insulin-like growth factor1 induces collagen type II expression through increased binding activity of Sox trio (Seifarth et al., 2009; Renard et al., 2012; Legendre et al., 2013; Demoor et al., 2014). Transforming growth factor β1 initiates the condensation of MSCs to chondrocytes for the onset of chondrogenesis, increases the collagen type II gene expression levels during the early stage of chondrogenesis and inhibits the terminal differentiation of chondrocytes via increasing the expression of parathyroid hormone-related peptide (Li et al., 2005a; Demoor et al., 2014). Bone morphogenic protein 2 plays a pivotal role in the expression of the mature form of collagen type II (Rosen et al., 1994; Gouttenoire et al., 2010; Demoor et al., 2014).

WNT signaling is a well-studied pathway for differentiation and hypertrophy (Ripmeester et al., 2018). WNTs establish a large family of cysteine-rich morphogens that have an essential role in cartilage, bone and joint development. *In vivo* mice studies indicated that WNT signaling extended cell survival and inhibited the differentiation of chondrocytes toward hypertrophy (Zhu et al., 2008, 2009). WNT5a and WNT5b are important during differentiation of MSCs to chondrocytes (Church et al., 2002), chondrocyte proliferation and cartilage homeostasis

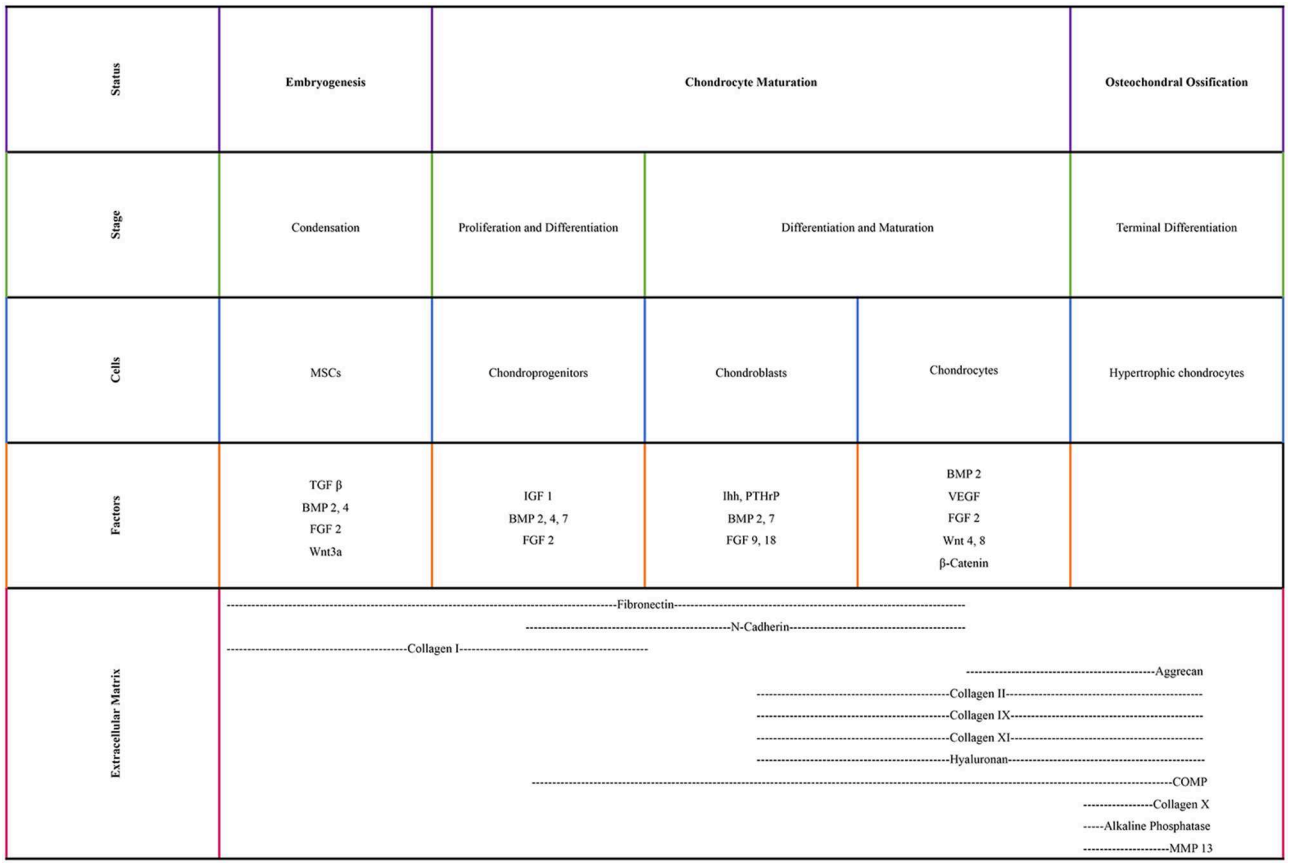

FIGURE 1 | Biological factors and extracellular molecules involved in chondrogenesis.

(Sharma et al., 2013). However, overexpression of WNTs has been reported to lead to OA-like diseases (Lodewyckx and Lories, 2009).

The surface zone of articular cartilage contains a subpopulation called cartilage progenitor cells. These flat cells are responsible for the appositional growth of the cartilage tissue and express high level of stem cell surface marker (Hiraoka et al., 2006) and exhibit a significant degree of plasticity, in terms of differentiation toward chondrogenic, osteogenic, and adipogenic pathways (Morrison et al., 1997; Dowthwaite et al., 2004). Upon injury to a healthy cartilage, they migrate and emerged to the injury site. During OA progression, changes in the distribution of cartilage progenitors suggests that these cells may be responsible for communication between articular cartilage and subchondral bone (Jiang and Tuan, 2015).

Cartilage Extracellular Matrix Composition and Architecture

Cartilage is mainly comprised of collagens (types II, VI, IX, X, XI); collagen type II is the predominant collagen that forms the 90–95% of the fibril network of the matrix and 60–85% of the dry weight of cartilage (Buckwalter and Mankin, 1997; Mow et al., 1999; Poole et al., 2001; Pearle et al., 2005; Lim et al., 2014). Bound carbohydrate groups found in collagen type II allow to interact with water more than other types of collagen. Together with collagen type II, types IX and XI form a macro-fibrillar structure/fiber network, which provides tensile strength. Collagen type IX is cross-linked to the surface of the macro-fibrils, whereas collagen type XI located within and on the surface of the macro-fibrils. Collagen type VI forms microfibrils in pericellular sites. Collagen type X is only synthesized by hypertrophic chondrocytes, which takes place in calcified cartilage (Cohen et al., 1998; Temenoff and Mikos, 2000; Poole et al., 2001). Proteoglycans consist of a protein core and one or more glycosaminoglycan chains. Hyaluronic acid, chondroitin sulfate, keratan sulfate, dermatan sulfate, and heparan sulfate are some of the glycosaminoglycans found in articular cartilage. The predominant proteoglycan is the large chondroitin sulfate proteoglycan 1, called aggrecan, which forms a strong, porous-permeable, fiber-reinforced material together with collagen fibrils. Aggrecan, as the name implies, forms an aggregate structure that does not allow proteoglycans to diffuse out of the matrix throughout joint loading, thus plays an important role during compressive loading. Decorin, biglycan, and fibromodulin are present in minor quantities and do not significantly affect the physical properties of the tissue, unlike aggrecan (Buckwalter and Mankin, 1997; Cohen et al., 1998).

From top to bottom the articular cartilage can be divided into four distinct layers with different compositions, cell morphologies, and physiological characteristics (**Figure 2**). The superficial zone is the thinnest zone, constitutes 10–20% of the total cartilage volume and is responsible for tensile properties of the tissue. It includes a high density of ellipsoid chondrocytes (24,000 cell/mm^3) with a parallel orientation to the surface. These ellipsoid chondrocytes synthesize high concentration of collagens [mainly type II and type IX collagen fibers with small diameter (20 nm) and parallel arrangement to the surface] and low concentration of proteoglycans; for this reason, this zone has the highest concentration of water. As a result of its construction, this zone protects deeper zones from shear, tensile, and compressive forces. Below the superficial zone, the transitional zone represents 40–60% of the total cartilage volume and has a lower cell density (10,300 cells/mm^3). This middle zone shows more typical morphologic features of a hyaline cartilage, with more spherical cells, higher fiber diameter and higher aggrecan content (Temenoff and Mikos, 2000; Poole et al., 2001; Bhosale and Richardson, 2008; Sohier et al., 2008; Nazempour and Van Wie, 2016). Situated between the transitional zone and the calcified cartilage is the deep zone, which represents almost 30% of the total cartilage volume. It provides a great strength against compressive forces and contains the lowest cell density among all of the zones (7,700 cells/mm^3). The cells in this zone are large and spherical and organized perpendicularly to the joint surface. Although the lowest cell density, the proteoglycan content and the fiber diameter (120 nm) are maximal in this zone. Between the deep zone and the subchondral bone, the calcified zone is located and constitutes an excellent interface that integrates with less resilient subchondral bone. There is a visible border between the deep and calcified zone, called tidemark. The calcified zone has a small volume of ellipsoid cells with an abundant calcified ECM, shows a very low metabolic activity. The chondrocytes in this zone exhibit a hypertrophic phenotype and, uniquely, they express collagen type X that can calcify surrounding ECM (Sohier et al., 2008; Sophia Fox et al., 2009).

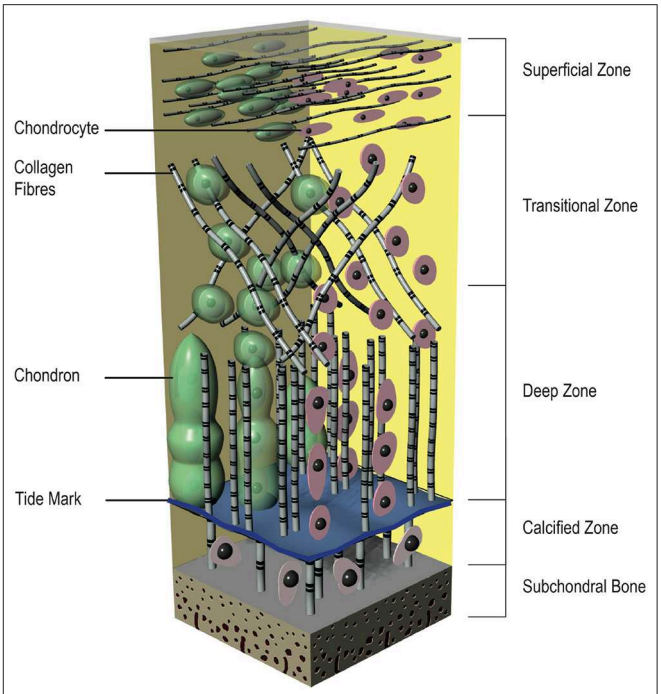

FIGURE 2 | A simplified graphical illustration of articular cartilage.

ELECTROSPINNING

The History

Electrospinning is a highly versatile technique that produces ultrafine fibers with a diameter in the nano- to micro- meter range by using electrostatic fields. It has become popular in a wide range of biomedical and industrial applications, as it can produce fibrous mats with controlled orientations, sizes, porosity, mechanical properties, and with high surface area to volume ratio (**Figure 3**). In 1882, Lord Rayleigh first described electrospray, which inspired the idea of the electrospinning process. He investigated "The Rayleigh instability"; a highly charged droplet is unstable and would break down into smaller droplets when passes through a voltage gradient. After his initial work, the electrospraying of aqueous solutions achieved by the workmanship of Zeleny; his work made possible the current state of electrospinning. It is considered a direct extension of electrospraying, considering that continuous fibers are produced in electrospinning, whereas small droplets are produced in electrospraying. In 1934, Formhals achieved a feasible method to get fine fibers from a cellulose acetate solution and took out a variety of U.S. patents on this technology. In 1966, Simons observed that the use of more viscous solutions resulted in longer fibers. Later, Baumgarten discovered that the diameter of acrylic fibers could be controlled by the feed rate of the infusion pump. Despite these advances and patents in the field of electrospinning until the 1990s, there was no commercial interest in this technique. From the beginning of 1990's, as nanotechnology became a popular research area, the interest of electrospinning has increased (Li et al., 2007; Molnár and Vas, 2012; Braghirolli et al., 2014).

The Setup

The electrospinning process is a simple, efficient spinning method that produces nanoscale to microscale fibers from polymer solutions or melts using electrostatic forces. It is a relatively easy to setup process, as it requires a syringe (polymer solution reservoir) with a small diameter needle (to charge the polymer solution), a flow control pump for reproducibility, a high voltage supply to produce a charged polymer jet and a collector. If the syringe is not set horizontally, the polymer flow can be driven by gravity. The voltage supply usually ranges from 10 to 50 kV (subject to solution viscosity, solvent volatility, etc.). The collector is usually a stationary plate, although advances in engineering have allowed the use of a rotating cylinder for the production of anisotropic fibers.

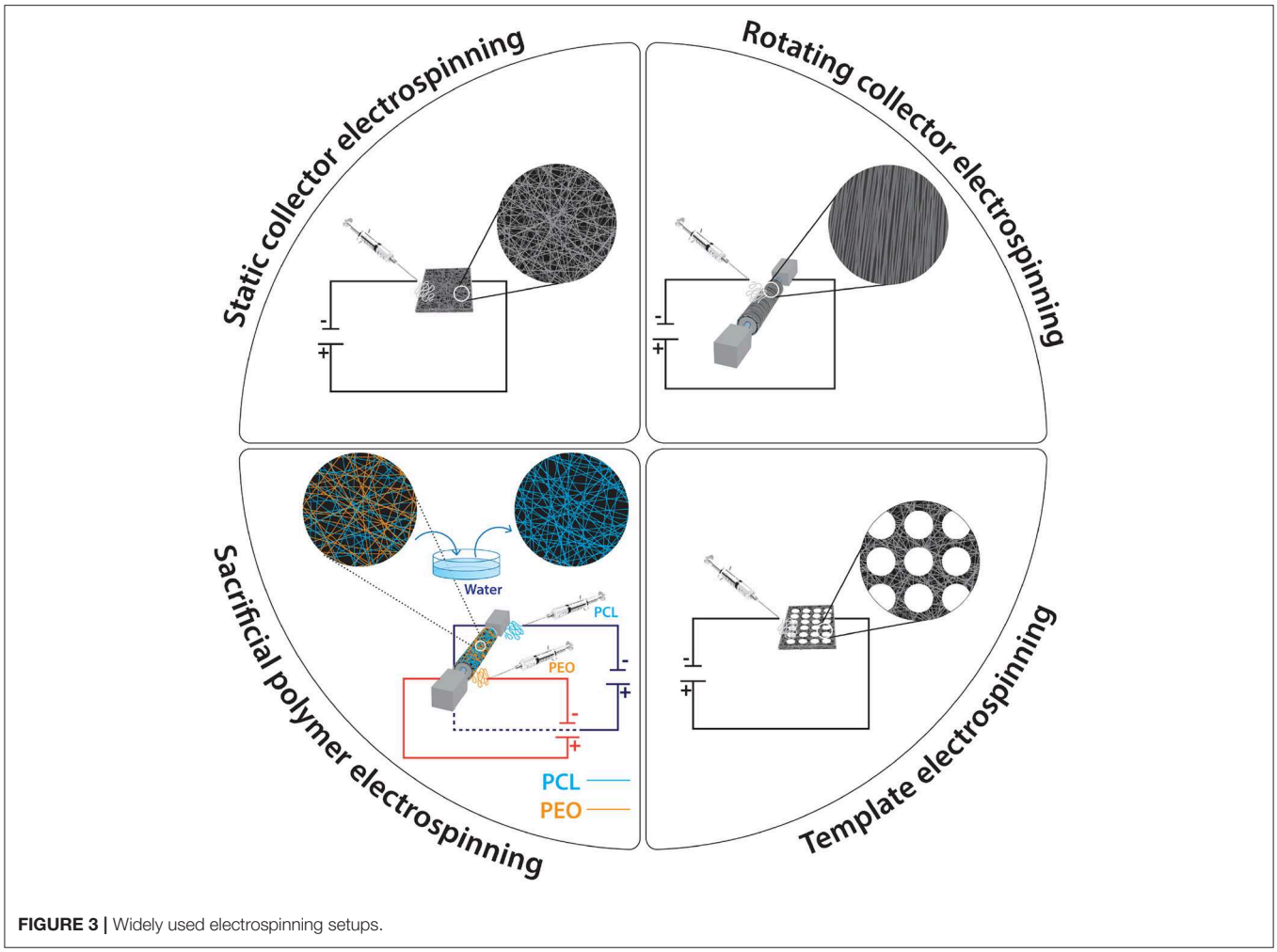

FIGURE 3 | Widely used electrospinning setups.

The Process

Electrospinning begins when the polymer solution emerges from the spinneret by the electrostatic forces. While it is extruded from the syringe, it forms a semi-spherical droplet at the end of the needle and due to the induction of charges on the polymer droplet, it causes instability within the polymer solution. When the reciprocal repulsion of the charges is enough to overcome the surface tension, a conical shape cone, known as Taylor cone, is formed via the elongation of polymer droplet. A liquid jet is the formed that flows through the direction of electric field. During this journey from the spinneret to the collector, the solvent in the liquid jet evaporates, increasing the surface charge on the jet. This increasing surface charge causes instability in the polymer jet and the polymer jet divides geometrically to compensate for the instability. First, it divides into two jets and, as the process continues, it divides into more and more jets. The action of the spinning force, which is caused by the electrostatic force on the continuously splitting polymer droplets, produces the non-woven nanofibers, which are deposited on the collector (Li and Tuan, 2009; Liu et al., 2012; Haider et al., 2015). Despite the electrospinning process seems quite simple, a number of process parameters should be adjusted in order to get desired morphology of nanofibers without droplets or beads (Pillay et al., 2013). These parameters can be divided 3 major group: solution parameters; process parameters; and ambient parameters.

Solution Parameters

All solution parameters (e.g., concentration, molecular weight, viscosity, surface tension, conductivity) are related to each other and affect the architectural features of the produced mat. The concentration of the solution is crucial for fiber formation to occur. Thus, an optimized solution concentration should be designated for each polymer. When the concentration is very low, the electrospinning process does not occur, instead of this, electrospraying is achieved via obtaining polymeric nano/micro particles, because of the low viscosity and high surface tensions of the solution. As the concentration goes a little higher, a mixture of beads and fibers occurs. A further increase in concentration changes the bead morphology from spherical to spindle-like. When the concentration reaches a suitable level, smooth fibers are obtained. Above this level, an increase in concentration results in an increase in fiber diameter. If the concentration is too high, instead of fibers, helix-shaped micro-ribbons are observed. The molecular weight of the polymer significantly affects the

morphology of fibers, due to its effect on the entanglement of polymer chains in solution. When the concentration is fixed, decreasing the molecular weight causes bead, instead of fiber, formation. When increasing the molecular weight, the number of beads and droplets is decreased and smooth fibers are obtained. Considering that each of the solution parameters has an effect on each other, molecular weight reflects the entanglement of the polymer chains, thus it affects viscosity and variance in viscosity can cause different surface tension, which plays an important role in bead formation. The solution viscosity, which can be adjusted by the polymer concentration, is one of the key factors in terms of fiber morphology. Low viscosity prohibits continuous and smooth fiber production, whilst at a high viscosity, longer stress relaxation time occurs, which causes hard ejection of the jets from the polymer solution. At optimal viscosity, uniform in diameter fibers are produced.

Surface tension determines the boundaries of the electrospinning process. Higher surface tension causes instability of the jets and yields sprayed droplets. The solvent and the polymer used as well as the addition of ionizable salts determine the solution conductivity. It has been shown that an increased conductivity causes a decrease in the diameter of the electrospun fibers, whilst low conductivity produces fibers with beads. Natural polymers are polyelectrolytic in nature and the ions present increase the charge carrying capacity of the jet. Further, the addition of ionic salts, such as KH_2PO_4, NaH_2PO_4 and NaCl, affect fiber morphology and diameter and allow production of bead-less fibers with relatively smaller diameters (Bhardwaj and Kundu, 2010; Li and Wang, 2013).

Process Parameters

The process parameters (e.g., voltage, flow rate, distance between needle and collector, collector's features) are also playing a crucial role in the production of reproducible fibers. Obviously, the voltage is crucial in the electrospinning process. When the applied voltage overcomes the threshold voltage, fibrous scaffolds can be produced. When the other parameters are fixed, increasing voltage can cause the formation of beads and droplets. With respect to the influence of voltage on fiber diameter, two contradictory theories exist. High voltages are associated with more polymer ejections and thus larger in diameter fibers. On the other hand, increasing the applied voltage results in smaller in diameter fibers due to the electrostatic repulsive force on the fluid jet. Greater Columbic forces and stronger electric field, arising from high voltages, induce increased stretching of the solution, which results in reduction in the fiber diameter and rapid evaporation of the solvent. The flow rate influences the jet velocity and the material transfer rate. High flow rates produce large in diameter fibers, whilst lower flow rates are more desirable for reproducible fiber production, as they provide sufficient drying time to the jet to reach the collector (Subbiah et al., 2005; Pham et al., 2006; Bhardwaj and Kundu, 2010). The morphology of the fibers is also affected by the distance between the tip of the needle and the collector. Too long or too short distances cause beaded morphology; therefore, an optimal distance should be identified to allow the fiber to dry before reaching the collector (Ki et al., 2005; Hassiba et al., 2016). Having said that, a study has argued that of the other parameters are optimal, the distance has no crucial effect on fiber size and morphology (Pham et al., 2006). The collector acts as a conductive substrate, where the charged fibers are collected. Its conductivity affects the arrangement of the fibers, because of its influence on the charge of the deposited fibers; a low in conductivity collector causes the deposited fibers to detain some of their charges and this causes a repelling effect to the incoming fibers. Customarily, flat aluminum collectors are used, but they are often associated with detachment issues that affect morphology and mechanical properties (Stanger et al., 2009; Pillay et al., 2013). Alternative collector conformations include porous metals of variable porosity and pore shape (Fuller et al., 2016, 2019), wire mesh (Wang et al., 2005), pin (Sundaray et al., 2004), grids (Li et al., 2004), liquid bath (Ki et al., 2007), rotating rods or wheels and parallel or gridded bars for anisotropic fiber production (Xu et al., 2004). It is also worth noting that fibers have also been produced using a non-conductive collector and an AC high voltage electrospinning, instead of a normal DC high voltage (Kessick et al., 2004).

Ambient Parameters

Ambient parameters (e.g., humidity, temperature) also have an impact on the morphology of the fibers. Relative humidity can make the fibers thicker or thinner based on chemical nature of the polymer. In general, high humidity prohibits solvent evaporation and results in beaded or flat mats, as opposed to fibrous mats. High temperatures, due to reduction in surface tension and viscosity, yield small in diameter fibers (De Vrieze et al., 2009).

ELECTROSPUN POLYMERS IN CARTILAGE ENGINEERING

Overview of Polymers Used in Cartilage Engineering

Up to now, numerous natural, synthetic and composite polymers have been electrospun and assessed for cartilage engineering; the critical issues for all of them are their compositional, structural, mechanical, degradation, and biocompatibility properties. The degradation products of natural polymers can be smoothly eliminated from the body and that is why they have been used extensively in cartilage repair and regeneration (**Table 1**). However, their degradation by the harsh solvents used in the electrospinning process (Yang et al., 2008; Zeugolis et al., 2008) requires heavy cross-linking to stabilize them, which frequently associated with cytotoxicity *in vitro* and foreign body response *in vivo* (Delgado et al., 2015), their fast degradation rate for a tissue that has slow recovery time and their potential immune responses and microbial/viral contaminants have restricted the use of natural polymers in the fabrication of electrospun scaffolds for cartilage engineering (Schmidt and Baier, 2000; Lavik and Langer, 2004). Synthetic polymers are in general stronger than natural polymers, can withheld the electrospinning process without any noticeable losses and offer controllable biodegradability (Cheung et al., 2007; Li et al., 2007; Zhang et al., 2009); for these

TABLE 1 | Electrospun natural polymers used in cartilage engineering.

Polymer	Solvent	Fiber diameter	Fiber orientation	Cell type	*in vivo*	Reference
Collagen II	Hexafluoroisopropanol	110–1,750 nm	Random	Human chondrocytes	–	Matthews et al., 2003
Collagen II	Hexafluoroisopropanol	70–2,740 nm	Random	Immortalized human chondrocytes	–	Shields et al., 2004
Chitosan	Proprietary composition	3,000 nm	Aligned	Canine chondrocytes	–	Subramanian et al., 2005
Chitosan	Hexafluoroisopropanol/ Methylene chloride	20–300 nm	Random	Bovine chondrocytes	–	Shim et al., 2009
Gelatin	Trifluoroethanol/Glacial acetic acid	100–1,000 nm	Random	Calf chondrocytes	–	Skotak et al., 2010
Keratin	Sodium carbonate–bicarbonate buffer/Sodium dodecyl sulfate	4,800 nm	Random	Human ADSCs	–	Xu et al., 2014

reasons, synthetic (**Table 2**) and composites (**Table 3**) polymers are extensively used in cartilage engineering.

Poly(α-hydroxy esters) [e.g., poly(glycolic acid) (PGA), poly(lactic acid) (PLA), poly(ε-caprolactone) (PCL) and their copolymers] are used extensively for tissue engineering applications, as they are well-characterized and FDA approved for clinical use. The simplest linear aliphatic polyester is PGA. It is considered as a promising biomaterial due to the natural absorption of its degradation products; however, its rapid degradation rate makes it an inappropriate candidate for cartilage engineering. PLA is more hydrophobic than PGA with an addition of a methyl group; however, it is readily soluble in commonly used organic solvents. Based on the position of the methyl group, it has three isomers, which are poly(L-lactic acid) (PLLA), poly(D,L-lactic acid) (PDLLA), and poly(D-lactic acid) (PDLA). Compared to PGA, PLA degrades slowly (from 1 to over 2 years) because of the hydrophobic characteristics. However, the tensile strength and modulus of elasticity of PLA is lower than PGA. Although the use of PLA and PGA is limited for hard tissue regeneration, such as cartilage tissue, due to their relatively weak mechanical properties (Cheung et al., 2007), one study showed that bidirectionally aligned and layered PLA electrospun mats loaded with human meniscus cells in an ECM hydrogel displayed ∼5-fold higher tensile modulus to the randomly aligned scaffolds; they had comparable tensile modulus to the human meniscus in the circumferential direction and they maintained physiological meniscus cells gene expression for COLA1A1, SOX9, and COMP (Baek et al., 2015).

In general, electrospun copolymers of poly(α-hydroxy esters) with tailored properties can be readily obtained and are extensively used in tissue engineering and regenerative medicine. When six commercially available poly(α-hydroxy esters) were incubated in physiological solutions, the PGA and PLGA50:50 scaffolds showed superior mechanical properties than the PLLA and PCL scaffolds; the PLLA and PCL scaffolds sustained their robust scaffold structure; and the PGA, PDLLA, PLGA50:50, and PLGA85:15 scaffolds exhibited a severe structural destruction due to polymer degradation. In terms of cell proliferation, PLLA scaffolds promoted the highest rate of proliferation between all polymers when seeded with chondrocytes and human BMSCs (Li et al., 2006a). A study that compared different PLGA ratios (75:25, 50:50) and a blend of 75:25 and 50:50 PLGA showed that the tensile modulus of the 75:25 and 50:50 PLGA scaffolds were similar to human skin and slightly lower than human cartilage, respectively (Shin et al., 2006). Due to its relatively cheap cost, high stability in ambient conditions, long degradation rate and the long regeneration time of cartilage tissue, PCL is favored in cartilage repair and regeneration, with numerous studies having demonstrated that electrospun PCL scaffolds promote cartilage cell proliferation, cartilage ECM synthesis and deposition and chondrogenic differentiation of various stem cell populations. Further, PCL nanofibrous scaffolds have shown higher chondrogenic differentiation, as judged by sGAG synthesis, of BMSCs than cell pellet cultures in TGF-β1 serum free media (Li et al., 2005b).

The Influence of Architectural Features on Cell Response

Over the years, numerous studies gave assessed the influence of architectural features (e.g., fiber orientation, fiber diameter, scaffold porosity) on cell fate. It has been shown that both aligned and random PLLA/PCL (Shafiee et al., 2014) and PCL/PLGA (Zamanlui et al., 2018) scaffolds support nasal septum-derived progenitor and human BMSCs, respectively, adhesion, proliferation and chondrogenesis. However, their proliferation was higher on the random scaffolds, whilst their differentiation was higher on the aligned scaffolds, rendering such conformation suitable for the superficial zone of the articular cartilage that exhibits an aligned orientation. Although both aligned nano- and micro- fibrous electrospun PCL scaffolds sustained growth of human BMSCs, the nano-fibrous scaffolds showed the highest chondrogenic activity, as judged by produced sGAG and collagen type II mRNA expression, suggesting that this combination may be suitable form for the superficial zone, which normally shows the highest level of collagen type II than the any other zone (Wise et al., 2009). Similar results were obtained with nano-fibrous, as opposed to micro-fibrous or smooth (film) PLLA (Li et al., 2006b) or PLDLA (Wimpenny et al., 2012) scaffolds; the nano-fibrous architecture maintained chondrocyte-like morphology and enhanced cartilage-specific mRNA expression and ECM synthesis. One should however note that not only the fiber size, but also the pore size has an important role in chondrogenesis. For example, micro-size PLLA

TABLE 2 | Electrospun synthetic polymers used in cartilage engineering.

Polymer	Solvent	Fiber diameter	Fiber orientation	Cell type	*in vivo*	Reference
PCL	Tetrahydrofuran /Dimethylformamide	700 nm	Random	Fetal bovine chondrocytes	–	Li et al., 2003
PCL	Chloroform /Dimethylformamide	400–1,400 nm	Random	Human BMSCs	–	Alves da Silva et al., 2010
PCL	Methylene chloride/Dimethylformamide	500–3,000 nm	Aligned	Human BMSCs	–	Wise et al., 2009
PCL	Dimethylformamide/Tetrahydrofuran	500–900 nm	Random	Human BMSCs	–	Li et al., 2005b
PCL	Dimethylformamide/Tetrahydrofuran	300–1,500 nm	Random	Swine chondrocytes Human BMSCs	Swine model	Li et al., 2006a, 2009
PCL	Chloroform/Dimethylformamide	175–875 nm	Random	Human chondrocytes Human Wharton's jelly stem cells	–	Guimarães et al., 2010; Alves da Silva et al., 2017
PCL	Hexafluoroisopropanol	900–4,600 nm	Aligned and random	Bovine Chondrocytes	–	McCullen et al., 2012
PCL	Hexafluoroisopropanol	1,570 ± 500 nm (aligned) 2,340 ± 740 nm (random)	Aligned and random	Rat BMSCs	–	Munir et al., 2019
PCL PCL-Polyurethane	Tetrafluoroethylene/N, N-dimethylacetamide	200–1,600 nm	Random	Human BMSCs	–	Kuo et al., 2014
PLGA	Dimethylformamide/Tetrahydrofuran	400–700 nm	Random	Porcine chondrocytes	–	Shin et al., 2006
PGA PDLLA PLLA PLGA PCL	Hexafluoroisopropanol Tetrahydrofuran/Dimethylformamide Chloroform/Dimethylformamide Tetrahydrofuran/Dimethylformamide	300–1,500 nm	Random	Human BMSCs Bovine chondrocytes	–	Li et al., 2006a
Poly(p-dioxanone) PLGA	Hexafluoroisopropanol	1,220–1,870 nm	Aligned and random	Human BMSCs	–	Rowland et al., 2016
Co-poly(ether)esterurethane Polyetherimide Poly(p-dioxanone)	Hexafluoroisopropanol Dimethylacetamide	2,000–3,500 nm	Aligned and random	Porcine chondrocytes	–	Schneider et al., 2012
PLLA	Chloroform/Dimethylformamide	500–15,000 nm	Random	Bovine chondrocytes	–	Li et al., 2006b
PLLA	Chloroform/Dimethylformamide	300–1,500 nm	Random	Human BMSCs	–	Li et al., 2006a
PLLA	Hexafluoroisopropanol Chloroform Dichloromethane	290–9,000 nm	Random	Human BMSCs	–	Janjanin et al., 2008; Shanmugasundaram et al., 2011
PLA	Dichloromethane/Dimethylacetamide	700–3,840 nm	Aligned and random	Human vascular and avascular meniscus cells	–	Baek et al., 2015
PLG	Dichloromethane	3,000–14,000 nm	Random	–	Rabbit model	Toyokawa et al., 2010

fibers of 5 and 9 μm in diameter and with pore sizes of 27 and 29 μm respectively were more chondrogenic (e.g., aggrecan, chondroadherin, sox9, collagen type II) than nano-size PLLA fibers of 300 nm and 600 nm to 1,400 nm in diameter and with pore sizes of 2 and 3 μm respectively (Shanmugasundaram et al., 2011).

Electrospinning and Bioreactors

Considering that cells *in vivo* are subjected to numerous tissue-specific cues, modern molecular delivery (Pugliese et al., 2018) and tissue engineering (Calejo et al., 2019) employ multifactorial approaches to recapitulate the *in vivo* niche *in vitro*. To this end, electrospun fibers have joined forces with other *in vitro* microenvironment modulators to either maintain native chondrocyte phenotype or to direct stem cells toward chondrogenic lineage, especially now that it is clear that a stable chondrocyte phenotype is still elusive (Graceffa et al., 2018, 2019). For example, dynamic culture systems combined with electrospun scaffolds have shown beneficial effects in cartilage engineering (Martin et al., 2007; Janjanin et al., 2008;

TABLE 3 | Electrospun composite polymers used in cartilage engineering.

Polymers	Solvent	Fiber diameter	Fiber orientation	Cell type	*in vivo*	Reference
Hydroxy apatite/PLGA/Collagen I	Hexafluoroisopropanol	421 ± 208 nm	Random	Human stem cells (tissue was not specified)	–	Mouthuy et al., 2010, 2016
PCL/Fibrin	Chloroform/Methanol	250–8,800 nm	Random	Human umbilical cord stem cells	–	Levorson et al., 2013
PCL/Cartilage derived matrix	Hexafluoroisopropanol	560–580 nm	Random	Human ADSCs	–	Garrigues et al., 2014
PLLA/Multi walled carbon nano tubes	Dichloromethane/ Dimethylformamide	1,332–3,390 nm	Random	Human BMSCs	–	Holmes et al., 2013
PLGA/Hydroxy apatite/Zein	Hexafluoroisopropanol	200–500 nm	Random	Human umbilical cord stem cells	Rabbit model	Lin et al., 2015
PLLA/Polyethylene glycol/Polyhedral oligomeric silsesquioxane	Chloroform/Dimethylformamide	483–884 nm	Random	Human BMSCs	–	Gomez-Sanchez et al., 2014
Collagen type I/PLCL	Hexafluoroisopropanol	237 ± 65 nm	Random	Rabbit chondrocytes	Mice model	He et al., 2013
PLA/PCL	Chloroform/Dimethylformamide	400–500 nm	Random	Human chondrocytes	–	Thorvaldsson et al., 2008
PLLA/Silk fibroin	Trifluoroacetic acid/Hexafluoroisopropanol	770 ± 160 nm	Random	Rabbit chondrocytes	–	Li et al., 2016
PLDLA nano-fibers/PLDLA micro-fibers	Chloroform/Dimethylformamide	418–728 nm	Aligned and random	Bovine chondrocytes	–	Wimpenny et al., 2012
Gelatin/PCL	Acetic acid/Tetrafluoroethylene	434 ± 130 nm	Random	Coculture of rabbit bone marrow stromal cells and rabbit chondrocytes (75:25)	Mice model	He et al., 2015
PVA/PCL	Chloroform/Dimethylformamide	300–800 nm	Random	Rabbit BMSCs	Rabbit model	Shafiee et al., 2011
PLLA/PCL	Chloroform	100–1,900 nm	Aligned and random	Human nasal septum derived progenitors	–	Shafiee et al., 2014
Poly(3-hydroxybutyrate-co-3-hydroxyvalerate)	Tetrafluoroethylene	600 nm	Random	Rabbit chondrocytes	–	Kwon et al., 2007
Gelatin/PCL	Dichloromethane/ Dimethylbenzene/Span 20/ Formic Acid/Ethyl ester	305 ± 72 nm	Random	Mouse iPSCs	Rabbit model	Liu et al., 2014a
PDLA/PLLA PDLA/PCL	Dichloromethane/Dimethylformamide Tetrahydrofuran/Dimethylformamide Dichloromethane/Dimethylformamide	503–1,000 nm	Random	Canine chondrocytes	–	Wright et al., 2014
PDLLA/Bioglass®	Dimethyl carbonate	100–200 nm	Random	Mouse chondrocyte cell line	–	Yunos et al., 2013
Poly(3-hydroxybutyrate)/Poly(3-hydroxyoctanoate)	Chloroform	336–744 nm	Random	Human chondrocytes	–	Ching et al., 2016
PLA/Carbon nanotubes/Gelatin	Dichloromethane/ Dimethylformamide Acetic acid	112–289 nm	Random	Human chondrocytes	–	Markowski et al., 2015
PLCL/Collagen type I	Hexafluoroisopropanol	20,000 ± 10,000 nm	Aligned and honeycomb	Rabbit BMSCs	–	Zheng et al., 2016
Poly(vinyl alcohol) methacrylate/Poly(vinyl alcohol) methacrylate-Chondroitin sulfate methacrylate	Ultra-pure water	410–500 nm	Random	Goat BMSCs	Rat model	Coburn et al., 2012

(Continued)

TABLE 1 | Continued

Polymers	Solvent	Fiber diameter	Fiber orientation	Cell type	*in vivo*	Reference
Gelatin/PLLA	Methylene chloride/Dimethylformamide	222 ± 14 nm	Random	Rabbit chondrocytes	Rabbit model	Chen and Su, 2011
Hyaluronic acid/Collagen I	Sodium hydroxide/Dimethylformamide	226–357 nm	Random	Bovine chondrocytes	–	Kim et al., 2008
PCL/Collagen I/Hyaluronic acid/Tricalcium phosphate	Chloroform	6,480 ± 1,640 nm	Aligned	Human BMSCs	Rabbit model	Liu et al., 2014b
PLGA/3,4,6-O-Bu3GlcNAc	Dichloromethane	20,000–2,000 nm	Random	Human chondrocytes	Rat model	Kim et al., 2016
PLA/Gelatin PLA/Gelatin/Hyaluronic acid	Hexafluoroisopropanol	Not specified	Random	Rat chondrocytes	Rabbit model	Chen et al., 2016
Poly(ethylene oxide-terephthalate)/Poly(butylene terephtalate)	Chloroform/Hexafluoroisopropanol	10,000 ± 2,800 nm	Random	Bovine chondrocytes	–	Moroni et al., 2008
PCL/PLA	Chloroform/Ethanol	1,430–3,160 nm	Random	–	Rabbit model	Islas-Arteaga et al., 2018
PLLA/PEG	Chloroform/Dimethylformamide	1,000 nm	Random	Chondrocytes/Stem cells (Species and tissue were not specified)	–	Mirzaei et al., 2017
PCL/PEO	Tetrahydrofuran/ Dimethylformamide/Ethanol	471 ± 133 nm	Aligned	Rabbit synovial stem cells	Rabbit model	Shimomura et al., 2019
Poly(hydroxybutyrate)/Chitosan ± Al_2O_3	Trifluoroacetic acid	300–550 nm	Random	Rabbit chondrocytes	–	Sadeghi et al., 2016; Toloue et al., 2019
PLA/Gelatin/Resveratrol	Hexafluoroisopropanol	200–2,200 nm	Random	–	SD rat model	Yu et al., 2018
Cellulose/Silk	Trifluoroacetic acid/glacial acetic acid	68 ± 17 nm	Random	Human BMSCs	–	Begum et al., 2018
PCL/Phytochemicals	Ethyl acetate	316 ± 7 nm	Random	Human meniscus cells	–	Venugopal et al., 2019
PCL/Graphene oxide/Collagen microporous construct	Dichloromethane/ Dimethylformamide	1,200–2,000 nm	Random	–	–	Girão et al., 2018
Sodium cellulose sulfate/Gelatin	Deionized water/Ethanol	1,700–3,700 nm	Random	Human BMSC pellets	–	Huang et al., 2018
Poly (3-hydroxybutyrate)/Chitosan/β-Tricalcium phosphate	Trifluoroacetic acid	400–1,200 nm	Random	Rabbit chondrocytes	–	Keikhaei et al., 2019
PLLA/Polydopamine/Chondroitin sulfate	Dichloromethane	3,000–7,000 nm	Aligned	Rabbit chondrocytes/ Rabbit BMSCs	Rabbit model	Ren et al., 2019
PCL/PLGA	Chloroform/Dimethylformamide	400–1,200 nm	Random	Human BMSCs	–	Zamanlui et al., 2018
Gelatin/Chondroitin sulfate	Tetrafluoroethylene/Water	189–230 nm	Random	Human BMSCs	–	Honarpardaz et al., 2019
PCL/Polytetrahydrofuran urethane/Collagen I	Hexafluoroisopropanol	444 ± 67 nm	Random	Rat femoral marrow stem cells	SD rat model	Jiang et al., 2018
Gelatin/PLGA	Hexafluoroisopropanol	∼1,000 nm	Random	Primary rabbit chondrocytes	Mice model	Chen et al., 2019

Khorshidi et al., 2016). A flow perfusion bioreactor, promoted chondrogenic differentiation of human BMSCs, as judged by increased expression of cartilage-associated genes (e.g., aggrecan, collagen type II, SOX9) and enhanced cell proliferation and ECM synthesis. However, there was no significant difference between bioreactor culture and static control culture, suggesting that the media fluid flow and the orientation of the electrospun meshes can also have an impact (Alves da Silva et al., 2010). Using a custom mold, PLLA electrospun scaffolds seeded with BMSCs and media supplemented with TGF-β1/IGF-1, after 42 days in a bioreactor system, the produced construct exhibited the highest (in comparison to TGF-β1 alone culture) Young's modulus values and collagen type II and aggrecan expression; a significant time-dependent increase in sGAG and hydroxyproline content was also reported (Janjanin et al., 2008).

Improving Cell Infiltration and Nutrient/Waste Transport

Highly dense/small porosity electrospun scaffolds often cause low cell infiltration and limited nutrient access to the deeper sides of the cartilage tissue (Nam et al., 2007; Skotak et al., 2011; Coburn et al., 2012). To enhance cellular infiltration and nutrient/excrete transport, various ingenious engineering approaches have been assessed over the years, including combination of nano-micro fibrous scaffolds (Kim et al., 2008; Thorvaldsson et al., 2008; Levorson et al., 2013), salt leaching techniques (Wright et al., 2014), controlled fiber density (Coburn et al., 2012), electrospinning in liquids (Thorvaldsson et al., 2008), and sacrificial fibers (Baker et al., 2008; Whited et al., 2011), with remarkable results. For example, an electrospun scaffold comprised of PCL microfibers and fibrin nanofibers resulted in higher human umbilical cord blood MSCs infiltration and GAG synthesis than PCL microfibres and PCL micro- and nano-fibers (Levorson et al., 2013). Electrospinning of PVA/methacrylate/chondroitin sulfate in ethanol bath enhanced goat BMSCs infiltration, proliferation and chondrogenesis *in vitro* and cartilage regeneration *in vivo*, even without cells or any other exogenous factor (Thorvaldsson et al., 2008). Salt leaching of chitosan hydrogels reinforced with either PDLA/PLLA or PDLA/PCL has been shown to increase porosity; however, the PDLA/PLLA-based scaffolds provided a favorable elastic modulus for articular cartilage, whilst the PDLA/PCL-based scaffolds exhibited better biological response (Slivka et al., 2001; Wright et al., 2014).

From Two-Dimensional to Three-Dimensional Constructs

To more closely imitate the native three-dimensional cartilage architecture, multi-layer horizontally, randomly, and vertically aligned fibers PCL fibers in a graphene-oxide-collagen microporous network have been developed (Girão et al., 2018). To imitate the three-dimensional cartilage architecture and composition, PCL/cartilage-derived matrix electrospun fibers were produced in single- and multi- layered conformations; the resultant multi-layered scaffolds enhanced chondrogenesis of human ADSCs, as judged by increased sGAG synthesis and increased gene expression of collagen type X, but had lower elastic modulus to PCL-alone scaffolds (Garrigues et al., 2014). Despite these significant advancements, scalability of such constructs is of concern. For this reason, electrospinning has been combined with other fabrication technologies for the development of three-dimensional constructs that closely imitate native cartilage architectural features. For example, electrospinning with rapid prototyping resulted in scaffolds with acceptable mechanical properties that supported bovine chondrocyte growth and cartilage-ECM synthesis for 4 weeks *in vitro* (Moroni et al., 2008). Electrospinning combined with freeze-drying has been shown to yield scaffolds that supported rabbit BMSC growth *in vitro* (Zheng et al., 2016) and to successfully regenerate osteochondral defects in a rabbit model (Liu et al., 2014b). More complex scaffolds have also been prepared and demonstrated efficacy in a mice model using electrospinning, three-dimensional printing and freeze drying (Chen et al., 2019).

Preclinical Data

It is worth noting that all small animal *in vivo* data have shown promising results. For example, in nude mice, layer-by-layer sandwich constructs of collagen/PLCL seeded with rabbit auricular chondrocytes reached 83% Young's modulus of native auricular cartilage after 12 weeks of implantation (He et al., 2013). PVA with chondroitin sulfate electrospun fibers in a rat osteochondral defect model resulted in enhanced chondrogenesis, compared to the empty control group (Coburn et al., 2012). Resveratrol-PLA-gelatin scaffolds resulted in faster healing than PLA-gelatin scaffolds in a rat articular cartilage defect model 12 weeks post-implantation (Yu et al., 2018). In a rabbit cartilage defect model, aligned PLLA-polydopamine-chondroitin sulfate fibers facilitated the filling of defects and the regeneration of hyaline cartilage-like tissue (Ren et al., 2019). In rabbit meniscal defects, aligned PCL fibers (produced with sacrificial PEO fibers) combined with a tissue engineered construct derived from synovial mesenchymal stem cells significantly contributed to the prevention of meniscal extrusion, exerted a chondroprotective effect and meniscal defects were repaired with a fibrocartilaginous tissue (Shimomura et al., 2019). In the only large animal model *in vivo* work (7 mm full thickness cartilage defect swine model), PCL fibers loaded with human BMSCs showed the most complete repair, generated hyaline cartilage-like tissue and had the highest equilibrium compressive stress of 1.5 MPa in the regenerated cartilage after 6 months of implantation, in comparison to PCL scaffolds alone and PCL/allogenic chondrocytes constructs (Li et al., 2009). Despite these profound preclinical data, no clinical studies are available to-date in cartilage engineering.

Critical Analysis and Outlook

Electrospinning has been adopted in tissue engineering and regenerative medicine since the 1990's. Since then, a substantial amount of work has been conducted, as evidenced by the wealth of scientific publications available (e.g., 8,103 papers in PubMed; term searched "electrospinning" in all fields). In cartilage space, the electrospinning technology is still at its infancy, which can be substantiated by the low number of scientific publications available (e.g., 155 papers in PubMed; terms searched "electrospinning" and "cartilage" in all fields). Nonetheless, significant strides (e.g., development of three-dimensional tissue equivalents that, to a certain extent, replicate the complex cartilage architecture and composition and have resulted in promising *in vivo* data in small animal preclinical models) have been achieved. However, it is also apparent that large animal experimentation and clinical translation are lagging behind for cartilage and also other clinical indications (e.g., only 5 clinical studies appear at clinicaltrials.gov, term searched "electrospinning" in all studies). This limited technology transfer from benchtop to large animal models and to clinical setting may be attributed to scalability and infrastructure costs required to produce reproducible fibers (e.g., controlled temperature/humidity chambers, automated systems, variable

collectors, multi-syringe systems). Considering though that electrospun scaffolds have started becoming commercially and clinically available (Ryan et al., 2015), we believe that in the years to come they will also be assessed in cartilage engineering.

We also believe that in the years to come electrospun scaffolds together with other *in vitro* microenvironment modulators will play a crucial role in the development of functional cell therapies for cartilage engineering. For example, the positive impact of bioreactors in musculoskeletal tissue engineering has been well-established (Peroglio et al., 2018) and electrospun scaffolds coupled with bioreactors have shown promise to-date, even for complex structures, such as the cartilage-bone interface (Baumgartner et al., 2019). Further, considering that extracellular matrix is key modulator of cell fate through provision of biophysical, biochemical, and biological signals (Guilak et al., 2009; Watt and Huck, 2013; Kumar et al., 2017; Muncie and Weaver, 2018; Smith et al., 2018; Novoseletskaya et al., 2019), strategies that enhance and accelerate native extracellular matrix synthesis [e.g., hypoxia (Taheem et al., 2019)] and deposition [e.g., macromolecular crowding (Graceffa and Zeugolis, 2019)] coupled with electrospinning are likely to lead to more biomimetic three-dimensional cartilage equivalents. It is also worth noting, that although the cell-sheet/scaffold-free technology has shown promise in human cartilage engineering (Sato et al., 2019), only thin layers of tissue can be developed, which imposes the need of either multi-layered approaches that are often associated with delamination and cell death in the middle layers due to poor nutrient/waste transport (Sekine et al., 2011) or multiple surgeries (Shimizu et al., 2006; Komae et al., 2017). Considering that advances in engineering are now allowing the development of porous electrospun scaffolds (Ameer et al., 2019), we believe that temperature-responsive electrospun scaffolds will play a key role in the development of scaffold-free three-dimensional tissue-like surrogates in the years to come.

CONCLUSIONS

Electrospinning can produce nano- to micro-range fibrous constructs that closely imitate the architecture of native tissues. Further, has the capacity to deliver cells and therapeutic molecules at the side of injury. Advancements in fabrication methods have addressed scalability issues and have allowed the development of porous structures than enable cell infiltration and growth for prolonged periods of times. Despite all these advantages, electrospun scaffolds have yet to be assessed comprehensively in preclinical models and clinical setting, which has compromised wide acceptance of this pioneering technology in biomedicine.

AUTHOR CONTRIBUTIONS

All authors listed have made a substantial, direct and intellectual contribution to the work, and approved it for publication.

FUNDING

This work was supported by Science Foundation Ireland, Career Development Award (Grant No. 15/CDA/3629) and Science Foundation Ireland/European Regional Development Fund (Grant No. 13/RC/2073).

REFERENCES

Alexopoulos, L. G., Haider, M. A., Vail, T. P., and Guilak, F. (2003). Alterations in the mechanical properties of the human chondrocyte pericellular matrix with osteoarthritis. *J. Biomech. Eng.* 125, 323–333. doi: 10.1115/1.1579047

Alexopoulos, L. G., Youn, I., Bonaldo, P., and Guilak, F. (2009). Developmental and osteoarthritic changes in Col6a1-knockout mice: Biomechanics of type VI collagen in the cartilage pericellular matrix. *Arthritis Rheum.* 60, 771–779. doi: 10.1002/art.24293

Alves da Silva, M., Martins, A., Costa-Pinto, A. R., Monteiro, N., Faria, S., Reis, R. L., et al. (2017). Electrospun nanofibrous meshes cultured with Wharton's jelly stem cell: an alternative for cartilage regeneration, without the need of growth factors. *Biotechnol. J.* 12:1700073. doi: 10.1002/biot.201700073

Alves da Silva, M. L., Martins, A., Costa-Pinto, A. R., Costa, P., Faria, S., Gomes, M., et al. (2010). Cartilage tissue engineering using electrospun PCL nanofiber meshes and MSCs. *Biomacromolecules* 11, 3228–3236. doi: 10.1021/bm100476r

Ameer, J., Pr, A., and Kasoju, N. (2019). Strategies to tune electrospun scaffold porosity for effective cell response in tissue engineering, *J. Funct. Biomater.* 10:E30. doi: 10.3390/jfb10030030

Archer, C. W., and Francis-West, P. (2003). The chondrocyte, *Int. J. Biochem. Cell Biol.* 35, 401–404. doi: 10.1016/S1357-2725(02)00301-1

Baek, J., Chen, X., Sovani, S., Jin, S., Grogan, S. P., and D'Lima, D. D. (2015). Meniscus tissue engineering using a novel combination of electrospun scaffolds and human meniscus cells embedded within an extracellular matrix hydrogel. *J. Orthop. Res.* 33, 572–583. doi: 10.1002/jor.22802

Baker, B. M., Gee, A. O., Metter, R. B., Nathan, A. S., Marklein, R. A., Burdick, J. A., et al. (2008). The potential to improve cell infiltration in composite fiber-aligned electrospun scaffolds by the selective removal of sacrificial fibers. *Biomaterials* 29, 2348–2358. doi: 10.1016/j.biomaterials.2008.01.032

Baumgartner, W., Otto, L., Hess, S., Stark, W., Märsmann, S., Bürgisser, G., et al. (2019). Cartilage/bone interface fabricated under perfusion: spatially organized commitment of adipose-derived stem cells without medium supplementation. *J. Biomed. Mater Res. B.* 107, 1833–1843. doi: 10.1002/jbm.b.34276

Begum, R., Su, B., Perriman, A., Scarpa, F., and Kafienah, W. (2018). Electrospun cellulose-silk composite nanofibres direct mesenchymal stem cell chondrogenesis in the absence of biological stimulation. *bioRxiv* 434316. doi: 10.1101/434316

Bhardwaj, N., and Kundu, S. C. (2010). Electrospinning: a fascinating fiber fabrication technique. *Biotechnol. Adv.* 28, 325–347. doi: 10.1016/j.biotechadv.2010.01.004

Bhosale, A. M., and Richardson, J. B. (2008). Articular cartilage: Structure, injuries and review of management. *Br. Med. Bull.* 87, 77–95. doi: 10.1093/bmb/ldn025

Bi, W., Deng, J. M., Zhang, Z., Behringer, R. R., and de Crombrugghe, B. (1999). Sox9 is required for cartilage formation. *Nat. Genet.* 22:85. doi: 10.1038/8792

Braghirolli, D. I., Steffens, D., and Pranke, P. (2014). Electrospinning for regenerative medicine: a review of the main topics. *Drug Discov. Today* 19, 743–753. doi: 10.1016/j.drudis.2014.03.024

Buckwalter, J., and Mankin, H. (1997). Articular cartilage: tissue design and chondrocyte-matrix interactions. *Instr. Course. Lect.* 47, 477–486.

Buttle, D. J., Fowles, A., Ilic, M. Z., and Handley, C. J. (1997). "Aggrecanase" activity is implicated in tumour necrosis factor alpha mediated cartilage aggrecan breakdown but is not detected by an in vitro assay. *Mol. Pathol.* 50, 153–159. doi: 10.1136/mp.50.3.153

Calejo, I., Costa-Almeida, R., Reis, R., and Gomes, M. (2019). *A Physiology-Inspired Multifactorial Toolbox in Soft-to-Hard Musculoskeletal Interface Tissue Engineering*. Trends Biotechnol. Available online at: https://www.sciencedirect.com/science/article/pii/S0167779919301520

Camp, C. L., Stuart, M. J., and Krych, A. J. (2014). Current concepts of articular cartilage restoration techniques in the knee. *Sports Health*. 6, 265–273. doi: 10.1177/1941738113508917

Casanellas, I., García-Lizarribar, A., Lagunas, A., and Samitier, J. (2018). Producing 3D biomimetic nanomaterials for musculoskeletal system regeneration. *Front. Bioeng. Biotechnol*. 6:128. doi: 10.3389/fbioe.2018.00128

Casanova, M., Reis, R., Martins, A., and Neves, N. (2018). The use of electrospinning technique on osteochondral tissue engineering. *Adv. Exp. Med. Biol*. 1058, 247–263. doi: 10.1007/978-3-319-76711-6_11

Cecil, D. L., Johnson, K., Rediske, J., Lotz, M., Schmidt, A. M., and Terkeltaub, R. (2005). Inflammation-induced chondrocyte hypertrophy is driven by receptor for advanced glycation end products. *J. Immunol*. 175, 8296–8302. doi: 10.4049/jimmunol.175.12.8296

Chen, J.-P., and Su, C.-H. (2011). Surface modification of electrospun PLLA nanofibers by plasma treatment and cationized gelatin immobilization for cartilage tissue engineering. *Acta Biomater*. 7, 234–243. doi: 10.1016/j.actbio.2010.08.015

Chen, W., Chen, S., Morsi, Y., El-Hamshary, H., El-Newhy, M., Fan, C., et al. (2016). Superabsorbent 3D scaffold based on electrospun nanofibers for cartilage tissue engineering. *ACS Appl. Mater Interfaces*. 8, 24415–24425. doi: 10.1021/acsami.6b06825

Chen, W., Xu, Y., Liu, Y., Wang, Z., Li, Y., Jiang, G., et al. (2019). Three-dimensional printed electrospun fiber-based scaffold for cartilage regeneration. *Materi Des*. 179:107886. doi: 10.1016/j.matdes.2019.107886

Cheng, A., Schwartz, Z., Kahn, A., Li, X., Shao, Z., Sun, M., et al. (2019). Advances in porous scaffold design for bone and cartilage tissue engineering and regeneration. *Tissue Eng. Part B*. 25, 14–29. doi: 10.1089/ten.teb.2018.0119

Cheung, H.-Y., Lau, K.-T., Lu, T.-P., and Hui, D. (2007). A critical review on polymer-based bio-engineered materials for scaffold development. *Composites B*. 38, 291–300. doi: 10.1016/j.compositesb.2006.06.014

Ching, K. Y., Andriotis, O. G., Li, S., Basnett, P., Su, B., Roy, I., et al. (2016). Nanofibrous poly(3-hydroxybutyrate)/poly(3-hydroxyoctanoate) scaffolds provide a functional microenvironment for cartilage repair. *J Biomater. Appl*. 31, 77–91. doi: 10.1177/0885328216639749

Church, V., Nohno, T., Linker, C., Marcelle, C., and Francis-West, P. (2002). Wnt regulation of chondrocyte differentiation. *J. Cell Sci*. 115, 4809–4818. doi: 10.1242/jcs.00152

Coburn, J. M., Gibson, M., Monagle, S., Patterson, Z., and Elisseeff, J. H. (2012). Bioinspired nanofibers support chondrogenesis for articular cartilage repair. *Proc. Natl. Acad. Sci. U.S.A*. 109, 10012–10017. doi: 10.1073/pnas.1121605109

Cohen, N. P., Foster, R. J., and Mow, V. C. (1998). Composition and dynamics of articular cartilage: structure, function, and maintaining healthy state. *J. Orthop. Sports Phys. Ther*. 28, 203–215. doi: 10.2519/jospt.1998.28.4.203

Correa, D., and Lietman, S. A. (2017). Articular cartilage repair: Current needs, methods and research directions. *Semin Cell Dev. Biol*. 62, 67–77. doi: 10.1016/j.semcdb.2016.07.013

De Vrieze, S., Van Camp, T., Nelvig, A., Hagström, B., Westbroek, P., and De Clerck, K. (2009). The effect of temperature and humidity on electrospinning. *J. Mater Sci*. 44, 1357–1362. doi: 10.1007/s10853-008-3010-6

Decker, R. S., Koyama, E., and Pacifici, M. (2015). Articular cartilage: Structural and developmental intricacies and questions. *Curr. Osteoporos. Rep*. 13, 407–414. doi: 10.1007/s11914-015-0290-z

Delgado, L., Bayon, Y., Pandit, A., and Zeugolis, D. (2015). To cross-link or not to cross-link? Cross-linking associated foreign body response of collagen-based devices. *Tissue Eng. Part B*. 21, 298–313. doi: 10.1089/ten.teb.2014.0290

Demoor, M., Ollitrault, D., Gomez-Leduc, T., Bouyoucef, M., Hervieu, M., Fabre, H., et al. (2014). Cartilage tissue engineering: molecular control of chondrocyte differentiation for proper cartilage matrix reconstruction. *Biochim. Biophys. Acta*. 1840, 2414–2440. doi: 10.1016/j.bbagen.2014.02.030

Dowthwaite, G., Bishop, J., Redman, S., Khan, I., Rooney, P., Evans, D., et al. (2004). The surface of articular cartilage contains a progenitor cell population. *J. Cell Sc*. 117, 889–897. doi: 10.1242/jcs.00912

Flannery, C. R., Little, C. B., Hughes, C. E., and Caterson, B. (1998). Expression and activity of articular cartilage hyaluronidases. *Biochem. Biophys. Res. Commun*. 251, 824–829. doi: 10.1006/bbrc.1998.9561

Fuller, K., Gaspar, D., Delgado, L., Pandit, A., and Zeugolis, D. (2016). Influence of porosity and pore shape on structural, mechanical and biological properties of poly ϵ-caprolactone electro-spun fibrous scaffolds. *Nanomedicine* 11, 1031–1040. doi: 10.2217/nnm.16.21

Fuller, K., Gaspar, D., Delgado, L., and Zeugolis, D. (2019). Development macro-porous electro-spun meshes with clinically relevant mechanical properties - A technical note. *Biomed. Mater*. 14:024103. doi: 10.1088/1748-605X/aaf929

Garg, K., and Bowlin, G. L. (2011). Electrospinning jets and nanofibrous structures. *Biomicrofluidics* 5:13403. doi: 10.1063/1.3567097

Garrigues, N. W., Little, D., Sanchez-Adams, J., Ruch, D. S., and Guilak, F. (2014). Electrospun cartilage-derived matrix scaffolds for cartilage tissue engineering. *J. Biomed. Mater. Res. A*. 102, 3998–4008. doi: 10.1002/jbm.a.35068

Girão, A. F., Semitela, Â., Ramalho, G., Completo, A., and Marques, P. A. (2018). Mimicking nature: Fabrication of 3D anisotropic electrospun polycaprolactone scaffolds for cartilage tissue engineering applications. *Composites B* 154, 99–107. doi: 10.1016/j.compositesb.2018.08.001

Goldring, M. B. (2012). Chondrogenesis, chondrocyte differentiation, and articular cartilage metabolism in health and osteoarthritis. *Ther. Adv. Musculoskelet Dis*. 4, 269–285. doi: 10.1177/1759720X12448454

Goldring, M. B., Otero, M., Plumb, D. A., Dragomir, C., Favero, M., El Hachem, K., et al. (2011). Roles of inflammatory and anabolic cytokines in cartilage metabolism: signals and multiple effectors converge upon MMP-13 regulation in osteoarthritis. *Eur. Cell Mater*. 21, 202–220. doi: 10.22203/eCM.v021a16

Gomez-Sanchez, C., Kowalczyk, T., Ruiz De Eguino, G., Lopez-Arraiza, A., Infante, A., Rodriguez, C. I., et al. (2014). Electrospinning of poly(lactic acid)/polyhedral oligomeric silsesquioxane nanocomposites and their potential in chondrogenic tissue regeneration. *J. Biomater. Sci. Polym. Ed*. 25, 802–825. doi: 10.1080/09205063.2014.910151

Gouttenoire, J., Bougault, C., Aubert-Foucher, E., Perrier, E., Ronzière, M.-C., Sandell, L., et al. (2010). BMP-2 and TGF-β1 differentially control expression of type II procollagen and α10 and α11 integrins in mouse chondrocytes. *Eur. J. Cell Biol*. 89, 307–314. doi: 10.1016/j.ejcb.2009.10.018

Graceffa, V., Vinatier, C., Guicheux, J., Evans, C., Stoddart, M., Alini, M., et al. (2018). State of art and limitations in genetic engineering to induce stable chondrogenic phenotype. *Biotechnol. Adv*. 36, 1855–1869. doi: 10.1016/j.biotechadv.2018.07.004

Graceffa, V., Vinatier, C., Guicheux, J., Stoddart, M., Alini, M., and Zeugolis, D. (2019). Chasing chimeras - The elusive stable chondrogenic phenotype. *Biomaterials* 192, 199–225. doi: 10.1016/j.biomaterials.2018.11.014

Graceffa, V., and Zeugolis, D. (2019). Carrageenan enhances chondrogenesis and osteogenesis in human bone marrow stem cell culture. *Eur. Cell Mater*. 37, 310–332. doi: 10.22203/eCM.v0637a19

Guilak, F., Cohen, D., Estes, B., Gimble, J., Liedtke, W., and Chen, C. (2009). Control of stem cell fate by physical interactions with the extracellular matrix. *Cell Stem Cell*. 5, 17–26. doi: 10.1016/j.stem.2009.06.016

Guimarães, A., Martins, A., Pinho, E. D., Faria, S., Reis, R. L., and Neves, N. M. (2010). Solving cell infiltration limitations of electrospun nanofiber meshes for tissue engineering applications. *Nanomedicine* 5, 539–554. doi: 10.2217/nnm.10.31

Haider, A., Haider, S., and Kang, I.-K. (2015). A comprehensive review summarizing the effect of electrospinning parameters and potential applications of nanofibers in biomedical and biotechnology. *Arab. J. Chem*. 11, 1165–1188. doi: 10.1016/j.arabjc.2015.11.015

Hassiba, A. J., El Zowalaty, M. E., Nasrallah, G. K., Webster, T. J., Luyt, A. S., Abdullah, A. M., et al. (2016). Review of recent research on biomedical applications of electrospun polymer nanofibers for improved wound healing. *Nanomedicine*11, 715–737. doi: 10.2217/nnm.15.211

He, X., Feng, B., Huang, C., Wang, H., Ge, Y., Hu, R., et al. (2015). Electrospun gelatin/polycaprolactone nanofibrous membranes combined with a coculture of bone marrow stromal cells and chondrocytes for cartilage engineering. *Int. J. Nanomedicine* 10, 2089–2099. doi: 10.2147/IJN.S79461

He, X., Fu, W., Feng, B., Wang, H., Liu, Z., Yin, M., et al. (2013). Electrospun collagen/poly(L-lactic acid-co-epsilon-caprolactone) hybrid nanofibrous membranes combining with sandwich construction model

for cartilage tissue engineering. *J. Nanosci. Nanotechnol*. 13, 3818–3825. doi: 10.1166/jnn.2013.7436

Hiraoka, K., Grogan, S., Olee, T., and Lotz, M. (2006). Mesenchymal progenitor cells in adult human articular cartilage. *Biorheology* 43, 447–454. doi: 10.1002/art.20269

Holmes, B., Castro, N. J., Li, J., Keidar, M., and Zhang, L. G. (2013). Enhanced human bone marrow mesenchymal stem cell functions in novel 3D cartilage scaffolds with hydrogen treated multi-walled carbon nanotubes. *Nanotechnology* 24:365102. doi: 10.1088/0957-4484/24/36/365102

Homandberg, G., Meyers, R., and Williams, J. (1993). Intraarticular injection of fibronectin fragments causes severe depletion of cartilage proteoglycans *in vivo*. *J. Rheumatol*. 20, 1378–1382.

Homandberg, G. A., and Hui, F. (1996). Association of proteoglycan degradation with catabolic cytokine and stromelysin release from cartilage cultured with fibronectin fragments. *Arch. Biochem. Biophys*. 334, 325–331. doi: 10.1006/abbi.1996.0461

Honarpardaz, A., Irani, S., Pezeshki-Modaress, M., Zandi, M., and Sadeghi, A. (2019). Enhanced chondrogenic differentiation of bone marrow mesenchymal stem cells on gelatin/glycosaminoglycan electrospun nanofibers with different amount of glycosaminoglycan. *J. Biomed. Mater Res. A*. 107, 38–48. doi: 10.1002/jbm.a.36501

Hu, K., Xu, L., Cao, L., Flahiff, C. M., Brussiau, J., Ho, K., et al. (2006). Pathogenesis of osteoarthritis-like changes in the joints of mice deficient in type IX collagen. *Arthritis. Rheum*. 54, 2891–2900. doi: 10.1002/art.22040

Huang, G. P., Molina, A., Tran, N., Collins, G., and Arinzeh, T. L. (2018). Investigating cellulose derived glycosaminoglycan mimetic scaffolds for cartilage tissue engineering applications. *J. Tissue Eng. Regen. Med*. 12, e592–e603. doi: 10.1002/term.2331

Hunter, D. J., McDougall, J. J., and Keefe, F. J. (2008). The symptoms of osteoarthritis and the genesis of pain. *Rheum. Dis. Clin. North Am*. 34, 623–643. doi: 10.1016/j.rdc.2008.05.004

Hunziker, E. B. (2002). Articular cartilage repair: Basic science and clinical progress. A review of the current status and prospects. *Osteoarthr. Cartilage* 10, 432–463. doi: 10.1053/joca.2002.0801

Ikeda, T., Kamekura, S., Mabuchi, A., Kou, I., Seki, S., Takato, T., et al. (2004). The combination of SOX5, SOX6, and SOX9 (the SOX trio) provides signals sufficient for induction of permanent cartilage. *Arthritis. Rheum*. 50, 3561–3573. doi: 10.1002/art.20611

Islas-Arteaga, N. C., Raya Rivera, A., Esquiliano Rendon, D. R., Morales-Corona, J., Ontiveros-Nevares, P. G., Flores Sánchez, M. G., et al. (2018). Electrospun scaffolds with surfaces modified by plasma for regeneration of articular cartilage tissue: a pilot study in rabbit. *Int. J. Polym. Mater Pol. Biomat*. 68, 1–10. doi: 10.1080/00914037.2018.1534109

Janjanin, S., Li, W. J., Morgan, M. T., Shanti, R. M., and Tuan, R. S. (2008). Mold-shaped, nanofiber scaffold-based cartilage engineering using human mesenchymal stem cells and bioreactor. *J. Surg. Res*. 149, 47–56. doi: 10.1016/j.jss.2007.12.788

Jiang, T., Kai, D., Liu, S., Huang, X., Heng, S., Zhao, J., et al. (2018). Mechanically cartilage-mimicking poly (PCL-PTHF urethane)/collagen nanofibers induce chondrogenesis by blocking NF–kappa B signaling pathway. *Biomaterials* 178, 281–292. doi: 10.1016/j.biomaterials.2018.06.023

Jiang, Y., and Tuan, R. (2015). Origin and function of cartilage stem/progenitor cells in osteoarthritis. *Nat. Rev. Rheumatol*. 11, 206–212. doi: 10.1038/nrrheum.2014.200

Keikhaei, S., Mohammadalizadeh, Z., Karbasi, S., and Salimi, A. (2019). Evaluation of the effects of β-tricalcium phosphate on physical, mechanical and biological properties of Poly (3-hydroxybutyrate)/chitosan electrospun scaffold for cartilage tissue engineering applications. *Mater. Technol*. 34, 615–625. doi: 10.1080/10667857.2019.1611053

Kessick, R., Fenn, J., and Tepper, G. (2004). The use of AC potentials in electrospraying and electrospinning processes. *Polymer* 45, 2981–2984. doi: 10.1016/j.polymer.2004.02.056

Khorshidi, S., Solouk, A., Mirzadeh, H., Mazinani, S., Lagaron, J. M., Sharifi, S., et al. (2016). A review of key challenges of electrospun scaffolds for tissue-engineering applications. *J. Tissue Eng. Regen. Med*. 10, 715–738. doi: 10.1002/term.1978

Ki, C. S., Baek, D. H., Gang, K. D., Lee, K. H., Um, I. C., and Park, Y. H. (2005). Characterization of gelatin nanofiber prepared from gelatin–formic acid solution. *Polymer* 46, 5094–5102. doi: 10.1016/j.polymer.2005.04.040

Ki, C. S., Kim, J. W., Hyun, J. H., Lee, K. H., Hattori, M., Rah, D. K., et al. (2007). Electrospun three-dimensional silk fibroin nanofibrous scaffold. *J. Appl. Polym*. 106, 3922–3928. doi: 10.1002/app.26914

Kim, C., Shores, L., Guo, Q., Aly, A., Jeon, O. H., Kim do, H., et al. (2016). Electrospun microfiber scaffolds with anti-inflammatory tributanoylated N-acetyl-d-glucosamine promote cartilage regeneration. *Tissue Eng. Part A*. 22, 689–697. doi: 10.1089/ten.tea.2015.0469

Kim, T. G., Chung, H. J., and Park, T. G. (2008). Macroporous and nanofibrous hyaluronic acid/collagen hybrid scaffold fabricated by concurrent electrospinning and deposition/leaching of salt particles. *Acta Biomater*. 4, 1611–1619. doi: 10.1016/j.actbio.2008.06.008

Komae, H., Sekine, H., Dobashi, I., Matsuura, K., Ono, M., Okano, T., et al. (2017). Three-dimensional functional human myocardial tissues fabricated from induced pluripotent stem cells. *J. Tissue Eng. Regen. Med*. 11, 926–935. doi: 10.1002/term.1995

Kumar, A., Placone, J., and Engler, A. (2017). Understanding the extracellular forces that determine cell fate and maintenance. *Development* 144, 4261–4270. doi: 10.1242/dev.158469

Kuo, Y. C., Hung, S. C., and Hsu, S. H. (2014). The effect of elastic biodegradable polyurethane electrospun nanofibers on the differentiation of mesenchymal stem cells. *Colloids Surf. B*. 122, 414–422. doi: 10.1016/j.colsurfb.2014.07.017

Kurz, B., Lemke, A. K., Fay, J., Pufe, T., Grodzinsky, A. J., and Schünke, M. (2005). Pathomechanisms of cartilage destruction by mechanical injury. *Ann. Anat*. 187, 473–485. doi: 10.1016/j.aanat.2005.07.003

Kwon, O. H., Lee, I. S., Ko, Y. G., Meng, W., Jung, K. H., Kang, I. K., et al. (2007). Electrospinning of microbial polyester for cell culture. *Biomed. Mater*. 2, S52–S58. doi: 10.1088/1748-6041/2/1/S08

Lavik, E., and Langer, R. (2004). Tissue engineering: current state and perspectives. *Appl. Microbiol. Biotechnol*. 65, 1–8. doi: 10.1007/s00253-004-1580-z

Lefebvre, V., and Smits, P. (2005). Transcriptional control of chondrocyte fate and differentiation. *Birth. Defects Res. C*. 75, 200–212. doi: 10.1002/bdrc.20048

Legendre, F., Ollitrault, D., Hervieu, M., Bauge, C., Maneix, L., Goux, D., et al. (2013). Enhanced hyaline cartilage matrix synthesis in collagen sponge scaffolds by using siRNA to stabilize chondrocytes phenotype cultured with bone morphogenetic protein-2 under hypoxia. *Tissue Eng. Part C*. 19, 550–567. doi: 10.1089/ten.tec.2012.0508

Levorson, E. J., Raman Sreerekha, P., Chennazhi, K. P., Kasper, F. K., Nair, S. V., and Mikos, A. G. (2013). Fabrication and characterization of multiscale electrospun scaffolds for cartilage regeneration, *Biomed Mater*. 8:014103. doi: 10.1088/1748-6041/8/1/014103

Li, D., Wang, Y., and Xia, Y. (2004). Electrospinning nanofibers as uniaxially aligned arrays and layer-by-layer stacked films. *Adv. Mater*. 16, 361–366. doi: 10.1002/adma.200306226

Li, G., Shi, S., Lin, S., Zhou, T., Shao, X., Huang, Q., et al. (2018). Electrospun fibers for cartilage tissue regeneration. *Curr. Stem Cell Res. Ther*. 13, 591–599. doi: 10.2174/1574888X13666180417120508

Li, J., Chen, G., Xu, X., Abdou, P., Jiang, Q., Shi, D., et al. (2019). Advances of injectable hydrogel-based scaffolds for cartilage regeneration. *Regen Biomater*. 6, 129–140. doi: 10.1093/rb/rbz022

Li, T.-F., O'Keefe, R. J., and Chen, D. (2005a). TGF-β signaling in chondrocytes. *Front. Biosci*. 10, 681–688. doi: 10.2741/1563

Li, W. J., Chiang, H., Kuo, T. F., Lee, H. S., Jiang, C. C., and Tuan, R. S. (2009). Evaluation of articular cartilage repair using biodegradable nanofibrous scaffolds in a swine model: a pilot study. *J. Tissue Eng. Regen Med*. 3, 1–10. doi: 10.1002/term.127

Li, W. J., Cooper, J. A. Jr., Mauck, R. L., and Tuan, R. S. (2006a). Fabrication and characterization of six electrospun poly(alpha-hydroxy ester)-based fibrous scaffolds for tissue engineering applications. *Acta Biomater*. 2, 377–385. doi: 10.1016/j.actbio.2006.02.005

Li, W. J., Danielson, K. G., Alexander, P. G., and Tuan, R. S. (2003). Biological response of chondrocytes cultured in three-dimensional nanofibrous poly(epsilon-caprolactone) scaffolds. *J. Biomed. Mater. Res. A*. 67, 1105–1114. doi: 10.1002/jbm.a.10101

Li, W. J., Jiang, Y. J., and Tuan, R. S. (2006b). Chondrocyte phenotype in engineered fibrous matrix is regulated by fiber size. *Tissue Eng.* 12, 1775–1785. doi: 10.1089/ten.2006.12.1775

Li, W. J., Shanti, R. M., and Tuan, R. S. (2007). *Electrospinning Technology for Nanofibrous Scaffolds in Tissue Engineering*. Nanotechnologies for the life sciences. doi: 10.1002/9783527610419.ntls0097

Li, W. J., and Tuan, R. S. (2009). Fabrication and application of nanofibrous scaffolds in tissue engineering. *Curr. Protocols Cell Biol.* 42, 25.22. 21–25.22.12. doi: 10.1002/0471143030.cb2502s42

Li, W. J., Tuli, R., Okafor, C., Derfoul, A., Danielson, K. G., Hall, D. J., et al. (2005b). A three-dimensional nanofibrous scaffold for cartilage tissue engineering using human mesenchymal stem cells. *Biomaterials* 26, 599–609. doi: 10.1016/j.biomaterials.2004.03.005

Li, Y., and Xu, L. (2015). Advances in understanding cartilage remodeling. *F1000Res.* 4:642. doi: 10.12688/f1000research.6514.1

Li, Z., Liu, P., Yang, T., Sun, Y., You, Q., Li, J., et al. (2016). Composite poly(l-lactic-acid)/silk fibroin scaffold prepared by electrospinning promotes chondrogenesis for cartilage tissue engineering. *J. Biomater. Appl.* 30, 1552–1565. doi: 10.1177/0885328216638587

Li, Z., and Wang, C. (eds.). (2013). "Effects of working parameters on electrospinning," in *One-Dimensional Nanostructures. SpringerBriefs in Materials* (Berlin, Heidelberg: Springer), 15–28. doi: 10.1007/978-3-642-36427-3_2

Lim, E.-H., Sardinha, J. P., and Myers, S. (2014). Nanotechnology biomimetic cartilage regenerative scaffolds. *Arch. Plast Surg.* 41, 231–240. doi: 10.5999/aps.2014.41.3.231

Lin, Y. X., Ding, Z. Y., Zhou, X. B., Li, S. T., Xie de, M., Li, Z. Z., et al. (2015). *In vitro* and *in vivo* evaluation of the developed PLGA/HAp/Zein scaffolds for bone-cartilage interface regeneration. *Biomed. Environ. Sci.* 28, 1–12. doi: 10.3967/bes2015.001

Liu, J., Nie, H., Xu, Z., Niu, X., Guo, S., Yin, J., et al. (2014a). The effect of 3D nanofibrous scaffolds on the chondrogenesis of induced pluripotent stem cells and their application in restoration of cartilage defects. *PLoS ONE* 9:e111566. doi: 10.1371/journal.pone.0111566

Liu, W., Thomopoulos, S., and Xia, Y. (2012). Electrospun nanofibers for regenerative medicine. *Adv. Healthc Mater.* 1, 10–25. doi: 10.1002/adhm.201100021

Liu, X., Liu, S., Liu, S., and Cui, W. (2014b). Evaluation of oriented electrospun fibers for periosteal flap regeneration in biomimetic triphasic osteochondral implant. *J. Biomed. Mater Res B.* 102, 1407–1414. doi: 10.1002/jbm.b.33119

Liu, Y., Liu, L., Wang, Z., Zheng, G., Chen, Q., and Luo, E. (2018). Application of electrospinning strategy on cartilage tissue engineering. *Curr. Stem Cell Res. Ther.* 13, 526–532. doi: 10.2174/1574888X13666180628163515

Lodewyckx, L., and Lories, R. J. (2009). WNT Signaling in osteoarthritis and osteoporosis: What is the biological significance for the clinician? *Curr. Rheumatol. Rep.* 11, 23–30. doi: 10.1007/s11926-009-0004-6

MacLean, H. E., Kim, J. I., Glimcher, M. J., Wang, J., Kronenberg, H. M., and Glimcher, L. H. (2003). Absence of transcription factor c-maf causes abnormal terminal differentiation of hypertrophic chondrocytes during endochondral bone development. *Dev. Biol.* 262, 51–63. doi: 10.1016/S0012-1606(03)00324-5

Markowski, J., Magiera, A., Lesiak, M., Sieron, A. L., Pilch, J., and Blazewicz, S. (2015). Preparation and characterization of nanofibrous polymer scaffolds for cartilage tissue engineering. *J. Nanomat.* 2015:564087. doi: 10.1155/2015/564087

Martin, I., Miot, S., Barbero, A., Jakob, M., and Wendt, D. (2007). Osteochondral tissue engineering, *J Biomech.* 40, 750–765. doi: 10.1016/j.jbiomech.2006.03.008

Matthews, J. A., Boland, E. D., Wnek, G. E., Simpson, D. G., and Bowlin, G. L. (2003). Electrospinning of collagen type II: a feasibility study. *J. Bioact. Compat. Pol.* 18, 125–134. doi: 10.1177/0883911503018002003

Matzat, S. J., van Tiel, J., Gold, G. E., and Oei, E. H. (2013). Quantitative MRI techniques of cartilage composition. *Quant. Imaging Med. Surg.* 3, 162–174. doi: 10.3978/j.issn.2223-4292.2013.06.04

McCullen, S. D., Autefage, H., Callanan, A., Gentleman, E., and Stevens, M. M. (2012). Anisotropic fibrous scaffolds for articular cartilage regeneration. *Tissue Eng. Part A.* 18, 2073–2083. doi: 10.1089/ten.tea.2011.0606

Mirzaei, S., Karkhaneh, A., Soleimani, M., Ardeshirylajimi, A., Seyyed Zonouzi, H., and Hanaee-Ahvaz, H. (2017). Enhanced chondrogenic differentiation of stem cells using an optimized electrospun nanofibrous PLLA/PEG scaffolds loaded with glucosamine. *J. Biomed. Mater. Res. A.* 105, 2461–2474. doi: 10.1002/jbm.a.36104

Molnár, K., and Vas, L. (2012). "Electrospun composite nanofibers and polymer composites," in *Synthetic Polymer-Polymer Composites*, eds D. Bhattacharyya and S. Fakirov (Munchen: Carl Hanser Verlag GmbH & Co. KG), 301–349. doi: 10.3139/9781569905258.010

Moroni, L., Schotel, R., Hamann, D., de Wijn, J. R., and van Blitterswijk, C. A. (2008). 3D fiber-deposited electrospun integrated scaffolds enhance cartilage tissue formation. *Adv. Funct. Mater.* 18, 53–60. doi: 10.1002/adfm.200601158

Morrison, S., Shah, N., and Anderson, D. (1997). Regulatory mechanisms in stem cell biology. *Cell* 88, 287–298. doi: 10.1016/S0092-8674(00)81867-X

Mouthuy, P. A., El-Sherbini, Y., Cui, Z., and Ye, H. (2016). Layering PLGA-based electrospun membranes and cell sheets for engineering cartilage-bone transition. *J. Tissue Eng. Regen. Med.* 10, E263–E274. doi: 10.1002/term.1765

Mouthuy, P. A., Ye, H., Triffitt, J., Oommen, G., and Cui, Z. (2010). Physico-chemical characterization of functional electrospun scaffolds for bone and cartilage tissue engineering. *Proc. Inst. Mech. Eng. H.* 224, 1401–1414. doi: 10.1243/09544119JEIM824

Mow, V. C., Wang, C. C., and Hung, C. T. (1999). The extracellular matrix, interstitial fluid and ions as a mechanical signal transducer in articular cartilage. *Osteoarthr. Cartilage* 7, 41–58. doi: 10.1053/joca.1998.0161

Muir, H. (1995). The chondrocyte, architect of cartilage. Biomechanics, structure, function and molecular biology of cartilage matrix macromolecules. *Bioessays* 17, 1039–1048. doi: 10.1002/bies.950171208

Muncie, J., and Weaver, V. (2018). The physical and biochemical properties of the extracellular matrix regulate cell fate. *Curr. Top. Dev. Biol.* 130, 1–37. doi: 10.1016/bs.ctdb.2018.02.002

Munir, N., McDonald, A., and Callanan, A. (2019). A combinatorial approach: cryo-printing and electrospinning hybrid scaffolds for cartilage tissue engineering. *Bioprinting* 16:e00056. doi: 10.1016/j.bprint.2019.e00056

Musumeci, G., Castrogiovanni, P., Leonardi, R., Trovato, F. M., Szychlinska, M. A., Di Giunta, A., et al. (2014). New perspectives for articular cartilage repair treatment through tissue engineering: a contemporary review. *World J. Orthop.* 5:80. doi: 10.5312/wjo.v5.i2.80

Nam, J., Huang, Y., Agarwal, S., and Lannutti, J. (2007). Improved cellular infiltration in electrospun fiber via engineered porosity. *Tissue Eng.* 13, 2249–2257. doi: 10.1089/ten.2006.0306

Nazempour, A., and Van Wie, B. J. (2016). Chondrocytes, mesenchymal stem cells, and their combination in articular cartilage regenerative medicine. *Ann. Biomed. Eng.* 44, 1325–1354. doi: 10.1007/s10439-016-1575-9

Novoseletskaya, E., Grigorieva, O., Efimenko, A., and Kalinina, N. (2019). Extracellular matrix in the regulation of stem cell differentiation. *Biochemistry.* 84, 232–240. doi: 10.1134/S0006297919030052

Pearle, A. D., Warren, R. F., and Rodeo, S. A. (2005). Basic science of articular cartilage and osteoarthritis. *Clin. Sports Med.* 24, 1–12. doi: 10.1016/j.csm.2004.08.007

Peroglio, M., Gaspar, D., Zeugolis, D., and Alini, M. (2018). Relevance of bioreactors and whole tissue cultures for the translation of new therapies to humans. *J. Orthop. Res.* 36, 10–21. doi: 10.1002/jor.23655

Pham, Q. P., Sharma, U., and Mikos, A. G. (2006). Electrospinning of polymeric nanofibers for tissue engineering applications: a review. *Tissue Eng.* 12, 1197–1211. doi: 10.1089/ten.2006.12.1197

Pillay, V., Dott, C., Choonara, Y. E., Tyagi, C., Tomar, L., Kumar, P., et al. (2013). A review of the effect of processing variables on the fabrication of electrospun nanofibers for drug delivery applications. *J. Nanomat.* 2013:22. doi: 10.1155/2013/789289

Poole, A. R., Kojima, T., Yasuda, T., Mwale, F., Kobayashi, M., and Laverty, S. (2001). Composition and structure of articular cartilage: a template for tissue repair:*Clin. Orthop. Relat. Res.* 391, S26–S33. doi: 10.1097/00003086-200110001-00004

Pugliese, E., Coentro, J., and Zeugolis, D. (2018). Advancements and challenges in multidomain multicargo delivery vehicles. *Adv. Mater.* 30:e1704324. doi: 10.1002/adma.201704324

Ren, X., Li, J., Li, J., Jiang, Y., Li, L., Yao, Q., et al. (2019). Aligned porous fibrous membrane with a biomimetic surface to accelerate cartilage regeneration. *Chem. Eng. J.* 370, 1027–1038. doi: 10.1016/j.cej.2019.03.271

Renard, E., Porée, B., Chadjichristos, C., Kypriotou, M., Maneix, L., Bigot, N., et al. (2012). Sox9/Sox6 and Sp1 are involved in the insulin-like growth factor-I-mediated upregulation of human type II collagen gene expression in articular chondrocytes. *J. Mol. Med*. 90, 649–666. doi: 10.1007/s00109-011-0842-3

Ripmeester, E., Timur, U., Caron, M., and Welting, T. (2018). Recent insights into the contribution of the changing hypertrophic chondrocyte phenotype in the development and progression of osteoarthritis. *Front. Bioeng. Biotechnol*. 6:18. doi: 10.3389/fbioe.2018.00018

Rosen, V., Nove, J., Song, J. J., Thies, R. S., Cox, K., and Wozney, J. M. (1994). Responsiveness of clonal limb bud cell lines to bone morphogenetic protein 2 reveals a sequential relationship between cartilage and bone cell phenotypes. *J. Bone Miner Res*. 9, 1759–1768. doi: 10.1002/jbmr.5650091113

Rowland, D. C., Aquilina, T., Klein, A., Hakimi, O., Alexis-Mouthuy, P., Carr, A. J., et al. (2016). A comparative evaluation of the effect of polymer chemistry and fiber orientation on mesenchymal stem cell differentiation. *J. Biomed. Mater Res. A*. 104, 2843–2853. doi: 10.1002/jbm.a.35829

Ryan, C., Fuller, K., Larrañaga, A., Biggs, M., Bayon, Y., Sarasua, J., et al. (2015). An academic, clinical and industrial update on electrospun, additive manufactured and imprinted medical devices. *Expert. Rev. Med. Devices*. 12, 601–612. doi: 10.1586/17434440.2015.1062364

Sadeghi, D., Karbasi, S., Razavi, S., Mohammadi, S., Shokrgozar, M. A., and Bonakdar, S. (2016). Electrospun poly(hydroxybutyrate)/chitosan blend fibrous scaffolds for cartilage tissue engineering. *J. Appl. Polym*. 133, 171. doi: 10.1002/app.44171

Sato, M., Yamato, M., Mitani, G., Takagaki, T., Hamahashi, K., Nakamura, Y., et al. (2019). Combined surgery and chondrocyte cell-sheet transplantation improves clinical and structural outcomes in knee osteoarthritis. *NPJ. Regen. Med*. 4:4. doi: 10.1038/s41536-019-0069-4

Schmidt, C. E., and Baier, J. M. (2000). Acellular vascular tissues: natural biomaterials for tissue repair and tissue engineering. *Biomaterials* 21, 2215–2231. doi: 10.1016/S0142-9612(00)00148-4

Schneider, T., Kohl, B., Sauter, T., Kratz, K., Lendlein, A., Ertel, W., et al. (2012). Influence of fiber orientation in electrospun polymer scaffolds on viability, adhesion and differentiation of articular chondrocytes. *Clin. Hemorheol. Microcirc*. 52, 325–336. doi: 10.3233/CH-2012-1608

Seifarth, C., Csaki, C., and Shakibaei, M. (2009). Anabolic actions of IGF-I and TGF-ß1 on interleukin-1ß-treated human articular chondrocytes: evaluation in two and three dimensional cultures. *Histol. Histopathol*. 24, 1245–1262. doi: 10.14670/HH-24.1245

Sekine, W., Haraguchi, Y., Shimizu, T., Umezawa, A., and Okano, T. (2011). Thickness limitation and cell viability of multi-layered cell sheets and overcoming the diffusion limit by a porous-membrane culture insert. *J. Biochip. Tissue Chip*. S1:007. doi: 10.4172/2153-0777.S1-007

Shafiee, A., Seyedjafari, E., Sadat Taherzadeh, E., Dinarvand, P., Soleimani, M., and Ai, J. (2014). Enhanced chondrogenesis of human nasal septum derived progenitors on nanofibrous scaffolds. *Mater. Sci. Eng. C* 40, 445–454. doi: 10.1016/j.msec.2014.04.027

Shafiee, A., Soleimani, M., Chamheidari, G. A., Seyedjafari, E., Dodel, M., Atashi, A., et al. (2011). Electrospun nanofiber-based regeneration of cartilage enhanced by mesenchymal stem cells. *J. Biomed. Mater. Res.* A 99, 467–478. doi: 10.1002/jbm.a.33206

Shanmugasundaram, S., Chaudhry, H., and Arinzeh, T. L. (2011). Microscale versus nanoscale scaffold architecture for mesenchymal stem cell chondrogenesis. *Tissue Eng. Part A* 17, 831–840. doi: 10.1089/ten.tea.2010.0409

Sharma, A. R., Jagga, S., Lee, S.-S., and Nam, J.-S. (2013). Interplay between cartilage and subchondral bone contributing to pathogenesis of osteoarthritis. *Int. J. Mol. Sci*. 14, 19805–19830. doi: 10.3390/ijms141019805

Shields, K. J., Beckman, M. J., Bowlin, G. L., and Wayne, J. S. (2004). Mechanical properties and cellular proliferation of electrospun collagen type II. *Tissue Eng.* 10, 1510–1517. doi: 10.1089/1076327042500373

Shim, I. K., Suh, W. H., Lee, S. Y., Lee, S. H., Heo, S. J., Lee, M. C., et al. (2009). Chitosan nano-/microfibrous double-layered membrane with rolled-up three-dimensional structures for chondrocyte cultivation. *J. Biomed. Mater. Res. A* 90, 595–602. doi: 10.1002/jbm.a.32109

Shimizu, T., Sekine, H., Yang, J., Isoi, Y., Yamato, M., Kikuchi, A., et al. (2006). Polysurgery of cell sheet grafts overcomes diffusion limits to produce thick, vascularized myocardial tissues. *FASEB J.* 20, 708–710. doi: 10.1096/fj.05-4715fje

Shimomura, K., Rothrauff, B. B., Hart, D. A., Hamamoto, S., Kobayashi, M., Yoshikawa, H., et al. (2019). Enhanced repair of meniscal hoop structure injuries using an aligned electrospun nanofibrous scaffold combined with a mesenchymal stem cell-derived tissue engineered construct. *Biomaterials* 192, 346–354. doi: 10.1016/j.biomaterials.2018.11.009

Shin, H. J., Lee, C. H., Cho, I. H., Kim, Y. J., Lee, Y. J., Kim, I. A., et al. (2006). Electrospun PLGA nanofiber scaffolds for articular cartilage reconstruction: mechanical stability, degradation and cellular responses under mechanical stimulation *in vitro*. *J. Biomater. Sci. Polym. Ed*. 17, 103–119. doi: 10.1163/156856206774879126

Shlopov, B. V., Lie, W.-R., Mainardi, C. L., Cole, A. A., Chubinskaya, S., and Hasty, K. A. (1997). Osteoarthritic lesions. Involvement of three different collagenases. *Arthritis Rheum*. 40, 2065–2074. doi: 10.1002/art.1780401120

Skotak, M., Noriega, S., Larsen, G., and Subramanian, A. (2010). Electrospun cross-linked gelatin fibers with controlled diameter: the effect of matrix stiffness on proliferative and biosynthetic activity of chondrocytes cultured *in vitro*. *J. Biomed. Mater Res. A* 95, 828–836. doi: 10.1002/jbm.a.32850

Skotak, M., Ragusa, J., Gonzalez, D., and Subramanian, A. (2011). Improved cellular infiltration into nanofibrous electrospun cross-linked gelatin scaffolds templated with micrometer-sized polyethylene glycol fibers. *Biomed. Mater*. 6:055012. doi: 10.1088/1748-6041/6/5/055012

Slivka, M. A., Leatherbury, N. C., Kieswetter, K., and Niederauer, G. G. (2001). Porous, resorbable, fiber-reinforced scaffolds tailored for articular cartilage repair. *Tissue Eng.* 7, 767–780. doi: 10.1089/107632701753337717

Smith, L., Cho, S., and Discher, D. (2018). Stem cell differentiation is regulated by extracellular matrix mechanics. *Physiology* 33, 16–25. doi: 10.1152/physiol.00026.2017

Sohier, J., Moroni, L., van Blitterswijk, C., de Groot, K., and Bezemer, J. M. (2008). Critical factors in the design of growth factor releasing scaffolds for cartilage tissue engineering. *Expert Opin. Drug Deliv*. 5, 543–566. doi: 10.1517/17425247.5.5.543

Sophia Fox, A. J., Bedi, A., and Rodeo, S. A. (2009). The basic science of articular cartilage: structure, composition, and function. *Sports Health*. 1, 461–468. doi: 10.1177/1941738109350438

Stanger, J., Tucker, N., Wallace, A., Larsen, N., Staiger, M., and Reeves, R. (2009). The effect of electrode configuration and substrate material on the mass deposition rate of electrospinning. *J. Appl. Polym*. 112, 1729–1737. doi: 10.1002/app.29663

Subbiah, T., Bhat, G., Tock, R., Parameswaran, S., and Ramkumar, S. (2005). Electrospinning of nanofibers. *J. Appl. Polym*. 96, 557–569. doi: 10.1002/app.21481

Subramanian, A., Vu, D., Larsen, G. F., and Lin, H.-Y. (2005). Preparation and evaluation of the electrospun chitosan/PEO fibers for potential applications in cartilage tissue engineering. *J. Biomater. Sci. Polym Ed*. 16, 861–873. doi: 10.1163/1568562054255682

Sun, A., Lin, H., Beck, A., Kilroy, E., and Tuan, R. (2015). Projection stereolithographic fabrication of human adipose stem cell-incorporated biodegradable scaffolds for cartilage tissue engineering. *Front. Bioeng. Biotechnol*. 3:115. doi: 10.3389/fbioe.2015.00115

Sundaray, B., Subramanian, V., Natarajan, T., Xiang, R.-Z., Chang, C.-C., and Fann, W.-S. (2004). Electrospinning of continuous aligned polymer fibers. *Appl. Phys. Lett*. 84, 1222–1224. doi: 10.1063/1.1647685

Taheem, D., Jell, G., and Gentleman, E. (2019). Hypoxia inducible factor-1α in osteochondral tissue engineering. *Tissue Eng Part B*. https://www.liebertpub.com/doi/full/10.1089/ten.teb.2019.0283

Temenoff, J. S., and Mikos, A. G. (2000). Review: tissue engineering for regeneration of articular cartilage. *Biomaterials* 21, 431–440. doi: 10.1016/S0142-9612(99)00213-6

Thorvaldsson, A., Stenhamre, H., Gatenholm, P., and Walkenstrom, P. (2008). Electrospinning of highly porous scaffolds for cartilage regeneration. *Biomacromolecules* 9, 1044–1049. doi: 10.1021/bm701225a

Toloue, E. B., Karbasi, S., Salehi, H., and Rafienia, M. (2019). Evaluation of mechanical properties and cell viability of poly (3-hydroxybutyrate)-chitosan/Al2O3nanocomposite scaffold for cartilage tissue engineering. *J. Med. Signals Sens*. 9, 111–116. doi: 10.4103/jmss.JMSS_56_18

Torio, C., and Moore, B. (2013). *National Inpatient Hospital Costs: The Most Expensive Conditions by Payer*. Statistical Brief.

Toyokawa, N., Fujioka, H., Kokubu, T., Nagura, I., Inui, A., Sakata, R., et al. (2010). Electrospun synthetic polymer scaffold for cartilage repair without cultured cells in an animal model. *Arthroscopy* 26, 375–383. doi: 10.1016/j.arthro.2009.08.006

van der Weyden, L., Wei, L., Luo, J., Yang, X., Birk, D. E., Adams, D. J., et al. (2006). Functional knockout of the matrilin-3 gene causes premature chondrocyte maturation to hypertrophy and increases bone mineral density and osteoarthritis. *Am. J. Pathol.* 169, 515–527. doi: 10.2353/ajpath.2006.050981

Van Spil, W. E., Kubassova, O., Boesen, M., Bay-Jensen, A.-C., and Mobasheri, A. (2019). Osteoarthritis phenotypes and novel therapeutic targets. *Biochem. Pharmacol.* 165, 41–48. doi: 10.1016/j.bcp.2019.02.037

Venugopal, E., Sahanand, K. S., Bhattacharyya, A., and Rajendran, S. (2019). Electrospun PCL nanofibers blended with Wattakaka volubilis active phytochemicals for bone and cartilage tissue engineering. *Nanomedicine* 21:102044. doi: 10.1016/j.nano.2019.102044

Vonk, L. A., de Windt, T. S., Kragten, A. H., Beekhuizen, M., Mastbergen, S. C., Dhert, W. J., et al. (2014). Enhanced cell-induced articular cartilage regeneration by chondrons: the influence of joint damage and harvest site. *Osteoarthr. Cartilage* 22, 1910–1917. doi: 10.1016/j.joca.2014.08.005

Wadhwa, S., Embree, M., Ameye, L., and Young, M. F. (2005a). Mice deficient in biglycan and fibromodulin as a model for temporomandibular joint osteoarthritis. *Cells Tissues Organs*. 181, 136–143. doi: 10.1159/000091375

Wadhwa, S., Embree, M. C., Kilts, T., Young, M. F., and Ameye, L. G. (2005b). Accelerated osteoarthritis in the temporomandibular joint of biglycan/fibromodulin double-deficient mice. *Osteoarthr. Cartilage* 13, 817–827. doi: 10.1016/j.joca.2005.04.016

Wang, X., Um, I. C., Fang, D., Okamoto, A., Hsiao, B. S., and Chu, B. (2005). Formation of water-resistant hyaluronic acid nanofibers by blowing-assisted electro-spinning and non-toxic post treatments. *Polymer* 46, 4853–4867. doi: 10.1016/j.polymer.2005.03.058

Watt, F., and Huck, W. (2013). Role of the extracellular matrix in regulating stem cell fate. *Nat. Rev. Mol. Cell. Biol.* 14, 467–473. doi: 10.1038/nrm3620

Whited, B. M., Whitney, J. R., Hofmann, M. C., Xu, Y., and Rylander, M. N. (2011). Pre-osteoblast infiltration and differentiation in highly porous apatite-coated PLLA electrospun scaffolds. *Biomaterials* 32, 2294–2304. doi: 10.1016/j.biomaterials.2010.12.003

Wilusz, R. E., Sanchez-Adams, J., and Guilak, F. (2014). The structure and function of the pericellular matrix of articular cartilage *Matrix Biol.* 39, 25–32. doi: 10.1016/j.matbio.2014.08.009

Wimpenny, I., Ashammakhi, N., and Yang, Y. (2012). Chondrogenic potential of electrospun nanofibres for cartilage tissue engineering. *J. Tissue Eng. Regen. Med.* 6, 536–549. doi: 10.1002/term.459

Wise, J. K., Yarin, A. L., Megaridis, C. M., and Cho, M. (2009). Chondrogenic differentiation of human mesenchymal stem cells on oriented nanofibrous scaffolds: engineering the superficial zone of articular cartilage, *Tissue Eng. Part A*. 15, 913–921. doi: 10.1089/ten.tea.2008.0109

Wright, L. D., McKeon-Fischer, K. D., Cui, Z., Nair, L. S., and Freeman, J. W. (2014). PDLA/PLLA and PDLA/PCL nanofibers with a chitosan-based hydrogel in composite scaffolds for tissue engineered cartilage. *J. Tissue Eng. Regen Med.* 8, 946–954. doi: 10.1002/term.1591

Wuelling, M., and Vortkamp, A. (2011). "Chondrocyte proliferation and differentiation," in *Cartilage and Bone Development and Its Disorders* (Karger Publishers), 1–11. doi: 10.1159/000328081

Xu, C. Y., Inai, R., Kotaki, M., and Ramakrishna, S. (2004). Aligned biodegradable nanofibrous structure: a potential scaffold for blood vessel engineering. *Biomaterials* 25, 877–886. doi: 10.1016/S0142-9612(03)00593-3

Xu, H., Cai, S., Xu, L., and Yang, Y. (2014). Water-stable three-dimensional ultrafine fibrous scaffolds from keratin for cartilage tissue engineering. *Langmuir* 30, 8461–8470. doi: 10.1021/la500768b

Yang, L., Fiti,é, C., van der Werf, K., Bennink, M., Dijkstra, P., and Feijen, J. (2008). Mechanical properties of single electrospun collagen type I fibers. *Biomaterials* 29, 955–962. doi: 10.1016/j.biomaterials.2007.10.058

Yoshida, C. A., Yamamoto, H., Fujita, T., Furuichi, T., Ito, K., Inoue, K.-,i., et al. (2004). Runx2 and Runx3 are essential for chondrocyte maturation, and Runx2 regulates limb growth through induction of Indian hedgehog. *Genes Dev.* 18, 952–963. doi: 10.1101/gad.1174704

Youn, I., Choi, J. B., Cao, L., Setton, L. A., and Guilak, F. (2006). Zonal variations in the three-dimensional morphology of the chondron measured *in situ* using confocal microscopy. *Osteoarthr. Cartilage* 14, 889–897. doi: 10.1016/j.joca.2006.02.017

Yu, F., Li, M., Yuan, Z., Rao, F., Fang, X., Jiang, B., et al. (2018). Mechanism research on a bioactive resveratrol–PLA–gelatin porous nano-scaffold in promoting the repair of cartilage defect. *Int. J. Nanomedicine* 13:7845. doi: 10.2147/IJN.S181855

Yunos, D. M., Ahmad, Z., Salih, V., and Boccaccini, A. R. (2013). Stratified scaffolds for osteochondral tissue engineering applications: electrospun PDLLA nanofibre coated Bioglass(R)-derived foams. *J. Biomater. Appl.* 27, 537–551. doi: 10.1177/0885328211414941

Zamanlui, S., Mahmoudifard, M., Soleimani, M., Bakhshandeh, B., Vasei, M., and Faghihi, S. (2018). Enhanced chondrogenic differentiation of human bone marrow mesenchymal stem cells on PCL/PLGA electrospun with different alignments and compositions. *Int. J. Polym. Mater. Pol. Biomat.* 67, 50–60. doi: 10.1080/00914037.2017.1297941

Zelzer, E., Glotzer, D. J., Hartmann, C., Thomas, D., Fukai, N., Soker, S., et al. (2001). Tissue specific regulation of VEGF expression during bone development requires Cbfa1/Runx2. *Mech. Dev.* 106, 97–106. doi: 10.1016/S0925-4773(01)00428-2

Zeugolis, D., Khew, S., Yew, E., Ekaputra, A., Tong, Y., Yung, L., et al. (2008). Electro-spinning of pure collagen nano-fibres - Just an expensive way to make gelatin? *Biomaterials* 29, 2293–2305. doi: 10.1016/j.biomaterials.2008.02.009

Zhang, L., Hu, J., and Athanasiou, K. A. (2009). The role of tissue engineering in articular cartilage repair and regeneration. *Crit. Rev. Biomed. Eng.* 37, 1–57. doi: 10.1615/CritRevBiomedEng.v37.i1-2.10

Zhang, Y., and Jordan, J. (2010). Epidemiology of osteoarthritis. *Clin Geriatr. Med.* 26, 355–369. doi: 10.1016/j.cger.2010.03.001

Zhang, Y., Liu, X., Zeng, L., Zhang, J., Zuo, J., Zou, J., et al. (2019). Polymer fiber scaffolds for bone and cartilage tissue engineering. *Adv. Funct. Mater.* 29:1903279. doi: 10.1002/adfm.201903279

Zheng, X., Wang, W., Liu, S., Wu, J., Li, F., Cao, L., et al. (2016). Enhancement of chondrogenic differentiation of rabbit mesenchymal stem cells by oriented nanofiber yarn-collagen type I/hyaluronate hybrid. *Mater. Sci. Eng. C.* 58, 1071–1076. doi: 10.1016/j.msec.2015.07.066

Zhu, M., Chen, M., Zuscik, M., Wu, Q., Wang, Y. J., Rosier, R. N., et al. (2008). Inhibition of beta-catenin signaling in articular chondrocytes results in articular cartilage destruction. *Arthritis. Rheum.* 58, 2053–2064. doi: 10.1002/art.23614

Zhu, M., Tang, D., Wu, Q., Hao, S., Chen, M., Xie, C., et al. (2009). Activation of beta-catenin signaling in articular chondrocytes leads to osteoarthritis-like phenotype in adult beta-catenin conditional activation mice. *J. Bone Miner Res.* 24, 12–21. doi: 10.1359/jbmr.080901

Conflict of Interest: The authors declare that the research was conducted in the absence of any commercial or financial relationships that could be construed as a potential conflict of interest.

frontiers in Bioengineering and Biotechnology

ORIGINAL RESEARCH
published: 19 February 2020
doi: 10.3389/fbioe.2020.00107

Multiparametric Optical Bioimaging Reveals the Fate of Epoxy Crosslinked Biomeshes in the Mouse Subcutaneous Implantation Model

Vadim Elagin[1], Daria Kuznetsova[1], Ekaterina Grebenik[2], Denis A. Zolotov[3], Leonid Istranov[2], Tatiana Zharikova[2], Elena Istranova[2], Anastasia Polozova[1], Dmitry Reunov[1], Alexandr Kurkov[2], Anatoly Shekhter[2], Elvira R. Gafarova[2], Victor Asadchikov[3], Sergey M. Borisov[4], Ruslan I. Dmitriev[2,5], Elena Zagaynova[1] and Peter Timashev[2,6,7]*

[1] *Institute of Experimental Oncology and Biomedical Technologies, Privolzhsky Research Medical University, Nizhny Novgorod, Russia,* [2] *Institute for Regenerative Medicine, Sechenov First Moscow State Medical University, Moscow, Russia,* [3] *Shubnikov Institute of Crystallography, Federal Scientific Research Centre "Crystallography and Photonics" Russian Academy of Sciences, Moscow, Russia,* [4] *Institute of Analytical Chemistry and Food Chemistry, Graz University of Technology, Graz, Austria,* [5] *School of Biochemistry and Cell Biology, University College Cork, Cork, Ireland,* [6] *Institute of Photonic Technologies, Federal Scientific Research Centre "Crystallography and Photonics" Russian Academy of Sciences, Moscow, Russia,* [7] *Department of Polymers and Composites, N.N.Semenov Institute of Chemical Physics, Moscow, Russia*

Biomeshes based on decellularized bovine pericardium (DBP) are widely used in reconstructive surgery due to their wide availability and the attractive biomechanical properties. However, their efficacy in clinical applications is often affected by the uncontrolled immunogenicity and proteolytic degradation. To address this issue, we present here *in vivo* multiparametric imaging analysis of epoxy crosslinked DBPs to reveal their fate after implantation. We first analyzed the structure of the crosslinked DBP using scanning electron microscopy and evaluated proteolytic stability and cytotoxicity. Next, using combination of fluorescence and hypoxia imaging, X-ray computed microtomography and histology techniques we studied the fate of DBPs after subcutaneous implantation in animals. Our approach revealed high resistance to biodegradation, gradual remodeling of a surrounding tissue forming the connective tissue capsule and calcification of crosslinked DBPs. These changes were concomitant to the development of hypoxia in the samples within 3 weeks after implantation and subsequent induction of angiogenesis and vascularization. Collectively, presented approach provides new insights on the transplantation of the epoxy crosslinked biomeshes, the risks associated with its applications in soft-tissue reconstruction and can be transferred to studies of other types of implants.

Keywords: decellularized tissue, biomeshes, bovine pericardium, epoxy crosslinking, hypoxia, *in vivo* biodegradation, optical bioimaging, PLIM

OPEN ACCESS

Edited by:
Dimitrios I. Zeugolis, National University of Ireland Galway, Ireland

Reviewed by:
Pavel Makarevich, Lomonosov Moscow State University, Russia
Ferdinand Köckerling, Vivantes Hospital, Germany
Karin Strigård, Umeå University, Sweden
Igor Adameyko, Karolinska Institutet (KI), Sweden

****Correspondence:***
Vadim Elagin
elagin.vadim@gmail.com

Specialty section:
This article was submitted to Tissue Engineering and Regenerative Medicine, a section of the journal Frontiers in Bioengineering and Biotechnology

Received: *06 September 2019*
Accepted: *03 February 2020*
Published: *19 February 2020*

Citation:
Elagin V, Kuznetsova D, Grebenik E, Zolotov DA, Istranov L, Zharikova T, Istranova E, Polozova A, Reunov D, Kurkov A, Shekhter A, Gafarova ER, Asadchikov V, Borisov SM, Dmitriev RI, Zagaynova E and Timashev P (2020) Multiparametric Optical Bioimaging Reveals the Fate of Epoxy Crosslinked Biomeshes in the Mouse Subcutaneous Implantation Model. Front. Bioeng. Biotechnol. 8:107. doi: 10.3389/fbioe.2020.00107

INTRODUCTION

Biomeshes based on decellularized bovine pericardium (DBP) are widely used in reconstructive surgery by virtue of their ready availability and attractive biomechanical properties (Baharuddin et al., 2002; Colombo et al., 2009; Guerette et al., 2009; Limpert et al., 2009; Schlee et al., 2012; Mallis et al., 2017). They are already being applied to intracardiac surgery (Gabbay et al., 1984), abdominal wall repair (Limpert et al., 2009), treatment of gingival recession (Schlee et al., 2012), bone and periodontal defects (Stavropoulos et al., 2011), duraplastics (Baharuddin et al., 2002), ophthalmology (Gupta et al., 2002; Koay et al., 2008; Quaranta et al., 2013), the repair of rectovaginal septum defects (Guerette et al., 2009), as dental membranes and venous stent covers (Colombo et al., 2009). However, the xenogenic nature of the biomesh source prompts an immune response in the human body and facile biodegradation. Elimination of immunogenicity is usually achieved by means of decellularization and/or crosslinking. In early 1990s, epoxy compounds attracted a wide attention as a class of crosslinkers owing to their anti-calcification effect. Epoxy compounds are proved to prevent biodegradation and calcification of bioprosthetic materials while preserving their pliability and cytocompatibility (Imamura et al., 1989; Xi et al., 1992; Sung et al., 1993; Bre et al., 2014; Rezvova and Kudryavceva, 2018). However, these findings are valid for native, intrinsically immunogenic, tissues; while no comprehensive *in vivo* studies on acellular epoxy crosslinked biomeshes were performed. Currently, decellularization is a prerequisite preliminary step in the fabrication process for providing satisfactory integration of the xenomaterial into the patient's tissue (Oswal et al., 2007; Dong et al., 2009; Mendoza-Novelo et al., 2011; Stavropoulos et al., 2011; Pagoulatou et al., 2012). The effects of the epoxy crosslinking on acellular biomeshes have been comprehensively investigated *in vitro* (Perme et al., 2009; Grebenik et al., 2019), while the data on the structural alterations undergoing upon implantation are incomplete and often are based on the use of very diverse experimental assessment methodologies.

Currently, dominating methods for analysis of biomeshes' behavior in animal model are histology and direct mechanical measurements. Potentially, employment of novel cutting-edge techniques will enable to obtain frequently missing information on calcification dynamics, vascularization and hypoxia and other factors-dependent tissue remodeling. Thus, fluorescence stereomicroscopy permits to assess a biodegradation rate based on fluorescence signal intensity. Alterations in a collagen fiber structure can be studied by a non-linear microscopy techniques. X-ray computed microtomography provides information about interaction between biomeshes and animal body. Studying oxygenation and metabolism is highly important for tracking vascularization.

In present work, we have performed a complex *in vitro/in vivo* imaging study of the process of implant integration into living tissue using promising biomesh based on an epoxy compound, ethylene glycol diglycidyl ether (EGDE) crosslinked DBP. Our approach is based on a set of advanced techniques including fluorescence stereo microscopy, X-ray computed microtomography, multiphoton tomography based on two-photon excitation fluorescence (TPEF), and second harmonic generation (SHG), and phosphorescent nanosensor-mediated O_2 (hypoxia) imaging. This is a first instance for combining such highly informative multi-parametric analysis of the transplantation efficiency and subcutaneous integration of the epoxy crosslinked biomeshes. Altogether, this approach is attractive for the characterization of the material behavior with *in vivo* models and is useful for planning and adequate clinical treatment.

MATERIALS AND METHODS

Biomesh Preparation

Bovine pericardia were obtained directly from a local slaughterhouse and transported to our laboratory in a cold hypertonic solution. The pericardia were carefully cleaned of excess fat and connective tissue. The decellularization was achieved by treatment of the tissue with a mixture of 1M sodium hydroxide and 0.85M sodium sulfate for 2 h at 20°C followed by rinsing with water and neutralization with 4% (wt/v) boric acid for 1 h. The decellularized tissues were then rinsed with water thrice for 30 min, under continuous shaking. Decellularization success was assessed with the aid of the nuclear stain, ethidium homodimer (EthD-1), using a Nikon A1 MP confocal microscopy system (Nikon Instruments) with a 561 nm laser (Em: 570–620 nm). Decellularized tissues were then crosslinked in a phosphate buffer (pH 9) containing 5% (wt/v) of EGDE – a protocol adopted from Grebenik et al. (2019). Crosslinked samples were extensively washed, lyophilized and then sterilized with γ-radiation.

Scanning Electron Microscopy

For SEM study, 1 cm^2 sample patches or transverse 23 μm-thick microtome sections were prepared. Prior to sectioning, the biomeshes were dehydrated in ethanol and embedded in paraffin. The sections were mounted on standard microscopy slides, deparaffinized, plated with gold in a Magnetron Sputtering System LEYBOLD LH Z400 (Germany) and examined with a Zeiss Supra 40VP scanning electron microscope (Carl Zeiss Group, Germany) using an acceleration voltage of 10 kV and a working distance of 4.3 mm.

MTT-Test

An MTT [3-(4,5-dimethylthiazol-2-yl)-2,5-diphenyltetrazolium bromide] extraction test was adopted from ISO 10993. Sample extracts were prepared as follows: tissue specimens (three 1 cm^2 pieces) were finely minced and incubated in 1 ml of culture medium for 24 h at 37°C. Serial dilutions of the intact (non-crosslinked) and epoxy crosslinked samples in DMEM/F12 culture medium supplemented with 100 U/mL streptomycin, 100 g/mL penicillin, 1% (v/v) GlutaMAX (Gibco), 5% (v/v) fetal bovine serum (HyClone); with positive control [sodium dodecyl sulfate (SDS)] and negative control (culture medium alone) in triplicates (100 μl) were added to a subconfluent monolayer of L929 murine fibroblast cells in 96-well plates. The plates

were then incubated for a further 24 h at 37°C in 5% (v/v) CO_2 in air before the effects of the extracts on cell viability were determined using the MTT-test. For the MTT-test, the extract and control media were replaced with 100 μL of the MTT solution (0.5 mg/mL in medium without supplements) and were incubated in a CO_2-incubator at 37°C for 3 h. After discarding the MTT solution, 100 μL aliquots of dimethyl sulfoxide were added to all the wells and the plates swayed. The color developed was quantified by measuring absorbance at 550 nm (reference 650 nm) using a microplate photometer *(Multiskan FC,* Thermo scientific).

In vitro Biodegradation Assay

The susceptibility to collagenase digestion was studied in Collagenase A (from *Clostridium histolyticum*) solution. Approximately, 4 mg (dry weight in triplicates) of each sample were weighed. To the weighed samples, 0.2 ml aliquots of 2.5 mg/ml Collagenase A solution in Tris buffer (50 mM, pH 7.4) containing 10 mM calcium chloride and 0.02 mg/ml sodium azide (Paneco, Russia) were added. The samples were incubated at 37°C for 24 h. Then, the samples were centrifuged at 12,000 rpm for 10 min (using an A-14, Thermo Electron Corporation, Jouan-type centrifuge), washed with phosphate buffered saline (PBS), and the remaining tissue samples then dried in an oven at 60°C for 20 h. Finally, they were weighed and the weight loss was calculated by a paired comparison of before and after the treatments. The biodegradation in papain was studied in a solution of papain (Karipazim, Georgia, 100 U/ml) prepared in Tris buffer (50 mM, pH 8) containing 10 mM cysteine, 20 mM ethylenediaminetetraacetic acid (EDTA) and 0.02% sodium azide (Paneco, Russia) after 6 days, followed by the same measurement protocol.

Analysis of Biomeshes Degradation in Animal Model

All *in vivo* experiments were approved by the Ethics committee of the Privolzhsky Research Medical University (Nizhny Novgorod, Russia). We performed *in vivo* experiments on 30 male BALB/c mice (the mean weight body 20 g). The animals were divided into two equal groups. The animals were anesthetized with Zoletil (80 mg kg^{-1}) and fixed on a support holder. The mouse back hairs were shaved and the underlying skin cleaned and sterilized using chlorhexidine gluconate. Throughout the surgical procedures all strict sterility measures were upheld for survival surgeries. 7-mm incisions were made on the dorsal section of each mouse to implant the intact and epoxy crosslinked DBP samples. The biomeshes were separately and independently implanted into each mouse (2 samples of DBP of the same type). The incisions were sutured and medical glue was topically applied to the surgery sites to prevent infection. 10 samples of each DBP type were harvested and analyzed with following techniques at each time point (3, 6, and 12 weeks) after the implantation.

Fluorescence Stereomicroscopy

The main components of the DBP samples are collagen and elastin fibers. Collagen and elastin have several fluorescent moieties in the ultraviolet and visible spectral regions (Croce and Bottiroli, 2014) that may account for the DBP fluorescence. To assess biodegradation of the biomeshes, we used a special technique developed earlier for bone implants having a fluorescence signal (Timashev et al., 2016; Kuznetsova et al., 2017). In brief, we analyzed the fluorescence of implanted pericardium tissue using an Axio Zoom V16 (Carl Zeiss, Germany) fluorescence stereomicroscope and ImageJ 1.43u software (National Institutes of Health, United States). In the fluorescence images, the areas of all the samples were identified and the 'Integrated density' (IntDen) parameter was measured. The area of the biomeshes was evaluated with the 'Area' parameter. In addition, we made light images of both the intact and the crosslinked samples to visualize growing blood vessels.

Multiphoton Tomography Analysis

A multiphoton tomograph (MPTflex®, JenLab, Germany) was used to image the TPEF and the SHG of the DBP samples. The images were acquired through a 40×, 1.3 NA oil immersion objective. The excitation wavelength was set at 750 nm for acquiring the both TPEF and SHG signals of collagen. Backward-directed SHG signals were detected in the 373–387 nm range. A 409–660 nm emission filter was used for TPEF acquisition. The acquisition time of an XY image (512 × 512 pixels and 220 × 220 μm) was approximately 15 s. TPEF and SHG images were taken through the samples from the surface at z-steps of 10 μm. At least 5 z-stacks were acquired for each sample. For each image in the acquired stacks the average values of the photon intensities for TPEF and SHG were calculated by manually selecting 30 × 30 pixel zones as regions of interest.

X-Ray Computed Microtomography

The explants were dehydrated in ethanol, embedded in paraffin and analyzed using a custom-built X-ray microtomograph as described in Buzmakov et al. (2018). This microtomograph was equipped with a laboratory X-ray source GE ISOVOLT 3003 with a tube having Cu anode (energy E_{Ka1} = 8 keV) anode. The measurements were performed in monochromatic radiation using a pyrolityc graphite crystal C (0001) (monochromatization dE/E = 0.1). The total 400 projections were obtained, each 0.5° apart, and recorded by CCD-detector with 9 × 9 μm pixel size. The exposure time for each projection was 5 s. The 3D images were acquired by a modified algebraic method using CGLS regularization (Buzmakov et al., 2019).

Histological and Immunohistochemical Analysis of Harvested Samples

For histological, immunohistochemical and confocal microscopy analysis, tissue samples with implanted intact DBP and EGDE biomeshes were fixed in 10% neutral buffered formalin. The samples were dehydrated and embedded in paraffin. Ten sections from the middle of each paraffin block were prepared with a Leica SM 2000 microtome (Germany). Transverse serial 4 μm thick sections were stained with hematoxylin and eosin and van Gieson's picrofuchsin to analyze the general histoarchitecture

of the tissues and collagen structures. Von Kossa staining was applied to assess the degree of calcification.

In immunohistochemical study, endothelial cells of blood vessels were visualized with rabbit monoclonal antibodies to CD31 (ab182981, Abcam, United States) at 1:2000 dilution. Goat anti-rabbit IgG cross-adsorbed antibody conjugated with Alexa Fluor 488 (A-11008, Thermo Fisher Scientific, United States) was applied as secondary antibody at 1:1000 dilution. Immunohistochemical study with primary mouse monoclonal antibodies to CD 68 (KP1 clone, ÌÀ5-13324, Thermo Fisher Scientific, United States) at 1:100 dilution and biotin-goat anti-mouse IgG (H + L) secondary antibodies (Life Technologies Corporation, United States) at 1:500 dilution was performed to visualize macrophage and giant cell reaction.

We investigated the histological and immunohistochemical samples by light and fluorescent microscopy using a LEICA DM4000 B LED microscope equipped with a LEICA DFC7000 T digital video camera and LAS V4.8 software (Leica Microsystems, Germany).

NucBlue^{TM} Fixed Cell Reagent (Invitrogen) was used for staining cell nuclei. The tissue sections were deparaffinized and stained for 30 min at 37°C according to the manufacturer instructions followed by thorough rinsing with PBS. Fluoromount^{TM} Aqueous Mounting Medium (Sigma) was applied to the tissue sections then covered with a coverslip and sealed. For confocal imaging, we used the LSM 880 Airyscan (Carl Zeiss, Jena, Germany) scanning laser confocal microscope.

The morphometric study of tissue reaction to scaffold implantation was performed using the microscopic images taken at the magnification of × 630 in 10 representative fields of view (FOV). We analyzed the numbers of cells invading the scaffolds and in scaffold capsules, the capsule thickness, the degree of vascularization of the scaffolds and their capsules. The degree of maturation of scaffold capsules and the degree of calcification and resorption of scaffold material were also assessed by a semi-quantitative evaluation (**Supplementary Tables S1, S2**).

Nanosensor-Mediated O_2 Imaging

Conjugated polymer-based cationic SI-0.2^+ and zwitter-ionic SI-$0.1^+/0.1^-$ and SI-$0.05^+/0.15^-$ were synthesized and handled as described previously (Dmitriev et al., 2015). Briefly, nanosensors respond to changes in phosphorescence intensity and lifetime with increasing at low O_2 (hypoxia) and decreasing at high O_2. These changes can be calibrated and used for quantification (Papkovsky and Dmitriev, 2018). Due to their highly charged surface groups, nanosensors can stick and remain bound to various protein-based scaffold materials. For biomeshes staining, non- and EGDE-crosslinked DBP scaffolds were incubated with different SI nanosensors (100 μg/ml, 1 h, 37°C) in PBS, subsequently washed with PBS (1–2 times) and used for *in vitro* and *in vivo* experiments.

For *in vitro* evaluation of stability, SI-$0.1^+/0.1^-$ stained scaffolds were incubated in PBS supplemented with 10% fetal bovine serum (Sigma) over 0–14 days period at 37°C and measured on a custom-made phosphorescence lifetime imaging (PLIM) microscope as described previously (Dmitriev et al., 2013). Briefly, samples were imaged using 10x/0.3 Neofluar objective (Zeiss) using 390 nm LED and emission collected with 635 nm long pass filter. The acquired images were exported as RGB TIFF files and measured (with background correction) in ImageJ (Fiji.sc) software.

For *in vivo* evaluation SI-$0.1^+/0.1^-$ – stained samples were implanted subcutaneously to Balb/c female mice. Each animal was bearing both intact DBP and EGDE samples. Sensor phosphorescence was measured on explanted samples after 1, 2 and 3 weeks, using confocal scanning system for macroscopic objects DCS-120 MACRO (Becker & Hickl GmbH, Germany). Phosphorescence was excited by 375 nm diode laser with 60 ps pulse width and emission collected with 610 nm long pass filter. The phosphorescence signal was collected for 60 s. The acquired images had 256 × 256 pixels in resolution and 1024 time channels. The field of view was 10 m × 10 mm. The calculation of phosphorescence lifetime was done in SPCImage (Becker & Hickl GmbH, Germany) using the mono-exponential fitting as described previously (Dmitriev et al., 2015).

Statistical Analysis

The mean values (M) and standard deviations (σ) were calculated for all the data. A one-way ANOVA with Fisher's *post hoc* test and a Student's *t*-test were used to compare the data ($p \leq 0.05$ was considered statistically significant).

The morphometry study results were statistically analyzed using a standard program package GraphPad Prism version 8.2 (GraphPad Software, San Diego, CA, United States) and Statistica version 12.0 (StatSoft, Inc., Tulsa, OK, United States). Anderson–Darling test, D'Agostino & Pearson test, and Shapiro–Wilk test used for testing the normality of distribution of data. Then the geometric mean was accounted for a parameter "the capsule thickness" in 10 field of view in each tissue sample, for other parameter median were performed. The normally distributed data was accounted using two-way ANOVA followed by Sidak's multiple compassion test. Other data was accounted with compassions in Mann–Whitney *U*-test. The differences between the studied groups was considered statistically significant at *p*-value less than 0.05.

RESULTS

Sample Preparation and Characterization

The bovine pericardium tissue was successfully decellularized using alkaline treatment as was indicated by staining the samples with EthD-1 before and after decellularization. Confocal laser scanning microscopy revealed numerous stained cell nuclei present on the smooth side of the native pericardium tissue, whereas there were almost no cell nuclei on the decellularized sample (**Supplementary Figure S1**).

Scanning electron microscopy was performed to assess the structural properties of the intact and epoxy crosslinked DBPs. The SEM analysis showed that the micro- and ultrastructural properties of the intact DBP and EGDE samples were different (**Figure 1**). The intact DBP had a compact unbroken arrangement of fibers with axial periodicities (D-period) of the collagen

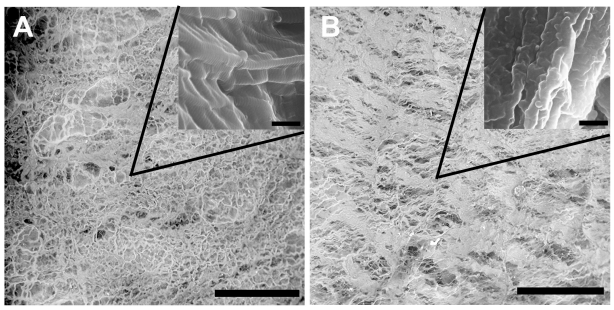

FIGURE 1 | Scanning electron microscopy characterization of the intact **(A)** and epoxy crosslinked DBP **(B)**. Scale bar is 200 μm. The inserts are the same sample at higher magnification, scale bar is 500 nm.

molecules. Crosslinking with EGDE affected the axial periodicity and changed the surface pattern, increasing the roughness. The average pore size was 10–140 μm in intact DBP and 10–130 μm – after epoxy crosslinking. However, the shape of the pores shifted from oval to more elongate with the tendency to fiber tightening and parallel packing. The fibril thickness increased upon crosslinking from 111.9 ± 20.8 to 117.1 ± 11.2 nm.

In vitro Assessment of Biocompatibility of the Intact and Epoxy Crosslinked Biomeshes

To evaluate the biocompatibility of the biomeshes we carried out MTT enzymatic reduction assays. The metabolic activity of actively respiring L929 murine fibroblast cells was found not to be influenced by the presence of EGDE crosslinks (**Figure 2A**). EGDE did not increase the cytotoxicity level of the biomeshes, and the relative cell viability was above 70% for the highest concentration of the sample extracts. SDS was used as a positive control, causing a remarkable level of cell death (IC_{50} ∼ 0.03 mg/ml).

Analysis of the biodegradation of the DBP samples in Collagenase and Papain solutions revealed that the EGDE biomeshes possessed a level of proteolytic stability several orders higher than that of the intact DBP (**Figure 2B**).

Analysis of Biomeshes Degradation in Animal Model

Both intact and epoxy crosslinked DBP samples were found to have strong fluorescence signals. The integral value of the signal intensity of the samples depends on the fiber structure and the total amount of protein in the pericardium tissue. The loss of fluorescence signal with time *in vivo* is proportional to the decrease in size of the DBP as it is degraded. Measurement of the signal intensity over time can therefore provide a relative assessment of DBP biodegradation. Collagen type I being a constituent of DBP is known to have strong SHG signal. The overall value of the mean signal intensity of the samples depends on the fiber structure and its packing.

Before implantation the intact and EGDE samples could be visualized as square-shaped structures with clear borders on stereomicroscopy (**Supplementary Figure S2**). The area and the fluorescence signal intensity (IntDen) were considered as 100%. Three weeks later, the borders of the samples still retained their shape, with the sample area still being about 97–99% of its initial value for all samples (**Figure 2C**), while the IntDen signal level had dropped by around two to three times (37% for the intact DBP and 45% for the EGDE sample; **Figure 2D**). Six weeks after the implantation the intact and epoxy crosslinked DBPs showed no further significant changes as compared with those at the 3-week time point. The areas were 85 and 95% for the intact and EGDE biomeshes respectively. The intact DBP had a more pronounced tendency toward a decrease in area. The IntDen signal level was 30% for the intact DBP and 44% for the EGDE sample. By week 12, the intact DBP area was 77% of its initial value, and its signal level had decreased to 16%. The EGDE biomeshes presented a more stable structure. Their areas and IntDen signals showed almost no change as compared to those at 3 and 6 weeks.

To evaluate the structure-functional alterations of DBPs during biodegradation we performed analysis of the shape of fibers as well as of the TPEF and SHG signal intensities by multiphoton tomography. The intact DBP samples were presented by dense collagen fibers with random direction (**Supplementary Figure S3**). The entangled collagen fibers had generally a cord-like shape and a tape-shape in a less. It was detected that the EGDE biomeshes consisted of dense regular collagen fibers were parallel to each other. By week 12 the intact DBP samples consisted of randomly oriented tape-shaped collagen fibers. No cord-like fibers were observed in the samples. In contrast, collagen fibers in the epoxy crosslinked DBPs did not change either shape or orientation. Analysis of intensities either TPEF or SHG revealed that both DBP samples had equal levels of each before implantation. However, biodegradation of the intact DBP led to a decrease of the TPEF value relative to that of the SHG, whereas, in the EGDE samples, the TPEF intensity dominated (**Supplementary Figure S3**).

X-ray computed microtomography was used to analyze macrostructural alterations of biomeshes. The average values of the linear absorption coefficient were calculated for both DBPs samples at 3rd, 6th, and 12th week after implantation (**Figure 3A**). The intact DBPs demonstrated the stable value over the experimental period. In contrast, the absorption coefficient of EGDE biomeshes dramatically increased at 12 week after implantation. For each sample, the values higher than 0.3 mm^{-1} were selected to build the distribution histogram (**Figure 3B**).

Interaction of the Intact and Epoxy Crosslinked Biomeshes With Recipient's Body

Morphological and morphometric analyses (**Figures 4–6** and **Supplementary Tables S1, S2**) and confocal microscopy analysis (**Supplementary Figure S4**) were performed in order to explain the changes in the intensity of fluorescence, SHG signal and X-ray absorption. 3 weeks after the operation, mature granulation tissue surrounded biomeshes of both DBP types forming a relatively thin capsules (**Figure 4**). Sponge shaped biomeshes had

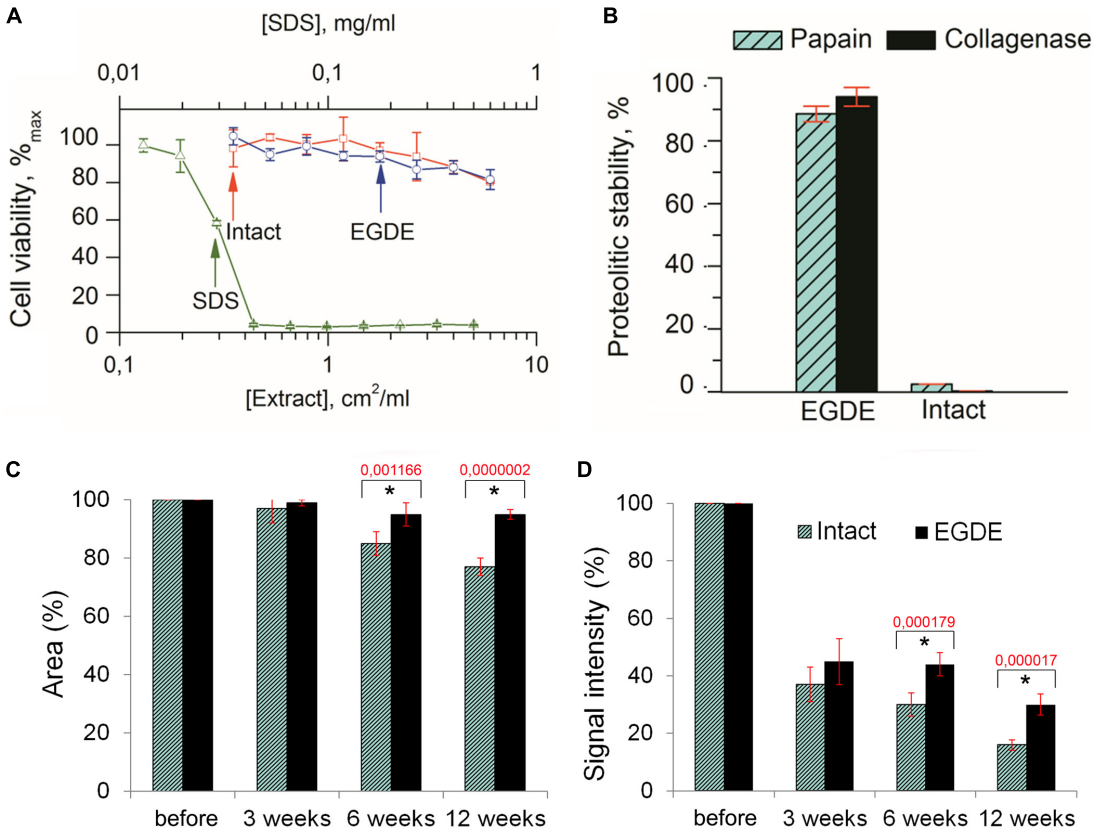

FIGURE 2 | Biodegradation analysis of the pericardium tissue *in vitro* **(A,B)** and *in vivo* **(C,D)**. **(A)** Cytotoxicity assays of an intact and of an EGDE biomeshes with murine fibroblasts L929 (SDS was used as a positive control); **(B)** biodegradation of the intact DBP and EGDE samples in Collagenase and Papain solutions; **(C)** quantitative analysis of the fluorescence signal intensity; **(D)** quantitative analysis of the implants area. *N* = 10, data shown as mean ± SD. *Statistically significant differences are presented between the intact and the EGDE samples, *p*-values are shown.

eosinophilic and fuchsinophilic septa. The capsules consisted of fibroblasts, sporadic small-caliber blood vessels, macrophages, foreign body giant cells, lymphocytes, and rare neutrophils. The capsules around intact DBP biomeshes were more mature than around epoxy crosslinked DBPs (**Figure 4**). However, the differences were statistically insignificant (**Supplementary Table S3**). They formed numerous septa in the peripheral pores of the biomeshes with rare small capillaries. In the EGDE samples, these septa were visually absent. The macrophage and fibroblast invasion into the intact DBP implant was more pronounced than that in the EGDE group (**Figures 4**, **5** and **Supplementary Figure S4, Table S3**). 6 weeks after the implantation, intact DBP biomesh material was severely resorbed by numerous macrophages inside and outside the scaffolds (**Supplementary Table S3**) and rare giant foreign body cells were present (**Figure 6**); the capsule was mature. Its connective tissue septa occupied most of the superficial pores and some deep pores of the biomeshes (**Figure 4**). The septa were very thin and consisted of immature connective tissue with an extremely scarce number of vessels and fibroblasts. In the epoxy crosslinked DBPs, the capsules had a similar structure, but it was noted to have a more prominent hyperemia, vascularization, and thickness (**Supplementary Table S3**). Moreover, rare connective tissue septa were observed only in the surficial pores and contained a significant number of giant cells (**Figures 4**, **6**). The number of giant cells in both scaffold and surrounding capsule were similar to that in intact DBP group (**Supplementary Table S3**). Unlike the intact DBP samples, peripheral septa in this group were modestly calcified (**Figures 4**, **5**), yet statistically insignificant. 12 weeks after the implantation of intact DBP biomeshes, structure of the capsules and connective tissue septa did not significantly differ from the previous period. However, connective tissue septa occupied almost all pores (**Figure 4** and **Supplementary Figure S4**), the number of fibroblasts insight and outside the scaffolds decreased. The resorption was statistically different from that of EGDE group (**Supplementary Table S3**). In the EGDE biomeshes, capsules, and connective tissue septa structures did not differ much from the previous time point as well. However, the EGDE biomesh material underwent an intensive calcification increasing tissue fragility and resulting in large defects that occurred after implantation during the life of the animal (**Figures 4**, **5** and **Supplementary Table S3**). The defects were filled with septa consisting of immature connective tissue with a weak inflammatory infiltration and a prominent hyperemia. At the same time, the number of fibroblasts in the scaffolds and surrounding capsule decreased,

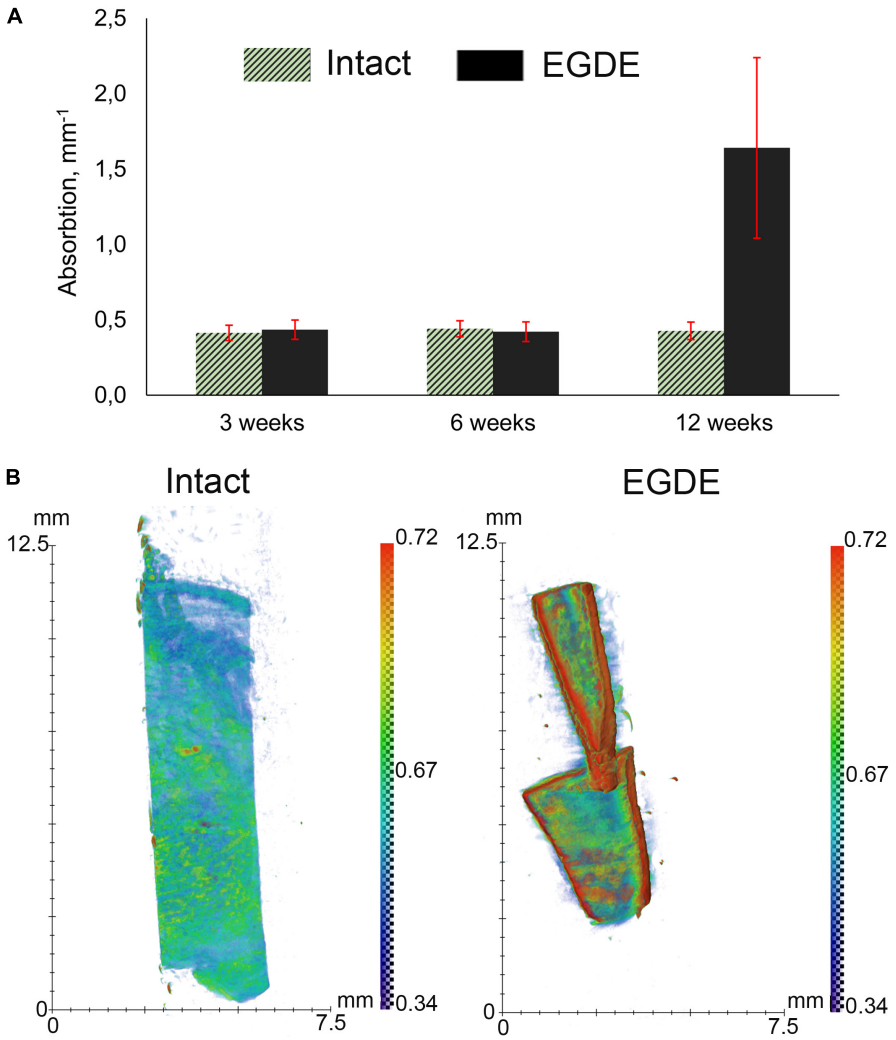

FIGURE 3 | X-ray computed microtomography analysis of DBP samples: **(A)** average absorption coefficients of the samples at 3, 6, and 12 weeks after subcutaneous implantation; **(B)** X-ray absorption histogram of the samples after 12 weeks. The data show a threefold increase in the X-ray absorption by the EGDE samples at 12 week after implantation. *N* = 10, data shown as mean ± SD.

and the capsule became thinner that in the intact DBP group (**Supplementary Table S3**). In spite of the prominent hyperemia in EDGE group, the total number of blood vessels outside the scaffold decreased compared to the previous time point and was comparable with that in intact DBP group (**Supplementary Table S3**).

We looked if the capsule formation could affect hypoxia in the implanted biomeshes. To test this, we used PLIM microscopy with the help of O_2-sensitive nanosensors. Recent success in design of O_2-and pH- sensing 'hybrid' tissue engineering materials (Jenkins et al., 2015; Yazgan et al., 2017; O'Donnell et al., 2018; Roussakis et al., 2019; Schilling et al., 2019) prompted us to stain the pericardial biomeshes with O_2-sensitive polymer nanoparticles. We hypothesized that charged nanoparticles could experience hydrophobic interactions and provide strong non-specific adsorption with the crosslinker or the polypeptide chains of the DBPs. We evaluated a promising cationic and zwitter-ionic (mixed charge) SI nanosensors with ratiometric and two-photon excited blue/red emission (Dmitriev et al., 2015) for staining of the scaffolds (**Supplementary Figure S5**). The brightest signals were observed for zwitter-ionic SI-$0.1^{+}/0.1^{-}$ nanoparticles, which were chosen for subsequent *in vivo* experiments. We further evaluated the stability of the staining by incubating them in serum-containing PBS over the 2 weeks time at 37°C and found negligible decrease in the fluorescence of the stained scaffolds over the tested period (**Supplementary Figure S6**). Interestingly, both intact and epoxy crosslinked DBPs displayed stability of the staining with O_2-sensitive nanoparticles. *In vivo* study showed that the mean values of phosphorescence lifetime of the sensor increased during the experiment, indicating decrease of oxygenation levels (**Figures 7A,B**). After 3 weeks the τ values of the EDGE samples grew in two times compared to those before implantation and reached nearly 0% O_2 values (∼55 μs).

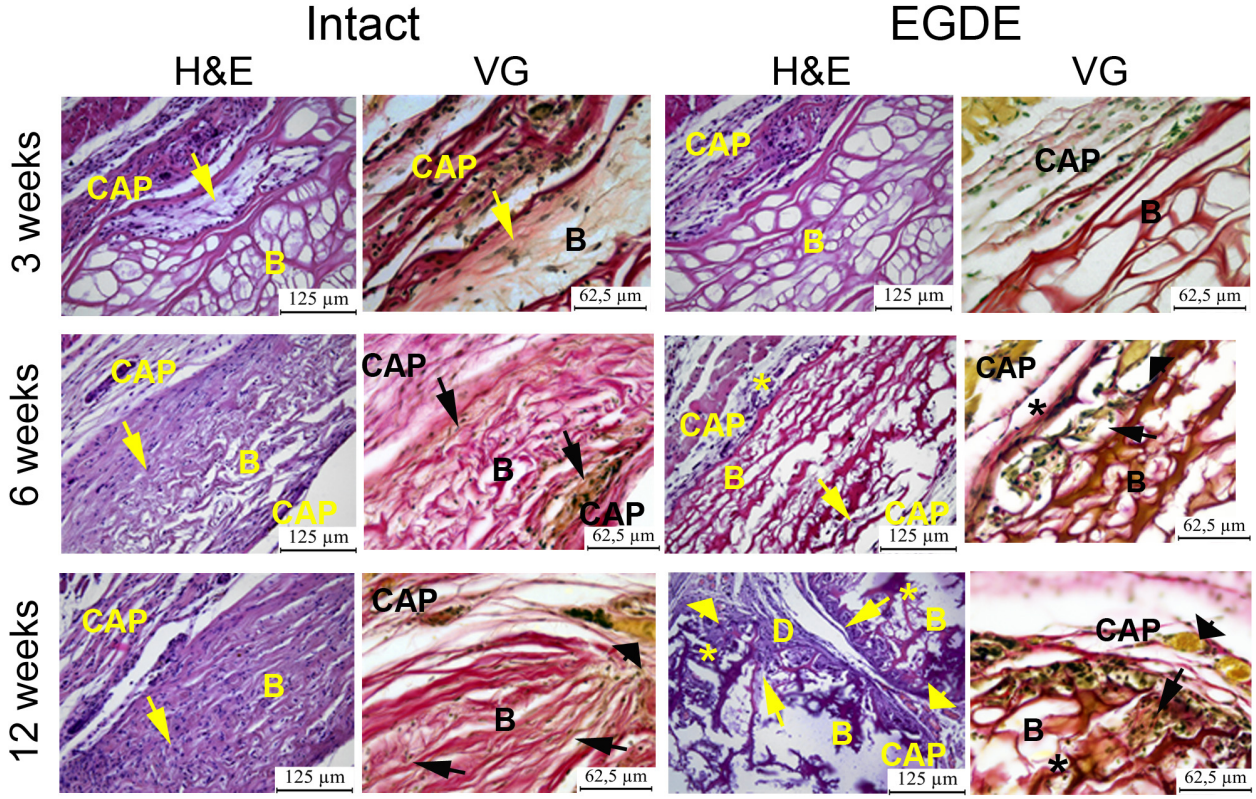

FIGURE 4 | Histological analysis of intact DBP and EGDE biomeshes 3, 6, and 12 weeks after the implantation. Implanted DBP biomeshes (B) were surrounded by a capsule (CAP) consisting of mature granulation tissue (3 weeks) or mature connective tissue (6 and 12 weeks), which grew into pores forming connective tissue septa (arrows) containing blood vessels. Calcification (*) and defects (D) of some parts of the implants' material were determined. Hyperemia (arrowheads) of the periphery of scaffolds. Scale bar for hematoxylin and eosin (H&E) staining is 125 μm, for van Gieson (VG) staining is 65.5 μm.

A vascular network formation was observed in the capsule around the EGDE samples 6 weeks after the implantation. Vascular networks could be seen both at the borders and in the centers of all the EGDE samples by fluorescence stereo microscopy (**Figure 8**). By contrast, the capsule around the intact DBP samples were absolutely free from vascularization. The content of the blood vessels was assessed by CD31 immunohistochemical staining.

DISCUSSION

Biomeshes constitute frequently used collagen-based matrix derived from biological tissue through a decellularization process. Grafted biomeshes act as a regenerative framework that supports remodeling and new collagen deposition (Bielli et al., 2018). The effectiveness of transplantation depends on the ability of the biomeshes to integrate into the host tissue promoting the *de novo* formation of tissues similar to the normal ones. The post-implantation fate of biomeshes is therefore crucial for biomaterial selection, determining the long-term success of a tissue-engineered graft (Sung et al., 2004).

A great number of approaches are aimed to understand and improve the tissue remodeling of biomeshes (Sun et al., 2013). Since the crosslinking of the decellularized biomaterials impacts on both biodegradation and tissue regeneration (Bielli et al., 2018), stabilization with new crosslinkers and elimination of immunogenicity are highly important (Xu and Wang, 2012; Ma et al., 2014; Rothamel et al., 2014; Wang et al., 2016). The influence of these parameters on the regeneration of the tissues needs to be comprehensively investigated before such biomaterials can be appropriately selected for biomedical applications. There have been many studies in which the effects of decellularization and crosslinking have been evaluated *in vitro* (Pagoulatou et al., 2012; Xu and Wang, 2012; Bielli et al., 2018). Importantly, the rates of biomesh biodegradation can differ drastically between the *in vitro* and *in vivo* settings. However, only a small number of studies controlled the biodegradation rate of pericardium tissue after implantation into animals (Rothamel et al., 2005, 2014; Gardin et al., 2015). Unfortunately, most of these studies were based on histological and morphometric analysis of harvested implants.

In this work we took advantage of various *state-of-the-art* techniques helping to understand biodegradation of biomeshes: non-invasive fluorescence imaging developed for *in vivo* estimation of the dynamics of the biodegradation rate of such implants (Timashev et al., 2016; Kuznetsova et al., 2017), *in vivo* imaging of implant (de)oxygenation using O_2-PLIM, *ex vivo*

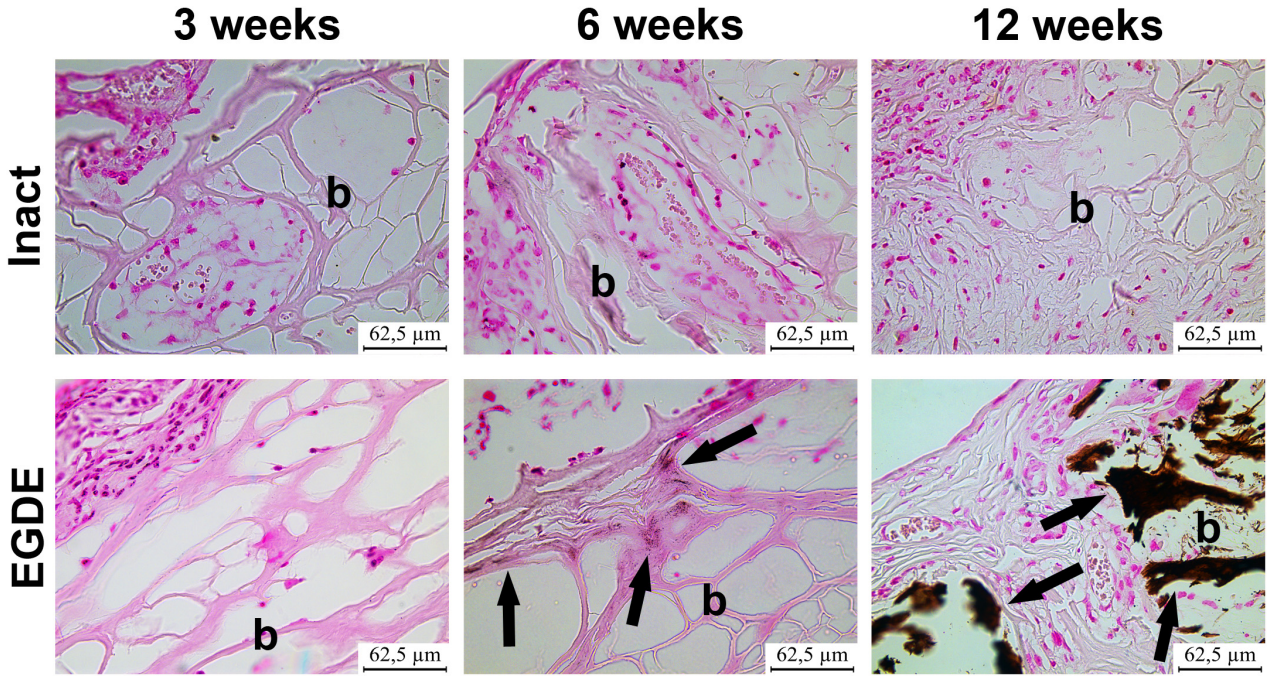

FIGURE 5 | Analysis of calcification of intact DBP and EGDE biomeshes (b) 3, 6, and 12 weeks after the implantation: EGDE with intensive calcification (arrows). The von Kossa staining, scale bar is 62.5 μm.

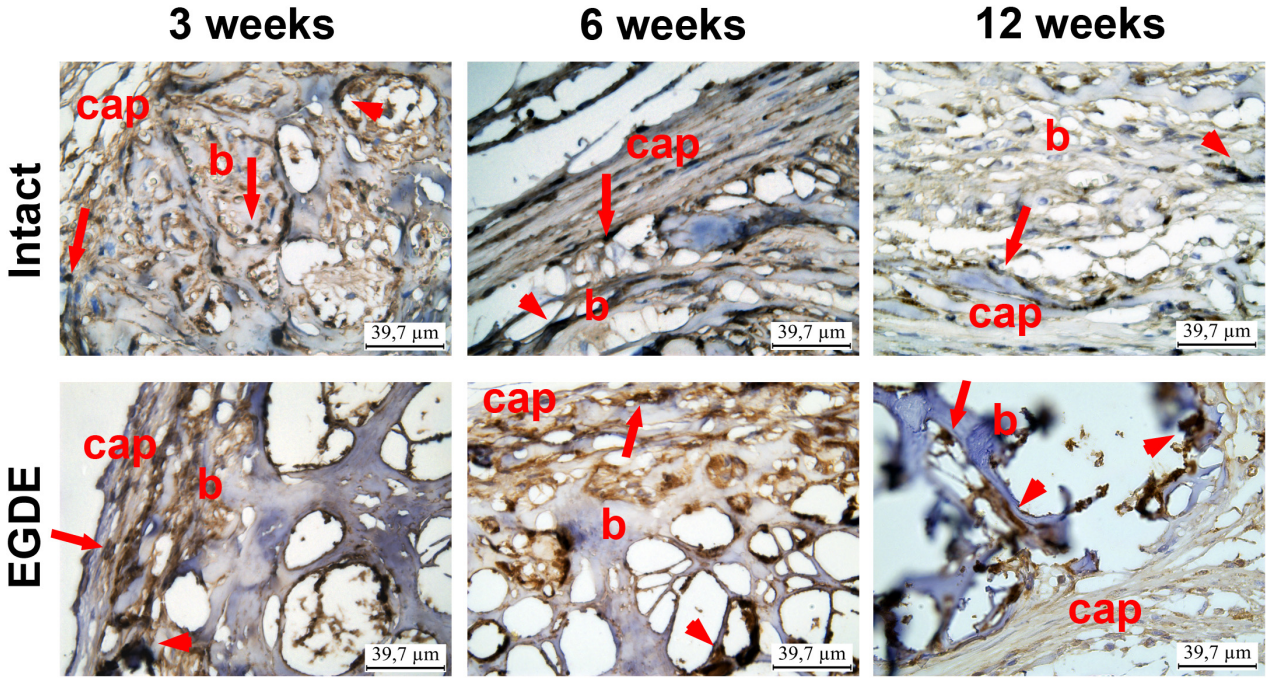

FIGURE 6 | Immunohistohistochemical analysis of intact DBP and EGDE biomeshes 3, 6, and 12 weeks after the implantation. CD 68 expression in macrophages (arrows) and giant cells (arrowheads) in biomeshes (b) and in their capsules (cap). Scale bar is 39.7 μm.

using multiphoton tomography, and conventional histological techniques. Before the implantation, we analyzed proteolytic stability and cytotoxicity of DBP samples *in vitro* (**Figure 2**). Our results demonstrated cytocompatibility of all DBP samples. We found that proteolytic stability of the intact and EGDE biomeshes showed different tendencies and rates of biodegradation and

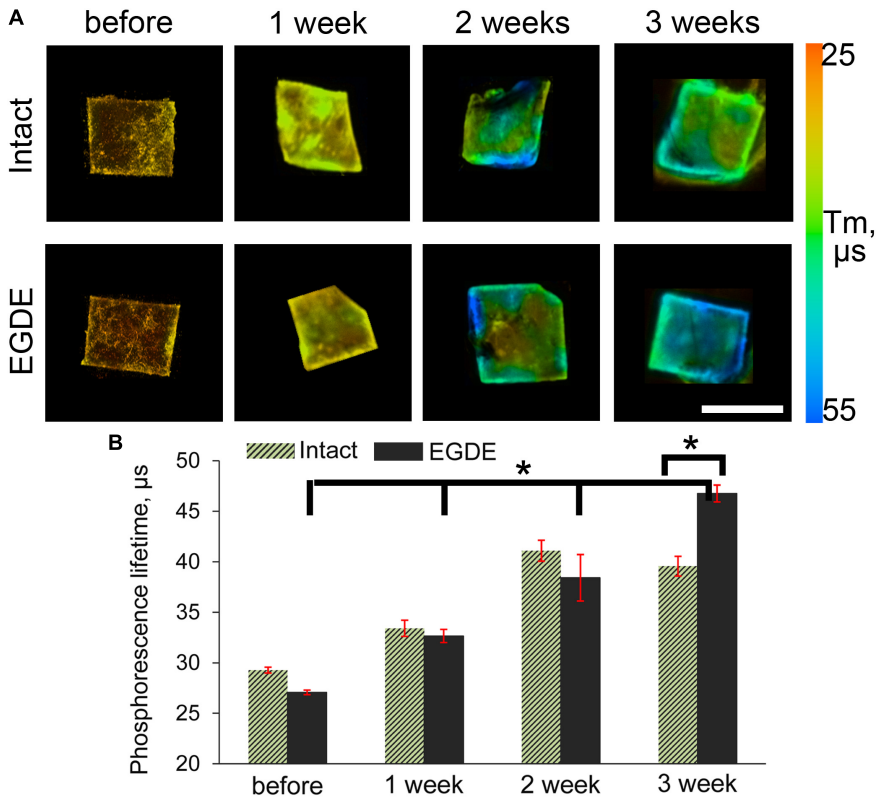

FIGURE 7 | PLIM imaging of intact DBP and EGDE biomeshes: **(A)** hypoxia progress in DBP biomeshes implanted subcutaneously to Balb/c mice; **(B)** quantification of the mean phosphorescence lifetime (τm, μs) of O_2-sensitive nanoparticles. Scale bar is 5 mm. $N = 3$, data shown as mean ± SD. *Statistically significant differences, $p < 0.001$.

higher stability for EGDE samples. In a good agreement with literature, that epoxy crosslinking provides appropriate proteolytic stability but has no substantial effect on cytotoxicity, unlike that typical of traditional glutaraldehyde treatment (Sung et al., 1999; Delgado et al., 2015). However, we demonstrated that the differences in the proteolytic resistance of the intact and of the epoxy crosslinked DBPs were less profound in the experiments *in vivo* compared with the data from corresponding tests *in vitro* (Ma et al., 2014). Fluorescence technique revealed a reduction in the area of only 20% in the case of intact DBP samples (**Figure 2C** and **Supplementary Figure S2**). Meanwhile the signal intensities of both fluorescence and SHG decreased about five times (**Figure 2D** and **Supplementary Figure S3**). Histological analysis revealed that the both DBP samples were surrounded by capsule consisted of connective tissue. The capsule leads to attenuation of signal intensities and increase the light scattering effects. Moreover, inflammatory cells and fibroblasts presented in capsule provided remodeling collagen fiber. Changes in collagen structure were found in both DBP samples (**Supplementary Figure S3**). The next reason of signal intensities reduction is the significant calcification of the EGDE biomeshes revealed by histological analysis and X-ray microtomography. The calcification also increases fragility, which is likely to cause alteration of the surrounding tissues and supports the inflammatory reaction with severe angiomatosis and hyperemia (up to 12 weeks after implantation). Although earlier *in vitro* studies showed no effect of epoxy compounds on biomesh calcification while incubation in calcium phosphate solution (Vasudev and Chandy, 1997) or with cells grown on its surface (Connolly et al., 2005). Calcification of implants is a negative effect violating the main function of an implant. Currently patients with breast implants face the such problem (Toscani et al., 2013). Polymer medical devices used in cardiology are also subject to calcification (Schlieper et al., 2008). Characteristics of the implant surface considerably influence the calcification process, either due to its chemical composition (Kim et al., 2007) or due to its roughness (Wang et al., 2004; Grebenik et al., 2018). Surface chemistry influences the calcification process by complexation of chemical groups on the material surface with calcium or phosphorus ions leading to the mineralization. Calcification of the epoxy crosslinked DBP implants may be induced by several reasons. Firstly, using scanning electron microscopy, we have established a change in the topology of DBP as a result of epoxy crosslinking with the formation of roughnesses. Secondly, the appearance of inflammatory cells, first of all, macrophages, into the implantation area was established. It was earlier shown, that macrophages are colocalized with calcification areas for the atherosclerotic changes and the inflammation degree correlates with the calcification degree (Aikawa et al., 2007). Thirdly, increased vascularization of the

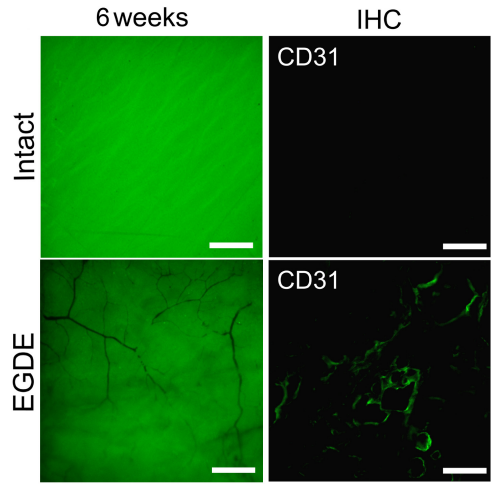

FIGURE 8 | Estimation of the DBP vascularization: fluorescence bioimaging (fluorescence stereo microscopy, the scale bar is 500 μm); CD31 immunohistochemically (IHC) staining of a DBP cross-section 12-weeks after implantation (fluorescence microscopy, the scale bar is 100 μm).

peripheral parts of the implant and impaired outflow from the deep layers can provoke the accumulation of calcium salts from the blood. Probably, calcification-capable implants may be used to regenerate bone tissue, but this requires a careful future study.

Vascularization of the peripheral parts of the EGDE implant is supported by CD31 immunohistochemical staining that revealed endothelial cells migration. According to published data, the endothelial cells migration may be caused by chemoattractants, contained in large quantities in the extracellular matrix. Several studies have shown that the biodegradation products of the extracellular matrix of the pigs' small intestine are capable to induce angiogenesis, mitogenesis, and cell differentiation (Hodde et al., 2001; Reing et al., 2009). However, in our work it was shown that the EGDE-treated DBP practically did not change in size during 90 days of biodegradation. Therefore, the chemoattractant release was prohibited compared to the intact sample. According to some studies, the calcification may trigger angiogenesis. *In vitro* study showed that calcification of extracellular matrix stimulates the synthesis and release of endothelial cell stimulating angiogenesis factor (ESAF) (Brown et al., 1994). It was also shown that scaffolds based on hydroxyapatite and dentin are able to stimulate angiogenesis during subcutaneous implantation in mice (Rucker et al., 2008). Thus, the calcification is the most appropriate mechanism of endothelial cell stimulation.

We also presented an innovative approach to understand implant oxygenation by labeling it with O_2-sensing phosphorescent probe (**Figure 7**). While in general the methodology of *in vivo* O_2 imaging is not new, until recently it was mostly focused on the use of vasculature- and interstitial space- specific probes (Esipova et al., 2019). Labeling scaffold materials with O_2 probe having long retention time opens new prospective area in the implant-based imaging. Even though it was not achieved here, hypoxia imaging of surrounding scaffold area can represent exciting future venue for research. Thus, PLIM imaging confirmed strong implant deoxygenation during the first 3 weeks, which explains angiomatosis along the periphery of the epoxy crosslinked DBPs. It is known that angiogenesis is a component of chronic inflammation: many cells are capable of producing angiogenic factors when their environment becomes hypoxic or inflammatory (Jackson et al., 1997). In the case with EGDE sample, hypoxic conditions could be the main factor promoting the vasculogenesis and very interesting for future studies. The following decrease in the number of blood vessels and fibroblasts and the capsule thinning along with the prominent hyperemia are related to the connective tissue reorganization in chronic hypoxia and inflammation.

For the first time, we observed the coincidence of calcification and peripheral angiogenesis of the epoxy crosslinked DBPs, associated with hypoxic conditions inside the biomesh. In our work, we report on angiomatosis along the periphery of the epoxy crosslinked DBPs. This appeared in the remodeled tissue and no angiogenesis was detected in the implant itself. The hypoxia was likely caused by the increased proteolytic stability and calcification of the biomesh prohibiting and slowing down the tissue remodeling. *In vitro* biodegradation of the EGDE samples was much slower compared to the intact DBP both, in collagenase and papain solutions. In the work of Umashankar et al. (2012) glutaraldehyde-crosslinked DPB exhibited similar angiogenesis pattern in the periphery of the implant, chronic inflammation observed and related calcification.

Some works have shown that bone grafts containing a graded structure of bone tissue and a branching structure of vessel networks can promote both osteogenesis and angiogenesis (Serbo and Gerecht, 2013; Mercado-Pagan et al., 2015). Understanding of this phenomenon is critical for the design of new therapeutic approaches in soft tissue engineering.

In conclusion, we have carried out a complex *in vivo* study of the effects of epoxy crosslinking on the process of implant integration into living tissue. Structural studies were performed with highly informative and precise techniques including scanning electron microscopy, fluorescence stereo microscopy, X-ray computed microtomography, multiphoton tomography combined with TPEF and SHG. Epoxy crosslinked DBPs presented more stable structures. However, the differences in the proteolytic resistance of the intact and epoxy crosslinked DBP samples was less marked in the experiments *in vivo*. Using fluorescence bioimaging we have estimated vascularization of the implanted DBPs. We observed, for the first time, to the best of our knowledge, the promotion of biomesh vascularization with epoxy compound crosslinking associated with prohibited remodeling of the host tissue and hypoxia. The analysis of TPEF and SHG intensities revealed structural changes of the biomeshes after inoculation into a living organism. Severe calcification of EGDE samples was detected at 12^{th} week after subcutaneous implantation using histological analysis and X-ray computed microtomography. These results illustrate the effect of epoxy crosslinking on the development of DBP calcification in living organism. This unfavorable result should stimulate detailed studies such biomaterials. Presented multimodal imaging approach

allows estimating the safety and long-term outcome of the biomesh used for soft tissue reconstruction.

DATA AVAILABILITY STATEMENT

All datasets generated for this study are included in the article/**Supplementary Material**.

ETHICS STATEMENT

The animal study was reviewed and approved by Ethics committee of the Privolzhsky Research Medical University.

AUTHOR CONTRIBUTIONS

VE, DK, and EG: study concept and design. VE, DK, EG, DZ, AP, AK, ERG, and RD: data acquisition and analysis. LI, TZ, EI, DR, AS, VA, and SB: quality control of the data. VE, DK, EG, AK, and RD: manuscript preparation. EZ and PT: manuscript review. All authors read and approved the submitted version.

FUNDING

The part of the project dedicated to the acquisition and modification of the biomeshes is supported by Russian academic excellence project "5–100" and Russian Foundation for Basic Research grant No. 18-29-06059 mk. The structural/functional characterization of the samples was performed with the support of the Russian Science Foundation grant No. 18-15-00401. The synthesis of O_2-sensing phosphorescent probe was supported by Science Foundation Ireland (SFI) 18/IF/6238.

SUPPLEMENTARY MATERIAL

The Supplementary Material for this article can be found online at: https://www.frontiersin.org/articles/10.3389/fbioe.2020.00107/full#supplementary-material

REFERENCES

Aikawa, E., Nahrendorf, M., Figueiredo, J. L., Swirski, F. K., Shtatland, T., Kohler, R. H., et al. (2007). Osteogenesis associates with inflammation in early-stage atherosclerosis evaluated by molecular imaging in vivo. *Circulation* 116, 2841–2850. doi: 10.1161/circulationaha.107.732867

Baharuddin, A., Go, B. T., Firdaus, M. N., and Abdullah, J. (2002). Bovine pericardium for dural graft: clinical results in 22 patients. *Clin. Neurol. Neurosurg.* 104, 342–344. doi: 10.1016/s0303-8467(02)00029-x

Bielli, A., Bernardini, R., Varvaras, D., Rossi, P., Di Blasi, G., Petrella, G., et al. (2018). Characterization of a new decellularized bovine pericardial biological mesh: structural and mechanical properties. *J. Mech. Behav. Biomed. Mater.* 78, 420–426. doi: 10.1016/j.jmbbm.2017.1012.1003

Bre, L. P., McCarthy, R., and Wang, W. (2014). Prevention of bioprosthetic heart valve calcification: strategies and outcomes. *Curr. Med. Chem.* 21, 2553–2564. doi: 10.2174/0929867321666131212151216

Brown, R. A., McFarland, C. D., Kayser, M., and McLaughlin, B. (1994). Calcification-linked angiogenesis and bone growth. *Bone* 15, 112–113. doi: 10.1016/8756-3282(94)90906-7

Buzmakov, A. V., Asadchikov, V. E., Zolotov, D. A., Chukalina, M. V., Ingacheva, A. S., and Krivonosov, Y. S. (2019). Laboratory X-ray microtomography: ways of processing experimental data. *Bull. Russian Acad. Sci.: Phys.* 83, 146–149. doi: 10.3103/s1062873819020060

Buzmakov, A. V., Asadchikov, V. E., Zolotov, D. A., Roshchin, B. S., Dymshits, Y. M., Shishkov, V. A., et al. (2018). Laboratory microtomographs: design and data processing algorithms. *Crystallogr. Rep.* 63, 1057–1061. doi: 10.1134/s106377451806007x

Colombo, A., Almagor, Y., Gaspar, J., and Vonderwalde, C. (2009). The pericardium covered stent (PCS). *EuroIntervention* 5, 394–399. doi: 10.4244/v5i3a61

Connolly, J. M., Alferiev, I., Clark-Gruel, J. N., Eidelman, N., Sacks, M., Palmatory, E., et al. (2005). Triglycidylamine crosslinking of porcine aortic valve cusps or bovine pericardium results in improved biocompatibility, biomechanics, and calcification resistance: chemical and biological mechanisms. *Am. J. Pathol.* 166, 1–13. doi: 10.1016/s0002-9440(10)62227-4

Croce, A. C., and Bottiroli, G. (2014). Autofluorescence spectroscopy and imaging: a tool for biomedical research and diagnosis. *Eur. J. Histochem.* 58:2461.

Delgado, L. M., Bayon, Y., Pandit, A., and Zeugolis, D. I. (2015). To cross-link or not to cross-link? Cross-linking associated foreign body response of collagen-based devices. *Tissue Eng.. Part B Rev.* 21, 298–313. doi: 10.1089/ten.TEB.2014.0290

Dmitriev, R. I., Borisov, S. M., Dussmann, H., Sun, S., Muller, B. J., Prehn, J., et al. (2015). Versatile conjugated polymer nanoparticles for high-resolution O2 imaging in cells and 3D tissue models. *ACS Nano* 9, 5275–5288. doi: 10.1021/acsnano.5b00771

Dmitriev, R. I., Zhdanov, A. V., Nolan, Y. M., and Papkovsky, D. B. (2013). Imaging of neurosphere oxygenation with phosphorescent probes. *Biomaterials* 34, 9307–9317. doi: 10.1016/j.biomaterials.2013.08.065

Dong, X., Wei, X., Yi, W., Gu, C., Kang, X., Liu, Y., et al. (2009). RGD-modified acellular bovine pericardium as a bioprosthetic scaffold for tissue engineering. *J. Mater. Sci. Mater Med.* 20, 2327–2336. doi: 10.1007/s10856-009-3791-4

Esipova, T. V., Barrett, M. J. P., Erlebach, E., Masunov, A. E., Weber, B., and Vinogradov, S. A. (2019). Oxyphor 2P: a high-performance probe for deep-tissue longitudinal oxygen imaging. *Cell Metabolism* 29, 736.e7–744.e7. doi: 10.1016/j.cmet.2018.12.022

Gabbay, S., Bortolotti, U., Wasserman, F., Tindel, N., Factor, S. M., and Frater, R. W. (1984). Long-term follow-up of the ionescu-shiley mitral pericardial xenograft. *J. Thorac. Cardiovasc. Surg.* 88(5 Pt 1), 758–763. doi: 10.1016/s0022-5223(19)35444-3

Gardin, C., Ricci, S., Ferroni, L., Guazzo, R., Sbricoli, L., De Benedictis, G., et al. (2015). Decellularization and delipidation protocols of bovine bone and pericardium for bone grafting and guided bone regeneration procedures. *PLoS One* 10:e0132344. doi: 10.1371/journal.pone.0132344

Grebenik, E. A., Grinchenko, V. D., Churbanov, S. N., Minaev, N. V., Shavkuta, B. S., Melnikov, P. A., et al. (2018). Osteoinducing scaffolds with multi-layered biointerface. *Biomed. Mater.* 13:054103. doi: 10.1088/1748-605X/aac4cb

Grebenik, E. A., Istranov, L. P., Istranova, E. V., Churbanov, S. N., Shavkuta, B. S., Dmitriev, R. I., et al. (2019). Chemical cross-linking of xenopericardial biomeshes: a bottom-up study of structural and functional correlations. *Xenotransplantation* 22:12506. doi: 10.1111/xen.12506

Guerette, N. L., Peterson, T. V., Aguirre, O. A., Vandrie, D. M., Biller, D. H., and Davila, G. W. (2009). Anterior repair with or without collagen matrix reinforcement: a randomized controlled trial. *Obstet Gynecol.* 114, 59–65. doi: 10.1097/AOG.1090b1013e3181a1081b1041

Gupta, M., Puri, P., and Rennie, I. G. (2002). Use of bovine pericardium as a wrapping material for hydroxyapatite orbital implants. *Br. J. Ophthalmol.* 86, 288–289. doi: 10.1136/bjo.86.3.288

Hodde, J. P., Record, R. D., Liang, H. A., and Badylak, S. F. (2001). Vascular endothelial growth factor in porcine-derived extracellular matrix. *Endothelium* 8, 11–24. doi: 10.3109/10623320109063154

Imamura, E., Sawatani, O., Koyanagi, H., Noishiki, Y., and Miyata, T. (1989). Epoxy compounds as a new cross-linking agent for porcine aortic leaflets:

subcutaneous implant studies in rats. *J. Card Surg.* 4, 50–57. doi: 10.1111/j.1540-8191.1989.tb00256.x

Jackson, J. R., Seed, M. P., Kircher, C. H., Willoughby, D. A., and Winkler, J. D. (1997). The codependence of angiogenesis and chronic inflammation. *Faseb J.* 11, 457–465. doi: 10.1096/fasebj.11.6.9194526

Jenkins, J., Dmitriev, R. I., Morten, K., McDermott, K. W., and Papkovsky, D. B. (2015). Oxygen-sensing scaffolds for 3-dimensional cell and tissue culture. *Acta Biomater.* 16, 126–135. doi: 10.1016/j.actbio.2015.1001.1032

Kim, M.-S., Choi, Y.-J., Noh, I., and Tae, G. (2007). Synthesis and characterization of in situ chitosan-based hydrogel via grafting of carboxyethyl acrylate. *J. Biomed. Mater. Res. Part A* 83A, 674–682. doi: 10.1002/jbm.a.31278

Koay, A. C., Yew, Y. H., Ngo, C. T., Loo, V. P., Intan, G., and Chua, C. N. (2008). The use of preserved bovine pericardium for emergency temporizing graft in corneal perforation. *Med. J. Malaysia* 63, 421–422.

Kuznetsova, D., Ageykin, A., Koroleva, A., Deiwick, A., Shpichka, A., Solovieva, A., et al. (2017). Surface micromorphology of cross-linked tetrafunctional polylactide scaffolds inducing vessel growth and bone formation. *Biofabrication* 9:025009. doi: 10.1088/1758-5090/aa6725

Limpert, J. N., Desai, A. R., Kumpf, A. L., Fallucco, M. A., and Aridge, D. L. (2009). Repair of abdominal wall defects with bovine pericardium. *Am. J. Surg.* 198, e60–e65. doi: 10.1016/j.amjsurg.2009.1001.1027

Ma, B., Wang, X., Wu, C., and Chang, J. (2014). Crosslinking strategies for preparation of extracellular matrix-derived cardiovascular scaffolds. *Regen Biomater.* 1, 81–89. doi: 10.1093/rb/rbu1009

Mallis, P., Michalopoulos, E., Dimitriou, C., Kostomitsopoulos, N., and Stavropoulos-Giokas, C. (2017). Histological and biomechanical characterization of decellularized porcine pericardium as a potential scaffold for tissue engineering applications. *Biomed. Mater. Eng.* 28, 477–488. doi: 10.3233/bme-171689

Mendoza-Novelo, B., Avila, E. E., Cauich-Rodriguez, J. V., Jorge-Herrero, E., Rojo, F. J., Guinea, G. V., et al. (2011). Decellularization of pericardial tissue and its impact on tensile viscoelasticity and glycosaminoglycan content. *Acta Biomater.* 7, 1241–1248. doi: 10.1016/j.actbio.2010.11.017

Mercado-Pagan, A. E., Stahl, A. M., Shanjani, Y., and Yang, Y. (2015). Vascularization in bone tissue engineering constructs. *Ann. Biomed. Eng.* 43, 718–729. doi: 10.1007/s10439-015-1253-3

O'Donnell, N., Okkelman, I. A., Timashev, P., Gromovykh, T. I., Papkovsky, D. B., and Dmitriev, R. I. (2018). Cellulose-based scaffolds for fluorescence lifetime imaging-assisted tissue engineering. *Acta Biomaterialia* 80, 85–96. doi: 10.1016/j.actbio.2018.09.034

Oswal, D., Korossis, S., Mirsadraee, S., Wilcox, H., Watterson, K., Fisher, J., et al. (2007). Biomechanical characterization of decellularized and cross-linked bovine pericardium. *J. Heart Valve Dis.* 16, 165–174.

Pagoulatou, E., Triantaphyllidou, I. E., Vynios, D. H., Papachristou, D. J., Koletsis, E., Deligianni, D., et al. (2012). Biomechanical and structural changes following the decellularization of bovine pericardial tissues for use as a tissue engineering scaffold. *J. Mater. Sci. Mater. Med.* 23, 1387–1396. doi: 10.1007/s10856-012-4620-8

Papkovsky, D. B., and Dmitriev, R. I. (2018). Imaging of oxygen and hypoxia in cell and tissue samples. *Cell. Mo. Life Sci.* 75, 2963–2980. doi: 10.1007/s00018-018-2840-x

Perme, H., Sharma, A., Kumar, N., Singh, H., Maiti, S., and Singh, R. (2009). In-vivo biocompatibility evaluation of crosslinked cellular and acellular bovine pericardium. *Indian J. Anim. Sci.* 79, 658–661.

Quaranta, L., Riva, I., and Floriani, I. C. (2013). Outcomes of using a sutureless bovine pericardial patch graft for Ahmed glaucoma valve implantation. *Eur. J. Ophthalmol.* 23, 738–742. doi: 10.5301/ejo.5000260

Reing, J. E., Zhang, L., Myers-Irvin, J., Cordero, K. E., Freytes, D. O., Heber-Katz, E., et al. (2009). Degradation products of extracellular matrix affect cell migration and proliferation. *Tissue Eng. Part A* 15, 605–614. doi: 10.1089/ten.tea.2007.0425

Rezvova, M. A., and Kudryavceva, Y. A. (2018). Modern approaches to chemical modification of proteins in biological tissues: consequences and application. *Russian J. Bioorganic Chem.* 44, 19–31. doi: 10.1134/s1068162018010144

Rothamel, D., Benner, M., Fienitz, T., Happe, A., Kreppel, M., Nickenig, H. J., et al. (2014). Biodegradation pattern and tissue integration of native and cross-linked porcine collagen soft tissue augmentation matrices - an experimental study in the rat. *Head Face Med.* 10:10. doi: 10.1186/1746-1160X-1110-1110

Rothamel, D., Schwarz, F., Sager, M., Herten, M., Sculean, A., and Becker, J. (2005). Biodegradation of differently cross-linked collagen membranes: an experimental study in the rat. *Clin. Oral. Implants Res.* 16, 369–378. doi: 10.1111/j.1600-0501.2005.01108.x

Roussakis, E., Ortines, R. V., Pinsker, B. L., Mooers, C. T., Evans, C. L., Miller, L. S., et al. (2019). Theranostic biocomposite scaffold membrane. *Biomaterials* 212, 17–27. doi: 10.1016/j.biomaterials.2019.05.007

Rucker, M., Laschke, M. W., Junker, D., Carvalho, C., Tavassol, F., Mulhaupt, R., et al. (2008). Vascularization and biocompatibility of scaffolds consisting of different calcium phosphate compounds. *J. Biomed. Mater. Res. A* 86, 1002–1011. doi: 10.1002/jbm.a.31722

Schilling, K., El Khatib, M., Plunkett, S., Xue, J., Xia, Y., Vinogradov, S. A., et al. (2019). Electrospun fiber mesh for high-resolution measurements of oxygen tension in cranial bone defect repair. *ACS Appl. Mater. Interfaces* 11, 33548–33558. doi: 10.1021/acsami.9b08341

Schlee, M., Ghanaati, S., Willershausen, I., Stimmlmayr, M., Sculean, A., and Sader, R. A. (2012). Bovine pericardium based non-cross linked collagen matrix for successful root coverage, a clinical study in human. *Head Face Med.* 8:6. doi: 10.1186/1746-1160X-1188-1186

Schlieper, G., Kruger, T., Djuric, Z., Damjanovic, T., Markovic, N., Schurgers, L. J., et al. (2008). Vascular access calcification predicts mortality in hemodialysis patients. *Kidney Int.* 74, 1582–1587. doi: 10.1038/ki.2008.458

Serbo, J. V., and Gerecht, S. (2013). Vascular tissue engineering: biodegradable scaffold platforms to promote angiogenesis. *Stem. Cell Res. Ther.* 4:8. doi: 10.1186/scrt1156

Stavropoulos, A., Chiantella, G., Costa, D., Steigmann, M., Windisch, P., and Sculean, A. (2011). Clinical and histologic evaluation of a granular bovine bone biomaterial used as an adjunct to GTR with a bioresorbable bovine pericardium collagen membrane in the treatment of intrabony defects. *J. Periodontol.* 82, 462–470. doi: 10.1902/jop.2010.100331

Sun, W. Q., Xu, H., Sandor, M., and Lombardi, J. (2013). Process-induced extracellular matrix alterations affect the mechanisms of soft tissue repair and regeneration. *J. Tissue Eng.* 4:2041731413505305. doi: 10.1177/2041731413505305

Sung, H. J., Meredith, C., Johnson, C., and Galis, Z. S. (2004). The effect of scaffold degradation rate on three-dimensional cell growth and angiogenesis. *Biomaterials* 25, 5735–5742. doi: 10.1016/j.biomaterials.2004.01.066

Sung, H. W., Chang, Y., Chiu, C. T., Chen, C. N., and Liang, H. C. (1999). Crosslinking characteristics and mechanical properties of a bovine pericardium fixed with a naturally occurring crosslinking agent. *J. Biomed. Mater. Res.* 47, 116–126. doi: 10.1002/(sici)1097-4636(199911)47:2<116::aid-jbm2>3.0.co;2-j

Sung, H. W., Shen, S. H., Tu, R., Lin, D., Hata, C., Noishiki, Y., et al. (1993). Comparison of the cross-linking characteristics of porcine heart valves fixed with glutaraldehyde or epoxy compounds. *Asaio J.* 39, M532–M536.

Timashev, P., Kuznetsova, D., Koroleva, A., Prodanets, N., Deiwick, A., Piskun, Y., et al. (2016). Novel biodegradable star-shaped polylactide scaffolds for bone regeneration fabricated by two-photon polymerization. *Nanomedicine* 11, 1041–1053. doi: 10.2217/nnm-2015-0022

Toscani, M., Rizzo, M. I., Spinelli, G., Sanese, G., Cerbelli, B., Soda, G., et al. (2013). Breast implant complication: calcifications in the double capsule. *Plast. Reconstr. Surg.* 131, 462e–464e. doi: 10.1097/PRS.0b013e31827c7377

Umashankar, P. R., Mohanan, P. V., and Kumari, T. V. (2012). Glutaraldehyde treatment elicits toxic response compared to decellularization in bovine pericardium. *Toxicol. Int.* 19, 51–58. doi: 10.4103/0971-6580.94513

Vasudev, S. C., and Chandy, T. (1997). Effect of alternative crosslinking techniques on the enzymatic degradation of bovine pericardia and their calcification. *J. Biomed Mater. Res.* 35, 357–369. doi: 10.1002/(sici)1097-4636(19970605)35:3<357::aid-jbm10>3.0.co;2-c

Wang, Y., Bao, J., Wu, X., Wu, Q., Li, Y., Zhou, Y., et al. (2016). Genipin crosslinking reduced the immunogenicity of xenogeneic decellularized porcine whole-liver matrices through regulation of immune cell proliferation and polarization. *Sci. Rep.* 6:24779. doi: 10.1038/srep24779

Wang, Y.-W., Wu, Q., and Chen, G.-Q. (2004). Attachment, proliferation and differentiation of osteoblasts on random biopolyester

poly(3-hydroxybutyrate-co-3-hydroxyhexanoate) scaffolds. *Biomaterials* 25, 669–675. doi: 10.1016/s0142-9612(03)00561-1

Xi, T., Ma, J., Tian, W., Lei, X., Long, S., and Xi, B. (1992). Prevention of tissue calcification on bioprosthetic heart valve by using epoxy compounds: a study of calcification tests in vitro and in vivo. *J. Biomed. Mater. Res.* 26, 1241–1251. doi: 10.1002/jbm.820260913

Xu, C., and Wang, Y. (2012). Collagen cross linking increases its biodegradation resistance in wet dentin bonding. *J. Adhes Dent* 14, 11–18. doi: 10.3290/j.jad.a21494

Yazgan, G., Dmitriev, R. I., Tyagi, V., Jenkins, J., Rotaru, G. M., Rottmar, M., et al. (2017). Steering surface topographies of electrospun fibers: understanding the mechanisms. *Sci. Rep.* 7:158. doi: 10.1038/s41598-017-00181-0

Conflict of Interest: The authors declare that the research was conducted in the absence of any commercial or financial relationships that could be construed as a potential conflict of interest.

frontiers in Bioengineering and Biotechnology

ORIGINAL RESEARCH
published: 27 March 2020
doi: 10.3389/fbioe.2020.00262

Extracellular Matrix From Decellularized Wharton's Jelly Improves the Behavior of Cells From Degenerated Intervertebral Disc

Letizia Penolazzi[1†], Michela Pozzobon[2,3†], Leticia Scussel Bergamin[1], Stefania D'Agostino[2,3], Riccardo Francescato[2], Gloria Bonaccorsi[4], Pasquale De Bonis[5], Michele Cavallo[5], Elisabetta Lambertini[1] and Roberta Piva [1*]*

[1] Department of Biomedical and Specialty Surgical Sciences, University of Ferrara, Ferrara, Italy, [2] Stem Cells and Regenerative Medicine Lab, Fondazione Istituto di Ricerca Pediatrica Città della Speranza, Padua, Italy, [3] Department of Women and Children Health, University of Padova, Padua, Italy, [4] Section of Obstetrics and Gynecology, Department of Morphology, Surgery and Experimental Medicine, University of Ferrara, and S. Anna University Hospital, Ferrara, Italy, [5] Department of Neurosurgery, University of Ferrara, and S. Anna University Hospital, Ferrara, Italy

Regenerative therapies for intervertebral disc (IVD) injuries are currently a major challenge that is addressed in different ways by scientists working in this field. Extracellular matrix (ECM) deriving from decellularized non-autologous tissues has been established as a biomaterial with remarkable regenerative capacity and its potential as a therapeutic agent is rising. In the present study, we investigated the potential of decellularized Wharton's jelly matrix (DWJM) from human umbilical cord to act as an ECM-based scaffold for IVD cell culturing. An efficient detergent-enzymatic treatment (DET) was used to produce DWJM maintaining its native microarchitecture. Afterward, immunofluorescence, biochemical assays and electron microscopy analysis showed that DWJM was able to produce sizeable 3D cell aggregates, when combined with human mesenchymal stromal cells isolated from WJ (MSCs) and IVD cells. These latter cells are characterized by the loss of their chondrocyte-like phenotype since they have been isolated from degenerated IVD and *in vitro* expanded to further de-differentiate. While the effect exerted by DWJM on MSCs was essentially the induction of proliferation, conversely, on IVD cells the DWJM promoted cell differentiation toward a discogenic phenotype. Notably, for the first time, the ability of DWJM to improve the degenerated phenotype of human IVD cells was demonstrated, showing that the mere presence of the matrix maintained the viability of the cells, and positively affected the expression of critical regulators of IVD homeostasis, such as SOX2, SOX9, and TRPS1 transcription factors at specific culture time. Our data are in line with the hypothesis that the strengthening of cell properties in terms of viability and expression of specific proteins at precise times represents an important condition in the perspective of guiding the recovery of cellular functionality and triggering regenerative potential. Currently, there

OPEN ACCESS

Edited by:
Dimitrios I. Zeugolis, National University of Ireland Galway, Ireland

Reviewed by:
Sibylle Grad, AO Foundation, Switzerland
Silvia Lopa, Istituto Ortopedico Galeazzi (IRCCS), Italy

***Correspondence:**
Michela Pozzobon
m.pozzobon@irpcds.org; michela.pozzobon@unipd.it
Roberta Piva
piv@unife.it

[†] These authors have contributed equally to this work

Specialty section:
This article was submitted to Tissue Engineering and Regenerative Medicine, a section of the journal Frontiers in Bioengineering and Biotechnology

Received: *12 December 2019*
Accepted: *13 March 2020*
Published: *27 March 2020*

Citation:
Penolazzi L, Pozzobon M, Bergamin LS, D'Agostino S, Francescato R, Bonaccorsi G, De Bonis P, Cavallo M, Lambertini E and Piva R (2020) Extracellular Matrix From Decellularized Wharton's Jelly Improves the Behavior of Cells From Degenerated Intervertebral Disc. Front. Bioeng. Biotechnol. 8:262. doi: 10.3389/fbioe.2020.00262

are no definitive surgical or pharmacological treatments for IVD degeneration (IDD) able to restore the disc structure and function. Therefore, the potential of DWJM to revert degenerated IVD cells could be exploited in the next future an ECM-based intradiscal injectable therapeutic.

Keywords: Wharton's jelly, intervertebral disc cells, TRPS1, decellularized matrix, scaffold

INTRODUCTION

The intervertebral disc (IVD) is a natural composite system bonding two adjacent vertebrae. IVD degeneration (IDD) is a phenomenon that can occur as a result of the natural aging, trauma or pathological conditions, and represents one of the main causes of lower back pain that, when it becomes chronic and debilitating, has a serious socio-economic impact (Roughley, 2004; Murray et al., 2012; Geurts et al., 2018; Fujii et al., 2019). To date, spinal fusion surgery is the treatment of choice for IDD aimed at removing the painful symptoms and the degenerated part of the disc (Amin et al., 2017). However, the surgical approach cannot slow down the degenerative process or restore the normal mechanical functionality of the disc, and management of chronic low back pain remains complicated (Schizas et al., 2010; Ohtori et al., 2011). In the recent years, several tissue engineering strategies have been developed and proposed as potential innovative approaches in IDD therapeutic treatment. In all its anatomical and functional complexity starting from the nucleus pulposus (NP, highly hydrophilic, rich of proteoglycans and collagen, with shock absorbing function), up to the annulus (AF, lamellar fibrocartilaginous tissue, with containment function) and cartilaginous endplates (a more rigid tissue acting as interface between disc and vertebrae), the IVD is attracting considerable interest from the scientists involved in tissue engineering field (Buckley et al., 2018; Farrugia et al., 2019; Tendulkar et al., 2019). In particular, several studies aim at developing innovative bio-inspired scaffolds, in order to counteract extracellular matrix (ECM) loss following degeneration/inflammation, and support functional recovery by endogenous damaged microenvironment (Coogan et al., 2016; Van Uden et al., 2017; Gullbrand et al., 2018). In this scenario, decellularized ECM deriving from autologous or non-autologous tissues represents an important advance in this field, as ideal system to deliver chemokines and growth factors, and provides adequate biomechanical microarchitecture also in the damaged IVD microenvironment (D'Este et al., 2018; Hensley et al., 2018; Liu et al., 2019; Ventre et al., 2019; Zhao et al., 2019). Obviously, obtaining autologous ECM from human IVD is not feasible, but recent evidences based on decellularized ECM from IVD of animal origin are encouraging (Illien-Jünger et al., 2016; Lin et al., 2016; Zhou et al., 2018; Xu et al., 2019). However, these scaffolds, which are potentially implantable in humans, can have non-negligibile side effects because of immunological reactions and pathogen transmission risk (Zhou et al., 2018). Interesting alternatives can come from tissues for which obtaining the ECM can be easily achieved, both from a technical and ethical point of view. In these terms, the perinatal tissues may represent a valuable opportunity.

In the current study, we produced decellularized ECM obtained from human Wharton's jelly (WJ) of full term human umbilical cord, and investigated its potential as bio-inspired scaffold affecting the behavior of IVD cells. WJ is a mucous connective tissue that surrounds the umbilical cord vessels and is covered by a layer of simple amniotic epithelium (Ferguson and Dodson, 2009). The recent characterization of WJ suggests that its composition is particularly similar to that of IVD. In particular, the abundance of hyaluronic acid (HA) makes this tissue strongly hydrated, viscous and suitable as potential substitute of NP (Jadalannagari et al., 2017; Bullard et al., 2019). In addition, WJ, being rich in growth factors and cytokines (Penolazzi et al., 2010; Jadalannagari et al., 2017; Najar et al., 2018; Kehtari et al., 2019) is particularly attractive for potential application in tissue engineering (Beiki et al., 2017; Basiri et al., 2019; Li et al., 2019; Walker et al., 2019). In recent years, different methods to decellularize the WJ have been developed and compared, aimed at producing a scaffold able to sustain cell viability and proliferation, and preserve the native ECM microstructure and secretion profile (Stocco et al., 2014; Beiki et al., 2017; Jadalannagari et al., 2017).

Here, we produced decellularized Wharton's jelly matrix (DWJM) with an efficient method based on detergent-enzymatic treatment (DET) cycle (Piccoli et al., 2016). The ability of DWJM to generate sizeable 3D cell aggregates was investigated by using human cells from degenerated IVD as cellular model of disease, and human mesenchymal stromal cells isolated from WJ (MSCs) as control cellular model. For the first time, we demonstrated the ability of DWJM to improve the degenerated phenotype of IVD cells isolated from herniated lumbar disc, expanded and further de-differentiated during the passage in culture. When combined with DWJM, the IVD cells were viable and recovered their chondrogenic-like phenotype through the expression of important proteins such as SOX2, SOX9, and TRPS1, previously recognized as critical regulators of IVD homeostasis (Penolazzi et al., 2019).

Therefore, we proposed DWJM as innovative scaffold mimicking the ECM of IVD microenvironment, and able to restore the chondrocyte-like cell phenotype.

MATERIALS AND METHODS

Cells

Human umbilical cords (all from natural deliveries, $n = 5$) were collected after mothers' consent and approval of the Ethics Committee of the University of Ferrara and S. Anna Hospital (protocol approved on November 19th, 2006). Harvesting

procedures of WJ from umbilical cord were conducted in full accordance with the Declaration of Helsinki as adopted by the 18th World Medical Assembly in 1964 and successively revised in Edinburgh (2000) and the Good Clinical Practice guidelines. Cords were processed within 4 h and stored in sterile saline until use (Penolazzi et al., 2012). Typically, the cord was rinsed several times with sterile phosphate-buffered saline (PBS) before processing and was cut into pieces (2–4 cm in length). Single pieces were dissected, after separating the epithelium of each section along its length, to expose the underlying WJ. The soft gel tissue was then finely chopped. The same tissue (2–3 mm^2 pieces) was placed directly into a 25 cm^2 flask for culture expansion in 10% Fetal Calf Serum (Euroclone S.p.A., Milan, Italy) Dulbecco's Modified Eagle's Medium (DMEM) low-glucose supplemented with antibiotics (100 μg/mL streptomycin, 100 U/mL penicillin), at 37°C in a humidified atmosphere of 5% CO_2. After 5–7 days, the culture medium was removed and then changed twice a week. At 70–80% confluence, cells were scraped off by 0.05% trypsin-ethylenediaminetetraaceticacid (EDTA) (Sigma Aldrich, St. Louis, United States) washed, counted by hemocytometric analysis, assayed for viability, and used thereafter for *in vitro* experiments (passages P2–P3).

Surgical herniated human disc tissues were obtained from six patients (patients' age was between 31 and 77 years, mean age 59 years, three males and three females, Pfirrmann grade 3–4), using research protocol approved by Ethics Committee of the University of Ferrara and S. Anna Hospital (protocol approved on November 17th, 2016). Patients were operated for the herniated lumbar disc through a microsurgical posterior approach. Disc sampling was obtained from the central core of the disc, in order to avoid anterior and posterior longitudinal ligament, annulus and calcified portion of the disc. Lumbar intervertebral disc tissues (1–2 cm^3) were collected, cut into small pieces, and subjected to mild digestion in 15 mL centrifuge tube with only 1 mg/mL type IV collagenase (Sigma-Aldrich, St. Louis, United States) for 5 h at 37°C in DMEM high glucose/F12 (Euroclone S.p.A., Milan, Italy) as previously described (Penolazzi et al., 2019). After digestion, cell suspension was filtered with a Falcon™ 70 μm Nylon Cell strainer (BD Biosciences, Franklin Lakes, NJ, United States). Subsequently 300 × *g* centrifugation was conducted for 10 min, the supernatant discarded, the cells resuspended in basal medium (DMEM/F12 containing 10% fetal calf serum, 100 μg/mL streptomycin, 100 U/mL penicillin, and 1% Glutamine) (Euroclone) and seeded in polystyrene culture plates (Sarstedt, Nümbrecht, Germany) at 10000 cells/cm^2. The cells were maintained in culture at 37°C in a humidified atmosphere with 5% CO_2. P0 cells were expanded by growing for a period not exceeding a week until subconfluent, detaching by trypsinization, and maintained in culture for more than two passages to obtain IVD cells that were used for later experiments. As already demonstrated after monolayer culture expansion, cells isolated from human lumbar IVD become de-differentiated, lose their chondrogenic-like phenotype resembling the degeneration process (Penolazzi et al., 2018).

Decellularization

Several fragments of WJ were treated up to three cycles of the DET as previously described (Piccoli et al., 2016). Briefly: samples were washed two times in PBS and then placed in deionized water with 3% Penicillin/streptomicyn. For each DET cycle, samples were gently shacked in deionized water at 4°C for 24 h, then in 4% sodium deoxycholate (SDC-Sigma-Aldrich) at room temperature (RT) for 4 h, and finally in 2000 kU DNase-I (Sigma-Aldrich) in 1 M NaCl at RT for 3 h. (One cycle is formed by water/SDC/DNAse). After each cycles, samples underwent DNA extraction (Trizol, Invitrogen) and DNA quantification (Nanodrop). Decellularized samples were further dehydrated and used as scaffold for subsequent experiments.

DWJM Seeding and Culture

Decellularized Wharton's jelly matrix fragments (2–4 mg) were presoaked with DMEM high glucose for 1 h, seeded with 200–400 × 10^3 cells and cultured in polypropylene tubes up to 14 days. Culture medium (DMEM high glucose/F12 or DMEM low glucose with 10% FCS) was added to cover the entire scaffold and changed twice a week. Each experiment refers to a single sample and the cells from the same donor are characterized before and after seeding.

Biochemical Assay

The collagen content was quantified using a commercially available assay kit (Hydroxyproline Assay Kit, BioVision, Milpitas, CA, United States). The proteoglycan content was determined by measuring the amount of sulfated glycosaminoglycans (sGAG) in the papain-digested samples (Fresh WJ and DWJM) using the 1,9-dimethylmethylene blue (DMMB, Sigma-Aldrich) dye binding assay and spectrophotometry (Farndale et al., 1986). Samples were first lyophilized (dry weight, 30 mg) and then digested in papain buffer (250 μL papain in PBS at pH 6.0 with 150 mM sodium chloride, 55 nM sodium citrate, 5 mM cysteine-HCl, and 5 mM Na_2EDTA) at 60°C for 12 h. After digestion, the supernatant fluid was incubated with DMMB and measured at 530 nm by a Microplate Absorbance Reader (Sunrise™, Tecan, Männedorf-Switzerland).

DNA Quantification

The DNA was extracted from both native and decellularized WJ. Six WJ specimens (wet weight, 25 mg) were used. The DNA was extracted using the DNA isolation kit (ReliaPrep gDNA Tissue Miniprep System, Promega, Fitchburg, WI, United States) and then quantified according to standard protocols by measuring the absorbance at 260/280 nm using a spectrophotometer (NanoDrop ND 1000; Thermo Scientific, Waltham, MA, United States).

Histology and Immunofluorescence

Histological analyses were performed on frozen sections (7–10 μm thick) using haematoxylin and eosin (H&E) kit for rapid frozen section and Alcian Blue (AB) for glycosaminoglycan hematoxylin staining (all from Bio-Optica, Milan, Italy) under manufacturer's instruction. For immunofluorescence analyses, frozen sections were permeabilized with 0.5% Triton X-100 (Sigma-Aldrich) in PBS for 10 min at RT, saturated with 10% horse serum (HS) (Thermo Fisher Scientific, WA, United States) in PBS for 12 min and with mouse serum (Sigma-Aldrich,

dilution 1:10) for 15 min at RT. The samples were incubated with primary antibodies (**Supplementary Table S1**) for 1 h at 37°C and then with labeled secondary antibodies (**Supplementary Table S1**) for 1 h at 37°C. Nuclei were counterstained with fluorescent mounting medium plus 100 ng/ml 4′,6-diamidino-2-phenylindole (DAPI) (Sigma-Aldrich). Images were captured using an DMI6000B confocal microscope (Leica Microsystems, Wetzlar, Germany). The cell count percentage has been performed comparing the positive cells with all the nuclei present in the field (the number multiplied per 100). Percentage of seeded area, defined as DAPI fluorescence in all the seeded area (panoramic picture of the whole sections was made), and laminin and fibronectin mean fluorescence intensity has been calculated using Fiji 30 software as already performed elsewhere (Kim et al., 2016; Quarta et al., 2017, 2018) using 8 bit image and threshold (n = 6, 10 fields per each sample). All counts were made by two blinded operators.

Electron Microscopy

The analysis of the morphological architecture, the porous structure, and the adhesion/integration of MSCs and IVD cells to DWJM was performed by different microscopic techniques, namely: inverted optical microscopy (Nikon Diafophot, Tokyo, Japan), scanning electron microscopy (SEM; Cambridge S360 microscope; Cambridge Instruments, Cambridge, United Kingdom), and transmission electron microscopy (TEM; ZEISS EM 910 electron microscope; Zeiss, Oberkochen, Germany). Samples for the electron microscopy, were fixed in glutaraldehyde 2.5% buffered solution and osmium tetroxide 2% buffered solution and dehydrated; for SEM analysis, samples were gold coated (Edward Sputter S150), while for TEM analysis, samples were araldite embedded (ACM Fluka Sigma-Aldrich) and the ultra-thin sections of a selected area were contrasted with uranyl acetate lead citrate. The pore size was estimated using SEM images, counting a minimum of 100 pores from different places on the cross section of the scaffolds. The pore sizes were analyzed by using Fiji 30 software.

Proliferation and Viability

Viability assay was performed as previously described (Penolazzi et al., 2010). For Propidium Iodide and Calcein-AM analysis, cells were visualized under a fluorescence microscope (Nikon, Optiphot-2, Nikon corporation, Japan) using the filter block for fluorescein. Dead cells were stained in red, whereas viable ones appeared in green. The proliferation rate of MSCs and IVD cells was determined by using the alamarBlue™ assay (Invitrogen Corporation, Carlsbad, CA, United States). The test is based on the metabolic activity of proliferating cells that results in a chemical reduction of alamarBlue™ reagent, previously added to the *in vitro* cultured cells. Briefly, at sequential time points a medium containing 5% alamarBlue™ was added to the cells, at 37°C and 5% CO_2. After 4 h of incubation, 200 μL samples of culture medium were withdrawn, centrifuged, and subsequently placed on 96-well plates. Visible light absorption of the collected samples was determined at 570 and 620 nm by a Microplate Absorbance Reader (Sunrise™, Tecan). Final values were calculated as the difference in absorbance units between the reduced and oxidized forms of alamarBlue™.

Statistical Analysis

Image-based counts and measurements were performed with Fiji 30 software (Mayachitra, Santa Barbara, CA, United States). For each analysis, at least five random pictures were used for data output. All graphs displayed were produced with GraphPad software 5 or 6 (GraphPad Software Inc., CA, United States). Data are expressed as means ± SD. Statistical significance was analyzed by unpaired Student's t-test. P-value below 0.05 was considered to be statistically significant.

RESULTS

Preparation and Characterization of Decellularized Human Wharton's Jelly Matrix

The overview of the different steps of the experiment plan is schematically shown in **Figure 1A**. First, WJ from umbilical cord (fresh WJ) was decellularized by using a protocol based on DET, as already reported (Piccoli et al., 2016). Different WJ samples were subjected to one or more cycles of treatment in order to obtain DWJM by a complete cell removal. After each cycle, the gross appearance of treated tissues, DNA content and the ECM composition (laminin and fibronectin fluorescence) were analyzed demonstrating that one DET cycle was sufficient to achieve more than 95% of nuclei depletion, keeping the morphology of the sample (**Figure 1B** and **Supplementary Figure S1**). As shown in **Figure 1B**, the amount of DNA was below the value of 50 ng/mg of tissue which is the threshold concentration of residual DNA to avoid adverse host responses (Crapo et al., 2011). Preservation of native tissue architecture was investigated by sGAG content evaluation and electron microscopy analysis. The structure of the DWJM retained sGAG (**Figure 1B**) and collagen network (**Figure 1C**) similar to fresh WJ. In particular, SEM imaging revealed the maintenance of the ECM fibrillary microstructure after decellularization, together with the presence of irregular spaces between the fibrils that range from 0.5 to several microns (**Figure 1C**). Collagen quantification of the fresh and decellularized samples was not significantly different (41.5 ± 2.1 μg/mg for fresh WJ and 39.8 ± 0.65 μg/mg for the DWJM-**Figure 1D**). TEM showed the absence of intact cells and the presence of collagen fibers mainly running in the same orientation (**Figure 1E**). Accordingly, after decellularization, pore size modification was found. In particular, DWJM showed a significant increase in pore diameter (**Figure 1F**), which is a desired effect in order to facilitate cellular infiltration and subsequent recellularization of the decellularized matrix used as a scaffold.

Other primary ECM components such as non-collagenous fibronectin and laminin glycoproteins which participate in cell proliferation, adhesion, migration, differentiation activities, and reparative ECM role, were investigated in DWJM. As reported in **Figure 1G**, substantial levels of fibronectin and laminin were

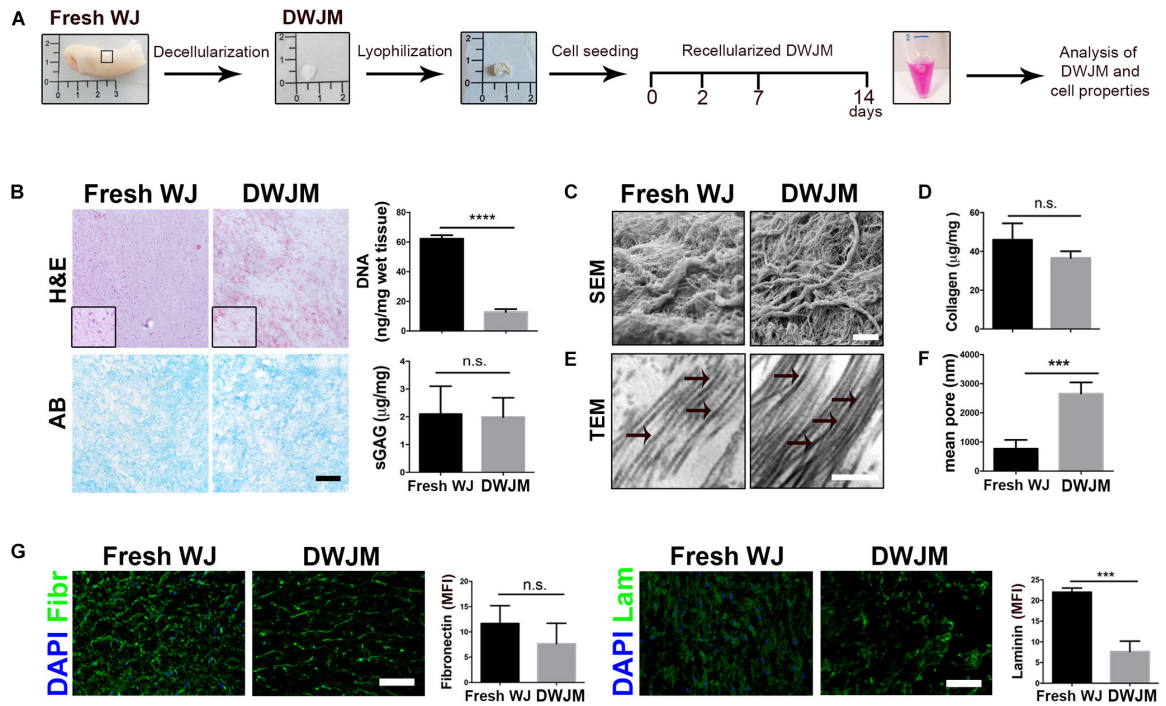

FIGURE 1 | Preparation and characterization of decellularized human Wharton's jelly matrix (DWJM). **(A)** Scheme of the different steps of the experimental plan: the gross appearance of Wharton's jelly freshly isolated (Fresh WJ), Wharton's jelly after decellularization (DWJM) and lyophilization process has been reported. After seeding of IVD cells or MSCs cells, the recellularized DWJM was kept in culture up to 14 days and then investigated. **(B)** Representative images of the histological analysis performed on Fresh WJ and DWJM by hematoxylin-eosin (H&E) and Alcian Blue (AB) staining. In the graphs the quantification of the residual DNA and total sulfated proteoglycans and glycosaminoglycans (sGAG) content is also reported. $^{****}p < 0.0001$; n.s., non-significant. Bar: 50 μm. **(C)** Representative images of SEM analysis of Fresh WJ and DWJM. Bar: 5 μm. **(D)** The quantification of the total collagen content (μg/mg of tissue) is reported in the graph. n.s., non-significant. **(E)** Representative images of TEM analysis of Fresh WJ and DWJM. Bar: 200 nm; black arrows indicate collagen fibers with visible cross-striation pattern. **(F)** Mean diameter of the pores (nm) is reported in the graph. $^{***}p < 0.001$; 10 analyzed fields, $n = 3$. **(G)** Representative images of the immunofluorescence analysis of Fibronectin (Fibr, in green), and Laminin (Lam, green) expression performed on Fresh WJ and DWJM. Nuclei were counterstained with DAPI (in blue); the results are expressed as mean fluorescence intensity (MFI, arbitrary unit) evaluated for 10 fields, $n = 3$. $^{***}p < 0.001$; n.s., non-significant. Bars: 50 μm.

detected by fluorescent immunostaining, after decellularization, even if laminin content appeared to be less preserved.

As a whole, the decellularization process was effective in generating a cell-free porous matrix with its native microarchitecture and composition.

Properties of the Cells Seeded on Decellularized Wharton's Jelly Matrix

In order to investigate the ability of DWJM to act as a scaffold for intervertebral disc cell culturing, human cells from degenerated intervertebral disc (namely IVD cells) were combined with the matrix and cultured in polypropylene tubes up to 14 days without soluble differentiation inducers. The effect of DWJM on IVD cells was compared with that on human MSCs from WJ, in terms of viability, proliferation and matrix interaction. By Calcein AM/Propidium Iodide staining, it was appreciable the ability of the cells to uniformly adhere to DWJM. As shown in **Figure 2A**, the cells were viable and able to maintain their spindle shape morphology. No major difference was observed when comparing the viability of both cell sources after 7 days of culture. However, alamarBlue™ assay highlighted that growth rate of IVD cells was significantly slower compare to MSCs (**Figure 2A**), although the proliferation ability of these two cell types is absolutely comparable in 2D culture conditions (Penolazzi et al., 2018 and data not shown).

This was confirmed by fluorescence microscopy analysis of DAPI-stained cells which revealed a lower percentage of cell-seeding area in DWJM combined with IVD cells than in DWJM combined with MSCs (**Figure 2B**).

Scanning and transmission electron microscopic analysis clearly revealed the ability of the cells to create cell-cell and cell-matrix interconnections (**Figure 2C**). Electron-dense areas close to the cellular membrane as specific points of contact with matrix surface were appreciable. Intriguingly, abundant vesicles budding from the IVD cells surface were found. In particular, TEM analysis revealed that these vesicles, 100–200 nm in size (117.18 ± 20 nm, mean diameter), were distributed all over the cellular membrane.

The Effect of DWJM on Degenerated Intervertebral Disc Cells

In a next step, we explored the potential of DWJM to restore the chondrocyte-like phenotype that belongs to healthy IVD cells and that is lost during degeneration/de-differentiation process.

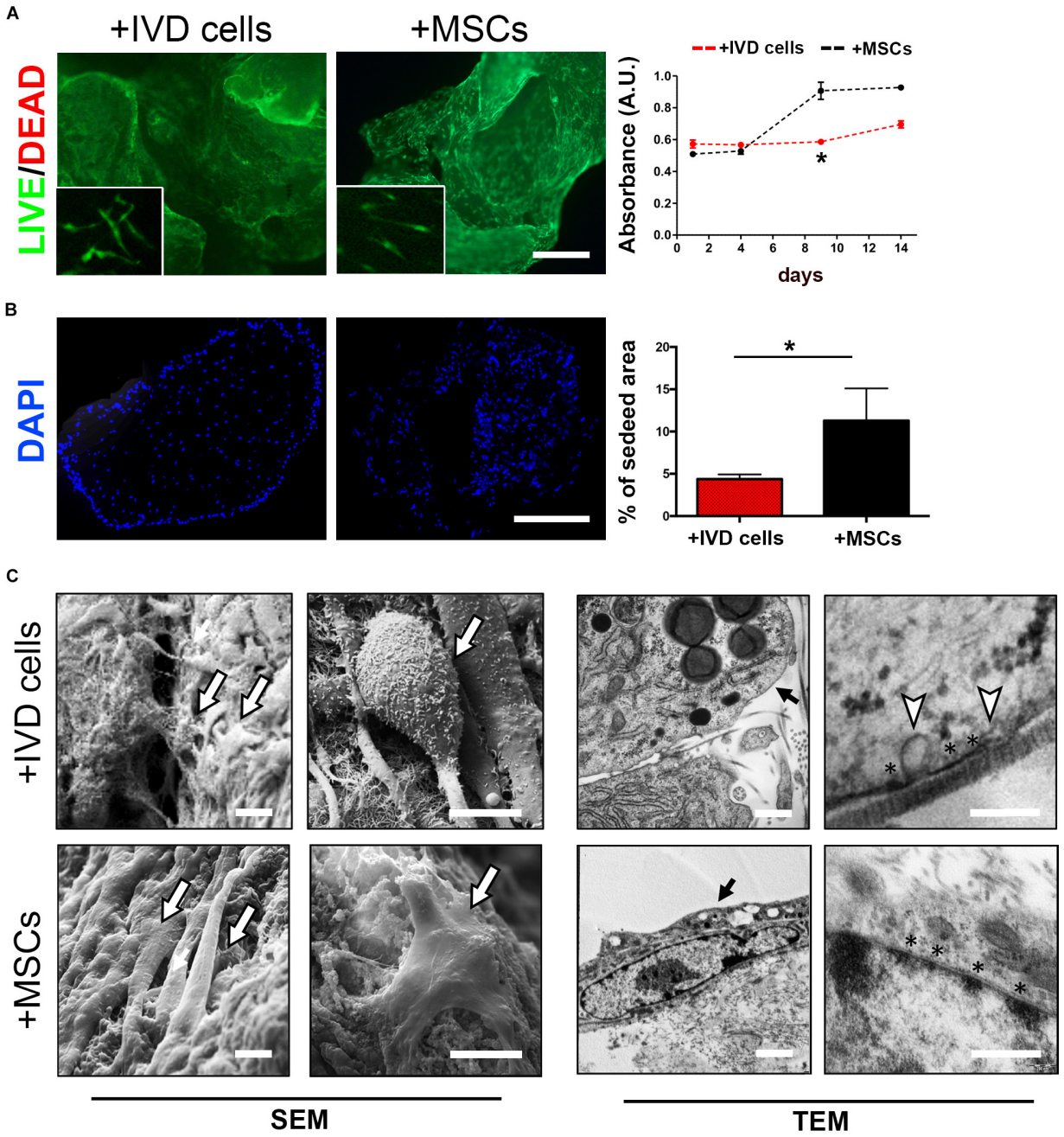

FIGURE 2 | DWJM combined with chondrocyte – like IVD cells or mesenchymal stromal cells (MSCs) from WJ. **(A)** Effect on cell viability was determined by Calcein-AM/Propidium Iodide double staining after 7 days of culture. Dead cells (red cells) were undetectable. High magnification images are shown in the insets. Effect on cell proliferation was determined by alamarBlue^{TM} assay in IVD cells (red dotted lane) and MSCs (black dotted lane) cultured up to 14 days, data are presented as mean absorbance (A.U., absorbance unit ± SD, $n = 3$). **(B)** Effect on cell distribution was determined fluorescence microscopy analysis of DAPI-stained cells cultured up to 14 days. The percentage of seeded area is reported in the graph, $n = 6$. *$p < 0.05$. Bar: 200 μm. **(C)** Representative images of SEM and TEM analysis. The presence of seeded cells on the DWJM surface is indicated by the arrows. Asterisks (*) indicate electron-dense areas close to the cellular membrane, white triangles indicate the presence of vesicles budding from the cell surface. Bars: 2 μm (SEM images); 200 nm (TEM images).

In particular, we evaluated the expression of three transcription factors that are lost in degenerated IVD microenvironment: SOX2, a well known stemness regulator, SOX9, the primary driver during the early stages of chondrogenic differentiation, and TRPS1, recently identified as pro-discogenic factor. As previously demonstrated (Penolazzi et al., 2019), the expression of these proteins always decreases during the passages in culture, as the cells undergo de-differentiation. Interestingly,

as shown in **Figure 3**A and **Supplementary Figures S2–S4**, immunofluorescence analysis revealed that culturing degenerated IVD cells on DWJM up-regulated the expression of these transcription factors with a specific timing that resembles the early and late phases of discogenic/chondrogenic differentiation. In fact, a progressive increase of SOX2 and SOX9 expression levels was observed in the first seven days of culture, suggesting a cellular activity both in terms of stemness and differentiation supported by the presence of DWJM. In a second phase, between day 7 and day 14, a down-regulation of SOX2 and SOX9 together with an up-regulation of TRPS1 was observed, suggesting the achievement of a more mature cellular phenotype.

On the contrary, culturing MSCs on DWJM weakly affected the expression of the transcription factors analyzed (**Figure 3B**). **Figure 3C** well summarizes the switch on and off of the proteins, according to the cell type.

DISCUSSION

It has been repeatedly shown that there is no effective treatment protecting the IVD from degeneration. In the regenerative approaches in IVD tissue engineering aimed at restoring the AF and NP function, important results are expected from the development of specific biomimetic scaffolds. In the present study, we investigated the potential of DWJM as ECM-based scaffold able to provide appropriate physical and chemical milieu for IVD cells. For the first time, we demonstrated the ability of DWJM to improve the degenerated phenotype of human IVD cells. De-differerentiated human IVD cells and DWJM were combined in a 3D culture condition without differentiating agents, cytokines or growth factors, showing that the mere presence of the matrix positively affected the expression of critical regulators of IVD homeostasis, such as SOX2, SOX9, and TRPS1 (Penolazzi et al., 2019).

Wharton's jelly from umbilical cord is becoming increasingly proposed as an ideal source for obtaining scaffold useful for tissue engineering application (Beiki et al., 2017; Basiri et al., 2019). WJ is easy to obtain as biological waste material, is non-immunogenic, and its use presents no ethical concerns (Forraz and McGuckin, 2011). WJ contains abundant collagenic structural proteins (collagen I, III, VI, and XII), other ECM components such as fibronectin, lumican, heparin sulfate, and growth factors (TGFβ, FGFβ, VEGF) (Jadalannagari et al., 2017). It has been demonstrated that DWJM is able to retain many chemotactic factors and soluble bioactive factors positively affecting cell viability and function (Basiri et al., 2019). Therefore, for these different reasons DWJM has been proposed as potential therapeutic agent in many areas (Jadalannagari et al., 2017; Kehtari et al., 2019; Li et al., 2019). A still unexplored field is represented by the degenerated IVD. For the first time, in the current study we cultured human de-differentiated IVD cells from degenerated IVD in combination with DWJM. The attempt to restore the properties of the IVD cells through the peculiar characteristics of the DWJM, meets the need to develop alternative methods to the use of cell-based therapy that in many cases proved to be a failure (Sakai and Andersson, 2015). It has been in fact demonstrated that degradation and loss of ECM proteins associated with the upregulation of proteinases, such as ADAMTSs and MMPs, and downregulation of TIMPs (Vo et al., 2013), in the degenerated IVD produces a physicochemical microenvironment which is hostile for the engraftment of many types of transplanted cells such as MSCs from bone marrow or stromal adipose derived cells, compromising the cell-based therapy outcome in different clinical trials (Tendulkar et al., 2019).

The benefit derived from the presence of the DWJM is demonstrated by evidence we obtained and is distinguishable in two different phases. In a first phase, corresponding to the first seven days in culture, the presence of SOX2, a well known stemness regulator, and SOX9, the primary driver during the early stages of chondrogenesis, has been appreciably highlighted. The progressive increase of SOX2 and SOX9 expression levels in the first seven days of culture, suggests a functional cellular activity both in terms of stemness and differentiation supported by the presence of DWJM. Otherwise, the expression of SOX2 and SOX9 in degenerated IVD cells in culture was very low or undetectable as by us previously demonstrated (Penolazzi et al., 2019). It is noteworthy, that, regarding in particular SOX9, there is a growing interest on therapeutic approach based on protein targeting, by adenoviral vector (AdSOX9) intradiscal injection aimed at increasing the percentage of positive resident cells (Paul et al., 2003), or by delivery of SOX9-transduced MSCs (Sun et al., 2014). In a second phase, between day 7 and day 14, IVD cells combined with DWJM showed a down-regulation of SOX2 and SOX9 together with an up-regulation of TRPS1, a chondrogenic transcription factor previously identified by us as chondroprotective and associated with the lower grade of disc degeneration (Penolazzi et al., 2019).

Our data are in line with the hypothesis that the strengthening of cell properties in terms of viability and expression of specific proteins at precise times represents an important condition in the perspective of guiding the recovery of cellular functionality and triggering regenerative potential. Therefore, the potential of DWJM to revert degenerated IVD cells can be exploited to carry out an ECM-based intradiscal injectable therapeutic (Tukmachev et al., 2016; Wachs et al., 2017; Porzionato et al., 2018; Zhou et al., 2018). In other words, the presence of DWJM could be sufficient to further the functional recovery of the endogenous cells in the degenerated IVD microenvironment. Otherwise, when MSCs were combined with DWJM, the main effect was a significant increase in cell proliferation, suggesting that these cells reseeded in the ECM they produced, just maintain their primitive phenotype without moving toward discogenic differentiation.

Moreover, it is worth considering also important technical aspects that arise from the data collected in the current study: i. producing an informative 3D culture system based on DWJM even with a low number of cells like those that can be obtained from a human IVD biopsy; ii. providing a cell culture – based platform available as a preclinical experimental model which can be exposed to different treatments mimicking pathophysiological IVD microenvironment (hypoxia, dynamic culture condition, mechanical forces), as an alternative to animal models such as

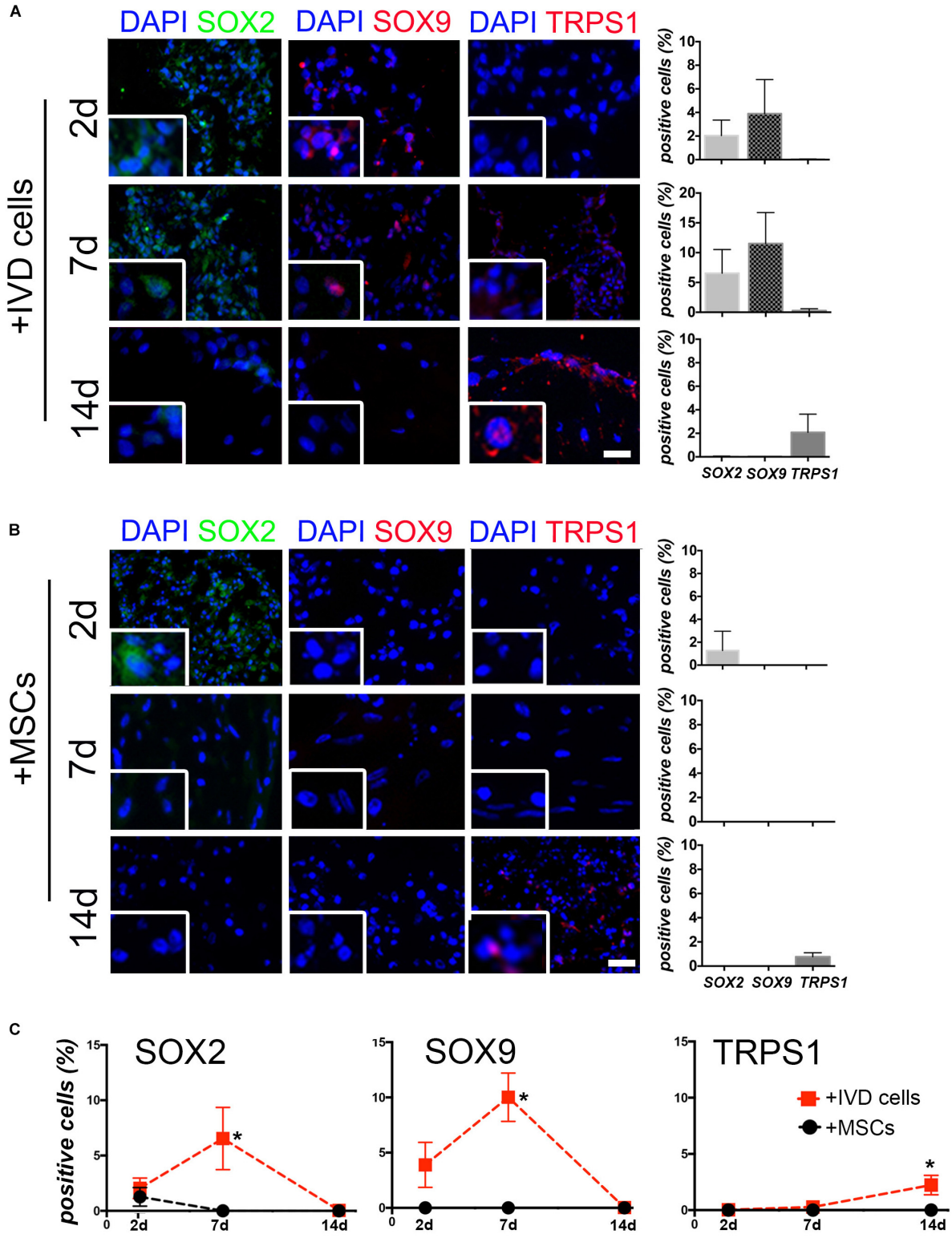

FIGURE 3 | The effect of DWJM on degenerated IVD cells. Representative images of the immunofluorescence analysis of SOX2, SOX9, and TRPS1 expression performed on DWJM combined with IVD cells **(A)** or with MSCs **(B)** after 2d, 7d, and 14d (days) of culture. Nuclei were counterstained with DAPI (in blue); bars: 50 μm. High magnification images are shown in the insets. The percentage of positive cells (±SD) for each transcription factor is reported in the graphs (10 analyzed fields, $n = 6$). **(C)** Lines plot showing the average percentage (±SD) of SOX2, SOX9, and TRPS1 positive cells over the time are reported. *$p < 0.05$. Statistical analysis was performed for DWJM combined with IVD cells versus MSCs.

rodents, rabbit or other large quadrupeds (Alini et al., 2008); iii. making available an ECM – based product characterized not only by biological properties suitable for cell survival and function, but also easy of handling for clinical application. DWJM can be easily stored as lyophilized powder, and also modified as ready-to use injectable hydrogel treatment for intraoperative application (Tukmachev et al., 2016; Wachs et al., 2017; Porzionato et al., 2018; Zhou et al., 2018).

Finally, we should also consider some limitations of this study as well as further investigation to demonstrate the potential of DWJM employment in restoring IVD integrity and functionality. First, we demonstrated the maintenance of ECM microarchitecture after decellularization process, however, further analysis are needed to define the relationship between ECM and IVD cells, and cell-cell interactions. In particular, being cell adhesion a critical event affecting cellular signaling, survival, growth, and phenotype, cell surface receptors such as integrin subunits, distribution of fibronectin, laminin and collagen receptors, the involvement of Focal Adhesion Kinase (FAK) and Integrin-linked Kinase (ILK) pathways (Cukierman et al., 2002) deserve further study. This aspect could help to better understand IVD cell differentiation mechanisms. Second, there are some recent studies that have focused on the effect of decellularized IVD ECM on treating disc degeneration in animal models (Lin et al., 2016; Illien-Jünger et al., 2016; Zhou et al., 2018). It would be interesting to compare the properties of this matrix with DWJM in order to optimize specific tissue engineering applications. Moreover, SEM and TEM microscopy revealed the presence of numerous extracellular vesicles (EVs) in DWJM combined with IVD cells. It remains to investigate whether the effect of DWJM on improving the IVD cell phenotype should be attributed to the 3D environment itself, to the native WJ microenvironment and the bioactive molecules of a rich ECM that are preserved after decellularization, or to a specific paracrine activity of the IVD cells triggered by the DWJM itself. Recent evidence suggests that the production of EVs often happens when cells are combined with collagen based biomaterials (McNeill et al., 2019). It will be particularly interesting to understand how DWJM is able to induce EVs production when combined with IVD cells but not with MSCs from Wharton's jelly. Therefore, in order to improve the comprehension of the mechanism underlying the action supported by DWJM, and to develop innovative therapeutics for spine injuries based on single molecules, in the next future it will be useful to analyze also EVs protein content.

DATA AVAILABILITY STATEMENT

All datasets generated for this study are included in the article/**Supplementary Material**.

ETHICS STATEMENT

The studies involving human participants were reviewed and approved by the Ethics Committee of the University of Ferrara and S. Anna Hospital. The patients/participants provided their written informed consent to participate in this study.

AUTHOR CONTRIBUTIONS

LP, MP, EL, and RP: conceptualization, experimental design, and writing. LP, LB, SD'A, and RF: methodology and visualization. GB, PD, and MC: supervision and data collection.

FUNDING

This work has been supported by the Fondo di Ateneo per la Ricerca 2018 (University of Ferrara) and Associazione Puzzle, Padua. MP is funded by University of Padova, Grant number GRIC15AIPF, Assegno di Ricerca Senior.

ACKNOWLEDGMENTS

The authors would like to thank Paola Boldrini and Daniela Palmeri, Centro di Microscopia Elettronica, University of Ferrara, for technical assistance. This work contributes to the COST Action CA17116 "International Network for Translating Research on Perinatal Derivatives into Therapeutic Approaches (SPRINT)," supported by COST (European Cooperation in Science and Technology).

SUPPLEMENTARY MATERIAL

The Supplementary Material for this article can be found online at: https://www.frontiersin.org/articles/10.3389/fbioe.2020.00262/full#supplementary-material

REFERENCES

Alini, M., Eisenstein, S. M., Ito, K., Little, C., Kettler, A. A., Masuda, K., et al. (2008). Are animal models useful for studying human disc disorders/degeneration? *Eur. Spine J.* 17, 2–19. doi: 10.1007/s00586-007-0414-y

Amin, R. M., Andrade, N. S., and Neuman, B. J. (2017). Lumbar disc herniation. *Curr. Rev. Musculoskelet. Med.* 10, 507–516. doi: 10.1007/s12178-017-9441-4

Basiri, A., Farokhi, M., Azami, M., Ebrahimi-Barough, S., Mohamadnia, A., Rashtbar, M., et al. (2019). A silk fibroin/decellularized extract of Wharton's jelly hydrogel intended for cartilage tissue engineering. *Prog. Biomater.* 8, 31–42. doi: 10.1007/s40204-019-0108-7

Beiki, B., Zeynali, B., and Seyedjafari, E. (2017). Fabrication of a three dimensional spongy scaffold using human Wharton's jelly derived extra cellular matrix for wound healing. *Mater. Sci. Eng. C Mater. Biol. Appl.* 78, 627–638. doi: 10.1016/j.msec.2017.04.074

Buckley, C. T., Hoyland, J. A., Fujii, K., Pandit, A., Iatridis, J. C., and Grad, S. (2018). Critical aspects and challenges for intervertebral disc repair and regeneration—Harnessing advances in tissue engineering. *JOR Spine* 1:e1029. doi: 10.1002/jsp2.1029

Bullard, J. D., Lei, J., Lim, J. J., Massee, M., Fallon, A. M., and Koob, T. J. (2019). Evaluation of dehydrated human umbilical cord biological properties for wound care and soft tissue healing. *J. Biomed. Mater. Res. B Appl.Biomater.* 107, 1035–1046. doi: 10.1002/jbm.b.34196

Coogan, J. S., Francis, W. L., Eliason, T. D., Bredbenner, T. L., Stemper, B. D., Yoganandan, N., et al. (2016). Finite element study of a lumbar intervertebral disc nucleus replacement device. *Front. Bioeng. Biotechnol.* 4:93. doi: 10.3389/fbioe.2016.00093

Crapo, P. M., Gilbert, T. W., and Badylak, S. F. (2011). An overview of tissue and whole organ decellularization processes. *Biomaterials* 32, 3233–3243. doi: 10.1016/j.biomaterials.2011.01.057

Cukierman, E., Pankov, R., and Yamada, K. M. (2002). Cell interactions with three-dimensional matrices. *Curr. Opin. Cell Biol.* 14, 633–639. doi: 10.1016/s0955-0674(02)00364-362

D'Este, M., Eglin, D., and Alini, M. (2018). Lessons to be learned and future directions for intervertebral disc biomaterials. *Acta Biomater.* 15, 13–22. doi: 10.1016/j.actbio.2018.08.004

Farndale, R. W., Buttle, D. J., and Barrett, A. J. (1986). Improved quantitation and discrimination of sulphated glycosaminoglycans by use of dimethylmethylene blue. *Biochim. Biophys. Acta* 883, 173–177. doi: 10.1016/0304-4165(86)90306-5

Farrugia, B., Smith, S. M., Shu, C. C., and Melrose, J. (2019). Spatiotemporal expression of 3-B-3(-) and 7-D-4 chondroitin sulfation, tissue remodeling, and attempted repair in an ovine model of intervertebral disc degeneration. *Cartilage* [Epub ahead of print]. doi: 10.1177/1947603519876354

Ferguson, V. L., and Dodson, R. B. (2009). Bioengineering aspects of the umbilical cord. *Eur. J. Obstet. Gynecol. Reprod. Biol.* 144, S108–S113. doi: 10.1016/j.ejogrb.2009.02.024

Forraz, N., and McGuckin, C. P. (2011). The umbilical cord: a rich and ethical stem cell source to advance regenerative medicine. *Cell Prolif.* 44(Suppl. 1), 60–69. doi: 10.1111/j.1365-2184.2010.00729.x

Fujii, K., Yamazaki, M., Kang, J. D., Risbud, M. V., Cho, S. K., Qureshi, S. A., et al. (2019). Discogenic back pain: literature review of definition, diagnosis, and treatment. *JBMR Plus* 3:e10180. doi: 10.1002/jbm4.10180

Geurts, J. W., Willems, P. C., Kallewaard, J., van Kleef, M., and Dirksen, C. (2018). The impact of chronic discogenic low back pain: costs and patients' burden. *Pain Res. Manag.* 2018, 1–8. doi: 10.1155/2018/4696180

Gullbrand, S. E., Ashinsky, B. G., Bonnevie, E. D., Kim, D. H., Engiles, J. B., Smith, L. J., et al. (2018). Long-term mechanical function and integration of an implanted tissue-engineered intervertebral disc. *Sci. Transl. Med.* 10:eaau0670. doi: 10.1126/scitranslmed.aau0670

Hensley, A., Rames, J., Casler, V., Rood, C., Walters, J., Fernandez, C., et al. (2018). Decellularization and characterization of a whole intervertebral disk xenograft scaffold. *J. Biomed. Mater. Res. A* 106, 2412–2423. doi: 10.1002/jbm.a.36434

Illien-Jünger, S., Sedaghatpour, D. D., Laudier, D. M., Hecht, A. C., Qureshi, S. A., and Iatridis, J. C. (2016). Development of a bovine decellularized extracellular matrix-biomaterial for nucleus pulposus regeneration. *J. Orthop. Res.* 34, 876–888. doi: 10.1002/jor.23088

Jadalannagari, S., Converse, G., McFall, C., Buse, E., Filla, M., Villar, M. T., et al. (2017). Decellularized Wharton's Jelly from human umbilical cord as a novel 3D scaffolding material for tissue engineering applications. *PLoS One* 12:e0172098. doi: 10.1371/journal.pone.0172098

Kehtari, M., Beiki, B., Zeynali, B., Hosseini, F. S., Soleimanifar, F., Kaabi, M., et al. (2019). Decellularized Wharton's jelly extracellular matrix as a promising scaffold for promoting hepatic differentiation of human induced pluripotent stem cells. *J. Cell. Biochem.* 120, 6683–6697. doi: 10.1002/jcb.27965

Kim, J. T., Kasukonis, B. M., Brown, L. A., Washington, T. A., and Wolchok, J. C. (2016). Recovery from volumetric muscle loss injury: a comparison between young and aged rats. *Exp. Gerontol.* 83, 37–46. doi: 10.1016/j.exger.2016.07.008

Li, D., Chiu, G., Lipe, B., Hopkins, R. A., Lillis, J., Ashton, J. M., et al. (2019). Decellularized Wharton's jelly matrix: a biomimetic scaffold for ex vivo hematopoietic stem cell culture. *Blood Adv.* 3, 1011–1026. doi: 10.1182/bloodadvances.2018019315

Lin, X., Fang, X., Wang, Q., Hu, Z., Chen, K., Shan, Z., et al. (2016). Decellularized allogeneic intervertebral disc: natural biomaterials for regenerating disc degeneration. *Oncotarget* 7, 12121–12136. doi: 10.18632/oncotarget.7735

Liu, C., Jin, Z., Ge, X., Zhang, Y., and Xu, H. (2019). Decellularized annulus fibrosus matrix/chitosan hybrid hydrogels with basic fibroblast growth factor for annulus fibrosus tissue engineering. *Tissue Eng Part A* 25, 1605–1613. doi: 10.1089/ten.TEA.2018.0297

McNeill, B., Ostojic, A., Rayner, K. J., Ruel, M., and Suuronen, E. J. (2019). Collagen biomaterial stimulates the production of extracellular vesicles containing microRNA-21 and enhances the proangiogenic function of CD34+ cells. *FASEB J.* 33, 4166–4177. doi: 10.1096/fj.201801332R

Murray, C. J., Vos, T., Lozano, R., Naghavi, M., Flaxman, A. D., Michaud, C., et al. (2012). Disability-adjusted life years (DALYs) for 291 diseases and injuries in 21 regions, 1990-2010: a systematic analysis for the Global Burden of Disease Study 2010. *Lancet* 380, 2197–2223. doi: 10.1016/S0140-6736(12)61689-4

Najar, M., Fayyad-Kazan, M., Meuleman, N., Bron, D., Fayyad-Kazan, H., and Lagneaux, L. (2018). Immunological impact of Wharton's Jelly mesenchymal stromal cells and natural killer cell co-culture. *Mol. Cell Biochem.* 447, 111–124. doi: 10.1007/s11010-018-3297-9

Ohtori, S., Koshi, T., Yamashita, M., Yamauchi, K., Inoue, G., Suzuki, M., et al. (2011). Surgical versus nonsurgical treatment of selected patients with discogenic low back pain: a small-sized randomized trial. *Spine* 36, 347–354. doi: 10.1097/BRS.0b013e3181d0c944

Paul, R., Haydon, R. C., Cheng, H., Ishikawa, A., Nenadovich, N., Jiang, W., et al. (2003). Potential use of Sox9 gene therapy for intervertebral degenerative disc disease. *Spine* 28, 755–763. doi: 10.1097/01.BRS.0000058946.64222.92

Penolazzi, L., Lambertini, E., Bergamin, L. S., Roncada, T., De Bonis, P., Cavallo, M., et al. (2018). MicroRNA-221 silencing attenuates the degenerated phenotype of intervertebral disc cells. *Aging* 10, 2001–2015. doi: 10.18632/aging.101525

Penolazzi, L., Lambertini, E., Scussel Bergamin, L., Gandini, C., Musio, A., De Bonis, P., et al. (2019). Reciprocal regulation of TRPS1 and miR-221 in intervertebral disc cells. *Cells* 8:E1170. doi: 10.3390/cells8101170

Penolazzi, L., Mazzitelli, S., Vecchiatini, R., Torreggiani, E., Lambertini, E., Johnson, S., et al. (2012). Human mesenchymal stem cells seeded on extracellular matrix-scaffold: viability and osteogenic potential. *J. Cell. Physiol.* 227, 857–866. doi: 10.1002/jcp.22983

Penolazzi, L., Tavanti, E., Vecchiatini, R., Lambertini, E., Vesce, F., Gambari, R., et al. (2010). Encapsulation of mesenchymal stem cells from Wharton's jelly in alginate microbeads. *Tissue Eng. C Methods* 16, 141–155. doi: 10.1089/ten.TEC.2008.0582

Piccoli, M., Urbani, L., Alvarez-Fallas, M. E., Franzin, C., Dedja, A., Bertin, E., et al. (2016). Improvement of diaphragmatic performance through orthotopic application of decellularized extracellular matrix patch. *Biomaterials* 74, 245–255. doi: 10.1016/j.biomaterials.2015.10.005

Porzionato, A., Stocco, E., Barbon, S., Grandi, F., Macchi, V., and De Caro, R. (2018). Tissue-engineered grafts from human decellularized extracellular matrices: a systematic review and future perspectives. *Int. J. Mol. Sci.* 19:E4117. doi: 10.3390/ijms19124117

Quarta, M., Cromie, M., Chacon, R., Blonigan, J., Garcia, V., Akimenko, I., et al. (2017). Bioengineered constructs combined with exercise enhance stem cell-mediated treatment of volumetric muscle loss. *Nat. Commun.* 8:15613. doi: 10.1038/ncomms15613

Quarta, M., Cromie Lear, M. J., Blonigan, J., Paine, P., Chacon, R., and Rando, T. A. (2018). Biomechanics show stem cell necessity for effective treatment of volumetric muscle loss using bioengineered constructs. *NPJ Regen. Med.* 3:18. doi: 10.1038/s41536-018-0057-0

Roughley, P. J. (2004). Biology of intervertebral disc aging and degeneration: involvement of the extracellular matrix. *Spine* 29, 2691–2699. doi: 10.1097/01.brs.0000146101.53784.b1

Sakai, D., and Andersson, G. B. (2015). Stem cell therapy for intervertebral disc regeneration: obstacles and solutions. *Nat. Rev. Rheumatol.* 11, 243–256. doi: 10.1038/nrrheum.2015.13

Schizas, C., Kulik, G., and Kosmopoulos, V. (2010). Disc degeneration: current surgical options. *Eur. Cells Mater.* 20, 306–315. doi: 10.22203/ecm.v020a25

Stocco, E., Barbon, S., Dalzoppo, D., Lora, S., Sartore, L., Folin, M., et al. (2014). Tailored PVA/ECM scaffolds for cartilage regeneration. *Biomed. Res. Int.* 2014:762189. doi: 10.1155/2014/762189

Sun, W., Zhang, K., Liu, G., Ding, W., Zhao, C., Xie, Y., et al. (2014). Sox9 gene transfer enhanced regenerative effect of bone marrow mesenchymal stem cells on the degenerated intervertebral Disc in a rabbit model. *PLoS One* 9:e93570. doi: 10.1371/journal.pone.0093570

Tendulkar, G., Chen, T., Ehnert, S., Kaps, H. P., and Nüssler, A. K. (2019). Intervertebral disc nucleus repair: hype or hope? *Int. J. Mol. Sci.* 20:E3622. doi: 10.3390/ijms20153622

Tukmachev, D., Forostyak, S., Koci, Z., Zaviskova, K., Vackova, I., Vyborny, K., et al. (2016). Injectable extracellular matrix hydrogels as scaffolds for spinal cord injury repair. *Tissue Eng. A* 22, 306–317. doi: 10.1089/ten.TEA.2015.0422

Van Uden, S., Silva-Correia, J., Oliveira, J. M., and Reis, R. L. (2017). Current strategies for treatment of intervertebral disc degeneration: substitution and regeneration possibilities. *Biomater. Res.* 21:22. doi: 10.1186/s40824-017-0106-6

Ventre, M., Coppola, V., Natale, C. F., and Netti, P. A. (2019). Alligned fibrous decellularized cell derived matrices for mesenchymal stem cell amplification. *J. Biomed. Mater. Res. A* 107, 2536–2546. doi: 10.1002/jbm.a.36759

Vo, N. V., Hartman, R. A., Yurube, T., Jacobs, L. J., Sowa, G. A., and Kang, J. D. (2013). Expression and regulation of metalloproteinases and their inhibitors in intervertebral disc aging and degeneration. *Spine J.* 13, 331–341. doi: 10.1016/j.spinee.2012.02.027

Wachs, R. A., Hoogenboezem, E. N., Huda, H. I., Xin, S., Porvasnik, S. L., and Schmidt, C. E. (2017). Creation of an injectable in situ gelling native extracellular matrix for nucleus pulposus tissue engineering. *Spine J.* 17, 435–444. doi: 10.1016/j.spinee.2016.10.022

Walker, J. T., Keating, A., and Davies, J. E. (2019). "Stem cells: umbilical cord/wharton's jelly derived," in *Cell Engineering and Regeneration. Reference Series in Biomedical Engineering.*, eds J. Gimble, D. Marolt, R. Oreffo, H. Redl, and S. Wolbank (Cham: Springer). doi: 10.1007/978-3-319-37076-7_10-1

Xu, J., Liu, S., Wang, S., Qiu, P., Chen, P., Lin, X., et al. (2019). Decellularised nucleus pulposus as a potential biologic scaffold for disc tissue engineering. *Mater. Sci. Eng. C* 99, 1213–1225. doi: 10.1016/j.msec.2019.02.045

Zhao, R., Liu, W., Xia, T., and Yang, L. (2019). Disordered mechanical stress and tissue engineering therapies in intervertebral disc degeneration. *Polymers* 11:e1151. doi: 10.3390/polym11071151

Zhou, X., Wang, J., Huang, X., Fang, W., Tao, Y., Zhao, T., et al. (2018). Injectable decellularized nucleus pulposus-based cell delivery system for differentiation of adipose-derived stem cells and nucleus pulposus regereration. *Acta Biomat.* 81, 115–128. doi: 10.1016/j.actbio.2018.09.044

Conflict of Interest: The authors declare that the research was conducted in the absence of any commercial or financial relationships that could be construed as a potential conflict of interest.

frontiers in Bioengineering and Biotechnology

ORIGINAL RESEARCH
published: 31 March 2020
doi: 10.3389/fbioe.2020.00243

Sodium Hyaluronate Supplemented Culture Media as a New hMSC Chondrogenic Differentiation Media-Model for *in vitro/ex vivo* Screening of Potential Cartilage Repair Therapies

*Graziana Monaco[1,2], Alicia Jennifer El Haj[3], Mauro Alini[1] and Martin James Stoddart[1,2]**

[1] AO Research Institute Davos, Davos, Switzerland, [2] School of Pharmacy and Bioengineering, Faculty of Medicine and Health Sciences, Keele University, Guy Hilton Research Centre, Thornburrow Drive, Stoke-on-Trent, United Kingdom, [3] Healthcare Technology Institute, Institute of Translational Medicine, University of Birmingham, Birmingham, United Kingdom

OPEN ACCESS

Edited by:
Dimitrios I. Zeugolis, National University of Ireland Galway, Ireland

Reviewed by:
Gunil Im, Dongguk University Ilsan Hospital, South Korea
Martijn van Griensven, cBITE, MERLN Institute, Maastricht University, Netherlands

***Correspondence:**
Martin James Stoddart
martin.stoddart@aofoundation.org

Specialty section:
This article was submitted to Tissue Engineering and Regenerative Medicine, a section of the journal Frontiers in Bioengineering and Biotechnology

Received: 15 December 2019
Accepted: 09 March 2020
Published: 31 March 2020

Citation:
Monaco G, El Haj AJ, Alini M and Stoddart MJ (2020) Sodium Hyaluronate Supplemented Culture Media as a New hMSC Chondrogenic Differentiation Media-Model for in vitro/ex vivo Screening of Potential Cartilage Repair Therapies. Front. Bioeng. Biotechnol. 8:243. doi: 10.3389/fbioe.2020.00243

Surgical strategies to treat articular cartilage injury such as microfracture, expose human bone marrow stem cells (hMSCs) to synovial fluid and its components. High molecular weight hyaluronan (hMwt HA) is one of the most abundant bioactive macromolecules of healthy synovial fluid (hSF) and it plays an important role in the protection of opposing articular cartilage surfaces within the synovial joint. Although hMwt HA has been extensively used to attempt the engineering of the cartilage tissue, its effect as media supplement has not been established. Indeed, current media are often simple in their composition and doesn't recapitulate the rheological and biological features of hSF. In addition, critical *in vivo* molecules that can potentially change the chondrogenic behavior of hBMSCs to make the *in vitro* results more predictive of the real *in vivo* outcome, are lacking. In order to be one step closer to the *in vivo* physiology of hSF, a new culture media supplemented with physiological level of hMwt HA was developed and the effect of the hMwt HA on the chondrogenesis of hMSCs that would be present in a traumatic defect after marrow stimulation techniques, was investigated. hBMSC-seeded fibrin-polyurethane constructs were cultured in a serum free chondropermissive control medium (HA- TGFβ-). This medium was further supplemented with 10 ng/mL TGFβ1 (HA- TGFβ+) or 2 mg/ml hMwt HA 1.8 MDa (HA+ TGFβ-) or both (HA+ TGFβ+). Alternatively, 1 MDa HA was mixed with the fibrin at 0.2 mg/ml (HASc TGFβ+). The effect of hMwt HA on hMSC differentiation was investigated at the gene expression level by RT-qPCR and total DNA, sulfated glycosaminoglycans and Safranin O staining were evaluated. Addition of hMwt HA to the culture media, significantly increased the synthesis of sulfated glycosaminoglycans, especially in the early days of chondrogenesis, and reduced the upregulation of the hypertrophic cartilage marker collagen X. hMwt HA added inside the fibrin gel

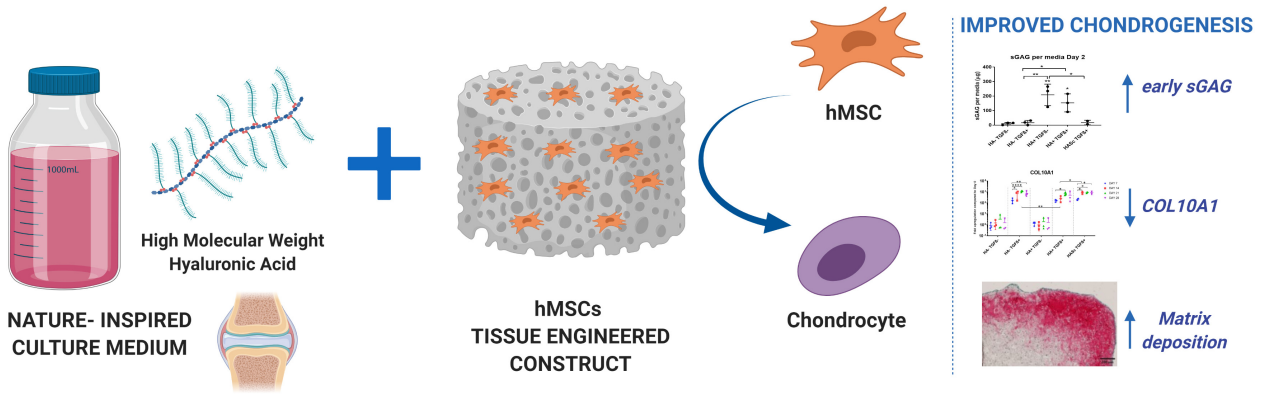

GRAPHICAL ABSTRACT | Bioengineered media model for hMSCs chondrogenic differentiation.

(HASc TGF+) led to the best matrix deposition. hMwt HA can be one key medium component in a more reliable *in vitro/ex vivo* system to reduce *in vitro* artifacts, enable more accurate pre-screening of potential cartilage repair therapies and reduce the need for animal studies.

Keywords: hyaluronic acid, mesenchymal stem cells, chondrogenic differentiation media, glycosaminoglycan, collagen X, hypertrophy, articular cartilage, synovial fluid

INTRODUCTION

Articular cartilage is a complex anisotropic tissue which consists of a superficial zone, middle zone, deep zone, and calcified zone. Each zone has a well-defined structure with characteristic collagen fiber organization and is mainly populated by the chondrocyte, which is responsible for extracellular matrix maintenance (Klein et al., 2009; Stoddart et al., 2009).

Articular cartilage covers the osseous ends of articulating diarthrosis also known as synovial joints and in this anatomical context is in contact with Synovial fluid.

The synovial fluid (SF) of healthy joints normally functions as a biological lubricant as well as a biochemical depot through which nutrients and regulatory cytokines are transported.

Synovial fluid which is derived from the ultrafiltration of the blood plasma and glycoproteins, is concentrated inside the joint by passing through the synovium, a fibrous, highly vascularized membrane whose internal layer macrophage-like synovial cells (type A) and type B synoviocytes resides.

High molecular weight hyaluronan (HA), is one of the major components of healthy SF that undergoes dynamic regulation during cartilage damage and inflammation. It plays an important role in the protection of opposing articular cartilage surfaces by improving joint lubrication, but is also involved in nutrient transport to the articular cartilage tissue, it has an excellent osmotic buffering property to maintain water homeostasis inside the joint, acts as pressure regulator and thanks to its gel-like structure, prevents tissue formation in the synovial space (McDonald and Levick, 1995; Laurent et al., 1996; Lynch et al., 1998).

Hyaluronan is composed of a repetitive sequence disaccharide unit which consist of 1,3-beta-D-N-acetylglucosamine and 1,4-beta-D-glucuronic acid and possess particular features that makes it a unique biopolymer (Jiang et al., 2006). It is produced by specific multipass transmembrane enzymes, the HA synthases 1–3, located on the inner surfaces of the plasma membranes (Weigel et al., 1997; Itano and Kimata, 2002; Kogan et al., 2007) and is continuously secreted into the joint and cleared with a half-life of 0.5–1 day in rabbit or sheep (Brown and Laurent, 1991; Fraser et al., 1993).

In healthy synovial fluid high molecular weight hyaluronan can achieve a molecular mass of 6–10 mega Dalton ($>10^6$ Dalton) but when inflammation or oxidative stress occurs, an accelerated HA degradation into smaller fragments has been observed (Noble, 2002; Jiang et al., 2011; Fakhari and Berkland, 2013). As such, the molecular weight of HA inside the SF is representative of the physio-pathological condition of the tissue. High molecular weight HA (10^5–10^7 Da) is protective for synovial joint and articular cartilage showing anti-inflammatory, anti-angiogenic properties, stimulation of chondrocyte proliferation and production of cartilage matrix and scavenging function against cellular debris and oxidizing systems (Laurent et al., 1996; Gigante and Callegari, 2011; Gallo et al., 2019). Conversely, low molecular weight HA is pro-inflammatory, pro-angiogenic and immune-stimulatory reflecting a tissue under stress as happen in rheumatoid/inflamed joints (Jiang et al., 2011; Gallo et al., 2019).

Due to its avascular nature, partial thickness defects or disease of articular cartilage cannot be easily accessed by stem cells. This condition associated with low metabolic activity,

make unsuccessful self-healing and repair (Hunziker, 2000; Huey et al., 2012).

Microfracture treatment of articular cartilage injury is the standard clinical practice to facilitate the access of mesenchymal stem cells (MSCs) that reside in the bone marrow cavity of the subchondral bone at the injured site, promoting cartilage regeneration (Steadman et al., 2001; Kang et al., 2008; Oussedik et al., 2015). These cells would be exposed to synovial fluid and the HA contained within.

Human mesenchymal stem cells derived from bone marrow (hBM MSCs) represent an attractive cell source for cartilage tissue engineering and regenerative medicines approaches, are the best described, the most advanced in clinical use and can differentiate in cartilage or bone (Wakitani et al., 2002; Parekkadan and Milwid, 2010; de Vries-van Melle et al., 2014). hBM MSCs can be easily harvested and isolated from bone marrow aspirates with limited donor site morbidity; in addition, following expansion BM MSCs maintain multilineage potential (Hegewald et al., 2004; Gardner et al., 2013). It has been shown that MSCs are able to repair both the subchondral bone and the overlying articular cartilage, and many studies describe how MSCs are useful in cartilage repair after injury or disease such as osteoarthritis (Wakitani et al., 1994; Wakitani et al., 2002).

One of the main problems associated with the chondrogenic differentiation of hBM MSCS *in vitro,* is that MSC-derived chondrocytes undergo hypertrophic differentiation that causes the neo-formed cartilage to undergo endochondral ossification (Johnstone et al., 1998).

HA has been extensively used as a polymer in scaffolds or hydrogel form, alone or in combination with MSCs to produce engineered cartilage with native tissue properties (Radice et al., 2000; Solchaga et al., 2000; Huerta-Ángeles et al., 2018; Li et al., 2018; Gallo et al., 2019).

Although it represents one of the most abundant macromolecules of the synovial fluid, it has not been extensively studied as media supplement to evaluate its effect on chondrogenesis.

Indeed, culture media currently used to induce chondrogenic differentiation of hMSCs are often simple in their composition and doesn't recapitulate the rheological and biological features of knee joint synovial fluid (Heng et al., 2004).

In this study, we hypothesize that a chondropermissive medium containing a physiological concentration (2 mg/ml) of exogenous high molecular weight HA 1.8 MDa (hMwt HA), both alone and in combination with TGFβ1, will enhance human MSC chondrogenesis in an MSC-based tissue engineered construct. This study also evaluated the possibility of supplementing a fibrin:polyurethane scaffold with 1 MDa hyaluronic acid to improve the quality of the fibrin gel-stem cell constructs for the same purpose above. A smaller molecular weight HA was used due to issues relating to handling and viscosity. Both sizes function as high molecular weight HA when considering their biological function.

Thus, our aim is to investigate the effect of hMwt HA supplemented in culture media, or inside the scaffold, on the chondrogenesis of hBM MSCs.

MATERIALS AND METHODS

Poly(Ester-Urethane) Scaffolds Preparation

Poly(ester-urethane) porous sponge (PU) were prepared by using hexamethylene diisocyanate, poly (1-caprolactone) diol and isosorbide diol (1,4: 3,6-dianhydro-D-sorbitol) via a salt leaching-phase inverse technique (Gorna and Gogolewski, 2002). By this procedure interconnected macroporosity ranging from 90 to 300 μm has been uniformly achieved within the sponge. The PU sponge was cut by water-jet (CUTEC AG, Basel, Switzerland) producing cylindrical scaffolds (8 mm diameter × 4 mm height) sterilized in a cold cycle at 37°C via ethylene oxide process and degassed under vacuum for 6 days before to usage.

Isolation of Human Bone Marrow Derived MSCs

Bone marrow was obtained with full ethical approval (KEK-ZH-NR: 2010–0444/0) and the written consent from patients undergoing routine operations due to bone fracture.

The MSCs were isolated from three different marrow aspirates (two female 1939 and 1992, one male 1958) using Ficoll density separation (Sigma-Aldrich, Buchs, Switzerland) (**Table 1**).

Mononuclear cells were collected from the interphase and the adherent cell fraction was seeded at a density of 50,000 cells/cm^2 and left to attach for 96 hrs in alpha minimum essential medium (αMEM) (Gibco, Carlsbad, CA, United States), 10% MSC tested fetal bovine serum (FBS) (Pan Biotech, Aidenbach, Germany), 5 ng/ml basic fibroblast growth factor (bFGF) (Peprotech, Rocky Hill, CN, United States) and 1% penicillin/streptomycin (Gibco). When the majority of colonies were confluent, the cells were passaged and seeded into fresh flasks at a cell density of 3,000 cells/cm^2. The chondrogenic potential of each donor was confirmed using standard techniques.

The hBMSCs isolated from each donor were used separately in three independent experiments.

Scaffold Seeding and Chondrogenic Differentiation

hMSCs at passage 3 were trypsinized, suspended in a 150 μl fibrinogen-thrombin-solution and evenly seeded at a cell density of 5 × 10^6 cells/150 μl in cylindrical (8 × 4 mm) macroporous polyurethane (PU) scaffolds. The constructs were fed with four different media for 28 days. Control medium was serum free basal medium containing DMEM high glucose, supplemented with 1% ITS+, 1% Pen/Strep, 1% non-essential

TABLE 1 | Legend of the donor details investigated under static conditions.

Donor	Age	Sex
1	79	Female
2	60	Male
3	26	Female

amino acid, 50 μg/ml ascorbate-2-phosphate, 5 μM ε-amino-caproic acid (EACA), 10^{-7} M dexamethasone (HA- TGFβ-). This media was further supplemented with 10 ng/mL TGF-β1 (HA- TGFβ+) or with 0.2% 1.8 MDa HA (HA+ TGFβ-) or with both (HA+ TGFβ+). When present, TGF-β1 was only added to the medium. Where mentioned above, the HA groups were supplemented with 1.8 MDa HA (*Stanford Chemicals*) to simulate the synovial fluid concentration under normal conditions (2.3 mg/ml) (Fam et al., 2007). In an additional group, 1 MDa HA (ALB Technology) was added at 0.02% directly into the PU scaffolds (HASc TGFβ+) fed with standard chondrogenic media (HA- TGFβ+).

The culture medium was changed every second day, and conditioned medium was collected for biochemical analysis.

Gene Expression Analysis: RNA Isolation, cDNA Synthesis, Real Time qPCR

After 7, 14, 21, and 28 days of chondrogenic culture, constructs were harvested, and total RNA was isolated using TRI Reagent (MRC, Cincinnati, OH/Molecular Research Centre Inc.). Total RNA was isolated at day 0 to assess basal gene expression levels.

TaqMan reverse transcription was then performed using 1 μg of total RNA sample, random hexamer primers and TaqMan reverse transcription reagents (Applied Biosystems, Carlsbad, CA, United States).

Real-time PCR was performed using the QuantStudio 6 Flex real-time PCR system (Applied Biosystems). A panel of human genes associated with chondrogenic markers (COL2A1, ACAN, Sox9), the hypertrophic marker COL10A1, osteogenic markers (RunX2; ALP; OC), the Hyaluronan receptor CD44, hyaluronan synthases (HAS1, HAS2, HAS3) and transforming growth factor receptors 1 and 2 (TGFβ-R1 and TGFβ-R2) were investigated.

Primers for RPLP0, COL2A1, COL10A1, ACAN, RunX2, and OC mRNA were synthesized by Microsynth AG (Balgach, Switzerland) (**Table 2**). Primers for Sox9, ALP, CD44, HAS1, HAS2, HAS3, TGFβ_RI, TGFβ_RII were purchased from Applied Biosystems (Warrington, United Kingdom) (**Table 3**).

Relative quantification of target mRNA was determined according to the comparative CT method with hRPLP0 as endogenous control. In addition, the level of gene expression for each gene was determined relative to day 0 monolayer via a ΔΔCT comparison.

TABLE 3 | Assays on demand used for qRT-PCR.

Gene	Assays on demand (ID)
Sox9	Hs00165814_m1
ALP	Hs00758162_m1
CD44	Hs01075861_m1
HAS1	Hs00987418_m1
HAS2	Hs00193435_m1
HAS3	Hs00193436_m1
TGFβ_RI	Hs00610320_m1
TGFβ_RII	Hs00234253_m1

Sox9, SRY (sex determining region Y)-box 9 cartilage transcription factor; ALP, alkaline phosphatase; CD44, hyaluronan receptor; HAS1, hyaluronan synthase 1; HAS2, hyaluronan synthase 2; HAS3, hyaluronan synthase 3; TGFβ_RI, transforming growth factor β1 Receptor 1; TGFβ_RII, transforming growth factor β1 Receptor 2.

Sulfated Glycosaminoglycans and DNA Quantification

After 28 days of culture, constructs were digested with 1ml proteinase K 0.5 mg/ml at 56°C for 16 h. Total DNA content was measured spectrofluorometrically following reaction with Bisbenzimide Hoechst 33258 dye (Polysciences Inc., Warrington, PA, United States) with purified calf thymus DNA as standard (Lubio Science, Luzern, Switzerland) (Labarca and Paigen, 1980).

Sulfated glycosaminoglycans (GAG) retained within the scaffolds was determined by a direct spectrophotometric microassay according to the dimethylmethylene blue dye method (Sigma-Aldrich, Buchs, Switzerland) at pH 1.5, using bovine chondroitin 4-sulfate sodium salt from bovine trachea (Fluka, St. Louis, MO, United States) (Farndale et al., 1986). Total GAG content of the culture media was also measured to assess the release of matrix molecules from the constructs. All samples containing hyaluronan were blanked with media containing 0.2% hyluronan and DMMB at pH 1.5 was used to eliminate the noisy signal due to the residual interaction between DMMB and Hyaluronan.

Histology and Staining

After 28 days of culture, the constructs were fixed in 70% methanol and 10 μm specimen sections were cut by cryostat, stained with Safranin O and counterstained with Fast Green

TABLE 2 | Human oligonucleotide primers and probes used for qRT-PCR.

Gene	Primer forward (5′–3′)	Primer reverse (5′–3′)	Probe (5′ FAM-3′ TAMRA)
COL2A1	5′-GGC AAT AGC AGG TTC ACG TAC A-3′	5′-GAT AAC AGT CTT GCC CCA CTT ACC-3′	5′-CCT GAA GGA TGG CTG CAC GAA ACA TAC-3′
COL10A1	5′-ACG CTG AAC GAT ACC AAA TG-3′	5′-TGC TAT ACC TTT ACT CTT TAT GGT GTA-3′	5′-ACT ACC CAA CAC CAA GAC ACA GTT CTT CAT TCC-3′
ACAN	5′-AGT CCT CAA GCC TCC TGT ACT CA-3′	5′-CGG GAA GTG GCG GTA ACA-3′	5′-CCG GAA TGG AAA CGT GAA TCA GAA TCA ACT-3′
RunX2	5′-AGC AAG GTT CAA CGA TCT GAG AT-3′	5′-TTT GTG AAG ACG GTT ATG GTC AA-3′	5′-TGA AAC TCT TGC CTC GTC CAC TCC G-3′
OC	5′-AAG AGA CCC AGG CGC TAC CT-3′	5′-AAC TCG TCA CAG TCC GGA TTG-3′	5′-ATG GCT GGG AGC CCC AGT CCC-3′
RPLP0	5′-TGG GCA AGA ACA CCA TGA TG-3′	5′-CGG ATA TGA GGC AGC AGT TTC-3′	5′-AGG GCA CCT GGA AAA CAA CCC AGC-3′

RPLP0, ribosomal protein large P0 housekeeping gene; COL2A1, collagen type 2; COL10A1, collagen type 10; ACAN, aggrecan; RunX2, runt-related transcription factor 2; OC, osteocalcin.

to detect proteoglycan presence and proteoglycan-depleted, collagen-rich areas.

Statistical Analysis

The data were produced from three individual experiments, each carried out with hMSC from a different donor. All experiments were performed in triplicate, quadruplicate or quintuplicates for each group at different timepoints in order to reduce methodological variability. Each measurement was performed in duplicate. Analyses were done between the appropriate control group and treatment groups as well as between different treatment groups, using one way or two ways ANOVA with Tukey's *Post-hoc* testing whenever required. A significance level of $p < 0.05$ was applied and data are presented as Mean and

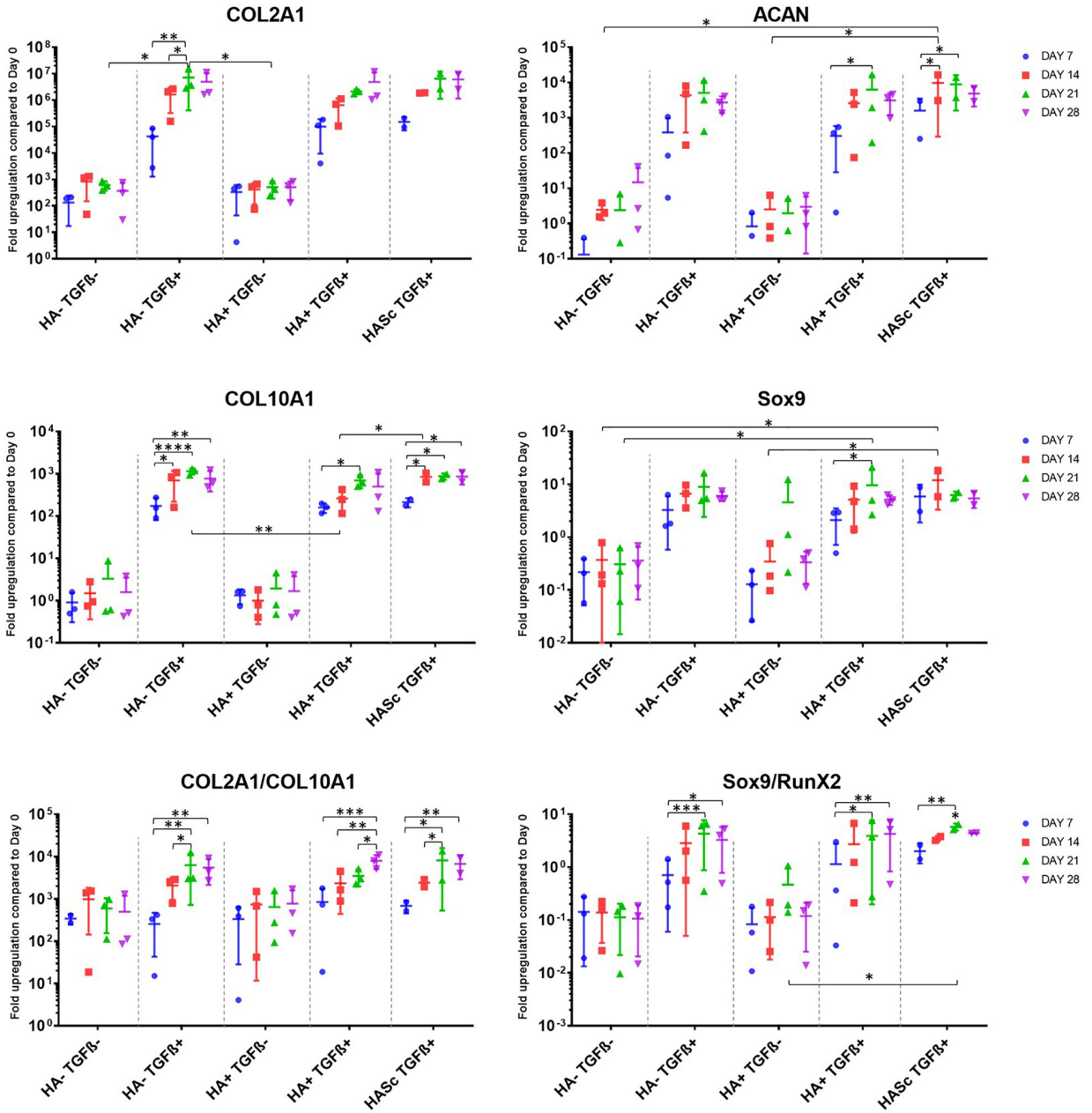

FIGURE 1 | Gene expression measured by qRT-PCR of chondrogenically differentiating hBMSCs-based constructs fed with standard chondropermissive media (HA-TGF-) supplemented with 0.2% sodium hyaluronate (HA+) or without (HA-) and with 10 ng/ml TGFβ1 (TGFβ+) or without (TGFβ-) and harvested at days 7, 14, 21, and 28. Sodium hyaluronate supplemented in media containing TGFβ1 (HA+ TGF+) supports the chondrogenic gene expression of ACAN and Sox9 and reduces the upregulation of the hypertrophic cartilage marker collagen type X. Relative quantification of target mRNA was performed according to the comparative Ct method. Values represent the mean ± SD of three independent hBMSC donors in experimental quadruplicate. Statistical significance was defined as $*p < 0.05$, $**p < 0.01$, $***p < 0.001$, and $****p < 0.0001$.

STDev. Analyses were carried out using the GraphPadPrism 7 software (GraphPad Software Inc., La Jolla, CA, United States).

RESULTS

Gene Expression Analysis

A panel of genes associated with chondrogenic differentiation (Collagen type II, Aggrecan, Sox9) were investigated, as well as Collagen type X associated with hMSCs hypertrophic differentiation, genes associated with osteogenic differentiation (RunX2, OC, ALP) and receptors of TGFβ1 (TGFβ_RI, TGFβ_RII) (**Figure 1**). To gain further understanding of the underlying mechanism, the hyaluronan receptor (CD44) and hyaluronan synthases (HAS1, HAS2, HAS3) were also investigated.

All donors displayed the same trends to a varying degree of magnitude. Among the chondrogenic markers, an overall upregulation of the genes involved in chondrogenic differentiation was observed when the culture media was supplemented with TGFβ1.

All media supplemented with TGFβ showed an overall collagen type II upregulation when compared with TGFβ-free media. The three media formulations containing TGFβ showed a similar profile in terms of expression levels and trend among the different timepoints analyzed. The hypertrophic marker Collagen type X was significantly upregulated from days 7 to 14, 21, and 28 in all the constructs fed with standard chondrogenic media (HA-TGFβ+) with a significant peak at day 21. However, when Hyaluronan is added to the culture media (HA+ TGF+) there is an overall reduction of collagen 10 upregulation at all timepoints. In the second and the last week of chondrogenesis there was no significant increase of collagen 10 compared with day 7. As with HA into the media (HA+ TGFβ+), HA inside the scaffold (HASc TGFβ+) also contributes to reducing the upregulation of the collagen 10 at days 21 and 28 when compared with standard chondrogenic media (HA-TGFβ+). However, the HASc TGF+ group showed a significantly higher Collagen 10 expression from days 7 to 14 compared with HA+ TGF+ group.

All TGFβ supplemented media showed a similar profile with a higher COL2A1/COL10A1 ratio compared with TGFβ depleted media. However, among the TGFβ1 supplemented media, only the group where HA was added (HA+ TGFβ+), showed a significant and progressive increase of the COL2/Col10 ratio from days 7, 14, and 21 to 28. Indeed, for HA depleted media (HA-TGF+), the ratio appears to reach a peak at day 21 although no further significant increase of the ratio was observed from days 21 to 28. When HA was added inside the scaffold (HASc TGF+ group) the COL2A1/COL10A1 ratio reached a peak at day 21 and significantly contributed to an increased ratio from days 7 to 28.

As observed for collagen type II, aggrecan upregulation was observed upon TGFβ supplementation. However, further addition of hyaluronan led to statistically significant increases (**Figure 1**). Only the groups where hyaluronan was present in the culture media (HA+ TGF+) or added inside the scaffold (HASc TGF+) showed a significant upregulation of aggrecan gene expression from days 7 to 21 in both groups and from day 7 to 14 in the HASc group.

The expression of ACAN at day 14 in HASc TGF+ group was significantly higher compared to the media TGFβ depleted at the same timepoint.

Sox9 expression in the three TGFβ-supplemented media was similar and higher than TGFβ-free media. However, only in groups containing HA do the differences become significant (**Figure 1**).

In the HASc TGF+ group Sox9 was upregulated earlier at day 14 when it reaches the peak.

The Sox9/Runx2 ratio behaved similarly to the COL2/10 ratio and showed an overall upregulation when the media is supplemented with TGFβ. Particularly, standard chondrogenic media (HA-TGFβ+) showed a significant increase of the ratio from days 7 to 21 and 28. HA supplemented chondrogenic media (HA+ TGF+), also significantly increased the Sox9/RunX2 ratio from days 7 to 21 and 28. In addition, the average value observed in HA+ TGF+ group at day 28, although not significantly different from day 21, showed a tendency to increase compared with day 21, contrary to that seen in the other two TGFβ supplemented groups.

HASc TGF+ group showed a similar profile of HA-TGF+ group with a significant increase of the ratio from days 7 to 21, but not from days 7 to 28.

TGFβRI and II appear to respond in the opposite way to TGFβ supplementation. When the media is TGFβ supplemented, the TGFβRI is more expressed compared with TGF free media groups. Contrarily TGFβRII appear to be slightly less expressed when media is supplemented with TGF compared to TGF free media groups. These observations did not reach significance so the data is not shown.

None of the osteogenic markers (RunX2, ALP, OC), were affected by TGFβ or HA supplementation (data not shown). The expression of HAS 1, 2, and 3 was also largely unaffected by media supplementation (data not shown). CD44 was slightly downregulated over time in all the groups. However, despite a similar trend, no significant downregulation was observed upon media supplementation (data not shown).

Sulfated Glycosaminoglycan and DNA Quantification

After 4 weeks in culture, no significant differences were observed in DNA content among different groups compared with the control (**Figure 2**). An overall significant increase in sulfated GAG per scaffold/DNA ratio was observed when the medium was supplemented with TGFβ. We also investigated the sGAG and DNA content. After 28 days of chondrogenesis the GAG/DNA ratio per scaffold (**Figure 2B**) showed a similar GAG deposition in all the media supplemented with TGFβ1, which was significantly higher if compared with the control media (HA-TGF-) and with the hMwt HA supplemented media (HA+ TGF-). However, as it has been shown that part of the sGAG produced within the polyurethane: fibrin scaffold used in this study, are released into the culture media (Wu et al., 2017), the sGAG/DNA ratio per scaffold does not

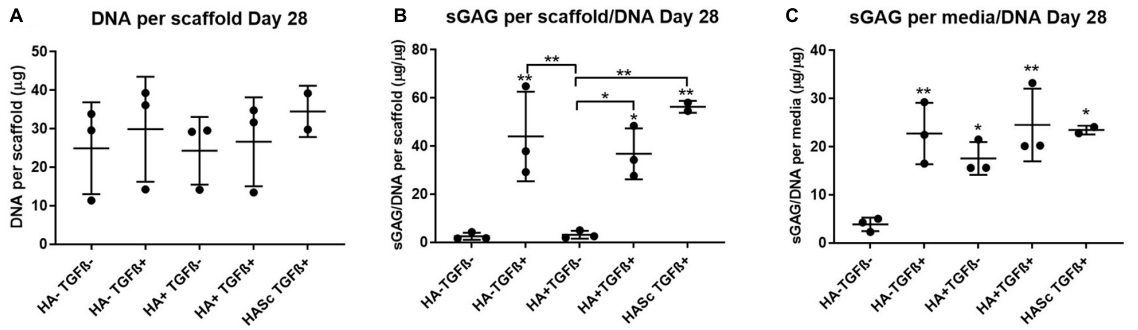

FIGURE 2 | Biochemical analysis of chondrogenically differentiated constructs after 4 weeks in culture shows a significantly higher GAG/DNA when hyaluronic acid is supplemented in culture media (HA+ TGF-). **(A)** Bisbenzimide Höchst 33528 dye was used to quantify the DNA in proteinase K digests of scaffolds. Dimethylmethylene blue (DMMB) at pH 1.5 was used to determine the total amount of sulfated glycosaminoglycan (GAG) produced by mesenchymal stem cells (MSCs). The GAG/DNA ratio was calculated from total DNA and GAG values to show the production of GAG relative to the MSCs present in each group from the proteinase K construct digests **(B)** and the collected culture media **(C)**. All culture media samples containing HA were blanked with media containing HA. Values represent the mean ± SD of three independent hBMSC donors in experimental triplicate or quadruplicate. Statistical significance was defined as $^{*}p < 0.05$, and $^{**}p < 0.01$.

reflect the total amount of sGAG produced by the hMSCs. For this reason, the sGAG/DNA per media was investigated and surprisingly the HA+ TGF- group free from the growth factor TGFβ1, produced significantly higher sGAG/DNA after 28 days of chondrogenesis when compared with the control media HA-TGF- (**Figure 2C**).

Media GAG showed an overall significant increase in all the experimental groups compared with the control group (HA-TGF-). Particularly, the HA supplemented chondropermissive media TGFβ free (HA+ TGF-), showed a significantly higher media GAG compared with the control group. Also, HA inside the constructs (HASTGF+) were significantly higher than the control.

With HA containing media (mainly HA+ TGF- and less markedly HA+ TGF+) a significant amount of sGAG was produced by the hMSCs and released into the culture media within the first week (**Figures 3**, **4**). Within the first week of chondrogenesis, the level of GAG in the media supplemented with HA alone (HA+ TGFβ-) was significantly and consistently higher among all three donors when compared with the control TGFβ free medium (HA-TGFβ-) and the standard chondrogenic media containing active TGFβ (HA- TGFβ+) ($^{**}p < 0.01$; $^{*}p < 0.05$) (**Figures 3**, **4**). Particularly, after 2 days of chondrogenic culture, the chondropermissive media supplemented with HA (HA+ TGF-) had significantly higher ($p < 0.01$) GAG release when compared with the standard chondropermissive media (HA-TGFβ-), with the standard chondrogenic media (HA-TGFβ+) ($p < 0.01$) and with the HASTGFβ+ group ($p < 0.05$). The sGAG/DNA of the HA+ TGF- group was comparable with all the other groups fed with TGFβ1 containing media.

At the same timepoint, the GAG level of the standard chondrogenic media HA-supplemented (HA+ TGFβ+) was also significantly higher compared to the control chondropermissive media (HA-TGFβ-) and to the chondrogenic media (HA-TGFβ+).

On day 4, HA+ TGFβ- continued to be significantly higher if compared to HA-TGFβ+ and by day 7, the average value of HA+ TGFβ- continued to be higher than HA-TGFβ+.

However, hyaluronan supplemented chondropermissive media (HA+ TGFβ-) continued to be significantly different from the chondropermissive media control (HA-TGFβ-) until day 18 of chondrogenic culture.

After 14 days of chondrogenesis, the GAG media content of the HA+ TGFβ+ group was greater than the HA+ TGFβ- group and it continued to increase over time until day 28.

By day 16, the GAG released by the HASTGFβ+ group slightly exceeded the average value of all other groups and at the same timepoint became significantly higher than the HA-TGFβ- group, continuing to increase until the end of chondrogenic culture.

Histology and Safranin O/Fast Green Staining

In order to show the deposition of sulfated GAGs, after 28 days of chondrogenesis the differentiated constructs were stained with Safranin O and counterstained with Fast green (**Figures 5A–N**). Positive Safranin O staining was present along the upper and lateral surface of the constructs when the media was supplemented with TGFβ alone (HA-TGF+) and with both factors (HA+ TGF+) with the exception of donor 1 where a slight Safranin O staining was observed only when the media was supplemented with both HA and TGFβ factors (HA+ TGF+).

Stronger positive staining was present in the same region of the constructs when hyaluronan was added directly into fibrin embedding the scaffolds fed with standard chondrogenic media (HASc TGFβ+ group). No staining was observed in the constructs fed with TGFβ1 free media.

DISCUSSION

Chondrogenic differentiation of mesenchymal stem/stromal cells is routinely evaluated using either monolayer, pellet culture

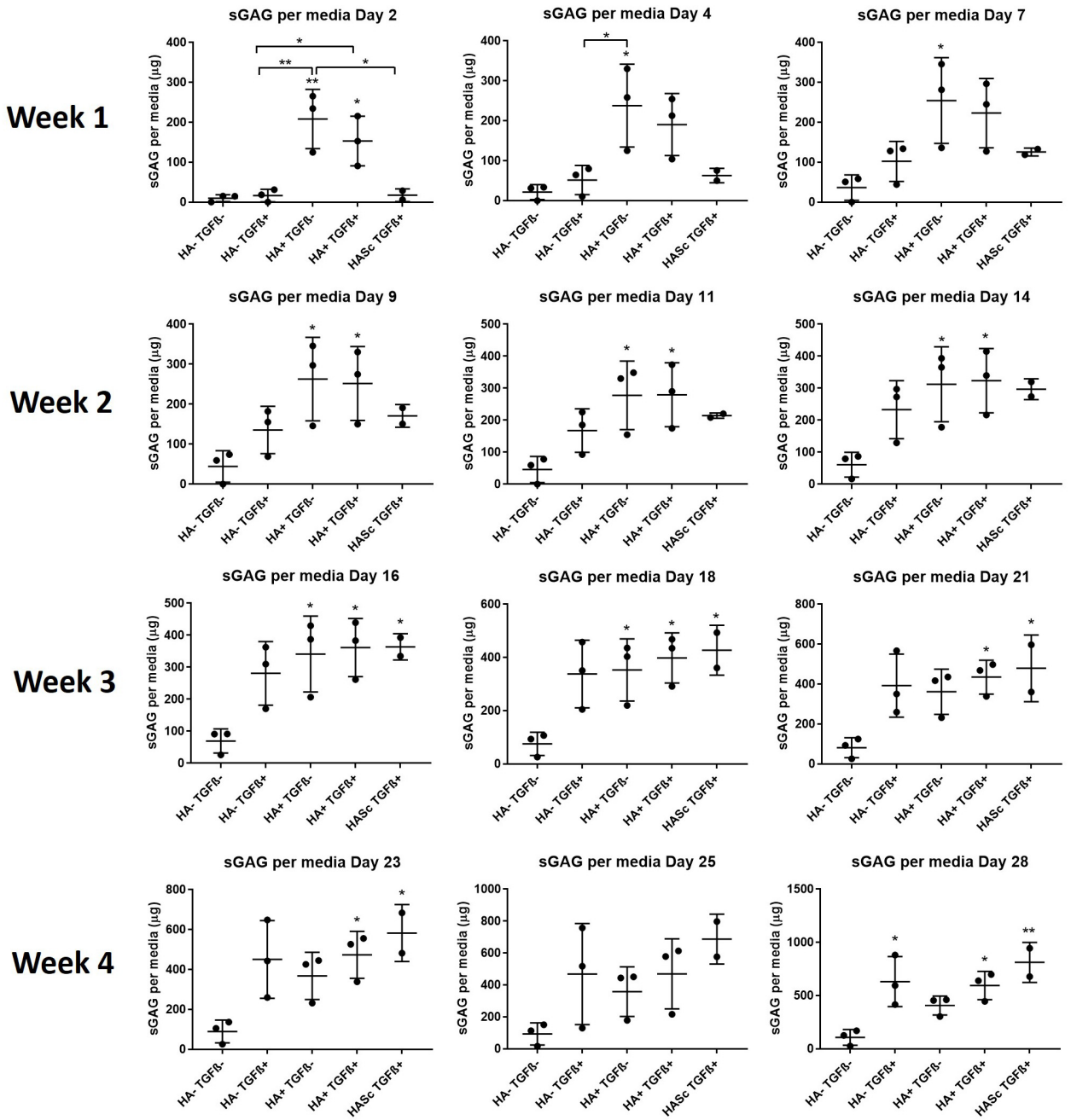

FIGURE 3 | GAG produced and released into culture media from chondrogenically differentiated hBMSC-based constructs over 4 weeks in culture. Chondropermissive medium supplemented with 0.2% sodium hyaluronate (HA+ TGF-) significantly increase sulfated GAG production detected in culture media in the early days of the hBMSC chondrogenesis in the absence of TGFβ. HA supplemented in standard chondrogenic media (HA+ TGF+) did also lead to significant increase in sulfated GAG. sGAG content in culture medium was determined spectrophotometrically following reaction with 1.9-dimethylmethylene blue (DMMB) pH 1.5. All samples containing HA were blanked with medium containing HA. Values represent the mean ± SD of three independent hBMSC donors in experimental quadruplicate or quintuplicate. Statistical significance was defined as $^{*}p < 0.05$, and $^{**}p < 0.01$.

in presence of TGFβ1, or three-dimensional fibrin matrices and insulin-like growth factor-1 (Johnstone et al., 1998; Yoo et al., 1998; Worster et al., 2000, 2001). Thus, most of the *in vitro* culture models to investigate cartilage repair therapies are highly simplified and critical *in vivo* signals that can potentially change the chondrogenic behavior of hBMSCs are lacking.

Particularly relevant *in vivo* functions come from synovial fluid, including acting as a shock absorber and friction reducer, supply of oxygen, nutrients and removal of metabolic waste and

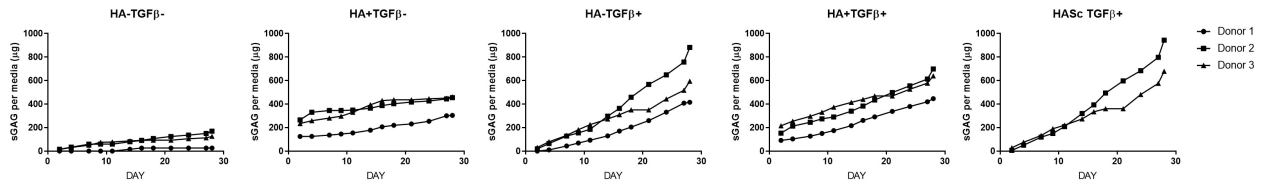

FIGURE 4 | Cumulative sGAG produced and released into culture media from chondrogenically differentiated hBMSC-based constructs along 4 weeks in culture.

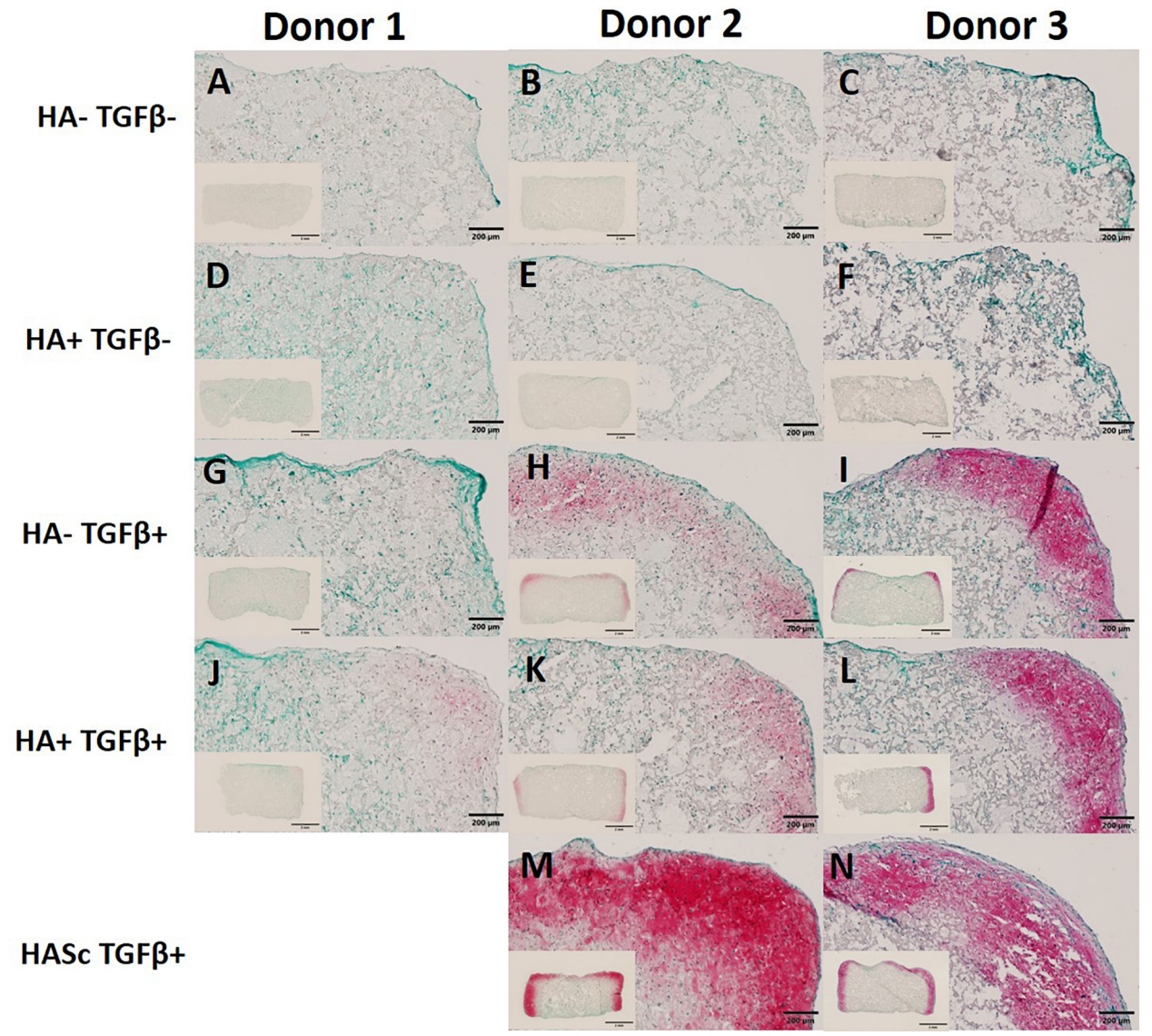

FIGURE 5 | Differentiated constructs stained with safranin O and counterstained with Fast Green after 4 weeks of chondrogenic culture. Images showing higher magnification of the right upper side and the full section of the constructs for three independent hBMSC donors. The HASc TGF+ group shows the best matrix deposition. Scale bar full section: 200 µm, scale bar overview images: 2 mm. Images **(A–C)** show the control group fed with chondropermissive media (HA-TGF–); Images **(D–F)** show the constructs fed with chondropermissive media supplemented with HA (HA+ TGF-); Images **(G–I)** show the constructs fed with chondrogenic media (HA-TGF+); Images **(J–L)** show the constructs fed with chondrogenic media supplemented with HA (HA+ TGF+); Images **(M,N)** show the constructs containing HA and fed with chondrogenic media (HASc TGF+).

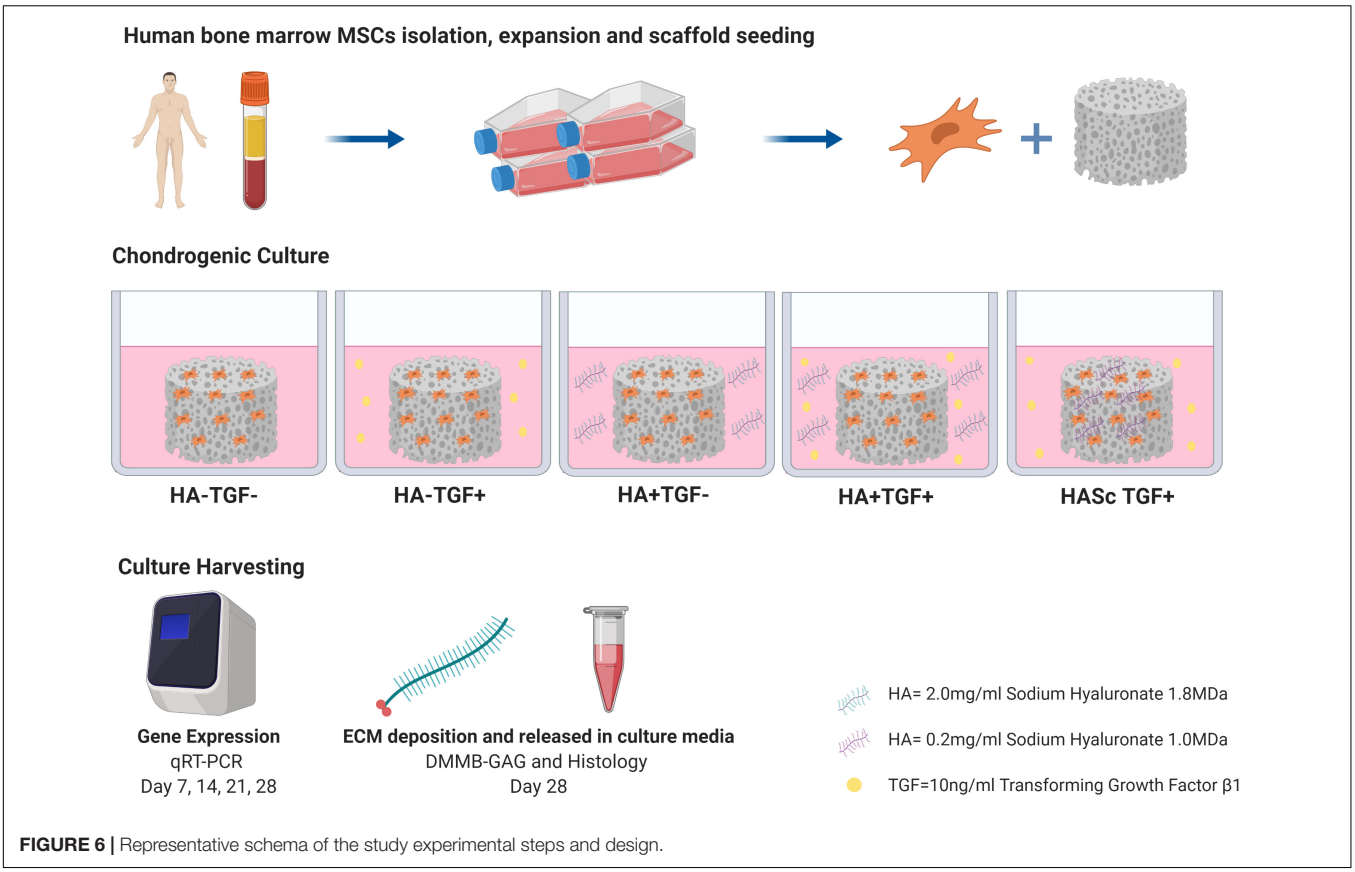

FIGURE 6 | Representative schema of the study experimental steps and design.

CO_2 from articular chondrocytes (Davies, 1966; Tamer, 2013). Some of these functions are reproduced in *in vitro* models by the cell culture media. However, synovial fluid is known to contain hMwt HA, which to date has been absent from the majority of culture media used in *in vitro* culture systems. This limits the efficacy and reliability of *in vitro* tests, placing a higher burden on *in vivo* models.

To be one step closer to synovial fluid composition, the present study investigated the effect of a chondrogenic media supplemented with a physiological concentration of exogenous hMwt HA, on the differentiation of hBMSCs in a 3D environment (**Figure 6**). In the present study a pharmaceutical grade HA was used with very low endotoxin contamination ($\leq$0.02 eu/mg or $\leq$0.05 eu/mg).

Our findings show that monolayer expanded hBMSCs when fed with chondropermissive media supplemented with hMwt HA alone or combined with TGFβ1 undergo, within 28 days, chondrogenic differentiation in 3D microporous polyurethane:fibrin culture system.

Particularly, upon the addition of hMwt HA to chondropermissive medium, we observed: (1) a reduced upregulation of the hypertrophic marker collagen type X, as well as a positive effect on Sox9 and ACAN gene expression level in culture media further supplemented with TGFβ1, (2) a significantly higher sGAG production and release in the culture media within the first week of chondrogenesis and especially in the first 48 h, (3) a more marked extracellular matrix deposition when hMwt HA was supplemented inside the scaffold, (4) consistent and reproducible trends in three different hMSC donors over 28 days of chondrogenic culture.

hMwt HA Reduces the Expression of Collagen Type X in TGFβ1 Containing Media

Several studies proposed a beneficial effect of hMwt HA in tissue repair following injury or inflammation and the potential role of hyaluronic acid on the differentiation of hMSCs (Shinomura and Kimata, 1990; Jiang et al., 2007; Salamanna et al., 2019). Hypertrophy is one of the main problems related with MSC differentiation in exogenous TGF-β containing media (Johnstone et al., 1998; Goldring et al., 2006). As a result, new protocols to prevent hypertrophy need to be developed to address a stable chondrogenic phenotype, which will help to enable the use of MSCs in clinics. Exogenous hyaluronan, in combination with anti-inflammatory signals, has been shown to act as disease modifying drugs following intra articular delivery with anti-hypertrophic and pro-chondrogenic effects (Prasadam et al., 2013). Similar results were observed when hyaluronic acid was added in a composite 3D collagen gel to address *in vitro* chondrogenesis of human adipose-derived mesenchymal stem cells in co-culture with human chondrocytes. The reduced upregulation of collagen type X appeared to be dose dependent with the best collagen type X reduction at 5%

HA (Amann et al., 2017). A reduction of peri-chondrocyte type X collagen was also observed following intraarticular injection of allogeneic MSCs in combination with hyaluronic acid in rabbits (Chiang et al., 2016). The present study confirms the previous findings since the addition of hMwt HA to the chondrogenic media containing TGFβ1 (HA+ TGF+) reproducibly reduced the upregulation of the hypertrophic marker collagen X after 28 days of chondrogenesis. HA inside the scaffold (HASc TGF+) also contributed to reducing the upregulation of collagen type X compared with HA-TGF+, but less markedly than hyaluronic acid supplemented media (HA+ TGF+).

In addition to the reduced upregulation of collagen type X, previous studies have shown an enhanced expression of the chondrogenic markers Sox9 and aggrecan when hMSCs were cultured on hyaluronic acid-coated dishes and the media was supplemented with TGFβ3 (Bhang et al., 2011). The enhanced chondrogenic differentiation of hMSCs due to the interactions with both a specific cell-adhesion matrix as hyaluronic acid and a soluble growth factor as TGFβ3 was shown to be additive (Bhang et al., 2011). The beneficial effect of hyaluronic acid on the upregulation of Sox9 expression was also highlighted in another study conducted by Amann et al. using 1% hyaluronic acid in a 3D collagen hydrogel (Wu et al., 2010; Amann et al., 2017). In the present work we also observed a beneficial effect of the hMwt HA in combination with TGFβ1, on the expression of human chondrogenic markers Sox9 and ACAN. Particularly we observed a statistically significant improvement of the expression level of both genes between days 7 and 21 in media supplemented with both TGFβ1 and hyaluronic acid. HA inside the scaffold significantly upregulated ACAN but did not contribute to a significant upregulation of Sox9 and collagen II, showing a similar profile to the other TGFβ containing media groups.

Upon the addition of hMwt HA, we did not observe a significant upregulation of collagen type II. However, the collagen type II/X mRNA ratio, a chondrocyte differentiation marker, was significantly upregulated over 28 days. A similar upregulation was also present for the HA-TGF+ group but in this case no significant upregulation was observed between days 21 and 28 due to a peak at day 21. This peak was always present for collagen type II, X, and II/X ratio in the HA-TGF+ group. The addition of HA in the culture media appears to attenuate this peak and this attenuation was particularly evident for collagen type X and the II/X ratio. This attenuation could be beneficial for the reduction of unwanted hMSC hypertrophy, which in the standard culture media (HA-TGF+) seems to be particularly pronounced at day 21.

In the present study, CD44 (a cell surface HA receptor; Aruffo et al., 1990) gene expression was unaffected suggesting the possible absence of interaction between exogenous HA and the receptor. This lack of interaction could be due to the high molecular weight of HA used in the present study (1,000 and 1,800 KDa). Several studies reports that low molecular weight fragments (50 KDa) derived from HA degradation bind and activate CD44 receptors during inflammation, promoting cytokine expression (Campo et al., 2009, 2012). However, high molecular weight HA (1,000–7,000 KDa) does not bind CD44 and therefore, does not activate biochemical mediators of damage (Campo et al., 2009; Avenoso et al., 2018). Thus, the lack of upregulation of CD44 indirectly suggests that the hMwt HA did not degrade over time.

hMwt HA-Supplemented Media Induces a Significant Increase of Early sGAG Synthesis

Chondrocytes embedded in a collagen gel, showed an enhanced sGAG synthesis as well as chondrocyte proliferation after treatment with 0.1 mg/ml 800 KDa HA (Kawasaki et al., 1999).

Akmal et al. (2005) partly confirmed the results of the previous study and showed that HA supplemented culture media in the range between 0.1 and 1 mg/ml enhanced chondrocyte metabolic activity and DNA synthesis, facilitating the deposition of GAG in cartilage tissue between days 9 and 14. Amann et al. (2017) found a significant increase in sGAG production by adipose mesenchymal stem cells seeded in a collagen gel supplemented with different concentrations of HA, with the best GAG/DNA ratio observed with 1% 1.5–1.8 MDa HA. Wu et al. (2017) supplemented the culture media with different concentrations of 1.8 MDa HA and, differently from the previous studies, observed that 2 mg/ml promoted a better preservation of chondrocyte phenotype under joint-kinematic-mimicking treatment especially in terms of collagen type II/I ratio.

None of the studies described above investigated the effect of continuous exposure to hMwt HA supplemented culture media on the chondrogenic differentiation behavior of human bone marrow derived MSCs over 28 days. This could also explain why, in the present work, under static conditions we observed an improvement of the chondrogenic phenotype and an attenuation of the hMSC hypertrophic differentiation following a longer and more constant exposure of the developing constructs to hMwt HA.

In the present work two different types of hyaluronic acid were used: a 1,800 kDa HA was supplemented at 2 mg/ml in the culture media and 1,000 kDa HA was added inside the fibrin gel at 0.2 mg/ml. 1,800 kDa is closer to the size found in synovial fluid, whereas 1,000 kDa was used in the scaffold due to its ease of handling and mixing with the fibrin. Differently from the previous work, in our study we didn't observe proliferation since the hMSCs DNA content did not increase from days 0 to 28 following the addition of hMwt HA. This might suggest that hMSCs seeded in the polyurethane:fibrin composite were more committed toward chondrogenic differentiation rather than proliferation and hMwt HA did not affect this behavior. It is also necessary to consider that the studies previously described used mainly chondrocytes and not MSCs. Thus, we can assume that the commitment level of the cell type affects the response to hyaluronic acid and based on previous studies, chondrocytes are more inclined to proliferation than MSCs which, in our study, appeared to be more prone to differentiation with the proper stimuli.

The reasons for the early GAG production and release into the media are unclear but previous studies have shown that hyaluronic acid promoted a chondroprotective effect following intra articular injection *in vivo,* with an increase of the

endogenous proteoglycan and glycosaminoglycan synthesis and a suppression of the degradation (Kobayashi et al., 2004; Altman et al., 2015). HA promoted the mobilization of the newly synthesized proteoglycan from the pericellular matrix to the interterritorial cartilage matrix, providing protection against degradation and contributing to the strengthening of the interterritorial cartilage matrix (Kikuchi et al., 2001; Altman et al., 2015). This mobilization could have happened also in our system but due to the early sGAG production, we could hypothesize that there is insufficient pericellular ECM to be able to retain the newly produced ECM causing its release into the media.

The early GAG production might also be explained by another interesting phenomena: macromolecular crowding. Macromolecular crowding (MMC), a biophysical phenomenon known to accelerate *in vitro* biological processes, accelerate and increases ECM deposition (Minton, 2001; Kumar et al., 2015; Shendi et al., 2019). The crowded environment is achieved by supplementation of the culture media with a synthetic or natural macromolecule (Kumar et al., 2015). Thanks to the excluded volume effect exerted by the macromolecule, the culture media better recapitulates the crowded physiological *in vivo* environment and this is the reason of the *in vitro* acceleration of biological processes as ECM deposition (Kumar et al., 2015; Prewitz et al., 2015). Previous studies suggested that MMC can enhance GAG deposition during hMSC differentiation (Welter et al., 2009; Prewitz et al., 2015) and have shown culture media supplemented with 0.2% 1.8 MDa hyaluronic acid acts as macromolecular crowding agent (Zhou et al., 2008; Shendi et al., 2019). Therefore, the early sGAG production observed within the first week of chondrogenesis and particularly within the first 48 h of culture, could be explained by a potential macromolecular crowding effect exerted by hyaluronic acid supplemented in culture media. However, we did not observe an increased expression of collagen type I, II, III, or aggrecan.

hMwt HA in Fibrin Gel Enhances the ECM Deposition

Histological analysis of ECM deposition provided evidence of positive Safranin O staining when the media was supplemented with TGFβ1. Addition of HA in the culture media slightly improved the ECM deposition. However, when HA was added inside the scaffold a stronger ECM deposition was observed. Simple mixing of HA to a fibrin composite as performed here would be a clinically applicable carrier gel that could be used to deliver MSCs locally into a cartilage defect. Our results indicate this would be beneficial when considering matrix deposition.

In a previous study it was observed that HA inside a hydrogel might affect cell behavior as it reduces oxygen concentration (Amann et al., 2017). Several studies suggest that low oxygen is favorable for chondrocyte phenotype maintenance and could be used as stimulus for hMSC chondrogenic differentiation (Buckley et al., 2010; Sheehy et al., 2012).

Exogenous hyaluronic acid injected into rabbit knee joints was incorporated into articular cartilage (Antonas et al., 1973). This incorporation could happen also over time in our system when the differentiating hMSCs are in contact with exogenous HA supplemented directly in the fibrin gel or in the culture media. HA supplemented in media or in the fibrin gel might facilitate the accumulation of extracellular matrix since HA is one of the main components, thus explaining the better extracellular matrix deposition in HASc TGF+ group.

In addition, the gene expression results of Sox9, ACAN and collagen type 10, the sGAG deposition and the histological analysis, suggests that the location of hyaluronic acid might play a role on the chondrogenic response of hMSCs seeded inside a 3D scaffold.

Despite mesenchymal stem cells holding great promise for the treatment of orthopedic injury and disease, donor variation during chondrogenic differentiation has severely hindered their clinical use (Kim et al., 2018). Donor variation makes interpretation of the results more difficult and often, when statistical analysis is performed on several donors, some useful results can be hidden. In these cases, it is better to aim at personalized medicine and to study the behavior of individual donors.

In the present study, despite the small donor variation observed, the trends of gene expression analysis, sGAG production and deposition, and histological analysis was consistent, reliable and reproducible among three different human mesenchymal stem cell donors.

CLINICAL SIGNIFICANCE AND POTENTIAL APPLICATIONS

In vitro models aim to recapitulate the complexity of *in vivo* systems. Most of the work on chondrogenic differentiation of hMSCs use a culture media with a very simple composition which is an oversimplification of the *in vivo* system. In order to mimic more closely the *in vivo* physiology, current models need to be improved to reflect the complexity of the synovial joint environment and to try to more accurately predict *in vivo* outcomes. In the current climate of animal welfare and "3Rs," more accurate *in vitro* models will be crucial to prevent *in vitro* artifacts and to enable more accurate prescreening of potential cartilage repair therapies. Producing reliable results *in vitro* that are more representative of the *in vivo* outcome, will also help to reduce the need for animal studies. Therefore, in addition to the standard approaches that aim to engineer cartilage tissue, it is worth to pursue the bioengineering of a more complex culture media. In addition, the association of HA media with human mesenchymal stem cells and fibrin gel, which is currently used in clinical practice, makes the whole system more relevant for clinics. HA supplemented media, being one step closer to the synovial fluid, can be used to make preclinical testing systems more predictable of clinics for several applications:

(1) to screen and evaluate potential cartilage and osteochondral repair therapies which involves the use of human MSCs (differentiating cartilage) or human chondrocytes (mature cartilage) in *in vitro* models or *ex vivo* systems simulating traumatic defects or diseases,

(2) to screen new biomaterials designed for tissue engineering and clinical application purposes,
(3) to screen new drug candidates for cartilage regeneration and osteochondral repair,
(4) to study the behavior of autologous or allogeneic human stem cell for intra articular joint injection in 2D/3D *in vitro* environments,
(5) to potentially increase the clinical effectiveness of tissue engineered constructs developed in a more synovial fluid-like environment.

CONCLUSION AND PERSPECTIVES

Overall, our results demonstrate that the constant supplementation of 1.8 MDa hMwt HA at 2 mg/ml to the culture media or the addition of 1 MDa hMwt HA into the scaffolds at 0.2 mg/ml, had a positive effect on the intrinsic capacity of hMSCs to produce ECM. Increased sGAG production occurred especially in the early days of chondrogenesis when the hMwt HA was supplemented in culture media; while a better matrix deposition was observed when hMwt HA was added in the scaffold. Considering all the evidence mentioned above, further studies are ongoing to investigate the composition of the ECM released into the culture media and deposited inside the constructs.

First it would be interesting to understand the underlying mechanism by which the addition of HA into the media leads to an increased early production and why this effect decreases with time in culture. Finding these answers would allow a better understanding how to prevent the release of the sGAG and this would help to rapidly establish an initial ECM pericellular matrix. This would function as an improved baseline to assist in the effective deposition of further ECM that might contribute to a final improved/stronger ECM quality and quantity.

Eventually, physicochemical culture media factors that affect the cellular response and matrix deposition, such as viscosity (Laurent and Ogston, 1963; Laurent, 1995), osmolality (Laurent and Ogston, 1963; Urban et al., 1993; Palmer et al., 2001), diffusion properties (Hansen et al., 2016), and the potential interaction between HA and other molecules in the culture media (Kuznetsova et al., 2015), should be further investigated.

At the gene expression level, exogenous hMwt HA reduced the upregulation of the hypertrophic cartilage marker collagen type X. Therefore, a more stable hMSC chondrogenic differentiation can also be achieved through the development of a more physiological synovial-like bioengineered culture media. The bioengineered media might also reproduce *in vitro* another important function exerted by hMwt HA *in vivo*, namely its function as a shock absorber and friction reducer during dynamic loading. It is an ideal lubricant in the synovial joints due to its shear-dependent viscosity (Laurent et al., 1996; Morgese et al., 2018). Sliding motion and dynamic compression induces hMSCs chondrogenesis (Schatti et al., 2011) and joint-kinematic-mimicking mechanical loading combined with HA media improves matrix production in a bovine chondrocyte cartilage engineered model (Wu et al., 2017). In addition, specific stimuli mimicking human articular joint kinematics may promote the development of a functional articular surface–synovial interface (Grad et al., 2005). For these reasons it will be of high interest to perform additional studies in this direction to further increase the complexity by including mechanical stimuli typically experienced within articular joints. This will be possible thanks to our joint-simulating bioreactor that mimics the knee joint kinematics (Wimmer et al., 2004; Schatti et al., 2011). Thus, future work will include long-term loading experiments over several weeks to investigate if the lubricating capability of HA supplemented media can act synergistically with joint kinematic motion to address the chondrogenic differentiation behavior of hMSCs. This study will be useful on experimental level to improve our understanding of the homeostasis mechanisms of articulating joints and on a clinical level might serve as baseline to improve knee joint rehabilitation protocols after trauma or disease.

DATA AVAILABILITY STATEMENT

All relevant datasets generated for this study are included in the article.

ETHICS STATEMENT

The studies involving human participants were reviewed and approved by the Cantonal Ethics Commission, University of Zurich, Zurich (Ethics Commission reference number KEK ZH Nr 2010-0444/0). The patients provided their written informed consent to participate in this study.

AUTHOR CONTRIBUTIONS

GM designed and performed the experiments, analyzed the data, and wrote the manuscript. GM and MS reviewed and edited the manuscript. MS and MA worked on funding acquisition. MS, MA, and AE supervised the whole work. All authors reviewed the results and approved the final version of the manuscript.

FUNDING

This research was funded by AO Foundation, Switzerland.

ACKNOWLEDGMENTS

We thank David Eglin (AO Research Institute Davos) for producing the polyurethane scaffolds.

REFERENCES

Akmal, M., Singh, A., Anand, A., Kesani, A., Aslam, N., Goodship, A., et al. (2005). The effects of hyaluronic acid on articular chondrocytes. *Bone Joint J.* 87, 1143–1149.

Altman, R. D., Manjoo, A., Fierlinger, A., Niazi, F., and Nicholls, M. (2015). The mechanism of action for hyaluronic acid treatment in the osteoarthritic knee: a systematic review. *BMC Musculoskel. Disord.* 16:321. doi: 10.1186/s12891-015-0775-z

Amann, E., Wolff, P., Breel, E., van Griensven, M., and Balmayor, E. R. (2017). Hyaluronic acid facilitates chondrogenesis and matrix deposition of human adipose derived mesenchymal stem cells and human chondrocytes co-cultures. *Acta Biomater.* 52, 130–144. doi: 10.1016/j.actbio.2017.01.064

Antonas, K., Fraser, J., and Muirden, K. (1973). Distribution of biologically labelled radioactive hyaluronic acid injected into joints. *Ann. Rheum. Dis.* 32:103. doi: 10.1136/ard.32.2.103

Aruffo, I., Stamenkovic, M. Melnick, Underhill, C. B., and Seed, B. (1990). CD44 is the principal cell surface receptor for hyaluronate. *Cell* 61, 1303–1313. doi: 10.1016/0092-8674(90)90694-a

Avenoso, A., D'Ascola, M., Scuruchi, G. M., Calatroni, A., Saitta, A., Campo, S., et al. (2018). Hyaluronan in the experimental injury of the cartilage: biochemical action and protective effects. *Inflamm. Res.* 67, 5–20. doi: 10.1007/s00011-017-1084-9

Bhang, S. H., Jeon, J. Y., La, W. G., Seong, J. Y., Hwang, J. W., Ryu, S. E., et al. (2011). Enhanced chondrogenic marker expression of human mesenchymal stem cells by interaction with both TGF-β3 and hyaluronic acid. *Biotechnol. Appl. Biochem.* 58, 271–276. doi: 10.1002/bab.39

Brown, T., and Laurent, U. (1991). Turnover of hyaluronan in synovial joints: elimination of labelled hyaluronan from the knee joint of the rabbit. *Exp. Physiol.* 76, 125–134. doi: 10.1113/expphysiol.1991.sp003474

Buckley, C. T., Vinardell, T., and Kelly, D. J. (2010). Oxygen tension differentially regulates the functional properties of cartilaginous tissues engineered from infrapatellar fat pad derived MSCs and articular chondrocytes. *Osteoarthrit. Cartil.* 18, 1345–1354. doi: 10.1016/j.joca.2010.07.004

Campo, G. M., Avenoso, A., Campo, S., D'Ascola, A., Traina, P., and Calatroni, A. (2009). Differential effect of molecular size HA in mouse chondrocytes stimulated with PMA. *Biochim. Biophys. Acta Gen.Subj.* 1790, 1353–1367. doi: 10.1016/j.bbagen.2009.07.003

Campo, G. M., Avenoso, A., D'Ascola, A., Scuruchi, M., Prestipino, V., Calatroni, A., et al. (2012). Hyaluronan in part mediates IL-1beta-induced inflammation in mouse chondrocytes by up-regulating CD44 receptors. *Gene* 494, 24–35. doi: 10.1016/j.gene.2011.11.064

Chiang, E.-R., Ma, H.-L., Wang, J.-P., Liu, C.-L., Chen, T.-H., and Hung, S.-C. (2016). Allogeneic mesenchymal stem cells in combination with hyaluronic acid for the treatment of osteoarthritis in rabbits. *PLoS One* 11:e0149835. doi: 10.1371/journal.pone.0149835

Davies, D. (1966). "Paper 7: properties of synovial fluid," in *Proceedings of the Institution of Mechanical Engineers, Conference Proceedings*, (London: SAGE Publications), 25–29. doi: 10.1243/pime_conf_1966_181_203_02

de Vries-van Melle, M. L., Tihaya, M. S., Kops, N., Koevoet, W., Murphy, J. M., Verhaar, J., et al. (2014). Chondrogenic differentiation of human bone marrow-derived mesenchymal stem cells in a simulated osteochondral environment is hydrogel dependent. *Eur. Cell Mater.* 27, 112–123. doi: 10.22203/ecm.v027a09

Fakhari, A., and Berkland, C. (2013). Applications and emerging trends of hyaluronic acid in tissue engineering, as a dermal filler and in osteoarthritis treatment. *Acta Biomater.* 9, 7081–7092. doi: 10.1016/j.actbio.2013.03.005

Fam, H., Bryant, J., and Kontopoulou, M. (2007). Rheological properties of synovial fluids. *Biorheology* 44, 59–74.

Farndale, R. W., Buttle, D. J., and Barrett, A. J. (1986). Improved quantitation and discrimination of sulphated glycosaminoglycans by use of dimethylmethylene blue. *Biochim. Biophys. Acta* 883, 173–177. doi: 10.1016/0304-4165(86)90306-5

Fraser, J. R. E., Kimpton, W. G., Pierscionek, B. K., and Cahill, R. N. (1993). *The Kinetics Of Hyaluronan In Normal And Acutely Inflamed Synovial Joints: Observations With Experimental Arthritis In Sheep, Seminars In Arthritis And Rheumatism*. Amsterdam: Elsevier, 9–17.

Gallo, N., Nasser, H., Salvatore, L., Natali, M. L., Campa, L., Mahmoud, M., et al. (2019). Hyaluronic acid for advanced therapies: promises and challenges. *Eur. Polymer J.* 177, 134–147. doi: 10.1016/j.eurpolymj.2019.05.007

Gardner, O., Archer, C. W., Alini, M., and Stoddart, M. J. (2013). Chondrogenesis of mesenchymal stem cells for cartilage tissue engineering. *Histol. Histopathol.* 28, 23–42. doi: 10.14670/HH-28.23

Gigante, A., and Callegari, L. (2011). The role of intra-articular hyaluronan (Sinovial®) in the treatment of osteoarthritis. *Rheumatol. Intern.* 31, 427–444. doi: 10.1007/s00296-010-1660-6

Goldring, M. B., Tsuchimochi, K., and Ijiri, K. (2006). The control of chondrogenesis. *J. Cell. Biochem.* 97, 33–44. doi: 10.1002/jcb.20652

Gorna, K., and Gogolewski, S. (2002). In vitro degradation of novel medical biodegradable aliphatic polyurethanes based on ε-caprolactone and Pluronics® with various hydrophilicities. *Polym. Degrad. Stab.* 75, 113–122. doi: 10.1016/s0141-3910(01)00210-5

Grad, S., Lee, C. R., Gorna, K., Gogolewski, S., Wimmer, M. A., and Alini, M. (2005). Surface motion upregulates superficial zone protein and hyaluronan production in chondrocyte-seeded three-dimensional scaffolds. *Tissue Eng.* 11, 249–256. doi: 10.1089/ten.2005.11.249

Hansen, M. M., Meijer, L. H., Spruijt, E., Maas, R. J., Rosquelles, M. V., Groen, J., et al. (2016). Macromolecular crowding creates heterogeneous environments of gene expression in picolitre droplets. *Nat. Nanotechnol.* 11:191. doi: 10.1038/nnano.2015.243

Hegewald, J., Ringe, J., Bartel, I., Krüger, M., Notter, D., Barnewitz, C., et al. (2004). Hyaluronic acid and autologous synovial fluid induce chondrogenic differentiation of equine mesenchymal stem cells: a preliminary study. *Tissue Cell* 36, 431–438. doi: 10.1016/j.tice.2004.07.003

Heng, B. C., Cao, T., and Lee, E. H. (2004). Directing stem cell differentiation into the chondrogenic lineage in vitro. *Stem Cells* 22, 1152–1167. doi: 10.1634/stemcells.2004-0062

Huerta-Ángeles, G., Nešporová, K., Ambrožová, G., Kubala, L., and Velebnı, V. (2018). An effective translation: the development of hyaluronan-based medical products from the physicochemical, and preclinical aspects. *Front. Bioeng. Biotechnol.* 6:62. doi: 10.3389/fbioe.2018.00062

Huey, D. J., Hu, J. C., and Athanasiou, K. A. (2012). Unlike bone, cartilage regeneration remains elusive. *Science* 338, 917–921. doi: 10.1126/science.1222454

Hunziker, E. B. (2000). Articular cartilage repair: problems and perspectives. *Biorheol. Oxford* 37, 163–164.

Itano, N., and Kimata, K. (2002). Mammalian hyaluronan synthases. *IUBMB Life* 54, 195–199.

Jiang, D., Liang, J., and Noble, P. W. (2007). Hyaluronan in tissue injury and repair. *Annu. Rev. Cell Dev. Biol.* 23, 435–461. doi: 10.1146/annurev.cellbio.23.090506.123337

Jiang, D., Liang, J., and Noble, P. W. (2011). Hyaluronan as an immune regulator in human diseases. *Physiol. Rev.* 91, 221–264. doi: 10.1152/physrev.00052.2009

Jiang, D., Liang, J., Li, Y., and Noble, P. W. (2006). The role of Toll-like receptors in non-infectious lung injury. *Cell Res.* 16:693. doi: 10.1038/sj.cr.7310085

Johnstone, B., Hering, T. M., Caplan, A. I., Goldberg, V. M., and Yoo, J. U. (1998). In vitrochondrogenesis of bone marrow-derived mesenchymal progenitor cells. *Exp. Cell Res.* 238, 265–272. doi: 10.1006/excr.1997.3858

Kang, S.-W., Bada, L. P., Kang, C.-S., Lee, J.-S., Kim, C.-H., Park, J.-H., et al. (2008). Articular cartilage regeneration with microfracture and hyaluronic acid. *Biotechnol. Lett.* 30, 435–439. doi: 10.1007/s10529-007-9576-2

Kawasaki, K., Ochi, M., Uchio, Y., Adachi, N., and Matsusaki, M. (1999). Hyaluronic acid enhances proliferation and chondroitin sulfate synthesis in cultured chondrocytes embedded in collagen gels. *J. Cell. Physiol.* 179, 142–148. doi: 10.1002/(sici)1097-4652(199905)179:2<142::aid-jcp4>3.0.co;2-q

Kikuchi, T., Yamada, H., and Fujikawa, K. (2001). Effects of high molecular weight hyaluronan on the distribution and movement of proteoglycan around chondrocytes cultured in alginate beads. *Osteoarthrit. Cartil.* 9, 351–356. doi: 10.1053/joca.2000.0395

Kim, M., Erickson, I. E., Huang, A. H., Garrity, S. T., Mauck, R. L., and Steinberg, D. R. (2018). Donor variation and optimization of human mesenchymal stem cell chondrogenesis in hyaluronic acid. *Tissue Eng. Part A* 24, 1693–1703. doi: 10.1089/ten.TEA.2017.0520

Klein, T. J., Malda, J., Sah, R. L., and Hutmacher, D. W. (2009). Tissue engineering of articular cartilage with biomimetic zones. *Tissue Eng. Part B Rev.* 15, 143–157. doi: 10.1089/ten.TEB.2008.0563

Kobayashi, K., Matsuzaka, S., Yoshida, Y., Miyauchi, S., Wada, Y., and Moriya, H. (2004). The effects of intraarticularly injected sodium hyaluronate on levels of intact aggrecan and nitric oxide in the joint fluid of patients with knee osteoarthritis. *Osteoarthrit. Cartil.* 12, 536–542. doi: 10.1016/j.joca.2004.03.005

Kogan, G., Soltes, L., Stern, R., and Mendichi, R. (2007). "Hyaluronic acid: a biopolymer with versatile physico-chemical and biological properties," in *The Book "Handbook of Polymer Research: Monomers, Oligomers, Polymers and Composites*, eds R. A. Pethrick, A. Ballada, and G. E. Zaikov (Hauppauge, NY: Nova Science Publishers), 393–439.

Kumar, P., Satyam, A., Fan, X., Collin, E., Rochev, Y., Rodriguez, B. J., et al. (2015). Macromolecularly crowded in vitro microenvironments accelerate the production of extracellular matrix-rich supramolecular assemblies. *Sci. Rep.* 5:8729. doi: 10.1038/srep08729

Kuznetsova, I. M., Zaslavsky, B. Y., Breydo, L., Turoverov, K. K., and Uversky, V. N. (2015). Beyond the excluded volume effects: mechanistic complexity of the crowded milieu. *Molecules* 20, 1377–1409. doi: 10.3390/molecules20011377

Labarca, C., and Paigen, K. (1980). A simple, rapid, and sensitive DNA assay procedure. *Anal. Biochem.* 102, 344–352. doi: 10.1016/0003-2697(80)90165-7

Laurent, T. C. (1995). An early look at macromolecular crowding. *Biophys. Chem.* 57, 7–14. doi: 10.1016/0301-4622(95)00048-3

Laurent, T. C., Laurent, U. B., and Fraser, J. R. E. (1996). The structure and function of hyaluronan: an overview. *Immunol. Cell Biol.* 74, a1–a7. doi: 10.1038/icb.1996.32

Laurent, T., and Ogston, A. (1963). The interaction between polysaccharides and other macromolecules. 4. The osmotic pressure of mixtures of serum albumin and hyaluronic acid. *Biochem. J.* 89:249. doi: 10.1042/bj0890249

Li, L., Duan, X., Fan, Z., Chen, L., Xing, F., Xu, Z., et al. (2018). Mesenchymal stem cells in combination with hyaluronic acid for articular cartilage defects. *Sci. Rep.* 8:9900. doi: 10.1038/s41598-018-27737-y

Lynch, T., Caron, J., Arnoczky, S., Lloyd, J., Stick, J., and Render, J. (1998). Influence of exogenous hyaluronan on synthesis of hyaluronan and collagenase by equine synoviocytes. *Am. J. Vet. Res.* 59, 888–892.

McDonald, J., and Levick, J. (1995). Effect of intra-articular hyaluronan on pressure-flow relation across synovium in anaesthetized rabbits. *J. Physiol.* 485, 179–193. doi: 10.1113/jphysiol.1995.sp020722

Minton, A. P. (2001). The influence of macromolecular crowding and macromolecular confinement on biochemical reactions in physiological media. *J. Biol. Chem.* 276, 10577–10580. doi: 10.1074/jbc.r100005200

Morgese, G., Benetti, E. M., and Zenobi-Wong, M. (2018). Molecularly engineered biolubricants for articular cartilage. *Adv. Healthc. Mater.* 7:1701463. doi: 10.1002/adhm.201701463

Noble, P. W. (2002). Hyaluronan and its catabolic products in tissue injury and repair. *Matrix Biol.* 21, 25–29. doi: 10.1016/s0945-053x(01)00184-6

Oussedik, S., Tsitskaris, K., and Parker, D. (2015). Treatment of articular cartilage lesions of the knee by microfracture or autologous chondrocyte implantation: a systematic review. *Arthroscopy J. Arthroscop. Relat. Surg.* 31, 732–744. doi: 10.1016/j.arthro.2014.11.023

Palmer, G., Raia, F., Mauck, R., Valhmu, W., and Hung, C. (2001). Time-dependent aggrecan gene expression of articular chondrocytes in response to hyperosmotic loading. *Osteoarthrit. Cartil.* 9, 761–770. doi: 10.1053/joca.2001.0473

Parekkadan, B., and Milwid, J. M. (2010). Mesenchymal stem cells as therapeutics. *Ann. Rev. Biomed. Eng.* 12, 87–117. doi: 10.1146/annurev-bioeng-070909-105309

Prasadam, X., Mao, W. Shi, Crawford, R., and Xiao, Y. (2013). Combination of MEK-ERK inhibitor and hyaluronic acid has a synergistic effect on anti-hypertrophic and pro-chondrogenic activities in osteoarthritis treatment. *J. Mol. Med.* 91, 369–380. doi: 10.1007/s00109-012-0953-5

Prewitz, M. C., Stißel, A., Friedrichs, J., Träber, N., Vogler, S., Bornhäuser, M., et al. (2015). Extracellular matrix deposition of bone marrow stroma enhanced by macromolecular crowding. *Biomaterials* 73, 60–69. doi: 10.1016/j.biomaterials.2015.09.014

Radice, M., Brun, P., Cortivo, R., Scapinelli, R., Battaliard, C., and Abatangelo, G. (2000). Hyaluronan-based biopolymers as delivery vehicles for bone-marrow-derived mesenchymal progenitors. *J. Biomed. Mater. Res.* 50, 101–109. doi: 10.1002/(sici)1097-4636(200005)50:2<101::aid-jbm2>3.0.co;2-m

Salamanna, F., Giavaresi, G., Parrilli, A., Martini, L., Aldini, N. N., Abatangelo, G., et al. (2019). Effects of intra-articular hyaluronic acid associated to Chitlac (arty-duo®) in a rat knee osteoarthritis model. *J. Orthop. Res.* 37, 867–876. doi: 10.1002/jor.24259

Schatti, O., Grad, S., Goldhahn, J., Salzmann, G., Li, Z., Alini, M., et al. (2011). A combination of shear and dynamic compression leads to mechanically induced chondrogenesis of human mesenchymal stem cells. *Eur. Cell Mater.* 22:b97.

Sheehy, E. J., Buckley, C. T., and Kelly, D. J. (2012). Oxygen tension regulates the osteogenic, chondrogenic and endochondral phenotype of bone marrow derived mesenchymal stem cells. *Biochem. Biophys. Res. Commun.* 417, 305–310. doi: 10.1016/j.bbrc.2011.11.105

Shendi, D., Marzi, J., Linthicum, W., Rickards, A., Dolivo, D., Keller, S., et al. (2019). Hyaluronic acid as a macromolecular crowding agent for production of cell-derived matrices. *Acta Biomater.* 100, 292–305. doi: 10.1016/j.actbio.2019.09.042

Shinomura, T., and Kimata, K. (1990). Precartilage condensation during skeletal pattern formation: limb bud/precartilage mesenchymal condensation/cartilage differentiation/extracellular matrix. *Dev. Growth Diff.* 32, 243–248. doi: 10.1111/j.1440-169x.1990.00243.x

Solchaga, L. A., Yoo, J. U., Lundberg, M., Dennis, J. E., Huibregtse, B. A., Goldberg, V. M., et al. (2000). Hyaluronan-based polymers in the treatment of osteochondral defects. *J. Orthop. Res.* 18, 773–780. doi: 10.1002/jor.1100180515

Steadman, J. R., Rodkey, W. G., and Rodrigo, J. J. (2001). Microfracture: surgical technique and rehabilitation to treat chondral defects. *Clin. Orthop. Relat. Res.* 391, S362–S369.

Stoddart, M. J., Grad, S., Eglin, D., and Alini, M. (2009). Cells and biomaterials in cartilage tissue engineering. *Regen. Med.* 4, 81–98. doi: 10.2217/17460751.4.1.81

Tamer, T. M. (2013). Hyaluronan and synovial joint: function, distribution and healing. *Interdiscipl. Toxicol.* 6, 111–125. doi: 10.2478/intox-2013-0019

Urban, J., Hall, A., and Gehl, K. (1993). Regulation of matrix synthesis rates by the ionic and osmotic environment of articular chondrocytes. *J. Cell. Physiol.* 154, 262–270. doi: 10.1002/jcp.1041540208

Wakitani, S., Goto, T., Pineda, S. J., Young, R. G., Mansour, J. M., Caplan, A. I., et al. (1994). Mesenchymal cell-based repair of large, full-thickness defects of articular cartilage. *JBJS* 76, 579–592. doi: 10.2106/00004623-199404000-00013

Wakitani, S., Imoto, K., Yamamoto, T., Saito, M., Murata, N., and Yoneda, M. (2002). Human autologous culture expanded bone marrow mesenchymal cell transplantation for repair of cartilage defects in osteoarthritic knees. *Osteoarthrit. Cartil.* 10, 199–206. doi: 10.1053/joca.2001.0504

Weigel, P. H., Hascall, V. C., and Tammi, M. (1997). Hyaluronan synthases. *J. Biol. Chem.* 272, 13997–14000.

Welter, J., Pelyak, M., Penick, K., Solchaga, L., and Goldberg, V. (2009). 494 extracellular matrix deposition by chondrogenically differentiating human mesenchymal stem cells is enhanced by macromolecular crowding. *Osteoarthrit. Cartil.* 17:S265.

Wimmer, M. A., Grad, S., Kaup, T., Hänni, M., Schneider, E., Gogolewski, S., et al. (2004). Tribology approach to the engineering and study of articular cartilage. *Tissue Eng.* 10, 1436–1445. doi: 10.1089/ten.2004.10.1436

Worster, A. A., Brower-Toland, B. D., Fortier, L. A., Bent, S. J., Williams, J., and Nixon, A. J. (2001). Chondrocytic differentiation of mesenchymal stem cells sequentially exposed to transforming growth factor-β1 in monolayer and insulin-like growth factor-I in a three-dimensional matrix. *J. Orthop. Res.* 19, 738–749. doi: 10.1016/s0736-0266(00)00054-1

Worster, A. A., Nixon, A. J., Brower-Toland, B. D., and Williams, J. (2000). Effect of transforming growth factor β1 on chondrogenic differentiation of cultured equine mesenchymal stem cells. *Am. J. Vet. Res.* 61, 1003–1010. doi: 10.2460/ajvr.2000.61.1003

Wu, S.-C., Chang, J.-K., Wang, C.-K., Wang, G.-J., and Ho, M.-L. (2010). Enhancement of chondrogenesis of human adipose derived stem cells in a hyaluronan-enriched microenvironment. *Biomaterials* 31, 631–640. doi: 10.1016/j.biomaterials.2009.09.089

Wu, Y., Stoddart, M. J., Wuertz-Kozak, K., Grad, S., Alini, M., and Ferguson, S. J. (2017). Hyaluronan supplementation as a mechanical regulator of cartilage

tissue development under joint-kinematic-mimicking loading. *J. R. Soc. Interf.* 14:20170255. doi: 10.1098/rsif.2017.0255

Yoo, J. U., Barthel, T. S., Nishimura, K., Solchaga, L., Caplan, A. I., Goldberg, V. M., et al. (1998). The chondrogenic potential of human bone-marrow-derived mesenchymal progenitor cells. *JBJS* 80, 1745–1757.

Zhou, H.-X., Rivas, G., and Minton, A. P. (2008). Macromolecular crowding and confinement: biochemical, biophysical, and potential physiological consequences. *Annu. Rev. Biophys.* 37, 375–397. doi: 10.1146/annurev.biophys.37.032807.125817

Conflict of Interest: The authors declare that the research was conducted in the absence of any commercial or financial relationships that could be construed as a potential conflict of interest.

frontiers in Bioengineering and Biotechnology

ORIGINAL RESEARCH
published: 17 April 2020
doi: 10.3389/fbioe.2020.00278

Tissue Engineering Using Vascular Organoids From Human Pluripotent Stem Cell Derived Mural Cell Phenotypes

Maria Markou[1,2], Dimitrios Kouroupis[2], Fotios Badounas[3], Athanasios Katsouras[2], Athena Kyrkou[2], Theodore Fotsis[1,2], Carol Murphy[2] and Eleni Bagli[2]**

[1] Laboratory of Biological Chemistry, Medical School, University of Ioannina, Ioannina, Greece, [2] Foundation for Research and Technology-Hellas, Department of Biomedical Research, Institute of Molecular Biology and Biotechnology, Ioannina, Greece, [3] Transgenic Technology Laboratory, Inflammation Group, Department of Immunology, Hellenic Pasteur Institute, Athens, Greece

OPEN ACCESS

Edited by:
Dimitrios I. Zeugolis, National University of Ireland Galway, Ireland

Reviewed by:
Roberto Gramignoli, Karolinska Institutet (KI), Sweden
Lorenzo Fassina, University of Pavia, Italy
Kan Liu, University of Nebraska-Lincoln, United States

***Correspondence:**
Carol Murphy
carol_murphy@imbb.forth.gr
Eleni Bagli
elenibgl@hotmail.com

Specialty section:
This article was submitted to Tissue Engineering and Regenerative Medicine, a section of the journal Frontiers in Bioengineering and Biotechnology

Received: *18 January 2020*
Accepted: *16 March 2020*
Published: *17 April 2020*

Citation:
Markou M, Kouroupis D, Badounas F, Katsouras A, Kyrkou A, Fotsis T, Murphy C and Bagli E (2020) Tissue Engineering Using Vascular Organoids From Human Pluripotent Stem Cell Derived Mural Cell Phenotypes. Front. Bioeng. Biotechnol. 8:278. doi: 10.3389/fbioe.2020.00278

Diffusion is a limiting factor in regenerating large tissues (100–200 μm) due to reduced nutrient supply and waste removal leading to low viability of the regenerating cells as neovascularization of the implant by the host is a slow process. Thus, generating prevascularized tissue engineered constructs, in which endothelial (ECs) and mural (MCs) cells, such as smooth muscle cells (SMCs), and pericytes (PCs), are preassembled into functional *in vitro* vessels capable of rapidly connecting to the host vasculature could overcome this obstacle. Toward this purpose, using feeder-free and low serum conditions, we developed a simple, efficient and rapid *in vitro* approach to induce the differentiation of human pluripotent stem cells-hPSCs (human embryonic stem cells and human induced pluripotent stem cells) to defined SMC populations (contractile and synthetic hPSC-SMCs) by extensively characterizing the cellular phenotype (expression of CD44, CD73, CD105, NG2, PDGFRβ, and contractile proteins) and function of hPSC-SMCs. The latter were phenotypically and functionally stable for at least 8 passages, and could stabilize vessel formation and inhibit vessel network regression, when co-cultured with ECs *in vitro*. Subsequently, using a methylcellulose-based hydrogel system, we generated spheroids consisting of EC/hPSC-SMC (vascular organoids), which were extensively phenotypically characterized. Moreover, the vascular organoids served as focal starting points for the sprouting of capillary-like structures *in vitro*, whereas their delivery *in vivo* led to rapid generation of a complex functional vascular network. Finally, we investigated the vascularization potential of these vascular organoids, when embedded in hydrogels composed of defined extracellular components (collagen/fibrinogen/fibronectin) that can be used as scaffolds in tissue engineering applications. In summary, we developed a robust method for the generation of defined SMC phenotypes from hPSCs. Fabrication of vascularized tissue constructs using hPSC-SMC/EC vascular organoids embedded in chemically defined matrices is a significant step forward in tissue engineering and regenerative medicine.

Keywords: mural cells, tissue engineering, induced pluripotent stem cells, smooth muscle cells, vascularization, vascular organoids, spheroids, regenerative medicine

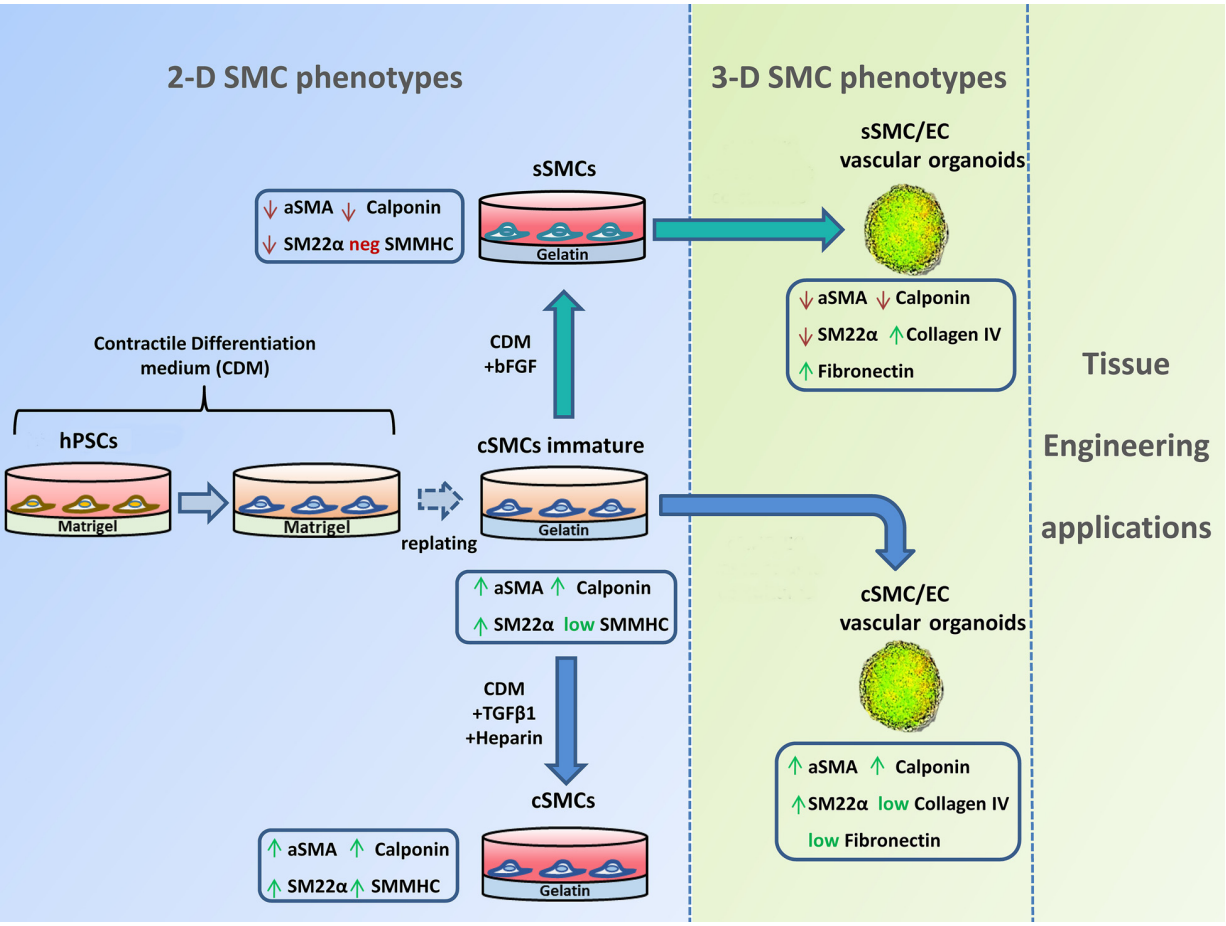

GRAPHICAL ABSTRACT | A quick and robust method has been developed to generate both contractile smooth muscle cells (cSMCs) and synthetic SMCs (sSMCs) from human pluripotent stem cells (hPSCs). According to our differentiation protocol, a combination of low serum conditions and subsequent seeding of the cells on gelatin, as ECM coating, can rapidly generate from hPSCs an immature cSMC phenotype (αSMA^{high}, Calponinhigh, $SM22^{high}$, $SMMHC^{+}$) that remain stable and without signs of senescence for at least 8 passages. Short treatment with TGFβ1 and heparin induce maturation of the cSMCs seen by the upregulated expression of SMMHC. In contrast, short-term FGF2 exposure of immature cSMCs result in downregulation of αSMA, Calponin, and SM22α expression, consistent with the development of sSMCs. The assembly of cSMC and sSMC subtypes with endothelial cells (ECs) into 3D spheroid co-cultures (vascular organoids), preserve their phenotypic features and serve as focal points for the sprouting of capillary-like structures *in vitro*. Finally, 3D SMC vascular organoid delivery *in vivo* result into rapid generation of a complex and functional vascular network.

INTRODUCTION

Regenerative Medicine is an interdisciplinary field of research and clinical applications, focused on repair, replacement, or regeneration of cells, tissues, or organs to restore impaired function resulting from congenital defects, disease and trauma (Heidary Rouchi and Mahdavi-Mazdeh, 2015). A major requirement for viability and function of the implantable construct is the availability of blood vessels to support its *in vivo* growth. Vascularization remains a critical obstacle in engineering thicker, metabolically demanding organs, such as heart muscle, brain and liver as regenerating tissue over 100–200 μm exceeds the capacity of nutrient supply and waste removal by diffusion, and requires a vascular network (Carmeliet and Jain, 2000; Jain, 2005). It takes several weeks for a scaffold to become fully vascularized *in vivo* (Nillesen et al., 2007), and without a rapid and high level of vascularization of the transplanted grafts, the majority of cells fail to survive the early post-transplantation phase. Therefore, the development of strategies that enhance the angiogenic process represents one of the major research topics in the field of tissue engineering.

The current classical approach is based on the isolation, expansion and seeding of endothelial cells (ECs) onto a suitable scaffold before *in vivo* implantation (Schechner et al., 2000). Although ECs implanted *in vivo* can form an immature vascular network, the ineffective integration of this network into the host vasculature causes regression of the vessels within a few days (Jain et al., 2005; Au et al., 2009). Moreover, the generated capillaries are leaky and unable to properly control permeability, contributing to tissue edema (Hashizume et al., 2000; Melero-Martin et al., 2008). Therefore,

a particular challenge for the tissue-engineering community is to induce vascularization of ischemic tissues with blood vessels that are functionally normal. To promote the maturation and stability of nascent vasculatures, ECs must functionally interact with mural cells (MCs), such as vascular smooth muscle cells (vSMCs).

MCs are primarily responsible for stabilization, inhibition of regression, contraction of the vessel as well as production and deposition of extracellular matrix (ECM) proteins (Shepro and Morel, 1993; Chistiakov et al., 2015). Interactions between MCs and ECs are critical in the process of vascular development (Armulik et al., 2005; Regan and Majesky, 2009; Trkov et al., 2010). MCs are composed of vSMC, surrounding larger vessels, such as arteries and veins, and pericytes (PCs), typically surrounding smaller microvessels and capillaries. However, heterogeneities exist within the subtypes (Hedin and Thyberg, 1987; Kusuma and Gerecht, 2013) and the existence of transitional cell phenotypes has recently been suggested in the literature (Holm et al., 2018). As a result, MCs exhibit overlapping marker expression and cannot be distinguished by one marker alone; instead, a combination of markers is required for their identification. Regarding vSMCs, two distinct phenotypes have been identified: synthetic and contractile (Hedin and Thyberg, 1987; Beamish et al., 2010). Both participate in neovascularization, but synthetic vSMCs predominate in the embryo and in diseased or injured adult vessels, while contractile vSMCs predominate in healthy adult vessels. In this context, understanding distinctions between MCs and the molecular mechanisms underlining their phenotypic stability and plasticity, will enable improved therapeutics in a tissue-specific manner. However, although the role of MCs in engineering vascularized constructs for therapeutic applications is unquestionable (Wanjare et al., 2013b; Dar and Itskovitz-Eldor, 2015), their dynamic phenotypic nature has not been extensively studied mainly due to limitations of isolation/expansion and phenotypic plasticity during *in vitro* culture of primary MCs (Cathery et al., 2018).

Selection of the suitable cell source for vascular tissue engineering as well as development of functional capillaries in the fabricated construct are crucial and can be a challenge. Human pluripotent stem cells (hPSCs), including induced PSCs (iPSCs), and embryonic stem cells (ESCs), can differentiate into the three germ layers. They have an unlimited ability to self-renew, making them easy to expand and, despite limitations of the current differentiation procedures (Liu and Zheng, 2019), represent an unlimited source of cells for therapeutic use. The generation of iPSCs, although laborious and expensive, overcomes the ethical problems associated with the clinical use of stem cells and provides the possibility of using autologous cells (Takahashi and Yamanaka, 2006). Using PSCs, the generation of defined phenotypes of MCs can be achieved and offers great potential for studying their plasticity and interactions with ECs. Furthermore, adequate number of cells for tissue engineering applications can be produced, a known obstacle of using primary cells. However, due to the dynamic nature of MCs, one must ensure stability of their phenotype and functionality upon *in vivo* administration.

Over the last few years it has become apparent that when cells are cultured in three-dimension (3D) they adhere to each other via ECM and form natural cell-cell contacts, which transmit physiological information regulating cell growth, migration, differentiation, and survival (Derda et al., 2009; Bhang et al., 2011) resembling the native environment. Spheroidal aggregation has been shown to stabilize ECs and render them responsive to the activities of survival factors (Korff and Augustin, 1998) and, moreover, when spheroids of cultured ECs were embedded in a variety of biomaterials, they served as focal starting points of outgrowing capillary sprouts (Korff et al., 2004; Alajati et al., 2008). In this context, mixed spheroids consisting of ECs and defined populations of MCs, could guarantee the physiological microenvironment for their function and offer the potential for multiple tissue engineering applications.

In the present study, we first induced the differentiation of hESCs and hiPSCs, generated by our group (Kyrkou et al., 2016), to defined SMC subtypes, which were extensively phenotypically and functionally analyzed. The SMCs were then used in a (3D) spheroidal co-culture model with primary human ECs, generating vascular organoids, in order to elucidate the potential of early and robust generation of mature neovessels *in vivo* for tissue engineering applications.

MATERIALS AND METHODS

Cell Culture

hPSCs

hiPSCs were generated from human fibroblasts as previously described (Kyrkou et al., 2016), and the H1 hESC line was purchased from Wicell Research Institute (Madison, WI, United States). hPSCs were cultured on six-well tissue culture plates coated with hESC-qualified Matrigel (Corning, 354277) in mTeSR1 medium (StemCell Technologies, 05850) at 37°C and 5% CO_2. Every 4–6 days, cells were passaged enzymatically using 1 mg/ml dispase (Invitrogen, 17105-041) for 2 min at 37°C. hPSC colonies were then harvested, dissociated into small clumps and replated onto Matrigel-coated 6-well plates (ratio 1:6).

Human ECs

ECs from umbilical vein (HUVEC) were cultured in M199 (Gibco) medium supplemented with 20% fetal calf serum (FCS), 47 μg/ml endothelial cell growth supplement (ECGS), 4.7 μ/ml heparin (Sigma) and 1% penicillin-streptomycin as previously described (Bellou et al., 2012).

Differentiation Protocol

To generate contractile SMCs (cSMCs), hPSCs plated on matrigel were cultured in contractile differentiation medium (CDM) consisting of basal medium (Lonza, PT-3273) supplemented with 2.5% FCS (Gibco, 10270-106) and glutamax (Gibco, 35050) for 9 days with daily medium changes. On day 9, cells were detached enzymatically using 0.05% Trypsin-EDTA (Gibco, 25300-054) and replated on gelatin (0.1% Gelatin-Millipore, ES-006-B) coated dishes and cultured in CDM until confluency (2–3 days).

Medium was changed every second day. For generation of a mature phenotype of cSMCs, the differentiated hPSC-cSMCs were induced with 5 ng/ml TGFβ1 (Peprotech) and 50 μ/ml heparin (Sigma, H-3149) in CDM, for 2 days.

To generate synthetic SMCs (sSMCs), hPSC-cSMCs were seeded on gelatin coated dishes for 24 h and subsequently the medium was changed to either CDM supplemented with 2 ng/ml FGF2 (Immunotools, 11343623) or synthetic differentiation medium (SDM) for 48 h. SDM medium consisted of a basal medium (ScienCell, 1201-b) supplemented with 2% FCS, and a combination of growth factors (ScienCell, 1252) 2 ng/ml EGF, 2 ng/ml FGF2 and 2 ng/ml IGF-I.

Generation of Vascular Organoids/Spheroids

Vascular organoids (spheroids consisted of hPSC-SMC/ECs) and cell spheroids (consisted of ECs) were created using methylcellulose (Sigma, M0512) and the hanging drop technique as previously described (Korff and Augustin, 1998). In brief, each vascular organoid was generated from 1,000 cells at a ratio 1:9 hPSC-SMCs:ECs in 10 μl solution (EGM-2 medium/methylcellulose solution:4:1), cultured in a hanging drop for 2 days at 37°C and 5% CO_2.

Immunophenotyping

Flow cytometry analysis of the cells was performed as previously described (Tsolis et al., 2016). Briefly, 2.0×10^5 cells were incubated with FITC/PE/APC-conjugated anti-human primary monoclonal antibodies (**Supplementary Table S1**). Dead cells were excluded using 2 μg/ml 7-Amino-actinomycin D (7-AAD) viability staining solution (Invitrogen, Thermo Fisher Scientific, Waltham, MA, United States). Background fluorescence was established using isotype controls and data were acquired using CyFlow (Partec, Münster, Germany) collecting a minimum of 20,000 events. The analysis was performed using FlowMax software.

Western Blot Analysis

Protein extraction was performed from whole cell lysates and quantified with BCA Protein Assay kit (Thermo Scientific, 23225). Samples were prepared, subjected to SDS-PAGE and blotted onto a nitrocellulose membrane, as previously described (Bellou et al., 2012). Specific proteins were detected following incubation with primary antibodies (**Supplementary Table S2**) and peroxidase-conjugated secondary antibodies (**Supplementary Table S2**). Quantification of band intensities was performed using Quantity One Analysis software (BIO-RAD).

Immunofluorescence

Adherent cells: Indirect immunofluorescence on adherent cells was performed as previously described (Bellou, 2012 #68) using primary and secondary antibodies (listed in **Materials and Methods Supplementary**). Cell nuclei were stained using propidium iodide-PI (Sigma), samples were mounted in moviol-dabco, and images of nine fields were taken on a Leica TCS SP5 confocal microscope using HCX PL APO CS 40 × 1.25 OIL objective.

Vascular organoids/spheroids: Vascular organoids or spheroids consisting of 1,000 cells/spheroid were fixed in 3.7% paraformaldehyde for 1 h at RT, permeabilized with 0.2% Triton-X/0.9% gelatin solution for 1 h, and 0.5% Triton-X/0.9% gelatin solution for 15 min, and incubated with primary antibodies overnight at 4°C (**Supplementary Table S2**). Next day, the vascular organoids were washed 5x with 0.2% Triton-X and incubated with secondary antibodies for 1 h (**Supplementary Table S2**). After rinsing 5x with 0.2% Triton-X and incubation with Draq5 (Thermo Fisher Scientific) for 10 min, images were taken on a Leica TCS SP5 confocal microscope using HCX PL APO CS 40 × 1.25 OIL objective. At least 10 vascular organoids or spheroids were analyzed per experiment.

Quantitative Real Time-PCR (qRT-PCR)

Total RNA was extracted using RNeasy Midi kit (NucleoSpin) according to manufacturer's instructions, and quantified using NanoDrop™ 1000 Spectrophotometer (Thermo Fisher Scientific). 10ng of RNA were quantified by QuantiTect SYBR Green RT-PCR Kit (Qiagen, 204243) using a LightCycler® 2.0 thermocycler (Roche Diagnostics). For each target transcript primers were selected using DnaStar software (**Supplementary Table S3**). All samples were analyzed in triplicates per experiment. Expression of the *Smooth Muscle 22-alpha (SM22α), CNN1, CD105, Platelet-Derived Growth Factor Receptor Beta (PDGFRB)* and *NG2* transcripts was calculated using a standard curve of RNA isolated from Adipose-derived stem cells. For *Smooth Muscle Myosin Heavy Chain (SMMHC)* mean values were normalized to *Glyceraldehyde-3-Phosphate Dehydrogenase (GAPDH)* and for each transcript the relative expression was calculated using the $2-\Delta CT$ method (Kouroupis et al., 2016).

Contraction Assay

40,000 hESC-cSMCs attached on 24 well plates were induced to contract with 10^{-5}M carbachol (Sigma) in plain DMEM for 30 min at 37°C. Cells were stained with calceinAM (eBioscience, 65-0853). A series of time-lapse images with a 20X (s plan fluor elwd) objective were taken using IncuCyte (IncuCyte ZOOM 2016B). Quantification of the contracted cells/total number of cells was performed in 4 fields/well (6 wells/experiment).

Cell Proliferation Assay

40,000 hPSC-cSMCs or hPSC-sSMCs were seeded in a 24 well plate in CDM and SDM respectively. After 6 h cells were counted (t = 0) or cultured in DMEM 2% FCS. Cell counting was also performed 24 and 48 h post-seeding by the addition of 0.2% trypan blue (Sigma, T815). Average cell number was evaluated from triplicates for each time point and for each cell type.

Migration Assay (Wound Healing)

The migration of hPSC-cSMCs and hPSC-sSMCs was assessed using a wound healing assay. Cells were cultured to confluence

and a "wound gap" was created by scratching a strip on the cell monolayer using a 200 μl pipet tip. Cells were washed with PBS, and cultured in DMEM 0.5% FCS. Optical microscope images of cell migration were taken in a time course every 1 h with a 5X objective. The average number of migrated cells from triplicates was measured with ImageJ software.

Gelatin Zymography

Zymographic assays were performed to determine matrix metalloproteinase (MMP) activity as previously described (Panopoulou et al., 2005) at cell lysates and conditioned medium (secretome) as well. In brief, hPSC-cSMCs and hPSC-sSMCs were seeded in a 24 well plate in CDM and SDM respectively. After 24 h medium was changed to serum free DMEM medium, and cells were cultured for 72 h. Whole cell lysates were centrifuged at 16,100rcf for 20 min and the concentration of total proteins was quantified with BCA Protein Assay kit. Conditioned media were collected and centrifuged at 1,000rcf for 10 min, to eliminate dead cells. Samples prepared in non-reducing conditions and containing equal amount of total protein were loaded to a gel supplemented with 1 mg/ml gelatin and subjected to SDS-PAGE at 4°C. Regarding the conditioned media, the volume from each sample that was loaded was normalized to protein concentration of the cell lysate. Gel was washed with a solution containing 2.5% Triton X-100, 50 mM Tris-HCL pH7.5, 5 mM $CaCL_2$, 1 μM $MgCL_2$ and incubated with 1% Triton X-100, 50 mM Tris-HCL pH7.5, 5 mM $CaCL_2$, 1 μM $MgCL_2$ solution at 37°C overnight. Then whole gel was stained with staining solution (40% methanol, 10% acetic acid, 0.5 g/100 ml Coomassie blue) for 30 min, rinsed with H_2O, and destained with 40% methanol, 10% acetic acid until bands could clearly be seen. Areas of enzyme activity appeared as white bands against a dark blue background. Gels were scanned, images were modified to be in black and white and then they were inverted so that the areas of enzyme activity appeared black. Quantification of band intensities was performed using Quantity One Analysis software. Alternatively, cell lysate samples prepared as for gelatin zymography were subjected to SDS-PAGE and blotted onto a nitrocellulose membrane. Tubulin was detected (western blot analysis section), in order to confirm equal samples loading.

Multipotency of hPSC-SMC Subtypes

Cultured hPSC-cSMCs and hPSC-sSMCs were expanded *in vitro* under standard conditions to passage 3 and then subjected to osteogenesis and chondrogenesis differentiation induction protocols, in duplicates, as previously described (Vlaikou et al., 2017).

In vitro Angiogenesis Assay

Monocells: hPSC-cSMCs/sSMCs and ECs were stained with the general membrane staining kit (PKH26, and PKH67 Fluorescent Cell Linker Kits, Sigma-Aldrich) according to manufacturer's instructions and seeded as monocells at a ratio of 1:9 (hPSC-SMCs:ECs) on a polymerized layer of matrigel in μ-Slide Angiogenesis plates (ibidi, 81501) in triplicates. Images from at least 5 fields/well were taken every 1 h for 48 h with a confocal microscope at 10X magnification. The newly formed network was evaluated using ImageJ software[1].

Vascular organoids/spheroids: Spheroids and vascular organoids (spheroids consisting of hPSC-SMC/EC) were plated on polymerized matrigel, collagen I (3 mg/ml), collagen I (3 mg/ml) with fibronectin (100 ng/ml) (Benning et al., 2018), and fibrin gel (2 mg/ml) (Nakatsu et al., 2003) in μ-Slide Angiogenesis plates and cultured in EGM-2 medium (1 spheroid/well). Media changes were performed every 2 days and spheroid sprouting was observed daily. Images from at least 3 vascular organoids or spheroids were taken on day 1and 3 using Leica TCS SP5 confocal microscope.

Tubulogenesis Assay

hPSC-cSMCs and hPSC-sSMCs in duplicates were seeded in the inner surface of ibidi dishes (81156, μ-Dish 35 mm). When confluent, 40,000 HUVECs were added on the cell monolayer and medium was changed to EGM-2 (Lonza, CC-3162). The medium was changed again on day 2. After 4 days cells were fixed and immunofluorescence was performed. Images were taken from the whole plate using Leica TCS SP5 confocal microscope and the formed tube-like network was evaluated with ImageJ software.

In vivo Angiogenesis Plug Assay

Formation of new blood vessels *in vivo* was evaluated using the matrigel plug assay. The experimental protocol was approved by the Committee for Animal Research Studies of the University of Ioannina (No14144). All the experimental procedures were in agreement with European Union directives (EU Directive 2010/63). Appropriate measures were taken to minimize pain or discomfort to the animals. Six to eight weeks old female NSG (NOD/SCID) mice were used. Animals were housed in individually ventilated cages in the animal house facility of University of Ioannina, under a 12 h light/dark cycle, pathogen-free conditions and they had free access to food and water.

ECs spheroids and hPSC-SMC/ECs as vascular organoids (300 spheroids/animal) or as monocells (300,000 cells/animal) were mixed with 200 μl cold matrigel (Corning, 354234), 200 ng/ml vascular endothelial growth factor (VEGF) (Immunotools, 11343663), 800 ng/ml FGF2, and 0.1 ng/ml heparin and injected subcutaneously into the abdominal tissue along the peritoneal midline into mice. Four days after the injection mice were euthanized and matrigel plugs were removed and fixed in 4% paraformaldehyde. Four animals per group were used according to G Power analysis. The statistical review was performed by a biomedical statistician.

Immunohistochemistry (IHC)

Samples were embedded in optimal cutting temperature (OCT) compound or in paraffin and 5μm sections were cut from each sample using Thermo Shandon cryotome E. Staining with hematoxylin and eosin and IHC was performed for all samples. Staining for CD31, CD34, and αSMA was carried out using the EnVision™ FLEX, High pH (Link) (Code K8000). Briefly,

[1]http://image.bio.methods.free.fr

the sections were hydrated in ddH_2O. Endogenous peroxidase activities were quenched in 3% H_2O_2 for 10 min at RT. Samples were then incubated with CD31, CD34, and αSMA accordingly, at RT for 1 h. Secondary EnVision FLEX/HRP (DAKO) was then applied for 30 min, followed by treatment with substrate/chromogen (DAKO) for 5–10 min. Slides were counterstained using Mayer's Hematoxyl in solution. Images from at least 5 fields/section and 3 sections/implant were acquired on an Olympus BX-50 microscope.

Statistical Analysis

Data were analyzed using SPSS 22.0 (SPSS, Inc). Continuous data were expressed as mean ± SD. Normality tests were carried out. *T*-test or Mann–Whitney test was performed accordingly (comparisons between two conditions) or ANOVA (comparisons between more than two conditions). Significant probability values were also corrected for multiple testing (Bonferroni correction). Categorical data were presented as counts and chi-square test was performed. The *P* values obtained were 2-tailed and determined to be significant at $P \leq 0.05$.

RESULTS

Differentiation of hPSCs to cSMCs and sSMCs

In a previous study we have generated mesenchymal stem cells (MSCs) from iPSCs by culturing them in a differentiation medium containing 10% FCs (Kouroupis et al., 2016). Since high serum is known to downregulate the expression of contractile proteins (Wanjare et al., 2013a), the key phenotypic feature of SMCs, we modified our differentiation strategy and developed a simple and quick differentiation protocol to induce the differentiation of hPSCs to cSMCs using CDM containing 2.5% FCS. After 9 days of culturing the cells in CDM, a distinct population of cells was positive for the typical mesenchymal marker CD44 (48.3 ± 0.6%) and to a lesser extent was positive for the general mesoderm marker CD73 (Boyd et al., 2009; Vodyanik et al., 2010), CD105 and NG2 (**Figure 1A**). Cells were then enzymatically removed, replated without sorting and cultured in CDM on gelatin coated dishes. When confluent (after 2–3 days), the cells exhibited high expression levels of the contractile proteins αSMA, Calponin, SM22α, implying a commitment to cSMCs (**Figure 1B**). In agreement, 78.4% ± 0.04 of the cells (from four independent experiments) contracted after treatment with carbachol (**Figure 1C**). Moreover, cells tested positive for typical markers expressed by MSCs as well as by MCs including CD44, CD73, CD105, CD29, and NG2 (**Figure 1A**). This cSMC phenotype was stable for at least 8 passages (data not shown).

In order to induce the transition of hPSC-cSMCs to hPSC-sSMCs, we added FGF2 to the differentiation medium, a growth factor known to induce the phenotypic switch from primary cSMCs to sSMCs (Jackson and Reidy, 1993). After 2 days of treatment the protein expression of the contractile proteins was downregulated, a fact consistent with the development of the synthetic phenotype (**Figure 1D** and **Supplementary Figure S1A**). Given that other growth factors have also a similar effect (Holycross et al., 1992), we treated the cells with SDM (basal medium containing 2% FCS, supplemented with a combination of growth factors including EGF, FGF2, and IGF-I) and the contractile proteins as well as their gene expression were downregulated and were almost undetectable after 3–4 days (**Figure 1D** and **Supplementary Figures S1B,C**). Upon further phenotypic characterization of hPSC-cSMCs and hPSC-sSMCs no significant change in the surface expression of the mesenchymal/MC markers CD29, CD44, CD73, CD105, NG2 was found between the two subtypes (**Figure 2A**). However, there were statistically significant fewer cells expressing αSMA, Calponin, SM22α in hPSC-sSMCs (similar to adipose derived-MSCs, AD-MSCs) compared to hPSC-cSMCs (**Figures 2B,C**). Finally, the pluripotent markers Nanog and Sox2 were undetectable from the first passage in both phenotypes (**Supplementary Figure S1D**).

The expression of SMMHC, a marker of cSMC maturation, was detectable, albeit at a low level, in hPSC-cSMCs indicating an immature phenotype of the cells (Wanjare et al., 2013a). We then attempted to induce maturation by exposure of differentiated hESC-cSMCs to TGFβ1/heparin. Indeed, after 24 h of treatment a significantly upregulated gene expression of the contractile protein SMMHC (ninefold induction) was observed (**Supplementary Figure S2A**). The protein expression of the other contractile proteins was increased but did not reach statistical significance (**Supplementary Figure S2B**). Notably, the proliferation potential of the hESC-cSMCs TGFβ1/heparin treated cells was decreased compared to hESC-cSMCs (**Supplementary Figure S2C**), all consistent with the acquisition of a mature phenotype (Wanjare et al., 2013a).

Functional characterization of these two cell subtypes (hPSC-cSMCs and hPSC-sSMCs) revealed that hPSC-sSMCs exhibited higher proliferation and migration potential (**Figures 3A,B**) and increased deposition of ECM (fibronectin, collagen IV) (**Figure 3C**), compared to hPSC-cSMCs. Moreover, increased MMP-2 activity both in the conditioned medium and in the cell extract and MMP-9 activity in the cell extract was found in hPSC-sSMCs compared to hPSC-cSMCs (**Figure 3D**). All of the above results are consistent with the phenotypes of primary sSMCs and cSMCs (Beamish et al., 2010; Cecchettini et al., 2011).

Finally, both cell subtypes demonstrated similar potential to differentiate toward chondrogenic and osteogenic lineages (**Supplementary Figure S3A**).

MC Functionality of hPSC-cSMCs and hPSC-sSMCs

To explore whether our SMC derivatives could assist in vessel formation by ECs and stabilization of the neovasculature, both cell subtypes were co-cultured with primary human ECs on matrigel matrix (*in vitro* angiogenesis assay). A fixed ratio of 9:1 ECs:SMCs (hPSC-cSMCs or hPSC-sSMCs) similar to the average ratio of MC:ECs found in vascular beds *in vivo* was used (Shepro and Morel, 1993). As shown in **Figure 4A** both

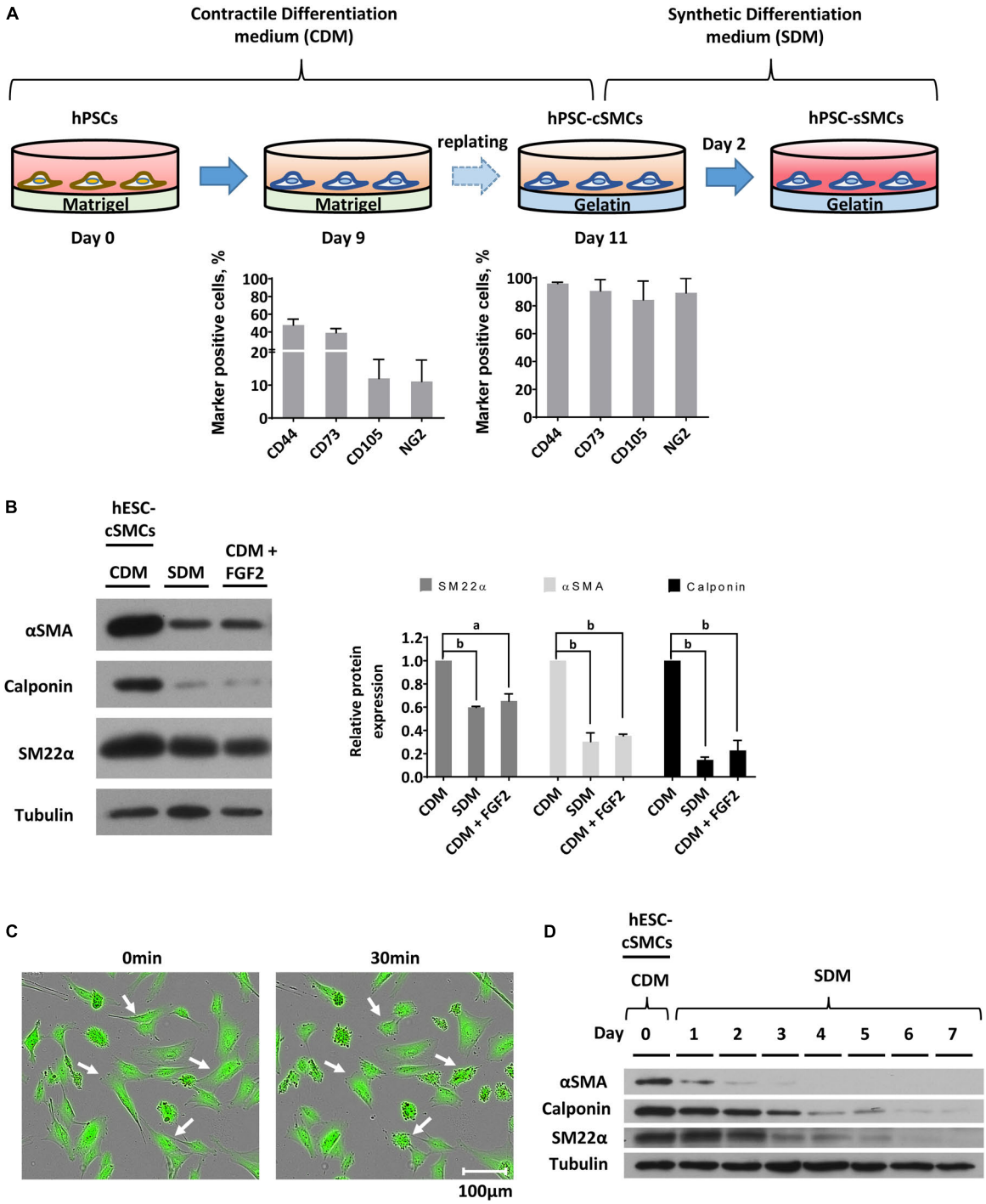

FIGURE 1 | Differentiation of hPSCs to cSMCs and sSMCs. **(A)** Overview of the differentiation procedure and histograms presenting the percentage of the cells expressing the surface markers CD44, CD73, CD105, NG2 evaluated by flow cytometry analysis on day 9 (left histogram) and on day 11 (right histogram) of the differentiation process. The means ± SD were calculated from three independent experiments. **(B)** Cells on day 11 of the differentiation process (hESC-cSMCs) were further cultured in CDM, SDM, or CDM supplemented with FGF2 for 48 h. Whole-cell lysates were analyzed by SDS-PAGE and immunoblotted with antibodies recognizing αSMA, Calponin and SM22α. Quantification of band intensities for each contractile protein is presented in graphs (right). Each bar represents the intensity of the contractile protein normalized to the density of tubulin (loading control) and expressed as fold change relative to cells in CDM. The means ± SD were calculated from three independent experiments, $^{a}P < 0.05$, $^{b}P < 0.01$. **(C)** Images of hESC-cSMCs stained with calcein before (left image) and 30 min after the addition of carbachol (10^{-5}M) (right image). Some contracted cells are indicated with white arrows. This is a representative image of three independent experiments. Scale bar, 100 μm. **(D)** The medium of hESC-cSMCs cultured in CDM was changed to SDM (day 0). Protein expression levels of αSMA, Calponin, SM22α from whole-cell lysates were evaluated daily until day 7 by western blot analysis. Tubulin levels served as loading control. This is a representative image of two independent experiments.

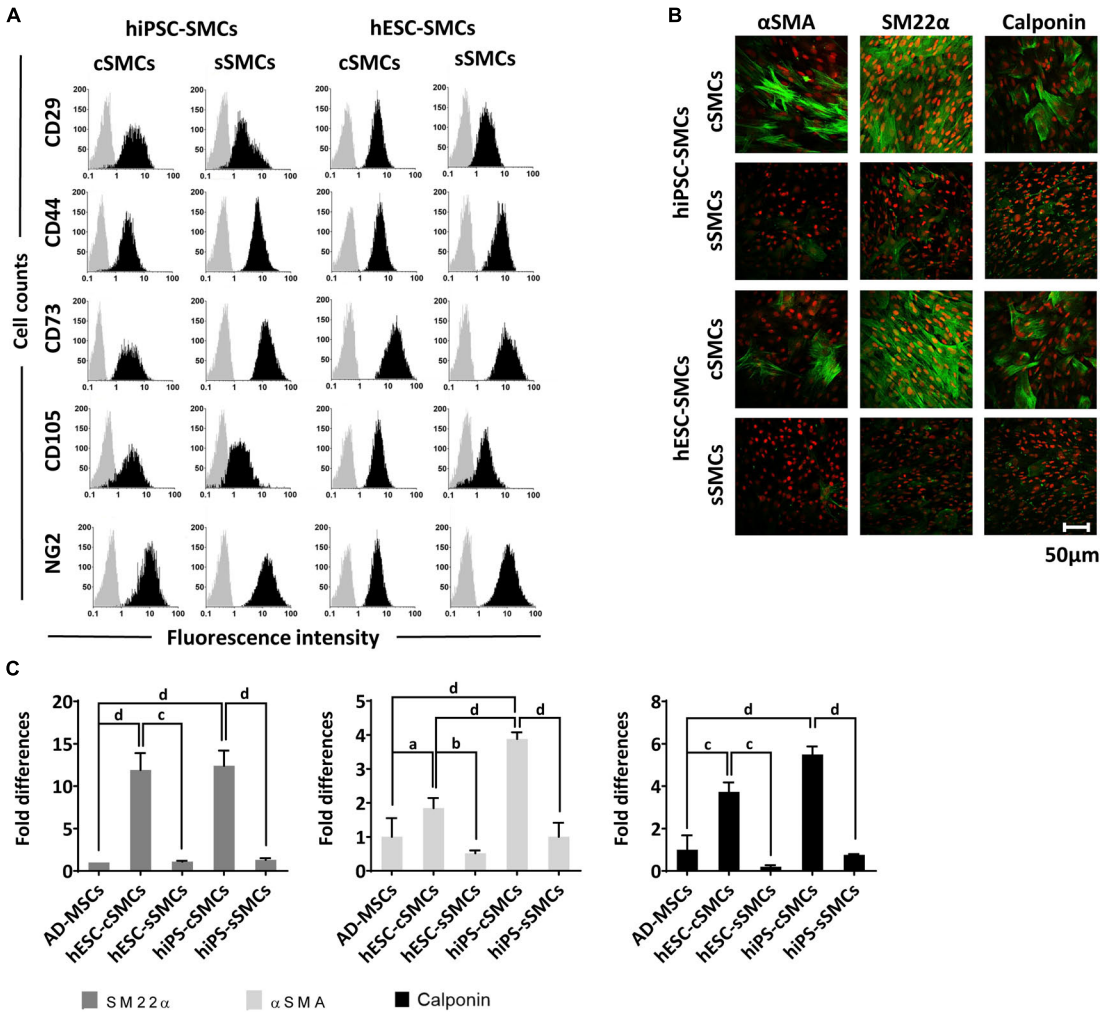

FIGURE 2 | Phenotypic analysis of hPSC-cSMCs and hPSC-sSMCs. **(A)** The panel shows representative flow cytometry histograms of hiPSC-cSMCs, hiPSC-sSMCs, hESC-cSMCs, and hESC-sSMCs (columns from left to right). The histograms of the samples stained with the isotypic IgGs are shown in light gray, whereas the samples stained with fluorochrome-conjugated antibodies are overlaid in black. Each histogram is a representative of at least three independent experiments. **(B)** Immunofluorescence analysis performed on hiPSC-cSMCs, hiPSC-sSMCs, hESC-cSMCs, and hESC-sSMCs. Green fluorescence indicates cells positive for αSMA (left column), SM22α (middle column), and Calponin (right column) whereas red indicates nuclei (PI stain). Images were taken on Leica TCS SP5 confocal microscope and they are representative of three independent experiments. Scale bar, 50 μm. **(C)** Relative numbers of cells expressing SM22α, αSMA and Calponin from AD-MSCs, hESC-cSMCs, hESC-sSMCs, hiPSC-cSMCs, and hiPSC-sSMCs (histograms left, middle and right respectively) are expressed as fold differences based on quantification of the immunofluorescence analysis **(B)**. The means ± SD were calculated from three independent experiments, $^{a}P < 0.05$, $^{b}P < 0.01$, $^{c}P < 0.001$, $^{d}P < 0.001$.

hPSC-cSMCs and hPSC-sSMCs integrated into the ECs network. Furthermore, no statistically significant difference could be detected between hESC-cSMCs + ECs, hESC-sSMCs + ECs and ECs alone regarding morphometric parameters of the capillary-like structures quantified by ImageJ software (**Supplementary Table S1**). Moreover, both cell subtypes stabilized the vascular network and inhibited its regression, a key feature of MCs (**Figure 4B**). On the contrary, AD-MSCs or hiPSC-MSCs (Kouroupis et al., 2016) used in the same experimental set up could not rescue the ECs network from regression (**Supplementary Figure S3B**), implying that hPSC-cSMCs and hPSC-sSMCs, although exhibiting some features of MSCs, are functional MCs. We next explored the ability of hPSC-cSMCs and hPSC-sSMCs monolayers to induce ECs tubulogenesis. When ECs were added on top of a hPSC-sSMC monolayer, they were organized into a significantly more complex network, as evaluated with various morphometric parameters, compared to that developed by ECs added on a hPSC-cSMC monolayer (**Figure 4C**). Moreover, immunostaining of collagen IV (a component of vascular basement membrane) in the hPSC-sSMC + EC co-culture clearly demarcated the generated vascular tubules indicating a more mature network compared to hPSC-cSMC + ECs, where a less continuous and lower staining intensity was observed (**Figure 4D**). No significant difference in EC or SMC number was found between the two conditions that could account for this effect (data not shown). Furthermore, more

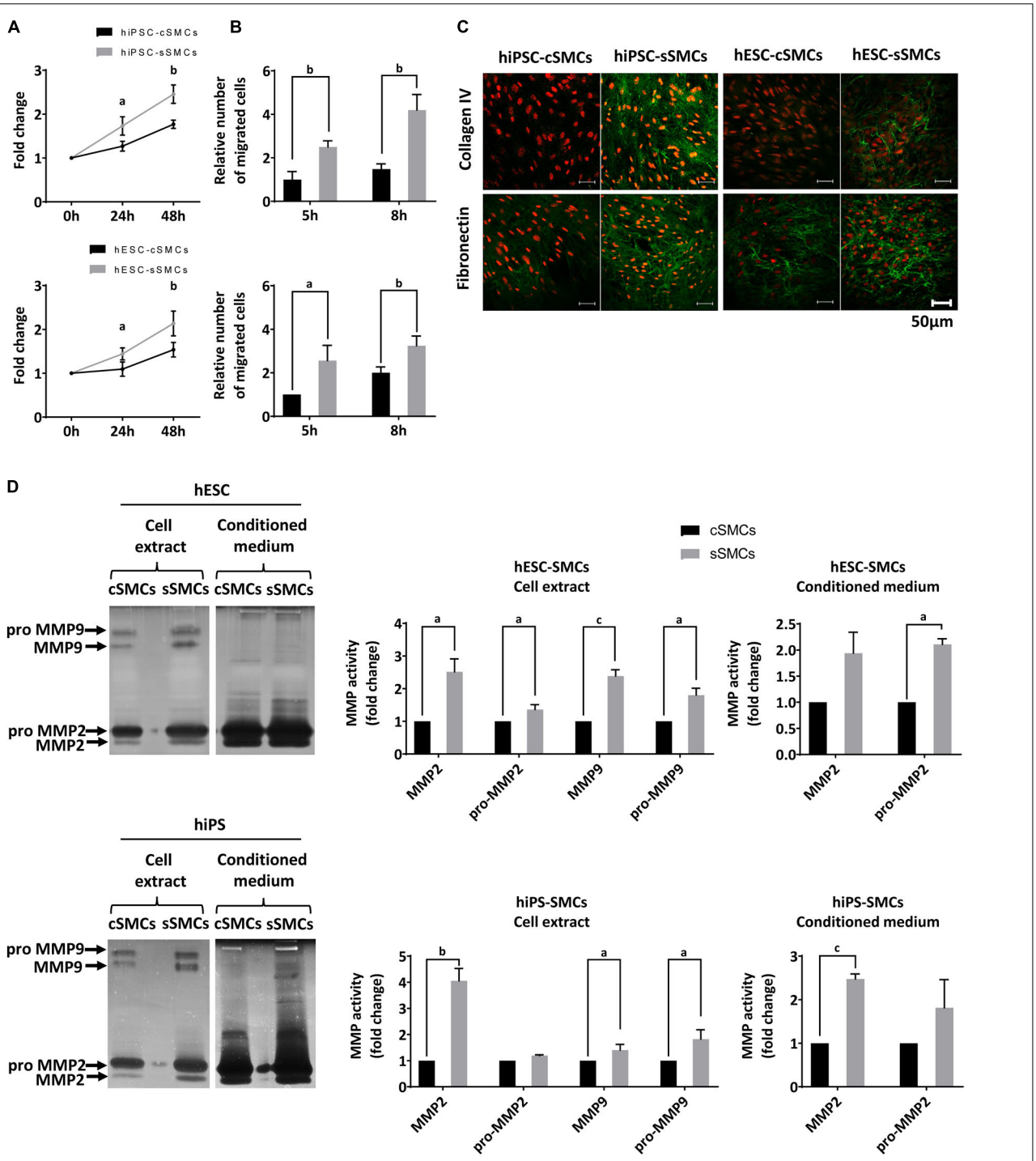

FIGURE 3 | Functional analysis of hPSC-cSMCs and hPSC-sSMCs. **(A)** Proliferation assay. Numbers of hiPSC-cSMCs, hiPSC-sSMCs (upper graph) and hESC-cSMCs, hESC-sSMCs (lower graph) are expressed as fold change at 24 and 48 h relative to 0 h and presented as means ± SD from three independent experiments. $^{a}P < 0.05$, $^{b}P < 0.01$. **(B)** Migration assay. Relative number of migrated hiPSC-cSMCs, hiPSC-sSMCs (upper chart) and hESC-sSMCs, hESC-cSMCs (lower chart) at 5 and 8 h using the wound healing assay are presented as means ± SD from three independent experiments. $^{a}P < 0.05$, $^{b}P < 0.01$. **(C)** Extracellular matrix deposition. Immunofluorescence analysis performed on hiPSC-cSMCs, hiPSC-sSMCs, hESC-cSMCs, and hESC-sSMCs. Green fluorescence indicates Collagen IV (upper panel) and Fibronectin (lower panel), whereas red fluorescence indicates nuclei (PI stain). Images were taken on Leica TCS SP5 confocal microscope and are representative of three independent experiments. Scale bar, 50 µm. **(D)** MMP2 and 9 activity. hESC-cSMC, hESC-sSMC (upper image) and hiPSC-cSMCs, hiPSC-sSMCs (lower image) cell extracts and conditioned media were assessed using gelatin zymography. The images are inverted photos of the zymograms and are representative of three independent experiments. Relative MMP activities were evaluated by quantification of band intensities and are presented in the charts. Data are expressed as means ± SD from three independent experiments. $^{a}P < 0.05$, $^{b}P < 0.01$, $^{c}P < 0.001$.

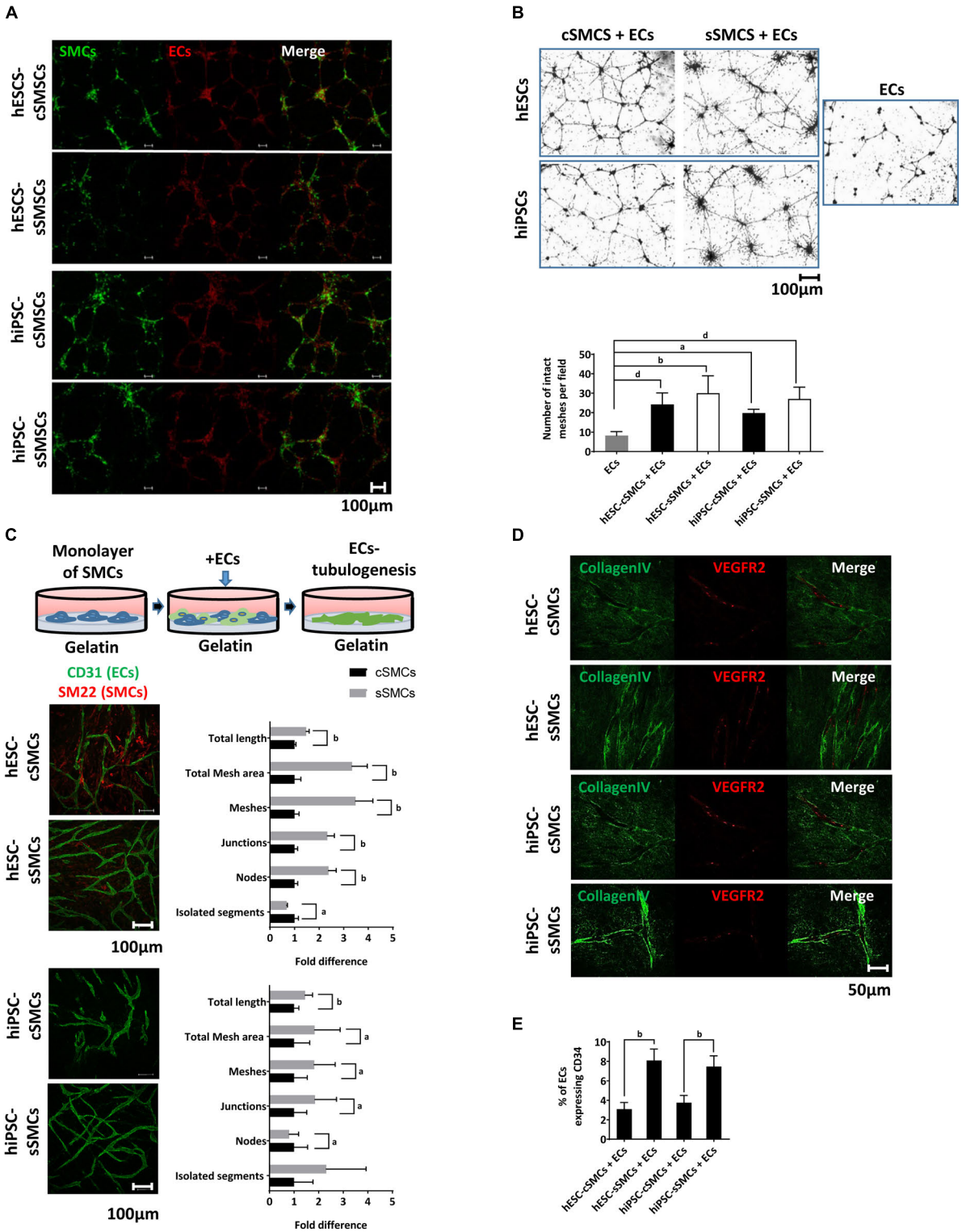

FIGURE 4 | MC function of hPSC-cSMCs and hPSC-sSMCs. **(A)** *In vitro* angiogenesis assay. hESC-cSMCs, hESC-sSMCs, hiPSC-cSMCs, and hiPSC-sSMCs labeled with PKH67, shown in green, were mixed in a ratio 1:9 with primary ECs labeled with PKH26, shown in red, and allowed to generate a vascular network on matrigel for 8 h. Merged fluorescence images are shown in right column of each panel. Images were taken on Leica TCS SP5 confocal microscope and are representative of three independent experiments. Scale bar, 100 μm. **(B)** Regression analysis. Phase-contrast images of hESC-cSMCs + ECs, hESC-sSMCs + ECs (upper left panel), hiPSC-cSMCs + ECs, hiPSC-sSMCs + ECs (lower left panel) and ECs (right panel) derived vascular networks on matrigel at 48 h are shown.

(Continued)

FIGURE 4 | Continued
Images were taken on Zeiss axiovert 100, and are representative of three independent experiments. Number of intact meshes representing the vascular network integrity for each condition are shown in the chart. Graph data are expressed as means ± SD from three independent experiments. $^{a}P < 0.05$, $^{b}P < 0.01$, $^{d}P < 0.001$. Scale bar, 100 μm. **(C)** Tubulogenesis assay. ECs were plated on a monolayer of hESC-cSMCs, hESC-sSMCs (upper images) or hiPSC-cSMCs, hiPSC-sSMCs (lower images) and allowed to generate tubule-like structures (illustration). Green fluorescence indicates ECs (CD31 staining). Images were taken on Leica TCS SP5 confocal microscope and are representative of three independent experiments. Morphometric analysis of the hESC-cSMCs + ECs, hESC-sSMCs + ECs and hiPSC-cSMCs + ECs, hiPSC-sSMCs + ECs tube-like structures is presented in the charts and expressed as fold change between the two conditions regarding various parameters. Analysis was performed with ImageJ software. Graph data are expressed as means ± SD from three independent experiments. $^{a}P < 0.05$, $^{b}P < 0.01$. Scale bar, 100 μm. **(D)** Immunofluoresence analysis of the hESC-cSMCs + ECs, hESC-sSMCs + ECs and hiPSC-cSMCs + ECs, hiPSC-sSMCs + ECs tube-like structures was performed. Green fluorescence indicates Collagen IV expression (left column) whereas red fluorescence indicates ECs (VEGFR2 staining) and the merge is shown in the right column. Images were taken on Leica TCS SP5 confocal microscope and are representative of three independent experiments. Scale bar, 100 μm. **(E)** The percentage of ECs expressing CD34 in hESC-cSMCs + ECs, hESC-sSMCs + ECs, hiPSC-cSMCs + ECs and hiPSC-sSMCs + ECs tube-like structures is presented in the chart. CD34 positive ECs were evaluated after cell detachment, double-staining with anti-CD31-FITC, anti-CD34-PE antibodies and flow cytometry analysis. The percentage of CD34 + /CD31 + cells ratio is expressed in the chart as means ± SD from three independent experiments. $^{b}P < 0.01$.

CD34 + ECs, indicating more tip cells (Siemerink et al., 2012) and therefore higher angiogenic potential, were found in the hPSC-sSMC + EC co-cultures compared to hPSC-cSMC + EC co-cultures (**Figure 4E**).

Generation of Vascular Organoids: Characterization and *in vitro* Functionality

In order to maintain the stability of the phenotype of hPSC derived SMC subtypes and also maximize their MC function by resembling the 3D native tissue environment, we generated a 3D spheroidal co-culture model with human ECs.

First, we analyzed self-organization of 1,000 hPSC-SMC/ECs into one vascular organoid, when co-cultured in EGM2 medium/methylcellulose using the hanging drop method. SMCs (hPSC-cSMCs or hPSC-sMCs):ECs, at a 1:9 cell ratio, co-cultures aggregated rapidly and condensed into 3D vascular organoids within 48 h. Using pre-labeled cells, as well as indirect immunofluorescence, we observed that ECs were distributed on the surface of the vascular organoids whereas SMCs were located underneath the ECs (**Figure 5**). Immunofluoresence analysis of the cells revealed that hPSC-cSMCs highly expressed contractile proteins compared to hPSC-sSMCs, indicating a phenotype identical to that observed, when the cells were cultured in monolayers (**Figure 5**). In the same context, hPSC-sSMC/EC vascular organoids were characterized by increased deposition of ECM compared to hPSC-cSMC/EC vascular organoids (**Figure 5**).

In addition to phenotypical characterization, we tested the angiogenic potential of hPSC-SMC/EC vascular organoids in the matrigel sprouting assay *in vitro*. When vascular organoids were placed on matrigel, sprouts originated from them and were organized into a capillary-like network (**Figure 6A**), which was histomorphologically intact for longer period of time compared to the network generated by monocells (data not shown). Interestingly, unlike AD-MSC/EC mixed spheroids, at hPSC-SMC/EC vascular organoids both hESC–SMCs subtypes and ECs co-assembled in the sprouts (**Figures 6A,B**). Morphometric analysis of the sprouts originating from the vascular organoids revealed significantly longer sprouts originating from hPSC-sSMC/ECs compared to hPSC-cSMC/ECs (**Figure 6B**). Moreover, the network derived from hPSC-SMC/EC vascular organoids invaded into the matrigel, whereas the network generated by hPSC-SMCs + ECs monocells, remained on the surface of the matrigel (**Figure 6C**).

In order to explore further the angiogenic potential of the hPSC-SMC/EC vascular organoids in a more defined matrix, which, unlike matrigel, is devoid any incorporated growth factors, we generated hydrogels consisting of ECM components, such as collagen I, fibronectin and fibrinogen. As shown in **Figure 7**, hPSC-cSMC/EC and hPSC-sSMC/EC vascular organoids exhibited a sprouting profile similar to matrigel. Interestingly, hPSC-SMCs and ECs as monocells failed to generate any network, when seeded on these matrices (data not shown).

In vivo Functionality of Vascular Organoids/Spheroids

To compare *in vivo* functionality of the differentiated cells, we employed a matrigel plug assay using our hESC–SMCs subtypes mixed with primary human ECs as monocells. After 4 days of subcutaneous transplantation, more vessel structures of human origin with lumen and a broader distribution of vascular diameter were found in the vascular networks of dual cell implants (EC and hESC-cSMC) compared and to sole EC implants (**Figure 8A**). hESC-SMCs, however, could not induce capillary growth, when they were implanted in matrigel plugs without ECs (data not shown).

We then wanted to test our hypothesis that hESC-SMC (cSMC or sSMC)/EC vascular organoids, when implanted in a matrigel plug, would lead to an earlier maturation and stabilization of the vascular network compared to sole EC spheroid implants. Analysis of the vascular structures derived from human ECs in implants harvested from mice as early as 4 days after implantation, revealed significantly more luminal vessels in spheroid implants (vascular organoids or EC spheroids) compared to mono-EC implants (**Figure 7A**). Moreover, higher number of human vessels with lumen

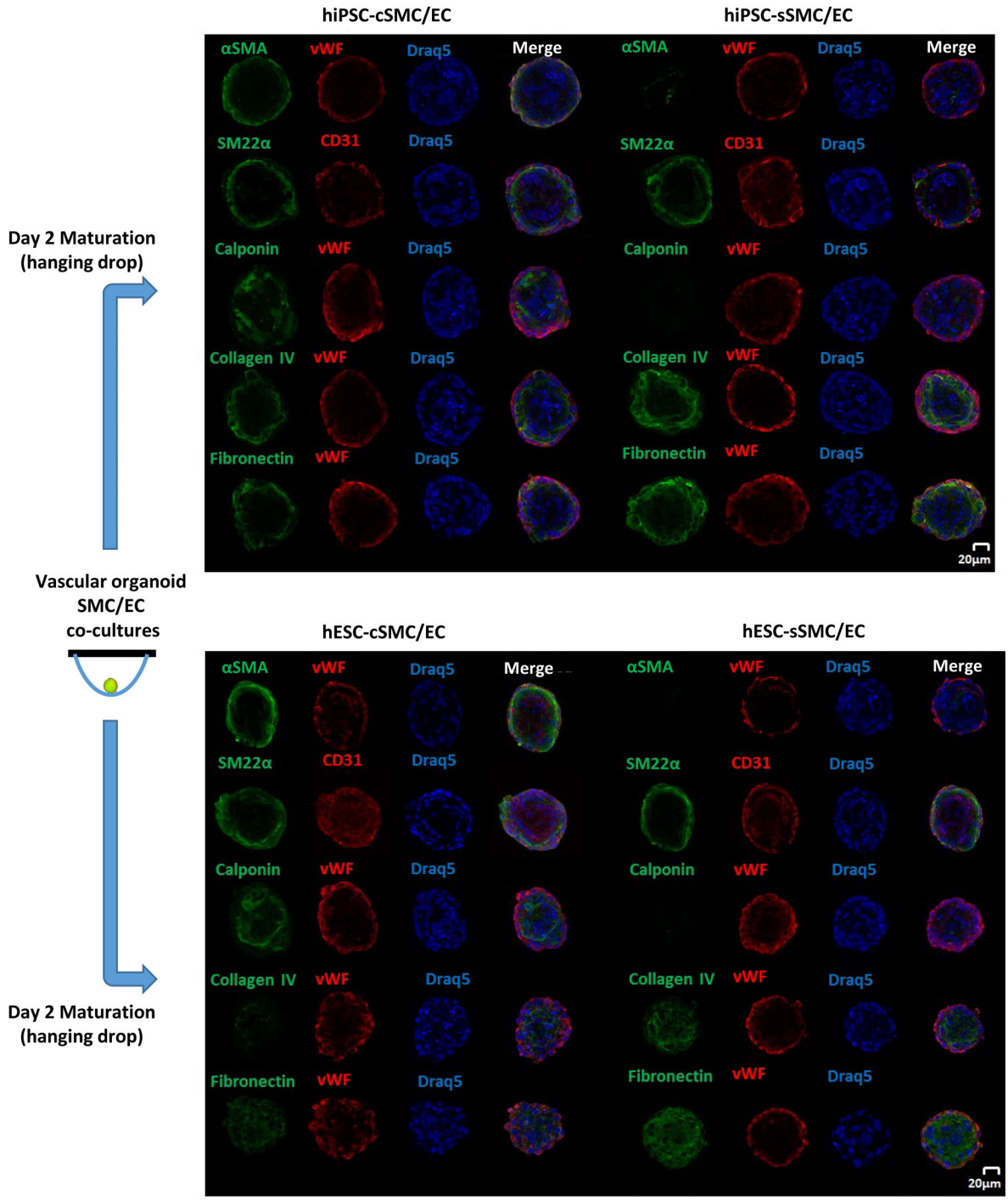

FIGURE 5 | Generation and Immunophenotypic characterization of vascular organoids. Vascular organoids were generated in 2 days using the hanging drop method (illustration). Immunofluoresence analysis was performed on vascular organoids consisting of hiPSC-cSMC/EC, hiPSC-sSMC/EC **(upper panel)** and hESC-cSMC/EC, hESC-sSMC/EC **(lower panel)**. Green fluorescence indicates either SMCs expressing αSMA (1st line), SM22α (2nd line), Calponin (3rd line), Collagen IV expression (4th line), and Fibronectin expression (5th line) whereas red indicates ECs (von Willebrand or CD31 staining) and blue indicate nuclei (Draq5 staining). Images were taken on Leica TCS SP5 confocal microscope and are representative of at least three independent experiments. Scale bar, 20 μm.

were found in hESC-SMC (cSMC and sSMC)/EC vascular organoid implants compared to hESC-cSMCs + ECs monocell implants.

Further analysis with respect to vessel diameter and classification according to their size revealed that more hCD31 positive vascular luminal structures and with greater

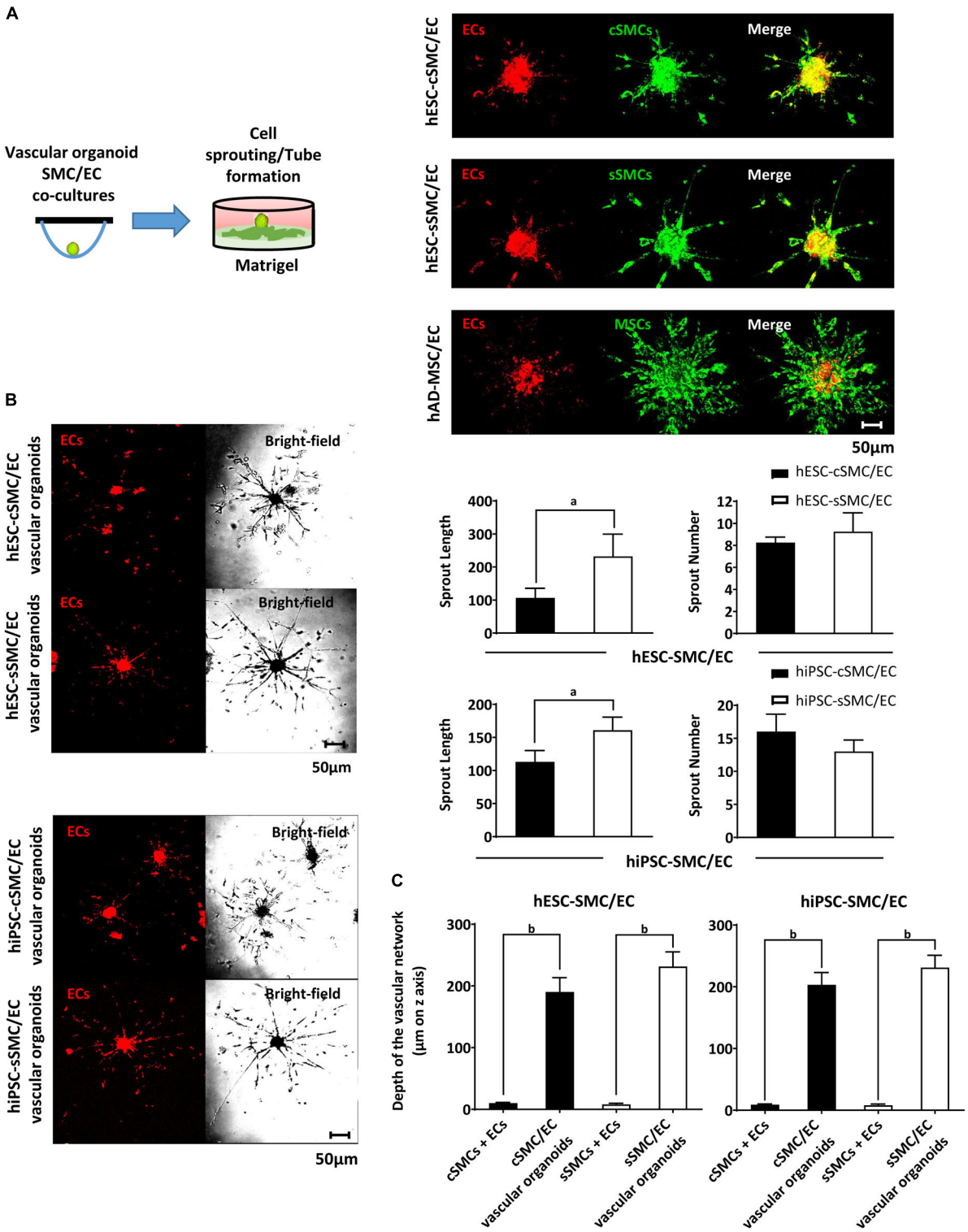

FIGURE 6 | Functional characterization of vascular organoids *in vitro.* **(A)** hPSC-SMC subtype/EC vascular organoids generated using the hanging drop method, were added on matrigel and allowed to develop sprouts (illustration). Representative images of hESC-cSMC/EC, hESC-sSMC/EC vascular organoids and hAD-MSC/EC spheroids 3d after their addition to matrigel. Red immunofluorescence indicates ECs (prelabeled with PKH26, left column), green fluorescence indicates hESC-cSMCs, hESC-sSMCs, and hAD-MSCs (pre-labeled with PKH67, middle column) and the merge is shown in the right column. Images were taken on Leica TCS SP5 confocal microscope and are representative of at least three independent experiments. Scale bar, 50 μm. **(B)** Representative images of

(Continued)

FIGURE 6 | Continued
hESC-cSMC/EC, hESC-sSMC/EC vascular organoids (upper panel) and hiPSC-cSMC/EC, hiPSC-sSMC/EC vascular organoids (lower panel) 3d after their addition on matrigel. Red immunofluorescence indicates ECs (prelabeled with PKH26, left column), whereas phase-contrast images of the same microscopic field are shown on the right column. Images were taken on Leica TCS SP5 confocal microscope and are representative of at least three independent experiments. Scale bar, 50 μm. Charts presenting length of sprouts (left) and number of sprouts (right) from hESC-cSMC/EC, hESC-sSMC/EC vascular organoids (upper charts) and hiPSC-cSMC/EC, hiPSC-sSMC/EC vascular organoids (lower charts). Images were taken 3d after the vascular organoids were plated on matrigel. Number and length of the sprouts were quantified using imageJ software and they are expressed as means ± SD from three independent experiments. $^{a}P < 0.05$. **(C)** Charts presenting the depth of the vascular network from hESC-cSMCs + ECs, hESC-sSMCs + ECs single cells or equal number of cells organized as vascular organoids (left chart) and hiPSC-cSMCs/ECs, hiPSC-sSMCs/ECs single cells or equal number of cells organized as vascular organoids (right chart). Images were taken 3d after single cells or vascular organoids had been plated on matrigel. Distance of vascular network invasion in the matrigel was quantified on Leica TCS SP5 confocal microscope (z axis) and it is expressed as mean ± SD from three independent experiments. $^{b}P < 0.01$.

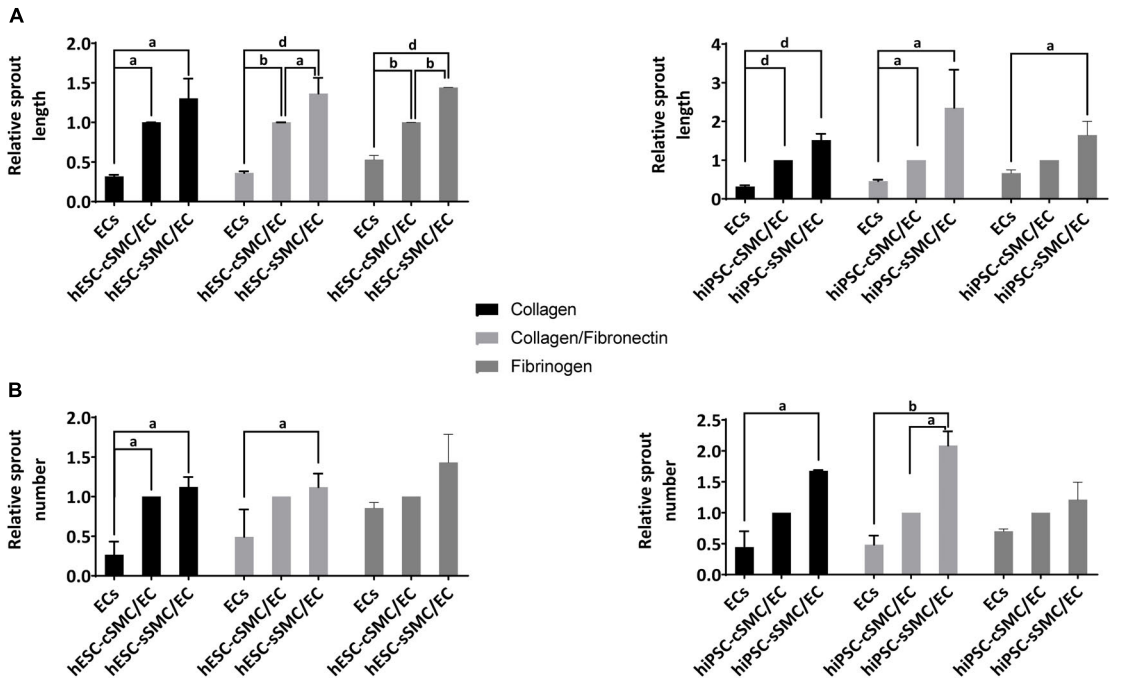

FIGURE 7 | Functional characterization of vascular organoids on hydrogels composed of defined ECM components. hPSC-SMC subtype/EC vascular organoids were added on hydrogels composed of collagen, collagen/fibronectin or fibrinogen and allowed to develop sprouts for 24 h. Length and number of sprouts were quantified using imageJ software. **(A)** Relative sprout length and **(B)** relative number of sprouts between EC spheroids and hPSC-cSMC/EC, hPSC-sSMC/EC vascular organoids from three independent experiments are presented in the charts. $^{a}P < 0.05$, $^{b}P < 0.01$, $^{d}P < 0.0001$.

lumen diameter were found in the hESC-cSMC/EC vascular organoid implants compared to mixed or sole EC monocell implants (**Figure 8A**). Statistically significant more vascular structures of human origin expressing CD34 (hCD34+) were observed in hESC-SMC (cSMC and sSMC)/EC vascular organoids compared to EC spheroid implants (**Figures 8A,B**). hESC-sSMC/EC vascular organoid implants had also more hCD34 positive structures compared to hESC-cSMC/EC vascular organoid implants, a result which is in agreement with the increased expression of CD34 in ECs, when co-cultured with hESC-sSMC (**Figure 4E**). Moreover, human vasculature that emerged from implanted hESC-cSMC/EC and hESC-sSMC/EC vascular organoids formed more anastomoses with mouse vasculature and more perfused blood vessels compared to EC spheroids (**Figure 8B**).

As shown in **Figure 8B**, in implants containing hESC-cSMC/EC and hESC-sSMC/EC vascular organoids, significantly more blood vessels were covered with αSMA-positive cells, compared to EC spheroid implants, indicating that vessels were probably stabilized by hESC-cSMC and hESC-sSMC.

To test the origin of the mural layer of the newly formed vessels, experiments were conducted in which red labeled hESC-cSMC/hESC-sSMC in vascular organoids with EC were implanted into mice. At day 2 following implantation, ECs started assembling into tubes originating from the vascular organoids and immunofluoresence analysis revealed red labeled cSMCs in close proximity to ECs tubes (green hCD31 staining), indicating human donor origin of the MCs of the assembled vessels (**Figure 8C**). Indeed, 4 days post-implantation red labeled hESC-cSMCs and hESCs-sSMCs where found next to human vascular structures (**Figure 8C**). The possibility however that murine PCs or SMCs were also recruited from surrounding mouse tissue cannot be excluded. Overall, these results show that EC spheroids displayed lower ability to form stable and perfused

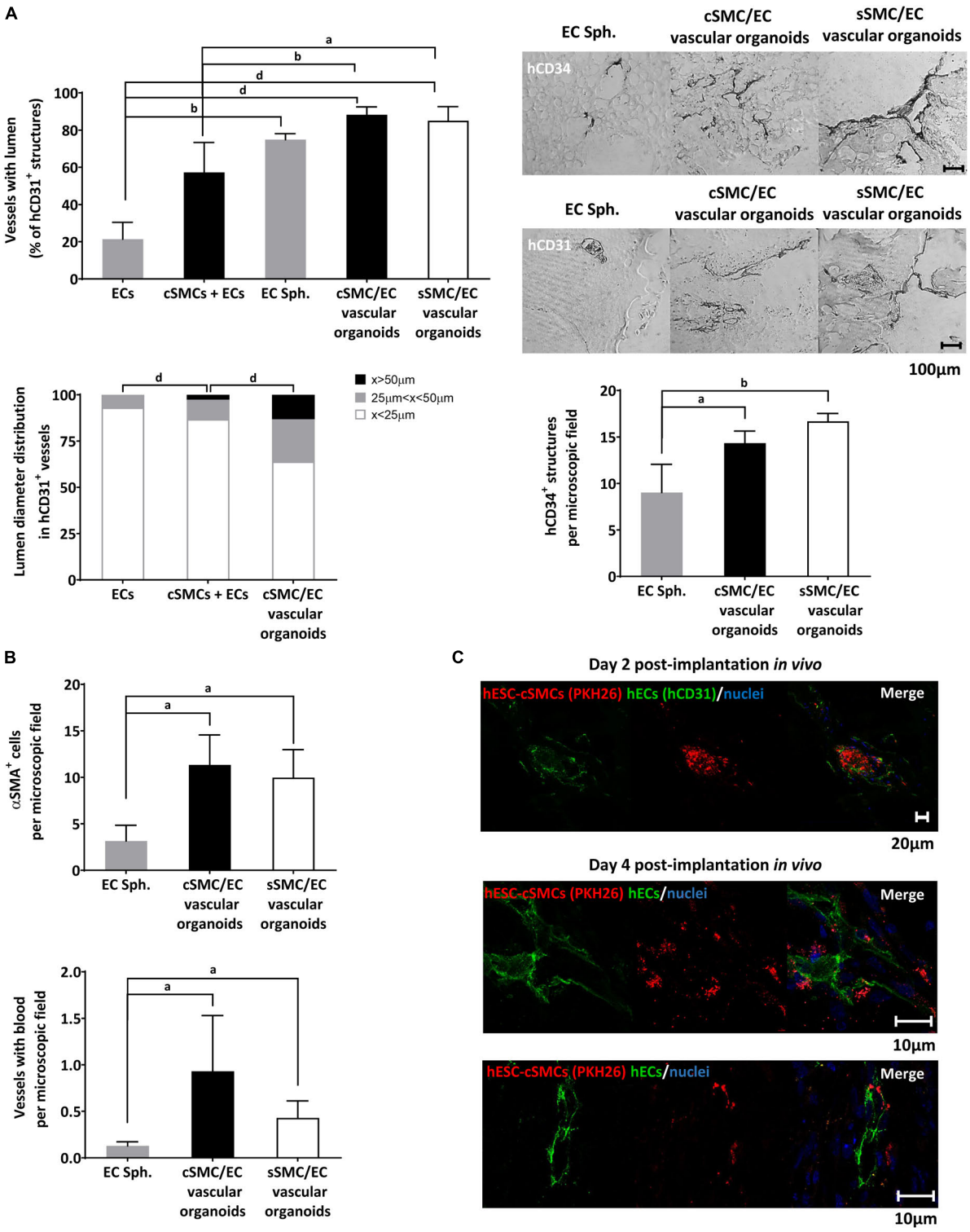

FIGURE 8 | Functional characterization of vascular organoids *in vivo.* **(A)** Chart presenting percentage of vessels of human origin (anti-hCD31 positive) with lumens in ECs, hESC-cSMCs + ECs single cell matrigel implants and in EC spheroids, hESC-cSMC/EC, hESC-sSMC/EC vascular organoid matrigel implants, 4 days after the implantation (upper). Vascular structures of human origin (anti-hCD31 positive) with lumen were quantified per microscopic field and expressed as percentage of the total anti-hCD31 positive structures. Chart presenting the lumen distribution of human vascular structures (anti-hCD31 positive) in ECs, hESC-cSMC/EC single cell matrigel implants and in hESC-cSMC/EC vascular organoid matrigel implants, 4 days after the implantation (left). Chart presenting the number of anti-hCD34

(Continued)

FIGURE 8 | Continued
positive structures in EC spheroid, hESC-cSMC/EC and hESC-sSMC/EC vascular organoid matrigel implants, 4 days after the implantation (right). All quantifications were performed in at least five fields and three sections per implant. All graph data are expressed as means ± SD from four animals per condition. $^{a}P < 0.05$, $^{b}P < 0.01$, $^{d}P < 0.001$. Representative images of sections stained with anti-hCD34 antibody (upper panel) or anti-hCD31 antibody (lower panel) using immunohistochemistry in EC spheroids, hESC-cSMC/EC, and hESC-sSMC/EC vascular organoid matrigel implants (images from left to right), 4 days after the implantation. Scale bar, 100 μm. **(B)** *In vivo* analysis of vessel maturation and perfusion. Sections from EC spheroids, hESC-cSMC/EC and hESC-sSMC/EC vascular organoid matrigel implants 4 days after implantations were stained with anti-αSMA antibody and the number of positive cells per microscopic field was quantified and presented in the upper chart. Vascular structures containing red blood cells/microscopic field in EC spheroid, hESC-cSMC/EC and hESC-sSMC/EC vascular organoid matrigel implants 4 days after implantation are presented in the lower histogram. All quantifications were performed in at least five fields and three sections per implant. All graph data are expressed as means ± SD from four animals per condition. $^{a}P < 0.05$. **(C)** Immunofluoresence analysis of sections from ECs spheroids, hESC-cSMC/EC and hESC-sSMC/EC vascular organoid matrigel implants 2 days (upper panel) and 4 days (lower panels) after implantation. Green fluorescence indicates human ECs (anti-hCD31-FITC staining) (left images), red fluorescence indicates hESC-cSMCs or hESC-sSMCs (prelabeled with PKH26) and blue fluorescence indicates nuclei (Draq5 staining). Merged images are shown (right images). Images were taken on Leica TCS SP5 confocal microscope and are representative of 2 animals (2 days) and 4 animals (4 days). Scale bars, 10, 20 μm.

vascular networks as early as in 4 days compared to vascular organoids containing either SMC subtype.

DISCUSSION

In the current study, we developed a quick and robust method to generate both cSMCs and sSMCs from hPSCs. Moreover, the assembly of these SMC subtypes into 3D spheroid co-cultures served as focal points for the sprouting of capillary-like structures *in vitro* and their delivery *in vivo* led to rapid generation of a complex functional vascular network.

In our previous study (Kouroupis et al., 2016) hiPSCs were fully committed to the mesodermal lineage by gradually increasing the serum concentration to 10% for 20 days *in vitro*. Since serum downregulates the expression of contractile proteins (Wanjare et al., 2013b), using a short-term (11 days) reduced-serum induction protocol, we have successfully induced hPSCs toward the cSMC phenotype (spindle-shaped morphology, >90–95% positivity for NG2, and CD29, CD44, CD73, CD105 mesodermal markers, high expression of early contractile markers αSMA, Calponin, and SM22α, low expression of the maturation marker SMMHC),which contracted when exposed to carbachol (Owens et al., 2004; Rensen et al., 2007). Kumar et al. (2017) have also generated cSMCs from hiPSCs using a longer differentiation protocol through a mesenchymoangioblast intermediate population, by exposure of cells first to high serum-containing media (Wanjare et al., 2013a), followed by low-serum induction. According to our differentiation protocol, a combination of low serum conditions and subsequent seeding of the cells on gelatin, as ECM coating, was adequate to rapidly generate an immature cSMC phenotype (αSMA^{high}, $Calponin^{high}$, $SM22^{high}$, $SMMHC^{+}$) that remained stable and without signs of senescence for at least 8 passages. Furthermore, short treatment with TGFβ1 (Chen et al., 2016) and heparin (Hashimoto et al., 2005) induced maturation of the hPSC-cSMCs seen by the upregulated expression of SMMHC, the most mature marker that demarcates the contractile vSMCs (Wanjare et al., 2013a). Finally, we induced transition of hPSC-cSMC to sSMCs (hPSC-sSMC), a phenotype present during neovascularization, embryonic vessel development and in injured or diseased vessels during vessel remodeling (Wanjare et al., 2013b), by the addition of FGF2, a mitogen known to promote primary vascular cSMC conversion to sSMCs (Jackson and Reidy, 1993). Indeed, short-term FGF2 exposure (2 days) resulted in downregulation of αSMA, Calponin, and SM22α expression, consistent with the development of hPSC-sSMCs. In addition, hPSC-sSMCs exhibited characteristic functions of sSMCs (Hao et al., 2003; Rensen et al., 2007), such as increased cell proliferation and migration, ECM protein deposition and upregulated MMP-2 and 9 activity compared to hPSC-cSMCs.

Both hPSC-cSMCs and sSMCs exhibited similar multipotent potential giving rise to osteocytes and chondrocytes, a typical feature of mesenchymal precursors which has been also described in MCs (Crisan et al., 2008; Speer et al., 2009; Majesky et al., 2017). In fact, it has been shown that some adult multipotent stromal cells might belong to a subset of MCs (Crisan et al., 2008). Indeed, *in vitro* tri-lineage differentiation of PCs has been documented (Farrington-Rock et al., 2004; Crisan et al., 2008), however this has been questioned regarding SMCs (Nguyen et al., 2013; Tang et al., 2013). Using fate mapping and lineage tracing approaches the multilineage potential for osteogenic and chondrogenic differentiation of SMCs has been attributed either to a reprogramming-like process of differentiated SMCs that leads to the generation of multipotent progenitor cells (Speer et al., 2009; Majesky et al., 2017) or to the presence of a progenitor cell population, such as multipotent vascular stem cells-MVSCs in the SMC culture that gives rise to both SMCs subtypes and to other lineages as well (Tang et al., 2012) or to another mesenchymal precursor (Kumar et al., 2017).}. The lack of SMC culture homogeneity at a specific differentiation stage, which may include immature and partially differentiated MVSCs, and also the specificity of the marker used for the lineage tracing might explain the disparity of the various reports (Nguyen et al., 2013; Tang et al., 2013). Based on these studies, our hPSC-cSMCs having a rather immature phenotype (proliferation potential, low expression of SMMHC) could exhibit multilineage potential as well. However, the existence of a minor partially differentiated subpopulation in the hPSC-SMCs culture cannot be excluded.

MCs are committed to stabilize the vasculature by paracrine and cell-cell interactions with neighboring ECs (Armulik et al., 2011). However, characterization of cSMCs and sSMCs derived from hPSCs regarding their MC function is limited in the literature. Our study reveals that both cell subtypes integrate in the EC network on matrigel and inhibit its regression, two essential features of MCs and important aspects for the use of

these cells in tissue engineering applications. AD-MSCs as well as hiPSC-MSCs (Kouroupis et al., 2016) failed to inhibit the EC network regression indicating that our generated cells, although exhibiting some phenotypic and functional features of MSCs, display mainly MC functions. Furthermore, both cSMCs and sSMCs monolayers induced EC tubulogenesis. Notably, sSMCs stimulated the organization of a more complex and expanded EC network compared to cSMCs as indicated by morphometric parameters, generation of a vascular basement membrane structure and higher percentage of ECs expressing CD34, a marker of tip cells (Siemerink et al., 2012). This differential effect of the two subtypes could be either due to specific SMC subtype-EC interactions or to increased extracellular deposition of fibronectin and collagen IV by sSMCs that could act as a provisional matrix promoting the EC tubulogenesis. These results are in agreement with the physiological role of sSMCs during both neovascularization in the embryo and vascular remodeling in adult blood vessels (Wanjare et al., 2013b).

In line with these findings, the generated SMC derivatives could demonstrate an important building block toward the study of developmental processes and diseases implicating these cell subtypes. In addition, they could also be used for the reconstruction of physiologically relevant vasculature. Specifically, the use of a rather immature but committed hPSC-cSMC, exhibiting both proliferation (unlike mature cSMCs) and maturation potential, might be favorable for tissue engineering applications. However, transplantation of mono-cells *in vivo* is usually characterized by low survival rate (Hayashi et al., 2004). Moreover, the lack of SMC culture homogeneity at a specific differentiation stage, the SMC phenotypic plasticity as well as the fact that SMC phenotype and function are tightly regulated by their surrounding microenvironment and by their organization within the tissue (Rensen et al., 2007), all indicate a high risk of SMCs to acquire an unfavorable (inflammatory) phenotype, when implanted as monocells in a hostile environment (Chistiakov et al., 2015). These obstacles could be overcome by the generation of 3D cell structures (small-scale vascular organoids) containing both ECs and SMCs subtypes, which unlike traditional 2D monolayer cultures, would provide enhanced cell–cell interactions that closely mimic the natural/physiological tissue microenvironment with beneficial effects on cell survival, phenotypic stability and function, when transplanted *in vivo* (Derda et al., 2009; Bhang et al., 2011). In Korff and Augustin (1998) introduced 3D EC spheroids as an *in vitro* model exhibiting angiogenic responses and sprouting behavior *in vivo*. Since then, multi-cellular spheroids have become a common 3D cell culture system, generated either from one or many cell types for multiple applications (reviewed in Laschke and Menger, 2017). Accordingly, we efficiently generated for the first time 3D SMC-EC vascular organoids using both hPSC-SMC subtypes (cSMCs and sSMCs) and ECs. Randomly mixed hPSC-cSMCs:ECs or hPSC-sSMCs:ECs in a fixed ratio of 1:9 underwent self-assembly into a segregated 3D structure similar to primary vSMC/EC spheroids (Korff et al., 2001) representing the physiological assembly of a normal blood vessel. Specifically, they were characterized by a multicellular spheroidal SMC core and an outer EC layer, which can be regarded as an inside-out assembly of a resting vessel wall. Phenotypic analysis of hPSC-SMCs, when co-cultured with ECs in vascular organoids, showed preservation of the two subtype signatures, since coalescence of hPSC-cSMCs/ECs were characterized by high expression of contractile proteins (Calponin, αSMA and SM22α) whereas hPSC-SMC/EC 3D vascular organoids significantly enhanced the deposition of ECM proteins, such as fibronectin and collagen IV. Implantation of the generated vascular organoids in matrigel or hydrogels composed of individual ECM components led to increased capillary network sprouting, which was characterized by SMC-EC co-alignment within the generated sprouts. However, since MCs are characterized by high plasticity involving a continuum of cell phenotypes, from PCs to SMCs, including transitional cell phenotypes as well (Holm et al., 2018), the acquisition of a phenotype closer to PCs by the SMC derivatives in the generated capillary-like network cannot be excluded. hPSC-sSMC/EC vascular organoids gave rise to longer sprouts compared to hPSC-cSMC/EC probably due to the migratory profile and higher MMP2 activity (and subsequent ECM degradation) of hPSC-sSMC, both associated with vessel remodeling. hPSC-SMC subtype/EC vascular organoids were superior to EC spheroids regarding sprouting, while hPSC-SMC and EC monocells failed to generate a capillary like network in simple ECM hydrogels. In summary, the generated SMC-EC vascular organoids preserved the phenotypic and functional signatures of the two SMCs subtypes, and exhibited the potential to give rise to a durable (compared to mono-cells) 3D vascular network *in vitro*.

Upon subcutaneous implantation in mice, hESC-SMC/EC vascular organoids not only generated more lumenized vascular structures and with greater diameter compared to ECs and hESC-SMCs/ECs monocell implants, but also formed more hCD31 + /CD34 + vessels, more anastomoses with the recipient's vasculature and more perfused vessels compared to EC spheroids. Therefore, the matrigel plug assay strongly demonstrated the capacity of both hESC-cSMC/EC and hESC-sSMC/EC vascular organoids to serve as focal starting points of outgrowing capillary sprouts consisting of both SMCs and ECs in order to generate, in a short time frame, mature human vascular structures with the ability to anastomose with resident vasculature *in vivo*. However, although we observed pre-stained hPSC-SMCs aligned along the vessels from the human ECs, we cannot exclude the participation of MCs from the host as well. Given that SMC subtypes were unable to induce neovascularization, when implanted alone (without ECs) *in vivo* as monocells, it seems that their role in the 3D vascular organoids is mainly on vascular remodeling and stabilization. Furthermore, an additional positive effect of hESC-SMC on hEC survival (Korff et al., 2001) could account for the increased number of vascular structures of human origin in the vascular organoid implants compared to EC spheroid implants. Our 3D spheroid approach is also flexible and versatile enough to enable further modifications (reviewed in Kouroupis et al., 2018), various applications regarding specific disease models, routes of administration (injectable), types of scaffolds, length of observation, which might further uncover the differential effect of hPSC-cSMC and hPSC-sSMC on vascular remodeling *in vivo*.

In summary, we developed a rapid differentiation protocol for hPSCs toward immature cSMCs, which can further mature after a short TGFβ1/heparin treatment or be induced to sSMCs after a short induction with FGF2. The phenotypic modulation of vascular SMCs is an important vascular injury repair mechanism and therefore, it plays a major role in the pathogenesis of a number of diseases, including atherosclerosis, restenosis and transplant vasculopathy (Beamish et al., 2010; Chistiakov et al., 2015). Our innovative differentiation strategy, unlike the previously reported protocols, offers the possibility of studying, in the same simple experimental set up, the molecular mechanisms underlying phenotypic plasticity of the generated hPSC-SMCs. Given that FGF-TGFβ signaling antagonism is reported as the primary regulator of the SMC phenotypes, our protocol is an ideal model to study this mechanism.

Based on the recent perception that MCs consist of a phenotypic continuing spectrum with PCs at the one end and SMCs on the other, it seems that using our differentiation protocol we generated MCs whose features cluster in the SMC phenotypic area, without excluding the existence of transitional cell types. Heterogeneity and spatiotemporal variation in protein expression is characteristic of MCs and therefore, it must be taken into consideration, when tissue engineering approaches are designed, where preservation or induction of an organ specific functional MC subtype is needed. hPSC-cSMCs, for instance, could be used as a homeostatic vSMC pool in cases of chronic inflammatory conditions or tissue transplantation (such as human pancreatic islet transplantation), whereas in the case of trauma, highly proliferative hPSC-sSMC would boost the matrix deposition and neovascularization locally *in vivo*. In this context, our simple approach of fabricating 3D vascular organoids of SMC subtypes and ECs and analyzing their phenotype and function is novel and is the first step in designing more complex 3D tissue engineering constructs (by also including organ specific cells and growth factors). Therefore, by fine tuning the phenotypic MC profile we will be able to understand the organotypically differentiated MCs and their functional plasticity and contribution to organ specific health and disease conditions. Accordingly, we propose a flexible, small-scale 3D organoid-like platform consisting of hPSC-SMC/ECs, which seems to be superior to mixed monocells and sole ECs regarding the development of a mature vasculature *in vivo* and is ready-to-use for various tissue engineering applications. Finally, these vascular organoids are a defined *in vitro* model for studying the paracrine interactions between ECs and SMC subtypes that regulate vessel assembly, phenotype modulation, maturation, maintenance and vessel destabilization in a way that mimics the physiological assembly of the normal vasculature and therefore might serve as a platform for drug development, including estimations of compound preclinical toxicity and potential metabolic liability.

DATA AVAILABILITY STATEMENT

All datasets generated for this study are included in the article/**Supplementary Material**.

ETHICS STATEMENT

The animal study was reviewed and approved by the Regional Directorate of Rural Economy and Veterinary Medicine, Epirus Region, Greece.

AUTHOR CONTRIBUTIONS

MM performed the experiments and drafted the manuscript. DK conceived the study, performed the experiments, and drafted the manuscript. AKy generated the hiPSCs. FB performed the immunohistochemistry. AKa generated the hydrogels. TF conceived the study and interpreted results. CM conceived the study, interpreted results, and edited the manuscript. EB conceived the study, performed the experiments, guided the experiments, interpreted results, and drafted and edited the manuscript.

FUNDING

This research supported by (a) the European Social Fund (ESF) and the Greek State [LS7 (2012)]. The research project is implemented within the framework of the Action «Supporting Postdoctoral Researchers» of the Operational Program "Education and Lifelong Learning" (Action's Beneficiary: General Secretariat for Research and Technology), (b) Greece and the European Union (European Social Fund-ESF) through the Operational Programme «Human Resources Development, Education and Lifelong Learning 2014–2020» in the context of the project "Generation of distinct phenotypes of mural cells from differentiation of human pluripotent stem cells: application in the generation of vascularized tissueengineered constructs" (5047550). MM was supported by a Ph.D. fellowship from the State Scholarships Foundation (IKY).

ACKNOWLEDGMENTS

We thank Dr. Dimitrios Stellas at Centre for Basic Research, Biomedical Research Foundation of the Academy of Athens, Greece for his technical contribution on animal model interventions. We thank the confocal laser microscope facility of the IMBB-University of Ioannina for the use of the Leica TCS-SP scanning confocal microscope. We acknowledge BioImaging-GR: MIS 5002755 funded by NSRF 2014–2020 and co-financed by Greece and the European Regional Development Fund for the IncuCyte.

SUPPLEMENTARY MATERIAL

The Supplementary Material for this article can be found online at: https://www.frontiersin.org/articles/10.3389/fbioe.2020.00278/full#supplementary-material

REFERENCES

Alajati, A., Laib, A. M., Weber, H., Boos, A. M., Bartol, A., Ikenberg, K., et al. (2008). Spheroid-based engineering of a human vasculature in mice. *Nat. Methods* 5, 439–445. doi: 10.1038/nmeth.1198

Armulik, A., Abramsson, A., and Betsholtz, C. (2005). Endothelial/pericyte interactions. *Circ. Res.* 97, 512–523. doi: 10.1161/01.RES.0000182903.16652.d7

Armulik, A., Genové, G., and Betsholtz, C. (2011). Pericytes: developmental, physiological, and pathological perspectives, problems, and promises. *Dev. Cell* 21, 193–215. doi: 10.1016/j.devcel.2011.07.001

Au, P., Tam, J., Duda, D. G., Lin, P. C., Munn, L. L., Fukumura, D., et al. (2009). Paradoxical effects of PDGF-BB overexpression in endothelial cells on engineered blood vessels *in vivo*. *Am. J. Pathol.* 175, 294–302. doi: 10.2353/ajpath.2009.080887

Beamish, J. A., He, P., Kottke-Marchant, K., and Marchant, R. E. (2010). Molecular regulation of contractile smooth muscle cell phenotype: implications for vascular tissue engineering. *Tissue Eng. Part B Rev.* 16, 467–491. doi: 10.1089/ten.TEB.2009.0630

Bellou, S., Karali, E., Bagli, E., Al-Maharik, N., Morbidelli, L., Ziche, M., et al. (2012). The isoflavone metabolite 6-methoxyequol inhibits angiogenesis and suppresses tumor growth. *Mol. Cancer* 11:35. doi: 10.1186/1476-4598-11-35

Benning, L., Gutzweiler, L., Trondle, K., Riba, J., Zengerle, R., Koltay, P., et al. (2018). Assessment of hydrogels for bioprinting of endothelial cells. *J. Biomed. Mater. Res. A* 106, 935–947. doi: 10.1002/jbm.a.36291

Bhang, S. H., Cho, S. W., La, W. G., Lee, T. J., Yang, H. S., Sun, A. Y., et al. (2011). Angiogenesis in ischemic tissue produced by spheroid grafting of human adipose-derived stromal cells. *Biomaterials* 32, 2734–2747. doi: 10.1016/j.biomaterials.2010.12.035

Boyd, N. L., Robbins, K. R., Dhara, S. K., West, F. D., and Stice, S. L. (2009). Human embryonic stem cell-derived mesoderm-like epithelium transitions to mesenchymal progenitor cells. *Tissue Eng. Part A* 15, 1897–1907. doi: 10.1089/ten.tea.2008.0351

Carmeliet, P., and Jain, R. K. (2000). Angiogenesis in cancer and other diseases. *Nature* 407, 249–257. doi: 10.1038/35025220

Cathery, W., Faulkner, A., Maselli, D., and Madeddu, P. (2018). Concise review: the regenerative journey of pericytes toward clinical translation. *Stem Cells* 36, 1295–1310. doi: 10.1002/stem.2846

Cecchettini, A., Rocchiccioli, S., Boccardi, C., and Citti, L. (2011). Vascular smooth-muscle-cell activation: proteomics point of view. *Int. Rev. Cell Mol. Biol.* 288, 43–99. doi: 10.1016/B978-0-12-386041-5.00002-9

Chen, P. Y., Qin, L., Li, G., Tellides, G., and Simons, M. (2016). Fibroblast growth factor (FGF) signaling regulates transforming growth factor beta (TGFbeta)-dependent smooth muscle cell phenotype modulation. *Sci. Rep.* 6:33407. doi: 10.1038/srep33407

Chistiakov, D. A., Orekhov, A. N., and Bobryshev, Y. V. (2015). Vascular smooth muscle cell in atherosclerosis. *Acta Physiol.* 214, 33–50. doi: 10.1111/apha.12466

Crisan, M., Yap, S., Casteilla, L., Chen, C. W., Corselli, M., Park, T. S., et al. (2008). A perivascular origin for mesenchymal stem cells in multiple human organs. *Cell Stem Cell* 3, 301–313. doi: 10.1016/j.stem.2008.07.003

Dar, A., and Itskovitz-Eldor, J. (2015). Therapeutic potential of perivascular cells from human pluripotent stem cells. *J. Tissue Eng. Regen. Med.* 9, 977–987. doi: 10.1002/term.1698

Derda, R., Laromaine, A., Mammoto, A., Tang, S. K., Mammoto, T., Ingber, D. E., et al. (2009). Paper-supported 3D cell culture for tissue-based bioassays. *Proc. Natl. Acad. Sci. U.S.A.* 106, 18457–18462. doi: 10.1073/pnas.0910666106

Farrington-Rock, C., Crofts, N. J., Doherty, M. J., Ashton, B. A., Griffin-Jones, C., and Canfield, A. E. (2004). Chondrogenic and adipogenic potential of microvascular pericytes. *Circulation* 110, 2226–2232. doi: 10.1161/01.CIR.0000144457.55518.E5

Hao, H., Gabbiani, G., and Bochaton-Piallat, M.-L. (2003). Arterial smooth muscle cell heterogeneity. *Arterioscler. Thromb. Vasc. Biol.* 23, 1510–1520. doi: 10.1161/01.ATV.0000090130.85752.ED

Hashimoto, T., Kihara, M., Sato, K., Imai, N., Tanaka, Y., Sakai, M., et al. (2005). Heparin recovers AT1 receptor and its intracellular signal transduction in cultured vascular smooth muscle cells. *FEBS Lett.* 579, 281–284. doi: 10.1016/j.febslet.2004.11.093

Hashizume, H., Baluk, P., Morikawa, S., McLean, J. W., Thurston, G., Roberge, S., et al. (2000). Openings between defective endothelial cells explain tumor vessel leakiness. *Am. J. Pathol.* 156, 1363–1380. doi: 10.1016/S0002-9440(10)65006-7

Hayashi, M., Li, T. S., Ito, H., Mikamo, A., and Hamano, K. (2004). Comparison of intramyocardial and intravenous routes of delivering bone marrow cells for the treatment of ischemic heart disease: an experimental study. *Cell Transplant.* 13, 639–647.

Hedin, U., and Thyberg, J. (1987). Plasma fibronectin promotes modulation of arterial smooth-muscle cells from contractile to synthetic phenotype. *Differentiation* 33, 239–246. doi: 10.1111/j.1432-0436.1987.tb01563.x

Heidary Rouchi, A., and Mahdavi-Mazdeh, M. (2015). Regenerative medicine in organ and tissue transplantation: shortly and practically achievable? *Int. J. Organ. Transplant. Med.* 6, 93–98.

Holm, A., Heumann, T., and Augustin, H. G. (2018). Microvascular mural cell organotypic heterogeneity and functional plasticity. *Trends Cell Biol.* 28, 302–316. doi: 10.1016/j.tcb.2017.12.002

Holycross, B. J., Blank, R. S., Thompson, M. M., Peach, M. J., and Owens, G. K. (1992). Platelet-derived growth factor-BB-induced suppression of smooth muscle cell differentiation. *Circ. Res.* 71, 1525–1532. doi: 10.1161/01.res.71.6.1525

Jackson, C. L., and Reidy, M. A. (1993). Basic fibroblast growth factor: its role in the control of smooth muscle cell migration. *Am. J. Pathol.* 143, 1024–1031.

Jain, R. K. (2005). Normalization of tumor vasculature: an emerging concept in antiangiogenic therapy. *Science* 307, 58–62. doi: 10.1126/science.1104819

Jain, R. K., Au, P., Tam, J., Duda, D. G., and Fukumura, D. (2005). Engineering vascularized tissue. *Nat. Biotechnol.* 23, 821–823. doi: 10.1038/nbt0705-821

Korff, T., and Augustin, H. G. (1998). Integration of endothelial cells in multicellular spheroids prevents apoptosis and induces differentiation. *J. Cell Biol.* 143, 1341–1352. doi: 10.1083/jcb.143.5.1341

Korff, T., Kimmina, S., Martiny-Baron, G., and Augustin, H. G. (2001). Blood vessel maturation in a 3-dimensional spheroidal coculture model: direct contact with smooth muscle cells regulates endothelial cell quiescence and abrogates VEGF responsiveness. *FASEB J.* 15, 447–457. doi: 10.1096/fj.00-0139com

Korff, T., Krauss, T., and Augustin, H. G. (2004). Three-dimensional spheroidal culture of cytotrophoblast cells mimics the phenotype and differentiation of cytotrophoblasts from normal and preeclamptic pregnancies. *Exp. Cell Res.* 297, 415–423. doi: 10.1016/j.yexcr.2004.03.043

Kouroupis, D., Kyrkou, A., Triantafyllidi, E., Katsimpoulas, M., Chalepakis, G., Goussia, A., et al. (2016). Generation of stem cell-based bioartificial anterior cruciate ligament (ACL) grafts for effective ACL rupture repair. *Stem Cell Res.* 17, 448–457. doi: 10.1016/j.scr.2016.04.016

Kouroupis, D., Sanjurjo-Rodriguez, C., Jones, E., and Correa, D. (2018). Mesenchymal stem cell functionalization for enhanced therapeutic applications. *Tissue Eng. Part B Rev.* 25, 55–77. doi: 10.1089/ten.teb.2018.0118

Kumar, A., D'Souza, S. S., Moskvin, O. V., Toh, H., Wang, B., Zhang, J., et al. (2017). Specification and diversification of pericytes and smooth muscle cells from Mesenchymoangioblasts. *Cell Rep.* 19, 1902–1916. doi: 10.1016/j.celrep.2017.05.019

Kusuma, S., and Gerecht, S. (2013). Recent progress in the use of induced pluripotent stem cells in vascular regeneration. *Expert Rev. Cardiovasc. Ther.* 11, 661–663. doi: 10.1586/erc.13.54

Kyrkou, A., Stellas, D., Syrrou, M., Klinakis, A., Fotsis, T., and Murphy, C. (2016). Generation of human induced pluripotent stem cells in defined, feeder-free conditions. *Stem Cell Res.* 17, 458–460. doi: 10.1016/j.scr.2016.05.006

Laschke, M. W., and Menger, M. D. (2017). Spheroids as vascularization units: from angiogenesis research to tissue engineering applications. *Biotechnol. Adv.* 35, 782–791. doi: 10.1016/j.biotechadv.2017.07.002

Liu, L. P., and Zheng, Y. W. (2019). Predicting differentiation potential of human pluripotent stem cells: Possibilities and challenges. *World J. Stem Cells* 11, 375–382. doi: 10.4252/wjsc.v11.i7.375

Majesky, M. W., Horita, H., Ostriker, A., Lu, S., Regan, J. N., Bagchi, A., et al. (2017). Differentiated smooth muscle cells generate a subpopulation of resident vascular progenitor cells in the adventitia regulated by Klf4. *Circ. Res.* 120, 296–311. doi: 10.1161/CIRCRESAHA.116.309322

Melero-Martin, J. M., De Obaldia, M. E., Kang, S. Y., Khan, Z. A., Yuan, L., Oettgen, P., et al. (2008). Engineering robust and functional vascular networks

in vivo with human adult and cord blood-derived progenitor cells. *Circ. Res.* 103, 194–202. doi: 10.1161/CIRCRESAHA.108.178590

Nakatsu, M. N., Sainson, R. C., Aoto, J. N., Taylor, K. L., Aitkenhead, M., Perez-del-Pulgar, S., et al. (2003). Angiogenic sprouting and capillary lumen formation modeled by human umbilical vein endothelial cells (HUVEC) in fibrin gels: the role of fibroblasts and Angiopoietin-1. *Microvasc. Res.* 66, 102–112. doi: 10.1016/s0026-2862(03)00045-1

Nguyen, A. T., Gomez, D., Bell, R. D., Campbell, J. H., Clowes, A. W., Gabbiani, G., et al. (2013). Smooth muscle cell plasticity: fact or fiction? *Circ. Res.* 112, 17–22. doi: 10.1161/CIRCRESAHA.112.281048

Nillesen, S. T., Geutjes, P. J., Wismans, R., Schalkwijk, J., Daamen, W. F., and van Kuppevelt, T. H. (2007). Increased angiogenesis and blood vessel maturation in acellular collagen-heparin scaffolds containing both FGF2 and VEGF. *Biomaterials* 28, 1123–1131. doi: 10.1016/j.biomaterials.2006.10.029

Owens, G. K., Kumar, M. S., and Wamhoff, B. R. (2004). Molecular regulation of vascular smooth muscle cell differentiation in development and disease. *Physiol. Rev.* 84, 767–801. doi: 10.1152/physrev.00041.2003

Panopoulou, E., Murphy, C., Rasmussen, H., Bagli, E., Rofstad, E. K., and Fotsis, T. (2005). Activin A suppresses neuroblastoma xenograft tumor growth via antimitotic and antiangiogenic mechanisms. *Cancer Res.* 65, 1877–1886. doi: 10.1158/0008-5472.CAN-04-2828

Regan, J. N., and Majesky, M. W. (2009). Building a vessel wall with notch signaling. *Circ. Res.* 104, 419–421. doi: 10.1161/CIRCRESAHA.109.194233

Rensen, S. S., Doevendans, P. A., and van Eys, G. J. (2007). Regulation and characteristics of vascular smooth muscle cell phenotypic diversity. *Neth. Heart J.* 15, 100–108. doi: 10.1007/bf03085963

Schechner, J. S., Nath, A. K., Zheng, L., Kluger, M. S., Hughes, C. C., Sierra-Honigmann, M. R., et al. (2000). In vivo formation of complex microvessels lined by human endothelial cells in an immunodeficient mouse. *Proc. Natl. Acad. Sci. U.S.A.* 97, 9191–9196. doi: 10.1073/pnas.152242297

Shepro, D., and Morel, N. M. (1993). Pericyte physiology. *FASEB J.* 7, 1031–1038. doi: 10.1096/fasebj.7.11.8370472

Siemerink, M. J., Klaassen, I., Vogels, I. M., Griffioen, A. W., Van Noorden, C. J., and Schlingemann, R. O. (2012). CD34 marks angiogenic tip cells in human vascular endothelial cell cultures. *Angiogenesis* 15, 151–163. doi: 10.1007/s10456-011-9251-z

Speer, M. Y., Yang, H. Y., Brabb, T., Leaf, E., Look, A., Lin, W. L., et al. (2009). Smooth muscle cells give rise to osteochondrogenic precursors and chondrocytes in calcifying arteries. *Circ. Res.* 104, 733–741. doi: 10.1161/CIRCRESAHA.108.183053

Takahashi, K., and Yamanaka, S. (2006). Induction of pluripotent stem cells from mouse embryonic and adult fibroblast cultures by defined factors. *Cell* 126, 663–676. doi: 10.1016/j.cell.2006.07.024

Tang, Z., Wang, A., Wang, D., and Li, S. (2013). Smooth muscle cells: to be or not to be? Response to Nguyen et Al. *Circ. Res.* 112, 23–26. doi: 10.1161/CIRCRESAHA.112.281055

Tang, Z., Wang, A., Yuan, F., Yan, Z., Liu, B., Chu, J. S., et al. (2012). Differentiation of multipotent vascular stem cells contributes to vascular diseases. *Nat. Commun.* 3:875. doi: 10.1038/ncomms1867

Trkov, S., Eng, G., Di Liddo, R., Parnigotto, P. P., and Vunjak-Novakovic, G. (2010). Micropatterned three-dimensional hydrogel system to study human endothelial-mesenchymal stem cell interactions. *J. Tissue Eng. Regen. Med.* 4, 205–215. doi: 10.1002/term.231

Tsolis, K. C., Bagli, E., Kanaki, K., Zografou, S., Carpentier, S., Bei, E. S., et al. (2016). Proteome changes during transition from human embryonic to vascular progenitor cells. *J. Proteome Res.* 15, 1995–2007. doi: 10.1021/acs.jproteome.6b00180

Vlaikou, A. M., Kouroupis, D., Sgourou, A., Markopoulos, G. S., Bagli, E., Markou, M., et al. (2017). Mechanical stress affects methylation pattern of GNAS isoforms and osteogenic differentiation of hAT-MSCs. *Biochim. Biophys. Acta* 1864, 1371–1381. doi: 10.1016/j.bbamcr.2017.05.005

Vodyanik, M. A., Yu, J., Zhang, X., Tian, S., Stewart, R., Thomson, J. A., et al. (2010). A mesoderm-derived precursor for mesenchymal stem and endothelial cells. *Cell Stem Cell* 7, 718–729. doi: 10.1016/j.stem.2010.11.011

Wanjare, M., Kuo, F., and Gerecht, S. (2013a). Derivation and maturation of synthetic and contractile vascular smooth muscle cells from human pluripotent stem cells. *Cardiovasc. Res.* 97, 321–330. doi: 10.1093/cvr/cvs315

Wanjare, M., Kusuma, S., and Gerecht, S. (2013b). Perivascular cells in blood vessel regeneration. *Biotechnol. J.* 8, 434–447. doi: 10.1002/biot.201200199

Conflict of Interest: The authors declare that the research was conducted in the absence of any commercial or financial relationships that could be construed as a potential conflict of interest.

frontiers in Bioengineering and Biotechnology

ORIGINAL RESEARCH
published: 24 April 2020
doi: 10.3389/fbioe.2020.00336

Primary Human Osteoblasts Cultured in a 3D Microenvironment Create a Unique Representative Model of Their Differentiation Into Osteocytes

*Gabriele Nasello[1,2], Pilar Alamán-Díez[1], Jessica Schiavi[3], María Ángeles Pérez[1], Laoise McNamara[3] and José Manuel García-Aznar[1]**

[1] Multiscale in Mechanical and Biological Engineering (M2BE), University of Zaragoza, Zaragoza, Spain, [2] Biomechanics Section, Department of Mechanical Engineering, KU Leuven, Leuven, Belgium, [3] Mechanobiology and Medical Device Research Group (MMDRG), National University of Ireland Galway, Galway, Ireland

Microengineered systems provide an *in vitro* strategy to explore the variability of individual patient response to tissue engineering products, since they prefer the use of primary cell sources representing the phenotype variability. Traditional *in vitro* systems already showed that primary human osteoblasts embedded in a 3D fibrous collagen matrix differentiate into osteocytes under specific conditions. Here, we hypothesized that translating this environment to the organ-on-a-chip scale creates a minimal functional unit to recapitulate osteoblast maturation toward osteocytes and matrix mineralization. Primary human osteoblasts were seeded in a type I collagen hydrogel, to establish the role of lower (2.5×10^5 cells/ml) and higher (1×10^6 cells/ml) cell density on their differentiation into osteocytes. A custom semi-automatic image analysis software was used to extract quantitative data on cellular morphology from brightfield images. The results are showing that cells cultured at a high density increase dendrite length over time, stop proliferating, exhibit dendritic morphology, upregulate alkaline phosphatase (ALP) activity, and express the osteocyte marker dental matrix protein 1 (DMP1). On the contrary, cells cultured at lower density proliferate over time, do not upregulate ALP and express the osteoblast marker bone sialoprotein 2 (BSP2) at all timepoints. Our work reveals that microengineered systems create unique conditions to capture the major aspects of osteoblast differentiation into osteocytes with a limited number of cells. We propose that the microengineered approach is a functional strategy to create a patient-specific bone tissue model and investigate the individual osteogenic potential of the patient bone cells.

Keywords: bone-on-a-chip, osteoblast differentiation, microfluidics, osteocyte, primary human cells, dendrite formation, *in vitro* bone model

OPEN ACCESS

Edited by:
Maria Chatzinikolaidou, University of Crete, Greece

Reviewed by:
Anne Bernhardt, Dresden University of Technology, Germany
Lorenzo Fassina, University of Pavia, Italy

***Correspondence:**
José Manuel García-Aznar
jmgaraz@unizar.es

Specialty section:
This article was submitted to Tissue Engineering and Regenerative Medicine, a section of the journal Frontiers in Bioengineering and Biotechnology

Received: *06 December 2019*
Accepted: *26 March 2020*
Published: *24 April 2020*

Citation:
Nasello G, Alamán-Díez P, Schiavi J, Pérez MÁ, McNamara L and García-Aznar JM (2020) Primary Human Osteoblasts Cultured in a 3D Microenvironment Create a Unique Representative Model of Their Differentiation Into Osteocytes. Front. Bioeng. Biotechnol. 8:336. doi: 10.3389/fbioe.2020.00336

1. INTRODUCTION

The comprehension of biological mechanisms in bones has a pivotal role in the development of successful clinical treatments. The developing field of bone engineering aims to take advantage of the innate repair capacity of this tissue (O'Brien, 2011), but the variability in the outcome of the products is one of the main limitations for their clinical translation. For example, the

individual heterogeneous response in newly formed bone tissue formation leads to drastic changes in the scaffold design (Reznikov et al., 2019). *In vitro* models can explore the impact of individual response in tissue engineering products, but they require a bone cell source representing the phenotype variability.

Osteoblasts experience marked transitional stages during bone formation, involving changes in cell morphology and gene expression. Osteoblasts express ALP to provide phosphate ions and initiate the mineralization process (Chai et al., 2012). They also secrete osteocalcin (OCN), bone sialoprotein 2 (BSP2), and osteopontin (OPN) until the end of the mineralization phase (Franz-Odendaal et al., 2006). When osteoblasts turn to a more mature phenotype, they reduce ALP expression, become embedded in a mineralized matrix and form an interconnected network of osteocytes (Boukhechba et al., 2009). During this transition, osteoblasts upregulate characteristic proteins as E11 and dentin matrix protein 1 (DMP1) (Atkins et al., 2011). The expression of sclerostin (Sost gene) is associated with the final stage of osteocyte differentiation (Bonewald, 2011; Prideaux et al., 2016). However, osteoblasts can have three other possible fates but the mechanism regulating this transition is not clearly understood yet: they can become bone-lining cells (inactive osteoblasts), undergo apoptosis, or transdifferentiate into chondroid-depositing cells (Dallas and Bonewald, 2010). Gene expression profiles (Boukhechba et al., 2009; Sun et al., 2017) and immunohistochemistry stainings (Uchihashi et al., 2013; Sun et al., 2015; McGarrigle et al., 2016) in traditional 3D culture systems showed that the expression of osteoblast and osteocyte markers *in vitro* corresponded to the *in vivo* expression at the same differentiation stages (Franz-Odendaal et al., 2006).

In this context, *in vitro* bone tissue models are a prerequisite tool for answering specific questions of cell biology, where minimal platforms are mandatory for effective research on human tissue function (Wittkowske et al., 2016; Pirosa et al., 2018; de Wildt et al., 2019). While traditional tissue engineering aims to recapitulate whole organs *in vitro*, organ-on-chip systems "combines the key features of specific tissue microenvironments and architecture within a microfabricated device, facilitating the creation of 3D models that exhibit functional hallmarks of native tissues" (Zhang et al., 2018). They provide minimal units mimicking specific features of living organs and human physiology, as the tissue barrier properties of the human gut and lung, the parenchymal function of cardiac and hepatic tissue, the multiorgan interactions between the lymph node and the skin (Huh et al., 2011; Osaki et al., 2018; Ronaldson-Bouchard and Vunjak-Novakovic, 2018; Zhang et al., 2018).

Bone models on a chip were developed in recent years to reveal different elements of bone biology, each one based on a critical advantage of microengineered devices over traditional 2D or 3D macroscale *in vitro* systems. For example, the use of optically transparent materials allowed the monitoring of osteoblast motility in a confined 3D environment (Movilla et al., 2018). The results of this study elucidated the effect of ECM degradation and its architecture on osteoblast migration, by applying growth factor gradients or interstitial fluid flow (Del Amo et al., 2018). Moreover, the culture chamber geometries facilitate the reproduction of 3D organ-level structures. Microengineered devices highlighted how a 3D microvasculature integrates with the mineralized bone tissue microenvironment and enhances osteogenic differentiation of cells in the surrounding tissue construct (Bertassoni et al., 2014; Jusoh et al., 2015). Organ function relies on the presence of biomechanical and biochemical stimuli. Mechanical, electrical, and chemical stimuli can simultaneously stimulate cells cultured in organ-on-chip systems (Zhang et al., 2018). The use of compartmentalized culture environments promotes the selective application of those stimuli to different cell types. A 2D microfluidic platform with osteoclasts and osteocytes cultured in separate compartments was key to observe the cross-talk between mechanically stimulated osteocytes, osteoclast precursors and unstimulated osteocytes (You et al., 2008; Middleton et al., 2017). In general, microfabrication techniques applied to cell biology aims to develop advanced human disease models by the inclusion of pathological factors. For example, organ-on-a-chip systems with an *ex vivo* decellularized bone matrix or an osteo-cell conditioned extracellular matrix (ECM) have recreated the interplay between cancer and endothelial cells with the bone matrix in metastatic colonization (Bersini et al., 2014; Marturano-Kruik et al., 2018). Such systems consisted of a bone-like microenvironment including a monolayer of endothelial cells, which provided the capacity to obtain quantitative data on the extravasation of breast cancer cells. They were proposed as an advanced model to screen novel organ-specific therapeutics, since the osteo-cell conditioned microenvironment secreted specific chemokines affecting the extravasation process (Bersini et al., 2014).

Osteocytes are the central regulators of bone homeostasis *in vivo*. Their regulatory activity on both processes of bone formation and resorption relies on the secretion of specific proteins to interact with osteoblasts and osteoclasts (Bonewald, 2011). Mature osteocytes are the only bone cells expressing sclerostin after matrix mineralization, which suppresses osteoblast activity and inhibits further bone formation (Poole et al., 2005). On the other hand, the receptor activator of nuclear factor-kB ligand (RANKL) is a cytokine that controls osteoclastogenesis and has a fundamental role in bone remodeling. The expression of RANKL by osteocytes is ten times higher than by osteoblasts in normal mice and its specific deletion in osteocytes induces osteopetrosis (Nakashima et al., 2011).

The effect of osteocyte activities to other bone cells is a vital function that requires advanced *in vitro* models to be investigated. Traditional *in vitro* cultures replicated essential features of the interaction between osteoblasts and osteocytes, such as osteoblast maturation and matrix mineralization. These systems consisted of 3D collagen hydrogels/sponges and human osteoblast-like cells (Atkins et al., 2009; Bernhardt et al., 2019; Skottke et al., 2019) or mouse clonal cell-lines (MC3T3-E1 and IDG-SW3) (Woo et al., 2011; McGarrigle et al., 2016), with the last ones usually preferred due to the excessive number of cells required. On a micro-scale, a 2D layer of MC3T3-E1 cells spontaneously formed a mineralized collagenous matrix in long-term cultures (up to 1 month) (Hao et al., 2018). Cells were mainly present in the apical and basal layers of the matrix, possibly due to excessive proliferation of the mouse cell-line. No previous bone-on-a-chip device has

differentiated primary human osteoblasts into osteocytes while embedded in a 3D extracellular matrix. There is a need for a novel microengineered model to explore the interaction between the two cell types.

Microfabricated platforms facilitate the use of cells derived from patients, thus creating models of human physiology with higher clinical impact. Primary and mature human cells are difficult to extract in large amounts, proliferate slowly and tend to dedifferentiate rapidly. Those systems require a limited amount of cells and aim to recreate the native microenvironment: they provide an approach to culture cells representing the variability of the cell phenotype (Zhang et al., 2018). This is a key advantage of the organ-on-a-chip over traditional technologies, considering the growing concern about the use of immortalized cell-lines for reliable human models (Lorsch et al., 2014). Cell-lines could lead to different results with respect to primary cells from the same species. For example, murine early osteocyte cell-line MLO-A5 created an interconnected 3D network in a microfluidic perfusion device (Gu et al., 2015) but produced a highly mineralized and dense tissue compared to primary murine bone cells (Sun et al., 2015).

We developed a bone-on-a-chip device to translate the findings of traditional macro-models on differentiated osteocyte networks to the scale of micro-devices. We hypothesized that the combination of primary human cells and a 3D fibrous collagen matrix in a microengineered platform creates a more robust model to recapitulate osteoblast maturation toward osteocytes and matrix mineralization. We developed a 3D cell culture system where the structural and biochemical microenvironment induced (1) the mineralization of a collagen matrix and (2) the differentiation of primary human osteoblasts into osteocytes. The specific aims were to determine the osteogenic behavior of osteoblasts embedded in a collagen type I hydrogel in terms of: (1) cellular morphology, (2) dendrite tracking, (3) cell proliferation, (4) ALP activity, (5) calcium deposition, and (6) synthesis of specific osteoblasts and osteocytes markers, respectively, BSP2 and DMP1, as well as the role of cell density in the formation of a bone tissue model.

2. MATERIALS AND METHODS

2.1. Cell culture

The low quantity needed for bone-on-a-chip experiments and the stability in the expression of the most critical genes during *in vitro* culture (Sun et al., 2017) favored the choice of primary human osteoblasts (HOBs) for the bone tissue model presented in this study.

HOBs were purchased from PromoCell (C-12720, Germany). These cells are fully differentiated osteoblasts isolated from femoral trabecular bone tissue from the knee or the hip joint region of healthy single donor. HOBs from two different donors were used (donor 1: caucasian female 86 years, donor 2: caucasian male 74 years). Cells were cultured under standard conditions (5% CO_2, 37°C), in cell expansion medium containing standard Dulbecco's Modified Eagle Medium (DMEM low glucose; Thermo Fisher Scientific, MA) supplemented with 10% fetal bovine serum (FBS; Thermo Fisher Scientific), 100 U/mL penicillin, 100 μg/mL streptomycin, and 2 mM L-glutamine (all Lonza, Switzerland). At each passage, cells were washed with phosphate buffered saline (PBS; Lonza), detached with TrypLE^{TM} Express (Invitrogen, CA) and plated in T25 cell culture flasks (Thermo Fisher Scientific) at a density of 15,000 cells/cm^2. Cells were used at passage 4–7 and mixed to the collagen gel solution. Final cell densities of 2.5×10^5 (low) and 1×10^6 cells/ml (high) were based on recent findings on osteocyte differentiation in traditional *in vitro* systems (McGarrigle et al., 2016).

Once loaded to the organ-on-a-chip devices, HOBs were cultured under static conditions in cell osteogenic medium, containing cell expansion medium supplemented with 50 μM ascorbic acid and 10 mM β-glycerol phosphate (both Sigma-Aldrich). Those supplements are widely accepted to induce osteogenic differentiation of stem cells *in vitro* and deposition of mineralized extracellular matrix (Langenbach and Handschel, 2013).

2.2. Bone-on-a-Chip System

Bone-on-a-chip devices were fabricated in poly(dimethlysiloxane) (PDMS) by soft lithography, following the methodology described by Shin et al. (2012).A commercial product was used to produce the silicone elastomer (Sylgard 184 Silicone Elastomer Kit, Dow Chemical, Germany), which comprises a polymeric base and a silicone resin solution as curing agent. The two liquid parts were mixed in a 10 (base) :1 (curing agent) ratio and poured in a master made of SU-8 where the microengineered geometry was patterned with a photolithography technique. The masters were then placed in a vacuum desiccator for one hour, to remove air bubbles in the PDMS solution, and kept in a dry oven overnight to cure the mixture. Later, dermal biopsy punches were used to create the reservoirs for cell culture media and the hydrogel inlets to the culture chamber (**Figure 1A**). PDMS devices followed a wet and a dry autoclave cycle before being bonded to a 35 mm glass (Ibidi, Germany) by plasma treatment (PDC-32G Basic Plasma Cleaner, Harrick Plasma, NY, USA) under vacuum conditions (**Figure 1B**). They were then coated with PDL (poly-D-lysine; 1 mg/ml in phosphate buffered saline; Sigma-Aldrich, Germany) and washed after 4 h to enhance matrix adhesion. Before use, the devices were left in a dry oven at 80°C for 48 h to restore the hydrophobicity of the bonded surfaces (Shin et al., 2012).

A previously developed geometry that consists of a central culture chamber divided into three compartments was selected for this study (Del Amo et al., 2017). Briefly, the length of a single compartment was 2.5 mm, the width was 1.145 mm, and the average height was 290 μm (**Figure 1A**). The chip uses equally spaced (175 μm) trapezoidal columns to separate the compartments and support the hydrogel via surface tension: gel contraction occurs only on the lateral channels while the 3D culture environment is maintained in the central channel during the whole experiment.

Cell laden collagen hydrogels, with a final collagen concentration of 6 mg/ml, were prepared by mixing in an ice bath collagen type I solution (Rat Tail; 8.9 mg/ml; Corning,

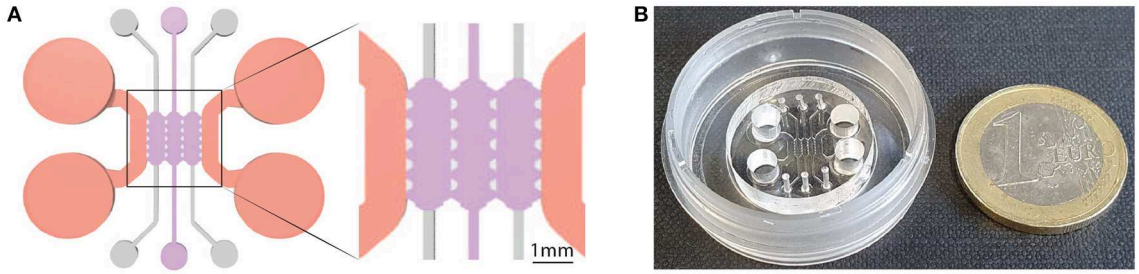

FIGURE 1 | Geometry of the bone-on-a-chip system. **(A)** 2D top view of the bone-on-a-chip system and detail of the culture chamber divided into three compartments by trapezoidal columns. The cell laden collagen hydrogels (purple) were loaded through the central compartment, while cell culture media (pink) was provided through the lateral channels. The height of the culture chamber is 290 ± 20 μm. **(B)** Picture of the bone-on-a-chip system bonded to a 35 mm glass.

NY), 10x Dulbecco's phosphate buffered saline (DPBS; Sigma-Aldrich), 0.5 M NaOH (Sigma-Aldrich) to adjust the pH to 7.4–7.6, and human osteoblasts suspended in cell expansion medium. After gently pipetting the solution into the culture chamber, it polymerized for 20 min in a humid chamber at 37°C.

The temperature and the pH conditions mentioned above induced a self-assembled gelation process of the collagen hydrogels, where collagen fibers are physically crosslinked (Chuang et al., 2018). During the polymerization process, collagen fibers create an interpenetrating polymer network in presence of living cells (Rowe and Stegemann, 2006). The microarchitecture and the mechanical properties of the collagen fibrous hydrogels used in this study were characterized in previous studies (Moreno-Arotzena et al., 2015; Del Amo et al., 2018). In the present work, we selected the 6 mg/ml gel because its Young modulus (∼0.72 kPa, from Valero et al., 2018) was comparable to the one (∼0.58 kPa) that allowed a homogeneous cell distribution in a 3D matrix and enhanced osteocytic differentiation of MC3T3-E1 cells (McGarrigle et al., 2016).

2.3. Phalloidin and DAPI Fluorescence Staining

Morphological analysis of cell phenotype is commonly used to assess osteoblast-osteocyte differentiation (Mullen et al., 2013). Cells were fixed after 21 days of culture using 4% (w/v) paraformaldehyde (PFA, Thermo Fisher Scientific) for 30 min, blocked overnight in PBS with 5% bovine serum albumin (BSA) and incubated overnight with Phalloidin-TRITC (0.1 mg/ml in PBS, Sigma Aldrich) and DAPI (0.01 mg/ml in PBS, Invitrogen). Samples were observed with a confocal microscope (Zeiss LSM880, Zeiss, Germany). Maximum intensity and 3D volumetric images were generated from z-stacks using ImageJ software (v 1.49, NIH).

2.4. Cell Dendrite Tracking

Brightfield images of the same samples were taken to track changes in dendrite morphology. Devices were observed at 10x and 20x magnification over the 21 days of culture with an inverted brightfield microscope (Nikon D-Eclipse C1, Japan) and focused in the middle of the culture chamber. Z-stacks were obtained with a distance of 5 μm between each slice and for a maximum thickness of 100 μm. A minimum number of 3 stacks were taken for each cell density at each timepoint.

A custom semi-automatic image analysis software was developed with Python programming language to track cell dendrite length over time. Original z-stacks images were opened with the Bio-format software tool (Linkert et al., 2010) and processed with the scikit-image library (van der Walt et al., 2014). After cells were manually contoured, an automatic algorithm computed the medial axis transform of the binary cell mask. An Otsu's thresholding algorithm later separated the cell body primary and secondary dendrites from the cell body. The software quantified the length of cell primary protrusions, defined as the longest branches starting from the cell body, and detected cell-cell connections if cell boundaries were in the same image of the z-stack.

Osteocytes exhibit exploratory dendrites that extend and retract from the surrounding extracellular matrix before forming a fully developed osteocyte network (McGarrigle et al., 2016). Cell primary protrusions longer than 10 μm were defined as dendrites, as previously described (Mullen et al., 2013).

2.5. DNA Content

Osteoblasts move from a proliferative (preosteoblast) to a quiescent phase (mature osteoblasts/osteocytes) during differentiation (Franz-Odendaal et al., 2006). Thus, DNA content was measured using the Hoechst 33,258 DNA assay to monitor cell proliferation over time. Cells were isolated by digesting the collagen matrix overnight in a solution of collagenase from *Clostridium histolyticum* (Sigma-Aldrich, 2 mg/ml, ≥ 125 CDU/mg) and centrifugating cell suspension at 13,000 rpm for 15 min. 100 μl of Hoechst buffer [1 mM EDTA, 10 mM Tris (hydroxymethyl) aminomethane and 0.1 M Sodium Chloride at pH 7.4, all reagents from Sigma-Aldrich] was added to the pellet. Cells were lysed by applying 3 cycles of freezing (−80°C)-thawing procedure before running the biochemical assay. Later, 20 μl of cells lysate or DNA standards were suspended in 200 μl of Hoechst dye solution (0.1% v/v, Sigma-Aldrich) and added in a 96-well plate in triplicate. Fluorescence was then measured (excitation: 380 nm; emission: 440 nm) using a fluorescence spectrophotometer (Synergy HT

Multi-mode microplate reader, BioTek Instruments, VT, USA). Readings were converted to DNA content using a standard curve, according to the manufacturer's protocol, with samples containing no cells subtracted as background.

2.6. Extracellular ALP Activity

The metalloenzyme ALP initiates the calcification process by providing inorganic phosphates (Coleman, 1992; Golub and Boesze-Battaglia, 2007). It is used as a marker for osteoblast activity, since ALP expression changes over time when osteoblast differentiation occurs (Atkins et al., 2009). Extracellular ALP activity was measured using a colorimetric assay of enzyme activity (SIGMAFAST p-NPP Kit, Sigma Aldrich). It uses p-nitrophenyl phosphate (pNPP) as colorimetric substrate that changes absorbance when dephosphorylated by ALP. Cell culture media was changed and sampled after 2 h at days 3, 7, 14, 21, and stored at −80°C. After thawing, 40 μl of medium were added to a 96-well plate in triplicate with 50 μl of pNPP solution (Birmingham et al., 2012). Samples were incubated at room temperature in the dark for 1 h, and absorbance was read at 405 nm with a spectrophotometer. Readings were converted to ALP production using a standard curve, with samples containing no ALP subtracted as background. ALP production was normalized by the DNA content of each sample in order to get comparable estimations of ALP activity between samples with different initial cell seeding density.

2.7. Mineralization

Calcein green staining (Sigma Aldrich) was performed to analyze calcium deposition without affecting cell viability after 7, 14, and 21 days (Schiavi et al., 2015). Calcein was dissolved in 0.5 M NaOH solution (Sigma Aldrich) at 2.5 mg/ml. After mixing, the solution was sterilized with a 0.2 μm Nylon filter, wrapped with aluminum foil and stored at 4°C. Cells were incubated with calcein (25 μg/ml in osteogenic media) (Sigma) for 5 days, washed 3 times in PBS and fixed using 4% (w/v) PFA. Samples were imaged with a confocal microscope (λ_{ex} = 470–509 nm) and maximum intensity images were generated from z-stacks using ImageJ software.

2.8. Immunofluorescent Staining

BSP2 is a non-collagenous protein upregulated by osteoblasts during the tissue mineralization and downregulated when osteocyte differentiation occurs. DMP1 is an extracellular matrix protein associated with osteocytes. BSP2 and DMP1 immunofluorescent stainings indicate whether cells cultured in the bone-on-a-chip samples synthetized osteoblast or osteocyte markers, respectively (Atkins et al., 2009; Dallas and Bonewald, 2010).

Cells were fixed after 7, 14, 21 days of culture using 4% (w/v) PFA for 30 min and blocked overnight with 5% BSA. Later, samples were incubated at 4°C overnight with mouse monoclonal BSP2 (Santa Cruz Biotechnology, sc-73630, Texas) or DMP1 (Santa Cruz, sc-73633) antibody at a dilution of 1:100 in PBS with 0.5% BSA. After washing 3 times for 5 min with PBS, samples were incubated at 4°C for 6 h with the relevant secondary antibody (for BSP2, goat anti-mouse Alexa Fluor® 555, Molecular Probes, Oregon, A21424; for DMP1, goat anti-mouse Alexa Fluor® 633, Molecular Probes, A21052) at a dilution of 1:50 in PBS with 0.5% BSA. Cell nuclei were then counterstained with DAPI and samples were observed with a confocal microscope. Maximum intensity images were generated from z-stacks using ImageJ software.

2.9. Statistics

All experiments were conducted in technical triplicates ($n = 3$) with two independent experiments, by using different donors. Python programming language was used to run all the statistical analyses. We used one-way analysis of variance (ANOVA) for all the biochemical analyses to assess significant differences between timepoints, followed by pair-wise multiple comparison procedure (Tukey's HSD test). Linear regression models described the variation of dendrite length over time. Experimental data are presented as mean ± 95% of confidence interval if not otherwise specified. P-value < 0.05 was considered significant.

3. RESULTS AND DISCUSSION

Recent advances in mimicking bone with microengineered platforms are reducing the gap between the tissue and other more developed organ-on-chip models but, to our knowledge, they did not reach to show the development of a device with differentiated osteocytes and a 3D mineralized matrix.

Given that primary human osteoblasts embedded in a 3D fibrous collagen matrix is an optimal environment to encourage osteocyte differentiation (Atkins et al., 2009; Woo et al., 2011; McGarrigle et al., 2016), we hypothesized that the same environment translated to organ-on-a-chip scale recapitulates two key *in vivo* bone properties: osteoblast maturation and matrix mineralization. To determine the development of mature bone formation, we investigated the major aspects underlying osteoblast-osteocyte differentiation: cell morphology variation, mineralization, and protein synthesis.

3.1. Cells Show Dendritic Morphology While Increasing Primary Dendrite Length Over Time

The osteoblast-osteocyte differentiation is a complex mechanism, still under investigation, with relevant changes in cell morphology, polarization, cytoplasmic volume, number of cell organelles, proliferation, gene expression, type of collagen deposited, and bone deposition rate. During these transitional stages, the extension of cellular dendrites or pseudopodia is the one of most recognizable variations (Franz-Odendaal et al., 2006).

To observe this morphological change, we stained actin filaments at the latest timepoint (21 days) and we qualitatively observed that cells at high density exhibited a dendritic morphology as well as initial interconnections. On the other hand, cells at low density kept an aligned morphology with a limited amount of dendrites (**Figure 2**).

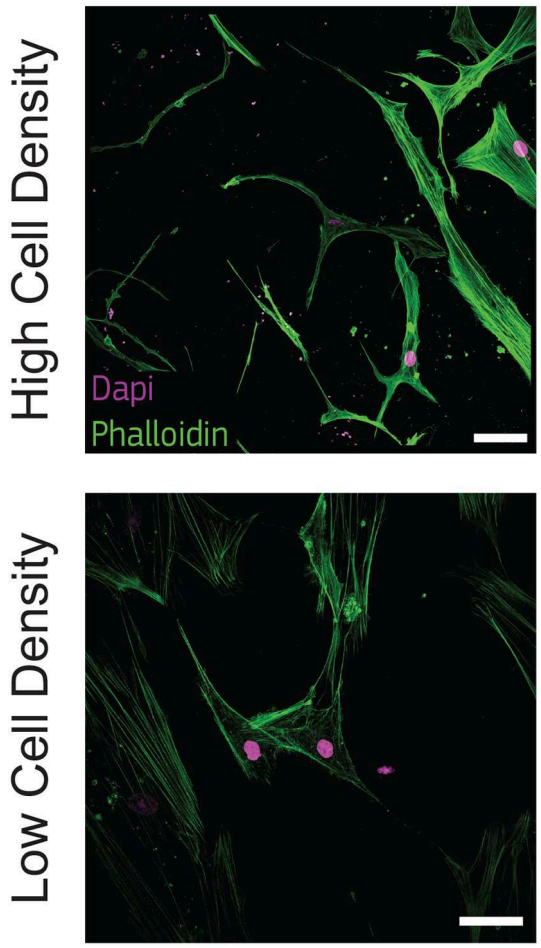

FIGURE 2 | Cells cultured at high density show dendritic morphology. Representative confocal images of cell nuclei (DAPI) and actin filaments (phalloidin) after 21 days of culture in bone-on-a-chip samples at high and low cell density. Scale bar, 50 μm.

Osteoblasts were already classified with a spread, aligned, transitional, or dendritic morphology during their differentiation into osteocytes *in vitro* (Mullen et al., 2013), and mineralizing conditions enhanced the development of a stellate morphology (Atkins et al., 2009). Microfluidics showed that pre-osteoblastic mouse cells adhere and spread differently along a stiffness gradient, but it did not highlight any morphological variation (Almodóvar et al., 2013). Here, the difference in cell shape suggests that human osteoblasts cultured at 1×10^6 cells/ml (high density) are more differentiated into osteocytes than cells cultured at 2.5×10^5 cells/ml (low density) (**Figure 2**). The dendritic morphology for the high density group reported here is consistent with the results in a traditional 3D *in vitro* systems, where mouse bone cells cultured at a low cell density (2.5×10^5 cells/ml) had a lower percentage of dendritic cells with respect to cells cultured at high density (2×10^6 cells/ml) (McGarrigle et al., 2016). Dendritic protrusions of primary human osteoblasts in collagen hydrogels is documented in the literature for initial cell seeding densities lower than 2.5×10^5 cells/ml (Atkins et al., 2009; Bernhardt et al., 2019; Skottke et al., 2019 In these cases, the maximum collagen concentration in the hydrogel was 3 mg/ml, which is half of the 6 mg/ml used in our study. Hydrogels with lower collagen concentration have lower mechanical properties (Chuang et al., 2018), which favor a dendritic cell morphology even at lower cell seeding densities (McGarrigle et al., 2016). Osteoblast differentiation was reduced in hydrogels with low collagen concentration when they were modified with biomimetically or strontium-doped mineralized collagen, confirming that the higher stiffness of the matrix delays the differentiation for low cell seeding densities (Bernhardt et al., 2019). On the other hand, hydrogel contraction limits the use of high cell seeding densities. Our bone-on-a-chip system, where trapezoidal columns within the culture chamber reduces the hydrogel contraction, facilitated the use of hydrogels with higher collagen concentration, thus favoring the culture of cells at higher seeding densities and the exhibition of a dendritic morphology at higher collagen concentrations.

Experimental biology requires novel automatic tools for image analysis to support the conversion of microscopy images into quantitative data (Eliceiri et al., 2012). To demonstrate a consistent change in cellular morphology, a customed image analysis software was developed to automatically separate cell body from dendrites, after a manual selection of the cell boundary (**Figure 3B**). The software quantified the cell dendrite length and detected cell-cell connections of cells in the same image of the z-stack (**Figure S1**, **Video S1**).

Cells cultured at high density experiences a significant dendrite growth of 1.01 ± 0.25 μm/day (**Figure 3C**) over the whole period of culture, confirming osteoblast change to a dendritic morphology compared to the lower density.

Cells cultured at low density did not increase dendrite length over time (**Figure 3C**). This analysis did not show a quantitative change in cell morphology for the low density group, as suggested by the aligned shape observed in confocal imaging (**Figure 2**).

Compared to traditional *in vitro* culture, the ratio between the volumes of culture and the fewer number of cells used in microengineered devices make quantitative image analyses more representative of the whole cell population present in each sample. The number of cells tracked in this study ($n \approx 50$ cells per timepoint) is 100 times lower than the total amount of cells in our samples (≈5,000 cells), while in traditional systems it is usually 1,000,000 times lower. Moreover, the high control of the geometries of the organ-on-a-chip culture chamber allows the identification of the same image location at each timepoint. The combination of the organ-on-chip technology with a semi-automatic software that decreases operator-dependent errors produce a more accurate and reliable platform for quantitative image analysis.

The evaluation of cell-cell connections showed a limited variation over time, due to the requirement for cell boundaries to be on the same image of the z-stack (**Video S1**). However, we observed a slight increase in cell connections for cells cultured at high density over time (**Figure 3A**). Osteoblasts did not form an interconnected network, they rather showed exploratory dendrites to create transient connections and position themselves

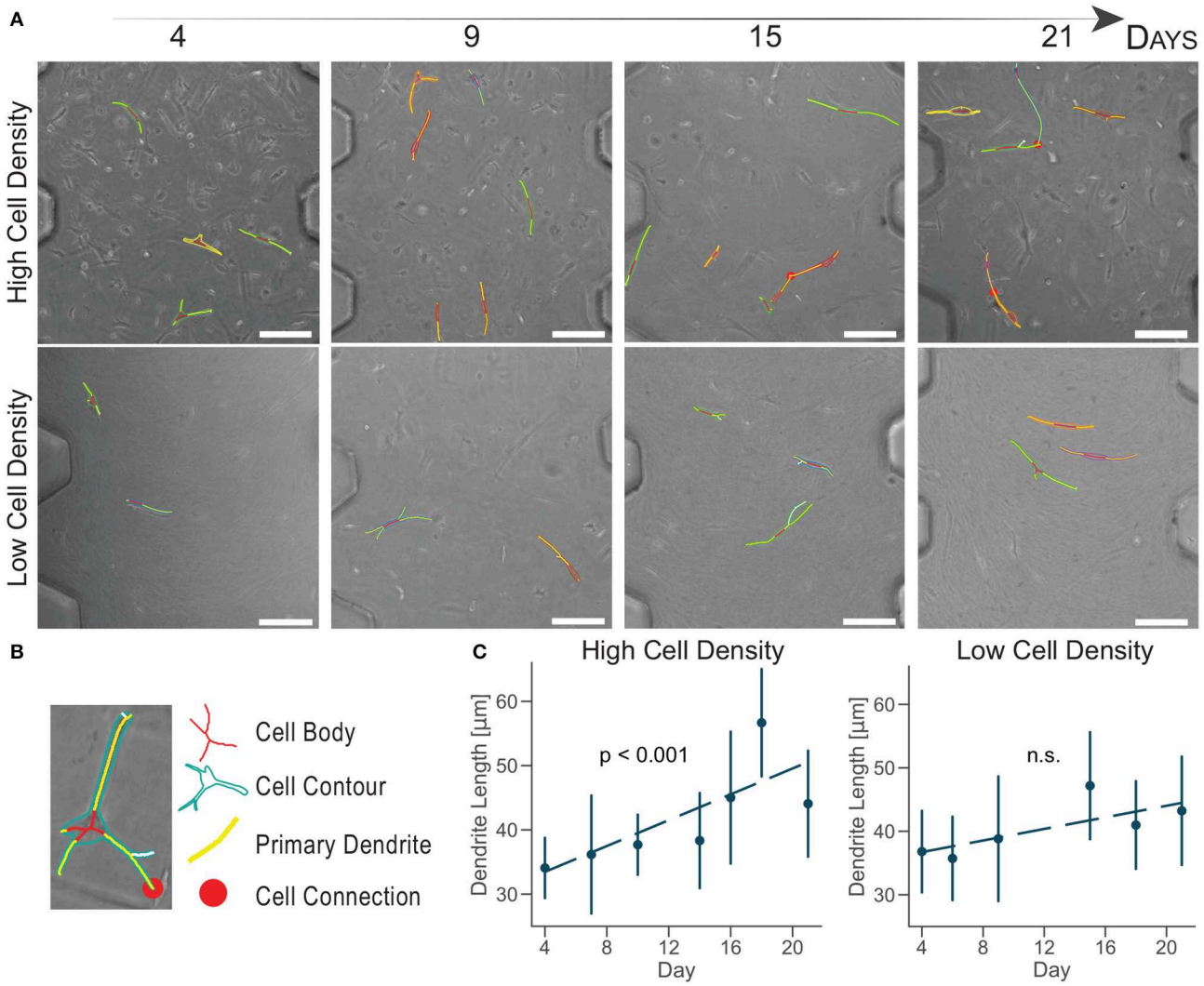

FIGURE 3 | Cells cultured at high density increase primary dendrite length over time. **(A)** Brightfield images of cultured human osteoblasts with superimposed tracking. Scale bar = 150 μm. **(B)** Cell image detail. Identification of the cell body, contour, primary dendrites, and connection with a semi-automatic algorithm. **(C)** Primary dendrite length measured with a customed software for dendrite tracking. Linear regression model in dashed lines ($n \approx 50$ cells per timepoint). Data are mean ±95% c.i.

in the extracellular matrix (Zhang et al., 2006; McGarrigle et al., 2016). The dendritic morphology at the end of the culture and the increase in exploratory dendrite length indicated that osteoblasts cultured at high density underwent differentiation into an early osteocytic phenotype.

3.2. Alkaline Phosphatase (ALP) Upregulation Is Associated With the Interruption of Cell Proliferation

The cessation of cell proliferation and collagen matrix production follows the secretion of soft osteoid that surrounds osteoblasts initiating differentiation (Atkins et al., 2011). To determine whether the culture microenvironment regulated cell proliferation in our bone-on-a-chip, we degraded the 3D collagen matrix, extracted cells and quantified the evolution of the DNA content.

DNA content had a negative trend over time for the high cell density group, as suggested by the lower DNA content at day 14 compared to day 3 (**Figure 4**). The amount of DNA measured from a unique cell type is proportional to the total number of cells. Thus, osteoblasts were not proliferating in our bone-on-a-chip system, plausibly because they were undergoing a differentiation process. Only a limited proportion of osteoblasts differentiates into osteocyte *in vivo* while the rest of the population follows other fates, including apoptosis (Franz-Odendaal et al., 2006). If cells seeded at high density were differentiating into osteocytes, the decreasing trend in the DNA amount confirmed that our microenvironment also induced the apoptosis of a subpart of the osteoblast population.

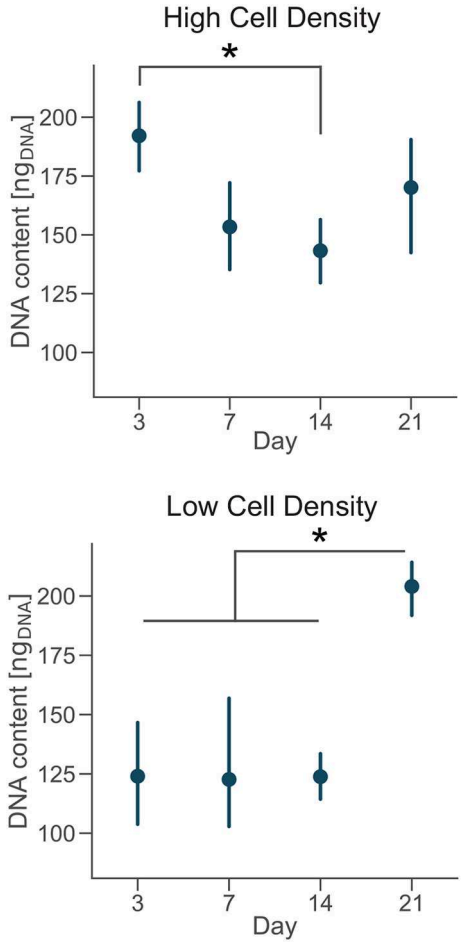

FIGURE 4 | Cells cultured at low density proliferate over time. DNA content of each group at day 3, 7, 14, and 21. Point plots denote the mean of $n = 6$ samples with error bars representing 95% of confidence interval. *Represents statistical significance ($p < 0.05$) between indicated groups using one-way ANOVA with Tukey's *post-hoc* test.

A 3D culture environment made of a microbeads assembly already showed that osteoblastic cells cultured in a microfluidic system stop proliferating, compared to a control group cultured in a plate where cells were proliferating. The cell number quantification in the microbead assembly was estimated by the ratio of the number of cells and the number of microbeads imaged (Sun et al., 2017). Here, we developed a protocol to get a more direct measure of the amount of cells over time in the microengineered sample.

In the low cell density group, by day 21 the DNA content was significantly higher than early timepoints (**Figure 4**), suggesting that cells started proliferating under these culture conditions. Our results show that after an initial period of quiescence, osteoblasts seeded at low density maintained their proliferative capacity in our bone-on-a-chip, supporting the hypothesis that they were not differentiating into osteocytes. The use of primary human cells was crucial to capture the difference between proliferative and non-proliferative conditions in the bone-on-a-chip model. Cell-lines have high proliferation rates which make them not very suitable to study this precise aspect of bone cells function (Clover and Gowen, 1994). For example, a mouse osteoblast cell-line (MC3T3-E1) showed to proliferate even if cells were differentiating into osteocytes and creating an interconnected network between dendritic cells (McGarrigle et al., 2016). The combination of primary human cells and microengineered technology give a valid solution to culture cells representative of the *in vivo* phenotype maximizing the number of samples. Such system is a unique representative model of osteoblast proliferation in a physiologic 3D environment.

The transition from a proliferative to a quiescent phase during osteoblast differentiation is concomitant to the upregulation of ALP and its later reduction (Boukhechba et al., 2009). To assess osteoblast secretion of ALP during culture, we quantified the evolution of enzyme activity in the culture media and the effect of cell density.

Extracellular ALP activity was normalized by the DNA content and showed an upregulation for the high density group compared to the low density in both donors (**Figure 5**). The ALP activity had increasing trend for cells cultured at high density, even if the magnitudes of the ALP measurements were higher for donor 2 compared to the donor 1. Moreover, cells from the donor 1 showed a significantly higher ALP activity by day 7 followed by a decreasing trend (**Figure 5A**). Differences in trends of the ALP measurements might be related to inter-donor variability, and more specifically to the differences in age and sex between donors. Cells from the younger male donor (donor 2) had higher absolute ALP activity and didn't show the trend observed in donor 1. However, the upregulation of ALP activity for cells cultured at higher density confirmed the higher potential for matrix mineralization and osteogenic differentiation for both donors. In tissue engineering, the upregulation of ALP expression relates to osteogenesis and is a precursor to mineralization of the tissue (Golub and Boesze-Battaglia, 2007). Previous studies in microfluidic devices only showed the upregulation of ALP activity at the end of the culture, proving that those platforms promoted osteogenesis (Leclerc et al., 2006; Jang et al., 2008; Hao et al., 2018). Here, we measured the temporal evolution of ALP activity during the whole culture and it suggested that osteoblasts cultured at high density had a phase of increase of mineralization in the first week of culture and later continued the differentiation process.

Calcein is a fluorochrome binding calcium at bone mineralization front (Yeh et al., 2018), thus identifying newly mineralized matrix. Calcium staining with calcein at days 7, 14, and 21 showed that primary human osteoblasts mineralized the extracellular matrix over the whole period of culture. Images qualitatively confirmed the results of ALP activity, with a higher presence of calcium ions for the cells cultured at high density (**Figure S2**). Our results suggest that the low cell density tested (2.5×10^5 cells/ml) was insufficient to initiate osteoblasts differentiation in this hydrogel and they needed to proliferate more before undertaking this pathway.

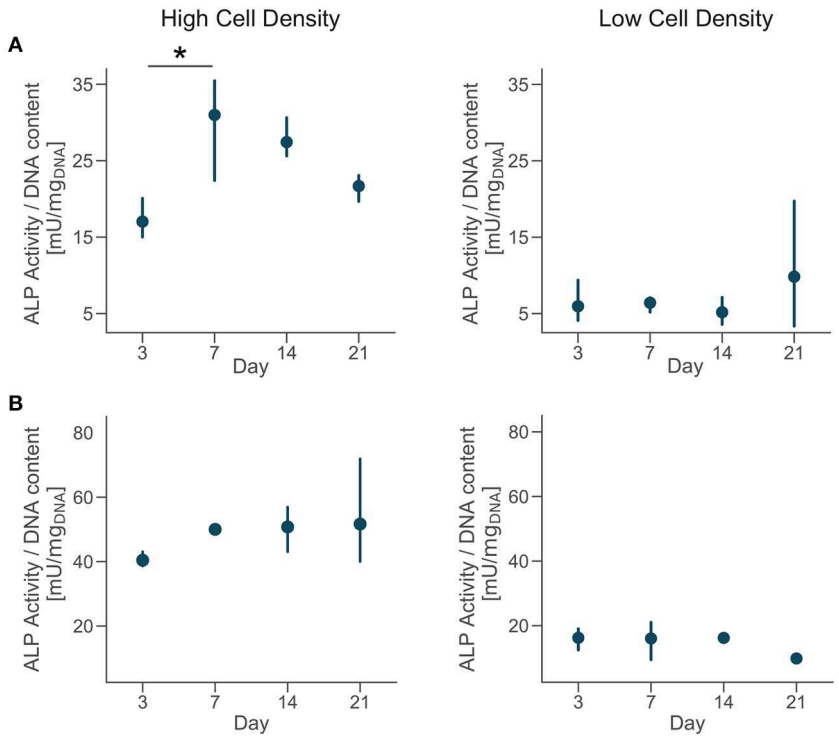

FIGURE 5 | Cells cultured at high density upregulate alkaline phosphatase (ALP) activity. Extracellular ALP activity of each group at day 3, 7, 14, and 21. Point plots denote the mean of $n = 3$ samples (row A—donor 1, row B—donor 2) with error bars representing 95% of confidence interval. *Represents statistical significance ($p < 0.05$) between indicated groups using one-way ANOVA with Tukey's *post-hoc* test.

3.3. Cell Density Regulates Osteoblast/Osteocyte Marker Synthesis

Osteoblasts transitional stages during bone formation involve changes in cell morphology and protein synthesis. As we found differences in cell morphology, protrusion length dynamics, proliferation, and osteogenesis, we investigated the qualitative expression of bone matrix proteins. We selected two specific proteins BSP2 and DMP1, representative of osteoblast and osteocyte phenotype respectively, to determine the effect of cell density on their production.

Immunofluorescent staining for BSP2 demonstrated positive synthesis within the proximity of cells in the earliest days of culture for both cell density groups, confirming the initial osteoblast phenotype of the cells used at the beginning of the experiment. Osteoblasts cultured at low density produced BSP2 at all timepoints (**Figure 6**), suggesting that no transition to osteocyte occurred for this group. On the contrary, the high density group reduced BSP2 expression at the end of the culture (21 days, **Figure 6**). The lower presence of BSP2 denoted that cells cultured at high density group changed differentiation stage in the bone-on-a-chip devices. BSP2 expression is characteristic of osteoblast phenotype, even if it was observed in lower amounts in osteocytes (Franz-Odendaal et al., 2006). Another osteocytic marker needs to determine whether cells of the high density group underwent this specific fate.

Low presence of DMP1 staining were observed for cells cultured at low density (**Figure 7**), supporting that cells of this group experienced a limited transition into the osteocyte stage during the whole culture period. DMP1 was more expressed by the human osteoblasts cultured at high density at all timepoints (**Figure 7**). The faster osteoblasts transition to osteocytes was confirmed by the presence of this osteocytic marker, together with the decreased presence of the osteoblast marker BSP2 (**Figure 6**). The positive DMP1 staining for cells cultured at high density reported here is consistent with the results in a traditional 3D *in vitro* systems, where cells cultured at higher density (2×10^6 cells/ml) produced more DMP1 as dispersed nodules within the surrounding matrix (McGarrigle et al., 2016).

3.4. Cells Cultured at Higher Density Differentiate Faster Into Osteocytes

Overall, our data showed how the 3D microenvironment in our bone-on-a-chip regulated osteoblast-osteocyte differentiation (**Figure 8**). The microengineered technology created a highly controllable environment to study the maturation of primary human bone cells in a 3D extracellular matrix made of the most abundant organic component in bone tissue. A custom semi-automatic image analysis software led to the extraction of quantitative data on the cellular morphology from microscopy images. In addition, the use of primary human cells at high cell density was crucial to mimic the physiological

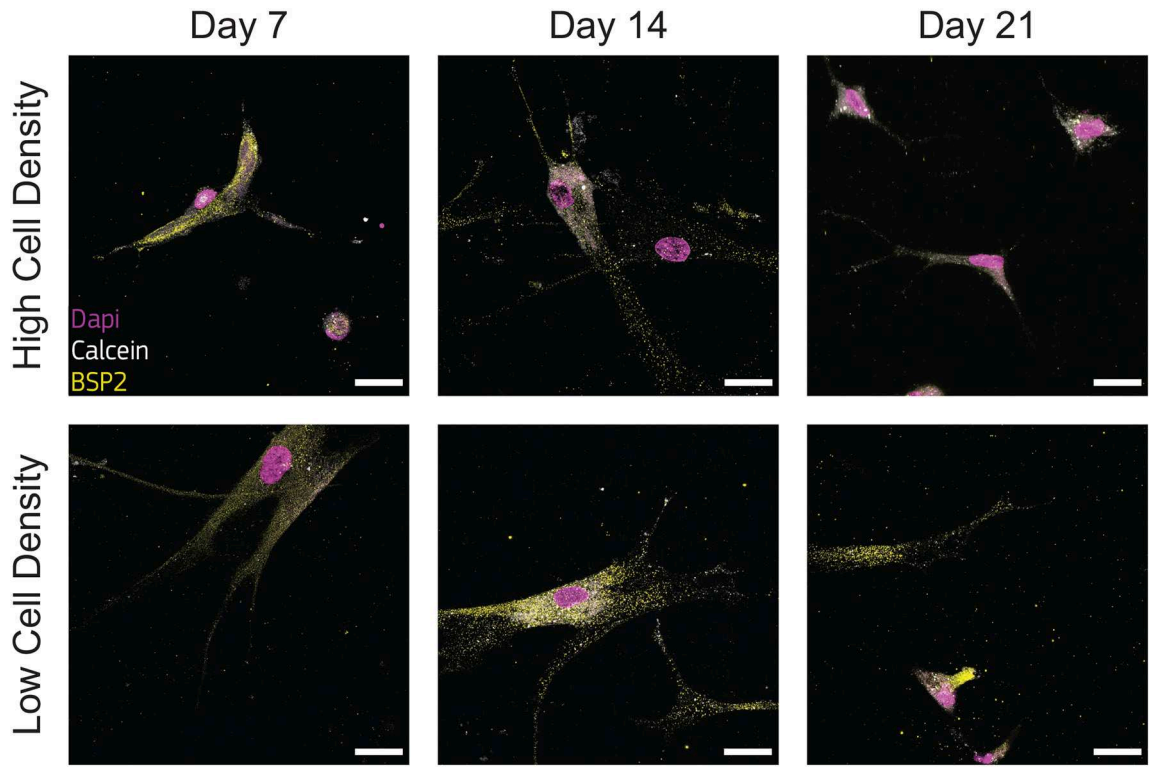

FIGURE 6 | Cells cultured at low density synthesize bone sialoprotein 2 (BSP2) at all timepoints. Representative confocal images of cell nuclei (DAPI), calcium ions (calcein), and BSP2 in bone-on-a-chip samples cultured at high and low cell density. Scale bar, 30 μm.

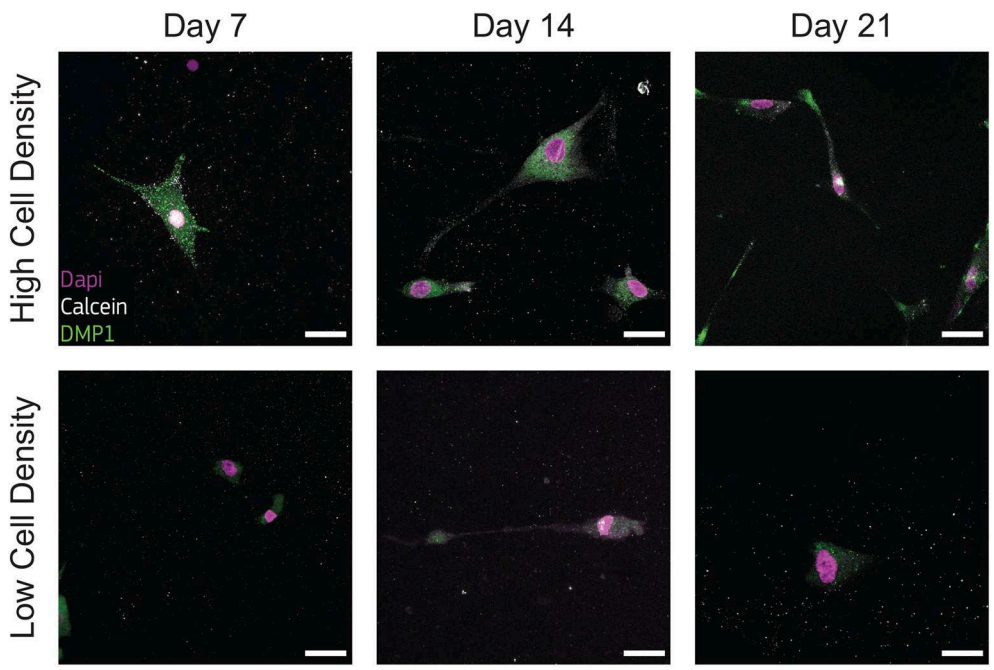

FIGURE 7 | Cells cultured at high density synthesize dental matrix protein 1 (DMP1). Representative confocal images of cell nuclei (DAPI), calcium ions (calcein), and DMP1 in bone-on-a-chip samples cultured at high and low cell density. Scale bar, 30 μm.

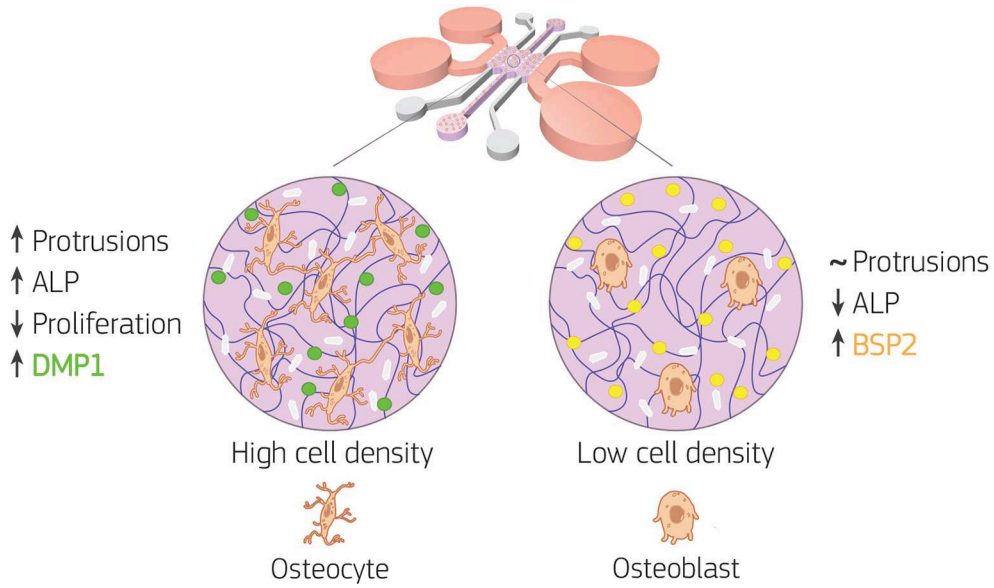

FIGURE 8 | Bone-on-a-chip development with two cell seeding densities. Primary human osteoblasts were encapsulated in type I collagen hydrogel (purple in the figure) at 2.5×10^5 (low cell density) and 1×10^6 (high cell density) cells/ml, then loaded in the bone-on-a-chip devices and cultured up to 21 days to study matrix mineralization and cell differentiation into osteocytes. Cell morphology, dendrite tracking, DNA content, alkaline phosphatase (ALP) production, calcium deposition (white in the figure), and immunofluorescent staining of bone sialoprotein 2 (BSP2, yellow in the figure) and dentin matrix protein 1 (DMP1, green in the figure) were performed to assess the osteogenic phenotype of the cells. At low cell density, the biochemical 3D microenvironment induced only the expression of osteoblast markers (ALP, BSP2). While the change in cell morphology, the upregulation of ALP and the expression of DMP1 suggested that osteoblast transition to osteocytes occurred faster for cells cultured at high density.

shift from proliferative to non-proliferative conditions during the differentiation process. The expression of characteristics osteoblast and osteocyte markers confirmed differentiation with changes in synthesis of extracellular matrix proteins. Furthermore, by 21 days of *in vitro* culture, osteoblasts cultured at high density increased the protrusion length over time, exhibited dendritic morphology, did not increase cell number, upregulated ALP activity, downregulated BSP2 synthesis and produced more DMP1. Thus they underwent changes in cell morphology, proliferation, mineral deposition and protein production that are specific of the differentiation into osteocytes. Conversely, osteoblasts cultured at low density had constant protrusion length up to 21 days, proliferated, had constant ALP activity and produced only BSP2. They consistently exhibited no transition toward the osteocytic phenotype.

One limitation of this study is the presence of a 3D hydrogel embedding cells in a narrow space that made RNA purification not possible after extraction for gene expression analysis. Moreover, the cell extraction protocol took one night for the complete digestion of the collagen matrix, which would inexorably affect results from PCR. Previous works on cell differentiation in microfluidic systems focused on the protein expression rather than gene profiles (Kim et al., 2011; Li et al., 2014; Park et al., 2015; Zhang et al., 2015; Agrawal et al., 2017), considering the technical challenges and that protein biosynthesis depends on transcript levels as well as other factors such as the local availability of resources (Liu et al., 2016). We believe that our results on dendritic morphology, cell proliferation, alkaline phsphatase activity and protein synthesis firmly indicate osteoblasts differentiation and the effectiveness of the microengineered technology used.

4. CONCLUSIONS

Traditional *in vitro* systems already showed that primary human osteoblasts embedded in a 3D fibrous collagen matrix differentiates into osteocytes under specific conditions. Here, we translated the findings of traditional macro-models on osteoblast differentiation to the organ-on-a-chip scale. We created a minimal functional unit that captures the major aspects underlying the differentiation of primary human osteoblasts into osteocytes, which depends on the cell seeding density. A custom image analysis software was developed to support the semi-automatic analysis of cell dendrite elongation. Only the human osteoblasts seeded at higher density underwent the change in cell morphology, proliferation, mineral deposition and protein synthesis that are specific of the differentiation into osteocytes. The use of the microengineered technology to study the maturation of primary human osteoblasts in a 3D fibrous extracellular matrix takes advantage of the limited number of cells required by these systems, creating a unique platform to represent the phenotype variability as well as to elucidate the role of single or simultaneous stimulation in osteoblast maturation. From a clinical perspective, the bone-on-a-chip presented in this work provides the minimal functional

microenvironment to build patient-specific bone models to study the individual osteogenic potential and the effect of alternative therapies.

DATA AVAILABILITY STATEMENT

Raw data is available upon request to the corresponding author. The image analysis software used for cell protrusion tracking in this study was developed in Python 3, and is available under github.com/gabnasello/cellprotrusiontracker-frontiers2020.

AUTHOR CONTRIBUTIONS

GN, PA-D, and JS designed the experiments. GN and PA-D carried out the experiments. GN developed the image analysis software. GN, JS, MP, LM, and JG-A participated in study design. GN analyzed the results and wrote the manuscript. All authors discussed the results and approved the final version of the manuscript.

FUNDING

This work has emanated from research conducted with financial support of the European Union's Horizon 2020 research and innovation programme under the Marie Skłodowska-Curie grant agreement No. 722535 (CuraBone project), of Science Foundation Ireland (SFI) co-funded under under grant number 14/IA/2884 and of the Spanish Ministry of Economy and Competitiveness (Spain) through the research project DPI 2017-84780-C2-1-R.

ACKNOWLEDGMENTS

The authors would like to thank Dr. Carlos Borau for his valuable help with the development of the image analysis software for cell protrusion tracking.

SUPPLEMENTARY MATERIAL

The Supplementary Material for this article can be found online at: https://www.frontiersin.org/articles/10.3389/fbioe.2020.00336/full#supplementary-material

REFERENCES

Agrawal, G., Aung, A., and Varghese, S. (2017). Skeletal muscle-on-a-chip: an *in vitro* model to evaluate tissue formation and injury. *Lab Chip* 17, 3447–3461. doi: 10.1039/C7LC00512A

Almodóvar, J., Crouzier, T., Selimović, S., Boudou, T., Khademhosseini, A., and Picart, C. (2013). Gradients of physical and biochemical cues on polyelectrolyte multilayer films generated via microfluidics. *Lab Chip* 13:1562. doi: 10.1039/c3lc41407h

Atkins, G., Findlay, D., Anderson, P., and Morris, H. (2011). Target genes: bone proteins, in *Vitamin D, 3rd Edn, Vol. 25*, eds D. Feldman, J. W. Pike, and J. S. Adams (Cambridge, MA: Elsevier), 411–424. doi: 10.1016/B978-0-12-381978-9.10023-X

Atkins, G. J., Welldon, K. J., Wijenayaka, A. R., Bonewald, L. F., and Findlay, D. M. (2009). Vitamin K promotes mineralization, osteoblast-to-osteocyte transition, and an anticatabolic phenotype by gamma-carboxylation-dependent and -independent mechanisms. *Am. J. Physiol. Cell Physiol.* 297, C1358–C1367. doi: 10.1152/ajpcell.00216.2009

Bernhardt, A., Weiser, E., Wolf, S., Vater, C., and Gelinsky, M. (2019). Primary human osteocyte networks in pure and modified collagen gels. *Tissue Eng. Part A* 25, 1347–1355. doi: 10.1089/ten.tea.2018.0338

Bersini, S., Jeon, J. S., Dubini, G., Arrigoni, C., Chung, S., Charest, J. L., et al. (2014). A microfluidic 3D *in vitro* model for specificity of breast cancer metastasis to bone. *Biomaterials* 35, 2454–2461. doi: 10.1016/j.biomaterials.2013.11.050

Bertassoni, L. E., Cecconi, M., Manoharan, V., Nikkhah, M., Hjortnaes, J., Cristino, A. L., et al. (2014). Hydrogel bioprinted microchannel networks for vascularization of tissue engineering constructs. *Lab Chip* 14, 2202–2211. doi: 10.1039/C4LC00030G

Birmingham, E., Niebur, G. L., McHugh, P. E., Shaw, G., Barry, F. P., and McNamara, L. M. (2012). Osteogenic differentiation of mesenchymal stem cells is regulated by osteocyte and osteoblast cells in a simplified bone niche. *Eur. Cells Mater.* 23, 13–27. doi: 10.22203/eCM.v023a02

Bonewald, L. F. (2011). The amazing osteocyte. *J. Bone Miner. Res.* 26, 229–238. doi: 10.1002/jbmr.320

Boukhechba, F., Balaguer, T., Michiels, J. F., Ackermann, K., Quincey, D., Bouler, J. M., et al. (2009). Human primary osteocyte differentiation in a 3D culture system. *J. Bone Miner. Res.* 24, 1927–1935. doi: 10.1359/jbmr.090517

Chai, Y. C., Carlier, A., Bolander, J., Roberts, S. J., Geris, L., Schrooten, J., et al. (2012). Current views on calcium phosphate osteogenicity and the translation into effective bone regeneration strategies. *Acta Biomater.* 8, 3876–3887. doi: 10.1016/j.actbio.2012.07.002

Chuang, C.-H., Lin, R.-Z., Melero-Martin, J. M., and Chen, Y.-C. (2018). Comparison of covalently and physically cross-linked collagen hydrogels on mediating vascular network formation for engineering adipose tissue. *Artif. Cells Nanomed. Biotechnol.* 46(Suppl. 3), S434S447. doi: 10.1080/21691401.2018.1499660

Clover, J., and Gowen, M. (1994). Are MG-63 and HOS TE85 human osteosarcoma cell lines representative models of the osteoblastic phenotype? *Bone* 15, 585–591. doi: 10.1016/8756-3282(94)90305-0

Coleman, J. E. (1992). Structure and mechanism of alkaline phosphatase. *Annu. Rev. Biophys. Biomol. Struct.* 21, 441–483. doi: 10.1146/annurev.bb.21.060192.002301

Dallas, S. L., and Bonewald, L. F. (2010). Dynamics of the transition from osteoblast to osteocyte. *Ann. N. Y. Acad. Sci.* 1192, 437–443. doi: 10.1111/j.1749-6632.2009.05246.x

de Wildt, B. W., Ansari, S., Sommerdijk, N. A., Ito, K., Akiva, A., and Hofmann, S. (2019). From bone regeneration to three-dimensional *in vitro* models: tissue engineering of organized bone extracellular matrix. *Curr. Opin. Biomed. Eng.* 10, 107–115. doi: 10.1016/j.cobme.2019.05.005

Del Amo, C., Borau, C., Movilla, N., Asín, J., and García-Aznar, J. M. (2017). Quantifying 3D chemotaxis in microfluidic-based chips with step gradients of collagen hydrogel concentrations. *Integr. Biol.* 9, 339–349. doi: 10.1039/C7IB00022G

Del Amo, C., Olivares, V., Cóndor, M., Blanco, A., Santolaria, J., Asín, J., et al. (2018). Matrix architecture plays a pivotal role in 3D osteoblast migration: the effect of interstitial fluid flow. *J. Mech. Behav. Biomed. Mater.* 83, 52–62. doi: 10.1016/j.jmbbm.2018.04.007

Eliceiri, K. W., Berthold, M. R., Goldberg, I. G., Ibá nez, L., Manjunath, B. S., Martone, M. E., et al. (2012). Biological imaging software tools. *Nat. Methods* 9, 697–710. doi: 10.1038/nmeth.2084

Franz-Odendaal, T. A., Hall, B. K., and Witten, P. E. (2006). Buried alive: how osteoblasts become osteocytes. *Dev. Dyn.* 235, 176–190. doi: 10.1002/dvdy.20603

Golub, E. E., and Boesze-Battaglia, K. (2007). The role of alkaline phosphatase in mineralization. *Curr. Opin. Orthop*. 18, 444–448. doi: 10.1097/BCO.0b013e3282630851

Gu, Y., Zhang, W., Sun, Q., Hao, Y., Zilberberg, J., and Lee, W. Y. (2015). Microbead-guided reconstruction of the 3D osteocyte network during microfluidic perfusion culture. *J. Mater. Chem. B* 3, 3625–3633. doi: 10.1039/C5TB00421G

Hao, S., Ha, L., Cheng, G., Wan, Y., Xia, Y., Sosnoski, D. M., et al. (2018). A spontaneous 3D bone-on-a-chip for bone metastasis study of breast cancer cells. *Small* 14, 1–10. doi: 10.1002/smll.201702787

Huh, D., Hamilton, G. A., and Ingber, D. E. (2011). From 3D cell culture to organs-on-chips. *Trends Cell Biol*. 21, 745–754. doi: 10.1016/j.tcb.2011.09.005

Jang, K., Sato, K., Igawa, K., Chung, U.-I., and Kitamori, T. (2008). Development of an osteoblast-based 3D continuous-perfusion microfluidic system for drug screening. *Anal. Bioanal. Chem*. 390, 825–832. doi: 10.1007/s00216-007-1752-7

Jusoh, N., Oh, S., Kim, S., Kim, J., and Jeon, N. L. (2015). Microfluidic vascularized bone tissue model with hydroxyapatite-incorporated extracellular matrix. *Lab Chip* 15, 3984–3988. doi: 10.1039/C5LC00698H

Kim, C., Lee, K. S., Bang, J. H., Kim, Y. E., Kim, M.-C., Oh, K. W., et al. (2011). 3-Dimensional cell culture for on-chip differentiation of stem cells in embryoid body. *Lab Chip* 11:874. doi: 10.1039/c0lc00516a

Langenbach, F., and Handschel, J. (2013). Effects of dexamethasone, ascorbic acid and β-glycerophosphate on the osteogenic differentiation of stem cells *in vitro*. *Stem Cell Res. Ther*. 4:117. doi: 10.1186/scrt328

Leclerc, E., David, B., Griscom, L., Lepioufle, B., Fujii, T., Layrolle, P., et al. (2006). Study of osteoblastic cells in a microfluidic environment. *Biomaterials* 27, 586–595. doi: 10.1016/j.biomaterials.2005.06.002

Li, S., Glynne-Jones, P., Andriotis, O. G., Ching, K. Y., Jonnalagadda, U. S., Oreffo, R. O. C., et al. (2014). Application of an acoustofluidic perfusion bioreactor for cartilage tissue engineering. *Lab Chip* 14, 4475–4485. doi: 10.1039/C4LC00956H

Linkert, M., Rueden, C. T., Allan, C., Burel, J.-M., Moore, W., Patterson, A., et al. (2010). Metadata matters: access to image data in the real world. *J. Cell Biol*. 189, 777–782. doi: 10.1083/jcb.201004104

Liu, Y., Beyer, A., and Aebersold, R. (2016). On the dependency of cellular protein levels on mRNA abundance. *Cell* 165, 535–550. doi: 10.1016/j.cell.2016.03.014

Lorsch, J. R., Collins, F. S., and Lippincott-Schwartz, J. (2014). Fixing problems with cell lines. *Science* 346, 1452–1453. doi: 10.1126/science.1259110

Marturano-Kruik, A., Nava, M. M., Yeager, K., Chramiec, A., Hao, L., Robinson, S., et al. (2018). Human bone perivascular niche-on-a-chip for studying metastatic colonization. *Proc. Natl. Acad. Sci. U.S.A*. 115, 1256–1261. doi: 10.1073/pnas.1714282115

McGarrigle, M. J., Mullen, C. A., Haugh, M. G., Voisin, M. C., and McNamara, L. M. (2016). Osteocyte differentiation and the formation of an interconnected cellular network *in vitro*. *Eur. Cells Mater*. 31, 323–340. doi: 10.22203/eCM.v031a21

Middleton, K., Al-Dujaili, S., Mei, X., Günther, A., and You, L. (2017). Microfluidic co-culture platform for investigating osteocyte-osteoclast signalling during fluid shear stress mechanostimulation. *J. Biomech*. 59, 35–42. doi: 10.1016/j.jbiomech.2017.05.012

Moreno-Arotzena, O., Meier, J., del Amo, C., and García-Aznar, J. (2015). Characterization of fibrin and collagen gels for engineering wound healing models. *Materials* 8, 1636–1651. doi: 10.3390/ma8041636

Movilla, N., Borau, C., Valero, C., and García-Aznar, J. (2018). Degradation of extracellular matrix regulates osteoblast migration: a microfluidic-based study. *Bone* 107, 10–17. doi: 10.1016/j.bone.2017.10.025

Mullen, C. A., Haugh, M. G., Schaffler, M. B., Majeska, R. J., and McNamara, L. M. (2013). Osteocyte differentiation is regulated by extracellular matrix stiffness and intercellular separation. *J. Mech. Behav. Biomed. Mater*. 28, 183–194. doi: 10.1016/j.jmbbm.2013.06.013

Nakashima, T., Hayashi, M., Fukunaga, T., Kurata, K., Oh-hora, M., Feng, J. Q., et al. (2011). Evidence for osteocyte regulation of bone homeostasis through RANKL expression. *Nat. Med*. 17, 1231–1234. doi: 10.1038/nm.2452

O'Brien, F. J. (2011). Biomaterials & scaffolds for tissue engineering. *Mater. Today* 14, 88–95. doi: 10.1016/S1369-7021(11)70058-X

Osaki, T., Sivathanu, V., and Kamm, R. D. (2018). Vascularized microfluidic organ-chips for drug screening, disease models and tissue engineering. *Curr. Opin. Biotechnol*. 52, 116–123. doi: 10.1016/j.copbio.2018.03.011

Park, J., Lee, B. K., Jeong, G. S., Hyun, J. K., Lee, C. J., and Lee, S.-H. (2015). Three-dimensional brain-on-a-chip with an interstitial level of flow and its application as an *in vitro* model of Alzheimer's disease. *Lab Chip* 15, 141–150. doi: 10.1039/C4LC00962B

Pirosa, A., Gottardi, R., Alexander, P. G., and Tuan, R. S. (2018). Engineering *in-vitro* stem cell-based vascularized bone models for drug screening and predictive toxicology. *Stem Cell Res. Ther*. 9:112. doi: 10.1186/s13287-018-0847-8

Poole, K. E., Van Bezooijen, R. L., Loveridge, N., Hamersma, H., Papapoulos, S. E., Löwik, C. W., et al. (2005). Sclerostin is a delayed secreted product of osteocytes that inhibits bone formation. *FASEB J*. 19, 1842–1844. doi: 10.1096/fj.05-4221fje

Prideaux, M., Findlay, D. M., and Atkins, G. J. (2016). Osteocytes: the master cells in bone remodelling. *Curr. Opin. Pharmacol*. 28, 24–30. doi: 10.1016/j.coph.2016.02.003

Reznikov, N., Boughton, O. R., Ghouse, S., Weston, A. E., Collinson, L., Blunn, G. W., et al. (2019). Individual response variations in scaffold-guided bone regeneration are determined by independent strain- and injury-induced mechanisms. *Biomaterials* 194, 183–194. doi: 10.1016/j.biomaterials.2018.11.026

Ronaldson-Bouchard, K., and Vunjak-Novakovic, G. (2018). Organs-on-a-chip: a fast track for engineered human tissues in drug development. *Cell Stem Cell* 22, 310–324. doi: 10.1016/j.stem.2018.02.011

Rowe, S. L., and Stegemann, J. P. (2006). Interpenetrating collagen-fibrin composite matrices with varying protein contents and ratios. *Biomacromolecules* 7, 2942–2948. doi: 10.1021/bm0602233

Schiavi, J., Keller, L., Morand, D.-N., Isla, N. D., Huck, O., Lutz, J. C., et al. (2015). Active implant combining human stem cell microtissues and growth factors for bone-regenerative nanomedicine. *Nanomedicine* 10, 753–763. doi: 10.2217/nnm.14.228

Shin, Y., Han, S., Jeon, J., Yamamoto, K., Zervantonakis, I., Sudo, R., et al. (2012). Microfluidic assay for simultaneous culture of multiple cell types on surfaces or within hydrogels. *Nat. Protoc*. 7, 1247–1259. doi: 10.1038/nprot.2012.051

Skottke, J., Gelinsky, M., and Bernhardt, A. (2019). *In vitro* co-culture model of primary human osteoblasts and osteocytes in collagen gels. *Int. J. Mol. Sci*. 20:1998. doi: 10.3390/ijms20081998

Sun, Q., Choudhary, S., Mannion, C., Kissin, Y., Zilberberg, J., and Lee, W. (2017). *Ex vivo* construction of human primary 3D-networked osteocytes. *Bone* 105, 245–252. doi: 10.1016/j.bone.2017.09.012

Sun, Q., Gu, Y., Zhang, W., Dziopa, L., Zilberberg, J., and Lee, W. (2015). *Ex vivo* 3D osteocyte network construction with primary murine bone cells. *Bone Res*. 3:15026. doi: 10.1038/boneres.2015.26

Uchihashi, K., Aoki, S., Matsunobu, A., and Toda, S. (2013). Osteoblast migration into type I collagen gel and differentiation to osteocyte-like cells within a self-produced mineralized matrix: a novel system for analyzing differentiation from osteoblast to osteocyte. *Bone* 52, 102–110. doi: 10.1016/j.bone.2012.09.001

Valero, C., Amaveda, H., Mora, M., and García-Aznar, J. M. (2018). Combined experimental and computational characterization of crosslinked collagen-based hydrogels. *PLoS ONE* 13:e0195820. doi: 10.1371/journal.pone.0195820

van der Walt, S., Schönberger, J. L., Nunez-Iglesias, J., Boulogne, F., Warner, J. D., Yager, N., et al. (2014). scikit-image: image processing in Python. *PeerJ* 2:e453. doi: 10.7717/peerj.453

Wittkowske, C., Reilly, G. C., Lacroix, D., and Perrault, C. M. (2016). *In vitro* bone cell models: impact of fluid shear stress on bone formation. *Front. Bioeng. Biotechnol*. 4:87. doi: 10.3389/fbioe.2016.00087

Woo, S. M., Rosser, J., Dusevich, V., Kalajzic, I., and Bonewald, L. F. (2011). Cell line IDG-SW3 replicates osteoblast-to-late-osteocyte differentiation *in vitro* and accelerates bone formation *in vivo*. *J. Bone Miner. Res*. 26, 2634–2646. doi: 10.1002/jbmr.465

Yeh, S. C. A., Wilk, K., Lin, C. P., and Intini, G. (2018). *In vivo* 3D histomorphometry quantifies bone apposition and skeletal progenitor cell differentiation. *Sci. Rep*. 8:5580. doi: 10.1038/s41598-018-23785-6

You, L., Temiyasathit, S., Lee, P., Kim, C. H., Tummala, P., Yao, W., et al. (2008). Osteocytes as mechanosensors in the inhibition of bone resorption due to mechanical loading. *Bone* 42, 172–179. doi: 10.1016/j.bone.2007.09.047

Zhang, B., Korolj, A., Lai, B. F. L., and Radisic, M. (2018). Advances in organ-on-a-chip engineering. *Nat. Rev. Mater.* 3, 257–278. doi: 10.1038/s41578-018-0034-7

Zhang, K., Barragan-Adjemian, C., Ye, L., Kotha, S., Dallas, M., Lu, Y., et al. (2006). E11/gp38 selective expression in osteocytes: regulation by mechanical strain and role in dendrite elongation. *Mol. Cell. Biol.* 26, 4539–4552. doi: 10.1128/MCB.02120-05

Zhang, W., Gu, Y., Hao, Y., Sun, Q., Konior, K., Wang, H., et al. (2015). Well plate-based perfusion culture device for tissue and tumor microenvironment replication. *Lab Chip* 15, 2854–2863. doi: 10.1039/C5LC00341E

Conflict of Interest: The authors declare that the research was conducted in the absence of any commercial or financial relationships that could be construed as a potential conflict of interest.

frontiers in Bioengineering and Biotechnology

ORIGINAL RESEARCH
published: 24 April 2020
doi: 10.3389/fbioe.2020.00290

A Novel Scaffold-Based Hybrid Multicellular Model for Pancreatic Ductal Adenocarcinoma—Toward a Better Mimicry of the *in vivo* Tumor Microenvironment

*Priyanka Gupta[1], Pedro A. Pérez-Mancera[2], Hemant Kocher[3], Andrew Nisbet[4], Giuseppe Schettino[5,6] and Eirini G. Velliou[1]**

[1] Bioprocess and Biochemical Engineering Group (BioProChem), Department of Chemical and Process Engineering, University of Surrey, Guildford, United Kingdom, [2] Department of Molecular and Clinical Cancer Medicine, University of Liverpool, Liverpool, United Kingdom, [3] Centre for Tumour Biology and Experimental Cancer Medicine, Barts Cancer Institute, Queen Mary University of London, London, United Kingdom, [4] Department of Medical Physics and Biomedical Engineering, University College London, London, United Kingdom, [5] Department of Physics, University of Surrey, Guildford, United Kingdom, [6] Medical Radiation Science Group, The National Physical Laboratory, Teddington, United Kingdom

OPEN ACCESS

Edited by:
Dimitrios I. Zeugolis, National University of Ireland Galway, Ireland

Reviewed by:
Shin Hamada, Tohoku University, Japan
Romano Pirola, University of New South Wales, Australia

***Correspondence:**
Eirini G. Velliou
e.velliou@surrey.ac.uk

Specialty section:
This article was submitted to Tissue Engineering and Regenerative Medicine, a section of the journal Frontiers in Bioengineering and Biotechnology

Received: *17 January 2020*
Accepted: *19 March 2020*
Published: *24 April 2020*

Citation:
Gupta P, Pérez-Mancera PA, Kocher H, Nisbet A, Schettino G and Velliou EG (2020) A Novel Scaffold-Based Hybrid Multicellular Model for Pancreatic Ductal Adenocarcinoma—Toward a Better Mimicry of the in vivo Tumor Microenvironment. Front. Bioeng. Biotechnol. 8:290. doi: 10.3389/fbioe.2020.00290

With a very low survival rate, pancreatic ductal adenocarcinoma (PDAC) is a deadly disease. This has been primarily attributed to (i) its late diagnosis and (ii) its high resistance to current treatment methods. The latter specifically requires the development of robust, realistic *in vitro* models of PDAC, capable of accurately mimicking the *in vivo* tumor niche. Advancements in the field of tissue engineering (TE) have helped the development of such models for PDAC. Herein, we report for the first time a novel hybrid, polyurethane (PU) scaffold-based, long-term, multicellular (tri-culture) model of pancreatic cancer involving cancer cells, endothelial cells, and stellate cells. Recognizing the importance of ECM proteins for optimal growth of different cell types, the model consists of two different zones/compartments: an inner tumor compartment consisting of cancer cells [fibronectin (FN)-coated] and a surrounding stromal compartment consisting of stellate and endothelial cells [collagen I (COL)-coated]. Our developed novel hybrid, tri-culture model supports the proliferation of all different cell types for 35 days (5 weeks), which is the longest reported timeframe *in vitro*. Furthermore, the hybrid model showed extensive COL production by the cells, mimicking desmoplasia, one of PDAC's hallmark features. Fibril alignment of the stellate cells was observed, which attested to their activated state. All three cell types expressed various cell-specific markers within the scaffolds, throughout the culture period and showed cellular migration between the two zones of the hybrid scaffold. Our novel model has great potential as a low-cost tool for *in vitro* studies of PDAC, as well as for treatment screening.

Keywords: pancreatic cancer, multicellular tumor model, 3D model, endothelial cells, pancreatic stellate cells, scaffold-assisted tumor model, polyurethane scaffold

INTRODUCTION

Pancreatic ductal adenocarcinoma (PDAC) is the fourth leading cause of cancer-related deaths worldwide and accounts for about 7% of all cancer-related deaths (Siegel et al., 2018). The 5-year survival rate is about 9% and has barely improved over the last decades (Cancer.Net, 2019). These dismal figures for PDAC are due to its late-stage diagnosis, early and rapid metastasis, along with a high resistance to currently available treatment options (mainly, chemotherapy and radiotherapy) (Kleeff et al., 2016). The latter is attributed to the complex tumor microenvironment (TME) of PDAC. The PDAC's TME consists of a cocktail of cellular, biochemical, biomechanical, and structural components, which interact in complex ways and contribute to the disease progression. More specifically, the stellate cells of the TME are known to produce very high amounts of extracellular matrix (ECM) proteins, leading to the so-called desmoplastic or fibrotic reaction. The increase of matrix proteins, e.g., collagen, fibronectin (FN), also results in tumor vessel collapse, along with the formation of aberrant, disorganized vessel networks (Longo et al., 2016). Overall, fibrosis/desmoplasia contributes to the high resistance of PDAC to treatment (Seicean et al., 2015; Chand et al., 2016; Totti et al., 2017; Ansari et al., 2018; Totti et al., 2018).

Traditionally, research on PDAC is conducted in (i) 2D *in vitro* systems (Onishi et al., 2012; Sato et al., 2018; Zhang et al., 2018; Serri et al., 2019) or in (ii) animal models, primarily mice (Awasthi et al., 2011; Dovzhanskiy et al., 2012; Courtin et al., 2013; Shinoda et al., 2018; Zhang et al., 2018; Awasthi et al., 2019). Although 2D systems are cheap, easy to use, and reproducible, they are unable to mimic accurately key *in vivo* characteristics like the TME structure, stiffness, the cellular spatial orientation, the cellular cross-talk, the cell-ECM interactions, or the environmental gradients (Onishi et al., 2012; Adcock et al., 2015; Jaidev et al., 2015; Totti et al., 2017; Chim and Mikos, 2018). Animal models can accurately mimic the *in vivo* conditions and hence are widely used for laboratory research and pre-clinical trials (Pérez–Mancera et al., 2012; Courtin et al., 2013; Bermejo-Rodríguez and Pérez-Mancera, 2015; Erstad et al., 2018; Humpton et al., 2019; Yan et al., 2019). However, such systems are expensive, difficult to use, and are not easily reproducible (Pérez–Mancera et al., 2012; Adcock et al., 2015; Ireland et al., 2016; Yan et al., 2019).

Advancements in the field of tissue engineering (TE) have enabled the development of different types of 3D *in vitro* models that realistically mimic *in vivo* tissue niches, including tumor tissues. Current 3D models of pancreatic tumors include (i) spheroids (from cell lines) or organoids (from primary tissue) (Froeling et al., 2009; Matsuda et al., 2010; Longati et al., 2013; Wen et al., 2013; Boj et al., 2015; Chiellini et al., 2016; Di Maggio et al., 2016; Ware et al., 2016; Brancato et al., 2017), (ii) hydrogels (Ki et al., 2014; Chiellini et al., 2016; Brancato et al., 2017; Okumura et al., 2019), and (iii) polymeric scaffolds based systems (He et al., 2013; Raza et al., 2013; Wang et al., 2013; Ricci et al., 2014; Chand et al., 2016; Totti et al., 2018). Overall, such 3D models have substantial advantages as compared to 2D systems and animal models. These include low cost and higher reproducibility, as compared to animal models and provision of more realistic structure, cell–cell and cell–ECM interactions, and realistic distribution of parameters, such as nutrients and oxygen concentration, as compared to 2D systems (Fernandes et al., 2009; Wang et al., 2016; Totti et al., 2017). For example, Longati et al. (2013) showed increased matrix protein secretion and increased resistance to the chemotherapeutic agent Gemcitabine in 3D spheroids, as compared to 2D systems for PANC-1 pancreatic cancer cell lines. Similarly, an increase in chemo-resistance in 3D spheroids when compared to 2D was also reported by Wen et al. (2013) for PANC-1 and MIA PaCa-2 cell lines. Ki et al. (2014) encapsulated COLO-357 cells within poly(ethylene glycol)-based hydrogels enhanced with collagen I (COL) fibrils to mimic the PDAC's desmoplasia and observed enhanced cell proliferation and epithelial–mesenchymal transition (EMT) within gels enriched with COL. Long-term (i.e., some weeks), culture of pancreatic cancer cells within polymeric scaffolds and hydrogels has been reported in some studies (Ricci et al., 2014; Chiellini et al., 2016; Totti et al., 2018; Gupta et al., 2019). Chiellini et al. carried out long-term (28 days) culture of BxPC-3 cell lines within micro-structured chitosan (mCS)-based or polyelectrolyte complex (mPEC) hydrogels. It was reported that cells in the hydrogels were able to maintain cancer features, like loss of cell polarity, which were not present in 2D. Furthermore, increase in matrix stiffness enhanced the expression of tumor-specific markers (Chiellini et al., 2016). We have also recently reported long-term (more than 5 weeks) culture of various PDAC cell lines, i.e., PANC-1, AsPC-1, BxPC-3, in polyurethane (PU) polymeric scaffolds wherein cell clustering, cell proliferation, and matrix protein production followed *in vivo*-like trends (Totti et al., 2018). We also reported that the model was able to mimic a clinically relevant response to various treatment protocols (Gupta et al., 2019).

However, all of the above models are monocellular, taking into consideration only pancreatic cancer cells. Therefore, they cannot recapitulate accurately the cellular complexity of the PDAC TME, which contains a plethora of different cell types, e.g., endothelial cells, stellate cells, which are crucial for the disease progression and resistance to treatment (Wehr et al., 2011; Hamada et al., 2012; Karnevi et al., 2016; Bynigeri et al., 2017). It is therefore important to recapitulate, in addition to the structural and biochemical complexity, features of the biological complexity of the PDAC TME. There are very limited multicellular 3D PDAC models, such as spheroids/organoids or hydrogel-based systems (Froeling et al., 2009; Di Maggio et al., 2016; Longo et al., 2016; Priwitaningrum et al., 2016; Ware et al., 2016; Brancato et al., 2017; Kuen et al., 2017; Noel et al., 2017; Shoval et al., 2017; Lazzari et al., 2018). Most multicellular PDAC models consist of two cells types involving cancer cells co-cultured with fibroblasts/stellate cells, endothelial cells, mesenchymal stem cells (MSCs), or immune cells. For example, Froeling et al. used COL and Matrigel to create spheroids of pancreatic cancer cells (Capan-1 and PaCa-3) with activated stellate cells or the normal fibroblastic cell line MRC-5 for 7 days. An increase in the number of invasive cancer cells and a decrease in the expression of cytokeratin (suggesting EMT) was observed in presence of stellate cells and MRC-5 fibroblasts (Froeling et al., 2009). Similarly,

Drifka et al. employed a collagen-coated microchannel spheroid-based co-culture of cancer cells (PANC-1) and primary stellate cells. Stellate cells facilitated collagen fiber alignment and helped cancer cell migration through the matrix (Drifka et al., 2016). Kuen et al. showed that the co-culture of cancer cells (PaTu-8902, BxPC-3, HPAC, and MiaCaPa-2) and MRC-5 fibroblasts in a spheroid model induced the production of immunosuppressive cytokines, highlighting the immunosuppressive role of different cell types within the tumor niche (Kuen et al., 2017). Ware et al. (2016) observed an impaired diffusion of Gemcitabine (1000 μM) in PDAC spheroids (PANC-1, AsPC-1, BxPC-3, Capan-1, and MIA PaCa-2) when they contained primary stellate cells as compared to mono-cellular cancer cell spheroids. Similarly, an increased resistance to oxaliplatin treatment in co-culture of patient-derived cancer associated fibroblasts (CAFs) with pancreatic cancer cells (MIA PaCa-2 and AsPC-1) in spheroids was observed by Broekgaarden et al. (2019). There are very few studies reporting co-culture of cancer cells with endothelial cells. Shoval et al. (2017) performed a 72-h co-culture with BxPC-3 PDAC cells and endothelial cells (HUVECs) in a spheroid model, wherein it was shown that the HUVECs mainly grew at the periphery of the spheroids and were unable to form vascular structures within the spheroids.

Among the multicellular PDAC studies, there are very limited studies of PDAC involving the presence of three cell types, and all those studies are in spheroid-type systems for a relatively short time period (24 h to 7 days). For example Beckermann et al. (2008) co-cultured pancreatic cancer cells (Capan-1, MIA-PaCa2, COLO-357, and BxPC-3), endothelial cells (HUVECs), and normal primary fibroblast cells in a spheroid model for 24 h. Di Maggio et al. (2016) developed a spheroid (Matrigel and COL-assisted)-based tri-culture model involving cancer cells (Capan-1, COLO-357, and AsPC-1), HUVECs, and activated pancreatic stellate cells (PS-1) and cultured it for 7 days. A gradual depletion of CD-31 positive HUVECs was observed in the spheroid system over time. Similarly, Lazzari et al. developed a co-culture model, which included cancer cells (PANC-1), HUVECs, and the fibroblast cell line MRC-5 for a period of 7 days. No endothelial cells were observed in the system after 4 days in culture. Furthermore, higher resistance to gemcitabine and doxorubicin was observed in the multicellular spheroids as compared to the monocellular ones (Lazzari et al., 2018).

Overall, spheroid-type multicellular models are valuable and suitable for molecular analysis and for fast drug response studies; however, they have certain limitations. Due to their spatial characteristics, artificially high diffusion gradients in terms of nutrients and oxygen can be formed, resulting in necrotic cores at the center and decreasing cellular proliferation very quickly (within a few days) (Burdett et al., 2010; Nath and Devi, 2016; Totti et al., 2017). Consequently, they are difficult to maintain over a long period of time (weeks or months) without re-suspending the cells to form fresh cellular aggregates. Such re-suspension can disturb the formed TME and cell–cell, cell–ECM interactions. Furthermore, it is difficult to robustly control the spheroid size and shape (Burdett et al., 2010; Nath and Devi, 2016; Totti et al., 2017). Hydrogel-type spheroids have better structure than simple cell-aggregates; however, they have relatively weak mechanical strength, making their long-term maintenance in culture challenging (Hoffman, 2012; Totti et al., 2017).

Polymer scaffold-assisted 3D structures can overcome several of the limitations associated with spheroids and hydrogels. They can provide a more robust mechanical strength and tunability allowing for much longer cultures (up to months), and they can be tuned to have appropriate internal structure, pore size, type, and distribution, enabling the recapitulation of the spatial organization of different cell types in a multicellular system, as well as allowing for proper diffusion of oxygen and other nutrients (O'Brien, 2011; Ricci et al., 2014; Velliou et al., 2015; Totti et al., 2017, 2018; Gupta et al., 2019). To the best of our knowledge, to date, there is no scaffold-assisted, multicellular model for PDAC.

The aim of this work was to address the above challenge *via* the development of a novel, multicellular, hybrid, PU scaffold-based model involving PANC-1 cancer cells, human microvascular endothelial cells (HMECs), and PS-1 pancreatic stellate cells. More specifically, building on our previously developed monocellular PU scaffold (Totti et al., 2018; Gupta et al., 2019), we performed appropriate zonal surface modification of the scaffolds with FN or COL to support growth and proliferation of different cells of the PDAC TME and we monitored proliferation, spatial organization, ECM secretion, and cellular interactions for a total of 5 weeks.

MATERIALS AND METHODS

Polymer Scaffold Preparation and Surface Modification

Polyurethane scaffolds were fabricated via the thermal induced phase separation method, as reported previously (Velliou et al., 2015; Totti et al., 2018). The scaffolds were then cut at appropriate sizes (see sections "Single Scaffold-Based 3D Cell Culture" and "Scaffold-Based Zonal 3D Cell Culture") and sterilized by exposing them to 70% ethanol (3 h) and UV ray (1 h). As previously reported, the average pore size of the scaffolds was 100–150 μm, the porosity was 85–90%, and the elastic modulus, 20 ± 2 kPa. It should be stated that the stiffness of the scaffolds was similar to that of PDAC *ex vivo* tissue (Chantarojanasiri and Kongkam, 2017; Pozzi et al., 2017; Rice et al., 2017).

Thereafter, as previously described, the generated scaffolds were surface modified (adsorption) with FN or COL for ECM mimicry (Totti et al., 2018; Gupta et al., 2019).

2D Cell Culture

The human pancreatic adenocarcinoma cell line PANC-1 (Sigma–Aldrich, Merck, United Kingdom) was expanded in Dulbecco's modified Eagle's medium (DMEM) with high glucose (Sigma–Aldrich, Merck, United Kingdom) supplemented with 10% fetal bovine serum (FBS, Fisher Scientific, United Kingdom), 1% penicillin/streptomycin (Fisher Scientific, United Kingdom), and 2 mM L-glutamine (Sigma–Aldrich, Merck, United Kingdom) in a humidified incubator at 37°C with 5% CO_2.

The HMEC line CRL-*3243* (ATCC, United Kingdom) was expanded in MCDB 131 medium (GIBCO, Thermo Fisher, United Kingdom), supplemented with 10% FBS, 1% penicillin/streptomycin, 2 mM L-glutamine, 10 ng/ml epidermal growth factor (SIGMA–Aldrich, Merck, United Kingdom), and 1 μg/ml hydrocortisone (SIGMA–Aldrich, Merck, United Kingdom) in a humidified incubator at 37°C with 5% CO_2.

The immortalized human pancreatic stellate cells (PS-1) were expanded in DMEM/F12 medium (GIBCO, Thermo Fisher, United Kingdom) supplemented with 10% FBS, 1% penicillin/streptomycin, and 2 mM L-glutamine in a humidified incubator at 37°C with 5% CO_2.

All cells were passaged regularly on reaching 80–90% confluency with TrypLE (GIBCO, Thermo Fisher, United Kingdom) until the required cell densities were obtained.

3D Cell Culture

Single Scaffold-Based 3D Cell Culture

Uncoated, FN- or COL-coated scaffolds were tested to analyze their ability to support PS-1 and HMEC cells in mono-culture, co-culture (PANC-1 + HMEC or PANC-1 + PS-1), and tri-culture (PANC-1 + PS-1 + HMEC).

For mono-culture experiments, 0.5×10^6 cells were seeded in each scaffold ($5 \times 5 \times 5$-mm^3-sized) (re-suspended in a total of 30 μl of cell culture media per scaffold) (Totti et al., 2018; Gupta et al., 2019). For the co-culture and tri-culture experiments, 0.25×10^6 cells per cell type were seeded in each scaffold ($5 \times 5 \times 5$-mm^3-sized), placed in 24 well plates, and cultured for 28 days (4 weeks), as per our previously established protocol (Totti et al., 2018; Gupta et al., 2019).

Scaffold-Based Zonal 3D Cell Culture

The single scaffold-based analysis for mono-, co-, and tri-cultures showed that different cell types prefer different ECM presence on the scaffold surface (see section "Results"). Therefore, to recapitulate that, a zonal scaffold architecture was designed. More specifically, as shown in **Figure 1**, two separate zones (a hollow cuboid with dimensions of approximately $7 \times 7 \times 5$ mm^3 and a solid inner cylinder of diameter of approximately 2 mm and height of 5 mm) were created/cut from the PU scaffold (prepared as described in section "Polymer Scaffold Preparation and Surface Modification") using a biopsy punch. The outer cuboid was coated with COL, while the inner cylinder was coated with FN through passive absorption, as described in Section "Polymer Scaffold Preparation and Surface Modification." HMEC and PS-1 stellate cells were seeded into the hollow cuboid in different ratios. As previously described, immediately after seeding, the scaffolds were placed in the incubator and cultured per our established protocol (Totti et al., 2018; Gupta et al., 2019) (section "Single Scaffold-Based 3D Cell Culture"). Based on our monocellular studies (**Figure 2**; Totti et al., 2018), we observed that PANC-1 cancer cells expanded at a faster rate in comparison to PS-1 and HMEC cells. Hence, to avoid the cancer cells' over-growing, as compared to the endothelial and stellate cells, we cultured the supporting cells (PS-1 and HMEC) for 7 days. On day 7, PANC-1 cells were seeded into the solid inner cylinder in a similar manner and then plugged inside the hollow cuboid to assemble to complete hybrid zonal model. The final ratios tested for PANC-1: HMEC: PS-1 were 1:1:1, 1:2:2, and 1:2:9, based on both ratios reported in literature for spheroid systems and on our initial trials (see single-scaffold-based experiments in sections "Single Scaffold-Based 3D Cell Culture" and "Scaffold-Based Zonal 3D Cell Culture") (Froeling et al., 2009; Di Maggio et al., 2016; Lazzari et al., 2018). Thereafter, the tri-culture was monitored for an additional 28 days (4 weeks). Separate inner and outer scaffold compartments were also cultured for the same duration of the experiment as controls for the individual zones.

Alamar Blue Viability Assay

The Alamar Blue assay was carried out every week per the manufacturer's instructions, to assess the cellular metabolic activity of the 3D cultures. Briefly, 10% Alamar Blue (Thermo Scientific, United Kingdom) solution was prepared in complete cell culture medium and added to the scaffolds followed by 2–3 h incubation at 37°C. At the end of the incubation period, change in Alamar Blue fluorescence was measured using BioTek, Plate reader (BioTek, United Kingdom) at 530 nm excitation and 590 nm emission.

Immunofluorescence Assay

In situ immunofluorescence (IF) staining of the scaffolds took place for the spatial determination of (i) the different cell types, CD-31 (HMEC), αSMA (PS-1), and pan-Cytokeratin (PANC-1), (ii) the cell proliferation (Ki-67), and (iii) the ECM production (COL). More specifically, scaffolds were snap frozen at specific time points in liquid nitrogen for 15 min and then preserved at -80°C until sectioning, as previously described (Allenby et al., 2017, 2019; Tahlawi et al., 2019). Prior to IF staining, scaffolds were sectioned and fixed for 4 h in 4% w/v paraformaldehyde (Sigma–Aldrich, Merck, United Kingdom). For intracellular proteins, scaffold sections were permeabilized for 2 h with 0.1% Triton-X solution (Sigma–Aldrich, Merck, United Kingdom), followed by 3 h blocking using 10% donkey serum solution. For membrane associated proteins, blocking was carried out without permeabilization. The primary antibody staining was carried out overnight, followed by overnight secondary antibody and DAPI co-staining. Each step employed a solvent containing 1% w/v bovine serum albumin (Sigma–Aldrich, Merck, United Kingdom) and 0.5% v/v Tween-20 (Promega, United Kingdom). For multi-panel staining involving both cell membrane and intracellular proteins, blocking, primary, secondary and DAPI staining solutions were made using 1% BSA, 0.5% Tween-20, and 0.1% Saponin (SIGMA–Aldrich, Merck, United Kingdom) solution to facilitate gentle permeabilization without the use of Triton-X.

Confocal Laser Scanning Microscopy (CLSM) Imaging

Immunofluorescent samples were imaged with a Nikon Ti-Eclipse inverted confocal microscope (Nikon Instruments, Europe) and processed with the NIS-Elements software using the following lasers and filters: (i) 405 (for DAPI), (ii) 488 (for Alexa

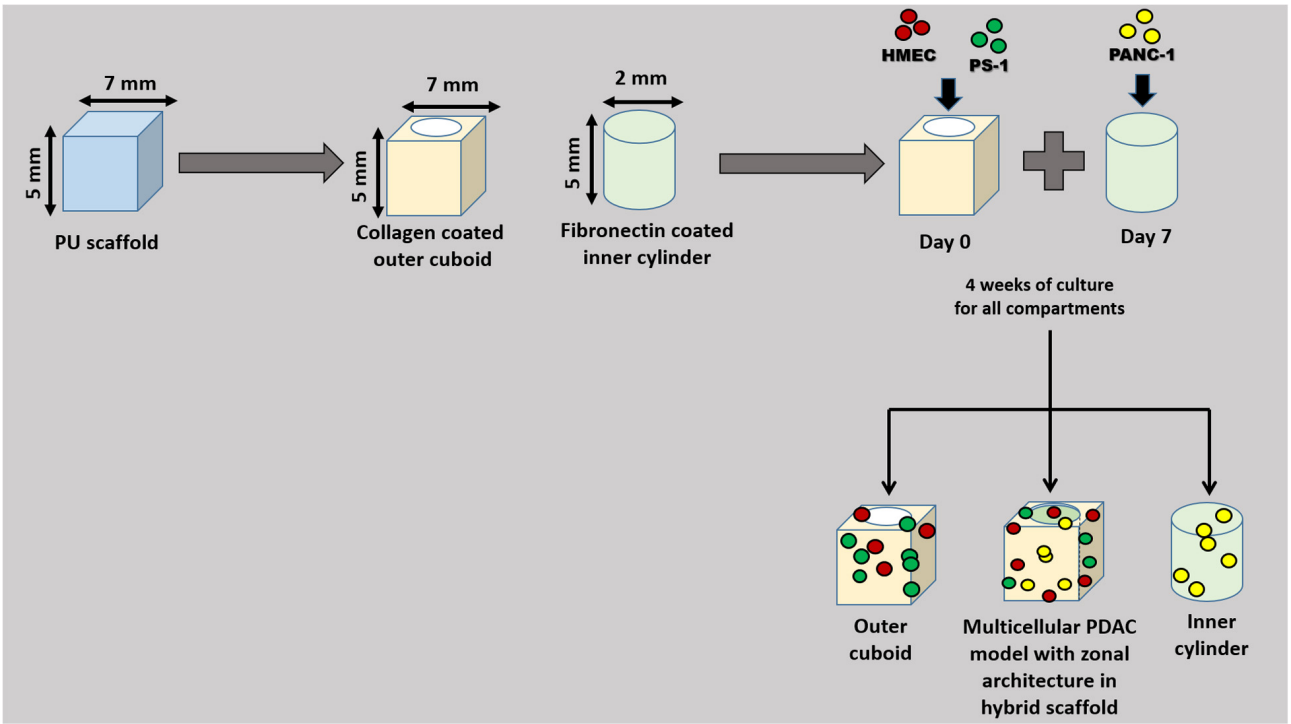

FIGURE 1 | Schematic diagram of the zonal architecture development for the scaffold-assisted multicellular model of PDAC. Polyurethane (PU) scaffolds were appropriately cut to design the zonal architecture. Different cells types were seeded at different time points and at different locations of the scaffold. The tri-culture system was monitored for 28 days (for a total experimental period of 35 days).

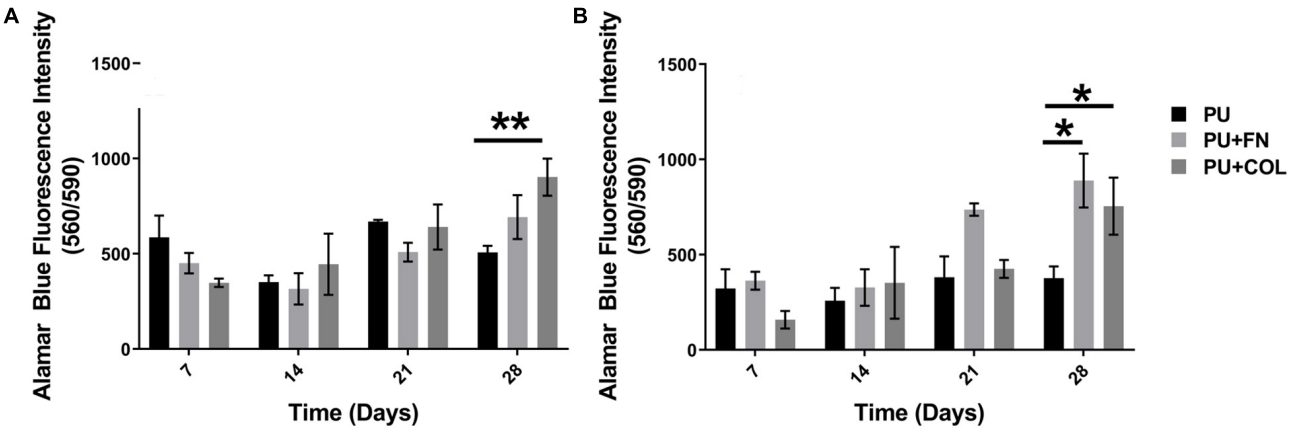

FIGURE 2 | Overall cellular metabolic activity as determined by the Alamar Blue metabolic assay within different PU scaffolds configurations (uncoated-PU, fibronectin-FN-coated, and collagen-COL-coated). **(A)** HMEC. **(B)** PS-1. *$p \leq 0.05$, **$p \leq 0.01$.

Fluor 488, Dylight 488), (iii) 561 (for Alexa Fluor 555, Dylight 550), and (iv) 643 nm (for Alexa Fluor 647, Dylight 650) for two sequential scans. Confocal images were captured using a 10x dry objective, with a 512 × 512-pixel resolution and 5–10 μm Z-stack distance, as previously described (Totti et al., 2018; Gupta et al., 2019). Multiple scaffolds as well as multiple areas and sections per scaffold were imaged to ensure reproducibility. Representative images are presented in this manuscript.

Statistical Analysis

Statistical analysis was performed for at least three independent experiments ($n \geq 3$) with at least three replicates per time point. Analysis of variance (ANOVA), followed by the Tukey's multiple comparison test, using the Graph Pad Prism® software (version 8.00 for Windows) to determine data statistical significance ($p < 0.05$). The error bars in the graphs represent standard error of mean.

RESULTS

Long-Term Mono-Culture of Stellate Cells and Endothelial Cells on PU Scaffolds

We have previously reported that PANC-1 pancreatic cancer cells are able to grow on PU scaffolds for over 28 days (4 weeks), forming dense cell clusters and secreting substantial amounts of COL in FN coated scaffolds (Totti et al., 2018). Similarly, in this work, mono-cultures of HMEC endothelial cells and PS-1 stellate cells were established on PU scaffolds both uncoated and coated with either FN or COL for 28 days (section "Single Scaffold-Based 3D Cell Culture"). Cell growth and viability were assessed weekly using the Alamar Blue viability assay (section "Alamar Blue Viability Assay"). As observed in **Figure 2**, both HMEC and PS-1 cells were able to attach and grow on the PU scaffolds for 28 days. At the end of 28 days, HMEC showed significantly higher cell viability on COL-coated scaffolds in comparison to uncoated ones. PS-1 stellate cells showed a significantly higher preference for coated scaffolds (FN or COL) over uncoated ones in terms of cellular metabolic activity as measured by the Alamar Blue assay (**Figure 2**).

Single PU Scaffold-Based Co-Culture and Tri-Culture of Stellate (PS-1), Endothelial (HMEC), and Cancer Cells (PANC-1)

As observed in the mono-culture experimental systems (section "Long-Term Monoculture of Stellate Cells and Endothelial Cells on PU Scaffolds"), both the PS-1 and HMEC cells were able to grow on PU scaffolds for 28 days and showed a preference for ECM protein coated scaffolds in comparison to those uncoated (**Figure 2**). Also, in our previously published work (Totti et al., 2018), we have reported that PANC-1 cells were able to grow on PU scaffolds (both coated and uncoated) for 28 days (4 weeks), with higher proliferation being observed in FN-coated scaffolds. Therefore, based on the results of the mono-cultures, we established co-culture and tri-culture systems using PU scaffolds, either uncoated or coated (FN or COL). Protein coatings enable the determination of the effects of different ECM proteins on such complex multicellular 3D models. As described in section "Single Scaffold-Based 3D Cell Culture," different combinations of the three cell types (PANC-1 + HMEC, PANC-1 + PS-1, and PANC-1 + HMEC + PS-1) were added to the scaffolds and cultured for 28 days. The overall cellular metabolic activity as an indication of the overall cell viability was monitored at regular intervals *via* the Alamar Blue Viability Assay (**Figure 3**).

As can be seen in **Figure 3**, the co-cultures as well as the tri-culture involving PANC-1, PS-1, and HMEC cells were all viable throughout the duration of our experiment (28 days). Significantly higher number of viable cells were observed on PU scaffolds coated with FN or COL in comparison to the uncoated scaffolds, similar to the HMEC and PS-1 mono-cultures (**Figure 2**; section "Long-Term Monoculture of Stellate Cells and Endothelial Cells on PU Scaffolds"), as well as in comparison to our previously published work for cancer cells (PANC-1) mono-culture (Totti et al., 2018). At the end of 28 days, sectioning and *in situ* fluorescence imaging of different cell-specific markers was conducted (i) to monitor the growth of all different cell types and (ii) to enable the assessment of the cell spatial distribution within the scaffolds (**Figure 4**). More specifically, HMEC cells were identified by CD-31 marker, stellate cells were identified by αSMA, and PANC-1 cells were stained for pan-Cytokeratin (section "Immunofluorescence Assay"). It is worth pointing out that most cancer cell lines are a heterogeneous mixture of cells at different stages of differentiation, hence not all cancer cells express the same proteins/markers (in this case, pan-Cytokeratin). Therefore, for our confocal laser scanning microscopy (CLSM) imaging in co and tri-culture systems, cells that only showed DAPI (nucleus) staining and no cell specific markers are assumed to be PANC-1 cancer cells.

As seen in **Figure 4**, all three cell types—i.e., cancer, endothelial, and stellate cells—were present within the PU scaffolds at the end of the 28-day culture period for both ECM coatings. The growth rate though of different cell types varied depending on the coating. For example, although FN-coated scaffolds promoted the growth of all cell types (both in co- and tri-culture systems, **Figures 4A–C**), for the co-culture of PANC-1 cancer cells and PS-1 stellate cells, the growth of PANC-1 was higher as compared to PS-1 cells (**Figure 4A**). More specifically, the PS-1 stellate cells were mainly found toward the periphery of the model, while PANC-1 cells were distributed throughout the whole scaffold. In contrast, COL-coating helped in a more homogenous growth and distribution of PS-1 stellate cells in a PANC-1 and PS-1 co-culture system (**Figure 4D**). The co-culture of PANC-1 cancer cells and HMEC endothelial cells also showed a similar trend. FN-coated scaffolds promoted the growth of PANC-1 over HMEC cells (**Figure 4B**), although in contrast to PS-1 (**Figure 4A**), HMEC cells were more evenly distributed within the FN-coated scaffolds (**Figure 4B**). COL-coating showed a significant increase in the number of endothelial cells within the scaffold resulting in dense cellular clusters (**Figure 4E**), clearly highlighting HMEC cells' preference for COL matrix protein. Nonetheless, both FN- and COL-coating were able to support a tri-culture tumor model within the PU scaffolds (**Figures 4C,F**). Similar to the co-cultures (**Figures 4A,B**), FN-coated PU scaffolds favored PANC-1 cancer cells over the HMEC and PS-1 cells (**Figure 4C**). The growth of the stellate cells was particularly suppressed within this system. In contrast, the COL-coated scaffolds promoted the growth of HMEC and PS-1 cells, resulting in a more homogenous distribution of all three cells types within the tumor model (**Figure 4F**).

PU Scaffold-Based Hybrid Zonal Multicellular Model of PDAC With Tri-Culture of Stellate (PS-1), Endothelial (HMEC), and Cancer Cells (PANC-1)

Overall, our observations on the co-culture and tri-culture systems above [section "Single PU Scaffold-Based Co-Culture and Tri-Culture of Stellate (PS-1), Endothelial (HMEC), and Cancer Cells (PANC-1)"], highlighted that the cellular

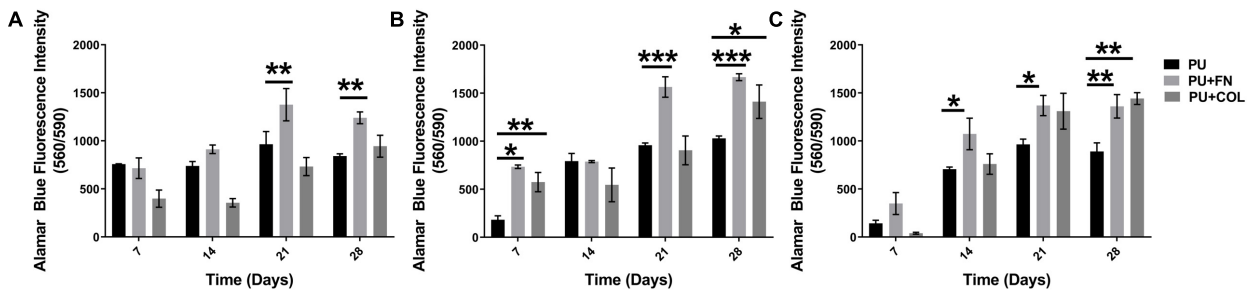

FIGURE 3 | Overall cellular metabolic activity as determined by the Alamar Blue metabolic assay within different PU scaffolds configurations (uncoated, fibronectin-FN-coated, and collagen-COL-coated). **(A)** PANC-1 + HMEC. **(B)** PANC-1 + PS-1. **(C)** PANC-1 + HMEC + PS-1. $^{*}p \leq 0.05$, $^{**}p \leq 0.01$, $^{***}p \leq 0.001$.

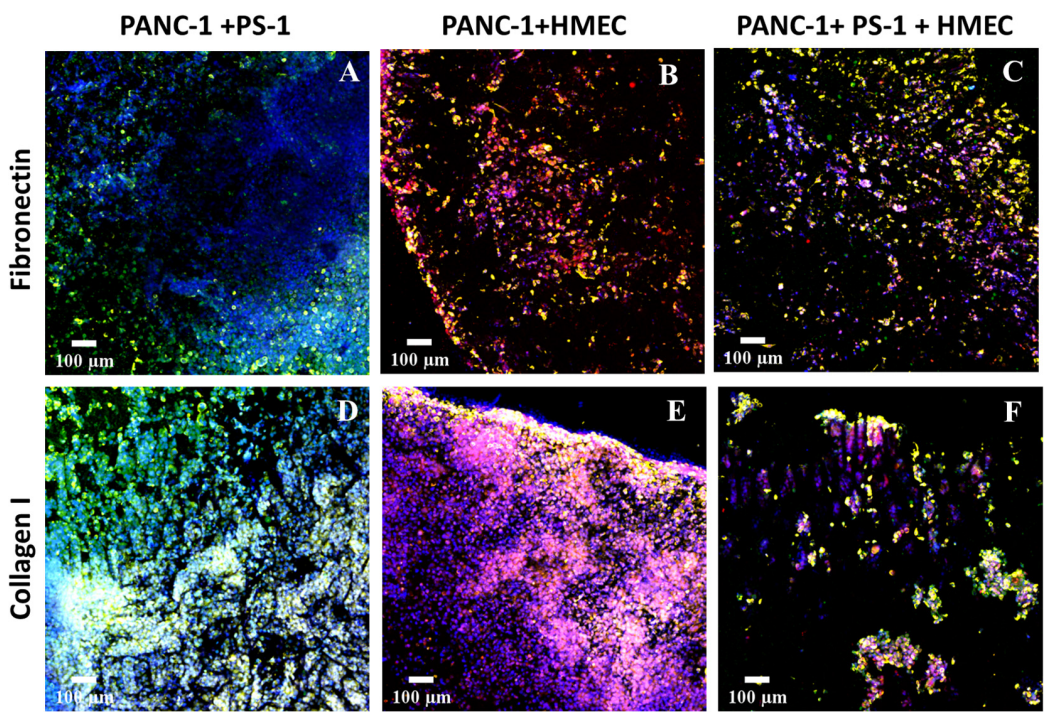

FIGURE 4 | Representative immunofluorescence CLSM images of sections of the 3D scaffolds after 28 days (4 weeks) of culturing multiple cell types in fibronectin-coated **(A–C)** and collagen I-coated **(D–F)** coated scaffolds: PANC-1 PDAC cell lines are in yellow (pan-Cytokeratin staining), PS-1 stellate cells are in green (αSMA staining), and HMEC endothelial cells are in red/pink (CD-31 staining). All cells were stained with DAPI, as well (blue). Scale bar = 100 µm.

interactions and cellular growth rates of different cell types in a mixed culture are affected by the ECM protein coating of the PU scaffolds. Specifically, for our PDAC model, PANC-1 cancer cells prefer FN coating, while the HMEC endothelial cells prefer COL. PS-1 stellate cells prefer coated scaffolds, both FN and COL, over uncoated ones. Thus, we further designed a hybrid zonal PU scaffold-based model with different ECM-coatings (**Figure 1**). More specifically, as described in Section "Scaffold-Based Zonal 3D Cell Culture," PS-1 and HMEC cells were cultured in a COL-coated external scaffold (stromal compartment), while PANC-1 was grown in an FN-coated inner scaffold (tumor compartment). This configuration enabled (i) tailoring of the ECM to the cell needs and (ii) a better zonal recapitulation of the cell distribution in the PDAC TME. The zonal model was monitored and analyzed at a compartmental level and as a whole (both compartments). More specifically, the following compartments were monitored: (i) FN-coated inner cylinder compartment containing PANC-1 cancer cells, (ii) COL-coated outer cuboid compartment containing HMEC and PS-1 cells, and (iii) the complete hybrid model containing both the inner and the outer compartment (see also section "Scaffold-Based Zonal 3D Cell Culture" and **Figure 1**).

Fibronectin-Coated PU Inner Cylinder Compartment of the Hybrid Scaffold (Containing PANC-1 Cells)

A mono-culture of PANC-1 cancer cells in the FN-coated inner scaffold compartment was monitored for 28 days, since for our hybrid model PANC-1 cancer cells were added 7 days after the

development of the outer cuboid (see also **Figure 1** and section "Scaffold-Based Zonal 3D Cell Culture"). Cell proliferation (Ki-67), secretion of ECM (i.e., human specific COL), and expression of cell specific markers (pan-Cytokeratin and CD-24) were assessed at regular intervals via immunostaining and CLSM imaging [see also sections "Immunofluorescence Assay" and "Confocal Laser Scanning Microscopy (CLSM) Imaging"].

As observed in **Figure 5**, Ki-67 positive proliferative cancer cells were observed throughout the entire culture period (top panel). Multiple PANC-1 cells within the scaffolds expressed both pan-Cytokeratin and CD-24 cellular markers (**Figure 5**, middle panels), highlighting the heterogeneous nature of the cancer cell population for the PANC-1 cell line (Schüssler et al., 1992; Aghamaliyev et al., 2015; Pei et al., 2016; Haeberle and Esposito, 2019). *In vivo*, COL is overexpressed by pancreatic tumor cells (Imamura et al., 1995) and hence is considered to be an important parameter for the development of a robust *in vitro* model of PDAC. As observed, PANC-1 cells were able to secrete COL within the FN-coated inner compartment of the hybrid scaffold throughout the culture period, the amount increasing with time

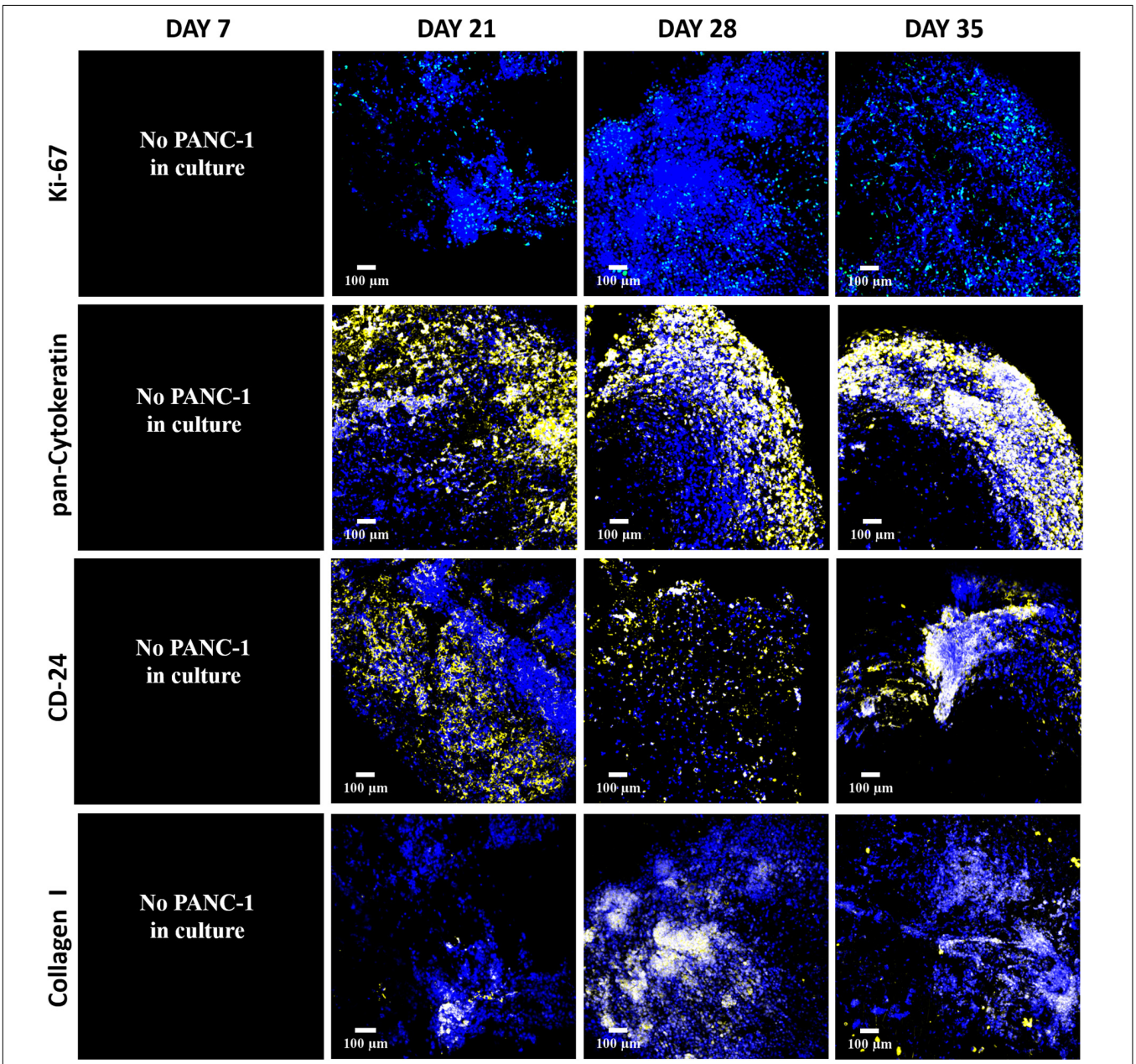

FIGURE 5 | Representative immunofluorescence CLSM images of fibronectin-coated PU inner cylinder of the hybrid scaffold with PANC-1 cells over 28 days of culture. **Top panel:** Ki-67 positive (green) proliferative cells. **Second panel:** Pan-Cytokeratin positive (yellow) PANC-1 cells. **Third panel:** CD-24 positive (yellow) PANC-1 cells. **Bottom panel:** Collagen I secretion (yellow) by the PANC-1 cells. Cell nuclei in all images were stained with DAPI (blue). Scale bar = 100 µm.

(**Figure 5**, bottom panel). Overall, these results highlight that in our FN-coated inner scaffold PANC-1 cancer cells (tumor zone) remain viable, are proliferative and secrete COL throughout the culture period of 28 days.

Collagen I-Coated PU Outer Compartment of the Hybrid Scaffold (Containing HMEC Endothelial and PS-1 Stellate Cells)

Similar to independently studying the inner cylinder of the hybrid scaffold [section "Fibronectin-Coated PU Inner Cylinder Compartment of the Hybrid Scaffold (Containing PANC-1 Cells)," **Figure 5**] the outer cuboid scaffold consisting of PS-1 and HMEC cells (i.e., recapitulating the stromal compartment of the TME) was independently studied for 35 days (see also **Figure 1** and section "Scaffold-Based Zonal 3D Cell Culture"). More specifically, three different ratios of PS-1 and HMEC cells were assessed to study the effect of seeding densities on the evolution of different cells (see also section "Scaffold-Based Zonal 3D Cell Culture"). As previously described [section "Fibronectin-Coated PU Inner Cylinder Compartment of the Hybrid Scaffold (Containing PANC-1 Cells)"], the cellular morphology, cell proliferation, ECM secretion, and cell-specific marker expressions were assessed at regular intervals. As shown in **Figure 6**, Ki-67 positive proliferative cells were present within the outer scaffold throughout the entire culture period (35 days). Furthermore, at the beginning of the culturing period (day 7), a clear distinction between the different ratios is observed in terms of cell number, i.e., higher seeding density of the HMEC and PS-1 cells showed more proliferating cells. However, by day 21, all three cell ratios under study show a high cell number and a uniform cellular distribution within the scaffolds. However, the number of proliferative cells decreased toward the end of the experimental time (day 35) for all three seeding ratios assessed (**Figure 6**).

Cell-specific immunostaining for phenotypic markers was carried out to identify the density and spatial distribution of PS-1 (αSMA) and HMEC (CD-31) cells within the outer cuboid scaffold. **Figure 7** shows representative images immunostaining for cell specific markers.

As can be seen in **Figure 7**, on day 7, the experimental systems with equal number of PS-1 and HMEC cells (**Figure 7**, top and middle panels) showed relatively similar distribution of the two cell types, while the presence of excess PS-1 in the third experimental system (**Figure 7**, bottom panel) resulted in the stellate cells growing significantly and suppressing the growth of the HMEC endothelial cells. On day 21 (week 3), all three conditions showed a high number of PS-1 stellate cells. HMEC endothelial cells were mainly visible in conditions with equal ratio of PS-1 and HMEC, although their cell number was generally lower than the PS-1 cells. For the 2:9 (PS-1:HMEC) ratio, similar to day 7, CD-31 positive HMEC cells were not very visible within the co-culture (**Supplementary Figure S1**). The αSMA-staining also showed fiber-like structure and an aligned nature of the activated stellate cells within the scaffolds, especially for the experiment with abundance of PS-1, i.e., 2:9 ratio. Toward the end of the culture period, at days 28 and 35 (weeks 4 and 5), although cells were present within the scaffolds, their numbers decreased. Furthermore, the morphology of the cells (particularly the stellate cells) changed and loss of cell-specific markers (CD-31 and αSMA) was observed (**Figure 7**).

Activated pancreatic stellate cells are known to secrete extensive ECM proteins (primarily COL), resulting as previously described, in desmoplasia/fibrosis (Apte et al., 2004; Armstrong et al., 2004; McCarroll et al., 2014). Hence, immunostaining for human-specific COL was carried out for the outer cuboid scaffold.

Excessive COL secretion was observed within our outer cuboid scaffold (**Figure 8**). On day 7, the amount of COL was directly proportional to the number of stellate cells, i.e., higher number of PS-1 resulted in higher amount of COL secretion. For all three conditions, COL secretion increased with time in the early days of the culture (up to day 28). Similar to the cell-specific marker expressions, toward the end of the culture period, a decrease in COL amount was observed (day 35).

Complete, Hybrid, Zonal, Multi-Compartmental, Multicellular Model of PDAC Containing Cancer Cells (PANC-1), Endothelial Cells (HMEC), and Stellate Cells (PS-1)

As reported in Sections "Fibronectin-Coated PU Inner Cylinder Compartment of the Hybrid Scaffold (Containing PANC-1 Cells)" and "Collagen I-Coated PU Outer Compartment of the Hybrid Scaffold (Containing HMEC Endothelial and PS-1 Stellate Cells)," both the inner and outer scaffolds of our hybrid model were individually viable for the entire duration of the experiment, i.e., 28 days for the inner scaffold and 35 days for outer scaffold. All three cell types remained in a proliferative state (**Figures 5**, **6**), expressed cell-specific markers (**Figures 5**, **7**), and produced their own COL matrix protein (**Figures 5**, **8**). Thereafter, a multicellular PDAC *in vitro* model was developed by assembling the inner and outer compartments (section "Scaffold-Based Zonal 3D Cell Culture") to obtain a hybrid, zonal, tri-culture PDAC model containing PANC-1 cancer cells, HMEC endothelial cells, and PS-1 stellate cells (for more details, see section "Scaffold-Based Zonal 3D Cell Culture" and **Figure 1**). As per the experiments of the separate scaffold compartments [sections "Fibronectin-Coated PU Inner Cylinder Compartment of the Hybrid Scaffold (Containing PANC-1 Cells)" and "Collagen I-Coated PU Outer Compartment of the Hybrid Scaffold (Containing HMEC Endothelial and PS-1 Stellate Cells)"] the cell proliferation, cell-specific marker expression (pan-Cytokeratin, CD-31, and αSMA), and COL secretion in the hybrid scaffold were monitored regularly.

As can be seen in **Figure 9**, Ki-67 positive proliferative cells were visible in the hybrid scaffold throughout the entire experimental time period, both in the inner and outer scaffold for all seeding ratios (**Figure 9**). On day 21, outer and inner rings were separately visible (**Figure 9**, first vertical panel). However, for later time points (i.e., days 28 and 35), the two sections of the scaffolds could not be easily distinguished, especially for the conditions with higher cell numbers, indicating the homogeneous merging of the two compartments (**Figure 9**).

As can be seen in **Figure 10**, for the cell specific phenotypic markers expression, at day 21 (2 weeks post-assembling the

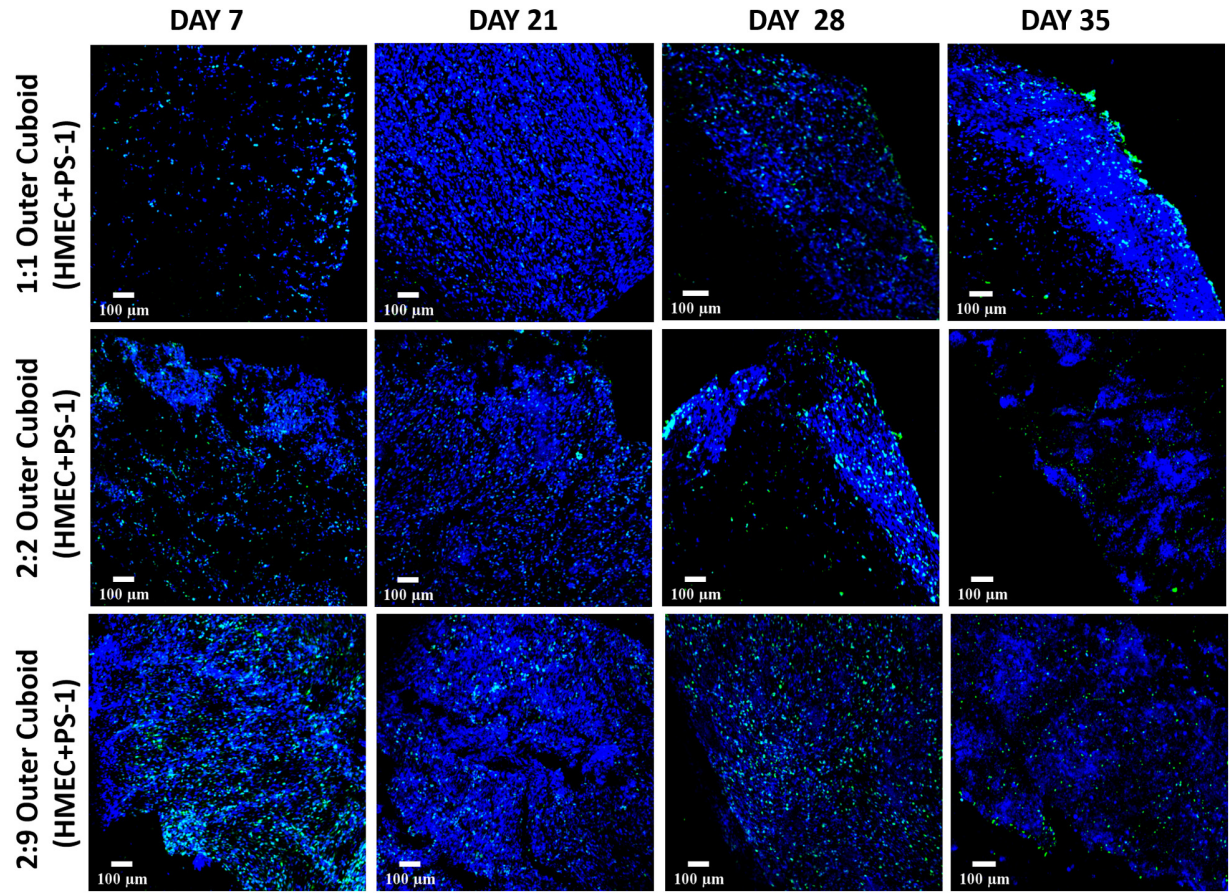

FIGURE 6 | Representative immunofluorescence CLSM images of collagen I-coated PU outer cuboid compartment of the hybrid scaffold with Ki-67 positive (green) proliferative PS-1 and HMEC cells over 35 days of culture. **Top panel:** PS-1:HMEC = 1:1 (PS-1 = 0.25 × 10^6 cells, HMEC = 0.25 × 10^6 cells), **Middle panel:** PS-1:HMEC = 2:2 (PS-1 = 0.5 × 10^6 cells, HMEC = 0.5 × 10^6 cells), **Bottom panel:** PS1:HMEC = 9:2 (PS-1 = 2.25 × 10^6 cells, HMEC = 0.5 × 10^6 cells). Nuclei for all images were stained with DAPI (blue). Scale bar = 100 µm.

hybrid model), all three cell types expressed their specific markers. More specifically, pan-Cytokeratin positive PANC-1 cells were visible within the FN-coated inner cylinder compartment, while an abundance of αSMA positive PS-1 stellate cells was observed in the collagen-coated outer cuboid scaffold compartment. Parallel alignment of the stellate cells was visible for all three seeding densities. CD-31 positive HMEC endothelial cells were present within the dense stellate-cell-rich compartment for all three cell ratios under study (indicated with red arrows in **Figure 10**), but they were more visible in the experiments where PS-1 and HMEC were in equal numbers (1:1:1 and 1:2:2 hybrid scaffolds). Similar to the experiments of the independent outer cuboid scaffold (**Figure 7**), changes in cellular morphology and loss of cellular markers were observed on day 28 and were further enhanced at the end of the culture period (day 35).

As mentioned earlier, the fibrotic reaction and the presence of excessive ECM protein (desmoplasia) are hallmarks for PDAC. Hence, COL secretion by the different cells was assessed within our zonal multicellular model (**Figure 11**). Similar to the separate experiments for the inner and outer scaffold compartments (**Figures 5**, **8**), at the beginning of the culture (day 21), cancer cells in the inner scaffold compartment showed very little COL secretion, while the stellate cells in the outer scaffold compartment showed extensive COL protein production (**Figure 11**, left panel). As time progressed, more COL secretion was observed by both the PS-1 cells and the PANC-1 cells. At the end of the 35 days (**Figure 11**, right panel), a slight decrease in COL in the model was observed, in alignment with the loss of cellular marker expressions and the morphology changes (**Figure 10**).

Cellular migration and cellular interactions between the tumor and the stromal cells within a cancer niche are important aspects for cancer metastasis (Keleg et al., 2003; Xu et al., 2010). As our hybrid multicellular model consists of two different scaffold zones/compartments, the ability of the cells, especially the PANC-1 cancer cells to migrate from one compartment to the other is an important requirement for the physiological relevance of the model. As observed in **Figure 12**, at day 21 (2 weeks post-assembly of the hybrid scaffold), cellular migration was observed for all three cell ratios under study. More specifically, for the 1:1:1 hybrid model (**Figure 12**, left panel), PANC-1 cells (yellow arrows in **Figure 12**) migrated

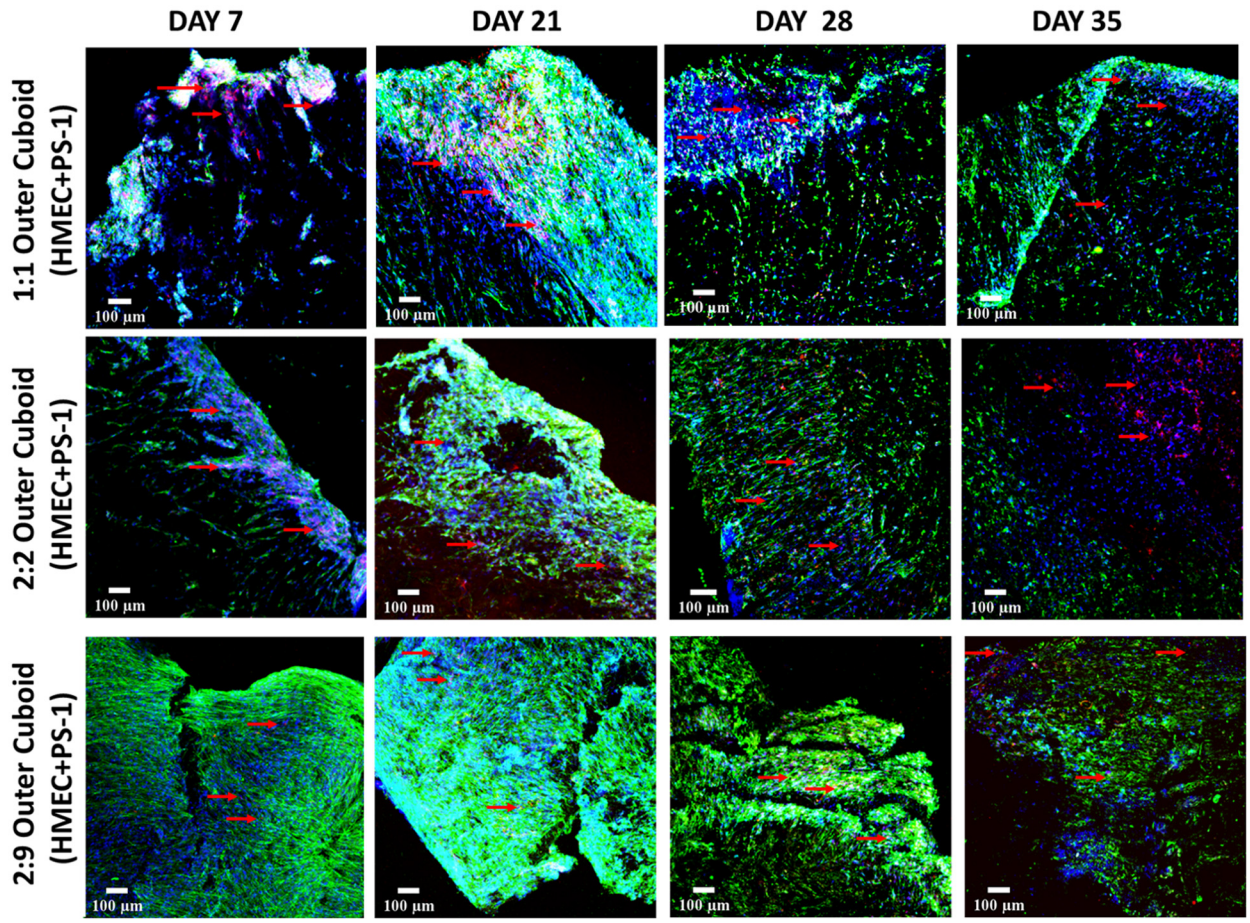

FIGURE 7 | Representative immunofluorescence CLSM images of collagen I-coated PU outer cuboid scaffold compartment of the hybrid scaffold with HMEC (CD-31, red) and PS-1 (αSMA, green) cell distribution over 35 days of culture. **Top panel:** PS-1:HMEC = 1:1 (PS-1 = 0.25 × 10^6 cells, HMEC = 0.25 × 10^6 cells), **Middle panel:** PS-1:HMEC = 2:2 (PS-1 = 0.5 × 10^6 cells, HMEC = 0.5 × 10^6 cells), **Bottom panel:** PS-1:HMEC = 9:2 (PS-1 = 2.25 × 10^6 cells, HMEC = 0.5 × 10^6 cells). Nuclei for all images were stained with DAPI (blue). Endothelial cells are pointed with red arrow. Scale bar = 100 µm.

from the inner to the outer scaffold compartment containing stellate and endothelial cells while the PS-1 stellate cells (green arrows in **Figure 12**) bridge the two zones. HMEC (red arrow) migration was also observed. For the 1:2:2 (**Figure 12**, middle panel) and 1:2:9 (**Figure 12**, right panel) cell ratios in the hybrid scaffolds, all three cell types (yellow, green, and red) are observed together primarily at the junction of the two scaffold compartments.

Overall, our results show the successful development of a novel hybrid, zonal, multicellular scaffold-based PDAC *in vitro* model containing pancreatic cancer, stellate, and endothelial cells. The model was successfully maintained in culture for a total of 35 days (5 weeks), although cellular/culture aging was observed after 28 days (4 weeks).

DISCUSSION

Overall, in this work, we developed, characterized, and maintained long-term (35-day) novel PU scaffold-based, multicellular, *in vitro* models of pancreatic cancer consisting of pancreatic cancer (PANC-1), stellate (PS-1), and endothelial (HMEC) cells.

Single Homogeneous Scaffold-Based Multicellular Model of PDAC

Our novel PU scaffold-based *in vitro* PDAC model was able to maintain cell viability and expression of cell specific markers for 28 days (4 weeks) in both FN- and COL-coated PU scaffolds for all co- and tri-cultures under study (**Figures 3**, **4**). Different cell types showed growth, which was dependent on the type of ECM proteins used to coat the scaffolds. More specifically, the presence of FN enhanced the growth of cancer cells (PANC-1) within the multicellular systems (co-culture and tri-culture), while COL assisted in a more even distribution and higher number of stellate (PS-1) and endothelial (HMEC) cells (**Figure 4**). It is worth noting that previous published research, wherein such multicellular models consisting of cancer, endothelial, and stellate/fibroblast cells

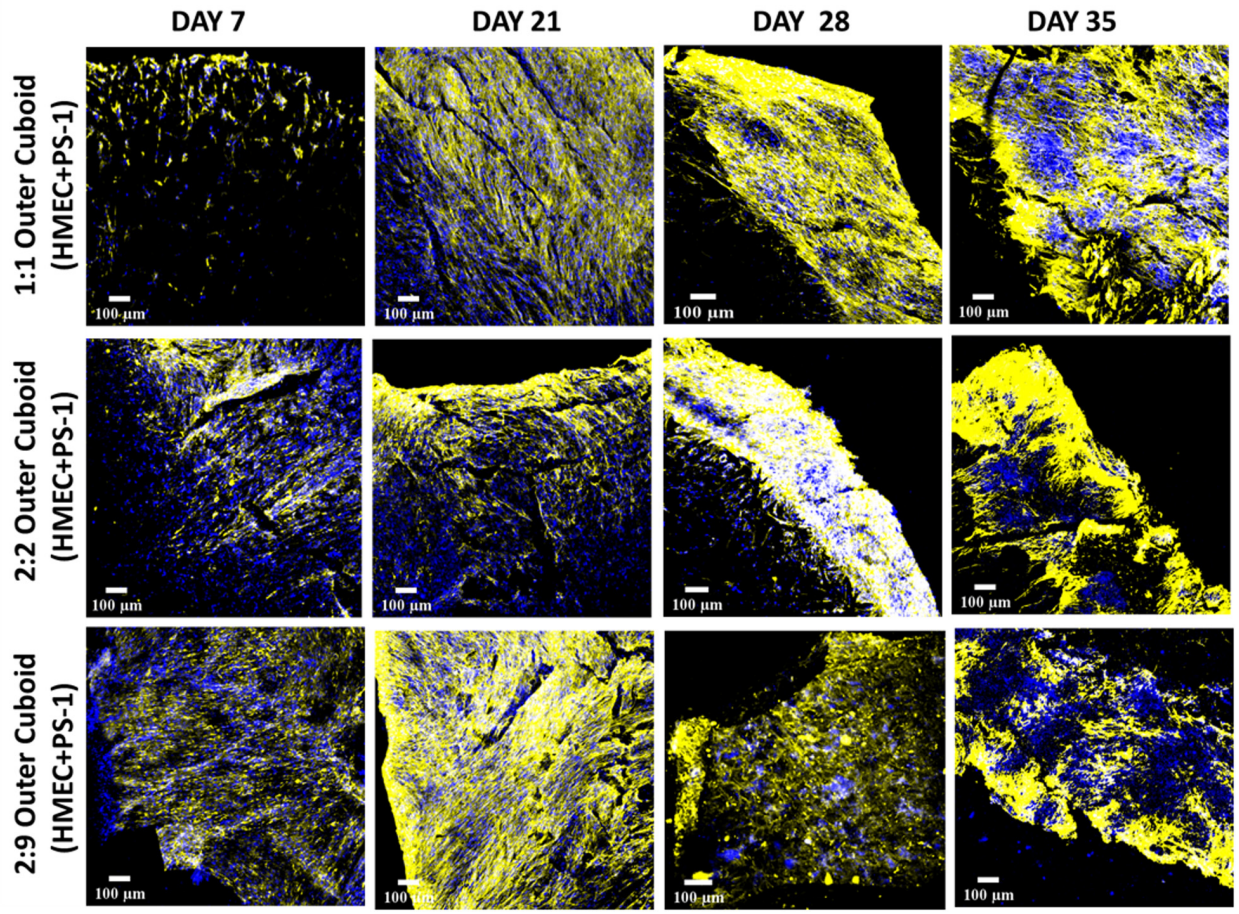

FIGURE 8 | Representative immunofluorescence CLSM images of collagen I (rat tail)-coated PU outer cuboid compartment of the hybrid scaffold for human specific collagen I secretion (yellow) over 35 days of culture. **Top panel:** PS-1:HMEC = 1:1 (PS-1 = 0.25 × 10^6 cells, HMEC = 0.25 × 10^6 cells), **Middle panel:** PS-1:HMEC = 2:2 (PS-1 = 0.5 × 10^6 cells, HMEC = 0.5 × 10^6 cells), **Bottom panel:** PS-1:HMEC = 9:2 (PS-1 = 2.25 × 10^6 cells, HMEC = 0.5 × 10^6 cells). Nuclei for all images were stained with DAPI (blue). Scale bar = 100 µm.

were attempted, a depletion of the supporting cells (endothelial and fibroblast/stellate) was observed at a very early stage of culture (day 4) (Di Maggio et al., 2016; Lazzari et al., 2018). In contrast, our polymer scaffold-based model was successful in maintaining the complex multicellular model of PDAC for 28 days (4 weeks).

Novel Hybrid, PU Scaffold-Based Multicellular PDAC Model

Based on our observations above (section "Single Homogeneous Scaffold-Based Multicellular Model of PDAC"), it was evident that different cell types within the tumor niche prefer different ECM proteins for high growth and survival. Hence, to account for this, we designed a novel hybrid, multi-compartmental multicellular model consisting of (i) an external/outer collagen-coated cuboid compartment for growth of the stromal cells, i.e., stellate and endothelial cells, and (ii) an internal/inner FN-coated cylindrical compartment for growth of the pancreatic cancer cells (**Figure 1**). We observed cell growth and proliferation (**Figure 9**), presence of cell-specific markers (**Figure 10**), the production of COL (**Figure 11**), as well as cell migration (**Figure 12**) within our novel hybrid model over a period of 35 days (5 weeks). Previous studies focusing on multicellular, *in vitro* models of pancreatic cancers have all been spheroids/cell aggregate based and were maintained in culture for a relatively short time period, i.e., between 24 h and 7 days (Froeling et al., 2009; Di Maggio et al., 2016; Ware et al., 2016; Lazzari et al., 2018). To the best of our knowledge, we report here for the first time, a long-term (35-day) PU scaffold-based, hybrid, zonal, multicellular (cancer, stellate, and endothelial cells) model of the PDAC tumor niche.

Characterization of Separate Inner (PANC-1) and Outer Compartment (HMEC, PS-1) Compartments of the Hybrid Scaffold

Prior to the development of the hybrid zonal scaffold, we studied independently the two scaffold compartments of the hybrid scaffold to monitor long term the evolution of the three different cell types (**Figure 1**).

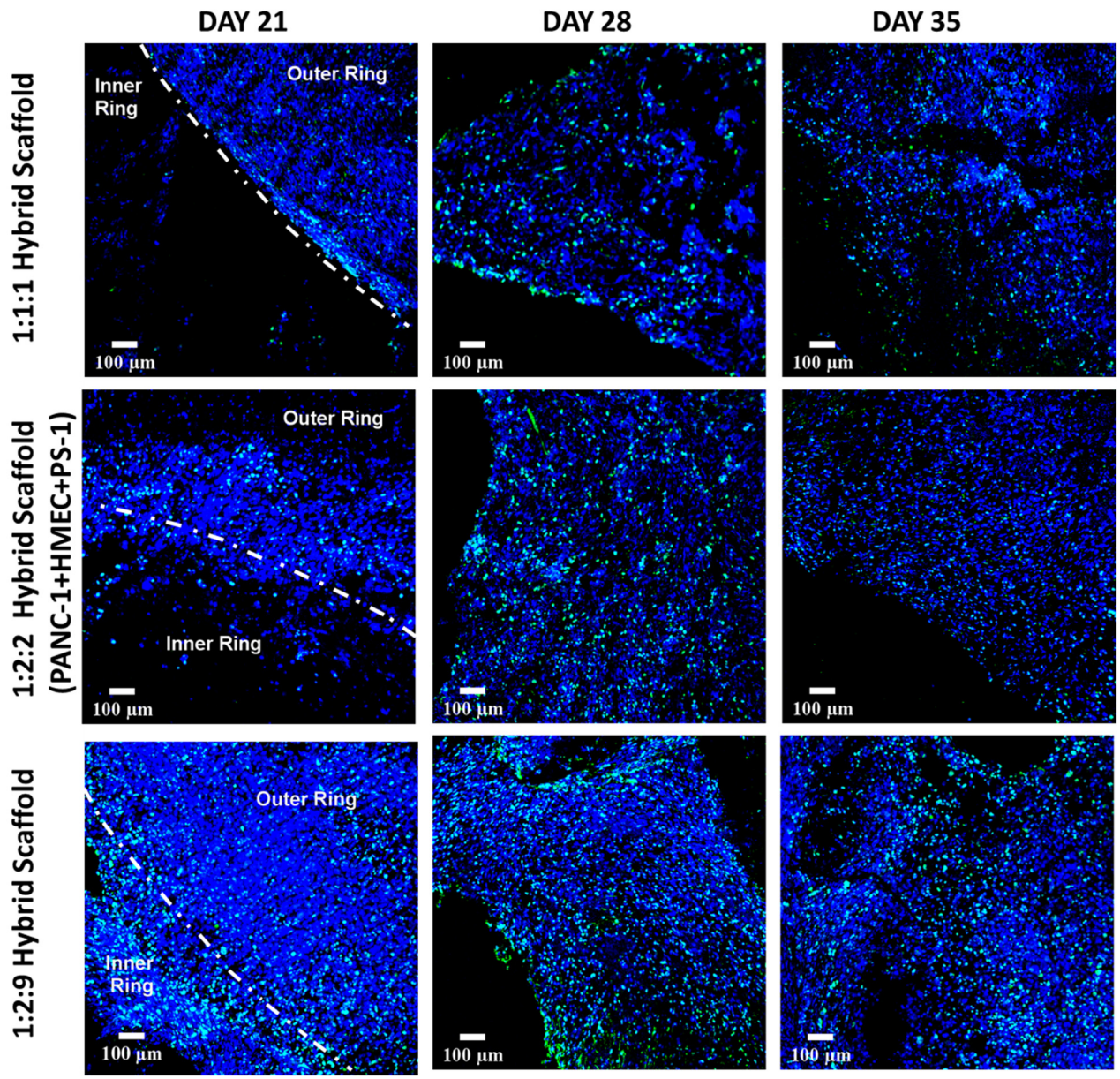

FIGURE 9 | Representative immunofluorescence CLSM images for Ki-67 positive (green) proliferative cells within the complete multicellular hybrid scaffold, containing both the collagen I-coated outer cuboid and the fibronectin-coated inner cylinder, over 35 days of culture. **Top panel:** PANC-1:HMEC:PS-1 = 1:1:1 (PANC-1 = 0.25 × 10^6 cells, PS-1 = 0.25 × 10^6 cells, HMEC = 0.25 × 10^6 cells), **Middle panel:** PANC-1:HMEC:PS-1 = 1:2:2 (PANC-1 = 0.25 × 10^6 cells, PS-1 = 0.5 × 10^6 cells, HMEC = 0.5 × 10^6 cells), **Bottom panel:** PANC-1:HMEC:PS-1 = 1:2:9 (PANC-1 = 0.25 × 10^6 cells, PS-1 = 2.25 × 10^6 cells, HMEC = 0.5 × 10^6 cells). Nuclei for all images were stained with DAPI (blue). Scale bar = 100 µm.

Inner fibronectin-coated cylinder scaffold compartment (PANC-1 cells)

We have previously demonstrated that PANC-1 cancer cells prefer FN-coated PU scaffolds for long-term cell proliferation and for mimicking various *in vivo* characteristics like COL production, realistic hypoxic gradients, and treatment resistance (Totti et al., 2018; Gupta et al., 2019). Hence, we cultured PANC-1 cancer cells on FN-coated cylindrical PU scaffolds for 28 days [see also sections "Scaffold-Based Zonal 3D Cell Culture" and "Fibronectin-Coated PU Inner Cylinder Compartment of the Hybrid Scaffold (Containing PANC-1 Cells)"].

As shown in **Figure 5**, PANC-1 cancer cells were able to proliferate within the FN-coated cylinder scaffold compartment for the entire duration of the experiment. We also monitored the secretion of COL as it is an important feature of the PDAC TME *in vivo* (Apte et al., 2004; Armstrong et al., 2004; Shintani et al., 2006; Shields et al., 2011). We observed COL production by the PANC-1 cancer cells as early as 14 days

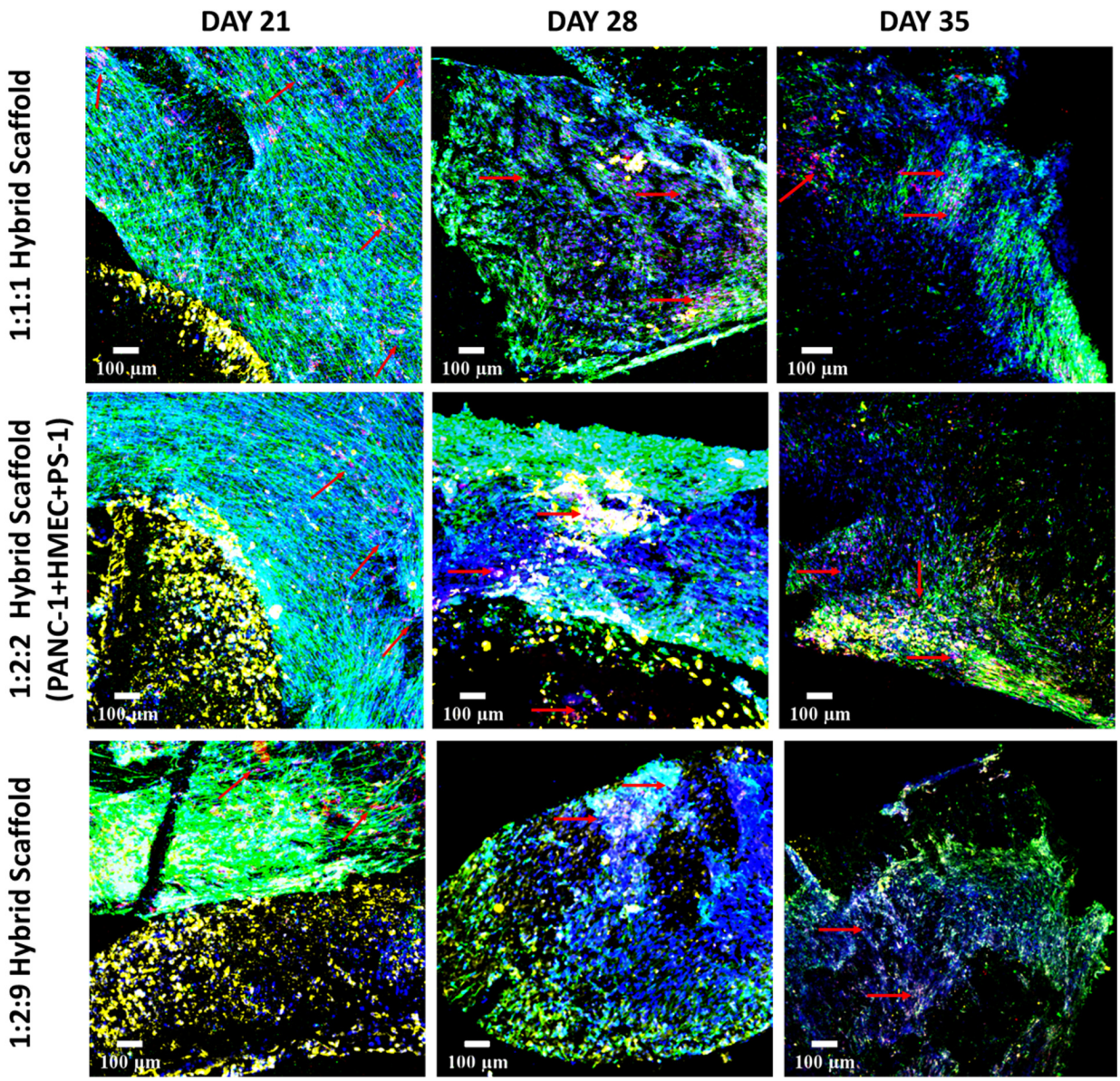

FIGURE 10 | Representative immunofluorescence CLSM images showing the cellular distribution of PANC-1 (pan-Cytokeratin, yellow), HMEC (CD-31, red), and PS-1 (αSMA, green) within the complete hybrid scaffold containing both the collagen I-coated outer cuboid and the fibronectin-coated inner cylinder, over 35 days of culture. **Top panel:** PANC-1:HMEC:PS-1 = 1:1:1 (PANC-1 = 0.25 × 10^6 cells, PS-1 = 0.25 × 10^6 cells, HMEC = 0.25 × 10^6 cells), **Middle panel:** PANC-1:HMEC:PS- = 1:2:2 (PANC-1 = 0.25 × 10^6 cells, PS-1 = 0.5 × 10^6 cells, HMEC = 0.5 × 10^6 cells), **Bottom panel:** PANC-1:HMEC:PS-1 = 1:2:9 (PANC-1 = 0.25 × 10^6 cells, PS-1 = 2.25 × 10^6 cells, HMEC = 0.5 × 10^6 cells). Nuclei for all images were stained with DAPI (blue). Endothelial cells are pointed with red arrow. Scale bar = 100 µm.

post-cell seeding, which increased throughout the culture period (**Figure 5**). These observations are in agreement to our previously published monocellular model of PDAC on FN-coated PU cubic scaffolds (Totti et al., 2018). Furthermore, with respect to the upregulation of cell-specific markers, PANC-1 cells contained a heterogeneous mixture of cells positive for both pan-Cytokeratin and CD-24 throughout the entire culture period (**Figure 5**), indicating that the PANC-1 cells were able to maintain their neoplastic characteristics long term.

Outer collagen-coated cuboid compartment (PS-1, HMEC cells)

As observed in the mono-culture study (**Figure 2A**), HMEC endothelial cells preferred COL-coated scaffolds over uncoated or FN-coated ones. This is in agreement to previously published literature, wherein endothelial cells' preference for COL matrix over other materials, like alginate and fibrin, has been reported (Rioja et al., 2016; Nguyen et al., 2017). PS-1 stellate cells showed a preference for coated scaffolds over those uncoated (**Figure 2B**)

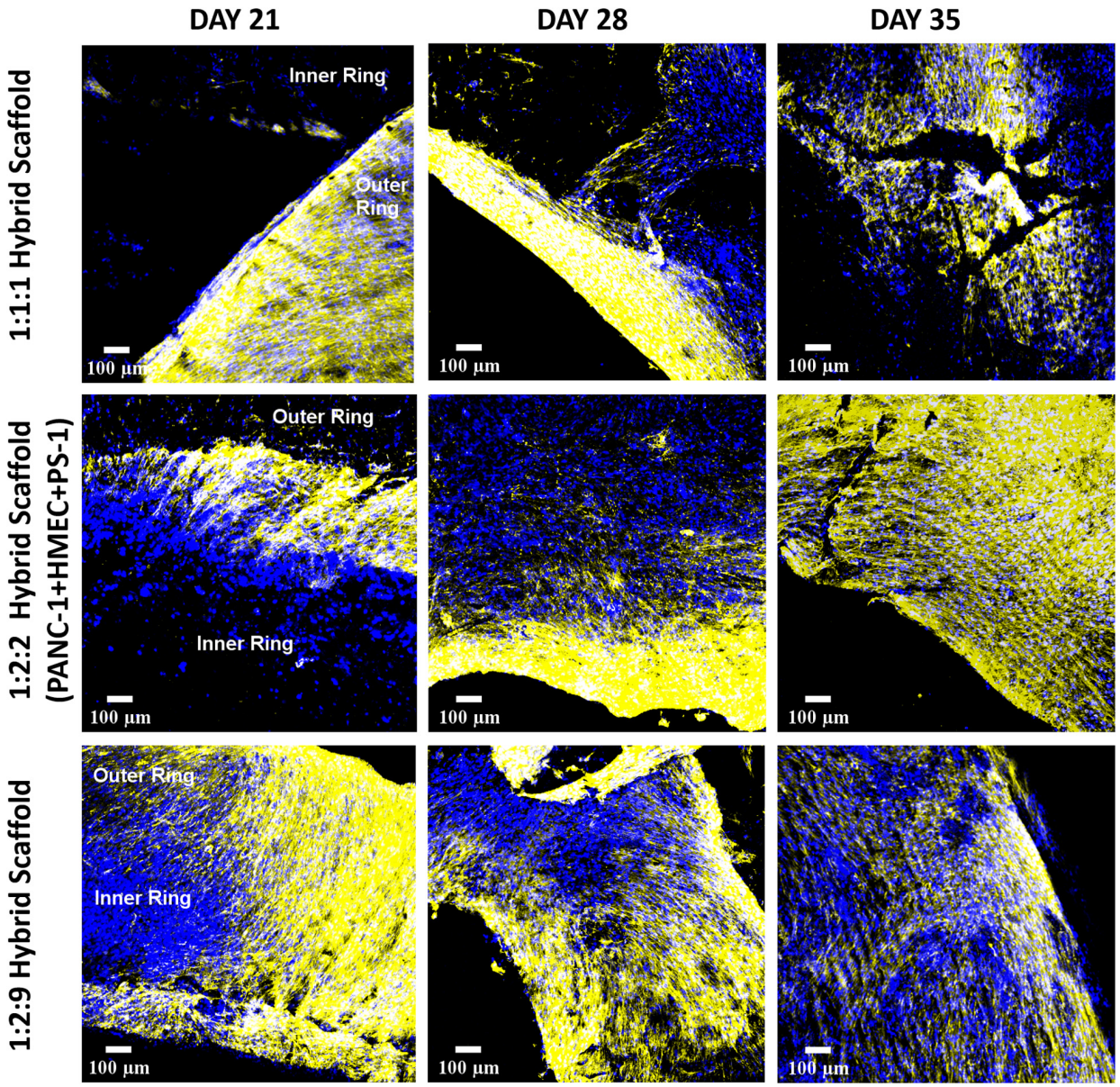

FIGURE 11 | Representative immunofluorescence CLSM images showing collagen I (human) ECM protein secretion within the complete multicellular hybrid scaffold containing both the collagen I (rat tail)-coated outer cuboid and the fibronectin-coated inner cylinder, over 35 days of culture. **Top panel:** PANC-1:HMEC:PS-1 = 1:1:1 (PANC-1 = 0.25 × 10^6 cells, PS-1 = 0.25 × 10^6 cells, HMEC = 0.25 × 10^6 cells), **Middle panel:** PANC-1:HMEC:PS-1 = 1:2:2 (PANC-1 = 0.25 × 10^6 cells, PS-1 = 0.5 × 10^6 cells, HMEC = 0.5 × 10^6 cells), **Bottom panel:** PANC-1:HMEC:PS-1 = 1:2:9 (PANC-1 = 0.25 × 10^6 cells, PS-1 = 2.25 × 10^6 cells, HMEC = 0.5 × 10^6 cells). Nuclei for all images were stained with DAPI (blue). Scale bar = 100 µm.

but did not show any specific preference for either COL or FN. Froeling et al. (2009) have reported a similar observation wherein PS-1 cells grew similarly in presence of collagen, FN, and Matrigel. Therefore, COL was selected to coat the external stromal compartment of the hybrid scaffolds. As described in Section "Scaffold-Based Zonal 3D Cell Culture," three different rations of stellate and endothelial cells were studied. Ki-67 positive proliferative cells were present in all three cell ratios under study (1:1, 2:2, and 2:9; HMEC:PS-1) throughout the entire culture period (35 days). However, we observed a decrease in the total cell number toward the end of the culture period, i.e., from day 28 days onward (**Figure 6**). As observed in **Figure 7**, for the 1:1 and 2:2 cell ratios (i.e., the conditions with equal number of HMEC and PS-1 cells), both HMEC and PS-1 cell were present within the PU scaffolds. PS-1 stellate cells had aligned fibril cellular morphology, which supports their active state (Bachem et al., 1998; Masamune et al., 2003). CD-31 positive HMEC cells were visible within the PS-1 fibrous stroma. These cellular markers and close interactions between PS-1 and HMEC cells were clearly observed until day 21 of culture. However,

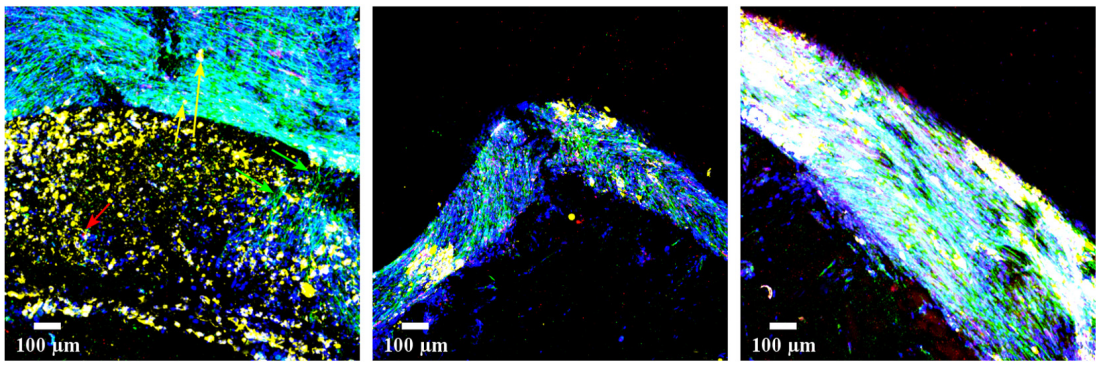

FIGURE 12 | Representative immunofluorescence CLSM image of the hybrid scaffold demonstrating cellular migration of PANC-1 (pan-Cytokeratin, yellow), HMEC (CD-31, red), and PS-1 (αSMA, green) at day 21 (2 weeks post-assembly of hybrid scaffold) between the inner and the outer scaffold compartments. **Left panel:** PANC-1:HMEC:PS-1 = 1:1:1 (PANC-1 = 0.25 × 10^6 cells, PS-1 = 0.25 × 10^6 cells, HMEC = 0.25 × 10^6 cells), **Middle panel:** PANC-1:HMEC:PS-1 = 1:2:2 (PANC-1 = 0.25 × 10^6 cells, PS-1 = 0.5 × 10^6 cells, HMEC = 0.5 × 10^6 cells), **Right panel:** PANC-1:HMEC:PS-1 = 1:2:9 (PANC-1 = 0.25 × 10^6 cells, PS-1 = 2.25 × 10^6 cells, HMEC = 0.5 × 10^6 cells). Nuclei for all images were stained with DAPI (blue). Migration shown by cell-specific arrow: PANC-1 = yellow, PS-1 = green, HMEC = red. Scale bar = 100 µm.

on day 28 and beyond, we observed changes in the cellular morphology of the PS-1 cells, i.e., a loss of their fibril-like structure (**Figure 7**). We also observed a decrease in cell number, loss of cell-specific markers, and a separation of the two cell types, which could be attributed to the natural aging of the cells. We have previously observed a similar cellular aging within our mono-culture model (PANC-1 cells only), wherein a decrease in cell number was seen after 28 days of culture (Gupta et al., 2019). However, it is difficult to compare our observations with existing literature as, to the best of our knowledge, there are no similar long-term (35-day) studies. For the 2:9 cell ratio, wherein an abundance of PS-1 stellate cells were present, the fibrous cellular morphology of the stellate cells was observed as early as day 7 (**Figure 7**). Due to the abundance of stellate cells, the growth of HMEC endothelial cells was reduced within this system, and a relatively low number CD-31 positive cells were observed (**Figure 7**). Overall, we did not observe any sprouting and vessel formation within our co-culture, which may suggest a need for more specialized media containing growth factors promoting angiogenesis like VEGF, or those found in Matrigel, to promote structured angiogenesis (Gerhardt et al., 2003; Son et al., 2006; Eichmann and Simons, 2012; Siemerink et al., 2012; Yin et al., 2018). It should be highlighted that although we observed some degree of cellular aging from day 28 (4 weeks) onward, both cell types (HMEC and PS-1) were present within our COL-coated PU cuboid scaffold compartment for 35 days (**Figure 7**), which is significantly longer than currently reported co-cultures of stellate cells and endothelial cells (Di Maggio et al., 2016). More specifically, Di Maggio et al. (2016) developed a hydrogel-based system consisting of Matrigel and COL, wherein co-culture of PS-1 stellate cells and HUVECs, as well as the effects of PS-1 stellate cells on HUVECs, were assessed for 96 h. In that system, the presence of stellate cells along with collagen and Matrigel assisted in endothelial cell sprouting and the formation of a luminal structure. Generally, activated pancreatic stellate cells have been well-established to be the key element behind the ECM-rich (primarily COL), fibrotic/desmoplastic TME of pancreatic cancer (Apte et al., 2012; Suklabaidya et al., 2018). To assess the PS-1 stellate cells' capability of mimicking this desmoplastic feature in our system, human-specific COL immunostaining was carried out. High amounts of COL were observed within our outer cuboid scaffold compartment for all three cell ratios under study (**Figure 8**). Furthermore, COL showed aligned structures (**Figure 8**), which are known to support/promote metastasis of pancreatic cancer cells (Drifka et al., 2016). Thus, we demonstrated successfully the development and long-term (35-day) maintenance of endothelial and stellate cells scaffold-assisted co-culture, which can act as a "supporting" compartment for our novel hybrid tri-culture model of PDAC. To the best of our knowledge, this is the longest reported co-culture of stellate cells and endothelial cells in a 3D *in vitro* model.

Characterization of Hybrid, Scaffold-Assisted Multicellular Model of PDAC

Following the assessments of the independent inner and outer scaffold compartments, the complete hybrid zonal *in vitro* model of PDAC was assembled and studied. Very few studies are available for multicellular *in vitro* models of PDAC involving cancer cells, endothelial cells, and stellate/fibroblast cells to mimic the fibrosis, and all of these studies were carried out for a relatively short period of time (24 h to 7 days). For example, Beckermann et al. (2008) cultured a multicellular model of PDAC involving MIA PaCa-2 pancreatic cancer cells, primary fibroblasts, and HUVECs in a spheroid system for 24 h. Similarly, Lazzari et al. (2018) developed a multicellular spheroid-based model of PANC-1 cancer cells, MRC-5 fibroblasts, and HUVECs and assessed the effects of chemotherapeutic agents (gemcitabine

and doxorubicin) within it. The model was viable for 4 days, beyond which loss of HUVECs and MRC-5 fibroblasts was observed. Di Maggio et al. (2016) developed a hydrogel-based tri-culture of PDAC with cancer cells (Capan-1, AsPC-1, and COLO-357), HUVECs, and stellate cells (PS-1). The system was cultured for 7 days. A significant decrease in the number of endothelial cells (HUVECs) in the developed hydrogel-based tri-culture system was observed after 72 h. In contrast to the currently reported spheroid-based studies, our hybrid, PU highly porous scaffold-based, zonal model of PDAC was able to support all three cell types for a total of 35 days (5 weeks) making it the longest reported *in vitro* model of PDAC. Further studies to elucidate the reasons behind the progressive loss of the supporting cells (endothelial and stellate cells) in 3D models would be informative.

As previously described, our novel hybrid scaffold-based multicellular model was characterized via immunostaining and CLSM imaging to assess cell growth and proliferation, ECM protein secretion and maintenance of cellular morphology and phenotypic characteristics (**Figures 9–11**). We have successfully demonstrated that our hybrid scaffold could maintain proliferating cells (**Figure 9**) expressing cell-specific markers (**Figure 10**) throughout the entire culture period (35 days). Furthermore, our model showed extensive COL secretion by the stellate cells and even the cancer cells to some extent, indicating its ability to mimic *in vitro* the PDAC desmoplastic nature (**Figure 11**). This fibrotic desmoplastic nature of PDAC is a key reason behind the resistance of pancreatic cancer to currently available therapeutic methods; therefore, recapitulating it *in vitro* is key for more accurate treatment screening trials (Chand et al., 2016; Bynigeri et al., 2017; Ansari et al., 2018). We also observed cellular migration across the two zones by all three cell types, highlighting that the cells are able to overcome the physical barrier of being in two separate scaffolds zones (**Figure 12**). Cellular migration by the cancer cells and the stromal cells, along with cross-talk between them has been linked with PDAC metastasis (Keleg et al., 2003; Xu et al., 2010; Tuveson and Neoptolemos, 2012; Zhan et al., 2017). Hence, this characteristic of our model can be exploited to study the metastatic properties of PDAC. In terms of total cell numbers in our hybrid scaffolds, as expected, differences were observed for different seeding ratios. Nonetheless, the different seeding ratios of the three cell types all showed similar characteristics in terms of cell proliferation (**Figure 9**), expression of phenotypic markers (**Figure 10**), and COL production (**Figure 11**). The choice of seeding density for future work would depend on the specific aim of the work. For example, if the aim would be to study the effect of desmoplasia, then high number of stellate cells (1:2:9 ratio) would be an ideal choice; however, if the aim would be to study more in depth the interactions between the different cell types, conditions with equal number of stellate and endothelial cells would be more appropriate, promoting the presence of higher amounts of endothelial cells. Furthermore, the availability of PDAC models with different ratios of the cells involved is important to account for tumor variability among patients and even intra-tumoral variability for the same patient, since fibrotic intensity as well as vascularization levels differ between patients (Junttila and De Sauvage, 2013; Koay et al., 2016; Verbeke, 2016). Coupled with the feasibility of maintaining a long-term robust culture, our hybrid model's ability to mimic desmoplasia and to account for tumor/patient variability, highlights the possibility of using it to (i) study the mechanisms behind PDAC's therapeutic resistance, (ii) assess the effects of therapeutic methods, both traditional (chemo and radiotherapy) (Adcock et al., 2015; Kuen et al., 2017; Al-Ramadan et al., 2018; Gupta et al., 2019) and novel (proton therapy) (Hong et al., 2011, 2014; Terashima et al., 2012), (iii) conduct fractionated radiation screening (Schellenberg et al., 2008; Mahadevan et al., 2010; Loehrer et al., 2011), and (iv) promote personalized treatment screening.

CONCLUSION

Overall in this study, we have developed and characterized a novel PU scaffold-assisted multicellular hybrid *in vitro* model of PDAC, with specific ECM protein-coated zones for the tumor compartment and the stromal compartment. More specifically, we have developed, characterized, and maintained for a month a novel tri-culture of pancreatic cancer (PANC-1), endothelial (HMEC), and stellate (PS-1) cells. The inner compartment of the scaffold was FN-coated and contained cancer cells, which were surrounded by an external collagen-coated scaffold compartment consisting of stellate and endothelial cells. Overall, such configuration enabled a more accurate recapitulation of the zonal distribution of different cell types of the pancreatic TME. The developed hybrid zonal model was able to (i) support long-term growth and proliferation of cancer (PANC-1), endothelial (HMEC), and stellate (PS-1) cells for up to 35 days (5 weeks), (ii) allow the maintenance of cell specific morphology and phenotypic markers, (iii) form dense desmoplastic region through abundant sections of COL protein, and (iv) demonstrate cellular migration between the different zones. With the capability of mimicking several key characteristics of the PDAC tumor (desmoplasia, cellular migration), the model shows great potential for future use in a range of applications from basic cancer studies to personalized healthcare. Future work on this model will focus on (i) further validation of the model's robustness with patient samples, (ii) assessment of the model's capability to mimic the PDAC's treatment resistance, and (iii) incorporation of immune cells with the help of perfusion bioreactor.

DATA AVAILABILITY STATEMENT

The datasets generated for this study are available on request to the corresponding author.

AUTHOR CONTRIBUTIONS

PG contributed to conception and design of experiments, conduction of experiments, data collection, data analysis and interpretation, and manuscript writing. PP-M contributed to data interpretation and manuscript reviewing. HK contributed

to provision of PS-1 stellate cells and manuscript reviewing. AN contributed to data interpretation and manuscript reviewing. GS contributed to data interpretation and manuscript reviewing. EV contributed to conception of scientific work, data interpretation, manuscript writing and reviewing, and financial support of work.

FUNDING

This work was supported by the Chemical and Process Engineering Department of the University of Surrey, Impact Acceleration Grant (IAA-KN9149C) from the University of Surrey, IAA–EPSRC Grant (RN0281J), and the Royal Society. PG was supported by the Commonwealth Rutherford Post-Doctoral Fellowship. EV is grateful to the Royal Academy of Engineering for an Industrial Fellowship.

SUPPLEMENTARY MATERIALS

The Supplementary Material for this article can be found online at: https://www.frontiersin.org/articles/10.3389/fbioe.2020.00290/full#supplementary-material

FIGURE S1 | Representative image of IF staining of outer cuboid with green (PS-1) and red (HMEC) separate channels. Scale bar = 100 μm.

REFERENCES

Adcock, A. F., Trivedi, G., Edmondson, R., Spearman, C., and Yang, L. (2015). Three-dimensional (3D) cell cultures in cell-based assays for in-vitro evaluation of anticancer drugs. *J. Anal. Bioanal. Tech.* 6:2.

Aghamaliyev, U., Birgin, E., and Rückert, F. (2015). Pancreatic ductal adenocarcinoma stem cells. *Pancreat. Disord. Ther.* 5, S2–S5.

Allenby, M. C., Misener, R., Panoskaltsis, N., and Mantalaris, A. (2017). A quantitative three-dimensional image analysis tool for maximal acquisition of spatial heterogeneity data. *Tissue Eng. Part C Methods* 23, 108–117. doi: 10.1089/ten.tec.2016.0413

Allenby, M. C., Panoskaltsis, N., Tahlawi, A., Dos Santos, S. B., and Mantalaris, A. (2019). Dynamic human erythropoiesis in a three-dimensional perfusion bone marrow biomimicry. *Biomaterials* 188, 24–37. doi: 10.1016/j.biomaterials.2018.08.020

Al-Ramadan, A., Mortensen, A. C., Carlsson, J., and Nestor, M. V. (2018). Analysis of radiation effects in two irradiated tumor spheroid models. *Oncology Lett.* 15, 3008–3016.

Ansari, D., Friess, H., Bauden, M., Samnegård, J., and Andersson, R. (2018). Pancreatic cancer: disease dynamics, tumor biology and the role of the microenvironment. *Oncotarget* 9:6644.

Apte, M., Pirola, R., and Wilson, J. (2012). Pancreatic stellate cells: a starring role in normal and diseased pancreas. *Front. Physiol.* 3:344. doi: 10.3389/fphys.2012.00344

Apte, M. V., Park, S., Phillips, P. A., Santucci, N., Goldstein, D., Kumar, R. K., et al. (2004). Desmoplastic reaction in pancreatic cancer: role of pancreatic stellate cells. *Pancreas* 29, 179–187. doi: 10.1097/00006676-200410000-00002

Armstrong, T., Packham, G., Murphy, L. B., Bateman, A. C., Conti, J. A., Fine, D. R., et al. (2004). Type I collagen promotes the malignant phenotype of pancreatic ductal adenocarcinoma. *Clin. Cancer Res.* 10, 7427–7437. doi: 10.1158/1078-0432.ccr-03-0825

Awasthi, N., Kronenberger, D., Stefaniak, A., Hassan, M. S., Von Holzen, U., Schwarz, M. A., et al. (2019). Dual inhibition of the PI3K and MAPK pathways enhances nab-paclitaxel/gemcitabine chemotherapy response in preclinical models of pancreatic cancer. *Cancer Lett.* 459, 41–49. doi: 10.1016/j.canlet.2019.05.037

Awasthi, N., Schwarz, M. A., and Schwarz, R. E. (2011). Enhancing cytotoxic agent activity in experimental pancreatic cancer through EMAP II combination therapy. *Cancer Chemother. Pharmacol.* 68, 571–582. doi: 10.1007/s00280-010-1514-7

Bachem, M. G., Schneider, E., Groß, H., Weidenbach, H., Schmid, R. M., Menke, A., et al. (1998). Identification, culture, and characterization of pancreatic stellate cells in rats and humans. *Gastroenterology* 115, 421–432. doi: 10.1016/s0016-5085(98)70209-4

Beckermann, B., Kallifatidis, G., Groth, A., Frommhold, D., Apel, A., Mattern, J., et al. (2008). VEGF expression by mesenchymal stem cells contributes to angiogenesis in pancreatic carcinoma. *Br. J. Cancer* 99, 622–631. doi: 10.1038/sj.bjc.6604508

Bermejo-Rodríguez, C., and Pérez-Mancera, P. A. (2015). Use of DNA transposons for functional genetic screens in mouse models of cancer. *Curr. Opin. Biotechnol* 35, 103–110. doi: 10.1016/j.copbio.2015.05.005

Boj, S. F., Hwang, C.-I., Baker, L. A., Chio, I. I. C., Engle, D. D., Corbo, V., et al. (2015). Organoid models of human and mouse ductal pancreatic cancer. *Cell* 160, 324–338.

Brancato, V., Comunanza, V., Imparato, G., Corà, D., Urciuolo, F., Noghero, A., et al. (2017). Bioengineered tumoral microtissues recapitulate desmoplastic reaction of pancreatic cancer. *Acta Biomater.* 49, 152–166. doi: 10.1016/j.actbio.2016.11.072

Broekgaarden, M., Anbil, S., Bulin, A.-L., Obaid, G., Mai, Z., Baglo, Y., et al. (2019). Modulation of redox metabolism negates cancer-associated fibroblasts-induced treatment resistance in a heterotypic 3D culture platform of pancreatic cancer. *Biomaterials* 222:119421. doi: 10.1016/j.biomaterials.2019.119421

Burdett, E., Kasper, F. K., Mikos, A. G., and Ludwig, J. A. (2010). Engineering tumors: a tissue engineering perspective in cancer biology. *Tissue Eng. Part B Rev.* 16, 351–359. doi: 10.1089/ten.teb.2009.0676

Bynigeri, R. R., Jakkampudi, A., Jangala, R., Subramanyam, C., Sasikala, M., Rao, G. V., et al. (2017). Pancreatic stellate cell: Pandora's box for pancreatic disease biology. *World J. Gastroenterol.* 23:382. doi: 10.3748/wjg.v23.i3.382

Cancer.Net (2019). Available online at: https://www.cancer.net/cancer-types/pancreatic-cancer/statistics (accessed March 1, 2020).

Chand, S., O'hayer, K., Blanco, F. F., Winter, J. M., and Brody, J. R. (2016). The landscape of pancreatic cancer therapeutic resistance mechanisms. *Intern. J. Biol. Sci.* 12:273. doi: 10.7150/ijbs.14951

Chantarojanasiri, T., and Kongkam, P. (2017). Endoscopic ultrasound elastography for solid pancreatic lesions. *World J. Gastro. Endosc.* 9:506. doi: 10.4253/wjge.v9.i10.506

Chiellini, F., Puppi, D., Piras, A. M., Morelli, A., Bartoli, C., and Migone, C. (2016). Modelling of pancreatic ductal adenocarcinoma in vitro with three-dimensional microstructured hydrogels. *RSC Adv.* 6, 54226–54235. doi: 10.1039/c6ra08420f

Chim, L. K., and Mikos, A. G. (2018). Biomechanical forces in tissue engineered tumor models. *Curr. Opin. Biomed. Eng.* 6, 42–50. doi: 10.1016/j.cobme.2018.03.004

Courtin, A., Richards, F. M., Bapiro, T. E., Bramhall, J. L., Neesse, A., Cook, N., et al. (2013). Anti-tumour efficacy of capecitabine in a genetically engineered mouse model of pancreatic cancer. *PLoS One* 8:e67330. doi: 10.1371/journal.pone.0067330

Di Maggio, F., Arumugam, P., Delvecchio, F. R., Batista, S., Lechertier, T., Hodivala-Dilke, K., et al. (2016). Pancreatic stellate cells regulate blood vessel density in the stroma of pancreatic ductal adenocarcinoma. *Pancreatology* 16, 995–1004. doi: 10.1016/j.pan.2016.05.393

Dovzhanskiy, D. I., Arnold, S. M., Hackert, T., Oehme, I., Witt, O., Felix, K., et al. (2012). Experimental in vivo and in vitro treatment with a new histone deacetylase inhibitor belinostat inhibits the growth of pancreatic cancer. *BMC Cancer* 12:226. doi: 10.1186/1471-2407-12-226

Drifka, C. R., Loeffler, A. G., Esquibel, C. R., Weber, S. M., Eliceiri, K. W., and Kao, W. J. (2016). Human pancreatic stellate cells modulate 3D collagen alignment to promote the migration of pancreatic ductal adenocarcinoma cells. *Biomed. Microdev.* 18:105.

Eichmann, A., and Simons, M. (2012). VEGF signaling inside vascular endothelial cells and beyond. *Curr. Opin. Cell Biol.* 24, 188–193. doi: 10.1016/j.ceb.2012.02.002

Erstad, D. J., Sojoodi, M., Taylor, M. S., Ghoshal, S., Razavi, A. A., Graham-O'regan, K. A., et al. (2018). Orthotopic and heterotopic murine models of pancreatic cancer and their different responses to FOLFIRINOX chemotherapy. *Dis. Models Mechan.* 11:dmm034793. doi: 10.1242/dmm.034793

Fernandes, T. G., Diogo, M. M., Clark, D. S., Dordick, J. S., and Cabral, J. M. S. (2009). High-throughput cellular microarray platforms: applications in drug discovery, toxicology and stem cell research. *Trends Biotechnol.* 27, 342–349. doi: 10.1016/j.tibtech.2009.02.009

Froeling, F. E., Mirza, T. A., Feakins, R. M., Seedhar, A., Elia, G., Hart, I. R., et al. (2009). Organotypic culture model of pancreatic cancer demonstrates that stromal cells modulate E-cadherin, β-catenin, and Ezrin expression in tumor cells. *Am. J. Pathol.* 175, 636–648. doi: 10.2353/ajpath.2009.090131

Gerhardt, H., Golding, M., Fruttiger, M., Ruhrberg, C., Lundkvist, A., Abramsson, A., et al. (2003). VEGF guides angiogenic sprouting utilizing endothelial tip cell filopodia. *J. Cell Biol.* 161, 1163–1177. doi: 10.1083/jcb.200302047

Gupta, P., Totti, S., Pérez-Mancera, P. A., Dyke, E., Nisbet, A., Schettino, G., et al. (2019). Chemoradiotherapy screening in a novel biomimetic polymer based pancreatic cancer model. *RSC Adv.* 9, 41649–41663. doi: 10.1039/c9ra09123h

Haeberle, L., and Esposito, I. (2019). Pathology of pancreatic cancer. *Transl. Gastroenterol. Hepatol.* 4:50.

Hamada, S., Masamune, A., Takikawa, T., Suzuki, N., Kikuta, K., Hirota, M., et al. (2012). Pancreatic stellate cells enhance stem cell-like phenotypes in pancreatic cancer cells. *Biochem. Biophys. Res. Commun.* 421, 349–354. doi: 10.1016/j.bbrc.2012.04.014

He, Q., Wang, X., Zhang, X., Han, H., Han, B., Xu, J., et al. (2013). A tissue-engineered subcutaneous pancreatic cancer model for antitumor drug evaluation. *Intern. J. Nanomed.* 8:1167. doi: 10.2147/ijn.s42464

Hoffman, A. S. (2012). Hydrogels for biomedical applications. *Adv. Drug Deliv. Rev.* 64, 18–23.

Hong, T. S., Ryan, D. P., Blaszkowsky, L. S., Mamon, H. J., Kwak, E. L., Mino-Kenudson, M., et al. (2011). Phase I study of preoperative short-course chemoradiation with proton beam therapy and capecitabine for resectable pancreatic ductal adenocarcinoma of the head. *Intern. J. Radiat. Oncol.* 79, 151–157. doi: 10.1016/j.ijrobp.2009.10.061

Hong, T. S., Ryan, D. P., Borger, D. R., Blaszkowsky, L. S., Yeap, B. Y., Ancukiewicz, M., et al. (2014). A phase 1/2 and biomarker study of preoperative short course chemoradiation with proton beam therapy and capecitabine followed by early surgery for resectable pancreatic ductal adenocarcinoma. *Intern. J. Radiat. Oncol.* 89, 830–838. doi: 10.1016/j.ijrobp.2014.03.034

Humpton, T. J., Alagesan, B., Denicola, G. M., Lu, D., Yordanov, G. N., Leonhardt, C. S., et al. (2019). *Oncogenic Kras* induces Nix-mediated mitophagy to promote pancreatic cancer. *Cancer Discov.* 9, 18–1409.

Imamura, T., Iguchi, H., Manabe, T., Ohshio, G., Yoshimura, T., Wang, Z. H., et al. (1995). Quantitative analysis of collagen and collagen subtypes I, III, and V in human pancreatic cancer, tumor-associated chronic pancreatitis, and alcoholic chronic pancreatitis. *Pancreas* 11, 357–364. doi: 10.1097/00006676-199511000-00007

Ireland, L., Santos, A., Ahmed, M. S., Rainer, C., Nielsen, S. R., Quaranta, V., et al. (2016). Chemoresistance in pancreatic cancer is driven by stroma-derived insulin-like growth factors. *Cancer Res.* 76, 6851–6863. doi: 10.1158/0008-5472.can-16-1201

Jaidev, L. R., Krishnan, U. M., and Sethuraman, S. (2015). Gemcitabine loaded biodegradable PLGA nanospheres for in vitro pancreatic cancer therapy. *Mater. Sci. Eng. C* 47, 40–47. doi: 10.1016/j.msec.2014.11.027

Junttila, M. R., and De Sauvage, F. J. (2013). Influence of tumour microenvironment heterogeneity on therapeutic response. *Nature* 501:346. doi: 10.1038/nature12626

Karnevi, E., Rosendahl, A. H., Hilmersson, K. S., Saleem, M. A., and Andersson, R. (2016). Impact by pancreatic stellate cells on epithelial-mesenchymal transition and pancreatic cancer cell invasion: adding a third dimension in vitro. *Exp. Cell Res.* 346, 206–215. doi: 10.1016/j.yexcr.2016.07.017

Keleg, S., Büchler, P., Ludwig, R., Büchler, M. W., and Friess, H. (2003). Invasion and metastasis in pancreatic cancer. *Mol. Cancer* 2:14.

Ki, C. S., Lin, T.-Y., Korc, M., and Lin, C.-C. (2014). Thiol-ene hydrogels as desmoplasia-mimetic matrices for modeling pancreatic cancer cell growth, invasion, and drug resistance. *Biomaterials* 35, 9668–9677. doi: 10.1016/j.biomaterials.2014.08.014

Kleeff, J., Korc, M., Apte, M., La Vecchia, C., Johnson, C. D., Biankin, A. V., et al. (2016). Pancreatic cancer. *Nat. Rev. Dis. Prim.* 2:16022.

Koay, E. J., Amer, A. M., Baio, F. E., Ondari, A. O., and Fleming, J. B. (2016). Toward stratification of patients with pancreatic cancer: Past lessons from traditional approaches and future applications with physical biomarkers. *Cancer Lett.* 381, 237–243. doi: 10.1016/j.canlet.2015.12.006

Kuen, J., Darowski, D., Kluge, T., and Majety, M. (2017). Pancreatic cancer cell/fibroblast co-culture induces M2 like macrophages that influence therapeutic response in a 3D model. *PLoS One* 12:e0182039. doi: 10.1371/journal.pone.0182039

Lazzari, G., Nicolas, V., Matsusaki, M., Akashi, M., Couvreur, P., and Mura, S. (2018). Multicellular spheroid based on a triple co-culture: a novel 3D model to mimic pancreatic tumor complexity. *Acta Biomater.* 78, 296–307. doi: 10.1016/j.actbio.2018.08.008

Loehrer, P. J. Sr., Feng, Y., Cardenes, H., Wagner, L., Brell, J. M., Cella, D., et al. (2011). Gemcitabine alone versus gemcitabine plus radiotherapy in patients with locally advanced pancreatic cancer: an eastern cooperative oncology group trial. *J. Clin. Oncol.* 29:4105. doi: 10.1200/JCO.2011.34.8904

Longati, P., Jia, X., Eimer, J., Wagman, A., Witt, M.-R., Rehnmark, S., et al. (2013). 3D pancreatic carcinoma spheroids induce a matrix-rich, chemoresistant phenotype offering a better model for drug testing. *BMC Cancer* 13:95. doi: 10.1186/1471-2407-13-95

Longo, V., Brunetti, O., Gnoni, A., Cascinu, S., Gasparini, G., Lorusso, V., et al. (2016). Angiogenesis in pancreatic ductal adenocarcinoma: a controversial issue. *Oncotarget* 7:58649.

Mahadevan, A., Jain, S., Goldstein, M., Miksad, R., Pleskow, D., Sawhney, M., et al. (2010). Stereotactic body radiotherapy and gemcitabine for locally advanced pancreatic cancer. *Intern. J. Rad. Oncol. Biol. Phys.* 78, 735–742.

Masamune, A., Kikuta, K., Satoh, M., Satoh, K., and Shimosegawa, T. (2003). Rho kinase inhibitors block activation of pancreatic stellate cells. *Br. J. Pharmacol.* 140, 1292–1302. doi: 10.1038/sj.bjp.0705551

Matsuda, Y., Ishiwata, T., Kawamoto, Y., Kawahara, K., Peng, W.-X., Yamamoto, T., et al. (2010). Morphological and cytoskeletal changes of pancreatic cancer cells in three-dimensional spheroidal culture. *Med. Mol. Morphol.* 43, 211–217. doi: 10.1007/s00795-010-0497-0

McCarroll, J. A., Naim, S., Sharbeen, G., Russia, N., Lee, J., Kavallaris, M., et al. (2014). Role of pancreatic stellate cells in chemoresistance in pancreatic cancer. *Front. Physiol.* 5:141. doi: 10.3389/fphys.2014.00141

Nath, S., and Devi, G. R. (2016). Three-dimensional culture systems in cancer research: Focus on tumor spheroid model. *Pharmacol. Therap.* 163, 94–108. doi: 10.1016/j.pharmthera.2016.03.013

Nguyen, B.-N. B., Moriarty, R. A., Kamalitdinov, T., Etheridge, J. M., and Fisher, J. P. (2017). Collagen hydrogel scaffold promotes mesenchymal stem cell and endothelial cell coculture for bone tissue engineering. *J. Biomed. Mater. Res. Part A* 105, 1123–1131. doi: 10.1002/jbm.a.36008

Noel, P., Muñoz, R., Rogers, G. W., Neilson, A., Von Hoff, D. D., and Han, H. (2017). Preparation and metabolic assay of 3-dimensional spheroid co-cultures of pancreatic cancer cells and fibroblasts. *J. Vis. Exper.* 2017:e56081.

O'Brien, F. J. (2011). Biomaterials & scaffolds for tissue engineering. *Mater. Today* 14, 88–95.

Okumura, T., Ohuchida, K., and Nakamura, M. (2019). "An in vitro three-dimensional organotypic model to analyze peripancreatic fat invasion in pancreatic cancer: a culture system based on collagen gel embedding," in *Pancreatic Cancer*, ed. G. Su (New York, NY: Humana Press), 135–141. doi: 10.1007/978-1-4939-8879-2_11

Onishi, H., Morifuji, Y., Kai, M., Suyama, K., Iwasaki, H., and Katano, M. (2012). Hedgehog inhibitor decreases chemosensitivity to 5-fluorouracil and gemcitabine under hypoxic conditions in pancreatic cancer. *Cancer Sci.* 103, 1272–1279. doi: 10.1111/j.1349-7006.2012.02297.x

Pei, X., Zhu, J., Yang, R., Tan, Z., An, M., Shi, J., et al. (2016). CD90 and CD24 Co-expression is associated with pancreatic intraepithelial neoplasias. *PLoS One* 11:e0158021. doi: 10.1371/journal.pone.0158021

Pérez–Mancera, P. A., Guerra, C., Barbacid, M., and Tuveson, D. A. (2012). What we have learned about pancreatic cancer from mouse models. *Gastroenterology* 142, 1079–1092. doi: 10.1053/j.gastro.2012.03.002

Pozzi, R., Parzanese, I., Baccarin, A., Giunta, M., Conti, C. B., Cantù, P., et al. (2017). Point shear-wave elastography in chronic pancreatitis: a promising tool for staging disease severity. *Pancreatology* 17, 905–910. doi: 10.1016/j.pan.2017.10.003

Priwitaningrum, D. L., Blondé, J.-B. G., Sridhar, A., Van Baarlen, J., Hennink, W. E., Storm, G., et al. (2016). Tumor stroma-containing 3D spheroid arrays:

a tool to study nanoparticle penetration. *J. Control. Rel.* 244, 257–268. doi: 10.1016/j.jconrel.2016.09.004

Raza, A., Ki, C. S., and Lin, C.-C. (2013). The influence of matrix properties on growth and morphogenesis of human pancreatic ductal epithelial cells in 3D. *Biomaterials* 34, 5117–5127. doi: 10.1016/j.biomaterials.2013.03.086

Ricci, C., Mota, C., Moscato, S., D'alessandro, D., Ugel, S., Sartoris, S., et al. (2014). Interfacing polymeric scaffolds with primary pancreatic ductal adenocarcinoma cells to develop 3D cancer models. *Biomatter* 4:e955386. doi: 10.4161/21592527.2014.955386

Rice, A., Cortes, E., Lachowski, D., Cheung, B., Karim, S., Morton, J., et al. (2017). Matrix stiffness induces epithelial–mesenchymal transition and promotes chemoresistance in pancreatic cancer cells. *Oncogenesis* 6:e352. doi: 10.1038/oncsis.2017.54

Rioja, A. Y., Tiruvannamalai Annamalai, R., Paris, S., Putnam, A. J., and Stegemann, J. P. (2016). Endothelial sprouting and network formation in collagen- and fibrin-based modular microbeads. *Acta Biomater.* 29, 33–41. doi: 10.1016/j.actbio.2015.10.022

Sato, Y., Yamada, S., Takeda, S., Hattori, N., Nakamura, K., Tanaka, H., et al. (2018). Effect of Plasma-Activated Lactated Ringer's Solution on Pancreatic Cancer Cells In Vitro and In Vivo. *Ann. Surg. Oncol.* 25, 299–307. doi: 10.1245/s10434-017-6239-y

Schellenberg, D., Goodman, K. A., Lee, F., Chang, S., Kuo, T., Ford, J. M., et al. (2008). Gemcitabine chemotherapy and single-fraction stereotactic body radiotherapy for locally advanced pancreatic cancer. *Intern. J. Rad. Oncol. Biol. Phys.* 72, 678–686. doi: 10.1016/j.ijrobp.2008.01.051

Schüssler, M., Skoudy, A., Ramaekers, F., and Real, F. X. (1992). Intermediate filaments as differentiation markers of normal pancreas and pancreas cancer. *Am. J. Pathol.* 140:559.

Seicean, A., Petrusel, L., and Seicean, R. (2015). New targeted therapies in pancreatic cancer. *World J. Gastroenterol.* 21:6127. doi: 10.3748/wjg.v21.i20.6127

Serri, C., Quagliariello, V., Iaffaioli, R. V., Fusco, S., Botti, G., Mayol, L., et al. (2019). Combination therapy for the treatment of pancreatic cancer through hyaluronic acid-decorated nanoparticles loaded with quercetin and gemcitabine: a preliminary in vitro study. *J. Cell. Physiol.* 234, 4959–4969. doi: 10.1002/jcp.27297

Shields, M. A., Dangi-Garimella, S., Redig, A. J., and Munshi, H. G. (2011). Biochemical role of the collagen-rich tumour microenvironment in pancreatic cancer progression. *Biochem. J.* 441, 541–552. doi: 10.1042/bj20111240

Shinoda, S., Kaino, S., Amano, S., Harima, H., Matsumoto, T., Fujisawa, K., et al. (2018). Deferasirox, an oral iron chelator, with gemcitabine synergistically inhibits pancreatic cancer cell growth in vitro and in vivo. *Oncotarget* 9, 28434–28444.

Shintani, Y., Hollingsworth, M. A., Wheelock, M. J., and Johnson, K. R. (2006). Collagen I Promotes metastasis in pancreatic cancer by activating c-Jun NH2-terminal Kinase 1 and Up-regulating N-Cadherin expression. *Cancer Res.* 66, 11745–11753. doi: 10.1158/0008-5472.can-06-2322

Shoval, H., Karsch-Bluman, A., Brill-Karniely, Y., Stern, T., Zamir, G., Hubert, A., et al. (2017). Tumor cells and their crosstalk with endothelial cells in 3D spheroids. *Sci. Rep.* 7:10428.

Siegel, R. L., Kimberly, M., and Jemal, A. (2018). Cancer statistics. *CA Cancer J. Clin.* 68, 7–30. doi: 10.3322/caac.21332

Siemerink, M. J., Klaassen, I., Vogels, I. M. C., Griffioen, A. W., Van Noorden, C. J. F., and Schlingemann, R. O. (2012). CD34 marks angiogenic tip cells in human vascular endothelial cell cultures. *Angiogenesis* 15, 151–163. doi: 10.1007/s10456-011-9251-z

Son, K.-N., Hwang, J., Kwon, B. S., and Kim, J. (2006). Human CC chemokine CCL23 enhances expression of matrix metalloproteinase-2 and invasion of vascular endothelial cells. *Biochem. Biophys. Res. Commun.* 340, 498–504. doi: 10.1016/j.bbrc.2005.12.037

Suklabaidya, S., Dash, P., Das, B., Suresh, V., Sasmal, P. K., and Senapati, S. (2018). Experimental models of pancreatic cancer desmoplasia. *Lab. Invest.* 98:27. doi: 10.1038/labinvest.2017.127

Tahlawi, A., Klontzas, M. E., Allenby, M. C., Morais, J. C., Panoskaltsis, N., and Mantalaris, A. (2019). RGD-functionalized polyurethane scaffolds promote umbilical cord blood mesenchymal stem cell expansion and osteogenic differentiation. *J. Tissue Eng. Regener. Med.* 13, 232–243.

Terashima, K., Demizu, Y., Hashimoto, N., Jin, D., Mima, M., Fujii, O., et al. (2012). A phase I/II study of gemcitabine-concurrent proton radiotherapy for locally advanced pancreatic cancer without distant metastasis. *Radiother. Oncol.* 103, 25–31. doi: 10.1016/j.radonc.2011.12.029

Totti, S., Allenby, M. C., Dos Santos, S. B., Mantalaris, A., and Velliou, E. G. (2018). A 3D bioinspired highly porous polymeric scaffolding system for in vitro simulation of pancreatic ductal adenocarcinoma. *RSC Adv.* 8, 20928–20940. doi: 10.1039/c8ra02633e

Totti, S., Vernardis, S. I., Meira, L., Pérez-Mancera, P. A., Costello, E., Greenhalf, W., et al. (2017). Designing a bio-inspired biomimetic in vitro system for the optimization of ex vivo studies of pancreatic cancer. *Drug Discov. Today* 22, 690–701. doi: 10.1016/j.drudis.2017.01.012

Tuveson, D. A., and Neoptolemos, J. P. (2012). Understanding metastasis in pancreatic cancer: a call for new clinical approaches. *Cell* 148, 21–23. doi: 10.1016/j.cell.2011.12.021

Velliou, E. G., Dos Santos, S. B., Papathanasiou, M. M., Fuentes-Gari, M., Misener, R., Panoskaltsis, N., et al. (2015). Towards unravelling the kinetics of an acute myeloid leukaemia model system under oxidative and starvation stress: a comparison between two- and three-dimensional cultures. *Bioprocess Biosyst. Eng.* 38, 1589–1600. doi: 10.1007/s00449-015-1401-z

Verbeke, C. (2016). Morphological heterogeneity in ductal adenocarcinoma of the pancreas–Does it matter? *Pancreatology* 16, 295–301. doi: 10.1016/j.pan.2016.02.004

Wang, D.-D., Liu, W., Chang, J.-J., Cheng, X., Zhang, X.-Z., Xu, H., et al. (2016). Bioengineering three-dimensional culture model of human lung cancer cells: an improved tool for screening EGFR targeted inhibitors. *RSC Adv.* 6, 24083–24090. doi: 10.1039/c6ra00229c

Wang, X., Zhang, X., Fu, Z., and Yin, H. (2013). A bioengineered metastatic pancreatic tumor model for mechanistic investigation of chemotherapeutic drugs. *J. Biotechnol.* 166, 166–173. doi: 10.1016/j.jbiotec.2013.05.008

Ware, M. J., Keshishian, V., Law, J. J., Ho, J. C., Favela, C. A., Rees, P., et al. (2016). Generation of an in vitro 3D PDAC stroma rich spheroid model. *Biomaterials* 108, 129–142. doi: 10.1016/j.biomaterials.2016.08.041

Wehr, A. Y., Furth, E. E., Sangar, V., Blair, I. A., and Yu, K. H. (2011). Analysis of the human pancreatic stellate cell secreted proteome. *Pancreas* 40:557. doi: 10.1097/mpa.0b013e318214efaf

Wen, Z., Liao, Q., Hu, Y., You, L., Zhou, L., and Zhao, Y. (2013). A spheroid-based 3-D culture model for pancreatic cancer drug testing, using the acid phosphatase assay. *Braz. J. Med. Biol.* 46, 634–642. doi: 10.1590/1414-431x20132647

Xu, Z., Vonlaufen, A., Phillips, P. A., Fiala-Beer, E., Zhang, X., Yang, L., et al. (2010). Role of pancreatic stellate cells in pancreatic cancer metastasis. *Am. J. Pathol.* 177, 2585–2596.

Yan, X., Zhou, L., Wu, Z., Wang, X., Chen, X., Yang, F., et al. (2019). High throughput scaffold-based 3D micro-tumor array for efficient drug screening and chemosensitivity testing. *Biomaterials* 198, 167–179. doi: 10.1016/j.biomaterials.2018.05.020

Yin, D., Fu, C., and Sun, D. (2018). Silence of lncRNA UCA1 represses the growth and tube formation of human microvascular endothelial cells through miR-195. *Cell Physiol. Biochem* 49, 1499–1511. doi: 10.1159/000493454

Zhan, H.-X., Zhou, B., Cheng, Y.-G., Xu, J.-W., Wang, L., Zhang, G.-Y., et al. (2017). Crosstalk between stromal cells and cancer cells in pancreatic cancer: new insights into stromal biology. *Cancer Lett.* 392, 83–93. doi: 10.1016/j.canlet.2017.01.041

Zhang, J. W., Zhao, F., and Sun, Q. (2018). Metformin synergizes with rapamycin to inhibit the growth of pancreatic cancer in vitro and in vivo. *Oncology Lett.* 15, 1811–1816.

Conflict of Interest: The authors declare that the research was conducted in the absence of any commercial or financial relationships that could be construed as a potential conflict of interest.

frontiers in Bioengineering and Biotechnology

ORIGINAL RESEARCH
published: 29 April 2020
doi: 10.3389/fbioe.2020.00376

Computational Modeling of Human Mesenchymal Stromal Cell Proliferation and Extra-Cellular Matrix Production in 3D Porous Scaffolds in a Perfusion Bioreactor: The Effect of Growth Factors

Mohammad Mehrian[1,2], *Toon Lambrechts*[2,3], *Ioannis Papantoniou*[2,4,5] *and Liesbet Geris*[1,2,6*]

[1] *Biomechanics Research Unit, GIGA In silico Medicine, University of Liège, Liège, Belgium,* [2] *Prometheus, The Division of Skeletal Tissue Engineering, KU Leuven, Leuven, Belgium,* [3] *M3-BIORES, KU Leuven, Leuven, Belgium,* [4] *Skeletal Biology and Engineering Research Center, KU Leuven, Leuven, Belgium,* [5] *Institute of Chemical Engineering Sciences (ICEHT), Foundation for Research and Technology – Hellas (FORTH), Patras, Greece,* [6] *Biomechanics Section, KU Leuven, Leuven, Belgium*

OPEN ACCESS

Edited by:
Dimitrios I. Zeugolis, National University of Ireland Galway, Ireland

Reviewed by:
Antonella Motta, University of Trento, Italy
Eirini Velliou, University of Surrey, United Kingdom

***Correspondence:**
Liesbet Geris
liesbet.geris@uliege.be

Specialty section:
This article was submitted to Tissue Engineering and Regenerative Medicine, a section of the journal Frontiers in Bioengineering and Biotechnology

Received: *28 September 2019*
Accepted: *06 April 2020*
Published: *29 April 2020*

Citation:
Mehrian M, Lambrechts T, Papantoniou I and Geris L (2020) Computational Modeling of Human Mesenchymal Stromal Cell Proliferation and Extra-Cellular Matrix Production in 3D Porous Scaffolds in a Perfusion Bioreactor: The Effect of Growth Factors. Front. Bioeng. Biotechnol. 8:376. doi: 10.3389/fbioe.2020.00376

Stem cell expansion on 3D porous scaffolds cultured in bioreactor systems has been shown to be beneficial for maintenance of the original cell functionality in tissue engineering strategies (TE). However, the production of extracellular matrix (ECM) makes harvesting the progenitor cell population from 3D scaffolds a challenge. Medium composition plays a role in stimulating cell proliferation over extracellular matrix (ECM) production. In this regard, a computational model describing tissue growth inside 3D scaffolds can be a great tool in designing optimal experimental conditions. In this study, a computational model describing cell and ECM growth in a perfusion bioreactor is developed, including a description of the effect of a (generic) growth factor on the biological processes taking place inside the 3D scaffold. In the model, the speed of cell and ECM growth depends on the flow-induced shear stress, curvature and the concentrations of oxygen, glucose, lactate, and growth factor. The effect of the simulated growth factor is to differentially enhance cell proliferation over ECM production. After model calibration with historic in-house data, a multi-objective optimization procedure is executed aiming to minimize the total experimental cost whilst maximizing cell growth during culture. The obtained results indicate there are multiple optimum points for the medium refreshment regime and the initial growth factor concentration where a trade-off is made between the final amount of cells and the culture cost. Finally, the model is applied to experiments reported in the literature studying the effects of perfusion-based cell culture and/or growth factor supplementation on cell expansion. The qualitative similarities between the simulation and experimental results, even in the

absence of proper model calibration, reinforces the generic character of the proposed modeling framework. The model proposed in this study can contribute to the cost efficient production of cell-based TE products, ultimately contributing to their affordability and accessibility.

Keywords: computational modeling, mesenchymal stromal cell, perfusion bioreactor, growth factors, optimization, tissue engineering, experimental costs

INTRODUCTION

The field of tissue engineering (TE) is constantly evolving but the development of a robust and reproducible tissue engineered advanced therapy medicinal product (ATMP) remains a challenge. Although several studies have shown the potential of TE ATMPs for *in vivo* tissue regeneration (Chai et al., 2012; Roberts et al., 2012), this has been mostly obtained with methods that relied on manual operations. In this respect, bioreactors could play an important role in creating a successful clinical product by contributing in achieving an automated, controlled, and monitored process environment for cell expansion and/or combination product culture (Schneider et al., 2010; Salter et al., 2011). This environment is then amenable to optimization and standardization through the use of *in silico* strategies.

Furthermore, the perfused flow through scaffold pores inside a bioreactor will expose cells to proper mechanical stimuli, which is shown to be beneficial in cell growth and differentiation, as well as ensuring the supply of nutrients such as glucose and removal of metabolic waste such as lactate (Martin et al., 2004; Haycock, 2011). During 3D growth, cells secrete extracellular matrix (ECM) depending on different culture conditions such as the composition of the medium, the frequency of medium refreshment in the bioreactor, the scaffold geometry and the flow rate (Papantoniou et al., 2014b; Sonnaert et al., 2017). Although the presence of ECM has shown to be advantageous for maintaining the potency of the expanded cells (Li and Pei, 2010; Pei et al., 2011), recovering the cells from the 3D scaffold is a challenging procedure. For the purpose of cell expansion in 3D scaffolds, we need to limit the ECM production and increase the cell proliferation. The use of growth factors in the culture medium is a necessity that can significantly increase proliferation or differentiation of cells toward a specific lineage and affect the amount and extracellular matrix that is produced by the differentiating cells (Hankemeier et al., 2005; Rodrigues et al., 2010; Mishra et al., 2016).

Computational models are useful tools in unraveling the complexity involved in neotissue (combination of cells and the extracellular matrix they produce) growth inside 3D scaffolds as they enable us to investigate the effect of a wide range of factors affecting the tissue formation during the culture period, assisting in designing and optimizing the best culture procedure (Lemon et al., 2007; Carlier et al., 2014; Chapman et al., 2014; Misener et al., 2014; Guyot et al., 2015; Shakhawath Hossain et al., 2015; Mehrian et al., 2018).

In a previous study we have developed a computational model describing neotissue growth inside 3D scaffolds in a perfusion bioreactor (Mehrian et al., 2018), taking into account influences of geometry, flow-induced shear stress, oxygen, glucose, lactate, and pH. We have furthermore applied various optimization methods to derive culture conditions leading to maximal filling of the scaffold at minimal cost (Mehrian and Geris, 2020). In contrast to that previous optimization objective, in this study, we do not focus on the optimization of the combination product (scaffold + neotissue) but rather we focus on the use of the perfusion bioreactor set-up to perform 3D cell expansion. Thereto, we have enhanced the previous model by replacing the neotissue variable by two separate variables, one for cell volume and one for ECM volume. The interaction between cell growth and ECM production, as well as the dependence of both variables on external factors, is an intricate process with many quantitative relations currently unquantified (or even uncharacterized). The method presented here provides a framework that can be continuously updated with new information related to a specific biological application in order to increase its biological relevance. In this study, model calibration was carried out based on historic results obtained in our perfusion bioreactor set-up. A (generic) growth factor variable was added to the model, with distinct effects on cell proliferation vs. matrix production. As different input parameters of the model such as refreshment time, refreshment amount and the initial concentration of the growth factor(s) in the medium greatly impact not only the cell and ECM production but also the cost of culture, a multi-objective optimization was run to find the combination of the aforementioned parameters leading to maximum cell volume in the most cost efficient manner. Finally, we have applied the model to two studies reported in the literature where (static or dynamic) cell culture was carried out under the presence of a range of growth factor concentrations. Due to lack of proper calibration information, the comparison remains at the qualitative level. The similarity in trends observed between experimental and simulation results however, further reinforces the generic character of the proposed modeling framework.

METHODS

Experimental Set-Up

The experiments used in this study have been extensively described in Papantoniou et al. (2014b) and Sonnaert et al. (2017). Briefly, the cells used in this experiment are human Periosteum Derived Cells (hPDCs), chosen for their pluripotency and their bone forming capacity (De Bari et al., 2006). hPDCs were isolated from periosteal biopsies of different donors as described in Eyckmans and Luyten (2006). All procedures were approved by the ethics committee for Human Medical Research

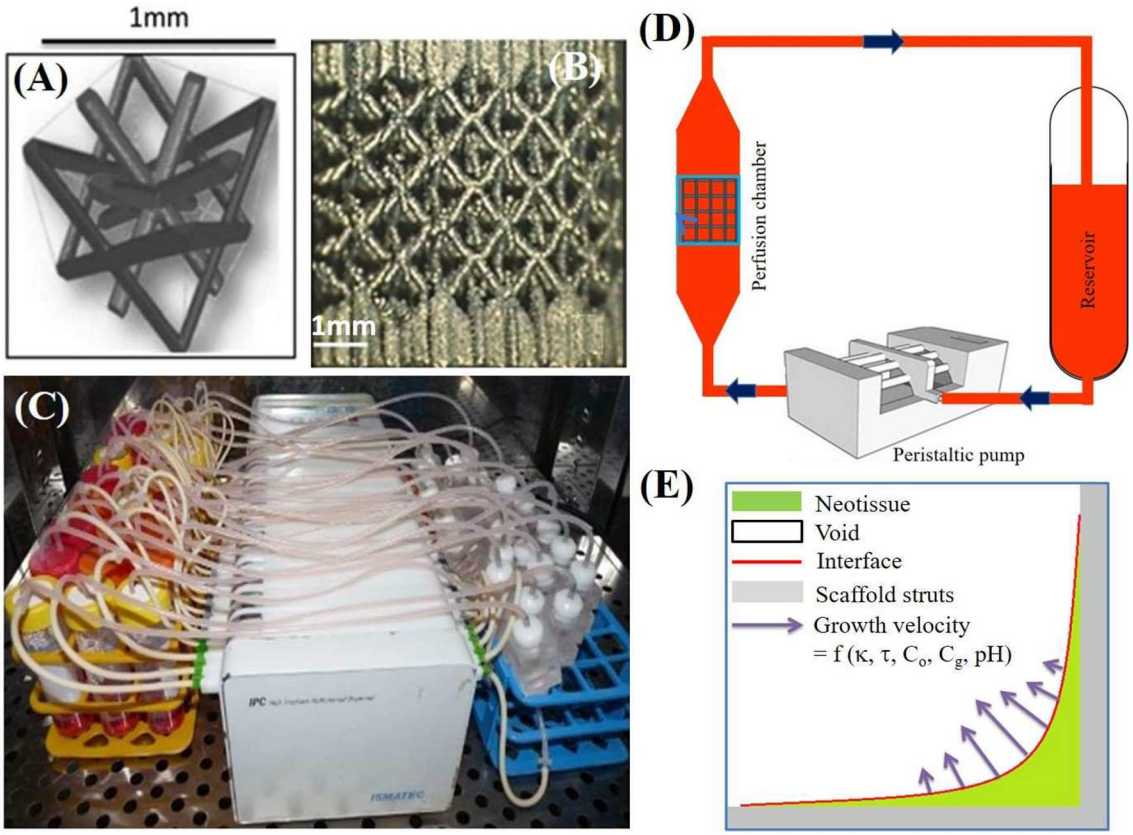

FIGURE 1 | (A) The parametric unit cell of the computer-aided design of the porous Ti scaffolds, which consists entirely of identical beams with constant circular cross sections (0.1 mm) and a beam length of 0.9 mm. **(B)** A typical image of a selective laser melting produced Ti scaffold. **(C)** An image of the in-house developed perfusion bioreactor equipped with parallel perfusion circuits. **(D)** Schematic representation of the bioreactor setup used for three-dimensional (3D) dynamic culture, consisting of a medium reservoir containing 10 mL of medium, a peristaltic pump forcing the culture medium through the porous scaffold that was positioned in the perfusion chamber. **(E)** Schematic representation of simulated neotissue growth inside scaffold with growth velocity a function of curvature (κ), flow induced shear stress (τ), oxygen concentration (C_o), glucose concentration (C_g), and pH. Adapted from Papantoniou et al. (2014b) and Guyot et al. (2015).

(KU Leuven) and explicit patient (or parental) consent was obtained. Cells were expanded in the Dulbecco's modified Eagle's medium with high glucose (Invitrogen) containing 10% fetal bovine serum (BioWhittaker) and 1% antibiotic–antimycotic (100 units/mL penicillin, 100 mg/mL streptomycin, and 0.25 mg/mL amphotericin B; Invitrogen). The seeding density used for the two-dimensional (2D) culture dish hPDC expansion was 6000 cells/cm^2. hPDCs were passaged at 80–90% confluency. At the time of experiment, cells were trypsinized with Tryple Express (Invitrogen) to be seeded on 3D additive manufactured open porous Ti6Al4V scaffolds (Ø = 6 mm, h = 6 mm, and a diamond unit cell with porosity = 73 ± 1%, strut diameter = 245 ± 2 μm, and pore size = 755 ± 3 μm), produced on an in-house developed selective laser melting machine (Van der Stok et al., 2013) (**Figures 1A,B**). The obtained TE constructs were cultured in an in-house developed perfusion bioreactor equipped with seven parallel perfusion circuits (**Figures 1C,D**). Each perfusion chamber, holding a single scaffold, was connected to an individual medium reservoir (disposable 50-mL Falcon tubes; BD Biosciences) containing 10 mL of the cell culture medium via a Tygon (Cole Parmer) tubing and via a two-stop tubing (BPT; Cole Parmer) connected to a peristaltic pump (IPC-24; Ismatec SA). Two different perfusion flow rates were used for the bioreactor culture: the low flow rate used was 0.04 ml/min, while the high flow rate was 4 ml/min. In this study, only the former (low) flow rate was used. Basic Growth Medium in the reservoir was fully refreshed (100%) every 2 days for the entire culture period (not taking into account the volume of medium sitting in the tubing and bioreactor chamber). Filling of the scaffold with neotissue was quantified by means of contrast-enhanced nanofocus computed tomography (CE-nano-CT) as described in Papantoniou et al. (2014b). The DNA content was determined using a highly quantitative and selective DNA assay (Quant-iT^{TM} dsDNA HS kit, Invitrogen) as described in Sonnaert et al. (2017).

Model Set-Up

In a previous study (Mehrian et al., 2018), we developed a computational model describing the neotissue growth inside 3D scaffolds as a function of several geometrical (see **Figure 1E**),

TABLE 1 | Overview of all model variables.

Model variable	Meaning
V_n	Neotissue volume
C_o	Oxygen concentration
C_g	Glucose concentration
C_{la}	Lactate concentration
κ	Curvature
pH	pH level
τ	Shear stress
V_{ECM}	Volume fraction of ECM
V_{Cell}	Volume fraction of proliferating cells
gf	Growth factor concentration
p	Refreshment period
a	Fraction of the medium being refreshed

chemical and physical factors, homogenized in space. In the following, we briefly describe this model, and explain the updated equations describing the evolution of cell volume and ECM volume as separate variables in the model. A detailed description can be found in the **Supplementary Material** and in Mehrian et al. (2018). An overview of all model variables with their respective symbols is provided in **Table 1**.

Neotissue Volume

$$\frac{dV_n}{dt} = A\, f_s(\tau)\; f_c(\kappa)\; h_1(C_o)\; h_2\left(C_g\right)\; h_3\left(pH\right)\; \frac{V_n}{K_{V_n} + \lambda V_n} \quad (1)$$

Equation (1) expresses the neotissue volume (V_n) as a function of the concentrations of oxygen (C_o) and glucose (C_g), pH level (pH), mean curvature (κ) of the neotissue-void interface inside the 3D scaffold and the shear stress (τ) caused by the medium flow that is perfused through the scaffold as described in Guyot (2015).

The shear stress (τ) influence is incorporated in the model based on Chapman et al. (2014) through (Equation 2) where there exist an optimal shear stress range that enhances the growth (between a_1 and a_2) in the model. High shear stress values ($\tau \geq a_3$) could be detrimental to tissue growth which results in no growth in our model. The values of the parameters a_1, a_2, and a_3 used in this study are shown in **Table 2**.

$$f_s(\tau) = \begin{cases} 0.5 + \frac{0.5\tau}{a_1}, & 0 \leq \tau < a_1 \\ 1, & a_1 \leq \tau < a_2 \\ \frac{\tau - a_2}{a_2 - a_3}, & a_2 \leq \tau < a_3 \\ 0, & a_3 \leq \tau \end{cases} \quad (2)$$

The function describing the effect of curvature on growth is expressed using a linear function:

$$f_c(\kappa) = \begin{cases} \kappa, & \kappa > 0 \\ 0, & \kappa \leq 0 \end{cases} \quad (3)$$

The influence of oxygen and glucose concentrations on the produced neotissue in Equation (1) is taken into account through the functions h_1 and h_2 where neotissue volume reduces when the species level decreases. **Table 2** shows the values of K_o and K_g used in this study.

TABLE 2 | Overview of all parameter values used in this study.

Parameter	Value	References
β_1	255	Mehrian et al., 2018
β_2	$3.6*10^5$	Mehrian et al., 2018
γ	0.6716	Mehrian et al., 2018
a_1	0.01	Chapman et al., 2014
a_2	0.03	Chapman et al., 2014
a_3	0.05	Chapman et al., 2014
V_o	$1.09*10^{-17}$mol/cell/s	Lambrechts et al., 2014
V_g	$9.5*10^{-17}$mol/cell/s	Zhou et al., 2013
K_o	$1.82*10^{-3}$mM	Carlier et al., 2014
K_g	0.3 mM	Shakhawath Hossain et al., 2015
ϕ_{cells}	$2.5*10^{13}$cells/m^3	Guyot, 2015
A_1	0.216	This study (GA)
A_2	$5.612*10^{12}$	This study (GA)
λ	$1.2836*10^{-4}$ s^{-1}	This study (half-life of 1.5 h)
α_1	0.975 $\frac{ng}{ml}$	This study (GA)
α_2	12.09	This study (GA)
α_3	0.1 $\frac{ng}{ml}$	This study (GA)

$$h_1(C_o) = \frac{C_o}{K_o + C_o} \quad (4)$$

$$h_2\left(C_g\right) = \frac{C_g}{K_g + C_g} \quad (5)$$

Lactate production in the medium is directly related to the medium pH level and negative influences the neotissue growth. Wuertz et al. (2009) described a detrimental effect of pH on cell fate using (Equation 8) where the neotissue growth rate decreases linearly when the medium pH level decreases.

$$h_3\left(pH\right) = \begin{cases} 1, & pH > 7.1 \\ \frac{4}{3}pH - 8.5, & 7.1 \leq pH < 6.375 \\ 0, & pH \leq 6.375 \end{cases} \quad (6)$$

The supply of nutrients such as oxygen and glucose and the removal of waste product (lactate in our model) in the bioreactor set-up are modeled using (Equations 7–10). In these equations, the right-hand side terms show the production or consumption of the species by the cells, modeled using Michaelis-Menten kinetics with ϕ_{cells} being the cell density within the neotissue, V_i the consumption rate and K_i the Michaelis-Menten with $i = o$ for oxygen and $i = g$ for glucose.

$$\frac{dC_o}{dt} = -\beta_1\; V_n\, \phi_{cells}\, V_o\; \frac{C_o}{K_o + \gamma C_o} \quad (7)$$

$$\frac{dC_g}{dt} = -\beta_2\; V_n\, \phi_{cells}\, V_g\; \frac{C_g}{K_g + C_g} \quad (8)$$

$$\frac{dC_{la}}{dt} = 2\; V_n\, \phi_{cells}\, V_g\; \frac{C_g}{K_g + C_g} \quad (9)$$

$$pH = 7.4 - 0.0406 C_{la} \quad (10)$$

The medium refreshment in the model is simulated by setting the glucose (C_g) and lactate (C_{la}) values to their initial amounts at the requested refreshment time. As in the bioreactor set-up, there is a leakage of oxygen, oxygen value is not reinitialized at each refreshment point. For partial medium refreshment, a percentage weighed average was calculated with the current values of the variables and the medium values. For a more detailed explanation on different model parameters, we refer the reader to the **Supplementary Materials** or Mehrian et al. (2018).

Cell Volume and ECM Volume

At this point, using the current state of the equations we cannot make a distinction between cell and ECM compartments in the neotissue. Given that we want to be able to control cell proliferation vs. matrix production, the variable expressing neotissue volume (V_n) in Equation (1) is separated into two variables – one for the cell compartment and one for the ECM compartment, based on Lemon et al. (2007) and shown in Equations (11) and (12).

$$\frac{dV_{ECM}}{dt} = A_1 f_s(\tau)\ f_c(\kappa)\ h_1(C_o)\ h_2\left(C_g\right)\ h_3\left(pH\right)\ V_{Cell}\left(V_T - V_{Cell} - V_{ECM}\right) \quad (11)$$

$$\frac{dV_{Cell}}{dt} = A_2 f_s(\tau)\ f_c(\kappa)\ h_1(C_o)\ h_2\left(C_g\right)\ h_3\left(pH\right)\ V_{Cell}\ V_{ECM}\left(V_T - V_{Cell} - V_{ECM}\right) \quad (12)$$

The volume fraction of ECM (V_{ECM}) in Equation (11) is not only affected by chemical (e.g., oxygen) and physical (e.g., curvature) factors (see Equation 1), but is also considered to be influenced by the cell volume (V_{Cell}). In addition, the production of ECM is limited by the presence of cells, ECM and the total available space (V_T). In Equation (12), the volume fraction of proliferated cells (V_{Cell}) is considered to be proportional to V_{ECM} to simulate the stimulatory effect of extracellular matrix proteins such as the extra-cellular protein Dickkopf-1 (Dkk-1) on cell proliferation (Gregory et al., 2003; Lemon et al., 2007).

To investigate whether all the chemical and physical factors affecting the neotissue volume (V_n) in Equation (1) should remain present in each of the two separated (Equations 11, 12), a literature review was conducted to study the effect of each factor on cell proliferation and matrix production.

Shear stress is believed to enhance cell proliferation and differentiation in 3D scaffolds in the presence of fluid flow (Datta et al., 2006; Stiehler et al., 2009). Using different flow rates, mineralized matrix deposition and cell proliferation is increased compared to the static culture (Bancroft et al., 2002; Papantoniou et al., 2014b). MSC cells are shear sensitive and shear responsive with fluid flow induced shear stress affecting their growth and phenotypic state. However, high shear stresses have been seen to be detrimental to MSCs either due to detachment from the scaffolds or due to mechanical damage (McCoy and O'Brien, 2010). The exact thresholds and parameters to describe these processes are dependent on the cell type. In this study, we perform a model calibration procedure based on historic data obtained for hPDCs during culture in a perfusion bioreactor. For this specific cell type and scaffold geometry we have indeed observed that excessively high shear stress affects local growth of neotissue (Papantoniou et al., 2014a). The shear stress magnitudes observed in that study match those in our computational investigation. In this study, the flow rate is kept at a fixed value of 0.04 ml/min.

Scaffold pore size influences the MSCs proliferations and matrix deposition (Oh et al., 2010; Nava et al., 2016) which is an indication of curvature in Equations (11) and (12). In Matsiko et al. (2014), it is shown that scaffolds with the largest mean pore size (300 μm), will result in higher cell proliferation and matrix deposition. In a recent review on curvature topography, Callens et al. (2019) summarize the evidence demonstrating that curvature is driving neotissue formation in a 3D context (which is the baseline assumption of the computational framework).

There are numerous studies showing the effect of oxygen on cell proliferation and differentiation (Choi et al., 2014; Atashi et al., 2015). In Grayson et al. (2006), hMSCs were cultured under two different oxygen conditions (normoxic 20% and hypoxic 2%). Differentiation and proliferation of cells was reported to be higher under hypoxic conditions.

Glucose is the main nutrient for cell growth in our model, but high glucose concentrations could suppress cell proliferation as it is shown in Kato et al. (2016). In this paper, authors compared cell proliferation and differentiation in four different concentrations of glucose (from 5.5 to 24 mM), where the lowest glucose concentration resulted in the best outcome.

In Singh (2014), the author has shown the influence of pH level on cell proliferation and differentiation by comparing the viability of staining MSCs cultured in medium with different pH levels at 21% oxygen where an increased presence of dead cells at lower pH levels was observed. Additionally, the effect of pH on cell proliferation and differentiation could be derived indirectly from the effect of glucose on cells in Equations (8)–(10).

In order to compare model output and experimental results, the experimentally DNA content (Sonnaert et al., 2017) was converted into an indication of the amount of cells and further into a volume measure by multiplying the amount of cells by the typical volume of a single hMSC, taken to be of spherical shape with a diameter of 20 μm (Lemon et al., 2007). Using this hypothesis, the volume of each hMSC will be $4.2{*}10^3 um^3$. In Docheva et al. (2008), the authors measured the volume of each hMSC by atomic force microscopy on fibrous substrates (polystyrene and collagen I) and glass. Taking the average volume of hMSCs on these substrates results in a volume of $4.16{*}10^3 um^3$ for each hMSC, which is similar to the previous method. The volume fraction of the cells is obtained by dividing the cell volume to the total available space of the scaffold (V_T).

Growth Factor

Making a distinction between cells and ECM in the model enables us to add a (generic) growth factor to the model equations with a differential effect on proliferation of cells vs. ECM production as shown in Equations (11) and (12). In this study, given the application in cell expansion, the described effect of the

growth factor is to enhance cell proliferation and limit the ECM production.

$$\frac{dV_{ECM}}{dt} = A_1 f_s(\tau)\ f_c(\kappa)\ h_1(C_o)\ h_2(C_g)\ h_3(pH)\ V_{Cell} (V_T - V_{Cell} - V_{ECM})\frac{\alpha_1}{1+gf} \quad (13)$$

$$\frac{dV_{Cell}}{dt} = A_2 f_s(\tau)\ f_c(\kappa)\ h_1(C_o)\ h_2(C_g)\ h_3(pH)\ V_{Cell}\ V_{ECM} (V_T - V_{Cell} - V_{ECM})\frac{\alpha_2 \cdot gf}{\alpha_3 + gf} \quad (14)$$

$$\frac{dgf}{dt} = -\lambda\, gf \quad (15)$$

The effect of growth factor is incorporated in Equations (13) and (14). Degradation of growth factor is expressed in Equation (15). Parameter λ is calculated based on the half-life of the growth factor which is in the range of a few hours for the growth factors that are typically used in the context of cell expansion. In this model, we have assumed the half-life of the growth factor to be 1.5 h. Parameters $A_1, A_2,\ \alpha_1, \alpha_2,\ and\ \alpha_3$ are obtained using a genetic algorithm procedure explained in the following sections.

Model Implementation, Calibration, and Optimization

Model Implementation

The model developed in this study was composed of six model variables (C_o, C_g, C_{la}, V_{ECM}, V_{CELL}, gf) and implemented in MATLAB®. The initial concentration of different model species are as follows; glucose: 25 $\frac{mol}{m^3}$, oxygen: 0.192 $\frac{mol}{m^3}$, and lactate is zero. The initial cell volume is 1.39% of the available space of the scaffold, which corresponds to the 10^5 initial seeded cells onto the scaffold. The initial ECM volume is zero. For the initial value of the growth factor, we have assumed that the baseline value for growth factor concentration in the medium corresponds to 1 $\frac{ng}{ml}$.

Model Calibration

In order to find the best set of model parameters ($A_1, A_2,\ \alpha_1, \alpha_2,\ and\ \alpha_3$) resulting in the closest model outcome to experimental data, a genetic algorithm was used with the goal to minimize the distance between experimental values (red dots) and model predictions at certain time points. The values of all model parameters are shown in **Table 2**.

Model Optimization: Cost Function

The goal in multi-objective optimization (MOO) is to reach a compromise between several conflicting objectives, in the context of this study that would be to maximize the cell volume whilst minimizing the cost. For solving the MOO problem we have used Particle swarm optimization (PSO) technique which is a recent approach inspired by the choreography of a bird flock. PSO was first introduced by Kennedy and Eberhart (1995) and has been found to be successful in a wide variety of optimization tasks (Kennedy, 2006). In order to find the best answer to the problem, a random population of candidates called "particles" are created. Each particle moves in the search space based on its position and velocity following a mathematical formula. The movement of the particles is influenced by the local best and global best-known positions by the total population and the velocity of each particle updates according to its distance from the best-known positions. This process for finding the best answer is repeated until the population converges or the algorithm reaches the maximum (pre-defined) number of iterations. In this study, the optimization problem was run using 100 initial candidates and stopped after 50 iterations. In order to reach the best answer to the problem, the Pareto frontier (Horn, 1997) is calculated. Pareto optimality is a state in which it is impossible to improve the value of one objective function without worsening the value of the other. In other words, we are looking for the border between the infeasible and the suboptimal in our problem.

The function that we aim to minimize in our MOO problem describes the associated costs of labor and culture medium, including the growth factor, and is expressed in Equation (16).

$$C = \left(M + Gf_i(P_g)\right)\left(1 + \frac{24d}{p}a\right) + (L)\ (1 + \frac{24d}{p}) \quad (16)$$

In this equation, C is the total cost of the experiment, M is the cost of the medium used for one medium exchange that is 0.2611€ and L is the labor costs for one medium refreshment that is 6.8€. Gf_i is the initial concentration of the growth factor, P_g is the price for 10ml (the reservoir capacity of the bioreactor) of the used growth factor, d is the total days in which the experiment lasts, p is the refreshment period and a is the fraction of the medium being refreshed each time ($0 \leq a \leq 1$).

Model Validation Using Experimental Data

We have compared the outcome of the model developed in this study with two other experimental studies looking into the (combined) effects of perfusion and growth factors dosing on the proliferation of MSC-type of cells. In Eom et al. (2014), the authors studied the effect of four different growth factors (FGF-2, FGF-4, EGF, and HGF) on the proliferation of the bone marrow-derived mesenchymal stem cells (BMSCs) derived from three healthy donors (aged 21–40 years) in a dose dependent manner (1, 5, and 10 ng/ml) for 3 days. The cells were cultured in 75 cm^2 flasks and the culture medium was changed twice weekly. In another study Koller et al. (1993) used hematopoietic stem cells cultured in a 2D+ perfusion environment with the cytokine concentration of 1.5 ng/ml and the culture medium was changed every 5 days by 50%. Due to lack of experimental data, proper model calibration for the aforementioned specific set-ups is not feasible. Therefore, simulations were conducted using the model optimized for 3D perfusion-based culture with hPDCs. As a result, only qualitative comparisons are made.

RESULTS

Model Calibration Using Experimental Data

The model is calibrated using the experimental data with a flow rate of 0.04 ml/min for the cell and ECM compartments (**Figure 2**). In the experiments, the medium was refreshed every 2 days by 100% during 28 days of culture. In order to be able to consider the effect of growth factor in the experimental data, it

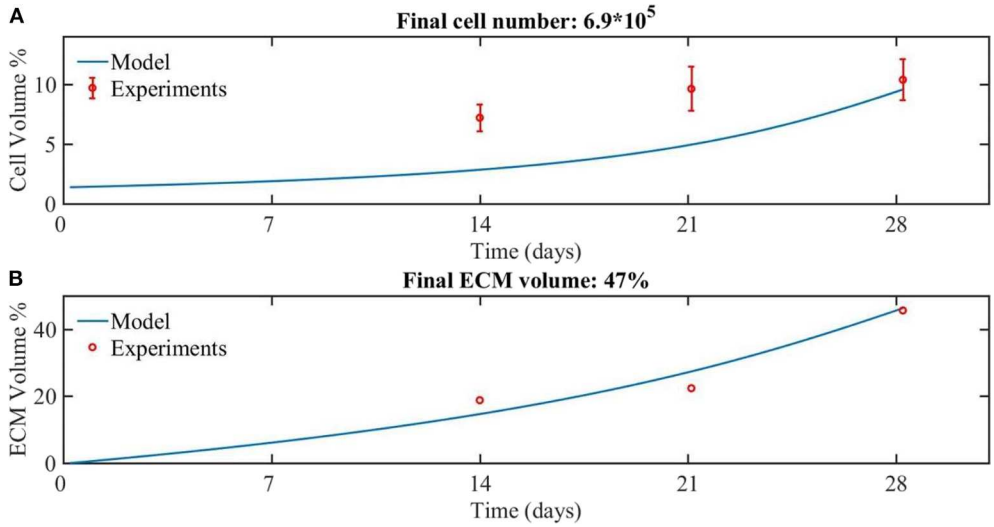

FIGURE 2 | The experimental (red dots) and modeling (blue line) results for the growth of **(A)** cells and **(B)** ECM volume over 28 days of culture. The amount of cells was experimentally estimated based on DNA quantification (Sonnaert et al., 2017). Results are shown as mean ± standard deviation. The ECM volume was measured by contrast-enhance nanofocus CT imaging (Papantoniou et al., 2014b).

is assumed that in the culture medium the concentration of the growth factor was at its baseline level of 1.

Comparing the numerical and experimental cell volume (**Figure 2A**), the numerical results (continuous line) showed a longer lag phase compared to the experimental data (dots), but the final cell volume was similar to the experimental data. The corresponding cell number at day 28 was calculated based on the cell volume, being $6.9*10^5$ cells. The experimental values obtained from the nanoCT imaging included the cell compartment as well as the ECM compartment. Therefore, for the sake of comparison with model outcome, the experimentally estimated cell volume was subtracted from the experimentally measured total volume to obtain the ECM volume. A good correspondence is obtained between numerical and experimental results for the ECM volume (**Figure 2B**).

Model Predictions for Cell and ECM Volume

In order to investigate the effect of different doses of the growth factor and the medium refreshment regime on the cell and ECM production, six different cases were considered, being 3 growth factor concentrations, the baseline concentration of growth factors, and 10 and 100 times the baseline concentration, and two medium refreshment regimes, every 48 h by 100% or every 72 h by 50%. The results are shown in **Figure 3**.

Both the growth factor concentration and the refreshment regime influence the growth of the cell and ECM compartments. For the case where the medium was changed every 72 h by 50%, increasing the dose of growth factor did not result in a substantial increase in cell or ECM production (**Figures 3A,B**), especially for higher doses of growth factor (10 and 100). For the case where the medium was refreshed every 48 h by 100%, ECM production was not much effected by the increase in growth factor concentrations whereas the difference in cell volume using different concentrations of growth factor was noticeable. Increasing the growth factor concentration from 10 to 100 did not result in a strong increase in cell proliferation due to the saturation effect (Equation 14). In order to find the best refreshment time and amount for the medium exchange during the culture period as well as the best concentration of the growth factor, a Multi-Objective-Optimization (MOO) problem was solved using Particle Swarm Optimization (PSO) with the goal to minimize all associated costs explained in Equation (16) and maximize the cell proliferation in the scaffold.

Multi-Objective Optimization

Figure 4 shows the Pareto front for the two objectives of our problem: cell volume and total cost.

Figure 4A shows the Pareto front for maximizing the cell number during 28 days of culture and **Figure 4B** the corresponding refreshment time, refreshment amount, and the initial concentration of growth factor (colors). All the points on the calculated Pareto front are considered as optimum points but there exists a single point which is known as the sweet spot on the Pareto front (**Figure 4A**, point M), where a good compromise between cost of experiment and scaffold filling percentage is obtained. At this point, around 80% of the scaffold is filled by the cells with the cost of 492€ which corresponds to refreshing the medium every 12 h by 65% with the growth factor concentration of 7 (**Figure 4B**, point M). Moving from this point toward the right-hand side of the Pareto front will result in slightly higher cell numbers (5% more cells), but at a considerably higher culture cost as this regime would require more frequent medium

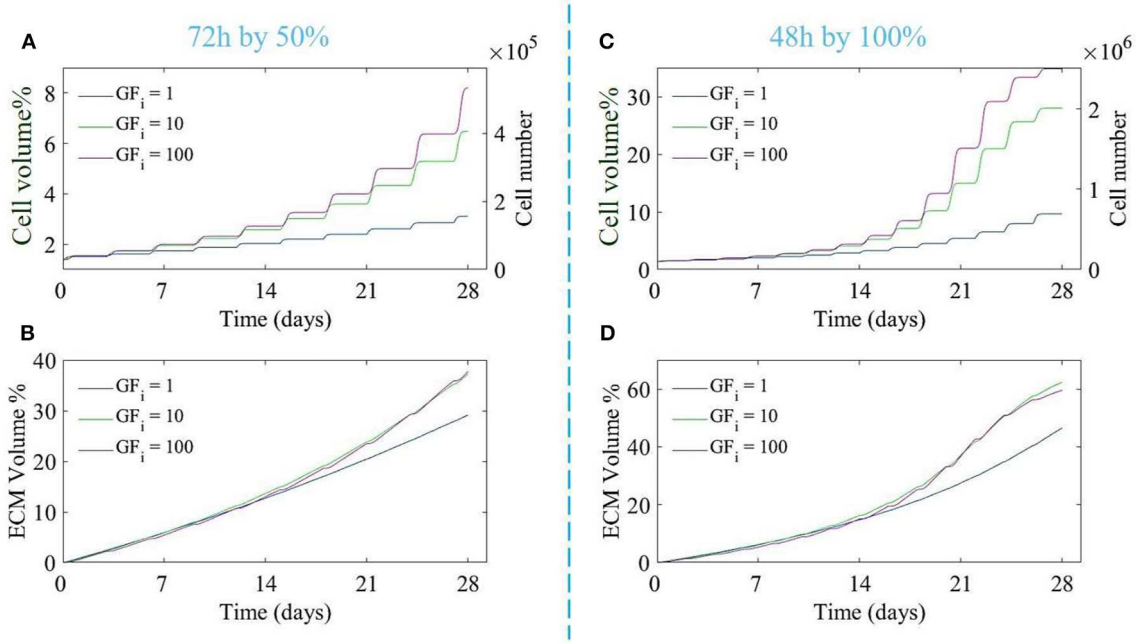

FIGURE 3 | The proliferation of cells **(A,C)** and production of ECM **(B,D)** over 28 days of culture for different initial growth factor concentrations of 1 (blue line), 10 (green line), and 100 (magenta line), and for two different medium refreshments regimes: **(A,B)** medium refreshed every 72 h by 50%, and **(C,D)** medium refreshed every 48 h by 100%. The cell growth is shown by the cell volume % on the left axis and the equivalent cell number on the right axis **(A,C)**.

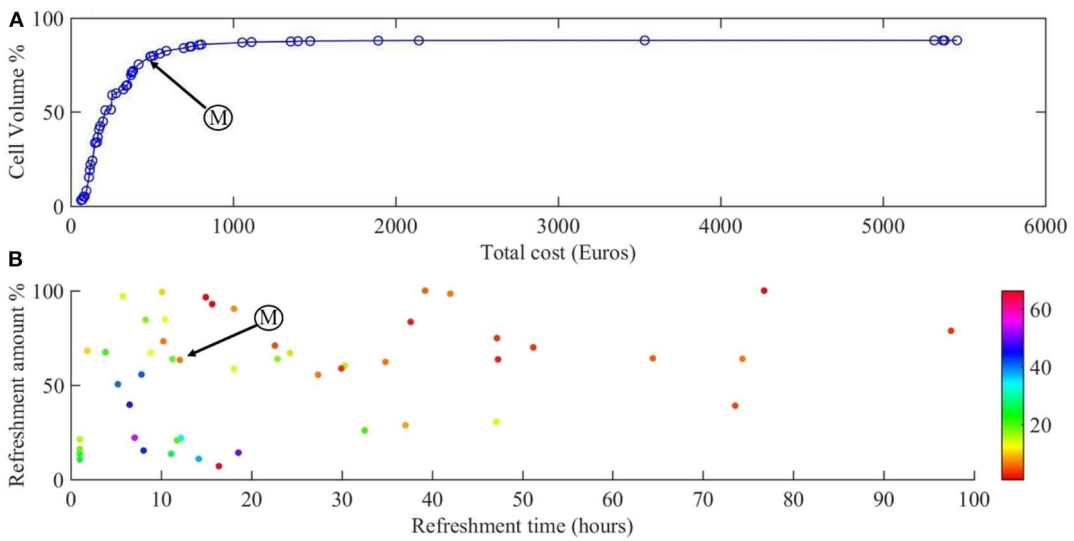

FIGURE 4 | Results of the multi-objective optimization. **(A)** Pareto front for the cell volume and total cost of the experiment. **(B)** The refreshment time and refreshment amounts corresponding to the points on the Pareto front, with growth factor concentration indicated in color. Point M is the sweet spot on the Pareto front where the best compromise between cost of experiment and scaffold filling percentage is obtained.

refreshments and higher concentrations of growth factor. Most of the expensive solutions are shown in **Figure 4B** in the bottom-left corner where the frequency of medium refreshment is very high (<15 h) and the concentration of the growth factor is the highest (light colors) compared to other solutions. For example, it is proposed that if we refresh the medium every 7 h by 40% using 50 times of the initial concentration of growth factor, the final cell volume would be around 87% with a total calculated cost of 1,411€ whereas we can reach 80% of cell volume with a total calculated cost of 500€.

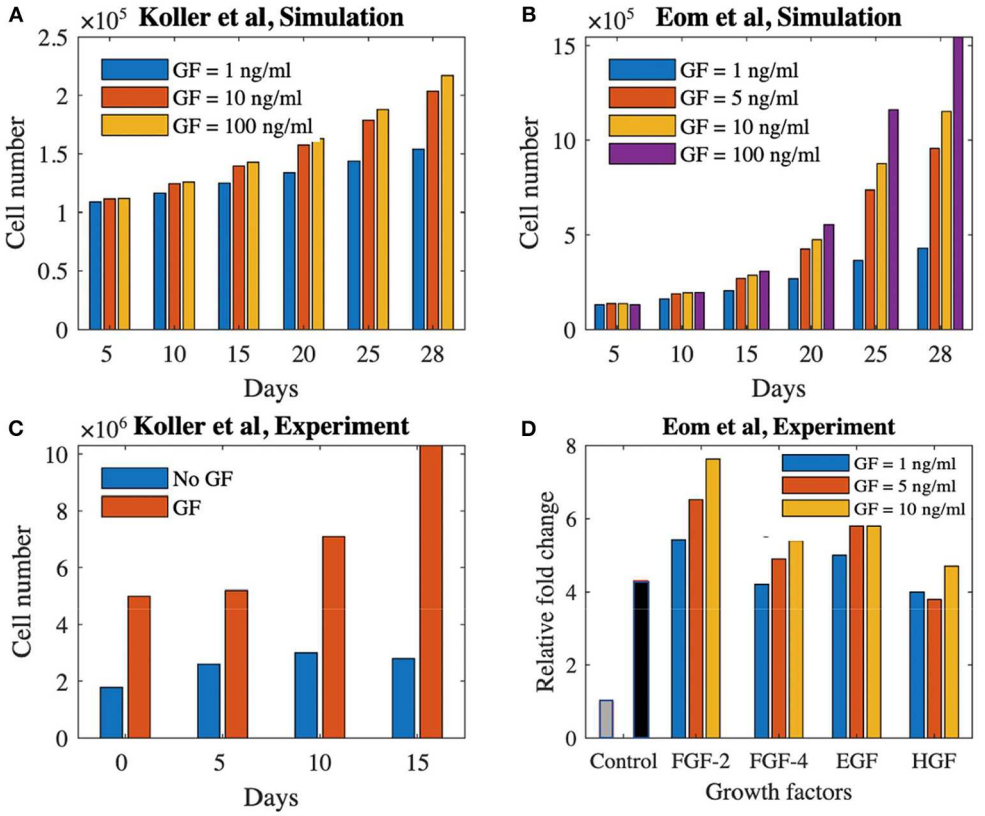

FIGURE 5 | Proliferation potential of cells treated with growth factors in static and dynamics culture set-ups. **(A)** Simulation result of cell proliferation (Koller et al., 1993) using three different concentrations of a growth factor. **(B)** Cell proliferation with and without growth factor for the experimental study of Koller et al. (1993). **(C)** Simulation result of cell proliferation (Eom et al., 2014) using four different concentrations of a generic growth factor. **(D)** Cell proliferation using four different growth factors with three different concentrations at day 3 (Eom et al., 2014). The gray and black bars shows the control group (no growth factor) at day 0 and 3, respectively. GF, growth factor.

Comparison With Other Experimental Studies

Figure 5 shows the comparison between our model predictions and the two aforementioned experimental studies (Koller et al., 1993; Eom et al., 2014). **Figure 5A** shows simulation results for the Koller et al. set-up (medium refreshment every 120 h by 50%, no flow), focusing on cell number increase over 28 days of culture using different growth factor concentrations (1, 10, and 100 ng/ml). **Figure 5B** shows the experimental data from Koller et al. (1993) where the cell proliferation is shown with and without growth factors during 15 days of culture time. Despite obvious quantitative differences (in time and amount of cells) owing to lack of model calibration, the same qualitative trends are visible.

Figure 5C shows the simulation results for the Eom et al. study where four different concentrations of growth factor (1, 5, 10, and 100 ng/ml) are used during 28 days of culture time in a 2D+ perfusion set-up (medium is refreshed every 55 h by 100%). The experimental results of Eom et al. are shown in **Figure 5D** where the relative fold change in cell proliferation for the four different growth factors up until days 3 is presented compared to static controls. Again, in absence of proper calibration, only qualitative comparison is possible, showing similar trends in cell proliferation for different growth factors doses between our simulations and the experimental data.

DISCUSSION

In this study we have further extended a previous model describing neotissue growth inside 3D scaffolds. Given that here the intended use of the bioreactor set-up and associated model was situated in the context of cell expansion, rather than the production of neotissue, separate equations have been developed to describe the cell and ECM volume. Subsequently, the effect of a generic growth factor has been incorporated in the model, allowing for a differential stimulation of cell proliferation over ECM production. Using this model, a multi-objective optimization strategy has been implemented, using PSO, with the aim of maximizing cell number while minimizing the corresponding experimental costs. The calculated Pareto front proposed multiple optimum points that we can choose from, depending on the desired cell number and its associated cost. Finally, a qualitative

comparison was made with experimental results reported in the literature, showing qualitative similarities despite obvious quantitative differences due to absence of proper calibration which reinforces the generic character the of proposed modeling platform. This study provides an *in silico* framework that, when calibrated for a particular cell type of interest, allows to identify meaningful culture regimen optima. This can provide an important support to a decision-making process that is currently mainly empirical.

The developed model in this study could be used to predict the cell number in 3D scaffolds cultured in a bioreactor set-up. One of the main issues accompanied with using 3D scaffolds for the purpose of cell expansion is the recovery of the cells from the scaffold at the end of culture, a process that is still largely an under-investigated field (Abbasalizadeh and Baharvand, 2013; dos Santos et al., 2013). In the perfusion set-up used in this study, Sonnaert et al. (2015) tested three different reagents to release the cells from the 3D culture surface and the best outcome was obtained using the collagenase reagent where 76% of the cells were recovered from the scaffold. They set the time point for cell recovery at 13 days to prevent over-confluence. This time point was chosen with respect to the metabolic activity measurements which is a frequently used measure for the amount of proliferated cells inside the scaffold. The model presented in this paper (after complete validation with dedicated experimental studies) will enable us to track cell growth during the whole culture period and therefore, to have a better estimate on the best cell recovery moment.

Notwithstanding the issues surrounding the recovery of cells from the 3D substrate, cell expansion in 3D scaffolds has many advantages compared to conventional 2D cultures. In 2D culture flasks, the cell expansion procedure becomes more labor intensive for each additional passage until the required amount of cells is reached. Whereas in the 3D expansion process, multiple scaffolds can be cultured in parallel with minimum interference from the operator. Additionally, 3D cell culture will result in a more robust and reliable cell expansion process. In Papadimitropoulos et al. (2014), the authors compared the MSC expansion in 2D flasks and 3D scaffolds and observed a similar proliferation capacity in the two methods, although a 4.3-fold higher clonogenicity capacity and a higher differentiation capacity toward all lineages was reported in 3D culture. Furthermore, in Lambrechts et al. (2016), authors compared the 2D with 3D cell culture and they observed a 2.5 lower variability on cell yield (normalized by culture surface) for the bioreactor culture compared to the flask-based expansion. Therefore, in time, 3D cell culture could replace most of the 2D cell culture. In this regard, the model developed in this study is a step forward in moving from manual tissue engineering strategies toward a more integrated and automated solution for expanding stem cells by providing an appropriate tool that predicts the cell proliferation during culture time. Furthermore, the proposed optimization strategy in this study would minimize the use of growth factors as they are one of the main sources of cost in the experiments and therefore, brings us one step closer in development of an affordable tissue engineered ATMP. In this study we have taken the current commercial price of typical growth factors used in a TE context (BMP-2). In the future it can be replaced with any other growth factor which enhances the cell proliferation over cell differentiation. One of the main limitations in this study is that due to the lack of experimental data, we were unable to fully validate the final model for the early time points as well as for the equations related to the incorporation of growth factors, which therefore remain mostly conceptual.

In terms of verification and validation of the model, all necessary verification steps have been executed and described in our previously published body of work (Guyot et al., 2015; Mehrian et al., 2018). As to validation of the model, we have used input from different studies to either qualitatively or quantitatively validate specific model predictions. As to the relative volumes of cells and ECM, we have partially validated the model with pre-existing experimental data (Papantoniou et al., 2014b), where we assumed the concentration of the growth factor at its baseline level of 1 in the culture medium. Adding growth factors during culture increases the proliferation potential (**Figures 3**, **5A,C**). The saturation of the growth factor effect that was observed in the simulations has been reported in Mishra et al. (2016), where the authors showed that increasing the growth factor dosage by 10-fold did not significantly increase the proliferation rate of the cells. Also Eom et al. (2014; **Figure 5D**) showed that increasing the growth factor dose does not increase the proliferation capacity in a linear manner. Despite qualitative correspondence, there are substantial qualitative difference in both time and cell volume between the simulations and experimental results shown in **Figure 5**. Due to lack of data regarding several aspects of the experimental set-ups used by Koller et al. (1993) and Eom et al. (2014), model calibration could not be carried out. Several set-up specific elements explain the observed quantitative differences. In the study by Koller et al. (1993) hematopoietic stem cells were used, which are quite different from the hPDCs used in our model calibration experiments. Furthermore, these hematopoietic stem cells were cultured under perfusion on a 2D+ substrate made of bone marrow stroma (layer-substrate) which is quite a different environment form the 3D scaffold and neotissue environment provided to the hPDCs in our set-up. Given these differences, it is encouraging that the model is able to qualitatively capture the growth factor influenced cell growth even for different types of cells. The cell type used in Eom et al. (2014) is more similar to our study, however the culture set-up (static, 2D culture plastic) and medium are different. This leads to a quantitative difference (temporal behavior and amount of cells) whilst showing a qualitative agreement between simulation results (**Figure 5C**) and experimental results (**Figure 5D**) especially for the FGF-2 growth factor. These results are in line with the model predictions presented in this study (**Figure 2**) where we show that there exists a saturation level (as it is implemented in the equations) for the effect of the growth factors on the proliferation of the MSC–type of cells. In order to go from these conceptual qualitative demonstrations toward tangible quantitative predictions for specific cell sources, model parameters will need to be calibrated with appropriate detailed data from dedicated experiments.

In conclusion, we have developed a computational model describing the cell and ECM production inside 3D scaffolds during perfusion bioreactor culture and we have optimized the performance of the model resulting in maximum cell number minimizing the associated costs of experiment. The developed model in this study could contribute in the trend moving from 2D cell cultures to a more promising cell expansion process in 3D environment.

DATA AVAILABILITY STATEMENT

The datasets generated for this study are available on request to the corresponding author.

ETHICS STATEMENT

The studies involving human participants were reviewed and approved by Ethics committee for Human Medical Research (KU Leuven). The patients/participants provided their written informed consent to participate in this study.

AUTHOR CONTRIBUTIONS

MM developed the computational model and wrote the manuscript. TL, IP, and LG contributed to the interpretation of the results. LG conceived and supervised the overall project. All authors commented on the manuscript.

FUNDING

This research leading to these results has received funding from the European Research Council under the European Union's Horizon 2020 research & innovation programme (ERC CoG 772418) and the Belgian National Fund for Scientific Research (FNRS) grant FRFC 2.4564.12 and T025413F. IP was funded by Fonds Wetenschappelijk Onderzoek (FWO) Fellowship (Project No. 12O7916N).

SUPPLEMENTARY MATERIAL

The Supplementary Material for this article can be found online at: https://www.frontiersin.org/articles/10.3389/fbioe.2020.00376/full#supplementary-material

REFERENCES

Abbasalizadeh, S., and Baharvand, H. (2013). Technological progress and challenges towards cGMP manufacturing of human pluripotent stem cells based therapeutic products for allogeneic and autologous cell therapies. *Biotechnol. Adv.* 31, 1600–1623. doi: 10.1016/j.biotechadv.2013.08.009

Atashi, F., Modarressi, A., and Pepper, M. S. (2015). The role of reactive oxygen species in mesenchymal stem cell adipogenic and osteogenic differentiation: a review. *Stem Cells Dev.* 24, 1150–1163. doi: 10.1089/scd.2014.0484

Bancroft, G. N., Sikavitsas, V. I., Van Den Dolder, J., Sheffield, T. L., Ambrose, C. G., Jansen, J. A., et al. (2002). Fluid flow increases mineralized matrix deposition in 3D perfusion culture of marrow stromal osteoblasts in a dose-dependent manner. *Proc. Natl. Acad. Sci. U.S.A.* 99, 12600–12605. doi: 10.1073/pnas.202296599

Callens, S. J., Uyttendaele, R. J., Fratila-Apachitei, L. E., and Zadpoor, A. A. (2019). Substrate curvature as a cue to guide spatiotemporal cell and tissue organization. *Biomaterials* 232:119739. doi: 10.1016/j.biomaterials.2019.119739

Carlier, A., van Gastel, N., Geris, L., Carmeliet, G., and Van Oosterwyck, H. (2014). Size does matter: an integrative *in vivo-in silico* approach for the treatment of critical size bone defects. *PLoS Comput. Biol.* 10:e1003888. doi: 10.1371/journal.pcbi.1003888

Chai, Y. C., Roberts, S. J., Desmet, E., Kerckhofs, G., van Gastel, N., Geris, L., et al. (2012). Mechanisms of ectopic bone formation by human osteoprogenitor cells on CaP biomaterial carriers. *Biomaterials* 33, 3127–3142. doi: 10.1016/j.biomaterials.2012.01.015

Chapman, L. A., Shipley, R. J., Whiteley, J. P., Ellis, M. J., Byrne, H. M., and Waters, S. L. (2014). Optimising cell aggregate expansion in a perfused hollow fibre bioreactor via mathematical modelling. *PLoS ONE* 9:e105813. doi: 10.1371/journal.pone.0105813

Choi, J. R., Pingguan-Murphy, B., Abas, W. A. B. W., Azmi, M. A. N., Omar, S. Z., Chua, K. H., et al. (2014). Impact of low oxygen tension on stemness, proliferation and differentiation potential of human adipose-derived stem cells. *Biochem. Biophys. Res. Commun.* 448, 218–224. doi: 10.1016/j.bbrc.2014.04.096

Datta, N., Pham, Q. P., Sharma, U., Sikavitsas, V. I., Jansen, J. A., and Mikos, A. G. (2006). *In vitro* generated extracellular matrix and fluid shear stress synergistically enhance 3D osteoblastic differentiation. *Proc. Natl. Acad. Sci. U.S.A.* 103, 2488–2493. doi: 10.1073/pnas.0505661103

De Bari, C., Dell'Accio, F., Vanlauwe, J., Eyckmans, J., Khan, I. M., Archer, C. W., et al. (2006). Mesenchymal multipotency of adult human periosteal cells demonstrated by single-cell lineage analysis. *Arthritis Rheum.* 54, 1209–1221. doi: 10.1002/art.21753

Docheva, D., Padula, D., Popov, C., Mutschler, W., Clausen-Schaumann, H., and Schieker, M. (2008). Researching into the cellular shape, volume and elasticity of mesenchymal stem cells, osteoblasts and osteosarcoma cells by atomic force microscopy. *J. Cell. Mol. Med.* 12, 537–552. doi: 10.1111/j.1582-4934.2007.00138.x

dos Santos, F. F., Andrade, P. Z., da Silva, C. L., and Cabral, J. M. (2013). Bioreactor design for clinical-grade expansion of stem cells. *Biotechnol. J.* 8, 644–654. doi: 10.1002/biot.201200373

Eom, Y. W., Oh, J. E., Lee, J. I., Baik, S. K., Rhee, K. J., Shin, H. C., et al. (2014). The role of growth factors in maintenance of stemness in bone marrow-derived mesenchymal stem cells. *Biochem. Biophys. Res. Commun.* 445, 16–22. doi: 10.1016/j.bbrc.2014.01.084

Eyckmans, J., and Luyten, F. P. (2006). Species specificity of ectopic bone formation using periosteum-derived mesenchymal progenitor cells. *Tissue Eng.* 12, 2203–2213. doi: 10.1089/ten.2006.12.2203

Grayson, W. L., Zhao, F., Izadpanah, R., Bunnell, B., and Ma, T. (2006). Effects of hypoxia on human mesenchymal stem cell expansion and plasticity in 3D constructs. *J. Cell. Physiol.* 207, 331–339. doi: 10.1002/jcp.20571

Gregory, C. A., Singh, H., Perry, A. S., and Prockop, D. J. (2003). The Wnt signaling inhibitor dickkopf-1 is required for reentry into the cell cycle of human adult stem cells from bone marrow. *J. Biol. Chem.* 278, 28067–28078. doi: 10.1074/jbc.M300373200

Guyot, Y. (2015). *A multiphysics multiscale computational framework for the simulation of perfusion bioreactor processes in bone tissue engineering* (PhD thesis), Université de Liège. Retrieved from: https://orbi.uliege.be/handle/2268/189105 (accessed January 01, 2020).

Guyot, Y., Luyten, F., Schrooten, J., Papantoniou, I., and Geris, L. (2015). A three-dimensional computational fluid dynamics model of shear stress distribution during neotissue growth in a perfusion bioreactor. *Biotechnol. Bioeng.* 112, 2591–2600. doi: 10.1002/bit.25672

Hankemeier, S., Keus, M., Zeichen, J., Jagodzinski, M., Barkhausen, T., Bosch, U., et al. (2005). Modulation of proliferation and differentiation of human bone marrow stromal cells by fibroblast growth factor 2: potential implications

for tissue engineering of tendons and ligaments. *Tissue Eng.* 11, 41–49. doi: 10.1089/ten.2005.11.41

Haycock, J. W. (2011). 3D cell culture: a review of current approaches and techniques. *Methods Mol. Biol.* 695, 1–15. doi: 10.1007/978-1-60761-984-0_1

Horn J. (1997). "Multicriterion decision making," in *Handbook of Evolutionary Computation*, Vol. 1, eds T. Bäck, D. Fogel, and Z. Michalewicz (IOP Publishing Ltd.; Oxford University Press), F1.9:1–F1.9:15.

Kato, H., Taguchi, Y., Tominaga, K., Kimura, D., Yamawaki, I., Noguchi, M., et al. (2016). High glucose concentrations suppress the proliferation of human periodontal ligament stem cells and their differentiation into osteoblasts. *J. Periodontol.* 87, e44–e51. doi: 10.1902/jop.2015.150474

Kennedy J. (2006). "Swarm intelligence," in *Handbook of Nature-Inspired and Innovative Computing*, ed A. Y. Zomaya (Boston, MA: Springer).

Kennedy, J., and Eberhart, R. (1995). "Particle swarm optimization," *Paper Presented at the Proceedings of IEEE International Conference on Neural Networks* (Perth, WA, Australia), 4.

Koller, M. R., Bender, J. G., Miller, W. M., and Papoutsakis, E. T. (1993). Expansion of primitive human hematopoietic progenitors in a perfusion bioreactor system with IL-3, IL-6, and stem cell factor. *Biotechnology* 11, 358–363. doi: 10.1038/nbt0393-358

Lambrechts, T., Papantoniou, I., Rice, B., Schrooten, J., Luyten, F. P., and Aerts, J.-M. (2016). Large-scale progenitor cell expansion for multiple donors in a monitored hollow fibre bioreactor. *Cytotherapy* 18, 1219–1233. doi: 10.1016/j.jcyt.2016.05.013

Lambrechts, T., Papantoniou, I., Sonnaert, M., Schrooten, J., and Aerts, J. M. (2014). Model-based cell number quantification using online single-oxygen sensor data for tissue engineering perfusion bioreactors. *Biotechnol. Bioeng.* 111, 1982–1992. doi: 10.1002/bit.25274

Lemon, G., Waters, S. L., Rose, F. R., and King, J. R. (2007). Mathematical modelling of human mesenchymal stem cell proliferation and differentiation inside artificial porous scaffolds. *J. Theor. Biol.* 249, 543–553. doi: 10.1016/j.jtbi.2007.08.015

Li, J., and Pei, M. (2010). Optimization of an *in vitro* three-dimensional microenvironment to reprogram synovium-derived stem cells for cartilage tissue engineering. *Tissue Eng. Part A* 17, 703–712. doi: 10.1089/ten.tea.2010.0339

Martin, I., Wendt, D., and Heberer, M. (2004). The role of bioreactors in tissue engineering. *Trends Biotechnol.* 22, 80–86. doi: 10.1016/j.tibtech.2003.12.001

Matsiko, A., Gleeson, J. P., and O'Brien, F. J. (2014). Scaffold mean pore size influences mesenchymal stem cell chondrogenic differentiation and matrix deposition. *Tissue Eng. Part A* 21, 486–497. doi: 10.1089/ten.tea.2013.0545

McCoy, R. J., and O'Brien, F. J. (2010). Influence of shear stress in perfusion bioreactor cultures for the development of three-dimensional bone tissue constructs: a review. *Tissue Eng Part B Rev.* 16, 587–601. doi: 10.1089/ten.teb.2010.0370

Mehrian, M., and Geris, L. (2020). Optimizing neotissue growth inside perfusion bioreactors with respect to culture and labor cost: a multi-objective optimization study using evolutionary algorithms. *Comput. Methods Biomechan. Biomed. Eng.* 23, 285–294. doi: 10.1080/10255842.2020.1719081

Mehrian, M., Guyot, Y., Papantoniou, I., Olofsson, S., Sonnaert, M., Misener, R., et al. (2018). Maximizing neotissue growth kinetics in a perfusion bioreactor: an *in silico* strategy using model reduction and Bayesian optimization. *Biotechnol. Bioeng.* 115, 617–629. doi: 10.1002/bit.26500

Misener, R., Gar,í, M. F., Rende, M., Velliou, E., Panoskaltsis, N., Pistikopoulos, E. N., et al. (2014). Global superstructure optimisation of red blood cell production in a parallelised hollow fibre bioreactor. *Comput. Chem. Eng.* 71, 532–553. doi: 10.1016/j.compchemeng.2014.10.004

Mishra, R., Sefcik, R. S., Bishop, T. J., Montelone, S. M., Crouser, N., Welter, J. F., et al. (2016). Growth factor dose tuning for bone progenitor cell proliferation and differentiation on resorbable poly (propylene fumarate) scaffolds. *Tissue Eng. Part C Methods* 22, 904–913. doi: 10.1089/ten.tec.2016.0094

Nava, M. M., Draghi, L., Giordano, C., and Pietrabissa, R. (2016). The effect of scaffold pore size in cartilage tissue engineering. *J. Appl. Biomater. Funct. Mater.* 14, e223–e229. doi: 10.5301/jabfm.5000302

Oh, S. H., Kim, T. H., Im, G. I., and Lee, J. H. (2010). Investigation of pore size effect on chondrogenic differentiation of adipose stem cells using a pore size gradient scaffold. *Biomacromolecules* 11, 1948–1955. doi: 10.1021/bm100199m

Papadimitropoulos, A., Piccinini, E., Brachat, S., Braccini, A., Wendt, D., Barbero, A., et al. (2014). Expansion of human mesenchymal stromal cells from fresh bone marrow in a 3D scaffold-based system under direct perfusion. *PLoS ONE* 9:e102359. doi: 10.1371/journal.pone.0102359

Papantoniou, I., Guyot, Y., Sonnaert, M., Kerckhofs, G., Luyten, F. P., Geris, L., et al. (2014a). Spatial optimization in perfusion bioreactors improves bone tissue-engineered construct quality attributes. *Biotechnol. Bioeng.* 111, 2560–2570. doi: 10.1002/bit.25303

Papantoniou, I., Sonnaert, M., Geris, L., Luyten, F. P., Schrooten, J., and Kerckhofs, G. (2014b). Three-dimensional characterization of tissue-engineered constructs by contrast-enhanced nanofocus computed tomography. *Tissue Eng. Part C Methods* 20, 177–187. doi: 10.1089/ten.tec.2013.0041

Pei, M., He, F., and Kish, V. L. (2011). Expansion on extracellular matrix deposited by human bone marrow stromal cells facilitates stem cell proliferation and tissue-specific lineage potential. *Tissue Eng. Part A* 17, 3067–3076. doi: 10.1089/ten.tea.2011.0158

Roberts, I., Baila, S., Rice, R. B., Janssens, M. E., Nguyen, K., Moens, N., et al. (2012). Scale-up of human embryonic stem cell culture using a hollow fibre bioreactor. *Biotechnol. Lett.* 34, 2307–2315. doi: 10.1007/s10529-012-1033-1

Rodrigues, M., Griffith, L. G., and Wells, A. (2010). Growth factor regulation of proliferation and survival of multipotential stromal cells. *Stem Cell Res. Ther.* 1:32. doi: 10.1186/scrt32

Salter, E., Goh, B., Hung, B., Hutton, D., Ghone, N., and Grayson, W. L. (2011). Bone tissue engineering bioreactors: a role in the clinic? *Tissue Eng. Part B Rev.* 18, 62–75. doi: 10.1089/ten.teb.2011.0209

Schneider, C. K., Salmikangas, P., Jilma, B., Flamion, B., Todorova, L. R., Paphitou, A., et al. (2010). Challenges with advanced therapy medicinal products and how to meet them. *Nat. Rev. Drug Disc.* 9, 195–201. doi: 10.1038/nrd3052

Shakhawath Hossain, M., Bergstrom, D., and Chen, X. (2015). A mathematical model and computational framework for three-dimensional chondrocyte cell growth in a porous tissue scaffold placed inside a bi-directional flow perfusion bioreactor. *Biotechnol. Bioeng.* 112, 2601–2610. doi: 10.1002/bit.25678

Singh, S. (2014). *Effects of different ph and oxygen levels on proliferation and chondrogenic differentiation of human mesenchymal stem cells cultured in hydrogels* (Master's thesis). Chalmers University of Technology, Gothenburg, Sweden.

Sonnaert, M., Luyten, F. P., Schrooten, J., and Papantoniou, I. (2015). Bioreactor-based online recovery of human progenitor cells with uncompromised regenerative potential: a bone tissue engineering perspective. *PLoS ONE* 10:e0136875. doi: 10.1371/journal.pone.0136875

Sonnaert, M., Papantoniou, I., Bloemen, V., Kerckhofs, G., Luyten, F., and Schrooten, J. (2017). Human periosteal-derived cell expansion in a perfusion bioreactor system: proliferation, differentiation and extracellular matrix formation. *J. Tissue Eng. Regen. Med.* 11, 519–530. doi: 10.1002/term.1951

Stiehler, M., Bünger, C., Baatrup, A., Lind, M., Kassem, M., and Mygind, T. (2009). Effect of dynamic 3-D culture on proliferation, distribution, and osteogenic differentiation of human mesenchymal stem cells. *J. Biomed. Mat. Res. Part A* 89, 96–107. doi: 10.1002/jbm.a.31967

Van der Stok, J., Van der Jagt, O. P., Amin Yavari, S., De Haas, M. F., Waarsing, J. H., Jahr, H., et al. (2013). Selective laser melting-produced porous titanium scaffolds regenerate bone in critical size cortical bone defects. *J. Orthop. Res.* 31, 792–799. doi: 10.1002/jor.22293

Wuertz, K., Godburn, K., and Iatridis, J. C. (2009). MSC response to pH levels found in degenerating intervertebral discs. *Biochem. Biophys. Res. Commun.* 379, 824–829. doi: 10.1016/j.bbrc.2008.12.145

Zhou, X., Holsbeeks, I., Impens, S., Sonnaert, M., Bloemen, V., Luyten, F., et al. (2013). Noninvasive real-time monitoring by AlamarBlue® during *in vitro* culture of three-dimensional tissue-engineered bone constructs. *Tissue Engineering Part C Methods* 19, 720–729. doi: 10.1089/ten.tec.2012.0601

Conflict of Interest: The authors declare that the research was conducted in the absence of any commercial or financial relationships that could be construed as a potential conflict of interest.

frontiers in Bioengineering and Biotechnology

ORIGINAL RESEARCH
published: 30 April 2020
doi: 10.3389/fbioe.2020.00400

Tripolyphosphate-Crosslinked Chitosan/Gelatin Biocomposite Ink for 3D Printing of Uniaxial Scaffolds

*Tiziana Fischetti[1,2], Nehar Celikkin[1], Nicola Contessi Negrini[2,3], Silvia Farè[2,3] and Wojciech Swieszkowski[1]**

[1] Faculty of Materials Science and Engineering, Warsaw University of Technology, Warsaw, Poland, [2] Department of Chemistry, Materials and Chemical Engineering "G. Natta", Politecnico di Milano, Milan, Italy, [3] INSTM, National Consortium of Materials Science and Technology, Local Unit Politecnico di Milano, Milan, Italy

OPEN ACCESS

Edited by:
Maria Chatzinikolaidou, University of Crete, Greece

Reviewed by:
Julietta V. Rau, Italian National Research Council, Italy
Shinn-Jyh Ding, Chung Shan Medical University, Taiwan

***Correspondence:**
Wojciech Swieszkowski
wojciech.swieszkowski@pw.edu.pl

Specialty section:
This article was submitted to Tissue Engineering and Regenerative Medicine, a section of the journal Frontiers in Bioengineering and Biotechnology

Received: *17 January 2020*
Accepted: *08 April 2020*
Published: *30 April 2020*

Citation:
Fischetti T, Celikkin N, Contessi Negrini N, Farè S and Swieszkowski W (2020) Tripolyphosphate-Crosslinked Chitosan/Gelatin Biocomposite Ink for 3D Printing of Uniaxial Scaffolds. Front. Bioeng. Biotechnol. 8:400. doi: 10.3389/fbioe.2020.00400

Chitosan is a natural polymer widely investigated and used due to its antibacterial activity, mucoadhesive, analgesic, and hemostatic properties. Its biocompatibility makes chitosan a favorable candidate for different applications in tissue engineering (TE), such as skin, bone, and cartilage tissue regeneration. Despite promising results obtained with chitosan 3D scaffolds, significant challenges persist in fabricating hydrogel structures with ordered architectures and biological properties to mimic native tissues. In this work, chitosan has been investigated aiming at designing and fabricating uniaxial scaffolds which can be proposed for the regeneration of anisotropic tissues (i.e., skin, skeletal muscle, myocardium) by 3D printing technology. Chitosan was blended with gelatin to form a polyelectrolyte complex in two different ratios, to improve printability and shape retention. After the optimization of the printing process parameters, different crosslinking conditions were investigated, and the 3D printed samples were characterized. Tripolyphosphate (TPP) was used as crosslinker for chitosan-based scaffolds. For the optimization of the printing temperature, the sol-gel temperature of the chitosan-gelatin blend was determined by rheological measurements and extrusion temperature was set to 20°C (i.e., below sol-gel temperature). The shape fidelity and surface morphology of the 3D printed scaffolds after crosslinking was dependent on crosslinking conditions. Interestingly, mechanical properties of the scaffolds were also significantly affected by the crosslinking conditions, nonetheless the stability of the scaffolds was strongly determined by the content of gelatin in the blend. Lastly, *in vitro* cytocompatibility test was performed to evaluate the interactions between L929 cells and the 3D printed samples. 2% w/v chitosan and 4% w/v gelatin hydrogel scaffolds crosslinked with 10% TPP, 30 min at 4°C following 30 min at 37°C have shown cytocompatible and stable characteristics, compared to all other tested conditions, showing suitable properties for the regeneration of anisotropic tissues.

Keywords: chitosan, gelatin, 3D printing, ionic crosslinking, uniaxial tissue engineering, scaffolds

INTRODUCTION

Chitosan is a natural polysaccharide derived from the partial deacetylation of chitin, a polymer present in the exoskeleton of crustaceans, insects and fungi (Elieh-Ali-Komi and Hamblin, 2016). The chitosan chemical structure is constituted by D-glucosamine and N-acetyl-D-glucosamine linked by β-(1-4) glycosidic bonds, in which the glucosamine is the main repeating unit. Amino groups present in D-glucosamine can be protonated in acidic aqueous solutions (pH < 6), bringing to the formation of a polycationic polymer (Croisier and Jérôme, 2013). For its polycationic behavior, chitosan can form ionic complexes with different anionic species, both deriving from natural or synthetic sources, as lipids, proteins, DNA, polystyrenesulphate, oleate and dextran sulfate (Rinaudo, 2006; Chen et al., 2007; Kim et al., 2008; Schwarz et al., 2012; Ng et al., 2016). Chitosan exhibits other intrinsic properties thanks to its polycationic nature, such as antibacterial (Ong et al., 2008) and antifungal activity (Aranaz et al., 2009), and mucoadhesive (Sogias et al., 2008), analgesic (Aranaz et al., 2009) and hemostatic properties (Ong et al., 2008). Chitosan is abundantly used in biomaterials science, food industry, biomedical, and pharmaceutical applications (Ravi Kumar, 2000; Rinaudo, 2006) and it offers the advantage of being easily processable into gels (Huang et al., 2011), membranes (Lin et al., 2013), nanofibers (Jayakumar et al., 2010), beads (Buranachai et al., 2010), nanoparticles (Moreira et al., 2016; Thandapani et al., 2017), scaffolds (Jana et al., 2013; Rodríguez-Vázquez et al., 2015), and porous foams (Ji et al., 2011).

Anisotropic tissues enable highly elaborate functions of living organisms (Haque et al., 2010). When these tissues are impaired by pathological conditions or trauma, their regeneration is challenging and it has been poorly investigated. Tissue engineering (TE) scaffolds for anisotropic tissues have to satisfy the requirement of creating regional and directional anisotropy in three-dimensional space. To obtain this, the design and obtainment of patterns able to induce cell orientation along one preferential direction is needed, together with the enhancement of the mechanical properties in this direction (De France et al., 2017). The most used techniques to generate anisotropy *in vitro* are the use of mechanical force (Haque et al., 2010; Nardinocchi and Teresi, 2016), directional freeze-casting (Chen et al., 2012; Bai et al., 2013) and micro-patterning (Li et al., 2014). In recent years, 3D printing technology has been also considered as valid alternative to fabricate anisotropic patterns for TE. This technique exploits the use of a 3D CAD which is later converted into a code, and manufacturing of a 3D construct with desired architecture is then obtained (Murphy and Atala, 2014). The main advantages of 3D printing are the automation and reproducibility of the process, with the precise deposition control of the scaffold structure based on the 3D model. Additionally, the possibility to obtain 3D printed physical constructs based on clinical images (e.g., CT, MRI) allows obtaining patient specific scaffolds, which makes 3D printing particularly useful for TE.

Despite 3D printing technology has been extensively investigated for TE applications, materials choice and optimization of printing parameters for defined micro-architectures are still compelling (Chia and Wu, 2015). Chitosan-based scaffolds for skin (Ng et al., 2016), bone (Demirtaş et al., 2017), and cartilage regeneration (Ye et al., 2014) fulfill the needed requirements in terms of cell viability (Elviri et al., 2017; Pollot et al., 2017); however, chitosan possesses poor printability and weak mechanical properties (Ng et al., 2016). For this reason, 3D printing of pristine chitosan is extremely challenging, and further modifications are required to increase the printability of chitosan-based scaffolds (Ng et al., 2016; Demirtaş et al., 2017). For example, gelatin can be used to improve the printability and shape fidelity of the printed construct (Golden and Tien, 2007; Neal et al., 2014; Hinton et al., 2015; Ng et al., 2016).

In this study, gelatin is blended with chitosan to improve the printability and shape fidelity of the printed constructs. The rheological characteristics of chitosan – gelatin blend with different chitosan/gelatin ratios are investigated. The printing process in terms of printing parameters (i.e., temperature, extrusion pressure, deposition speed) is optimized. Different crosslinking conditions are tested for the 3D printed constructs (0–180° fiber configuration), characterized through the coherence of printed fiber diameter to CAD design, mechanical and stability properties. The suitability of the scaffolds for anisotropic TE is evaluated by a preliminary *in vitro* cytocompatibility test. Through the abovementioned characterizations and evaluations, here, we propose the use of chitosan – gelatin blends as biomaterial ink and tripolyphosphate (TPP) as crosslinker to print uniaxial 3D scaffolds, for the first time.

MATERIALS AND METHODS

Materials

Chitosan (low molecular, 50–190 kDa, 75–85% deacetylation), gelatin (bovine skin, type B), sodium tripolyphosphate (TPP), and phosphate buffered saline (PBS) were purchased from Sigma Aldrich.

Preparation of CHIGEL Hydrogel Blends

Chitosan-gelatin (CHIGEL) hydrogel blends were prepared in two different chitosan:gelatin ratios (1:2 and 1:3 w:w), identified in the following as 1CHI2GEL and 1CHI3GEL. For their preparation, 3% (w/v) chitosan was dissolved in 2% (v/v) acetic acid under magnetic stirring for 3 h at room temperature. Gelatin, 12% (w/v) and 18% (w/v), was dissolved in PBS and stirred at 40°C. Before forming the chitosan-gelatin blend, the pH of 3% chitosan solution was increased to 4.7 by addition of 0.5 M NaOH; gelatin, at this pH value, starts to form the polyelectrolyte complex between the negative charges of gelatin and the positive charges of chitosan. Consequently, gelatin was added to chitosan solution, and the pH of the chitosan-gelatin blend was adjusted to 6.5 by addition of NaOH. Indeed, at this pH (i.e., 6.5), chitosan amino groups are deprotonated and form insoluble weak chitosan polymer.

Rheological Characterization

The rheological properties of the hydrogel blends were evaluated using ARES rheometer (TA Instruments, New Castle, DE, United States) with cone-plate geometry (diameter 50 mm, cone angle 0.1 rad), setting the gap at 50 μm. An oscillatory strain sweep test was firstly performed, with strain range 0–10% and frequency 1 Hz. This test was performed to study the values of the strain amplitude within the linear viscoelastic region (LVR); the shear strain value was chosen equal to 5%. To evaluate the sol-gel transition temperature, storage modulus (G') and loss modulus (G") of 1CHI2GEL and 1CHI3GEL were measured in the temperature range 4–40°C, with an increasing temperature ramp of 2°C/min. The complex viscosity (η*) of 1CHI2GEL and 1CHI3GEL was investigated for shear rates ranging from 0.1 to 100 s^{-1} at 20°C (i.e., optimized printing temperature).

Optimization of 3D Printing Process and Crosslinking of CHIGEL Scaffolds

A 3D Bioplotter (EnvisionTEC GmbH, Germany) was used to fabricate 3D printed scaffolds using an extrusion-based 3D printing technique. 3D printed scaffolds were designed to have dimensions corresponding to 12 mm × 10 mm × 2 mm. The scaffolds were printed with a 23G (inner diameter, ID = 330 μm) needle. Printing parameters were evaluated in the range 1–4 bar for the extrusion pressure and 2–30 mm/s for the deposition speed. After the optimization process, the parameters were set to 2.5 bar for the extrusion pressure and to 10 mm/s for the deposition speed. The obtained 3D printed scaffold was constituted by five layers, each formed by parallel superimposed fibers. The fiber orientation in adjacent layers was set to 0–180°, to ease the mimic of the anisotropic tissue architecture in longitudinal direction. Distance between the fibers was set to 1 mm, as for lower values fibers joined between each other, due to partial fiber collapse. The value of layer thickness (LT) was set at 250 μm, as from literature the ideal value of LT is the 80% of the needle size dimension, to favor the surface contact between consecutive deposited layers (Mozetic et al., 2017). The temperature during the printing process, previously assessed by rheological characterization, was set at 20°C, to have the CHIGEL in a gel state. The temperature of the base plate was set at 4°C, to guarantee the maintenance of the shape during the printing process, due to the gelation of gelatin at low temperatures (i.e., $T < T_{sol-gel}$).

After the printing process, the printed scaffolds were immersed in 10% w/v TPP crosslinker. The overall crosslinking time of the 3D printed structure was set to 60 min, due to chitosan slow gelation rate with TPP (Gan et al., 2005). The following three different crosslinking conditions were tested: (i) 3D printed structure kept at 4°C for 60 min with TPP, (ii) 3D printed structure kept at 4°C for 30 min and moved to 37°C for the remaining 30 min, or (iii) 3D printed structure kept at 4°C for 10 min and moved to 37°C for the remaining 50 min. The two selected temperatures, 4 and 37°C, in which CHIGEL blend exhibits a gel and solution state, respectively, were chosen to evaluate the thermo-sensitive behavior of the blends and to detect any differences within the considered conditions, for different exposition time. In all these cases, after 60 min of TPP crosslinking, TPP solution was removed and replaced with PBS, to remove possible unreacted residuals. The identification acronyms for the considered chitosan/gelatin structures are summarized for each ratio and crosslinking condition in **Table 1**.

Scanning Electron Microscopy (SEM) Observation

The morphology of the 3D printed structures for each crosslinking condition and ratio was observed by SEM (**Table 1**). Briefly, the samples were dehydrated in a graded ethanol series concentration (50, 70, 80, 90, 100%, 10 min for each) and then with hexamethyldisalazane (HDMS). To prepare samples for SEM observation, scaffolds were sputtered with 7 nm gold and the morphology was observed with proX desktop (Phenom) SEM at 10 kV, with different magnifications (285X, 1850X, 4600X).

Fourier Transform Infrared Spectroscopy (FTIR)

Fourier transform infrared spectroscopy analysis was performed on pristine chitosan and gelatin powders, and CHIGEL blends (**Table 1**) constituting the 3D printed structures. FTIR analysis was performed to detect the possible interactions between chitosan and gelatin in the considered blends, and to attain the differences among the crosslinking conditions and ratio (**Table 1**). Analyses were performed with Q5000 FTIR (TA Instruments, New Castle, DE, United States); the spectra were recorded in absorbance mode in the 4000–400 cm^{-1} range, with a 4 cm^{-1} resolution and 128 scans.

Mechanical Characterization

Compression mechanical tests were performed on the 3D printed scaffolds for each ratio and crosslinking condition (**Table 1**) using a dynamic mechanical analyzer (DMA Q800, TA Instrument, New Castle, DE, United States) in unconfined compression mode to test the suitability of the obtained structures in mimicking the mechanical properties of anisotropic tissues. Samples ($n = 3$, 12 mm × 10 mm × 2 mm), were incubated at 37°C in 2 ml of 0.02% w/v sodium azide solution for 48 h, and then tested. Tests were performed in strain-controlled mode at 37°C, after a 5 min isotherm at 37°C, by applying a compressive strain rate of 2.5% min^{-1} down to −30% strain (0.001 N preload force). Then, the compression force was removed, and an unload phase was performed at 5% min^{-1}. The following mechanical parameters were evaluated from the obtained stress-strain curves: elastic modulus (calculated as the slope of the curve in the 0–5% range, $E_{0-5\%}$), stiffness at maximum load (calculated as the slope of the curve in the 25–30% range, $E_{25-30\%}$), maximum stress (calculated as the stress corresponding to 30% strain, σ_{max}), residual strain (calculated as the strain corresponding to null strain at the end of the unload phase ε_{res}), and hysteresis area (calculated as the area between the loading and unloading curves, H) (Negrini et al., 2020).

TABLE 1 | Initial and final concentrations of chitosan (*) and gelatin (**) used to form 1:2 and 1:3 Chitosan: Gelatin blend ratios (identified as 1CHI2GEL and 1CHI3GEL, respectively).

	Initial concentrations	Final concentrations	Identification name	Crosslinking condition		
				60_0	30_30	10_50
*Chitosan-**Gelatin	*3%w/v-**12%w/v	*2%w/v-**4%w/v	1_2 Chito_Gel	1CHI2GEL 60_0	1CHI2GEL 30_30	1CHI2GEL 10_50
	*3%w/v-**18%w/v	*2%w/v-**6%w/v	1_3 Chito_Gel	1CHI3GEL 60_0	1CHI3GEL 30_30	1CHI3GEL 10_50

In the last column on the right, the coding system declined for each ratio used (1CHI2GEL, 1CHI3GEL) and crosslinking condition (60_0,30_30,10_50) is reported.

Shape Fidelity Characterization

The shape fidelity of the 3D printed samples was investigated for each ratio (1CHI2GEL, 1CHI3GEL) and crosslinking condition (60_0, 30_30, 10_50). Measurements were acquired immediately after the crosslinking time-period, considering the dimensions of the printed samples (i.e., length, width, height), fiber diameter, and distance between fibers. For each ratio and crosslinking condition considered in this study, the measurements of samples (n = 4) were obtained. As regarding the fiber dimensions, the diameter of each fiber for each condition was measured at seven different points and averaged. The same was performed for the measurements of the distance between the fibers, defined as the distance between the axes of two adjacent fibers (**Supplementary Figure S1**). The dimensions were acquired with an optical microscope (Leica TCS SP8). Quantitative measurements for the different conditions were compared to the theoretical ones, using the equation (Eq. 1):

$$\text{Accurancy}\,[\%] \;=\; \frac{100}{\mathrm{n}} * \sum_{1}^{\mathrm{n}} \left(1 - \frac{|\mathrm{dr} - \mathrm{ds}|}{\mathrm{ds}}\right) \qquad (1)$$

where d_r is the measured sample dimension, d_s the theoretical dimension (i.e., d_s = 12 mm, 10 mm, 1,25 mm, 330 μm, and 1 mm for length, width, height, needle size, and distance between fibers, respectively), n is the number of the considered samples ($n = 4 \times 7$ different points).

Stability Test

Stability test was performed on the samples of each ratio and each evaluated crosslinking condition to evaluate the residual weight (RW%) of samples after immersion in water at 37°C. Samples (n = 5 for each condition) were weighted in wet condition, i.e., immediately after the crosslinking (W_0). Consequently, samples immersed in 2 ml of 0.02% w/v sodium azide in distilled water at 37°C. At established time points (t = 1, 3, 24, 48 h, 3, 7, 14, 21 days) samples were removed from the solution, gently swabbed with tissue paper and weighted (W_t). Residual weight (RW%) was calculated with the following equation (Eq. 2):

$$\mathrm{RW}\% \;=\; \frac{\mathrm{W_t}}{\mathrm{W_0}} \times 100 \qquad (2)$$

In vitro Cytocompatibility of the CHIGEL Scaffolds

Preliminary *in vitro* cytocompatibility test was performed using L929 fibroblasts cell line to test cytocompatibility of the materials constituting the 3D structures and the different crosslinking conditions performed. After the physico-chemical and mechanical characterization, only 1CHI2GEL ratio and 30_30, 10_50 crosslinking conditions were considered. To prevent any contamination, gelatin and chitosan powders were sterilized by UV light (λ = 100–280 nm) for 30 min. The 3D structures (12 mm × 10 mm × 2 mm) were printed in sterile condition, then washed in sterile PBS overnight to remove potential residues and put in contact with L929 cells (from mouse C3H/An, ECACC, United Kingdom). For each tested condition, n = 4 replicates were considered. Positive control was constituted by L929 cells cultured in complete DMEM and 0.1% Triton X100 (i.e., dead cells), and negative control was constituted by L929 cells cultured in complete DMEM (i.e., live cells), representing the worst and the optimal cells viability condition, respectively. 3D printed CHIGEL scaffolds were seeded with 3×10^4 cells/well, and cultured in Dulbecco's Modified Eagle Medium (DMEM, Gibco, Grand Island, MA, United States) supplemented with 10% FBS (EuroClone S.p.A., Pero, Italy), and 100 μg/mL Penicillin-Streptomycin (10,000 U/mL, Gibco) at 37°C, 5% CO_2, up to 72 h. Subsequently, 24 and 72 h after seeding, CellTiter Cell Proliferation Assay (MTS, Promega, Fitchburg, WI, United States) was performed to evaluate the metabolic activity (FLUOstar Omega UV/Vis spectrometer, BMG LabTech, Ortenberg, Germany) of fibroblasts on the 3D printed CHIGEL hydrogels. Metabolic activity was evaluated by UV spectrophotometer (FLUOstar Omega), considering the absorbance at λ = 490 nm. Percentage cell viability was calculated by using the following equation (Eq. 3):

$$\text{Cell Viability}\,(\%) \;=\; \frac{\mathrm{A_S} - \mathrm{A_P}}{\mathrm{A_N} - \mathrm{A_P}} * 100 \qquad (3)$$

where A_S,A_P, and A_N are the sample absorbance, the positive control absorbance, and the negative control absorbance, respectively. Cytocompatibility results were reported in terms of cell viability (%) and compared to the negative control (i.e., cells in complete DMEM seeded on tissue culture plastic).

Statistical Analysis

Results are expressed as mean ± standard deviation. One-way ANOVA with Tukey's multiple comparison tests were

performed using GraphPad Prism software to investigate statistical difference between data populations. A p-value (p) < 0.05 was considered as statistically significant.

RESULTS AND DISCUSSION

Rheological Characterization and Printing Temperature Optimization

The rheological characterization for 1CHI2GEL, 1CHI3GEL was performed in the range 4–40°C, to determine the sol-gel transition temperature ($T_{sol-gel}$) of the two blends. $T_{sol-gel}$ was detected at 25.5 ± 1.0°C for 1CHI2GEL (4% w/v gelatin, **Figure 1A**), and at 26.4 ± 0.9°C for 1CHI3GEL, (6% w/v gelatin, **Figure 1B**). The results showed that the chitosan–gelatin blends were in a gel state below the gel point temperatures, and in a liquid-like state above them.

To optimize printing temperature, extrusion at different temperatures (T = 18, 20, 23°C), all below the $T_{sol-gel}$ transition (T = 25.5 and 26.4°C), were evaluated (**Figure 1C**) to ensure the shape fidelity when gelatin is in the gel state. For both 1CHI2GEL and 1CHI3GEL blends at 18°C, the extrusion was not smooth; in fact, irregular fragments were obtained. At 20°C, the extrusion was continuous, and it was possible to obtain smooth fibers. On the contrary, at 23°C, temperature closer to the $T_{sol-gel}$, the gel was weak and not able to maintain a good shape fidelity. Thus, 20°C was selected as the temperature to extrude the gels during the printing process, for both the CHIGEL ratios considered in the study. At this temperature, the complex viscosity η* of 1CHI2GEL and 1CHI3GEL, in function of the shear rate (**Figure 1D**), was investigated. For both the blends (1CHI2GEL and 1CHI3GEL), a slightly increase in η* was observed up to shear rate values equal to 0.2 s^{-1}; in fact, the gels had to overcome the yield stress point at this value. Then, a continuous decrease in viscosity for both the ratios was detected, until 1 Pa·s at 100 s^{-1}. The decrease in viscosity with increasing shear rate (i.e., shear thinning response) is the typical behavior of non-Newtonian fluids. Hydrogels showing shear thinning behavior are particularly suitable in extrusion-based 3D printing systems (Costantini et al., 2016; Ng et al., 2016); indeed, they are characterized by a decrease in viscosity under applied shear, as it occurs during the extrusion of the gel through the needle in the 3D printing process.

Optimization of the Printing Process

After the rheological characterization and the selection of the printing temperature (T = 20°C), the optimization of the printing parameters (i.e., extrusion pressure and deposition speed) was attained. The optimal combination of these parameters was selected as the one allowing for the continuous extrusion of structurally stable 3D structures. First, the extrusion pressure was optimized (range 1–4 bar). In particular, 1, 2.5, and 4 bar pressure values were considered (**Figure 2A**). P = 1 bar was not sufficient to extrude the hydrogel through the needle; P = 2.5 bar allowed for the extrusion of a continuous and steady fiber; P = 4 bar resulted in dispersion of cluster of material. After the selection of the optimal extrusion pressure (P = 2.5 bar), this was combined with different values of deposition speed (range 2–30 mm/s). In particular, 2, 10, 20, 30 mm/s deposition speed values were considered. In **Figure 2B**, single fiber diameters were reported as the extrusion speed varies. In particular, the fiber diameter decreased for increasing speed values; in fact, by increasing the speed values, the 3D printer does not have enough time to deposit the hydrogel fiber, resulting in progressive fiber thinning or lack of deposition on the surface of the platform (Ng et al., 2016). Combining the selected pressure (P = 2.5 bar) with the different values of deposition speed, it was noticed that for P = 2.5 bar and speed = 2 mm/s, merged fibers were obtained (**Figure 2C_i**). By increasing speed, a shear thinning of the fibers in some points (speed = 20 mm/s, **Figure 2C_iii**) and lack of the deposited hydrogel in other points (speed = 30 mm/s, **Figure 2C_iv**) were observed. The optimal values that allowed detecting all the deposited fibers and obtaining continuous deposition of the hydrogels were found for P = 2.5 bar and speed = 10 mm/s (**Figure 2C_ii**). The optimized printing parameters are summarized in **Table 2**, and the 3D printed structure obtained with the optimized parameters is shown in **Figure 2D**. The use of the optimized printing parameters allowed obtaining comparable results for the different chitosan/gelatin ratio considered in this study (i.e., 1CHI2GEL and 1CHI3GEL). The higher gelatin content in the 1CHI3GEL, resulting in higher viscosity (i.e., higher number of interactions between the positively charged amine groups from chitosan and the negatively charged carboxylate groups from gelatin) did not significantly affect the gel extrusion. Indeed, the viscosity values reported for 1CHI2GEL and 1CHI3GEL are very close between each other (**Figure 1D**) and overlap from 10 to 100 s^{-1}, demonstrating the possible use of the same printing parameters (P = 2.5 bar, speed = 10mm/s).

Crosslinking Effects on 3D Printed Structures

Post Crosslinking Processing

The 3D printing of chitosan scaffolds was possible through formation of a polyelectrolyte complex between chitosan and gelatin, as the latter works as thickener and support material (Piard et al., 2019). However, to ensure the stability of the 3D printed structure after 3D printing process and to be able to handle the scaffolds without losing their structural integrity, 10% w/v TPP crosslinker was used as crosslinker. TPP was poured on the 3D printed structure immediately after the printing process. TPP has been previously used to crosslink chitosan beads (Buranachai et al., 2010), nanoparticles (Gan et al., 2005; Thandapani et al., 2017), and films (Liao and Ho, 2011); however, the use of TPP to crosslink 3D chitosan-based printed scaffolds has been poorly investigated (Serra et al., 2015). TPP crosslinker could represent an optimal choice and substitution to other chitosan crosslinkers, such as glutaraldehyde and genipin. Indeed, glutaraldehyde, the most common agent used to crosslink chitosan, may have a cytotoxic effect on cells if its residues are not completely eliminated (Liao and Ho, 2011; Serra et al., 2015). Genipin, a natural compound that shows a significantly lower level of cytotoxicity compared

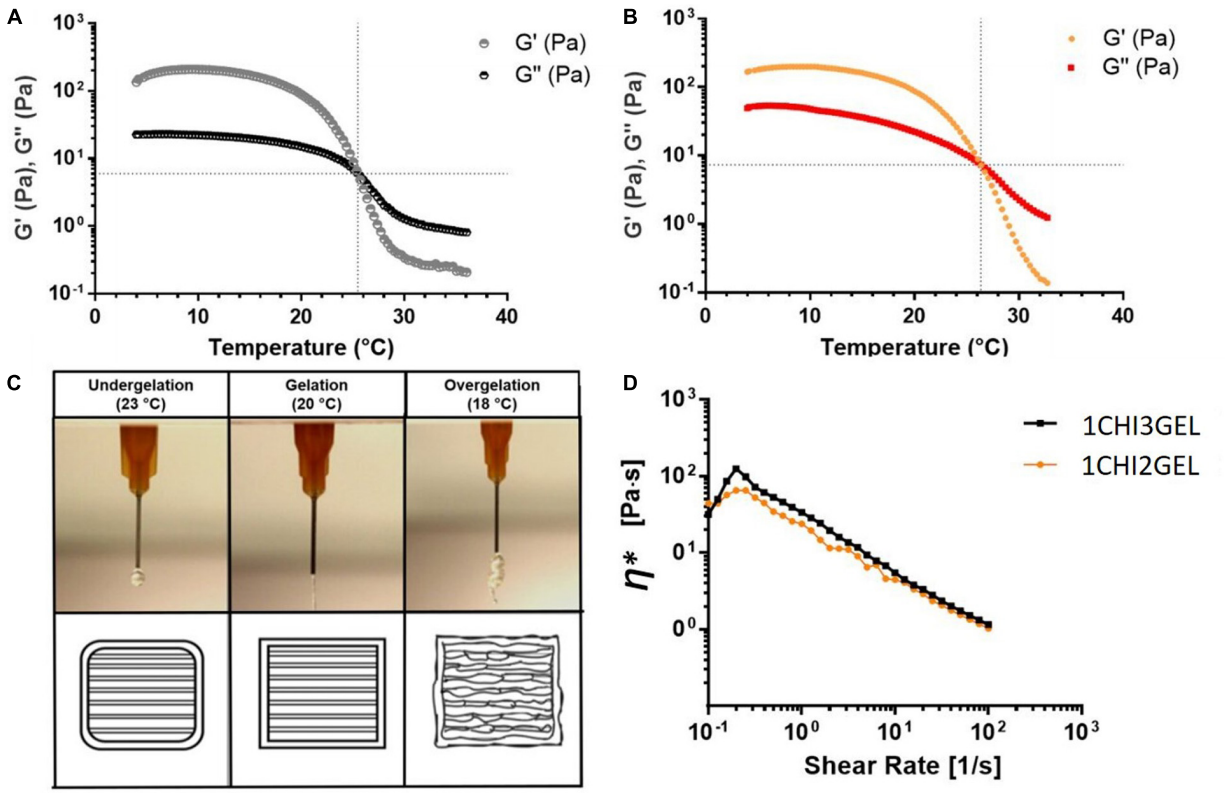

FIGURE 1 | Rheological characterization of chitosan – gelatin blends. Storage (G′) and loss (G″) moduli at varying temperatures for **(A)** 1CHI2GEL, and **(B)** 1CHI3GEL. **(C)** Extrusion of the gel at varying temperatures (18, 20, 23°C). **(D)** Complex viscosity η* behavior in function of the shear rate for 1CHI2GEL and 1CHI3GEL.

to glutaraldehyde, is a highly priced reagent (Gattazzo et al., 2018). In this work, TPP crosslinking has been performed at different temperatures, 4 and 37°C (**Table 1**). Due to gelatin stability at 4°C, 60_0 crosslinking condition shows the best results in terms of shape integrity and retention just after the crosslinking (**Figures 3A,D**). On the contrary, as the gelatin has predominant liquid-like behavior at 37°C, for 10_50 and 30_30 crosslinking conditions, the structures tend to collapse and lose the retention (**Figures 3B,C,E,F**).

FT-IR Analysis

The interactions between chitosan and gelatin within the blend and the effect of the TPP crosslinking for each crosslinking condition (**Table 1**) were evaluated by FT-IR analysis. FT-IR spectrum of pristine chitosan and gelatin powders were considered as controls. Chitosan exhibited polysaccharide peaks at approximately 815 and 1151 cm^{-1}. The peaks at 1251 cm^{-1}, 1579 cm^{-1}, and 1647 correspond, respectively, to C-N and N-H vibrations in amide III, to N-H and C-N vibrations in amide II and to C = O and N-H vibrations in amide I (the peak of the acetyl group) (**Table 3**). The IR spectrum of gelatin is characterized by peaks at 1235 cm^{-1}, 1524 cm^{-1}, 1628 cm^{-1}, 3071 cm^{-1}, corresponding respectively, to C-N, N-H vibrations in amide III, to N-H and C-N vibrations in amide II, to C = O and N-H vibrations in amide I (peak of carbonyl group), and to N-H vibrations in Amide A (**Table 3**). From the comparison between the spectra of the pristine materials and the ones obtained from the blend for each crosslinking condition, some shifts and disappearance of some peaks were detected (**Figures 4A,B**). In particular, in all the FTIR spectra acquired for CHIGEL, for each ratio and crosslinked condition, it was observed that the carbonyl groups shifted from 1628 cm^{-1} to 1640 cm^{-1}, and the amino groups shifted from 1579 cm^{-1} to 1540 cm^{-1}. It was also noticed that the gelatin peak at 2934 cm^{-1} attributed to amide B, and the one at 1397 cm^{-1}, related to amide III, disappeared in the blend, due to the chitosan-gelatin electrostatic interactions (**Table 3**).

Similar results were reported in previous FT-IR spectra performed on chitosan-gelatin blend (Hajiabbas et al., 2015; Ng et al., 2016). Besides the interaction between chitosan and gelatin within the blend, the peak at 1151 cm^{-1} (evidenced with the purple rectangle in **Figure 4**) could also be hypothesized to represent the interaction between TPP crosslinker, as reported in previous works (Gan et al., 2005; Bhumkar and Pokharkar, 2006). However, this interaction could not be detected in the spectra, due to the overlapping with the saccharide peak of chitosan. Within the spectra of the blends for each ratio (**Figure 4A** for 1CHI2GEL, **Figure 4B** for 1CHI3GEL) and crosslinking condition, no differences were detected, as the interacting groups were the same.

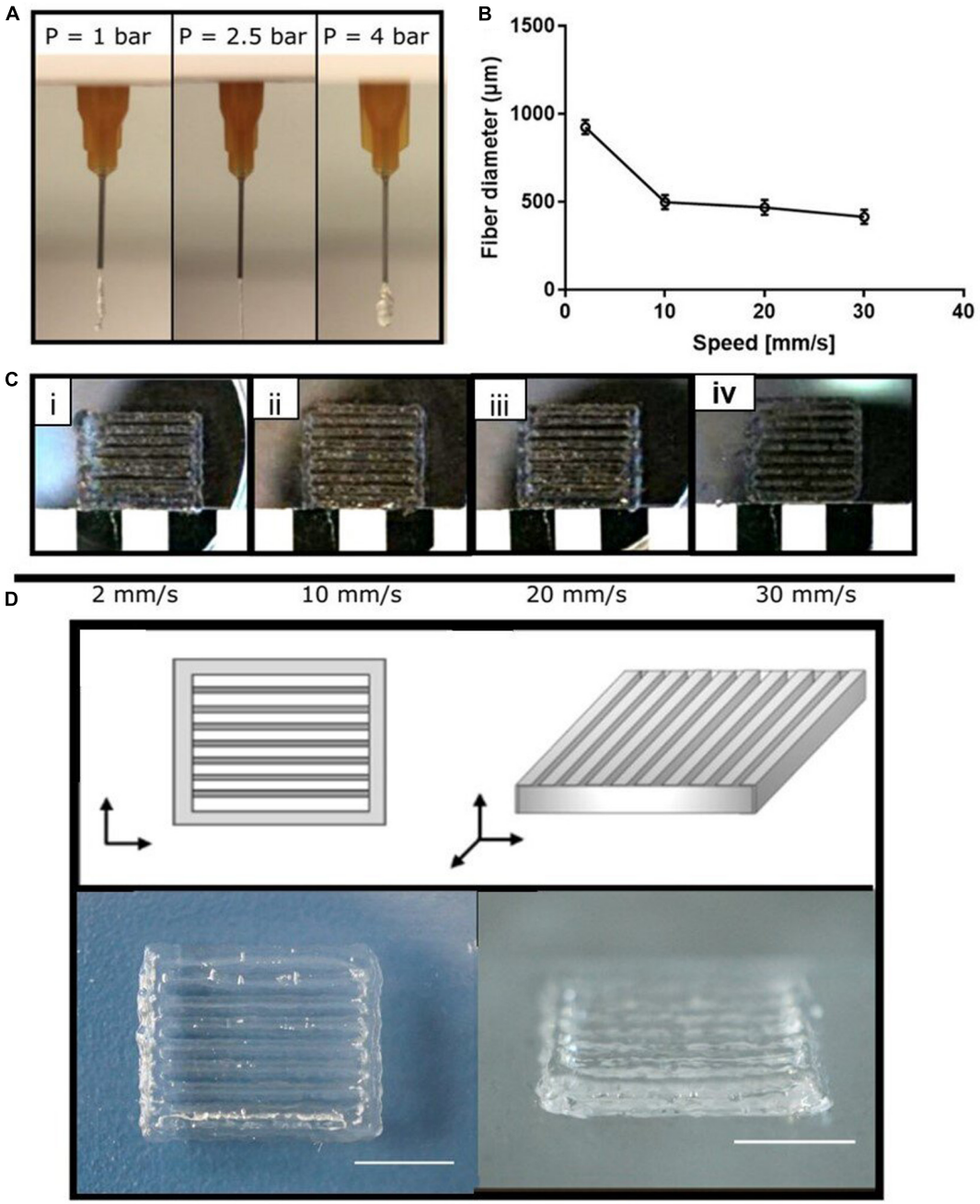

FIGURE 2 | Optimization of the chitosan-gelatin blend printing parameters. **(A)** Extrusion of the blend at different pressures. **(B)** Printed fiber diameter at different speed values. **(C)** Effect of the combination between the selected pressure (P = 2.5 bar) and different speed values; **(D)** on the top panel schematic representation of the 3D designed scaffold and on the lower panel frontal and lateral view of the obtained 3D printed scaffold (i.e., 1CHI2GEL, 2% w/v chitosan, 4% w/v gelatin).

SEM Morphology

The surface morphology of 1CHI2GEL and 1CHI3GEL for each crosslinking condition (60_0, 30_30, 10_50) was investigated by SEM (**Figures 5A–F**). Qualitative differences can be detected between the 60_0 (**Figures 5E,F**) and both the 30_30 (**Figures 5C,D**) and 10_50 (**Figures 5A,B**) crosslinking conditions, for both the considered blends. The surface morphology of the 60_0 scaffold was rougher compared to the others, where this difference became more evident between the 60_0 and the 10_50 structures. The roughness characterizing the 60_0 condition of crosslinking that was performed at 4°C could be attributed to the presence of gelatin, which is in the gel state at low temperatures. In 30_30 and 10_50 conditions, the roughness effect is reduced, as the samples were maintained at 37°C, temperature at which gelatin is in liquid state. It is likely that, at 37°C, gelatin dissolves and a coating-like structure is generated

TABLE 2 | Optimized printing parameters for the chitosan-gelatin blend.

Parameters	Values
Cartridge temperature [°C]	20
Plate temperature [°C]	4
Pressure [bar]	2.5
Speed [mm/s]	10
Layer thickness [μm]	250
Distance between fibers [mm]	1
Fiber orientation	0/180°

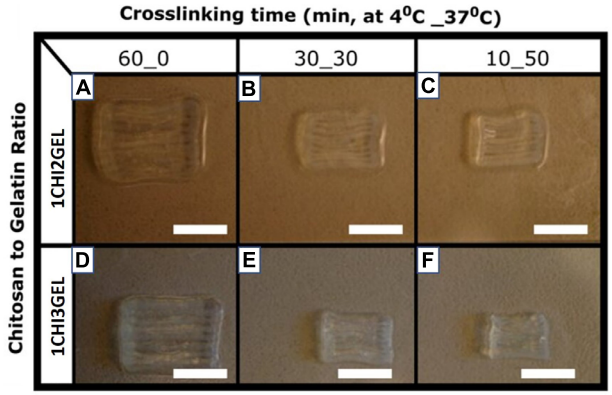

FIGURE 3 | Printed structure obtained for each ratio (1CHI2GEL on the top, and 1CHI3GEL on the bottom) and for each crosslinking condition performed, respectively, 60_0, 30_30, and 10_50. Scale bar: 5 mm. From a qualitative point of view, **(A,D)** 60_0 crosslinking condition shows the best results in terms of shape integrity, while **(B,E)** 30_30 and **(C,F)** 10_50 lose the structural integrity.

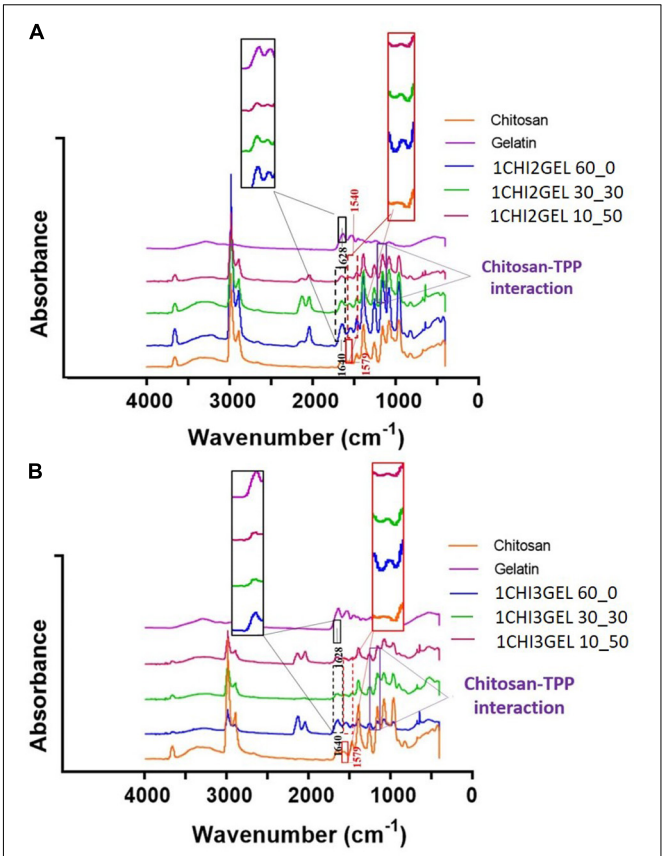

FIGURE 4 | FTIR characterization of 3D printed chitosan- gelatin scaffolds. **(A)** FT-IR spectra of both pure chitosan and gelatin material, and different crosslinking conditions for 1CHI2GEL. The black and red boxes report a magnification of the shifts in the blends spectra, compared to the pristine material spectra. **(B)** FT-IR spectra of both pure chitosan and gelatin material, and different crosslinking conditions for 1CHI3GEL.

on the 3D printed sample surface, giving it a more homogenous aspect. This morphological difference is more evident in 10_50 condition compared to the 30_30, as the first is maintained at 37°C for longer time.

Compressive Mechanical Characterization

Mechanical compression tests were performed on the printed samples for each ratio (i.e., 1CHI2GEL, 1CHI3GEL) and for each crosslinking condition (**Table 1**). Stress-strain curves (**Figure 6A**) were all characterized by a load phase, in which the stress increased until the maximum stress value (σ_{max}), corresponding to the maximum applied strain (ε = 30%), and an unload phase, when the stress decreased gradually while removing the strain. The different behavior of the load and unload phase for the considered configurations, corresponding to the loss of energy during the mechanical test, is due to the viscoelastic nature of the blends constituting the scaffolds. The mechanical testing results were reported in **Figure 6** for all the considered samples. The elastic modulus values ($E_{0-5\%}$, **Figure 6B**) showed there was no significant difference ($p > 0.05$) between the

TABLE 3 | FT-IR main chemical groups of chitosan, gelatin, and chitosan-gelatin blend.

Functional groups	Chitosan peaks	Gelatin peaks	Chitosan-gelatin blend
Saccharidic group	815, 1151 cm^{-1}	_	Not reported
C-N, N-H vibrations in amide III	1251 cm^{-1}	1235 cm^{-1}	Not reported
C-N, N-H vibrations in amide II	1579 cm^{-1}	1524 cm^{-1}	1540 cm^{-1}
C = O, N-H vibrations in amide I	1647 cm^{-1}	1628 cm^{-1}	1640 cm^{-1}
N-H vibrations in amide A	_	3071 cm^{-1}	/
C = H vibrations in amide B	_	2934 cm^{-1}	/

Shift in the chitosan-gelatin blend, Peak disappearance (/) in the chitosan-gelatin blend.

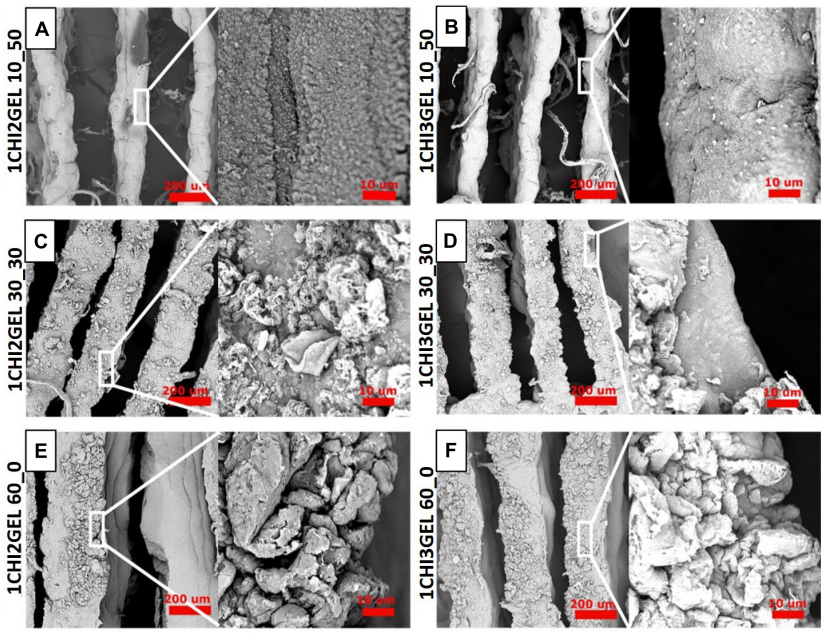

FIGURE 5 | Morphological characterization of 3D printed chitosan-gelatin scaffolds. **(A–F)** SEM morphology of both the ratio and the crosslinking conditions (60_0, 30_30, 10_50) at different magnifications (Scale bar: 200 μm, 10 μm).

crosslinking conditions or gelatin/chitosan ratio. Regarding the stiffness ($E_{25-30\%}$, **Figure 6C**), the highest value was detected for the 1CHI3GEL and 10_50 crosslinking condition, with a significant difference ($p < 0.05$) compared to the 1CHI3GEL and both 60_0 and 30_30 conditions. The same trend was observed for the maximum stress (σ_{max}, **Figure 6D**). Hence, higher concentration of gelatin in the 1_3 ratio (6 vs. 4% w/v in 1CHI2GEL ratio) and the longer crosslinking period at 37°C (t = 50 min vs. 0 and 30 min in 60_0 and 30_30, respectively) contribute to an increase in mechanical properties for 10_50 condition, compared to 60_0 and 30_30 crosslinking conditions. Considering the residual deformation values (**Figure 6E**), the lowest value, related to a higher elastic behavior of the scaffolds, was attained for the 1CHI3GEL crosslinked under the 10_50 condition. Hence, a higher ability to recover the deformation after the exerted compression was detected for 10_50 condition, with significant difference ($p < 0.05$) compared to the 1CHI3GEL 30_30 crosslinking condition. The hysteresis area (**Figure 6F**) of the 1CHI3GEL 10_50 was the highest (i.e., higher viscous behavior of the structure), with significant difference ($p < 0.05$) compared to the 1CHI3GEL 30_30 condition. This means that the energy loss during the compression test for the 1CHI3GEL of the 10_50 condition was higher. The compressive elastic modulus obtained in this study for the 3D printed samples is found to be in a range between 0.53 ± 0.27 kPa (for the 60_0 of 1CHI3GEL) and 0.79 ± 0.14 kPa (for the 10_50 of 1CHI3GEL). These results were expected, as hydrogels suffer from weak mechanical properties (Vedadghavami et al., 2017). For the purpose of this study, the obtained range has to be compared to the elasticity range of native anisotropic tissues, as 4.5–8 kPa in skin (Karimi and Navidbakhsh, 2014), 12 kPa in skeletal (Gilbert et al., 2010), and 10–15 kPa in myocardial tissues (Pok et al., 2013). Indeed, it is well known that 3D scaffolds substitute extracellular matrix (ECM), whose mechanical properties regulate cell behavior, in terms of proliferation and differentiation. The obtainment of values closer to the ones of the native tissues is mandatory to obtain a scaffold able to provide the proper mechanical stimuli for the desired application. As it can be observed from the elastic moduli (**Figure 6B**), the ones obtained in this study are lower compared to the ones of the anisotropic tissues previously mentioned, but in the same order of magnitude. Moreover, it has been already reported that soft hydrogels can be used for the regeneration of non-loading areas, or for soft tissue regeneration (i.e., skin) (Kim et al., 2007). Testing higher concentrations of the polymers constituting the blend and crosslinker agents (Bettadapur et al., 2016; Gattazzo et al., 2018), adding growth factors (Rutledge et al., 2014; Castro et al., 2015) or using a bioreactor (Gauvin et al., 2011; Heher et al., 2015) could help reaching the desired values. In addition, the cells seeded on the 3D printed structures may produce ECM, allowing to increase the mechanical properties of the scaffold.

Effect of Crosslinking Conditions on Scaffold Dimensions, Fiber Size and Distance Between the Fibers

To determine the effect of different crosslinking conditions, overall dimensions (i.e., length, width, height), fiber diameter and distance between fibers of the printed samples were measured for each ratio (1CHI2GEL and 1CHI3GEL) and crosslinking condition (60_0, 30_30, 10_50). The differences in the overall scaffold dimensions can be qualitatively observed comparing

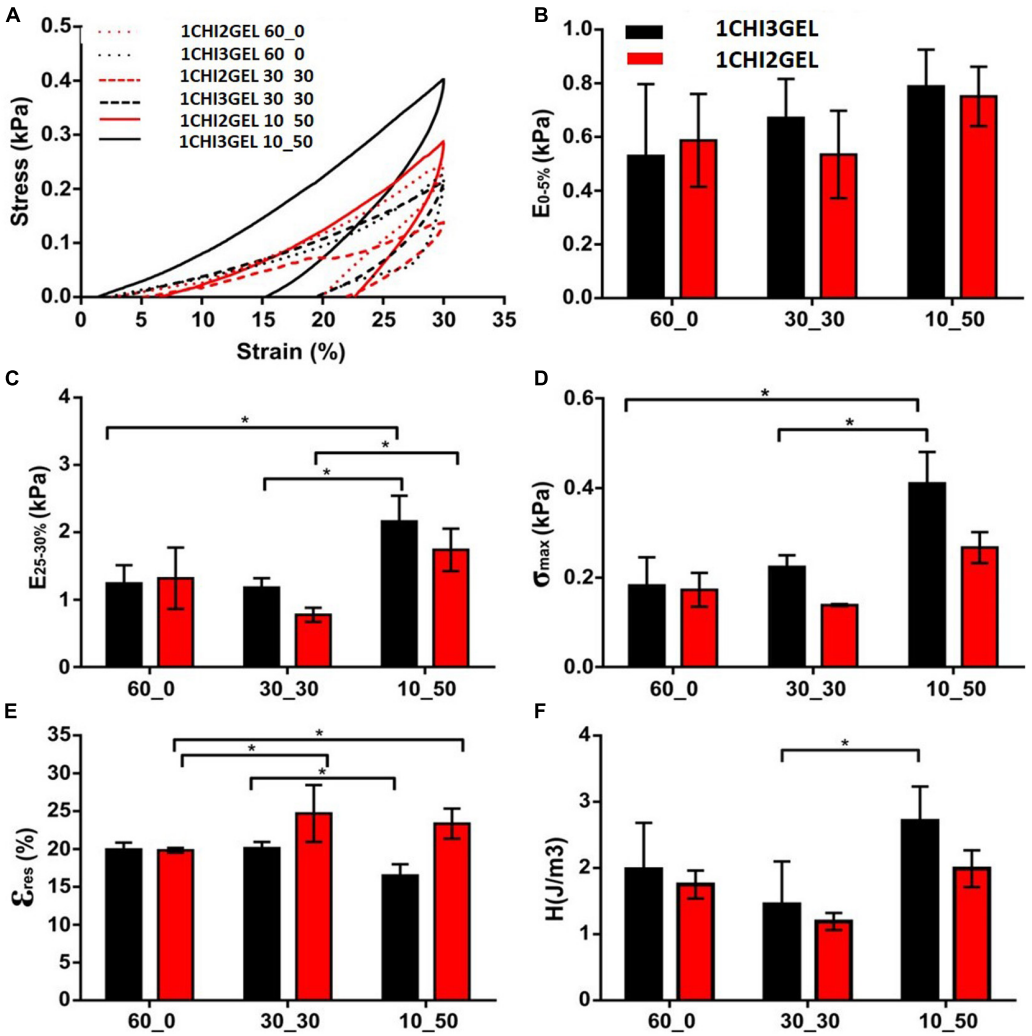

FIGURE 6 | Mechanical characterization of 3D printed chitosan-gelatin scaffolds. **(A)** Representative stress-strain curves obtained for the 60_0, 30_30, 10_50 crosslinking conditions, and for the considered ratio (1CHI2GEL and 1CHI3GEL). Mechanical parameters calculated from the curves: **(B)** elastic modulus, **(C)** stiffness, **(D)** maximum stress, **(E)** residual deformation and **(F)** hysteresis area (*$p < 0.05$).

the 60_0 condition to both 30_30 and 10_50 conditions (**Figure 3**). Chitosan/gelatin ratio (1CHI2GEL and 1CHI3GEL) did not cause any significant change ($p > 0.05$) in the scaffold dimensions, for any crosslinking conditions performed (**Figures 7A–C**). Scaffolds crosslinked under 60_0 condition had the closest dimensions to the CAD model (i.e., 98.4%, 97.9%, and 98.4% for length, width, height, respectively, **Figures 7A–C**), probably caused by the fact that these scaffolds were kept for all the crosslinking period at 4°C. In fact, at this temperature, gelatin is in a gel-like state, ensuring the maintenance of the 3D structure shape during the crosslinking as during the 3D printing process, in which the temperature of the base plate was set at 4°C. On the contrary, in the 30_30 and 10_50 crosslinking condition, the obtained values of length, width and height (**Figures 7A–C**) were statistically lower ($p < 0.05$) compared to the set ones and to the ones detected for 60_0 condition (i.e., 64.5%, 66.5%, 92.8% in 30_30 condition, and 62.1%, 63.8%, 93.6% in 10_50 condition, reported for length, width, height, respectively). This is due to the fact that, when samples are kept for 30 and 50 min at 37°C (in the 30_30 and 10_50 condition, respectively), gelatin is in a liquid-like state, resulting in the loss of shape and structural integrity (Piard et al., 2019). Indeed, as reported in a previous study (Dragusin et al., 2012), incubation at 37°C causes disintegration of the physical network of gelatin, due to the protein change from helix to coil above $T_{sol-gel}$. Regarding fiber diameter and distance between fibers (**Figure 7_D** for fiber diameters, **Figure 7_E** for distance between fibers), for the fiber diameters obtained with the 60_0 condition (513.2 ± 27.4 μm), the dimensions are significantly different ($p < 0.05$) compared to the needle size dimension (ID = 330 μm), indicating a collapse of the fibers after the deposition. On the contrary, the fiber diameters obtained with the 30_30 (353.0 ± 44.9 μm) and 10_50 (334.1 ± 29.5 μm) conditions were closer to the needle size ($p > 0.05$), as consequence of the global reduction of the samples

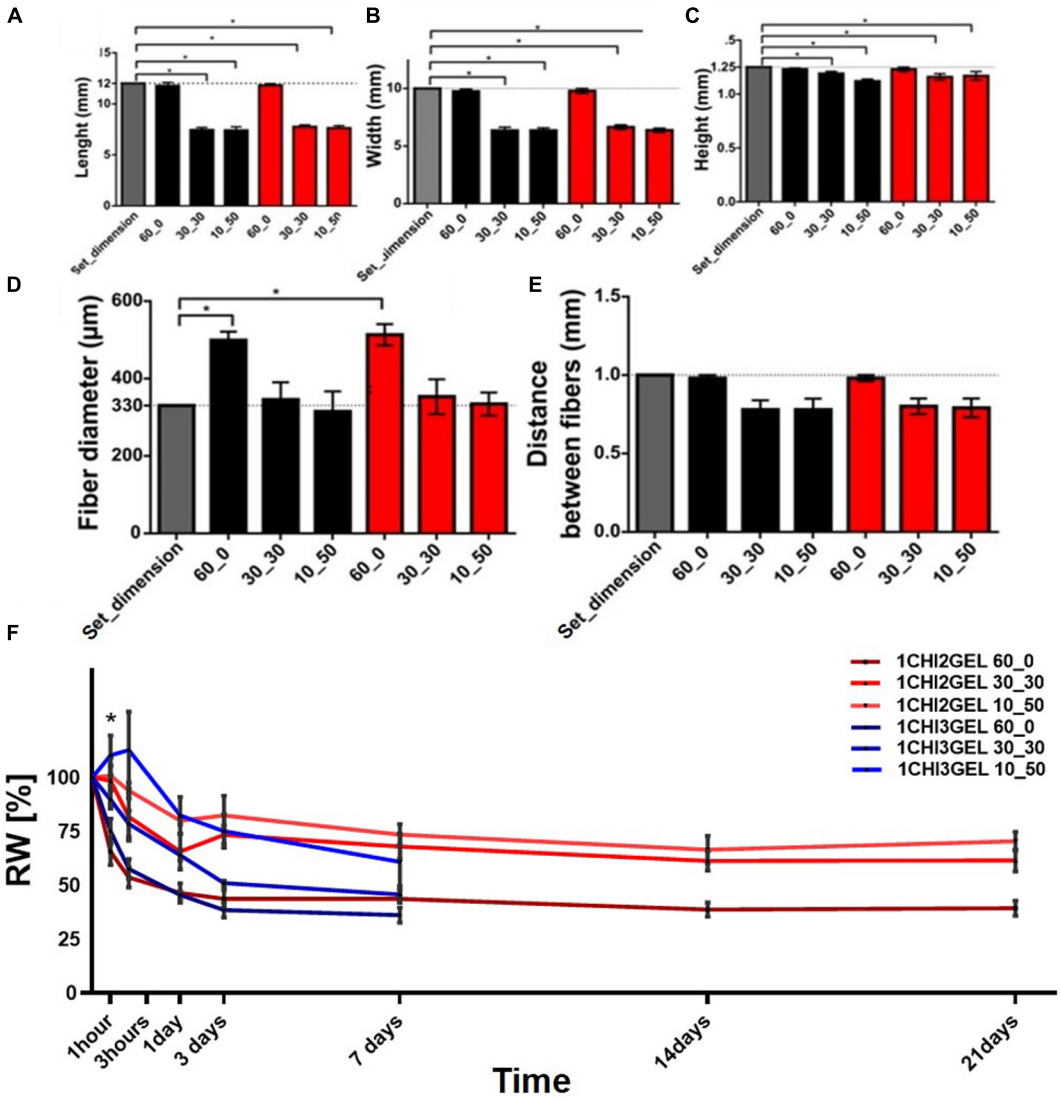

FIGURE 7 | Printing accuracy and stability of 3D printed chitosan-gelatin scaffolds. The measurements have been acquired just after crosslinking time period. Dimensional values for each crosslinking condition with respect to **(A)** the length set dimension (12 mm), **(B)** width set dimension (10 mm), **(C)** height set dimension (1.25 mm). **(D)** Fiber diameter and **(E)** distance between fibers (compared to the set one, 1 mm) for each different crosslinking condition, **(F)** weight variation for both the ratio and the three crosslinking conditions considered in the study (*$p < 0.05$).

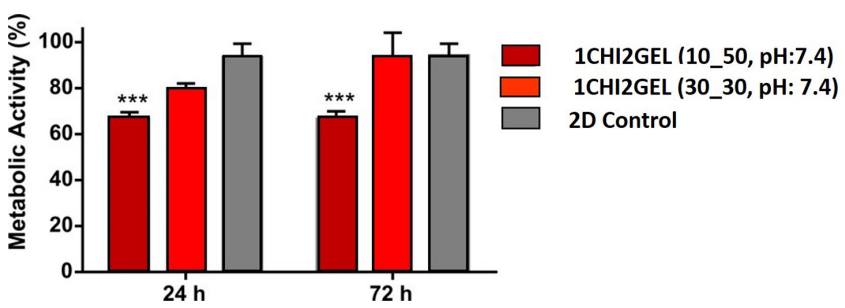

FIGURE 8 | *In vitro* cytotoxicity test performed on the 1CHI2GEL scaffolds crosslinked under different crosslinking conditions (***$p < 0.001$).

size in these conditions. Regarding the distance between the fibers, no significant difference was found ($p > 0.05$) for the considered crosslinking conditions, even if in 30_30 and 10_50 conditions the distance between the fibers was slightly decreased. Indeed, it is well known that cells have a different behavior on biomaterials composed of nano-scale architecture compared to micro-scale features (Kumbar et al., 2008). For instance, within anisotropic tissues, it has been reported that human skin fibroblasts show higher proliferation on fibers diameters in the range 350–1100 nm (Kumbar et al., 2008); for skeletal muscle tissue fiber diameter dimensions should be comprised in a range between 10 and 100 μm, to mimic as much as possible the diameter of adult muscle fiber, and 50–100 μm for the distance between the fibers (Cooper et al., 2010). Regarding myocardial regeneration, it has been shown that mimicking the hierarchical structure through the simultaneous deposition of microfibers (2–4 μm) and nanofibers (50–300 nm) favor cell-matrix interactions (Sreerekha et al., 2013). Comparing the values of the printed fiber diameters and distance between them obtained in this work, these are one order of magnitude higher than the ones desirable to mimic the native structure of anisotropic tissues and the ones obtained with other techniques [e.g., electrospinning (Kumbar et al., 2008; Cooper et al., 2010; Sreerekha et al., 2013), replica molding (Altomare et al., 2010) and soft lithography (Boldrin et al., 2007; Hwang et al., 2017)] used in anisotropic tissue regeneration. These techniques allow to obtain fiber diameter measurements at the nanometer scale, enhancing the substrate-cell interaction. Nonetheless, they did not fully satisfy mimicking native 3D tissue and manufacturing 3D constructs, being not able to reach and reproduce the real thickness value of anisotropic tissues [thickness of skin tissue ∼ 1–3 mm (Kumbar et al., 2008), skeletal muscle tissue ∼ 2–2.5 mm (Bian and Bursac, 2009), and myocardial tissue ∼ 1 cm (Sreerekha et al., 2013)]. On the contrary, 3D printing technology has the potential to build 3D constructs able to provide suitable microenvironment in which cells are spatially organized in 3D tissues, important requirement for the repair and regeneration of anisotropic tissues. Moreover, despite the 3D printing intrinsic limitations related to needle diameter size and selected printing parameters, very promising results for anisotropic tissues regeneration have been already reported (Lee et al., 2014; Costantini et al., 2017).

Stability Test

Stability test was performed *in vitro* on the printed samples for each gel ratio (1CHI2GEL and 1CHI3GEL) and crosslinking condition (60_0, 30_30, and 10_50), maintaining the samples at 37°C up to 21 days (**Figure 7F**). Considering the same crosslinking condition, no significant difference ($p > 0.05$) was observed between the two gel ratios for the first 24 h. After 24 h, residual weight differences between the crosslinking conditions of both chitosan/gelatin ratio became significant ($p < 0.05$). In particular, the scaffolds of 1CHI2GEL samples show a swelling behavior (i.e., absorbing aqueous media) mainly between 24 h up to 3 days, followed by a progressive weight stabilization up to 21 days. The scaffolds of 1CHI3GEL after 24 h started to lose weight dramatically until complete disintegration of the 3D printed samples at 7 days.

When the stability test and mechanical testing results have taken together, we can assert the coexisting effects of bulk and surface erosion mechanisms (Storti and Lattuada, 2017). We hypothesize that in the early time points (during the first 48 h) the effect of surface erosion, which causes reduction in size without changing polymer structure properties, overcomes bulk erosion. Indeed, through the macroscopic observation of the 3D printed structures (**Figures 3A–F**), we can assess the change in dimensions. Moreover, when the stability has been further studied with SEM over 21 days, effect of surface erosion can clearly be seen at early time points while, at later time points, crumbling around the fibers starts, causing the 3D printed scaffolds losing their structural integrity (**Supplementary Figures S4, S5**). Moreover, the scaffolds have been evaluated over 21 days by FTIR analysis (**Supplementary Figures S2, S3**), and shift in the amide peaks indicated that the bulk erosion took place at later time points, when bulk erosion becomes dominant. Hence, mechanical properties evaluated at 48 h were not affected by bulk erosion effect, thus resulting higher in 1CHI3GEL. Over time, at later time points, the effect of chains cleaving due to bulk erosion on 1CHI3GEL becomes more dominant than in 1CHI2GEL, and this could be imputed to the higher presence of gelatin in 1CHI3GEL. Higher presence of gelatin is related with higher hydrophilicity and, thus, the effect of water penetrating the bulk cleaving hydrolytically chemical bonds bringing to the rupture of long chains into water-soluble fragments is higher (Rey-Vinolas et al., 2019). It has been reported that gelatin dissolution in presence of water is quicker when gelatin is in higher concentration (Kathuria et al., 2009; Nieto-Suárez et al., 2016), as in 1CHI3GEL. Although it has been observed that the presence of chitosan in a gelatin scaffold reduces its degradation rate, stabilizing the network, the influence of chitosan in our study was not sufficient to prevent gelatin loss in the 1CHI3GEL.

Comparing 60_0, 30_30, and 10_50 conditions, it can be observed that weight variation was not significant ($p > 0.05$) between 30_30 and 10_50 for any time point of the stability test. In 10_50, even a small swelling behavior was observed within the first hour (Huang et al., 2005). In particular, 1CHI2GEL 30_30 and 10_50 conditions show higher weight stability and no significant weight trend changes than 1CHI3GEL ones, mostly after 24 h. On the contrary, the difference between the 60_0 crosslinking condition and the other two (30_30 and 10_50) can be detected for all the considered timepoints for the both chitosan/gelatin ratios, specifically significant ($p < 0.05$) mainly within 3 h as the scaffolds tend to stabilize. The steep weight loss of the 60_0 condition compared to the others can be explained considering the crosslinking temperature of the samples. The samples in 60_0 were crosslinked at 4°C for 60 min at which gelatin was in its gel state (i.e., T = 25.5 ± 1°C for 1CHI2GEL, T = 26.4 ± 0.95°C for 1CHI3GEL). Thus, during crosslinking, gelatin was stable, the volume of the printed constructs was constant, and gelatin did not leach out from the structure. On the contrary, samples in 30_30 and 10_50 condition were at 37°C (above sol-gel temperature) during part of the crosslinking period, thus causing gelatin dissolution until stabilization. Proof of these considerations is the fact that the initial weight of the samples crosslinked with 30_30 and 10_50 conditions was lower

than those of 60_0. Gelatin weight loss in the 3D samples was due to its temperature dependence, occurred as it was not crosslinked, in fact TPP only ionically crosslinked chitosan material.

In a previously reported study, using TPP as crosslinker for chitosan and gelatin blends, Yan et al. (2005) 3D printed tissue culture scaffolds with 0–90° orientation. In this study, the biomaterial ink composition has been chosen as 1:10 chitosan:gelatin and the crosslinking conditions was indicated as 3% (w/v) TPP for 5 min followed by glutaraldehyde crosslinking (0.25%) to further stabilize the structure. Authors have shown the stability of the constructs over 14 days, with cytocompatible characteristics (Yan et al., 2005). In comparison to the previously reported literature, the lower gelatin concentration in the blend, the higher TPP crosslinking concentration and TPP crosslinking time used in this study enabled us to create stable scaffolds up to 21 days in 0–180° orientation, without using additional crosslinkers.

In vitro Cytocompatibility Test

For the *in vitro* cytocompatibility test, 1CHI2GEL crosslinked using 30_30 and 10_50 crosslinking conditions was tested. In fact, considering the results obtained in the stability test, only 10_50 and 30_30 crosslinking conditions of the 1CHI2GEL demonstrate good stability. Cell viability (**Figure 8**) was measured 66% at 24 h and 67% at 72 h for the 10_50 condition, and 79.7% at 24 h, to 91% at 72 h for the 30_30 condition, respectively, compared to the negative control group (i.e., 97%). This difference between 10_50 and 30_30 condition may be imputed to the higher gelatin diffusion to the media in the 30_30 condition, thus resulting in changes in the media composition. In the stability test, even if the residual weight percentages between these two groups is not statistically significant, lower residual weight of the scaffolds crosslinked under 30_30 condition can be noticed. In the first 24 h, the lower metabolic activity of the cells compared to the negative control group can be explained due to the leaching of gelatin to the media and changings in the composition of the media. However, over 72 h period it was observed that cells in contact with the scaffolds crosslinked 30_30 condition have shown comparable metabolic activity to negative control group while the cells in contact with the scaffolds crosslinked 10_50 condition have not shown any improvement regarding their metabolic activity. Hence, the best results were obtained with the 30_30 condition of the 1CHI2GEL, as they showed an increased cell viability at 72 h with no significant difference compared to the negative control. As a good interaction between the cells and the material is required by bioprinting, the mentioned condition was considered the optimal candidate for future 3D bioprinting experiment.

CONCLUSION

In this study, chitosan-gelatin blend hydrogel was investigated as suitable bioink in 3D printing technology applications. The printing parameters (i.e., printing temperature, extrusion pressure, dispensing speed) were successfully optimized to obtain reproducible 3D printed anisotropic structures replicating the CAD design. Among the tested crosslinking conditions, chitosan/gelatin ratio, physico-mechanical and biological properties, 1CHI2GEL 30_30 was selected as the eligible formulation to be considered, thus paving the way for potential applications in anisotropic TE field. Briefly, for both CHI/GEL ratios, fiber diameters and distance between the fibers obtained in the 30_30 and 10_50 were found to be more suitable for future applications in anisotropic TE, although 60_0 crosslinking condition resulted the best in terms of shape retention. For all the crosslinking conditions and ratio tested, the obtained compression test values were of the same order of magnitude of the *in vivo* anisotropic tissue values. 3D printed scaffolds with 1CHI2GEL ratio and crosslinked with 30_30 and 10_50 conditions have shown better stability compared to all the conditions of 1CHI3GEL samples, as the latter disintegrated after 7 days. Therefore, 1CHI3GEL ratio was excluded from the study and it was not further considered in the cytocompatibility testing. Lastly, cell viability evaluated *in vitro* on 1CHI2GEL samples was higher in the 30_30 condition, compared to the 10_50 condition. In comparison to the previously reported studies, the lower gelatin concentration in the blend, the higher TPP crosslinking concentration and TPP crosslinking time used in this study enabled us to create stable cytocompatible scaffolds for 3D anisotropic tissue constructs.

DATA AVAILABILITY STATEMENT

All datasets generated for this study are included in the article/**Supplementary Material**.

AUTHOR CONTRIBUTIONS

NCe, NCo, and WS designed the study. TF and NCe performed the experimental work and analyses. TF, NCe, NCo, SF, and WS contributed to data discussion and wrote/edited the manuscript.

FUNDING

This study was financially supported by the National Centre for Research and Developments in the framework of the project "Consolidation of 3D printing, cell biology and material technology for the development of bioprinted meat – A prototype study" (grant No. PL-TWIII/5/2016).

SUPPLEMENTARY MATERIAL

The Supplementary Material for this article can be found online at: https://www.frontiersin.org/articles/10.3389/fbioe.2020.00400/full#supplementary-material

REFERENCES

Altomare, L., Gadegaard, N., Visai, L., Tanzi, M. C., and Farè, S. (2010). Biodegradable microgrooved polymeric surfaces obtained by photolithography for skeletal muscle cell orientation and myotube development. *Acta Biomater.* 6, 1948–1957. doi: 10.1016/j.actbio.2009.12.040

Aranaz, I., Mengibar, M., Harris, R., Panos, I., Miralles, B., Acosta, N., et al. (2009). Functional characterization of chitin and chitosan. *Curr. Chem. Biol.* 3, 203–230.

Bai, H., Polini, A., Delattre, B., and Tomsia, A. P. (2013). Thermoresponsive composite hydrogels with aligned macroporous structure by ice-templated assembly. *Chemi. Mater.* 25, 4551–4556. doi: 10.1021/cm4025827

Bettadapur, A., Suh, G. C., Geisse, N. A., Wang, E. R., Hua, C., Huber, H. A., et al. (2016). Prolonged culture of aligned skeletal myotubes on micromolded gelatin hydrogels. *Sci. Rep.* 6, 1–14. doi: 10.1038/srep28855

Bhumkar, D. R., and Pokharkar, V. B. (2006). Studies on effect of pH on cross-linking of chitosan with sodium tripolyphosphate: a technical note. *AAPS PharmSciTech* 7, E138–E143. doi: 10.1208/pt070250

Bian, W., and Bursac, N. (2009). Engineered skeletal muscle tissue networks with controllable architecture. *Biomaterials* 30, 1401–1412. doi: 10.1016/j.biomaterials.2008.11.015

Boldrin, L., Elvassore, N., Malerba, A., Flaibani, M., Cimetta, E., Piccoli, M., et al. (2007). Satellite cells delivered by micro-patterned scaffolds: a new strategy for cell transplantation in muscle diseases. *Tissue Engi.* 13, 253–262. doi: 10.1089/ten.2006.0093

Buranachai, T., Praphairaksit, N., and Muangsin, N. (2010). Chitosan/Polyethylene glycol beads crosslinked with tripolyphosphate and glutaraldehyde for gastrointestinal drug delivery. *AAPS PharmSciTech* 11, 1128–1137. doi: 10.1208/s12249-010-9483-z

Castro, N. J., Patel, R., and Zhang, L. G. (2015). Design of a novel 3D printed bioactive nanocomposite scaffold for improved osteochondral regeneration. *Cell. Mol. Bioeng.* 8, 416–432. doi: 10.1007/s12195-015-0389-4

Chen, M., Zhu, J., Qi, G., He, C., and Wang, H. (2012). Anisotropic hydrogels fabricated with directional freezing and radiation-induced polymerization and crosslinking method. *Mater. Lett.* 89, 104–107. doi: 10.1016/j.matlet.2012.08.087

Chen, Y., Mohanraj, V. J., Wang, F., and Benson, H. A. E. (2007). Designing chitosan-dextran sulfate nanoparticles using charge ratios. *AAPS PharmSciTech* 8:E98. doi: 10.1208/pt0804098

Chia, H. N., and Wu, B. M. (2015). Recent advances in 3D printing of biomaterials. *J. Biol. Eng.* 9:4. doi: 10.1186/s13036-015-0001-4

Cooper, A., Jana, S., Bhattarai, N., and Zhang, M. (2010). Aligned chitosan-based nanofibers for enhanced myogenesis. *J. Mater. Chem.* 20:8904. doi: 10.1039/c0jm01841d

Costantini, M., Idaszek, J., Szöke, K., Jaroszewicz, J., Dentini, M., Barbetta, A., et al. (2016). 3D bioprinting of BM-MSCs-loaded ECM biomimetic hydrogels for in vitro neocartilage formation. *Biofabrication* 8:35002. doi: 10.1088/1758-5090/8/3/035002

Costantini, M., Testa, S., Mozetic, P., Barbetta, A., Fuoco, C., Fornetti, E., et al. (2017). Microfluidic-enhanced 3D bioprinting of aligned myoblast-laden hydrogels leads to functionally organized myofibers in vitro and in vivo. *Biomaterials* 131, 98–110. doi: 10.1016/j.biomaterials.2017.03.026

Croisier, F., and Jérôme, C. (2013). Chitosan-based biomaterials for tissue engineering. *Eur. Polym. J.* 49, 780–792. doi: 10.1016/j.eurpolymj.2012.12.009

De France, K. J., Yager, K. G., Chan, K. J. W., Corbett, B., Cranston, E. D., and Hoare, T. (2017). Injectable anisotropic nanocomposite hydrogels direct in situ growth and alignment of myotubes. *Nano Lett.* 17, 6487–6495. doi: 10.1021/acs.nanolett.7b03600

Demirtaş, T. T., Irmak, G., and Gümüşderelioğlu, M. (2017). A bioprintable form of chitosan hydrogel for bone tissue engineering. *Biofabrication* 9:035003. doi: 10.1088/1758-5090/aa7b1d

Dragusin, D. M., Van Vlierberghe, S., Dubruel, P., Dierick, M., Van Hoorebeke, L., Declercq, H. A., et al. (2012). Novel gelatin-PHEMA porous scaffolds for tissue engineering applications. *Soft Matter* 8, 9589–9602. doi: 10.1039/c2sm25536g

Elieh-Ali-Komi, D., and Hamblin, M. R. (2016). Chitin and chitosan: production and application of versatile biomedical nanomaterials. *Int. J. Adv. Res.* 4, 411–427.

Elviri, L., Foresti, R., Bergonzi, C., Zimetti, F., Marchi, C., Bianchera, A., et al. (2017). Highly defined 3D printed chitosan scaffolds featuring improved cell growth. *Biomed. Materi.* 12, 1–11. doi: 10.1088/1748-605X/aa7692

Gan, Q., Wang, T., Cochrane, C., and McCarron, P. (2005). Modulation of surface charge, particle size and morphological properties of chitosan-TPP nanoparticles intended for gene delivery. *Collo. Surfaces B Biointerfaces* 44, 65–73. doi: 10.1016/j.colsurfb.2005.06.001

Gattazzo, F., De Maria, C., Rimessi, A., Donà, S., Braghetta, P., Pinton, P., et al. (2018). Gelatin-genipin-based biomaterials for skeletal muscle tissue engineering. *J. Biomed. Mater. Res.Part B Appl. Biomater.* 106, 2763–2777. doi: 10.1002/jbm.b.34057

Gauvin, R., Parenteau-Bareil, R., Larouche, D., Marcoux, H., Bisson, F., Bonnet, A., et al. (2011). Dynamic mechanical stimulations induce anisotropy and improve the tensile properties of engineered tissues produced without exogenous scaffolding. *Acta Biomater.* 7, 3294–3301. doi: 10.1016/j.actbio.2011.05.034

Gilbert, P. M., Havenstrite, K. L., Magnusson, K. E. G., Sacco, A., Leonardi, N. A., Kraft, P., et al. (2010). Supplem. substrate elasticity regulates skeletal muscle stem cell. *Science* 1078, 1078–1081. doi: 10.1126/science.1191035

Golden, A. P., and Tien, J. (2007). Fabrication of microfluidic hydrogels using molded gelatin as a sacrificial element. *Lab Chip* 7, 720–725.

Hajiabbas, M., Mashayekhan, S., Nazaripouya, A., Naji, M., Hunkeler, D., Rajabi Zeleti, S., et al. (2015). Chitosan-gelatin sheets as scaffolds for muscle tissue engineering. *Artif. Cells, Nanomedi. Biotechnol.* 43, 124–132. doi: 10.3109/21691401.2013.852101

Haque, M. A., Kamita, G., Kurokawa, T., Tsujii, K., and Gong, J. P. (2010). Unidirectional alignment of lamellar bilayer in hydrogel: one-dimensional swelling, anisotropic modulus, and stress/strain tunable structural color. *Adv. Mater.* 22, 5110–5114. doi: 10.1002/adma.201002509

Heher, P., Maleiner, B., Prüller, J., Teuschl, A. H., Kollmitzer, J., Monforte, X., et al. (2015). A novel bioreactor for the generation of highly aligned 3D skeletal muscle-like constructs through orientation of fibrin via application of static strain. *Acta Biomater.* 24, 251–265. doi: 10.1016/j.actbio.2015.06.033

Hinton, T. J., Jallerat, Q., Palchesko, R. N., Park, J. H., Grodzicki, M. S., Shue, H.-J., et al. (2015). Three-dimensional printing of complex biological structures by freeform reversible embedding of suspended hydrogels. *Sci. Adv.* 1:e1500758. doi: 10.1126/sciadv.1500758

Huang, Y., Onyeri, S., Siewe, M., Moshfeghian, A., and Madihally, S. V. (2005). In vitro characterization of chitosan-gelatin scaffolds for tissue engineering. *Biomaterials* 26, 7616–7627. doi: 10.1016/j.biomaterials.2005.05.036

Huang, Z., Yu, B., Feng, Q., Li, S., Chen, Y., and Luo, L. (2011). In situ-forming chitosan/nano-hydroxyapatite/collagen gel for the delivery of bone marrow mesenchymal stem cells. *Carbohydr. Polym.* 85, 261–267. doi: 10.1016/j.carbpol.2011.02.029

Hwang, Y., Seo, T., Hariri, S., Choi, C., and Varghese, S. (2017). Matrix topographical cue-mediated myogenic differentiation of human embryonic stem cell derivatives. *Polymers* 9:580. doi: 10.3390/polym9110580

Jana, S., Cooper, A., and Zhang, M. (2013). Chitosan scaffolds with unidirectional microtubular pores for large skeletal myotube generation. *Adv. Healthc. Mater.* 2, 557–561. doi: 10.1002/adhm.201200177

Jayakumar, R., Prabaharan, M., Nair, S. V., and Tamura, H. (2010). Novel chitin and chitosan nanofibers in biomedical applications. *Biotechnol. Adv.* 28, 142–150. doi: 10.1016/j.biotechadv.2009.11.001

Ji, C., Annabi, N., Khademhosseini, A., and Dehghani, F. (2011). Fabrication of porous chitosan scaffolds for soft tissue engineering using dense gas CO2. *Acta Biomater.* 7, 1653–1664. doi: 10.1016/j.actbio.2010.11.043

Karimi, A., and Navidbakhsh, M. (2014). Material properties in unconfined compression of gelatin hydrogel for skin tissue engineering applications. *Biomed. Tech* 59, 479–486. doi: 10.1515/bmt-2014-0028

Kathuria, N., Tripathi, A., Kar, K. K., and Kumar, A. (2009). Synthesis and characterization of elastic and macroporous chitosan-gelatin cryogels for tissue engineering. *Acta Biomater.* 5, 406–418. doi: 10.1016/j.actbio.2008.07.009

Kim, I.-Y., Seo, S.-J., Moon, H.-S., Yoo, M.-K., Park, I.-Y., Kim, B.-C., et al. (2008). Chitosan and its derivatives for tissue engineering applications. *Biotechnol. Adv.* 26, 1–21. doi: 10.1016/j.biotechadv.2007.07.009

Kim, J., Kim, I. S., Cho, T. H., Lee, K. B., Hwang, S. J., Tae, G., et al. (2007). Bone regeneration using hyaluronic acid-based hydrogel with bone morphogenic protein-2 and human mesenchymal stem cells. *Biomaterials* 28, 1830–1837. doi: 10.1016/j.biomaterials.2006.11.050

Kumbar, S. G., Nukavarapu, S. P., James, R., Nair, L. S., and Laurencin, C. T. (2008). Electrospun poly(lactic acid-co-glycolic acid) scaffolds for skin tissue engineering. *Biomaterials* 29, 4100–4107. doi: 10.1016/j.biomaterials.2008.06.028

Lee, V., Singh, G., Trasatti, J. P., Bjornsson, C., Xu, X., Tran, T. N., et al. (2014). Design and fabrication of human skin by three-dimensional bioprinting. *Tissue Eng. Part C Methods* 20, 473–484. doi: 10.1089/ten.tec.2013.0335

Li, G., Zhao, X., Zhao, W., Zhang, L., Wang, C., Jiang, M., et al. (2014). Porous chitosan scaffolds with surface micropatterning and inner porosity and their effects on Schwann cells. *Biomaterials* 35, 8503–8513. doi: 10.1016/j.biomaterials.2014.05.093

Liao, C. T., and Ho, M. H. (2011). The fabrication of biomimetic chitosan scaffolds by using SBF treatment with different crosslinking agents. *Membranes* 1, 3–12. doi: 10.3390/membranes1010003

Lin, W. C., Lien, C. C., Yeh, H. J., Yu, C. M., and Hsu, S. H. (2013). Bacterial cellulose and bacterial cellulose-chitosan membranes for wound dressing applications. *Carbohydr.te Polym.* 94, 603–611. doi: 10.1016/j.carbpol.2013.01.076

Moreira, C. D. F., Carvalho, S. M., Mansur, H. S., and Pereira, M. M. (2016). Thermogelling chitosan-collagen-bioactive glass nanoparticle hybrids as potential injectable systems for tissue engineering. *Mater. Sci. Eng. C* 58, 1207–1216. doi: 10.1016/j.msec.2015.09.075

Mozetic, P., Giannitelli, S. M., Gori, M., Trombetta, M., and Rainer, A. (2017). Engineering muscle cell alignment through 3D bioprinting. *J. Biomed. Materi. Res.Part A* 105, 2582–2588. doi: 10.1002/jbm.a.36117

Murphy, S. V., and Atala, A. (2014). 3D bioprinting of tissues and organs. *Nat. Biotechnol.* 32, 773–785. doi: 10.1038/nbt.2958

Nardinocchi, P., and Teresi, L. (2016). Actuation performances of anisotropic gels. *J. Appl. Phys.* 120, 1–11. doi: 10.1063/1.4969046

Neal, D., Sakar, M. S., Ong, L.-L. S., and Asada, H. H. (2014). Formation of elongated fascicle-inspired 3D tissues consisting of high-density, aligned cells using sacrificial outer molding. *Lab Chip* 14, 1907–1916. doi: 10.1039/c4lc00023d

Negrini, N. C., Celikkin, N., Tarsini, P., Farè, S., and Święszkowski, W. (2020). Three-dimensional printing of chemically crosslinked gelatin hydrogels for adipose tissue engineering. *Biofabrication* 12:025001. doi: 10.1088/1758-5090/ab56f9

Ng, W. L., Yeong, W. Y., and Naing, M. W. (2016). Polyelectrolyte gelatin-chitosan hydrogel optimized for 3D bioprinting in skin tissue engineering. *Int. J. Bioprint.* 2, 53–62. doi: 10.18063/IJB.2016.01.009

Nieto-Suárez, M., López-Quintela, M. A., and Lazzari, M. (2016). Preparation and characterization of crosslinked chitosan/gelatin scaffolds by ice segregation induced self-assembly. *Carbohydr. Polym.* 141, 175–183. doi: 10.1016/j.carbpol.2015.12.064

Ong, S. Y., Wu, J., Moochhala, S. M., Tan, M. H., and Lu, J. (2008). Development of a chitosan-based wound dressing with improved hemostatic and antimicrobial properties. *Biomaterials* 29, 4323–4332. doi: 10.1016/j.biomaterials.2008.07.034

Piard, C., Baker, H., Kamalitdinov, T., and Fisher, J. (2019). Bioprinted osteon-like scaffolds enhance in vivo neovascularization. *Biofabrication* 11:025013. doi: 10.1088/1758-5090/ab078a

Pok, S., Myers, J. D., Madihally, S. V., and Jacot, J. G. (2013). A multilayered scaffold of a chitosan and gelatin hydrogel supported by a PCL core for cardiac tissue engineering. *Acta Biomater.* 9, 5630–5642. doi: 10.1016/j.actbio.2012.10.032

Pollot, B. E., Rathbone, C. R., Wenke, J. C., and Guda, T. (2017). Natural polymeric hydrogel evaluation for skeletal muscle tissue engineering. *J. Biomed. Mater. Res. Part B Appl. Biomater.* 0075, 1–8. doi: 10.1002/jbm.b.33859

Ravi Kumar, M. N. (2000). A review of chitin and chitosan applications. *React. Funct. Polym.* 46, 1–27. doi: 10.1016/S1381-5148(00)00038-9

Rey-Vinolas, S., Engel, E., and Mateos-Timoneda, M. (2019). "Polymers for Bone Repair," in *Bone Repair Biomaterials*, 2nd Edn. ed J. A. Planell, (Amsterdam: Elsevier Ltd).

Rinaudo, M. (2006). Chitin and chitosan: properties and applications. *Prog. Polym. Sci.* 31, 603–632. doi: 10.1016/j.progpolymsci.2006.06.001

Rodríguez-Vázquez, M., Vega-Ruiz, B., Ramos-Zúñiga, R., Saldaña-Koppel, D. A., and Quiñones-Olvera, L. F. (2015). Chitosan and its potential use as a scaffold for tissue engineering in regenerative medicine. *BioMed Res. Int.* 2015:821279. doi: 10.1155/2015/821279

Rutledge, K., Cheng, Q., Pryzhkova, M., Harris, G. M., and Jabbarzadeh, E. (2014). Enhanced differentiation of human embryonic stem cells on Extracellular matrix-containing Osteomimetic scaffolds for bone tissue engineering. *Tissue Eng. - Part C Methods* 20, 865–874. doi: 10.1089/ten.tec.2013.0411

Schwarz, S., Wong, J. E., Bornemann, J., Hodenius, M., Himmelreich, U., Richtering, W., et al. (2012). Polyelectrolyte coating of iron oxide nanoparticles for MRI-based cell tracking. *NanomedNanotechnol.Bio.Med.* 8, 682–691. doi: 10.1016/j.nano.2011.08.010

Serra, I. R., Fradique, R., Vallejo, M. C. S., Correia, T. R., Miguel, S. P., and Correia, I. J. (2015). Production and characterization of chitosan/gelatin/β-TCP scaffolds for improved bone tissue regeneration. *Mater. Sci. Eng. C* 55, 592–604. doi: 10.1016/j.msec.2015.05.072

Sogias, I. A., Williams, A. C., and Khutoryanskiy, V. V. (2008). Why is chitosan mucoadhesive? *Biomacromolecules* 9, 1837–1842. doi: 10.1021/bm800276d

Sreerekha, P. R., Menon, D., Nair, S. V., and Chennazhi, K. P. (2013). Fabrication of electrospun poly (lactide-co-glycolide)-fibrin multiscale scaffold for myocardial regeneration in vitro. *Tissue Eng. Part A* 19, 849–859. doi: 10.1089/ten.tea.2012.0374

Storti, G., and Lattuada, M. (2017). "Synthesis of bioresorbable polymers for medical applications," in *Bioresorbable Polymers for Biomedical Applications: From Fundamentals to Translational Medicine*, eds G. Perale, and J. Hilborn, (Amsterdam: Elsevier), 153–179. doi: 10.1016/b978-0-08-100262-9.00008-2

Thandapani, G., Supriya Prasad, P., Sudha, P. N., and Sukumaran, A. (2017). Size optimization and in vitro biocompatibility studies of chitosan nanoparticles. *Int. J. Biol. Macromol.* 104, 1794–1806. doi: 10.1016/j.ijbiomac.2017.08.057

Vedadghavami, A., Minooei, F., Mohammadi, M. H., Khetani, S., Rezaei Kolahchi, A., Mashayekhan, S., et al. (2017). Manufacturing of hydrogel biomaterials with controlled mechanical properties for tissue engineering applications. *Acta Biomater.* 62, 42–63. doi: 10.1016/j.actbio.2017.07.028

Yan, Y., Wang, X., Pan, Y., Liu, H., Cheng, J., Xiong, Z., et al. (2005). Fabrication of viable tissue-engineered constructs with 3D cell-assembly technique. *Biomaterials* 26, 5864–5871. doi: 10.1016/j.biomaterials.2005.02.027

Ye, K., Felimban, R., Traianedes, K., Moulton, S. E., Wallace, G. G., Chung, J., et al. (2014). Chondrogenesis of infrapatellar fat pad derived adipose stem cells in 3D printed chitosan scaffold. *PLoS One* 9:e99410. doi: 10.1371/journal.pone.0099410

Conflict of Interest: The authors declare that the research was conducted in the absence of any commercial or financial relationships that could be construed as a potential conflict of interest.

frontiers in Bioengineering and Biotechnology

ORIGINAL RESEARCH
published: 05 May 2020
doi: 10.3389/fbioe.2020.00406

Aged Tendon Stem/Progenitor Cells Are Less Competent to Form 3D Tendon Organoids Due to Cell Autonomous and Matrix Production Deficits

*Zexing Yan[1], Heyong Yin[1], Christoph Brochhausen[2], Christian G. Pfeifer[1], Volker Alt[1] and Denitsa Docheva[1,3]**

[1] Experimental Trauma Surgery, Department of Trauma Surgery, University Regensburg Medical Centre, Regensburg, Germany, [2] Institute of Pathology, University of Regensburg, Regensburg, Germany, [3] Department of Medical Biology, Medical University of Plovdiv, Plovdiv, Bulgaria

Tendons are dense connective tissues, which are critical for the integrity and function of our musculoskeletal system. During tendon aging and degeneration, tendon stem/progenitor cells (TSPCs) experience profound phenotypic changes with declined cellular functions that can be linked to the known increase in complications during tendon healing process in elderly patients. Tissue engineering is a promising approach for achieving a complete recovery of injured tendons. However, use of autologous cells from aged individuals would require restoring the cellular fitness prior to implantation. In this study, we applied an established cell sheet model for *in vitro* tenogenesis and compared the sheet formation of TSPC derived from young/healthy (Y-TSPCs) versus aged/degenerative (A-TSPCs) human Achilles tendon biopsies with the purpose to unravel differences in their potential to form self-assembled three-dimensional (3D) tendon organoids. Using our three-step protocol, 4 donors of Y-TSPCs and 9 donors of A-TSPCs were subjected to cell sheet formation and maturation in a period of 5 weeks. The sheets were then cross evaluated by weight and diameter measurements; quantification of cell density, proliferation, senescence and apoptosis; histomorphometry; gene expression of 48 target genes; and collagen type I protein production. The results revealed very obvious and significant phenotype in A-TSPC sheets characterized by being fragile and thin with poor tissue morphology, and significantly lower cell density and proliferation, but significantly higher levels of the senescence-related gene markers and apoptotic cells. Quantitative gene expression analyses at the mRNA and protein levels, also demonstrated abnormal molecular circuits in the A-TSPC sheets. Taken together, we report for the first time that A-TSPCs exhibit profound deficits in forming 3D tendon tissue organoids, thus making the cell sheet model suitable to investigate the molecular mechanisms involved in tendon aging and degeneration, as well as examining novel pharmacologic strategies for rejuvenation of aged cells.

Keywords: tendon age-related degeneration, tendon stem/progenitor cells, tenogenesis, 3D cell sheet model, tendon regeneration

OPEN ACCESS

Edited by:
Dimitrios I. Zeugolis, National University of Ireland Galway, Ireland

Reviewed by:
Andreas Traweger, Paracelsus Medical University, Austria
Zi Yin, Zhejiang University, China

***Correspondence:**
Denitsa Docheva
denitsa.docheva@ukr.de

Specialty section:
This article was submitted to Tissue Engineering and Regenerative Medicine, a section of the journal Frontiers in Bioengineering and Biotechnology

Received: *10 December 2019*
Accepted: *09 April 2020*
Published: *05 May 2020*

Citation:
Yan Z, Yin H, Brochhausen C, Pfeifer CG, Alt V and Docheva D (2020) Aged Tendon Stem/Progenitor Cells Are Less Competent to Form 3D Tendon Organoids Due to Cell Autonomous and Matrix Production Deficits. Front. Bioeng. Biotechnol. 8:406. doi: 10.3389/fbioe.2020.00406

INTRODUCTION

Tendons are dense connective tissues, which are critical for the integrity and function of our musculoskeletal system (Schiele et al., 2013; Docheva et al., 2015; Costa-Almeida et al., 2019). Tendons are hierarchically organized and have an extracellular matrix (ECM) consisting mainly of collagen type I and a smaller portion of other collagens and proteoglycans (Yan et al., 2018). After injury, tendons need a long period for rehabilitation, especially in aged patients, accompanied with higher failure risk and unsatisfactory repair outcomes (Hirzinger et al., 2014). Tissue aging involves many intrinsic and extrinsic processes and it is frequently linked with tissue degeneration, tendon rupture incidence as well as reduced healing capacity (Gumucio et al., 2014; Schneider et al., 2018; Steinmann et al., 2020). In general, aging is reflected by a decline in organ and tissue homeostasis (de Lucas et al., 2018). Many studies on age-related diseases have revealed that a diminished stem cell pool is responsible for adult tissue degeneration (Zhang et al., 2018). However, the exact molecular mechanism behind tendon aging and degeneration remain by large unclear.

By carrying out a direct comparison between TSPCs derived from young/healthy (Y-TSPC) and aged/degenerative (A-TSPC) Achilles tendons, we have reported that A-TSPCs exhibit in two dimensional (2D) culture profound phenotypic changes with a decline in multiple cellular functions (Kohler et al., 2013). Moreover, microarray analysis showed a distinct transciptomal shift mRNA in A-TSPCs, namely, genes related to cell-cell and cell-matrix contacts, cytoskeleton and cell motility were significantly dysregulated (Kohler et al., 2013). F-actin imaging as well as quantitative kinetic analysis of cytoskeleton turnover, demonstrated that A-TSPCs have accumulation of robust actin stress fiber with slow turnover that correlated with the significantly reduced migratory and *in vitro* would healing potential of these cells (Kohler et al., 2013).

Self-assembled three-dimensional (3D) organoids, whereby cells form connections naturally between each other and to the deposited ECM, are considered as a promising culture models to investigate tissue formation *in vitro*. One widely used scaffold-free approach is the cell pellet model for *in vitro* chondrogenesis. For tenogenesis, more a tube-like cell sheet, composed of a multi-layered cellular architecture and ECM-rich patches, can be fabricated *in vitro* (Ni et al., 2013). These organoids maintain natural microenvironment and own autocrine and paracrine signaling pathways. Our recent results on 3D cell sheets formed by mesenchymal stem cells and TSPCs provided evidences for the suitability of this model to study *in vitro* tenogenic differentiation (Hsieh et al., 2018).

Thus, in this study we hypothesized that A-TSPCs will exhibit significant differences to Y-TSPCs in their potential to form 3D tendon organoids and our aims were first, to characterize the quality of the tendon sheets and second to outline dominant cellular and molecular traits underlying the expected A-TSPC phenotype.

Abbreviations: ACAN, aggrecan; ACTA2, alpha-actin 2; ADSC, adipose-derived stem cell; AR, aspect ratio; A-TSPC, aged tendon stem/progenitor cell; BMSC, bone mesenchymal stem cell; BSA, bovine serum albumin; CDKN2a, cyclin-dependent kinase Inhibitor 2a; COL, collagen; COMP, cartilage oligomeric matrix protein; DCN, decorin; DES, desmin; ELISA, enzyme-linked immunosorbent assay; ECM, extracellular matrix; FMOD, fibromodulin; FN, fibronectin; LPL, lipopretionlipase; NAR, nuclear aspect ratio; OSX, osterix; PBS, phosphate buffered saline; PLOD, procollagen-Lysine,2-Oxoglutarate 5-Dioxygenase 1; RT, room temperature; TEM, transmission electron microscopy; TGFB1, transforming growth factor beta 1; THBS, thrombospondin; TNC, tenascin C; TUNEL, terminal deoxynucleotidyl transferase dUTP nick end labeling; Y-TSPC, young tendon stem/progenitor cell.

MATERIALS AND METHODS

Cell Culture

Primary Y-TSPCs (n = 4) and A-TSPCs (n = 9) were collected from human non-injured Achilles tendon biopsies with an average age of 28 ± 5 years and 61 ± 13 years, respectively, and extensively validated and characterized in 2D culture (Kohler et al., 2013; Popov et al., 2015) (Ethical Grant No. 166-08 of the Medical Faculty of the Ludwig-Maximilians-University, Munich). Details on donor cohort demographics, clinical indications, histological examination, inclusion and exclusion criteria are published in the **Supplementary Information** of Kohler et al. (2013). In short, The Y-TSPC cohort was limited to only n = 4 due to the rarity of such clinical samples. The donors for the A-TSPC cohort were validated for degenerative status by histological examination. For extraction and purification of the cells, the tendon tissue was minced into small pieces, digested with 0.15% collagenase II (Worthington, Lakewood, NJ, United States) enzymatically in culture medium at 37°C overnight, then filtered with sterile nylon mesh (100 μm pore size), and centrifuged at 500 *g* for 10 min. No enrichment step was implemented. Afterward, the pelleted cells were resuspended and expanded in DMEM/Ham's F-12 medium with glutamine (365.3 mg/L), 1 × MEM amino acids, 10% FBS and 1% L-ascorbic acid-2-phosphate. Stem/progenitor character of the cells was verified in Kohler et al. (2013) by FACS and immunohistochemistry for MSC-related markers positive markers CD44, CD73, CD90, CD105, CD146 (pericyte marker), Musashi-1 and STRO-1 as well as negative markers CD19, CD34, CD45, HLA-DR) revealing a very homogeneous populations. Tendon-related genes such as the transcription factors Scleraxis, Eya1, and Six1, the tendon marker gene tenomodulin and several ECM proteins abundant in tendon (collagen types I and III, COMP, decorin, and tenascin C) were validated (Kohler et al., 2013). Self-renewal and tri-lineage differentiation assays were also carried (Kohler et al., 2013). For passaging, 60% confluent cells were detached by trypsin. Cells were used in the study at passage 2–6.

Cell Sheet Formation

The cell sheet protocol, depicted in **Figure 1A**, comprises of a three-step procedure: expansion, stimulation and maturation (Hsieh et al., 2018). The three-step procedure is required for the self-assembly process of the cell sheet with (1) expansion – formation of confluent cell layer; (2) stimulation - for apical deposition of ECM and enrichment cell-ECM interactions

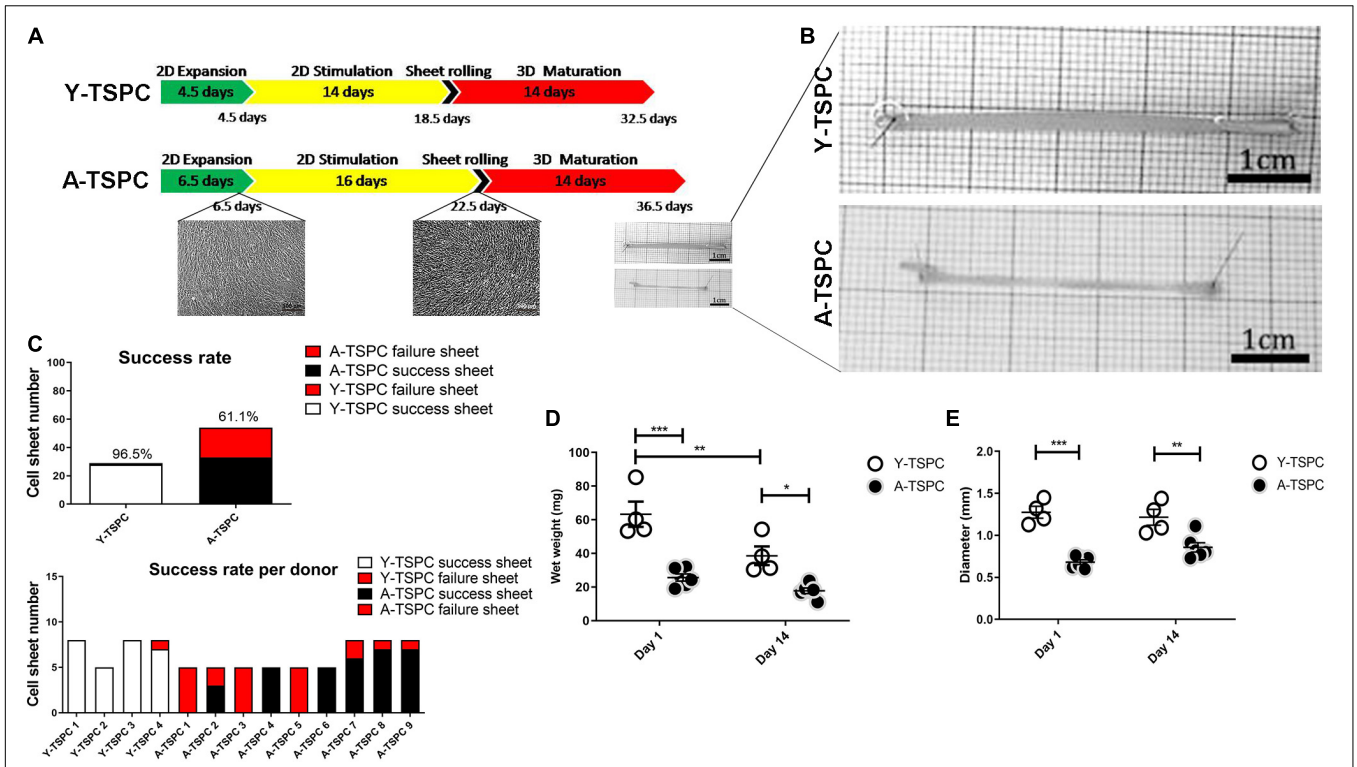

FIGURE 1 | Cell sheet procedure and gross morphological data. **(A)** Cartoon depicting the 3-step protocol for cell sheet formation. **(B)** Representative macroscopy images Y-TSPC and A-TSPC sheets at day 14. **(C)** Success rate of all donors (upper panel) success rate of each individual donor (lower panel). **(D)** Comparison of TSPC sheet wet weight at day 1 and 14. **(E)** Comparison of TSPC sheet diameter at day 1 and 14. Y-TSPC $n = 4$; A-TSPC $n = 9$; $^{*}p < 0.05$, $^{**}p < 0.01$, and $^{***}p < 0.001$.

(glucose for energy supply, and ascorbic acid to serve as anti-oxidant and co-factor for collagen synthesis); and (3) maturation - by tendon specific ECM production and organization in the 3D space (TGF- β3 mediated signaling is critical for tenogenesis (Havis et al., 2014, 2016). In the expansion step, both cell types (8×10^3 cells/cm^2) were cultured in 10 cm^2 cell culture dishes (Falcon, New York, United States) until reaching full confluence in the basic medium. In the stimulation step, cells were supplemented with high glucose DMEM containing 10% FBS and 50 μg/mL ascorbic acid for 14 (Y-TSPCs) or 16.5 days (A-TSPCs). Afterwards, the continuous cell monolayers were detached manually with a cell scraper, rolled into a 3D tube-like cell sheet, stretched 10% manually and fixed with small pins in non-adhesive culture dish (Corning, New York, United States). In the last maturation step, all formed cell sheets were cultured for 14 days in maturation media containing high glucose DMEM with 10 ng/ml TGF-β3 and 50 μg/mL ascorbic acid.

Cell Sheet Wet Weight and Diameter Analysis

Cell sheets wet weight and diameter were measured at day 1 and day 14 of the maturation step. For diameter evaluation, following algorithm was applied: (1) 5–8 sheets/donor were imaged; (2) 6 images/sheet were implemented; 5 diameters/image were measured manually and the mean was calculated; (3) the diameter of each sheet was analyzed as the mean from 6 images; (4) the diameter for each donor was expressed as mean diameter of 5–8 sheets. 4 Y-TSPC cell sheet and 9 A-TSPC cell sheet donors were applied. The quantitative data was processed with GraphPad Prism v.5 software (GraphPad software, CA, United States).

Cell Sheet Fixation and Cryo Cutting

Y-TSPC ($n = 4$ donors) and A-TSPC ($n = 6$ donors) cell sheets (2 sheets/donor) were fixed with 4% paraformaldehyde, cryoprotected with 10, 20, 30% sucrose/phosphate-buffered saline (PBS) gradient (Sigma-Aldrich Corporation, St Louis, United States) and embedded in Tissue-Tek (Sakura Finetek, Alphen aan den Rijn, Netherlands). Cryosections (10 μm thick) were collected with cryotome (Leica, Wetzlar, Germany), and stored until use at −20°C. Prior to staining, sections were equilibrated at room temperature and rehydrated with PBS for 5 min.

H&E (Hematoxylin and Eosin) Staining and Nuclear Angle Deviation Analysis

4 Y-TSPC ($n = 4$ donors) and 6 A-TSPC ($n = 6$ donors), the sheets (1 sheet/donor) were placed in Hematoxylin solution for 3 min, rinsed with 0.1% HCl in PBS for dedifferentiation, washed in tap water for 5 min, immersed in Eosin solution for 3 min (both from Carl Roth, Karlsruhe, Baden-Württemberg,

Germany), rinsed with distilled water for 30 s and covered with Depex (Serva, Heidelberg, Germany). H&E staining images were made with Nikon digital sight DS-U camera mounted at Nikon eclipse TE2000-U microscope (Nikon, Tokyo, Japan) and used for analysis of nuclear angular deviation. Since healthy resident cells in tendon tissue are well aligned to the tensile axis (muscle to bone), this parameter is useful to assess the quality of the 3D sheet organization, and the lesser the deviation the better the alignment. The following algorithm was implemented: (1) 9 images at x20 magnification were taken randomly from each cell sheet; (2) 9 randomly chosen nuclei per image were assessed (81 nuclei/sheet); (3) the angles between the longitudinal axis of the cell sheet and the long axis of the nuclei were determined with the "angular" tool of the AxioVision software v 4.8 (Carl Zeiss, Jena, Germany); (4) 324 and 486 angles for Y- and A-TSPC cohorts were analyzed, respectively; (5) the distribution of nuclear angle deviation for each cell type was generated with GraphPad Prism.

Nuclear Staining and Cell Density Analysis

Cryosections of Y-TSPC (n = 4 donors) and A-TSPC (n = 6 donors) sheets (1 sheet/donor) were rehydrated in water for 5 min, then stained with 4′,6-diamidino-2-phenylindole (DAPI; 1:10 × 10^3 dilution in H2O) for 5 min at room temperature (RT) and fluoroprotected with Mowiol 4-88 (Roth, Karlsruhe, Germany). Fluorescent images were acquired at 20x magnification with an Olympus XC10 camera on an Olympus BX61 fluorescence microscope (Olympus, Japan). In brief, (1) 9 randomly taken DAPI images/sheet were analyzed with ImageJ (v1.45s software National Institutes of Health, Bethesda, MD, United States)[1] software; (2) each image was converted into grayscale by using "threshold" adjustment tool; (3) total nuclear number and the nuclear aspect ratio (NAR) were quantified automatically with "analyze particles" tool; (4) the average cell (nuclei) density/sheet as well as per cell cohort was calculated and expressed per mm; (5) the frequency of different NAR for each cohort was generated with GraphPad Prism. Round cells are represented by NAR value close to 1, while flattened cells near to 0.

F-Actin Staining

Cryosections of Y-TSPC (n = 4 donors) and A-TSPC (n = 6 donors) sheets (1 sheet/donor) were rehydrated in water for 5 min and permeabilizated with 0.2% Triton-X (Sigma-Aldrich) for 30 min at RT. Afterward, 1:200 phalloidin-AF488 in 1%BSA in PBS solution (Sigma-Aldrich) was applied for 60 min at RT. DAPI was used for nuclear counter-staining.

Resazurin Assay and DNA Quantification

Resazurin assay was performed on the last day of the stimulation step according to the manufacturer's instructions (Sigma-Aldrich). Relative immunofluorescence was measured with fluorescent ELISA reader (TECAN, Zurich, Switzerland). Y-TSPC (n = 3 donors) and A-TSPC (n = 3 donors) 2D monolayers (3 dishes/donor) were evaluated.

Cell proliferation was estimated in 3D by DNA quantification of Y-TSPC (n = 3 donors) and A-TSPC (n = 3 donors) sheets (1 sheet/donor). All samples were digested with papain for 16 h at 60°C. Next, the DNA content was quantified by using a PicoGreen DNA kit (Invitrogen, Carlsbad, CA, United States) following the manufacturer's instructions. A standard curve based on known DNA concentration was applied to determine the total DNA content of the samples. Relative immunofluorescence was measured with TECAN.

TUNEL (Terminal Deoxynucleotidyl Transferase dUTP Nick end Labeling) Staining and Quantification

Cell apoptosis was detected by TUNEL staining of Y-TSPC (n = 4 donors) and A-TSPC (n = 6 donors) sheets (one sheet/donor). Samples were treated with 0.2% hyaluronidase (Sigma-Aldrich) for 1 h, and then permeabilized with 0.2% Triton-X. TUNEL reaction was carried out at 37°C for 1 h. Afterward, DAPI counterstaining (1:10 × 10^3 dilution in H_2O) was applied and the samples were mounted for imaging. 10 µl DNase in 70 µl RNA free buffer (Qiagen, Hilden, Germany) was applied. DNA-treated samples were used as a positive control. Apoptotic cell number was measured as follow: (1) 6 images/sheet were randomly taken at x20 magnification; (2) all images were analyzed by ImageJ software; (3) apoptotic cells were counted manually and average number per donor and per cohort were expressed per mm^2.

RNA Isolation, cDNA Synthesis and Real Time Polymerase Chain Reaction (PCR)

Y-TSPC (n = 3 donors) and A-TSPC (n = 3 donors) sheets (1 sheet/donor) were snap frozen ad cryocrushed, then used for total RNA extraction with Qiagen RNeasy Mini kit (Qiagen) following the manufacturer's instructions. For cDNA synthesis, 0.5 µg total RNA/sample and Transcriptor First-Strand cDNA Synthesis Kit (Roche, Mannheim, Germany) were used. Custom-designed Real-Time PCR plates with 48 different genes (**Table 1**) in format of 96-well/32+ by Bio-Rad (Bio-Rad Laboratories, Hercules, CA, United States) were implemented according to the manufacturer's instructions and our previously described protocols (Yin et al., 2019). Gene expression differences were calculated with the ΔΔCT method and presented as fold change of A-TSPC group to Y-TSPC group (control). Hypoxanthine-guanine phosphoribosyltransferase 1 gene (HPRT1), low abundant but also very stable, was implemented as housekeeper in calculating ΔCT. The CT values of HPRT1 were also used as indicative of gene abundance. The average CT value of HPRT1 was 27 (n = 6). From the 48 target genes, 38 genes had CT values lower than HPRT1. Threshold of HPRT1 Ct (27) + 3 Ct ≥ 30 Ct was set and genes with Ct ≥ 30 were considered not detectable or very low abundant, and therefore without fold change calculation. For cell senescence analysis, Real Time PCR for p16, p21, and p53 genes (**Table 2**) was performed as described by Kohler et al. (2013).

[1] https://imagej.nih.gov/ij/

TABLE 1 | Genes included in Real Time PCR Ready Custom Designed Plates analyzed in this study.

Target gene	Abbreviation	Category
Early growth response 1	EGR-1	Tendon transcription factor
Early growth response 2	EGR-2	Tendon transcription factor
Eyes absent homolog 1	EYA1	Tendon transcription factor
Eyes absent homolog 2	EYA2	Tendon transcription factor
Mohawk homeobox	MKX	Tendon transcription factor
Scleraxis homolog A	SCXA	Tendon transcription factor
SIX homeobox1	SIX1	Tendon transcription factor
SIX homeobox2	SIX2	Tendon transcription factor
Collagen, type I, alpha 1	COL1A1	Collagen gene
Collagen, type III, alpha 1	COL3A1	Collagen gene
Collagen, type V, alpha 1	COL5A1	Collagen gene
Collagen, type VI, alpha 1	COL6A1	Collagen gene
Collagen, type XII, alpha 1	COL12A1	Collagen gene
Collagen, type XIV, alpha 1	COL14A1	Collagen gene
Collagen, type XV, alpha 1	COL15A1	Collagen gene
Asporin	ASPN	Collagen cross-linker gene
Lysyl oxidase	LOX	Collagen cross-linker gene
Procollagen-Lysine,2-Oxoglutarate 5-Dioxygenase 1	PLOD1, LH1	Collagen cross-linker gene
Biglycan	BGN	Tendon-related matrix gene
Decorin	DCN	Tendon-related matrix gene
Ephrin type-A receptor 4	EPHA4	Tendon-related matrix gene
Fibromodulin	FMOD	Tendon-related matrix gene
Fibronectin 1	FN1	Tendon-related matrix gene
Lumican	LUM	Tendon-related matrix gene
Proteoglycan 4	PRG4	Tendon-related matrix gene
Tenascin C	TNC	Tendon-related matrix gene
Thrombospondin 2	THBS2	Tendon-related matrix gene
Thrombospondin 4	THBS4	Tendon-related matrix gene
Tenomodulin	TNMD	Tendon-related matrix gene
Aggrecan	ACAN	Other lineage gene
Collagen, type II, alpha 1	COL2A1	Other lineage gene
Alpha-actin-2	ACTA2,α-SMA	Other lineage gene
Cartilage oligomeric matrix protein	COMP	Other lineage gene
Desmin	DES	Other lineage gene
Integrin-binding sialoprotein	IBSP	Other lineage gene
Fucosyltransferase 4	FUT4	Other lineage gene
Lipoprotein lipase	LPL	Other lineage gene
Myogenic differentiation 1	MYOD1	Other lineage gene
Myogenin	MYOG	Other lineage gene
Nanog homebox pseudogene 8	NANOG	Other lineage gene
Octamer-binding transcription factor 4	Oct4, Pou5f1	Other lineage gene
Peroxisome proliferator-activated receptor gamma	PPARG	Other lineage gene
Runt-related transcription factor 2	RUNX2	Other lineage gene
Transcription factor Sp7	SP7, Osterix	Other lineage gene
SRY (sex-determining region Y)-box 9	SOX9	Other lineage gene
Transcription factor AP-2 alpha	TFAP2A	Other lineage gene
Transforming growth factor beta 1	TGF-β1	Other lineage gene
Transglutaminase 2	TGM2	Other lineage gene
Beta-2-Microglobulin	B2M	Reference gene
Glyceraldehyde 3-phosphate dehydrogenase	GAPDH	Reference gene
Hypoxanthine-guanine phosphoribosyltransferase 1	HPRT1	Reference gene

TABLE 2 | PCR for senescence-related genes p16, p21, p53.

Target gene	Primers	Annealing temperature [°C]	Cycle number	References
p16	F 5′-caacgcaccgaatagttacg-3′	57	35	Le Frere-Belda et al., 2004
	R 5′-agcaccaccagcgtgtc-3′			
p21	F 5′-gaacttcgactttgtcaccgag-3′	60	30	Alcantara et al., 2001
	R 5′-cgttttcgaccctgagagtctc-3′			
p53	F 5′-aaggaaatttgcgtgtggag-3′	58	35	Gan et al., 2005
	R 5′-ttctgacgcacacctattgc-3′			

Collagen I Immunofluorescent Staining and Enzyme-Linked Immunosorbent Assay (ELISA)

Cryosections of Y-TSPC (n = 4 donors) and 6 A-TSPC (n = 6 donors) sheets (1 sheet/donor) were treated for antigen retrieval with 1% pepsin for 15 min at RT blocked by 1% bovine serum albumin (BSA) for 1 h, and incubated with primary anti-collagen type I antibody (Sigma-Aldrich, Cat. Nr. C2456, 1:200 dilution) overnight at 4°C. Next day, anti-mouse FITC secondary antibody (Sigma-Aldrich) was applied for 1h at RT, and last DAPI counterstaining was done for 5 min. Fluorescent images were acquired with an Olympus XC10 camera on an Olympus BX61 fluorescence microscope. The amount of deposited collagen I protein was detected by ELISA. 3 Y-TSPC and 5 A-TSPC donors analyzed (1 sheet/donor). First, total protein was extracted with 10 μg/ml pepsin and 1 mg/mL elastase. Next, collagen I Elisa kit (Chondrex, Redmond, WA, United States) was used according to the manufacturer's instruction. The data was expressed as total collagen I content/DNA.

Transmission Electron Microscopy (TEM)

Transmission electron microscopy was applied to detect the ultrastructure of Y-TSPC (n = 3 donors) and A-TSPC (n = 5 donors) cell sheets. One cell sheet per donor was prepared for TEM analyses. After rinsing with PBS, samples were fixed with Karnovsky-fixatives (0.1M cacodylate-buffer with 2.5% glutaraldehyde and 2% paraformaldehyde), then enclosed within 4% low melting agarose, post-fixed with 1% osmium tetroxide at pH 7.3, dehydrated in graded ethanol, embedded in EMbed-812 epoxy resin (Science Services, Munich, Germany) and finally

polymerized for 48 h at 60°C into an EPON block. Each cell sheet was halved and embedded for longitudinal or cross-sectional cutting. Semithin sections from 0.75 μm thickness were cut and stained with toluidine blue and basic fuchsine. After selection of appropriate areas of interest, the EPON block was trimmed and ultrathin sections (80 nm thickness) were cut on Reichert Ultracut-S ultramicrotome (Leica, Bensheim, Germany). Sections were mounted on grids and stained with aqueous 2% uranyl acetate and lead citrate solution for 10 min each. Next, the sections were examined with a LEO912AB electron microscope (Zeiss, Oberkochen, Germany) operating at 100 kV. Images were taken with a side-mounted 2k x 2k-CCD-camera (TRS, Moorenweis, Germany). The number of elongated cells and apoptotic cells (images of 80 × 80 μm^2), as well as the diameter of the collagen fibers (images of 4 × 4 μm^2) were evaluated as follows: (1) 6 images/donor were implemented; (2) all images were analyzed by ImageJ; (3) each image was converted to grayscale by using "threshold" adjustment; (4) the number of elongated cells, apoptotic cells and collagen fibrils were counted manually and the data was expressed as the mean of counted objects per image area per donor; (5) the diameter of collagen fibrils was measured by "straight" tool manually as 20 randomly chosen fibrils per image were assessed (6 images/donor; 120 fibrils/donor; 360 fibrils for Y-TSPC group and 600 fibrils for A-TSPC group were analyzed); (6) the collagen diameter distribution per group was expressed by calculating the frequency of fibrils with different diameters (total of 360 fibrils for Y-TSPC group and total of 600 fibrils for A-TSPC group). In **Figures 4**, **5** representative images of Y-TSPC (n = 3 donors) and A-TSCP n = 5 (donors) are shown. GraphPad Prism v.5 software was used for quantitative data analyses and graphical data expression.

Statistics

GraphPad Prism v.5 software was used for expressing quantitative data and estimation of statistical significance. Unless distribution and frequency data, all data shows individual donors (dot plot) and mean values and standard deviations for each cohort. Statistical testing was performed with unpaired t-test. Difference were considered statistically significant when $^{*}p < 0.05$, $^{**}p < 0.01$, and $^{***}p < 0.001$.

RESULTS

A-TSPC Showed Inferior Sheets Formation With Higher Failure Rate

In the first expansion step, A-TSPCs needed 2 more days to reach full cell confluence than Y-TSPCs. In the stimulation step, Y-TSPCs took 14 days to form a cell sheet, whilst A-TSPCs required 16.5 days (**Figure 1A**). The gross appearances of sheets from both cell types were evaluated and compared (**Figure 1B**), showing that A-TSPC sheets were much thinner and smaller than Y-TSPC sheets. Then, as mentioned in the Materials and Methods, 4 Y-TSPC donors and 9 A-TSPC donors were used in the study, and the total success rate for Y-TSPC sheet formation was 96.5% with only 1 failed sheet from Y3-TSPC donor (ruptured) because of the over stretching when handled. In contrast, for the A-TSPC group the overall success rate of sheet formation was only 61.1% and certain donors namely A1-, A3-, and A5-TSPC being unable to form any sheet (**Figure 1C**). Next, cell sheet diameter and wet weight at day 1 and 14 were measured confirming that A-TSPC sheets were significantly smaller and lighter than Y-TSPC sheets at both the time points (**Figures 1D,E**).

A-TSPC Sheets Had Lower Cell Density, Disorganized Matrix and Poor Cell Alignment

The general tissue morphology of the cell sheets was revealed by H&E staining (**Figure 2A**) and analysis of the angle of nuclear deviation (**Figure 2B**). A-TSPC cells formed an inferior cell sheet with less matrix deposition and frequent gaps. Y-TSPC formed bigger cell sheet containing a large amount of aligned fibrous matrix with higher number of spindle-like shaped cells. In addition, the cells in the A-TSPC sheets were sparser and rounded compared to the Y-TSPC group. Cell orientation was assessed by estimating the angular deviation of the cell nuclei to the axial axis of the cell sheet. The results showed that in the Y-TSPC group, over 60% of the nuclei deviated 0° to 20° from the axial axis, and the average nuclear angle was 15.69°. In contrast, in the A-TSPC group, less than 30% of the nuclei deviated from 0° to 20°, and the average nuclear deviation was nearly twofold increased to 29.95°. Next, the cell density and frequency distribution of the nuclei aspect ratio, which represents the nuclei flattening, were quantified (**Figures 2C–E**) and revealed a significantly lower cell density in the aged group. Moreover, A-TSPC sheets contained significantly higher frequency of cells with NAR 0.8-0.9 corresponding to roundish cells. Analyses of the cell cytoskeleton via phalloidin fluorescent staining confirmed worse cell elongation and cytoskeletal organization in the A-TSPC group than the Y-TSPC group (**Figure 2F**).

A-TSPC Sheets Showed Reduced Metabolic and Proliferative Activities, Whilst Augmented Apoptosis, Senescence

For cell proliferation, Resazurin assay was carried out at the 2D cell monolayer level prior to sheet formation (day 18.5 for Y-TSPCs and day 22.5 for A-TSPC), followed by DNA content quantification. DNA was also quantified at the 3D cell sheet level at day 1 and day 14 (**Figures 3A–C**). The results showed that A-TSPC group contained significantly lower cell amount than Y-TSPC group, paralleled by significantly higher metabolic cell activity, in the 2D step. At the 3D level, the data suggested that after the collection of the cell sheets in the A-TSPC group there is further cell loss. In contrast, in the period day 1 to day 14 at the 3D level cell proliferation occurred in the Y-TSPC sheets as indicated by an increase in DNA content. Furthermore, TUNEL staining of Y-TSPC and A-TSPC cell sheets revealed that A-TSPC sheets have significantly more apoptotic cells than Y-TSPC sheets (**Figures 3D,E**). Cell senescence analysis was performed by quantitative PCR for the expression of cell cycle regulator genes

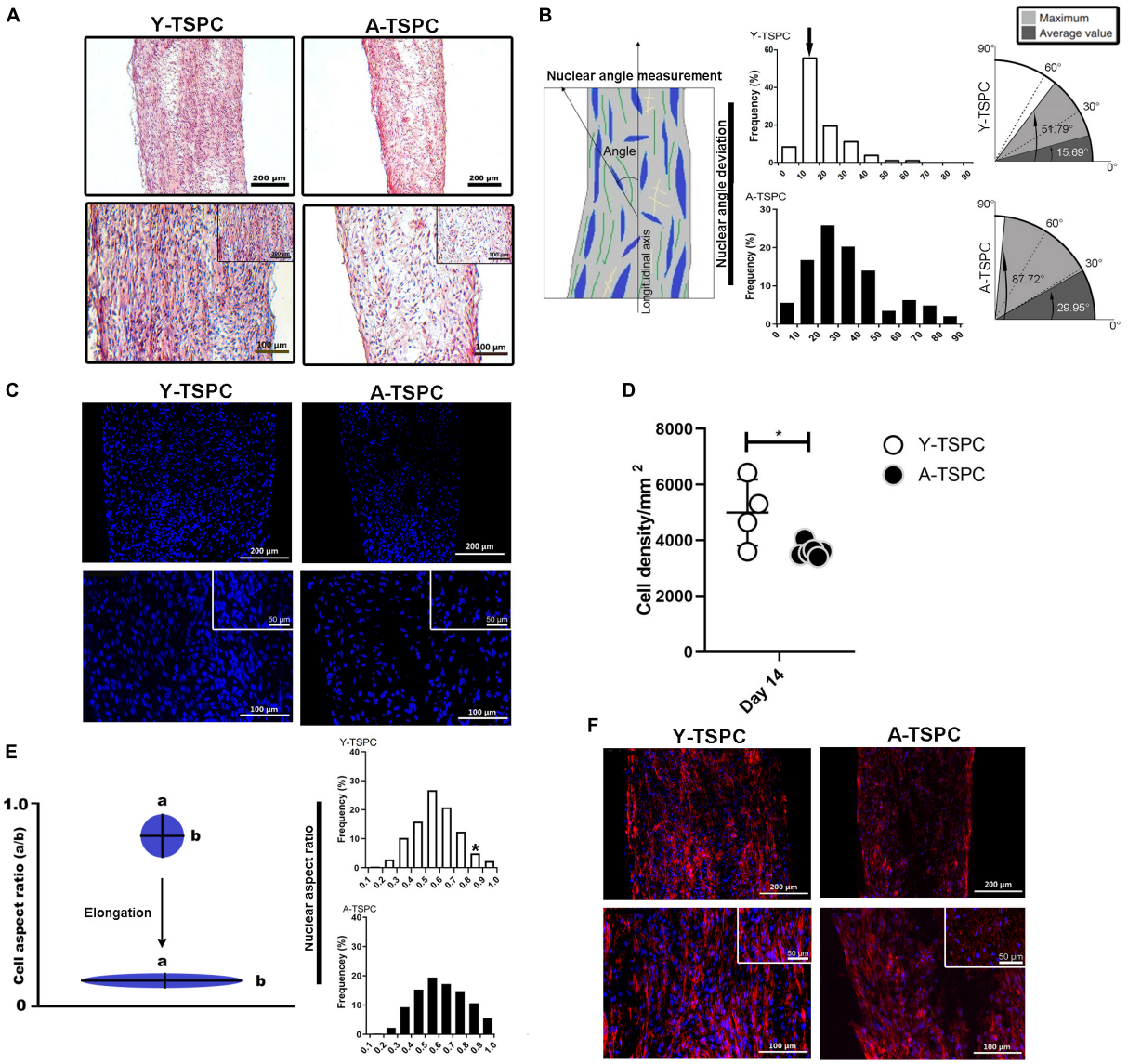

FIGURE 2 | Y-TSPC and A-TSPC histomorphometrical analyses. **(A)** Representative H&E images of Y-TSPC and A-TSPC sheets at day 14. **(B)** Frequency distribution of nuclear angle deviation (left panel) as well as maximum and average values of angular deviation (right panel, virtual angle between cell sheet longitudinal axis and nuclear axis). The arrow indicates the higher frequency of nuclear deviation of 10°–20° deviation in the Y-TSPC sheets. **(C)** Representative images of nuclear staining via DAPI (blue color) of Y-TPSC and A-TPSC sheets. **(D)** Average cell density of both groups. **(E)** Frequency distribution of NAR (nuclear aspect ratio, nucleus width versus length). The arrow indicates the higher tendency of NAR 0.8-1 (round cells) in A-TSPC group. (F) Representative F-actin images of Y-TSPC and A-TSPC sheets at day 14. Y-TSPC $n = 4$; A-TSPC $n = 6$; $^*p < 0.05^*$.

p16, p21, and p53 and it demonstrated a significant upregulation of p16 and p21 in the A-TSPC sheet group (**Figure 3F**).

A-TSPC Sheets Exhibited a Profound Phenotype at the Ultrastructural Level

The ultrastructure of Y-TSPC and A-TSPC sheets was revealed by TEM. In Y-TSPC sheets, cells appeared elongated and in many locations organized in parallel rows compared to A-TSPC sheets (**Figures 4a–l**). In addition, Y-TSPC sheets had higher cellular density (**Figures 4a–c**); the ECM was rich in collagen type I fibrils that were densely packed (**Figures 5a–c**). In contrast, A-TSPCs exhibited a rounded morphology within the sheets as well as their ECM was less dense and contained few sparsely distributed collagen fibrils (**Figures 4g–l**, **5g–i**). In the Y-TSPC sheets, plasmalemma vesicles at the cell membrane (**Figure 5d**) as well as cell protrusions (**Figures 4d–f**) and cell-cell contacts (**Figure 5e**) were frequently detected. They were also visible in A-TSPC sheets but very rarely (**Figures 4j–l**, **5j,k**). Interestingly, A-TSPC sheets contained multiple apoptotic bodies indicative of cells that undergo programmed cell death (**Figures 4g–i**, **5l**). Apoptotic cells were rare in sheets formed by Y-TSPCs

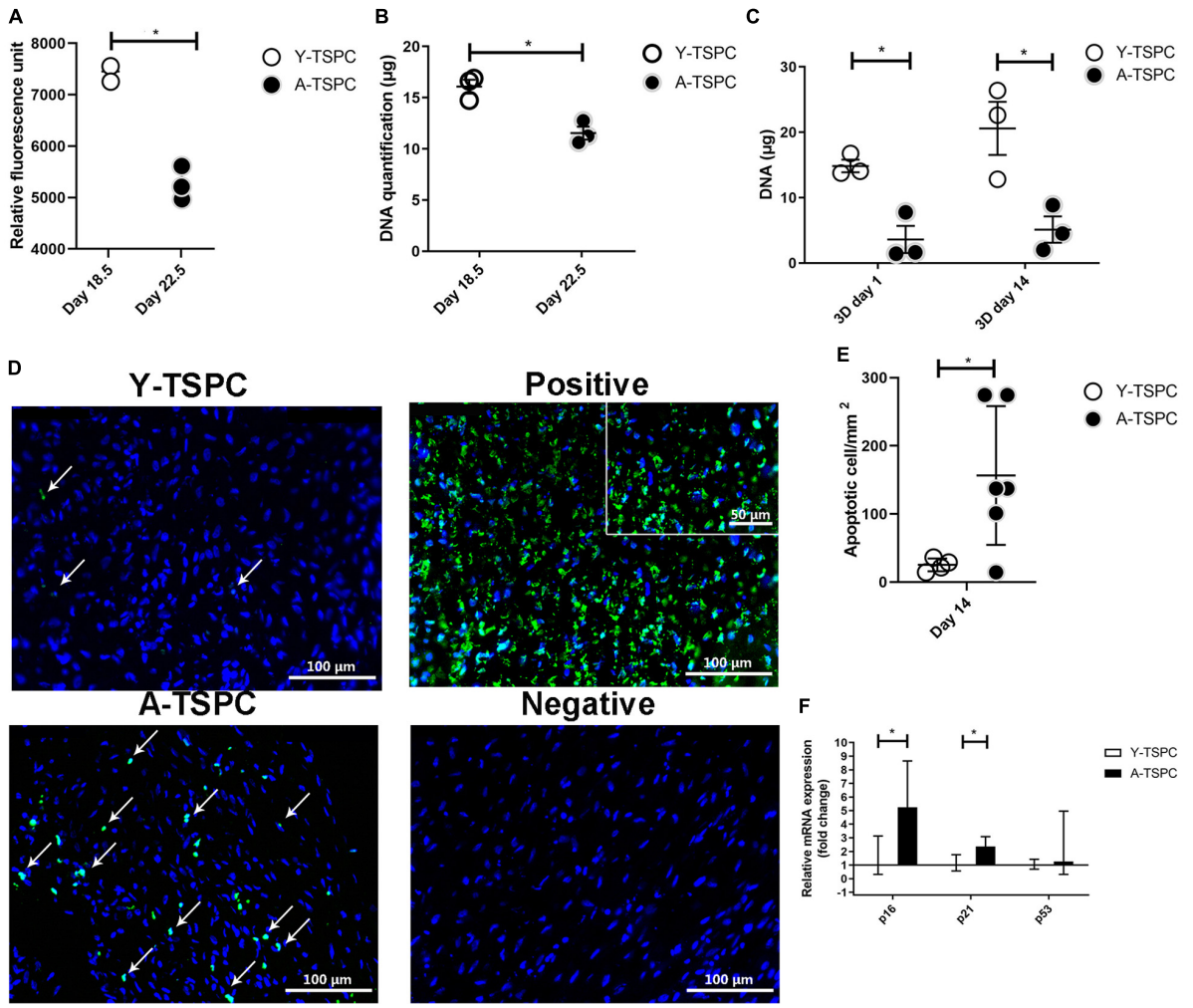

FIGURE 3 | Quantitative analyses of cell proliferation, apoptosis and senescence. **(A,B)** Resazurin assay and DNA quantification at 2D prior sheet collection. **(C)** DNA quantification at 3D day 1 and day 14. **(D)** Representative TUNEL/DAPI images at 3D day 14. Apoptotic cells appear in green. Positive control with DNase treated. Negative control with label solution only (without terminal transferase). **(E)** Quantification of average apoptotic cell number in the sheets at day 14. **(F)** Quantitative PCR analysis of p16, p21, and p53. Y-TSPC $n = 4$; A-TSPC $n = 6$; $^{*}p < 0.05$ and $^{***}p < 0.001$. For PCR, Y-TSPC $n = 3$; A-TSPC $n = 3$.

(**Figures 4a–c**, **5f**). However, both types of cells however were comparable regarding vacuoles and mitochondria (**Figures 4d–f,j–l**, **5d,e,j,k**). Next, quantification analysis of TEM image data confirmed the above observation and clearly showed that A-TSPC sheets had a significantly reduced number of elongated cells and collagen fibrils, but significantly increased number of apoptotic cells (**Figures 6A,B,D**). Regarding collagen fibril diameter distribution, both types of cell sheet were comparable with fibril diameter spanning 10–50 nm (**Figure 6C**). In all, the TEM analyses strongly confirmed the profound phenotype of the A-TSPC sheet at the ultrastructural level.

A-TSPC Sheets Contained Lower Collagen I Protein

In addition, to the TEM analysis, collagen type one deposition was further validated by conducting collagen I immunofluorescence staining and ELISA (**Figures 7A,B**). Our results clearly demonstrated that A-TSPC sheets had significantly lower collagen I protein content than Y-TSPC sheets.

A-TSPC Sheets Displayed Abnormal Gene Expression Profile

Real-time PCR for 48 different genes (**Table 1**) was carried out with mRNA/cDNA collected from Y-TSPC and A-TSPC sheets at day 14. Gene markers for other lineages, namely for cartilage - collagen 2a1 (COL2A1) (cartilage); for muscle – desmin (DES), myogenic differentiation 1 (MYOD1) and myogenin (MYOG); for bone – Sp7 (SP7, Osterix) and integrin-binding sialoprotein (IBSP); for fat – AP-2 alpha (TFAP2A) and lipoprotein lipase (LPL); and for embryonic lineage – Nanog homebox pseudogene 8 (NANOG) were not detectable. Several genes that are tendon-related – early growth response protein 2 (EGR2), eyes absent homolog 1 (EYA1), transglutaminase 2 (TGM2) and tenomodulin (TNMD) were also not detectable or very low

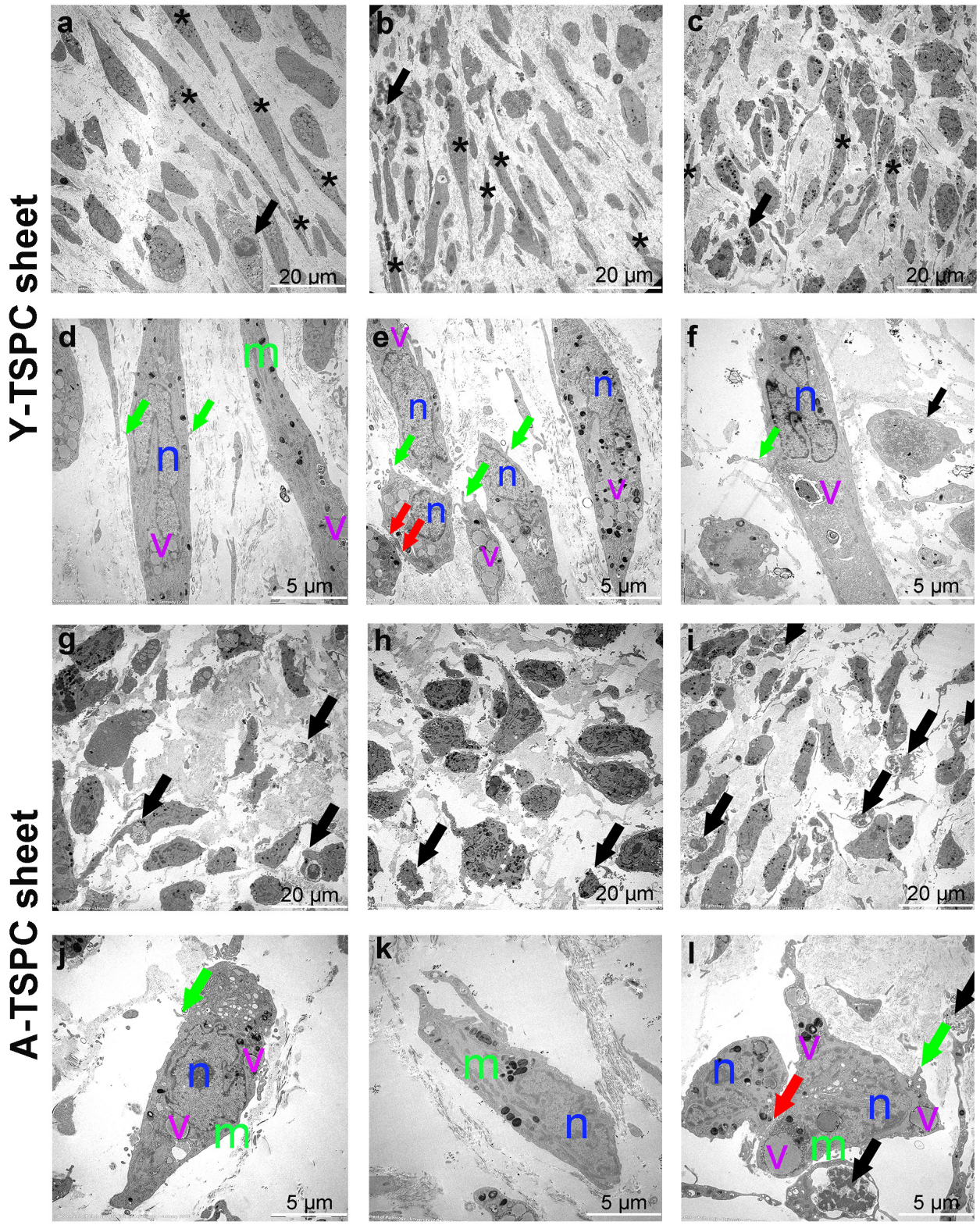

FIGURE 4 | Representative transmission electron microscopy (TEM) images of Y-TSPC and A-TSPC sheets. **(a–c)** Y-TSPC sheet cell arrangement, cell density and morphology. **(d–f)** Close view of Y-TSPC morphology and cell protrusions. **(g–i)** A-TSPC sheet cell arrangement, cell density and morphology. **(j–l)** Close view of A-TSPC morphology and cell protrusions. Black arrows, apoptotic cells; green arrows, cell protrusions; red arrows, cell–cell contact; m, mitochondria; n, nucleus; v, vacuoles; *, longitudinal cell; Y-TSPC $n = 3$, A-TSPC $n = 5$ were investigated.

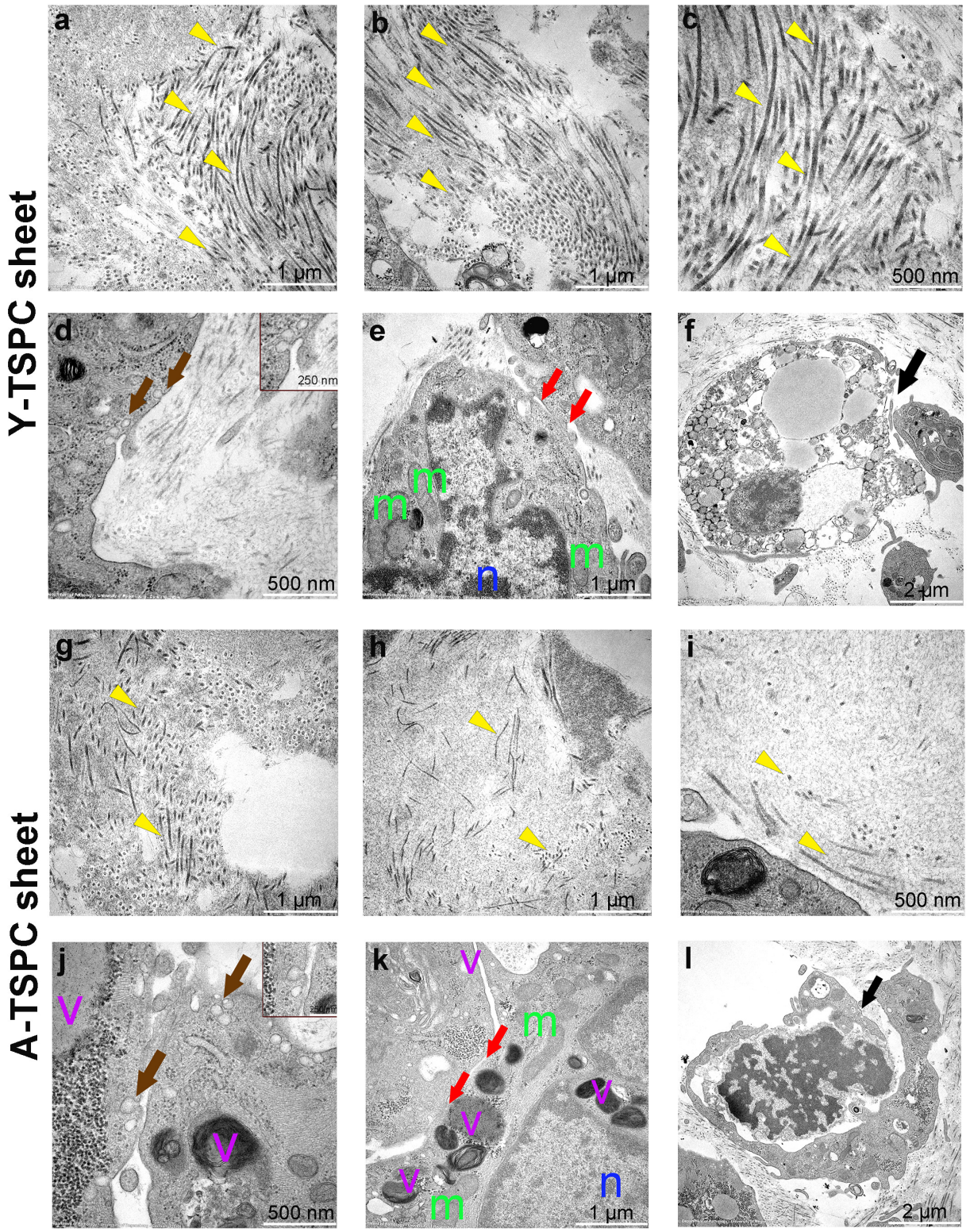

FIGURE 5 | Representative transmission electron microscopy (TEM) images of Y-TSPC and A-TSPC sheets. **(a–c)** Y-TSPC sheet collagen fibrils. **(d)** Y-TSPC sheet plasmalemma vesicles at the cell membrane. **(e)** Y-TSPC sheet cell-to-cell contacts between cells. **(f)** Y-TSPC sheet close view of apoptotic bodies. **(g–i)** A-TSPC sheet collagen fibrils. **(j)** A-TSPC sheet plasmalemma vesicles at the cell membrane. **(k)** A-TSPC sheet cell-to-cell contacts between cells. **(l)** A-TSPC sheet close view of apoptotic bodies. Arrow head, collagen fibrils; black arrows, apoptotic cells, brown arrows, plasmalemma vesicles; red arrows, cell–cell contact; m, mitochondria; n, nucleus; v, vacuoles; Y-TSPC $n = 3$, A-TSPC $n = 5$ were investigated.

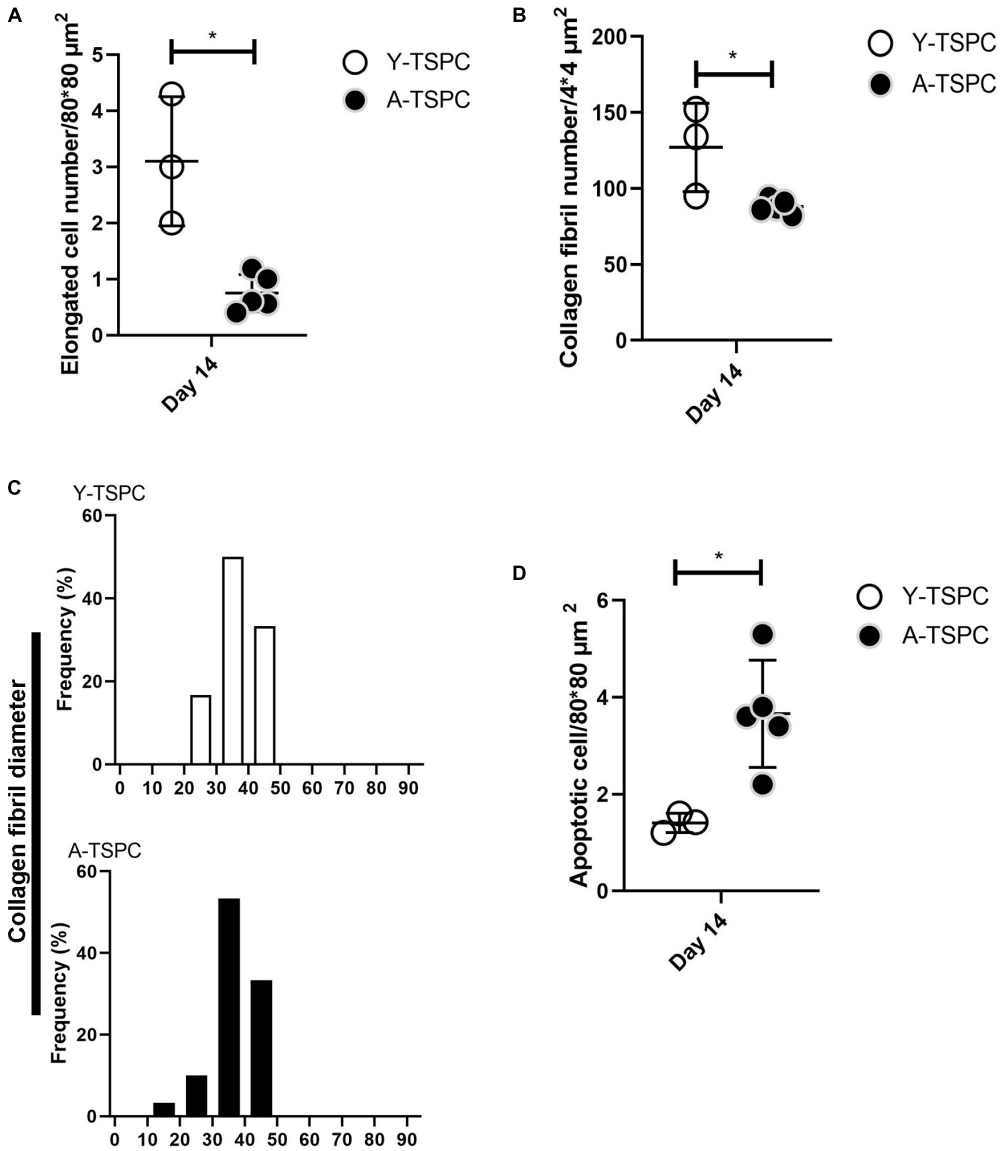

FIGURE 6 | Quantification of elongated cells **(A)**, collagen fibrils and diameter distribution **(B,C)** and apoptotic cell numbers **(D)** from TEM images. Y-TSPC $n = 3$; A-TSPC $n = 5$; for **(A,B,D)**, 6 images/donor were analyzed; for **(C)** 20 randomly chosen fibrils per image were assessed; $^*p < 0.05$.

abundant. The mRNA levels of tendon transcription factors (**Figure 7C**) were comparable between the two groups. Several collagen genes namely collagen 1a1 (COL1A1), collagen 3a1 (COL3A1), collagen 5a1 (COL5A1), collagen 6a1 (COL6A1), collagen 15a1 (COL15A1), had significantly lower expression in the A-TSPC sheets (**Figure 7D**). In addition, a gene related to collagen cross-linking such as procollagen-lysine, 2-oxoglutarate 5-dioxygenase 1 (PLOD1) and the matrix proteoglycans decorin (DCN), fibromodulin (FMOD), fibronection (FN), tenascin C (TNC) and thrombospondin 2 were also significantly downregulated in the A-TSPC sheets (**Figures 7E,F**). Regarding other lineage related genes, three genes aggrecan (ACAN), alpha-actin 2 (ACTA2), cartilage oligomeric matrix protein (COMP) were also found to be expressed to a lower extent in the A-TSPC group (**Figure 7G**). Altogether, this data demonstrated a fundamental matrix synthesis problem in the A-TSPC sheets.

DISCUSSION

Tendon injuries, which associate closely with aged-related tissue degeneration present great challenges to orthopedic and trauma surgery departments. Aged-related tissue degeneration has been previously linked to impaired functions of tissue-resident stem/progenitor cells (Smith et al., 2002; Rees et al., 2006; Asai et al., 2014). Han et al. suggested that with donor aging smooth muscle-derived MSCs have greatly diminished self-renewal and proliferation abilities but augmented senescence

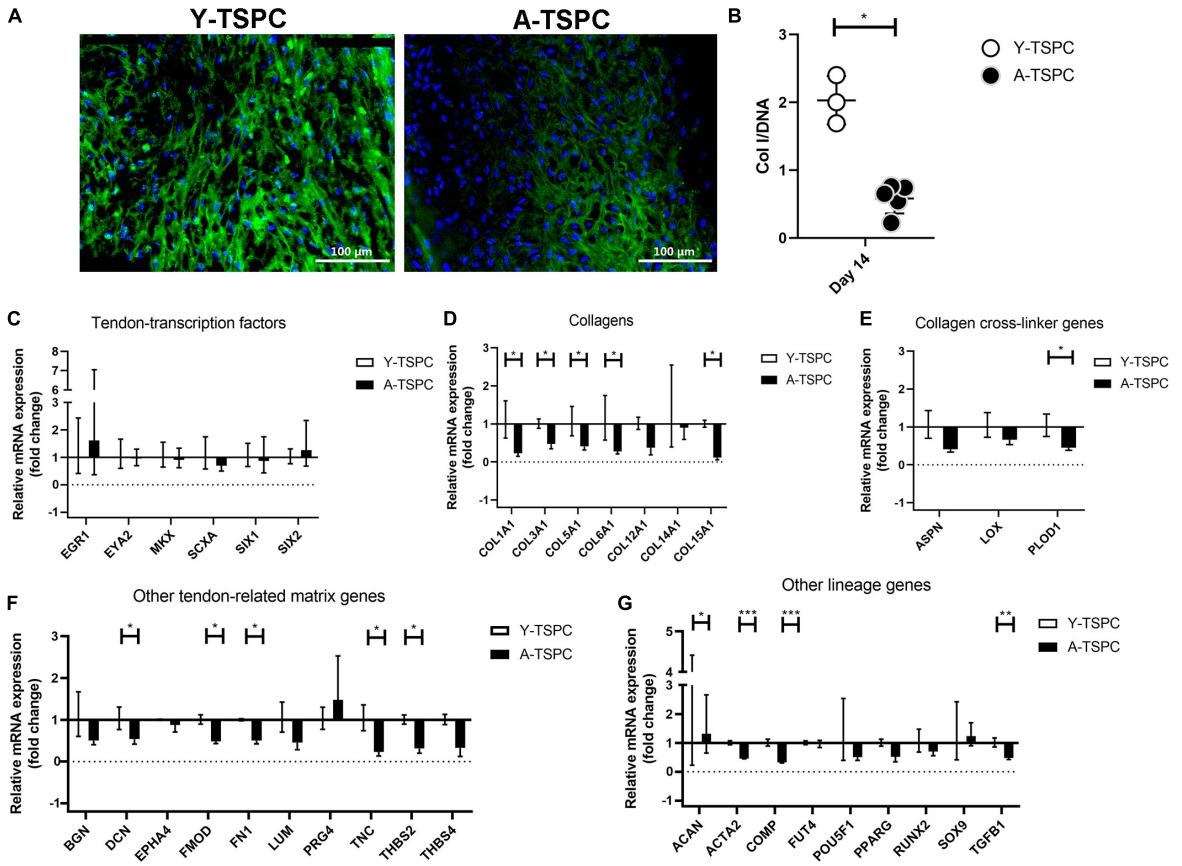

FIGURE 7 | Collagen I protein production and gene expression profiling by Real Time PCR. **(A)** Representative collagen I immunofluorescent images of Y-TSPC and A-TSPC sheets at day 14. **(B)** Quantitative analysis of collagen I by ELISA. For **(A,B)** Y-TSPC $n = 3$; A-TSPC $n = 6$. Normalization to DNA. Quantitative PCR analysis for tendon-transcription factors **(C)**, collagen genes **(D)**, cross-linker genes **(E)**, tendon-related ECM genes **(F)** other lineage genes **(G)**. Gene expression was calculated as fold change to Y-TSPC group. GAPDH was used as reference gene in each group. Non-detectable (Ct over 38 genes were not included in the graphs. For **(C–G)** Y-TSPC $n = 3$; A-TSPC $n = 3$; $^{*}p < 0.05$, $^{**}p < 0.01$, and $^{***}p < 0.001$.

(Han et al., 2010). In order to investigate how aging affects TSPCs, we compared the phenotypic difference between Achilles tendon-derived Y-TSPC from young/healthy and A-TSPC from aged/degenerative human donors. Our previous data in 2D culture, revealed that A-TSPC had a significantly reduced cell adhesion, migration and self-renewal abilities with distinct clonogenic deficits and premature entry into senescence (Kohler et al., 2013), suggesting that the TSPC pool is becoming exhausted in terms of size and functional fitness during tendon age-related degeneration.

Here, we applied a previously established cell sheet model (Hsieh et al., 2018) for *in vitro* tenogenesis and compared the sheet formation of Y-TSPCs and A-TSPCs with the purpose of unraveling differences in their potential to form 3D tendon organoids. Formation of cell sheets is an alternative scaffold-free approach to build an abundant ECM niche without elimination of the native connections between cells to cells and cells to ECM. Furthermore, the cell multilayer contains a natural microenvironment and maintains its own autocrine and paracrine signaling (Hsieh et al., 2018). Several growth factors such as members of the Transforming Growth Factor beta family, TGF-β1, β2, and β3, have been reported to be critical for tendon tissue formation, function and healing (Pryce et al., 2009; Maeda et al., 2011; Havis et al., 2014; Tan et al., 2020). Connective Tissue Growth Factor (CTGF) has also been linked to tenogenesis; for example, it is pro-tenogenic factor of adipose-derived stem cells (Shen et al., 2018; Li et al., 2019). Interestingly, Yin et al. (2016) have combined CTGF and TGF-β1 in a step-wise manner, which led to augmented tenogenic differentiation of MSCs, as well as to tendon-like tissue formation in the repair process of rat patella tendon defect. CTGF alone or in combination with TGF-β has also been associated with fibrocartilage formation in meniscal injury models (Lee et al., 2014; Tarafder et al., 2019). Therefore, as well as to minimize costs, we designed our study with administration of only one growth factor from the TGFβ family. However, it will be of great importance in follow up research to investigate the synergistic action of CTGF and TGFβ in the 3D tendon cell sheet model, which may result in quicker maturation of the cell sheets.

In the present study, our results clearly showed that A-TSPCs exhibit profound deficits in forming 3D tendon tissue organoids.

There are several possible explanations: A-TSPC sheets have (1) reduced cell proliferation; (2) augmented cell apoptosis and senescence; and (3) less ECM production.

Tissue and organ aging has a strong relationship with stem cell proliferation ability, apoptosis and senescence. Kasper et al. (2009) reported that the size of MSCs pool reduces in aged animals, compared to young animals. Yu et al. (2011) demonstrated that aged rhesus macaque BMSCs require longer population doubling time due to decreased proliferation capacity. In our study, cell proliferation was tested prior to sheet collection and at day 1 and 14, revealing that A-TSPC sheets have significantly lower cell density and proliferation rate than Y-TSPC sheets. Kawakami et al. (2019) communicated that progeroid mice contained higher numbers of apoptotic muscle stem/progenitor cells. Taylor et al. (2003) showed that in human colonic crypts, age-related DNA mutations are associated with stem cell apoptosis. By performing TUNEL assays for DNA damage, we observed that the A-TSPC sheets also contain more apoptotic cells than the Y-TSPC group. Furthermore, we found that senescence-related gene markers namely p16 and p21 (Campisi, 2005) were significantly upregulated in the A-TSPC group, This finding is in line with skeletal muscle aging, where local stem cells undergo a dysregulation in p16 signaling that is directly related to an augmentation in muscle tissue senescence. Interestingly, reducing p16 expression might be a way to postpone tissue and organ aging (Baker et al., 2011). Silencing of p16 expression can reduce the number of senescent cells thus restoring the regenerative potential of muscle tissue, which was shown by Sousa-Victor et al. (2014). In all, the above results indicated that A-TSPC 3D sheets, characterized with a lower cell density and proliferation potential, whilst having higher cell apoptosis and senescence, are significantly inferior then Y-TSPC sheets.

Tendon ECM is very fibrous and organized in parallel collagen fibers. Roughly 95% of the collagen is type I, with small levels of collagen types III, V, VI, XII, XIV, and XV. The non-collageneous proteins in the tendon ECM belong to proteoglycan and glycoprotein family and smaller amount of proteoglycans (e.g., decorin, biglycan, fibromodulin, lumican) such glycoproteins (e.g., COMP, TNC, PRG4. TNMD) (Docheva et al., 2015; Screen et al., 2015). In the current study, we could not detect TNMD gene expression in neither of the TSPC groups, most likely due to transcript loss in the cell expansion step. Rapid downregulation of TNMD mRNA in 2D and 3D cultured human TSPCs was previously described (Dex et al., 2017). The ECM provides a natural physical microenvironment for cellular connections and also regulates cellular processes such as proliferation and differentiation (Theocharis et al., 2016). Aged stem cells still possess multipotency and are capable of ECM deposition (Stolzing and Scutt, 2006; Yu et al., 2011). However, it has been reported that cell aging can lead to a reduction in COL content (Haut et al., 1992; Couppe et al., 2009). In our study, we found that A-TSPC sheets contained significantly less ECM with poor alignment when compared to the Y-TSPC sheets. Connor et al. (2019) showed that senescent fibroblast has downregulated COL1A1 and elastin gene expression, compared to young fibroblast. This is comparable to our study revealing in A-TSPC sheets had a significant lower COL1 expression at mRNA and protein levels. COL 3 and COL 5, fibrillar collagens expressed in the human tendon tissue, that are important for the optimal fibrillary formation and tissue quality (Kannus, 2000) were both also significantly downregulated in the A-TSPC group. Our results are in line with two omics studies. Proteomic analysis of engineered tendon constructs by young or aged equine tenocytes revealed that tendon aging was associated with altered ECM protein, and especially COL type I, III and IV as well as proteins involved in cell-matrix interaction and mechanotransduction such as calponin 1, paladin, caldesmon 1 and contracting (Turlo et al., 2018). Moreover, the data suggested a lower cytoskeleton turnover in the aged group (Turlo et al., 2018), confirming independently the findings in Kohler et al. (2013). Transcriptome comparison of uninjured human Achilles tendon tissue biopsies from young and old patients demonstrated with tendon age a differential expression of genes related to cellular function, growth and the cell cycle (Peffers et al., 2015). Interestingly, downregulation of COL transcripts and genes involved in the post translational modification of COL were also affected (Peffers et al., 2015). A gene called SPARC (secreted protein acidic and rich in cysteine) has been shown to play an important role in ECM assembly and particularly in dermal fibroblast to regulate processing of procollagen I and COL fibrilogenesis (Rentz et al., 2007; Bradshaw, 2009). Interestingly, tendon tissues from Sparc-deficient mice, also exhibited altered actin cytoskeleton as well as collagen fibrilogenesis defects (Gehwolf et al., 2016) and hence, will be relevant to assess in the future, SPARC expression levels in the A-TSPC sheets. On the contrary, the study by Couppe et al. (2014) suggested that the COL fibril numbers remain unchanged during aging in both animal and human tendon tissue, but the enzymatic or non-enzymatic cross-linkers of the fibrils, thereby their size, can be affected during aging (Svensson et al., 2016). We analyzed other genes related to COL fibril regulation such as proteoglycans (DCN, FMOD, FN1, TNC, THBS2, COMP) and PLOD1, and found several being significantly downregulated in the A-TSPC group. These novel molecular candidates can be the foundation in follow up studies to investigate molecular cascades in both directions – up and downstream in order to elucidate the molecular mechanisms leading to the deficiency in matrix synthesis by A-TSPCs. Altogether, this data indicates the A-TSPC group harbors significant ECM production deficit.

With aging some structural changes of the COL fibrils occur; as mentioned above, changes in their size, but also shape and even biomechanical properties (Rahmati et al., 2017). We carried out TEM and investigated COL fibril diameter size but found no significant differences between the groups. One possibility is that during *in vitro* culture without dynamic mechanical loading the lateral growth of the COL fibril size is limited. In future, it will be of interest to subject both type of sheets to periodic axial stretching, as well as to examine their biomechanical properties, for example by the means of Force Indentation Atomic Force Microscopy. Nevertheless, the TEM analyses independently validated that A-TSPC contained less and disorganized cells exhibiting round and apoptotic morphologies embedded in a very poor COL matrix. The structural and biomechanical properties of the ECM can profoundly affect cell behavior. Interestingly,

providing A-TSPCs with hydrogel environment consisting of aligned nanonfibers alleviated their aged phenotype (Yin et al., 2020). Hence, "engineering a healthy" ECM niche might be an attractive way to rejuvenate aged cells, support their growth and direct their fate decision and differentiation.

Our study has several shortcomings that need to be addressed in follow up research: (1) Due to the manual rolling of the cell sheets, some ECM and cells are lost, therefore standardizing this process will be of importance; (2) A time point longer that 14 days can be evaluated to investigate if the A-TSPC sheets further deteriorate; (3) As mentioned above, subjecting the 3D tendon organoids to periodic axial stretching will be relevant to examine if this can lead to sheet diameter growth. In addition, efforts to speed up the sheet formation process and to become more economic, regarding required cell numbers will be very important.

Taken together, our study reports as in 2D culture, so in 3D culture A-TSPCs show cell autonomous deficits namely, significantly reduced renewability but significantly increased senescence and apoptosis. Furthermore, we report the following novel findings: (1) A-TSPCs have a severe issue with ECM production, which was validated at the mRNA and protein levels; (2) they are less competent to organize the ECM and to properly align in the third dimension; (3) Q-PCR profiling identified novel molecular candidates such as collagen genes (COL I, III, V, VI, and XV) and proteoglycans (DCN, FMOD, FN1, TNC, THBS2, COMP, PLOD1) which can help to elucidate the exact molecular circuits behind the deficiency in ECM synthesis. Further validation at the protein level as well as "gain" and "loss" of function experiments will be of great interest to follow. Last but not least, the 3D sheet model can become very attractive for (1) developing an effective 3D tenogenic differentiation protocol for wide use similarly to the well-known and accepted chondorgenic in pellet cultures and (2) for screening of small pharmacological cues for rejuvenation of the A-TSPC sheets and to evaluate side effects of available or in development medications on tendon tissues.

DATA AVAILABILITY STATEMENT

The datasets generated for this study are available on request to the corresponding author.

ETHICS STATEMENT

The studies involving human participants were reviewed and approved by Ethics Committee of the Medical Faculty of the Ludwig-Maximilians-University, Munich (Ethical Grant No. 166-08). The patients/participants provided their written informed consent to participate in this study.

AUTHOR CONTRIBUTIONS

DD conceived and designed the study, analyzed the data, and wrote the manuscript. ZY designed and performed the experiments, analyzed the data, and wrote the manuscript. HY analyzed the data and edited the manuscript. CB conducted TEM experiments. CP and VA provided the clinical expertise. All co-authors have read and approved the manuscript.

FUNDING

DD acknowledges the financial support of the EU H2020-WIDESPREAD-05-2017-Twinning Grant "Achilles: Overcoming specific weakness in tendon biology to design advanced regenerative therapies" Proposal Nr. 810850. ZY is grateful for the support from the China Scholarship Council (CSC) (Grant No. 201708080098).

ACKNOWLEDGMENTS

The authors thank Daniela Drenkard for valuable technical assistance, Heiko Siegmund for the TEM technical support, and Dr. Girish Pattappa for English proofreading.

SUPPLEMENTARY MATERIAL

The Supplementary Material for this article can be found online at: https://www.frontiersin.org/articles/10.3389/fbioe.2020.00406/full#supplementary-material

REFERENCES

Alcantara, O., Kalidas, M., Baltathakis, I., and Boldt, D. H. (2001). Expression of multiple genes regulating cell cycle and apoptosis in differentiating hematopoietic cells is dependent on iron. *Exp. Hematol.* 29, 1060–1069. doi: 10.1016/s0301-472x(01)00683-x

Asai, S., Otsuru, S., Candela, M. E., Cantley, L., Uchibe, K., Hofmann, T. J., et al. (2014). Tendon progenitor cells in injured tendons have strong chondrogenic potential: the CD105-negative subpopulation induces chondrogenic degeneration. *Stem Cells* 32, 3266–3277. doi: 10.1002/stem.1847

Baker, D. J., Wijshake, T., Tchkonia, T., LeBrasseur, N. K., Childs, B. G., van de Sluis, B., et al. (2011). Clearance of p16Ink4a-positive senescent cells delays ageing-associated disorders. *Nature* 479, 232–236. doi: 10.1038/nature10600

Bradshaw, A. D. (2009). The role of SPARC in extracellular matrix assembly. *J. Cell Commun. Signal.* 3, 239–246. doi: 10.1007/s12079-009-0062-6

Campisi, J. (2005). Senescent cells, tumor suppression, and organismal aging: good citizens, bad neighbors. *Cell* 120, 513–522. doi: 10.1016/j.cell.2005.02.003

Costa-Almeida, R., Calejo, I., and Gomes, M. E. (2019). Mesenchymal stem cells empowering tendon regenerative therapies. *Int. J. Mol. Sci.* 20:3002. doi: 10.3390/ijms20123002

Couppe, C., Hansen, P., Kongsgaard, M., Kovanen, V., Suetta, C., Aagaard, P., et al. (2009). Mechanical properties and collagen cross-linking of the patellar tendon in old and young men. *J. Appl. Physiol.* 107, 880–886. doi: 10.1152/japplphysiol.00291.2009

Couppe, C., Svensson, R. B., Grosset, J. F., Kovanen, V., Nielsen, R. H., Olsen, M. R., et al. (2014). Life-long endurance running is associated with reduced glycation

and mechanical stress in connective tissue. *Age* 36:9665. doi: 10.1007/s11357-014-9665-9

de Lucas, B., Perez, L. M., and Galvez, B. G. (2018). Importance and regulation of adult stem cell migration. *J. Cell Mol. Med.* 22, 746–754. doi: 10.1111/jcmm.13422

Dex, S., Alberton, P., Willkomm, L., Sollradl, T., Bago, S., Milz, S., et al. (2017). Tenomodulin is required for tendon endurance running and collagen I fibril adaptation to mechanical load. *EBioMedicine* 20, 240–254. doi: 10.1016/j.ebiom.2017.05.003

Docheva, D., Muller, S. A., Majewski, M., and Evans, C. H. (2015). Biologics for tendon repair. *Adv. Drug Deliv. Rev.* 84, 222–239. doi: 10.1016/j.addr.2014.11.015

Gan, L., Yang, X. L., Liu, Q., and Xu, H. B. (2005). Inhibitory effects of thioredoxin reductase antisense RNA on the growth of human hepatocellular carcinoma cells. *J. Cell. Biochem.* 96, 653–664. doi: 10.1002/jcb.20585

Gehwolf, R., Wagner, A., Lehner, C., Bradshaw, A. D., Scharler, C., Niestrawska, J. A., et al. (2016). Pleiotropic roles of the matricellular protein Sparc in tendon maturation and ageing. *Sci. Rep.* 6:32635. doi: 10.1038/srep32635

Gumucio, J. P., Korn, M. A., Saripalli, A. L., Flood, M. D., Phan, A. C., Roche, S. M., et al. (2014). Aging-associated exacerbation in fatty degeneration and infiltration after rotator cuff tear. *J. Shoulder Elbow. Surg.* 23, 99–108. doi: 10.1016/j.jse.2013.04.011

Han, J., Liu, J. Y., Swartz, D. D., and Andreadis, S. T. (2010). Molecular and functional effects of organismal ageing on smooth muscle cells derived from bone marrow mesenchymal stem cells. *Cardiovasc. Res.* 87, 147–155. doi: 10.1093/cvr/cvq024

Haut, R. C., Lancaster, R. L., and DeCamp, C. E. (1992). Mechanical properties of the canine patellar tendon: some correlations with age and the content of collagen. *J. Biomech.* 25, 163–173. doi: 10.1016/0021-9290(92)90273-4

Havis, E., Bonnin, M. A., Esteves de Lima, J., Charvet, B., Milet, C., and Duprez, D. (2016). TGFbeta and FGF promote tendon progenitor fate and act downstream of muscle contraction to regulate tendon differentiation during chick limb development. *Development* 143, 3839–3851. doi: 10.1242/dev.136242

Havis, E., Bonnin, M. A., Olivera-Martinez, I., Nazaret, N., Ruggiu, M., Weibel, J., et al. (2014). Transcriptomic analysis of mouse limb tendon cells during development. *Development* 141, 3683–3696. doi: 10.1242/dev.108654

Hirzinger, C., Tauber, M., Korntner, S., Quirchmayr, M., Bauer, H. C., Traweger, A., et al. (2014). ACL injuries and stem cell therapy. *Arch. Orthop. Trauma Surg.* 134, 1573–1578. doi: 10.1007/s00402-014-2060-2

Hsieh, C. F., Yan, Z., Schumann, R. G., Milz, S., Pfeifer, C. G., Schieker, M., et al. (2018). In vitro comparison of 2D-Cell culture and 3d-cell sheets of scleraxis-programmed bone marrow derived mesenchymal stem cells to primary tendon stem/progenitor cells for tendon repair. *Int. J. Mol. Sci.* 19:2272. doi: 10.3390/ijms19082272

Kasper, G., Mao, L., Geissler, S., Draycheva, A., Trippens, J., Kuhnisch, J., et al. (2009). Insights into mesenchymal stem cell aging: involvement of antioxidant defense and actin cytoskeleton. *Stem Cells* 27, 1288–1297. doi: 10.1002/stem.49

Kawakami, Y., Hambright, W. S., Takayama, K., Mu, X., Lu, A., Cummins, J. H., et al. (2019). Rapamycin rescues age-related changes in muscle-derived stem/progenitor cells from progeroid mice. *Mol. Ther. Methods Clin. Dev.* 14, 64–76. doi: 10.1016/j.omtm.2019.05.011

Kohler, J., Popov, C., Klotz, B., Alberton, P., Prall, W. C., Haasters, F., et al. (2013). Uncovering the cellular and molecular changes in tendon stem/progenitor cells attributed to tendon aging and degeneration. *Aging Cell* 12, 988–999. doi: 10.1111/acel.12124

Lee, C. H., Rodeo, S. A., Fortier, L. A., Lu, C., Erisken, C., and Mao, J. J. (2014). Protein-releasing polymeric scaffolds induce fibrochondrocytic differentiation of endogenous cells for knee meniscus regeneration in sheep. *Sci. Transl. Med.* 6:266ra171. doi: 10.1126/scitranslmed.3009696

Le Frere-Belda, M. A., Gil Diez de Medina, S., Daher, A., Martin, N., Albaud, B., Heudes, D., et al. (2004). Profiles of the 2 INK4a gene products, p16 and p14ARF, in human reference urothelium and bladder carcinomas, according to pRb and p53 protein status. *Hum. Pathol.* 35, 817–824. doi: 10.1016/j.humpath.2004.01.019

Li, X., Pongkitwitoon, S., Lu, H., Lee, C., Gelberman, R., and Thomopoulos, S. (2019). CTGF induces tenogenic differentiation and proliferation of adipose-derived stromal cells. *J. Orthop. Res.* 37, 574–582. doi: 10.1002/jor.24248

Maeda, T., Sakabe, T., Sunaga, A., Sakai, K., Rivera, A. L., Keene, D. R., et al. (2011). Conversion of mechanical force into TGF-beta-mediated biochemical signals. *Curr. Biol.* 21, 933–941. doi: 10.1016/j.cub.2011.04.007

Ni, M., Rui, Y. F., Tan, Q., Liu, Y., Xu, L. L., Chan, K. M., et al. (2013). Engineered scaffold-free tendon tissue produced by tendon-derived stem cells. *Biomaterials* 34, 2024–2037. doi: 10.1016/j.biomaterials.2012.11.046

Peffers, M. J., Fang, Y., Cheung, K., Wei, T. K., Clegg, P. D., and Birch, H. L. (2015). Transcriptome analysis of ageing in uninjured human achilles tendon. *Arthritis Res. Ther.* 17:33. doi: 10.1186/s13075-015-0544-2

Popov, C., Kohler, J., and Docheva, D. (2015). Activation of EphA4 and ephb2 reverse signaling restores the age-associated reduction of self-renewal, migration, and actin turnover in human tendon stem/progenitor cells. *Front. Aging Neurosci.* 7:246. doi: 10.3389/fnagi.2015.00246

Pryce, B. A., Watson, S. S., Murchison, N. D., Staverosky, J. A., Dunker, N., and Schweitzer, R. (2009). Recruitment and maintenance of tendon progenitors by TGFbeta signaling are essential for tendon formation. *Development* 136, 1351–1361. doi: 10.1242/dev.027342

Rahmati, M., Nalesso, G., Mobasheri, A., and Mozafari, M. (2017). Aging and osteoarthritis: central role of the extracellular matrix. *Ageing Res. Rev.* 40, 20–30. doi: 10.1016/j.arr.2017.07.004

Rees, J. D., Wilson, A. M., and Wolman, R. L. (2006). Current concepts in the management of tendon disorders. *Rheumatology* 45, 508–521. doi: 10.1093/rheumatology/kel046

Rentz, T. J., Poobalarahi, F., Bornstein, P., Sage, E. H., and Bradshaw, A. D. (2007). SPARC regulates processing of procollagen I and collagen fibrillogenesis in dermal fibroblasts. *J. Biol. Chem.* 282, 22062–22071. doi: 10.1074/jbc.M700167200

Schiele, N. R., Marturano, J. E., and Kuo, C. K. (2013). Mechanical factors in embryonic tendon development: potential cues for stem cell tenogenesis. *Curr. Opin. Biotechnol.* 24, 834–840. doi: 10.1016/j.copbio.2013.07.003

Schneider, M., Angele, P., Jarvinen, T. A. H., and Docheva, D. (2018). Rescue plan for achilles: therapeutics steering the fate and functions of stem cells in tendon wound healing. *Adv. Drug Deliv. Rev.* 129, 352–375. doi: 10.1016/j.addr.2017.12.016

Screen, H. R., Berk, D. E., Kadler, K. E., Ramirez, F., and Young, M. F. (2015). Tendon functional extracellular matrix. *J. Orthop. Res.* 33, 793–799. doi: 10.1002/jor.22818

Shen, H., Jayaram, R., Yoneda, S., Linderman, S. W., Sakiyama-Elbert, S. E., Xia, Y., et al. (2018). The effect of adipose-derived stem cell sheets and CTGF on early flexor tendon healing in a canine model. *Sci. Rep.* 8:11078. doi: 10.1038/s41598-018-29474-8

Smith, R. K., Birch, H. L., Goodman, S., Heinegard, D., and Goodship, A. E. (2002). The influence of ageing and exercise on tendon growth and degeneration–hypotheses for the initiation and prevention of strain-induced tendinopathies. *Comp. Biochem. Physiol. A Mol. Integr. Physiol.* 133, 1039–1050. doi: 10.1016/s1095-6433(02)00148-4

Sousa-Victor, P., Gutarra, S., Garcia-Prat, L., Rodriguez-Ubreva, J., Ortet, L., Ruiz-Bonilla, V., et al. (2014). Geriatric muscle stem cells switch reversible quiescence into senescence. *Nature* 506, 316–321. doi: 10.1038/nature13013

Steinmann, S., Pfeifer, C. G., Brochhausen, C., and Docheva, D. (2020). spectrum of tendon pathologies: triggers, trails and end-state. *Int. J. Mol. Sci.* 21:844. doi: 10.3390/ijms21030844

Stolzing, A., and Scutt, A. (2006). Age-related impairment of mesenchymal progenitor cell function. *Aging Cell* 5, 213–224. doi: 10.1111/j.1474-9726.2006.00213.x

Svensson, R. B., Heinemeier, K. M., Couppe, C., Kjaer, M., and Magnusson, S. P. (2016). Effect of aging and exercise on the tendon. *J. Appl. Physiol.* 121, 1237–1246. doi: 10.1152/japplphysiol.00328.2016

Tan, G. K., Pryce, B. A., Stabio, A., Brigande, J. V., Wang, C., Xia, Z., et al. (2020). Tgfbeta signaling is critical for maintenance of the tendon cell fate. *eLife* 9:e52695. doi: 10.7554/eLife.52695

Tarafder, S., Gulko, J., Kim, D., Sim, K. H., Gutman, S., Yang, J., et al. (2019). Effect of dose and release rate of CTGF and TGFbeta3 on avascular meniscus healing. *J. Orthop. Res.* 37, 1555–1562. doi: 10.1002/jor.24287

Taylor, R. W., Barron, M. J., Borthwick, G. M., Gospel, A., Chinnery, P. F., Samuels, D. C., et al. (2003). Mitochondrial DNA mutations in human colonic crypt stem cells. *J. Clin. Investig.* 112, 1351–1360. doi: 10.1172/jci19435

Theocharis, A. D., Skandalis, S. S., Gialeli, C., and Karamanos, N. K. (2016). Extracellular matrix structure. *Adv. Drug Deliv. Rev.* 97, 4–27. doi: 10.1016/j.addr.2015.11.001

Turlo, A. J., Ashraf Kharaz, Y., Clegg, P. D., Anderson, J., and Peffers, M. J. (2018). Donor age affects proteome composition of tenocyte-derived engineered tendon. *BMC Biotechnol.* 18:2. doi: 10.1186/s12896-018-0414-5

Yan, Z., Yin, H., Nerlich, M., Pfeifer, C. G., and Docheva, D. (2018). Boosting tendon repair: interplay of cells, growth factors and scaffold-free and gel-based carriers. *J. Exp. Orthop.* 5:1. doi: 10.1186/s40634-017-0117-1

Yin, H., Caceres, M. D., Yan, Z., Schieker, M., Nerlich, M., and Docheva, D. (2019). Tenomodulin regulates matrix remodeling of mouse tendon stem/progenitor cells in an ex vivo collagen I gel model. *Biochem. Biophys. Res. Commun.* 512, 691–697. doi: 10.1016/j.bbrc.2019.03.063

Yin, H., Strunz, F., Yan, Z., Lu, J., Brochhausen, C., Kiderlen, S., et al. (2020). Three-dimensional self-assembling nanofiber matrix rejuvenates aged/degenerative human tendon stem/progenitor cells. *Biomaterials* 236:119802. doi: 10.1016/j.biomaterials.2020.119802

Yin, Z., Guo, J., Wu, T. Y., Chen, X., Xu, L. L., Lin, S. E., et al. (2016). stepwise differentiation of mesenchymal stem cells augments tendon-like tissue formation and defect repair in vivo. *Stem Cells Transl. Med.* 5, 1106–1116. doi: 10.5966/sctm.2015-0215

Yu, J. M., Wu, X., Gimble, J. M., Guan, X., Freitas, M. A., and Bunnell, B. A. (2011). Age-related changes in mesenchymal stem cells derived from rhesus macaque bone marrow. *Aging Cell* 10, 66–79. doi: 10.1111/j.1474-9726.2010.00646.x

Zhang, H., Menzies, K. J., and Auwerx, J. (2018). The role of mitochondria in stem cell fate and aging. *Development* 145:dev143420. doi: 10.1242/dev.143420

Conflict of Interest: The authors declare that the research was conducted in the absence of any commercial or financial relationships that could be construed as a potential conflict of interest.

frontiers in Bioengineering and Biotechnology

ORIGINAL RESEARCH
published: 05 May 2020
doi: 10.3389/fbioe.2020.00366

Microfluidic Biofabrication of 3D Multicellular Spheroids by Modulation of Non-geometrical Parameters

*Silvia Lopa[1†], Francesco Piraino[2†‡], Giuseppe Talò[1†], Valerio Luca Mainardi[3,4], Simone Bersini[1‡], Margherita Pierro[1‡], Luigi Zagra[5], Marco Rasponi[2] and Matteo Moretti[1,3]**

[1] IRCCS Istituto Ortopedico Galeazzi, Cell and Tissue Engineering Laboratory, Milan, Italy, [2] Department of Electronics, Information and Bioengineering, Politecnico di Milano, Milan, Italy, [3] Regenerative Medicine Technologies Laboratory, Ente Ospedaliero Cantonale, Lugano, Switzerland, [4] Laboratory for Biological Structures Mechanics, Chemistry, Material and Chemical Engineering Department "Giulio Natta," Politecnico di Milano, Milan, Italy, [5] IRCCS Istituto Ortopedico Galeazzi, Hip Department, Milan, Italy

Three-dimensional (3D) cell spheroids are being increasingly applied in many research fields due to their enhanced biological functions as compared to conventional two-dimensional (2D) cultures. 3D cell spheroids can replicate tissue functions, which enables their use both as *in vitro* models and as building blocks in tissue biofabrication approaches. In this study, we developed a perfusable microfluidic platform suitable for robust and reproducible 3D cell spheroid formation and tissue maturation. The geometry of the device was optimized through computational fluid dynamic (CFD) simulations to improve cell trapping. Experimental data were used in turn to generate a model able to predict the number of trapped cells as a function of cell concentration, flow rate, and seeding time. We demonstrated that tuning non-geometrical parameters it is possible to control the size and shape of 3D cell spheroids generated using articular chondrocytes (ACs) as cellular model. After seeding, cells were cultured under perfusion at different flow rates (20, 100, and 500 μl/min), which induced the formation of conical and spherical spheroids. Wall shear stress values on cell spheroids, computed by CFD simulations, increased accordingly to the flow rate while remaining under the chondroprotective threshold in all configurations. The effect of flow rate on cell number, metabolic activity, and tissue-specific matrix deposition was evaluated and correlated with fluid velocity and shear stress distribution. The obtained results demonstrated that our device represents a helpful tool to generate stable 3D cell spheroids which can find application both to develop advanced *in vitro* models for the study of physio-pathological tissue maturation mechanisms and to obtain building blocks for the biofabrication of macrotissues.

Keywords: microfluidic, spheroid, 3D culture, pellet culture, fluid dynamic

OPEN ACCESS

Edited by:
Dimitrios I. Zeugolis, National University of Ireland Galway, Ireland

Reviewed by:
Sourabh Ghosh, Indian Institute of Technology Delhi, India
Rodrigo Alvarenga Rezende, Centro de Tecnologia da Informação Renato Archer (CTI), Brazil

***Correspondence:**
Matteo Moretti
matteo.moretti@grupposandonato.it

[†] These authors have contributed equally to this work

*[‡] **Present address:***
Francesco Piraino, Quanterix Corporation, Billerica, MA, United States
Simone Bersini, Molecular and Cell Biology Laboratory, The Salk Institute for Biological Studies, La Jolla, CA, United States
Margherita Pierro, Bonalive Italia s.r.l., Perugia, Italy

Specialty section:
This article was submitted to Tissue Engineering and Regenerative Medicine, a section of the journal Frontiers in Bioengineering and Biotechnology

Received: *13 January 2020*
Accepted: *31 March 2020*
Published: *05 May 2020*

Citation:
Lopa S, Piraino F, Talò G, Mainardi VL, Bersini S, Pierro M, Zagra L, Rasponi M and Moretti M (2020) Microfluidic Biofabrication of 3D Multicellular Spheroids by Modulation of Non-geometrical Parameters. Front. Bioeng. Biotechnol. 8:366. doi: 10.3389/fbioe.2020.00366

INTRODUCTION

Three-dimensional (3D) cell spheroids have enhanced biological functions compared to conventional two-dimensional (2D) cultures (Pampaloni et al., 2007; Fang and Eglen, 2017). In particular, self-assembled 3D cell spheroids can replicate tissue functionality, representing useful models of tumorigenesis (Kwapiszewska et al., 2014; Ishiguro et al., 2017), embryonic development

(Nakazawa et al., 2013; Pettinato et al., 2014; Belair et al., 2017), and chondrogenesis (Sabatino et al., 2012; Lopa et al., 2013; Sridharan et al., 2018) that bridge the gap between classical *in vitro* studies and animal studies (Zorlutuna et al., 2012). Moreover, 3D cell spheroids are being increasingly applied as building blocks for tissue engineering applications due to the possibility of achieving *in vitro* tissue maturation before their assembly into macrotissues of desired shape by biofabrication techniques, such as bioprinting (Laschke and Menger, 2017). In this scenario, the development of platforms to achieve robust and reproducible 3D cell spheroid formation and tissue maturation appears as a crucial step to engineer advanced *in vitro* models and pave the way to tissue biofabrication.

Traditional methods for 3D cell spheroid formation include the culture on non-adhesive substrates, the use of rotating vessel bioreactors, the hanging-drop method, and the centrifugation in conical tubes. However, all these approaches are characterized by a limited control over the size and geometry of 3D cell spheroids. In the last years, several microwell platforms have been developed by microfabrication technologies to overcome this limitation (Selimovic et al., 2011; Piraino et al., 2012; Lopa et al., 2015; Lee et al., 2016), finding an important application in studies where cell function is strictly connected to the size and geometry of the 3D spheroid (Moreira Teixeira et al., 2012; Babur et al., 2013; Sridharan et al., 2015; Liu et al., 2017). These features are usually modulated by modifying the geometry of the microwells (Karp et al., 2007; Napolitano et al., 2007; Moeller et al., 2008; Sakai et al., 2010; Masuda et al., 2012), which is the main tunable parameter in static culture platforms.

Compared to static microwell systems, microfluidics offers the advantage to modulate additional parameters, such as flow rate and shear stress. The effect of these parameters is strictly dependent on the chip design. For example, it has been shown that the presence of microgrooves within microchannel strongly influences the fluid dynamic environment. Moreover, the modulation of microgrooves geometry (width and height) determines microcirculation areas and microscale shear stresses, in turn affecting cell trapping (Manbachi et al., 2008; Karimi et al., 2013; Khabiry and Jalili, 2015). However, given a fixed microfluidic chip design, the fluid flow can be tuned to obtain different fluid dynamics microenvironment, a possibility that is usually neglected in view of tuning cell trapping and 3D cell spheroid formation.

Computational fluid dynamics (CFD) modeling is a powerful tool that is being applied to assist microfluidic platforms design, allowing to unravel the factors determining specific hydrodynamic patterns, and study the influence of fluid dynamics on cell behavior (Huang et al., 2010). Interesting results have been provided by studies combining CFD simulations and experimental cell trapping, demonstrating that improved results can be achieved through the CFD-driven optimization of chip geometry (Khabiry et al., 2009; Cioffi et al., 2010) and thus proving the value of this computational-experimental approach. CFD modeling can also be exploited to investigate the effect of mechanical cues on cell behavior. For instance, mechanical factors are known to play a key role in tissue development *in vivo* (Mammoto and Ingber, 2010). Based on this, culture platforms compatible with the application of mechanical stimulation can be used to gain a better understanding of tissue maturation and exploit biophysical cues to enhance this process. In this scenario, CFD modeling is essential to interpret the experimental results and identify the biophysical determinants of cell behavior.

The aim of this study was to control cell trapping and 3D cell spheroid formation by tuning non-geometrical parameters within a perfused microfluidic environment through a computational–experimental approach. Here, articular chondrocytes (ACs) were used since chondrocytes are known as 3D spheroid-forming cells and as responsive to biophysical cues. CFD modeling was exploited to optimize chip geometry, while cell concentration, flow rate, and seeding time were modulated to control and generate a predictive model of cell trapping. CFD modeling was subsequently used to study the influence of fluid flow and shear stress on 3D cell spheroid formation and tissue maturation.

MATERIALS AND METHODS

Study Design

In this study, we evaluated the influence of multiple non-geometrical parameters, such as cell concentration, flow rate, and seeding time on cell trapping in a concave microfluidic chamber. Computational modeling was used to predict cell trapping and correlate the formation and biological response of 3D spheroids of human ACs with the fluid dynamic features associated to different flow rates.

Design and Optimization of the Microfluidic Chip Based on CFD Modeling

A microfluidic concave chamber was conceived, resembling the conical end-tip of a standard 1.5 ml tube routinely used to generate 3D cell spheroids. Computational modeling was used to optimize its geometry. At first, a preliminary chamber design was realized with a desktop CNC milling machine (MDX40, Roland DG) through a carbide round mill (Ø 400 μm). The chamber surface was characterized by the presence of micro-burrs. Images of the chamber were acquired using an IX71 inverted microscope (Olympus) and analyzed to reproduce the actual geometry in the numerical model. CFD modeling was exploited to verify whether a simplified (smooth) geometry of the chamber could be adopted in the simulations to replace the actual design. Chamber geometries were discretized by GAMBIT (Ansys Inc.) adopting a tetrahedral meshing scheme with about 2,000,000 elements. The steady-state Navier–Stokes equations for an incompressible fluid were then solved using the finite volume code ANSYS FLUENT (Ansys Inc.). In all the simulations, the following conditions were applied: no-slip boundary at walls, zero pressure at the outlet, and flat average velocity profiles at the inlet port. The velocity fields calculated by CFD simulations in both configurations were compared at different depths. The microfluidic chip geometry

was then analyzed by CFD modeling to verify whether the inclusion of an additional groove between the microchannels and the seeding chamber could be a suitable option to reduce the flow velocity in proximity of the chamber, hence favoring cell trapping by sedimentation.

Fabrication of the Microfluidic Device

Based on the results of the CFD simulations, the microfluidic device was designed to include a channel allowing for cell loading and medium perfusion, a groove to reduce the velocity of flowing cells, and a concave chamber for cell trapping and 3D spheroid culture.

The microfabrication consisted in the manufacturing of two layers obtained by replica molding of poly(dimethylsiloxane) (PDMS) and assembled together to obtain a continuous fluidic domain (Xia and Whitesides, 1998). The top layer mold was obtained by transferring the layout of a straight channel (40 mm long, 250 μm wide) onto a 4″ silicon wafer through photolithography, achieving a SU-8 50 (MicroChem Corp.) negative photoresist relief with a height of 150 μm. PDMS prepolymer and curing agent (Sylgard 184, Dow Corning), mixed in ratio 10:1 (w/w), were then poured on the mold, degassed, and cured in oven at 80°C for 120 min. PDMS was then demolded and inlet and outlet ports were realized through a 0.5 mm biopsy puncher. The bottom layer, including the culture chamber and the upstream and downstream groove, was obtained through a series of consecutive fabrication steps. At first, the fluidic volume of the chamber and the groove were machined on a flat 8 mm thick poly(methylmethacrylate) (PMMA) substrate with CNC milling machine (round mill, Ø 400 μm) at a final depth of 2.2 mm. PDMS prepolymer and curing agent, mixed in ratio 10:1 (w/w), were then poured on the PMMA mold, degassed, and cured in oven at 80°C for 120 min. Subsequently, the PDMS layer was removed from the mold, and its surface underwent an air plasma treatment (Harrick Plasma, United States), followed by 30 min of chloro-trimethyl-silane vapor deposition (Sigma-Aldrich) in a saturated atmosphere. PDMS was then used as mold, and fresh PDMS (10:1, w/w) was poured on top of it and cast on a hot plate at 150°C for 10 min. Finally, the obtained PDMS block was bonded to the top layer.

Cell Isolation and Expansion

Human articular cartilage was harvested aseptically from discarded tissue fragments obtained from osteoarthritic patients (Kellgren–Lawrence grade III–IV) undergoing routine arthroplasty surgical procedures, with patients' informed consent. ACs were isolated by macroscopically non-fibrillated regions of cartilage by enzymatic digestion of minced tissue. After digestion, cells were plated at 10^4 cells/cm^2 in complete medium (CM) added with 5 ng/ml FGF-2 and 1 ng/ml TGF-β1 (Lagana et al., 2014). After 2 weeks, cells were detached and suspended in CM at 5, 10, and 20 million (M) cells/ml for seeding.

Cell Trapping

Experimental Set-Up

Before use, microfluidic devices were cleaned by flowing 70% ethanol at 10 μl/min for 3 min and rinsing with phosphate buffer solution (PBS), and finally filled with CM. Cells were seeded using a syringe pump (PHD 22/2000, Harvard Apparatus). Different combinations of cell concentrations (5M, 10M, and 20M cells/mL), flow rates (1.25, 2.5, and 5 μl/min), and seeding times (10, 20, and 40 min) were tested as non-geometrical parameters able to modulate cell docking.

Generation of a Predictive Model for Cell Trapping

A statistical software (JMP, SAS Institute Inc.) was used to analyze the interactions between the analyzed non-geometrical parameters and to predict their effect on cell trapping. The number of trapped cells represented the output, whereas cell concentration, flow rate, and seeding time represented the input variables. All the experimental conditions and the relative number of trapped cells were included in the model. Experiments in an additional condition (i.e., 10M cells/ml, 2.5 μl/min, 60 min) were performed to test the model using the simulation tool provided by JMP with the following specifications: random error, five repetitions. The interaction plot and the correlation plot were drawn using the software to evaluate the interaction between cell concentration and flow rate or seeding time and to compare experimental and predicted results.

Dynamic Generation and Culture of 3D Cell Aggregates

Experimental Set-Up

3D cell aggregates were generated within the microfluidic device. The following parameters were used for the seeding phase: 10M cells/ml, 2.5 μl/min, 20 min. After seeding, devices were incubated at 37°C, 5% CO_2 and perfused with serum-free chondrogenic medium (Lopa et al., 2013) using an intermittent flow rate (1 min perfusion each hour). Three flow rates were tested: 20, 100, and 500 μl/min. Samples were cultured for 14 days.

Modeling of 3D Cell Spheroids Generated Under Different Flow Rates

Computational models were gleaned on the different aggregate geometries generated upon the tested flow conditions. Specifically, three models were developed: a filled chamber, a disk-shaped aggregate, and a spherical aggregate. The filled chamber model was generated creating a 3D surface above the concave chamber. The other models were developed by designing solid bodies inside the chamber: a disk ($Ø_{max}$ 1.9 mm, height 1.1 mm) or a solid sphere (Ø 1 mm).

Sample Analysis

DNA Assay

Immediately after seeding, the top layer of the chip was punched (Ø 2 mm) and cells trapped in the concave chamber were retrieved using a micropipette. Similarly, cell aggregates were retrieved from the microfluidic devices after 14 days of culture and digested with papain (60°C, 16 h). DNA quantification was performed by CyQUANT kit, according to the manufacturer's instructions. Fluorescence was

measured (λ_{ex} 485 nm–λ_{em} 535 nm) using a Victor X3 Plate Reader (Perkin Elmer).

Alamar Blue Assay

Cell metabolic activity was assessed through the Alamar Blue™ cell viability assay (Life Technologies). Briefly, cell spheroids were transferred to a 96-well plate and incubated with 10% Alamar Blue™ in HG-DMEM (37°C, 4 h). After incubation, the supernatant was harvested and fluorescence was measured (λ_{ex} 540 nm–λ_{em} 580 nm) using a Victor X3 Plate Reader. Fluorescence values were then normalized on the DNA content to obtain the metabolic activity per cell, defined as normalized metabolic activity.

Glycosaminoglycan Assay

After papain digestion, GAG content of cell aggregates was measured by dimethylmethylene blue assay (16 mg/ml, Sigma-Aldrich) with chondroitin sulfate as standard. Absorbance was read (λ 525 nm) using a Victor X3 Plate Reader.

Histological Evaluation

Cell aggregates were fixed in 4% neutral buffered formalin, dehydrated in a graded series of alcohols, individually embedded in paraffin, and sectioned at 4 μm. Sections were stained with hematoxylin and eosin to visualize cell and extracellular matrix distribution and with alcian blue to detect GAG deposition. Images were acquired using an Olympus IX71 microscope.

Statistical Analysis

Data are presented as mean + standard deviation (SD), except where otherwise noted. Each experimental condition was repeated at least three times ($n \geq 3$). Data were analyzed using GraphPad Prism. Data distribution was evaluated by means of D'Agostino and Pearson normality test. Comparison between two groups was performed by *t*-test for parametric or non-parametric data, depending on data normality. Comparison of multiple groups was performed by univariate analysis of variance (ANOVA) followed by Bonferroni's or Dunnet's *post hoc* tests for parametric and non-parametric data, respectively. Differences were considered significant when $p < 0.05$.

RESULTS

Design of the Microfluidic Chip

In CFD simulations, tetrahedral meshing schemes with up to 2,000,000 elements were adopted (**Figure 1A**). To study the local fluid dynamics of the microfluidic device while preserving computational time, smaller elements were used to discretize the volume of the chamber, in which cells are seeded, while larger tetrahedrons were employed for the microchannels, designed for cell loading. CFD modeling was applied to validate the use of a simplified chamber geometry (i.e., without micro-burrs deriving from micro-machining) instead of the actual chamber geometry in the simulations. No relevant differences were found in the velocity field at any depths between the simplified and the actual geometry at a flow rate equal to 2.5 μl/min (**Figure 1B**, average velocity difference 0.6%). Hence, the simplified chamber geometry was used in all the subsequent CFD simulations.

Subsequently, starting from the simplified chamber geometry, two computational models were generated with and without the groove upstream and downstream the chamber (**Figure 1C**). We demonstrated that the introduction of a 200 μm-deep groove reduced the flow velocity at different depths of the microchamber. Indeed, at a 2.5 μl/min flow rate, the average velocity at the top of the microchamber ($z = 0$ μm) changed from 46.34 μm/s without groove to 38.17 μm/s with groove (−18%). The average velocity decreased also at $z = 200$ μm from 35.37 μm/s without groove to 33.87 μm/s with groove (−4.2%). Based on the results of CFD optimization, the microfluidic chip was fabricated including the upstream and downstream groove (**Figure 2A**). The 3D rendering and geometrical features of the assembled device are illustrated in **Figure 2B**.

Cell Trapping Experiments

Based on CFD optimization, cell trapping experiments were performed to demonstrate that tuning multiple non-geometrical parameters allows controlling the number of trapped cells. An overview of the tested combinations is displayed as 3D matrix (**Figure 3A**).

The gradual filling of the chamber during cell seeding is shown in **Figure 3B**. The number of trapped cells starting from cell suspensions containing 10M and 20M cells/ml gradually increased over time for each single flow rate. However, a non-linear increase of the trapped cell number was observed when comparing different flow rates at the same time or the same flow rate at different times (**Figures 3C,D**). For instance, seeding 10M cells/ml at 1.25 μl/min for 40 min resulted in 200,000 trapped cells, but the application of twofold and fourfold higher flow rates (i.e., 2.5 and 5 μl/min) only led to increases of + 20 and + 62.5% in the trapped cell number, respectively. Similarly, seeding 10M cells/ml at 2.5 μl/min for 20 min resulted in 200,000 trapped cells, but using two- and fourfold higher seeding times (i.e., 40 and 80 min) only led to respective increases of + 20 and + 35% in the number of trapped cells. Similar results were obtained by grouping cell trapping data for specific flow rates (**Figures 3E,F**). Indeed, within each single cell concentration, the trapped cell number increased over time for both 2.5 and 5 μl/min flow rates, but in most cases, this increase was not directly proportional to the increase in time. To better represent this phenomenon, we grouped together the data derived from experimental conditions theoretically expected to result in an equivalent trapped cell number (**Figures 3G,H**). Comparison between experimental groups with the same cell concentration but different flow rates and seeding times revealed that cell seeding at the highest flow rate (i.e., 5 μl/min) applied for a short time corresponded to a lower number trapped cells compared to lower flow rates used for a longer time. Conversely, no relevant differences were found between experimental groups where 1.25 and 2.5 μl/min flow rates were applied. The aforementioned results demonstrated that the interplay among different parameters, such as cell concentration, flow rate, and

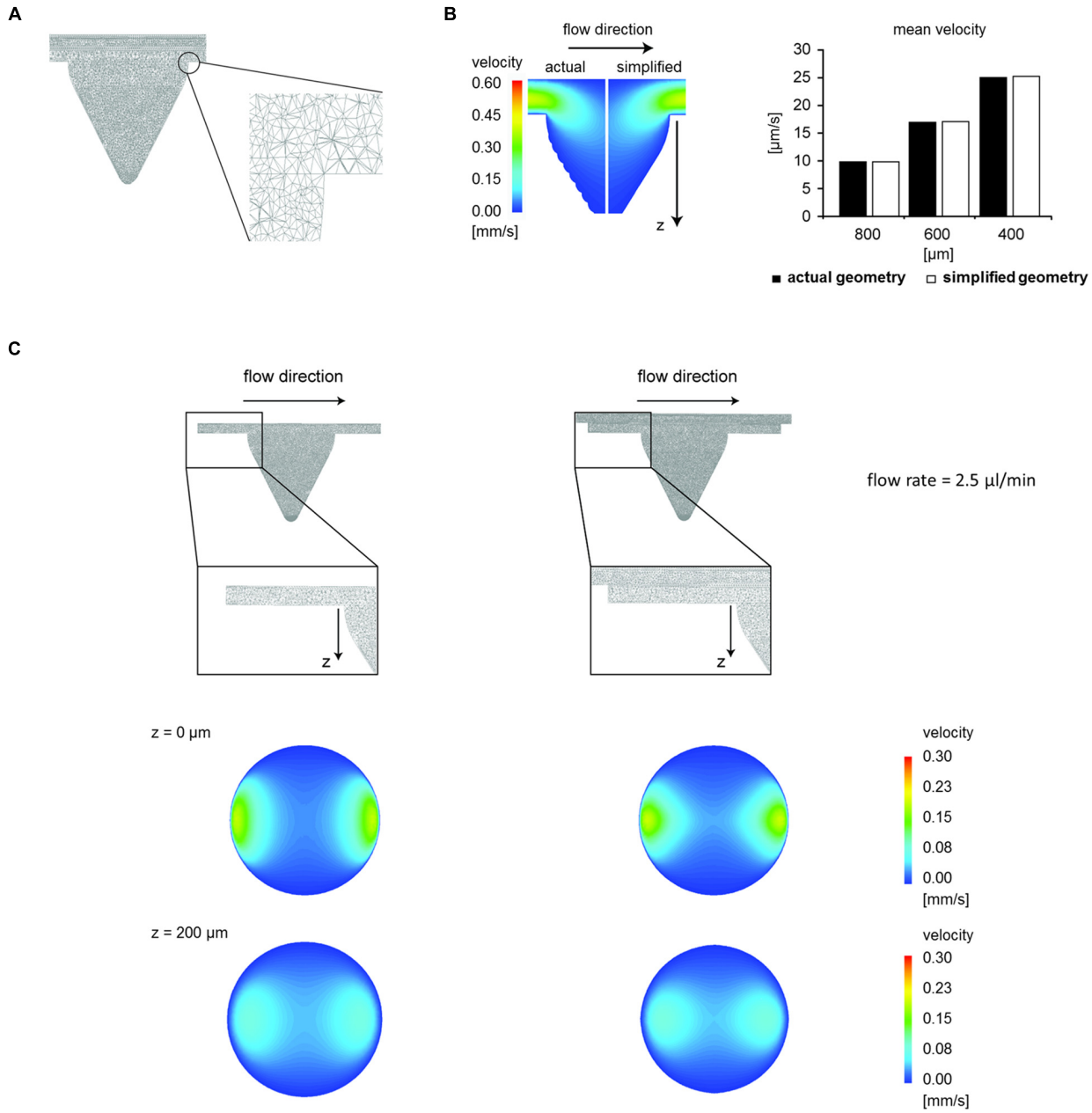

FIGURE 1 | Optimization of the microfluidic chip design. **(A)** Geometric discretization of the concave chamber used in the computational model. Section of the mesh corresponding to the longitudinal mirror plane, and zoom of a mesh detail. **(B)** Colorimetric map of velocity magnitude relative to the longitudinal mirror plane and comparison between mean velocity values computed within the simplified and the actual chamber geometry at different depths (flow rate 2.5 µl/min). **(C)** Comparison between two different configurations of the chip chamber (i.e., without or with a 0.2 mm-high groove). Meshing scheme and colorimetric maps of velocity magnitude relative to cross-sections of the concave chamber at different depths (flow rate 2.5 µl/min).

seeding time modulates the number of cells trapped into the seeding chamber.

Generation of a Predictive Model for Cell Trapping

Multiple interaction plots were drawn to describe the interactions between cell concentration and either the flow rate or the seeding time (**Figure 4A**). The interaction plots between cell concentration and flow rate generated parallel curves indicating that the trapped cell number increased similarly with increasing flow rates for 5M and 20M cells/ml (**Figure 4B**) and that the trapped cell number increased similarly with increasing cell concentrations at both 1.25 and 5 µl/min (**Figure 4C**). Differently, non-parallel curves were obtained by the correlation of seeding time and cell concentration. In particular, the trapped

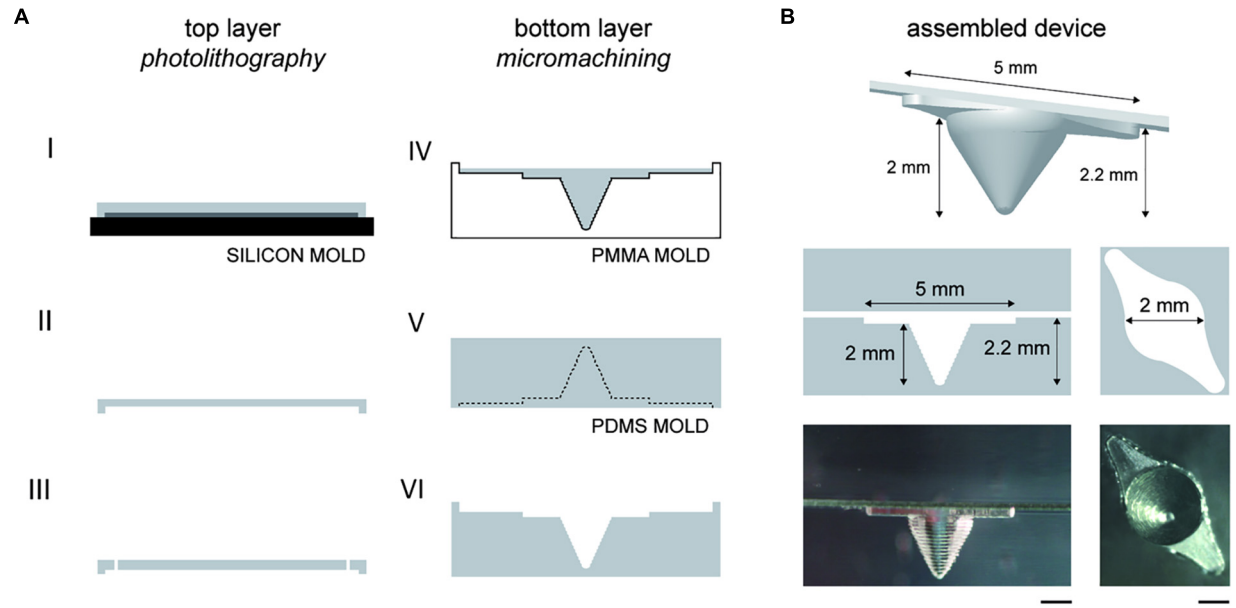

FIGURE 2 | Microfluidic chip fabrication. **(A)** Schematic of the fabrication process. The top layer mold was obtained by transferring the channel layout onto a silicon wafer by photolithography. PDMS was casted and cured (I). The PDMS layer was detached (II) and inlet/outlet ports were punched (III). The bottom layer was obtained through multiple fabrication steps. The chamber and the groove were machined on a PMMA substrate with a CNC milling machine. PDMS was poured on the PMMA mold and cured (IV). Subsequently, PDMS was detached and used as mold for PDMS casting (V). The PDMS layer was then detached (VI) and bonded to the top layer. **(B)** 3D rendering and lateral view of the assembled microfluidic device and top view of the concave chamber (scale bars: 1 mm).

cell number gradually increased over time when using a low cell concentration (5M cells/ml), whereas it reached a plateau with a high cell concentration (20M cells/ml) (**Figure 4D**). Accordingly, approximately the same number of cells trapped in the chamber after a long seeding phase (80 min) independently from the starting cell concentration, while the cell concentration correlated with the number of trapped cells after a short seeding phase (10 min) (**Figure 4E**). The cell trapping data obtained by testing multiple combinations of these three parameters were used to generate a model able to predict the number of trapped cells (**Figure 4F**). We tested the model with specific combinations of input parameters, and we found that the values predicted by the model were similar to the experimental values, as shown in the example in **Figure 4G**. Furthermore, the correlation analysis demonstrated that simulated cell number values obtained by testing the model with all the experimental input combinations significantly correlated with the values measured in our experiments (**Figure 4H**).

Generation of 3D Cell Spheroids

Based on the cell trapping results, the microfluidic devices were seeded with 10M cells/ml at 2.5 μl/min for 20 min to achieve 200,000 trapped cells in the chamber. Three conditions of intermittent medium perfusion (20, 100, or 500 μl/min for 1 min every hour) were applied for 14 days (**Figure 5A**). A representative time course describing cell aggregate generation is depicted in **Figure 5B**. Initially, the influence of different flow rates on the formation of 3D cell aggregates was evaluated. Application of a low flow rate (20 μl/min) did not result in the generation of stable 3D aggregates. Due to the impossibility to retrieve stable cell aggregates from chips perfused with 20 μl/min, these samples were excluded from the subsequent analyses. Culture under perfusion at 100 and 500 μl/min resulted in the formation of stable 3D cell aggregates (**Figure 5C**). In particular, a flow rate of 100 μl/min induced the formation of conical aggregates, while spherical aggregates formed at 500 μl/min. These results correlated with the different shear stress profiles exerted by the flow in the different perfusion conditions. CFD simulations were performed to compute wall shear stress profiles on the surface of the microchamber filled with cells. The maximum wall shear stress gradually increased from 6.31 (20 μl/min) to 32.12 mPa (100 μl/min) and reached a peak equal to 164.92 mPa at 500 μl/min flow rate. Similarly, the mean wall shear stress increased from 2.37 (20 μl/min) to 13.74 mPa (100 μl/min), reaching the highest value (63.89 mPa) at 500 μl/min.

Culture and Analysis of 3D Cell Spheroids

We compared cell number, normalized metabolic activity, and GAG production in cell aggregates cultured at 100 and 500 μl/min. In both conditions, cell number increased after 14 days compared to day 0 (dotted line, **Figure 6A**). Cell number and normalized metabolic activity in aggregates perfused at 100 and 500 μl/min were comparable (**Figures 6A,B**), while GAG production resulted to be higher in cell aggregates perfused at 100 μl/min compared to 500 μl/min (**Figure 6C**). Accordingly, in aggregates cultured at 100 μl/min, an abundant GAG deposition

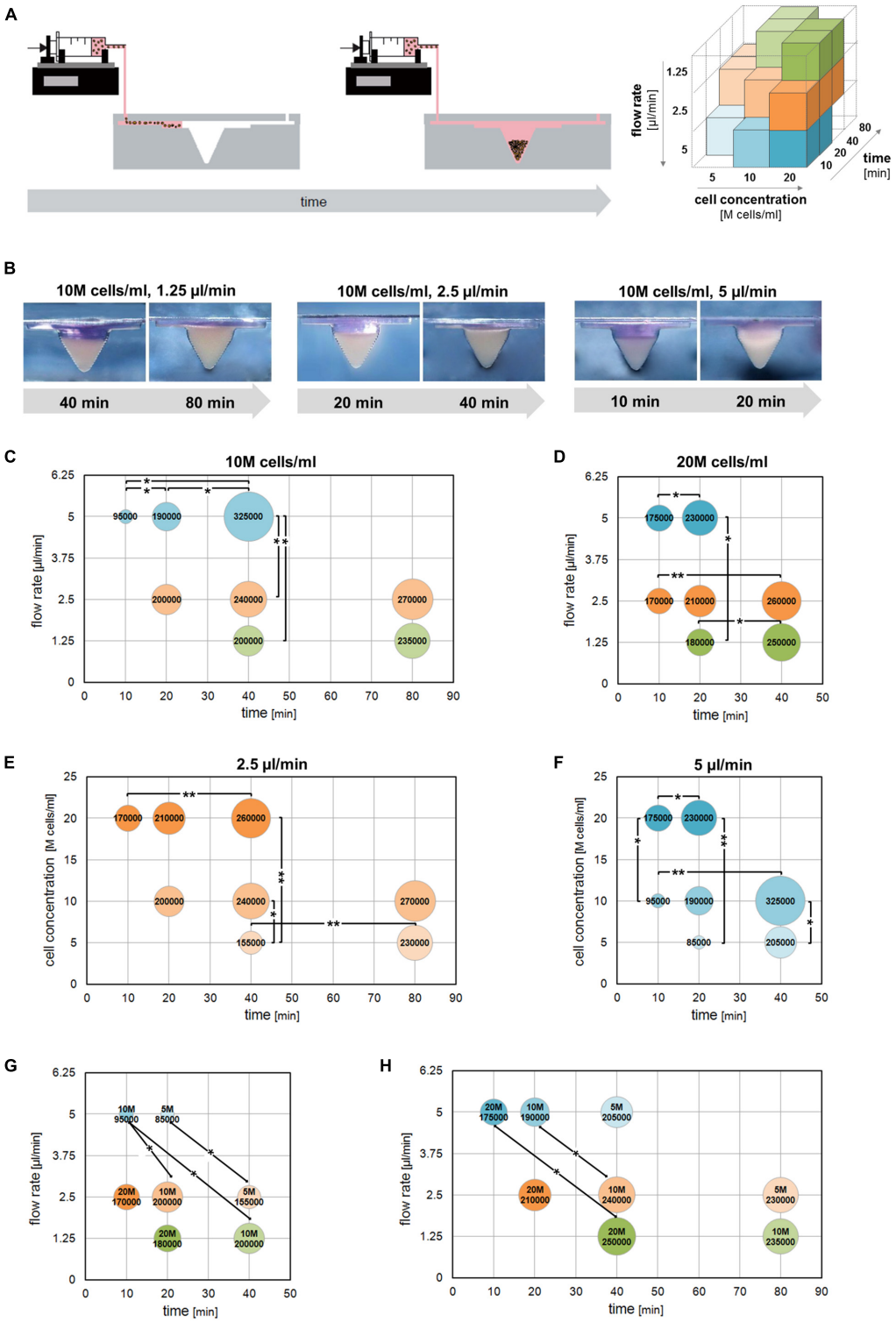

FIGURE 3 | Cell trapping analysis. **(A)** Schematic showing the experimental set-up. The tested experimental conditions are represented as a 3D matrix. **(B)** Representative side views showing the progressive cell trapping in the chamber for different cell concentrations and flow rates. **(C–H)** Bubble graphs showing the average number of cells trapped in the chamber in correspondence of specific combinations of cell concentrations, flow rates, and seeding times. The bubble size is proportional to the number of trapped cells indicated. **(C,D)** Number of trapped cells obtained using different flow rates and seeding times starting from 10M or 20M cells/ml. **(E,F)** Number of trapped cells obtained for different cell concentrations and seeding times applying 2.5 or 5 µl/min. **(G,H)** Number of trapped cells obtained using parameter combinations theoretically leading to the same outcome. All the experimental conditions were tested independently at least six times (*$p < 0.05$; **$p < 0.01$).

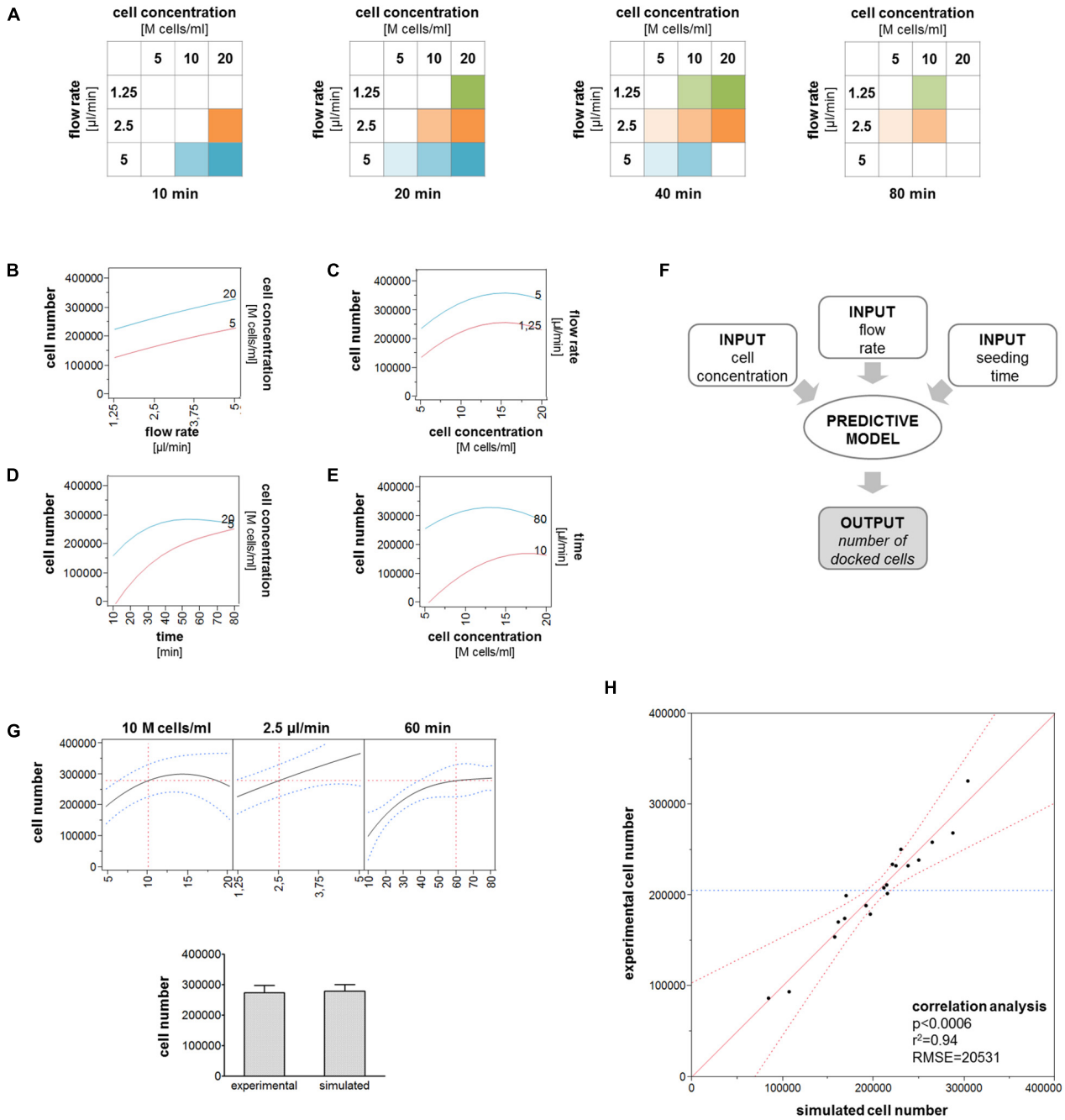

FIGURE 4 | Cell trapping model. **(A)** All the experimental conditions included in the model are represented as 2D matrices. **(B–E)** Interaction plots describing the relation between cell concentration and flow rate or seeding time. Lines describe the variation of the number of trapped cells in correspondence of the minimum and maximum values of the variable indicated in the right *y*-axis for increasing values of the variable indicating in the *x*-axis. **(F)** Schematic of the working principle of the predictive model. **(G)** Comparison between the numbers of trapped cells obtained experimentally and predicted by the model for the following parameters: 10M cells/ml, 2.5 µl/min, 60 min. **(H)** Correlation plot describing the correlation between the number of trapped cells experimentally measured and the number predicted by the model.

was observed, even though restricted to the upper region of the disk-shaped aggregate, which was directly exposed to the flow. In this region, cellularization was inferior compared to the lower region of the aggregate. In aggregates perfused at 500 µl/min, cells were more evenly distributed through the aggregate. Only in the upper region of the pellet, which was directly exposed to the medium flow, it was possible to detect a positive, yet weak, staining for GAGs.

To explain these data, the two perfusion conditions were analyzed through CFD modeling. Two different models were

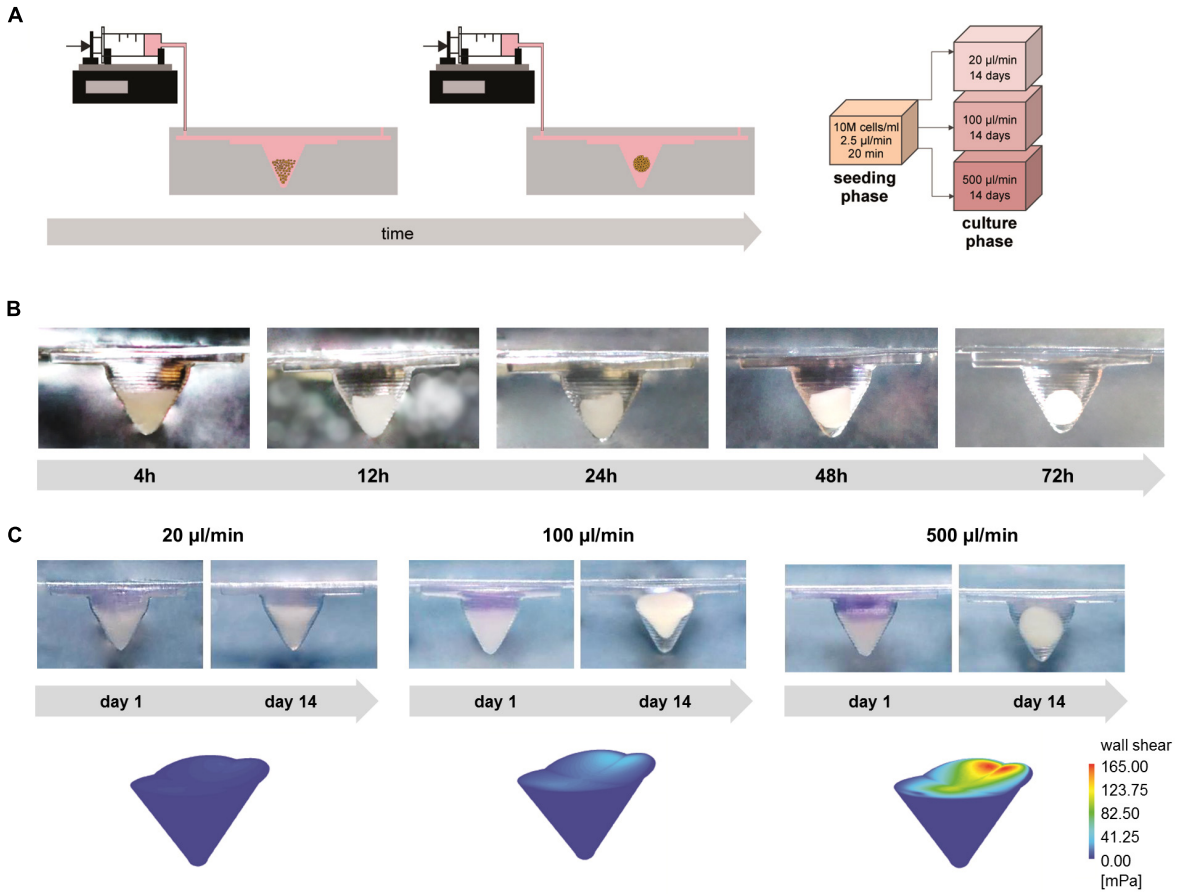

FIGURE 5 | 3D cell spheroid formation under different perfusion conditions. **(A)** Schematic showing the experimental set-up and the tested experimental conditions. **(B)** Side view of the concave chamber showing aggregate formation over time. **(C)** Representative pictures showing the process of spheroid formation and colorimetric maps of shear stresses applied on the concave chamber filled with cells under different perfusion conditions (scale bars: 1 mm).

applied to resemble the conical ($Ø_{max}$ 1.9 mm, height 1.1 mm) and the spherical (Ø 1 mm) cell aggregate generated at 100 and 500 µl/min, respectively (**Figure 6D**). Computational simulations allowed predicting velocity and wall shear stress profiles when aggregates were exposed to 100 or 500 µl/min flow rate. Consistently, fluid velocity was lower in the chamber exposed to 100 µl/min flow rate compared to the chamber exposed to 500 µl/min flow rate, reaching max values equal to 53.53 and 260.25 mm/s, respectively. As expected, in both conditions, the highest wall shear stress values were predicted in correspondence of the surfaces directly exposed to the flow. Remarkably, despite similar peak values were measured for the disk-shaped and the spherical aggregates (127.57 and 148.83 mPa, respectively), the upper surface of the disk-shaped aggregate was characterized by a more homogeneous wall shear stress distribution compared to that of the spherical aggregate. Indeed, the disk-shaped pellet showed two peek values of shear stress on lateral regions of its upper side (max 127.57 mPa, mean 34.37 mPa), while the spherical pellet showed a singular peak value of shear stress on its upper side (max 148.83 mPa, mean 18.38 mPa).

DISCUSSION

The use of 3D spheroids allows overcoming the boundaries of standard 2D cell cultures by creating environments more similar to biological tissues (Pampaloni et al., 2007; Fang and Eglen, 2017). Microfluidics enables the creation of highly controlled environments, reducing the use of cells and reagents and the associated costs, and allowing high-throughput analysis (Whitesides, 2006). For these reasons, in recent years, efforts have been made to integrate the generation and the culture of 3D spheroids in a single device, with promising outcomes in different fields (Brady et al., 2015; Lim and Park, 2018; Mulholland et al., 2018; Ko et al., 2019).

In view of the on-chip generation and culture of 3D spheroids, one of the main objectives is to achieve consistent cell deposition (Kang et al., 2010). This means that the method used for cell trapping and for the subsequent spheroid formation has to be reproducible, robust, and fully predictable. Furthermore, to aim for the routine application in the laboratory practice, ease-of-use of the microfluidic device should be pursued. For what concerns the output predictability, CFD modeling provides

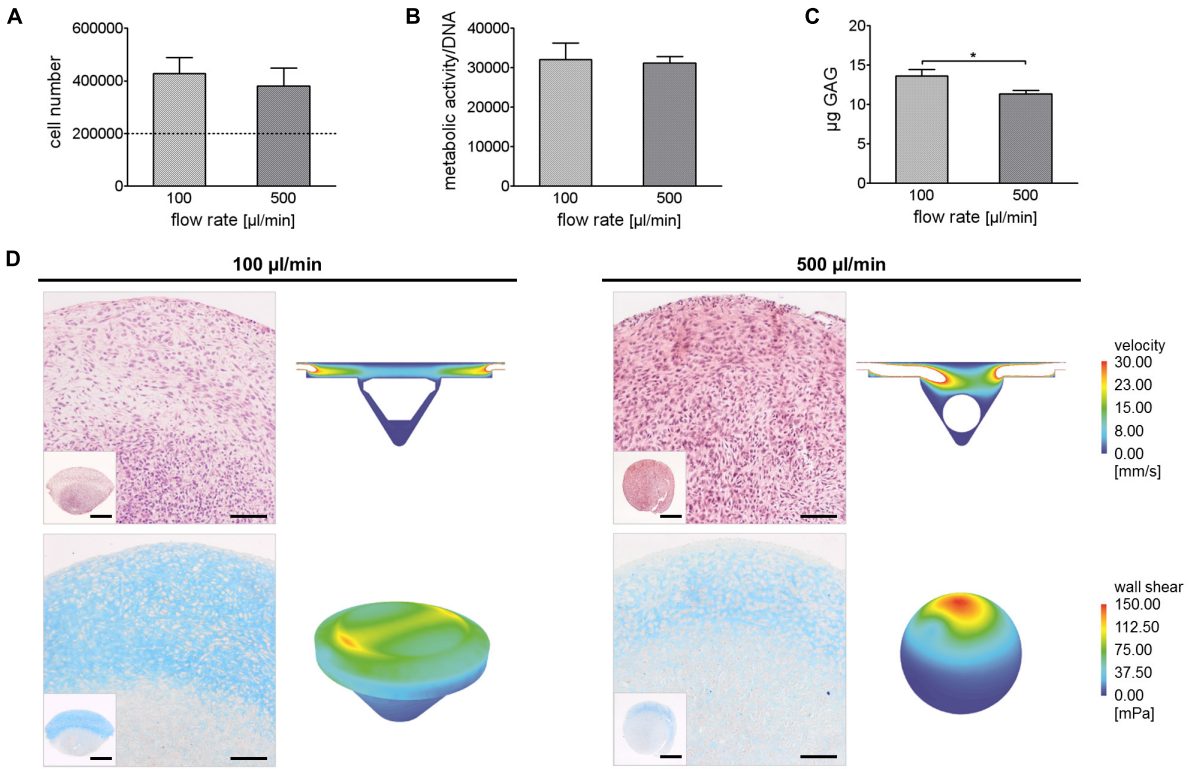

FIGURE 6 | Comparison of 3D aggregates generated under different perfusion conditions. **(A–C)** Quantification of cell number, normalized metabolic activity, and GAG content in 3D articular chondrocyte spheroids after 14 days of culture (*$p < 0.05$). **(D)** Hematoxylin/eosin (upper images) and Alcian Blue (lower images) staining of spheroids cultured in perfusion for 14 days under different flow regimen and respective velocity fields and shear stress colorimetric maps (scale bars: image 100 µm; inset 500 µm).

an invaluable tool to couple the local fluid dynamics with experimental outcomes which can be exploited both to rationally design the microfluidic device and to understand the influence of mechanical stimulation on cellular behavior.

In this study, we designed and tested a microfluidic device that allows obtaining spheroids with controlled cell number and culturing them in dynamic conditions. Here, we applied an integrated computational–experimental approach in all the phases of the study, from the design of the device to the interpretation of biological results.

Starting from standard approaches to obtain 3D spheroids by cell centrifugation, the chamber design was built with a conical geometry resembling 1.5 ml microcentrifuge tubes. In the design phase, CFD simulations were used to optimize the geometry of the microfluidic device by adding a groove before and after the conical chamber. This modification allowed modifying flow velocity field to favor cell trapping in the conical chamber. Indeed, as reported in previous studies, the combination of device geometry and flow velocity is a crucial factor for the improvement of cell trapping efficiency (Manbachi et al., 2008; Cioffi et al., 2010). However, our results showed that, given a combination of cell concentration, seeding time, and flow rate expected to result in the same number of trapped cells, increasing the fluid velocity above a certain threshold negatively affects cell trapping. In particular, when fluid velocity is higher, cells are dragged by the flow to continue their path along the channel balancing the effect of gravity force and resulting in a lower number of cells trapped within the conical chamber. These results are partially in contrast with a previous study which demonstrated that increasing the seeding flow rate in a microfluidic device with U-shaped collecting traps, it was possible to push back cells that, with lower flow rates, tended to escape from the traps before adhering to each other (Wu et al., 2008). This discrepancy indicates that fluid-dynamic assumptions cannot be easily generalized from one device to another, since the device geometry is determinant. On the other hand, our results showed that even seeding cells with low fluid velocity, it is possible to fill the conical chamber with cells, as also reported in a previous microfluidic model where gravity-driven flow was used to let cells settle in the cell culture chambers (Patra et al., 2013).

Cell trapping experiments based on the combination of cell concentration, flow rate, and seeding time were used to build a model able to predict the synergic effect of multiple non-geometrical parameters on the number of trapped cells. Using specific combinations of input parameters, the model was validated demonstrating its ability to predict the number of trapped cells obtained experimentally, thus supporting its use as a tool to plan new experiments saving time and resources in the optimization phase.

The conical chamber configuration proved to be suitable to support cell spheroid formation within 24 h after cell seeding, due to the synergic action of fluid flow and gravity sedimentation. Additionally, our device allowed the biophysical stimulation of the developing constructs, which resulted in the formation of stable cell spheroids, when adequate levels of shear stress were applied. Indeed, very low shear stress levels did not yield the formation of a stable spheroid. This result indicates that in our system cell trapping *per se* was not sufficient to induce stable cell aggregation, not even in the case of ACs that are intrinsically prone to form 3D aggregates. On the other hand, the other flow rates tested (i.e., 100 and 500 μl/min) were able to promote spheroid formation. Noticeably, even when cultured with the highest flow rate, the maximum shear stress (148.83 mPa) imposed on cells was well below 1 Pa, the threshold above which shear stress loses the chondroprotective potential and begins to be detrimental for cell survival (Mohtai et al., 1996; Wang et al., 2010; Gharravi et al., 2014). Interestingly, as expected, shear stress distribution on trapped cells was similar for both flow rates, with maximum shear values found in the top surface of cell aggregate on the opposite side from the inlet channel. However, culturing trapped cells with different flow rates allowed creating cell spheroids characterized by different size and shape, indicating that these features are strictly dependent on fluid dynamic parameters in our system. Indeed, lower shear stress values led to bigger and less rounded spheroids, while higher shear stress values led to smaller and more rounded spheroids. We hypothesized that this phenomenon was due to cell response to the fluid dynamic stimulation in the attempt to minimize shear stresses on pellet surface (Ota et al., 2011). Our hypothesis was confirmed by the hematoxylin and eosin staining. When spheroids were cultured with a low flow rate (i.e., 100 μl/min), cells tended to migrate toward the core region of the pellet forming a cell gradient, while when spheroids were cultured with a high flow rate (i.e., 500 μl/min), cells tended to be more evenly distributed and form more compact pellets. Finally, our results demonstrated that fluid dynamic stimulation plays a very important role also after spheroid formation influencing GAG deposition. These results are not unexpected, since in several studies, biophysical cues have been applied to stimulate 3D constructs through micro- and macro-scale systems, demonstrating their effects on chondrocyte phenotype (Raimondi et al., 2011; Mayer et al., 2016; Salinas et al., 2018; Occhetta et al., 2019; Sharifi and Gharravi, 2019). Alcian blue staining showed that, regardless of the flow rate, the pellet region in direct contact with culture medium was characterized by a higher amount of GAGs. This result is in accordance with several studies showing that AC metabolism is directly modulated by shear forces in a wide range of intensity (i.e., 0.01–1 Pa) acting on the cells through mechanotransduction processes and inducing the upregulation of cartilage-specific ECM components, such as GAG and other proteoglycans, as recently reviewed (Sharifi and Gharravi, 2019). It must be noted that the ACs used in this study were derived from osteoarthritic donor, albeit only macroscopically non-fibrillated regions of cartilage were harvested for cell isolation. This means that the redifferentiation potential of our cells may be lower compared to ACs obtained from healthy donors. However, our experience with osteoarthritic chondrocytes indicates that, when cultured in the presence of suitable growth factors combinations, these cells are able to redifferentiate and produce cartilage-specific matrix, in line with literature reports that indicate this cell source as suitable for cartilage tissue-engineering applications (Stoop et al., 2007; Hsieh-Bonassera et al., 2009; Lopa et al., 2013). Based on the similar effects induced by fluid flow on ACs derived from the most diverse sources (Sharifi and Gharravi, 2019), we can reasonably speculate that although absolute amounts of GAG produced by healthy and osteoarthritic chondrocytes may differ, a similar outcome can be expected in cell response to biophysical stimulation. The observed results may either depend on a direct effect of flow rate on GAG production or be the result of a combination of biophysical and biochemical stimuli. In fact, the supply of nutrients to cells *in vitro* is controlled largely by diffusion. For this reason, mass transfer of nutrients within static culture systems is limited, while it is increased by fluid motion in dynamic culture systems (Freed et al., 1994; Vunjak-Novakovic and Freed, 1998). In accordance with a previous study investigating the effect of fluid flow on chondrogenic differentiation of human mesenchymal stem cells (MSC) (Kock et al., 2014), it is possible that less compact and more porous pellets obtained with the lowest flow rate favor nutrient and oxygen diffusion toward the inner core, thus explaining the higher amount of GAG found in the spheroids cultured with the lowest flow rate. On the contrary, more compact and less porous pellets obtained with the highest flow rate may limit nutrient and oxygen diffusion toward the inner core, despite the presence of a higher flow rate. Additionally, increasing the flow rate could cause a superior wash-out of external GAG molecules as observed in several microfluidic and non-microfluidic systems (Mizuno et al., 2001; Saini and Wick, 2003; Villanueva et al., 2009; Kock et al., 2014). This hypothesis could not be confirmed since the quantification of GAG release in the medium was not planned in our experimental set-up. Indeed, the amount of GAG released in the medium was expected to be under the detection limit of standard assays, considering the volume of medium perfused in the chamber during culture and the limited number of cells contained in the pellet. However, based on the supporting evidences provided by the literature, we hypothesize that this factor can at least partially explain the lower amount of GAG observed in correspondence of the highest flow rate applied.

CONCLUSION

The described device meets the requirements for an easily accessible and consistent process to generate and culture 3D cell spheroids in a microfluidic set-up that could be upscaled to increase the throughput of the system. Our system allowed predicting the dimension and shape of the generated spheroid, proving to be highly reproducible and flexible. The particular advantage of the current system is the possibility to achieve different outcomes by simply tuning non-geometrical parameters without the need to modify the chip design. Considering the wide application of 3D cell spheroids, this platform holds a

great potential both to generate *in vitro* models related to different research fields and to produce mature building blocks for tissue biofabrication.

DATA AVAILABILITY STATEMENT

The datasets generated for this study are available on request to the corresponding author.

ETHICS STATEMENT

Ethical review and approval was not required for the study on human participants in accordance with the local legislation and institutional requirements. The patients/participants provided their written informed consent to participate in this study.

AUTHOR CONTRIBUTIONS

FP, MP, MR, and MM contributed to the conception and design of the study. SL, FP, GT, and MP performed the experiments and analyzed the data. SB and VM performed the computational analysis and analyzed the relative data. LZ provided the cartilage biopsies for articular chondrocyte isolation. SL, FP, GT, and VM wrote the manuscript. All authors contributed to manuscript revision and read and approved the submitted version.

FUNDING

This research was funded by the Italian Ministry of Health, Ricerca Corrente, Progetto "Approcci biomedici innovativi per le patologie e i disordini muscolo-scheletrici."

REFERENCES

Babur, B. K., Ghanavi, P., Levett, P., Lott, W. B., Klein, T., Cooper-White, J. J., et al. (2013). The interplay between chondrocyte redifferentiation pellet size and oxygen concentration. *PLoS One* 8:e58865. doi: 10.1371/journal.pone.0058865

Belair, D. G., Wolf, C. J., Wood, C., Ren, H., Grindstaff, R., Padgett, W., et al. (2017). Engineering human cell spheroids to model embryonic tissue fusion in vitro. *PLoS One* 12:e0184155. doi: 10.1371/journal.pone.0184155

Brady, M. A., Waldman, S. D., and Ethier, C. R. (2015). The application of multiple biophysical cues to engineer functional neocartilage for treatment of osteoarthritis. Part I: cellular response. *Tissue Eng. Part B Rev.* 21, 1–19. doi: 10.1089/ten.TEB.2013.0757

Cioffi, M., Moretti, M., Manbachi, A., Chung, B. G., Khademhosseini, A., and Dubini, G. (2010). A computational and experimental study inside microfluidic systems: the role of shear stress and flow recirculation in cell docking. *Biomed. Microdevices* 12, 619–626. doi: 10.1007/s10544-010-9414-5

Fang, Y., and Eglen, R. M. (2017). Three-dimensional cell cultures in drug discovery and development. *SLAS Discov.* 22, 456–472. doi: 10.1177/1087057117696795

Freed, L. E., Marquis, J. C., Langer, R., Vunjak-Novakovic, G., and Emmanual, J. (1994). Composition of cell-polymer cartilage implants. *Biotechnol. Bioeng.* 43, 605–614.

Gharravi, A. M., Orazizadeh, M., and Hashemitabar, M. (2014). Direct expansion of chondrocytes in a dynamic three-dimensional culture system: overcoming dedifferentiation effects in monolayer culture. *Artif. Organs* 38, 1053–1058. doi: 10.1111/aor.12295

Hsieh-Bonassera, N. D., Wu, I., Lin, J. K., Schumacher, B. L., Chen, A. C., Masuda, K., et al. (2009). Expansion and redifferentiation of chondrocytes from osteoarthritic cartilage: cells for human cartilage tissue engineering. *Tissue Eng. Part A* 15, 3513–3523. doi: 10.1089/ten.TEA.2008.0628

Huang, M. G., Fan, S. C., Xing, W. W., and Liu, C. T. (2010). Microfluidic cell culture system studies and computational fluid dynamics. *Math. Comput. Model.* 52, 2036–2042.

Ishiguro, T., Ohata, H., Sato, A., Yamawaki, K., Enomoto, T., and Okamoto, K. (2017). Tumor-derived spheroids: relevance to cancer stem cells and clinical applications. *Cancer Sci.* 108, 283–289. doi: 10.1111/cas.13155

Kang, E., Choi, Y. Y., Jun, Y., Chung, B. G., and Lee, S. H. (2010). Development of a multi-layer microfluidic array chip to culture and replate uniform-sized embryoid bodies without manual cell retrieval. *Lab Chip* 10, 2651–2654. doi: 10.1039/c0lc00005a

Karimi, A., Yazdi, S., and Ardekani, A. M. (2013). Hydrodynamic mechanisms of cell and particle trapping in microfluidics. *Biomicrofluidics* 7:21501. doi: 10.1063/1.4799787

Karp, J. M., Yeh, J., Eng, G., Fukuda, J., Blumling, J., Suh, K. Y., et al. (2007). Controlling size, shape and homogeneity of embryoid bodies using poly(ethylene glycol) microwells. *Lab Chip* 7, 786–794.

Khabiry, M., Chung, B. G., Hancock, M. J., Soundararajan, H. C., Du, Y., Cropek, D., et al. (2009). Cell docking in double grooves in a microfluidic channel. *Small* 5, 1186–1194. doi: 10.1002/smll.200801644

Khabiry, M., and Jalili, N. (2015). A microfluidic platform containing sidewall microgrooves for cell positioning and trapping. *Nanobiomedicine* 2:4. doi: 10.5772/60562

Ko, J., Ahn, J., Kim, S., Lee, Y., Lee, J., Park, D., et al. (2019). Tumor spheroid-on-a-chip: a standardized microfluidic culture platform for investigating tumor angiogenesis. *Lab Chip* 19, 2822–2833. doi: 10.1039/c9lc00140a

Kock, L. M., Malda, J., Dhert, W. J., Ito, K., and Gawlitta, D. (2014). Flow-perfusion interferes with chondrogenic and hypertrophic matrix production by mesenchymal stem cells. *J. Biomech.* 47, 2122–2129. doi: 10.1016/j.jbiomech.2013.11.006

Kwapiszewska, K., Michalczuk, A., Rybka, M., Kwapiszewski, R., and Brzozka, Z. (2014). A microfluidic-based platform for tumour spheroid culture, monitoring and drug screening. *Lab Chip* 14, 2096–2104. doi: 10.1039/c4lc00291a

Lagana, M., Arrigoni, C., Lopa, S., Sansone, V., Zagra, L., Moretti, M., et al. (2014). Characterization of articular chondrocytes isolated from 211 osteoarthritic patients. *Cell Tissue Bank.* 15, 59–66. doi: 10.1007/s10561-013-9371-3

Laschke, M. W., and Menger, M. D. (2017). Life is 3D: boosting spheroid function for tissue engineering. *Trends Biotechnol.* 35, 133–144. doi: 10.1016/j.tibtech.2016.08.004

Lee, G. H., Lee, J. S., Wang, X., and Hoon Lee, S. (2016). Bottom-up engineering of well-defined 3D microtissues using microplatforms and biomedical applications. *Adv. Healthc. Mater.* 5, 56–74. doi: 10.1002/adhm.201500107

Lim, W., and Park, S. (2018). A microfluidic spheroid culture device with a concentration gradient generator for high-throughput screening of drug efficacy. *Molecules* 23:3355. doi: 10.3390/molecules23123355

Liu, Z., Takeuchi, M., Nakajima, M., Hu, C., Hasegawa, Y., Huang, Q., et al. (2017). Three-dimensional hepatic lobule-like tissue constructs using cell-microcapsule technology. *Acta Biomater.* 50, 178–187. doi: 10.1016/j.actbio.2016.12.020

Lopa, S., Colombini, A., Sansone, V., Preis, F. W., and Moretti, M. (2013). Influence on chondrogenesis of human osteoarthritic chondrocytes in co-culture with donor-matched mesenchymal stem cells from infrapatellar fat pad and subcutaneous adipose tissue. *Int. J. Immunopathol. Pharmacol.* 26, 23–31.

Lopa, S., Piraino, F., Kemp, R. J., Di Caro, C., Lovati, A. B., Di Giancamillo, A., et al. (2015). Fabrication of multi-well chips for spheroid cultures and implantable constructs through rapid prototyping techniques. *Biotechnol. Bioeng.* 112, 1457–1471. doi: 10.1002/bit.25557

Mammoto, T., and Ingber, D. E. (2010). Mechanical control of tissue and organ development. *Development* 137, 1407–1420.

Manbachi, A., Shrivastava, S., Cioffi, M., Chung, B. G., Moretti, M., Demirci, U., et al. (2008). Microcirculation within grooved substrates regulates cell positioning and cell docking inside microfluidic channels. *Lab Chip* 8, 747–754. doi: 10.1039/b718212k

Masuda, T., Takei, N., Nakano, T., Anada, T., Suzuki, O., and Arai, F. (2012). A microfabricated platform to form three-dimensional toroidal multicellular aggregate. *Biomed. Microdevices* 14, 1085–1093. doi: 10.1007/s10544-012-9713-0

Mayer, N., Lopa, S., Talo, G., Lovati, A. B., Pasdeloup, M., Riboldi, S. A., et al. (2016). Interstitial perfusion culture with specific soluble factors inhibits type I collagen production from human osteoarthritic chondrocytes in clinical-grade collagen sponges. *PLoS One* 11:e0161479. doi: 10.1371/journal.pone.0161479

Mizuno, S., Allemann, F., and Glowacki, J. (2001). Effects of medium perfusion on matrix production by bovine chondrocytes in three-dimensional collagen sponges. *J. Biomed. Mater. Res.* 56, 368–375.

Moeller, H. C., Mian, M. K., Shrivastava, S., Chung, B. G., and Khademhosseini, A. (2008). A microwell array system for stem cell culture. *Biomaterials* 29, 752–763.

Mohtai, M., Gupta, M. K., Donlon, B., Ellison, B., Cooke, J., Gibbons, G., et al. (1996). Expression of interleukin-6 in osteoarthritic chondrocytes and effects of fluid-induced shear on this expression in normal human chondrocytes in vitro. *J. Orthop. Res.* 14, 67–73.

Moreira Teixeira, L. S., Leijten, J. C., Sobral, J., Jin, R., Van Apeldoorn, A. A., Feijen, J., et al. (2012). High throughput generated micro-aggregates of chondrocytes stimulate cartilage formation in vitro and in vivo. *Eur. Cell Mater.* 23, 387–399.

Mulholland, T., Mcallister, M., Patek, S., Flint, D., Underwood, M., Sim, A., et al. (2018). Drug screening of biopsy-derived spheroids using a self-generated microfluidic concentration gradient. *Sci. Rep.* 8:14672. doi: 10.1038/s41598-018-33055-0

Nakazawa, K., Yoshiura, Y., Koga, H., and Sakai, Y. (2013). Characterization of mouse embryoid bodies cultured on microwell chips with different well sizes. *J. Biosci. Bioeng.* 116, 628–633. doi: 10.1016/j.jbiosc.2013.05.005

Napolitano, A. P., Chai, P., Dean, D. M., and Morgan, J. R. (2007). Dynamics of the self-assembly of complex cellular aggregates on micromolded nonadhesive hydrogels. *Tissue Eng.* 13, 2087–2094.

Occhetta, P., Mainardi, A., Votta, E., Vallmajo-Martin, Q., Ehrbar, M., Martin, I., et al. (2019). Hyperphysiological compression of articular cartilage induces an osteoarthritic phenotype in a cartilage-on-a-chip model. *Nat. Biomed. Eng.* 3, 545–557. doi: 10.1038/s41551-019-0406-3

Ota, H., Kodama, T., and Miki, N. (2011). Rapid formation of size-controlled three dimensional hetero-cell aggregates using micro-rotation flow for spheroid study. *Biomicrofluidics* 5, 34105–3410515. doi: 10.1063/1.3609969

Pampaloni, F., Reynaud, E. G., and Stelzer, E. H. (2007). The third dimension bridges the gap between cell culture and live tissue. *Nat. Rev. Mol. Cell Biol.* 8, 839–845.

Patra, B., Chen, Y. H., Peng, C. C., Lin, S. C., Lee, C. H., and Tung, Y. C. (2013). A microfluidic device for uniform-sized cell spheroids formation, culture, harvesting and flow cytometry analysis. *Biomicrofluidics* 7:54114. doi: 10.1063/1.4824480

Pettinato, G., Wen, X., and Zhang, N. (2014). Formation of well-defined embryoid bodies from dissociated human induced pluripotent stem cells using microfabricated cell-repellent microwell arrays. *Sci. Rep.* 4:7402. doi: 10.1038/srep07402

Piraino, F., Selimovicì, S. E., Adamo, M., Pero, A., Manoucheri, S., Bok Kim, S., et al. (2012). Polyester μ-assay chip for stem cell studies. *Biomicrofluidics* 6:044109. doi: 10.1063/1.4766300

Raimondi, M. T., Bonacina, E., Candiani, G., Lagana, M., Rolando, E., Talo, G., et al. (2011). Comparative chondrogenesis of human cells in a 3D integrated experimental-computational mechanobiology model. *Biomech. Model. Mechanobiol.* 10, 259–268. doi: 10.1007/s10237-010-0232-8

Sabatino, M. A., Santoro, R., Gueven, S., Jaquiery, C., Wendt, D. J., Martin, I., et al. (2012). Cartilage graft engineering by co-culturing primary human articular chondrocytes with human bone marrow stromal cells. *J. Tissue Eng. Regen. Med.* 9, 1394–1403. doi: 10.1002/term.1661

Saini, S., and Wick, T. M. (2003). Concentric cylinder bioreactor for production of tissue engineered cartilage: effect of seeding density and hydrodynamic loading on construct development. *Biotechnol. Prog.* 19, 510–521.

Sakai, Y., Yoshida, S., Yoshiura, Y., Mori, R., Tamura, T., Yahiro, K., et al. (2010). Effect of microwell chip structure on cell microsphere production of various animal cells. *J. Biosci. Bioeng.* 110, 223–229. doi: 10.1016/j.jbiosc.2010.01.021

Salinas, E. Y., Hu, J. C., and Athanasiou, K. (2018). A guide for using mechanical stimulation to enhance tissue-engineered articular cartilage properties. *Tissue Eng. Part B Rev.* 24, 345–358. doi: 10.1089/ten.TEB.2018.0006

Selimovic, S., Piraino, F., Bae, H., Rasponi, M., Redaelli, A., and Khademhosseini, A. (2011). Microfabricated polyester conical microwells for cell culture applications. *Lab Chip* 11, 2325–2332. doi: 10.1039/c1lc20213h

Sharifi, N., and Gharravi, A. M. (2019). Shear bioreactors stimulating chondrocyte regeneration, a systematic review. *Inflamm. Regen.* 39:16. doi: 10.1186/s41232-019-0105-1

Sridharan, B., Laflin, A. D., and Detamore, M. S. (2018). Generating chondromimetic mesenchymal stem cell spheroids by regulating media composition and surface coating. *Cell. Mol. Bioeng.* 11, 99–115. doi: 10.1007/s12195-017-0517-4

Sridharan, B., Lin, S. M., Hwu, A. T., Laflin, A. D., and Detamore, M. S. (2015). Stem cells in aggregate form to enhance chondrogenesis in hydrogels. *PLoS One* 10:e0141479. doi: 10.1371/journal.pone.0141479

Stoop, R., Albrecht, D., Gaissmaier, C., Fritz, J., Felka, T., Rudert, M., et al. (2007). Comparison of marker gene expression in chondrocytes from patients receiving autologous chondrocyte transplantation versus osteoarthritis patients. *Arthritis Res. Ther.* 9:R60.

Villanueva, I., Klement, B. J., Von Deutsch, D., and Bryant, S. J. (2009). Cross-linking density alters early metabolic activities in chondrocytes encapsulated in poly(ethylene glycol) hydrogels and cultured in the rotating wall vessel. *Biotechnol. Bioeng.* 102, 1242–1250. doi: 10.1002/bit.22134

Vunjak-Novakovic, G., and Freed, L. E. (1998). Culture of organized cell communities. *Adv. Drug Deliv. Rev.* 33, 15–30.

Wang, P., Zhu, F., and Konstantopoulos, K. (2010). Prostaglandin E2 induces interleukin-6 expression in human chondrocytes via cAMP/protein kinase A- and phosphatidylinositol 3-kinase-dependent NF-kappaB activation. *Am. J. Physiol. Cell Physiol.* 298, C1445–C1456. doi: 10.1152/ajpcell.00508.2009

Whitesides, G. M. (2006). The origins and the future of microfluidics. *Nature* 442, 368–373.

Wu, L. Y., Di Carlo, D., and Lee, L. P. (2008). Microfluidic self-assembly of tumor spheroids for anticancer drug discovery. *Biomed. Microdevices* 10, 197–202.

Xia, Y., and Whitesides, G. M. (1998). Soft lithography. *Annu. Rev. Mater. Sci.* 28, 153–184.

Zorlutuna, P., Annabi, N., Camci-Unal, G., Nikkhah, M., Cha, J. M., Nichol, J. W., et al. (2012). Microfabricated biomaterials for engineering 3D tissues. *Adv. Mater.* 24, 1782–1804. doi: 10.1002/adma.201104631

Conflict of Interest: The authors declare that the research was conducted in the absence of any commercial or financial relationships that could be construed as a potential conflict of interest.

frontiers in Bioengineering and Biotechnology

ORIGINAL RESEARCH
published: 08 May 2020
doi: 10.3389/fbioe.2020.00388

Improvement of a Three-Layered *in vitro* Skin Model for Topical Application of Irritating Substances

Freia F. Schmidt, Sophia Nowakowski and Petra J. Kluger*

Reutlingen Research Institute, Reutlingen University, Reutlingen, Germany

In the field of skin tissue engineering, the development of physiologically relevant *in vitro* skin models comprising all skin layers, namely epidermis, dermis, and subcutis, is a great challenge. Increasing regulatory requirements and the ban on animal experiments for substance testing demand the development of reliable and *in vivo*-like test systems, which enable high-throughput screening of substances. However, the reproducibility and applicability of *in vitro* testing has so far been insufficient due to fibroblast-mediated contraction. To overcome this pitfall, an advanced 3-layered skin model was developed. While the epidermis of standard skin models showed an 80% contraction, the initial epidermal area of our advanced skin models was maintained. The improved barrier function of the advanced models was quantified by an indirect barrier function test and a permeability assay. Histochemical and immunofluorescence staining of the advanced model showed well-defined epidermal layers, a dermal part with distributed human dermal fibroblasts and a subcutis with round-shaped adipocytes. The successful response of these advanced 3-layered models for skin irritation testing demonstrated the suitability as an *in vitro* model for these clinical tests: only the advanced model classified irritative and non-irritative substances correctly. These results indicate that the advanced set up of the 3-layered *in vitro* skin model maintains skin barrier function and therefore makes them more suitable for irritation testing.

Keywords: three-layered skin model, *in vitro* skin irritation testing, alternatives to animal testing, tissue engineering, subcutis

OPEN ACCESS

Edited by:
Dimitrios I. Zeugolis, National University of Ireland Galway, Ireland

Reviewed by:
Thomas Biedermann, University of Zurich, Switzerland
Kar Wey Yong, University of Alberta, Canada

****Correspondence:***
Freia F. Schmidt
Freia.Schmidt@reutlingen-university.de

Specialty section:
This article was submitted to Tissue Engineering and Regenerative Medicine, a section of the journal Frontiers in Bioengineering and Biotechnology

Received: *18 January 2020*
Accepted: *07 April 2020*
Published: *08 May 2020*

Citation:
Schmidt FF, Nowakowski S and Kluger PJ (2020) Improvement of a Three-Layered in vitro Skin Model for Topical Application of Irritating Substances. Front. Bioeng. Biotechnol. 8:388. doi: 10.3389/fbioe.2020.00388

INTRODUCTION

The assessment of skin toxicity is an essential part of the analyzing the overall effect of chemicals and pharmaceutical products. As an ethical alternative for skin toxicity testing, and due to the limited transferability of results from animal assays to human reactions, *in vitro*-generated organ-like reconstructed human skin models have been developed using tissue engineering techniques. Global legislation has been committed to the development of alternative test methods, in accordance to the 3Rs (reduction, refinement, and replacement of animal experimentation) established by Russell et al. (1959).

Several skin models are currently commercially available from various producers and academic institutes. While, such models are used for skin corrosion, skin irritation, skin barrier formation, and skin absorption assays, amongst others, the only approved *in vitro* tests use epidermal models (OECD, 2019a,b). The absence of dermal and subcutaneous layers limits the application of the

models, as well as the crosstalk of the three skin layers, the regulation of skin morphology, homeostasis, and metabolic activity (Maas-Szabowski et al., 1999; Oesch et al., 2014; Wiegand et al., 2014). Different artificial skin models constituting an epidermal and dermal layer are available, however, the subcutaneous part of the skin in most current models is neglected.

As an endocrine and paracrine organ, adipose tissue plays an important role in the irritating and sensitizing reaction of tissue and in the storage and metabolization of drugs. Therefore, this part of the skin is crucial for the assessment of effects of drugs on the skin and for the storage of various substances. Many studies confirm that especially lipophilic adipose tissue can absorb harmful substances highlighting the need for test systems to categorize such substances. The process of accumulation of a substance in tissue has so far been neglected in most experiments (*in vivo*, as well as *in vitro*). A three-layered skin model reflects the native skin more accurately, as well as extending the test spectrum with new test substances and further endpoints. First efforts to generate three-layered skin models have been made using stem cells, which were differentiated into the adipogenic lineage (Bellas et al., 2012). However, stem cells are time-, material-, and cost-intensive. Additionally, subcutaneous layers created using stem cells have so far lacked a sufficient amount of functional adipocytes. As an alternative, using mature adipocytes to create a functional subcutis (Huber et al., 2016b) offers promising properties. They can be isolated in large numbers and are fully functional without the need for further differentiation from adipose tissue. To build up artificial connective tissue, collagen hydrogels are commonly used as the main protein component of the extracellular matrix of the native dermis are collagen type I and type III (Rossi et al., 2015). However, fibroblasts contract collagen-based hydrogels in culture resulting in the epidermal layer losing the close connection to the insert wall, and eventually leading to the loss of skin barrier function (Ackermann et al., 2010). To overcome the fibroblast-mediated contraction of hydrogels, different approaches were used so far. A reduced contraction of collagen hydrogels was caused by physical and chemical modifications, for example using plastic compression or cross-linking of the collagen matrix (Braziulis et al., 2012; Lotz et al., 2017). However, in these cases, the contraction cannot be completely prevented, and the modifications further influence cell behavior. To overcome these shortcomings, in this study we explored altered culture conditions to maintain the epidermal barrier function in collagen-based skin models.

We aimed to improve the barrier function of our already established model using a three-layered *in vitro* skin model, including an epidermis, dermis, and a subcutis by adapting the culture conditions. The novel skin model overcomes an epidermal shrinkage by applying keratinocytes to the insert membrane which separates the epidermis from the underlying dermis. Using this functional epidermis, various barrier function tests were performed highlighting that the modified system is superior in terms of epidermal barrier function. Additionally, modified skin models with an advanced construction were morphologically characterized and compared to native human skin. Finally, we evaluated the applicability of the three-layered skin models for irritation studies by analyzing the irritation potential of known substances. This is essential for their application as an alternative to animal testing.

MATERIALS AND METHODS

Human Tissue Samples

All research was carried out in accordance with the Declaration of Helsinki on human medical research. Patients gave written consent after being given information about the use of their probes. This as in accordance with the permission of the Landesärztekammer Baden-Württemberg (F-2012-078; for normal skin from elective surgeries).

Cell Isolation and Culture

Adult mature adipocytes were isolated as described previously byHuber et al. (2016a). Human fatty tissue was provided by Dr. Ziegler (Klinik Charlottenhaus, Stuttgart) (Huber et al., 2016a).

Primary keratinocytes and fibroblasts were isolated from biopsies of human foreskin of surgeries performed by Dr. Z. Yurrtas from Stuttgart. Their isolation was performed according to protocols previously described by Huber et al. Keratinocytes were used in passage 3 for all experiments.

Construction of Three-Layered Skin Models and Advanced Three-Layered Skin Models

The construction of three-layered skin models was based on the procedure previously described by Huber et al. (2016b) with some modifications. Three-layered skin models were composed in a collagen type I hydrogel (10 mg/mL from rat tail, Corning, United States) in 12-well plate inserts (Greiner Bio-One, 0.4 μm pore diameter). The subcutaneous layer, is made of collagen gel mixed with freshly isolated adipocytes and a gel neutralization buffer [10× DMEM/Ham's F12 (Biochrom) and 50 mM NaOH in demineralized water (1:1) with 0.2 M $NaHCO_3$ and 0.225 M HEPES (Serva Electrophoresis)] in a ratio of 4:4:1. 300 μL was pipetted into each insert and the gel run for 20 min at 37°C. The dermal layer consists of fibroblasts embedded in a collagen hydrogel. Collagen, fibroblast suspension and gel neutralization buffer were mixed in the same manner as described for the subcutaneous layer (ratio 4:4:1). Per skin model, 1.5×10^4 fibroblasts in 300 μL collagen solution were seeded above the adipose tissue layer. Then the models were incubated for another 20 min at 37°C. Inserts were placed into deep-well plates containing 5 mL of adipocyte maintenance 1 medium (ZenBio) supplemented with 1.44 mM $CaCl_2$ (Applichem) and 73 μg/mL ascorbic acid-2-phosphate (Sigma-Aldrich; =AM1-Air) and were incubated for 24 h. The next day, keratinocytes were obtained by accutase incubation (Sigma-Aldrich) for 20 min at 37°C and 5% CO_2. On each insert, $5 \times 10_5$ cells were seeded in 500 μL keratinocyte growth medium and allowed to attach for 1 h. Then 5 mL AM1-Air was added to the wells. After 24 h, the remaining medium in the insert was removed to allow airlift conditions for the keratinocytes.

For the advanced three-layered skin models, pieces of silicone tubing (1 cm width, 15 mm inner diameter, 2 mm wall thickness, cut into pieces of 20 mm height; Esska) were disinfected with 70% ethanol (Brenntag) and attached to the bottom of the cell culture inserts (Greiner Bio-One). Inserts were turned over and the dermal layer was pipetted into the piece of tubing, following the subcutaneous layer. Gels were prepared as described above for the previous three-layered skin model. After seeding, the inserts were turned over again and placed into a 12-deep-well plate containing 3 mL AM1-Air. After 24 h, keratinocytes were seeded onto the insert membrane and set to airlift culture after another 24 h. Three-layered skin models and advanced three-layered skin models were cultured for 15 days in AM1-Air until further evaluation.

Measurement of Epidermal Area

The area of the epidermis was measured at days 4, 7, and 14 using Image J by comparison to a set scale.

Determination of Skin Barrier by Topical Detergent Application

The barrier of skin and advanced skin models was tested by application of 1% Triton X-100 for 1.5 h at 37°C and 5% CO_2. Remaining Triton X-100 was aspirated and the skin models were washed twice with Phosphate buffered saline (PBS). The viability of the skin models was measured via a WST-1 assay (Takara Clontech), with absorbance measurement of 200 µL sample at 450 and 620 nm. Values were normalized to non-treated skin models.

Permeability Experiments With Fluorescent Molecules

The silicone tubes were removed from the inserts of the advanced skin models. Skin models and advanced skin models were placed into 12-well plates. AM1-Air medium (1 mL) was applied to the receiver compartment and 300 µL of fluorescent solution [1 mg/mL fluorescein isothiocyanate dextran (4 kDa, Sigma-Aldrich) in AM1-Air, 0.25 mg/mL fluorescein sodium (Roth) in AM1-Air] to the donor compartment. The plate was incubated at 37°C under agitation over 6 h. At defined time points (0.5, 1, 2, 4, 6 h), an aliquot (100 µL) was withdrawn from the receiver compartment and the removed liquid was replaced with AM1-Air medium. Fluorescence was measured by a micro-plate reader (Tecan) at 485/530 nm.

Irritation Experiments

Study Design

The irritation tests were performed according to the OECD test guideline 439 (OECD, 2019b). The reference substances (**Table 1**) comprised one irritant (category 2 substance) according to the United Nations Globally Harmonized System of Classification and Labelling of Chemicals (UN GHS), and one non-irritant (no category substance). Two controls were included in each test run. Phosphate buffered saline (Lonza) was applied to the top of the models as a negative control (non-irritant) and a 5% aqueous solution of sodium dodecyl sulfate (SDS; Sigma-Aldrich) served as positive control (irritating). All substances and controls were tested on three skin model replicates per test run.

TABLE 1 | List of two reference chemicals defined in the OECD performance standard Test No. 439 (*in vitro* Skin Irritation: Reconstructed Human Epidermis Test Method) to assess the predictive capacity of the skin models.

Test substances	Supplier	Physical state	UN GHS category
2-Propanol	Brenntag	Liquid, clear, colorless	No category (non-irritant)
Heptanal	Thermo Fisher Scientific	Liquid, clear, colorless	Category 2 (irritant)

Test Protocol

The skin irritation test was carried out according to the protocol published by Groeber et al. (2016) with some modifications. Briefly, 100 µL of the liquid test substances were applied to the skin models and advanced skin models. After a treatment time of 35 min at room temperature, the skin models were washed eight times with 600 µL PBS each and additionally immersed five times into 60 mL fresh PBS. After a post-exposure incubation of 42 h at 37°C and 5% CO_2, tissue viability was assessed via a WST-1 assay (TaKaRa Bio Europe, France). For that, skin models were cut out of the inserts and incubated with 1 mL WST-1 reagent in AM1-Air (1:10) for 30 min at 37°C and 5% CO_2. The WST-1 reduction was quantified by measuring the optical density at a wavelength of 450 and 620 nm using a micro-plate reader (Tecan). Tissue viability of treated models was normalized to the negative control (PBS), which was set to 100%.

Prediction/Evaluation Model

In this study, the prediction/evaluation model defined in the performance standards of the OECD test guideline 439 was used. A 50% threshold was used for the prediction/evaluation of skin irritation from viability measurements. A substance that reduced the average viability after the skin irritation test to below 50% was classified as "irritating" or "category 2" following the UN GHS system. Substances with mean viability above 50% were classified as "non-irritating" or "no category."

Quantification of Extracellular Interleukin Concentration by ELISA

To investigate the cytokine response following skin irritation, the extracellular interleukin (IL) concentration of IL-1α, IL-6 and IL-8 was quantified by ELISA (PeproTech). This was carried out according to the manufacturer's instructions. Briefly, supernatants were collected before and after the irritation test (42 h after the last medium change). Samples were diluted as follows: for IL-1α undiluted, for IL-8 1:50, and samples treated with 2-propanol 1:100, for IL-6 1:2 and samples treated with 1:10. For color development, 100 µL tetramethylbenzidine (TMB) substrate was added to each well. The reaction was stopped with 100 µL 1 M sulfuric acid (Thermo Fisher Scientific) and the absorption was measured at 450 nm with a wavelength correction of 620 nm (Tecan). The concentration of IL-1α, IL-6 and IL-8 was calculated using an evaluation excel sheet provided by PeproTech.

Hemalaun-Eosin Staining and Immunofluorescence Staining

Skin models were fixed using 4% paraformaldehyde (Roth) for 4 h and watered with demineralized water for several hours. After embedding tissues in paraffin, sections of 5 μm were generated. Hemalaun-eosin staining was performed according to a standard staining procedure.

For immunofluorescence staining, tissue sections were deparaffined according to a standard protocol. Sections for filaggrin, cytokeratin 10 and 14 and vimentin were heat demasked with a target retrieval buffer pH 6 and Ki67 and perilipin A with a target retrieval buffer pH 9 for 20 min in a preheated steamer. Tissue sections were blocked with 3% BSA in 0.1% Triton X-100 for 30 min. Primary antibodies (cytokeratin 10: 1:200, Santa Cruz; cytokeratin 14: 1:1000; and filaggrin: 1:500, both Boster Biological Technologies; Ki67: 1:100; and vimentin: 1:1000, both Abcam; perilipin A: 1:500, Sigma-Aldrich) were diluted with blocking solution and incubated overnight at 4°C. Secondary antibodies Alexa Fluor 488 (1:500, Abcam) and Cy3 (1:250, Jackson ImmunoResearch Laboratories) were used for 1 h at room temperature. Sections were covered with Fluoromount-G containing DAPI (Life Technologies) and a coverslip and analyzed with a fluorescence microscope (Zeiss).

Statistics

All experiments were repeated as indicated in figure legend The samples of three donors were examined. Data was compared using one-way analysis of variance (ANOVA) with repeated measurements and a mean value comparison according to Tukey using Origin Pro. Statistical significance was stated as $^{*}p < 0.05$.

RESULTS

The Advanced Construction of Skin Models Prevents Dermal-Mediated Contraction of the Epidermis

To understand what prevents dermal-mediated contraction of the epidermal layer of skin models, the new construction approach was compared to skin models cultured with a more common method (**Figure 1**). Freshly isolated adipocytes and fibroblasts were encapsulated into a collagen hydrogel and seeded into a silicone tube attached beneath the cell culture insert. The next day, keratinocytes were seeded into the insert directly on the PET membrane, which functions as an artificial basal membrane. The modified setup differs from the previous structure in which all three skin layers are inserted directly into the cell culture insert without the separating membrane between epidermal and dermal part.

To assess the capability of advanced skin models to resist cell-mediated contraction of the epidermal part, the epidermal layer was monitored periodically for 15 days (**Figure 2**). During the culture period, the epidermis of the common skin models continuously contracted by 17.68 ± 1.46% of the initial epidermal surface (**Figure 2A**). In opposition, no contraction was detected in the advanced skin models, whereby a surface area of 100% was retained (**Figure 2B**).

These observations suggest that the advanced skin models prevent dermal-mediated contraction of the epidermal layer, compared to more commonly used *in vitro* models.

Advanced Skin Models Show Improved Skin Barrier Functions

The barrier integrity is the most integral to the skin models and ensures reliable testing. Therefore, the resistance to a detergence (Triton X-100) and permeability assays with fluorescent molecules (0.25 mg/mL fluorescein sodium and 1 mg/mL FITC-dextran) were conducted on day 15 of the advanced skin models (**Figure 3**).

The viability of the models after Triton application was significantly reduced by 25.43 ± 12.46% for common/traditional skin models and to 53 ± 10.82% for the advanced models, compared to the respective untreated models (**Figure 3A**). Moreover, the mean viability value of the advanced skin models treated with Triton was significantly higher than that of the more traditional skin models, indicating a higher cell survival in the advanced skin model following detergent application.

To assess permeability, fluorescein sodium and FITC-dextran were applied topically to the skin models and incubated for 6 h. Samples were taken after 0.5, 1, 2, 4, and 6 h of treatment. Fluorescence values were normalized to the reference/untreated samples and displayed as a percentage. With the fluorescein sodium treatment, no significant difference in the mean values between the skin model approaches was observed for the first two sampling times [0.5 h: 3.47 ± 2.55% (traditional skin model), 0.2 ± 0.24% (advanced skin model), 1 h: 7.59 ± 4.59% (traditional skin model), 0.72 ± 0.7% (advanced skin model)]. From 2 h of starting the treatment the fluorescence values of the skin model (16.53 ± 8.29%, 31.11 ± 12.63%, 42.39 ± 16.13%) were significantly higher compared to the advanced traditional skin model (1.94 ± 1.63%, 4.94 ± 3.75%, 17.17 ± 5.38%; **Figure 3B**).

For FITC-dextran, the advanced skin models showed no measurable changes in permeability compared to the untreated. For the skin models, the relative fluorescence values were 0.28 ± 0.37% after 0.5 h of incubation, 0.83 ± 0.87% after 1 h, 1.94 ± 1.49% after 2 h, 3.83 ± 2.37% after 4 h and 6.45 ± 4.33% after 6 h (**Figure 3C**).

Advanced Skin Models Recapitulate the Morphology of Human Skin

To analyze the basic morphological features of the traditional skin models, H&E staining were conducted and compared to human skin samples. Both *in vitro* skin models formed a multilayered epidermis, a dermal compartment, and a subcutaneous layer (**Figure 4**). The architecture of the skin models and human skin were comparable. In the lower part of the epidermis, several layers of living cells can be identified both in the skin models and the human skin. These formed a defined stratum basale, granulosum, and spinosum. The epidermal keratinocytes showed a cuboid morphology typical of human keratinocytes in the basal layer. In both skin models,

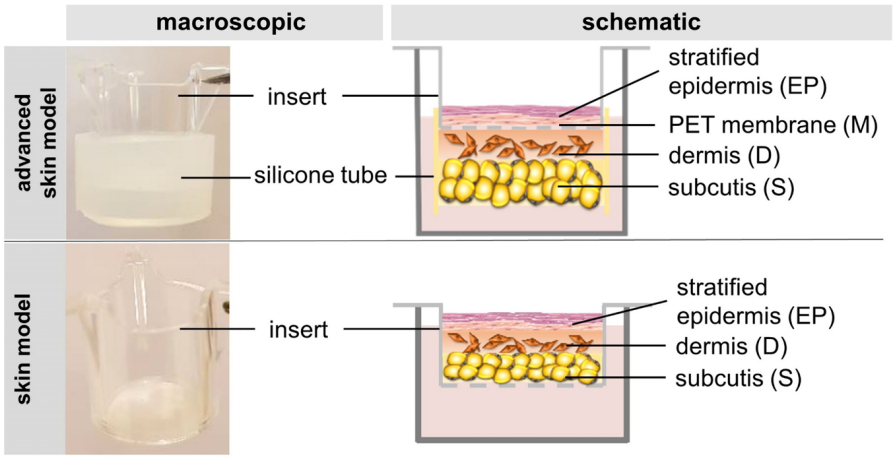

FIGURE 1 | The figure schematically depicts the construction of the skin model and the advanced skin model.

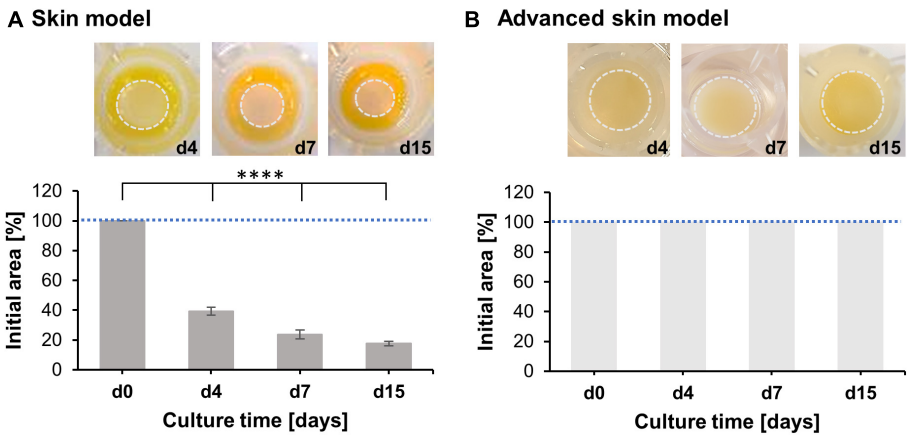

FIGURE 2 | Analysis of skin model area over time. Pictures show representative tissue models after 4, 7, and 15 days of culture. Dashed circles (light gray) indicate the contracted area of the epidermal-dermal part. Bar graphs outline percentages of the initial area at the respective days normalized to the area at day 0. Mean values are plotted with SD. Dashed blue lines highlight 100% of the initial skin model area. **(A)** Evaluation of skin model area (n = 3), **(B)** Evaluation of advanced skin model area (n = 3), level of significance ****$p < 0.0001$.

the stratum granulosum consisted of flat cells with certain cells lacking a nucleus. The stratum spinosum was also comparable the *in vitro* models and the human skin. However, human skin and skin models differed in the thickness of the stratum spinosum. This appeared to be regular in the skin models compared to the irregular thickness of the native model. This was due to the papillary bodies of the human skin. In the dermis of human skin, the fibroblasts were clustered whereas in the skin models fibroblasts were homogenously distributed throughout the dermal part and appeared more elongated and spindle-shaped as well as being less numerous. The underlying subcutis showed round-shaped adipocytes with detectable cell nuclei comparable to human adult adipose tissue. However, the subcutaneous layer of the skin models contained more intermediate matrix and the cells were not as densely packed as in the human adipose tissue.

The skin models were characterized using the three differentiation markers: Cytokeratin 10 and 14, and fillagrin (**Figure 5**). Ki67 staining was also carried out to assess cell proliferation in the epidermal layer (**Figure 5**). Human dermal fibroblasts were visualized via vimentin (**Figure 5**). Adipocytes of the subcutaneous layer were stained using the coating protein perlipin A (**Figure 5**). The co-localization of the epidermal differentiation markers cytokeration 10 and 14 and of filaggrin could be seen in the skin models as well as in human skin. Cytokeratin 10 was present as part of the intermediate filament network in the suprabasal layers, whereas cytkeratin 14 was most strongly represented in the basal layers. Fillagrin was found particularly in the stratum corneum. Proliferative cells were identified by Ki67 staining in the base layer of the epidermis, for both the skin models and human skin. The distribution of the skin fibroblasts in the skin portion of the models were identified by vimentin staining and comparable to the dermis of the human skin. The subcutis was visualized using the perlipin A coating

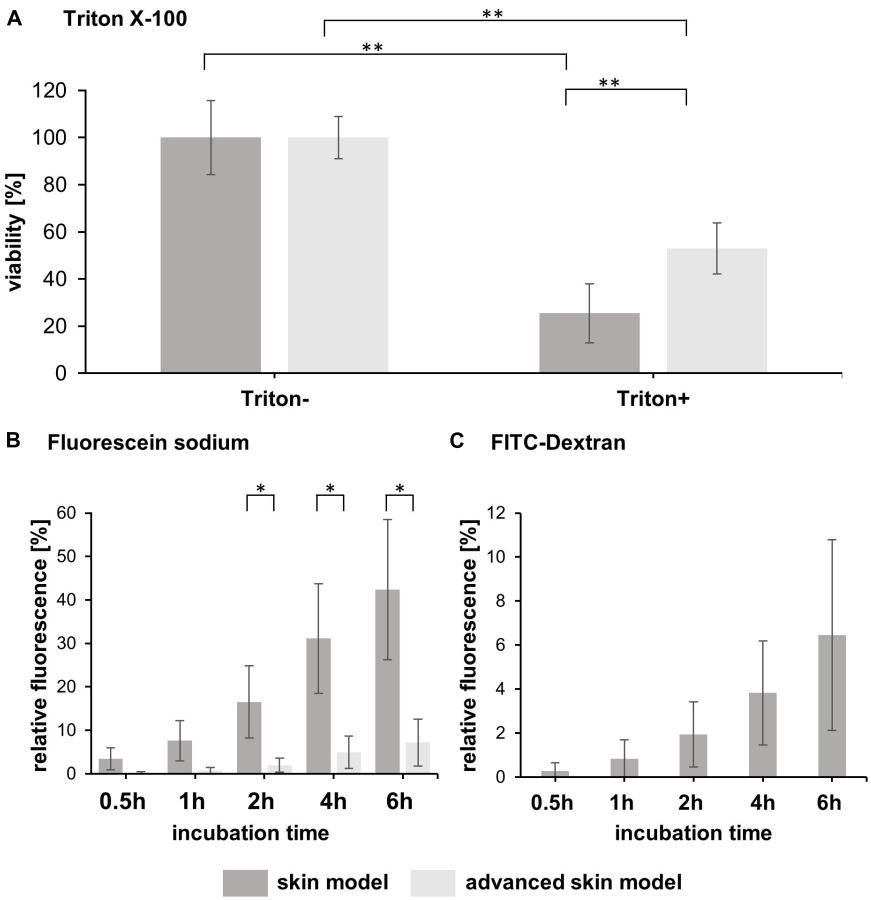

FIGURE 3 | Analysis of skin model barrier function. **(A)** The bar graph shows the percentual viability of skin models and advanced skin models after treatment with (Triton+) and without a detergent (Triton-) ($n = 3$). The values were normalized to the untreated skin model/advanced skin model which was set to 100%. Level of significance $^{**}p < 0.01$. **(B)** Fluorescein sodium and **(C)** FITC-dextran were applied topically to the skin models and permeability was assessed over a time period of 6 h with sampling at 0.5, 1, 2, 4, and 6 h after application. The bar graphs depict the percentage of relative fluorescence values normalized to a reference which was set to 100% (fluorescent stock solution in cell culture medium). For FITC-dextran, only values for skin models are shown, as the values for the advanced skin models were below the detection limit. Mean values are presented with SD ($n = 3$). Level of significance $^{*}p < 0.05$.

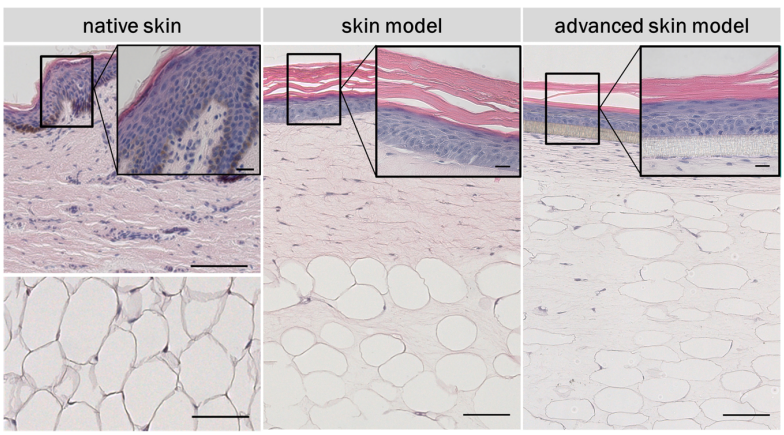

FIGURE 4 | H&E staining of *in vivo* and *in vitro* skin. The epidermis contains all characteristic layers: basal, spinous, granular and cornified layer. The artificial basal lamina (insert PET membrane) is shown for the advanced skin model. Cell nuclei are stained in purple/blue and plasma proteins, collagen, and keratins are stained in pink. Black arrows point at nuclei. Scale bars: 100 μm (low magnification), 20 μm (high magnification).

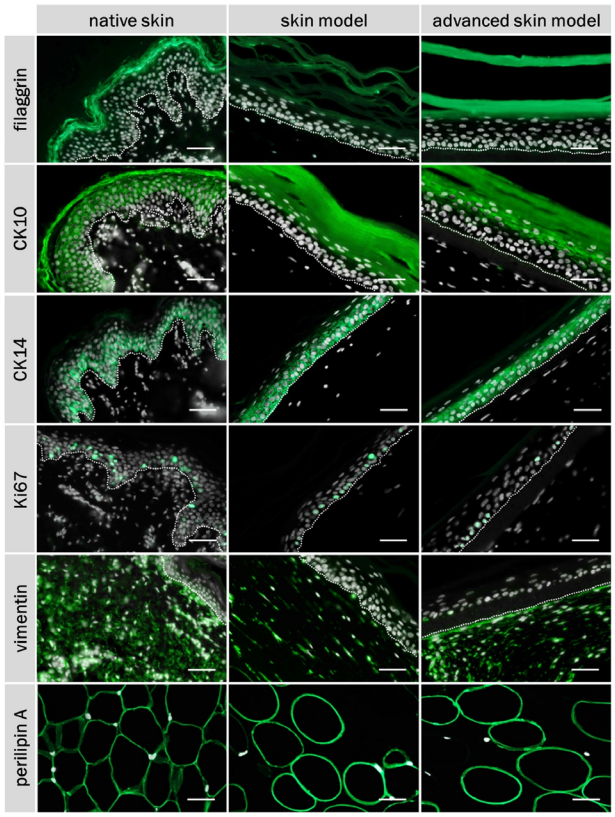

FIGURE 5 | Immunofluorescence staining of filaggrin, CK10, CK14, Ki67, vimentin, perilipin A, and DAPI of native skin and skin models. Cell nuclei (stained with DAPI) are illustrated in white, characteristic proteins (stained with respective specific antibody) in green. White dashed line shows epidermal-dermal border. Scale bar: 50 μm.

protein. Both skin models showed adipocysts completely coated with perlipin A. This corresponds to the native fat tissue structure.

Advanced Skin Models Are Suitable to Test the Irritation Potential of Substances

The irritation potential of substances is commonly detected by cell viability, after the topical application of the substance and a subsequent post-incubation time. A negative (PBS) and positive control (5% SDS solution) were included in every test run. The viability was assessed using a WST assay. Tissue viability of the negative control was set to 100% (**Figure 6A**). The positive control demonstrates the sensitivity of the tissue model to a known irritant. The mean viability of the positive control was always clearly below the threshold of 50% as defined in the prediction model (**Figure 6B**).

To identify the predictive capacity of the models, the *in vitro* classification obtained was compared to the reference *in vivo* UN GHS classifications. Both skin models classified the irritating substance heptanal (GHS cat. 2) correctly (**Figure 6D**). However, the traditional skin model misclassified 2-propanol (GHS no cat.) as irritating whereas the advanced skin model classified the substance correctly as non-irritating (**Figure 6C**).

The potential of a skin irritation reaction could be correlated to the release of cytokines (IL-1α, IL-6, and IL-8). The extracellular cytokine release/secretion of IL-1α, IL-8, and IL-6 was measured prior to the substance exposure and after the post-exposure phase of 48 h (**Figure 7**). The negative control had limited influence on the cytokine release in both skin models. The positive control lead to an increase in IL-1α secretion in both models, a decrease in IL-8 and IL-6 secretion in the traditional skin model, and an increase in IL-8 for the advanced model. When the models were treated with the strong irritant substance heptanal, both showed a significant increase in IL-1α secretion and a significant decrease in IL-8 and IL-6 secretion. The treatment of 2-propanol lead to an increase of IL-1α only in the traditional skin model, while the advanced skin model showed no reaction to the treatment. However, both test systems showed an increase of IL-8 and IL-6 following incubation with 2-propanol.

DISCUSSION

For the generation of *in vitro* skin models, accurately reproducing the different layers and components of human skin is critical. The simultaneous culture of different cell types is a difficult process, which has yet to be optimized. The use of collagen I hydrogels for the production of full thickness skin equivalents reflects closely human tissue, as the extracellular component of the connective tissue mainly consist of collagen I and III. However, the collagen hydrogels undergo a fibroblast-mediated contraction. The use of chemical modifications to avoid the contraction alters the cell behavior and leads to a reduced viability or/and inhibits cell proliferation (Lotz et al., 2017). The new approach we have established in this study has no influence on cell behavior as no unnatural cross-linking or toxic substances were used to alter the hydrogel construction. Since the rearrangement of existing collagen fibrils and synthesis of a new matrix by fibroblasts is a physiological process, its prevention is undesirable. Another approach uses self-assembled dermal equivalents, where isolated human fibroblasts produce their specific fibroblast-derived matrix (Berning et al., 2015). However, this process lasts around 4 weeks, followed by an epidermal differentiation of at least 14 days. This leads to high costs and minimizes the use as a high-throughput system, necessary in industry and clinical contexts. The standard skin models experienced a strong contraction during 15 days of culture, visible in a remaining surface area of 17%. These weak mechanical properties, caused by the strong fibroblast-mediated shrinkage of collagen gels, have already been reported by other research groups (El-Ghalbzouri et al., 2002; Boehnke et al., 2007; Lotz et al., 2017; Schimek et al., 2018). This diminishes the suitability of skin models as a test system for topically applied substances, as they do not cover the whole surface and the substance under investigation can openly diffuse through the insert membrane (Ackermann et al., 2010; Groeber et al., 2011). The advanced skin model developed in this study showed no reduction of the epidermal surface area due

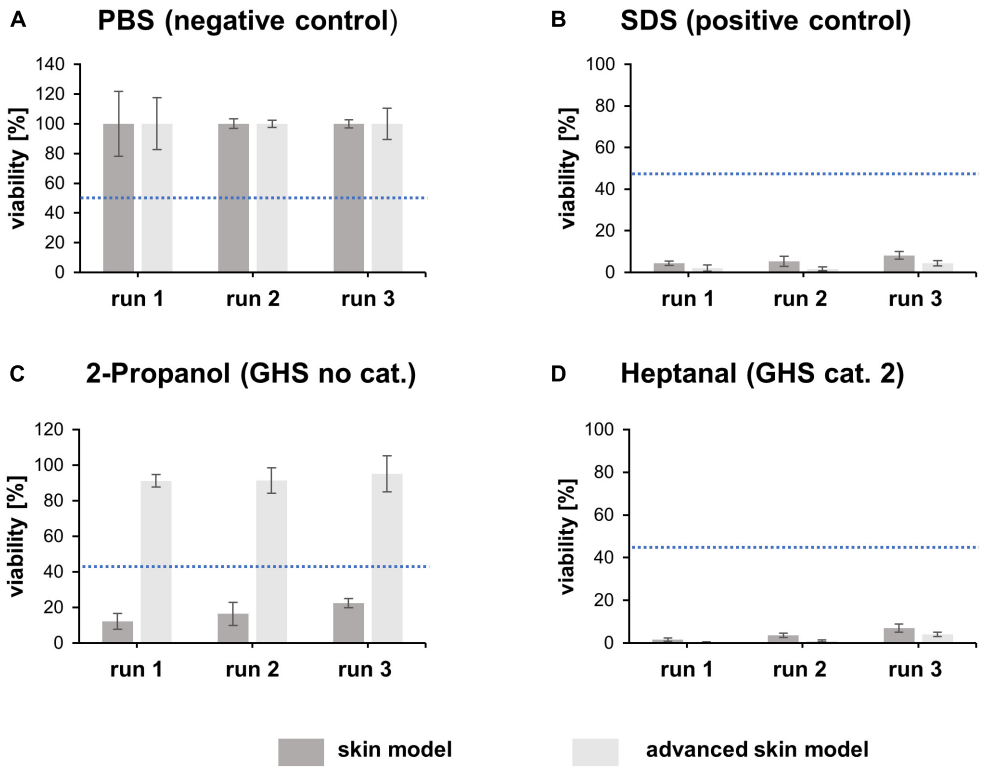

FIGURE 6 | Irritation test with heptanal, SDS, 2-propanol and PBS. The bar graphs represent the percentual viability of skin models/advanced skin models after treatment with PBS **(A)**, SDS **(B)**, 2-propanol **(C)**, and heptanal **(D)**. Treatment with PBS was set as negative control and treatment with SDS as positive control. All values were normalized to the negative control (set to 100%). Mean values are displayed with SD. Dashed blue lines highlight the threshold of 50% viability compared to the negative control (n = 3).

to shrinkage, sealing the complete insert surface and modeling a skin barrier more accurately. However, the epidermal part is separated from the dermis because keratinocytes were seeded into the insert directly on the PET membrane which functions as an artificial basal membrane.

A main function of human skin is to serve as a non-permeable barrier between the body and the environment (Elias, 2007). The barrier function of skin models is often assessed by topical application of substances, a suitable route for drug delivery (Naik et al., 2000; Torin Huzil et al., 2011). The presence of an intact skin barrier is also associated with resistance to chemicals (Mathes et al., 2014). The function of the barriers in skin models is crucial and should be tested by using substances that penetrate the skin such as fluorescein sodium and FITC-dextran or impair barrier structure such as Triton-X (El Ghalbzouri et al., 2008). The human skin is permeable for small molecules with molecular weights of <500 g/mol (Abd et al., 2016).FITC-dextran (4000 g/mol) showed no permeation through the advanced skin model whereas fluorescein sodium (∼380 g/mol) is able to permeate to a low extend (17% after 6 h of incubation), demonstrating the suitability of this *in vitro* model compared to currently available skin models. These findings attest an intact barrier function of the advanced skin model. The resistance of the skin models and advanced skin models to detergent application was tested by topical Triton-X application. Both skin models experienced a significant reduction in viability measured by WST-1 assay compared to untreated skin models. However, the advanced skin model maintained 53% viability and the skin model only 25% after 1.5 h of detergent application. This indicates a higher resistance of the advanced skin model to Triton X-100 penetration compared to the skin model, which demonstrated superiority in the advanced skin model permeability.

Human skin has a complex multilayered structure. Especially the formation of a stratified epidermis with the different layers, namely basal, spinous, granular and cornified layer comprising keratinocytes with distinct morphology and protein expression pattern, is critical for skin models and their barrier function (Baroni et al., 2012; Kumar and Jagannathan, 2018). No effects on epidermal differentiation and the building of the stratum corneum were observed. More over our model shows a comparable histological architecture to human skin. Taken together we developed a new method to generate volume stable 3-layered skin models showing typical morphological characteristics with a functional barrier for further testing.

In vitro skin models represent a valuable tool for substance testing in the cosmetic industry. Since the ban of animal testing for cosmetic research, the need and the requirement for skin models have increased significantly (SCCS, 2006). The OECD defines in its guideline 439 requirements which skin models

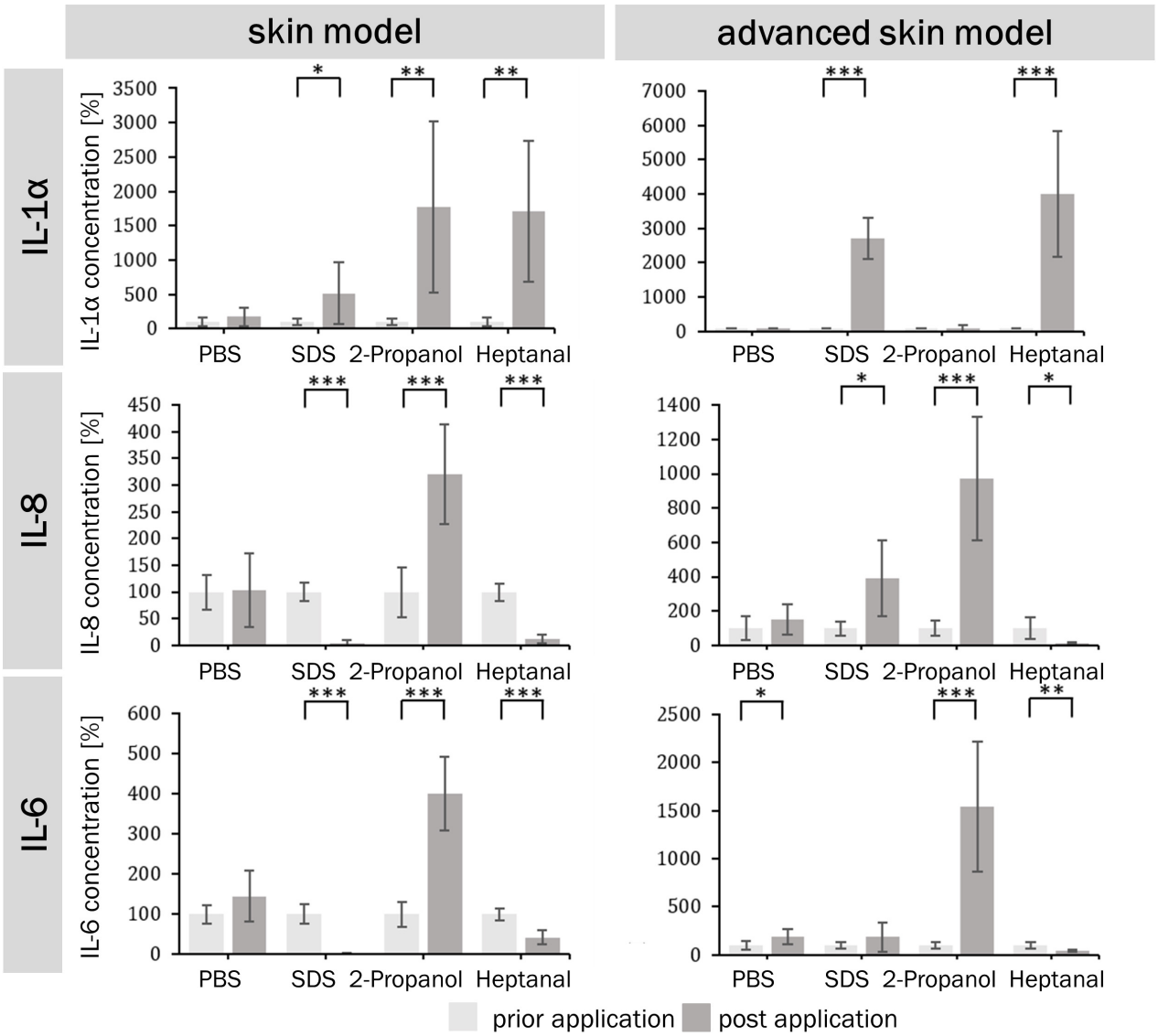

FIGURE 7 | Percentual IL-1α, IL-6, and IL-8 levels prior and post application of irritating and non-irritating substances. Bar graphs depict percentual concentration values of the cytokines IL-1α, IL-6, and IL-8 for of the skin model **(A,C,E)** and the advanced skin model **(B,D,F)** normalized to prior application of the different substances (light gray). Cytokines were detected by ELISA in the supernatants of the respective skin models 48 h after the last media change prior and post application of substances ($n = 3$). PBS served as negative control and SDS as positive control. Level of significance $^{*}p < 0.05$, $^{**}p < 0.01$, $^{***}p < 0.001$.

must met in order to be used in a standardized manner for the evaluation of skin irritation (OECD, 2019b). The performance standards state the need of necessary test methods, essential reference chemicals and must reliably and accurately define the results generated with the respective skin models (Liebsch et al., 2011). In this study, the OECD TG 439 was used as a basis to compare the traditional and advanced skin models in their ability to correctly classify an irritating and a non-irritating substance, as determined by viability after irritant exposure. The commonly used generation of skin models led to a misclassification of 2-propanol, whereas the advanced set-up classified both substances correctly. Misclassification of substances in *in vitro* irritation testing was previously reported in other studies where reconstructed epidermal models were used (Alepee et al., 2010; Jung et al., 2014; Groeber et al., 2016; Mewes et al., 2016). However, 2-propanol was never misclassified in other studies using epidermal models. However, the OECD acceptance criterion of ≥80% sensitivity, ≥70% specificity and ≥75% accuracy, doesn't require a correct classification of all 20 reference substances in a validation study. Nonetheless, it can be assumed that if 2-propanol is classified incorrectly, other substances will also be misclassified. The shrinkage of the epidermis leads to an impaired connection between the insert wall and the epidermis, which is highly accountable for the misclassification of 2-propanol. The next step should be the testing of all 20 reference chemicals

defined in the OECD performance standards for *in vitro* skin irritation testing.

Pro-inflammatory cytokines such as IL-1α, IL-6, and IL-8 are involved in skin reaction to irritants. Therefore, extracellular cytokine release can be used to define the irritation potential of substances. IL-1α is an important inflammatory mediator in the skin located in keratinocytes, where it is constitutively expressed and accumulates in the cytoplasm or as a membrane bound form (Dinarello, 1998; Grone, 2002). It is only released from cells with disrupted membranes, e.g., after detergent application, which results in the release of the cytoplasm (Osborne and Perkins, 1994). This correlates with the IL-1α concentrations of both skin models, which were elevated after irritant exposure. The skin model also showed increased IL-1α concentrations after 2-propanol application, which is consistent with the false classification of 2-propanol as irritating. An increase of IL-6 and IL-8 after 2-propanol exposure occurred for both models. These results demonstrate that these cytokines could be used to show the outcome of mild irritating effects, which cannot be detected in viability studies.

In conclusion, an advanced three-layered skin model suitable as *in vitro* test system for irritating substances was successfully established. Our *in vitro* test system enables the topical application of substances, as well as the analysis of the influence on adipose tissue and the introduction of new endpoints like drug deposition would be possible. This improved model is groundbreaking, in how it overcomes current obstacles of alternative methods for animal testing.

DATA AVAILABILITY STATEMENT

The datasets generated for this study are available on request to the corresponding author.

ETHICS STATEMENT

All research was carried out in accordance with the rules for investigation of human subjects as defined in the Declaration of Helsinki. Patients gave a written agreement according to the permission of the Landesärztekammer Baden-Württemberg (F-2012-078; for normal skin from elective surgeries).

AUTHOR CONTRIBUTIONS

FS and PK conceived and presented the idea, and supervised the findings of this work. FS and SN designed the study and analyzed the data. SN performed the experiments. All authors discussed the results and contributed to the final manuscript.

FUNDING

The authors kindly thank the "Ministerium für Ländlichen Raum und Verbraucherschutz Baden-Württemberg" (project title: Fat2Skin) for financial support of this work [Grant number 14-(34)-8402.43/0391 E].

REFERENCES

Abd, E., Yousef, S. A., Pastore, M. N., Telaprolu, K., Mohammed, Y. H., Namjoshi, S., et al. (2016). Skin models for the testing of transdermal drugs. *Clin. Pharmacol.* 8, 163–176. doi: 10.2147/cpaa.s64788

Ackermann, K., Borgia, S. L., Korting, H. C., Mewes, K. R., and Schafer-Korting, M. (2010). The Phenion full-thickness skin model for percutaneous absorption testing. *Skin Pharmacol. Physiol.* 23, 105–112. doi: 10.1159/000265681

Alepee, N., Tornier, C., Robert, C., Amsellem, C., Roux, M. H., Doucet, O., et al. (2010). A catch-up validation study on reconstructed human epidermis (SkinEthic RHE) for full replacement of the Draize skin irritation test. *Toxicol. In Vitro* 24, 257–266. doi: 10.1016/j.tiv.2009.08.024

Baroni, A., Buommino, E., De Gregorio, V., Ruocco, E., Ruocco, V., and Wolf, R. (2012). Structure and function of the epidermis related to barrier properties. *Clin. Dermatol.* 30, 257–262. doi: 10.1016/j.clindermatol.2011.08.007

Bellas, E., Seiberg, M., Garlick, J., and Kaplan, D. L. (2012). *In vitro* 3D full-thickness skin-equivalent tissue model using silk and collagen biomaterials. *Macromol. Biosci.* 12, 1627–1636. doi: 10.1002/mabi.201200262

Berning, M., Pratzel-Wunder, S., Bickenbach, J. R., and Boukamp, P. (2015). Three-dimensional *in vitro* skin and skin cancer models based on human fibroblast-derived matrix. *Tissue Eng. Part C Methods* 21, 958–970. doi: 10.1089/ten.TEC.2014.0698

Boehnke, K., Mirancea, N., Pavesio, A., Fusenig, N. E., Boukamp, P., and Stark, H. J. (2007). Effects of fibroblasts and microenvironment on epidermal regeneration and tissue function in long-term skin equivalents. *Eur. J. Cell Biol.* 86, 731–746. doi: 10.1016/j.ejcb.2006.12.005

Braziulis, E., Diezi, M., Biedermann, T., Pontiggia, L., Schmucki, M., Hartmann-Fritsch, F., et al. (2012). Modified plastic compression of collagen hydrogels provides an ideal matrix for clinically applicable skin substitutes. *Tissue Eng. Part C Methods* 18, 464–474. doi: 10.1089/ten.TEC.2011.0561

Dinarello, C. A. (1998). Interleukin-1, interleukin-1 receptors and interleukin-1 receptor antagonist. *Int. Rev. Immunol.* 16, 457–499. doi: 10.3109/08830189809043005

El Ghalbzouri, A., Siamari, R., Willemze, R., and Ponec, M. (2008). Leiden reconstructed human epidermal model as a tool for the evaluation of the skin corrosion and irritation potential according to the ECVAM guidelines. *Toxicol. In Vitro* 22, 1311–1320. doi: 10.1016/j.tiv.2008.03.012

El-Ghalbzouri, A., Gibbs, S., Lamme, E., Van Blitterswijk, C. A., and Ponec, M. (2002). Effect of fibroblasts on epidermal regeneration. *Br. J. Dermatol.* 147, 230–243. doi: 10.1046/j.1365-2133.2002.04871.x

Elias, P. M. (2007). The skin barrier as an innate immune element. *Semin. Immunopathol.* 29, 3–14.

Groeber, F., Holeiter, M., Hampel, M., Hinderer, S., and Schenke-Layland, K. (2011). Skin tissue engineering–*in vivo* and *in vitro* applications. *Adv. Drug Deliv. Rev.* 63, 352–366. doi: 10.1016/j.addr.2011.01.005

Groeber, F., Schober, L., Schmid, F. F., Traube, A., Kolbus-Hernandez, S., Daton, K., et al. (2016). Catch-up validation study of an *in vitro* skin irritation test method based on an open source reconstructed epidermis (phase II). *Toxicol. In Vitro* 36, 254–261. doi: 10.1016/j.tiv.2016.07.008

Grone, A. (2002). Keratinocytes and cytokines. *Vet. Immunol. Immunopathol.* 88, 1–12. doi: 10.1016/s0165-2427(02)00136-8

Huber, B., Borchers, K., Tovar, G. E., and Kluger, P. J. (2016a). Methacrylated gelatin and mature adipocytes are promising components for adipose tissue engineering. *J. Biomater. Appl.* 30, 699–710. doi: 10.1177/0885328215587450

Huber, B., Link, A., Linke, K., Gehrke, S. A., Winnefeld, M., and Kluger, P. J. (2016b). Integration of mature adipocytes to build-up a functional three-layered full-skin equivalent. *Tissue Eng. Part C Methods* 22, 756–764. doi: 10.1089/ten.TEC.2016.0141

Jung, K. M., Lee, S. H., Jang, W. H., Jung, H. S., Heo, Y., Park, Y. H., et al. (2014). KeraSkin-VM: a novel reconstructed human epidermis model for skin irritation tests. *Toxicol. In Vitro* 28, 742–750. doi: 10.1016/j.tiv.2014.02.014

Kumar, A., and Jagannathan, N. (2018). Cytokeratin: a review on current concepts. *Int. J. Orofac.* 2, 6–11.

Liebsch, M., Grune, B., Seiler, A., Butzke, D., Oelgeschlager, M., Pirow, R., et al. (2011). Alternatives to animal testing: current status and future perspectives. *Arch. Toxicol.* 85, 841–858. doi: 10.1007/s00204-011-0718-x

Lotz, C., Schmid, F. F., Oechsle, E., Monaghan, M. G., Walles, H., and Groeber-Becker, F. (2017). Cross-linked collagen hydrogel matrix resisting contraction to facilitate full-thickness skin equivalents. *ACS Appl. Mater. Interfaces* 9, 20417–20425. doi: 10.1021/acsami.7b04017

Maas-Szabowski, N., Shimotoyodome, A., and Fusenig, N. E. (1999). Keratinocyte growth regulation in fibroblast cocultures via a double paracrine mechanism. *J. Cell. Sci.* 112(Pt 12), 1843–1853.

Mathes, S. H., Ruffner, H., and Graf-Hausner, U. (2014). The use of skin models in drug development. *Adv. Drug Deliv. Rev.* 6, 81–102.

Mewes, K. R., Fischer, A., Zoller, N. N., Laubach, V., Bernd, A., Jacobs, A., et al. (2016). Catch-up validation study of an *in vitro* skin irritation test method based on an open source reconstructed epidermis (phase I). *Toxicol. In Vitro* 36, 238–253. doi: 10.1016/j.tiv.2016.07.007

Naik, A., Kalia, Y. N., and Guy, R. H. (2000). Transdermal drug delivery: overcoming the skins barrier function. *Pharm. Sci. Technol. Today* 3, 318–326. doi: 10.1016/s1461-5347(00)00295-9

OECD, (2019a). *Test No. 431: In Vitro Skin Corrosion: Reconstructed Human Epidermis (RHE) Test Method*. Paris: OECD.

OECD, (2019b). *Test No. 439: In Vitro Skin Irritation: Reconstructed Human Epidermis Test Method*. Paris: OECD.

Oesch, F., Fabian, E., Guth, K., and Landsiedel, R. (2014). Xenobiotic-metabolizing enzymes in the skin of rat, mouse, pig, guinea pig, man, and in human skin models. *Arch. Toxicol.* 88, 2135–2190. doi: 10.1007/s00204-014-1382-8

Osborne, R., and Perkins, M. A. (1994). An approach for development of alternative test methods based on mechanisms of skin irritation. *Food Chem. Toxicol.* 32, 133–142.

Rossi, A., Appelt-Menzel, A., Kurdyn, S., Walles, H., and Groeber, F. (2015). Generation of a three-dimensional full thickness skin equivalent and automated wounding. *J. Vis. Exp.* 96:52576. doi: 10.3791/52576

Russell, W. M. S., Burch, R. L., and Hume, C. W. (1959). *The Principles Of Humane Experimental Technique*. London: Methuen.

SCCS, (2006). *Notes of Guidance for the Testing of Cosmetic Ingredients and Their Safety Evaluation*. Brussels: Scientific Committee on Consumer Safety.

Schimek, K., Hsu, H. H., Boehme, M., Kornet, J. J., Marx, U., Lauster, R., et al. (2018). Bioengineering of a full-thickness skin equivalent in a 96-well insert format for substance permeation studies and organ-on-a-chip applications. *Bioengineering* 5:43. doi: 10.3390/bioengineering5020043

Torin Huzil, J., Sivaloganathan, S., Kohandel, M., and Foldvari, M. (2011). Drug delivery through the skin: molecular simulations of barrier lipids to design more effective noninvasive dermal and transdermal delivery systems for small molecules, biologics, and cosmetics. *Wiley Interdiscip. Rev. Nanomed. Nanobiotechnol.* 3, 449–462. doi: 10.1002/wnan.147

Wiegand, C., Hewitt, N. J., Merk, H. F., and Reisinger, K. (2014). Dermal xenobiotic metabolism: a comparison between native human skin, four *in vitro* skin test systems and a liver system. *Skin Pharmacol. Physiol.* 27, 263–275. doi: 10.1159/000358272

Conflict of Interest: The authors declare that the research was conducted in the absence of any commercial or financial relationships that could be construed as a potential conflict of interest.

frontiers in Bioengineering and Biotechnology

ORIGINAL RESEARCH
published: 14 May 2020
doi: 10.3389/fbioe.2020.00413

Elastin-Like Recombinamer Hydrogels for Improved Skeletal Muscle Healing Through Modulation of Macrophage Polarization

*Arturo Ibáñez-Fonseca[1†], Silvia Santiago Maniega[2†], Darya Gorbenko del Blanco[1†], Benedicta Catalán Bernardos[3], Aurelio Vega Castrillo[2], Ángel José Álvarez Barcia[4], Matilde Alonso[1], Héctor J. Aguado[2] and José Carlos Rodríguez-Cabello[1]**

[1] BIOFORGE (Group for Advanced Materials and Nanobiotechnology), CIBER-BBN, University of Valladolid, Valladolid, Spain, [2] Servicio de Traumatología, Hospital Clínico de Valladolid, Valladolid, Spain, [3] Servicio de Neurofisiología, Hospital Clínico de Valladolid, Valladolid, Spain, [4] Servicio de Investigación y Bienestar Animal, University of Valladolid, Valladolid, Spain

OPEN ACCESS

Edited by:
Dimitrios I. Zeugolis, National University of Ireland Galway, Ireland

Reviewed by:
Johannes Von den Hoff, Radboud University Nijmegen Medical Centre, Netherlands
Marie-noelle Giraud, Université de Fribourg, Switzerland

***Correspondence:**
José Carlos Rodríguez-Cabello
roca@bioforge.uva.es

[†]These authors have contributed equally to this work

Specialty section:
This article was submitted to Tissue Engineering and Regenerative Medicine, a section of the journal Frontiers in Bioengineering and Biotechnology

Received: *13 January 2020*
Accepted: *14 April 2020*
Published: *14 May 2020*

Citation:
Ibáñez-Fonseca A, Santiago Maniega S, Gorbenko del Blanco D, Catalán Bernardos B, Vega Castrillo A, Álvarez Barcia ÁJ, Alonso M, Aguado HJ and Rodríguez-Cabello JC (2020) Elastin-Like Recombinamer Hydrogels for Improved Skeletal Muscle Healing Through Modulation of Macrophage Polarization. Front. Bioeng. Biotechnol. 8:413. doi: 10.3389/fbioe.2020.00413

Large skeletal muscle injuries, such as a volumetric muscle loss (VML), often result in an incomplete regeneration due to the formation of a non-contractile fibrotic scar tissue. This is, in part, due to the outbreak of an inflammatory response, which is not resolved over time, meaning that type-1 macrophages (M1, pro-inflammatory) involved in the initial stages of the process are not replaced by pro-regenerative type-2 macrophages (M2). Therefore, biomaterials that promote the shift from M1 to M2 are needed to achieve optimal regeneration in VML injuries. In this work, we used elastin-like recombinamers (ELRs) as biomaterials for the formation of non- (physical) and covalently (chemical) crosslinked bioactive and biodegradable hydrogels to fill the VML created in the tibialis anterior (TA) muscles of rats. These hydrogels promoted a higher infiltration of M2 within the site of injury in comparison to the non-treated control after 2 weeks ($p < 0.0001$), indicating that the inflammatory response resolves faster in the presence of both types of ELR-based hydrogels. Moreover, there were not significant differences in the amount of collagen deposition between the samples treated with the chemical ELR hydrogel at 2 and 5 weeks, and this same result was found upon comparison of these samples with healthy tissue after 5 weeks, which implies that this treatment prevents fibrosis. The macrophage modulation also translated into the formation of myofibers that were morphologically more similar to those present in healthy muscle. Altogether, these results highlight that ELR hydrogels provide a friendly niche for infiltrating cells that biodegrades over time, leaving space to new muscle tissue. In addition, they orchestrate the shift of macrophage population toward M2, which resulted in the prevention of fibrosis in the case of the chemical hydrogel treatment and in a more healthy-like myofiber phenotype for both types of hydrogels. Further studies should focus in the assessment of the regeneration of skeletal muscle in larger animal models, where a more critical defect can be created and additional methods can be used to evaluate the functional recovery of skeletal muscle.

Keywords: skeletal muscle healing, volumetric muscle loss, biomaterials, elastin-like recombinamers, hydrogels, macrophage polarization, immunomodulation

INTRODUCTION

Large skeletal muscle injuries are the result of high energy traumatisms as a consequence of different events, such as car accidents or explosions, being very common in clinics (Zalavras and Patzakis, 2003; Corona et al., 2015). They usually involve a volumetric muscle loss (VML), which implies an impairment of muscle function, and their treatment is a challenge for the orthopedic surgeon (Grogan et al., 2011; Greising et al., 2018). Currently, the gold standard is scar tissue debridement or autologous muscle transfer, which substantially increases donor site morbidity and can cause severe problems, such as infections or non-functional transfers (Lin et al., 2004, 2007; Klinkenberg et al., 2013).

After acute injuries, like VML, a complex process is activated in order to restore muscle structure and function, mainly due to the activation, proliferation and differentiation of a quiescent population of resident muscle progenitor stem cells known as satellite cells (SCs) (Tedesco et al., 2010; Lepper et al., 2011). These steps are orchestrated by the inflammatory response: during the first hours post-damage, circulating monocytes start differentiating into pro-inflammatory type-1 macrophages (M1) that activate the proliferation of SCs from the surrounding tissue (Tidball and Villalta, 2010; Saclier et al., 2013). Then, as the muscle repair process advances, the phenotype of the macrophages shifts to anti-inflammatory type-2 macrophages (M2), which express and secrete cytokines that stimulate myogenic differentiation of the SCs toward myofibers, thus being essential for a successful healing (Tidball and Villalta, 2010; Saclier et al., 2013). A dysregulated macrophage response leads to a chronic inflammation that induces the formation of a non-contractile fibrotic tissue due to the activation and recruiting of fibroblasts that secrete extracellular matrix (ECM) components, mainly collagen, to fill the void generated by the VML before it can be repopulated by new myofibers, hence leading to functional deficits (Järvinen et al., 2005; Shin et al., 2014).

During the past few years, several strategies have been proposed to modulate the inflammatory response to enhance skeletal muscle repair, many of them involving the use of biological (mainly decellularized porcine ECM) (Greising et al., 2017) or biomaterial-based scaffolds (Grasman et al., 2015). Interestingly, some of them have shown to promote a M2-balanced response (Sicari et al., 2014; Boersema et al., 2016; Wang et al., 2019). These scaffolds are intended to give mechanical and biochemical support to the different types of cells involved in the regeneration process, such as SCs, and they need to be biodegradable to give space for the formation of new myofibers (Wolf et al., 2015; Bartolacci et al., 2019). One specific type of scaffolds are injectable hydrogels, which are made up of polymeric biomaterials that form 3D networks with high water content and permeability and that can be applied in a minimally invasive way. While some of them are made of natural biomaterials, e.g., alginate or chitosan, meaning that they are extracted from natural sources, some others are made of synthetic ones (Qazi et al., 2015; Wolf et al., 2015). These synthetic biomaterials offer a better control on the chemical composition, and hence a high reproducibility, although they usually lack biological activity (O'Brien, 2011).

Within the different types of synthetic biomaterials, we can identify recombinant polymers (recombinantly expressed structural proteins with repetitive domains) (Cappello et al., 1990; Tirrell et al., 1991), such as elastin-like recombinamers (ELRs) (Rodríguez-Cabello et al., 2009). These molecules derive from the repetition of the L-Val-L-Pro-Gly-X-Gly (VPGXG) pentapeptide found in natural elastin, where X can be any amino acid except L-Pro, and are able to self-assemble through hydrophobic interactions above the so-called transition temperature (T_t) (Urry et al., 1976; Urry, 2006; Ibáñez-Fonseca et al., 2019). Due to their recombinant nature, they can be precisely engineered at the DNA level to bear specific amino acids (Rodríguez-Cabello et al., 2009; Girotti et al., 2015). For instance, the introduction of lysines with amine groups that can be modified for covalent crosslinking through "click chemistry" strategies, like strain-promoted alkyne-azide cycloaddition (SPAAC), may allow the formation of chemical hydrogels (González de Torre et al., 2014; Madl et al., 2016). On the other hand, physical hydrogels can be achieved by the inclusion of amino acid sequences able to form stable non-covalent interactions (e.g., H-bonds), such as the repetitive domains found in silk fibroin from *Bombyx mori* silkworm that, in combination with the elastin-like building blocks, form hydrogels through a concomitant self-assembly above the T_t (Fernández-Colino et al., 2014; Ibáñez-Fonseca et al., 2020). Furthermore, the genetic fusion of bioactive sequences, including cell adhesion domains, like the L-Arg-Gly-L-Asp (RGD) tripeptide (Ruoslahti, 1996), or protease-sensitive sequences for improved biodegradation (Flora et al., 2019; Contessotto et al., under review), permits the obtaining of hydrogels with acquired functionalities. In this last regard, the inclusion of motifs sensitive to matrix metalloproteinase (MMP)-2, 9 and 13 provides a multipurpose platform able to be degraded in different *in vivo* environments (Lutolf et al., 2003; Chung et al., 2006; Contessotto et al., under review). Therefore, due to their intrinsic properties of high biocompatibility (Ibáñez-Fonseca et al., 2018), mechanical stability (Fernández-Colino et al., 2014; González de Torre et al., 2014), injectability (Martín et al., 2010; Fernández-Colino et al., 2014), and acquired bioactivity (Girotti et al., 2004; Ibáñez-Fonseca et al., 2017), ELR-based hydrogels have found several uses in tissue engineering and regenerative medicine (Coletta et al., 2017; Pescador et al., 2017; Staubli et al., 2017; Contessotto et al., under review), specially within the field of *in situ* tissue regeneration (Lee et al., 2016).

In this work, we propose the use of chemical and physical ELR-based hydrogels, both of them biodegradable, to improve the healing of skeletal muscle injuries. Our hypothesis is that ELR hydrogels will be able to modulate the macrophage response and facilitate the shift to pro-regenerative M2 macrophages. Moreover, the ELR hydrogels will provide a cell-friendly and biodegradable environment that will prevent the formation of fibrotic tissue in the area of the defect, and that will allow the development of new myofibers. Therefore, the objective of this study was to quantitatively analyze macrophage polarization and its effects on muscle healing, in terms of collagen deposition

(fibrosis) and muscle morphology, following ELR hydrogel treatment in a rat model of VML.

MATERIALS AND METHODS

ELRs Biosynthesis and Characterization

The ELRs used in this work were biosynthesized through recombinant DNA technology as described elsewhere (Rodríguez-Cabello et al., 2012). Briefly, the genes encoding for the recombinamers were cloned into a pET-25b(+) plasmid vector (Novagen, Merck, Germany) that was used to transform a BLR(DE3) strain of *Escherichia coli* (Novagen, Merck, Germany). An ELR-expressing clone was cultured in a 15-L bioreactor (Applikon Biotechnology B.V., Netherlands) and the ELR was purified by several cooling and heating cycles with centrifugation steps. Then, the highly pure ELR solution was dialyzed against ultra-pure water and filtered through 0.22 μm filters (Nalgene, Thermo Fisher Scientific, United States) for sterilization. Finally, the solution was freeze-dried prior to storage.

Two of the ELRs used in this work, namely HRGD6 and HE5, i.e., the ones used for the formation of chemically crosslinked hydrogels (or simply chemical hydrogels), were previously described (Costa et al., 2009; Contessotto et al., under review). HRGD6 has six cell adhesion RGD sequences per molecule, embedded within the lysine-containing elastin-like backbone, whereas the HE5 includes MMP-sensitive domains for biodegradation and lysine-rich crosslinking domains within a glutamic acid-containing elastin-like backbone. The presence of lysines in both ELRs makes them suitable for chemical modification and subsequent covalent crosslinking via "click chemistry" for the formation of chemical hydrogels (see below).

On the other hand, the silk-elastin-like recombinamer (SELR) used for the formation of physically crosslinked hydrogels, the so-called IKRS-MMP, was based on a previously designed SELR (Ibáñez-Fonseca et al., 2020), to which a MMP-sensitive domain, similar to the one included in the HE5, was included for biodegradation.

The characterization methods for every ELR batch included sodium dodecyl sulfate polyacrylamide gel electrophoresis (SDS-PAGE) and matrix-assisted laser desorption/ionization time-of-flight (MALDI-TOF) for the evaluation of the purity and the molecular weight, HPLC to determine the amino acid composition and differential scanning calorimetry (DSC) for the calculation of the transition temperature. Furthermore, the endotoxin levels were assessed by the limulus amebocyte lysate assay with the Endosafe®-PTS system (Charles River Laboratories, Inc., United States) and were always below 1 endotoxin unit/mg of ELR.

ELR Chemical Modification

The chemical modification of the ELRs was performed as previously described (González de Torre et al., 2014). On one hand, the ELR containing RGD cell-adhesion domains (HRGD6) was chemically modified with azide groups through the transformation of the ε-amine group found in the side chain of lysine residues, achieving a 55–65% of modification (from 14 to 16 modified lysines, out of 24), and giving a HRGD6-N_3. On the other hand, the ELR comprising MMP-sensitive motifs (HE5) was modified similarly, in this case to bear cyclooctyne (activated alkyne) groups, resulting in a 30–40% of modification (from 3 to 4 modified lysines, out of 9), and named HE5-C. These modified ELRs were used for the formation of covalently crosslinked "click" ELR-based hydrogels (chemical hydrogels).

ELR-Based Hydrogel Preparation and *in vivo* Administration

In this work, two different types of biodegradable hydrogels were used to evaluate their influence on muscle healing: non-covalently crosslinked SELR-based hydrogels (physical hydrogels) and covalently crosslinked "click" ELR-based hydrogels (chemical hydrogels), formed through SPAAC (González de Torre et al., 2014). In both cases, the recombinamers were dissolved in cold 1× PBS for 16–24 h at 4°C and the hydrogels were formed *in situ* just after the creation of the muscle defect.

In the case of the "click" ELRs, the HRGD6-N_3 and the HE5-C were dissolved separately and mixed prior to injection in a 1:1.8 ratio, since this was found to be the optimal proportion, taking into account the different molecular weights and modification percentage of the ELRs, finally giving 50 mg/mL hydrogels. The mixture was left for 8 min in an ice bath and afterward it was placed in the injury site with a pipette, where the hydrogel formation process was completed.

For the physical hydrogel (IKRS-MMP), the mono-component solution was left in an ice bath until its administration in the site of the defect with a pipette, similarly to the chemical hydrogel. In this case, the gelation was triggered by the change in the temperature of the solution that leads to an inverse temperature transition (ITT) and to the formation of a network through hydrophobic interactions. The hydrogel was further stabilized by the folding of silk domains into β-sheets, which results in crystallization (Fernández-Colino et al., 2014; Ibáñez-Fonseca et al., 2020).

In both cases, administration was easily performed with a pipette, taking advantage of the injectability of both hydrogels, and the gelation was instantaneous, which avoided the dilution of the hydrogel once implanted. Moreover, due to the inclusion of a MMP-sensitive amino acid sequence in the HE5 and IKRS-MMP, both types of hydrogels, i.e., chemical and physical, were biodegradable.

Animal Experiments

Ethical Statement

All animal experiments were conducted in accordance with the institutional guidelines for the care and use of experimental animals of the University of Valladolid (Spain) in accordance with Directive 2010/63/EU. The protocol was approved by the Committee of Ethics in Animal Experimentation and Welfare (CEEBA, for its Spanish acronym) of the University of Valladolid (protocol number 5402485).

Animal Care

A total of 19 three-month-old male Wistar rats were used in this study. The average weight was 400 g at the time of surgery. The animals were kept in cages with a light:dark cycle of 12:12 and provided with *ad libitum* food and water. An identification chip was placed in the interscapular region, inaccessible to the animals, to ensure masking during the study.

Experimental Groups

Four different groups were established through randomized classification: non-treated or empty (n = 11), treated with chemical biodegradable hydrogels (n = 11) or physical biodegradable hydrogels (n = 11), and non-injury or healthy group (n = 5). In the empty group, the VML was left untreated, whereas for the treated groups chemical and physical biodegradable hydrogels were placed in the injury area. No surgical procedure was done in the non-injury group.

Anesthesia

All surgical procedures were carried out under proper anesthesia. Intraperitoneal anesthesia of the animals was performed with ketamine-medetomidine at a dose of 0.125 mL per 100 g of animal weight.

Tibialis Anterior VML Injury

Our goal was to create a defect of at least a 20% of the weight of the tibialis anterior (TA) muscle, which was calculated according to the equation described by Wu et al. (2012), giving an average defect weight of 121 mg. A scheme of the TA VML injury has been included in **Supplementary Figure 1A**.

First, the inferior limbs of the animal were shaved using an electric shaver to facilitate subsequent procedures. Then, the animal was placed in the supine position on a heat blanket (to prevent hypothermia), and it was covered with a sterile drape, so that only the legs were accessible. Subsequently, a longitudinal incision was made in the skin from the knee to the ankle following the course of the TA muscle with a sterile no. 11 blade scalpel. The fascia was sectioned independently and separated from the muscle using blunt dissection to completely uncover the anterior surface of the TA.

Afterward, a transversal mark was made in the exposed muscle with a sterile marker, measuring 1cm from the tibial tuberosity with a rule. This mark would be the proximal limit of the defect. A second mark was made parallel to the first, 1 cm from it. In this way, the proximal and distal limits of the defect were delimited. Regarding the width of the VML, we left a margin of about 2 mm from the medial and lateral margins of the TA muscle. In this way, both the length and width of the defect were precisely delimited, whereas the depth was adjusted according to the volume of muscle needed to achieve the above calculated weight.

Once the defect was created, the corresponding treatment was applied, according to the groups defined above. For the administration of the hydrogel, the skin was first sutured with Vicryl rapid 2/0, and the skin was left partially open during the operation to minimize mobilization of the hydrogel during closure. Both chemical and physical hydrogels were formed instantaneously once implanted, as previously described in the hydrogel preparation section. Subsequently, the continuous suture was tensed and knotted. A self-adhesive bandage of both legs was made so that the rats could not contaminate or bite the wound.

Animals were provided with postoperative analgesia in food and drink. Specifically, ibuprofen was dissolved in water at a concentration of 10 mL/L of water for 3 days, and tramadol was administered masked in commercial hazelnut cocoa spread at a concentration of 1 mg/kg/day, calculated for 48 h.

Euthanasia

Animals were euthanized 2 and 5 weeks post-injury by intracardiac injection of phenobarbital, after being anesthetized to avoid suffering. Then, whole TA muscles were extracted for processing and analysis as described below.

Histological Processing

The TA muscles were harvested and divided into two halves in the middle area of the defect, and they were used to achieve both longitudinal and cross-sections (see **Supplementary Figure 1B** for a schematic representation). To this end, the samples were mounted on cork discs according to the direction of the muscle fibers using a small amount of optimum cutting temperature (OCT) mounting medium (VWR, United States). Then, the samples were frozen in 2-Methylbutane (Thermo Fisher Scientific, Belgium) previously chilled in liquid nitrogen. After freezing, the samples were stored at −80°C until further processing. Subsequently, 6 μm cross-section slices were cut in a cryostat (Thermo Fisher Scientific, United States) and stained with Harris' hematoxylin (Merck, Germany)/eosin-Y (Sigma-Aldrich, United States) (HE staining) and Picrosirius red (Abcam, United Kingdom) following the manufacturers' protocols.

Histomorphometry

Histomorphometry methods were used to quantify areas, number and size of myofibers, and collagen percentage. For this purpose, HE images of the whole muscle sections were obtained using a Nikon Eclipse 80i microscope (Nikon Corporation, Japan) coupled to an automated stage (Prior, United Kingdom) and a DS-Fi1 camera (Nikon Corporation, Japan), which were controlled with the NIS-Elements AR software (Nikon Corporation, Japan).

Within the samples, three different regions were differentiated: the remaining native tissue, the interface (tissue newly regenerated between the remaining muscle and the scaffold area, characterized by the presence of myofibers with internal nuclei) and the scaffold area (without myofibers). The sum of these last two areas give the area corresponding to the potentially injured tissue, i.e., the region where the VML was created (**Figure 1**), although it may not represent the wound area to its full extent. The three different areas were traced manually and measured using the Fiji distribution of the ImageJ software (Schindelin et al., 2012). The percentage of injury (interface and scaffold) area was normalized to the entire muscle area, whereas the percentage of the interface and scaffold areas were obtained by normalizing to the injury area.

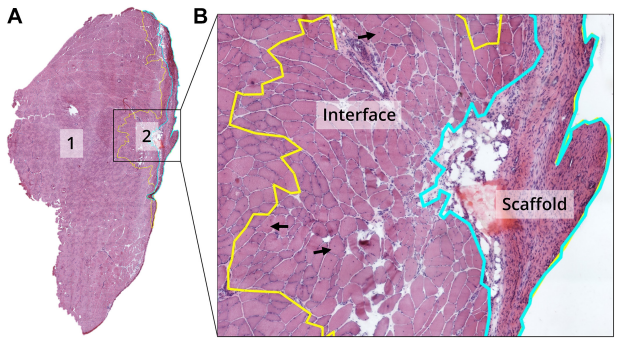

FIGURE 1 | Example of TA muscle cross-section and visual explanation of the different areas used for the quantifications. **(A)** Example picture of the hematoxylin–eosin (HE) staining of the entire TA muscle (×20 magnification), where we identified and manually traced the remaining native tissue (1) and the injury area (2). **(B)** Visual explanation of the division of the injury area into two clearly differentiated regions: interface (showing newly formed myofibers with central nuclei, highlighted with black arrows) and scaffold (no visible myofibers are present). Therefore, both the scaffold and interface areas conform the potentially injured/wounded region.

Automatic myofiber counting was performed using a customized macro that included the use of the Trainable Weka Segmentation tool in Fiji (ImageJ) (Arganda-Carreras et al., 2017). Myofiber size was determined by measuring the lesser diameter (minimal Feret's, defined as the closest distance between the two parallel tangents of the muscle fiber) of 100 fibers manually in four different locations (Briguet et al., 2004; Dubach-Powell et al., 2008; Pertl et al., 2013) in the interface region of each sample (n = 5 per group/time point). Data were represented as frequency distribution of size ranges with Gaussian distribution with GraphPad Prism 6.0 software. The quantification of the percentage of myofibers with internal nuclei was performed similarly by counting the nuclei of a total of 100 fibers in four different locations within the interface region of each sample (n = 5 per group/time point).

The entire muscle section was analyzed for collagen staining with Picrosirius red under bright-field and polarized light. The birefringent staining under polarized light is highly specific for type I and III mature collagen fibrils (Junqueira et al., 1979), and it was used for collagen quantification with a custom macro in Fiji (ImageJ).

Immunofluorescence Staining

Immunofluorescence stainigs were performed as previously described (Aurora et al., 2016) to detect macrophages: type-1 or pro-inflammatory macrophages (anti-CCR7 antibody, 1:200; ab32527, Abcam, United Kingdom) (Corona et al., 2013) and type-2 or anti-inflammatory macrophages (anti-mannose receptor (CD206) antibody, 1:200; ab64693, Abcam, United Kingdom) (Lankford et al., 2018). Alexa Fluor 488-labeled secondary antibody (1:500; ab150077, Abcam, United Kingdom) was used for final immunostaining in both cases. At least 16 non-overlapping images (20× magnification) of the injury region were randomly taken with a Nikon Eclipse Ti-E coupled to a Nikon DS-2MBWc digital camera (Nikon Corporation, Japan). The quantification of the number of cells in each image was obtained manually with Fiji (ImageJ).

Statistical Analysis

All the results are presented as means ± SD (n = 5, unless otherwise stated in figure caption). p-values were calculated using the one-way (differences between more than 2 groups) or 2-way ANOVA (including time-dependence) with Tukey's multiple comparisons test using GraphPad Prism 6.0 software. All p-values < 0.05 were considered significant. $^{*}p < 0.05$, $^{**}p < 0.01$, $^{***}p < 0.001$, $^{****}p < 0.0001$, nsd, not significantly different.

RESULTS

The VML injury was successfully created in the rat TA muscle as described above, and muscle samples were harvested at 2 and 5 weeks post-injury. No post-implantation mortality was detected and no implant rejection was observed. No significant differences between groups were found as regards initial animal body weight, defect weight and percentage of excised TA muscle (**Supplementary Table 1**).

To assess our hypothesis, we first performed immunostaining toward M1 ($CCR7^{+}$) and M2 ($CD206^{+}$) macrophages (**Figures 2A,B**, respectively) and quantified the number of each type of immune cells, observing that the injury areas of the samples treated with either the chemical or the physical hydrogels showed a significantly greater quantity of M2 than the empty (non-treated) samples ($p < 0.0001$) at 2 weeks post-injury (**Figure 2C**). Moreover, the presence of M1 in the hydrogel-treated samples was significantly lower than in the empty samples at this timepoint ($p < 0.0001$), thus giving a much higher M2/M1 ratio for the hydrogel-treated samples. These ratios were 0.75 ± 0.38 and 0.61 ± 0.23 for the groups treated with the chemical and with the physical hydrogel, respectively, while it was 0.11 ± 0.10 for the empty group. On the other hand, the quantity of M1 and M2 macrophages decreased for every group after 5 weeks, giving similar values for all of them (nsd). Nevertheless, the difference in M2 for the empty group between 2 and 5 weeks was not significant, meaning that the quantity of this type of macrophages did not peak at 2 weeks, contrarily to what we observed for the hydrogel-treated samples.

Since one of the main outcomes of a balanced macrophage response is the healing of the damaged tissue with a lesser amount of fibrosis, we performed Picrosirius red histological staining to observe collagen deposition in the muscle samples. For this purpose, we used polarized light (see **Supplementary Figure 2** for the bright-field pictures) to specifically differentiate and quantify collagen within the muscle sections for comparison between groups (**Figure 3A**). In particular, there were not significant differences in collagen deposition in the interface area (injury region with newly formed myofibers) between 2 and 5 weeks post-injury, although in the empty and physical hydrogel groups, but not in the chemical hydrogel one, there was a tendency toward increasing levels along time (**Figure 3B**). On the other

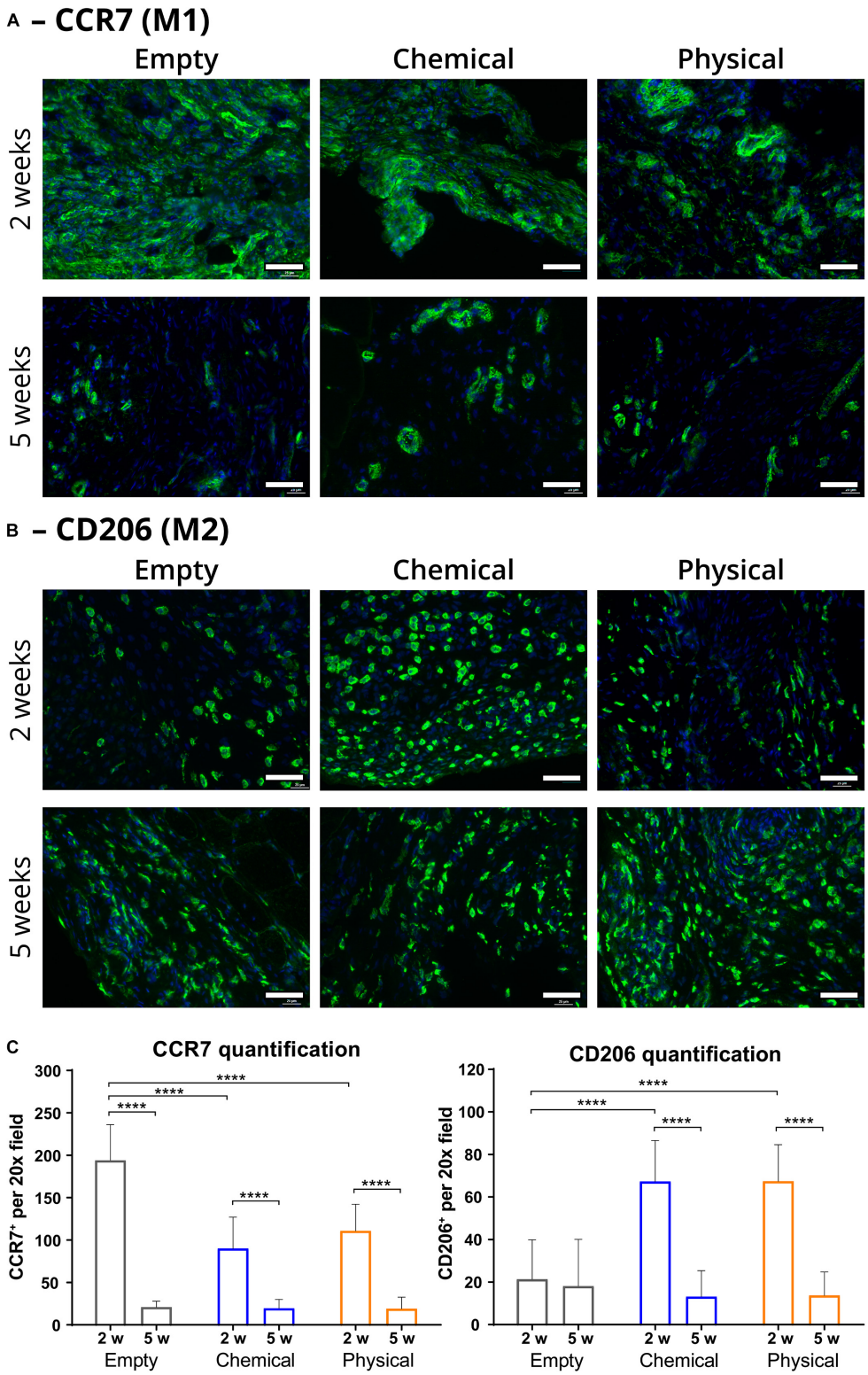

FIGURE 2 | Immunofluorescence representative images and quantification of macrophage populations in the injury area (scaffold and interface regions). **(A)** Type-1 macrophages (M1 or pro-inflammatory; in green) present in the injury area of samples from the empty (left), chemical (center), and physical (right) groups after 2 (top) and 5 weeks (bottom), labeled with an anti-CCR7 antibody. **(B)** Type-2 macrophages (M2 or anti-inflammatory; in green) present in the injury area of samples from the empty (left), chemical (center), and physical (right) groups after 2 (top) and 5 weeks (bottom), labeled with an anti-CD206 antibody. **(C)** Quantification of macrophage populations in the injury area (number of CCR7- or CD206-positive cells per 20× field) at 2 (2 w) and 5 weeks (5 w) post-injury. All the samples were counterstained with DAPI for nuclei. Scale bar = 50 μm. *n* = at least 16, which are the number of 20× fields used for the quantification. ****$p < 0.0001$.

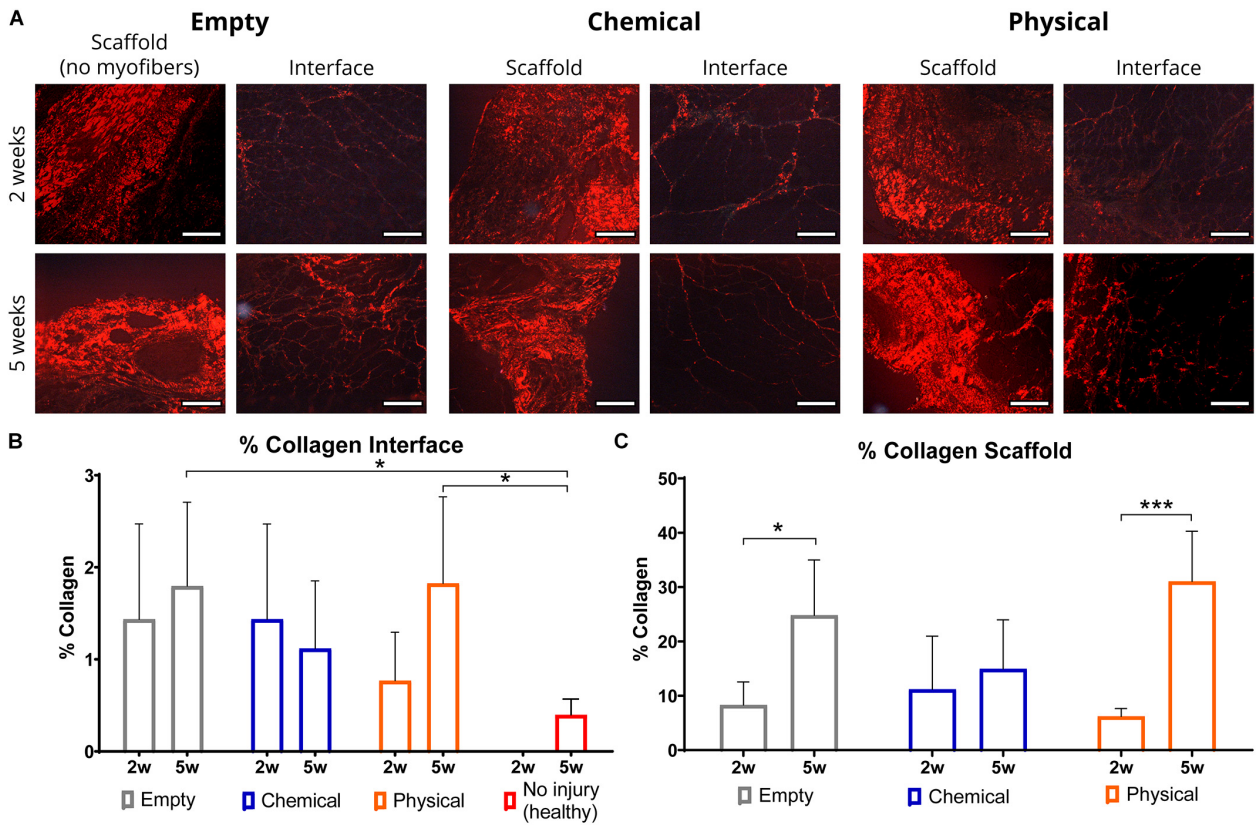

FIGURE 3 | Representative images and quantification for collagen staining with Picrosirius red. **(A)** Polarized light images from muscle samples of empty (left), chemical (center), and physical (right) groups for the scaffold (area without newly formed myofibers) and interface (area with newly formed myofibers) regions at 2 (top) and 5 weeks (bottom) post-injury. Scale bar = 100 μm. **(B,C)** Percentage of collagen in the interface (including no injury group at 5 weeks) and scaffold regions, normalized to their areas, after 2 and 5 weeks. $^{*}p < 0.05$, $^{***}p < 0.001$.

hand, there was a significant increase in collagen deposition in the scaffold area (injury region without newly formed myofibers) from 2 to 5 weeks for the empty and physical hydrogel groups ($p < 0.05$, respectively), whereas this was not observed for the chemical hydrogel-treated samples (**Figure 3C**). Moreover, the interface (remodeling) area of the samples treated with the chemical hydrogel after 5 weeks showed similar levels of collagen compared to the total percentage of collagen presented in the non-injured (healthy) samples (**Figure 3B**), while the empty and physical hydrogel groups presented significantly higher collagen levels ($p<0.05$).

Finally, we also performed hematoxylin and eosin (HE) staining of the muscle cross-sections to observe their morphology (see **Supplementary Figure 3** for the entire sections). In all the samples, we identified the remaining native tissue and the injury area, divided in the interface and the scaffold areas, as shown in **Figure 1**, which were subsequently quantified. Specifically, quantification of the interface and scaffold areas (**Figure 4A**) presented no significant differences between the different treatment groups (**Figures 4B,C**). Nevertheless, we observed significant differences in the muscles treated with the physical hydrogel between 2 and 5 weeks post-injury in both the interface and the scaffold areas (**Figures 4B,C**), suggesting a greater remodeling of the muscle tissue during this time. Moreover, we found an almost complete absence of myofibers with internal nuclei in the healthy tissue (**Supplementary Figure 4**), which suggests that the healing process only takes place in the interface and scaffold areas that represent the potentially injured region.

Further parameters, such as myofiber density, were also quantified. In this case, we found that the density in the interface area of samples from the empty group showed a significant decrease from 2 to 5 weeks ($p < 0.05$) (**Figure 5A**), which correlates to a lower myofiber number. On the other hand, no differences in the chemical and physical groups were observed. In addition, when samples harvested at 5 weeks from the three groups were compared to healthy samples (no injury), all of them showed a lower cell density, although in the groups treated with the physical hydrogel this difference was not significant (**Figure 5B**).

Another parameter that allowed the comparison between groups was the size of the myofibers, i.e., the cross-sectional minimal Feret's, which permits a reliable measurement of myofiber diameter independently of variations in sample orientation (Pertl et al., 2013). These results showed that the size of the myofibers found in the hydrogel-treated samples were

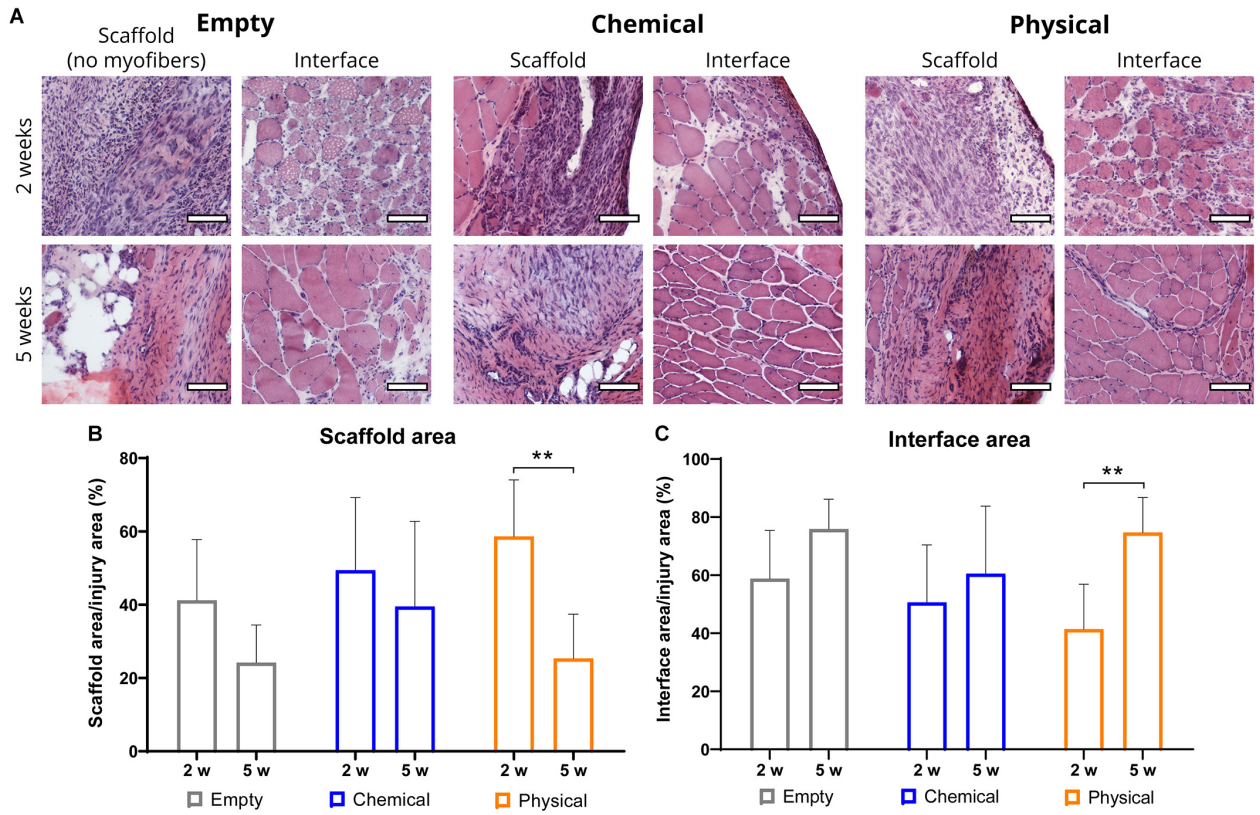

FIGURE 4 | (A) Representative images of the hematoxylin–eosin (HE) staining of sample cross-sections of the scaffold (area without newly formed myofibers) and interface (area with newly formed myofibers) regions (left and right for each group, respectively) of samples from the empty (left), chemical (center), and physical (right) groups at 2 (top) and 5 weeks (bottom) post-injury. Scale bar = 100 μm. **(B,C)** Percentage of the interface and scaffold areas, with respect to the injury area at 2 and 5 weeks post-injury. $^{**}p < 0.01$.

more similar to the size of the healthy ones than the cells in the empty samples at 5 weeks post-injury (**Figure 5C**), although all the injured groups presented smaller myofibers at 2 and 5 weeks than the uninjured samples.

DISCUSSION

The results obtained in this study show that the ELR hydrogels, both chemical and physical, promote a shift in macrophage polarization toward anti-inflammatory M2, highlighted by the higher M2/M1 ratio in comparison with the untreated control at 2 weeks post-injury. As aforementioned, M2 are known to secrete anti-inflammatory cytokines, while also regulating myogenic differentiation. Therefore, the increase in M2 for the hydrogel-treated samples at 2 weeks post-injury should promote a better regulation of the skeletal muscle repair in comparison with the untreated control, resulting in a morphology more similar to the healthy muscle and with a less amount of fibrotic/scar tissue. In this last regard, we studied collagen content by Picrosirius red staining, and it revealed that there was less collagen in the hydrogel-treated samples in comparison to the untreated control, especially in the case of the chemical hydrogel, which is indicative of a lesser fibrosis. Similarly, histological results through hematoxylin-eosin staining showed that the morphology of the muscle treated with the ELR hydrogels is more similar to the healthy one than the untreated control at 5 weeks post-injury, which is clearly evident when measuring specific parameters, such as myofiber density and diameter. This effect is consistent with the higher M2 response observed, which induces the maturation of the myofibers to give a more healthy-like muscle, while untreated samples, where the presence of M2 is much lower than in the treated samples at 2 weeks post-injury, show smaller myofibers, suggesting a lack of complete myogenic differentiation and muscle growth.

In this work, we show how the use of a bioactive and dynamic synthetic scaffold promotes an enhanced healing of injured skeletal muscle by itself, through the immunomodulation of the macrophage response that guides the repair process. The therapeutic strategy presented herein belongs to the field of *in situ* tissue regeneration, where a host cell recruitment is achieved (Lee et al., 2016), in this case without the use of external cells or growth factors, hence preventing potential side effects (Baldo, 2014). The immunomodulation shown by ELR hydrogels has also been observed in other works that used biological scaffolds, mainly decellularized urinary bladder matrix (UBM), to improve

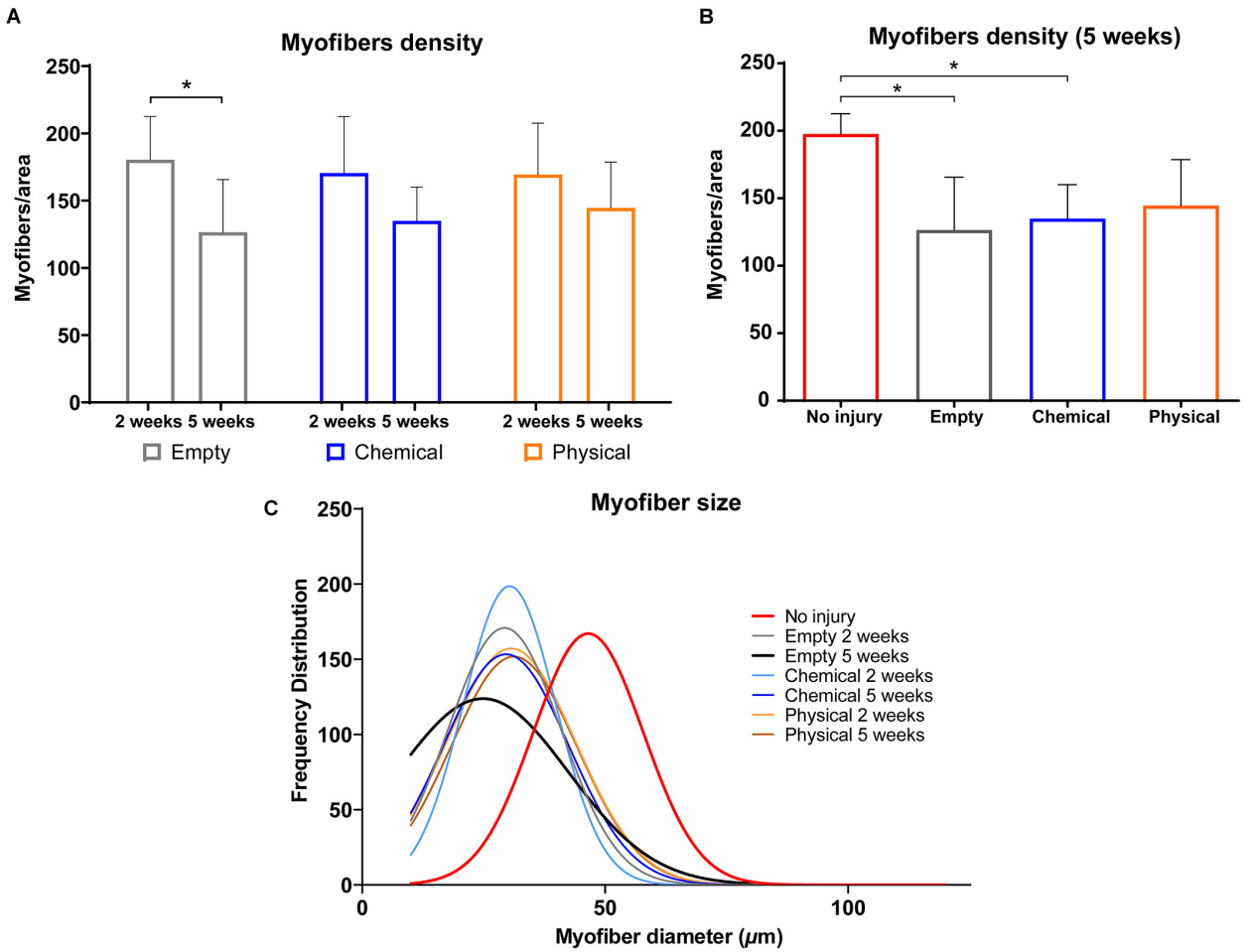

FIGURE 5 | Histomorphometric characterization of the HE-stained samples. **(A)** Myofiber density at 2 and 5 weeks post-injury for the empty (gray), chemical (blue) and physical (orange) groups. **(B)** Myofiber density after 5 weeks for the empty (gray), chemical (blue) and physical (orange) groups in comparison with no injury (healthy) samples (red). **(C)** Myofiber size distribution (number of myofibers with a specific diameter) for the different groups used in this study, i.e., empty, chemical, and physical, after 2 and 5 weeks, in comparison with the no injury (healthy) group. *$p < 0.05$.

the healing of VML injuries. In some of them, authors do not observe a shift from a M1 to a M2 response, and, as they state, this leads to an impaired muscle healing (Aurora et al., 2015, 2016; Greising et al., 2017), whereas some others report dissimilar results (Sicari et al., 2014; Dziki et al., 2016; Lee et al., 2019).

On the other hand, it has been suggested that the treatment with synthetic biomaterial-based scaffolds, comparable to the ELR hydrogels used in this work, also promote a M2-balanced immune response, with different examples using a photoresponsive hyaluronan hydrogel (Wang et al., 2019), a biohybrid pNIPAAm and UBM hydrogel (Zhu et al., 2018), keratin (Passipieri et al., 2017), or fibrin by itself (Tanaka et al., 2019). This strategy has several advantages in comparison with biological scaffolds, since the controlled synthesis of the biomaterials used for their fabrication does not rely on methods like decelullarization.

Regarding the immunomodulation mediated by ELR hydrogels, we suggest that, on one hand, the presence of RGD promotes a physiological interaction with the scaffolds, that hence resemble some of the properties of the native ECM. Another reason that may provide an explanation to the findings of this work is the fact that the ELR hydrogels used herein are biodegradable. This means that they act as a transient ECM-like scaffold, providing a dynamic environment that evolves as required by the cells involved in the healing process, which secrete MMPs relevant for the proteolysis of the hydrogels [mainly macrophages (Turner and Badylak, 2012)] and make space for the formation of regenerated tissue. Indeed, we found in a preliminary study that biodegradable ELR hydrogels are completely necessary for the healing of the VML injury, which otherwise is permanently occupied by the scaffold (**Supplementary Figure 5**). Previous studies have shown the importance of the biodegradation of ELR hydrogels with potential application in tissue engineering, influencing, for instance, vascularization (Staubli et al., 2017; Flora et al., 2019), which is considered one of the main events to achieve a successful

healing of damaged tissues. In addition, the filling of the void created through the VML with the ELR hydrogels impedes the formation of a large scar tissue (fibrosis) that usually impairs muscle healing (Järvinen et al., 2005; Turner and Badylak, 2012). Therefore, the use of biodegradable ELR hydrogels could provide a niche that promotes vascularization and replacement by newly formed skeletal muscle, resulting in an efficient healing.

This investigation has a main limitation, which is the lack of functional characterization of the TA muscles. Nevertheless, we aimed to delve into the effect of ELR hydrogels in the healing of VML injuries in terms of cell and molecular biology, in order to set the basis for future works with larger animal models (Pollot and Corona, 2016). These models will not only be more relevant as regards the future application of ELR hydrogels in the treatment of skeletal muscle injuries in humans, but they will also allow the use of non-invasive techniques already implemented in clinics for the determination of muscle function.

CONCLUSION

In conclusion, this study demonstrates that bioactive and biodegradable ELR hydrogels regulate the macrophage response by inducing M2 polarization after a VML injury. This immunomodulation results in an enhanced skeletal muscle healing, with a reduced collagen deposition and a muscle morphology more similar to the healthy tissue. Therefore, we confirmed that ELR hydrogels provide a cell-friendly and dynamic environment that induces M2 shift and supports an enhanced healing, especially in the case of the chemically crosslinked ELR hydrogel, which showed a reduced fibrosis. The work presented here paves the way for future studies in more relevant large animal models of VML treated with the chemical ELR hydrogel that include functional characterization.

DATA AVAILABILITY STATEMENT

Data associated with this study is available upon request to the corresponding author.

ETHICS STATEMENT

The animal study was reviewed and approved by the Comité de Ética en Experimentación y Bienestar Animal (CEEBA) de la Universidad de Valladolid (protocol number 5402485).

AUTHOR CONTRIBUTIONS

AI-F, SS, DG, MA, HA, and JR-C designed the study. AI-F, SS, DG, BC, ÁÁ, and HA performed the experiments. AI-F, SS, and DG wrote the manuscript. AV, MA, HA, and JR-C revised the manuscript. All authors approved the final version.

FUNDING

This work was funded by the Spanish Government (MAT2016-78903-R, RTI2018-096320-B-C22), Junta de Castilla y León (VA015U16, VA317P18), Interreg V A España Portugal POCTEP (0624_2IQBIONEURO_6_E) and Centro en Red de Medicina Regenerativa y Terapia Celular de Castilla y León.

ACKNOWLEDGMENTS

The authors acknowledge the support of the technicians from the Servicio de Investigación y Bienestar Animal (SIBA) of the University of Valladolid, and of Rocío García for the help in the bioproduction of the ELRs used in this work.

SUPPLEMENTARY MATERIAL

The Supplementary Material for this article can be found online at: https://www.frontiersin.org/articles/10.3389/fbioe.2020.00413/full#supplementary-material

REFERENCES

Arganda-Carreras, I., Kaynig, V., Rueden, C., Eliceiri, K. W., Schindelin, J., Cardona, A., et al. (2017). Trainable weka segmentation: a machine learning tool for microscopy pixel classification. *Bioinformatics* 33, 2424–2426. doi: 10.1093/bioinformatics/btx180

Aurora, A., Corona, B. T., and Walters, T. J. (2016). A porcine urinary bladder matrix does not recapitulate the spatiotemporal macrophage response of muscle regeneration after volumetric muscle loss injury. *Cells Tissues Organs* 202, 189–201. doi: 10.1159/000447582

Aurora, A., Roe, J. L., Corona, B. T., and Walters, T. J. (2015). An acellular biologic scaffold does not regenerate appreciable de novo muscle tissue in rat models of volumetric muscle loss injury. *Biomaterials* 67, 393–407. doi: 10.1016/j.biomaterials.2015.07.040

Baldo, B. A. (2014). Side effects of cytokines approved for therapy. *Drug Saf.* 37, 921–943. doi: 10.1007/s40264-014-0226-z

Bartolacci, J., Dziki, J., and Badylak, S. F. (2019). "12 - Scaffolds for skeletal muscle tissue engineering," in *Handbook of Tissue Engineering Scaffolds*, Vol. One, eds M. Mozafari, F. Sefat, and A. Atala (New York, NY: Woodhead Publishing), 245–258.

Boersema, G. S. A., Grotenhuis, N., Bayon, Y., Lange, J. F., and Bastiaansen-Jenniskens, Y. M. (2016). The effect of biomaterials used for tissue regeneration purposes on polarization of macrophages. *Biores. Open Access* 5, 6–14. doi: 10.1089/biores.2015.0041

Briguet, A., Courdier-Fruh, I., Foster, M., Meier, T., and Magyar, J. P. (2004). Histological parameters for the quantitative assessment of muscular dystrophy in the mdx-mouse. *Neuromuscul. Disord.* 14, 675–682. doi: 10.1016/j.nmd.2004.06.008

Cappello, J., Crissman, J., Dorman, M., Mikolajczak, M., Textor, G., Marquet, M., et al. (1990). Genetic engineering of structural protein polymers. *Biotechnol. Prog.* 6, 198–202. doi: 10.1021/bp00003a006

Chung, E. H., Gilbert, M., Virdi, A. S., Sena, K., Sumner, D. R., and Healy, K. E. (2006). Biomimetic artificial ECMs stimulate bone regeneration. *J. Biomed. Mater. Res. A* 79A, 815–826. doi: 10.1002/jbm.a.30809

Coletta, D. J., Ibáñez-Fonseca, A., Missana, L. R., Jammal, M. V., Vitelli, E. J., Aimone, M., et al. (2017). Bone regeneration mediated by a bioactive

and biodegradable extracellular matrix-like hydrogel based on elastin-like recombinamers. *Tissue Eng. A* 23, 1361–1371. doi: 10.1089/ten.tea.2017.0047

Corona, B. T., Garg, K., Ward, C. L., McDaniel, J. S., Walters, T. J., and Rathbone, C. R. (2013). Autologous minced muscle grafts: a tissue engineerin therapy for the volumetric loss of skeletal muscle. *Am. J. Physiol. Cell Physiol.* 305, C761–C775. doi: 10.1152/ajpcell.00189.2013

Corona, B. T., Rivera, J. C., Owens, J. G., Wenke, J. C., and Rathbone, C. R. (2015). Volumetric muscle loss leads to permanent disability following extremity trauma. *J. Rehabil. Res. Dev.* 52, 785–792. doi: 10.1682/JRRD.2014.07.0165

Costa, R. R., Custódio, C. A., Testera, A. M., Arias, F. J., Rodríguez-Cabello, J. C., Alves, N. M., et al. (2009). Stimuli-responsive thin coatings using elastin-like polymers for biomedical applications. *Adv. Funct. Mater.* 19, 3210–3218. doi: 10.1002/adfm.200900568

Dubach-Powell, J., Erb, M., Van Putten, M., Thirion, C., Barton, E., and Rüegg, M. A. (2008). *Quantitative Determination of Muscle Fiber Diameter (Minimal Feret's Diameter) and Percentage of Centralized Nuclei*. Available online at: www.treat-nmd.eu/downloads/file/sops/dmd/MDX/DMD_M.1.2.001.pdf (accessed April 12, 2020).

Dziki, J. L., Sicari, B. M., Wolf, M. T., Cramer, M. C., and Badylak, S. F. (2016). Immunomodulation and mobilization of progenitor cells by extracellular matrix bioscaffolds for volumetric muscle loss treatment. *Tissue Eng. Part A* 22, 1129–1139. doi: 10.1089/ten.TEA.2016.0340

Fernández-Colino, A., Arias, F. J., Alonso, M., and Rodríguez-Cabello, J. C. (2014). Self-Organized ECM-mimetic model based on an amphiphilic multiblock silk-elastin-like corecombinamer with a concomitant dual physical gelation process. *Biomacromolecules* 15, 3781–3793. doi: 10.1021/bm501051t

Flora, T., González de Torre, I., Alonso, M., and Rodríguez-Cabello, J. C. (2019). Use of proteolytic sequences with different cleavage kinetics as a way to generate hydrogels with preprogrammed cell-infiltration patterns imparted over their given 3D spatial structure. *Biofabrication* 11:035008. doi: 10.1088/1758-5090/ab10a5

Girotti, A., Orbanic, D., Ibáñez-Fonseca, A., Gonzalez-Obeso, C., and Rodríguez-Cabello, J. C. (2015). Recombinant technology in the development of materials and systems for soft-tissue repair. *Adv. Healthc. Mater.* 4, 2423–2455. doi: 10.1002/adhm.201500152

Girotti, A., Reguera, J., Rodríguez-Cabello, J. C., Arias, F. J., Alonso, M., and Testera, A. M. (2004). Design and bioproduction of a recombinant multi(bio)functional elastin-like protein polymer containing cell adhesion sequences for tissue engineering purposes. *J. Mater. Sci. Mater. Med.* 15, 479–484. doi: 10.1023/B:JMSM.0000021124.58688.7a

González de Torre, I., Santos, M., Quintanilla, L., Testera, A., Alonso, M., and Rodríguez Cabello, J. C. (2014). Elastin-like recombinamer catalyst-free click gels: characterization of poroelastic and intrinsic viscoelastic properties. *Acta Biomater.* 10, 2495–2505. doi: 10.1016/j.actbio.2014.02.006

Grasman, J. M., Zayas, M. J., Page, R. L., and Pins, G. D. (2015). Biomimetic scaffolds for regeneration of volumetric muscle loss in skeletal muscle injuries. *Acta Biomater.* 25, 2–15. doi: 10.1016/j.actbio.2015.07.038

Greising, S. M., Rivera, J. C., Goldman, S. M., Watts, A., Aguilar, C. A., and Corona, B. T. (2017). Unwavering pathobiology of volumetric muscle loss injury. *Sci. Rep.* 7:13179. doi: 10.1038/s41598-017-13306-2

Greising, S. M., Warren, G. L., Southern, W. M., Nichenko, A. S., Qualls, A. E., Corona, B. T., et al. (2018). Early rehabilitation for volumetric muscle loss injury augments endogenous regenerative aspects of muscle strength and oxidative capacity. *BMC Musculoskelet. Disord.* 19:173. doi: 10.1186/s12891-018-2095-6

Grogan, B. F., Hsu, J. R., and Skeletal Trauma Research Consortium (2011). Volumetric muscle loss. *J. Am. Acad. Orthop. Surg.* 19(Suppl. 1), S35–S37. doi: 10.5435/00124635-201102001-00007

Ibáñez-Fonseca, A., Alonso, M., Arias, F. J., and Rodríguez-Cabello, J. C. (2017). Förster resonance energy transfer-paired hydrogel forming silk-elastin-like recombinamers by recombinant conjugation of fluorescent proteins. *Bioconjug. Chem.* 28, 828–835. doi: 10.1021/acs.bioconjchem.6b00738

Ibáñez-Fonseca, A., Flora, T., Acosta, S., and Rodríguez-Cabello, J. C. (2019). Trends in the design and use of elastin-like recombinamers as biomaterials. *Matrix Biol.* 84, 111–126. doi: 10.1016/j.matbio.2019.07.003

Ibáñez-Fonseca, A., Orbanic, D., Arias, F. J., Alonso, M., Zeugolis, D. I., and Rodríguez-Cabello, J. C. (2020). Influence of the thermodynamic and kinetic control of self-assembly on the microstructure evolution of silk-elastin-like recombinamer hydrogels. *Small* doi: 10.1002/smll.202001244

Ibáñez-Fonseca, A., Ramos, T. L., González de Torre, I., Sánchez-Abarca, L. I., Muntión, S., Arias, F. J., et al. (2018). Biocompatibility of two model elastin-like recombinamer-based hydrogels formed through physical or chemical cross-linking for various applications in tissue engineering and regenerative medicine. *J. Tissue Eng. Regen. Med.* 12, e1450–e1460. doi: 10.1002/term.2562

Järvinen, T. A. H., Järvinen, T. L. N., Kääriäinen, M., Kalimo, H., and Järvinen, M. (2005). Muscle injuries: biology and treatment. *Am. J. Sports Med.* 33, 745–764. doi: 10.1177/0363546505274714

Junqueira, L. C. U., Bignolas, G., and Brentani, R. R. (1979). Picrosirius staining plus polarization microscopy, a specific method for collagen detection in tissue sections. *Histochem. J.* 11, 447–455. doi: 10.1007/bf01002772

Klinkenberg, M., Fischer, S., Kremer, T., Hernekamp, F., Lehnhardt, M., and Daigeler, A. (2013). Comparison of anterolateral thigh, lateral arm, and parascapular free flaps with regard to donor-site morbidity and aesthetic and functional outcomes. *Plast. Reconstr. Surg.* 131, 293–302. doi: 10.1097/PRS.0b013e31827786bc

Lankford, K. L., Arroyo, E. J., Nazimek, K., Bryniarski, K., Askenase, P. W., and Kocsis, J. D. (2018). Intravenously delivered mesenchymal stem cell-derived exosomes target M2-type macrophages in the injured spinal cord. *PLoS One* 13:e0190358. doi: 10.1371/journal.pone.0190358

Lee, H., Ju, Y. M., Kim, I., Elsangeedy, E., Lee, J. H., Yoo, J. J., et al. (2019). A novel decellularized skeletal muscle-derived ECM scaffolding system for in situ muscle regeneration. *Methods* 171, 77–85. doi: 10.1016/j.ymeth.2019.06.027

Lee, S. J., Yoo, J. J., and Atala, A. (2016). "Chapter 1 - Fundamentals of In Situ Tissue Regeneration," in *In Situ Tissue Regeneration*, eds S. J. Lee, J. J. Yoo, and A. Atala (Boston: Academic Press), 3–17.

Lepper, C., Partridge, T. A., and Fan, C.-M. (2011). An absolute requirement for Pax7-positive satellite cells in acute injury-induced skeletal muscle regeneration. *Development* 138, 3639–3646. doi: 10.1242/dev.067595

Lin, C.-H., Lin, Y.-T., Yeh, J.-T., and Chen, C.-T. (2007). Free functioning muscle transfer for lower extremity posttraumatic composite structure and functional defect. *Plast. Reconstr. Surg.* 119, 2118–2126. doi: 10.1097/01.prs.0000260595.85557.41

Lin, S.-H., Chuang, D. C.-C., Hattori, Y., and Chen, H.-C. (2004). Traumatic major muscle loss in the upper extremity: reconstruction using functioning free muscle transplantation. *J. Reconstr. Microsurg.* 20, 227–235. doi: 10.1055/s-2004-823110

Lutolf, M. P., Weber, F. E., Schmoekel, H. G., Schense, J. C., Kohler, T., Müller, R., et al. (2003). Repair of bone defects using synthetic mimetics of collagenous extracellular matrices. *Nat. Biotechnol.* 21, 513–518. doi: 10.1038/nbt818

Madl, C. M., Katz, L. M., and Heilshorn, S. C. (2016). Bio-orthogonally crosslinked, engineered protein hydrogels with tunable mechanics and biochemistry for cell encapsulation. *Adv. Funct. Mater.* 26, 3612–3620. doi: 10.1002/adfm.201505329

Martín, L., Arias, F. J., Alonso, M., García-Arévalo, C., and Rodríguez-Cabello, J. C. (2010). Rapid micropatterning by temperature-triggered reversible gelation of a recombinant smart elastin-like tetrablock-copolymer. *Soft Matter.* 6, 1121–1124. doi: 10.1039/B923684H

O'Brien, F. J. (2011). Biomaterials & scaffolds for tissue engineering. *Mater. Today* 14, 88–95. doi: 10.1016/S1369-7021(11)70058-X

Passipieri, J. A., Baker, H. B., Siriwardane, M., Ellenburg, M. D., Vadhavkar, M., Saul, J. M., et al. (2017). Keratin hydrogel enhances in vivo skeletal muscle function in a rat model of volumetric muscle loss. *Tissue Eng. Part A* 23, 556–571. doi: 10.1089/ten.tea.2016.0458

Pertl, C., Eblenkamp, M., Pertl, A., Pfeifer, S., Wintermantel, E., Lochmüller, H., et al. (2013). A new web-based method for automated analysis of muscle histology. *BMC Musculoskelet. Disord.* 14:26. doi: 10.1186/1471-2474-14-26

Pescador, D., Ibáñez-Fonseca, A., Sánchez-Guijo, F., Briñón, J. G., Arias, F. J., Muntión, S., et al. (2017). Regeneration of hyaline cartilage promoted by xenogeneic mesenchymal stromal cells embedded within elastin-like recombinamer-based bioactive hydrogels. *J. Mater. Sci. Mater. Med.* 28:115. doi: 10.1007/s10856-017-5928-1

Pollot, B. E., and Corona, B. T. (2016). "Volumetric muscle loss," in *Skeletal Muscle Regeneration in the Mouse: Methods and Protocols*, ed. M. Kyba (New York, NY: Springer), 19–31.

Qazi, T. H., Mooney, D. J., Pumberger, M., Geißler, S., and Duda, G. N. (2015). Biomaterials based strategies for skeletal muscle tissue engineering: existing

technologies and future trends. *Biomaterials* 53, 502–521. doi: 10.1016/j.biomaterials.2015.02.110

Rodríguez-Cabello, J. C., Girotti, A., Ribeiro, A., and Arias, F. J. (2012). "Synthesis of Genetically Engineered Protein Polymers (Recombinamers) as an Example of Advanced Self-Assembled Smart Materials," in *Nanotechnology in Regenerative Medicine: Methods and Protocols*, eds M. Navarro and J. A. Planell (Totowa, NJ: Humana Press), 17–38. doi: 10.1007/978-1-61779-388-2_2

Rodríguez-Cabello, J. C., Martín, L., Alonso, M., Arias, F. J., and Testera, A. M. (2009). "Recombinamers" as advanced materials for the post-oil age. *Polymer* 50, 5159–5169. doi: 10.1016/j.polymer.2009.08.032

Ruoslahti, E. (1996). RGD and other recognition sequences for integrins. *Annu. Rev. Cell Dev. Biol.* 12, 697–715. doi: 10.1146/annurev.cellbio.12.1.697

Saclier, M., Yacoub-Youssef, H., Mackey, A. L., Arnold, L., Ardjoune, H., Magnan, M., et al. (2013). Differentially activated macrophages orchestrate myogenic precursor cell fate during human skeletal muscle regeneration. *Stem Cells* 31, 384–396. doi: 10.1002/stem.1288

Schindelin, J., Arganda-Carreras, I., Frise, E., Kaynig, V., Longair, M., Pietzsch, T., et al. (2012). Fiji: an open-source platform for biological-image analysis. *Nat. Methods* 9:676. doi: 10.1038/nmeth.2019

Shin, E. H., Caterson, E. J., Jackson, W. M., and Nesti, L. J. (2014). Quality of healing: defining, quantifying, and enhancing skeletal muscle healing. *Wound Repair Regen.* 22, 18–24. doi: 10.1111/wrr.12163

Sicari, B. M., Dziki, J. L., Siu, B. F., Medberry, C. J., Dearth, C. L., and Badylak, S. F. (2014). The promotion of a constructive macrophage phenotype by solubilized extracellular matrix. *Biomaterials* 35, 8605–8612. doi: 10.1016/j.biomaterials.2014.06.060

Staubli, S. M., Cerino, G., Gonzalez de Torre, I., Alonso, M., Oertli, D., Eckstein, F., et al. (2017). Control of angiogenesis and host response by modulating the cell adhesion properties of an Elastin-Like Recombinamer-based hydrogel. *Biomaterials* 135, 30–41. doi: 10.1016/j.biomaterials.2017.04.047

Tanaka, R., Saito, Y., Fujiwara, Y., Jo, J.-I., and Tabata, Y. (2019). Preparation of fibrin hydrogels to promote the recruitment of anti-inflammatory macrophages. *Acta Biomater.* 89, 152–165. doi: 10.1016/j.actbio.2019.03.011

Tedesco, F. S., Dellavalle, A., Diaz-Manera, J., Messina, G., and Cossu, G. (2010). Repairing skeletal muscle: regenerative potential of skeletal muscle stem cells. *J. Clin. Invest.* 120, 11–19. doi: 10.1172/JCI40373

Tidball, J. G., and Villalta, S. A. (2010). Regulatory interactions between muscle and the immune system during muscle regeneration. *Am. J. Physiol. Regul. Integr. Comp. Physiol.* 298, R1173–R1187. doi: 10.1152/ajpregu.00735.2009

Tirrell, D. A., Fournier, M. J., and Mason, T. L. (1991). Genetic engineering of polymeric materials. *MRS Bull.* 16, 23–28. doi: 10.1557/S0883769400056505

Turner, N. J., and Badylak, S. F. (2012). Regeneration of skeletal muscle. *Cell Tissue Res.* 347, 759–774. doi: 10.1007/s00441-011-1185-7

Urry, D. W. (2006). *What Sustains Life? Consilient Mechanisms for Protein-Based Machines and Materials*. Boston: Birkhäuser Boston.

Urry, D. W., Okamoto, K., Harris, R. D., Hendrix, C. F., and Long, M. M. (1976). Synthetic, cross-linked polypentapeptide of tropoelastin: an anisotropic, fibrillar elastomer. *Biochemistry* 15, 4083–4089. doi: 10.1021/bi00663a026

Wang, H., Morales, R.-T. T., Cui, X., Huang, J., Qian, W., Tong, J., et al. (2019). A Photoresponsive Hyaluronan Hydrogel Nanocomposite for Dynamic Macrophage Immunomodulation. *Adv. Healthc. Mater.* 8:1801234. doi: 10.1002/adhm.201801234

Wolf, M. T., Dearth, C. L., Sonnenberg, S. B., Loboa, E. G., and Badylak, S. F. (2015). Naturally derived and synthetic scaffolds for skeletal muscle reconstruction. *Adv. Drug Deliv. Rev* 84, 208–221. doi: 10.1016/j.addr.2014.08.011

Wu, X., Corona, B. T., Chen, X., and Walters, T. J. (2012). A standardized rat model of volumetric muscle loss injury for the development of tissue engineering therapies. *Biores. Open Access* 1, 280–290. doi: 10.1089/biores.2012.0271

Zalavras, C. G., and Patzakis, M. J. (2003). Open fractures: evaluation and management. *JAAOS J. Am. Acad. Orth. Surg.* 11, 212–219.

Zhu, Y., Hideyoshi, S., Jiang, H., Matsumura, Y., Dziki, J. L., LoPresti, S. T., et al. (2018). Injectable, porous, biohybrid hydrogels incorporating decellularized tissue components for soft tissue applications. *Acta Biomater.* 73, 112–126. doi: 10.1016/j.actbio.2018.04.003

Conflict of Interest: The authors declare that the research was conducted in the absence of any commercial or financial relationships that could be construed as a potential conflict of interest.

frontiers in Bioengineering and Biotechnology

ORIGINAL RESEARCH
published: 15 May 2020
doi: 10.3389/fbioe.2020.00456

Optimisation of a Novel Bio-Substrate as a Treatment for Atrophic Age-Related Macular Degeneration

*Rachel McCormick[1], Ian Pearce[2], Stephen Kaye[1,2] and Atikah Haneef[1]**

[1] Department of Eye and Vision Science, Institute of Life Course and Medical Sciences, University of Liverpool, Liverpool, United Kingdom, [2] St Paul's Eye Unit, Royal Liverpool University Hospital, Liverpool, United Kingdom

Atrophic age-related macular degeneration (AMD) is the most common form of AMD accounting for 90% of patients. During atrophic AMD the waste/exchange pathway between the blood supply (choroid) and the retinal pigment epithelium (RPE) is compromised. This results in atrophy and death of the RPE cells and subsequently the photoreceptors leading to central blindness. Although the mechanisms behind AMD are unknown, the growth of fatty deposits known as drusen, have been shown to play a role in the disease. There is currently no treatment or cure for atrophic AMD. Much research focuses on developing a synthetic substrate in order to transplant healthy cells to the native Bruch's membrane (BM), however, the diseased native BM and related structures still leave potential for transplanted cells to succumb to disease. In this proof-of-concept work we electrospun poly(ethylene terephthalate) (PET) to fabricate a nanofibrous cytocompatible synthetic BM. The apical surface of the membrane was cultured with ARPE-19 cells and the underside was decorated with poly(lactic acid-co-glycolic acid) (PLGA) or poly(glycolic acid) (PGA) degradable nanoparticles by electrospraying. The membrane exhibited hydrophilicity, high tensile strength and structurally resembled the native BM. ARPE-19 cells were able to form a monolayer on the surface of the membrane and no cell invasion into the membrane was seen. The presence of both PLGA and PGA nanoparticles increased ARPE-19 cell metabolism but had no effect on cell viability. There was a decrease in pH of ARPE-19 cell culture media 7 days following culturing with the PLGA nanoparticles but this change was eliminated by 2 weeks; PGA nanoparticles had no effect on cell culture media pH. The fluorescent dye FITC was encapsulated into nanoparticles and showed sustained release from PLGA nanoparticles for 2 weeks and PGA nanoparticles for 1 day. Future work will focus on encapsulating biologically active moieties to target drusen. This could allow this novel bioactive substrate to be a potential treatment for atrophic AMD that would function two-fold: deliver the required monolayer of healthy RPE cells to the macula on a synthetic BM and remove diseased structures within the retina, restoring the waste/exchange pathway and preventing vision loss.

Keywords: AMD, electrospinning, electrospraying, nanoparticles, sustained release, composite, substrate, coaxial

OPEN ACCESS

Edited by:
Dimitrios I. Zeugolis, National University of Ireland Galway, Ireland

Reviewed by:
Christine A. Curcio, University of Alabama at Birmingham, United States
Thomas Ach, University Hospital Würzburg, Germany

***Correspondence:**
Atikah Haneef
atikahh@liverpool.ac.uk

Specialty section:
This article was submitted to Tissue Engineering and Regenerative Medicine, a section of the journal Frontiers in Bioengineering and Biotechnology

Received: *20 December 2019*
Accepted: *21 April 2020*
Published: *15 May 2020*

Citation:
McCormick R, Pearce I, Kaye S and Haneef A (2020) Optimisation of a Novel Bio-Substrate as a Treatment for Atrophic Age-Related Macular Degeneration. Front. Bioeng. Biotechnol. 8:456. doi: 10.3389/fbioe.2020.00456

INTRODUCTION

Age-related macular degeneration (AMD) is a progressive disease of the retina that is the leading form of blindness in developed countries. It is a form of central blindness that mainly affects people over the age of 50 years. Although the pathology of AMD is currently unknown, age is considered to be the main contributing factor to the manifestation of this disease (Nowak, 2006; Curcio and Johnson, 2013). There are two forms of AMD; neovascular and atrophic (nonexudative). Neovascular (or wet) AMD makes up 10% of all reported cases where new abnormal leaking blood vessels break through a layer underlying the retina called the BM leading to a loss of central vision. There has been significant developments and improvements in the management of neovascular AMD such as intravitreal injections of anti-vascular endothelial growth factor (anti-VEGF) to prevent any further growth of abnormal blood vessels. Nonexudative (or dry) AMD, however, makes up 90% of all cases. It is associated with a slowly progressive form of sight loss where fatty deposits known as drusen, form on BM leading to alterations and atrophy of the RPE. The RPE is the main source of nutrient/waste exchange; if the RPE fails it leads on to photoreceptor death, ultimately leading to central blindness (atrophic AMD) as the end stage of the disease. Although several risk factors for nonexudative AMD are known, there are no available treatments other than supportive optical aids and nutritional supplements that are recommended for a subset of patients with large drusen (Rudolf et al., 2008; Age-Related Eye Disease Study 2 Research Group, 2013).

Much research focuses on developing a synthetic cell transplantation substrate in order to transplant healthy RPE cells onto BM as a treatment for nonexudative AMD (Lu et al., 2012; Liu et al., 2014; Surrao et al., 2017; da Cruz et al., 2018; Tan et al., 2019). The underlying native diseased BM and related structures remain, however, which leaves the potential for healthy transplanted cells to eventually succumb to disease (White and Olabisi, 2017).

Recent research has explored using an anti-inflammatory, antiatherogenic peptide L-4F to reduce the accumulation of fatty deposits on BM of *Macaca fascicularis*, via intravitreal injection of L-4F (Rudolf et al., 2019). Those eyes injected with L-4F were found to have had clearance of the fatty deposits along the BM without harming surrounding ultrastructure in the retina. This is particularly interesting, as they described the drug to be well tolerated at even the highest dose, with the only adverse events attributed to the physical process of the injection. Interestingly they found that the effect of the drug was seen bilaterally, even though only one eye was injected with the drug while the other was meant to serve as a control (Rudolf et al., 2019).

Abbreviations: AMD, aged related macular degeneration; Best1, bestrophin 1; BM, bruch's membrane; DAPI, 4',6-diamidino-2-phenylindole; DMEM, dulbecco's modified eagles' media; DPBS, dulbecco's phosphate buffered saline; FITC, fluorescein-5-isothiocyanate; FTIR, fourier-transform infrared spectroscopy; NBF, neutral buffered formalin; PET, poly(ethylene terephthalate); PGA, poly(glycolic acid); PLGA, poly(lactic acid-co-glycolic acid); RPE, retinal pigment epithelium; SEM, scanning electron microscope; UTS, ultimate tensile strength; UV, ultraviolet; VEGF, vascular endothelial growth factor; WCA, water contact angle; YM, young's modulus.

There is, therefore, scope to provide a two-pronged approach for a potential treatment for nonexudative AMD. That is, a persistent bioactive substrate that would function two-fold; provide a permanent basement layer for transplantation of healthy RPE cells to the area required, while removing diseased structures (drusen) on the BM (Curcio and Johnson, 2013), using moieties such as L-4F. This would replenish the native BM nutrient/waste exchange pathway, preventing the progressive loss of photoreceptors, through a more controlled and localized effect. Our aim is to develop a bioactive persistent cell transplant substrate for the treatment for nonexudative AMD. This article describes the development of a composite membrane for this two-pronged approach, which includes the fabrication of a non-degradable electrospun membrane (adapted from a previously fabricated and tested membrane (Haneef and Downes, 2015) that will serve as a cell-culture substrate on the membrane's apical surface, nanoparticles are anticipated to be decorated on the underside of the membrane (opposite to where the cells will be cultured) electrosprayed to encapsulate biological moieties for sustained release to locally target drusen. Electrospraying parameters can be altered to control the degradation of the nanoparticles, thereby allowing a controlled release of these moieties. For the purpose of this paper we have encapsulated fluorescent dye FITC into the nanoparticles to exhibit the proof-of-concept, we have not yet chosen nor decided upon the biological moiety that would be used to target the drusen.

MATERIALS AND METHODS

Electrospinning of PET Scaffold

Poly(ethylene terephthalate) (PET) pellets (04301, Polysciences Inc.) were dissolved in neat 1,1,1-3,3,3-hexafluoroisopropanol (HFIP) (Apollo Scientific Ltd.) at a concentration of 17.5% (w/v). The fibres were collected for 15 min under laboratory conditions on a grounded plate covered with aluminium foil at a working distance of 15 cm, flow rate of 2 ml/h and a voltage of 25 kV.

Electrospraying of PLGA and PGA Nanoparticles

Poly(lactic acid-co-glycolic acid) 50/50 (PLGA) (26269, Polysciences Inc.) was dissolved in neat chloroform (Merck) at a concentration of 2% (w/v). Poly(glycolic acid) (06525, Polysciences Inc.) was dissolved in neat HFIP at a concentration of 1% (w/v) and left to stir overnight at room temperature. To encapsulate FITC into the nanoparticles, prior to electrospraying 2 mM of FITC was added to the polymer solutions and mixed thoroughly. The homogeneous polymer solution was introduced into a 10 mL plastic syringe and a blunt-tip needle attached. Any air bubbles were removed and the filled syringe was fixed in a mechanical syringe pump. All work was carried out at ambient conditions in a fume-hood. To assess initial nanoparticle formation, nanoparticles were sprayed into a glass dish filled with 0.1% (v/v) isopropanol (Merck) in dH_2O placed on a magnetic stirrer, connected to a grounding plate and left to spray for 1 h. Nanoparticles were then decorated on the basal surface of the electrospun membrane using the optimal electrospraying

parameters. Working parameters for PGA nanoparticles were 25 kV, 25 cm working distance, 2 ml/h flow rate; and for PLGA nanoparticles; 11 kV, 13 cm working distance, 0.5 ml flow rate (**Supplementary Figure S1**).

Fibre and Nanoparticle Diameter Measurements

Diameter measurements were undertaken to determine fibre/nanoparticle size and homogeneity between fabrication batches. The diameter of 50 fibres and nanoparticles from three different images of the electrospun fibres and electrosprayed nanoparticles were measured using ImageJ ($n = 3$).

Preparation of Fibres and Nanoparticles for SEM

Scanning electron microscopy (SEM) was undertaken to characterise the morphology of the fibres and nanoparticles. Electrospun membrane or 10 μl of electrosprayed nanoparticles suspended in solution was placed on a carbon tab (TAAB) mounted on an aluminium stub (TAAB). The nanoparticles were surrounded by a layer of silver dag (Merck) and were left overnight in a desiccator for the solution to evaporate. Membrane or nanoparticles were gold sputter coated (Quorum) and imaged using SEM (Quanta FEG250 ESEM) with EHT of 5 kV ($n = 3$).

Contact Angle Measurements

To measure the wettability and identify if membranes were hydrophilic or hydrophobic, WCA measurements were carried out. Electrospun membranes were cut into 3 cm × 1 cm rectangles. Samples were either untreated, UV treated (1 h), placed in ethanol, or placed in cell culture medium and left to dry before being measured for changes in wettability using sessile-drop goniometry on the DSA 100 (Kruss-Scientific) ($n = 6$). Briefly, a 5 μL water drop is recorded being released from a needle tip onto the membrane. A still is then taken from this video and the contact angle determined using the tangent method. Generally, a WCA smaller than 90° is considered hydrophilic and a WCA bigger than 90° is considered hydrophobic.

Tensile Testing

Mechanical properties of the electrospun membranes were determined using tensile testing. Quantitative tensile testing of the electrospun membrane was undertaken using UniVert tensile tester (CellScale) equipped with a 10 N load cell at a displacement rate of 12 mm/min. The membranes were cut into dog-bone shaped strips 2 cm in length by 0.5 cm in width and tested until failure or until the tensile tester had reached maximum distance ($n = 16$). Membrane thickness was measured using a digital micrometer (HITEC, 190-00, Farnell). For wet samples ($n = 7$), samples were soaked in dH_2O before mounting into the tensile tester.

FTIR

Fourier-transform infrared spectroscopy measurements were undertaken to determine changes in surface chemistry following membrane surface treatment. Electrospun membranes were cut into 3 cm × 1 cm rectangles. Samples were either untreated, UV treated (1 h), placed in ethanol, or placed in cell culture medium and left to dry before being measured using Vertex 70 Fourier Transform Infrared Spectrometer (Vertex) ($n = 6$).

Cell Culture

Electrospun membrane was cut into 1.5 cm^2 squares and placed in Scaffdex (Merck). ARPE-19 cells (ATCC-LGC, CRL-2302 passage 28–30) were seeded at a density of 50,000 cells/sample and incubated at 37°C, 5% CO_2, 98–99 % humidity and grown for 1 month or 3 months. Media consisted of DMEM:F12 (Merck) containing 10 % FCS (Thermofisher Scientific), 2.5 mg/L amphotericin B (Merck) and penicillin-streptomycin (Merck). Media was changed every 3 days. Controls were glass coverslips (Agar).

For long-term culture, the membrane was fabricated as aforementioned and then mounted onto a grounded water bath as described. Nanoparticles were sprayed onto the membrane using the described parameters followed by cutting and mounting into Scaffdex with the nanoparticle decorated side orientated to be the basal side. Cells were seeded onto the apical side and cultured as mentioned above.

Histology

We used histology to determine whether the cells had invaded across the thickness of the membrane. It is important the cells do not invade the entire membrane and culture only on the surface of the membrane. Cell cultured membranes were fixed in 10 % NBF for 15 min and processed for histological staining with Leica TP1020. Following processing, tissues were embedded for sectioning in paraffin wax and stained with Haemotoxylin and Eosin (H&E) using standard protocol, images were taken with Olympus BX60 microscope, 20x objective, no post-processing ($n = 4$).

Preparation of Cells for SEM

Scanning electron microscopy was used to visualise membrane coverage and cell morphology following cell culture. Cells were fixed in 1.5% Glutaraldehyde (Fluka) for 30 min at 4°C and dehydrated with graded ethanol; 2 × 3 min 50%, 2 × 3 min 70%, 2 × 3 min at 90%, 2 × 5 min at 100%. Hexamethyldisilane (HMDS, Merck) was added for 2 × 5 min and left overnight to evaporate. Samples were mounted on a carbon tab on an aluminium stub, gold sputter coated (Quorum) and imaged using SEM (Quanta FEG250 ESEM) with EHT of 5 kV ($n = 3$).

Immunofluorescence Staining

To visualise the presence of RPE characteristic proteins in the ARPE-19 cells cultured on electrospun membranes, we carried out immunofluorescence studies. Cell cultured membranes were harvested after 1 or 3 months of culture, washed with DPBS and fixed in 10% NBF for 15 min. Cells were permeabilised with 1% Triton-X for 10 min, blocked with 10% goat serum for 30 min and incubated with primary antibodies (**Table 1**) overnight at 4°C. The following day, cells were incubated with the appropriate secondary antibody for 1 h, followed by DAPI staining, and membrane placed on glass slides and mounted to coverslips with Vectorshield (Vectorlabs). Slides were viewed using the Zeiss

TABLE 1 | Primary antibody stains and the companies from where they were bought with corresponding catalogue numbers.

Primary antibody	Company (catalogue number)
Anti-Bestrophin/BEST1 antibody	Abcam (ab14927)
Anti-RPE65 antibody	Abcam (ab13826)
Anti-LRAT antibody	Abcam (ab166784)
Anti-PEDF antibody	Abcam (ab180711)
Anti-CRABP1 antibody	Abcam (ab235838)
Anti-MERTK antibody	Abcam (ab110108)
Anti-LAMP2 antibody [H4B4]	Abcam (ab25631)
Anti-USO1 antibody	Abcam (ab102470)
Anti-GULP antibody	Abcam (ab236893)
ZO-1	Thermofisher Scientific (61-7300)
Alexa Fluor 488 Phalloidin	Thermofisher Scientific (A12379)

ImagerM1 microscope, numerical aperture of x10 objective 0.2, Nikon camera, no post-processing ($n = 3$).

Resazurin Assay

To assess metabolism of cells cultured on the surface of the membranes, we used a resazurin cell metabolism assay. In this assay, resazurin (an oxidised non-fluorescent blue colored compound) is reduced by metabolically active cells to resorufin (a fluorescent pink product), which is detected via fluorescence measurement. Resazurin solution (5 mg resazurin salt in 40 mL DPBS) (PAA laboratories), was added to each sample (100 µl/ml) and returned to the incubator for 4 h. A 100 µl aliquot of media was taken from each sample and transferred into a black bottomed 96-well plate. Fluorescence was measured at 530–510 nm excitation and 590 nm emission using a fluorescence reader (FLUOstar OPTIMA, BMG LABTECH) ($n = 4$).

Barrier Assay

To assess the ability of the membrane to act as a barrier, we set up a barrier assay using FITC as the detectable dye to traverse the membrane on both a cellular and cell cultured membranes (Yeste et al., 2018). Scaffdex mounted membranes, with or without cells, were placed in 12 well plates with DPBS on the basal side of the membranes. On the apical side of the membranes, 1 mM FITC (Merck) in DPBS was added. Every 10 min, 100 µl of DPBS was taken from the basal side of the membranes and measured using the fluorescence reader (FLUOstar OPTIMA, BMG LABTECH) ($n = 4$).

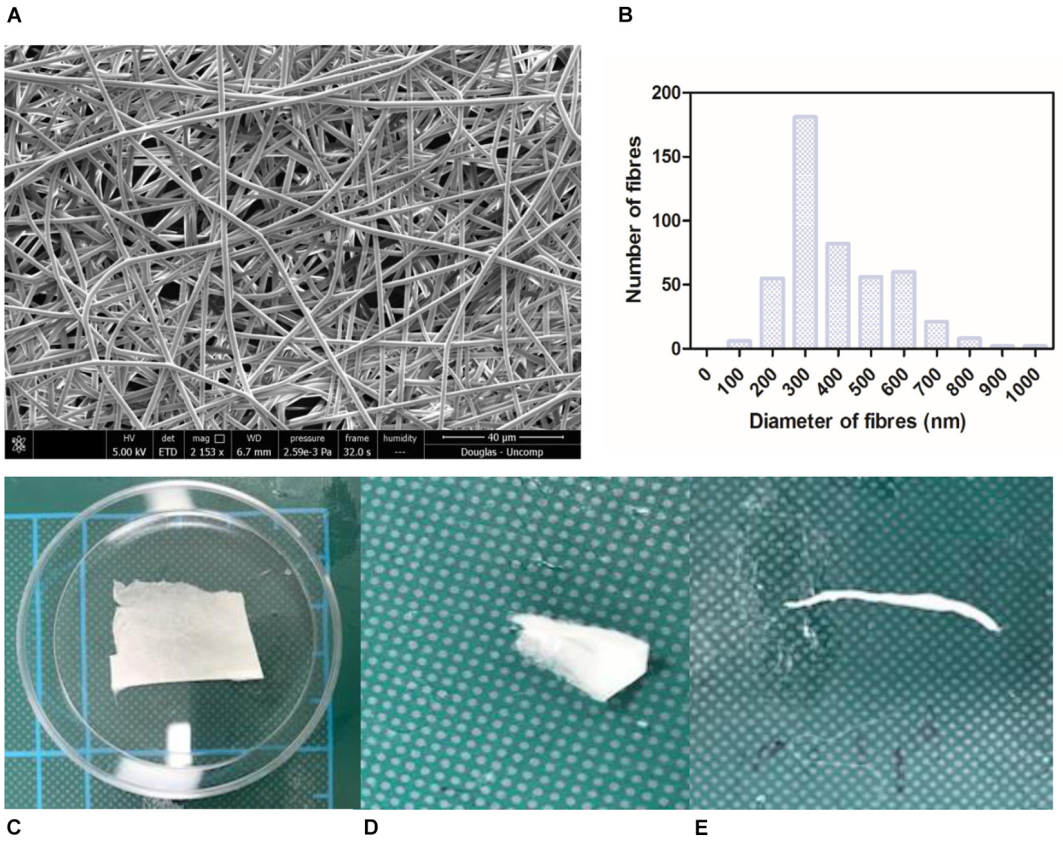

FIGURE 1 | SEM micrograph of 17.5 % PET electrospun membrane exhibiting ultrastructure of randomly orientated fibres **(A)** and corresponding histogram showing distribution of fibre diameter size; average diameter of 387 nm (+/−6.9) **(B)**. Photographs of material folded **(C)**, rolled **(D)**, twisted **(E)** without breaking denote good handleability of the material ($n = 3$). Scale shown = 5 cm.

Live/Dead Assay

Live/dead assays were undertaken to visualise the viability of cells grown on the membranes following culture with and without nanoparticles to assess the effect the presence of degrading nanoparticles had on the cells. Cell cultured membranes were washed in DPBS and following manufacturer's instructions (molecular probes) incubated with calcein AM and ethidium homodimer-1 for 30 min. The material was placed on glass slides and mounted to coverslips with Vectorshield (Vectorlabs). Slides were viewed using the Zeiss ImagerM1 microscope, x4 objective, Nikon camera, no post-processing ($n = 3$).

pH Measurements

Three pH measurements were taken from each well using a digital pH meter to assess if broad changes in pH due to nanoparticle degradation over time occurred that could affect cell viability (Mettler-Toledo) ($n = 6$).

Measurement of FITC Dye Release

Release of encapsulated FITC dye from the nanoparticles with time was assessed to determine how long the encapsulated moieties could be sustainably released. Following electrospraying, 10 ml of collected nanoparticles in 0.1% (v/v) isopropanol was kept at 37°C. An aliquot (1 ml) of solution was then collected at each time point and kept at −20°C until the final time point. For collection from cell cultures 1 ml of media was collected at each time point and media changed. A 100 μl aliquot was taken from each sample and transferred into a black bottomed 96-well plate. Fluorescence was measured at 530–510 nm excitation and 590 nm emission using a fluorescence reader (FLUOstar OPTIMA, BMG LABTECH) ($n = 4$).

Statistical Analysis

Data are presented as mean (+/− standard error) with n values noted within the text. Analysis was undertaken using GraphPad Prism software using t-tests or one-way ANOVA followed by the appropriate post-test noted within the text. Significance was $p < 0.05$.

RESULTS AND DISCUSSION

Characterisation of Electrospun PET: Morphology, FTIR, Hydrophilicity, Mechanical Properties, Barrier Assay, and Cell Culture

Scaffolds were characterized for adequate mechanical properties to undergo surgical handling and the ultrastructure was

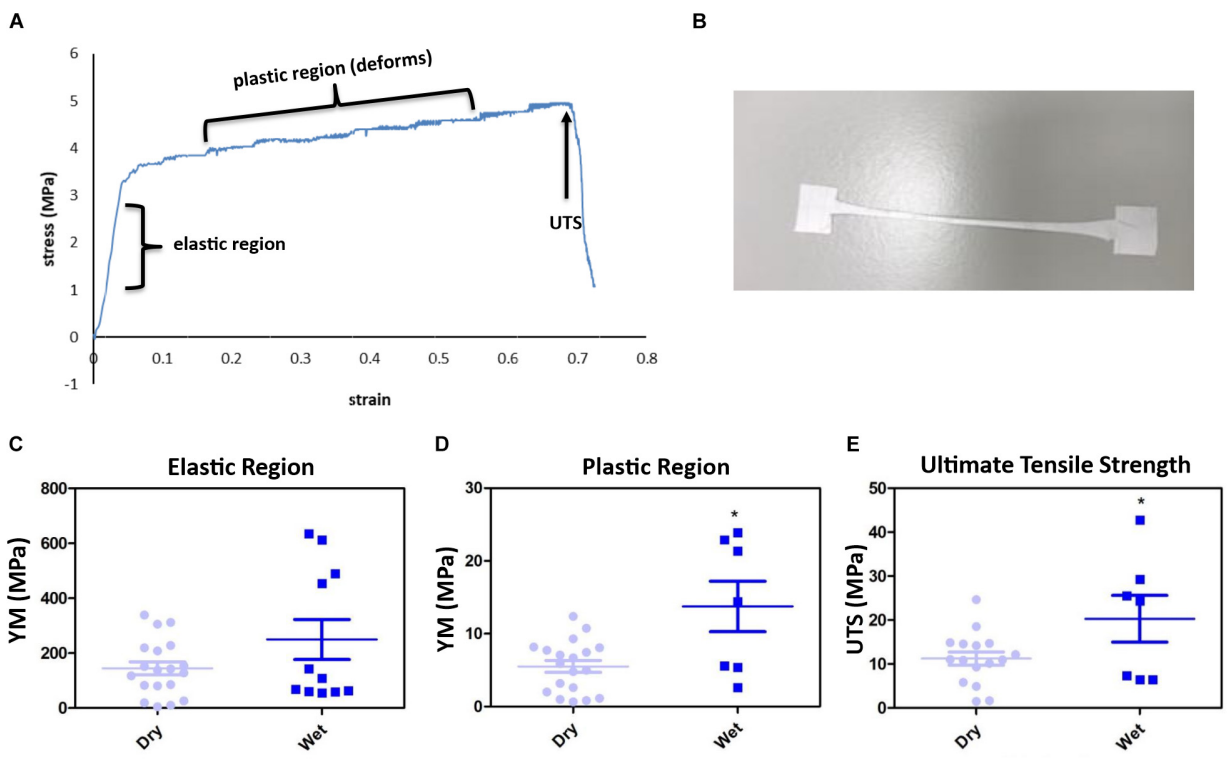

FIGURE 2 | The membranes gave an interesting stress vs. strain plot, as shown by the representative profile **(A)** and stretched to deformation **(B)**. Young's modulus (YM) for the elastic region (retains form) are high, with no significant difference between the dry [145.2 MPa (+/−23.46)] and wet (250.2 MPa (+/−73.08) membranes **(C)**, whereas the plastic region (deformation) YM significantly increased from 5.15 MPa (+/−0.82) (dry) to 13.75 MPa (+/−3.47) (wet) **(D)**, and the ultimate tensile strength (UTS) of the membrane significantly increased from 11.23 MPa (+/−1.5) (dry) to 20.29 MPa (+/−5.3) (wet) **(E)**. Significant difference $^*p < 0.05$ compared with dry material, t-test ($n = 16$ for dry, $n = 7$ for wet). Data presented: mean (+/− standard error).

characterized to match fibre morphology to mimic the native BM (Yamamoto and Yamashita, 1989; Del Priore et al., 2006). Surface chemistry was analyzed for presence of functional groups following surface treatment and hydrophilic properties measured using WCA. Barrier properties were analyzed with and without a monolayer of cells to ascertain any changes with cell culture.

Nanofibrous non-degradable PET fibres were produced in a collectable membrane form. SEM micrographs showed the

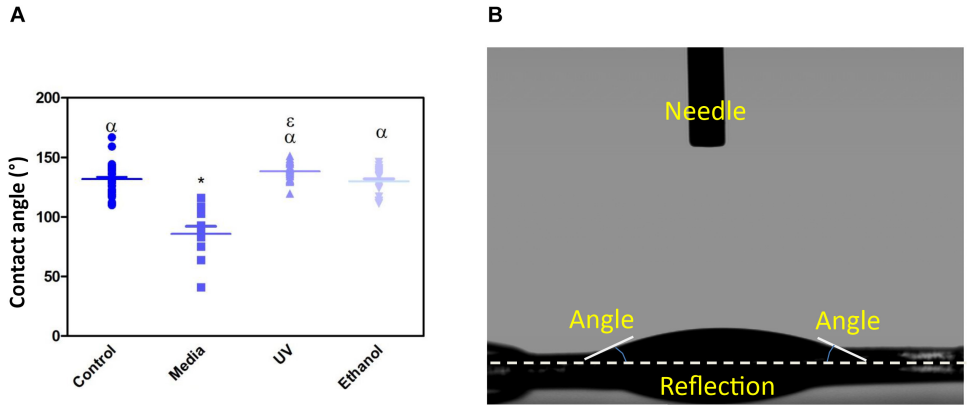

FIGURE 3 | (A) Shows a dot-plot exhibiting the WCA of PET untreated control, cell culture media treated, UV treated and ethanol treated membranes. Media treated membrane exhibited a significantly different decrease in WCA (85.8 ° +/−20) compared to control and all other treatments. One-way ANOVA followed by Tukey's *post hoc* test ($n = 6$). *$p < 0.05$ significantly different to untreated control, $\alpha = p < 0.05$ significantly different to cell culture media treated, $\varepsilon = p < 0.05$ significantly different to ethanol treated. Data presented: mean (+/− standard error). **(B)** shows the image taken of a water drop on top of the membrane, the flat droplet morphology shows the membrane is hydrophilic (note the white dashed line is the contact surface).

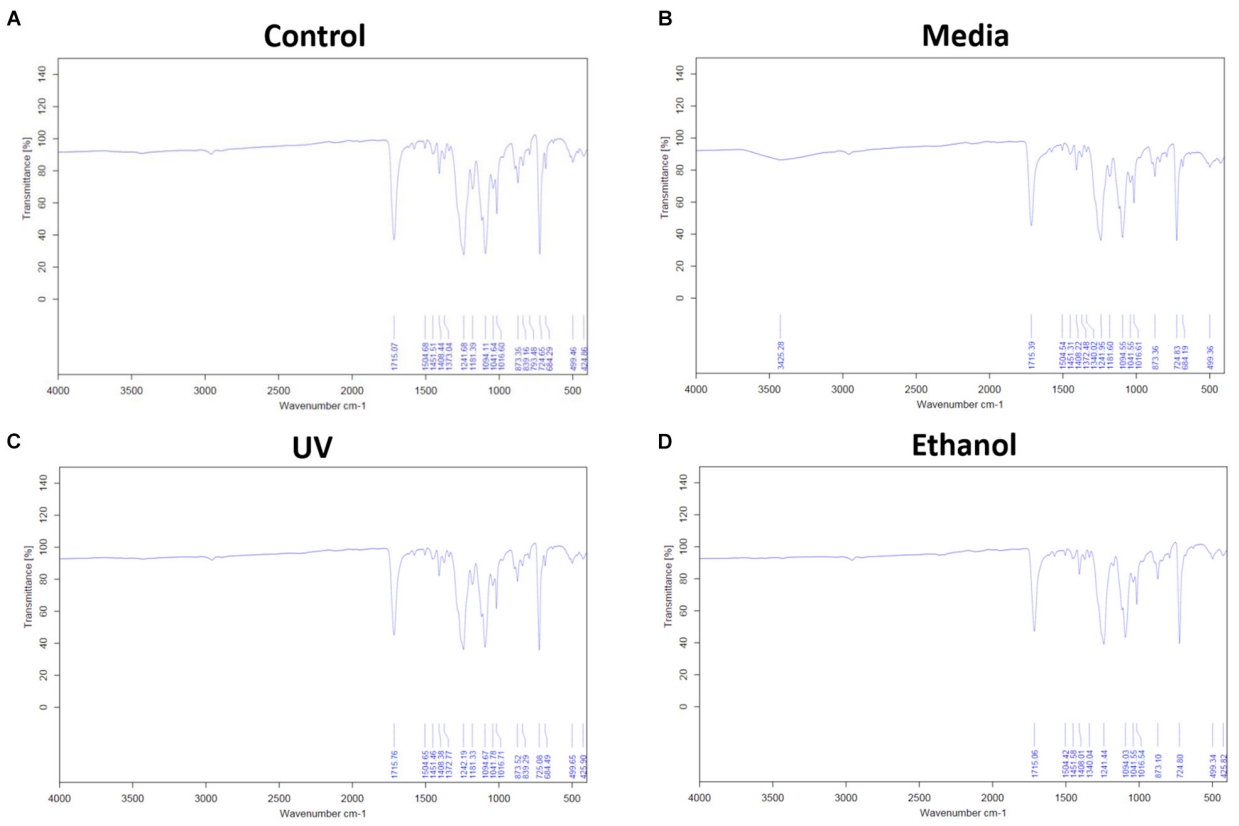

FIGURE 4 | (A) Shows the FTIR spectra of electrospun membrane untreated control, **(B)** shows the FTIR spectra of tissue culture media treated membrane, **(C)** shows the FTIR of ethanol treated membrane, and **(D)** shows the FTIR of the UV treated membrane. All spectra exhibit the characteristic PET carbonyl peak at ~1700 cm^{-1} with the media treated membrane exhibiting a peak at ~3400 cm^{-1} suggesting evidence of protein interaction ($n = 6$).

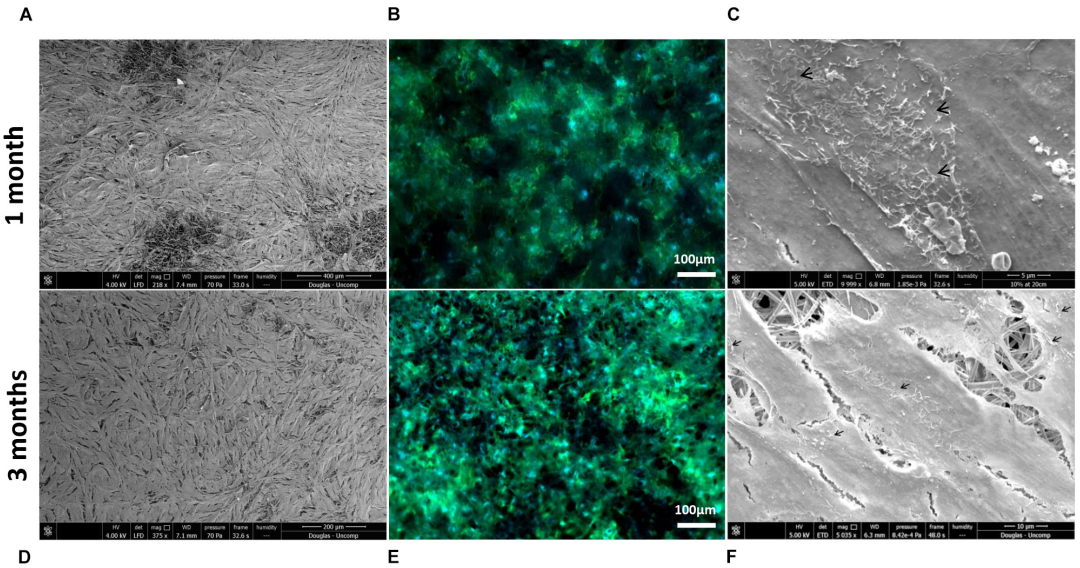

FIGURE 5 | Representative SEM micrographs and corresponding fluorescence images of DAPI/phalloidin stained ARPE-19 cells cultured on PET membranes for 1 month **(A–C)** and 3 months **(D–F)**. Cells populate the membrane with better coverage and more apparent phalloidin staining at 3 months culture. Microvilli (arrows) phenotypical of RPE cells are apparent by 1 month (n = 3).

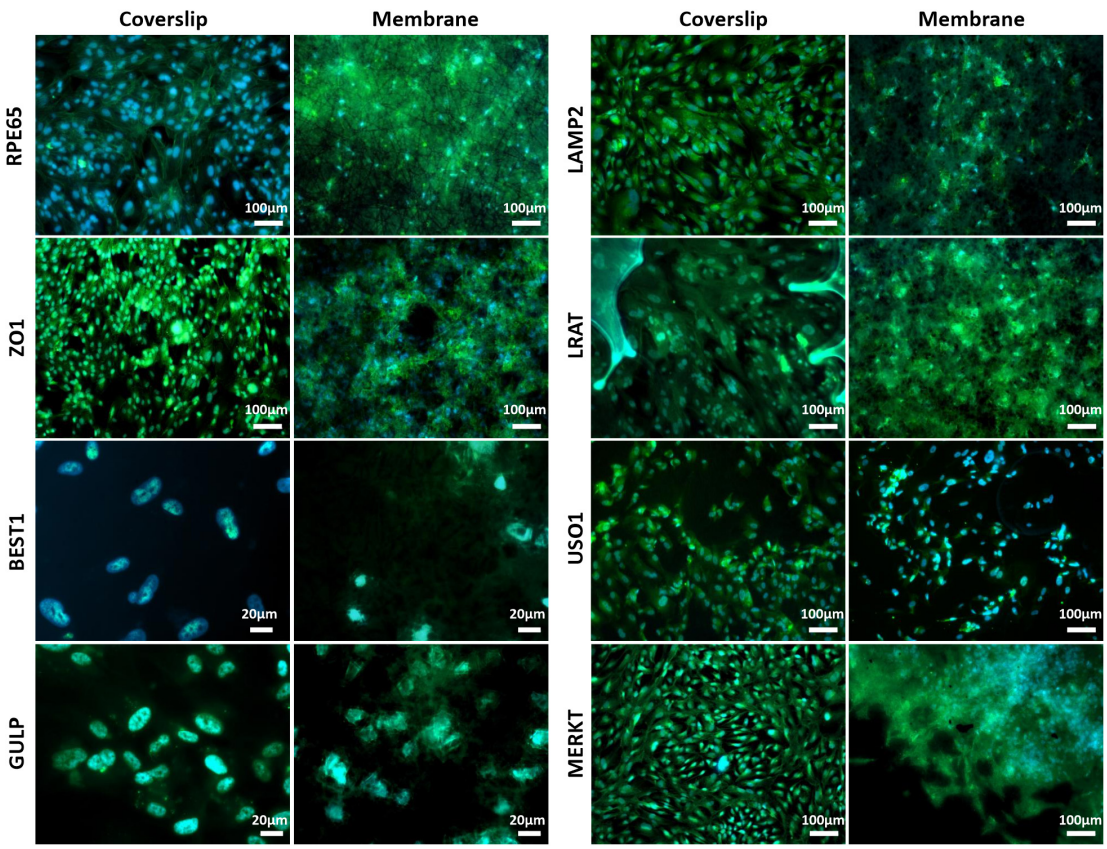

FIGURE 6 | Representative immunofluorescent images show RPE cells cultured on the electrospun membrane for 1 month stained positively for RPE cell marker proteins and RPE function proteins (green). Cells cultured on the membranes were difficult to image clearly due to the auto-fluorescent nature of the PET fibres. Upon comparison with the positive glass coverslip control, similar staining patterns are apparent, especially noticeable with BEST1, GULP and USO1. DAPI = blue nuclear stain (n = 3).

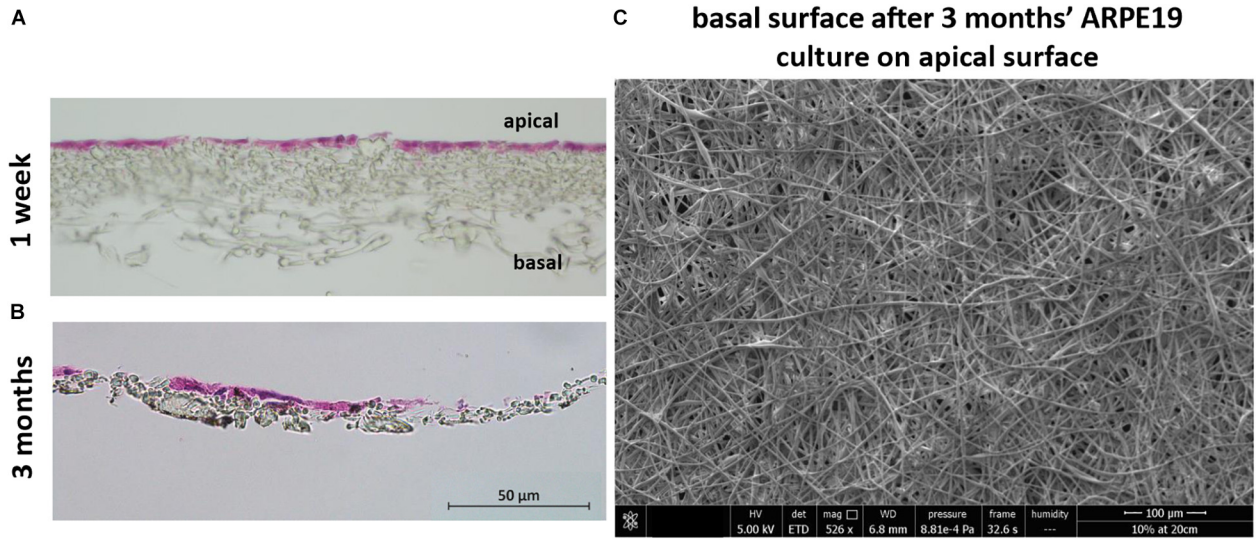

FIGURE 7 | The membrane does not allow invasion of cells through its architecture. H&E staining of cells cultured on the membrane for 1 week **(A)** up to 3 months **(B)** show the desired lack of cell invasion. The SEM micrograph **(C)** exhibits a lack of cells on the basal side of the membrane that had been seeded with ARPE-19 cells on its apical side and cultured for 3 months (n = 4).

membranes exhibited a randomly orientated fibrous mesh (**Figure 1A**); an open network of interconnected voids with average fibre diameter of 387 nm (+/−147.8) (**Figure 1B**). The membrane was able to undergo folding, rolling, and twisting without being destroyed; depicting the ease with which it could be handled and exhibiting adequate mechanical properties (**Figures 1C–E**). The handling properties were in agreement with previously published work, even though the concentration of the polymer solution used was lower than previous work (Haneef and Downes, 2015). Morphologically this electrospun membrane mimics native BM (Yamamoto and Yamashita, 1989) and electrospun PET has previously been reported to exhibit tolerance to subretinal insertion with a lack of inflammatory response (Liu et al., 2014).

The membrane gave an interesting stress vs. strain profile following tensile testing; exhibiting an elastic region (original form is retained following release of load) and a plastic region (membrane deforms indefinitely) before attaining failure exhibiting the UTS (**Figures 2A,B**). 16% of membranes tested did not break (**Supplementary Figure S2**). Soaking the membranes in dH_2O did not significantly change the YM of the elastic region (**Figure 2C**), however, the YM of the plastic region significantly increased from 5.5 MPa (+/−0.8) to 13.8 MPa (+/−3.5) and the UTS significantly increased from an average of 11.23 MPa (+/−1.5) to 20.29 MPa (+/−5.3) (**Figures 2D,E**). Wetting the membrane introduced hydrogen bonding between the fibres thereby increasing the YM of the plastic region and the UTS, while in the dry form the fibres did not have the water to provide the added interactions (Chen et al., 2018; Kurokawa et al., 2018).

Treatment of the membrane with cell culture media significantly increased hydrophilicity compared to all other treatment methods, whereas ethanol treatment resulted in an increase in the hydrophilicity compared only to UV treatment. WCA of control membranes averaged at 132.6° which decreased to 85.8° and 118.4° following treatment with media and ethanol, respectively (**Figures 3A,B** and **Supplementary Table S1**). FTIR spectra exhibit the characteristic carbonyl peak in PET membrane typical of the ester bond group within the polymer structure, denoted by the strong peak at ∼1700 cm^{-1} for C = O. No changes were detected for any of the membranes except the cell culture media treated membrane. A peak at ∼3400 cm^{-1} denoting the presence of O-H group was detected, suggesting that the

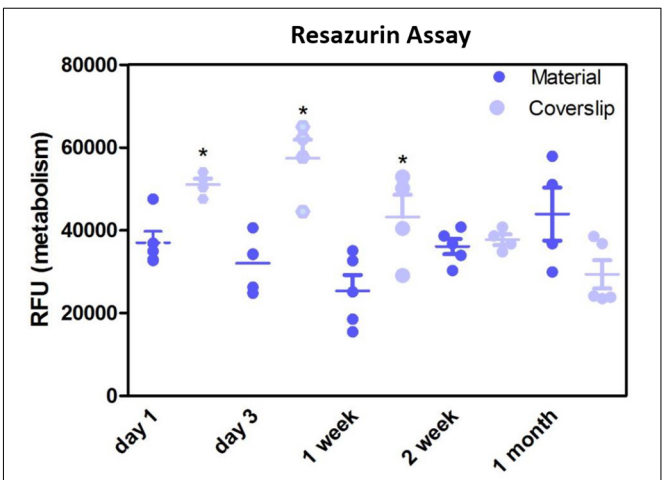

FIGURE 8 | Resazurin assay showed metabolism of cells cultured on the membranes was significantly lower in the initial 1 week of culture compared to glass coverslip controls. There was no significant difference in the metabolism of the cells thereafter up to 1 month. Significant difference *$p < 0.05$, one-way ANOVA followed by Bonferroni post-test (n = 4). Data presented: mean (+/− standard error).

surface of the membrane underwent a degree of functional group opening to form -COOH free groups that could be attributed to protein interaction or hydrolysis of the surface of the polymer (**Figures 4A–D**; Haneef and Downes, 2015; Kawai et al., 2019).

Scanning electron microscopy and phalloidin staining showed cells were able to form a monolayer when cultured on the membrane up to 3 months, with microvilli that are phenotypical of RPE cells (Thomson et al., 2011) presenting after 1-month's culture (**Figures 5A–F**). Although the auto-fluorescence of the membrane fibres made it challenging to see clearly, cells plated on the membrane stained positively for the characteristic proteins of RPE cells (Liao et al., 2010; Brandl et al., 2014) in comparison with

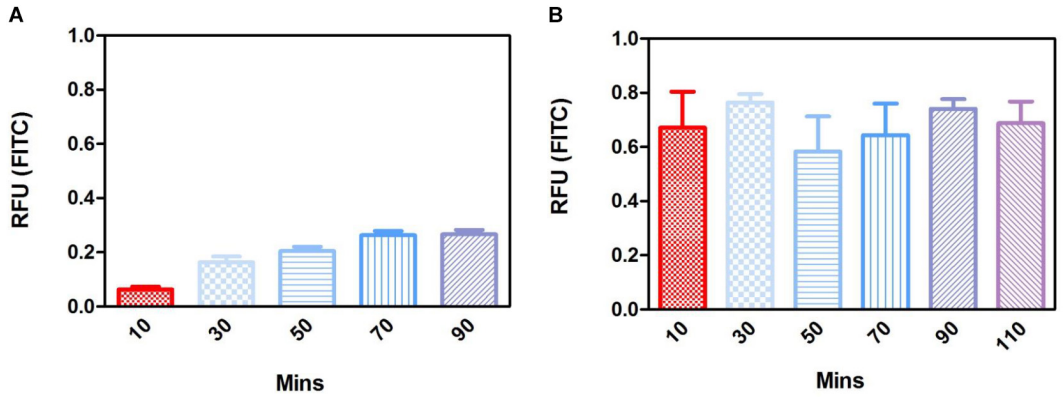

FIGURE 9 | Fluorescence barrier assays in the acellular substrate showed passive diffusion that plateaued FITC concentration across the membrane by 70 min **(A)**, whereas fluorescence in the 1-month cell cultured membrane plateaued in the first 10 min of measurement suggesting the active transport of FITC by the monolayer of cells **(B)** (n = 4). Data presented: mean (+/− standard error).

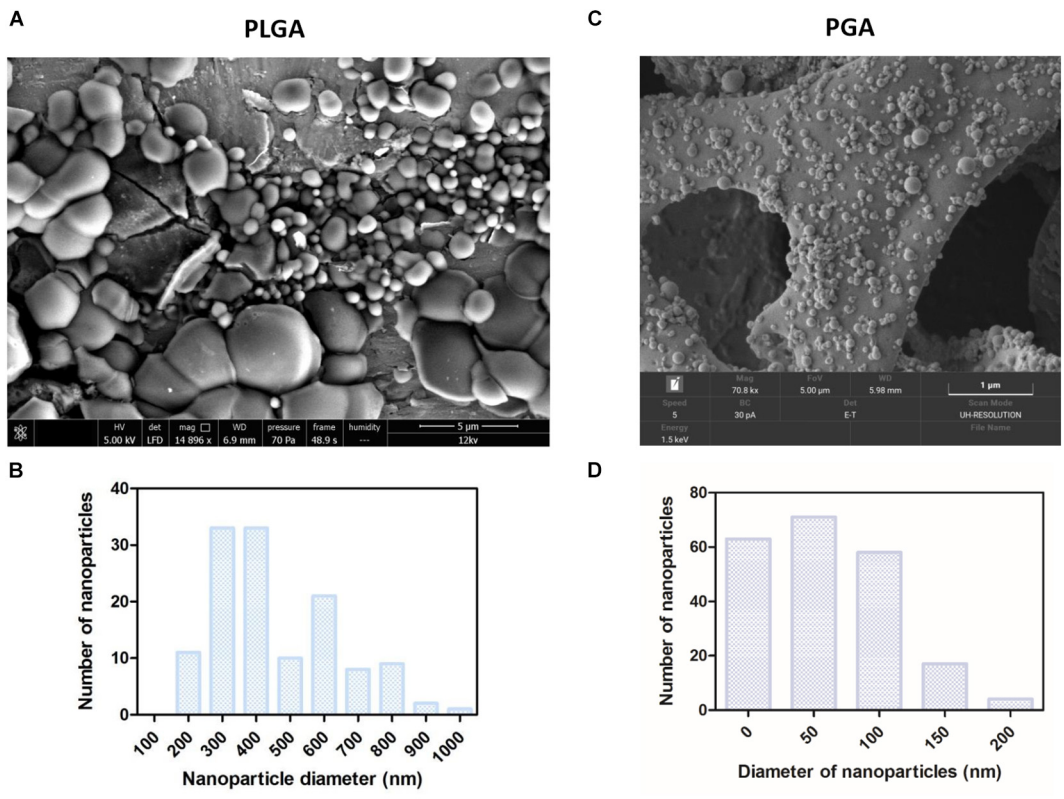

FIGURE 10 | SEM micrographs show PLGA nanoparticles **(A,B)** were larger than PGA nanoparticles **(C,D)** Corresponding histograms showed PLGA averaged at 480 nm (+/−252) with a broader range of particle sizes, whereas PGA averaged at 59 nm (+/−49) and exhibited less variation in particle size (n = 3). Data presented: mean (+/− standard error).

positive controls (**Figure 6**). This is particularly noticeable with BEST1 (bestrophin-1), a Ca^{2+}-activated Cl^{-} channel (CaCC) specifically expressed in the RPE of the eye (Kittredge et al., 2018), USO1 (General vesicular transport factor p115) and GULP (PTB domain-containing engulfment adaptor protein 1), an adaptor protein involved in phagocytosis (Park et al., 2008), an important function of RPE with involvement in the phagocytosis of photoreceptor outer segments (Sparrow et al., 2010).

H&E stained sections showed the lack of cell invasion in the bulk structure of the membrane, which was the desired characteristic at both 1 week and 3 months' culture (although some material loss was seen due to the histological processing method in month 3) (**Figures 7A,B**). This was further confirmed with SEM imaging showing the absence of any cells on the basal side of the membrane following cell culture on the apical side (**Figure 7C**).

Resazurin assays showed the metabolism of the cells cultured on the membrane was significantly lower compared to positive control in the initial first week of culture, thereafter, the metabolism was not significantly different to the positive control (**Figure 8**). This may have been due to cells not adhering as quickly due to the porosity of the membrane, as this difference in metabolism was overcome by 2 weeks. These data are in contrast to previous studies by our group that have shown RPE cells had increased metabolism when plated on an electrospun PET membrane (Haneef and Downes, 2015), however, the membrane formed in the previous study was electrospun for 1 h and had thinner fibres, giving the membrane a different morphology. Current results, as well as previously published work demonstrating adequate TEER measurements (Haneef and Downes, 2015) show that ARPE-19 cells were able to form a monolayer, express proteins and exhibit microvilli phenotypical to the RPE cells, after long-term culture on the current electrospun membrane.

To determine the permeability of the membrane a barrier assay was carried out on acellular membranes and on membranes cultured with ARPE-19 cells for 1 month, as this was when a monolayer had formed. The barrier assay on acellular membranes

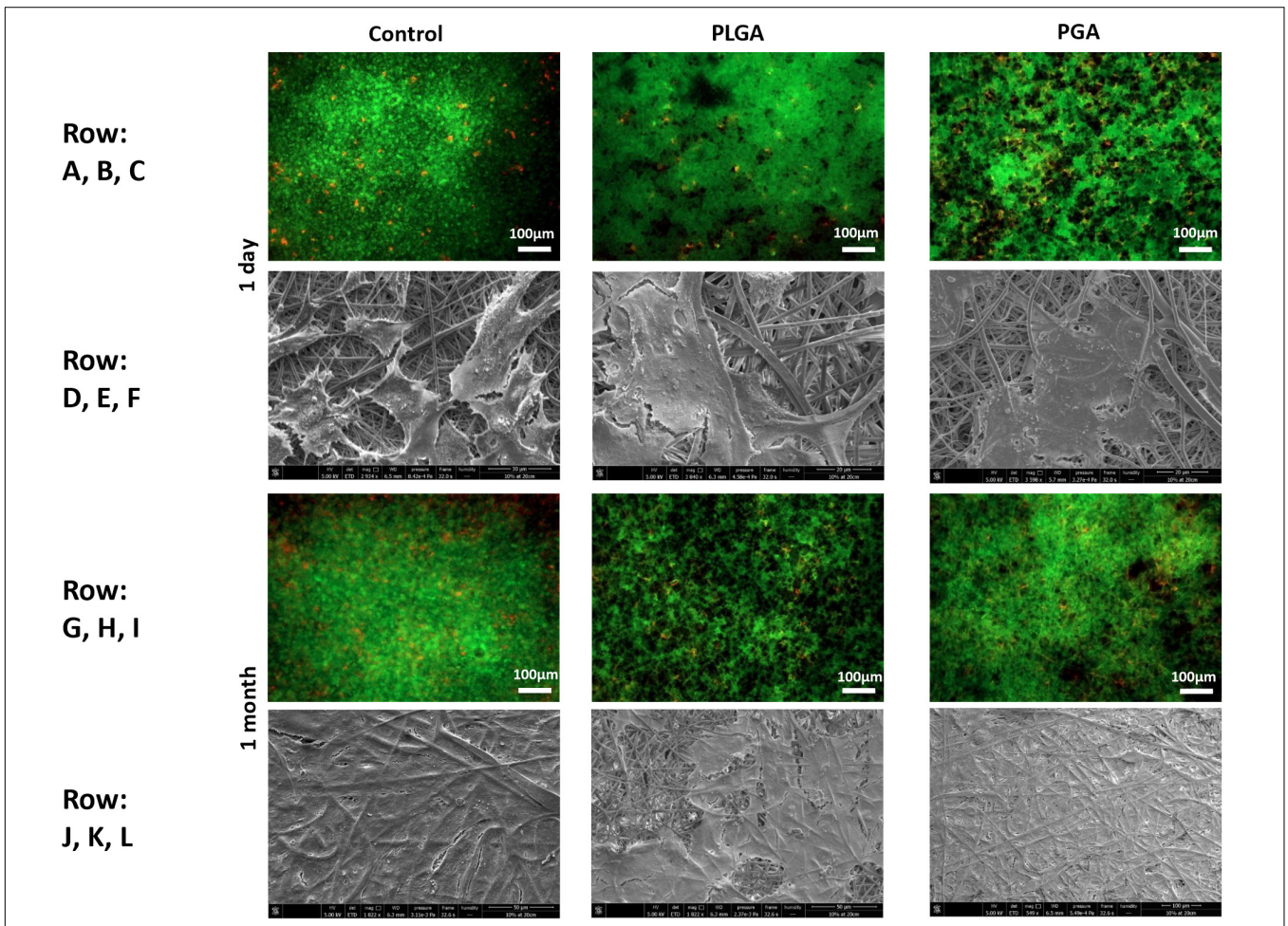

FIGURE 11 | Representative images of live/dead staining (green/red) and corresponding SEM micrographs of ARPE-19 cells after 1 day's culture **(A–F)**, 1 month's culture **(G–L)** on membrane only control, or with either PLGA or PGA nanoparticles decorated on the basal side of the membrane. Live/dead images show there is little difference between the three conditions with few dead cells present up to 1 month's culture. SEM micrographs show the progression in cells covering the membrane's apical surface (n = 3).

showed FITC was able to passively diffuse through the membrane in a time dependent manner, taking 80 min for maximum signal to be detected (**Figure 9A**). Cell cultured membranes showed the transport of FITC had increased with fluorescence plateauing within the first 10 min of culture, suggesting the monolayer of cells may be actively transporting the FITC across the membrane and functioning correctly (**Figure 9B**). These data showed that cells plated on the material did not affect the permeability of the membrane and shows it has the appropriate properties to act as an artificial BM.

Future experiments to confirm the ability of the RPE cells to perform phagocytosis when seeded on the PET membrane are needed. The presence of the phagocytosis marker MERKT in the ARPE-19 cells cultured on the PET membrane (**Figure 6**) suggested the cells had phagocytic potential. Furthermore, a study by da Cruz et al. (2018) have shown the ability of human embryonic RPE cells plated onto a PET membrane to phagocytose both *in vitro* and following surgical implantation.

Nanoparticles

Spherical nanoparticles were successfully fabricated with average nanoparticle diameters at 480 nm (+/−252) for PLGA and 59 nm (+/−49) for PGA (**Figures 10A–D**). Interestingly less variation in particle size was seen in PGA particles.

The nanoparticles did not affect ARPE-19 cell viability or morphology when compared with the membrane only control (**Figure 11**); cells attached 24 h following seeding and formed a monolayer by 1 month in the presence of nanoparticles. Resazurin assays showed the presence of nanoparticles induced a significant increase in cell metabolism compared to the membrane only control up to 2 weeks, which resolved thereafter up to 1 in month in culture (**Figure 12**). The increase in metabolism may be attributed to the change in pH as the nanoparticles degrade with time; it was found that the pH of the culture media decreased after 1 week for both PLGA and PGA nanoparticles (**Figure 13** and **Supplementary Table S2**). PLGA nanoparticles significantly decreased the pH up to 1 week's degradation compared to membrane only control. The metabolites of PLGA degradation are lactic acid and glycolic acid, which contribute to lowering the pH of the surrounding environment. It could also be attributed to the larger variation in particle size which could be contributing to the significant change in pH compared to PGA.

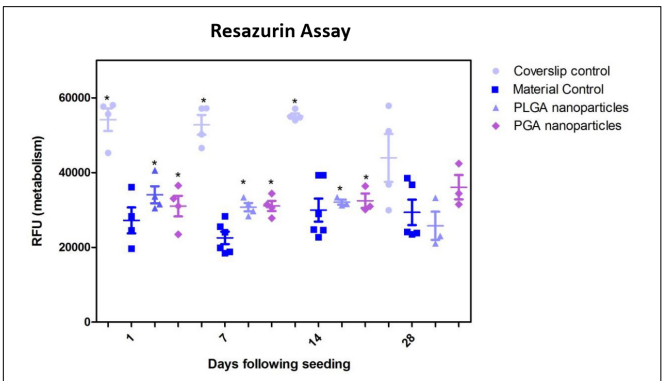

FIGURE 12 | Resazurin assay of ARPE-19 cells plated on membranes with PLGA or PGA nanoparticles decorated on the basal side showed significantly higher metabolism compared to membrane only controls for the first 14 days of culture. There was no significant difference in metabolism of the cells thereafter up to 1 month or compared with coverslip control. Significant difference $*p < 0.05$ compared with membrane control, one-way ANOVA followed by Bonferroni post-test ($n = 4$). Data presented: mean (+/− standard error).

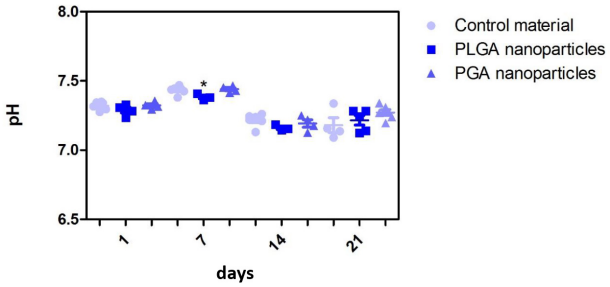

FIGURE 13 | Effect of degrading nanoparticles on pH of ARPE-19 culture media exhibited little change, with PLGA exhibiting a significant decrease compared to membrane only control in week 1, which resolved thereafter. Significant difference $*p < 0.05$ compared to PET membrane only control, one-way ANOVA followed by Bonferroni post-test ($n = 3$). Significant difference $*p < 0.05$ compared to PET membrane only control, one-way ANOVA followed by Bonferroni post-test ($n = 6$). Data presented: mean (+/− standard error).

Although a difference in metabolism of cells and pH of their surrounding environment was observed when cultured with nanoparticles; morphology and protein expression results suggest that the cells were not adversely affected by the membrane/nanoparticle composite.

Nanoparticle Degradation and FITC Release Profile

Short term degradation studies show that over 72 h, both PLGA and PGA nanoparticles degraded releasing FITC into solution (0.1 % isopropanol in dH_2O). PLGA nanoparticles exhibited a continuous release profile up to 72 h (**Figure 14A**) compared to the PGA nanoparticles, which exhibited sudden burst release of the dye after 3 h, which plateaued after 24 h (**Figure 14B**).

Long term (up to 28 days) degradation studies showed similar results as the short-term studies with PLGA nanoparticles continuing to sustainably release FITC into solution up to 14 days, decreasing thereafter (**Figure 14C**). PGA nanoparticles exhibited maximum release after 1 day, but exhibited considerable decrease in FITC release by day 7 onward (**Figure 14D**). This can be attributed to the faster degradation rate of PGA compared to PLGA and also to the higher surface area:volume ratio of significantly smaller nanoparticles of PGA, which would allow faster release of the dye, due to shorter diffusion pathway and faster degradation (Sharma et al., 2016). Observation of the resultant solution after 28 days degradation would suggest PLGA nanoparticles had released more FITC compared to PGA nanoparticles (**Supplementary Figure S3**), however, this could also be attributed to more

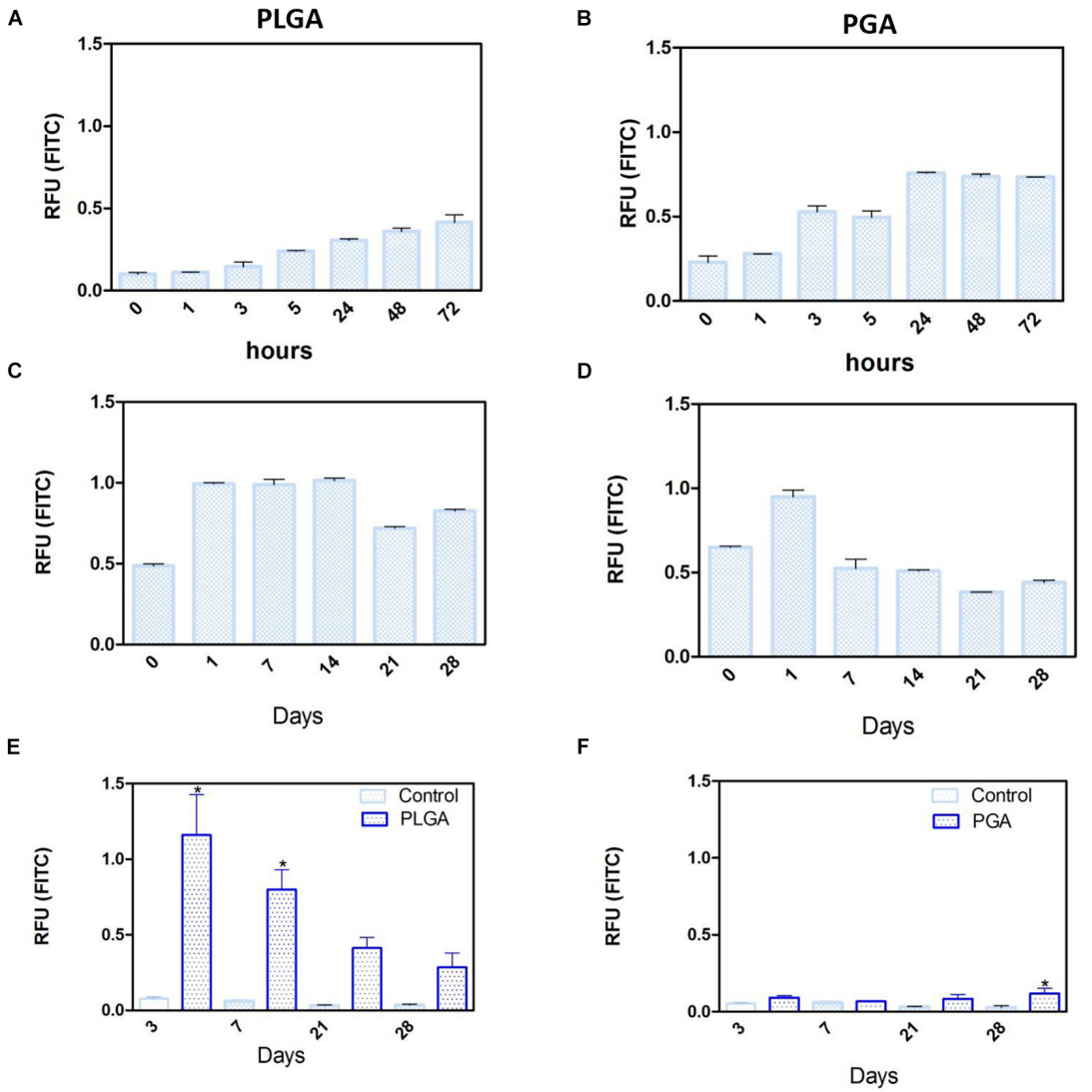

FIGURE 14 | Release of FITC from PLGA and PGA nanoparticles into a solution of 0.1% isopropanol over a short period of time **(A,B)**, long period of time **(C,D)** and the release of FITC into cell culture media **(E,F)** from nanoparticles electrosprayed onto the basal side of PET membrane. Significant difference $^*p < 0.05$ compared to PET membrane only control, one-way ANOVA followed by Bonferroni post-test ($n = 4$). Data presented: mean (+/− standard error).

FITC encapsulated. Encapsulation efficiency may explain these differences, particularly given the size difference and inter-variance in size of the produced nanoparticles; however, this was beyond the scope of this study.

Degradation studies on cell cultured PET membranes decorated with FITC encapsulated nanoparticles on the basal surface, showed PLGA nanoparticles exhibited release of FITC over 28 days. The majority of the dye release was observed up to 7 days for PLGA nanoparticles with fluorescence decreasing thereafter; however, PGA nanoparticles exhibited no significant change until after 28 days, with very little detected fluorescence in comparison to PLGA (**Figures 14E,F**) and upon comparison to degradation in isopropanol solution (**Figure 14B**). This would suggest that nanoparticle degradation in cell culture media rather than in isopropanol solution offers the nanoparticles a degree of protection from degradation. The effects of the ions, proteins, lipids and other components of the culture medium may confer a degree of stability to the nanoparticles (Moore et al., 2015) and is an important factor to consider in final implant design.

CONCLUSION

In this article we have described the development of a proof-of-concept composite bioactive membrane that has adequate mechanical properties, permeability and cytocompatibility. The membrane was able to maintain a monolayer of ARPE-19 cells that exhibited phenotypic microvilli structures on its apical surface while providing a sustained release of encapsulated moieties from the membrane's basal surface.

This composite bioactive membrane exhibits the potential to act as an artificial BM and a potential treatment for atrophic AMD as a novel bioactive cell transplant substrate; to the authors' knowledge the first of its kind to be developed as a potential treatment for atrophic AMD. There are still many aspects to optimize and analyse, hence, we are now focusing on the optimization and formation of co-axially electrosprayed nanoparticles to encapsulate biologically active moieties to target drusen, and have already achieved the coaxial encapsulation of FITC with Nile red as the outer shell via electrospraying (**Supplementary Figure S4**). Since electrospraying involves the use of compounds dissolved in solvents, care must be taken when encapsulating biologically active moieties to ensure their activity is not compromised. We have begun screening solvents for this purpose using enzyme activity agar assays (**Supplementary Figure S5**). Immediate work will entail using cell systems that replicate phenotypic RPE (Pilgrim et al., 2017; Chen et al., 2020) to test this composite membrane, carrying out gene transcription and protein expression profiling on cultured primary RPE cells, as well as photoreceptor outer-segment phagocytosis assays. Further work will then move toward using moieties such as L4-F, amongst others (Vavvas et al., 2016), to target drusen.

DATA AVAILABILITY STATEMENT

The raw data supporting the conclusion of this article will be made available by the authors, without undue reservation, to any qualified researcher.

AUTHOR CONTRIBUTIONS

RM performed the acquisition and undertook the analyses of the data and contributed to the writing of the manuscript. IP and SK provided critical evaluation on the progress of the work and guided the work through clinical relevance. SK also provided feedback on the manuscript. AH prepared, wrote, and revised the manuscript, obtained the funding and is also leading the research.

FUNDING

This work was funded by the EPSRC, Grant reference number: EP/S001468/1.

ACKNOWLEDGMENTS

The authors would like to acknowledge Alison Beckett (University of Liverpool) for her help with the SEM to image the fibrous membrane and Dr. Keith Arnold (Materials Innovations Factory, Liverpool) for his help with SEM in imaging the nanoparticles.

SUPPLEMENTARY MATERIAL

The Supplementary Material for this article can be found online at: https://www.frontiersin.org/articles/10.3389/fbioe.2020.00456/full#supplementary-material

REFERENCES

Age-Related Eye Disease Study 2 Research Group (2013). Lutein + zeaxanthin and omega-3 fatty acids for age-related macular degeneration: the age-related eye disease study 2 (AREDS2) randomized clinical trial. *JAMA* 309, 2005–2015.

Brandl, C., Zimmermann, S. J., Milenkovic, V. M., Rosendahl, S. M. G., Grassmann, F., Milenkovic, A., et al. (2014). In-depth characterisation of retinal pigment epithelium (RPE) Cells derived from human induced pluripotent stem cells (hiPSC). *Neuro Mol. Med.* 16, 551–564.

Chen, L., Cheng, H.-H., Xiong, J., Zhu, Y.-T., Zhang, H.-P., Xiong, X., et al. (2018). Improved mechanical properties of Poly(butylene succinate) membrane by co-electrospinning with gelatin. *Chin. J. Polymer Sci.* 36, 1063–1069.

Chen, X., Singh, D., Adelman, R. A., and Rizzolo, L. J. (2020). Unstimulated, serum-free cultures of retinal pigment epithelium excrete large mounds of drusen-like deposits. *Curr. Eye Res.* 30, 1–5.

Curcio, C. A., and Johnson, M. (2013). "Chapter 20 - structure, function, and pathology of bruch's membrane," in *Retina Anatomy and Physiology*, 5th Edn, eds S. J. Ryan, S. R. Sadda, and D. R. Hinton (London: W.B. Saunders), 465–481.

da Cruz, L., Fynes, K., Georgiadis, O., Kerby, J., Luo, Y. H., Ahmado, A., et al. (2018). Phase 1 clinical study of an embryonic stem cell–derived retinal pigment epithelium patch in age-related macular degeneration. *Nat. Biotechnol.* 36, 328–337.

Del Priore, L. V., Tezel, T. H., and Kaplan, H. J. (2006). Maculoplasty for age-related macular degeneration: Reengineering Bruch's membrane and the human macula. *Prog. Retinal Eye Res.* 25, 539–562.

Haneef, A. S., and Downes, S. (2015). Assessing the suitability of electrospun Poly(Ethylene Terephthalate) and polystyrene as cell carrier substrates for potential subsequent implantation as a synthetic Bruch's membrane. *Intern. J. Polyme. Mater. Polymer. Biomater.* 64, 320–332.

Kawai, F., Kawabata, T., and Oda, M. (2019). Current knowledge on enzymatic PET degradation and its possible application to waste stream management and other fields. *Appl. Microbiol. Biotechnol.* 103, 4253–4268.

Kittredge, A., Ji, C., Zhang, Y., and Yang, T. (2018). Differentiation, maintenance, and analysis of human retinal pigment epithelium cells: a disease-in-a-dish model for BEST1 mutations. *J. Visual. Exp.* 138:57791.

Kurokawa, N., Kimura, S., and Hotta, A. (2018). Mechanical properties of poly(butylene succinate) composites with aligned cellulose-acetate nanofibers. *J. Appl. Polymer Sci.* 135:45429.

Liao, J.-L., Yu, J., Huang, K., Hu, J., Diemer, T., Ma, Z., et al. (2010). Molecular signature of primary retinal pigment epithelium and stem-cell-derived RPE cells. *Hum. Mol. Genet.* 19, 4229–4238.

Liu, Z., Yu, N., Holz, F. G., Yang, F., and Stanzel, B. V. (2014). Enhancement of retinal pigment epithelial culture characteristics and subretinal space tolerance of scaffolds with 200 nm fiber topography. *Biomaterials* 35, 2837–2850.

Lu, B., Zhu, D., Hinton, D., Humayun, M. S., and Tai, Y.-C. (2012). Mesh-supported submicron parylene-C membranes for culturing retinal pigment epithelial cells. *Biomed. Microdev.* 14, 659–667.

Moore, T. L., Rodriguez-Lorenzo, L., Hirsch, V., Balog, S., Urban, D., Jud, C., et al. (2015). Nanoparticle colloidal stability in cell culture media and impact on cellular interactions. *Chem. Soc. Rev.* 44, 6287–6305.

Nowak, J. Z. (2006). Age-related macular degeneration (AMD): pathogenesis and therapy. *Pharmacol. Rep.* 58, 353–363.

Park, S.-Y., Kang, K.-B., Thapa, N., Kim, S.-Y., Lee, S.-J., and Kim, I.-S. (2008). Requirement of adaptor protein GULP during Stabilin-2-mediated cell corpse engulfment. *J. Biol. Chem.* 283, 10593–10600.

Pilgrim, M. G., Lengyel, I., Lanzirotti, A., Newville, M., Fearn, S., Emri, E., et al. (2017). Subretinal pigment epithelial deposition of drusen components including hydroxyapatite in a primary cell culture model. *Invest. Ophthalmol. Vis. Sci.* 58, 708–719.

Rudolf, M., Clark, M. E., Chimento, M. F., Li, C. M., Medeiros, N. E., and Curcio, C. A. (2008). Prevalence and morphology of druse types in the macula and periphery of eyes with age-related maculopathy. *Invest. Ophthalmol. Vis. Sci.* 49, 1200–1209.

Rudolf, M., Curcio, C. A., Schlötzer-Schrehardt, U., Sefat, A. M. M., Tura, A., Aherrahrou, Z., et al. (2019). Apolipoprotein A-I mimetic peptide L-4F removes bruch's membrane lipids in aged nonhuman primates. *Invest. Ophthalmol. Vis. Sci.* 60, 461–472.

Sharma, N., Madan, P., and Lin, S. (2016). Effect of process and formulation variables on the preparation of parenteral paclitaxel-loaded biodegradable polymeric nanoparticles: a co-surfactant study. *Asian J. Pharm. Sci.* 11, 404–416.

Sparrow, J. R., Hicks, D., and Hamel, C. P. (2010). The retinal pigment epithelium in health and disease. *Curr. Mol. Med.* 10, 802–823.

Surrao, D. C., Greferath, U., Chau, Y. Q., Skabo, S. J., Huynh, M., Shelat, K. J., et al. (2017). Design, development and characterization of synthetic Bruch's membranes. *Acta Biomater.* 64, 357–376.

Tan, E. Y. S., Sing, S. L., and Yeong, W. Y. (2019). *60 - Scaffolds For Retinal Repairs in Handbook of Tissue Engineering Scaffolds*. Sawston: Woodhead Publishing.

Thomson, H. A. J., Treharne, A. J., Walker, P., Grossel, M. C., and Lotery, A. J. (2011). Optimisation of polymer scaffolds for retinal pigment epithelium (RPE) cell transplantation. *Br. J. Ophthalmol.* 95:563.

Vavvas, D. G., Daniels, A. B., Kapsala, Z. G., Goldfarb, J. W., Ganotakis, E., Loewenstein, J. I., et al. (2016). Regression of some high-risk features of age-related macular degeneration (AMD) in patients receiving intensive statin treatment. *eBio Med.* 5, 198–203.

White, C. E., and Olabisi, R. M. (2017). Scaffolds for retinal pigment epithelial cell transplantation in age-related macular degeneration. *J. Tis. Eng.* 8:2041731417720841.

Yamamoto, T., and Yamashita, H. (1989). Scanning electron microscopic observation of Bruch's membrane with the osmium tetroxide treatment. *Br. J. Ophthamol.* 73, 162–167.

Yeste, J., Illa, X., Alvarez, M., and Villa, R. (2018). Engineering and monitoring cellular barrier models. *J. Biol. Eng.* 12:18.

Conflict of Interest: The authors declare that the research was conducted in the absence of any commercial or financial relationships that could be construed as a potential conflict of interest.

frontiers in Bioengineering and Biotechnology

ORIGINAL RESEARCH
published: 19 May 2020
doi: 10.3389/fbioe.2020.00384

Hybrid Injectable Sol-Gel Systems Based on Thermo-Sensitive Polyurethane Hydrogels Carrying pH-Sensitive Mesoporous Silica Nanoparticles for the Controlled and Triggered Release of Therapeutic Agents

Monica Boffito[1], Alessandro Torchio[1,2], Chiara Tonda-Turo[1], Rossella Laurano[1,2], Miguel Gisbert-Garzarán[3,4], Julia C. Berkmann[5], Claudio Cassino[6], Miguel Manzano[3,4], Georg N. Duda[5,7], María Vallet-Regí[3,4], Katharina Schmidt-Bleek[5,7] and Gianluca Ciardelli[1]*

[1] Department of Mechanical and Aerospace Engineering, Politecnico di Torino, Turin, Italy, [2] Department of Surgical Sciences, Università degli Studi di Torino, Turin, Italy, [3] Departamento de Química en Ciencias Farmacéuticas, Instituto de Investigación Sanitaria del Hospital, Universidad Complutense de Madrid, Madrid, Spain, [4] CIBER de Bioingeniería, Biomateriales y Nanomedicina (CIBER-BBN), Madrid, Spain, [5] Julius Wolff Institut, Charité - Universitätsmedizin Berlin, Berlin, Germany, [6] Department of Science and Technological Innovation, Università del Piemonte Orientale, Alessandria, Italy, [7] BIH Center for Regenerative Therapies, Charité - Universitätsmedizin Berlin, Berlin, Germany

OPEN ACCESS

Edited by:
Maria Chatzinikolaidou, University of Crete, Greece

Reviewed by:
Xin Zhao, Hong Kong Polytechnic University, Hong Kong
Tzu-Wei Wang, National Tsing Hua University, Taiwan

***Correspondence:**
Monica Boffito
monica.boffito@polito.it

Specialty section:
This article was submitted to Tissue Engineering and Regenerative Medicine, a section of the journal Frontiers in Bioengineering and Biotechnology

Received: *15 February 2020*
Accepted: *07 April 2020*
Published: *19 May 2020*

Citation:
Boffito M, Torchio A, Tonda-Turo C, Laurano R, Gisbert-Garzarán M, Berkmann JC, Cassino C, Manzano M, Duda GN, Vallet-Regí M, Schmidt-Bleek K and Ciardelli G (2020) Hybrid Injectable Sol-Gel Systems Based on Thermo-Sensitive Polyurethane Hydrogels Carrying pH-Sensitive Mesoporous Silica Nanoparticles for the Controlled and Triggered Release of Therapeutic Agents. Front. Bioeng. Biotechnol. 8:384. doi: 10.3389/fbioe.2020.00384

Injectable therapeutic formulations locally releasing their cargo with tunable kinetics in response to external biochemical/physical cues are gaining interest in the scientific community, with the aim to overcome the cons of traditional administration routes. In this work, we proposed an alternative solution to this challenging goal by combining thermo-sensitive hydrogels based on custom-made amphiphilic poly(ether urethane)s (PEUs) and mesoporous silica nanoparticles coated with a self-immolative polymer sensitive to acid pH (MSN-CS-SIP). By exploiting PEU chemical versatility, Boc-protected amino groups were introduced as PEU building block (PEU-Boc), which were then subjected to a deprotection reaction to expose pendant primary amines along the polymer backbone (PEU-NH_2, 3E18 -NH_2/$g_{PEU\text{-}NH2}$) with the aim to accelerate system response to external acid pH environment. Then, thermo-sensitive hydrogels were designed (15% w/v) showing fast gelation in physiological conditions (approximately 5 min), while no significant changes in gelation temperature and kinetics were induced by the Boc-deprotection. Conversely, free amines in PEU-NH_2 effectively enhanced and accelerated acid pH transfer (pH 5) through hydrogel thickness (PEU-Boc and PEU-NH_2 gels covered approximately 42 and 52% of the pH delta between their initial pH and the pH of the surrounding buffer within 30 min incubation, respectively). MSN-CS-SIP carrying a fluorescent cargo as model drug (MSN-CS-SIP-Ru) were then encapsulated within the hydrogels with no significant effects on their thermo-sensitivity. Injectability and *in situ* gelation at 37°C were demonstrated *ex vivo* through sub-cutaneous injection

in rodents. Moreover, MSN-CS-SIP-Ru-loaded gels turned out to be detectable through the skin by IVIS imaging. Cargo acid pH-triggered delivery from PEU-Boc and PEU-NH_2 gels was finally demonstrated through drug release tests in neutral and acid pH environments (in acid pH environment approximately 2-fold higher cargo release). Additionally, acid-triggered payload release from PEU-NH_2 gels was significantly higher compared to PEU-Boc systems at 3 and 4 days incubation. The herein designed hybrid injectable formulations could thus represent a significant step forward in the development of multi-stimuli sensitive drug carriers. Indeed, being able to adapt their behavior in response to biochemical cues from the surrounding physio-pathological environment, these formulations can effectively trigger the release of their payload according to therapeutic needs.

Keywords: thermo-sensitive hydrogels, polyurethane, pH-sensitive mesoporous silica nanoparticles, self-immolative polymer, triggered drug release, stimuli-responsive

INTRODUCTION

The design of injectable therapeutic formulations locally releasing their cargo with controlled and prolonged kinetics is becoming an urgent need in the biomedical field. Indeed, such an approach is expected to open a new chapter in the treatment of pathological states, with the huge potential to progressively overcome the typical drawbacks of gold standard administration approaches (e.g., need to repeatedly administer high drug dosages, undesired side effects, drug accumulation in non-target tissues and organs). Additionally, a proper engineering of newly designed injectable formulations could eventually lead to an in depth control over their properties, thus allowing the achievement of the best delivery profiles ensuring the cargo to be released within the therapeutic window in the target tissue for the required time interval. Among the potential approaches under investigation in the scientific community, the design of hydrogels for drug release applications is gaining huge interest, with an increasing number of research works on this topic published annually (a 10–15% annual increase has been registered over the last 10 years, PubMed's database). In their general definition, hydrogels are three-dimensional cross-linked networks able to absorb a remarkable amount of water/physiological fluids from the surrounding environment and characterized by a soft consistence, which makes them similar to living soft tissues (Ahmed, 2015; Ozcelik, 2016). Among the wide variety of available hydrogels, thermo-sensitive sol-gel systems that undergo a temperature-driven gelation with increasing temperature up to the physiological value represent a promising alternative as drug delivery systems (Boffito et al., 2014). Indeed, they are easily injectable in the sol/semi-gel state and perfectly take the shape of the defect cavity prior to complete gelation. Additionally, they can be easily loaded with therapeutic agents, which are then locally released over time in a sustained and controlled way. Interestingly, in the case of thermo-sensitive hydrogels based on amphiphilic polymers, both hydrophilic and hydrophobic drugs can be easily encapsulated at high concentration by exploiting the arrangement of the polymeric chains into micelles, which are also the driving-force for system transition from the sol to the gel state (Xi et al., 2014; Boffito et al., 2016, 2019a,b; Anggelia et al., 2019). Payload release from thermo-sensitive hydrogels is usually driven by passive diffusion, swelling/erosion or the co-presence of both diffusion and swelling/erosion phenomena (Huang et al., 2019). A further tuning of payload release kinetics and mechanism can be obtained by pre-loading therapeutic agents into nano- or micro-carriers, such as mesoporous silica or polymeric particles. For instance, Geng et al. (2011) incorporated vascular endothelial growth factor (VEGF)-loaded poly(lactic-*co*-glycolic acid) particles into Pluronic F127-based hydrogels for application in bladder reconstruction. Later, a similar approach was adopted by Chen et al. (2018) that reported the incorporation of VEGF-loaded polymeric microspheres into injectable thermo-sensitive hydrogels based on a star-shaped poly(D,L-lactic-*co*-glycolic acid)-*b*-methoxy poly(ethylene glycol) (PLGA-mPEG) block copolymer, demonstrating the capability of the gels to delay VEGF release from the particles. Pontremoli et al. (2018) reported the development of hybrid sol-gel systems based on a custom-made poly(ether urethane) (PEU) containing F127 as building block and ion-doped bioactive glasses (MBGs) in the form of nanoparticles or microspheres, demonstrating that the resulting composite formulations allowed a prolonged and sustained release of copper ions over time. Later, the same authors described similar injectable formulations co-releasing copper ions and ibuprofen (Boffito et al., 2019b). Interestingly, they demonstrated that drugs could be released from hybrid formulations with an anomalous mechanism resulting from the existence of a double diffusive barrier (i.e., the hydrogel and the mesoporous framework) the drug molecules must pass through before being released in the surrounding aqueous medium. On the other hand, in the case of therapeutic ion release, different mechanisms turned out to be involved in the progressive delivery of ion species, i.e., ion exchange reactions within the MBG framework followed by diffusion through the hydrogel network.

Additional control over payload release can be reached by providing the designed systems with the capability to respond to physical and/or biochemical cues from the surrounding

environment, thus making it possible to finely modulate and trigger the release of encapsulated therapeutics. For instance, reactive oxygen species (ROS)-dependent drug release was reported by Gupta et al. (2014) from thermo-sensitive hydrogels based on a ABC triblock polymer containing a ROS-sensitive poly(propylene sulfide) building block. Near-infrared (NIR) light-induced drug delivery was achieved by embedding gold nanorods into thermo-sensitive poly(N-isopropylacrylamide) (PNIPAM) hydrogels which underwent shrinkage upon local heating of the nanorods due to NIR light irradiation, resulting in the triggered release of encapsulated drugs (Jiang et al., 2019). Carbon nanotubes were also used with the same goal by Dong et al. (2017) that exploited their photo-thermal effect to trigger the release of doxorubicin from thermo-sensitive hydrogels based on a poly(ε-caprolactone)-*b*-poly(ethylene glycol)-*b*-poly(ε-caprolactone) (PCL-PEG-PCL) triblock copolymer. However, differently from the former approach, triggered release was achieved in this case by exploiting a gel-to-sol transition occurring within the hydrogels in response to local heating induced by NIR light application. Another widely explored stimulus to achieve a triggered drug release *in situ* exploits pH variations. The design of drug delivery systems able to respond to specific pH values, thus accelerating the release of their payload in well-defined conditions, could effectively represent a successful strategy in the treatment of all pathological conditions characterized by pH changes in the surrounding milieu [e.g., tumor and chronic skin wound environments are characterized by acid and alkaline pH, respectively (Kanamala et al., 2016; Bullock et al., 2019)]. The goal of triggering payload release in response to external pH is usually achieved by chemically modifying hydrogel-forming polymers. For instance, Guar gum was block copolymerized with PNIPAM by Lang et al. (2006) to provide thermo-sensitive PNIPAM-based hydrogels with additional pH-sensitivity (slower release of sinomenine hydrochloride at pH 6.8 compared to pH 1.0). More recently, N-isopropylacrylamide (NIPAM), itaconamic acid (AIM) and β-cyclodextrin (β-CD) were copolymerized to get a polymer which aqueous solutions showed responsiveness to temperature and pH provided by NIPAM and AIM, respectively, and additional capability to encapsulate drug molecules due to β-CD moieties (Rwei et al., 2016). Similar results were also published by Roy et al. (2019) that developed pH- and thermo-responsive gels by grafting and crosslinking PNIPAM and poly(methacrylic acid) on β-cyclodextrins for preferential release of metronidazole and ofloxacin at colonic pH (i.e., 7.4) instead of stomach pH (acid pH). As an alternative to this approach, pH-sensitive release of a cargo can be also achieved by blending hydrogel-forming materials with pH-sensitive polymers. For instance, Zhang et al. (2018) developed injectable hydrogels modulating doxorubicin release in response to external pH (i.e., faster release in acid pH environment) by mixing chitosan, hyaluronic acid and β-sodium glycerophosphate. Later, a similar approach was adopted by Chatterjee et al. (2019) that recently reported the design of dual-responsive (pH and temperature) hydrogels by blending F127, N,N,N-trimethyl chitosan and polyethylene glycolated hyaluronic acid. In the same year, tissue adhesive and acid pH-responsive hydrogels were designed starting from chitosan-grafted-dihydrocaffeic acid and oxidized pullulan that underwent chemical crosslinking via a Schiff base reaction upon mixing (Liang et al., 2019).

Finally, as a last approach to design pH-sensitive drug-releasing gels, composite formulations combining cargo-loaded particles within a hydrogel vehicle phase have been also described in literature. For instance, Wang et al. (2010) encapsulated molecularly imprinted pH-sensitive nanospheres loaded with dexamethasone-21 phosphate disodium into UV-crosslinked gels as potential coating of implantable biosensors. In the same year, chitosan/poly-γ-glutamic acid nanoparticles loaded with amoxicillin were incorporated into pH-sensitive alginate-based hydrogels (Chang et al., 2010). Later, triggered camptothecin (CPT) release at mild acid pH values was achieved by loading CPT-containing nanoparticles based on an acid-sensitive β-cyclodextrin derivative (i.e., acetalated-β-cyclodextrin) into supramolecular hydrogels prepared starting from graphene oxide and poly(vinyl alcohol) (Ye and Hu, 2016). Lastly, Qindeel et al. (2019) described hybrid formulations for transdermal drug delivery resulting from the encapsulation of pH-sensitive nanoparticles into Carbopol 934-based hydrogels.

Within this constantly evolving scenario, in the present work we proposed an alternative approach to design injectable therapeutical formulations showing concurrent temperature- and pH-sensitivity, which allow easy injection and gelation under mild conditions and triggered payload release, respectively. In detail, this goal was achieved by combining the thermo-sensitivity of a custom-made amphiphilic poly(ether urethane) and the pH responsiveness of mesoporous silica nanoparticles (MSNs), which pore openings have been plugged by a self-immolative polymer (SIP) sensitive to acid pH (MSN-CS-SIP). Furthermore, to accelerate system response to pH changes, thus making acid pH transmission from the surrounding environment through hydrogel thickness faster, the wide versatility of polyurethane chemistry was exploited to introduce pendant primary amines along PEU backbone. In detail, the PEU used in this work was synthesized by chain extending Poloxamer® 407 with an aliphatic non-toxic diisocyanate and an amino-acid derived diol containing Boc-protected amino-groups (NHP407). Then, amino group exposure along PEU backbone (SHP407) resulted from the optimization of the Boc deprotection procedure in terms of chloroform/trifluoroacetic acid volume ratio. The successful synthesis of NHP407 and SHP407 was demonstrated by Size Exclusion Chromatography (SEC), Fourier Transformed Infrared (FTIR) Spectroscopy, Proton Nuclear Magnetic Resonance (^{1}H NMR) Spectroscopy and Orange II Sodium Salt colorimetric assay. Then, thermo-sensitive hydrogels were designed by solubilizing the PEUs in aqueous media and their gelation was qualitatively and quantitatively characterized by tube inverting and rheological tests. The capability of the hydrogels to transmit the pH of the surrounding environment through their thickness was studied by means of contact tests with buffer solutions at different pH values (pH 5 and 7.4). Finally, MSN-CS-SIP were embedded within the hydrogels and the effect of particle encapsulation on the temperature-driven sol-to-gel transition of the hybrid formulations was investigated through rheology. SIP-coated MSNs carrying a fluorescent cargo

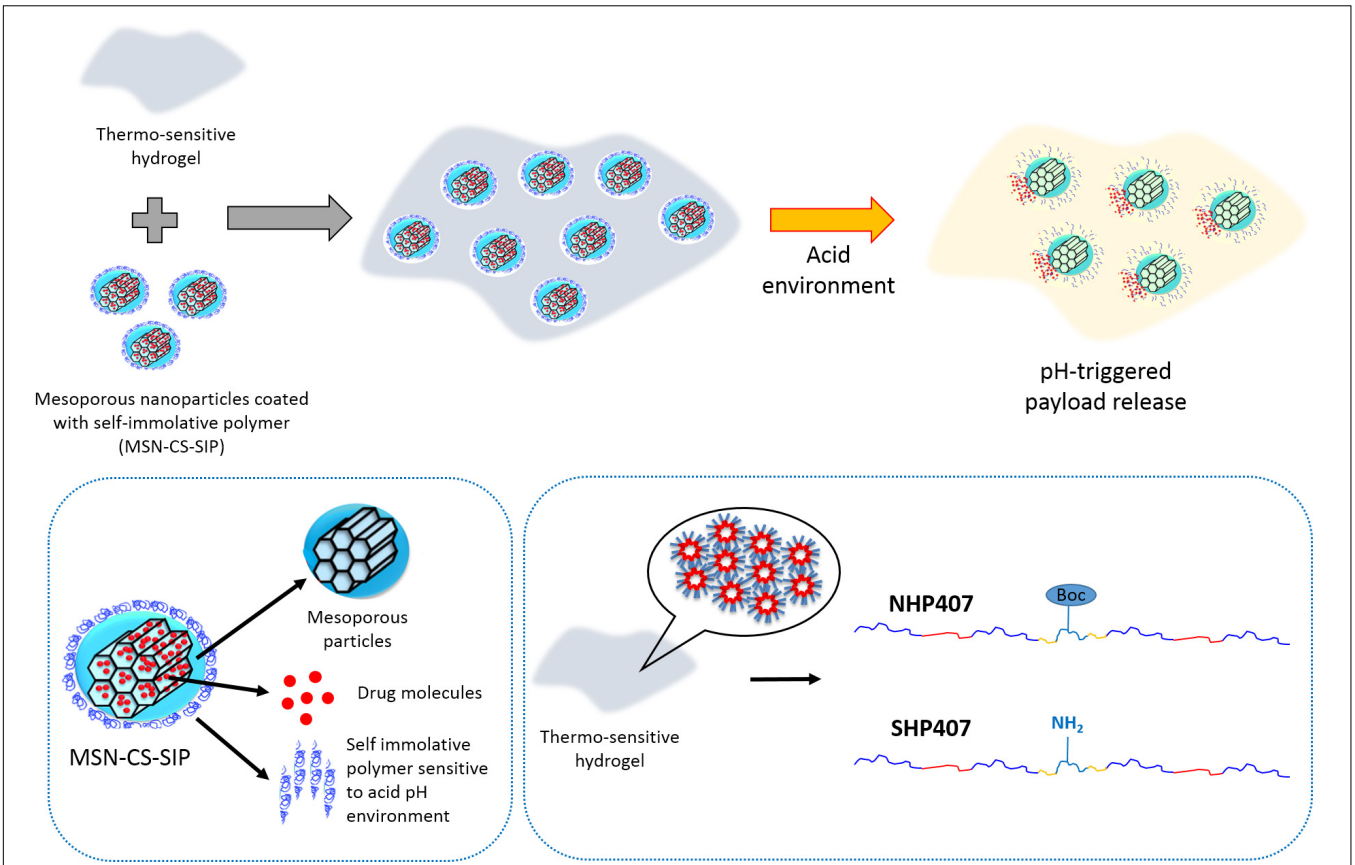

SCHEME 1 | Schematic representation of the overall strategy proposed in this work to design thermo- and pH-sensitive hydrogels.

as model drug were then encapsulated within the hydrogels and its pH-triggered release was investigated by incubating the gels in neutral and acid pH media. Injectability and *in situ* dispersion and gelation were finally assessed *ex vivo* through subcutaneous injection in rodents. **Scheme 1** summarizes the overall strategy we adopted to design the thermo- and pH-sensitive gels described in this work.

MATERIALS AND METHODS

Polymer Synthesis and Characterization

Materials

The building blocks used for PEU synthesis, i.e., Poloxamer® 407 (P407, poly(ethylene oxide)-poly(propylene oxide)-poly(ethylene oxide), PEO-PPO-PEO, $\overline{M}_n$ 12600 Da, 70% w/w PEO), 1,6-hexamethylene diisocyanate (HDI) and N-Boc serinol were purchased from Sigma Aldrich, Italy. Before use, they were treated to remove residual moisture and stabilizers. Briefly, P407 was dried under reduced pressure at 100°C for 8 h and then cooled down to 30°C under vacuum, N-Boc serinol was dried at room temperature (RT) under vacuum in a dessicator, HDI was distilled under reduced pressure and stored in a dessicator until use. Butynorate was purchased from Sigma Aldrich, Italy and used as received. All solvents were purchased from Carlo Erba Reagents, Italy in the analytical grade and used as received with the exception of 1,2-dichloroethane (DCE) which was anhydrified over activated molecular sieves (3 Å, Sigma Aldrich, Italy, activation at 120°C, atmospheric pressure, overnight) at RT and under nitrogen flow for 8 h. All required glassware for PEU synthesis was dried overnight at 120°C.

Poly(ether urethane) Synthesis

The poly(ether urethane) used in this work was synthesized according to Boffito et al. (2016). Briefly, the synthesis was carried out in solution (i.e., anhydrous DCE) under nitrogen flow through a pre-polymerization approach. Initially, P407 was solubilized in anhydrous DCE (20% w/v) and equilibrated at 80°C. Then, HDI (2:1 molar ratio with respect to P407) and butynorate (0.1% w/w with respect to P407) were added to the P407 solution and the prepolymerization step started. After 150 min, the temperature of the reaction mixture was lowered to 60°C, N-Boc serinol was added (3% w/v in anhydrous DCE) and the chain extension reaction was carried on for 90 min. Finally, upon temperature decrease to RT and passivation of residual isocyanate groups with MeOH, the synthesized PEU was collected by precipitation in excess petroleum ether (4:1 volume ratio with respect to DCE). PEU was then purified by precipitating its solution (30% w/v in DCE) in a mixture of diethyl ether and MeOH (98:2 v/v, 5:1 volume ratio with respect

to DCE). The polymer was finally collected by centrifugation (Hettich, MIKRO 220R, 6000 rpm, 0°C, 20 min), dried overnight under the fume hood and stored at 4°C under nitrogen until use.

Hereafter, the as-synthesized PEU will be referred to with the acronym NHP407, where N, H and P407 identify the chain extender, the diisocyanate and the macrodiol used for its synthesis, respectively.

Exposure of Free Amines Along Poly(ether urethane) Backbone

The selection of N-Boc serinol as PEU building block allowed the exposure of free amines along its backbone through a Boc-deprotection reaction. According to the protocols usually adopted in peptide synthesis reactions to deprotect Boc-protected amines of amino acids, the deprotection reaction was carried out in acid conditions (Blondelle and Houghten, 1993). Briefly, 10 g of NHP407 were solubilized in 225 ml of chloroform ($CHCl_3$) at RT for 120 min (under stirring at 250 rpm) and then 25 ml of trifluoroacetic acid (TFA) were added to the solution and the mixture (overall 4% w/v polymer concentration, $CHCl_3$/TFA 90/10 volume ratio) was left to react for 60 min at RT. At the end of the deprotection reaction, solvents were evaporated under vacuum using a rotary evaporator (Buchi Rotavapor Labortechnik AG) and the collected polymer was washed twice using chloroform (10% w/v) to completely evaporate TFA residues. Finally, the polymer was solubilized in distilled water (5% w/v) at 4°C overnight and dialyzed (cellulose membrane cut-off 10–12 kDa, Sigma Aldrich, Italy) against distilled water for 2 days (water refresh three times/day) to completely wash out Boc groups and residual $CHCl_3$ and TFA molecules. Deprotected polymer was then freeze dried (Martin Christ ALPHA 2–4 LSC) and stored under vacuum at 4°C until use. This deprotection protocol resulted from an optimization process, which is thoroughly described in **Supplementary Material**.

Hereafter, the collected polymer after the Boc-deprotection reaction will be referred to with the acronym SHP407.

Attenuated Total Reflectance Fourier Transform Infrared Spectroscopy

Attenuated Total Reflectance Fourier Transform Infrared (ATR-FTIR) spectroscopic analyses were performed to (i) assess the success of NHP407 synthesis, and (ii) verify the absence of degradation and $CHCl_3$/TFA residues in SHP407. ATR-FTIR spectra resulted from 16 scans registered at RT within the spectral range 6000–400 cm^{-1} (resolution 4 cm^{-1}) using a Perkin Elmer Spectrum 100 instrument equipped with an ATR accessory with diamond crystal (UART KRS5). Spectra analysis and peak identification were conducted using the Perkin Elmer Spectrum software.

Size Exclusion Chromatography

Number Average and Weight Average Molecular Weights ($\overline{M}_n$ and $\overline{M}_w$, respectively) and Polydispersity Index (D) of NHP407 and SHP407 samples were estimated using an Agilent Technologies 1200 Series (USA) instrument equipped with a Refractive Index detector (RID) and two Waters Styragel columns (HR2 and HR4). Analyses were conducted using tetrahydrofuran (THF, inhibitor-free, CHROMASOLV® Plus, for HPLC, ≥99.9%, Sigma Aldrich, Italy) as eluent at 35°C and 0.4 ml/min flow rate. SEC samples were prepared by filtering a polymer solution (2 mg/ml in THF) through a 0.45 μm syringe filter (Whatman). Registered RID signals as a function of elution time were then analyzed using Excel software (Microsoft Corporation) to estimate $\overline{M}_n$, $\overline{M}_w$, and D relative to a calibration curve based on polystyrene standards ($\overline{M}_n$ within the range 740–180,000 Da).

Proton Nuclear Magnetic Resonance Spectroscopy

Proton Nuclear Magnetic Resonance spectra of NHP407 and SHP407 samples were recorded in anhydrous deuterated dimethyl sulfoxide (DMSO-d6, 99.8% D with 0.03% TMS, Sigma Aldrich, Italy) by means of an Avance III Bruker spectrometer equipped with a 11.74 T superconducting magnet (500 MHz ^1H Larmor frequency), a Bruker BBFO direct probe and a Bruker BVT 3000 unit for temperature control. The spectra were registered at 25°C and resulted from 12 scans, with 10 s relaxation time. ^1H NMR spectra were referenced to TMS signal at 0 ppm.

Quantification of Exposed Amines Through Orange II Sodium Salt Colorimetric Assay

Primary amines exposed along polymer backbone upon Boc-removal were quantified according to the method recently published by Laurano et al. (2020) that adapted to water-soluble polymers the protocol usually used to quantify amino groups exposed on polymer surfaces (Noel et al., 2011). Briefly, the polymer was dissolved (0.04% w/v) in an Orange II Sodium Salt (Sigma Aldrich, Italy) aqueous solution (0.175 mg/ml in double distilled water, ddH_2O) previously adjusted at pH 3 and then the resulting solutions were incubated for 18 h at RT, in the dark. Samples were then dialyzed against ddH_2O (Sigma Aldrich, Italy, cellulose membrane cut-off 10–12 kDa) to wash out uncoupled dye molecules and freeze dried (Martin Christ ALPHA 2–4 LSC). Lastly, dye molecules were desorbed from lyophilized samples by solubilizing them in ddH_2O previously adjusted at pH 12 (1% w/v) for 2 h at RT, in the dark. Finally, after centrifugation (15°C, 6000 rpm, 10 min), the samples were analyzed using an UV–Vis spectrophotometer (PerkinElmer, Lambda 25) within the spectral range from 700 to 400 nm, being Orange characteristic peak at 485 nm. Exposed amines were then quantified referring to a calibration curve based on Orange-containing standards (1.75–29.2 μg/ml concentration) prepared in ddH_2O at pH 12.

Hydrogel Design and Characterization

Hydrogel Preparation Protocol

In order to obtain thermo-sensitive sol-gel systems, NHP407 and SHP407 were dissolved at a previously optimized concentration of 15% w/v (Boffito et al., 2016). Polymer solubilization was carried out at 5°C overnight using a mix of physiological solution (0.9% NaCl), phosphate buffer at pH 8 and phosphate buffered saline (PBS, pH 7.4) at 80/10/10 volume ratio. This mixture of buffered and not-buffered aqueous solutions was selected to make the developed sol-gel systems able to more easily transport acid pH from the surrounding environment (pH 5) to their core, while forcing initial hydrogel pH toward a neutral value. In order to

allow comparison among the samples and avoid results variance due to sample geometry and volume, all hydrogels (1 ml) were prepared in Bijou sample containers (Savatec, Italy, polystyrene vials with 17 mm inner diameter).

Tube Inverting Test

Hydrogel gelation potential was first qualitatively assessed by tube inverting test, which was performed in temperature ramp mode and in isothermal conditions at 37°C to estimate Lower Critical Gelation Temperature (LCGT) values and gelation time in physiological conditions, respectively. Briefly, LCGT values were estimated by progressively increasing hydrogel temperature from 4 to 70°C at 1°C/step, each step consisting in sample equilibration at the predefined temperature for 5 min followed by vial inversion for 30 s. At each step, "sol," "semi-gel," and "gel" states were defined by observing the presence of flow during the 30 s of vial inversion. Gelation time in physiological conditions was estimated by keeping the temperature constant at 37°C and inverting the vials after predefined time intervals of incubation at that temperature (i.e., from 1 to 10 min, 1 min/step). Conditions of "sol," "semi-gel," and "gel" were defined through vial inversion for 30 s.

Rheological Characterization

To better characterize hydrogel transition from the sol to the gel state, rheological characterization was performed through strain sweep, frequency sweep and temperature ramp tests. Strain sweep tests were conducted at 37°C and constant frequency (10 Hz) within the deformation range from 0.01 to 500% to characterize the designed gels in terms of their resistance to applied strain through the definition of their linear viscoelastic region (LVE, i.e., the strain range is which storage modulus -G′- is constant), the linearity limit (γ_L, i.e., the limiting value of the LVE region) and the yield stress (YS, i.e., the value of shear stress at the maximum of the loss modulus -G″-). Then, frequency sweep tests were performed within the LVE region, at three different temperatures (i.e., 25, 30, and 37°C) and angular frequency ranging between 0.1 and 100 rad/s to characterize the progressive transition from the sol to the gel state. At each tested temperature, the angular frequency at G′/G″ crossover ($\omega_{G'/G''\,crossover}$) was determined using Matlab (MathWorks, R2016b version). Finally, the temperature-driven sol-to-gel transition was investigated through temperature ramp tests at constant frequency (0.1 Hz) and rate (2°C/min) within the temperature range from 0 to 40°C. Gelation onset temperature (T_{onset}) was then identified at the minimum of viscosity. All tests were performed using a stress-controlled MCR302 Anton Paar rheometer equipped with a Peltier system for temperature control and a 50 mm parallel plate geometry. Before each analysis, the sample was poured on instrument lower plate at 0°C, heated at the test temperature, left to equilibrate for 10 min and finally analyzed. In the case of temperature ramp tests, equilibration was performed at 0°C.

Evaluation of Hydrogel pH Transfer Potential

Hydrogels based on NHP407 and SHP407 were qualitatively and quantitatively characterized in terms of their ability to transfer pH variation from the surrounding environment through their thickness. To quantitatively characterize hydrogel pH variation upon contact with environments at different pH values, samples were prepared as previously described and their initial pH was measured (Martini Instruments, Mi150, United States) in the sol state while keeping them in a water bath at 5°C. After complete gelation at 37°C (Memmert IF75, Schwabach, Germany) for 10 min, 1 ml of a buffer solution (phosphate buffered saline -PBS- pH 7.4 or acetate buffer at pH 5 (0.1 M), previously equilibrated at 37°C) was added to each sample. At predefined time intervals (15, 30, 45 min, 1 and 24 h), the residual buffer was withdrawn, the samples were incubated at 5°C to allow their sol-to-gel transition and finally hydrogel pH was measured. At each time point, hydrogel pH change was calculated according to Eq. 1.

$$Hydrogel\ pH\ change(\%) = \frac{pH_{to} - pH_{ti}}{pH_{to} - pH_{buffer}} \cdot 100 \qquad (1)$$

where pH_{to} and pH_{ti} are the measured pH values of hydrogels before (at t_o) and after incubation in the presence of a buffer for t_i minutes, and pH_{buffer} is the pH of the buffer (7.4 or 5) put in contact with the hydrogels.

Qualitative evaluation of the pH gradient moving through gel thickness was performed adding pH indicators to the hydrogels (phenol red, 0.1 mg/ml, for neutral/basic pH, and bromocresol purple, 0.1 mg/ml, for acid pH, Sigma Aldrich, Italy), which change their color in response to pH changes. Upon gelation at 37°C for 10 min, the prepared hydrogels containing pH indicators were incubated in the presence of acetate buffer at pH 5 or PBS according to the previously described protocol and then photographed at predefined time intervals.

Hydrogel Swelling and Stability in Aqueous Environment

The capability of the developed hydrogels to absorb fluids from the surrounding environment and undergo swelling/erosion phenomena was evaluated according to a recently published protocol (Boffito et al., 2019b). In detail, hydrogels were prepared as previously described and weighed (w_i). Upon gelation at 37°C for 10 min, 1 ml of buffer (PBS or acetate buffer at pH 5, equilibrated at 37°C) was added upon each gel and samples were again incubated at 37°C to simulate physiological conditions. Complete buffer refresh was performed every other day. At predefined time points (6 h, 1, 3, 7, and 14 days), residual buffer was removed and samples were weighed in their wet and dried states upon lyophilization (w_f and w_{f_dried}, respectively). Control samples, i.e., samples not-subjected to swelling and stability tests, were also prepared and freeze dried to evaluate hydrogel initial dried weight (w_{i_dried}). Finally, the percentage of hydrogel swelling (i.e., gel mass change in wet conditions) and dissolution/degradation (i.e., gel mass change in dry conditions) was evaluated according to equations reported by Boffito et al. (2016). In addition, at each time point swelling and dissolution/degradation data were correlated through the evaluation of the swelling ratio according to the formula reported by Park et al. (2009).

Ex vivo Characterization of the Developed Hydrogels

To test injectability and gelation potential of SHP407 hydrogel within an organism, a proof of concept cadaver study was carried out. In line with the 3R principles, the mice employed in this study had to be finalized for reasons beyond the outlined experiments. No additional animals had to be sacrificed, thereby exploiting the "reduce" of the 3R principles. The study was performed in accordance with the German Animal Welfare Act and was approved by the local animal protection authorities (LaGeSo; permit number: G 0293/17). Mice ($n = 2$) were finalized in deep anesthesia achieved by intraperitoneal (i.p.) injection of medetomidine and ketamine [medetomidine 1 mg/kg BW (Cepetor®, CP-Pharma, Germany) and ketamin 75 mg/kg BW (Inresa Arzneimittel, Germany)] followed by cervical dislocation directly prior to the injection of the SHP407 hydrogel (15% w/v). The rodents' physiological body temperature was maintained by a heating plate set to 37°C and exposure to red light. The external temperature of the immediate environment of the cadaver was controlled using a thermometer. SHP407 hydrogel was stained with food coloring for better visualization, kept on ice until usage, and 200 µl were injected subcutaneously (s.c.) into the neck region using a 18G needle. 5 min post injection, the skin pocket containing the injected hydrogel was opened and gel distribution and gelation were inspected visually and haptically. Additionally, an external fixator (RISytems, Switzerland) was mounted on the right femur, and a 0.7 mm osteotomy gap was created using a giggly saw. Via the 18G needle, the blue-colored gel was applied into the fracture gap in order to test the gel distribution in a wound cavity.

Particle Synthesis and Characterization

Materials

The following compounds were purchased from Sigma Aldrich Inc.: Tetraethyl orthosilicate (TEOS); Ammonium nitrate; Cetyltrimethylammonium bromide (CTAB); 4-Aminobenzyl alcohol (ABA); Phenyl chloroformate; N,N-Diisopropyl-ethylamine (DIPEA); Dibutyltin dilaurate (DBTDL); *tert*-butanol (*t*BuOH); Tris(2,2′-bipyridyl)dichlororuthenium(II) hexahydrate (Ru); (3-chloropropyl)triethoxysilane; Di-*tert*-butyl dicarbonate (BOC_2O); Dimethyl sulfoxide (DMSO); N,N-Dimethylformamide (DMF); Tetrahydrofuran (THF); Dichloromethane (DCM). The rest of the chemicals (ethanol, heptane, etc.) were of the best quality and employed as received.

Synthesis of Mesoporous Silica Nanoparticles

Mesoporous silica nanoparticles (MSNs) were synthesized following the Stöber method with some modifications (Baeza et al., 2014). Briefly, CTAB (1 g, 2.74 mmol), H_2O (480 ml) and NaOH (3.5 ml) were added to a 1l flask. Then, the solution was heated to 80°C and TEOS (5 ml, 22.39 mmol) was added dropwise over 20 min. Once the addition was completed, the solution was heated for further 2 h at 80°C under magnetic stirring. After that, the precipitate was centrifuged and washed twice with water and once with ethanol. Afterward, the surfactant was removed to obtain empty pores. For that purpose, the particles were refluxed in 350 ml of a NH_4NO_3 solution (10 mg/ml) in EtOH (95%) at 75°C for 2 h and subsequently centrifuged (Sorvall LEGEND XTR Centrifuge, Thermo Scientific; 9000 rpm, 15 min, 10°C). The process was repeated two more times. Finally, the nanoparticles were centrifuged, washed twice with water and once with ethanol and stored in absolute ethanol.

Synthesis of Self-Immolative Polymer (SIP)

(a) Phenyl(4-(hydroxymethyl)phenyl) carbamate (**1**)

Compound **1** was synthesized following a previously reported method (Gisbert-Garzarán et al., 2017). First, 4-aminobenzyl alcohol (1 g, 8.12 mmol) was dissolved in dry DMF (15 ml). Then, dry DIPEA (1.7 ml, 9.76 mmol) was added and the solution was placed in an ice bath. After that, phenyl chloroformate (1.12 ml, 8.83 mmol) was added dropwise, the ice bath was removed after 15 min and the reaction was stirred for 4 h. Afterward, the organic phase was extracted in ethyl acetate, washed with saturated ammonium chloride solution and finally dried over sodium sulfate. The solvent was partially evaporated and the resultant solution was precipitated in cold heptane and centrifuged (Sorvall LEGEND XTR Centrifuge, Thermo Scientific; 9000 rpm, 15 min, 10°C) twice in heptane.

(b) Tert-butyl(4-(hydroxymethyl)phenyl) carbamate (**2**) First, 4-aminobenzyl alcohol (1 g, 8.12 mmol) and di-*tert*-butyl dicarbonate (1.8 g, 8.12 mmol) were dissolved in dry THF (80 ml). Then, dry DIPEA (1.4 ml, 8.12 mmol) was added and the mixture was refluxed overnight. Afterward, the solvent was removed to obtain an oil that was dissolved in a small amount of ethyl acetate and precipitated in cold heptane. The solid was filtered off and dried under vacuum.

(c) Poly(phenyl(4-(hydroxymethyl)phenyl) carbamate (**3**) Compound **3** was synthesized following a modification of a previously reported method (Sagi et al., 2008). First, compound **1** (1 g, 4.12 mmol) was dissolved in dry DMSO (1.62 ml) and the solution was heated to 85°C. Then, DBTDL (5% mol) was added and the reaction was stirred for 2 h 30 min at 85°C. After that, compound **2** (223 mg, 1 mmol) in dry DMSO (0.5 ml) was injected and the solution was heated for further 2 h. Finally, the crude reaction mixture was precipitated in cold methanol, centrifuged (Sorvall LEGEND XTR Centrifuge, Thermo Scientific; 9000 rpm, 15 min, 10°C) and washed three times with methanol.

Synthesis of SIP-Coated Mesoporous Silica Nanoparticles

Mesoporous silica nanoparticles modified with (3-chloropropyl)triethoxysilane (MSN-CS)

Vacuum-dried MSNs (175 mg) were first dispersed in dry toluene (30 ml). Then, (3-chloropropyl)triethoxysilane (100 µl, 0.04 mmol) was added and the mixture was refluxed overnight. After that, the particles were isolated by centrifugation (Sorvall LEGEND XTR Centrifuge, Thermo Scientific; 9000 rpm, 15 min, 10°C), washed with toluene and ethanol and dried under vacuum.

SIP-coated mesoporous silica nanoparticles (MSN-CS-SIP)

First, vacuum-dried MSN-CS (175 mg) were dispersed in dry DMSO (25 ml). Separately, compound **3** (0.33 g, 0.1 mmol) was dissolved in dry DMSO (2.5 ml). Then, dry DIPEA (25.6 μl, 0.15 mmol) was added and the solution was stirred for 2 h for alcohol activation. After that, the polymer-containing solution was added dropwise to the nanoparticle dispersion and the mixture was heated to 80°C. Afterward, a second vial containing compound **3** in dry DMSO was activated for 2 h with dry DIPEA and subsequently added to the nanoparticle solution. Finally, a third vial containing compound **3** in DMSO was activated with dry DIPEA and added to the nanoparticle solution. After that, the whole reaction mixture was stirred overnight at 80°C. Finally, SIP-coated particles (MSN-CS-SIP) were centrifuged (Sorvall LEGEND XTR Centrifuge, Thermo Scientific; 9000 rpm, 15 min, 10°C), washed with DMSO, water and ethanol and dried under vacuum. For pH-triggered release experiments, the fluorescent red dye tris(2,2′-bipyridine)dichloro ruthenium (II) (Ru) was loaded into the MSN framework before SIP grafting according to Gisbert-Garzarán et al. (2017). Briefly, MSN-CS (175 mg) were incubated in a Ru solution (10.4 mg/ml in DMSO) at room temperature and under stirring for 24 h. Then, the dispersion was heated to 80°C and subjected to the previously described protocol. Ru containing MSNs will be referred to with the acronym MSN-CS-SIP-Ru.

Characterization of MSNs, SIP, MSN-CS, and MSN-CS-SIP

A step-by-step approach was adopted for the characterization of the synthesized mesoporous matrices and their coating, encompassing the analysis of compounds **1–3**, MSNs, MSN-CS (see **Supplementary File**) and culminating with the characterization of MSN-CS-SIP samples.

MSN-CS-SIP samples were characterized by Power X-Ray Diffraction (XRD) analyses performed using a Philips X'Pert diffractometer equipped with a Cu Kα radiation (wavelength 1.5406 Å). XRD patterns were registered within the 2θ range from 0.6° to 6°, with a step size of 0.02° and 5 s counting time/step. ATR-FTIR analyses were performed using a Nicolet Nexus instrument (Thermo Fisher Scientific) equipped with a Goldengate ATR accessory. Spectra resulted from the average of 64 scans within the spectral range 4000–400 cm^{-1} at 1 cm^{-1} resolution. Nitrogen adsorption and desorption isotherms were recorded on degassed samples (approximately 50 mg kept under vacuum at 40°C for 24 h) at 77 K using a Micromeritics ASAP 2020 equipment. Surface area and pore size distribution were estimated through the Brunauer-Emmett-Teller (BET) and the Barrett-Joyner-Halenda (BJH) methods, respectively. Pore volume was defined from the amount of N_2 adsorbed at a relative pressure of approximately 0.99. Thermogravimetric (TG) analyses were conducted using a Perkin Elmer Pyris Diamond TG/DTA instrument within the temperature range from RT to 600°C (5°C/min) to quantify the amount of organic phase present in the sample (10 mg).

Hybrid Hydrogel Design and Characterization

Preparation of Hybrid PEU/MSN-CS-SIP Sol-Gel Systems

Hybrid NHP407 and SHP407 hydrogels containing MSN-CS-SIP were prepared according to Boffito et al. (2019b). Briefly, PEU-based hydrogels were initially prepared according to the protocol described in section "Hydrogel preparation protocol" at higher concentration by solubilizing the polymer in the solution portion composed of physiological solution and phosphate buffer at pH 8 (0.1 M), which represents the 90% of the total aqueous solution volume required to solubilize the material at a final concentration of 15% w/v. Then, the residual 10% of aqueous solution (i.e., PBS) was used to prepare a MSN-CS-SIP-containing dispersion. In detail, MSN-CS-SIP were first dispersed at 50 mg/ml concentration in PBS through sonication (26 W, 20 kHz, Vibracell VCX130, Sonics, United States) for 3 min in a water-ice bath to avoid evaporation and then an aliquot was added to the previously solubilized PEU samples to reach final particle and polymer concentrations of 5 mg/ml and 15% w/v, respectively. Particle addition was performed with hydrogels in the sol state (at 5°C) and samples were vortexed for 30 s to homogeneously distribute the particle within the hybrid sol-gel systems.

Hereafter, MSN-CS-SIP-containing hydrogels will be referred to with the acronyms NHP407_MSN-CS-SIP and SHP407_MSN-CS-SIP.

Rheological Characterization of Hybrid Sol-Gel Systems

In order to investigate the effects of particle addition to hydrogels on their gelation potential, rheological characterization of the developed hybrid sol-gel systems was performed according to the previously described protocol (see section "Rheological characterization").

Payload Release Test

pH-triggered release studies were performed on hybrid hydrogels encapsulating MSN-CS-SIP particles previously loaded with the red dye Ru (MSN-CS-SIP-Ru) (hydrogel acronyms: NHP407_MSN-CS-SIP-Ru and SHP407_MSN-CS-SIP-Ru). Tests were performed according to the protocol published by Gisbert-Garzarán et al. (2017) with slight changes to adapt it to sol-gel systems. In detail, hybrid hydrogels were loaded in the sol state into 24 well cell culture inserts (transwell, Greiner, poly(ethylene terephthalate) membrane, 0.4 μm pore size) (400 μl gel/insert) and allowed to gel at 37°C for 10 min. Then, 1 ml of buffer (PBS pH 7.4 or acetate buffer at pH 5, equilibrated at 37°C) was added to each well containing an insert and release tests were conducted in physiological like conditions (i.e., in incubator at 37°C). Release medium was collected at predefined time intervals (1, 2, 4, 5, 24, 28, 72, 96, 168, and 336 h) and completely refreshed with the same volume of fresh buffer at 37°C. Collected release media were then analyzed through a plate reader (Perkin Elmer Victor X3) at a wavelength of 450 nm. For the quantification of released dye, a calibration curve was constructed starting from Ru standards prepared in PBS or

acetate buffer at pH 5 at different concentrations within the range 0–200 μg/ml.

Ex vivo Characterization of Hybrid Sol-Gel Systems

The gelation and dispersion of SHP407_MSN-CS-SIP-Ru hydrogel were studied similarly to SHP407 sol-gel system as such (section "*Ex vivo* Characterization of the Developed Hydrogels"). 200 μl of composite hydrogel (SHP407_MSN-CS-SIP-Ru), SHP407 hydrogel or MSN-CS-SIP-Ru dispersion (all kept on ice until usage) were injected s.c. into the neck region of just finalized murine cadavers (n = 4 mice) maintained at physiological body temperature. After 5 min, the cadavers were imaged using an *in vivo* imaging system (IVIS® Lumina, Caliper LifeSciences, MA; ex/em filter: 465 nm/Cy5.5). After imaging, the injection site was opened through a skin incision and the dispersion and appearance (i.e., sol or gel state) of the different injected materials were inspected visually and haptically.

Statistical Analysis

Statistical analysis of the collected data was performed using GraphPad Prism 5 for Windows (GraphPad Software, Inc., Version 5.03, 2009)[1]. In detail, Two-way ANOVA analyses followed by Bofferoni's multiple comparison tests were performed on data collected from swelling, dissolution/degradation, pH variation and release tests. Statistical differences were defined according to Boffito et al. (2016). Analyses were performed in triplicate and results are reported as mean ± standard deviation.

RESULTS

Chemical Characterization of NHP407 and SHP407

The as-synthesized NHP407 PEU containing P407 as building block was chemically characterized by Attenuated Total Reflectance Fourier Transform Infrared (ATR-FTIR) spectroscopy and Size Exclusion Chromatography (SEC). The effects of Boc-deprotection reaction on the integrity of PEU backbone were investigated by ATR-FTIR and SEC analyses, meanwhile the effective Boc group removal was assessed by Proton Nuclear Magnetic Resonance spectroscopy. Finally, exposed -NH_2 groups were colorimetrically quantified according to Laurano et al. (2020).

Characterization of NHP407 Poly(ether urethane)

Attenuated Total Reflectance Fourier Transform Infrared spectroscopic analyses were performed on both as-synthesized NHP407 and the starting P407 macrodiol for comparison (**Supplementary Figure S1**). As expected, NHP407 spectrum exhibited all the characteristic absorption bands of P407 at 2877 cm^{-1} (CH_2 stretching vibration), 1242 cm^{-1} (CH_2 rocking vibration) and 1099 cm^{-1} (asymmetric stretching of -CH_2-O-CH_2- groups typical of PEO blocks in P407). The formation of urethane bonds in NHP407 induced the appearance in its ATR-FTIR spectrum of new absorption peaks at 3347 cm^{-1} (N-H stretching vibration), 1720 and 1630 cm^{-1} (stretching vibration of carbonyl groups, amide I), and 1539 cm^{-1} (concurrent bending and stretching of N-H and C-N bonds, respectively). The absence of absorption peaks within 2200 and 2300 cm^{-1} proved the complete conversion of isocyanate groups.

NHP407 exhibited $\overline{M}_n$ and D values of 44600 Da and 1.42, respectively, as assessed by SEC analyses.

Characterization of SHP407 Poly(ether urethane)

With the aim to assess the integrity of PEU backbone upon treatment in $CHCl_3$/TFA mixture (90/10 v/v), ATR-FTIR, SEC and ^{1}H NMR analyses were performed on SHP407 samples and NHP407 as control. ATR-FTIR spectrum of SHP407 was completely overlapped with that of native NHP407 (**Supplementary Figure S1**) and no absorption peaks ascribable to residual $CHCl_3$ or TFA (e.g., C-Cl and C-F stretching vibration at 600–800 cm^{-1} and 1000–1400 cm^{-1}, respectively) were detected.

Estimated $\overline{M}_n$ value slightly decreased after the Boc-deprotection reaction ($\overline{M}_n$ and D of SHP407 were measured to be 40700 Da and 1.56, respectively), but this change was not significant considering the typical SEC analysis error (approximately 10%) (Trathnigg, 2000).

Supplementary Figure S2 reports the ^{1}H NMR spectra of NHP407 (control) and SHP407 samples. Magnified inserts in the spectral regions between 5.65–5.73 and 7.00–7.20 highlight the characteristic bands of urea and urethane N-H groups, respectively (Qin et al., 2019). The magnified insert of NHP407 spectrum within 1.31 and 1.41 ppm shows the co-presence of resonances typical of the methylene protons of HDI-deriving block (at 1.22 and 1.37 ppm) and the methyl protons of Boc caging groups (sharp singlet at 1.37 ppm, overlapped to HDI-derived signals) (Caddeo et al., 2019). Differently, the methylene protons adjacent to the urethane bonds appeared at 2.93 ppm. Upon treatment in acid conditions, the singlet at 1.37 due to Boc protons significantly decreased, indicating that the reaction conditions allowed an almost complete Boc removal (deprotection yield > 90%).

The number of exposed primary amines in SHP407 was colorimetrically quantified through the Orange II sodium salt assay. The effective exposure of amino groups along polymer chains was indirectly proved by the darker orange color of SHP407 solutions in ddH_2O at pH 12 compared to NHP407 control samples, which exhibited a weak orange color ascribable to physical adsorbance phenomena of dye molecules to polymer chains. Assuming that orange molecules and -NH_2 groups electrostatically interact at a 1:1 molecular ratio and subtracting the contribution of dye adsorbance to polymer chains, the number of exposed free primary amines along SHP407 was estimated to be 3.07E18 ± 1.63E17 -NH_2/g_{SHP407}.

[1]http://www.graphpad.com

Characterization of NHP407- and SHP407-Based Sol-Gel Systems

NHP407- and SHP407-based hydrogels (15% w/v), prepared by solubilizing the PEUs in aqueous medium (i.e., physiological solution/PBS/buffer at pH 8 at 80/10/10 v/v), were characterized in terms of their temperature-driven gelation, capability to change their pH in response to the external aqueous medium as well as swelling and stability in aqueous environments at different pH values. Finally, injectability, gelation and gel distribution upon subcutaneous injection were evaluated *ex vivo* in a rodent model.

Thermo-Sensitive Behavior of NHP407 and SHP407 Hydrogels

The gelation potential of NHP407- and SHP407-based sol-gel systems was first qualitatively evaluated by tube inverting test. LCGT values were measured to be 26 and 28°C (error ± 0.5°C) for NHP407 and SHP407 hydrogels, respectively. Tube inverting test in isothermal conditions at 37°C, instead, allowed the estimation of hydrogel gelation time in physiological conditions, which turned out to be 4 and 5 min (error ± 30 s) for NHP407 and SHP407 sol-gel systems, respectively. To obtain further insight on the sol-to-gel transition of NHP407 and SHP407 hydrogels, a thorough rheological characterization was performed by strain sweep, frequency sweep and temperature ramp tests (**Figure 1**). **Figure 1A** reports the trends of storage and loss moduli (G′ and G″) at 37°C as a function of strain in the range 0.01–500% for NHP407 and SHP407 gels. As expected for structured materials, when the strain (γ) exceeded a critical value (γ_L, limiting strain value of the LVE), G′ started to decrease, while G″ initially increased and then decreased, representing an overshoot behavior that can be correlated to a strain hardening effect. NHP407 and SHP407 hydrogels showed a similar behavior, but the NHP407-based sol-gel system was characterized by slightly higher critical deformation (γ_L of 18.6 and 11.6% for NHP407 and SHP407 gels, respectively) and mechanical strength (higher G′ values within the LVE) with respect to SHP407-based one (mean G′ value within LVE for NHP407 and SHP407 gels was 8880 and 6780 Pa, respectively). Gel Yield Stress (YS) was measured to be 1790 and 875 Pa for NHP407 and SHP407 formulations, respectively. Frequency sweep tests were conducted to study the progress of gel formation and development with increasing temperature (three different temperatures were tested, i.e., 25, 30, and 37°C) (**Figure 1C**). **Table 1** reports the G′/G″ crossover frequencies ($\omega_{G'/G''\text{crossover}}$) and the G′/G″ delta at 100 rad/s ($\Delta_{G'/G''\_100\ rad/s}$) for NHP407 and SHP407 gels at each tested temperature. No significant differences were observed between NHP407 and SHP407 hydrogels that were both characterized by G′ values becoming progressively constant with temperature increase, proving the progressive gel formation. At 37°C, indeed, both NHP407 and SHP407 gels turned out to be in the gel state with $\omega_{G'/G''\text{crossover}}$ lower than 0.1 rad/s. However, the kinetics of gel formation and development slightly slowed down in SHP407-based sol-gel system with respect to NHP407-based one, as shown by the slight increase in $\omega_{G'/G''\text{crossover}}$ at 25 and 30°C observed in SHP407 formulation compared to NHP407 one. The temperature-driven gelation of NHP407 and SHP407 sol-gel systems was also investigated by rheological temperature ramp tests (**Figure 1B**), which highlighted that SHP407-based formulation exhibited a similar gelation process compared to NHP407-based one. **Table 2** summarizes the characteristic parameters extracted from the measured temperature ramp curves: the gelation onset temperature (T_{onset}), viscosity at 0°C ($\eta_{0°C}$) and viscosity value at 25°C ($\eta_{25°C}$). As typical of solutions, viscosity initially decreased with increasing temperature until a minimum value was reached that was followed by a sharp viscosity increase. The temperature at the minimum of viscosity (T_{onset}) represents the onset of the gelation process, i.e., the temperature at which polymer chains started to aggregate into micelles. The formed micelles then tended to organize into a gel network as evidenced by the viscosity increase at higher temperatures. At a certain temperature of about 29–30°C, the viscosity of both the analyzed systems decreased with increasing temperature as a consequence of melt fracture phenomena due to gel mechanical failure induced by the application of a continuous strain rate (Boffito et al., 2016).

TABLE 1 | Frequency values at G′/G″ crossover ($\omega_{G'/G''\text{crossover}}$) and G′/G″ delta at 100 rad/s ($\Delta_{G'/G''\_100\ rad/s}$) for NHP407 and SHP407 hydrogels, evaluated at 25, 30, and 37°C.

	$\omega_{G'/G''\text{crossover}}$ (rad/s)		$\Delta_{G'/G''\_100\ rad/s}$ (Pa)	
	NHP407	**SHP407**	**NHP407**	**SHP407**
25°C	27.46	32.25	2130	1410
30°C	2.05	2.51	7670	5660
37°C	<0.1	<0.1	9650	7340

TABLE 2 | T_{onset}, $\eta_{0°C}$ and $\eta_{25°C}$ of NHP407 and SHP407 hydrogels, estimated from rheological temperature ramp tests.

	NHP407	**SHP407**
$\eta_{0°C}$ (Pa · s)	0.57	0.50
T_{onset} (°C)	16.03	16.36
$\eta_{25°C}$ (Pa · s)	201.7	230.2

Investigation of Hydrogel pH Transfer Potential

NHP407 and SHP407 gel ability to transfer pH changes through their thickness was tested in acid and neutral environments (i.e., pH 5 and 7.4). First, a quantitative evaluation was obtained through the measurement of hydrogel pH after incubation with buffers at different pHs (PBS, acetate buffer at pH 5) for predefined time intervals (0, 15, 30, 45 min, 1, 24 h) at 37°C (**Figures 2A,B**). NHP407- and SHP407-based hydrogels showed initial pH of 7.45 ± 0.10 and 7.67 ± 0.02, respectively. After 15 min contact with acetate buffer at pH 5, the pH of both hydrogels significantly decreased ($0.0001 < p < 0.001$) reaching values of 6.54 ± 0.06 and 6.50 ± 0.08 (no significant difference), respectively. However, although both the sol-gel systems reached a pH value of about 6.5, the initial pH of SHP407 hydrogels was significantly higher than that of NHP407 systems ($0.01 < p < 0.05$). Starting from 30 min incubation,

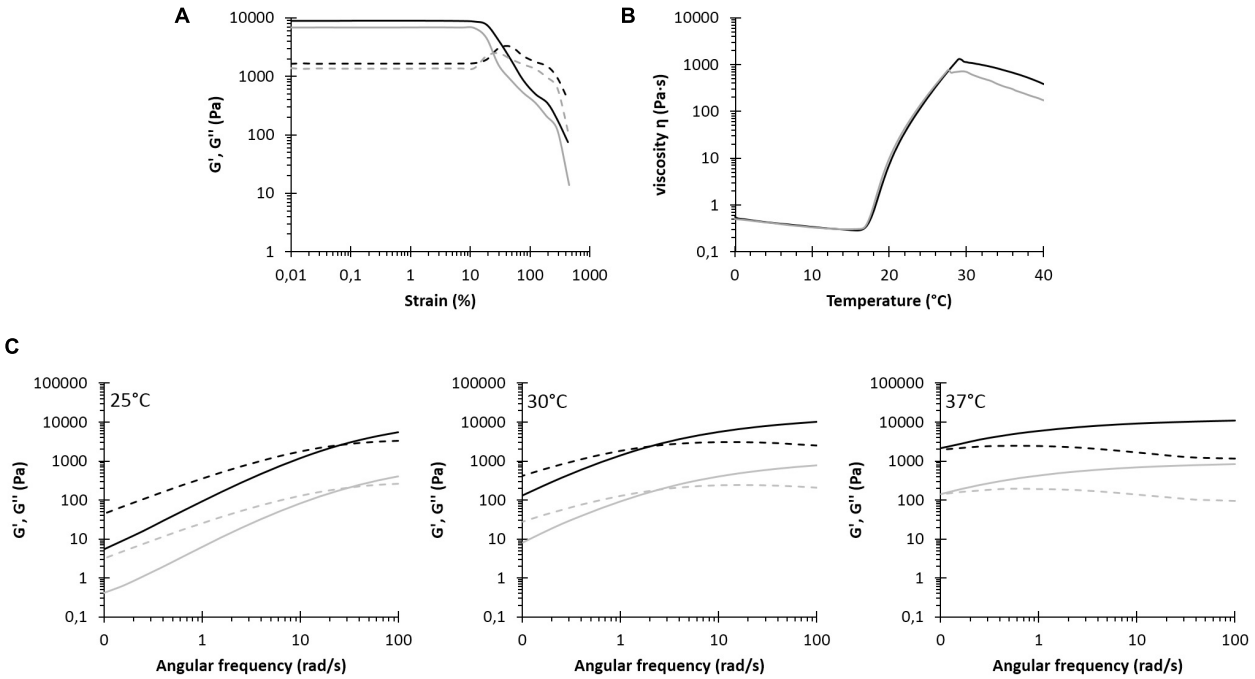

FIGURE 1 | Rheological characterization of NHP407 (black) and SHP407 (gray) hydrogels. **(A)** Storage (G′, continuous line) and loss (G″, dashed line) moduli trends as a function of applied strain at 37°C. **(B)** Trend of viscosity (η) as a function of temperature within 0–40°C temperature range. **(C)** G′ and G″ trends (continuous and dashed lines, respectively) as a function of angular frequency at 25, 30, and 37°C. G′ and G″ values of SHP407 hydrogels were divided by a factor of 10.

hydrogel pH progressively decreased toward the value of the surrounding aqueous medium, with no significant differences between NHP407 and SHP407 hydrogels at all investigated time points (after 24 h incubation in a buffer at pH 5, NHP407 and SHP407 gels reached a pH value of 5.32 ± 0.03 and 5.32 ± 0.00, respectively) (**Figure 2A**). The progressive change of hydrogel pH over time was then evaluated according to Eq. 1 (**Figure 2C**), highlighting that pH variations in SHP407-based hydrogels showed a faster kinetics compared to NHP407-based systems up to 45 min incubation time. For instance, NHP407 and SHP407 gels covered 42.01 ± 3.42 and 52.00 ± 0.65% ($0.01 < p < 0.05$) of the pH delta between their initial pH value and the pH of the buffer (i.e., pH 5) within the first 30 min of incubation, respectively. As control condition, pH transfer tests were also conducted by soaking the gels in neutral pH environment (i.e., PBS) (**Figure 2B**). As expected, both NHP407 and SHP407 hydrogels did not show significant pH variations at each analyzed time point, with the exception of 24 h incubation for SHP407-based formulation (from 60 min to 24 h incubation time, SHP407 hydrogel pH significantly decreased from 7.76 ± 0.01 to 7.61 ± 0.04, $0.01 < p < 0.05$). On the other hand, at each investigated time point the pH of SHP407 hydrogels was significantly higher than that of NHP407 sol-gel systems ($0.0001 < p < 0.001$), in accordance with its higher initial pH. After 24 h incubation in contact with PBS, NHP407 and SHP407 hydrogels exhibited pH values of 7.26 ± 0.02 and 7.61 ± 0.04, respectively. The progressive pH gradient moving through gel thickness was qualitatively evaluated observing the change in color of gels containing pH indicators and put in contact with acetate buffer at pH 5 or PBS (**Figure 2D**). In accordance with quantitative measurements, no changes in the color of the hydrogels were observed upon incubation in the presence of PBS, meaning that no gradient of pH change was moving through hydrogel thickness. Conversely, a progressive variation of gel color from blue to yellow was observed in gels incubated in acetate buffer at pH 5.

Investigation of Hydrogel Swelling and Stability in Aqueous Media

The capability of NHP407- and SHP407-based gels to absorb fluids from the surrounding environment undergoing swelling/erosion phenomena was evaluated at 37°C by incubating the samples in contact with PBS or acetate buffer at pH 5. Gel swelling [gel mass change in wet state (%)] and dissolution/degradation [gel mass change in dry state (%)] over time are reported in **Figures 3A,B**, meanwhile **Figure 3C** reports swelling ratio data evaluated at each time point according to Park et al. (2009).

Irrespective of the surrounding environment pH, swelling prevailed over erosion/dissolution (**Figures 3A,B**) up to 7 days incubation for both NHP407 and SHP407 gels. However, with increasing incubation time in aqueous media, hydrogel dissolution/degradation became progressively predominant over swelling, with a consequent deswelling (i.e., a decrease in swelling percentage) which assumed negative values when erosion/dissolution completely prevailed over absorption phenomena. In the presence of a buffer at pH 5, NHP407- and SHP407-based gels showed similar swelling behavior, with

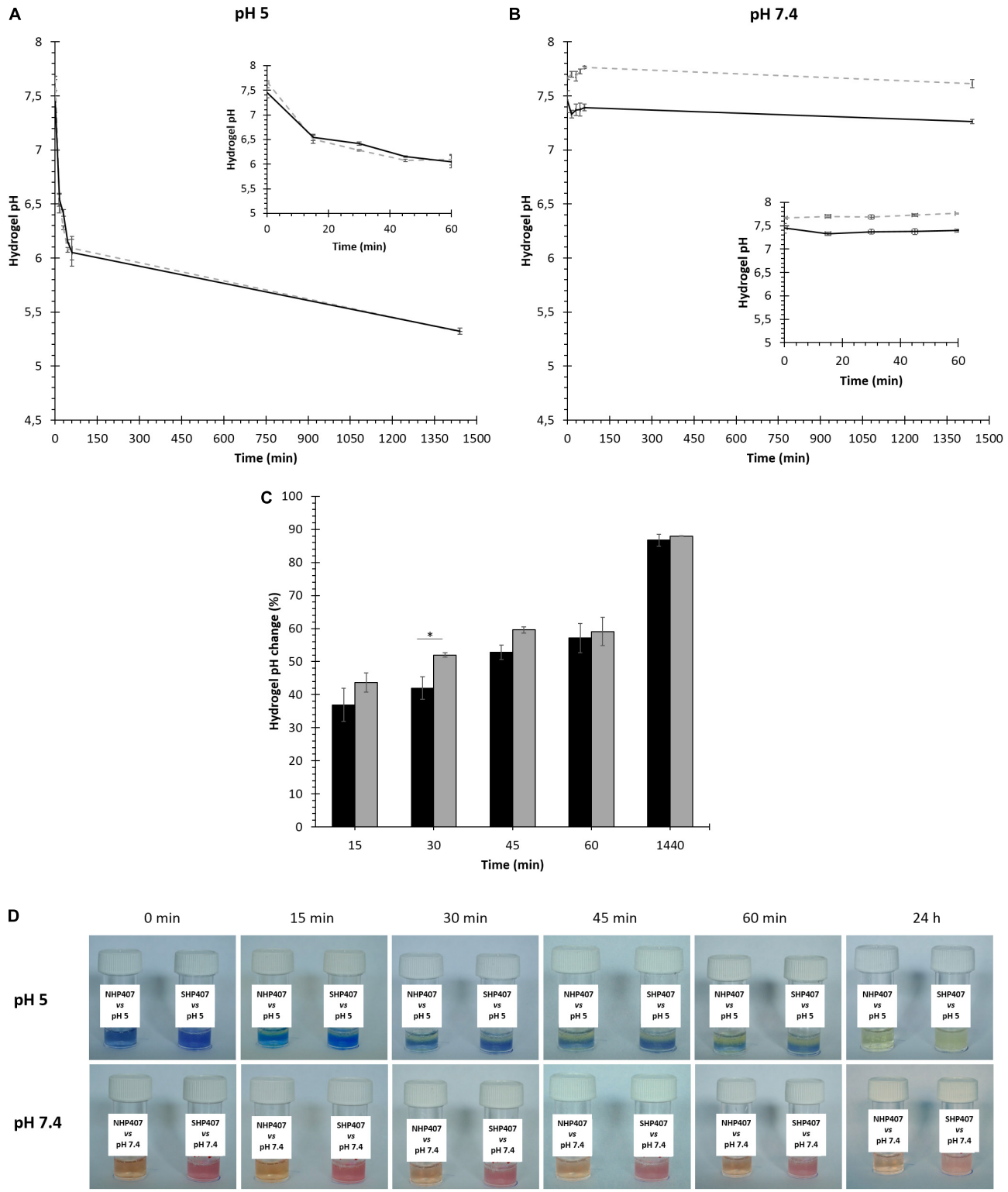

FIGURE 2 | Sensitivity of NHP407- and SHP407-based gels to environmental pH (pH 5 and 7.4). **(A,B)** NHP407 (black, continuous line) and SHP407 (gray, dashed line) hydrogel pH values after incubation in buffered solutions at pH 5 or 7.4 for different time intervals. Magnified inserts evidence the trend of hydrogel pH within the first 60 min incubation in aqueous medium. **(C)** Percentage of pH change (evaluated according to Eq. 1) in NHP407- (black) and SHP407- (gray) based hydrogels upon incubation in the presence of acetate buffer at pH 5 for different time intervals. **(D)** Representative images of NHP407 and SHP407 gels containing pH indicators (phenol red for neutral/basic pH and bromocresol purple for acid pH) which change their color in response to pH changes. Gels were soaked in acetate buffer solution at pH 5 or phosphate buffered solution at pH 7.4 for different time intervals.

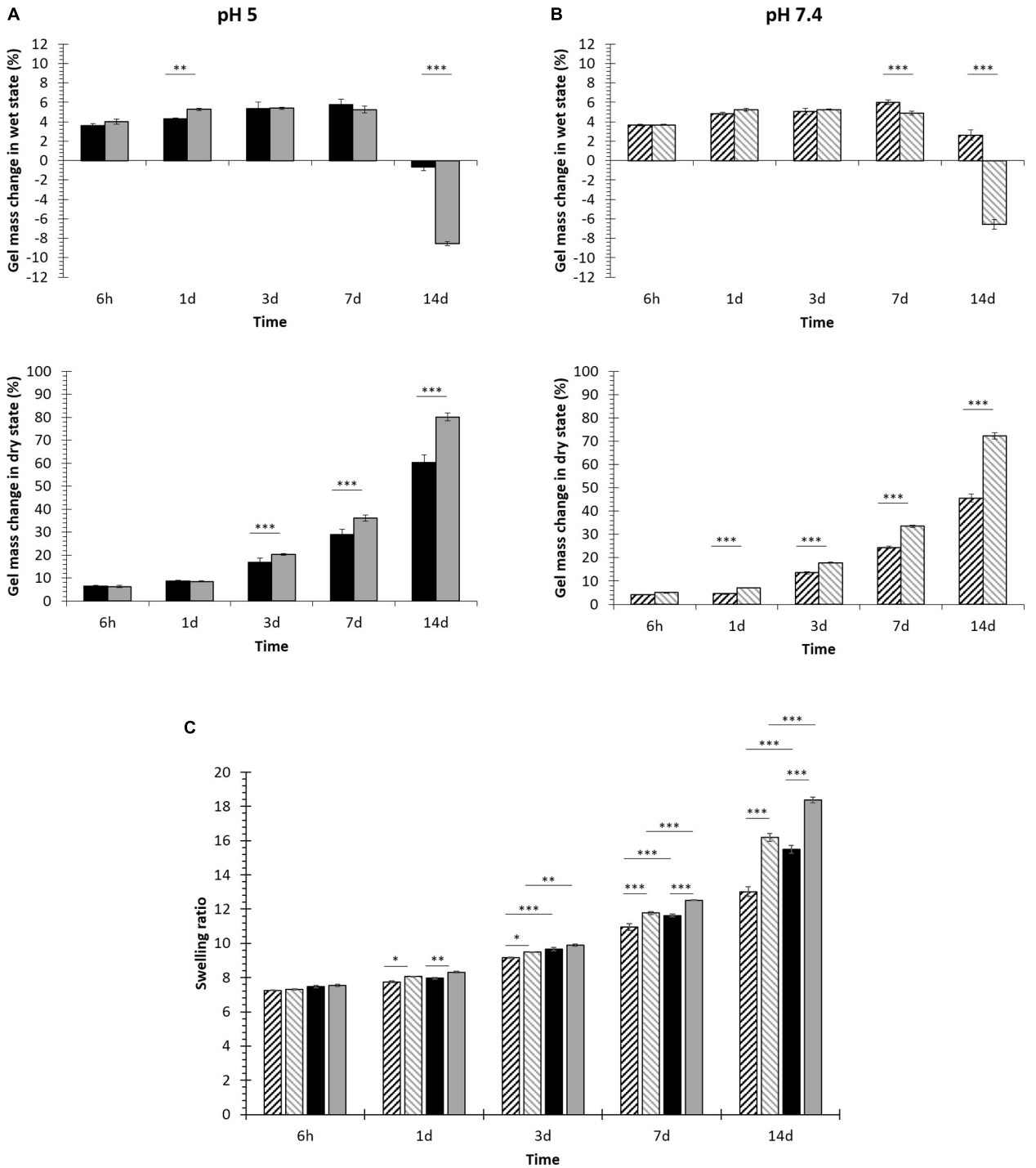

FIGURE 3 | NHP407 (black) and SHP407 (gray) gel behavior in aqueous environments at different pH values. **(A)** Percentage of swelling and dissolution over time for NHP407 and SHP407 gels incubated in an aqueous medium at pH 5. **(B)** Percentage of swelling and dissolution over time for NHP407 and SHP407 gels incubated in PBS (pH 7.4). **(C)** Swelling ratio evaluated for NHP407 (black) and SHP407 (gray) gels incubated in acetate buffer at pH 5 (plain) or PBS (patterned) for different time intervals (6 h, 1, 3, 7, and 14 days).

significantly different swelling percentages at 1 and 14 days incubation time. In the same environment, SHP407-based gels showed significantly higher dissolution compared to NHP407-based ones starting from 3 days incubation time ($0.0001 < p < 0.001$), reaching a dissolution of 78.98 ± 0.15 and $60.61 \pm 0.98\%$, respectively after 14 days incubation. Gels

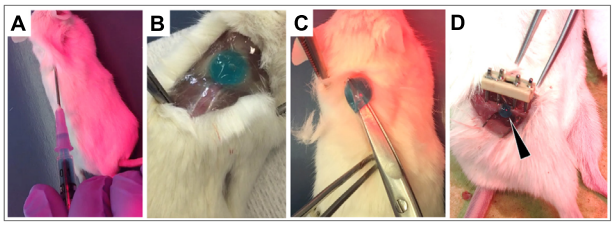

FIGURE 4 | Injection and gelation of SHP407 hydrogel *in situ* into murine cadavers. **(A)** Using an 18G needle, blue-colored SHP407 hydrogel was injected s.c. into the neck region. Physiological temperature of the organism was maintained using a heating pad and red light. **(B)** Solidified SHP407 gel 5 min post s.c. injection into the neck region. **(C)** Test of solidity by lifting the SHP407 gel up. **(D)** Solid SHP407 gel (black arrow) exclusively present within the osteotomy area 5 min post injection into the fracture gap.

immersed in PBS showed a similar swelling trend, with SHP407 gels undergoing significant deswelling compared to NHP407 ones. Similarly to data collected from hydrogels incubated in acid pH aqueous medium, SHP407 gels exhibited higher weight loss in the dry state compared to NHP407, with significant differences ($0.0001 < p < 0.001$) from 1 day incubation on. Hence, SHP407-based sol-gel systems showed higher destabilization compared to NHP407-based ones irrespective of the environmental pH surrounding them. This consideration was also proved by the analysis of swelling ratio data (**Figure 3C**), that evidenced a higher swelling ratio for SHP407 gels compared to NHP407 ones at each analyzed time point, at both pH 5 and pH 7.4. On the other hand, the swelling ratio for both NHP407 and SHP407 gels was higher at pH 5 compared to pH 7.4 at each time point, with significant differences on 3, 7 and 14 days incubation.

Ex vivo Evaluation of Hydrogel Injectability and Gelation

In order to study hydrogel injectability, dispersion and gelation *in situ* within an organism, *ex vivo* proof of concept studies were carried out working with murine cadavers. In detail, the dispersion and gelation of SHP407 hydrogel were investigated by injecting 200 μl subcutaneously (s.c.) in the neck region (**Figure 4A**). In **Figures 4B–D**, representative images of solid SHP407 gel at 5 min post injection are depicted. The blue color derives from food coloring that was previously confirmed to not affect gelation properties (data not shown). **Figure 4B** clearly shows a minimum dispersion of SHP407 sol-gel system as it presented as a coherent and spherical gel. **Figure 4C** demonstrates the solidity of SHP407 system, which allowed lifting the hydrogel using scissors. To study the dispersion and gelation of SHP407 in a more advanced application, a 0.7 mm femoral midshaft osteotomy was created in the cadaver and the hydrogel (∼15 μl) was introduced into the osteotomy gap using a 18G needle (**Figure 4D**). The spherical shape and the finding that the SHP407 gel remained in the gap region, without dripping onto the muscle tissue below the femur, further stresses the quick gelation and minimum dispersion *in situ*.

Particle Characterization

Mesoporous silica nanoparticles and SIP were initially synthesized and characterized separately (see **Supplementary Material**). In detail, MSNs were physico-chemically and morphologically characterized by XRD, ATR-FTIR spectroscopy, nitrogen adsorption and desorption analyses, TG analyses, DLS, SEM and TEM, meanwhile the SIP and its constituent blocks (i.e., compounds **1** and **2**) were characterized by ^{1}H NMR spectroscopy. The functionalization of MSNs with the pH-responsive polymeric coating was accomplished following a two-step synthetic protocol: (i) MSNs functionalization with an organosilane acting as linker between the surface and the SIP (MSN-CSs) and (ii) DIPEA-mediated alcohol activation and mixing with the particles (**Scheme 2**). SIP-coated MSNs (MSN-CS-SIP) resulting from the grafting of SIP on MSN surface were then characterized as MSNs as such to assess the effect of the coating procedure on particle physico-chemical and morphological properties.

Characterization of SIP-Coated Mesoporous Silica Nanoparticles

As observed in **Supplementary Figure S3A**, the diffraction maxima typical of mesoporous silica nanoparticles were still observable after the grafting of the SIP on top of mesoporous silica nanoparticles. The amount of organic matter incorporated was analyzed though TG analysis (**Supplementary Figure S3B**). The addition of the self-immolative coating increased the weight loss up to *ca.* 15%, compared to MSNs as such. The samples were further analyzed using ATR-FTIR spectroscopy (**Supplementary Figure S3C**), unrevealing the presence of new functional groups. For instance, vibration bands typical of the carbamate of the self-immolative polymer (C=O stretching vibration at 1630 cm^{-1}) were present in MSN-CS-SIP ATR-FTIR

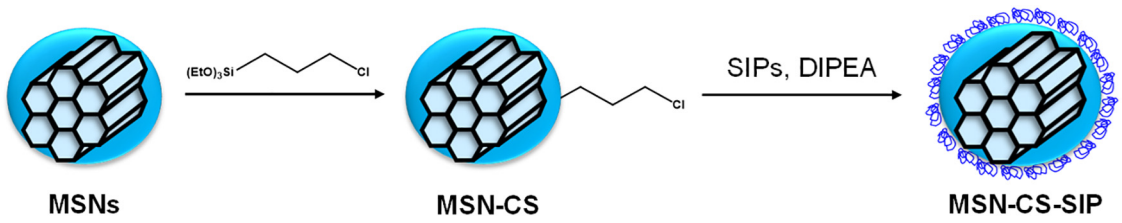

SCHEME 2 | Schematic representation of the coating of MSNs with the SIP. First, the nanoparticles were surface modified with a chloro alkoxysilane (MSN-CS) and then subjected to SIP grafting, leading to SIP-coated MSNs (MSN-CS-SIP).

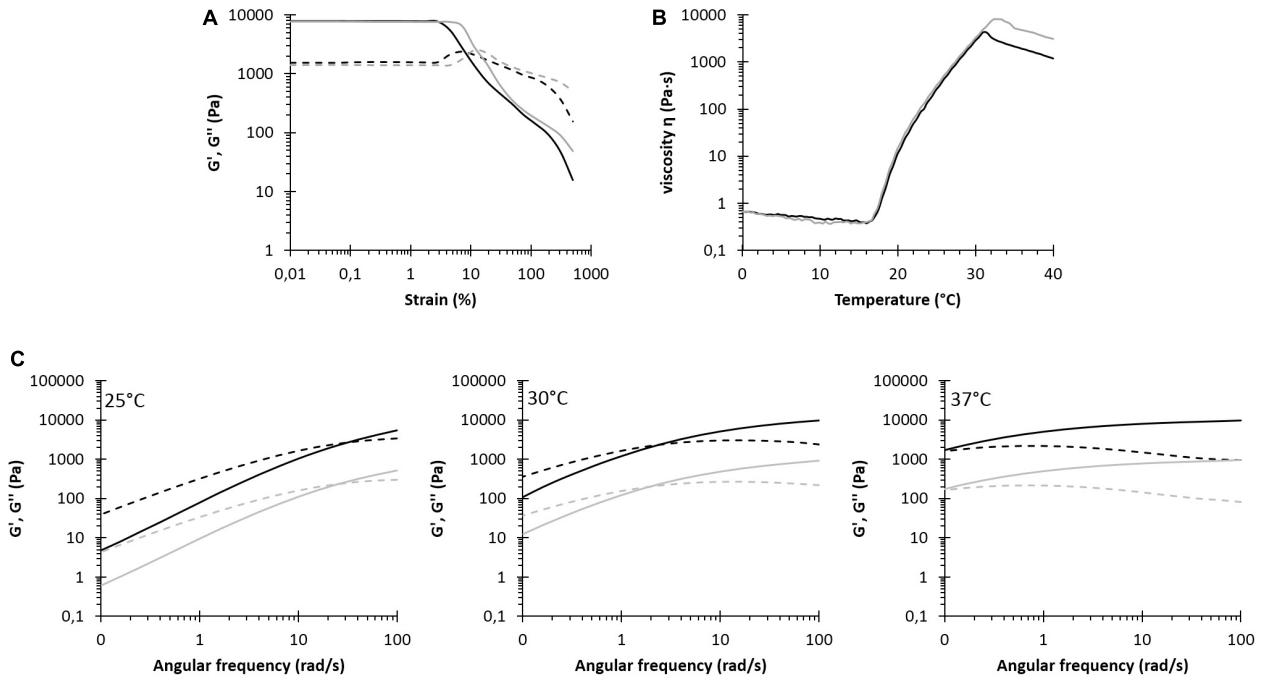

FIGURE 5 | Rheological characterization of NHP407_MSN-CS-SIP (black) and SHP407_MSN-CS-SIP (gray) hydrogels. **(A)** Storage (G′, continuous line) and loss (G″, dashed line) moduli trends as a function of applied strain at 37°C. **(B)** Trend of viscosity (η) as a function of temperature within 0–40°C range. **(C)** G′ and G″ trends (continuous and dashed lines, respectively) as a function of angular frequency at 25, 30, and 37°C. G′ and G″ values of SHP407_MSN-CS-SIP hydrogels were divided by a factor of 10.

spectrum. N_2 adsorption analysis (**Supplementary Figure S3D**) showed a reduction of the textural parameters after the SIP coating. In detail, the specific surface area decreased *ca.* 40% after SIP grafting (from *ca.* 1000 m^2/g for MSNs to *ca.* 650 m^2/g for MSN-CS-SIP).

Hybrid Hydrogel Characterization

NHP407- and SHP407-based hydrogels (15% w/v) encapsulating MSN-CS-SIP (5 mg/mL) were first characterized through rheological tests. Release tests against different pHs were conducted on hydrogels encapsulating MSN-CS-SIP previously loaded with a fluorescent dye as model drug (Ru). Finally, hybrid hydrogel injectability, gelation, distribution and detectability upon subcutaneous injection were evaluated *ex vivo* in a rodent model.

Thermo-Sensitive Behavior of NHP407 and SHP407 Hydrogels Encapsulating MSN-CS-SIP

In order to assess the effects of particle addition on hybrid hydrogel gelation, rheological characterization of NHP407_MSN-CS-SIP and SHP407_MSN-CS-SIP hydrogels was conducted by strain sweep, frequency sweep and temperature ramp tests (**Figure 5**). **Figure 5A** reports the trends of storage and loss moduli at 37°C as a function of applied strain within the range 0.01–500%. Both storage and loss moduli initially showed a constant value (within the LVE region) up to the linearity limit (γ_L) which turned out to be 2.83 and 7.25% for NHP407_MSN-CS-SIP and SHP407_MSN-CS-SIP gels, respectively. Moreover, within the linear viscoelastic region, G′ showed higher values than G″ for both NHP407_MSN-CS-SIP and SHP407_MSN-CS-SIP gels, proving that at 37°C the developed systems were in the gel state. NHP407_MSN-CS-SIP and SHP407_MSN-CS-SIP gels exhibited mean G′ values within the LVE region of 7800 and 7600 Pa, respectively, meanwhile their Yield Stress was measured to be 262 and 442 Pa. For strain value higher than γ_L, storage modulus started to decrease, while G″ increased reaching a maximum value (2350 and 2550 Pa for NHP407_MSN-CS-SIP and SHP407_MSN-CS-SIP gels, respectively), as typical for structured networks. After this maximum value was achieved, also G″ started to decrease as a consequence of macro-cracks development throughout the sample which finally led to its complete failure, with the hydrogel behaving as a sol (i.e., G″ > G′). Hydrogel progressive transition from the sol to the gel state with increasing temperature was investigated by frequency sweep tests conducted within the angular frequency range from 0 to 100 rad/s at 25, 30, and 37°C (**Figure 5C**). **Table 3** reports the frequency values at G′/G″ crossover ($\omega_{G'/G''\,crossover}$) and the G′/G″ delta at 100 rad/s ($\Delta_{G'/G''-100\ rad/s}$) for NHP407_MSN-CS-SIP and SHP407_MSN-CS-SIP evaluated at 25, 30, and 37°C. For both NHP407_MSN-CS-SIP and SHP407_MSN-CS-SIP, $\omega_{G'/G''\,crossover}$ value decreased with increasing temperature, as a sign of hydrogel temperature-drive gelation. On the other hand, particle encapsulation within SHP407-based systems led to lower $\omega_{G'/G''\,crossover}$ values compared to SHP407 hydrogels as such (at 25°C $\omega_{G'/G''\,crossover}$ of 32.25 and 25.96 Pa for SHP407 and SHP407_MSN-CS-SIP hydrogels, respectively) (see

section "Thermo-Sensitive Behavior of NHP407 and SHP407 Hydrogels"). Conversely, MSN-CS-SIP loading within NHP407 hydrogels resulted in slightly increased $\omega_{G'/G''\,crossover}$ values compared to NHP407 as such (at 25°C $\omega_{G'/G''\,crossover}$ increased from 27.46 rad/s for NHP407 to 30.98 rad/s for NHP407_MSN-CS-SIP). Despite these differences, at 37°C both the systems appeared to be in the gel state, but complete gel development (i.e., G′ independent over frequency) was not achieved, similarly, to NHP407 and SHP407 as such.

The trend of viscosity as a function of temperature for NHP407_MSN-CS-SIP and SHP407_MSN-CS-SIP is reported in **Figure 5B**, meanwhile the characteristic parameters of temperature ramp tests are summarized in **Table 4**. Initial viscosity slightly increased in MSN-CS-SIP-containing hybrid hydrogels compared to pure NHP407 and SHP407 sol-gel systems ($\eta_{0°C}$ values for SHP407_MSN-CS-SIP and SHP407 systems were 0.66 and 0.50, respectively). Similarly, viscosity values of MSN-CS-SIP-containing hydrogels slightly increased compared to hydrogels as such at each tested temperature within the analyzed range; for instance, at 25°C NHP407_MSN-CS-SIP and virgin NHP407 exhibited a viscosity of 265.0 and 201.7 Pa · s, respectively. On the other hand, the trend of the onset temperature of gelation for SHP407-based hybrid system was opposite, with SHP407_MSN-CS-SIP hydrogel showing a slightly lower T_{onset} value compared to virgin sol-gel system. No differences in T_{onset} were observed between NHP407 and NHP407_MSN-CS-SIP.

Payload Release Tests in Aqueous Environment at pH 5 or 7.4

The progressive release of the red dye tris(2,2′-bipyridine)dichloro ruthenium (II) (Ru) from SIP-coated MSNs embedded within NHP407 and SHP407 hydrogels (NHP407_MSN-CS-SIP-Ru and SHP407_MSN-CS-SIP-Ru) was investigated in aqueous environment at different pH values. **Figure 6A** reports payload release profiles over time from SHP407_MSN-CS-SIP-Ru gels incubated in pH 5 and pH 7.4 aqueous media. Similar trends were obtained also from NHP407_MSN-CS-SIP-Ru gels (data not reported). Additionally, at each analyzed time point, both NHP407_MSN-CS-SIP-Ru and SHP407_MSN-CS-SIP-Ru showed significantly higher Ru dye release in pH 5 buffer compared to PBS ($0.0001 < p < 0.001$). Furthermore, the exposure of free amines along SHP407 polymer chains induced an increased release of Ru molecules in acid pH environment from SHP407_MSN-CS-SIP-Ru compared to NHP407_MSN-CS-SIP-Ru at each analyzed time point (statistically significant differences at 72 and 96 h observation time, $0.01 < p < 0.05$) (**Figure 6B**). On the other hand, at pH 7.4, Ru release from SHP407_MSN-CS-SIP-Ru was not significantly higher (approximately 5–6%) than its release from NHP407_MSN-CS-SIP-Ru (**Figure 6C**). Conversely, in acid pH environment higher differences were detected at each investigated time interval, with released Ru amounts approximately 10% higher for SHP407_MSN-CS-SIP-Ru compared to NHP407_MSN-CS-SIP-Ru.

TABLE 3 | Frequency values at G′/G″ crossover ($\omega_{G'/G''\,crossover}$) and G′/G″ delta at 100 rad/s ($\Delta_{G'/G''\_100\ rad/s}$) for NHP407_MSN-CS-SIP and SHP407_MSN-CS-SIP evaluated at 25, 30 and 37°C.

	$\omega_{G'/G''\,crossover}$ (rad/s)		$\Delta_{G'/G''\_100\ rad/s}$ (Pa)	
	NHP407_MSN-CS-SIP	SHP407_MSN-CS-SIP	NHP407_MSN-CS-SIP	SHP407_MSN-CS-SIP
25°C	30.98	25.96	2060	2160
30°C	2.37	2.01	7220	6980
37°C	<0.1	<0.1	8840	8745

TABLE 4 | T_{onset}, $\eta_{0°C}$ and $\eta_{25°C}$ of NHP407_MSN-CS-SIP and SHP407_MSN-CS-SIP hydrogels estimated from rheological temperature ramp tests.

	NHP407_MSN-CS-SIP	SHP407_MSN-CS-SIP
$\eta_{0°C}$ (Pa · s)	0.64	0.66
T_{onset} (°C)	16.0	15.7
$\eta_{25°C}$ (Pa · s)	265.0	321.0

Ex vivo Evaluation of Hybrid Hydrogel Injectability and Gelation

Ex vivo evaluation of hybrid hydrogel injectability, gelation and distribution was conducted according to the protocol previously adopted for SHP407 hydrogel as such. In detail, hybrid SHP407 hydrogel embedding MSN-CS-SIP-Ru was compared with SHP407 hydrogels as such and MSN-CS-SIP-Ru aqueous dispersion. Moreover, the fluorescent nature of particles' cargo was utilized to study the detectability of the materials under the skin via an *in vivo* imaging system (IVIS). Prior to s.c. injection into murine cadavers, the fluorescence-based detectability of Ru-loaded MSN-CS-SIP within aqueous dispersion or upon incorporation within SHP407 hydrogel was confirmed using IVIS imaging (**Figure 7A**, ex/em filter: 465 nm/ Cy5.5). Then, the just finalized mice were injected with 200 µl of material at similar concentrations, maintained at physiological body temperature and imaged after 5 min of incubation using the IVIS. **Figure 7B** shows the fluorescence signal obtained from Ru-loaded MSNs (ex/em filter: 465 nm/ Cy5.5), which was detectable for animals 1, 3, and 4 in accordance to the nature of the injected material. In fact, animal 1 received an injection of MSN-CS-SIP-Ru dispersion, animal 2 an injection of SHP407 hydrogel as such and animals 3 and 4 were injected with the composite hydrogel SHP407_MSN-CS-SIP-Ru. By comparing animals 1 to 3 and 4, the animal that received MSN-CS-SIP-Ru suspended in physiological fluid already showed a less round shape of the fluorescence-positive injection area 5 min after injection. After the imaging, the injection site was uncovered (**Figure 7C**). The photographic pictures confirmed the previously seen low dispersion and good solidification of SHP407 hydrogel (animal 2), which was found to be similar to the distribution and gelation properties of the composite hydrogel (animals 3 and 4). On the contrary, MSN-CS-SIP-Ru injected as suspension in physiological fluid dispersed broadly as shown in the magnified image of the injection area. **Figure 7D** underlines the successful

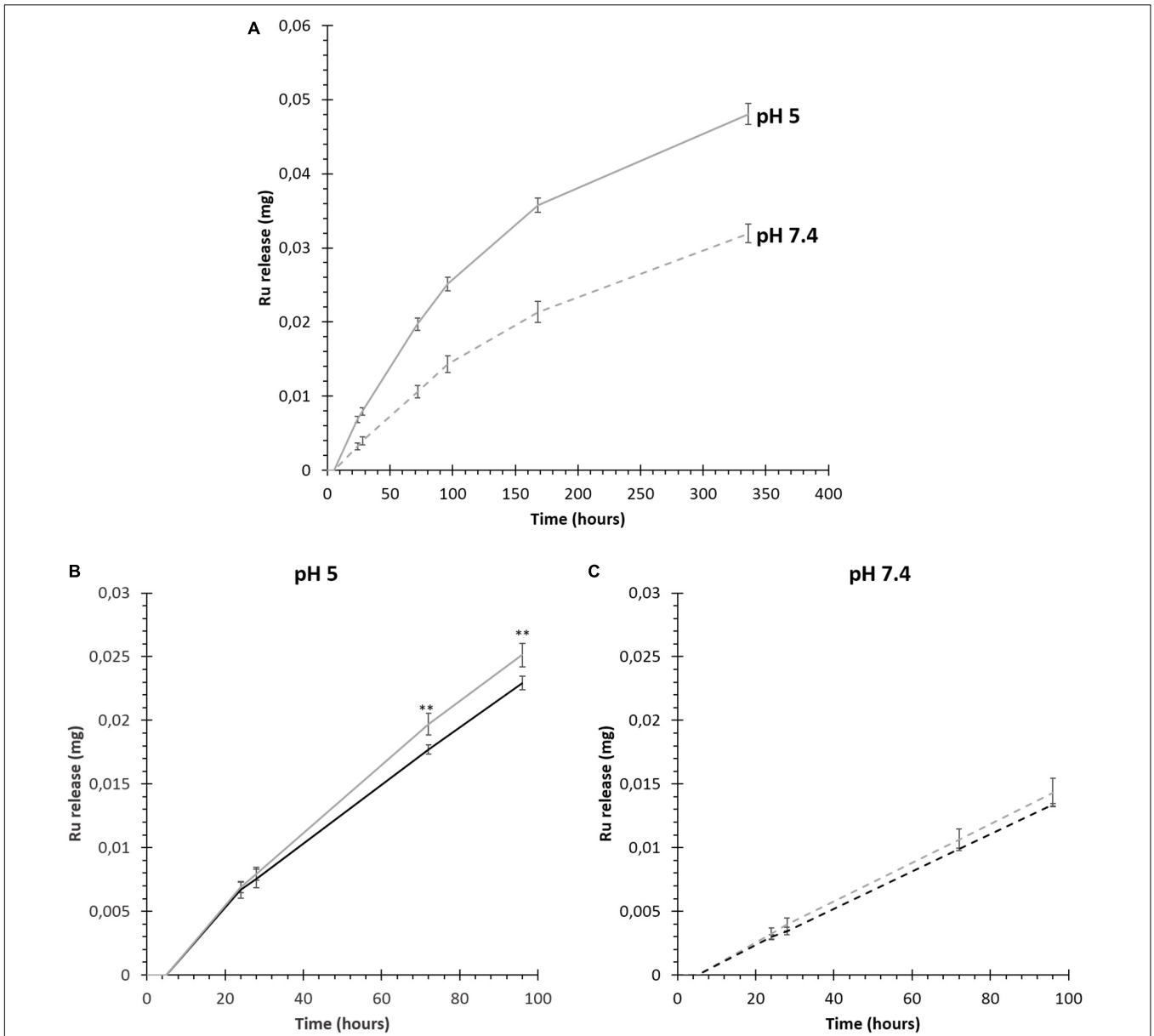

FIGURE 6 | Release of Ru dye from MSN-CS-SIP-Ru-containing hydrogels (NHP407_MSN-CS-SIP-Ru in black, SHP407_MSN-CS-SIP-Ru in gray) in aqueous media at pH 5 and pH 7.4. **(A)** Ru release from SHP407_MSN-CS-SIP-Ru hydrogels incubated in acetate buffer at pH 5 (continuous line) or in phosphate buffered saline (pH 7.4) (dashed line). **(B)** Trend of Ru release in pH 5 aqueous environment from NHP407_MSN-CS-SIP-Ru (black continuous line) and SHP407_MSN-CS-SIP-Ru hydrogels (gray continuous line) within the first 4 days of observation. **(C)** Ru release in PBS (pH 7.4) from NHP407_MSN-CS-SIP-Ru (black dashed line) and SHP407_MSN-CS-SIP-Ru hydrogels (gray dashed line) within the first 4 days of observation.

gelation of SHP407 as such and in composite with MSN-CS-SIP-Ru, as both could be lifted up as a whole using forceps (black arrows) and remained in their solid form after harvest from the injection site (**Figure 7D**, dashed pictures, top left).

DISCUSSION

In a scenario characterized by the progressive development and optimization of patient-specific smart therapeutic approaches, there is an urgent need of *ad hoc* designed injectable formulations with the potential to be finely tuned according to the pathological environment. Additionally, these injectable therapeutics could be designed to exhibit sensitivity to different physico-chemical stimuli, thus making them able to properly adapt their properties in response to external environment characteristics, with a consequent capability to smartly exert their function in the target tissue/organ. Within this complex and challenging scenario, in this work we attempted to design and thoroughly characterize a new injectable formulation responding

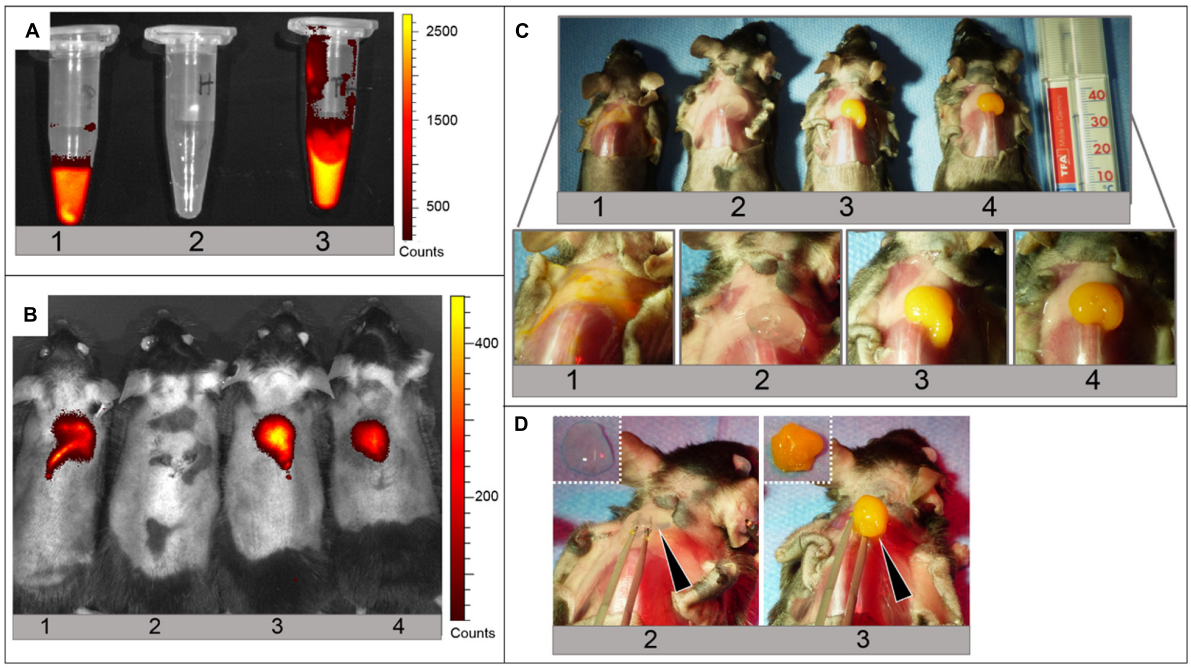

FIGURE 7 | Injection and gelation of MSN-CS-SIP-Ru aqueous dispersion, SHP407 hydrogel and SHP407_MSN-CS-SIP-Ru hybrid hydrogel *in situ* into murine cadavers. **(A)** IVIS read at ex/em filter: 465 nm/ Cy5.5 of MSN-CS-SIP-Ru aqueous dispersion (1), SHP407 hydrogel (2) and SHP407_MSN-CS-SIP-Ru hybrid hydrogel (3) before injection in the animal model. **(B)** IVIS read at ex/em filter: 465 nm/ Cy5.5 of murine cadavers with maintained physiological body temperature subjected to injection of MSN-CS-SIP-Ru aqueous dispersion **(1)**, SHP407 hydrogel **(2)** and SHP407_MSN-CS-SIP-Ru hybrid hydrogel **(3,4)**. Only those animals injected with samples containing Ru-loaded MSN-CS-SIP exhibited a fluorescence signal. **(C)** Photographic images of the animals previously measured in the IVIS (same numbering) including a magnification of the injection site. Solid materials can be seen in animal **(2–4)**, whereas MSN-CS-SIP-Ru were broadly dispersed in the animal injected with particle suspension (animal 1). **(D)** Test of gelation of SHP407 (animal 2) and SHP407_MSN-CS-SIP-Ru (animal 3) by lifting the material up (black arrows). The solid form was maintained after the harvest (dashed pictures, top left of each image).

to the aforementioned demands by exploiting the custom-made nature of its components. In fact, we combined amphiphilic PEU-based thermo-sensitive sol-gel systems with MSNs coated with a SIP providing them sensitivity to acid pH environments. Custom-made PEUs were used as alternative to commercially available Poloxamers® to develop thermo-sensitive hydrogels with improved gelation properties (i.e., lower critical gelation concentration, faster gelation in physiological conditions), mechanical strength and residence time in aqueous environments (Boffito et al., 2016). Additionally, PEU versatile chemistry was exploited to introduce free amines along the polymer backbone to provide the resulting material with an enhanced sensitivity to external pH environment. On the other hand, MSNs have been selected for their easy synthesis route, tunable pore morphology and dimension, suitability to surface functionalization to expose specific functional moieties and high surface area and pore volume, which are responsible for their high loading capacities of different payloads (e.g., drugs, growth factors) (Narayan et al., 2018; Zhou et al., 2018; Xu et al., 2019; Manzano and Vallet-Regí, 2020). However, mesoporous particles exhibit an open porous network that usually makes payload diffusion out from them very fast. In this regard, the introduction of gatekeepers closing the pore entrance and opening on-demand in the presence of specific conditions has been reported as a valuable strategy to control payload release (Wen et al., 2017). In this work, MSNs were surface functionalized with a self-immolative polymer caging their pore mouth and undergoing head to tail degradation in the presence of acid pH, thus inducing pore opening and acid-pH triggered cargo release, as already demonstrated by Gisbert-Garzarán et al. (2017). According to a bottom up approach, the key components of the therapeutic formulation, i.e. the hydrogel and the particles, were first designed and characterized as single entities and then they were assembled to develop hybrid sol-gel systems answering to the previously described needs.

An amphiphilic water soluble PEU with acronym NHP407 was synthesized using Poloxamer® 407, HDI and N-Boc serinol as building blocks. Successful NHP407 synthesis was proved by ATR-FTIR spectroscopy, SEC analyses and ^{1}H NMR spectroscopy. The comparison between native P407 and NHP407 ATR-FTIR spectra proved the synthesis of a PEU containing P407 blocks. Indeed, in addition to P407 typical absorption peaks, new bands characteristic of urethane bonds appeared in NHP407 spectrum (**Supplementary Figure S1**). Additionally, complete consumption of isocyanate groups was proved by the absence of –N=C=O characteristic peak around 2200–2300 cm^{-1}. Similarly, ^{1}H NMR spectrum of NHP407 (**Supplementary Figure S2**) showed the characteristic peaks of all the building blocks used for its synthesis, i.e., resonances ascribable to the PEO and PPO segments of P407 and to the methylene protons of HDI blocks and serinol moieties (Caddeo et al., 2019). In addition, methyl

protons of Boc caging groups showed their typical resonance at 1.37 ppm, in the form of a sharp singlet overlapped to HDI signals (Caddeo et al., 2019). Finally, the successful binding of NHP407 building blocks through urethane bonds was demonstrated by the signal within the spectral range between 5.65 and 5.73, which is typical of N-H groups of urethane groups (Qin et al., 2019). However, also side-reactions leading to urea bond formation occurred during NHP407 synthesis, as proved by the presence of a signal in its ^{1}H NMR spectrum within the spectral region from 7.00 to 7.20 ppm (attributed to urea N-H groups) and the peak at 1630 cm^{-1} in its ATR-FTIR spectrum (ascribed to urea carbonyl groups) (**Supplementary Figures S1, S2**; Laurano et al., 2020). Nevertheless, despite urea by-product formation, a high molecular weight polymer with a narrow molecular weight distribution was obtained (NHP407 $\overline{M}_n$ and D were measured to be 44600 Da and 1.42, respectively). NHP407 was designed to expose Boc-protected amines along its polymer chains, which could be made available through a deprotection reaction in acid conditions, similarly to protocols habitually adopted during peptide synthesis. In this work, the protocol for Boc caging group removal from NHP407 chains was optimized to maximize free amine exposure, while avoiding detrimental polymer degradation (see **Supplementary Material**). In the optimized conditions, NHP407 was treated in a $CHCl_3$/TFA mixture at 90/10 v/v, obtaining SHP407. ATR-FTIR spectrum of SHP407 was completely overlapped to that of native NHP407, confirming the retention of PEU chemical structure and the complete removal of both $CHCl_3$ and TFA (**Supplementary Figure S1**). Similarly, also ^{1}H NMR spectrum of SHP407 sample was completely overlapped to that of native NHP407, with the exception of the peak attributed to the methyl protons of Boc caging groups at 1.37 ppm (**Supplementary Figure S2**). This peak, indeed, significantly decreased its intensity in SHP407 compared to NHP407, thus proving an almost complete removal of the Boc groups (deprotection yield > 90%). SEC analyses evidenced a slight decrease in number average molecular weight upon the deprotection reaction, which, however, fell within the typical SEC analysis error (approximately 10%) (Trathnigg, 2000). The number of exposed free amines along SHP407 chains turned out to be 3.07E18 ± 1.63E17 -NH_2/g_{SHP407} corresponding to the 93–94% of the total theoretical number of amines present along PEU chains (i.e., approximately 2–3 primary amines exposed per each SHP407 chain), in agreement with ^{1}H NMR analyses. SHP407 and NHP407 were then used to prepare thermo-sensitive sol-gel systems at 15% w/v polymer concentration in a physiological solution/PBS/buffer at pH 8 mixture at 80/10/10 volume ratio. This polymer concentration was selected based on the previous characterization performed on NHP407-based hydrogels by Boffito et al. (2016), which evidenced the high potential of this formulation as injectable fast-gelling hydrogel. On the other hand, the composition of the aqueous medium used to solubilize the polymers was optimized to force hydrogel initial pH toward a neutral value (thus protecting the SIP from degradation), while maximizing the possibility to change its pH in response to environmental pH value being a not-buffered solution. Qualitative characterization through tube inverting test highlighted that SHP407-based formulation showed a slightly increased Lower Critical Gelation Temperature and gelation time at 37°C compared to NHP407-based system. These results were further confirmed by frequency sweep tests conducted at 25, 30, and 37°C (**Figure 1C** and **Table 1**) which evidenced a slightly slowed down kinetics of SHP407-based gel formation compared to NHP407-based one (e.g., at 25°C $\omega_{G'/G''crossover}$ of SHP407 and NHP407 sol-gel systems was measured to be 32.25 and 27.46, respectively). Furthermore, also the temperature of gelation onset (T_{onset}) was slightly higher in SHP407 sol-gel system compared to NHP407 one (T_{onset} of 16.03 and 16.36), respectively (**Figure 1B** and **Table 2**). This different behavior can be probably correlated to the different hydrophobicity of NHP407 and SHP407: being NHP407 more hydrophobic than SHP407 due to the presence of Boc caging groups, the conditions required to induce polymer chains rearrangement into micelles were more easily reached in NHP407 aqueous solution compared to SHP407 one. Conversely, SHP407-based micelles required slightly more time and higher temperature to form, but then they turned out to be able to easily and quickly arrange into a gel network similarly to NHP407 micelles. In fact, at 37°C both NHP407 and SHP407 systems exhibited $\omega_{G'/G''crossover}$ values lower than 0.1 rad/s and turned out to be in the gel state, although a not complete gel development was achieved. This result can be correlated to the presence in SHP407-based system of a higher number of hydrogen bonds due to the exposure of free -NH_2 groups, which contribute together with hydrophobic interactions to the progressive chain arrangement into micelles and their consequent aggregation to finally form a gel (Aoki et al., 1994; Laurano et al., 2019). This high degree of physical crosslinking within SHP407 gel was probably also responsible for its lower resistance to applied deformation (γ_L of 18.6 and 11.6% for NHP407 and SHP407 gels, respectively) and Yield Stress (YS of 1790 and 875 Pa for NHP407 and SHP407 gels, respectively) compared to NHP407-based one (**Figure 1A**). Despite these slight differences, the G′, G″ and viscosity trends reported in **Figure 1** and the data summarized in **Tables 1**, **2** clearly evidenced that the exposure of free amines along PEU chains did not detrimentally affect the thermo-responsiveness of SHP407 hydrogel that retained the capability to quickly undergo gelation in physiological conditions. As the final hybrid formulation has been designed to release the payload encapsulated into MSNs in response to a pH trigger, the capability of both NHP407 and SHP407 gels to transfer pH changes from the surrounding aqueous environment toward their core was quantitatively evaluated through hydrogel pH measurements upon incubation with buffered solutions at pH 5 or 7.4 for predefined time intervals (**Figures 2A–C**). The progressive pH gradient through gel thickness was also visually analyzed using pH indicators (**Figure 2D**). The exposure of free amino groups along SHP407 chains effectively accelerated the transfer of acid pH through gel thickness compared to NHP407-based system. Indeed, faster pH variation kinetics (hydrogel pH change defined according to Eq. 1 within the first 30 min incubation in pH 5 environment was measured to be 42 and 52% for NHP407 and SHP407 gels, respectively) and gradient movement toward the gel core were observed in SHP407-based hydrogel compared to NHP407-based one,

probably as a consequence of the progressive protonation of exposed -NH_2 along SHP407 chains in acid environment. However, after this initial accelerated pH change in SHP407-based gel up to approximately 45 min incubation, the trend of pH of both kinds of gels became almost the same, with the pH value progressively tending to 5. On the other hand, Boc-deprotection did not affect the behavior of the gels in contact with a neutral pH environment, with no statistically significant differences. Gel swelling and stability in aqueous media were evaluated in the same conditions used to evaluate pH transfer potential. Due to the physical interactions responsible for micelle packing and gel network formation, two distinct and concurrent phenomena can be distinguished upon gel incubation in an aqueous environment, i.e., swelling and erosion/dissolution. In fact, in a watery environment, the gel network tends to absorb fluids from the surrounding environment, undergoing swelling. However, absorbed water molecules also induce a progressive dissolution of the polymer chains, which constitute the micelles, resulting in erosion/dissolution of the gels and therefore a decrease in hydrogel dry weight. The trends of swelling and dissolution/degradation (**Figures 3A,B**) of NHP407 and SHP407 gels were similar with dissolution/erosion phenomena becoming predominant over swelling with increasing incubation time. No clear dependence of gel swelling/stability over the pH of the surrounding aqueous medium was observed. Indeed, irrespective of the pH of the surrounding aqueous medium, SHP407-based gels exhibited an increased destabilization compared to NHP407-based ones. This different behavior can be associated to SHP407 increased hydrophilicity and water-solubility, resulting from the removal of Boc caging groups rather than to a clear pH-responsiveness induced by the exposure of amino groups along polymer backbone. Hence, although the exposed primary amines along SHP407 chains made pH transfer through gel thickness faster, they did not provide the resulting gels with a marked pH-sensitivity, which would have conferred higher swelling to SHP407 gels compared to NHP407 systems in acid environment, as a consequence of the electrostatic repulsion forces arising among micelles upon amine protonation in acid media. Increasing the number of exposed functionalities along polymer chains would lead to the design of hydrogels with further accelerated pH change capability in acid media and significantly increased swelling potential in low pH environment. To achieve this goal different approaches could be adopted. For instance, the protocol for polymer synthesis could be optimized to introduce a higher number of amine-containing building blocks in each polymer chain. In this regard, Laurano et al. have recently reported a modified synthesis protocol resulting in the introduction along the backbone of a P407-based PEU of approximately 10E20 secondary amino groups/g_{PEU} (Laurano et al., 2020). Another possible route to be investigated consists in adapting the plasma treatment protocol developed by Laurano et al. (2019) to expose primary amines along polymer backbone using allylamine as monomer (Jeong et al., 2019) or ammonia gas (Mahmoudifard et al., 2017). In view of the final application of the developed formulation, SHP407 hydrogel injectability, dispersion and gelation *in situ* within an organism were demonstrated *ex vivo* using murine cadavers (**Figure 4**). Results of *ex vivo* studies concerning dispersion and gelation of SHP407 sol-gel systems were in line with *in vitro* studies, since proper solidification after 5 min of incubation in a 37°C environment was observed. The dispersion of SHP407 gel was quite low, as demonstrated by the spherical shape of the material upon visual inspection (**Figure 4B**). For future usage of the SHP407 as a place-keeper of e.g., pharmacologically active carrier-drug systems, the restricted dispersion is of outmost importance, since the location of the intervention would need to be precise and controllable. Moreover, penetration of deeper underlying tissues would not be favorable. Creating a femoral osteotomy and applying the SHP407 hydrogel into the fracture gap allowed for a more advanced application and confirmed the beneficial gelation and dispersion properties, as the hydrogel remained in the gap area and did not penetrate the tissues underneath the femur (**Figure 4D**).

As second component of the final hybrid formulation, pH-responsive nanoparticles were prepared as potential drug delivery systems by grafting a self-immolative polymer on the surface of mesoporous silica nanoparticles. The production of MSN-CS-SIP was carried out by first synthesizing and characterizing its building blocks, i.e., MSNs and SIP (see **Supplementary Material**). MSNs were then surface functionalized with the SIP in a two-step procedure according to **Scheme 2**. XRD patterns highlighted that the typical hexagonally ordered mesostructure of the particles was unaffected by the coating procedure (**Supplementary Figure S3A**). ATR-FTIR spectrum of MSN-CS-SIP sample exhibited the characteristic absorption bands of the SIP (i.e., CH and C=O stretching vibrations at approximately 3050 and 1630 cm^{-1}, respectively), thus proving the successful grafting of the SIP on MSN surface (**Supplementary Figure S3C**). Further confirmation of the presence of the polymeric coating covering the surface of the nanoparticles was provided by N_2 adsorption analysis (**Supplementary Figure S3A**) that evidenced a reduction of the characteristic textural parameters after the SIP coating (specific surface area of MSNs and MSN-CS-SIP were measured to be *ca.* 1000 vs. *ca.* 650 m^2/g, respectively), and TG analyses which showed the presence of a higher amount of organic material (corresponding to an increased weight loss within the 100–600°C temperature range) in MSN-CS-SIP compared to MSNs (**Supplementary Figure S3B**).

NHP407- and SHP407-based hydrogels encapsulating MSN-CS-SIP were finally prepared at 15% w/v and 5 mg/ml polymer and particle concentration, respectively. First, both NHP407_MSN-CS-SIP and SHP407_MSN-CS-SIP hydrogels were rheologically characterized to evaluate the effect of particle addition on the gelation potential and kinetics of the hybrid formulations (**Figure 5**). Particle embedding within PEU sol-gel systems turned out to affect both resistance to applied deformation and gelation kinetics of the resulting formulations. However, no detrimental effects hindering the transition from the sol to the gel state were observed. In fact, similarly to NHP407 and SHP407 hydrogels as such, both NHP407_MSN-CS-SIP and SHP407_MSN-CS-SIP systems appeared to be in the gel state at 37°C ($\omega_{G'/G''\,crossover}$ lower than 0.1 rad/s). Additionally, both the formulations did not exhibit a G′ trend independent over frequency, proving that the gel network

was not completely developed at physiological temperature (**Figure 5C** and **Table 3**). However, in terms of gelation kinetics, MSN-CS-SIP loading within the hydrogels turned out to have different effects on SHP407 and NHP407 sol-gel systems. SHP407 hybrid formulation showed a faster sol-to-gel transition compared to virgin SHP407 hydrogel, as suggested by the lower $\omega_{G'/G''crossover}$ values it exhibited at both 25 and 30°C (**Figure 5C** and **Table 3**). This behavior could be probably correlated to the presence of the polymeric coating covering the particles, which made them able to take part to the gelation process, acting as additional crosslinking points within the gel network thanks to the hydrogen bonds arising between them and SHP407 micelles. This hypothesis was further supported by the observed decrease in T_{onset} (from 16.36 to 15.7°C upon particle encapsulation) (**Figure 5B** and **Table 4**). Differently, particle embedding within NHP407-based sol-gel system had an opposite effect, as demonstrated by the slightly higher $\omega_{G'/G''crossover}$ values of NHP407_MSN-CS-SIP system with respect to NHP407 control hydrogel at both 25 and 30°C. The different behavior of NHP407-based hybrid hydrogel could be ascribed to the presence of Boc groups that acted as obstacles to H-bond formation due to steric hindrance and their caging activity of amino groups that, conversely, in SHP407 were available for hydrogen bonding. Irrespective of the nature of the constituent polymer, at 37°C the particles acted as defects within the gel network, lowering its resistance to applied deformation and Yield Stress (**Figure 5A**). These results further corroborated the previous hypothesis on the formation of hydrogen bonds between the SIP and SHP407 chains. In fact, a lower decrease of both γ_L and YS was observed for SHP407-based system compared to NHP407-based one (i.e., upon particle addition, γ_L decreased of 84.8 and 37.5% in NHP407- and SHP407-based systems, respectively. Decrease in YS was 85.4 and 49.5% in NHP407- and SHP407-based systems, respectively). Finally, the capability of hybrid formulations to release the payload previously encapsulated in MSN-CS-SIP was characterized in pH 5 and pH 7.4 aqueous media (**Figure 6**). Despite encapsulation within the gel phase, SIP-coated MSNs retained the capability to release their cargo. In fact, at both pH 5 and pH 7.4 environments, the Ru dye was progressively released from the hybrid hydrogels with no burst release. In accordance with the pH-responsiveness of the SIP, triggered Ru dye release in acid environment was successfully achieved from both NHP407_MSN-CS-SIP-Ru and SHP407_ MSN-CS-SIP-Ru (**Figure 6A**), thus proving that the progressive SIP degradation at acid pH and the opening of the pore entrances were not hindered by the embedding of the particles within a hydrogel phase. Furthermore, the exposure of free amino groups along SHP407 polymer chains turned out to effectively enhance Ru release from SHP407_MSN-CS-SIP-Ru compared to NHP407_MSN-CS-SIP-Ru (**Figure 6B**). This result is in agreement with the accelerated decrease in pH observed in SHP407 sol-gel systems compared to NHP407 ones, during incubation in acid pH environment (**Figure 2A**). On the other hand, no significant differences in Ru release were observed in neutral pH medium, in accordance with the similar pH trend SHP407 and NHP407 hydrogels exhibited upon incubation in this environment (**Figure 2B**). *Ex vivo* injectability and gelation were then assessed also for SHP407_MSN-CS-SIP-Ru hybrid formulation (**Figures 7C,D**). The capability of the hydrogel vehicle phase to localize the therapeutic formulation in the target area was demonstrated by s.c. injecting the hybrid formulation and comparing this to a MSN-CS-SIP-Ru aqueous dispersion that, in fact, tended to broadly disperse immediately upon application (**Figure 7C**). Additionally, the loading of the fluorescent cargo Ru into the MSNs allowed for a fluorescence-based detection of the particle dispersion as such, but also upon loading into the hydrogel, both *in vitro* (**Figure 7A**) as well as *in vivo* (**Figure 7B**). Hence, SHP407 gel showed ability to transmit fluorescent signals, which can be a crucial feature for potential proof-of-concept *in vivo* payload release studies.

CONCLUSION

The optimal therapeutic drug-release formulation should recapitulate in a sole device several features and fulfill a specific plethora of strict requirements. First, it must be easy to handle, injectable and able to completely fill body cavities or defects. Second, the capability to change its state and adapt itself to different scenarios is mandatory to allow injection, good distribution in the target tissue/organ and adequate residence time to properly exert its function. Third, it must progressively release its payload in a controlled way, avoiding undesired burst release and ensuring the delivery of active therapeutic agents within the target tissue/organ at a suitable concentration within the therapeutic window for the proper time frame. Last, it should possess high versatility allowing a wide possibility of tuning its composition. As an additional feature, smartness could make therapeutic formulations able to actively respond to external stimuli, such as physical and biochemical cues, thus allowing them to change their properties, with the consequent possibility to trigger and modulate cargo release. Within this challenging and highly demanding scenario, in this work we succeeded in developing formulations meeting the aforementioned demands and showing concurrent sensitivity to temperature and environmental pH. Thermo-responsiveness was successfully provided through the use of an amphiphilic polymer as hydrogel forming material to make the resulting formulations able to quickly gel in physiological conditions. On the other hand, mesoporous silica particles coated with a properly designed self-immolative polymer provided the resulting formulation with responsiveness to acid pH environment, resulting in accelerated delivery of their payload in specific conditions. *Ex vivo* demonstrated injectability, gelation and confined distribution of the newly designed formulations represent additional key features for their application in the biomedical field. Moreover, in view of a potential *in vivo* application, the here-developed formulations and their degradation products can be hypothesized to be suitable for complete excretion from the body. Indeed, mesoporous silica nanoparticles have been demonstrated in literature to undergo degradation/dissolution in simulated biological media, with a progressive increase in pore size and decrease in both porosity and surface area

(Cauda et al., 2010; Chen et al., 2015). On the other hand, the poly(ether urethane)s used as hydrogel-forming materials are susceptible to progressive hydrolytic or oxidative degradation, which could be also triggered by local environment properties [e.g., local pH (Mesa et al., 2005; Yang et al., 2006) and presence of specific ionic species (Boffito et al., 2019b)]. On the other hand, being dissolution the main phenomenon responsible for physical hydrogel disassembling in aqueous media in the short-term, also full-length polymer chain will probably circulate in the body and expected to be excreted via renal clearance [albumin -66 kDa- is usually referred to as a good estimate for glomerular molecular weight cut-off (Lin, 2009)].

The high potential of the here-proposed approach lies in its many compositional degrees-of-freedom and the custom-made nature of its constituents. The high versatility of poly(urethane) chemistry opens the way to the possibility to further increase the sensitivity of the gel phase to the surrounding environment through a proper selection of the building blocks or additional functionalization procedures. For instance, enzyme-sensitive blocks [e.g., matrix metalloproteinase-sensitive peptide sequences (Lutolf et al., 2003)] could be introduced into the polymer backbone allowing a further control over the stability of the system upon *in vivo* injection. On the other hand, according to recently reported data by some authors of the present work (Pontremoli et al., 2018; Boffito et al., 2019b), thermo-sensitive hydrogels based on custom-made poly(ether urethane)s have been demonstrated to allow mesoporous particle encapsulation at high concentration, thus making it possible to modulate cargo loading within a wide concentration range. In addition, the mesoporous nature of embedded particles allows the encapsulation of huge amounts of payload, thus further increasing the potential of the here-developed injectable formulations. Finally, also the custom-made nature of the self-immolative polymers opens the way to a further tuning of payload release profile. The multi-component nature of these hybrid hydrogels and the custom-made nature of its constituents will thus allow in the future to assemble *ad hoc* formulated therapeutics answering to the specific needs of each patient.

DATA AVAILABILITY STATEMENT

The raw data supporting the conclusions of this article will be made available by the authors, without undue reservation, to any qualified researcher.

ETHICS STATEMENT

The animal study was approved by the local animal protection authorities (Landesamt für Gesundheit und Soziales (LaGeSo); permit number: G 0293/17) and was performed in accordance with the German Animal Welfare Act.

AUTHOR CONTRIBUTIONS

This is a multi-disciplinary work that has been conducted by three main institutions (Politecnico di Torino, POLITO, Universidad Complutence de Madrid, UCM, and Charité - Universitätsmedizin Berlin, CHARITÉ). GC was responsible for POLITO's unit and coordinated the research activities, MB, AT, CT-T, and RL designed the thermo-sensitive hydrogels and executed all the experimental activities related to hydrogel fabrication and characterization. They were also responsible for the design and characterization of hybrid sol-gel systems. CC performed and interpreted ^{1}H NMR analyses. MV-R and MM were responsible for UCM's activities. MG-G synthesized and characterized pH-sensitive mesoporous silica nanoparticles and loaded them with the fluorescent cargo. GD, KS-B, and JB were responsible for the research activities carried out by CHARITÉ units. JB and KS-B planned and executed *ex vivo* injectability and gelation tests in rodents. Data interpretation responsibility was collectively shared by all the authors. MB wrote the whole manuscript with contribution on particle synthesis and characterization and *ex vivo* tests from MG-G and JB, respectively. All authors provided critical feedback and helped shape the research, analysis and manuscript.

FUNDING

This project has received funding from the European Union's Horizon 2020 Research and Innovation Programme under grant agreement no. 685872-MOZART (www.mozart project.eu). MV-R acknowledged the financial support from European Research Council through ERC-2015-AdG-694160 (VERDI) project.

ACKNOWLEDGMENTS

The authors would like to express their gratitude to Dr. Carsten Grötzinger, Charité - Universitätsmedizin Berlin, Germany, for his instrumental support by enabling the usage of the *in vivo* imaging system (IVIS).

SUPPLEMENTARY MATERIAL

The Supplementary Material for this article can be found online at: https://www.frontiersin.org/articles/10.3389/fbioe.2020.00384/full#supplementary-material

REFERENCES

Ahmed, E. M. (2015). Hydrogel: preparation, characterization, and applications: a review. *J. Adv. Res.* 6, 105–121. doi: 10.1016/j.jare.2013.07.006

Anggelia, M. R., Cheng, H. Y., Wen, C. J., Wang, A. Y. L., and Lin, C. H. (2019). A mixed thermosensitive hydrogel system for sustained delivery of Tacrolimus for immunosuppressive therapy. *Pharmaceutics* 11, 413. doi: 10.3390/pharmaceutics11080413

Aoki, T., Kawashima, M., Katono, H., Sanui, K., Ogata, N., Okano, T., et al. (1994). Temperature-responsive interpenetrating polymer networks constructed with poly(acrylic acid) and poly(N,N-dimethylacrylamide). *Macromolecules* 27, 947–952. doi: 10.1021/ma00082a010

Baeza, A., Guisasola, E., Torres-Pardo, A., González-Calbet, J. M., Melen, G. J., Ramirez, M., et al. (2014). Hybrid enzyme-polymeric capsules/mesoporous silica nanodevice for in situ cytotoxic agent generation. *Adv. Funct. Mater.* 24, 4625–4633. doi: 10.1002/adfm.201400729

Blondelle, S. E., and Houghten, R. A. (1993). Comparison of 55% TFA/CH2Cl2 and 100% TFA for Boc group removal during solid−phase peptide synthesis. *Int. J. Pept. Protein Res.* 41, 522–527. doi: 10.1111/j.1399-3011.1993.tb00473.x

Boffito, M., Gioffredi, E., Chiono, V., Calzone, S., Ranzato, E., Martinotti, S., et al. (2016). Novel polyurethane-based thermosensitive hydrogels as drug release and tissue engineering platforms: design and in vitro characterization. *Polym. Int.* 65, 756–769. doi: 10.1002/pi.5080

Boffito, M., Grivet Brancot, A., Lima, O., Bronco, S., Sartori, S., and Ciardelli, G. (2019a). Injectable thermosensitive gels for the localized and controlled delivery of biomolecules in tissue engineering/regenerative medicine. *Biomed. Sci. Eng.* 3:67. doi: 10.4081/bse.2019.67

Boffito, M., Pontremoli, C., Fiorilli, S., Laurano, R., Ciardelli, G., and Vitale-Brovarone, C. (2019b). Injectable thermosensitive formulation based on polyurethane hydrogel/mesoporous glasses for sustained co-delivery of functional ions and drugs. *Pharmaceutics* 11:501. doi: 10.3390/pharmaceutics11100501

Boffito, M., Sirianni, P., Di Rienzo, A. M., and Chiono, V. (2014). Thermosensitive block copolymer hydrogels based on poly(ε-caprolactone) and polyethylene glycol for biomedical applications: state of the art and future perspectives. *J. Biomed. Mater. Res. A* 103, 1276–1290. doi: 10.1002/jbm.a.35253

Bullock, A. J., Garcia, M., Shepherd, J., Rehman, I., and Sheila, M. (2019). Bacteria induced pH changes in tissue-engineered human skin detected non-invasively using Raman confocal spectroscopy. *Appl. Spectrosc. Rev.* 55, 158–171. doi: 10.1080/05704928.2018.1558232

Caddeo, S., Mattioli-Belmonte, M., Cassino, C., Barbani, N., Dicarlo, M., Gentile, P., et al. (2019). Newly-designed collagen/polyurethane bioartificial blend as coating on bioactive glass-ceramics for bone tissue engineering applications. *Mater. Sci. Eng. C* 96, 218–233. doi: 10.1016/j.msec.2018.11.012

Cauda, V., Schlossbauer, A., and Bein, T. (2010). Bio-degradation study of colloidal mesoporous silica nanoparticles: effect of surface functionalization with organo-silanes and poly(ethylene glycol). *Micropor. Mesopor. Mater.* 132, 60–71. doi: 10.1016/j.micromeso.2009.11.015

Chang, C. H., Lin, Y. H., Yeh, C. L., Chen, Y. C., Chiou, S. F., Hsu, Y. M., et al. (2010). Nanoparticles incorporated in pH-sensitive hydrogels as amoxicillin delivery for eradication of *Helicobacter pylori*. *Biomacromolecules* 11, 133–142. doi: 10.1021/bm900985h

Chatterjee, S., Hui, P. C.-L., Kan, C.-W., and Wang, W. (2019). Dual-responsive (pH/temperature) Pluronic F-127 hydrogel drug delivery system for textile-based transdermal therapy. *Sci. Rep.* 9:11658. doi: 10.1038/s41598-019-48254-6

Chen, D., Zhang, C., Huo, H., Ji, C., Sun, M., and Nie, L. (2018). Injectable temperature-sensitive hydrogel with VEGF loaded microspheres for vascularization and bone regeneration of femoral head necrosis. *Mater. Lett.* 229, 138–141. doi: 10.1016/j.matlet.2018.06.123

Chen, G., Teng, Z., Su, X., Liu, Y., and Lu, G. (2015). Unique biological degradation behavior of stöber mesoporous silica nanoparticles from their interiors to their exteriors. *J. Biomed. Nanotechnol.* 11, 722–729. doi: 10.1166/jbn.2015.2072

Dong, X., Wei, C., Liang, J., Liu, T., Kong, D., and Lv, F. (2017). Thermosensitive hydrogel loaded with chitosan-carbon nanotubes for near infrared light triggered drug delivery. *Colloids Surf. B Biointerfaces* 154, 253–262. doi: 10.1016/j.colsurfb.2017.03.036

Geng, H., Song, H., Qi, J., and Cui, D. (2011). Sustained release of VEGF from PLGA-nanoparticles mbedded thermo-sensitive hydrogel in full-thickness porcine bladder acellular matrix. *Nanoscale Res. Lett.* 6:312. doi: 10.1186/1556-276X-6-312

Gisbert-Garzarán, M., Lozano, D., Vallet-Regí, M., and Manzano, M. (2017). Self-immolative polymers as novel pH-responsive gate keepers for drug delivery. *RSC Adv.* 7, 132–136. doi: 10.1039/C6RA26771H

Gupta, M. K., Martin, J. R., Werfel, T. A., Shen, T., Page, J. M., and Duvall, C. L. (2014). Cell protective, ABC triblock polymer-based thermoresponsive hydrogels with ROS-triggered degradation and drug release. *J. Am. Chem. Soc.* 136, 14896–14902. doi: 10.1021/ja507626y

Huang, H., Qi, X., Chen, Y., and Wu, Z. (2019). Thermo-sensitive hydrogels for delivering biotherapeutic molecules: a review. *Saudi Pharm. J.* 27, 990–999. doi: 10.1016/j.jsps.2019.08.001

Jeong, Y. W., Jung, S., Han, J. J., Park, H. J., Kim, R. Y., Kim, B. H., et al. (2019). Effectiveness of surface treatment with amine plasma for improving the biocompatibility of maxillofacial plates. *Materials (Basel)* 12:2581. doi: 10.3390/ma12162581

Jiang, S., Wang, K., Dai, Y., Zhang, X., and Xia, F. (2019). Near-infrared light-triggered dual drug release using gold nanorod-embedded thermosensitive nanogel-crosslinked hydrogels. *Macromol. Mater. Eng.* 304:1900087. doi: 10.1002/mame.201900087

Kanamala, M., Wilson, W. R., Yang, M., Palmer, B. D., and Wu, Z. (2016). Mechanisms and biomaterials in pH-responsive tumour targeted drug delivery: a review. *Biomaterials* 85, 152–167. doi: 10.1016/j.biomaterials.2016.01.061

Lang, Y. Y., Li, S. M., Pan, W. S., and Zheng, L. Y. (2006). Thermo- and pH-sensitive drug delivery from hydrogels constructed using block copolymers of poly(N-isopropylacrylamide) and Guar gum. *J. Drug Deliv. Sci. Technol.* 16, 65–69. doi: 10.1016/s1773-2247(06)50010-3

Laurano, R., Boffito, M., Torchio, A., Cassino, C., Chiono, V., and Ciardelli, G. (2019). Plasma treatment of polymer powder as an effective tool to functionalize polymers: case study application on an amphiphilic polyurethane. *Polymers (Basel)* 11:E2109. doi: 10.3390/polym11122109

Laurano, R., Cassino, C., Ciardelli, G., Chiono, V., and Boffito, M. (2020). Polyurethane-based thiomers: a new multifunctional copolymer platform for biomedical applications. *React. Funct. Polym.* 146:104413. doi: 10.1016/j.reactfunctpolym.2019.104413

Liang, Y., Zhao, X., Ma, P. X., Guo, B., Du, Y., and Han, X. (2019). pH-responsive injectable hydrogels with mucosal adhesiveness based on chitosan-grafted-dihydrocaffeic acid and oxidized pullulan for localized drug delivery. *J. Colloid Interface Sci.* 536, 224–234. doi: 10.1016/j.jcis.2018.10.056

Lin, J. H. (2009). Pharmacokinetics of biotech drugs: peptides, proteins and monoclonal antibodies. *Curr. Drug Metab.* 10, 661–691. doi: 10.2174/138920009789895499

Lutolf, M. P., Lauer-Fields, J. L., Schmoekel, H. G., Metters, A. T., Weber, F. E., Fields, G. B., et al. (2003). Synthetic matrix metalloproteinase-sensitive hydrogels for the conduction of tissue regeneration: engineering cell-invasion characteristics. *Proc. Natl. Acad. Sci. U.S.A.* 100, 5413–5418. doi: 10.1073/pnas.0737381100

Mahmoudifard, M., Soleimani, M., and Vossoughi, M. (2017). Ammonia plasma-treated electrospun polyacrylonitryle nanofibrous membrane: the robust substrate for protein immobilization through glutaraldhyde coupling chemistry for biosensor application. *Sci. Rep.* 7:9441. doi: 10.1038/s41598-017-10040-7

Manzano, M., and Vallet-Regí, M. (2020). Mesoporous silica nanoparticles for drug delivery. *Adv. Funct. Mater.* 30, 3–5. doi: 10.1002/adfm.201902634

Mesa, M., Sierra, L., Patarin, J., and Guth, J. L. (2005). Morphology and porosity characteristics control of SBA-16 mesoporous silica. Effect of the triblock surfactant Pluronic F127 degradation during the synthesis. *Solid State Sci.* 7, 990–997. doi: 10.1016/j.solidstatesciences.2005.04.006

Narayan, R., Nayak, U. Y., Raichur, A. M., and Garg, S. (2018). Mesoporous silica nanoparticles: a comprehensive review on synthesis and recent advances. *Pharmaceutics* 10:E118. doi: 10.3390/pharmaceutics10030118

Noel, S., Liberelle, B., Robitaille, L., and De Crescenzo, G. (2011). Quantification of primary amine groups available for subsequent biofunctionalization of polymer surfaces. *Bioconjug. Chem.* 22, 1690–1699. doi: 10.1021/bc200259c

Ozcelik, B. (2016). "Degradable hydrogel systems for biomedical applications," in *Biosynthetic Polymers for Medical Applications,* Chapter 7, eds L. Poole-Warren, P. Martens, and R. Green (Amsterdam: Elsevier), 173–188. doi: 10.1016/B978-1-78242-105-4.00007-9

Park, H., Guo, X., Temenoff, J. S., Tabata, Y., Caplan, A. I., Kasper, F. K., et al. (2009). Effect of swelling ratio of injectable hydrogel composites on chondrogenic differentiation of encapsulated rabbit marrow mesenchymal stem cells in vitro. *Biomacromolecules* 10, 541–546. doi: 10.1021/bm801197m

Pontremoli, C., Boffito, M., Fiorilli, S., Laurano, R., Torchio, A., Bari, A., et al. (2018). Hybrid injectable platforms for the in situ delivery of therapeutic ions from mesoporous glasses. *Chem. Eng. J.* 340, 103–113. doi: 10.1016/j.cej.2018.01.073

Qin, J., Jiang, J., Ye, S., Wang, S., Xiao, M., Tao, Y., et al. (2019). High performance poly(urethane-: co-amide) from CO_2-based dicarbamate: an alternative to long chain polyamide. *RSC Adv.* 9, 26080–26090. doi: 10.1039/c9ra04646a

Qindeel, M., Ahmed, N., Sabir, F., Khan, S., and Ur-Rehman, A. (2019). Development of novel pH-sensitive nanoparticles loaded hydrogel for transdermal drug delivery. *Drug Dev. Ind. Pharm.* 45, 629–641. doi: 10.1080/03639045.2019.1569031

Roy, A., Maity, P. P., Bose, A., Dhara, S., and Pal, S. (2019). β-Cyclodextrin based pH and thermo-responsive biopolymeric hydrogel as a dual drug carrier. *Mater. Chem. Front.* 3, 385–393. doi: 10.1039/c8qm00452h

Rwei, S. P., Anh, T. H. N., Chiang, W. Y., Way, T. F., and Hsu, Y. J. (2016). Synthesis and drug delivery application of thermo- and pH-sensitive hydrogels: poly(β-CD-co-N-isopropylacrylamide-co-IAM). *Materials (Basel)* 9:E1003. doi: 10.3390/ma9121003

Sagi, A., Weinstain, R., Karton, N., and Shabat, D. (2008). Self-immolative polymers. *J. Am. Chem. Soc.* 8, 5434–5435. doi: 10.1021/ja801065d

Trathnigg, B. (2000). "Size-exclusion chromatography of polymers," in *Encyclopedia of Analytical Chemistry*, ed. R. A. Meyers (Chichester: Jonh Wiley & Sons Ltd), 8008–8034.

Wang, C., Javadi, A., Ghaffari, M., and Gong, S. (2010). A pH-sensitive molecularly imprinted nanospheres/hydrogel composite as a coating for implantable biosensors. *Biomaterials* 31, 4944–4951. doi: 10.1016/j.biomaterials.2010.02.073

Wen, J., Yang, K., Liu, F., Li, H., Xu, Y., and Sun, S. (2017). Diverse gatekeepers for mesoporous silica nanoparticle based drug delivery systems. *Chem. Soc. Rev.* 46, 6024–6045. doi: 10.1039/c7cs00219j

Xi, L., Wang, T., Zhao, F., Zheng, Q., Li, X., Luo, J., et al. (2014). Evaluation of an injectable thermosensitive hydrogel as drug delivery implant for ocular glaucoma surgery. *PLoS One* 9:e100632. doi: 10.1371/journal.pone.0100632

Xu, C., Lei, C., and Yu, C. (2019). Mesoporous silica nanoparticles for protein protection and delivery. *Front. Chem.* 7:290. doi: 10.3389/fchem.2019.00290

Yang, B., Guo, C., Chen, S., Junhe, M., Wang, J., Liang, X., et al. (2006). Effect of acid on the aggregation of poly(ethylene oxide)-poly(propylene oxide)-poly(ethylene oxide) block copolymers. *J. Phys. Chem. B* 110, 23068–23074. doi: 10.1021/jp0634149

Ye, Y., and Hu, X. (2016). A pH-sensitive injectable nanoparticle composite hydrogel for anticancer drug delivery. *J. Nanomater.* 2016:9816461. doi: 10.1155/2016/9816461

Zhang, W., Jin, X., Li, H., Zhang, R. R., and Wu, C. W. (2018). Injectable and body temperature sensitive hydrogels based on chitosan and hyaluronic acid for pH sensitive drug release. *Carbohydr. Polym.* 186, 82–90. doi: 10.1016/j.carbpol.2018.01.008

Zhou, Y., Quan, G., Wu, Q., Zhang, X., Niu, B., Wu, B., et al. (2018). Mesoporous silica nanoparticles for drug and gene delivery. *Acta Pharm. Sin. B* 8, 165–177. doi: 10.1016/j.apsb.2018.01.007

Conflict of Interest: The authors declare that the research was conducted in the absence of any commercial or financial relationships that could be construed as a potential conflict of interest.

frontiers in Bioengineering and Biotechnology

ORIGINAL RESEARCH
published: 25 May 2020
doi: 10.3389/fbioe.2020.00484

Hybrid Bioprinting of Chondrogenically Induced Human Mesenchymal Stem Cell Spheroids

*Lise De Moor[1], Sélina Fernandez[1], Chris Vercruysse[1], Liesbeth Tytgat[2], Mahtab Asadian[3], Nathalie De Geyter[3], Sandra Van Vlierberghe[2], Peter Dubruel[2] and Heidi Declercq[1,4]**

[1] Tissue Engineering Group, Department of Human Structure and Repair, Faculty of Medicine and Health Sciences, Ghent University, Ghent, Belgium, [2] Polymer Chemistry and Biomaterials Research Group, Department of Organic and Macromolecular Chemistry, Faculty of Sciences, Centre of Macromolecular Chemistry, Ghent University, Ghent, Belgium, [3] Research Unit Plasma Technology, Department of Applied Physics, Faculty of Engineering and Architecture, Ghent University, Ghent, Belgium, [4] Tissue Engineering Lab, Department of Development and Regeneration, Faculty of Medicine, KU Leuven Kulak, Kortrijk, Belgium

OPEN ACCESS

Edited by:
Dimitrios I. Zeugolis, National University of Ireland Galway, Ireland

Reviewed by:
Riccardo Levato, University Medical Center Utrecht, Netherlands
Jos Malda, Utrecht University, Netherlands

***Correspondence:**
Heidi Declercq
Heidi.Declercq@ugent.be;
Heidi.Declercq1@kuleuven.be

Specialty section:
This article was submitted to Tissue Engineering and Regenerative Medicine, a section of the journal Frontiers in Bioengineering and Biotechnology

Received: *13 January 2020*
Accepted: *27 April 2020*
Published: *25 May 2020*

Citation:
De Moor L, Fernandez S, Vercruysse C, Tytgat L, Asadian M, De Geyter N, Van Vlierberghe S, Dubruel P and Declercq H (2020) Hybrid Bioprinting of Chondrogenically Induced Human Mesenchymal Stem Cell Spheroids. Front. Bioeng. Biotechnol. 8:484. doi: 10.3389/fbioe.2020.00484

To date, the treatment of articular cartilage lesions remains challenging. A promising strategy for the development of new regenerative therapies is hybrid bioprinting, combining the principles of developmental biology, biomaterial science, and 3D bioprinting. In this approach, scaffold-free cartilage microtissues with small diameters are used as building blocks, combined with a photo-crosslinkable hydrogel and subsequently bioprinted. Spheroids of human bone marrow-derived mesenchymal stem cells (hBM-MSC) are created using a high-throughput microwell system and chondrogenic differentiation is induced during 42 days by applying chondrogenic culture medium and low oxygen tension (5%). Stable and homogeneous cartilage spheroids with a mean diameter of 116 ± 2.80 μm, which is compatible with bioprinting, were created after 14 days of culture and a glycosaminoglycans (GAG)- and collagen II-positive extracellular matrix (ECM) was observed. Spheroids were able to assemble at random into a macrotissue, driven by developmental biology tissue fusion processes, and after 72 h of culture, a compact macrotissue was formed. In a directed assembly approach, spheroids were assembled with high spatial control using the bio-ink based extrusion bioprinting approach. Therefore, 14-day spheroids were combined with a photo-crosslinkable methacrylamide-modified gelatin (gelMA) as viscous printing medium to ensure shape fidelity of the printed construct. The photo-initiators Irgacure 2959 and Li-TPO-L were evaluated by assessing their effect on bio-ink properties and the chondrogenic phenotype. The encapsulation in gelMA resulted in further chondrogenic maturation observed by an increased production of GAG and a reduction of collagen I. Moreover, the use of Li-TPO-L lead to constructs with lower stiffness which induced a decrease of collagen I and an increase in GAG and collagen II production. After 3D bioprinting, spheroids remained viable and the cartilage phenotype was maintained. Our findings demonstrate that hBM-MSC spheroids are able to differentiate into cartilage microtissues and display a geometry compatible with 3D bioprinting. Furthermore, for hybrid bioprinting of these spheroids,

gelMA is a promising material as it exhibits favorable properties in terms of printability and it supports the viability and chondrogenic phenotype of hBM-MSC microtissues. Moreover, it was shown that a lower hydrogel stiffness enhances further chondrogenic maturation after bioprinting.

Keywords: bioprinting, spheroids, chondrogenesis, differentiation, stem cell, fusion, self-assembly

INTRODUCTION

Articular cartilage, the connective tissue lining the articular surface of bones within diarthrodial joints, ensures load support, load transmission, and joint lubrication. It is characterized by a limited intrinsic healing and repair capacity because of its avascular and aneural nature. Therefore, articular cartilage lesions are prone to progress to osteoarthritis and patients are liable to suffer from joint instability in the long term (Fox et al., 2009, 2012).

Nowadays, articular cartilage defects are already being treated with cell-based regenerative therapies, such as autologous chondrocyte implantation (ACI). This two-step surgical procedure includes the isolation of autologous articular chondrocytes from a non-weight bearing region, the *in vitro* expansion and the reinjection into the defect site (Davies and Kuiper, 2019). Another commonly used approach is Matrix-assisted ACI (MACI) which is an *ex vivo* engineered hybrid construct, where isolated autologous chondrocytes are seeded onto a biomaterial, a bovine-derived type I/III collagen scaffold, before implantation in the defect (Foldager et al., 2012; Basad et al., 2015). However, the harvesting procedure to obtain chondrocytes can induce donor-site morbidity and the 2D expansion of articular chondrocytes is characterized by long *in vitro* culture periods and chondrocyte dedifferentiation to a more fibroblast-like phenotype featuring a decrease in collagen II, aggrecan, and glycosaminoglycans (GAG) (Caron et al., 2012; De Moor et al., 2019). This results in the generation of repair tissue which is biochemically and hence biomechanically inferior compared to the native cartilage (Knutsen et al., 2007). Therefore, new biofabrication strategies are being explored in the quest for novel regenerative therapies.

For the creation of cartilage constructs, a modular tissue engineering concept is emerging. This approach is inspired by developmental biology where complex tissues are comprised of repeating functional units (Nichol and Khademhosseini, 2009). Instead of starting from single cells, smaller tissue units such as cell sheets or cellular spheroids are used as building blocks to create larger tissues by self-assembly and fusion. The 3D spatial arrangement of cells into spheroids mimics the natural environment by creating cell–cell contacts and cell–extracellular matrix (ECM) interactions, enhancing cell differentiation (Mironov et al., 2009; Schon et al., 2017). Injection of spheroids can be used to treat cartilage defects instead of injecting a single cell suspension, whose dedifferentiation leads to inferior fibrous tissue. Spheroid maturation already starts *in vitro*, establishing a tissue specific ECM provoked by their high cellularity and cell density (Huang et al., 2016; De Moor et al., 2019). An example used in clinical trials are chondrospheres, 500–800 μm spheroids generated from autologous chondrocytes. The chondrospheres naturally adhere to the cartilage defect after injection and assemble and fuse at random (Anderer and Libera, 2002; Becher et al., 2017).

As an alternative to injecting or assembling spheroids at random, 3D printing technologies can be used to assemble the cellular building blocks in a directed manner with high spatial control in a complex predesigned configuration. In bio-ink based extrusion bioprinting, biomaterials can be used as viscous carriers for the deposition of cells or spheroids, to restrain them and to ensure shape fidelity of the printed construct (Moldovan et al., 2018). Moreover, hydrogels are widely used in cell-based cartilage regeneration as a pro-chondrogenic environment as they can mimic the biological and physical properties of the native ECM (Vega et al., 2017). Next to alginate or agarose hydrogels, commonly used for chondrocyte redifferentiation, gelatin-based hydrogels are an optimal candidate to use as an ink because of their low-cost, high water content, cell-interactive properties and resemblance with the natural ECM as a derivative from collagen (Cigan et al., 2016; Ewa-Choy et al., 2017; Pahoff et al., 2019). Methacrylamide-modified gelatin (gelMA), also frequently referred to as gelatin methacryloyl in the literature, is a modified photo-crosslinkable form of the natural polymer gelatin combining stability (after crosslinking) at 37°C and allowing interaction, adhesion and migration of cells by the presence of the integrin binding Arg-Gly-Asp (RGD) sequence. GelMA solutions are interesting for extrusion bioprinting as thermally initiated (reversible) gelation can create a viscous gel-like solution, ideal for extrusion, by applying a printing temperature below 30°C (Van Den Bulcke et al., 2000; Pepelanova et al., 2018). GelMA can be chemically crosslinked by a UV-induced chain growth polymerization mechanism in the presence of a photo-initiator (PI), which transfers the electromagnetic energy of the UV-light into chemical energy by generating radicals and initiating the polymerization (Tytgat et al., 2018). Hydrogel properties can be tailored by varying polymer concentration, crosslinking times or by using different PIs (Rouillard et al., 2011; Billiet et al., 2014; Loessner et al., 2016; Pahoff et al., 2019). Irgacure 2959 is a commonly used PI but its water solubility is very limited, therefore there is a shift to PIs with higher water solubility such as Li-TPO-L (Markovic et al., 2015; Tytgat et al., 2018). It has been demonstrated that gelMA supports cartilage-like matrix production when a suspension of single chondrocytes or mesenchymal stem cells (MSC) were embedded (Hu et al., 2009; Schuurman et al., 2013; Mouser et al., 2018; Pahoff et al., 2019). Recently, there has been an increased interest in the use of adult MSC in cartilage regeneration because of their multipotency and ability to differentiate into chondrogenic lineages after expansion *in vitro* and intra-articular injections of MSC have

been performed to reduce osteoarthritic pain or induce cartilage repair (Jo et al., 2014; Shin et al., 2018). The use of MSC would also eliminate the need for harvesting surgery within the damaged knee-joint or donor site. Spheroid formation of stem cells resembles the aggregation and condensation processes of mesenchymal progenitor cells during embryonic cartilage development (Ghosh et al., 2009). Next to culturing MSC in 3D, differentiation into the chondrogenic lineage can be induced by applying a chondrogenic culture medium containing growth factors such as transforming growth factor-β (TGF-β) and/or bone morphogenetic protein (BMP) (Ude et al., 2017). Further mimicking of the natural environment can be done by culturing in a low oxygen environment as hypoxia results in an increase of cartilage ECM molecules such as collagen II and aggrecan (Tan et al., 2011; Berneel et al., 2016).

For hyaline cartilage tissue engineering, mainly large diameter spheroids (>500 μm) are created using articular chondrocytes (Anderer and Libera, 2002; Armoiry et al., 2018). Though for bioprinting, small diameter spheroids with uniform shapes and sizes are necessary for compatibility with the print needle. In our previous study, we described the biofabrication of printable high quality cartilage microtissues starting from porcine chondrocytes (De Moor et al., 2019). However, to enhance clinical translation, we describe the high-throughput creation of small diameter human cartilage spheroids (<200 μm) by chondrogenic differentiation of human bone marrow-derived mesenchymal stem cells (hBM-MSC), applying chondrogenic culture medium and low oxygen tension (5%). To generate the spheroids, a low-cost non-adhesive microwell system is used (**Figure 1**). Moreover, the fusion capacity of the cartilage microtissues in suspension and within a hydrogel is investigated. We investigated if gelMA is a suitable conductive microenvironment for spheroid differentiation by extensive screening of ECM by histology. In the final phase of the study, the processing potential of the bio-ink, consisting of cartilage microtissues and gelMA, and the impact of the extrusion-based bioprinting on viability and cartilage phenotype were assessed (**Figure 1**).

MATERIALS AND METHODS

Cell Culture

Human Bone Marrow-derived Mesenchymal Stem Cells were purchased from PromoCell GmbH (C-12974, male donor age 65). Cells were cultured in MSC Growth Medium 2 (C-28009, PromoCell GmbH) supplemented with 50 U/ml penicillin and 50 μg/ml streptomycin (Life technologies) and maintained at 37°C in a humidified 5% CO_2-containing atmosphere. Cells were subcultured at 80% confluency. Passage 3–5 cells were used to generate spheroids in this study. Passage 3 cells were applied in the fusion experiments and passage 4 and 5 cells were used in all other experiments.

Fabrication of Non-adhesive Microwells

Spheroids are generated using a high-throughput non-adhesive agarose microwell system, as previously described (Gevaert et al., 2014; Berneel et al., 2016; Roosens et al., 2017; De Moor et al., 2018, 2019). In brief, polydimethylsiloxane (PDMS) molds (NaMiFab, Ghent University) with a diameter of 18 mm and a height of 3 mm, containing 1585 micropores of 400 μm diameter each, are used as a negative replica to create microwells (**Figure 1A**). A 4.5 w/v% Ultrapure agarose solution (Life technologies) dissolved in sterile phosphate buffered saline (PBS) was heated and poured on top of the PDMS mold. Once the agarose solidified, the agarose microwell was separated from the mold and placed in a 12-well plate.

Generation of 3D Microtissues

Cells were harvested and 500 μl of cell suspension, containing 5.0×10^5 cells, was seeded onto the microwell, resulting in approximately 315 cells per pore. One hour after seeding, cells lowered into the pores by gravitational force. To induce chondrogenesis, spheroids were cultured in a serum-free chondrogenic culture medium comprised of Dulbecco's Modified Eagle Medium/Nutrient Mixture F-12 (DMEM/F12, Life Technologies), 1 mM sodium pyruvate (Life technologies), 0.5% (v/v) ITS (Sigma-Aldrich), 10 U/mL penicillin, 10 μg/mL streptomycin, 100 μM dexamethasone (Sigma-Aldrich), 200 μM L-ascorbic acid-2-phosphate (Sigma-Aldrich), and 10 ng/mL TGF-β1 (Peprotech), in a low oxygen tension (5% O_2) incubator at 37°C. Spheroids were cultured up to 42 days and culture medium was refreshed after the first 24 h of culture and afterward every 2 days. Aggregation of the cells was evaluated microscopically (Olympus IX81) and spheroids were harvested after 7, 14, 21, 28, 35, and 42 days of culture. Spheroid morphology was analyzed with the Xcellence image software (Olympus). Spheroid diameter, area (A) and perimeter (p) were measured and circularity was calculated using the formula $f_{circularity} = (4\pi A)/p^2$. For the evaluation of diameter and circularity, 18 spheroids ($n = 3$), were assessed.

At Random Assembly of Spheroids: Fusion Assays

As spheroids were used as building blocks to create larger tissues, their capacity to fuse at random was tested by using two methods.

Fusion of Doublets

Spheroid doublets were formed based on the method of Susienka et al. (2016). Medium was carefully removed from two microwells containing immature 7-days-cultured spheroids. The recipient chip (microwell 2) was then transferred into a new 12-well plate. The walls of the donor chip (microwell 1) were removed using a punching device and the remaining central portion was gently inverted onto the recipient chip. After centrifugation, the donor chip was removed leaving the recipient chip with numerous spheroid doublets and 2 ml of chondrogenic medium was gradually added (**Figure 2A**). Images of 14 doublets were analyzed after 0, 2, 6, 8, 10, 24, 48, 72, 96, and 168 h of culture. Intersphere angle, doublet length, doublet width, and contact length (indicated in **Figure 2B**) of the fused doublets were measured in ImageJ.

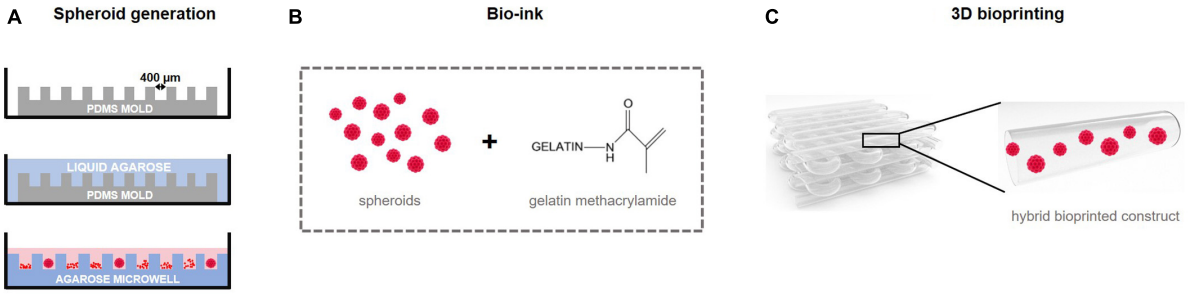

FIGURE 1 | Experimental study design. **(A)** Printable micro building blocks (spheroids) for the creation of a larger construct are generated in high-throughput using non-adhesive microwells. Agarose microwells are created by using a PDMS mold as a negative replica. After seeding, cells lower into the pores of the microwell and self-assemble into 3D cellular spheroids. **(B)** Spheroids are combined with a hydrogel precursor solution, a methacrylamide-modified gelatin for **(C)** 3D bio-ink based bioprinting of a construct using extrusion.

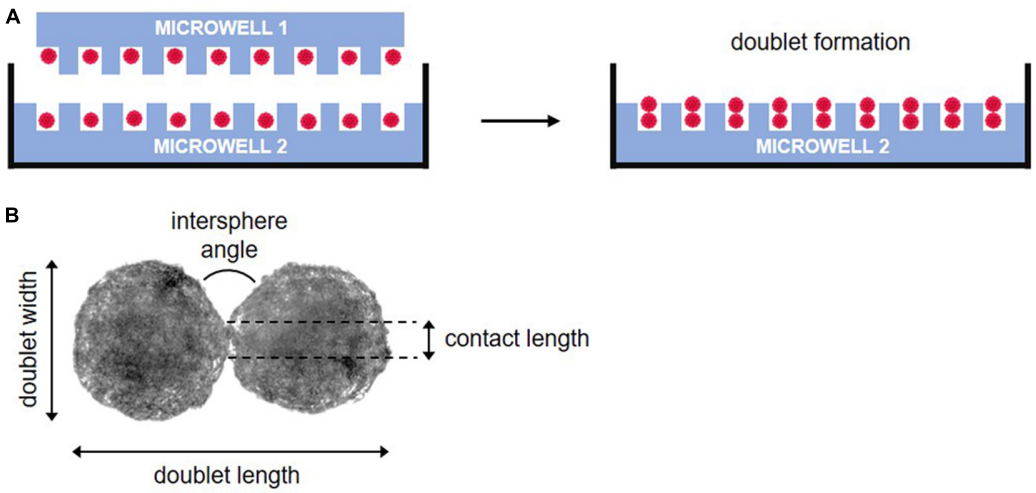

FIGURE 2 | Schematic representation of doublet fusion assay. **(A)** Spheroids are pairwise placed by inverting a donor microwell (microwell 1) on top of a recipient microwell (microwell 2) and after centrifugation, the donor microwell was removed, leaving spheroid doublets in microwell 2. **(B)** Morphological parameters measured during fusion.

Fusion of Multiple Spheroids

To assess the capacity of multiple spheroids to fuse into a macrotissue, 7-day-old spheroids were fused in an agarose coated well. A 2 w/v% agarose solution was prepared and a coating was applied in a 96-well plate (Greiner) by pipetting 300 µl per well and subsequently removing 270 µl. After 7 days of culture, spheroids of one microwell were harvested and resuspended in 160 µl chondrogenic medium. Per agarose coated well, 20 µl of the spheroid suspension was seeded, resulting in 200 spheroids per well. After seeding, 200 µl of chondrogenic medium was carefully added. Follow-up of the at random fusion was carried out at several time points: 0, 2, 6, 8, 24, 48, 72, 96, and 168 h.

Biopolymer and Photo-Initiator Preparation

Methacrylamide-modified gelatin was provided by the Polymer Chemistry and Biomaterials Research group (Ghent University) and was prepared by functionalization of the primary amines of the (hydroxy)lysine and ornithine side groups present in bovine type B gelatin (Rousselot) with methacrylic anhydride (Sigma-Aldrich) (Van Den Bulcke et al., 2000; Van Hoorick et al., 2017; Tytgat et al., 2019). Briefly, 100 g gelatin (0.000385 mol amines/g) was dissolved in 1 L phosphate buffer (pH 7.8) at 40°C. One equivalent of methacrylic anhydride (0.0385 mol, 5.7 ml) was added dropwise while stirring for 1 h. The mixture was dialyzed against distilled water using dialysis membranes for 24 h. The degree of substitution of purified gelatin methacrylamide was 78%, as determined by ^{1}H-NMR spectroscopy (Bruker AVANCE II 500 MHz). Freeze-dried gelMA was sterilized by a cold ethylene oxide treatment (AZ Sint-Jan, Bruges, Belgium) before use. 10 w/v% solutions of gelMA, dissolved in sterile autoclaved PBS while stirring at 37°C, were used. To initiate photo-crosslinking, Irgacure 2959 (1-[4-(2-hydroxyethoxy)-phenyl]-2-hydroxy-2-methyl-1-propane-1-one) (BASF) or lithium phenyl-2,4,6-trimethylbenzoylphosphinate (Li-TPO-L or LAP) (kindly provided by the Polymer Chemistry and Biomaterials Research

group, Ghent University, synthesized as previously reported by Markovic et al. (2015), dissolved in PBS, were used as PI. 2 mol%, relative to the amount of methacrylamides present was added to the gelMA solution. Before adding, stock solutions of 0.8 w/v% of Irgacure or Li-TPO-L were sterilized using a 0.22 μm pore filter (Millipore).

Hydrogel Characterization

To evaluate the effect of different PIs on the hydrogel properties, gel fraction, swelling ratio and Young's moduli of cell-free gelMA/Irgacure 2959 or gelMA/Li-TPO-L hydrogel samples were determined. Hydrogel disks (diameter = 10 mm, height = 2 mm) were prepared by pipetting 800 μl of a 10 w/v% gelMA solution, containing 2 mol% Irgacure 2959 or Li-TPO-L, relative to the amount of methacrylamides present in gelMA, in a 6-well plate. After 10 min of physical gelation at room temperature (RT), gels with Irgacure 2959 as PI were photo-crosslinked for 20 min with a UV-A broad spectrum light (365 nm, 4 mW/cm^2, UVP Inc.), gels with Li-TPO-L were crosslinked using a UV-LED incorporated in the RegenHu bioprinter for 60 s (365 nm, 200 mW/cm^2). Disks of 10 mm diameter were punched out using a punching device.

Gel Fraction and Swelling Ratio

Gel fraction and swelling ratio of the gels was determined. Samples were dried in a desiccator for 2 weeks and weighed (W_{d0}), followed by swelling overnight in PBS at 37°C and weighed again (W_s). Subsequently, the samples were dried and weighed again (W_{d1}). The gel fraction and swelling ratio were defined as:

$$Gel\ fraction\ (\%) = \frac{W_{d1}}{W_{d0}} \times 100$$

$$Swelling\ ratio\ (\%) = \frac{W_s - W_{d0}}{W_{d0}} \times 100$$

Compression Test

After crosslinking, hydrogel disks were compressed using a universal testing machine (LRXplus, Lloyd Instruments) equipped with a 100 N load cell, at a rate of 5 mm/min. Hydrogel disks were compressed at RT over a distance of 1 mm and Young's moduli (kPa) were calculated. All measurements were prepared in fivefold.

Encapsulation of Spheroids in gelMA

Spheroids were combined with gelMA as a viscous printing medium for bio-ink based bioprinting by extrusion (**Figure 1B**). To examine the effect of hydrogel properties and PI type on spheroid morphology, viability and phenotype, hydrogel encapsulation experiments without printing were performed. Spheroids were encapsulated in 10 w/v% gelMA containing either Irgacure 2959 or Li-TPO-L as PI. Spheroids were collected from the microwells after 14 days of culture by vigorously resuspending the culture medium. After centrifugation, supernatant was removed and the gelMA/PI solution was added to the spheroid pellet. Hydrogel disks of 250 μl were prepared by pipetting spheroid/gelMA/PI solution in a 48-well plate. Per 250 μl gel, spheroids of 3 microwells were encapsulated resulting in ±4755 spheroids/gel. After physical crosslinking for 10 min at RT, gelMA/Irgacure 2959 gels and gelMA/Li-TPO-L gels were photo-crosslinked as described above (see section "Hydrogel Characterization"). Gels were transferred to a 12-well plate and chondrogenic medium was added. Medium was exchanged after 24 h and then every other 2 days, encapsulated spheroids were cultured for 14 days.

Directed Assembly of Spheroids: 3D Extrusion-Based Bioprinting

The processing potential of the bio-ink, gelMA/Li-TPO-L containing 14-day-old spheroids, was evaluated using extrusion-based 3D bioprinting, to create controlled formation of a larger construct (**Figure 1C**). Spheroids from 8 microwells (±12680 spheroids) were collected by vigorously resuspending the culture medium. After centrifugation, supernatant was removed and 1.0 ml of a 10 w/v% gelMA/Li-TPO-L solution was added to the pellet of spheroids. As a control, constructs containing single cells instead of spheroids were also printed. 4 × 10^6 hBM-MSC were collected and 1.0 ml of a 10 w/v% gelMA/Li-TPO-L solution was added to the cell pellet. After homogenization, the bio-ink solution was transferred into a cartridge and placed into the cartridge heater at 25°C for 30 min. Scaffolds were produced using the 3D Discovery Instrument (RegenHU), operated by human machine interface (HMI) and BioCAD software, equipped with a pneumatic dispensing printhead. A polyethylene conical needle with an inner diameter of 0.41 mm was used to print the scaffold by extrusion at feed rate of 5 mm/s. The printed scaffolds (1.3×1.3 cm) contained four layers of bio-ink (two horizontal, two vertical), printed with a theoretical strut thickness of 0.328 mm (80% of the needle's inner diameter). A pressure of approximately 0.035 MPa was applied and manually adjusted during the printing process of the constructs. After printing, scaffolds were physically crosslinked at RT for 10 min and photopolymerization of the scaffolds was induced by the UV-LED incorporated in the RegenHu bioprinter for 60 s (365 nm, 200 mW/cm^2). All printing parameters are described in **Table 1**.

Scanning Electron Microscopy

Bioprinted scaffolds containing cartilage microtissues were washed two times with PBS and fixed in 2% glutaraldehyde in

TABLE 1 | Printing parameters.

Parameter	Value
Cartridge temperature	25°C
Extrusion pressure	0.035 MPa
Ambient temperature	21°C
Feed rate	5 mm/s
Needle diameter	0.41 mm
Theoretical strut thickness	0.328 mm
Layers	4
Spheroid concentration	±12680/ml
Physical crosslinking	10 min at 4°C
UV irradiation time	60 s

0.1 M cacodylatebuffer (pH 7.2) for 3 h at RT. Next, scaffolds were washed three times in 0.1 M cacodylatebuffer, dehydrated in graded alcohol concentrations (30 min of 50%, 70%, 85%, and 95%) and completely dried by using hexamethyldisilazane (Sigma-Aldrich). Once dried, scaffolds were first coated with a thin layer of gold making use of a sputter coater (JFC-1300 auto fine coater, JEOL) to avoid charge accumulation. Scanning electron microscopy (SEM) (JSM-6010 PLUS/LV; JEOL) images were used to examine the morphology of the scaffolds and spheroids, and were obtained with an accelerating voltage of 7 kV at a working distance of 11 mm.

Live/Dead Viability Assay

To determine cell viability, spheroids, hydrogel samples or bioprinted scaffolds were harvested, two times washed with PBS and incubated with calcein-AM (2 μg/ml, Anaspec) and propidium iodide (2 μg/ml, Sigma). After 10 min of incubation, spheroid viability was evaluated using an inverted fluorescence microscope (Olympus IX81) equipped with Xcellence software (Olympus).

(Immuno)Histochemical Evaluation of Proliferation and Extracellular Matrix Components

Spheroids of 2 microwells were collected and pooled for histological analysis. Hydrogels and bioprinted scaffolds were rinsed with PBS 2 times prior to fixation. All samples were fixed overnight at 4°C with 4% paraformaldehyde, dehydrated in graded alcohol concentrations and embedded in paraffin. Paraffin sections of 5 μm thickness were cut, deparaffinized, and rehydrated. Sections were stained with hematoxylin/eosin (HE) (VWR/Thermo Fisher), Alcian Blue, and Picrosirius Red (PSR), in accordance to standard protocols, to analyze overall morphology and ECM components as GAG and collagen, respectively.

The distribution of collagen type II and collagen type I was visualized by immunohistochemistry (IHC). Heat induced antigen retrieval was performed using citrate buffer (pH 6,0, 2 × 5 min) at 90°C, followed by 10 min incubation with 3% H_2O_2 to block endogenous peroxidase activity. After 30 min blocking with a blocking solution (1% w/v Bovine Serum Albumin, 5% v/v normal rabbit serum, 0.2% v/v Tween 20), sections were incubated with monoclonal mouse anti-collagen II antibody for 2 h at RT (1:50, sc-518017, SantaCruz) or a monoclonal mouse anti-collagen I antibody (1:50, sc-293182, SantaCruz) at 4°C overnight. This was followed by a biotinylated rabbit anti-mouse antibody (1:200, E0413, Dako) as secondary antibody for 30 min. After washing, sections were treated with streptavidin-horseradish peroxidase for 30 min (1:200, Dako) after which 3,3-diaminobenzidine tetrahydrochloride (DAB, Sigma) served as a chromogen to visualize the coupled secondary antibody.

To assess proliferation, sections were stained with a mouse monoclonal antibody against the proliferation marker Ki67 (1:50, M7240, Dako). Staining procedure was similar as described above. The number of $Ki67^+$ was manually counted and are reported in **Supplementary Figure S1**. All IHC stained sections were counterstained with Mayer's hematoxylin and examined using an Olympus BX51 microscope. Sections were thoroughly screened and only images representative for the majority of the spheroids, hydrogels and scaffolds were selected.

Histomorphometric evaluation was performed to quantify the presence of the ECM components (GAG, collagen type I and type II). In brief, histological images (20× objective, Olympus BX51) were analyzed using the color deconvolution ("Alcian Blue and H" and "H DAB" vector) method in Image J. Automatic thresholding (RenyiEntropy method) was applied for the selection of GAG, collagen type I and collagen type II positive regions within spheroids. Positive stained area is shown as a ratio to the region of interest (ROI), i.e., total area of all spheroids on the slide. All measurements were performed in sixfold.

Statistical Analysis

Data were analyzed using SPSS version 26.0 (SPSS GmbH Software) and are represented as the mean ± 95% confidence interval (CI). To test for normality of the variables, the Shapiro–Wilk test was used. The homogeneity of the variances was assessed with the Levene's test. For data with a non-normal distribution, a Kruskal–Wallis test was performed. For the analysis of data with a normal distribution and homogeneous variances, a one-way ANOVA and Tukey's *post hoc* test were performed. For data with a normal distribution with non-homogeneous variances, a Welch's ANOVA test followed by a Games-Howell *post hoc* test were executed. For hydrogel properties, where two groups were compared and groups were normally distributed, an independent samples *t*-test was performed. P values < 0.05 were considered significant.

RESULTS

Cartilage Microtissues

High-Throughput Formation of Cartilage Microtissues

Spheroids were created using a non-adhesive agarose microwell system (**Figure 1A**). After seeding of the hBM-MSC suspension on the microwells, cells lowered into the bottom of the pores by gravitational force within 1–2 h and cells were distributed over the entire surface of the pore. Cells self-assembled spontaneously into slightly irregular shaped spheroids after 1 day of culture (**Figure 3A**). With increasing culture time, spheroids became more rounded and compact which is accompanied by a significant reduction in diameter from 131.68 ± 2.80 μm on day 7 to 116,28 ± 6.89 μm on day 21. Diameter slightly increased to a mean diameter of 122.09 ± 6.38 μm after 42 days of culture (**Figure 3C**). The circularity of the spheroids remained stable (±88%) (**Figure 3D**). Live/dead staining with calcein-AM/PI (**Figure 3B**) revealed high cell viability, cell dead is mostly observed at the periphery of the spheroids and in detached single cells. Few dead cells can be detected in the core of the spheroids, especially after 42 days of culture (indicated by white arrows, **Figure 3B**).

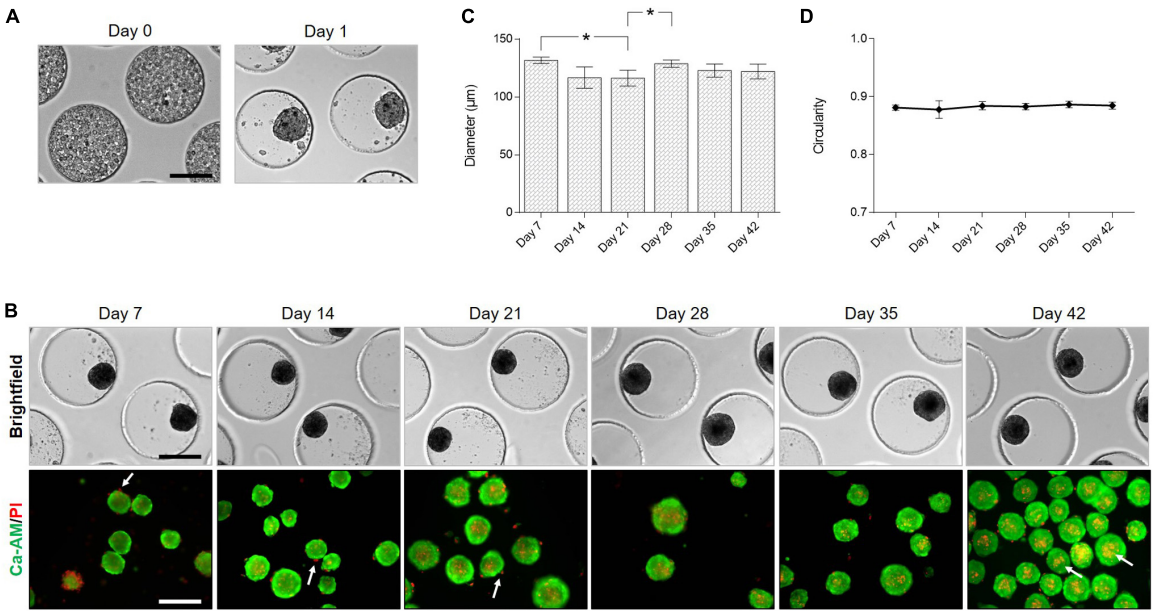

FIGURE 3 | Formation of cartilage microtissues: morphology and viability. **(A)** hBM-MSC lowered spontaneously into the pores of the microwell. After 1 day of culture irregular shaped spheroids were formed. **(B)** Light microscopy and live/dead staining of spheroids over time in culture, white arrows indicate dead cells. **(C)** Evaluation of spheroid diameter and **(D)** circularity (n = 3, Welch's ANOVA test followed by a *post hoc* Games-Howell, significant differences were marked as $^*p < 0.05$). All data are presented as mean ± 95% CI. All scale bars represent 200 µm.

Proliferation and Maturation of Cartilage Microtissues

Histological analysis was performed to screen overall morphology (HE), proliferation (Ki67), and cartilage ECM (**Figure 4**). HE staining shows the presence of nuclei throughout the spheroid. Nuclei appeared more flattened at the periphery of the spheroid (indicated by black arrows, **Figure 4A**). Spheroids displayed a cartilage-like morphology with lacunae with increasing culture time (indicated by white arrows, **Figure 4A**).

Proliferation within the spheroids was evaluated by performing an IHC staining against the proliferation marker Ki67. Staining showed that Ki67 positive cells were mostly located in the outer rim of the spheroids (**Figure 4A**). The highest number of $Ki67^+$ cells was reported after 7 days of culture (2.14 ± 0.85 cells/spheroid) (**Supplementary Figure S1**). On day 28, spheroids presented a significant higher number of Ki67 positive cells (1.31 ± 0.55 cells/spheroid) as compared to day 21 (0.31 ± 0.30 cells/spheroid), which correlates with the increase in diameter (**Figure 3C**). The number of Ki67 positive cells reduced after 35 and 42 days in culture (0.17 ± 0.26 and 0.08 ± 0.20 cells/spheroid, respectively (**Figure 4A** and **Supplementary Figure S1**).

To induce chondrogenic differentiation of hBM-MSC spheroids to mature cartilage microtissues, serum-free chondrogenic culture medium and low oxygen tension (5%) were applied. As the goal of our study is to develop articular cartilage-like microtissues, composition and distribution of cartilage specific ECM components was extensively screened. GAG were visualized by Alcian Blue staining. From day 7, slightly positive staining for GAG was detected (12.16 ± 2.57%), especially in the spheroid core. With increasing culture time, positive stained area and staining intensity both increased (46.13 ± 4.36% on day 42), resulting in the presence of GAG covering the entire spheroid area (**Figures 4A,B**). Picrosirius Red staining showed slightly positive collagen fibers in the 7-day-old spheroids and from 14 days in culture, mature fibrillar collagen was demonstrated (black arrows, **Figure 4A**). Starting from day 21, a clear presence of fibers especially located at the periphery of the spheroid was reported (black arrows, **Figure 4A**). This corresponds to the IHC localization of collagen type I, where fibers showed to be present exclusively in the outer rim of the spheroids, covering 2.49 ± 2.36% of the spheroid area after 7 days of culture and increased to 29.64 ± 4.90% after 42 days of culture (**Figures 4A,B**). This is in contrast to the distribution of collagen type II, which is more dispersed throughout the entire spheroid. Collagen type II manifested starting from 14 days of culture, mainly situated at the periphery covering 28.56 ± 3.52% of spheroid area, and the positively stained area increased with increasing culture time, stretching toward the center covering 61.83 ± 4.40% of the spheroid area on day 42 (**Figures 4A,B**). Some spheroids are devoid of collagen type II in the center but Alcian Blue staining shows the presence of GAG in the core of the spheroid (**Figure 4A**).

Cartilage Microtissue Fusion Into a Macrotissue

To investigate the potential and time frame of immature 7-day-old cartilage microtissues to fuse, spheroids were placed in close proximity to each other by performing a doublet

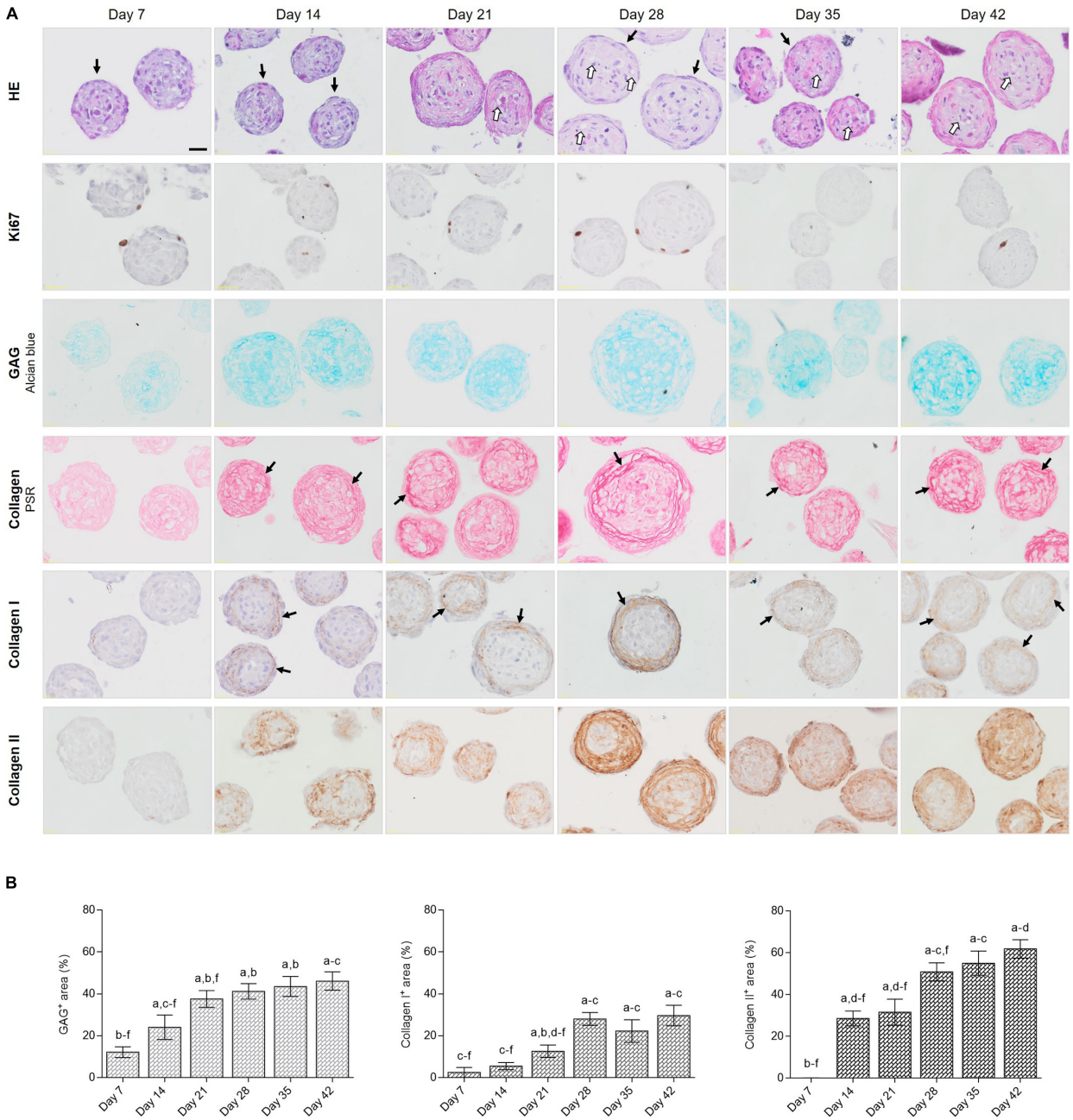

FIGURE 4 | (Immuno)histological evaluation of cartilage microtissues: proliferation and extracellular matrix. **(A)** HE staining was performed to assess overall morphology, black arrows indicate flattened nuclei of cells at the periphery and white arrows indicate lacunae. IHC staining for Ki67 indicated proliferating cells, Alcian Blue staining showed the presence of glycosaminoglycans (GAG). Collagen was visualized by Picrosirius Red (PSR) staining, black arrows indicate mature fibrillar collagens. IHC stainings for collagen type I and type II were performed, black arrows indicate collagen type I fibers. Scale bar 20 μm. **(B)** Quantification of GAG, collagen I and collagen II positive stained areas. All data are presented as mean ± 95% CI. Significant differences ($p < 0.05$) were marked [a] compared to day 7, [b] to day 14, [c] to day 21, [d] to day 28, [e] to day 35, and [f] to day 42 ($n = 6$, One-way ANOVA followed by a Tukey's *post hoc* test).

formation assay (**Figure 2**; Susienka et al., 2016). For the creation of spheroid doublets, the donor microwell was cropped and inversely stacked on the recipient microwell. After centrifugation spheroids of the donor microwell lowered into the wells of the recipient microwell, resulting in pairwise placement of spheroids, creating doublets (**Figure 5A**). Microwells comprising triplets and quadruplets were excluded for evaluation. During fusion, doublets rotated both clock- and counterclockwise in the pores of the microwell. To analyze the time span of fusion of a mature cartilage microtissue, morphological changes during the first hours of the fusion process were imaged. Doublet length, doublet width, intersphere angle and contact length between spheroids

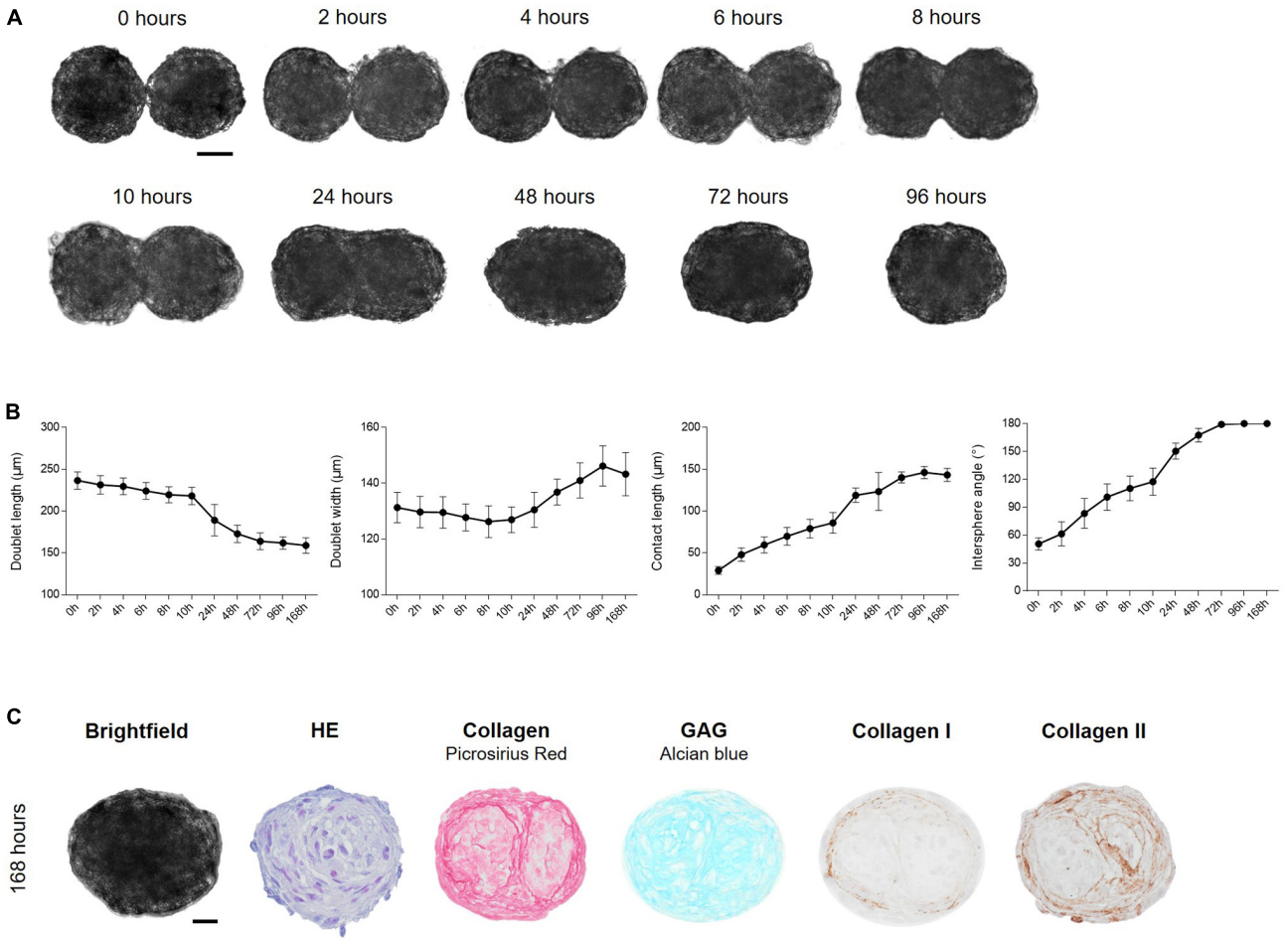

FIGURE 5 | Fusion of cartilage microtissue doublets. **(A)** Cartilage microtissues at maturation stage of 7 days were harvested and doublets were formed. Spheroid fusion was tracked for 168 h by light microscopy. Scale bar 50 µm. **(B)** Morphological parameters such as doublet length (µm), doublet width (µm), contact length (µm), and intersphere angle (°) were measured using Image J software. (n = 12, all data are presented as mean ± 95% CI). **(C)** Morphological and (immuno)histochemical evaluation of fused doublets after 168 h of culture. HE staining was performed to assess overall morphology, Alcian Blue staining showed the presence of glycosaminoglycans (GAG). Collagen was visualized by Picrosirius Red (PSR) staining and IHC stainings for collagen type I and type II were performed. Scale bar 20 µm.

were measured. Initial contact between spheroids occurs within the first hour (**Figure 5A**). As fusion progressed, doublet lengths shortened in function of time starting from 236.53 ± 10.24 µm to 158.91 ± 9.41 µm after 168 h. Intersphere angle and contact length increased in function of time at a similar rate. After 72 h of fusion, the intersphere angle reached a plateau (±179°) and did not change anymore in function of prolonged culture time. Contact length approached 140 µm which matches the width of the spheroids, indicating complete spheroid fusion. However, contact length and doublet width showed some minor deviations indicating continuous dynamic processes in the fused spheroids. The fused spheroid after 96 h indeed shows a more rounded morphology compared to the oval spheroid after 72 h (**Figures 5A,B**). Histological evaluation of the fused doublet after 168 h is shown in **Figure 5C**. Although HE staining shows a perfectly fused doublet, ECM stainings (PSR, Alcian Blue, collagen I, and II) clearly show the margins of the individual cartilage microtissues. Especially collagen type I (demonstrated by PSR and IHC) is situated at the periphery of the individual microtissues and the fused doublet (**Figure 5C**). The newly synthesized matrix surrounding the original individual spheroids is mainly composed of collagen II (**Figure 5C**).

To confirm if a large number of spheroids was able to fuse into a macrotissue, ±200 7-day-old spheroids were seeded in agarose coated 96-wells (**Figure 6**). Spheroids made contact within 2 h after seeding. After 24 h, margins between spheroids faded and no individual spheroids could be distinguished. Further compaction occurred and after 96 h, a circular construct of ±527 µm diameter was formed (**Figure 6A**). After 168 h of fusion, histology showed the presence of GAG throughout the entire fused tissue, collagen I and especially collagen II were present at the periphery of the fused tissue and at the periphery of the original individual spheroids, which still can be perceived with histology (**Figure 6B**).

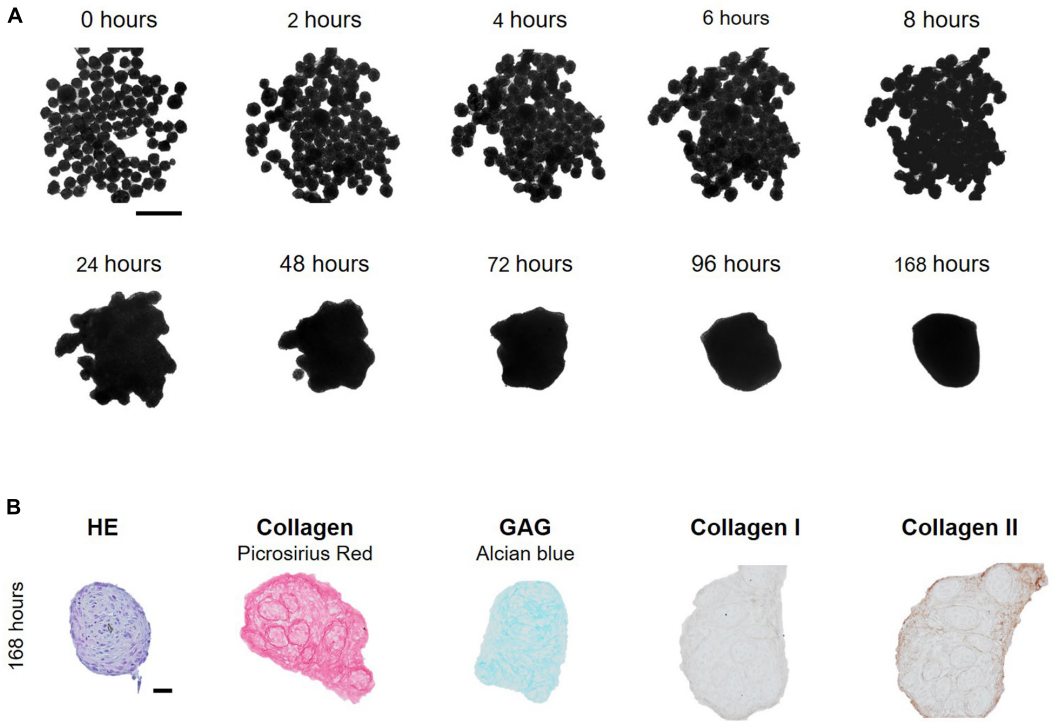

FIGURE 6 | Formation of a macrotissue by fusion of multiple cartilage microtissues. **(A)** Cartilage microtissues at maturation stage of 7 days were harvested and ± 200 spheroids were seeded per agarose coated 96-well. Spheroid fusion was tracked for 168 h. Scale bar 500 μm. **(B)** Morphological and (immuno)histochemical evaluation of the fused microtissues after 168 h of culture. HE staining was performed to assess overall morphology, Alcian Blue staining showed the presence of glycosaminoglycans (GAG). Collagen was visualized by Picrosirius Red (PSR) staining and IHC stainings for collagen type I and type II were performed. Scale bar 20 μm.

Encapsulation of Cartilage Microtissues in gelMA

Because spheroids started to developed a cartilage ECM after 14 days of culture, as demonstrated by GAG (24.06 ± 5.84%) and collagen type II content (28.56 ± 3.52%) (**Figures 4A,B**), spheroids at this maturation stage were selected to encapsulate in gelMA. To assess the impact of the biopolymer and PI on spheroid morphology, viability, phenotype, fusion and outgrowth, spheroids were encapsulated in hydrogel disks of 10 w/v% gelMA. Polymerization by UV-light was performed with 2 mol% Irgacure 2959 or Li-TPO-L and their effect on hydrogel properties was assessed as well.

Morphology, Viability and Fusion of Encapsulated Cartilage Microtissues

Spheroids encapsulated in gelMA displayed a round morphology (**Figure 7**). In the gelMA/Irgacure2959 hydrogels, cellular outgrowth was observed after 7 days. In contrast, when Li-TPO-L was used as a PI, more cellular outgrowth was observed after 7 and 14 days post encapsulation. After 14 days, cellular sprouts were spread within the entire hydrogel disk. Live/dead staining showed that spheroids and their cellular outgrowths remained viable in all hydrogels, regardless the PI used for photopolymerization (**Figure 7A**). Encapsulated spheroids located in near vicinity of each other still have the capacity to fuse, as indicated by the black and white arrows in **Figure 7B**. Nevertheless, spheroid fusion post encapsulation is strongly dependent on the position of the spheroids within the hydrogel and progresses slower. Only incomplete fusion is reached during the 14-day time frame of the encapsulation experiment, reaching an intersphere angle of ±127°. This is in contrast with the non-encapsulated spheroid doublets where complete fusion (intersphere angle of ±180°) is obtained after 72 h.

Physico-Chemical Properties of GelMA

The mechanical and physico-chemical properties including Young's modulus, gel fraction and swelling behavior were evaluated for cell-free gelMA hydrogel disks, crosslinked in the presence of Irgacure 2959 or Li-TPO-L (**Figure 7C**). Irgacure 2959 as PI resulted in samples with significantly higher Young's moduli (9.84 ± 1.22 kPa) compared to Li-TPO-L samples (6.69 ± 1.25 kPa).

The results of the swelling test indicate that all conditions were able to absorb large quantities of water, which mimics the content of native cartilage tissues as cartilage is mainly composed of water (80%). Li-TPO-L crosslinked hydrogels showed significantly higher swelling (565.1 ± 13.87%) compared to Irgacure 2959 crosslinked hydrogels (382.59 ± 27.78%). Irgacure 2959 crosslinked hydrogels had a lower gel fraction

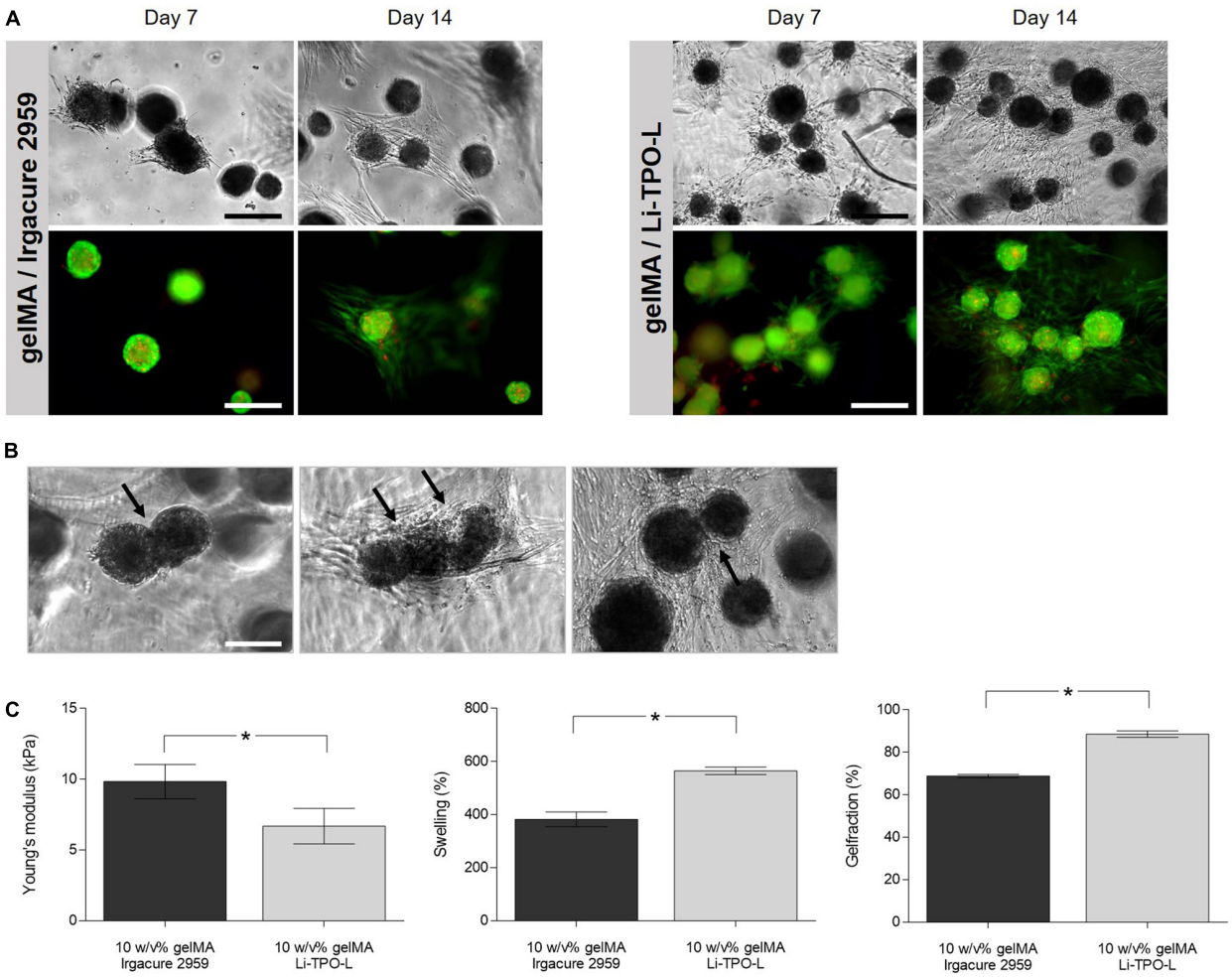

FIGURE 7 | Influence of gelMA properties on spheroid morphology, viability, and fusion. **(A)** Cartilage microtissues at maturation stage of 14 days were harvested and were encapsulated in gelMA using either Irgacure 2959 or Li-TPO-L as a photo-initiator. Morphology and viability of encapsulated spheroids 7 and 14 days post encapsulation. Scale bars 200 μm. **(B)** Cellular outgrowth and fusion of 14-day-matured cartilage microtissues within gelMA after 14 days of culture in the hydrogel, fused spheroids are indicated by the black arrows. **(C)** Young's modulus, gel fraction and swelling ratio were assessed on cell-free gelMA hydrogel samples ($n = 5$, independent samples t-test). All data are presented as mean ± 95% CI and significant differences were marked as $^*p < 0.05$.

(68.84% ± 0.81) compared to Li-TPO-L crosslinked hydrogels (88.61% ± 1.48).

Influence of GelMA on Proliferation and Cartilage Phenotype

Hematoxylin/eosin staining showed that the hydrogel encapsulation process did not change the morphology of the spheroids. In contrast, immunohistochemical staining for Ki67 demonstrates that encapsulated cells rarely proliferated, only few positive cells were found (0.29 ± 0.49 and 0.43 ± 0.53 cells/spheroid after 7 and 14 days of encapsulation, respectively) (**Figure 8**).

Histological analysis was performed to assess the effect of gelMA encapsulation on the cartilaginous phenotype of the spheroid. Alcian Blue staining showed the presence of GAG which increased with extending culture time, though not significantly, from 47.33 ± 3.46% 7 days post encapsulation to 54.52 ± 5.47 14 days post encapsulation (**Figures 8**, **11B**). Moreover, combination with gelMA seems to have a positive effect on GAG production, indicated by a significantly higher positively stained area by Alcian Blue staining in the encapsulated spheroids (**Figure 8**) as compared to the non-encapsulated spheroids (37.59 ± 4.00% and 41.19 ± 3.69% on day 21 and 28, respectively) (**Figures 4**, **11B**). For the evaluation of collagen content, PSR, collagen type I, and type II stainings were performed. Once encapsulated in gelMA, only slightly positive staining for collagen type I was observed. This reduction in collagen type I content in encapsulated spheroids (1.81 ± 1.01% 7 days post encapsulation and 4.68 ± 3.78% 14 days post encapsulation) was significant as compared to non-encapsulated controls (12.57 ± 2.97% and 28.04 ± 3.05% on day 21 and 28, respectively) (**Figure 11B**). Spheroids in gelMA/Li-TPO-L hydrogels showed a reduced presence of collagen type I as compared to gelMA/Irgacure 2959 hydrogels. Moreover,

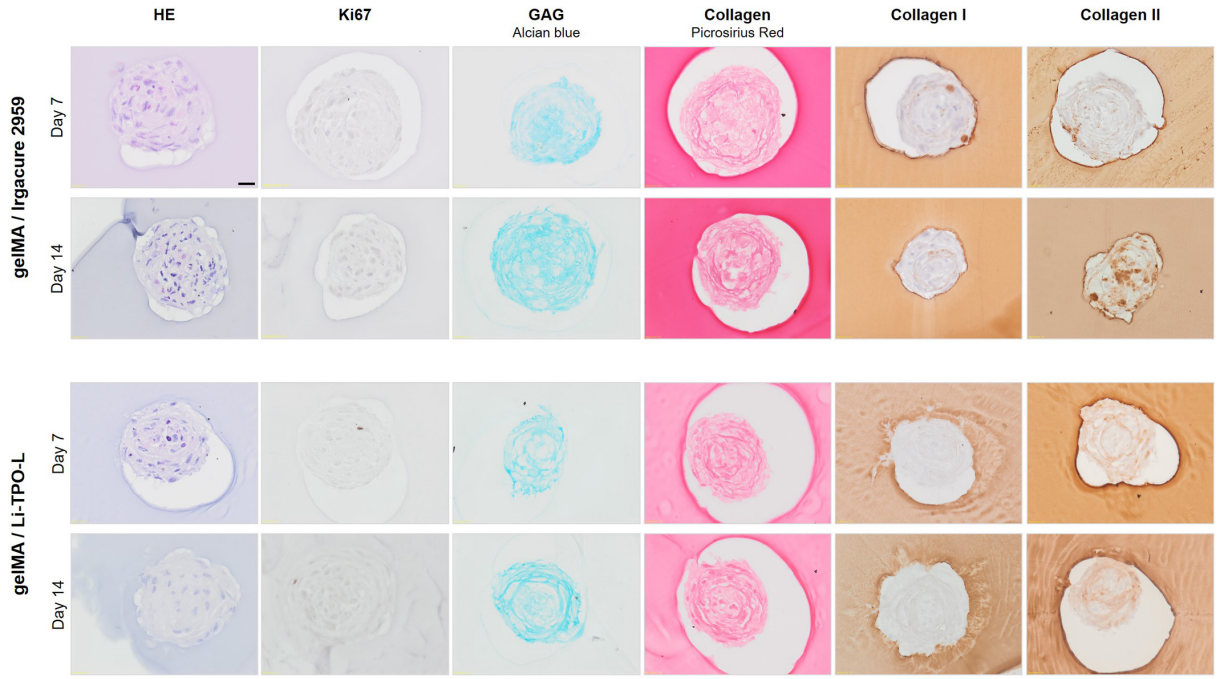

FIGURE 8 | Evaluation of cartilaginous phenotype 7 and 14 days post encapsulation in gelMA. Comparison of Irgacure 2959 or Li-TPO-L as a photo-initiator. HE staining was performed to assess overall morphology, IHC staining for Ki67 indicated proliferating cells, Alcian Blue staining showed the presence of glycosaminoglycans (GAG). Collagen was visualized by Picrosirius Red (PSR) staining and IHC stainings for collagen type I and type II were performed. Scale bar 20 μm.

spheroids encapsulated in gelMA/Li-TPO-L hydrogels had a higher and more dispersed collagen type II content (**Figure 8**). Collagen type II content was not affected by encapsulation (**Figure 11B**). Therefore, this condition was selected for further experiments.

Extrusion Bio-Ink Based 3D Bioprinting of Cartilage Microtissues

The processing potential of the bio-ink, consisting of gelMA/Li-TPO-L containing cartilage microtissues at maturation stage of 14 days was evaluated using extrusion-based 3D bioprinting (**Figure 9**). Processing parameters such as ambient temperature, cartridge temperature, needle type, and diameter, were optimized (**Table 1**).

Scaffolds (1.3 × 1.3 cm) composed of four layers in a 0/90° lay-down pattern were printed according to a computer-aided design (CAD), using an applied pressure of approximately 0.035 MPa [**Figure 9A**(a)]. Scaffolds displayed highly controlled macropore morphology, with pore sizes around 800 μm and struts with a mean thickness of 480.01 ± 20.90 μm (measured after 30 min immersion in culture medium post printing). Spheroids were dispersed throughout the entire scaffold [**Figure 9A**(b–f)]. SEM analysis was performed after 4 days of culture to investigate scaffold and spheroid morphology (**Figure 9B**). The dehydration process for SEM analysis caused shrinkage of the scaffold samples. SEM of the gelMA showed an organized networked structure. Spheroids show cellular outgrowth [white arrows, **Figure 9B**(c,e)] and when placed adjacent to each other, cellular sprouts made contact, initiating spheroid fusion [black arrow, **Figure 9B**(c)]. Brightfield images after 4 and 14 days of culture (**Figure 9C**) confirmed that after the printing process, spheroids were still able to grow out, and that is, dependent on their initial position, either on the outer surface of the printed construct or deeper into the hydrogel (**Figure 10D**). When deposited in close proximity to each other, spheroids were able to fuse in the printed construct [indicated by black arrows, **Figure 9C**(a,c)]. Culturing of the bioprinted scaffolds for 14 days, showed that scaffolds retained their 3D structure and that spheroids remained at their initial 3D spatial position (**Figure 10A**). The printing process did not affect spheroid viability as observed by live/dead staining (**Figures 10B–D**). 14 days post printing, spheroids and sprouts of nearly surfacing, partially protruding and fully encapsulated spheroids were still viable (**Figures 10B–D**). However, complete fusion of cartilage microtissues was not obtained yet.

Histological evaluation and macroscopic pictures confirmed the 3D printed pattern composed of struts and pores (**Figure 11**, first row). Microscopical histological evaluation showed that post printing spheroids displayed good morphology with intact nuclei throughout the entire spheroids. More importantly, spheroid ECM was not altered or did not deteriorate after enduring the printing process. 7 days post printing, spheroids displayed high GAG and collagen type II content, and low to no collagen type I presence, which is in line with the results of the encapsulation experiments, no significant differences were observed for the ECM components in comparison with

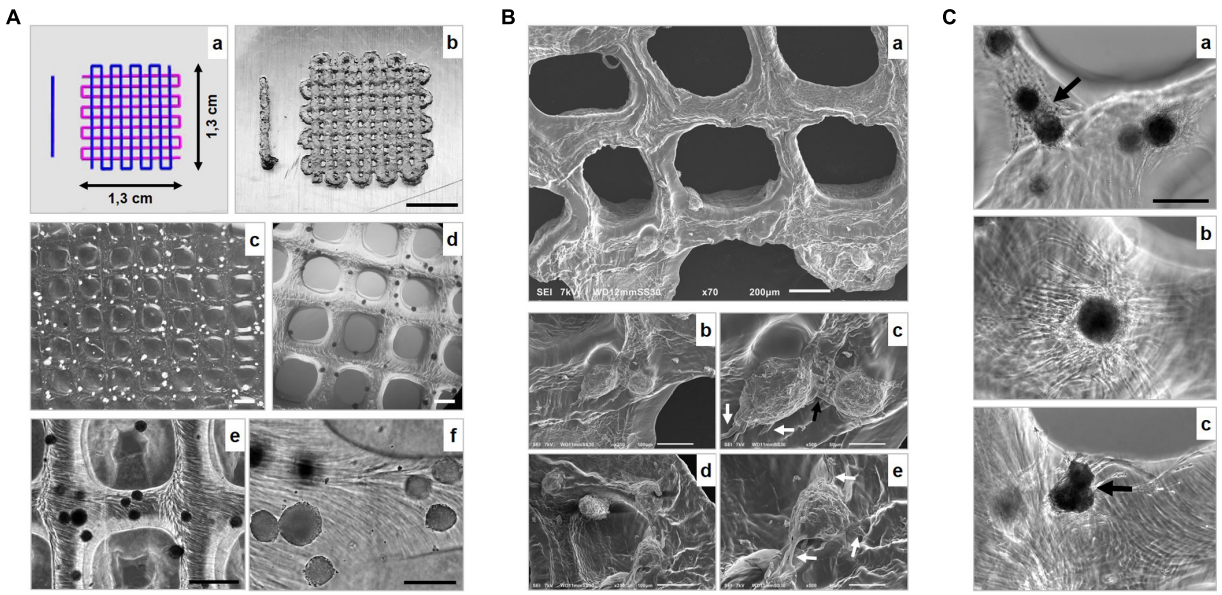

FIGURE 9 | 3D bioprinting of 14-day-mature cartilage microtissues in gelMA/Li-TPO-L **(A)** Representation of **(a)** the CAD model and **(b–f)** macroscopic to microscopic representation of the printed scaffolds. Scale bars 500 μm **(b)**, 800 μm **(c)**, 500 μm **(d,e)**, 200 μm **(f)**. **(B)** Scanning Electron Microscopy (SEM) evaluation of bioprinted scaffolds. Black arrow indicates cellular sprouts of adjacent spheroids making contact, initiating fusion **(b)** and white arrows **(b,c)** indicate cellular outgrowth. Scale bar 200 μm **(a)**, 100 μm **(b,d)**, 50 μm **(c,e)**. **(C)** Fusion and cellular outgrowth of spheroids 4 days **(a)** and 14 days **(b,c)** post printing within the gelMA. Black arrows indicate tissue fusion. Scale bar 200 μm.

the encapsulated spheroids (**Figures 11A,B**). Moreover, GAG and collagen type II content increased over time in culture from 43.40 ± 2.75% to 52.82 ± 5.63% and 36.79 ± 6.75% to 52.45 ± 4.15%, respectively, 7 and 14 days post printing (**Figure 11B**). Bioprinting of spheroids clearly outperformed the bioprinting with single cells (**Figure 12**). Constructs with single cells showed poor viability 7 days post printing and no chondrogenic differentiation was observed after 14 days. Spheroids seem to withstand the printing process better, probably because of their robust ECM.

DISCUSSION

Cell-based regenerative therapies for cartilage repair and regeneration are trending, with (M)ACI as a well-known example. However, this procedure often results in the creation of reparative tissue, with inferior quality and lacking durability when compared to the native tissue. This can be attributed to chondrocytes having the tendency to dedifferentiate during expansion in 2D culture (Dewan et al., 2014; Deng et al., 2016; Onofrillo et al., 2018; De Moor et al., 2019). Moreover, the application of individual cells fails to mimic the complex cell-cell and cell-matrix interactions present within a 3D tissue, which hinders the accurate imitation of the early events in tissue development (Gionet-Gonzales and Leach, 2018).

In the search for an alternative to freely inject or transplant cells into the defect site, 3D bioprinting holds a great promise to fabricate a tissue construct mimicking the native tissue by the directed assembly of microscale building blocks into a larger tissue construct. We explored a hybrid strategy combining cellular microtissues, biomaterials and 3D printing technology. For the first time, small spheroids of BM-MSC were generated using a cost-effective system and the potential of a low-cost modified version of the natural polymer gelatin (gelMA) was tested to serve as an instructive ink for cartilage microtissues to create a macroscale tissue. This work aimed to elucidate if BM-MSC spheroids are able to differentiate into cartilage microtissues and how they respond to encapsulation in a gelMA hydrogel environment. The promise of this approach is that in future studies cartilage microtissues of different maturation stages mimicking endochondral ossification could be printed in a stratified pattern resembling osteochondral interfaces. This stratified approach cannot be obtained by current clinical therapy with injecting of cells or spheroids (chondrospheres).

Prior to encapsulation of spheroids with gelMA, different culture times were evaluated to select the maturation stage of the cartilage microtissue (optimal spheroid diameter and ECM content). Self-assembled 3D cartilage microtissues from human BM-MSC were successfully generated using a non-adhesive agarose microwell system. This high-throughput technique allowed the controlled formation of spheroids with a mean diameter of 116.73 μm after 14 days of culture, which is an optimal geometry for deposition by the print needle. 3D microtissues can be created in several other ways, using pellet culture, spinner flask culture, hanging drop method, etc., the main disadvantages of these techniques are the heterogeneity of the spheroids (intervariability in dimensions is reflected in suboptimal chondrogenic differentiation), the quantity of the produced spheroids and the intensive manual labor for

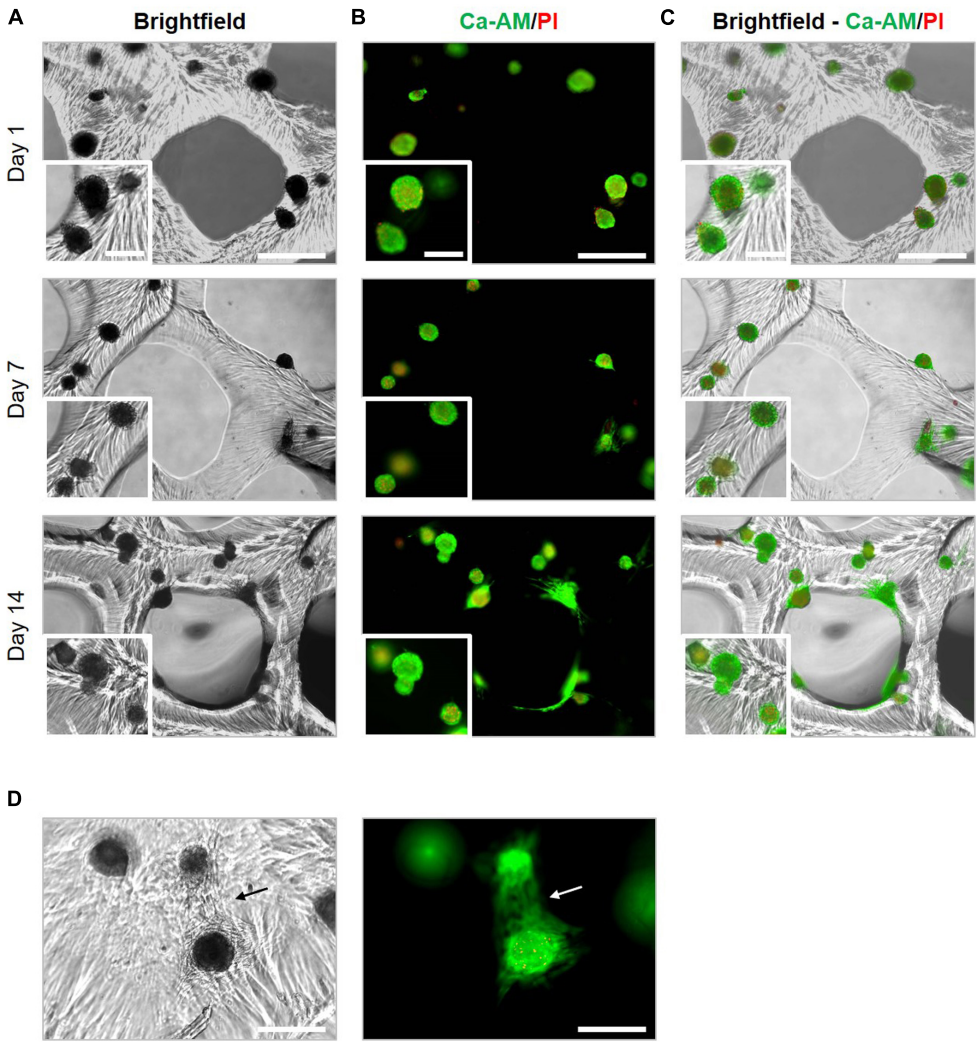

FIGURE 10 | Viability of cartilage microtissues post 3D bioprinting. The viability of spheroids bioprinted at maturation stage of 14 days was assessed by live/dead staining with ca-AM/PI after 1, 7, and 14 days post printing. **(A)** Brightfield images, **(B)** fluorescent images of ca-AM/PI staining and **(C)** merged brightfield and ca-AM/PI images. Scale bars 500 μm (overview) and 200 μm (insert). **(D)** Cell outgrowth within printed constructs 14 days post printing. Cells spreading out from a surfacing spheroid (lower spheroid) toward a deeper situated spheroid (upper spheroid). Scale bar 500 μm.

the exchange of culture medium and spheroid harvesting (Achilli et al., 2012).

In this study, the spheroids were homogeneous in shape and size, crucial for efficient deposition by 3D bioprinting. In addition to homogeneity and stability in diameter and circularity along the culture period, spheroids showed a high viability during chondrogenesis, which started from 14 days in culture, indicated by the manifestation of cartilage ECM components such as GAG and collagen II. Histological analysis also showed that GAG and collagen II increased over the 42 days of spheroid culture time. Chondrogenesis was induced by a low oxygen culture environment, mimicking the physiological concentration and the application of a serum-free chondrogenic culture medium containing TGF-β1. It has been described that TGF-βs contribute in the regulation of chondrogenic differentiation from the early to terminal stages, including condensation, proliferation, terminal differentiation and maintenance of articular chondrocytes. More specifically, the TGF-β1 signaling pathway induces mesenchymal condensation via up-regulation of N-cadherin and fibronectin and TGF-β1 treatment initiates chondrogenesis of mesenchymal progenitor cells (Wang et al., 2014). In this regard, it is important that spheroid cultures have a low variability in spheroid dimensions allowing to homogeneously differentiate into the cartilage phenotype and leading to thousands of cartilage microtissues at the same maturation stage.

Hydrogels have been widely used as 3D matrices for cell application. They are used as a medium for the retention of cells after injection in the cartilage defect site or as a carrier for cells or spheroids during bio-ink based extrusion printing to ensure shape fidelity of the construct (Moldovan et al., 2018; Li et al., 2019). Common biomaterials used in cartilage engineering are collagen, alginate, hyaluronic acid, etc., because of their

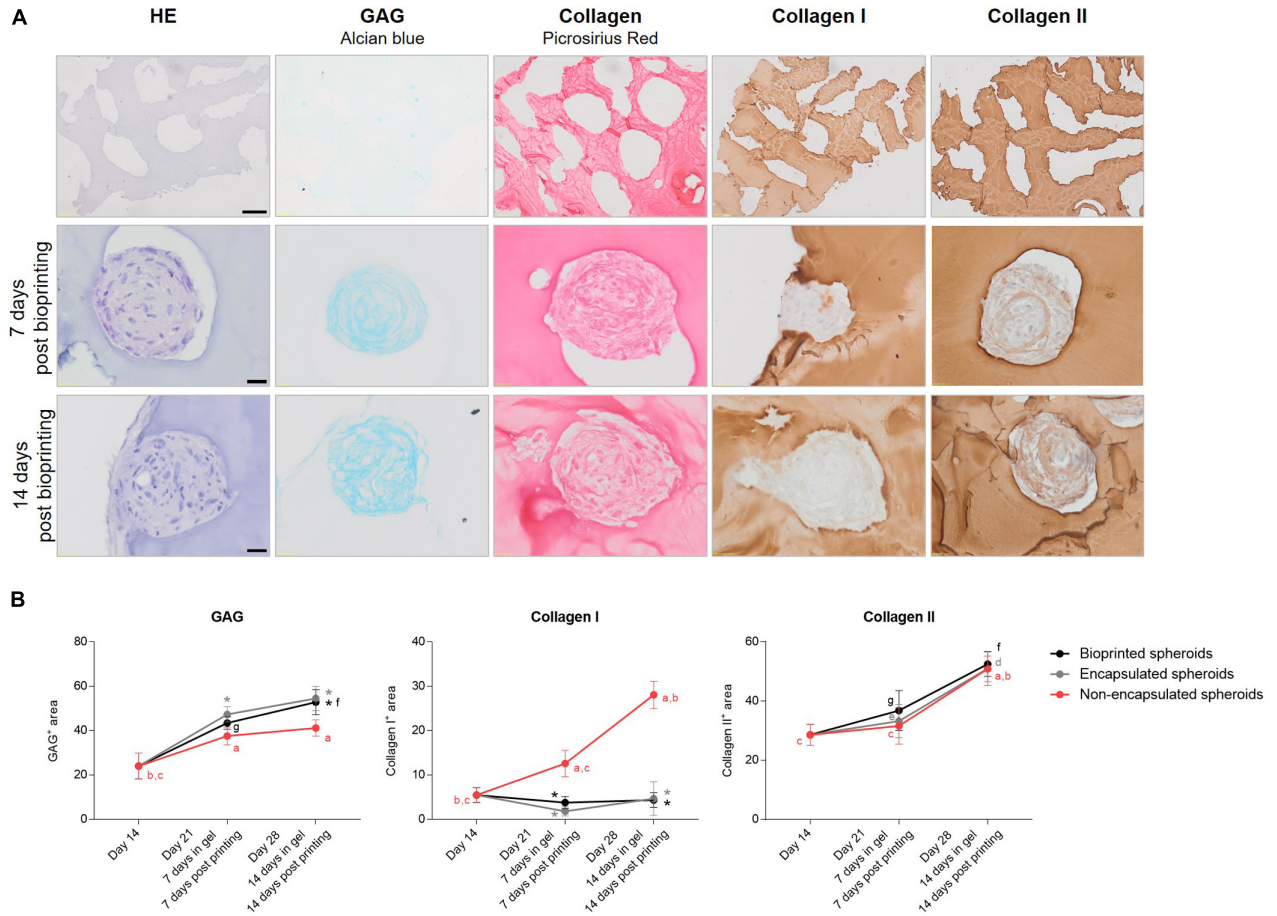

FIGURE 11 | Evaluation of cartilaginous phenotype of microtissues post printing. **(A)** HE staining was performed to assess overall morphology, Alcian Blue staining showed the presence of glycosaminoglycans (GAG). Collagen was visualized by Picrosirius Red (PSR) staining and IHC stainings for collagen type I and type II were performed. Scale bar 20 μm. **(B)** Graphs represent the quantification of GAG, collagen I and collagen II positive stained areas within bioprinted spheroids as compared to encapsulated spheroids in gelMA/Li-TPO-L and non-encapsulated spheroids from corresponding culture timepoints. All data are presented as mean ± 95% CI. For non-encapsulated spheroids, significant differences ($p < 0.05$) between culture timepoints were marked [a] compared to day 14, [b] to day 21, and [c] to day 28 spheroids. For encapsulated spheroids significant differences ($p < 0.05$) between culture timepoints were marked [d] compared to 7 days post encapsulation and [e] to 14 days post encapsulation. For bioprinted spheroids significant differences ($p < 0.05$) between culture timepoints were marked [f] compared to 7 days post printing and [g] to 14 days post printing. For both encapsulated (in gray) and bioprinted spheroids (in black) significant differences compared to the non-encapsulated spheroid controls were marked * ($n = 6$, One-way ANOVA followed by a Tukey's *post hoc* test).

resemblance with the native tissue ECM (Li et al., 2019). In this work gelMA was chosen because it has shown to be a permissive environment for neo-cartilage formation when cell suspensions of chondrocytes or MSC are encapsulated (Levato et al., 2017; Rothrauff et al., 2017). After encapsulation, cartilage microtissues proved to retain their geometry and although the crosslinking process involving UV-light could be detrimental for cell viability, it was preserved in the hydrogel. However, a shift in proliferative capacity was observed after embedding in gelMA, limited Ki67 positive cells were found in comparison to non-encapsulated spheroids. Although this lack of Ki67 staining, light microscopic evaluation showed the cellular outgrowth. Similar results were reported when spheroids of human adipose-derived MSC were encapsulated in 5, 7.5, and 10 w/v% gelMA hydrogels: sprouting was observed and was more pronounced in the softest gels (Žigon-Branc et al., 2019). In this study, outgrowth of cells was especially seen in the softer gelMA hydrogels crosslinked with Li-TPO-L as a PI. Interestingly, these hydrogels with a significantly lower Young's modulus did display a higher gel fraction than hydrogels crosslinked with Irgacure 2959. The latter is expected because a LED with higher intensity was used to crosslink the Li-TPO-L gels and Li-TPO-L has an absorption maximum at approximately 375 nm. Therefore, at the wavelength of 365 nm, it provides better reactivity compared to Irgacure 2959, whose absorption already tails out in this spectral range and Li-TPO-L also exhibits a higher efficiency and yield of radical formation (Markovic et al., 2015). It is hypothesized that crosslinking with Li-TPO-L probably results in a more homogenously distributed network throughout the entire hydrogel, as compared to Irgacure 2959 which possibly results in a more heterogeneously distributed crosslinked network with initial crosslinking at the surface and less transmission of the UV-light deeper in the gel, explaining

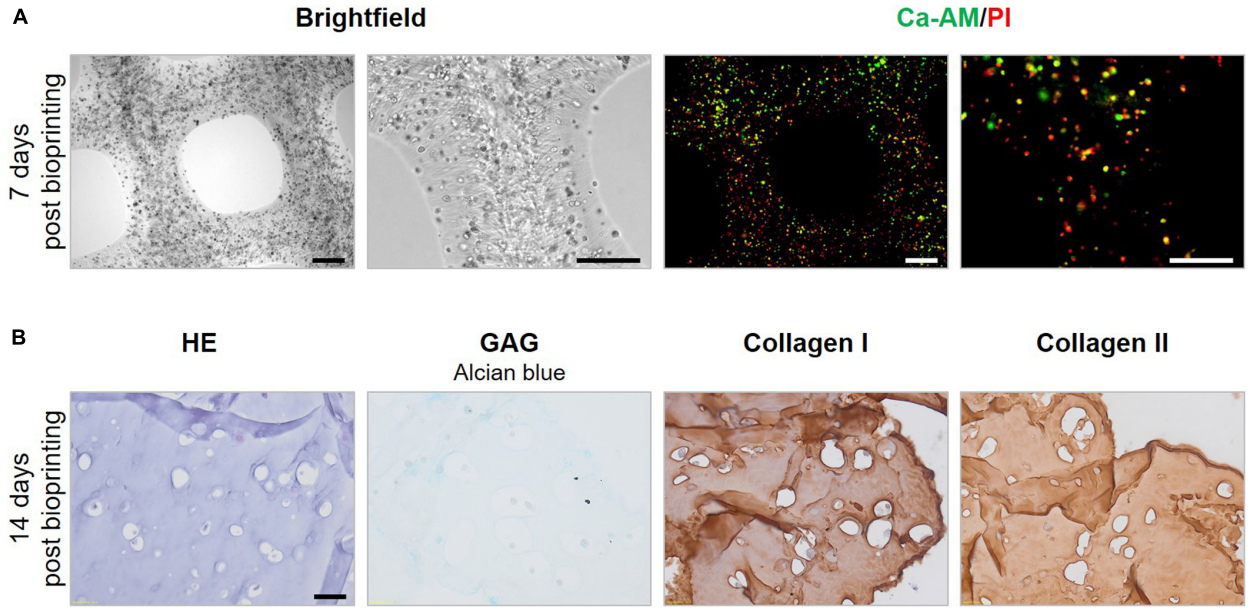

FIGURE 12 | Evaluation of bioprinted single cells. **(A)** Morphology and viability of bioprinted single cells 7 days post printing. Scale bars 200 μm. **(B)** HE staining was performed to assess overall morphology, Alcian Blue staining showed the presence of glycosaminoglycans (GAG) and IHC stainings for collagen type I and type II were performed. Scale bar 20 μm.

the higher mechanical strength but lower gel fraction. Moreover, different crosslinking times and light sources with different intensities were used to crosslink the Irgacure 2959 and Li-TPO-L gels, respectively, explaining the differences in mechanical properties and gel fraction.

Regardless of the hydrogel stiffness, the encapsulated chondrogenic induced spheroids presented a GAG- and collagen type II-rich ECM, increasing with time in culture in the hydrogel. It was already described by Salamon et al. (2014) that gelMA had a pro-chondrogenic impact on MSC. When adipose-derived MSC were seeded on top of gelMA films, an upregulation of Sox9, Sox5, and Col2a1 gene expression was described (Salamon et al., 2014). Moreover, seeding adipose-derived MSC on gelMA resulted in a stronger accumulation of GAG compared to controls (Salamon et al., 2014). We also observed that gelMA encapsulation had a cumulative effect on GAG production within spheroids and Roosens et al. (2019) reported the same trend when spheroids consisting of valvular interstitial cells were encapsulated. The constructs with lower stiffness resulted in a downregulation of collagen I and an increase in collagen II production. Žigon-Branc et al. (2019) also demonstrated that the extent of chondrogenic differentiation of MSC spheroids was more pronounced in softer hydrogels.

The bioprinting processability of spheroid-laden gelMA/Li-TPO-L bio-ink was improved after optimization of the printhead heater and environmental temperature. Hence, gelMA scaffolds with encapsulated cartilage microtissues demonstrated good shape-fidelity. Moreover, the printed scaffolds were stable for the entire culture period and spheroid viability and phenotype remained after enduring the printing process. For the creation of large scale constructs with relevant mechanical strength, the hydrogel can be reinforced with a synthetic polymer such as polycaprolactone (PCL), a popular polymer due to its superior rheological and viscoelastic properties (Woodruff and Hutmacher, 2010). Daly et al. (2016) co-deposited hydrogel bio-inks with PCL filaments and PCL-reinforced hydrogel scaffolds had compressive moduli (2 MPa) similar to that of native articular cartilage. Co-depositioning with PCL fibers can lead to stress shielding if the young's modulus of the implant is higher than the modulus of the surrounding tissue which will lead to the PCL fibers carrying most of the externally applied forces. It is important to keep this strain mismatch between implant and surrounding tissue limited, preventing poor implant performance and surrounding tissue damage (Wintermantel et al., 2001; Farag, 2017).

Recently, a material-free assembly method was used to create a cartilage construct starting from spheroids (Grogan et al., 2019). The Kenzan bioprinting method does not use any material support structure, but relies on natural cell-to-cell contact behavior and spheroid fusion after fixation upon microneedles that provide temporary support (Moldovan et al., 2017). Spheroids used for this method are characterized by a large diameter (>500 μm) (Grogan et al., 2019). However, creating viable tissues with large diameter is challenging due to the diffusion limit (100–200 μm) (Radisic et al., 2006; Liu et al., 2015). Especially centrally located cells of an engineered construct, lack sufficient supply of nutrients and oxygen, and are unable to dispose metabolic products (e.g., CO_2), causing poor viability (Alvarez-Pérez et al., 2005; Gaskell et al., 2016). For this reason, we opted to start from small diameter spheroids. Their ability to fuse is essential in this synergistic hybrid tissue engineering

approach, as tissue fusion is the fundamental biological process to build larger structures. When two spheroids were placed together, creating a doublet, cartilage microtissue fusion was completed after 72 h of culture as indicated by reaching a plateau of the intersphere angle. During the first 24 h of fusion, doublet length and width decreased, suggesting the compaction process. Doublet length further decreased but doublet width started to increase, approaching the measurements of the doublet length indicating that doublets started to compact and dynamically reorient to a circular shape. The fused doublet displayed cartilage specific molecules, GAG and collagen II, GAG were dispersed throughout the fused doublet, while collagen II was mainly present in the newly synthesized matrix surrounding the original individual spheroids. Doublet fusion of primary chondrocyte spheroids was already described by Parfenov et al. (2018) and Susienka et al. (2016) Both studies showed that sheep and human primary chondrocyte spheroids/doublets, respectively, were able to fuse (Susienka et al., 2016; Parfenov et al., 2018). Our study investigated, for the first time, fusion and morphological changes during chondrogenic induced BM-MSC doublet formation.

Doublet fusion could be transferred to fusion of multiple spheroids in an agarose coated well. A compact macrotissue was created after 96 h which showed increased circularity over time in culture. Notably, there was no presence of collagen type II in the center of the fused construct, this can be explained by the use of immature day 7 spheroids, where there is no manifestation of ECM, and the limited diffusion of nutrients into the core of the macrotissue. Spheroid fusion was still observed when spheroids were encapsulated in gelMA hydrogels in close proximity to each other, demonstrating the tissue-fusion-permissive potential of the hydrogel. This was confirmed after completing the printing process where spheroids within the scaffold structure were still able to fuse. However, we want to highlight the time discrepancy between spheroid fusion in the absence versus in the presence of a hydrogel. Complete fusion of spheroids is obtained after 72 h in absence of a hydrogel, as indicated by an intersphere angle of ±179°. When spheroids are encapsulated or bioprinted in gelMA, fusion is highly dependent on a close deposition of neighboring spheroids. Encapsulated spheroids in gelMA did not completely fuse during the 14-day time frame of the experiment, shown by an intersphere angle of 127°. This was in part due to the difference in age of the used spheroids, the spheroids used in the non-encapsulated fusion experiments were 7-day-old spheroids, while 14-day-matured spheroids were encapsulated or bioprinted. It has been described that fusion of older spheroids results in incomplete fusion showing the individual margins of the spheroids (De Moor et al., 2018). Nevertheless, while hydrogel degradation will occur *in vivo*, spheroids will have enhanced probability to fuse. This underlines the importance of research dedicated to find hydrogels or biomaterials with altered characteristics having the capability to enhance the functionality of bioprinted tissues. This field of smart biomaterials research will definitely have a positive impact on the biofabricated tissues.

Traditional ACI procedures using a cell suspension of chondrocytes, or MACI procedures using cells in combination with a scaffold, are indicated for large femoral defects of 2–10 cm^2 and 2 million autologous cells/cm^2 are applied (Foldager et al., 2012; Becher et al., 2017; Krill et al., 2018). Only 12–26 weeks after implantation of the single cell suspension, cartilage matrix develops (Becher et al., 2017; Krill et al., 2018). The major advantage of using spheroids instead of single cells is that, because of the high cell-cell contacts and cell density in 3D preculture, they already have developed a tissue specific ECM, before they are used for implantation (Bartz et al., 2016; De Moor et al., 2019). We believe the use of spheroids will lead to a less fibrous tissue than traditional ACI because they already possess a GAG- and collagen II-rich ECM. Moreover, spheroids combined with gelMA also displayed a significantly less fibrous and a more hyaline cartilage-like phenotype. Interestingly, bioprinting of spheroids seems to be more successful than bioprinting of single cells since constructs containing single cells showed poor viability, and more importantly no chondrogenic differentiation (**Figure 12**). When using spheroids as building blocks, the concentration of spheroids in the bio-ink needs to be optimized. One bioprinted construct of four layers was printed, with dimensions of 1.3 cm × 1.3 cm and thus covering an area of 1.69 cm^2, using ±167 µl of bio-ink. The concentration of spheroids in the bio-ink was 12680 spheroids/ml, thus 1 construct contained ±2113 spheroids/1.69 cm^2 which equals 1250 spheroids/cm^2. We suggest to increase the concentration in accordance with the clinically applied cell concentration in traditional ACI (2 million cells/cm^2), this corresponds with 4 seeded microwells and thus 6340 spheroids/cm^2. To achieve a similar concentration as in traditional ACI, the spheroid concentration in the bio-ink needs to be a fivefold higher (±63400 spheroids/ml, corresponding with 40 microwells). Enhanced fusion of spheroids will be the result of the increased spheroid concentration. *In vivo*, the gelMA scaffold will be prone to degradation, leading to softer hydrogels with impact on nutrient diffusion, spheroid fusion and cellular outgrowth.

Our study shows that 3D cartilage microtissues can be bioprinted while maintaining cell viability, 3D architecture, chondrogenic phenotype and their fusion capacity. The versatile fusion capacity of microtissues is interesting for future *in vivo* implantation as this shows the broad spectrum of application possibilities. Spheroids can be used as such, or in combination with gelMA as an injectable. Highly interesting is that a patient-specific implantable construct could be manufactured by 3D bioprinting of chondrogenic induced spheroids at various endochondral developmental stages giving the promise of treating stratified osteochondral defects.

DATA AVAILABILITY STATEMENT

The datasets generated for this study are available on request to the corresponding author.

AUTHOR CONTRIBUTIONS

LD and HD: participation in manuscript writing, study design, study performance, and data analysis. SF: performance of the experiments. MA and ND: scanning electron microscopy. LT, CV, SV, and PD: synthesis of gelMA and data interpretation regarding the material characterization. All authors reviewed the results and approved the final version of the manuscript.

FUNDING

HD acknowledges the Research Foundation Flanders (FWO) for supporting a Research Grant (1510414N) and Ghent University (Special Research Fund, BOF) (01B02315). ND has received funding from the European Research Council (ERC) under the European Union's Seventh Framework Program (FP/2007-2013)/ERC Grant Agreement 335929 (PLASMATS). The work of LT was supported by the FWO under a Ph.D. research fellowship (1S26616N).

ACKNOWLEDGMENTS

The authors would like to thank Prof. Dr. Jan Vanfleteren and NaMiFab Ghent University for kindly providing the PDMS molds, Prof. Dr. Björn Heindryckx and Prof. Dr. Jolanda van Hengel (Ghent University) for access to the low oxygen incubator. The authors would also like to thank Greet De Smet, Leen Pieters, and Johanna Aernoudt (Ghent University) for their technical assistance.

SUPPLEMENTARY MATERIAL

The Supplementary Material for this article can be found online at: https://www.frontiersin.org/articles/10.3389/fbioe.2020.00484/full#supplementary-material

FIGURE S1 | Number of Ki67$^+$ cells/spheroid. The number of Ki67$^+$ cells was manually counted on stained histological sections (5 μm) of the spheroids. Data are represented as mean ± 95% CI, significant differences ($p < 0.05$) were marked * ($n = 6$, Kruskal–Wallis test).

REFERENCES

Achilli, T.-M., Meyer, J., and Morgan, J. R. (2012). Advances in the formation, use and understanding of multi-cellular spheroids. *Expert Opin. Biol. Ther.* 12, 1347–1360. doi: 10.1517/14712598.2012.707181

Alvarez-Pérez, J., Ballesteros, P., and Cerdán, S. (2005). Microscopic images of intraspheroidal pH by 1H magnetic resonance chemical shift imaging of pH sensitive indicators. *Magn. Reson. Mater. Phys. Biol. Med.* 18, 293–301. doi: 10.1007/s10334-005-0013-z

Anderer, U., and Libera, J. (2002). In vitro engineering of human autogenous cartilage. *J. Bone Miner. Res.* 17, 1420–1429. doi: 10.1359/jbmr.2002.17.8.1420

Armoiry, X., Cummins, E., Connock, M., Metcalfe, A., Royle, P., Johnston, R., et al. (2018). Autologous chondrocyte Implantation with chondrosphere for treating articular cartilage defects in the knee: an evidence review group perspective of a NICE single technology appraisal. *Pharmacoeconomics* 37, 879–886. doi: 10.1007/s40273-018-0737-z

Bartz, C., Meixner, M., Giesemann, P., Roël, G., Bulwin, G.-C., and Smink, J. J. (2016). An ex vivo human cartilage repair model to evaluate the potency of a cartilage cell transplant. *J. Transl. Med.* 14:317. doi: 10.1186/s12967-016-1065-8

Basad, E., Wissing, F. R., Fehrenbach, P., Rickert, M., Steinmeyer, J., and Ishaque, B. (2015). Matrix-induced autologous chondrocyte implantation (MACI) in the knee: clinical outcomes and challenges. *Knee Surg. Sport Traumatol. Arthrosc.* 23, 3729–3735. doi: 10.1007/s00167-014-3295-3298

Becher, C., Laute, V., Fickert, S., Zinser, W., Niemeyer, P., John, T., et al. (2017). Safety of three different product doses in autologous chondrocyte implantation: results of a prospective, randomised, controlled trial. *J. Orthop. Surg. Res.* 12:71. doi: 10.1186/s13018-017-0570-577

Berneel, E., Philips, C., Declercq, H., and Cornelissen, R. (2016). Redifferentiation of high-throughput generated fibrochondrocyte micro-aggregates: impact of low oxygen tension. *Cells. Tissues Organs* 202, 369–381. doi: 10.1159/000447509

Billiet, T., Gevaert, E., De Schryver, T., Cornelissen, M., and Dubruel, P. (2014). The 3D printing of gelatin methacrylamide cell-laden tissue-engineered constructs with high cell viability. *Biomaterials* 35, 49–62. doi: 10.1016/j.biomaterials.2013.09.078

Caron, M. M. J., Emans, P. J., Coolsen, M. M. E., Voss, L., Surtel, D. A. M., Cremers, A., et al. (2012). Redifferentiation of dedifferentiated human articular chondrocytes: comparison of 2D and 3D cultures. *Osteoarthr. Cartil.* 20, 1170–1178. doi: 10.1016/j.joca.2012.06.016

Cigan, A. D., Roach, B. L., Nims, R. J., Tan, A. R., Albro, M. B., Stoker, A. M., et al. (2016). High seeding density of human chondrocytes in agarose produces tissue-engineered cartilage approaching native mechanical and biochemical properties. *J. Biomech.* 49, 1909–1917. doi: 10.1016/j.jbiomech.2016.04.039

Daly, A. C., Critchley, S. E., Rencsok, E. M., Kelly, D. J., and Sophia Fox, A. J. (2016). A comparison of different bioinks for 3D bioprinting of fibrocartilage and hyaline cartilage. *Biofabrication* 8:045002. doi: 10.1088/1758-5090/8/4/045002

Davies, R., and Kuiper, N. (2019). Regenerative medicine: a review of the evolution of autologous chondrocyte implantation (ACI) therapy. *Bioengineering* 6:22. doi: 10.3390/bioengineering6010022

De Moor, L., Beyls, E., and Declercq, H. (2019). Scaffold free microtissue formation for enhanced cartilage repair. *Ann. Biomed. Eng.* 48, 298–311. doi: 10.1007/s10439-019-02348-4

De Moor, L., Merovci, I., Baetens, S., Verstraeten, J., Kowalska, P., Krysko, D. V., et al. (2018). High-throughput fabrication of vascularized spheroids for bioprinting. *Biofabrication* 10:035009. doi: 10.1088/1758-5090/aac7e6

Deng, Z., Jin, J., Zhao, J., and Xu, H. (2016). Cartilage defect treatments: with or without cells? mesenchymal stem cells or chondrocytes? Traditional or matrix-assisted? A systematic review and meta-analyses. *Stem Cells Int.* 2016:9201492. doi: 10.1155/2016/9201492

Dewan, A. K., Gibson, M. A., Elisseeff, J. H., and Trice, M. E. (2014). Evolution of autologous chondrocyte repair and comparison to other cartilage repair techniques. *Biomed Res. Int.* 2014:272481. doi: 10.1155/2014/272481

Ewa-Choy, Y. W., Pingguan-Murphy, B., Abdul-Ghani, N. A., Jahendran, J., and Chua, K. H. (2017). Effect of alginate concentration on chondrogenesis of co-cultured human adipose-derived stem cells and nasal chondrocytes: a biological study. *Biomater. Res.* 21:19. doi: 10.1186/s40824-017-0105-107

Farag, M. M. (2017). "Design and manufacture of biodegradable products from renewable resources," in *Handbook of Composites From Renewable Materials*, eds V. Kumar, M. K. Thakur, and M. R. Kessler (Hoboken, NJ: John Wiley & Sons, Inc), 111–131. doi: 10.1002/9781119441632.ch23

Foldager, C. B., Gomoll, A. H., Lind, M., and Spector, M. (2012). Cell seeding densities in autologous chondrocyte implantation techniques for cartilage repair. *Cartilage* 3, 108–117. doi: 10.1177/1947603511435522

Fox, A. J. S., Bedi, A., and Rodeo, S. A. (2009). The basic science of articular cartilage: structure, composition, and function. *Sports Health* 1, 461–468. doi: 10.1177/1941738109350438

Fox, A. J. S., Bedi, A., and Rodeo, S. A. (2012). The basic science of human knee menisci: structure, composition, and function. *Sports Health* 4, 340–351. doi: 10.1177/1941738111429419

Gaskell, H., Sharma, P., Colley, H. E., Murdoch, C., Williams, D. P., and Webb, S. D. (2016). Characterization of a functional C3A liver spheroid model. *Toxicol. Res.* 5, 1053–1065. doi: 10.1039/c6tx00101g

Gevaert, E., Dollé, L., Billiet, T., Dubruel, P., van Grunsven, L., van Apeldoorn, A., et al. (2014). High throughput micro-well generation of hepatocyte micro-aggregates for tissue engineering. *PLoS One* 9:e105171. doi: 10.1371/journal.pone.0105171

Ghosh, S., Laha, M., Mondal, S., Sengupta, S., and Kaplan, D. L. (2009). In vitro model of mesenchymal condensation during chondrogenic development. *Biomaterials* 30, 6530–6540. doi: 10.1016/j.biomaterials.2009.08.019

Gionet-Gonzales, M. A., and Leach, J. K. (2018). Engineering principles for guiding spheroid function in the regeneration of bone, cartilage, and skin. *Biomed. Mater.* 13:034109. doi: 10.1088/1748-605X/aab0b3

Grogan, S. P., Dorthé, E. W., Glembotski, N. E., Gaul, F., and D'Lima, D. D. (2019). Cartilage tissue engineering combining microspheroid building blocks and microneedle arrays. *Connect. Tissue Res.* 61, 229–243. doi: 10.1080/03008207.2019.1617280

Hu, X., Ma, L., Wang, C., and Gao, C. (2009). Gelatin hydrogel prepared by photo-initiated polymerization and loaded with TGF-beta1 for cartilage tissue engineering. *Macromol. Biosci.* 9, 1194–1201. doi: 10.1002/mabi.200900275

Huang, B. J., Hu, J. C., and Athanasiou, K. A. (2016). Cell-based tissue engineering strategies used in the clinical repair of articular cartilage. *Biomaterials* 98, 1–22. doi: 10.1016/j.biomaterials.2016.04.018

Jo, C. H., Lee, Y. G., Shin, W. H., Kim, H., Chai, J. W., Jeong, E. C., et al. (2014). Intra-articular injection of mesenchymal stem cells for the treatment of osteoarthritis of the knee: a proof-of-concept clinical trial. *Stem Cells* 32, 1254–1266. doi: 10.1002/stem.1634

Knutsen, G., Drogset, J. O., Engebretsen, L., Grøntvedt, T., Isaksen, V., Ludvigsen, T. C., et al. (2007). A randomized trial comparing autologous chondrocyte implantation with microfracture. Findings at five years. *J. Bone Joint Surg. Am.* 89, 2105–2112. doi: 10.2106/JBJS.G.00003

Krill, M., Early, N., Everhart, J. S., and Flanigan, D. C. (2018). Autologous chondrocyte implantation (ACI) for knee cartilage defects. *JBJS Rev.* 6:e5. doi: 10.2106/JBJS.RVW.17.00078

Levato, R., Webb, W. R., Otto, I. A., Mensinga, A., Zhang, Y., van Rijen, M., et al. (2017). The bio in the ink: cartilage regeneration with bioprintable hydrogels and articular cartilage-derived progenitor cells. *Acta Biomater.* 61, 41–53. doi: 10.1016/J.ACTBIO.2017.08.005

Li, J., Chen, G., Xu, X., Abdou, P., Jiang, Q., Shi, D., et al. (2019). Advances of injectable hydrogel-based scaffolds for cartilage regeneration. *Regen. Biomater.* 6, 129–140. doi: 10.1093/rb/rbz022

Liu, J., Hilderink, J., Groothuis, T. A. M., Otto, C., van Blitterswijk, C. A., and de Boer, J. (2015). Monitoring nutrient transport in tissue-engineered grafts. *J. Tissue Eng. Regen. Med.* 9, 952–960. doi: 10.1002/term.1654

Loessner, D., Meinert, C., Kaemmerer, E., Martine, L. C., Yue, K., Levett, P. A., et al. (2016). Functionalization, preparation and use of cell-laden gelatin methacryloyl-based hydrogels as modular tissue culture platforms. *Nat. Protoc.* 11, 727–746. doi: 10.1038/nprot.2016.037

Markovic, M., Van Hoorick, J., Hölzl, K., Tromayer, M., Gruber, P., Nürnberger, S., et al. (2015). Hybrid tissue engineering scaffolds by combination of three-dimensional printing and cell photoencapsulation. *J. Nanotechnol. Eng. Med.* 6, 0210011–0210017. doi: 10.1115/1.4031466

Mironov, V., Visconti, R. P., Kasyanov, V., Forgacs, G., Drake, C. J., and Markwald, R. R. (2009). Organ printing: tissue spheroids as building blocks. *Biomaterials* 30, 2164–2174. doi: 10.1016/j.biomaterials.2008.12.084

Moldovan, N., Maldovan, L., and Raghunath, M. (2018). Of balls, inks and cages: hybrid biofabrication of 3D tissue analogs. *Int. J. Bioprint.* 5:1. doi: 10.18063/ijb.v5i1.167

Moldovan, N. I., Hibino, N., and Nakayama, K. (2017). Principles of the kenzan method for robotic cell spheroid-based three-dimensional bioprinting. *Tissue Eng. Part B Rev.* 23, 237–244. doi: 10.1089/ten.teb.2016.0322

Mouser, V. H. M., Levato, R., Mensinga, A., Dhert, W. J. A., Gawlitta, D., and Malda, J. (2018). Bio-ink development for three-dimensional bioprinting of hetero-cellular cartilage constructs. *Connect. Tissue Res.* 61, 137–151. doi: 10.1080/03008207.2018.1553960

Nichol, J. W., and Khademhosseini, A. (2009). Modular tissue engineering: engineering biological tissues from the bottom up. *Soft Matter.* 5, 1312–1319. doi: 10.1039/b814285h

Onofrillo, C., Duchi, S., O'Connell, C. D., Blanchard, R., O'Connor, A. J., Scott, M., et al. (2018). Biofabrication of human articular cartilage: a path towards the development of a clinical treatment. *Biofabrication* 10:045006. doi: 10.1088/1758-5090/aad8d9

Pahoff, S., Meinert, C., Bas, O., Nguyen, L., Klein, T. J., and Hutmacher, D. W. (2019). Effect of gelatin source and photoinitiator type on chondrocyte redifferentiation in gelatin methacryloyl-based tissue-engineered cartilage constructs. *J. Mater. Chem. B.* 7:2607. doi: 10.1039/C8TB02607F

Parfenov, V. A., Koudan, E. V., Bulanova, E. A., Karalkin, P. A., Das Pereira, F., Norkin, N. E., et al. (2018). Scaffold-free, label-free and nozzle-free biofabrication technology using magnetic levitational assembly. *Biofabrication* 10:034104. doi: 10.1088/1758-5090/aac900

Pepelanova, I., Kruppa, K., Scheper, T., and Lavrentieva, A. (2018). Gelatin-methacryloyl (GelMA) hydrogels with defined degree of functionalization as a versatile toolkit for 3D cell culture and extrusion bioprinting. *Bioengineering* 5:55. doi: 10.3390/bioengineering5030055

Radisic, M., Malda, J., Epping, E., Geng, W., Langer, R., and Vunjak-Novakovic, G. (2006). Oxygen gradients correlate with cell density and cell viability in engineered cardiac tissue. *Biotechnol. Bioeng.* 93, 332–343. doi: 10.1002/bit.20722

Roosens, A., Handoyo, Y. P., Dubruel, P., and Declercq, H. (2019). Impact of modified gelatin on valvular microtissues. *J. Tissue Eng. Regen. Med.* 13, 771–784. doi: 10.1002/term.2825

Roosens, A., Puype, I., and Cornelissen, R. (2017). Scaffold-free high throughput generation of quiescent valvular microtissues. *J. Mol. Cell. Cardiol.* 106, 45–54. doi: 10.1016/j.yjmcc.2017.03.004

Rothrauff, B. B., Shimomura, K., Gottardi, R., Alexander, P. G., and Tuan, R. S. (2017). Anatomical region-dependent enhancement of 3-dimensional chondrogenic differentiation of human mesenchymal stem cells by soluble meniscus extracellular matrix. *Acta Biomater.* 49, 140–151. doi: 10.1016/j.actbio.2016.11.046

Rouillard, A. D., Berglund, C. M., Lee, J. Y., Polacheck, W. J., Tsui, Y., Bonassar, L. J., et al. (2011). Methods for photocrosslinking alginate hydrogel scaffolds with high cell viability. *Tissue Eng. Part C Methods* 17, 173–179. doi: 10.1089/ten.tec.2009.0582

Salamon, A., van Vlierberghe, S., van Nieuwenhove, I., Baudisch, F., Graulus, G.-J., Benecke, V., et al. (2014). Gelatin-based hydrogels promote chondrogenic differentiation of human adipose tissue-derived mesenchymal stem cells in vitro. *Materials* 7, 1342–1359. doi: 10.3390/ma7021342

Schon, B. S., Hooper, G. J., and Woodfield, T. B. F. (2017). Modular tissue assembly strategies for biofabrication of engineered cartilage. *Ann. Biomed. Eng.* 45, 100–114. doi: 10.1007/s10439-016-1609-3

Schuurman, W., Levett, P. A., Pot, M. W., van Weeren, P. R., Dhert, W. J. A., Hutmacher, D. W., et al. (2013). Gelatin-methacrylamide hydrogels as potential biomaterials for fabrication of tissue-engineered cartilage constructs. *Macromol. Biosci.* 13, 551–561. doi: 10.1002/mabi.201200471

Shin, Y.-S., Yoon, J.-R., Kim, H.-S., and Lee, S.-H. (2018). Intra-articular injection of bone marrow-derived mesenchymal stem cells leading to better clinical outcomes without difference in mri outcomes from baseline in patients with knee osteoarthritis. *Knee Surg. Relat. Res.* 30, 206–214. doi: 10.5792/ksrr.17.201

Susienka, M. J., Wilks, B. T., and Morgan, J. R. (2016). Quantifying the kinetics and morphological changes of the fusion of spheroid building blocks. *Biofabrication* 8:045003. doi: 10.1088/1758-5090/8/4/045003

Tan, G.-K., Dinnes, D. L. M., Myers, P. T., and Cooper-White, J. J. (2011). Effects of biomimetic surfaces and oxygen tension on redifferentiation of passaged human fibrochondrocytes in 2D and 3D cultures. *Biomaterials* 32, 5600–5614. doi: 10.1016/j.biomaterials.2011.04.033

Tytgat, L., Baudis, S., Ottevaere, H., Liska, R., Thienpont, H., Dubruel, P., et al. (2018). "Photopolymerizable materials for cell encapsulation," in *3D Printing and Biofabrication*, eds A. Ovsianikov, J. Yoo, V. Mironov (Berlin: Springer International Publishing), 353–396. doi: 10.1007/978-3-319-45444-3_15

Tytgat, L., Van Damme, L., Hoorick, J., Van, Declercq, H., Thienpont, H., et al. (2019). Additive manufacturing of photo-crosslinked gelatin scaffolds for adipose tissue engineering. *Acta Biomater.* 94, 340–350. doi: 10.1016/j.actbio.2019.05.062

Ude, C. C., Chen, H. C., Norhamdan, M. Y., Azizi, B. M., Aminuddin, B. S., and Ruszymah, B. H. I. (2017). The evaluation of cartilage differentiations using transforming growth factor beta3 alone and with combination of bone morphogenetic protein-6 on adult stem

cells. *Cell Tissue Bank* 18, 355–367. doi: 10.1007/s10561-017-9638-9631

Van Den Bulcke, A. I., Bogdanov, B., De Rooze, N., Schacht, E. H., Cornelissen, M., and Berghmans, H. (2000). Structural and rheological properties of methacrylamide modified gelatin hydrogels. *Biomacromolecules* 1, 31–38. doi: 10.1021/bm990017d

Van Hoorick, J., Gruber, P., Markovic, M., Tromayer, M., Van Erps, J., Thienpont, H., et al. (2017). Cross-linkable gelatins with superior mechanical properties through carboxylic acid modification: increasing the two-photon polymerization potential. *Biomacromolecules* 18, 3260–3272. doi: 10.1021/acs.biomac.7b00905

Vega, S. L., Kwon, M. Y., and Burdick, J. A. (2017). Recent advances in hydrogels for cartilage tissue engineering. *Eur. Cells Mater.* 33, 59–75. doi: 10.22203/eCM.v033a05

Wang, W., Rigueur, D., and Lyons, K. M. (2014). TGFβ signaling in cartilage development and maintenance. *Birth Defect. Res. Part C Embryo Today Rev.* 102, 37–51. doi: 10.1002/bdrc.21058

Wintermantel, E., Mayer, J., and Goehring, T. N. (2001). Composites for biomedical applications. *Encyclop. Mater. Sci. Technol.* 1, 1371–1376. doi: 10.1016/b0-08-043152-6/00255-252

Woodruff, M. A., and Hutmacher, D. W. (2010). The return of a forgotten polymer—Polycaprolactone in the 21st century. *Prog. Polym. Sci.* 35, 1217–1256. doi: 10.1016/j.progpolymsci.2010.04.002

Žigon-Branc, S., Markovic, M., Van Hoorick, J., Van Vlierberghe, S., Dubruel, P., Zerobin, E., et al. (2019). Impact of hydrogel stiffness on differentiation of human adipose-derived stem cell microspheroids. *Tissue Eng. Part A* 25, 1369–1380. doi: 10.1089/ten.TEA.2018.0237

Conflict of Interest: The authors declare that the research was conducted in the absence of any commercial or financial relationships that could be construed as a potential conflict of interest.

frontiers in Bioengineering and Biotechnology

ORIGINAL RESEARCH
published: 04 June 2020
doi: 10.3389/fbioe.2020.00540

Human Melanocyte-Derived Spheroids: A Precise Test System for Drug Screening and a Multicellular Unit for Tissue Engineering

Irina M. Zurina[1,2,3], Anastasiya A. Gorkun[1,2,3], Ekaterina V. Dzhussoeva[1], Tamara D. Kolokoltsova[1,3], Dmitriy D. Markov[4], Nastasia V. Kosheleva[1,3,5], Sergey G. Morozov[1] and Irina N. Saburina[1,3]*

[1] Laboratory of Cell Biology and Developmental Pathology, FSBSI Institute of General Pathology and Pathophysiology, Moscow, Russia, [2] Department of Modern Biomaterials, Institute for Regenerative Medicine, Sechenov First Moscow State Medical University, Moscow, Russia, [3] FSBEI FPE Russian Medical Academy of Continuous Professional Education of the Russian Ministry of Healthcare, Moscow, Russia, [4] Institute of Molecular Genetics of the Russian Academy of Sciences, Moscow, Russia, [5] Faculty of Biology, Lomonosov Moscow State University, Moscow, Russia

OPEN ACCESS

Edited by:
Dimitrios I. Zeugolis, National University of Ireland Galway, Ireland

Reviewed by:
Elizabeth R. Balmayor, Maastricht University, Netherlands
Naresh Mahajan, Wake Forest School of Medicine, United States

***Correspondence:**
Irina M. Zurina
izurina@gmail.com

Specialty section:
This article was submitted to Tissue Engineering and Regenerative Medicine, a section of the journal Frontiers in Bioengineering and Biotechnology

Received: *11 November 2019*
Accepted: *05 May 2020*
Published: *04 June 2020*

Citation:
Zurina IM, Gorkun AA, Dzhussoeva EV, Kolokoltsova TD, Markov DD, Kosheleva NV, Morozov SG and Saburina IN (2020) Human Melanocyte-Derived Spheroids: A Precise Test System for Drug Screening and a Multicellular Unit for Tissue Engineering. Front. Bioeng. Biotechnol. 8:540. doi: 10.3389/fbioe.2020.00540

Pigmentation is the result of melanin synthesis, which takes place in melanocytes, and its further distribution. A dysregulation in melanocytes' functionality can result in the loss of pigmentation, the appearance of pigment spots and melanoma development. Tissue engineering and the screening of new skin-lightening drugs require the development of simple and reproducible *in vitro* models with maintained functional activity. The aim of the study was to obtain and characterize spheroids from normal human melanocytes as a three-dimensional multicellular structure and as a test system for skin-lightening drug screening. Melanocytes are known to lose their ability to synthesize melanin in monolayer culture. When transferred under non-adhesive conditions in agarose multi-well plates, melanocytes aggregated and formed spheroids. As a result, the amount of melanin elevated almost two times within seven days. MelanoDerm™ (MatTek) skin equivalents were used as a comparison system. Cells in spheroids expressed transcription factors that regulate melanogenesis: MITF and Sox10, the marker of developed melanosomes—gp100, as well as tyrosinase (*TYR*)—the melanogenesis enzyme and melanocortin receptor 1 (*MC1R*)—the main receptor regulating melanin synthesis. Expression was maintained during 3D culturing. Thus, it can be stated that spheroids maintain melanocytes' functional activity compared to that in the multi-layered MelanoDerm™ skin equivalents. Culturing both spheroids and MelanoDerm™ for seven days in the presence of the skin-lightening agent fucoxanthin resulted in a more significant lowering of melanin levels in spheroids. Significant down-regulation of gp100, MITF, and Sox10 transcription factors, as well as 10-fold down-regulation of *TYR* expression, was observed in spheroids by day 7 in the presence of fucoxanthin, thus inhibiting the maturation of melanosomes and the synthesis of melanin. MelanoDerm™ samples were characterized by significant down-regulation of only MITF, Sox10 indicating that spheroids formed a more sensitive system allowed for quantitative assays. Collectively, these data illustrate that normal melanocytes can assemble themselves into

spheroids—the viable structures that are able to accumulate melanin and maintain the initial functional activity of melanocytes. These spheroids can be used as a more affordable and easy-to-use test system than commercial skin equivalents for drug screening.

Keywords: melanocyte, melanogenesis, spheroid, 3D culture, drug screening, tissue engineering

INTRODUCTION

The pharmaceutical industry is one of the fastest-developing R&D systems. As long as new products are developed, discovery programs require more accurate and high-throughput *in vitro* systems for preclinical drug screening and testing. Currently, most *in vitro* studies are carried out using monolayer cultures of primary cells or immortalized cell lines. However, the efficacy of such approaches is now in doubt as 2D culture conditions do not fully reflect the complex 3D microenvironment (intercellular junctions, well-organized extracellular matrix, which cells have to make contact with, gradients of oxygen and nutrients) that surrounds cells *in vivo* (Fitzgerald et al., 2015).

Recently, 3D cell culture systems have been shown to model that microenvironment *in vitro*—they allow for maintaining cell morphology, viability, proliferation rate, and differentiation processes, as well as long-term culturing without disturbing the structural integrity (Antoni et al., 2015; Fitzgerald et al., 2015). Overall, this confirms that 3D cultures are more accurate and valuable in terms of predicting the clinical effects of tested drugs as compared to the 2D culture. There are now numerous technologies with which to obtain 3D cultures that can be divided into two categories: anchorage-independent and scaffold-based (Langhans, 2018). The first type of 3D culture is based on the ability of cells to self-organize in aggregates under non-adhesive conditions, including the hanging-drop technique, the use of low adhesion plates, and the magnetic cell levitation approach (Langhans, 2018). The use of multi-well non-adhesive plates is a simple way of obtaining a large number of spheroids of the same size and controlling their size by simply changing the cell concentrations (Koudan et al., 2017). In scaffold-based technologies, natural (ECM proteins) or synthetic scaffolds are used to provide mechanical support for cells, as well as to enable them to self-assemble in the preferred manner, similar to the native one (Langhans, 2018).

Numerous advantages of 3D cultures, mainly spheroids, have made them a widely used instrument for *in vitro* drug testing. The main area where spheroids are used is in the study of tumor cells and their resistance to different agents (Huang and Gao, 2018). That said, more researchers are now using 3D cultures for studying different pathologies and drug testing in cardiology (Figtree et al., 2017), neurology (Hartley and Brennand, 2017; Nzou et al., 2018), pulmonology (Surolia et al., 2017), orthopedics (Zigon-Branc et al., 2018), and endocrinology (Klaka et al., 2017; Ribeiro et al., 2018). New highly sensitive, yet easy-to-manipulate (and corresponding to the norms of bioethics) *in vitro* models are also required in cosmetic industries to study the efficacy and mechanisms of the effects of active drug substances or combined drugs.

The regulation of skin pigmentation, primarily skin lightening, is one of the most common processes in skin physiology, which is modified during cosmetological procedures. Active production of melanin, as well as its transfer from melanocytes to keratinocytes using special organelles—melanosomes—is one of the protective mechanisms of the skin against UV exposure. Melanin prevents the penetration of UV into the deeper layers of the skin and blocks the release of reactive oxygen species (ROS). Maintaining permanent skin pigmentation depends on a variety of sequential processes: migration of melanoblasts into tissue during embryogenesis, their viability and differentiation into melanocytes, the density of melanocytes in the skin, expression and functions of the enzymatic and structural components of melanosomes, synthesis of various types of melanin (eu- and pheomelanin), maturation and transportation of melanosomes in the dendritic processes of melanocytes and their transfer to keratinocytes, and, finally, the spread of melanin in the suprabasal layers of the skin (Yamaguchi and Hearing, 2007).

Therefore, to suppress hyperpigmentation and abnormal melanogenesis, the use of combined drugs that can affect different stages and levels of regulation of melanin synthesis is required. For example, fucoxanthin (algae pigment), which belongs to the carotenoid family and is used as a skin protector in cosmetology as a component in different drugs, has been shown to have multiple protective effects in various pathologies (Peng et al., 2011).

Currently, primary cultures of melanocytes and keratinocytes (Lei et al., 2002), the commercial tissue equivalents EpiSkin, MelanoDerm™ and others (Costin and Raabe, 2013; Meena and Mohandass, 2019) and tissue equivalents obtained from cells with induced pluripotency (iPSC) (Gledhill et al., 2015) are used to study *in vitro* the efficacy of drugs against hyperpigmentation. However, in this case, a simpler 3D model, namely, spheroids from melanocytes, could also be an effective tool for studying the mechanisms of anti-pigmentation drug efficacy. The 3D culturing of melanocytes in different systems has already been shown to reduce cell proliferation rates and increase their viability and functional activity (Lin et al., 2006; Lee et al., 2015; Hsiao and Young, 2019). The purpose of this study was to obtain and characterize spheroids from normal human melanocytes as a cellular module and as a test system for skin-lightening drug screening and to compare the efficacy of its use with MelanoDerm™ tissue equivalents.

MATERIALS AND METHODS

The study was conducted on the primary culture of human melanocytes (104-05N, CELL Applications, Inc.) and MelanoDerm™ tissue equivalents (MEL-300, MatTek Corporation).

Cultivation of MelanoDerm™ Tissue Equivalents

A set of tissue equivalents was transported to the laboratory (at +4°C). The samples located in special holders were transferred to six-well culture plates in individual wells. Each sample was placed on a stand (MEL-STND, MatTek Corporation) on a section between the water and the air phases. Tissue equivalents were cultured in a complete growth medium provided by the company along with the samples (EPI-100-NMM-113, MatTek Corporation) under standard conditions (37°C, 5% CO_2); the medium was replaced daily.

Fucoxanthin powder (3351-86-8, Anhui, China) was dissolved in saline buffer at a concentration of 500 μM (stock solution), then sterilized by filtration through a syringe filter (SLGP033RS, 0.22 μm, Millipore). For this study, the stock solution of fucoxanthin mixed with complete growth medium in a volume ratio of 1:10 (50 μM) was added to the experimental samples. The concentration of fucoxanthin was chosen based on the previously reported study on its protective effect on cell culture (Heo and Jeon, 2009) and our study of its cytotoxicity (data not published). An equivalent volume of saline buffer (1:10) was added to the control samples.

2D Cultivation of Human Melanocytes

The culture of human melanocytes was transported to the laboratory (at −20°C), and the cells were thawed in a water bath at 37°C. Cells were resuspended in a complete growth medium for melanocytes (135–500, CELL Applications, Inc.) and placed on Petri dishes (35 mm) at a density of 10^4 cells/cm^2. When the melanocytes reached a confluent state, the culture was passaged with Versene solution (R080p, PanEco) and 0.25% trypsin solution (R036p, PanEco). The full growth medium was replaced every 2 days. For further experimental studies, the culture of melanocytes at passage 4 was used to obtain spheroids.

3D Cultivation of Human Melanocytes

Human melanocytes were cultured under 3D non-adhesive conditions with and without the addition of the drug, to obtain three-dimensional spheroids and to study the effect of fucoxanthin on melanin accumulation by melanocytes under these conditions, which are closer to the native tissue compared to monolayer culture. Agarose plates were obtained by polymerizing 2% agarose type I (A6013, Sigma) in special plastic forms (12–256, 3D Petri Dishes, Microtissue) and were then placed in 12-well culture plates. Cell suspension was obtained from the monolayer melanocyte culture at passage 4, resuspended in the full growth medium, and placed in agarose plates at a concentration of 1×10^3 cells per micro-well. 50μM of fucoxanthin was added to experimental spheroids. In the control group, the same volume of sodium chloride (NaCl) buffer was added to the growth medium. The dynamics of spheroids' formation in agarose plates were monitored by the Cell-IQ live time-lapse system (CM Technologies, Finland) with photo registration every 20 min. The resulting spheroids were collected on Days 1, 3, and 7 for melanin concentration measurements and real-time PCR, and at Days 3 and 7 for immunocytochemical analysis.

Photometric Analysis of Melanin Concentration in MelanoDerm™ Tissue Equivalents and Spheroids From Human Melanocytes

Prior to photometric analysis, the samples of MelanoDerm™ (3 pieces of tissue equivalent per time point in experimental and control groups) and spheroids (256 spheroids per time point in experimental and control groups) were washed three times from the residues of the medium in PBS (pH = 7.4), after which they were stored at −20°C. To extract melanin, the samples were thawed and dried, and then 250 μl of Solvable solution (6NE9100, PerkinElmer) was added to each sample. Next, the samples were incubated for 18 h in a water bath at +60°C. After incubation, the samples were thoroughly mixed in a vortex mixer, undissolved particles were precipitated by centrifugation (5 min, 13,000 g), 100 μl of the supernatant was placed into a 96-well plate, and samples' optical densities were measured at a wavelength of 490 nm on a Multiscan GO plate photometer (Thermo Scientific, USA). A calibration curve was obtained by analyzing standard solutions with a known concentration of melanin prepared from dry matter (M863, Sigma-Aldrich). Measurements were performed in triplicate.

Fixation of MelanoDerm™ Tissue Equivalents and Spheroids From Human Melanocytes

For immunocytochemical analysis of melanocyte monolayer culture, cells were seeded on the cover glass. Before fixing the 3D culture, the spheroids were collected in the tube and centrifuged (1 min, 100 g). The resulting pellet was washed three times in phosphate-saline buffer solution (PBS, pH = 7.4). Cover glasses seeded with melanocytes and spheroids were then fixed in a 4% solution of paraformaldehyde (20 min, +4°C). MelanoDerm™ tissue equivalents were also washed three times with PBS from the remnants of the culture medium (5 min for each wash, pH = 7.4). The material was fixed in a 4% solution of paraformaldehyde (one day, +4°C).

Immunocytochemistry

After fixation, the MelanoDerm™ tissue equivalents samples were dehydrated in Isoprep histological processing solution (06-002/S, Biovitrum) and embedded in paraffin (01-007/1, Biovitrum). Next, a series of 9 μm sections was made on the microtome; the sections were placed on glass slides. Prior to immunocytochemical staining, the paraffin was removed from the sections in three changes of xylene (5 min each) and a series of alcohols with descending concentrations (1 min each) to distilled water. Next, the antigens were unmasked in citrate

buffer (pH = 6.0; 06-014, Biovitrum) for 3 min at +100°C under pressure. Cover glasses and spheroids were washed three times with PBS (5 min for each wash, pH = 7.4) from the remnants of PFA. All the following staining procedures were the same for 2D culture, spheroids, and tissue equivalent samples. Melanocytes in monolayer culture were incubated with primary antibodies against MEL5 (917801, BioLegend, 1:100). After preliminary preparations, sections and spheroids were incubated with primary antibodies against gp 100 (ab137078, Abcam, 1:100), Sox10 (ab155279, Abcam, 1:500), and MITF (ab122982, Abcam, 1:300). The result was visualized using secondary antibodies conjugated with the fluorochromes FITC (Em = 525 nm) and DyLight594 (Em = 617 nm). The nuclei were stained with a bisbenzimide fluorescent dye, i.e., Hoechst 33258 (0.002 mg/ml, 10 min, 25°C). After staining, the excess dye was removed in three changes of PBS (pH = 7.4). The resulting preparations were placed in Vitrogel mounting medium (12-001, Biovitrum) and analyzed in visible and ultraviolet light ranges using the Olympus Fluoview FV10 laser scanning confocal microscope (Olympus, Japan).

The obtained images of MelanoDerm™ sections and spheroids from melanocytes were analyzed for mean fluorescence intensity. Images were imported into ImageJ software and converted to a 16-bit format. The parameters "area integrated intensity" and "mean gray value" were measured in the area limited by the threshold. The corrected total cell fluorescence (CTCF) was calculated using the formula: CTCF = integrated density—(area of selected cell × mean fluorescence of background readings). Three images were measured for each marker and time point.

Analysis of Gene Expression by Real-Time Polymerase Chain Reaction

To perform real-time PCR, three pieces of MelanoDerm™ and 256 spheroids from melanocytes were used for each time point in experimental and control groups. Total RNA was isolated using a standard Trizol method (TRIReagent, Sigma, USA). The RNA was treated with Type I DNase (Fermentas, Germany) to remove any DNA contamination, and precipitated in 4M LiCl. The concentration of the obtained RNA was measured using a Nanodrop 8000 spectrophotometer (Thermo Scientific, USA); 2 μg of total RNA were used to synthesize cDNA. cDNA synthesis was performed using M-MLV reverse transcriptase (Evrogen, Russia) and random hexanucleotides (Sileks, Russia). The obtained samples were used to analyze the expression of the *MC1R* gene and the *TYR* gene. The sequences of the used primers are presented in **Table 1**. The analysis was performed on an automatic 7500 Real-Time PCR System amplifier (Applied Biosystems, USA) using a qPCRmix-HSSYBR + ROX mixture (Evrogen, Russia). The relative expression of *MC1R* and *TYR* genes was measured using the ΔΔCt method, normalized to *HsTBP* (Bookout et al., 2006).

TABLE 1 | Primers used in this research.

Primers	Primer sequence (5′-3′)	Length	Tm°C	Primer description
MC1R_For	GTGGTCTTCTTCCTGGCTATGC	22 bp	62.3	*MC1R*
MC1R_Rev	GGATGGTGAGGGTGACAGCG	20 bp	63.0	
TYR_For	TTCAAGAAGTTTATCCAGAAGCC	23 bp	57.7	*TYR*
TYR_Rev	CTTAATGTAGTCTTGAAAAGAGTC	24 bp	53.8	
HsTBP_For	CATGACTCCCGGAATCCCTATCTTT	25 bp	63.1	*HsTBP*
HsTBP_Rev	TGTTGCTGCTGCTGCCTTTGTT	22 bp	63.7	

Statistics

Statistical analysis was performed, and graphs were created using the Prism 8.0 GraphPad software package. Using the Shapiro-Wilk, hypotheses about the normality of the distributions of the studied parameters, and the Pearson $\chi 2$ test for the evaluation of fucoxanthin influence were tested. Both two-way ANOVA assay and multiple *t*-test were used consecutively to confirm the significant difference of data. The *p*-value was adjusted using the two-stage linear step-up procedure of Benjamini, Krieger, and Yekutieli, with Q = 5%. All the experiments were reproduced in triplicate; data are reported as the means ± SD of at least three experiments.

RESULTS

Study of Melanin Accumulation in 3D Cultures—Spheroids From Melanocytes and MelanoDerm™ Tissue Equivalent

Primary human melanocytes (CELL Applications) were first maintained in monolayer culture. During the first passages, melanocytes mostly had spindle-like morphology, with a tendency to the formation of dark aggregates (**Figure 1A**). By the fourth passage, cell morphology slightly changed—cells had more dendrites, while no aggregates were observed in the culture (**Figure 1B**). Cells were characterized by the positive staining against melanocyte-specific marker MEL5, also known as a tyrosinase-related protein-1 that is involved in melanin synthesis (**Figure 1C**).

The melanocytes at the fourth passage were placed in non-adhesive agarose multi-well plates to obtain 3D spheroid culture. Using the method of live time-lapse microscopy, we observed the dynamics of spheroid formation in the control culture and in the presence of fucoxanthin (**Figure 2A**). In the process of culturing cells under 3D conditions, general patterns of spheroid formation were observed—initial compaction took place during the first 24 h of cultivation and lasted up to 7 days. Moreover, by Day 7 both control and experimental spheroids became darker (**Figure 2A**), but the difference between groups could not be adequately assessed visually because spheroids were dense and not transparent.

MelanoDerm™ tissue equivalents are artificially created tissue samples consisting of layers of keratinocytes and melanocytes cultured on a porous membrane. Throughout the cultivation period, the samples accumulated melanin by increasing the number of melanocytes and autoregulating the intensity of pigment synthesis. The visual analysis showed that while on the first and third days the dynamics of samples darkening did not

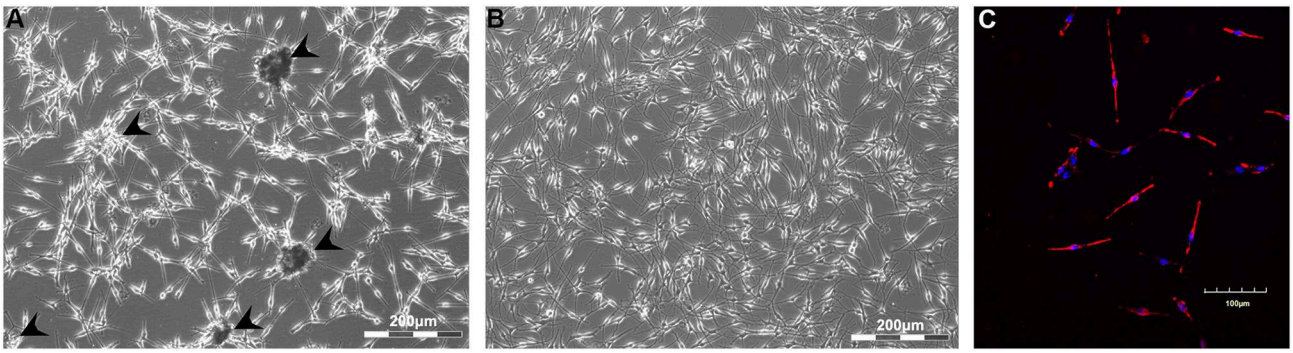

FIGURE 1 | Monolayer culture of human melanocytes at Passages 1 **(A)** and 4 **(B)**. Cells were shown to express Mel5—the marker of melanocytes **(C)**. Arrowheads indicate the sites of aggregates formation. **(A,B)**—Light phase-contrast microscopy; **(C)**—laser scanning confocal microscopy.

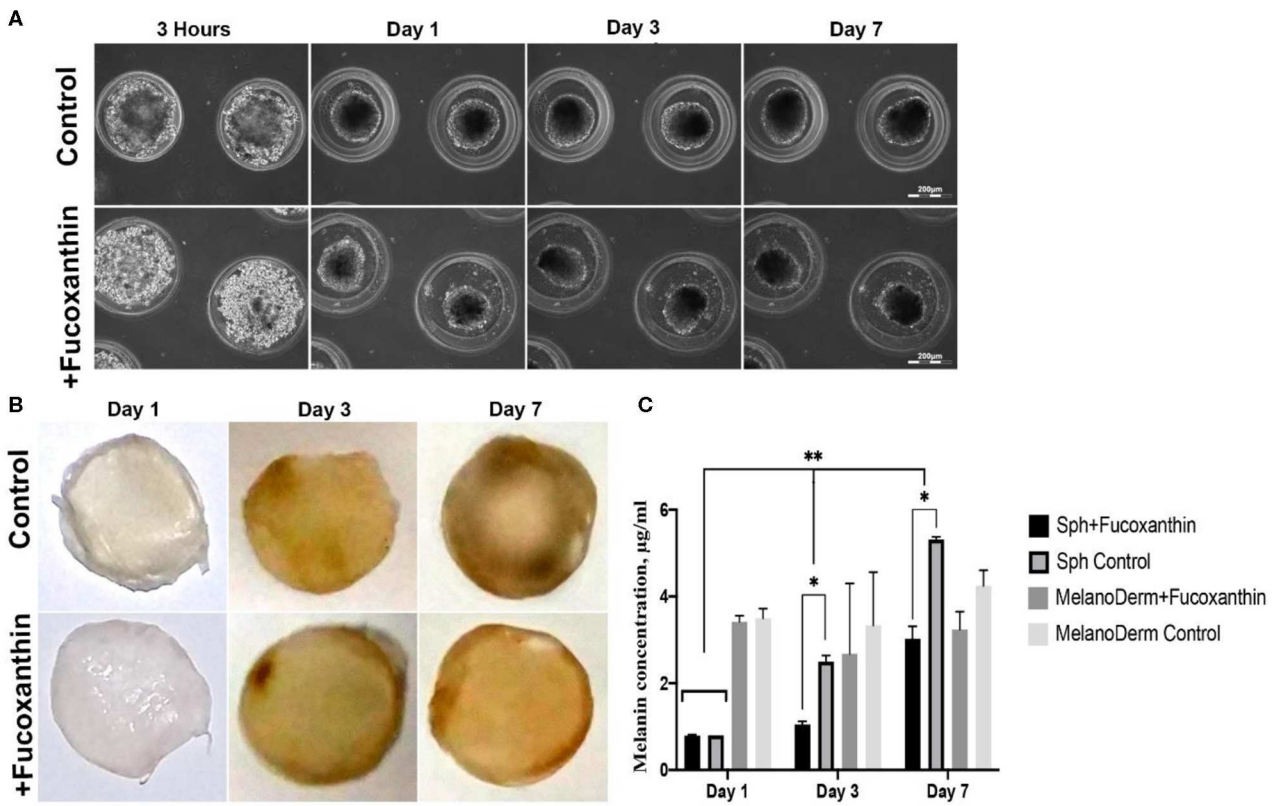

FIGURE 2 | Pigmentation of treated and untreated spheroids and skin equivalents. **(A)** Dynamics of the spheroid formation from a suspension of melanocytes under non-adhesive 3D conditions in a standard growth medium (control) and with the addition of fucoxanthin (experimental group). Phase-contrast live time-lapse microscopy (Cell-IQ, CM Technologies, Finland). **(B)** Pigment accumulation in MelanoDerm™ tissue equivalents at Days 1, 3, and 7 in the control group and the experimental group with the addition of fucoxanthin. All samples had the standard size—9 mm. Photos of samples dried before photometric analysis of melanin content. **(C)** Dynamics of melanin accumulation in melanocyte spheroids and MelanoDerm™ tissue equivalents in the presence of the lightening agent fucoxanthin (experimental group) and with a solution of sodium chloride (control group). *$p < 0.05$ for two-way ANOVA assay and multiple *t*-test. *, **$p < 0.05$ (*within one time-point, **between different time-points).

differ significantly, by Day 7, the experimental skin equivalents cultured in the presence of fucoxanthin were lighter compared to the control group (**Figure 2B**).

To support the visual data on melanin accumulation in these two types of 3D culture containing melanocytes, the spectrophotometric analysis of pigment concentration was performed. The obtained data confirmed the visual assessment of the intensity of melanin synthesis in control and experimental spheroids. As shown in **Figure 2C**, on Day 1 in 3D culture, the average concentration of melanin was similar in both groups, but,

on Days 3 and 7, melanin synthesis by spheroids in the presence of fucoxanthin was significantly lower than in the control group, as confirmed by statistical analysis.

The data from the visual observations of melanin accumulation in MelanoDerm™ were also confirmed using photometry (**Figure 2C**). The obtained results showed that melanin content in control and experimental groups was the same on the first day of cultivation, while, on Day 3, a decrease in the melanin content was observed in the experimental group relative to the control group. By Day 7, the final concentration of melanin in the experimental samples after cultivation with fucoxanthin was significantly lower than in the control group, but it slightly increased compared to Day 3 in the experimental group. However, no statistically significant difference was observed between the groups.

Immunocytochemical Analysis of 3D Cultures

To assess the effect of fucoxanthin on the expression of the key factors of melanogenesis gp 100, MITF and Sox10, immunocytochemical analysis of the MelanoDerm™ tissue equivalent sections and spheroids from melanocytes was performed.

Visual comparison of stained spheroids revealed no difference in the expression of gp100 on Day 3. However, there was up-regulation on Day 7 in the control group as compared to the fucoxanthin-present group (**Figure 3**). On the other hand, MITF expression was lower on day 3 and showed up-regulation on the day 7th in the spheroid control group as compared to the fucoxanthin present spheroid group (**Figure 3**). The expression of the Sox10 was higher on the 3rd day as well as 7th day in the spheroid control group as compared to the fucoxanthin-present spheroid group (**Figure 3**). We also analyzed the images using ImageJ for digital analysis (**Figure 5**). The data obtained were consistent with the visual analysis.

For the MelanoDerm™ group, it was shown that the expression level of gp100, which is responsible for the maturation of melanosomes, was increased in the MelanoDerm™ control group compared to the MelanoDerm™ experimental group on Day 7 of cultivation (**Figure 4**). On Days 3 and 7, there was a slight increase in the expression level of MITF in the presence of the drug, as well as in the MelanoDerm™ control group with a high level of expression of this transcription factor (**Figure 4**). Sox10 on Days 3 and 7 of cultivation was expressed in cell nuclei in the control MelanoDerm™ samples and practically not present in the experimental samples (**Figure 4**). These observations were supported by a quantitative analysis of the mean fluorescence intensity of the obtained images (**Figure 5**).

Real-Time PCR Analysis of Melanogenesis Factor Expression in MelanoDerm™ Tissue Equivalents and Spheroids From Human Melanocytes

Real-time PCR revealed the effect of fucoxanthin on the expression of tyrosinase (*TYR*)—one of the melanogenesis enzymes. That is, it was down-regulated by Day 7 in both spheroids and skin equivalents, compared to the corresponding control groups, but, in the case of spheroids, the difference between the control and experimental groups was significant on Days 1 and 7 (**Figure 6**). The gene expression of the main receptor regulating melanin synthesis, i.e., melanocortin receptor 1 (*MC1R*), was affected by fucoxanthin only in MelanoDerm™ culture, which was confirmed by statistical analysis (**Figure 6**).

DISCUSSION

The expanding ozone holes in the atmosphere lead to the growing danger of UV skin damage, making the pharmaceutical industry increase the production of new types of sun protection (Smit et al., 2009; Zastrow et al., 2017), which requires the new systems for testing them *in vitro*. At present, the mainly used test-systems are primary cultures of melanocytes and keratinocytes (Lei et al., 2002; Lee et al., 2020), melanoma cell lines (Kim et al., 2017; Lee et al., 2020), the commercial tissue equivalents (EpiSkin™, MelanoDerm™, and others) (Costin and Raabe, 2013; Kim et al., 2017; Meena and Mohandass, 2019; Lee et al., 2020), and tissue equivalents obtained from cells with induced pluripotency (iPSC) (Gledhill et al., 2015). These approaches have some limitations, including non-physiological conditions (for 2D cultures), difficulties in analysis, and expensiveness (for commercial tissue equivalents). The current study was aimed to assess the ability of spheroids from normal human melanocytes to maintain their functional activity (melanin synthesis) and to react to the addition of hypopigmentation agent fucoxanthin. Additionally, we compared spheroids' properties to 3D MelanoDerm™ skin tissue equivalents, which we considered as the closest available alternative.

Melanocytes had cell-specific dendritic morphology and expressed specific marker Mel5 at passage 4 in the standard monolayer system (**Figure 1**). However, cells were not able to accumulate melanin *in vitro,* which was corresponded by numerous studies (Chung et al., 2019). At the first passages, cells demonstrated a tendency to the spontaneous formation of dark aggregates attached to the surface, which has been previously reported only on specific culture surface (Lin et al., 2005). This effect was no longer observed at the further passages. When transferred in non-adhesive agarose microplates, melanocytes formed pigmented spheroids that accumulated melanin during cultivation. The same tendency was observed in commercial skin equivalent MelanoDerm™ (**Figure 2**).

In our study, we used the well-known skin-lightening compound fucoxanthin, which targets melanocytes, to validate the capability of both spheroids from melanocyte and skin equivalents of the tissue-specific reaction (the regulation of melanin synthesis). Fucoxanthin is a naturally occurring brown- or orange-colored pigment that belongs to the class of non-provitamin A carotenoids present in the chloroplasts of brown seaweeds (Martin, 2015). Fucoxanthin is well-known as the compound that affects different cellular pathways providing antioxidative effects (Martin, 2015) and hypopigmentation (Shimoda et al., 2010). Both spheroids from melanocyte and

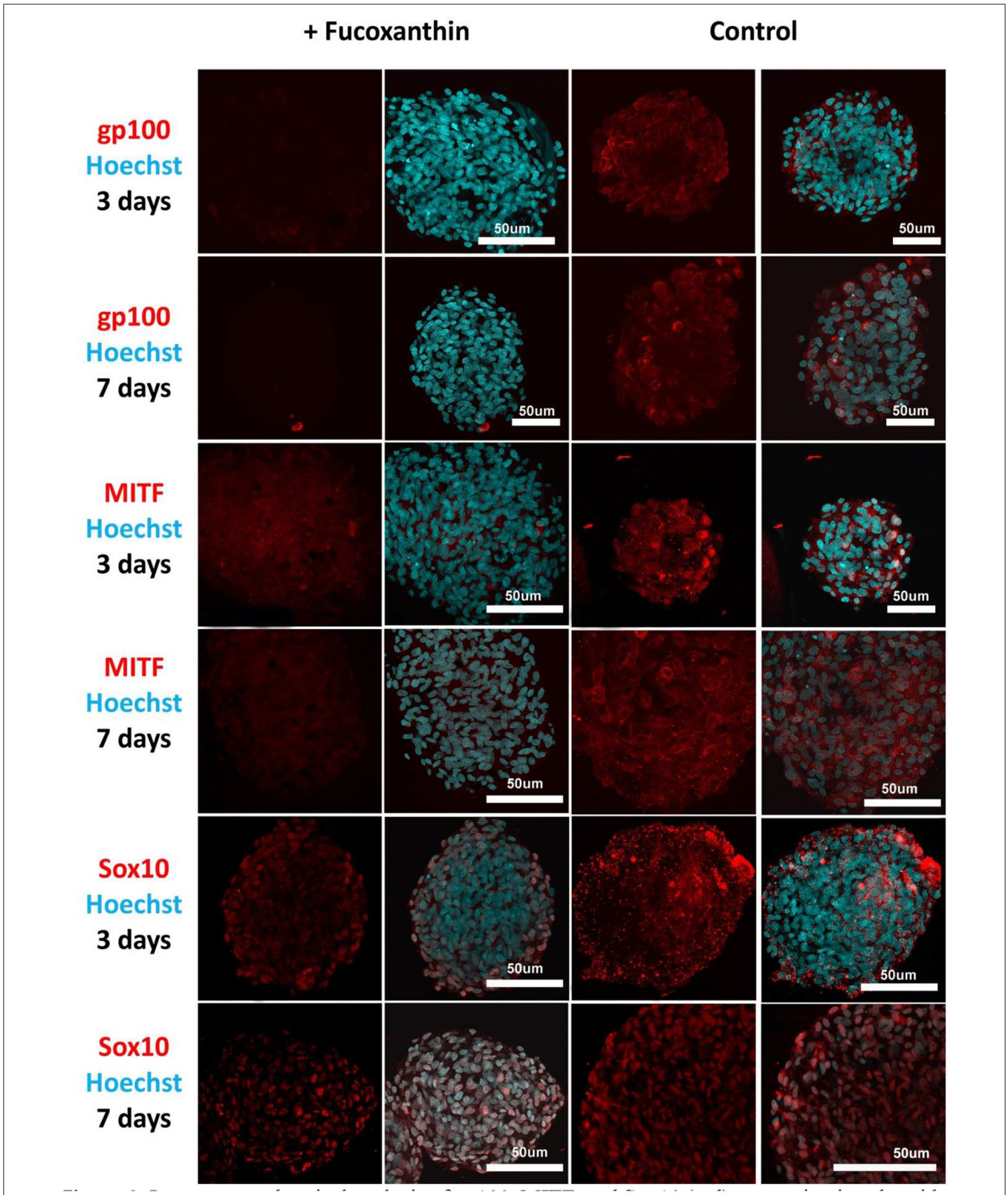

FIGURE 3 | Immunocytochemical analysis of gp100, MITF, and Sox10 (red) expression in spheroids from human melanocytes in the control and experimental groups on Days 3 and 7 in 3D culture. The nuclei are stained with Hoechst 33258 (blue). Laser-scanning confocal microscopy.

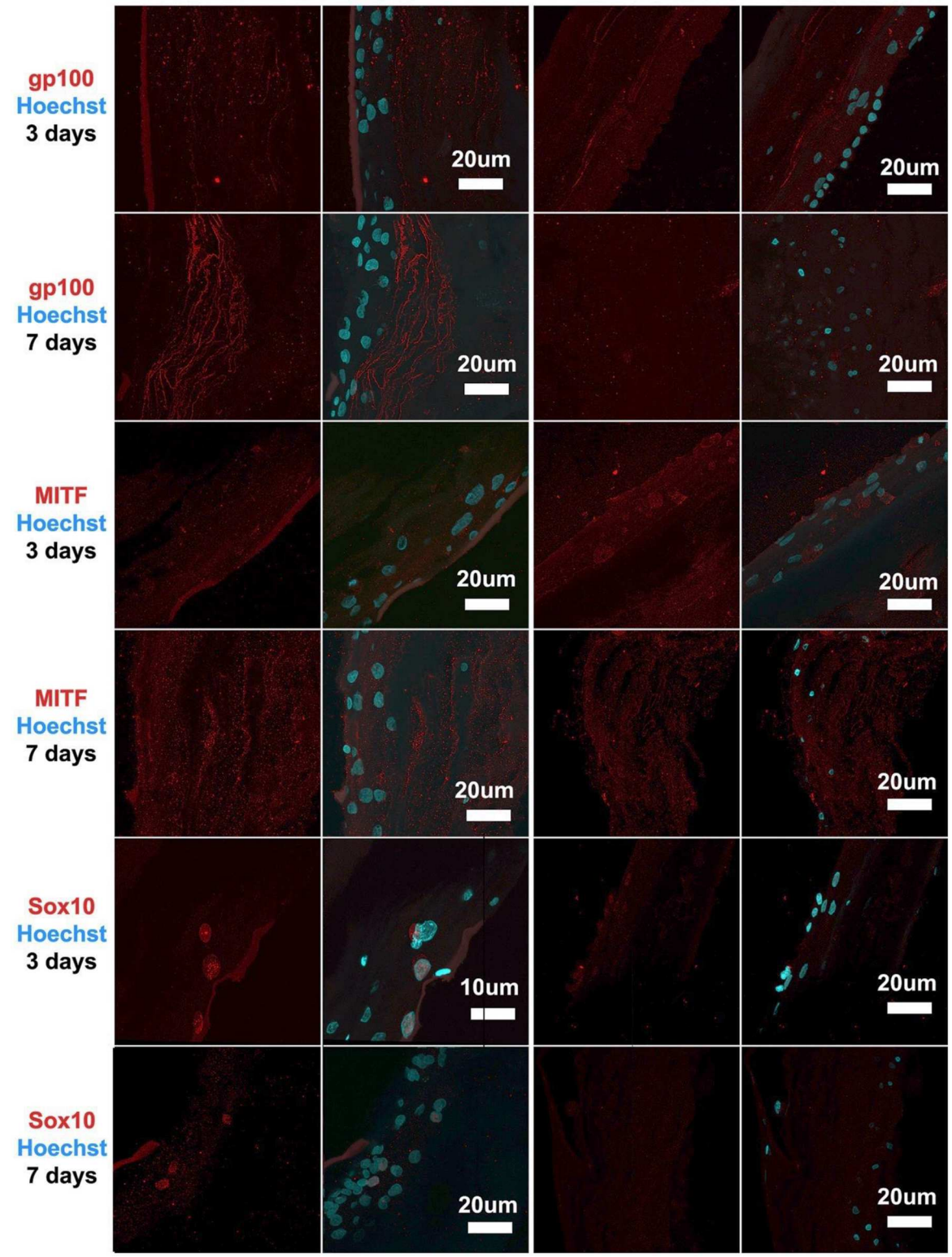

FIGURE 4 | Immunocytochemical analysis of gp100, MITF, and Sox10 (red) expression on sections of MelanoDerm™ tissue equivalents in the control and experimental groups on Days 3 and 7 of cultivation. The nuclei are stained with Hoechst 33258 (blue). Laser-scanning confocal microscopy.

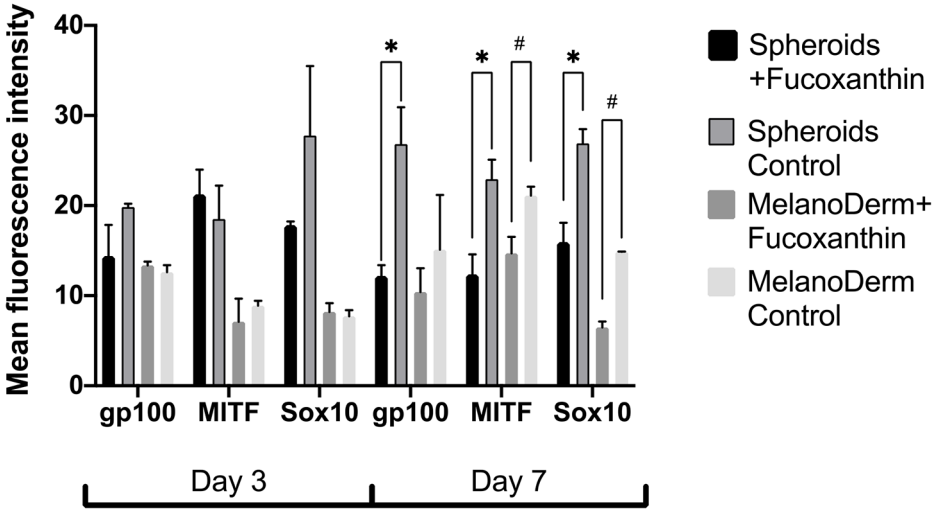

FIGURE 5 | The analysis of mean fluorescence intensity on the immunocytochemical staining images of spheroids and MelanoDerm™ sections in the experimental (in the presence of fucoxanthin) and control groups presenting an expression of gp100, MITF, and Sox10 on Days 3 and 7 in 3D culture. $*^{\#}p < 0.05$ for two-way ANOVA assay and multiple *t*-test.

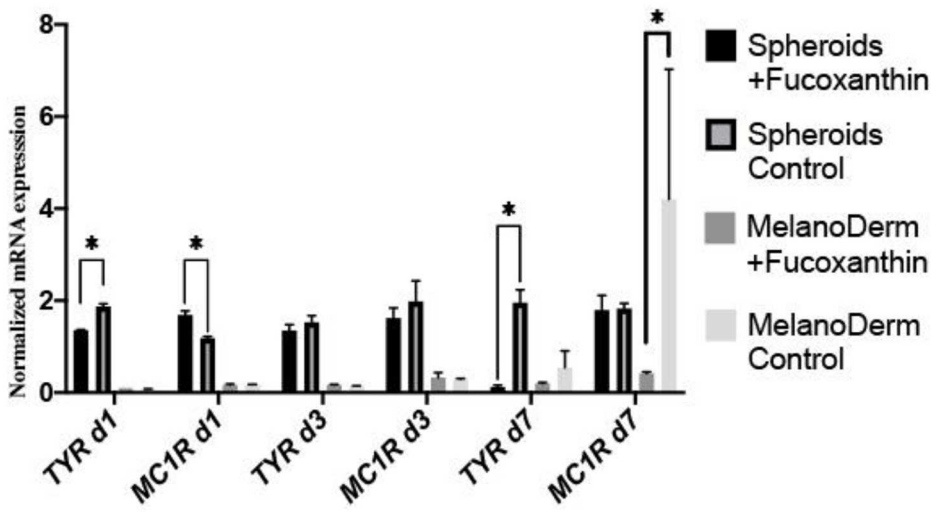

FIGURE 6 | Real-time PCR analysis of *TYR* and *MC1R* expression in MelanoDerm™ tissue equivalents and spheroids from human melanocytes on Days 1, 3, and 7 in the presence of fucoxanthin and in the control group with growth medium. $*p < 0.05$ for two-way ANOVA assay and multiple *t*-test.

MelanoDerm™ showed a decrease of melanin synthesis in the presence of fucoxanthin, but that difference between control and experimental groups was significant only for spheroids (**Figure 2**), probably, because they contained only melanocytes.

To confirm the mechanisms of fucoxanthin physiological influence, we studied the expression of key factors that regulate melanogenesis. Since the synthesis of melanin is a complex multi-stage process (**Figure 7**) controlled by both endogenous and exogenous factors, and fucoxanthin, as well as other carotenoids, is a multitargeting agent (Shimoda et al., 2012), we have analyzed elements from different levels of this melanogenesis signaling pathway (**Figure 7**).

The skin pigment synthesis starts with the activation of melanocortin 1 receptor (MC1R) by its agonists—α-melanocyte-stimulating hormone (αMSH) and adrenocorticotropic hormone (ACTH) (Slominski et al., 2004). This activation stimulates the cAMP/PKA cascade leading to the increased expression of the master regulator of melanocyte development, i.e., microphthalmia-associated transcription factor (MITF) (Yamaguchi and Hearing, 2007). MITF, in its turn, activates the expression of the *TYR* gene (tyrosinase), *PMEL17* (or gp100—premelanosome protein), and Bcl-2 (anti-apoptotic factor),

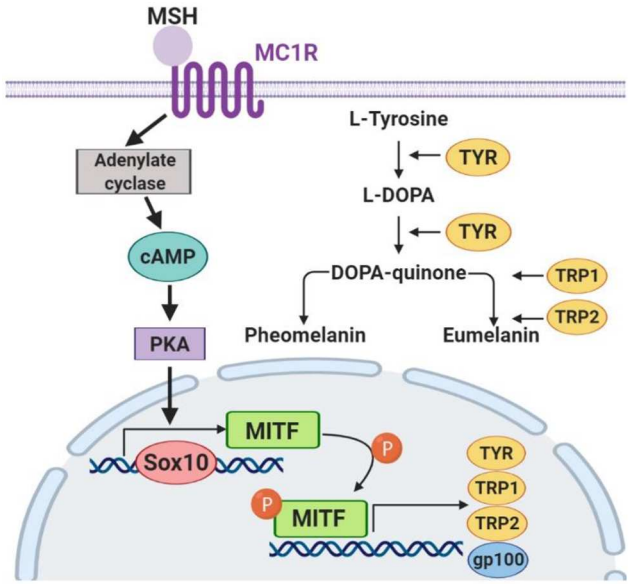

FIGURE 7 | The key components of the melanogenesis signaling pathway.

which leads to an increased synthesis of melanin (Lin and Fisher, 2007). The transcription factors Sox10 and PAX3, in synergistic terms, directly regulate the expression of MITF (Bondurand et al., 2000; Hou et al., 2006). In addition, the intensity of melanin synthesis in melanocytes directly depends on the amount and activity of the tyrosinase enzyme in the cells, which catalyzes the first two stages of melanin formation: hydroxylation of L-tyrosine into L-dihydroxyphenylalanine (L-DOPA) and subsequent oxidation of L-DOPA into L-dopaquinone.

As for the anti-melanogenic effect of fucoxanthin, it is shown to reduce TYR activity, the expression of MC1R, TYR-dependent receptor 1, cyclooxygenase 2 (COX-2), prostaglandin receptor 1 (EP1), which also indicates its anti-inflammatory properties (Shimoda et al., 2010). A general overview shows that fucoxanthin inhibits TYR and melanin production *in vitro* in B16 melanoma cells and *in vivo* in guinea-pigs and mice skin. It also suppressed PGE2, MSH, TRP1, and melanogenic stimulant receptors—EP1and MC1R *in vivo* (Azam et al., 2017). Based on these findings, we selected to assay the expression of *MC1R* and *TYR* mRNA (**Figure 6**).

Our study demonstrated significant down-regulating of *TYR* gene expression on days 1 and 7 for melanocyte spheroids and reduction of *MC1R* gene expression on day 7—for MelanoDerm™. Thus, melanocyte spheroids reproduced results described previously *in vitro* and *in vivo*, and MelanoDerm™ system showed results matched with *in vivo* studies. However, neither system showed both results.

Fucoxanthin is also interacting with other signaling pathways such as NF-κB and WNT/β-catenin pathways (Martin, 2015), which are also involved in melanogenesis (D'Mello et al., 2016). Using this fact, we have also analyzed other crucial factors of melanogenesis—the cellular expression of transcription factors Sox10 and MITF, and the expression of the melanosome maturation regulator—gp100/PMEL17 (**Figures 3**, **4**). Melanocyte spheroids and skin equivalent MelanoDerm™ equally showed the significant reduction of expression of the transcription factors MITF and Sox10 in the presence of fucoxanthin (**Figure 5**). However, only spheroid model has firstly revealed that the application of fucoxanthin can inhibit melanosome formation by significantly decreasing gp100 synthesis. Thus, in general, the spheroid model showed higher responsiveness to fucoxanthin, as confirmed by statistical analysis.

The obtained results indicate that, in the case of studies of agents that potentially affect pigment synthesis and physiology of melanocytes, spheroids can be used as a more affordable and reproducible drug-testing system. The preservation of native-like cell morphology and physiology in spheroids makes it possible to conduct a study on isolated cells instead of using expensive tissue equivalents consisting of different types of cells and requiring special conditions for culturing.

CONCLUSIONS

Collectively, these data illustrate that the 3D culture system can maintain the melanin accumulation *in vitro* compared to the MelanoDerm™ skin equivalents. Moreover, the obtained spheroids provided a sensitive response to the compound addition, recapitulated the *in vitro* and *in vivo*-like response (reduction of MITF, Sox10, and TYR expression), and showed new data (down-regulation of gp100 expression) that has not been previously reported using MelanoDerm™ or other skin tissue equivalents. Thus, melanocyte spheroids can be used as a convenient and affordable test system for screening drugs targeting melanocytes and potentially as building blocks for the tissue engineering of skin equivalents.

DATA AVAILABILITY STATEMENT

All datasets generated for this study are included in the article/supplementary material.

AUTHOR CONTRIBUTIONS

IZ, AG, and IS contributed to the conception and the design of the study. IZ wrote the first draft of the manuscript and prepared the submitted version together with AG. IZ and ED cultivated Skin Equivalents (MelanoDerm™) and spheroids, collected samples. ED and TK conducted all 2D cell culture works. AG accomplished the immunocytochemical analysis of all samples. DM performed the molecular assay and the photometric assay of all samples. NK provided statistical analysis and created the graphs. SM and IS supervised the study and edited the manuscript. All authors contributed to manuscript revision, read, and approved the submitted version.

FUNDING

This work was supported by The Special Federal Programme of the Russian Federation Government, Research Project No. 0520-2019-0026 (The Study of the Mechanisms of Ageing and Regeneration and the Development of Conditions for Obtaining Tissue-engineered Constructs Using 2D and 3D Cell Cultures).

ACKNOWLEDGMENTS

Part of the work using confocal microscopy was performed at the Faculty of Biology at Lomonosov Moscow State University (Equipment Complex for Tissue-engineering Technologies, Visualization and Microsurgery; ID: 9351669).

REFERENCES

Antoni, D., Burckel, H., Josset, E., and Noel, G. (2015). Three-dimensional cell culture: a breakthrough *in vivo*. *Int. J. Mol. Sci.* 16, 5517–5527. doi: 10.3390/ijms16035517

Azam, M. S., Choi, J., Lee, M.-S., and Kim, H.-R. (2017). Hypopigmenting effects of brown algae-derived phytochemicals: a review on molecular mechanisms. *Marine Drugs* 15:297. doi: 10.3390/md15100297

Bondurand, N., Pingault, V., Goerich, D. E., Lemort, N., Sock, E., Caignec, C. L., et al. (2000). Interaction among SOX10, PAX3 and MITF, three genes altered in waardenburg syndrome. *Hum. Mol. Genet.* 9, 1907–1917. doi: 10.1093/hmg/9.13.1907

Bookout, A. L., Cummins, C. L., Mangelsdorf, D. J., Pesola, J. M., and Kramer, M. F. (2006). High-throughput real-time quantitative reverse transcription PCR. *Curr. Protoc. Mol. Biol* 73, 15.8.1–15.8.28. doi: 10.1002/0471142727.mb1508s73

Chung, S., Lim, G. J., and Lee, J. Y. (2019). Quantitative analysis of melanin content in a three-dimensional melanoma cell culture. *Sci. Rep* 9, 1–9. doi: 10.1038/s41598-018-37055-y

Costin, G.-E., and Raabe, H. (2013). Optimizied *in vitro* pigmentation screening assay using a reconstructed three dimensional human skin model. *Rom. J. Biochem.* 50, 15–27.

D'Mello, S. A., Finlay, G. J., Baguley, B. C., and Askarian-Amiri, M. E. (2016). Signaling pathways in melanogenesis. *Int. J. Mol. Sci.* 17:1144. doi: 10.3390/ijms17071144

Figtree, G. A., Bubb, K. J., Tang, O., Kizana, E., and Gentile, C. (2017). Vascularized cardiac spheroids as novel 3D *in vitro* models to study cardiac fibrosis. *Cells. Tissues Organs.* 204, 191–198. doi: 10.1159/000477436

Fitzgerald, K. A., Malhotra, M., Curtin, C. M., O' Brien, F. J., and O' Driscoll, C. M. (2015). Life in 3D is never flat: 3D models to optimise drug delivery. *J. Control. Rel.* 215, 39–54. doi: 10.1016/j.jconrel.2015.07.020

Gledhill, K., Guo, Z., Umegaki-Arao, N., Higgins, C. A., Itoh, M., and Christiano, A. M. (2015). Melanin transfer in human 3D skin equivalents generated exclusively from induced pluripotent stem cells. *PloS ONE* 10:e0136713. doi: 10.1371/journal.pone.0136713

Hartley, B. J., and Brennand, K. J. (2017). Neural organoids for disease phenotyping, drug screening and developmental biology studies. *Neurochem. Int.* 106, 85–93. doi: 10.1016/j.neuint.2016.10.004

Heo, S.-J., and Jeon, Y.-J. (2009). Protective effect of fucoxanthin isolated from Sargassum siliquastrum on UV-B induced cell damage. *J. Photochem. Photobiol. B Biol.* 95, 101–107. doi: 10.1016/j.jphotobiol.2008.11.011

Hou, L., Arnheiter, H., and Pavan, W. J. (2006). Interspecies difference in the regulation of melanocyte development by SOX10 and MITF. *Proc. Natl. Acad. Sci. U.S.A.* 103, 9081–9085. doi: 10.1073/pnas.0603114103

Hsiao, W. C., and Young, T. H. (2019). Characteristics of melanocyte spheroids formed through different biomaterial-induced processes. *J. Formos. Med. Assoc.* 118, 152–161. doi: 10.1016/j.jfma.2018.02.010

Huang, B.-W., and Gao, J.-Q. (2018). Application of 3D cultured multicellular spheroid tumor models in tumor-targeted drug delivery system research. *J. Control. Rel.* 270, 246–259. doi: 10.1016/j.jconrel.2017.12.005

Kim, K., Leutou, A. S., Jeong, H., Kim, D., Seong, C. N., Nam, S.-J., et al. (2017). Anti-pigmentary effect of (-)-4-hydroxysattabacin from the marine-derived bacterium *Bacillus* sp. *Mar. Drugs* 15:138. doi: 10.3390/md15050138

Klaka, P., Grudl, S., Banowski, B., Giesen, M., Sattler, A., Proksch, P., et al. (2017). A novel organotypic 3D sweat gland model with physiological functionality. *PLoS ONE* 12:e0182752. doi: 10.1371/journal.pone.0182752

Koudan, E. V., Korneva, J. V., Karalkin, P. A., Gladkaya, I. S., Gryadunova, A. A., Mironov, V. A., et al. (2017). THe scalable standardized biofabrication of tissue spheroids from different cell types using nonadhesive technology. *3D Print. Addit. Manufac.* 4, 53–60. doi: 10.1089/3dp.2016.0044

Langhans, S. A. (2018). Three-dimensional *in vitro* cell culture models in drug discovery and drug repositioning. *Front. Pharmacol.* 9:6. doi: 10.3389/fphar.2018.00006

Lee, J., Lee, S., Roh, K., Jung, E., and Park, D. (2015). A novel culture system to induce melanin synthesis by three-dimensional spheroid culture. *Biotechnol. Bioproc. Eng.* 20, 194–200. doi: 10.1007/s12257-014-0415-8

Lee, S. H., Bae, I.-H., Lee, E.-S., Kim, H.-J., Lee, J., and Lee, C. S. (2020). Glucose exerts an anti-melanogenic effect by indirect inactivation of tyrosinase in melanocytes and a human skin equivalent. *Int. J. Mol. Sci.* 21:1736. doi: 10.3390/ijms21051736

Lei, T. C., Virador, V. M., Vieira, W. D., and Hearing, V. J. (2002). A melanocyte–keratinocyte coculture model to assess regulators of pigmentation *in vitro*. *Anal. Biochem.* 305, 260–268. doi: 10.1006/abio.2002.5665

Lin, J. Y., and Fisher, D. E. (2007). Melanocyte biology and skin pigmentation. *Nature* 445:843. doi: 10.1038/nature05660

Lin, S.-J., Jee, S.-H., Hsaio, W.-C., Lee, S.-J., and Young, T.-H. (2005). Formation of melanocyte spheroids on the chitosan-coated surface. *Biomaterials* 26, 1413–1422. doi: 10.1016/j.biomaterials.2004.05.002

Lin, S. J., Jee, S. H., Hsiao, W. C., Yu, H. S., Tsai, T. F., Chen, J. S., et al. (2006). Enhanced cell survival of melanocyte spheroids in serum starvation condition. *Biomaterials* 27, 1462–1469. doi: 10.1016/j.biomaterials.2005.08.031

Martin, L. J. (2015). Fucoxanthin and its metabolite fucoxanthinol in cancer prevention and treatment. *Mar. Drugs* 13, 4784–4798. doi: 10.3390/md13084784

Meena, S. N., and Mohandass, C. (2019). "Application of 3D cell culture techniques in cosmeceutical research," in *Advances in Biological Science Research: A Practical Approach,* eds S. N. Meena and M. M. Naik (London, UK: Academic Press), 469–484.

Nzou, G., Wicks, R. T., Wicks, E. E., Seale, S. A., Sane, C. H., Chen, A., et al. (2018). Human cortex spheroid with a functional blood brain barrier for high-throughput neurotoxicity screening and disease modeling. *Sci. Rep.* 8:7413. doi: 10.1038/s41598-018-25603-5

Peng, J., Yuan, J.-P., Wu, C.-F., and Wang, J.-H. (2011). Fucoxanthin, a marine carotenoid present in brown seaweeds and diatoms: metabolism and bioactivities relevant to human health. *Mar. Drugs* 9, 1806–1828. doi: 10.3390/md9101806

Ribeiro, D., Kvist, A. J., Wittung-Stafshede, P., Hicks, R., and Forslow, A. (2018). 3D-Models of insulin-producing beta-cells: from primary islet cells to stem cell-derived islets. *Stem Cell Rev. Rep.* 14, 177–188. doi: 10.1007/s12015-017-9783-8

Shimoda, H., Shan, S. J., Tanaka, J., and Maoka, T. (2012). β-Cryptoxanthin suppresses UVB-induced melanogenesis in mouse: involvement of the inhibition of prostaglandin E2 and melanocyte-stimulating hormone pathways. *J. Pharm. Pharmacol.* 64, 1165–1176. doi: 10.1111/j.2042-7158.2012.01495.x

Shimoda, H., Tanaka, J., Shan, S. J., and Maoka, T. (2010). Anti-pigmentary activity of fucoxanthin and its influence on skin mRNA expression of melanogenic molecules. *J. Pharm. Pharmacol.* 62, 1137–1145. doi: 10.1111/j.2042-7158.2010.01139.x

Slominski, A., Tobin, D. J., Shibahara, S., and Wortsman, J. (2004). Melanin pigmentation in mammalian skin and its hormonal regulation. *Physiol. Rev.* 84, 1155–1228. doi: 10.1152/physrev.00044.2003

Smit, N., Vicanova, J., and Pavel, S. (2009). The hunt for natural skin whitening agents. *Int. J. Mol. Sci.* 10, 5326–5349. doi: 10.3390/ijms10125326

Surolia, R., Li, F. J., Wang, Z., Li, H., Liu, G., Zhou, Y., et al. (2017). 3D pulmospheres serve as a personalized and predictive multicellular model for assessment of antifibrotic drugs. *JCI. Insight* 2:e91377. doi: 10.1172/jci.insight.91377

Yamaguchi, Y., and Hearing, V. J. (2007). "Melanocyte distribution and function in himan skin," in *From Melanocytes to Melanoma: The Progression to Malignancy,* eds V. J. Hearing and S. P. L. Leong (Totowa, NJ: Springer Science & Business Media), 101.

Zastrow, L., Meinke, M. C., Albrecht, S., Patzelt, A., and Lademann, J. (2017). From UV protection to protection in the whole spectral range of the solar radiation: new aspects of sunscreen development. *Adv. Exp. Med. Biol.* 996, 311–318. doi: 10.1007/978-3-319-56017-5_26

Zigon-Branc, S., Barlic, A., Knezevic, M., Jeras, M., and Vunjak-Novakovic, G. (2018). Testing the potency of anti-TNF-alpha and anti-IL-1beta drugs using spheroid cultures of human osteoarthritic chondrocytes and donor-matched chondrogenically differentiated mesenchymal stem cells. *Biotechnol. Prog.* 34, 1045–1058. doi: 10.1002/btpr.2629

Conflict of Interest: The authors declare that the research was conducted in the absence of any commercial or financial relationships that could be construed as a potential conflict of interest.

frontiers in Bioengineering and Biotechnology

ORIGINAL RESEARCH
published: 10 June 2020
doi: 10.3389/fbioe.2020.00583

Preclinical *ex-vivo* Testing of Anti-inflammatory Drugs in a Bovine Intervertebral Degenerative Disc Model

Zhen Li[1], *Yannik Gehlen*[1,2], *Fabian Heizmann*[1,2], *Sibylle Grad*[1], *Mauro Alini*[1], *R. Geoff Richards*[1,2], *David Kubosch*[2], *Norbert Südkamp*[2], *Kaywan Izadpanah*[2], *Eva Johanna Kubosch*[2] *and Gernot Lang*[2]*

[1] AO Research Institute Davos, Davos, Switzerland, [2] Department of Orthopedics and Trauma Surgery, Faculty of Medicine, Medical Center - Albert-Ludwigs-University of Freiburg, Albert-Ludwigs-University of Freiburg, Freiburg, Germany

Discogenic low back pain (LBP) is a main cause of disability and inflammation is presumed to be a major driver of symptomatic intervertebral disc degeneration (IDD). Anti-inflammatory agents are currently under investigation as they demonstrated to alleviate symptoms in patients having IDD. However, their underlying anti-inflammatory and regenerative activity is poorly explored. The present study sought to investigate the potential of Etanercept and Tofacitinib for maintaining disc homeostasis in a preclinical intervertebral disc (IVD) organ culture model within IVD bioreactors allowing for dynamic loading and nutrient exchange. Bovine caudal IVDs were cultured in a bioreactor system for 4 days to simulate physiological or degenerative conditions: (1) Phy—physiological loading (0.02–0.2 MPa; 0.2 Hz; 2 h/day) and high glucose DMEM medium (4.5 g/L); (2) Deg+Tumor necrosis factor α (TNF-α)—degenerative loading (0.32–0.5 MPa; 5 Hz; 2 h/day) and low glucose DMEM medium (2 g/L), with TNF-α injection. Etanercept was injected intradiscally while Tofacitinib was supplemented into the culture medium. Gene expression in the IVD tissue was measured by RT-qPCR. Release of nitric oxide (NO), interleukin 8 (IL-8) and glycosaminoglycan (GAG) into the IVD conditioned medium were analyzed. Cell viability in the IVD was assessed using lactate dehydrogenase and ethidium homodimer-1 staining. Immunohistochemistry was performed to assess protein expression of IL-1β, IL-6, IL-8, and collagen type II in the IVD tissue. Etanercept and Tofacitinib downregulated the expression of IL-1β, IL-6, IL-8, Matrix metalloproteinase 1 (MMP1), and MMP3 in the nucleus pulposus (NP) tissue and IL-1β, MMP3, Cyclooxygenase-2 (COX2), and Nerve growth factor (NGF) in the annulus fibrosus (AF) tissue. Furthermore, Etanercept significantly reduced the IL-1β positively stained cells in the outer AF and NP regions. Tofacitinib significantly reduced IL-1β and IL-8 positively stained cells in the inner AF region. Both, Etanercept and Tofacitinib reduced the GAG loss to the level under physiological culture condition. Etanercept and Tofacitinib are able to neutralize the proinflammatory and catabolic environment in the IDD organ culture model. However, combined anti-inflammatory and anabolic treatment may be required to constrain accelerated IDD and relieving inflammation-induced back pain.

Keywords: spine, regeneration, inflammation, intervertebral disc, disc degeneration, organ culture, bioreactor, 3R

OPEN ACCESS

Edited by:
Dimitrios I. Zeugolis, National University of Ireland Galway, Ireland

Reviewed by:
Gianluca Vadalà, Campus Bio-Medico University, Italy
Dilip Thomas, Stanford University, United States

***Correspondence:**
Gernot Lang
gernot.michael.lang@uniklinik-freiburg.de

Specialty section:
This article was submitted to Tissue Engineering and Regenerative Medicine, a section of the journal Frontiers in Bioengineering and Biotechnology

Received: *17 December 2019*
Accepted: *13 May 2020*
Published: *10 June 2020*

Citation:
Li Z, Gehlen Y, Heizmann F, Grad S, Alini M, Richards RG, Kubosch D, Südkamp N, Izadpanah K, Kubosch EJ and Lang G (2020) Preclinical ex-vivo Testing of Anti-inflammatory Drugs in a Bovine Intervertebral Degenerative Disc Model. Front. Bioeng. Biotechnol. 8:583. doi: 10.3389/fbioe.2020.00583

INTRODUCTION

Low back pain (LBP) is a main cause for disability and early retirement and remains an immense socioeconomic burden in modern societies (Hoy et al., 2014; Buchbinder et al., 2018; Clark and Horton, 2018). Symptomatic intervertebral disc degeneration (IDD) is one of the major causes of LBP and is characterized by early degradation of extracellular matrix (ECM), release of proinflammatory cytokines and altered spine biomechanics (Pye et al., 2004; Le Maitre et al., 2007a; Podichetty, 2007; Freemont, 2009). The pathophysiology of discogenic pain is complex and involves various factors such as trauma, mechanical overloading, oxidative stress, metabolic disorders, genetic preposition, and inflammation interacting with the peripheral and the central nervous system (Stirling et al., 2001; Rannou et al., 2003; Battie et al., 2019; Fujii et al., 2019). It is hypothesized, that IDD is associated with a "first hit" causing structural damage to the intervertebral disc (IVD) followed by an inflammatory response within the microenvironment of the IVD (Risbud and Shapiro, 2014). Proinflammatory cytokines such as tumor necrosis factor alpha (TNF-α) and interleukin 1 beta (IL-1β) are considered of crucial importance in the pathogenesis of IDD as they link the inflammatory process to accelerated tissue degeneration and pain (Risbud and Shapiro, 2014). Recent studies indicated that the presence of TNF-α causes an upregulation of major catabolic enzymes involving Matrix-Metalloproteinases (MMPs) and A Disintegrin and Metalloprotease with Thrombospondin Motifs (ADAMTS), contributing to advanced structural decay in IDD (Purmessur et al., 2013; Tian et al., 2013; Baptista et al., 2020; Zhou et al., 2020). Moreover, TNF-α is associated with the development of discogenic pain by upregulating pain transmitter substance P (SP) and by attracting nerve ingrowth into the outer annulus fibrosus (Freemont et al., 1997, 2002; Olmarker and Larsson, 1998; Igarashi et al., 2000; Risbud and Shapiro, 2014; Evashwick-Rogler et al., 2018).

Current therapies for discogenic pain include conservative as well as surgical treatment in severe scenarios, such as discectomy and fusion. Although commonly performed, the true benefit of current surgical therapies in patients with discogenic LBP remains questionable (Lurie et al., 2014). Presently, there are no causative therapeutic options for patients with failed conservative treatment who do not qualify for surgery.

In order to overcome current treatment barriers and improve patient care, biological approaches on IVD regeneration have gained increasing interest. According to the state of IVD degeneration, staged therapeutic concepts have been developed such as biomolecular, cell therapy, as well as tissue engineering (TE)-based treatments (Li et al., 2014, 2015, 2017; Pirvu et al., 2015; Mojica-Santiago et al., 2018; Pennicooke et al., 2018). In earlier stages of disc degeneration when viable cells are still present, the aim is to relieve pain and enhance the intradiscal metabolism by stopping the catabolic cascade of ECM breakdown and inflammation. As inflammation is presumed to be a major driver of symptomatic IDD, the use of anti-inflammatory biologicals as a novel treatment strategy for early stage IDD is a promising approach to consider.

TNF-α inhibitors, such as Infliximab, Adalimumab, or Etanercept, have been investigated for the treatment of rheumatoid arthritis (RA) and inflammatory bowel disease, and are commercially available for more than 15 years. These drugs are currently under investigation for the treatment of IDD, as observational studies demonstrated to partially alleviate discogenic as well as sciatic leg pain and reduce the risk for spine surgery when local application is performed (Cooper and Freemont, 2004; Genevay et al., 2004, 2012; Korhonen et al., 2004, 2006; Tobinick and Davoodifar, 2004; Autio et al., 2006; Cohen et al., 2009; Okoro et al., 2010; Ohtori et al., 2012; Williams et al., 2013; Pimentel et al., 2014; Sainoh et al., 2016). However, the encouraging findings of observational reports could not be confirmed in randomized controlled trials and recent meta-analysis failed to demonstrate the superiority of anti-TNF-a therapies. Nevertheless, studies indicated that Anti-TNF-a therapies reduced the risk of having spine surgery in cases of sciatica. All authors of the meta-analysis agreed that larger and better-designed studies may need to be performed on anti-TNF-a therapies against placebo since all included studies comprised small study populations. Although evidence exists to reduce symptoms, the detailed biological and mechanical effects of TNF-α inhibitors on degenerated IVDs need to be investigated before broad application can be implemented in patients with refractory discogenic pain.

In 2017, a novel orally administered anti-inflammatory agent, Tofacitinib, was licensed for the treatment of refractory RA in Europe (Milici et al., 2008; van Vollenhoven et al., 2012). Tofacitinib irreversibly inhibits Janus Kinase (JAK) 1 and 3, reduces symptoms and improves physical function in patients with RA (Fleischmann et al., 2012). TNF-α was shown to activate the JAK/signal transducers and activators of transcription (STAT) pathway, which serves as a decisive pathway for many proinflammatory cytokines, such as interleukin 6 (IL-6). The JAK-STAT3 participates in the pathogenesis of IDD and selective JAK-inhibition suppressed degenerative effects of pro-inflammatory cytokines in rat annulus fibrosus (AF) cells in a recent *in vitro* study (Suzuki et al., 2017). It is unknown whether the JAK-inhibitor Tofacitinib would show similar effects under more relevant IDD *ex vivo* experimental conditions compared to cell culture studies. Additionally, the cytocompatibility of these drugs toward disc cells needs to be determined if local administration is desired.

In vitro cell culture studies fail to simulate the complex microenvironment within IVDs realistically as they lack to represent the harsh and avascular 3D niche and/or dynamic loading conditions of the IVD. Recently, we have established a bovine degenerative *ex vivo* organ culture model to mimic the proinflammatory and mechanical micro-environment within an early stage degenerative IVD (Lang et al., 2018). This model is highly valuable as it allows for rapid and cost-efficient screening of novel drug therapies under relevant conditions.

The purpose of the present study was to evaluate the anti-inflammatory and anti-catabolic potential of TNF-α inhibitor Etanercept and the selective JAK-inhibitor Tofacitinib in early onset of IVD degeneration and to analyze their capability to maintain disc homeostasis within our recently established

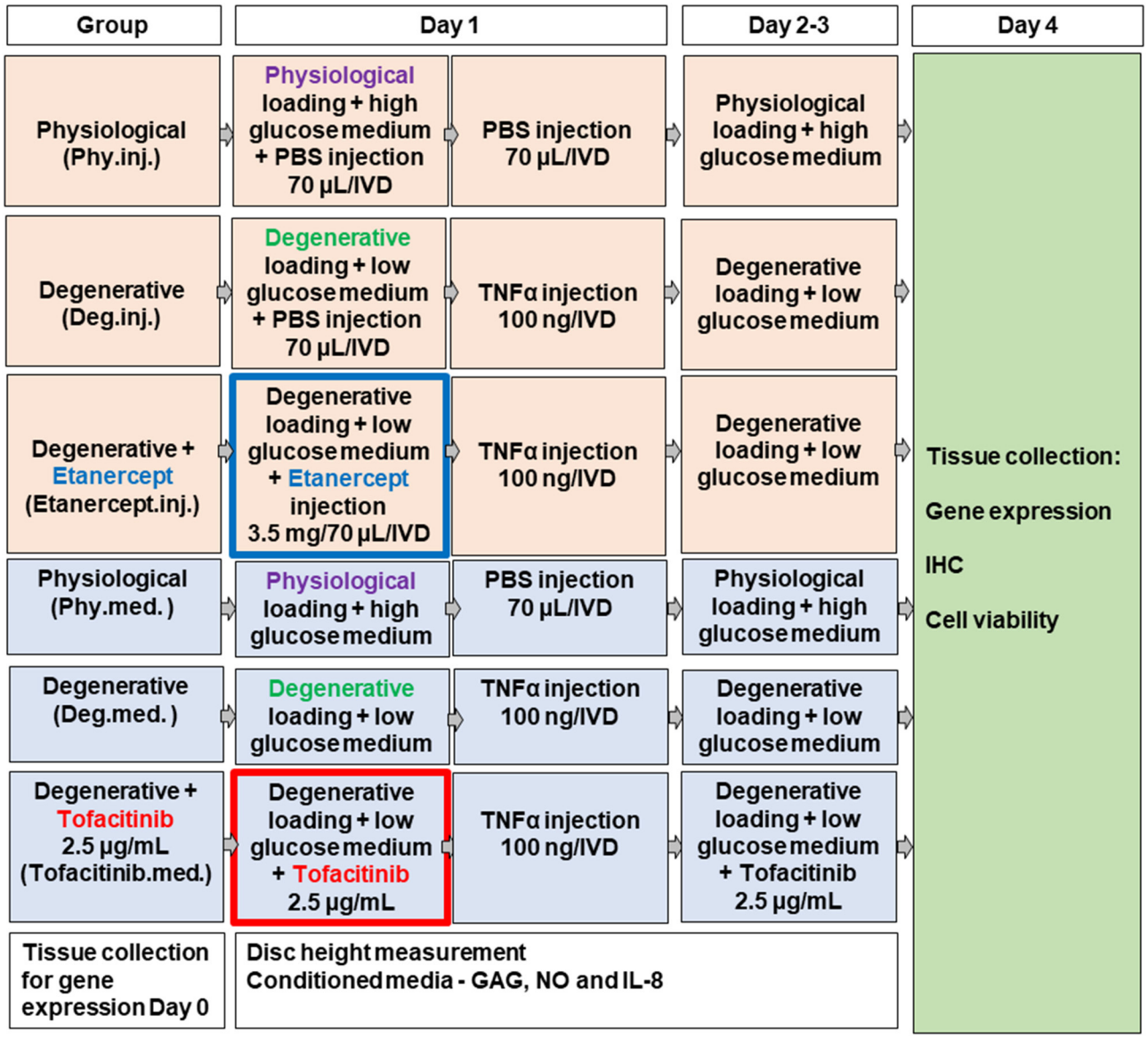

FIGURE 1 | Scheme of experimental setup.

degenerative and pro-inflammatory intervertebral disc organ culture model.

MATERIALS AND METHODS

IVD Dissection and Organ Culture

IVD dissection and organ culture were performed as described before (Lang et al., 2018). Experiments were performed using 16 bovine tails (6–12 months old) obtained from local abattoirs. IVDs were harvested and distributed among 3 experimental groups per tail (**Figure 1**). One disc from each tail was harvested as Day0 control. Discs from the same tail were randomly distributed among the different groups for equivalent distribution of dimensions. Initial average disc height was 11.02 ± 1.21 mm for Tofacitinib and 10.55 ± 1.35 mm for Etanercept experiment sets. The average diameter was 16.73 ± 2.42 and 16.76 ± 1.95 mm for Tofacitinib and Etanercept experiments, respectively. After removal of soft tissue, a band saw (Exakt Apparatebau, Norderstedt, Germany) was used to obtain single units with intact endplates. Capillary blood residues in the bony endplates were removed with a Pulsavac jet-lavage system (Zimmer, Warsaw, IN, USA). IVDs were initially washed with 10% Penicillin/Streptomycin (Pen/Strep) in phosphate-buffered saline (PBS, Sigma–Aldrich, St. Louis, MO, USA) for 15 min, then in 1% Pen/Strep (Sigma–Aldrich) for another 1 min. Hereafter, IVDs were incubated at 37°C, 85% humidity and 5% CO_2 under free swelling conditions in six-well plates containing Dulbecco's Modified Eagle Medium (DMEM, Sigma–Aldrich)

supplied with 2% fetal calf serum (FCS), 1% Pen/Strep, 1% ITS+ Premix (Discovery Labware, Inc., Bedford, MA, USA), 50 μg/mL ascorbate-2-phosphate (Sigma–Aldrich) and 50 μg/mL Primocin (InvivoGen, San Diego, CA, USA).

IVD Organ Culture Under Different Dynamic Loading and Nutrient Conditions

The procedure for disc harvesting and preparation, as well as the bioreactor used in this study, were the same as described previously (Lang et al., 2018). For this study, a bioreactor system was used to mimic relevant loading conditions of cultured IVDs. IVDs were placed in custom-made chambers filled with 4.5 mL IVD culture medium and were loaded for 4 days within a custom made bioreactor system under 2 different culture conditions (**Figure 1**) (Lang et al., 2018): (1) physiological cyclic sinusoidal loading (0.02–0.2 MPa; 0.2 Hz; 2 h/day) and high glucose DMEM (4.5 g/L) for **Phy** group, and (2) detrimental cyclic sinusoidal loading (0.32–0.5 MPa; 5 Hz; 2 h/day) and low glucose DMEM medium (2 g/L) for **Deg** group. The polycarbonate bioreactor was designed for the application of uniaxial loading and contained two porous plates. The discs were kept centered in the bioreactor by always maintaining a compressive load in order to ensure contact of bony endplates to the porous plates (Gantenbein et al., 2006; Junger et al., 2009). The entire system was maintained in an incubator kept at 37°C and 5% CO_2 and ambient O_2. Four bioreactor chambers were loaded with 1 disc each and the remaining discs were used as fresh d0 controls. The bioreactor system consists of 4 units, with each bioreactor unit independently pneumatically actuated (dSpace data acquisition and control card, dSPACE GmbH, Paderborn, Germany; Matlab-Simulink, MathWorks, Inc., Natick, MA, USA) under force control (load cell, Burster, Gernsbach, Germany, type 8432) (Gantenbein et al., 2006; Junger et al., 2009).

Between loading cycles, IVDs were cultured for free swelling recovery in six-well plates containing corresponding high or low glucose DMEM. Our previous study has shown that combination of 4 days of detrimental culture and single injection of TNF-α significantly upregulated the expression of key proinflammatory and catabolic genes, by mimicking the IVD microenvironment during the early phase of disc degeneration (Lang et al., 2018). Therefore, 100 ng recombinant human TNF-α (R&D systems, Zug, Switzerland) within 70 μl PBS/IVD was injected into the nucleus pulposus (NP) tissue of the Deg and Drug groups after the first dynamic loading cycle on day 1 to trigger inflammation. Control groups received 70 μL PBS which was shown not to influence cell phenotype and viability (Lang et al., 2018).

Anti-inflammatory Therapy via Etanercept or Tofacitinib

To investigate the anti-inflammatory and anti-catabolic effects of Etanercept and Tofacitinib, either TNF-α-inhibitor Etanercept (**Etanercept.inj.**) or the selective JAK3-inhibitor Tofacitinib (**Tofacitinib.med.**) were administered to the Drug group (**Figure 1**). Etanercept (3.5 mg/70 μl, Enbrel®, Pfizer, New York, NY, USA) was injected into the center of the NP with an 30G insulin needle after the first loading cycle followed by TNF-α injection 5 min later. Within the same experiment sets, 70 μl PBS was injected to Phy.inj. and Deg.inj. groups serving as positive or negative controls. The selected concentration of Etanercept at 3.5 mg per bovine caudal IVD (∼0.35 mg/mL) was based on literature. It has been reported that in a rat animal model, dosages of 0.1 or 1 mg of Etanercept were required to show appropriate effects on pain-related peptide expression in lumbar discs after intradiscal injection (Inage et al., 2016). A clinical study showed that single intradiscal administration of 10 mg Etanercept on patients with LBP could alleviate pain levels for 8 weeks after follow-up (Sainoh et al., 2016). Furthermore, Caliskan and coworkers investigated the effect of Etanercept on primary cell cultures (first-passage cultures of NP and AF cells) from intact human IVD tissue at doses of 0.1, 0.25, 0.5, 1, and 2 mg/mL (Caliskan et al., 2019). The Etanercept doses of >0.5 mg/mL were found to have cytotoxic effects. Hence the Etanercept concentration in the current study at 0.35 mg/mL is speculated to have no cytotoxic effect on disc cells. Olmarker et al. studied whether Etanercept prevents nucleus pulposus-induced functional and structural nerve root injury in a porcine experimental model by assessment of nerve conduction velocity and histology (Olmarker and Rydevik, 2001). Etanercept was applied at a dose of 12.5 mg by subcutaneous injection into pigs of ∼25 kg body weight during surgery followed by a second application 3 days later. Etanercept was found to reduce nerve fiber injury, intracapillary thrombus formation, intraneural edema formation, and to prevent a decrease of nerve conduction velocity. The average disc height for human lumbar IVDs was reported to be 10 mm and average disc diameter to be 35 mm (Bergknut et al., 2012). The average initial disc height of the bovine IVDs in this experiment was 10.55 mm and the average disc diameter was 16.76 mm. Thus, the disc volume ($V = \pi \cdot r^2 \cdot h$) of bovine caudal IVDs used in this study is around 2.34 cm^3, and the disc volume of human lumbar IVDs is around 9.62 cm^3, revealing a volume ratio of ∼1:4. Since 10 mg Etanercept injection into human lumbar IVDs was effective to relieve pain in patients according to Sainoh et al. (2016). The dose of 3.5 mg Etanercept chosen in this study is thus within an assumed therapeutic range in our model, considering the smaller distribution volume of the bovine IVDs.

For Tofacitinib, a dose of 10 mg Tofacitinib p.o. twice a day was proposed for the treatment of rheumatoid arthritis, with a body fluid volume of around 87 L and oral bioavailability of 74% (Fleischmann et al., 2016). Additionally, Suzuki and coworkers recently evaluated the anti-inflammatory effect of 100 mmol/L Tofacitinib (31240 μg/mL) on primary rat AF cells supplemented with the IL-6 *in vitro* and observed significant suppression of catabolic effects of IL-6 (Suzuki et al., 2017; NLM National Center for Biotechnology Information, 2020). In the current study, a concentration of 250 ng/mL tofacitinib citrate (Selleckchem, Munich, Germany) was first chosen to be added to the culture medium following every medium change to simulate a systemic application comparable to clinical application of the drug. Hence, the amount of a usual oral dose of 100 mg distributes to a serum concentration of 250 ng/mL. This concentration was based on the highest dose used in clinical study (Krishnaswami

et al., 2011). A 10 times higher concentration at 2.5 μg/mL was also tested to investigate the dose-response. Results of the pilot study showed that the higher dose of 2.5 μg/mL has a stronger trend to reduce the gene expression of proinflammatory markers in the NP tissue (**Supplementary Figure 1**). Thus, a concentration of 2.5 μg/mL tofacitinib citrate was selected in the main study. Tofacitinib citrate stock solution was dissolved in dimethyl sulfoxide (DMSO) at a concentration of 5 mg/mL. In the Deg group 0.05% DMSO was added to the culture medium as vehicle control. Addition of 0.05% DMSO did not cause any dysregulation on the inflammatory, catabolic, and anabolic markers in the vehicle control group.

Disc Height Change

Disc height was measured twice per day, after free swelling culture overnight and after each dynamic loading, to assess the extent of biomechanical alterations within cultured IVDs. The disc height loss and recovery percentage were assessed by calculation of the average of two measurements. Values were normalized to the initial dimensions right after dissection.

Gene Expression in IVD Tissue

RT-qPCR was performed to investigate gene expression levels of key proinflammatory, catabolic, and pain related markers as demonstrated before (Lang et al., 2018). From each IVD sample, 150 mg of NP and AF tissue were digested with 2 mg/mL pronase for 1 h at 37°C, then flash frozen, pulverized, and homogenized using liquid nitrogen and a TissueLyser (Qiagen, Venlo, Netherlands) (Caprez et al., 2018). Total mRNA was extracted using TRI Reagent (Molecular Research Center, Cincinnati, OH, USA) and reverse transcription was performed with a SuperScript VILO cDNA Synthesis Kit (Life Technologies, Carlsbad, CA, USA). Quantitative real-time PCR was performed using the Quant Studio Flex 6 instrument (Life Technologies) (Kazezian et al., 2017; Li et al., 2017). Custom designed bovine primers and TaqMan™ probes from Microsynth (Balgach, Switzerland; **Supplementary Table 1**) were used for amplification of Interleukin-1b (IL-1β), Interleukin-6 (IL-6), Matrix Metalloprotease (MMP) 1, 3, and 13. For amplification of ribosomal protein large P0 (RPLP0, Bt03218086_m1), IL-8 (Bt03211906_m1), NGF (Bt03817604_s1), and COX2 (Bt03214492_m1), gene expression assays from Applied Biosystems (Life Technologies) were used. Relative quantification of the target mRNA was performed using comparative Ct method with RPLP0 as endogenous control (Lopa et al., 2016).

Medium Analysis

Conditioned medium was collected for analysis of released matrix components and mediators daily before and after loading for further analysis. Glycosaminoglycan (GAG) content and levels of nitric oxide (NO) in the conditioned medium were determined using a modified DMMB method and a Griess Reagent Kit (Promega, Madison, WI, USA) (Farndale et al., 1986; Lang et al., 2018). The Griess Reagent Kit is based on the chemical reaction which utilizes sulfanilamide and N-1-napthylethylenediamine dihydrochloride (NED) under acidic (phosphoric acid) conditions. This system detects NO_2^- in various liquids. For the NO_2^- measurement, a nitrite standard reference curve was prepared for each assay. Hereafter, 50 μl of each sample was added to wells in duplicates. Fifty microliter of the Sulfanilamide Solution was dispensed to all experimental samples and wells containing the dilution series for the Nitrite Standard reference curve following incubation for 10 min at room temperature, protected from light. Additionally, 50 μl of the NED Solution was dispensed to all wells following incubation for 10 min, protected from light. Finally, the absorbance was measured in a plate reader (Victor3 Micro Plate Reader, PerkinElmer, Waltham, MA, USA) with a filter between 520 and 550 nm. For the modified DMMB method, a GAG standard reference curve was prepared for each assay utilizing 1 mg/ml chondroitinsulfate (Chondroitin 4-sulfate sodium salt from bovine trachea, mixture of isomers, Sigma-Aldrich) in distilled H_2O. Hereafter, 50 μl of each sample was added to wells in duplicates following the supplementation of 200 μl of DMMB color reagent [16 mg DMMB (1,9-Dimethyl-methylene blue, Sigma-Aldrich) in 1 L water containing 3.04 g glycine and 2.37 g NaCl)] to each well. Absorbance was read in a plate reader (Victor3 Micro Plate Reader) at 535 nm. Interleukin 8 (IL-8) protein content was measured with bovine IL-8 ELISA kits (Kingfisher Biotech, St. Paul, MN, USA).

Histology

After 4 days of culture, endplates were removed from one side and whole IVDs were snap frozen in Tissue Freezing Medium® (Leica Biosystems, Nussloch, Germany). Transverse sections (10 μm) were obtained using a cryostat (Microm, Dreieich, Germany). Immunohistochemistry (IHC) was performed to investigate protein expression of IL-1β, IL-6, IL-8, and collagen type II within the disc tissue. Cryosections were fixed in 70% and 100% methanol for 10 min each, then left airdry overnight. The slides were rinsed in deionized water and washed in 99% methanol with 0.3% H_2O_2 solution for 30 min. After blocking with goat serum (Vector Laboratories, Burlingame, CA, USA), the sections were probed with IL-1β (Kingfisher Biotech, KP1109B-100, 2 μg/mL), IL-6 (Kingfisher Biotech, KP0652B-100, 1 μg/mL) or IL-8 (Kingfisher Biotech, PB0273B-100, 5 μg/mL) antibodies at 4°C overnight. The sections were then incubated with a biotinylated goat-anti-rabbit secondary antibody (Vector Laboratories, #BA-1000) for IL-1β and IL-8, or goat-anti-chicken secondary antibody (Vector Laboratories, #BA-9010) for IL-6, followed by incubation with avidin-biotin-peroxidase (Vectastain Elite ABC kit, Vector Laboratories), and ImmPACT®DAB Peroxidase (HRP) Substrate (Vector Laboratories). For collagen type II IHC staining, after enzyme treatment with 1 U/mL hyaluronidase (Sigma-Aldrich), non-specific binding sites were blocked with horse serum (Vector Laboratories) for 1 h at RT. The primary antibody (CIIC1, 5 μg/mL, Developmental Studies Hybridoma Bank, University of Iowa, Iowa City, IA, USA) was incubated for 30 min at RT and detected using a secondary biotinylated anti-mouse antibody (Vector Laboratories) followed by incubation with avidin-biotin-peroxidase complex, and ImmPACT®DAB Peroxidase (HRP) Substrate. Negative control sections were incubated without the primary antibody. As described previously, cell viability was

assessed using lactate dehydrogenase (LDH) staining in 40% polypep solution and ethidium homodimer-1 staining (EthD-1, 1 μg/mL). The blue or blue/red staining indicates living cells, and red only staining indicates dead cells (Li et al., 2016b; Lang et al., 2018). For both IHC and LDH/ EthD-1 staining, 2 IVDs per group were analyzed. For each IVD sample, 4 images at each predefined anatomic region (NP, inner AF, and outer AF) were analyzed. In IL-1β, IL-6 and IL-8 IHC images, the percentage of positively stained cells was analyzed using Axioplan software (Zeiss, Oberkochen, Germany). In collagen type II IHC images, the staining optical density (OD)/area value was analyzed using Image-Pro Plus 6.0 software (Media Cybernetics, Rockville, MD, USA). In LDH/EthD-1 staining images, the percentage of alive cells was analyzed using Axioplan software (Zeiss).

Statistical Analysis

GraphPad Prism 7 software (GraphPad Software, Inc., La Jolla, CA, USA) was used for statistical analysis. D'Agostino-Pearson omnibus normality test was performed to assess if data were normally distributed. For data that were normally distributed, unpaired *t*-test was used to determine differences between two groups; one-way ANOVA was used to determine differences between three or more groups. For data that were not normally distributed, Mann–Whitney *U*-test was used to determine differences between two groups; Kruskal Wallis test was used to determine differences between three or more groups. A $p < 0.05$ was considered statistically significant.

RESULTS

Gene Expression

Gene expression levels of NP and AF tissues were normalized to Phy group. According to the results of the D'Agostino-Pearson omnibus normality test, the gene expression data were not non-normally distributed. Therefore, Kruskal Wallis test was used to detect the differences between the 3 groups: Phy, Deg, and Drug. Deg.inj. culture condition upregulated the expression of catabolic enzymes MMP1 ($p < 0.05$) and MMP3 ($p < 0.05$) in NP tissue (**Figure 2**). Deg.med. culture condition upregulated the expression of catabolic enzymes MMP3 ($p < 0.05$) in NP

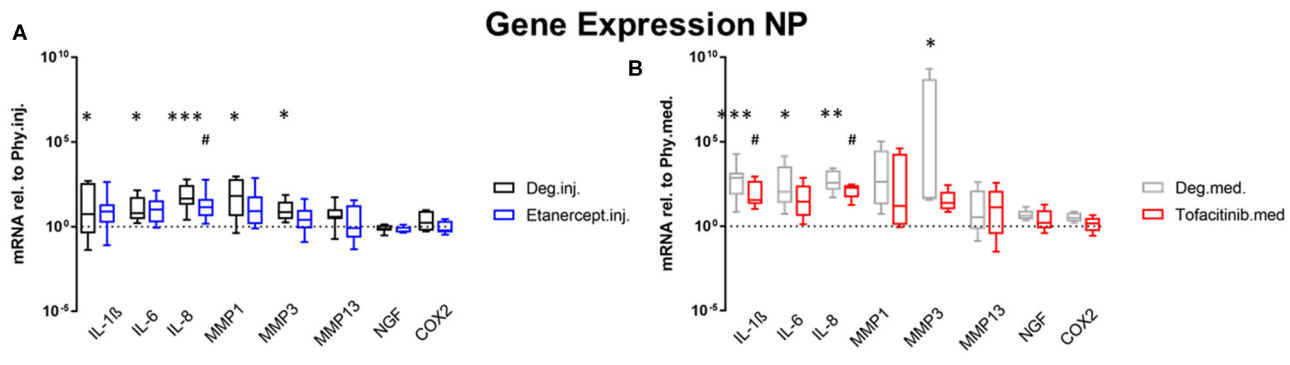

FIGURE 2 | Gene expression levels of NP tissue. Gene expression levels of NP tissue after 4 days of culture under Deg culture condition, with or without **(A)** Etanercept intradiscal injection. **(B)** Tofacitinib application into the medium, normalized to Phy group. $n = 8$, $^{*}p < 0.05$, $^{**}p < 0.01$, $^{***}p < 0.001$ Deg vs. Phy, $^{\#}p < 0.05$ Drug vs. Phy, min to max (bottom and top bar) with interquartile range (middle box). NP, Nucleus pulposus; IL, Interleukin; MMP, Matrix metalloproteinases; NGF, Nerve growth factor; COX-2, Cyclooxygenase-2.

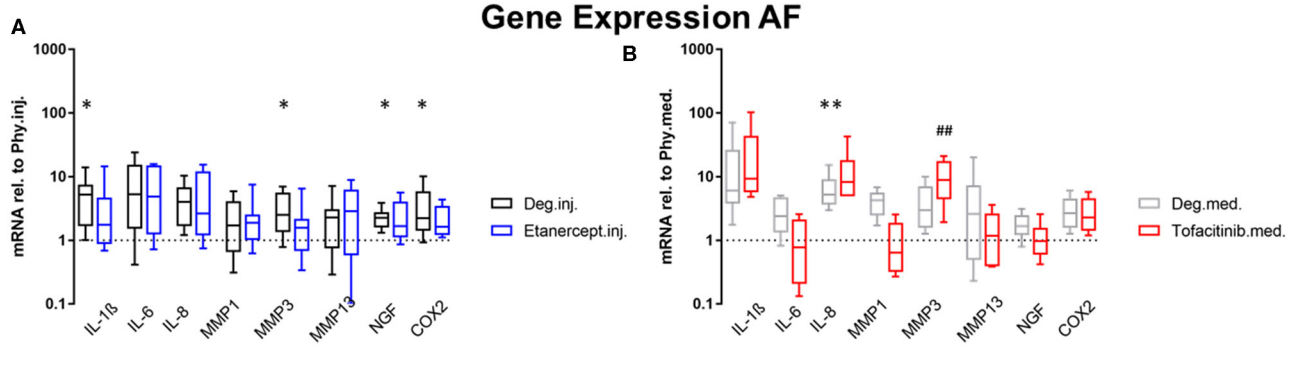

FIGURE 3 | Gene expression levels of AF tissue. Gene expression levels of AF tissue after 4 days of culture under Deg culture condition, with or without **(A)** Etanercept intradiscal injection. **(B)** Tofacitinib application into the medium, normalized to Phy group. $n = 8$, $^{*}p < 0.05$, $^{**}p < 0.01$ Deg vs. Phy, $^{\#\#}p < 0.01$ Drug vs. Phy, min to max (bottom and top bar) with interquartile range (middle box). AF, Annulus fibrosus; IL, Interleukin; MMP, Matrix metalloproteinases; NGF, Nerve growth factor; COX-2, Cyclooxygenase-2.

tissue (**Figure 2**). Detrimental culture conditions also resulted in a strong inflammatory response, indicated by a significant upregulation of proinflammatory markers, including IL-1β in NP (Deg.inj. and Deg.med.) and AF tissue (Deg.inj., $p < 0.05$), IL-6 in NP tissue (Deg.inj. and Deg.med., $p < 0.05$) and IL-8 in NP (Deg.inj. and Deg.med, $p < 0.05$) and AF tissue (Deg.med, $p < 0.05$) (**Figures 2**, **3**). COX2 ($p < 0.05$) and NGF ($p < 0.05$) showed a significant upregulation under Deg.inj. culture conditions in the AF (**Figure 3**). Overall, detrimental culture conditions, implying degenerative loading combined with the pro-inflammatory stimulus TNF-α, featured stronger effects in the NP than in AF tissue.

Compared to the Deg.inj. group, Etanercept treatment partially prevented the upregulation of IL-1β, IL-6, IL-8, MMP1, and MMP3 in the NP (**Figure 2**) and IL-1β, MMP3, COX2, and NGF in the AF (**Figure 3**), resulting in expression levels comparable with the Phy.inj. group. Compared to the Deg.med. group, Tofacitinib therapy partially prevented the increase of IL-1β, IL-6, IL-8, and MMP3 in the NP (**Figure 2**).

GAG, NO, and IL-8 Protein Release in Medium

Conditioned IVD medium was collected for investigation of GAG, NO, and IL-8 protein release ($n = 8$). The cumulative GAG release was normalized to the volume of each disc on day 0 after dissection, which was then normalized to the value of respective group on day 1 during 20 h of free swelling culture (**Figures 4A,B**) GAG release under Deg.med. culture condition was significantly enhanced compared to Phy.med. culture condition on Day 2 and Day 3 after loading ($p <$

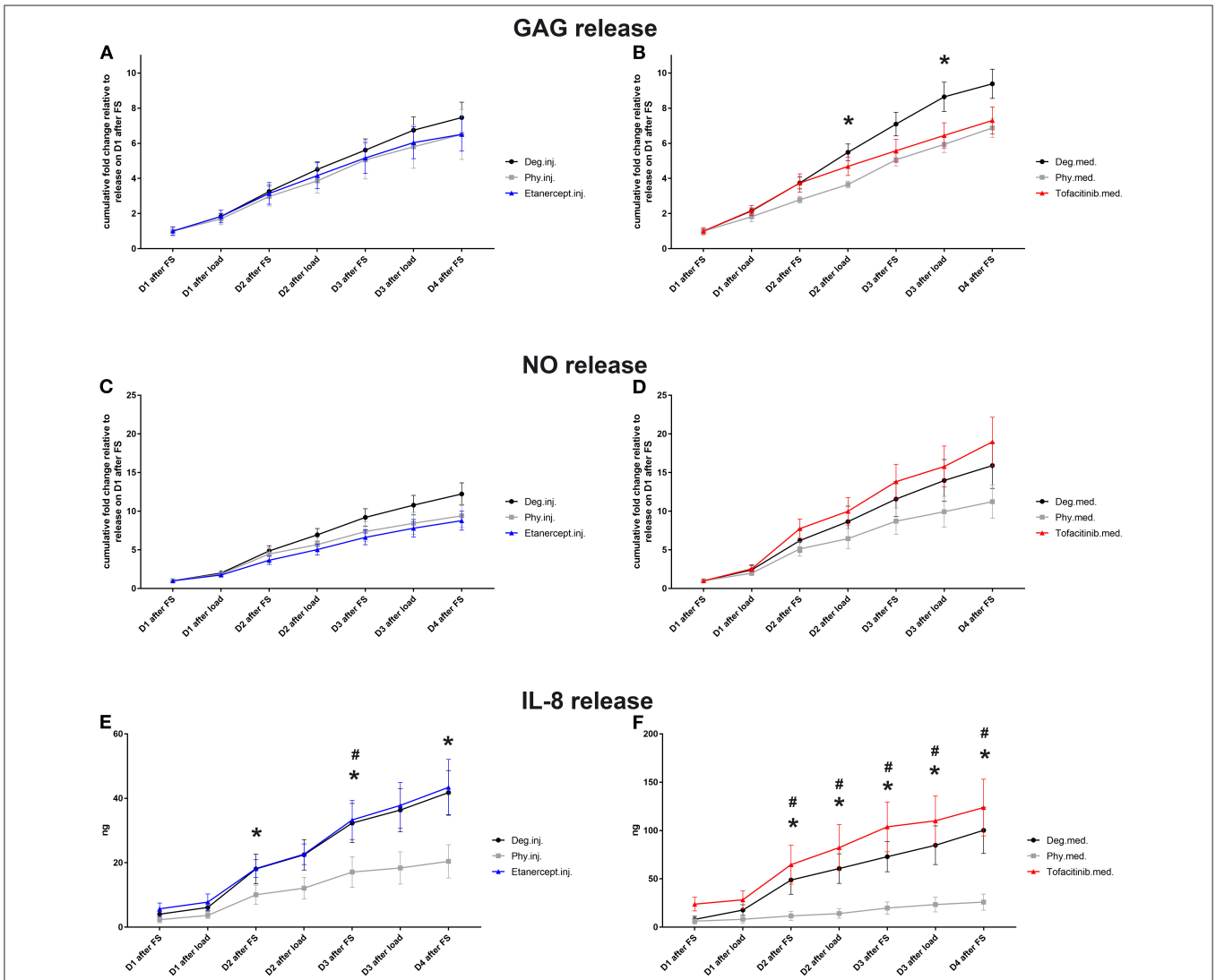

FIGURE 4 | GAG **(A,B)**, NO **(C,D)**, and IL-8 release **(E,F)** in IVD culture medium. Cumulative release of GAG, NO, and IL-8 into IVD conditioned medium during 20 h of free swelling culture (FS) and 2 h of dynamic loading (load); D, day; Means ± SEM, $n = 8$; $^{*}p < 0.05$ Phy vs. Deg; $^{\#}p < 0.05$ Phy vs. Drug; GAG, glycosaminoglycan; NO, nitric oxide.

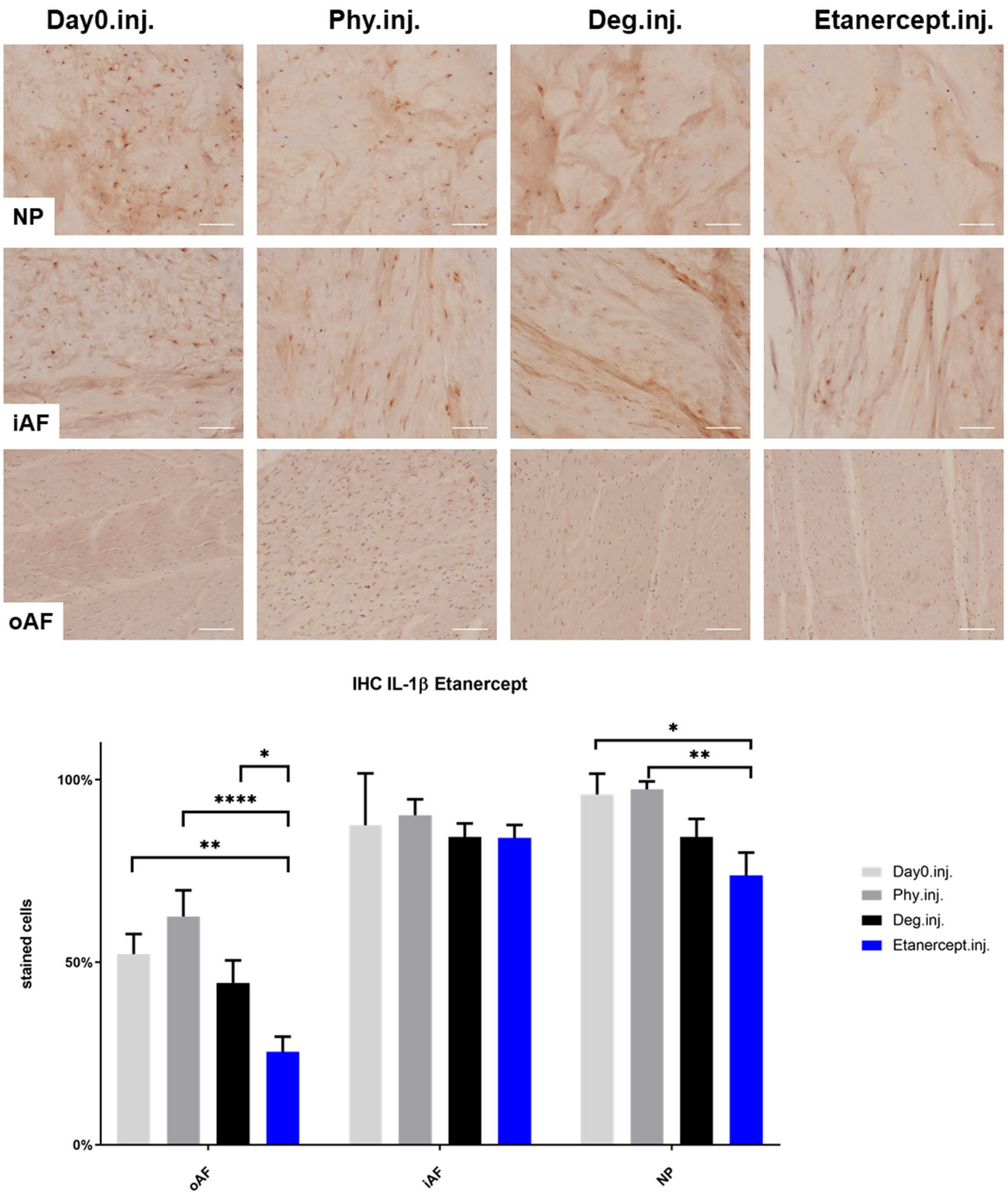

FIGURE 5 | IL-1β immunohistochemistry staining of IVD tissue from the Etanercept experiments. Representative IL-1β IHC image of NP region, inner AF region (iAF) and outer AF (oAF) region from day 0 control samples (Day0.inj.), IVDs cultured under physiological condition on day 4 (Phy.inj.), IVDs cultured under degenerative condition on day 4 (Deg.inj.), and IVDs cultured under degenerative condition and treated with Etanercept on day 4 (Etanercept.inj.). Scale bar: 100 μm. The percentage of positively stained cells were counted, as presented in the bar graph. $n = 8$, Means + SEM, $^{*}p < 0.05$, $^{**}p < 0.01$, $^{****}p < 0.0001$.

0.05). Deg.inj. condition also caused an enhanced release of GAG compared to Phy.inj. culture condition. Etanercept and Tofacitinib reduced the GAG loss to the level under physiological culture condition (**Figures 4A,B**). The cumulative NO release was normalized to the volume of each disc on day 0 after dissection, which was then normalized to the value of the respective group on day 1 during free swelling (**Figures 4C,D**). An increased NO release was observed under Deg.inj. and Deg.med. culture conditions compared to Phy.inj. and Phy.med. groups. Etanercept reduced the NO release, while Tofacitinib had no effect. Deg.inj. and Deg.med. culture conditions significantly upregulated IL-8 protein release compared to physiological culture conditions ($p < 0.05$) (**Figures 4E,F**). Furthermore, there was a peak of IL-8 release among all Deg and Drug groups after the TNF-α injection. Cumulation with time revealed an increasing difference of IL-8 release in the Deg groups compared to the Phy groups, indicating a constant increase of proinflammatory cytokines due to Deg treatment. Etanercept and Tofacitinib did not show any reduction effect on IL-8 release.

IL-1β, IL-6, and IL-8 Protein Expression in IVD Tissue

IHC was performed to investigate the protein expression of IL-1β, IL-6, and IL-8 within IVD tissue (**Figures 5–10**). For qualitative analysis, representative IL-1β, IL-6, and IL-8 IHC images were taken from the NP region, inner AF region, and outer AF region from day 0 control samples (Day0.inj.), IVDs cultured under physiological condition on day 4 (Phy.inj./Phy.med.), IVDs cultured under degenerative condition on day 4 (Deg.inj./Deg.med.), and IVDs cultured under degenerative condition and treated either with Etanercept (Etanercept.inj.) or Tofacitinib on day 4 (Tofacitinib.med.). Additionally, the percentage of positively stained cells were counted, as presented in the bar graphs (**Figures 5–10**). IHC revealed expression of proinflammatory cytokines IL-1β, IL-6, and IL-8 throughout all experimental groups. Trends of differences in the distribution of interleukins among the different IVD tissue types were observable. In general, physiological expression of IL-1β and IL-8 was more abundant in the NP whereas IL-6 featured higher expression levels in the AF. Degenerative culture condition reduced the percentage of IL-8 positively stained cells in the outer AF tissue compared with physiological group (Deg.inj; **Figure 7**), as well as the IL-6 positively stained cells in the NP tissue compared with day 0 group (Deg.med.; **Figure 9**). A reduction of IL-1β positively stained cells in the outer AF and NP regions after Etanercept treatment (**Figure 5**, $p < 0.05$), reduction of IL-1β positively stained cells in the inner AF region following Tofacitinib therapy (**Figure 8**, $p < 0.01$), as well as reduction of IL-8 positively stained cells in inner AF tissue after Tofacitinib (**Figure 10**, $p < 0.05$) were observed comparing to at least one of the other groups.

Collagen Type II Protein Expression in IVD Tissue

COL2 distribution was revealed by IHC in **Figures 11**, **12**. In NP tissue, COL2 was homogenously distributed in the tissue. The expression in inner AF tissue had a stripe shape, with some AF lamellae stained more intense and some other lamellae with lighter staining. The outer AF tissue showed very weak staining of COL2. After 4 days of culture, COL2 expression in the inner AF tissue of IVDs under Phy condition showed a decrease compared with Day0 healthy controls. The Deg and Drug groups showed a slightly higher COL2 staining intensity compared with the Phy group, while no difference was observed between the Deg and Drug groups.

Cell Viability in IVD Tissue

Cell viability of disc tissue was assessed after 4 days of culture. Degenerative loading combined with TNF-α injection decreased cell viability in the NP and iAF regions compared to the Phy and Day0 control groups ($p < 0.01$; **Figures 13**, **14**), whereas viability in the oAF tissue was not influenced by Deg treatment after 4 days of culture. Neither of the drugs did affect the cell viability under Deg condition during the observation time (**Figures 13**, **14**).

Disc Height Change

Degenerative loading and detrimental culture caused a significantly stronger disc height loss (∼20%) compared to the physiological loading protocol and culture (∼10%, $p < 0.001$) (**Figure 15**). During free swelling recovery, all IVDs could recover to the initial disc height before first loading (∼105–110%). This diurnal disc height change pattern was observed throughout the entire period of 3 days of repetitive dynamic load. The height loss in the detrimentally loaded groups seemed to increase by time, indicating progressive destruction of tissue. Whereas, the extent of height recovery demonstrated consistency. The drugs did not alter the potential of recovery or the height loss after loading during the observation time.

DISCUSSION

Detrimental Loading, Nutrient Deficiency, and TNF-α Injection Simulates Early-Stage Intervertebral Disc Degeneration

Proinflammatory cytokines are considered of crucial importance in the pathogenesis of IDD as they link the inflammatory process to accelerated tissue degeneration and pain. Previous work provided evidence, that the expression of proinflammatory cytokines such as TNF-α, IL1β, IL-6, and IL-8, is associated with the disease activity of IDD in human subjects and animal models (Le Maitre et al., 2005, 2007b; Bachmeier et al., 2007; Hoyland et al., 2008; Freemont, 2009; Freeman et al., 2013; Purmessur et al., 2013; Andrade et al., 2016; Sutovsky et al., 2017). In the present study, degenerative culture conditions combined with TNF-α injection stimulated proinflammatory gene expression (IL-1β, IL-6, and IL-8 in the NP and IL-1β, IL-8, and COX2 in the AF) and upregulated catabolic enzymes (MMP1 and MMP3) with a more profound increase in the NP compared with the AF tissue. These results support the work by Walter et al. and confirm our TNF-α intradiscal injection model, with a higher TNF-α gradient in the NP than in the AF (Walter et al., 2015a; Lang et al., 2018).

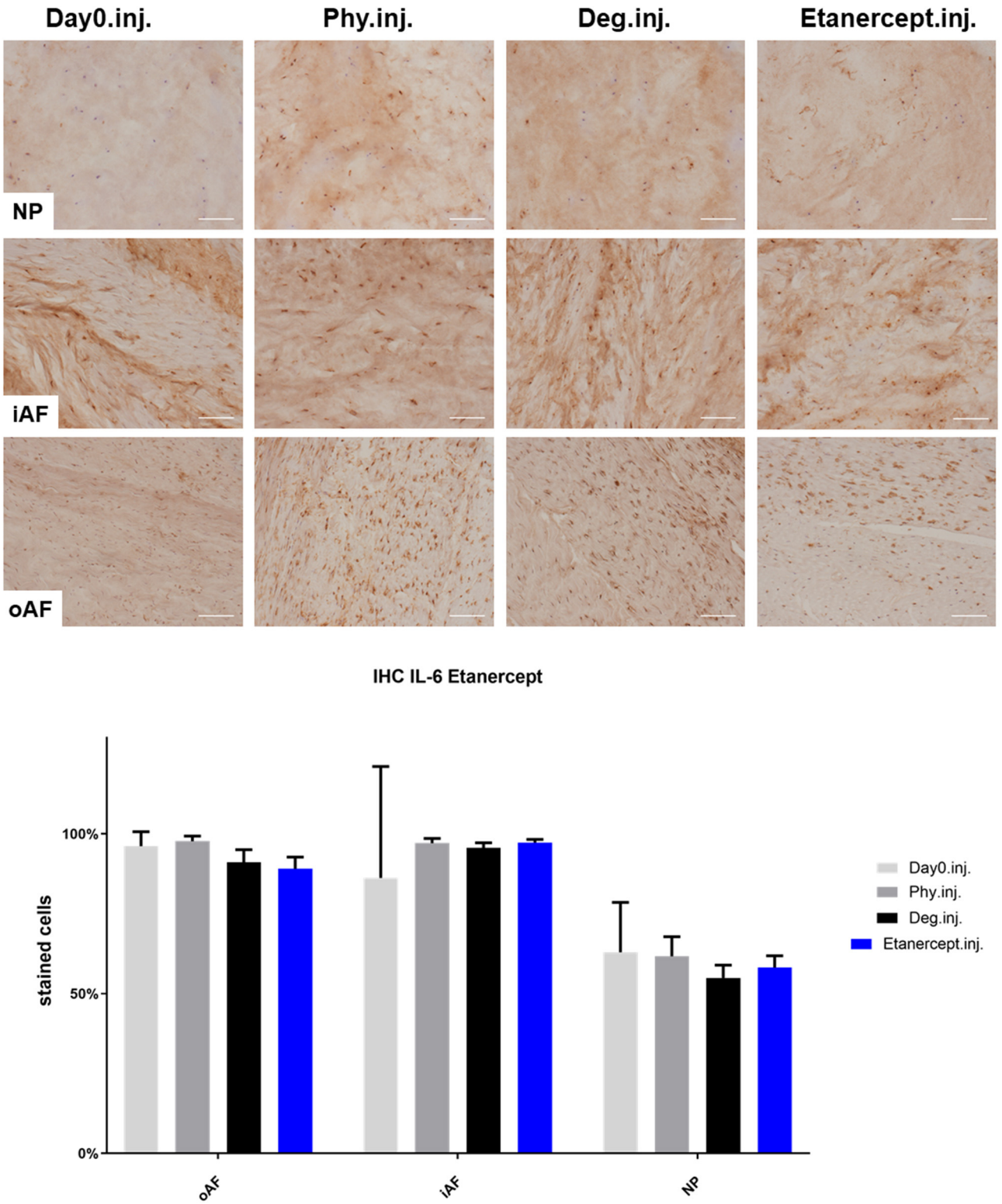

FIGURE 6 | IL-6 immunohistochemistry staining of IVD tissue from the Etanercept experiments. Representative IL-6 IHC image of NP region, inner AF region (iAF) and outer AF (oAF) region from day 0 control samples (Day0.inj.), IVDs cultured under physiological condition on day 4 (Phy.inj.), IVDs cultured under degenerative condition on day 4 (Deg.inj.), and IVDs cultured under degenerative condition and treated with Etanercept on day 4 (Etanercept.inj.). Scale bar: 100 μm. The percentage of positively stained cells were counted, as presented in the bar graph. $n = 8$, Means + SEM.

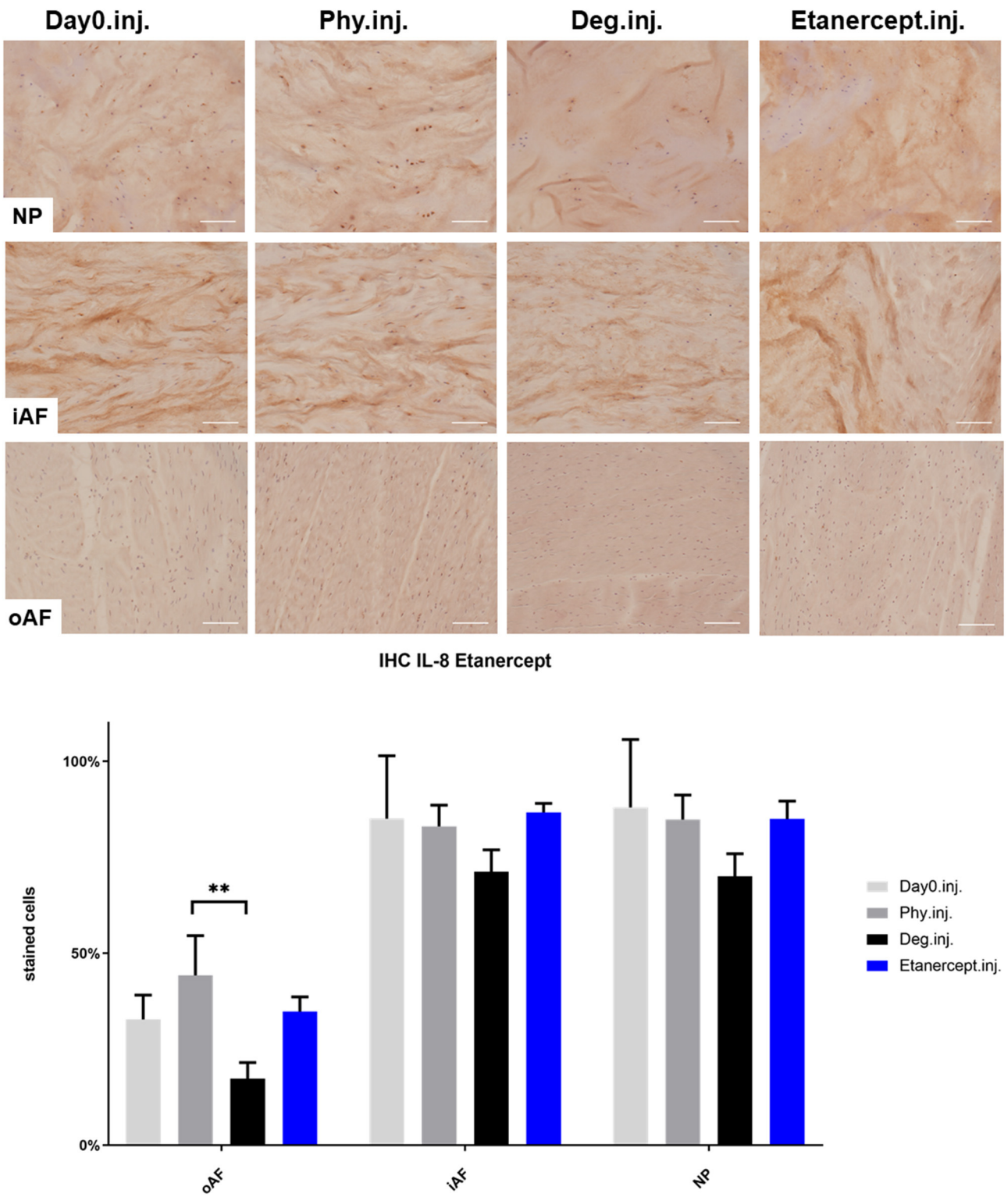

FIGURE 7 | IL-8 immunohistochemistry staining of IVD tissue from the Etanercept experiments. Representative IL-8 IHC image of NP region, inner AF region (iAF) and outer AF (oAF) region from day 0 control samples (Day0.inj.), IVDs cultured under physiological condition on day 4 (Phy.inj.), IVDs cultured under degenerative condition on day 4 (Deg.inj.), and IVDs cultured under degenerative condition and treated with Etanercept on day 4 (Etanercept.inj.). Scale bar: 100 μm. The percentage of positively stained cells were counted, as presented in the bar graph. $n = 8$, Means + SEM, $^{**}p < 0.01$.

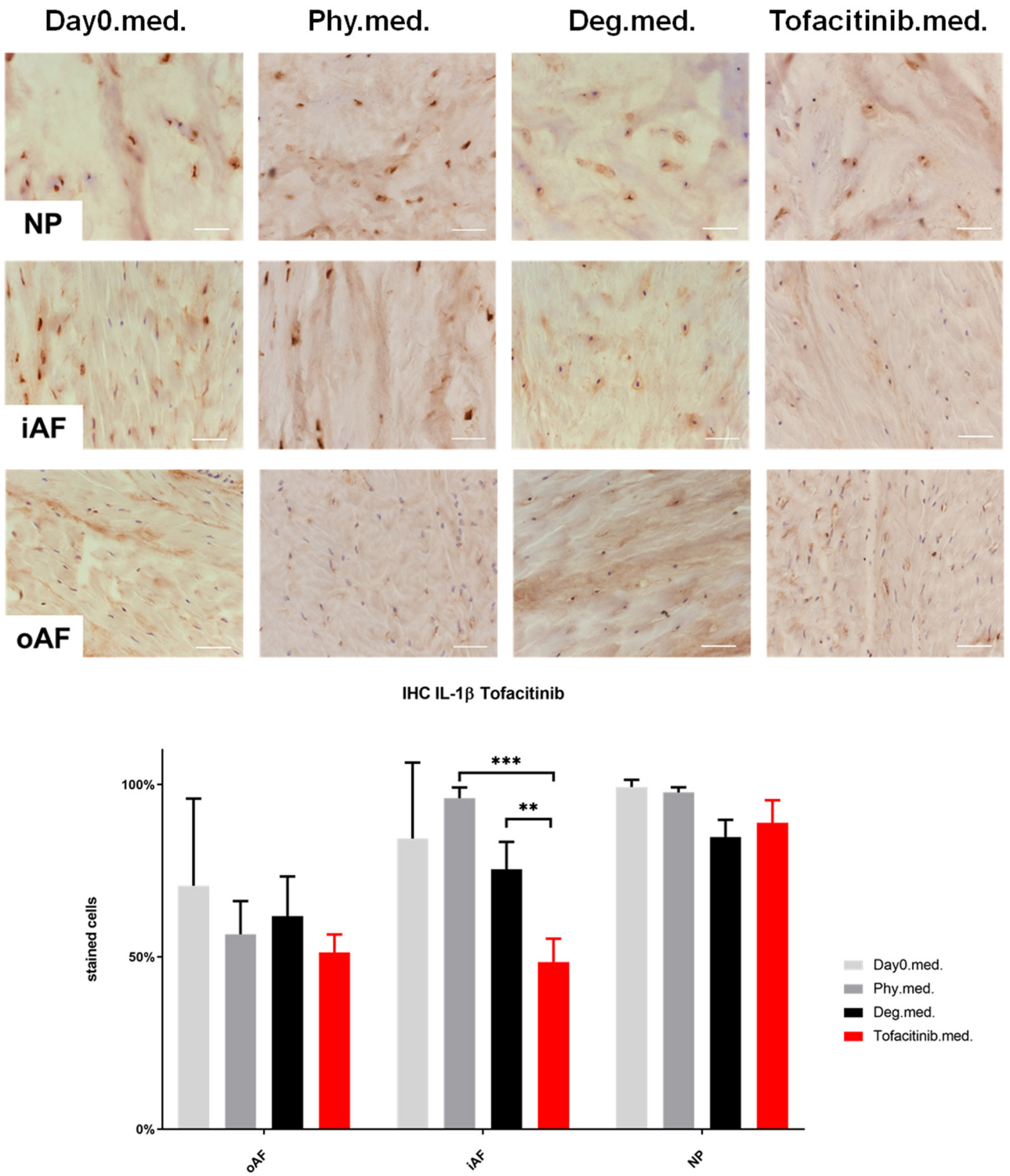

FIGURE 8 | IL-1β immunohistochemistry staining of IVD tissue from the Tofacitinib experiments. Representative IL-1β IHC image of NP region, inner AF region (iAF) and outer AF (oAF) region from day 0 control samples (Day0.med.), IVDs cultured under physiological condition on day 4 (Phy.med.), IVDs cultured under degenerative condition on day 4 (Deg.med.), and IVDs cultured under degenerative condition and treated with Tofacitinib on day 4 (Tofacitinib.med.). Scale bar: 100 μm. The percentage of positively stained cells were counted, as presented in the bar graph. $n = 8$, Means + SEM, $^{**}p < 0.01$, $^{***}p < 0.001$.

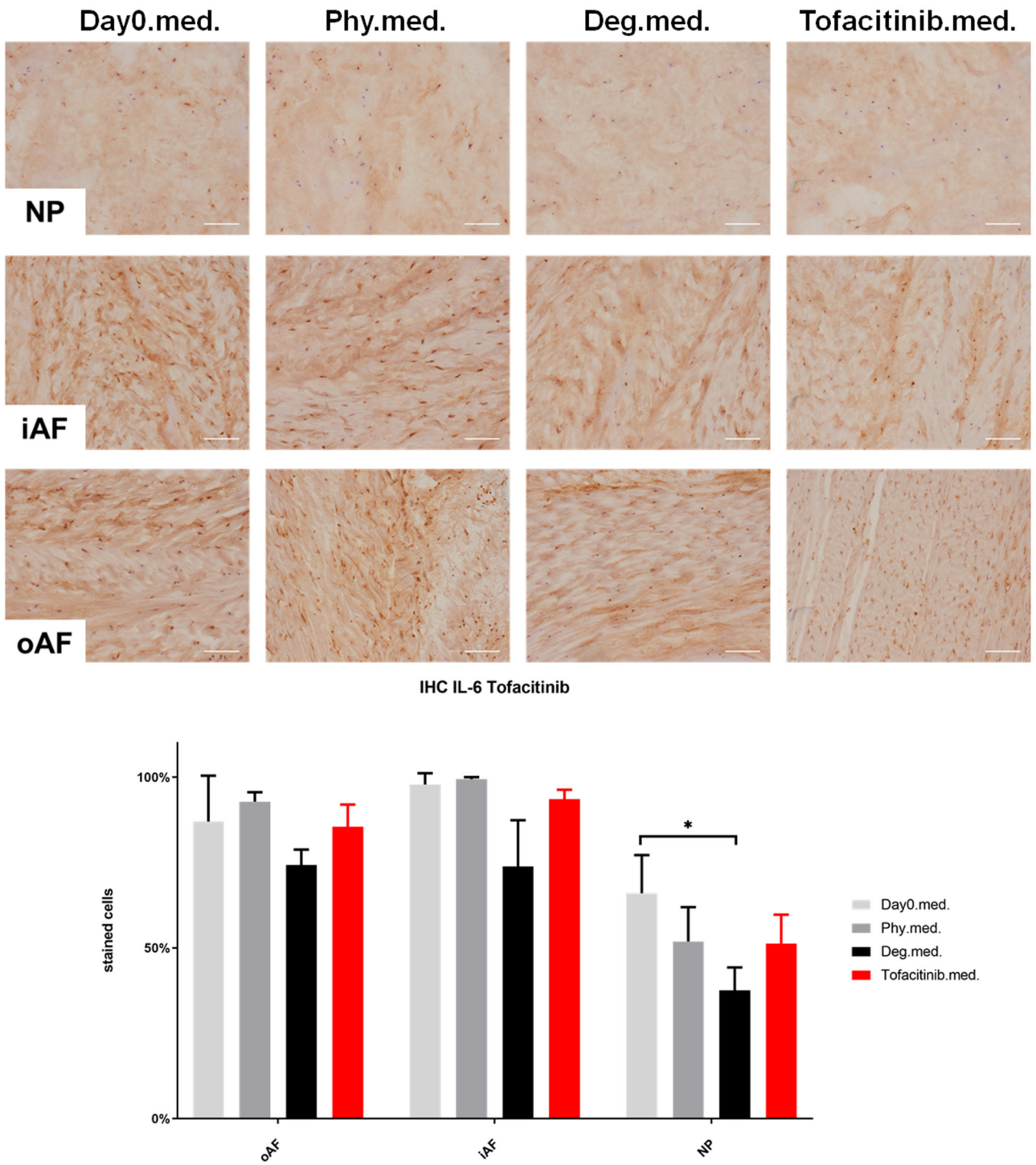

FIGURE 9 | IL-6 immunohistochemistry staining of IVD tissue from the Tofacitinib experiments. Representative IL-6 IHC image of NP region, inner AF region (iAF) and outer AF (oAF) region from day 0 control samples (Day0.med.), IVDs cultured under physiological condition on day 4 (Phy.med.), IVDs cultured under degenerative condition on day 4 (Deg.med.), and IVDs cultured under degenerative condition and treated with Tofacitinib on day 4 (Tofacitinib.med.). Scale bar: 100 μm. The percentage of positively stained cells were counted, as presented in the bar graph. $n = 8$, Means + SEM, $^{*}p < 0.05$.

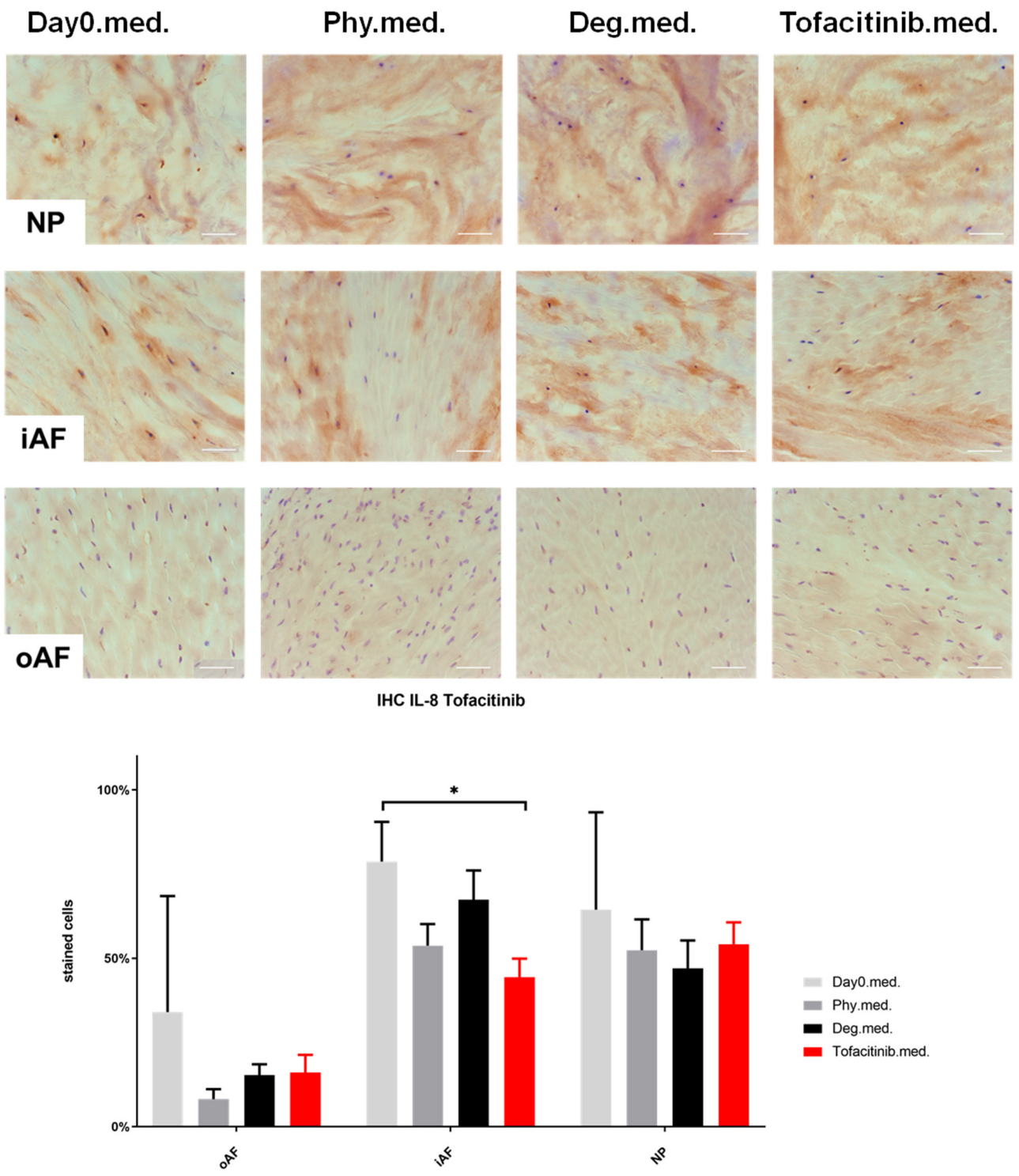

FIGURE 10 | IL-8 immunohistochemistry staining of IVD tissue from the Tofacitinib experiments. Representative IL-8 IHC image of NP region, inner AF region (iAF) and outer AF (oAF) region from day 0 control samples (Day0.med.), IVDs cultured under physiological condition on day 4 (Phy.med.), IVDs cultured under degenerative condition on day 4 (Deg.med.), and IVDs cultured under degenerative condition and treated with Tofacitinib on day 4 (Tofacitinib.med.). Scale bar: 100 μm. The percentage of positively stained cells were counted, as presented in the bar graph. $n = 8$, Means + SEM, $^{*}p < 0.05$.

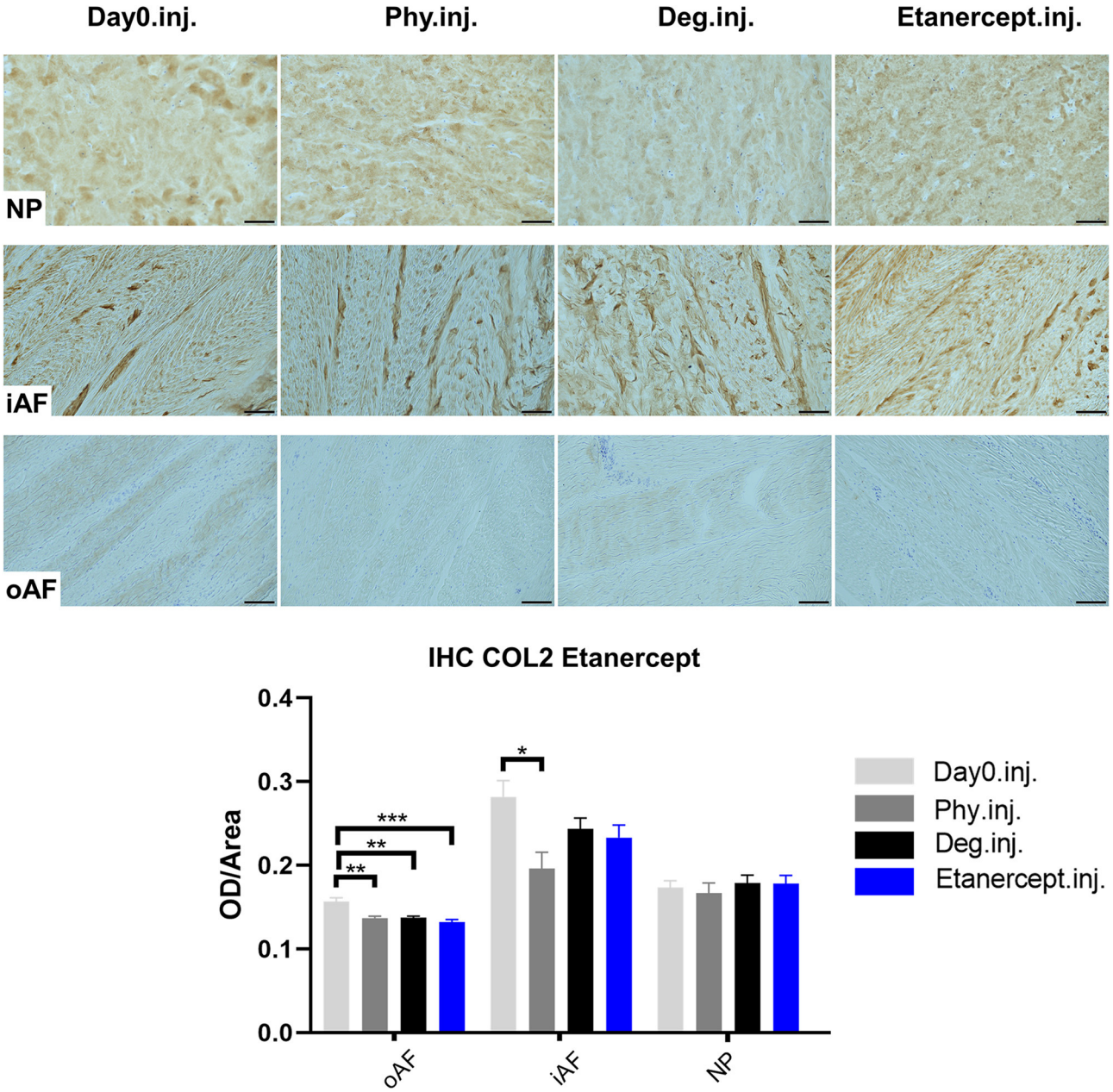

FIGURE 11 | Collagen type II immunohistochemistry staining of IVD tissue from the Etanercept experiments. Representative COL2 IHC image of NP region, inner AF region (iAF) and outer AF (oAF) region from day 0 control samples (Day0.inj.), IVDs cultured under physiological condition on day 4 (Phy.inj.), IVDs cultured under degenerative condition on day 4 (Deg.inj.), and IVDs cultured under degenerative condition and treated with Etanercept on day 4 (Etanercept.inj.). Scale bar: 100 μm. The staining optical density (OD)/area value was analyzed, as presented in the bar graph. $n = 8$, Means + SEM, $^{*}p < 0.05$, $^{**}p < 0.01$, $^{***}p < 0.001$.

Interestingly, degenerative and proinflammatory culture condition also induced gene expression of nerve growth factor (NGF) in the AF tissue, which is related with nociceptive nerve ingrowth and discogenic pain (Freemont et al., 1997; Nakawaki et al., 2019). Previous work has already indicated that, inflammatory cytokines such as IL-1β, TNF-α regulate local intradiscal NGF expression and subsequent ingrowth of small non-myelinated nerve fibers into the IVD (Abe et al., 2007; Miyagi et al., 2012, 2018; Nakawaki et al., 2019). Although our model lacks the opportunity to investigate pain behavioral changes due to IDD driven NGF expression as done by others (i.e., *in vivo* studies in rodents), upregulation of NGF in the AF tissue may be a hint for local intradiscal NGF production in our *ex vivo* system as observed in symptomatic IDD (Lai et al., 2015).

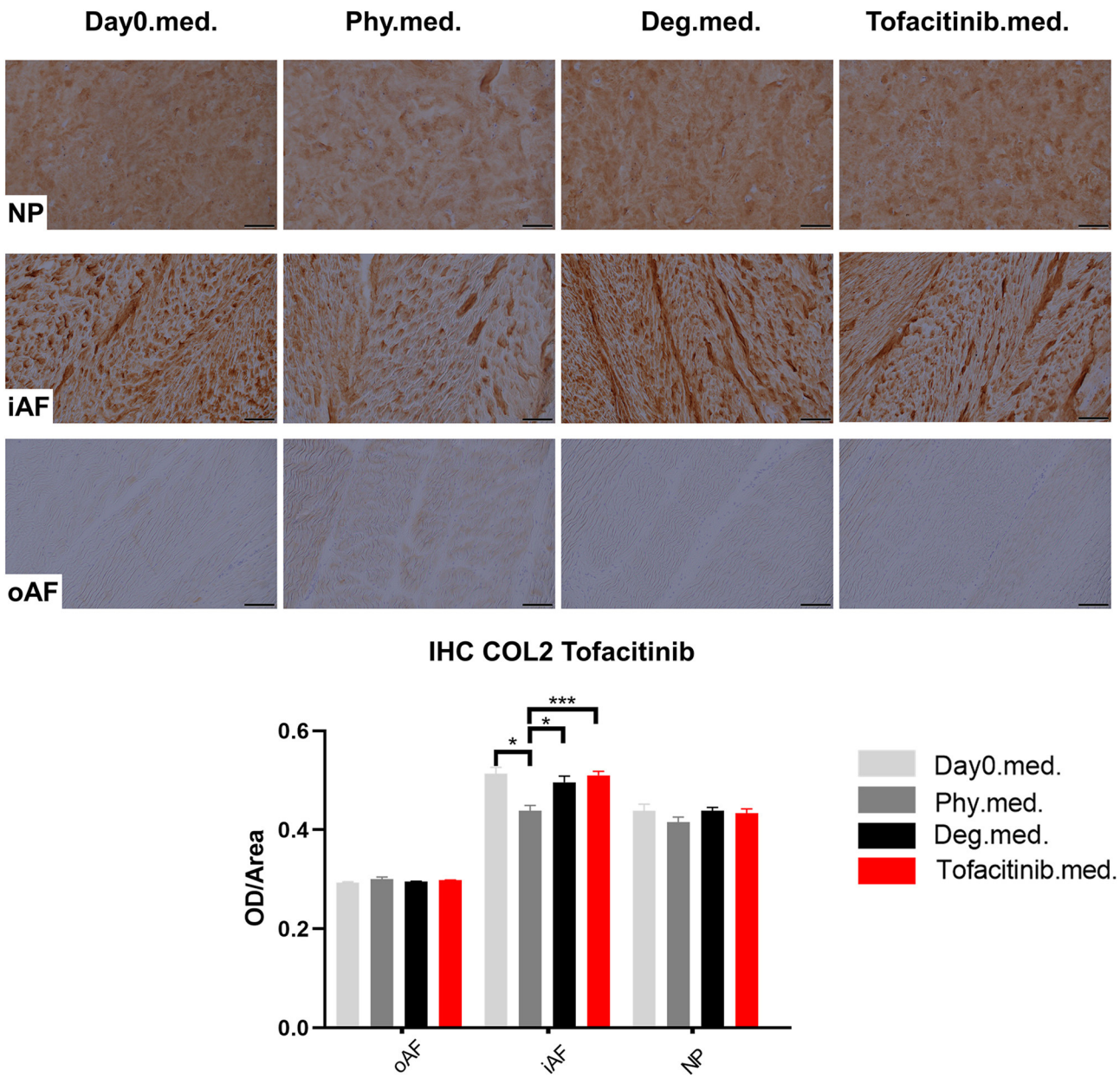

FIGURE 12 | Collagen type II immunohistochemistry staining of IVD tissue from the Tofacitinib experiments. Representative COL2 IHC image of NP region, inner AF region (iAF) and outer AF (oAF) region from day 0 control samples (Day0.med.), IVDs cultured under physiological condition on day 4 (Phy.med.), IVDs cultured under degenerative condition on day 4 (Deg.med.), and IVDs cultured under degenerative condition and treated with Tofacitinib on day 4 (Tofacitinib.med.). Scale bar: 100 μm. The staining optical density (OD)/area value was analyzed, as presented in the bar graph. $n = 8$, Means + SEM, $^{*}p < 0.05$, $^{***}p < 0.001$.

Additionally, degenerative culture conditions combined with TNF-α injection elevated the IL-8 protein release compared to physiological culture conditions, further indicating inflammatory disc condition consistent with our previous work (Lang et al., 2018). Likewise, GAG and NO release were enhanced due to the inflammatory and degenerate culture condition. The collagen type II and proteoglycan expression in the IVD were not reduced by degenerative culture condition compared to the Phy group, as indicated by IHC staining in the current study and Safranin O staining and GAG content quantification from previous study, respectively (Lang et al., 2018). This is due to the high intrinsic content of GAG and collagen type II within the young bovine discs, which did not show a reduction under Deg condition during the culture period. However, the enhanced GAG release into the culture medium indicates the early onset of matrix degradation.

The biomechanical response of IVDs under a degenerative proinflammatory stimulus was assessed via disc height change.

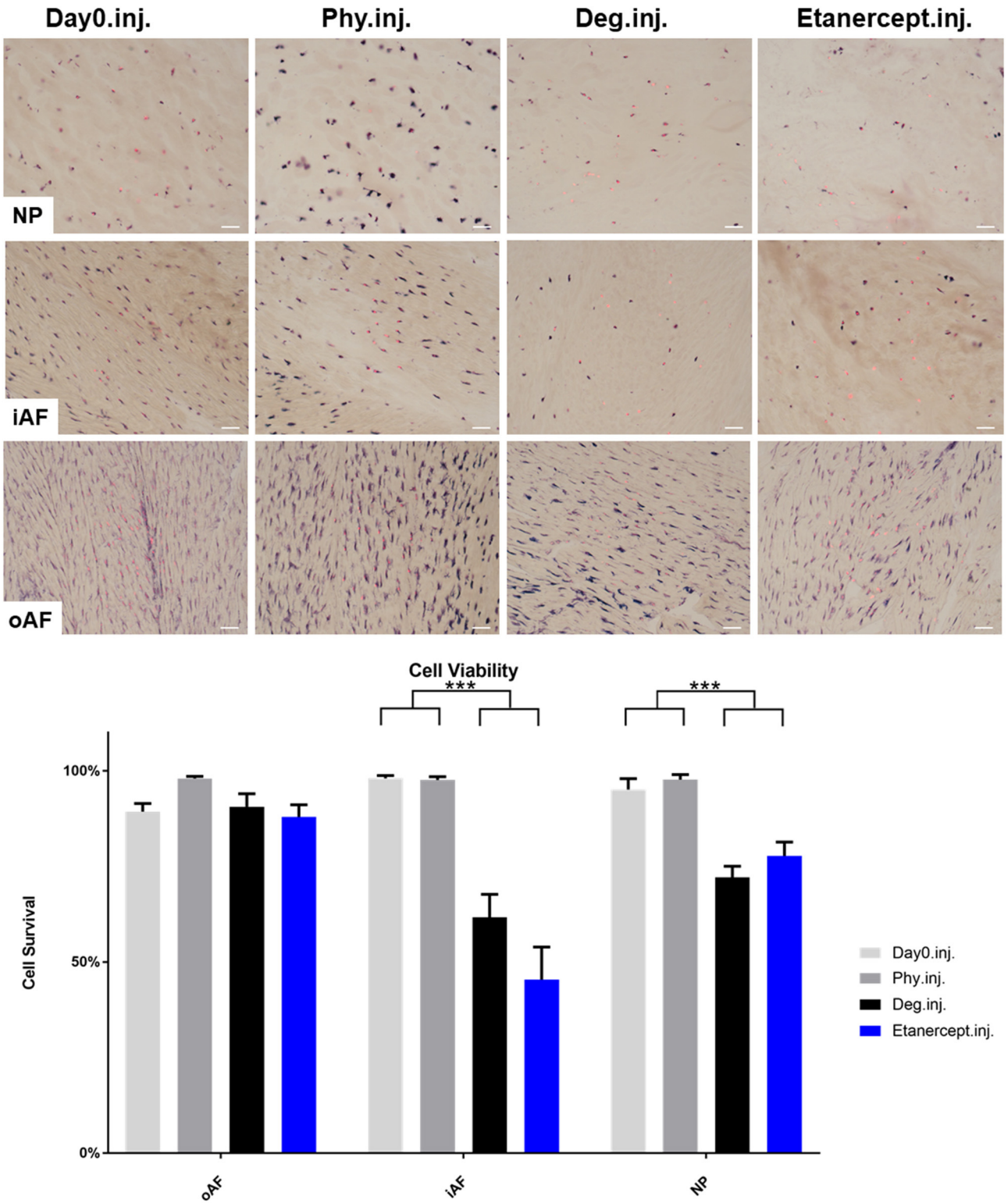

FIGURE 13 | Cell viability of IVD tissue from the Etanercept experiments. Representative LDH/ EthD-1 staining image of NP region, inner AF region (iAF) and outer AF (oAF) region from day 0 control samples (Day0.inj.), IVDs cultured under physiological condition on day 4 (Phy.inj.), IVDs cultured under degenerative condition on day 4 (Deg.inj.), and IVDs cultured under degenerative condition and treated with Etanercept on day 4 (Etanercept.inj.). Scale bar: 50 μm. The percentage of alive cells were counted, as presented in the bar graph. $n = 8$, Means + SEM, $^{***}p < 0.001$.

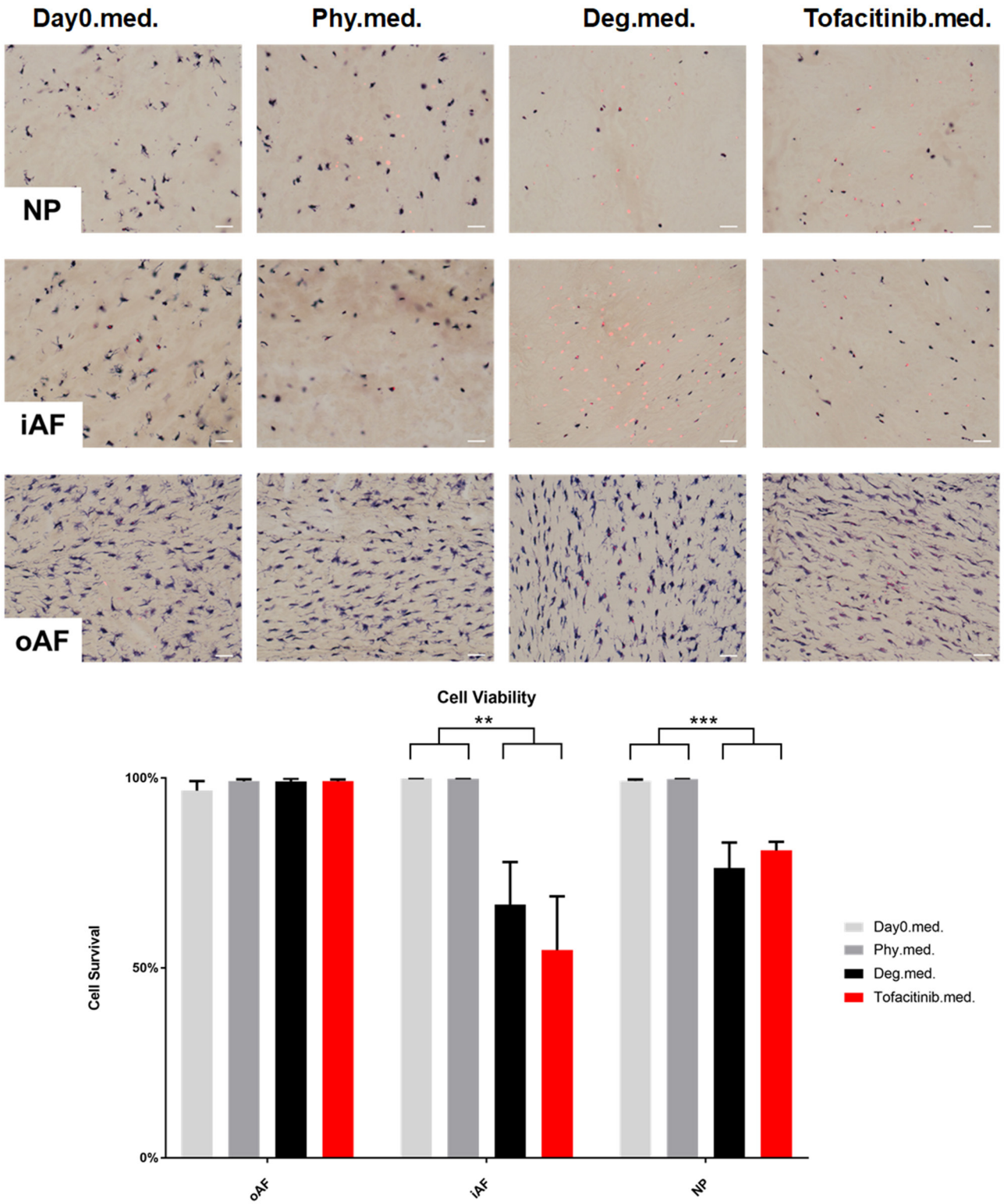

FIGURE 14 | Cell viability of IVD tissue from the Tofacitinib experiments. Representative LDH/ EthD-1 staining image of NP region, inner AF region (iAF) and outer AF (oAF) region from day 0 control samples (Day0.med.), IVDs cultured under physiological condition on day 4 (Phy.med.), IVDs cultured under degenerative condition on day 4 (Deg.med.), and IVDs cultured under degenerative condition and treated with Tofacitinib on day 4 (Etanercept.med.). Scale bar: 50 μm. The percentage of alive cells were counted, as presented in the bar graph. $n = 8$, Means + SEM, $^{**}p < 0.01$, $^{***}p < 0.001$.

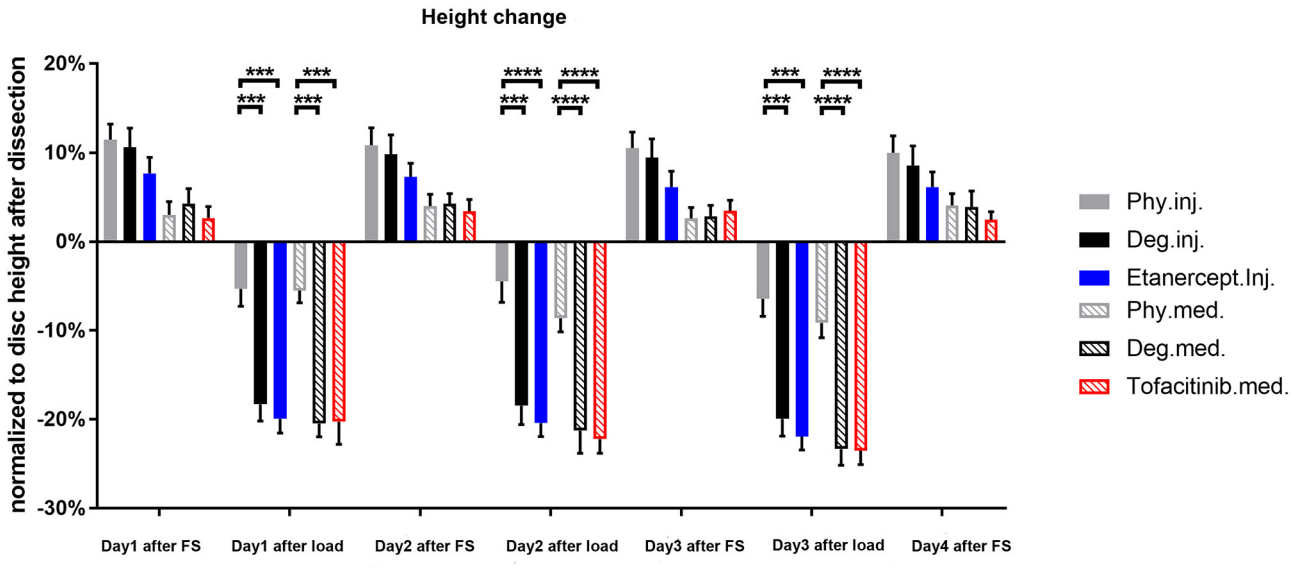

FIGURE 15 | Disc height change normalized to the original dimension after dissection. $n = 8$, means ± SEM, ***$p < 0.001$, ****$p < 0.0001$, FS, Free swelling.

Outcome indicates that a short-term application of degenerative loading increased temporary disc height loss of bovine IVDs. However, the disc height recovery capacity after free swelling did not differ between the groups, which is consistent to our previous study (Lang et al., 2018). Degenerative loading combined with TNF-α injection significantly decreased cell viability in the NP and inner AF tissue compared to the physiological and Day0 control groups.

In summary, the combination of detrimental dynamic loading, nutrient deficiency, and intradiscal TNF-α injection is able to simulate the proinflammatory and degenerative condition operative in IDD, highlighting the potential of our whole IVD organ culture model to efficiently screen and explore novel anti-inflammatory agents or regenerative therapies.

Etanercept and Tofacitinib Reduce Proinflammatory Activity in IDD

As far as we know, this is the first study evaluating anti-inflammatory effects of Etanercept and Tofacitinib within a proinflammatory and degenerative microenvironment of a whole organ IVD culture model. Both, Etanercept and Tofacitinib partially prevented the upregulation of proinflammatory cytokines in IVDs cultured under IDD-like conditions which supports outcome of previous *in vitro* studies on TNF-α inhibition (Likhitpanichkul et al., 2015; Walter et al., 2015b; Evashwick-Rogler et al., 2018). Moreover, our data confirms the concept of recent work investigating a potential involvement of the IL-6/JAK/STAT3 pathway in IDD (Suzuki et al., 2017). Pharmacological inhibition of JAK3 activity with CP690550 significantly suppressed the IL-6-mediated gene expression in human AF cells. Increased expression levels of IL-6 are associated with active discopathy (Kang et al., 1995; Watts et al., 1996; Pedersen et al., 2015). Milici et al. performed a rodent *in vivo* study to evaluate whether selective JAK3 inhibition can preserve cartilage in RA. Outcome revealed a dose dependent reduction of clinical and histological signs of joint inflammation following JAK-inhibition (Milici et al., 2008).

On protein level, Etanercept and Tofacitinib did not alter IL-8 protein release. Etanercept partially diminished the elevated release of proinflammatory mediator NO compared to IVDs cultured within a degenerative and proinflammatory microenvironment, while Tofacitinib did not. In summary, these results indicate a superior protective anti-inflammatory effect of Etanercept in the tested conditions compared with Tofacitinib. Within the IVD tissue, a region dependent anti-inflammatory effect of both drugs was observed, where Etanercept reduced the percentage of IL-1β positively stained cells in the oAF region, while Tofacitinib reduced the percentage of IL-1β and IL-8 positively stained cells in the iAF region.

Etanercept Shows a "Pain" Alleviation Effect

Intradiscal administration of Etanercept has shown to relieve pain at 4-weeks after injection in discogenic low back pain patients (Sainoh et al., 2016). In the current study, Etanercept reduced the expression of NGF in the AF tissue. Previous research by Kivitz et al. (2013) and Katz et al. (2011) investigated whether Tanezumab, a monoclonal antibody that specifically inhibits NGF, relieves chronic pain in a randomized controlled trial against naproxen and placebo. The authors concluded that Tanezumab provides greater improvement in pain, function, and global scores vs. placebo and naproxen in patients with chronic low back pain. These results indicate that Etanercept may alleviate discogenic pain by inhibition of NGF expression.

Etanercept and Tofacitinib Partially Diminish Matrix Catabolism in IDD

Etanercept and Tofacitinib prevented the upregulation of MMP1 and MMP3 catabolic gene expression in the NP tissue. In addition, both drugs reduced the GAG loss to the level under physiological culture condition. These results indicate that both drugs could prevent matrix degradation and slow down the catabolic pathology in disc degeneration. They are also consistent with previous research, where Tofacitinib was shown to reduce degenerative effects of proinflammatory cytokines in rat AF cells (Suzuki et al., 2017). IVD degeneration starts with GAG loss and fibrosis in the tissue. Therefore, these drugs which showed an inhibition effect on GAG loss under the degenerative condition are of important potential for clinical translation, to slow down the IVD degeneration process after traumatic injury.

Both biologicals tested in the present study are FDA approved drugs for the treatment of chronic inflammatory diseases such as RA, Psoriasis, and ulcerative colitis. These drugs have been implemented in daily clinical use with limited clinical side effects (Genevay et al., 2009; Fleischmann et al., 2012). Furthermore, Etanercept was proved successful in alleviating symptoms in patients with disabling discogenic or radicular LBP (Genevay et al., 2004, 2012; Cohen et al., 2009; Okoro et al., 2010; Ohtori et al., 2012; Freeman et al., 2013; Sainoh et al., 2016).

Strengths and Limitations

In contrast to previous models, the present organ culture system comprises a 3D IVD microenvironment combined with dynamic loading, which is more relevant than cell culture experiments (Ponnappan et al., 2011; Purmessur et al., 2013; Walter et al., 2015a; Krupkova et al., 2016; Teixeira et al., 2016). *In vitro* studies have several limitations when assessing inflammation and IVD homeostasis as the monolayer culture itself induces a dedifferentiation effect on IVD cell phenotype (Kluba et al., 2005). IVDs can be maintained viable under dynamic load in a bioreactor for several weeks while still having intact endplates (Illien-Junger et al., 2010; Li et al., 2015, 2016a, 2017). Here, we offer a relevant and easily modifiable whole organ culture system providing a straightforward and cost-efficient approach to rapidly screen a variety of therapies for IVD regeneration. Furthermore, the present organ culture system reduces the need for unnecessary animal studies and thus perfectly represents the 3R principles "reduce, replace, refine" while still delivering relevant answers on research questions. Probably, the observed changes on gene signaling are "early signs" which may cause alteration on protein expression when performing longer experiments. Hence, the limited effect of the drugs might be due to the short observation time. The current study was designed as a first screening step to investigate if Etanercept and Tofacitinib are able to inhibit or slow down this inflammation at the beginning of the signaling progression, which is the primary requisite for anti-inflammatory therapeutics that show an immediate response. Further analysis of another longer time point is warranted in future studies to evaluate the long-term effect of the drugs. In our experiments, neither Etanercept nor Tofacitinib were capable of maintaining initial cell viability during degenerative culture. Though targeting different signaling molecules, both drugs could partially reduce the detrimental effects. However, combined anti-inflammatory and anabolic treatment may be required to constrain accelerated IVD degeneration while relieving back pain and promoting disc regeneration.

Changes on gene expression level are the first alterations in the onset of degeneration which are later followed by protein and structural changes. The distinctive distribution of cytokines among different disc tissue regions in symptomatic IDD might offer a basis for tissue specific application of novel treatments, which needs further intensified investigation.

In addition, systemic reaction and interaction cannot be investigated in the present organ culture system. Certainly, this system fails to reproduce complex immunologic interactions. However, intradiscal injection of Etanercept in patients already demonstrated beneficial effects which were partially reproducible in our bioreactor system (Tellegen et al., 2018).

CONCLUSIONS

The combination of detrimental dynamic loading, nutrient deficiency and intradiscal TNF-α injection could simulate the proinflammatory and degenerative condition operative in active discopathy, highlighting the potential of our whole IVD organ culture model to efficiently screen and explore novel anti-inflammatory agents or regenerative therapies. In addition, Etanercept and Tofacitinib revealed their capability to slow down the degenerative cascade and neutralize the proinflammatory microenvironment in our early onset organ culture model. Combined anti-inflammatory and anabolic treatment may be required to constrain accelerated IVD degeneration while relieving back pain and promoting disc regeneration.

DATA AVAILABILITY STATEMENT

Datasets are available on request. The raw data supporting the conclusions of this article will be made available by the authors, without undue reservation, to any qualified researcher.

AUTHOR CONTRIBUTIONS

ZL: substantial contributions to study design, acquisition, analysis, interpretation of data, drafting the paper, revising it critically, and final approval. YG and FH: substantial contributions to acquisition of data, analysis, interpretation of data, revising the article critically, and final approval. DK, NS, KI, EK, RR, and MA: substantial contributions to study design, revising the article critically, and final approval. SG: substantial contributions to study design, interpretation of data, revising the article critically, and final approval. GL: substantial contributions to study design, interpretation of data, drafting the article, revising it critically, final approval, and takes responsibility for the integrity of the work as a whole, from inception to finished article.

FUNDING

This study was funded by the Foundation for the Promotion of Alternate and Complementary Methods to Reduce Animal

Testing (SET) under the project InflamoDisc [number 59], AO Foundation, and AO Spine International. GL was supported by the Berta-Ottenstein-Programme for Advanced Clinician Scientists, Faculty of Medicine, University of Freiburg. The article processing charge was funded by the Baden-Württemberg Ministry of Science, Research and Art and the University of Freiburg in the funding programme Open Access Publishing.

ACKNOWLEDGMENTS

We would like to acknowledge Nora Goudsouzian and Robert Peter (AO Research Institute Davos, Davos, Switzerland) for technical support. The collagen type II antibody was obtained from the Developmental Studies Hybridoma Bank, developed under the auspices of the NICHD and maintained by the University of Iowa, Department of Biology, Iowa City, IA, USA.

SUPPLEMENTARY MATERIAL

The Supplementary Material for this article can be found online at: https://www.frontiersin.org/articles/10.3389/fbioe.2020.00583/full#supplementary-material

Supplementary Figure 1 | Gene expression levels of NP tissue in Tofacitinib dose response experiment. Gene expression levels of NP tissue after 4 days of culture under Deg culture condition, with 250 ng/mL or 2.5 μg/mL Tofacitinib application into the medium, normalized to Phy group. $n = 2$. NP, Nucleus pulposus; IL, Interleukin; COX-2, Cyclooxygenase-2.

REFERENCES

Abe, Y., Akeda, K., An, H. S., Aoki, Y., Pichika, R., Muehleman, C., et al. (2007). Proinflammatory cytokines stimulate the expression of nerve growth factor by human intervertebral disc cells. *Spine* 32, 635–642. doi: 10.1097/01.brs.0000257556.90850.53

Andrade, P., Hoogland, G., Teernstra, O. P., van Aalst, J., van Maren, E., Daemen, M. A., et al. (2016). Elevated levels of tumor necrosis factor-alpha and TNFR1 in recurrent herniated lumbar discs correlate with chronicity of postoperative sciatic pain. *Spine J.* 16, 243–251. doi: 10.1016/j.spinee.2015.10.038

Autio, R. A., Karppinen, J., Niinimaki, J., Ojala, R., Veeger, N., Korhonen, T., et al. (2006). The effect of infliximab, a monoclonal antibody against TNF-alpha, on disc herniation resorption: a randomized controlled study. *Spine* 31, 2641–2645. doi: 10.1097/01.brs.0000244616.64962.9e

Bachmeier, B. E., Nerlich, A. G., Weiler, C., Paesold, G., Jochum, M., and Boos, N. (2007). Analysis of tissue distribution of TNF-alpha, TNF-alpha-receptors, and the activating TNF-alpha-converting enzyme suggests activation of the TNF-alpha system in the aging intervertebral disc. *Ann. N.Y. Acad. Sci.* 1096, 44–54. doi: 10.1196/annals.1397.069

Baptista, J. S., Traynelis, V. C., Liberti, E. A., and Fontes, R. B. V. (2020). Expression of degenerative markers in intervertebral discs of young and elderly asymptomatic individuals. *PLoS ONE* 15:e0228155. doi: 10.1371/journal.pone.0228155

Battie, M. C., Joshi, A. B., and Gibbons, L. E. (2019). Degenerative disc disease: what is in a name? *Spine* 44, 1523–1529. doi: 10.1097/BRS.0000000000003103

Bergknut, N., Rutges, J. P., Kranenburg, H. J., Smolders, L. A., Hagman, R., Smidt, H. J., et al. (2012). The dog as an animal model for intervertebral disc degeneration? *Spine* 37, 351–358. doi: 10.1097/BRS.0b013e31821e5665

Buchbinder, R., van Tulder, M., Oberg, B., Costa, L. M., Woolf, A., Schoene, M., et al. (2018). Low back pain: a call for action. *Lancet* 391, 2384–2388. doi: 10.1016/S0140-6736(18)30488-4

Caliskan, T., Sirin, D. Y., Karaarslan, N., Yilmaz, I., Ozbek, H., Akyuva, Y., et al. (2019). Effects of etanercept, a tumor necrosis factor receptor fusion protein, on primary cell cultures prepared from intact human intervertebral disc tissue. *Exp. Ther. Med.* 18, 69–76. doi: 10.3892/etm.2019.7559

Caprez, S., Menzel, U., Li, Z., Grad, S., Alini, M., and Peroglio, M. (2018). Isolation of high-quality RNA from intervertebral disc tissue via pronase predigestion and tissue pulverization. *JOR Spine* 1:e1017. doi: 10.1002/jsp2.1017

Clark, S., and Horton, R. (2018). Low back pain: a major global challenge. *Lancet* 391:2302. doi: 10.1016/S0140-6736(18)30725-6

Cohen, S. P., Bogduk, N., Dragovich, A., Buckenmaier, C. C. 3rd, Griffith, S., Kurihara, C., et al. (2009). Randomized, double-blind, placebo-controlled, dose-response, and preclinical safety study of transforaminal epidural etanercept for the treatment of sciatica. *Anesthesiology* 110, 1116–1126. doi: 10.1097/ALN.0b013e3181a05aa0

Cooper, R. G., and Freemont, A. J. (2004). TNF-alpha blockade for herniated intervertebral disc-induced sciatica: a way forward at last? *Rheumatology* 43, 119–121. doi: 10.1093/rheumatology/keh013

Evashwick-Rogler, T. W., Lai, A., Watanabe, H., Salandra, J. M., Winkelstein, B. A., Cho, S. K., et al. (2018). Inhibiting tumor necrosis factor-alpha at time of induced intervertebral disc injury limits long-term pain and degeneration in a rat model. *JOR Spine* 1:e1014. doi: 10.1002/jsp2.1014

Farndale, R. W., Buttle, D. J., and Barrett, A. J. (1986). Improved quantitation and discrimination of sulphated glycosaminoglycans by use of dimethylmethylene blue. *Biochim. Biophys. Acta* 883, 173–177. doi: 10.1016/0304-4165(86)90306-5

Fleischmann, R., Kremer, J., Cush, J., Schulze-Koops, H., Connell, C. A., Bradley, J. D., et al. (2012). Placebo-controlled trial of tofacitinib monotherapy in rheumatoid arthritis. *N. Engl. J. Med.* 367, 495–507. doi: 10.1056/NEJMoa1109071

Fleischmann, R., Kremer, J., Tanaka, Y., Gruben, D., Kanik, K., Koncz, T., et al. (2016). Efficacy and safety of tofacitinib in patients with active rheumatoid arthritis: review of key phase 2 studies. *Int. J. Rheum. Dis.* 19, 1216–1225. doi: 10.1111/1756-185X.12901

Freeman, B. J., Ludbrook, G. L., Hall, S., Cousins, M., Mitchell, B., Jaros, M., et al. (2013). Randomized, double-blind, placebo-controlled, trial of transforaminal epidural etanercept for the treatment of symptomatic lumbar disc herniation. *Spine* 38, 1986–1994. doi: 10.1097/01.brs.0000435140.61593.4c

Freemont, A. J. (2009). The cellular pathobiology of the degenerate intervertebral disc and discogenic back pain. *Rheumatology* 48, 5–10. doi: 10.1093/rheumatology/ken396

Freemont, A. J., Peacock, T. E., Goupille, P., Hoyland, J. A., O'Brien, J., and Jayson, M. I. (1997). Nerve ingrowth into diseased intervertebral disc in chronic back pain. *Lancet* 350, 178–181. doi: 10.1016/S0140-6736(97)02135-1

Freemont, A. J., Watkins, A., Le Maitre, C., Baird, P., Jeziorska, M., Knight, M. T., et al. (2002). Nerve growth factor expression and innervation of the painful intervertebral disc. *J. Pathol.* 197, 286–292. doi: 10.1002/path.1108

Fujii, K., Yamazaki, M., Kang, J. D., Risbud, M. V., Cho, S. K., Qureshi, S. A., et al. (2019). Discogenic back pain: literature review of definition, diagnosis, and treatment. *JBMR Plus* 3:e10180. doi: 10.1002/jbm4.10180

Gantenbein, B., Grunhagen, T., Lee, C. R., van Donkelaar, C. C., Alini, M., and Ito, K. (2006). An *in vitro* organ culturing system for intervertebral disc explants with vertebral endplates: a feasibility study with ovine caudal discs. *Spine* 31, 2665–2673. doi: 10.1097/01.brs.0000244620.15386.df

Genevay, S., Finckh, A., Mezin, F., Tessitore, E., and Guerne, P. A. (2009). Influence of cytokine inhibitors on concentration and activity of MMP-1 and MMP-3 in disc herniation. *Arthr. Res. Ther.* 11:R169. doi: 10.1186/ar2858

Genevay, S., Finckh, A., Zufferey, P., Viatte, S., Balague, F., and Gabay, C. (2012). Adalimumab in acute sciatica reduces the long-term need for surgery: a 3-year follow-up of a randomised double-blind placebo-controlled trial. *Ann. Rheum. Dis.* 71, 560–562. doi: 10.1136/annrheumdis-2011-200373

Genevay, S., Stingelin, S., and Gabay, C. (2004). Efficacy of etanercept in the treatment of acute, severe sciatica: a pilot study. *Ann. Rheum. Dis.* 63, 1120–1123. doi: 10.1136/ard.2003.016451

Hoy, D., March, L., Brooks, P., Blyth, F., Woolf, A., Bain, C., et al. (2014). The global burden of low back pain: estimates from the global burden of disease 2010 study. *Ann. Rheum. Dis.* 73, 968–974. doi: 10.1136/annrheumdis-2013-204428

Hoyland, J. A., Le Maitre, C., and Freemont, A. J. (2008). Investigation of the role of IL-1 and TNF in matrix degradation in the intervertebral disc. *Rheumatology* 47, 809–814. doi: 10.1093/rheumatology/ken056

Igarashi, T., Kikuchi, S., Shubayev, V., and Myers, R. R. (2000). 2000 Volvo Award winner in basic science studies: exogenous tumor necrosis factor-alpha mimics nucleus pulposus-induced neuropathology. Molecular, histologic, and behavioral comparisons in rats. *Spine* 25, 2975–2980. doi: 10.1097/00007632-200012010-00003

Illien-Junger, S., Gantenbein-Ritter, B., Grad, S., Lezuo, P., Ferguson, S. J., Alini, M., et al. (2010). The combined effects of limited nutrition and high-frequency loading on intervertebral discs with endplates. *Spine* 35, 1744–1752. doi: 10.1097/BRS.0b013e3181c48019

Inage, K., Orita, S., Yamauchi, K., Suzuki, T., Suzuki, M., Sakuma, Y., et al. (2016). Dose optimization for single intradiscal administration of the tumor necrosis factor-α inhibitor, etanercept, in rat disc injury models. *Asian Spine J.* 10, 619–623. doi: 10.4184/asj.2016.10.4.619

Junger, S., Gantenbein-Ritter, B., Lezuo, P., Alini, M., Ferguson, S. J., and Ito, K. (2009). Effect of limited nutrition on in situ intervertebral disc cells under simulated-physiological loading. *Spine* 34, 1264–1271. doi: 10.1097/BRS.0b013e3181a0193d

Kang, J. D., Georgescu, H. I., McIntyre-Larkin, L., Stefanovic-Racic, M., and Evans, C. H. (1995). Herniated cervical intervertebral discs spontaneously produce matrix metalloproteinases, nitric oxide, interleukin-6, and prostaglandin E2. *Spine* 20, 2373–2378. doi: 10.1097/00007632-199511001-00001

Katz, N., Borenstein, D. G., Birbara, C., Bramson, C., Nemeth, M. A., Smith, M. D., et al. (2011). Efficacy and safety of tanezumab in the treatment of chronic low back pain. *Pain* 152, 2248–2258. doi: 10.1016/j.pain.2011.05.003

Kazezian, Z., Li, Z., Alini, M., Grad, S., and Pandit, A. (2017). Injectable hyaluronic acid down-regulates interferon signaling molecules, IGFBP3 and IFIT3 in the bovine intervertebral disc. *Acta Biomater.* 52, 118–129. doi: 10.1016/j.actbio.2016.12.029

Kivitz, A. J., Gimbel, J. S., Bramson, C., Nemeth, M. A., Keller, D. S., Brown, M. T., et al. (2013). Efficacy and safety of tanezumab versus naproxen in the treatment of chronic low back pain. *Pain* 154, 1009–1021. doi: 10.1016/j.pain.2013.03.006

Kluba, T., Niemeyer, T., Gaissmaier, C., and Grunder, T. (2005). Human anulus fibrosis and nucleus pulposus cells of the intervertebral disc: effect of degeneration and culture system on cell phenotype. *Spine* 30, 2743–2748. doi: 10.1097/01.brs.0000192204.89160.6d

Korhonen, T., Karppinen, J., Malmivaara, A., Autio, R., Niinimaki, J., Paimela, L., et al. (2004). Efficacy of infliximab for disc herniation-induced sciatica: one-year follow-up. *Spine* 29, 2115–2119. doi: 10.1097/01.brs.0000141179.58778.6c

Korhonen, T., Karppinen, J., Paimela, L., Malmivaara, A., Lindgren, K. A., Bowman, C., et al. (2006). The treatment of disc-herniation-induced sciatica with infliximab: one-year follow-up results of FIRST II, a randomized controlled trial. *Spine* 31, 2759–2766. doi: 10.1097/01.brs.0000245873.23876.1e

Krishnaswami, S., Kudlacz, E., Wang, R., and Chan, G. (2011). A supratherapeutic dose of the Janus kinase inhibitor tasocitinib (CP-690,550) does not prolong QTc interval in healthy participants. *J. Clin. Pharmacol.* 51, 1256–1263. doi: 10.1177/0091270010379809

Krupkova, O., Hlavna, M., Amir Tahmasseb, J., Zvick, J., Kunz, D., Ito, K., et al. (2016). An inflammatory nucleus pulposus tissue culture model to test molecular regenerative therapies: validation with epigallocatechin 3-gallate. *Int. J. Mol. Sci.* 17:1640. doi: 10.3390/ijms17101640

Lai, A., Moon, A., Purmessur, D., Skovrlj, B., Winkelstein, B. A., Cho, S. K., et al. (2015). Assessment of functional and behavioral changes sensitive to painful disc degeneration. *J. Orthop. Res.* 33, 755–764. doi: 10.1002/jor.22833

Lang, G., Liu, Y., Geries, J., Zhou, Z., Kubosch, D., Sudkamp, N., et al. (2018). An intervertebral disc whole organ culture system to investigate proinflammatory and degenerative disc disease condition. *J. Tissue Eng. Regen. Med.* 12, e2051–e2061. doi: 10.1002/term.2636

Le Maitre, C. L., Freemont, A. J., and Hoyland, J. A. (2005). The role of interleukin-1 in the pathogenesis of human intervertebral disc degeneration. *Arthr. Res. Ther.* 7, R732–R745. doi: 10.1186/ar1732

Le Maitre, C. L., Hoyland, J. A., and Freemont, A. J. (2007a). Catabolic cytokine expression in degenerate and herniated human intervertebral discs: IL-1beta and TNFalpha expression profile. *Arthr. Res. Ther.* 9:R77. doi: 10.1186/ar2275

Le Maitre, C. L., Hoyland, J. A., and Freemont, A. J. (2007b). Interleukin-1 receptor antagonist delivered directly and by gene therapy inhibits matrix degradation in the intact degenerate human intervertebral disc: an in situ zymographic and gene therapy study. *Arthr. Res. Ther.* 9:R83. doi: 10.1186/ar2282

Li, Z., Kaplan, K. M., Wertzel, A., Peroglio, M., Amit, B., Alini, M., et al. (2014). Biomimetic fibrin-hyaluronan hydrogels for nucleus pulposus regeneration. *Regen. Med.* 9, 309–326. doi: 10.2217/rme.14.5

Li, Z., Lang, G., Chen, X., Sacks, H., Mantzur, C., Tropp, U., et al. (2016a). Polyurethane scaffold with in situ swelling capacity for nucleus pulposus replacement. *Biomaterials* 84, 196–209. doi: 10.1016/j.biomaterials.2016.01.040

Li, Z., Lang, G., Karfeld-Sulzer, L. S., Mader, K. T., Richards, R. G., Weber, F. E., et al. (2017). Heterodimeric BMP-2/7 for nucleus pulposus regeneration-*in vitro* and *ex vivo* studies. *J. Orthop. Res.* 35, 51–60. doi: 10.1002/jor.23351

Li, Z., Lezuo, P., Pattappa, G., Collin, E., Alini, M., Grad, S., et al. (2016b). Development of an *ex vivo* cavity model to study repair strategies in loaded intervertebral discs. *Eur. Spine J.* 25, 2898–2908. doi: 10.1007/s00586-016-4542-0

Li, Z., Peroglio, M., Alini, M., and Grad, S. (2015). Potential and limitations of intervertebral disc endogenous repair. *Curr. Stem. Cell Res. Ther.* 10, 329–338. doi: 10.2174/1574888X10666150305105114

Likhitpanichkul, M., Kim, Y., Torre, O. M., See, E., Kazezian, Z., Pandit, A., et al. (2015). Fibrin-genipin annulus fibrosus sealant as a delivery system for anti-TNFalpha drug. *Spine J.* 15, 2045–2054. doi: 10.1016/j.spinee.2015.04.026

Lopa, S., Ceriani, C., Cecchinato, R., Zagra, L., Moretti, M., and Colombini, A. (2016). Stability of housekeeping genes in human intervertebral disc, endplate and articular cartilage cells in multiple conditions for reliable transcriptional analysis. *Eur. Cell Mater.* 31, 395–406. doi: 10.22203/eCM.v031a25

Lurie, J. D., Tosteson, T. D., Tosteson, A. N., Zhao, W., Morgan, T. S., Abdu, W. A., et al. (2014). Surgical versus nonoperative treatment for lumbar disc herniation: eight-year results for the spine patient outcomes research trial. *Spine* 39, 3–16. doi: 10.1097/BRS.0000000000000088

Milici, A. J., Kudlacz, E. M., Audoly, L., Zwillich, S., and Changelian, P. (2008). Cartilage preservation by inhibition of Janus kinase 3 in two rodent models of rheumatoid arthritis. *Arthr. Res. Ther.* 10:R14. doi: 10.1186/ar2365

Miyagi, M., Ishikawa, T., Kamoda, H., Suzuki, M., Murakami, K., Shibayama, M., et al. (2012). ISSLS prize winner: disc dynamic compression in rats produces long-lasting increases in inflammatory mediators in discs and induces long-lasting nerve injury and regeneration of the afferent fibers innervating discs: a pathomechanism for chronic discogenic low back pain. *Spine* 37, 1810–1818. doi: 10.1097/BRS.0b013e31824ffac6

Miyagi, M., Uchida, K., Takano, S., Fujimaki, H., Aikawa, J., Sekiguchi, H., et al. (2018). Macrophage-derived inflammatory cytokines regulate growth factors and pain-related molecules in mice with intervertebral disc injury. *J. Orthop. Res.* 36, 2274–2279. doi: 10.1002/jor.23888

Mojica-Santiago, J. A., Lang, G. M., Navarro-Ramirez, R., Hussain, I., Härtl, R., and Bonassar, L. J. (2018). Resorbable plating system stabilizes tissue-engineered intervertebral discs implanted *ex vivo* in canine cervical spines. *JOR Spine* 1:e1031. doi: 10.1002/jsp2.1031

Nakawaki, M., Uchida, K., Miyagi, M., Inoue, G., Kawakubo, A., Satoh, M., et al. (2019). Changes in nerve growth factor expression and macrophage phenotype following intervertebral disc injury in mice. *J. Orthop. Res.* 37, 1798–1804. doi: 10.1002/jor.24308

NLM National Center for Biotechnology Information (2020). *Compound Summary Tofacitinib.* Available online at: https://pubchem.ncbi.nlm.nih.gov/compound/Tofacitinib

Ohtori, S., Miyagi, M., Eguchi, Y., Inoue, G., Orita, S., Ochiai, N., et al. (2012). Epidural administration of spinal nerves with the tumor necrosis factor-alpha inhibitor, etanercept, compared with dexamethasone for treatment of sciatica in patients with lumbar spinal stenosis: a prospective randomized study. *Spine* 37, 439–444. doi: 10.1097/BRS.0b013e318238af83

Okoro, T., Tafazal, S. I., Longworth, S., and Sell, P. J. (2010). Tumor necrosis alpha-blocking agent (etanercept): a triple blind randomized controlled trial of its use in treatment of sciatica. *J. Spinal. Disord. Tech.* 23, 74–77. doi: 10.1097/BSD.0b013e31819afdc4

Olmarker, K., and Larsson, K. (1998). Tumor necrosis factor alpha and nucleus-pulposus-induced nerve root injury. *Spine* 23, 2538–2544. doi: 10.1097/00007632-199812010-00008

Olmarker, K., and Rydevik, B. (2001). Selective inhibition of tumor necrosis factor-alpha prevents nucleus pulposus-induced thrombus formation, intraneural edema, and reduction of nerve conduction velocity: possible implications

for future pharmacologic treatment strategies of sciatica. *Spine* 26, 863–869. doi: 10.1097/00007632-200104150-00007

Pedersen, L. M., Schistad, E., Jacobsen, L. M., Roe, C., and Gjerstad, J. (2015). Serum levels of the pro-inflammatory interleukins 6 (IL-6) and−8 (IL-8) in patients with lumbar radicular pain due to disc herniation: a 12-month prospective study. *Brain Behav. Immun.* 46, 132–136. doi: 10.1016/j.bbi.2015.01.008

Pennicooke, B., Hussain, I., Berlin, C., Sloan, S. R., Borde, B., Moriguchi, Y., et al. (2018). Annulus fibrosus repair using high-density collagen gel: an *in vivo* ovine model. *Spine* 43, E208–e215. doi: 10.1097/BRS.0000000000002334

Pimentel, D. C., El Abd, O., Benyamin, R. M., Buehler, A. M., Leite, V. F., Mazloomdoost, D., et al. (2014). Anti-tumor necrosis factor antagonists in the treatment of low back pain and radiculopathy: a systematic review and meta-analysis. *Pain Physician* 17, E27–44.

Pirvu, T., Blanquer, S. B., Benneker, L. M., Grijpma, D. W., Richards, R. G., Alini, M., et al. (2015). A combined biomaterial and cellular approach for annulus fibrosus rupture repair. *Biomaterials* 42, 11–19. doi: 10.1016/j.biomaterials.2014.11.049

Podichetty, V. K. (2007). The aging spine: the role of inflammatory mediators in intervertebral disc degeneration. *Cell Mol. Biol.* 53, 4–18.

Ponnappan, R. K., Markova, D. Z., Antonio, P. J., Murray, H. B., Vaccaro, A. R., Shapiro, I. M., et al. (2011). An organ culture system to model early degenerative changes of the intervertebral disc. *Arthr. Res. Ther.* 13:R171. doi: 10.1186/ar3494

Purmessur, D., Walter, B. A., Roughley, P. J., Laudier, D. M., Hecht, A. C., and Iatridis, J. (2013). A role for TNFalpha in intervertebral disc degeneration: a non-recoverable catabolic shift. *Biochem. Biophys. Res. Commun.* 433, 151–156. doi: 10.1016/j.bbrc.2013.02.034

Pye, S. R., Reid, D. M., Smith, R., Adams, J. E., Nelson, K., Silman, A. J., et al. (2004). Radiographic features of lumbar disc degeneration and self-reported back pain. *J. Rheumatol.* 31, 753–758.

Rannou, F., Revel, M., and Poiraudeau, S. (2003). Is degenerative disk disease genetically determined? *Joint Bone Spine* 70, 3–5. doi: 10.1016/S1297-319X(02)00003-9

Risbud, M. V., and Shapiro, I. M. (2014). Role of cytokines in intervertebral disc degeneration: pain and disc content. *Nat. Rev. Rheumatol.* 10, 44–56. doi: 10.1038/nrrheum.2013.160

Sainoh, T., Orita, S., Miyagi, M., Inoue, G., Kamoda, H., Ishikawa, T., et al. (2016). Single intradiscal administration of the tumor necrosis factor-alpha inhibitor, etanercept, for patients with discogenic low back pain. *Pain Med.* 17, 40–45. doi: 10.1111/pme.12892

Stirling, A., Worthington, T., Rafiq, M., Lambert, P. A., and Elliott, T. S. (2001). Association between sciatica and propionibacterium acnes. *Lancet* 357, 2024–2025. doi: 10.1016/S0140-6736(00)05109-6

Sutovsky, J., Benco, M., Sutovska, M., Kocmalova, M., Pappova, L., Miklusica, J., et al. (2017). Cytokine and chemokine profile changes in patients with lower segment lumbar degenerative spondylolisthesis. *Int. J. Surg.* 43, 163–170. doi: 10.1016/j.ijsu.2017.06.024

Suzuki, S., Fujita, N., Fujii, T., Watanabe, K., Yagi, M., Tsuji, T., et al. (2017). Potential involvement of the IL-6/JAK/STAT3 pathway in the pathogenesis of intervertebral disc degeneration. *Spine* 42, E817–e824. doi: 10.1097/BRS.0000000000001982

Teixeira, G. Q., Boldt, A., Nagl, I., Pereira, C. L., Benz, K., Wilke, H. J., et al. (2016). A Degenerative/proinflammatory intervertebral disc organ culture: an *ex vivo* model for anti-inflammatory drug and cell therapy. *Tissue Eng. Part C Methods* 22, 8–19. doi: 10.1089/ten.tec.2015.0195

Tellegen, A. R., Rudnik-Jansen, I., Beukers, M., Miranda-Bedate, A., Bach, F. C., de Jong, W., et al. (2018). Intradiscal delivery of celecoxib-loaded microspheres restores intervertebral disc integrity in a preclinical canine model. *J. Control Release* 286, 439–450. doi: 10.1016/j.jconrel.2018.08.019

Tian, Y., Yuan, W., Fujita, N., Wang, J., Wang, H., Shapiro, I. M., et al. (2013). Inflammatory cytokines associated with degenerative disc disease control aggrecanase-1 (ADAMTS-4) expression in nucleus pulposus cells through MAPK and NF-kappaB. *Am. J. Pathol.* 182, 2310–2321. doi: 10.1016/j.ajpath.2013.02.037

Tobinick, E., and Davoodifar, S. (2004). Efficacy of etanercept delivered by perispinal administration for chronic back and/or neck disc-related pain: a study of clinical observations in 143 patients. *Curr. Med. Res. Opin.* 20, 1075–1085. doi: 10.1185/030079903125004286

van Vollenhoven, R. F., Fleischmann, R., Cohen, S., Lee, E. B., Garcia Meijide, J. A., Wagner, S., et al. (2012). Tofacitinib or adalimumab versus placebo in rheumatoid arthritis. *N. Engl. J. Med.* 367, 508–519. doi: 10.1056/NEJMoa1112072

Walter, B. A., Likhitpanichkul, M., Illien-Junger, S., Roughley, P. J., Hecht, A. C., and Iatridis, J. C. (2015a). TNFalpha transport induced by dynamic loading alters biomechanics of intact intervertebral discs. *PLoS ONE* 10:e0118358. doi: 10.1371/journal.pone.0118358

Walter, B. A., Purmessur, D., Likhitpanichkul, M., Weinberg, A., Cho, S. K., Qureshi, S. A., et al. (2015b). Inflammatory kinetics and efficacy of anti-inflammatory treatments on human nucleus pulposus cells. *Spine* 40, 955–963. doi: 10.1097/BRS.0000000000000932

Watts, M. E., Arnold, S., and Chaplin, D. J. (1996). Changes in coagulation and permeability properties of human endothelial cells *in vitro* induced by TNF-alpha or 5,6 MeXAA. *Br. J. Cancer Suppl.* 27, S164–167.

Williams, N. H., Lewis, R., Din, N. U., Matar, H. E., Fitzsimmons, D., Phillips, C. J., et al. (2013). A systematic review and meta-analysis of biological treatments targeting tumour necrosis factor alpha for sciatica. *Eur. Spine J.* 22, 1921–1935. doi: 10.1007/s00586-013-2739-z

Zhou, X., Hong, Y., and Zhan, Y. (2020). Karacoline, identified by network pharmacology, reduces degradation of the extracellular matrix in intervertebral disc degeneration via the NF-kappaB signaling pathway. *J. Pharm. Anal.* 10, 13–22. doi: 10.1016/j.jpha.2019.07.002

Conflict of Interest: The authors declare that the research was conducted in the absence of any commercial or financial relationships that could be construed as a potential conflict of interest.

frontiers in Bioengineering and Biotechnology

ORIGINAL RESEARCH
published: 16 June 2020
doi: 10.3389/fbioe.2020.00596

Evaluation of Fibrin-Agarose Tissue-Like Hydrogels Biocompatibility for Tissue Engineering Applications

Fernando Campos[1,2], *Ana Belen Bonhome-Espinosa*[2,3], *Jesús Chato-Astrain*[1,2], *David Sánchez-Porras*[1], *Óscar Darío García-García*[1,2], *Ramón Carmona*[4], *Modesto T. López-López*[2,3], *Miguel Alaminos*[1,2], *Víctor Carriel*[1,2*†] and *Ismael A. Rodriguez*[1,5†]

[1] Department of Histology and Tissue Engineering Group, Faculty of Medicine, University of Granada, Granada, Spain, [2] Instituto de Investigación Biosanitaria ibs.GRANADA, Granada, Spain, [3] Department of Applied Physics, Faculty of Science, University of Granada, Granada, Spain, [4] Department of Cell Biology, Faculty of Sciences, University of Granada, Granada, Spain, [5] Department of Histology, Faculty of Dentistry, National University of Cordoba, Cordoba, Argentina

OPEN ACCESS

Edited by:
Dimitrios I. Zeugolis, National University of Ireland Galway, Ireland

Reviewed by:
Michela Pozzobon, University of Padova, Italy
Wenguo Cui, Shanghai Jiao Tong University, China
John George Hardy, Lancaster University, United Kingdom

***Correspondence:**
Víctor Carriel
vcarriel@ugr.es

†These authors have contributed equally to this work

Specialty section:
This article was submitted to Tissue Engineering and Regenerative Medicine, a section of the journal Frontiers in Bioengineering and Biotechnology

Received: *16 January 2020*
Accepted: *15 May 2020*
Published: *16 June 2020*

Citation:
Campos F, Bonhome-Espinosa AB, Chato-Astrain J, Sánchez-Porras D, García-García ÓD, Carmona R, López-López MT, Alaminos M, Carriel V and Rodriguez IA (2020) Evaluation of Fibrin-Agarose Tissue-Like Hydrogels Biocompatibility for Tissue Engineering Applications. Front. Bioeng. Biotechnol. 8:596. doi: 10.3389/fbioe.2020.00596

Generation of biocompatible and biomimetic tissue-like biomaterials is crucial to ensure the success of engineered substitutes in tissue repair. Natural biomaterials able to mimic the structure and composition of native extracellular matrices typically show better results than synthetic biomaterials. The aim of this study was to perform an *in vivo* time-course biocompatibility analysis of fibrin-agarose tissue-like hydrogels at the histological, imagenological, hematological, and biochemical levels. Tissue-like hydrogels were produced by a controlled biofabrication process allowing the generation of biomechanically and structurally stable hydrogels. The hydrogels were implanted subcutaneously in 25 male Wistar rats and evaluated after 1, 5, 9, and 12 weeks of *in vivo* follow-up. At each period of time, animals were analyzed using magnetic resonance imaging (MRI), hematological analyses, and histology of the local area in which the biomaterials were implanted, along with major vital organs (liver, kidney, spleen, and regional lymph nodes). MRI results showed no local or distal alterations during the whole study period. Hematology and biochemistry showed some fluctuation in blood cells values and in some biochemical markers over the time. However, these parameters were progressively normalized in the framework of the homeostasis process. Histological, histochemical, and ultrastructural analyses showed that implantation of fibrin-agarose scaffolds was followed by a progressive process of cell invasion, synthesis of components of the extracellular matrix (mainly, collagen) and neovascularization. Implanted biomaterials were successfully biodegraded and biointegrated at 12 weeks without any associated histopathological alteration in the implanted zone or distal vital organs. In summary, our *in vivo* study suggests that fibrin-agarose tissue-like hydrogels could have potential clinical usefulness in engineering applications in terms of biosafety and biocompatibility.

Keywords: fibrin-agarose hydrogels, *in vivo* biocompatibility, blood and biochemical profile, histological assessment, biodegradation, tissue engineering

INTRODUCTION

The main objective of tissue engineering (TE) is to generate artificial biological substitutes to repair damaged human tissues and organs. Current tissue engineering protocols use different combinations of three basic components: cells, biocompatible and mechanically stable scaffolds and different bioactive factors to promote cell function and differentiation (Atala, 2012).

Scaffolds are essential tools in TE, since they define the biomechanical properties, physical dimensions, shape, and biological or physicochemical properties of bioengineered tissues (Campos et al., 2018). Among the numerous scaffolds used in TE, hydrogels have great potential due to their excellent biocompatibility due to their high hydration rate, diffusive and exchange properties allowing cell functions and viability (Ahmed et al., 2008; Carriel et al., 2014; Scionti et al., 2014). In this regard, one of the most widely used hydrogels in TE is fibrin, which offers some relevant advantages: low price, good cell-biomaterial interactions, fibrillary, and porous pattern and easy handling (Rosso et al., 2005; Swartz et al., 2005). Furthermore, fibrin hydrogels can be generated from the patient's own plasma and used in therapeutic protocols as an autologous product. Some of the bioartificial organs and tissues generated with fibrin hydrogels are skin (Meana et al., 1998; Helmedag et al., 2015; Keck et al., 2019), cornea (Alaminos et al., 2006), liver (Bruns et al., 2005; Wang and Liu, 2018), cardiovascular structures (Jockenhoevel et al., 2001; Mol et al., 2005; Myu Mai Ja et al., 2018), cartilage (Eyrich et al., 2007a,b; Almeida et al., 2016), and bone (Noori et al., 2017). Fibrin hydrogels have been used also as vehicles for delivering relevant products in wound regeneration (Banerjee et al., 2019). Although fibrin hydrogels have all the advantages indicated above, their biomechanical properties are typically poor as compared to the stiffness, flexibility, resistance, and strength of native tissues. In order to improve the biomechanical properties of fibrin hydrogels for tissue engineering applications, researchers combined this biomaterial with polyurethane (Lee et al., 2005), polycaprolactone-based polyurethane (Eyrich et al., 2007b; Wittmann et al., 2016) and polycaprolactone (Van Lieshout et al., 2006), among other biomaterials, with variable results.

Over the recent years, our group combined fibrin with agarose, a natural polysaccharide widely used in different laboratory applications and tissue engineering protocols (Alaminos et al., 2007). Fibrin-agarose tissue-like hydrogels (FATLH) allowed the successful biofabrication of different biological substitutes with promising *ex vivo* and *in vivo* results (Alaminos et al., 2006, 2007; Carriel et al., 2012, 2013, 2017a, 2019; Campos et al., 2016, 2018; Fernandez-Valades-Gamez et al., 2016; Rodriguez-Arco et al., 2016; Garcia-Martinez et al., 2017; Chato-Astrain et al., 2018). These studies demonstrated that the addition of agarose resulted in a significant improvement of the biomechanical properties as compared to fibrin hydrogels, especially when chemical crosslinkers were used (Campos et al., 2016, 2018). Potential clinical application of fibrin-agarose hydrogels are multiple, and include repair of damaged human organs such as the cornea (Alaminos et al., 2006), skin (Carriel et al., 2012), nerve (Carriel et al., 2013, 2017a; Chato-Astrain et al., 2018), oral mucosa (Garzon et al., 2013; Fernandez-Valades-Gamez et al., 2016), and cartilage (Garcia-Martinez et al., 2017), among others. In fact, our group has recently generated two of these models of bioartificial tissues that were approved as Advanced Therapies Medical Products (ATMP) by the National Medicines Agency in Spain (Agencia Española de Medicamentos y Productos Sanitarios—AEMPS) and are currently being used clinically in patients with and severe skin burns (Egea-Guerrero et al., 2019) and corneal ulcers (Gonzalez-Andrades et al., 2017; Rico-Sanchez et al., 2019). Although FATLH demonstrated very good results in preclinical studies in laboratory animals, a complete *in vivo* characterization of the mechanisms associated to FATLH biocompatibility is still needed.

Therefore, the aim of this study is to perform a time-course *in vivo* evaluation of the effects of FATLH grafted *in vivo* in laboratory animals to determine the stability of the graft over the time and the effect of the implant at the graft site (*in situ* response) and distal organs (liver, kidney, spleen, and lymph nodes). These studies were carried out at the histological (histochemical and ultrastructural) and laboratory levels (hematological and biochemical) as well as with magnetic resonance imaging (MRI).

MATERIALS AND METHODS

A brief description of the experimental plan is sumarized in **Figure 1**.

Generation of Fibrin-Agarose Tissue-Like Hydrogels (FATLH)

Fibrin-agarose tissue-like hydrogels (FATLH) were generated as previously described (Campos et al., 2016, 2018; Carriel et al., 2017a; Chato-Astrain et al., 2018). Briefly, to generate a FATLH with a volume of 10 ml, 7.6 ml of human plasma obtained from healthy blood donors were mixed with 750 μl of Dulbecco's modified Eagle's medium (DMEM) and 150 μl of tranexamic acid used as anti-fibrinolytic agent (Amchafibrin, Fides-Ecofarma, Valencia, Spain). Then, 500 μl of type VII agarose dissolved and melted in PBS to a final concentration of 2% were added to obtain a FATLH whose agarose content was 0.1%. Finally, 1 ml of a 1% $CaCl_2$ solution was added in order to promote the fibrin polymerization reaction and the mixture was carefully mixed and aliquoted in Petri dishes with a diameter of 6 mm (5 ml per dish). This solution was allowed to solidify in a cell incubator at 37°C for 24 h.

Biomechanical Evaluation of FATLH

FATLH were rheologically characterized to determine if these biomaterials are able to fulfill the basic biomechanical requirements of bioartificial tissues. The mechanical properties of FATLH were measured after 24 h of their preparation, with a controlled effort Haake MARS III rheometer (Thermo Fisher Scientific, USA). The measurement geometry used was parallel plates, which consisted of two disc with a diameter of 5 cm, where the surface in contact with the sample had

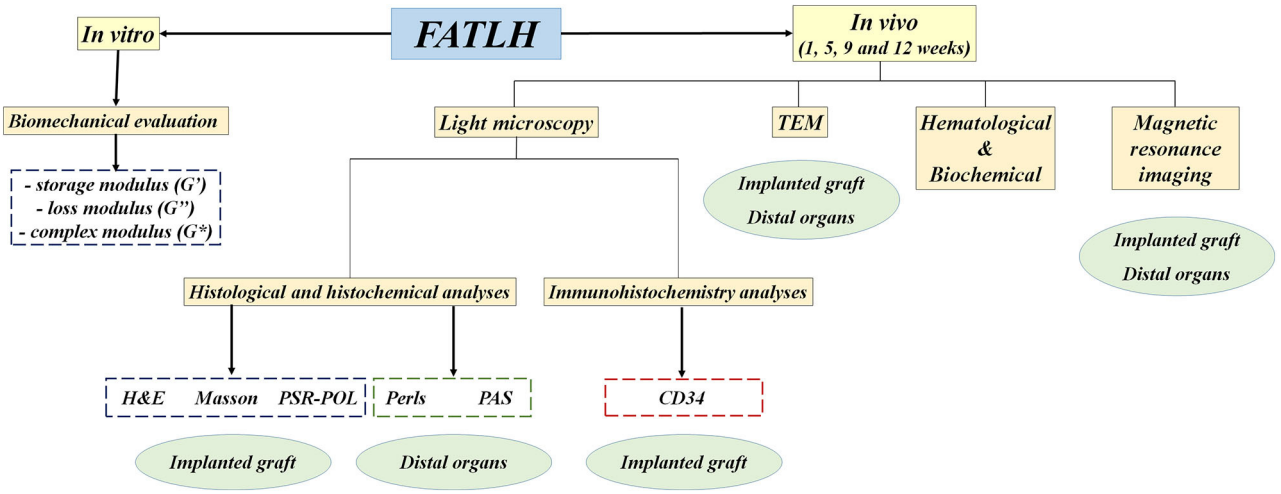

FIGURE 1 | Description of the experimental plan developed in this work. FATLH were generated in the laboratory and analyzed *in vitro* and *in vivo* in laboratory animals as described in the materials and methods section.

roughness to prevent surface sliding. We performed two kinds of oscillatory experiments: amplitude sweeps and frequency sweeps. These measurements were used to calculate the storage modulus (G'), the loss modulus (G''), and the complex modulus (G^*) as a function of shear strain frequency. In all cases, we maintained each frequency–amplitude pair during 5 oscillatory cycles, although we only used data for the last 3 cycles to rule out transients.

Laboratory Animals, Surgical Procedures, and Experimental Groups

For this study, 12-week-old male Wistar rats weighing 250–300 g were used. These animals were maintained in the Experimental Unit of the University Hospital Virgen de las Nieves of Granada (Spain) and housed in a temperature-controlled room ($21 \pm 1°C$) on a 12 h light/dark cycle with *ad libitum* access to tap water and standard rat chow. FATLH disc with 5 mm of diameter were subcutaneously implanted in the forelimb of each animal and evaluated after 1, 5, 9, and 12 weeks of follow-up ($n = 5$ in each time). Five healthy animals were used as controls (CTR) for all the analyses. Animals were euthanized by using anesthesia overdose and an infusion of a euthanasia agent followed by intracardiac perfusion of fixative. Experiments were performed according to the European Union and Spanish Government guidelines for the ethical care of animals (EU Directive No. 63/2010, RD 53/2013). Animal experimentation and the research work were approved by the local ethical committee (ref. 08-07-2019-121, AC17/013-NANOGSKIN).

Histological and Histochemical Analyses

To carry out the *in situ* histological and histochemical evaluations of the grafting area—the subcutaneous tissue containing implanted FATLH—and distal organs, tissue samples from perfused animals were processed and embedded in paraffin as previously described (Carriel et al., 2017b; Chato-Astrain et al., 2018). Histological sections (5 μm thickness) were hydrated and stained with hematoxylin-eosin (H&E) for general histological assessment. Masson trichrome and picrosirius red histochemical methods were used to evaluate the presence and remodeling of the collagen network in each tissue type. These histochemical methods, especially picrosirius staining, are specific for the identification of fibrillar collagen fibers (types I, II, and III) due to the interaction of strong anionic dyes (sirius red F3B and light green) with the cationic groups of the collagen molecules (Kiernan, 2008; Carriel et al., 2011). Both methods are useful tools in diagnostic pathology and tissue engineering research (Wick, 2008; Chato-Astrain et al., 2018; Carriel et al., 2019). Images were taken using a Nikon Eclipse light microscope. At the same time, the Picrosirius Red Polarization Method (PSR-POL) method was used to identify and quantify the specific types of collagen fibers (mature fibers vs. recently synthetized fibers) as previously reported (Drifka et al., 2016; Chato-Astrain et al., 2020). Tissue sections stained with H&E and Masson trichrome were used to quantify the presence of specific cell types within the grafting site and in the grafted biomaterial using a morphological approach. In short, four expert histologists examined each tissue sample (controls and implants grafted for 1, 5, 9, and 12 weeks) and quantified the presence of local connective-tissue cells (i.e., fibroblasts and other cell types), pro-inflammatory cells (neutrophils and lymphocytes), and macrophages in a tissue area corresponding to 0.1 mm^2. For each sample, we quantified 9 tissue areas inside the biomaterial and 9 tissue areas at the host grafting site. Tissue sections stained with H&E were also used to determine the biodegradation rate of the grated biomaterials. For this purpose, low magnification images were obtained from the implant site of each animal, which were analyzed using the Image J software (National Institute of Health, USA). In each case, the thickness of the implanted graft was quantified, and results were shown as percentage of biodegraded biomaterial as compared to the original graft implanted at time 0 used as a reference. A total of 10 measurements were obtained for each experimental group.

To evaluate the liver glycogen content and the basal membrane of renal glomeruli, the periodic acid-Schiff (PAS) histochemical method was used (Kiernan, 2008). To identify the presence of iron (Fe^{+3}) in lymphatic node and spleen histological sections were stained with Perl's histochemical method (Perl's) contrasted with H&E as described previously (Rodriguez-Arco et al., 2016).

Finally, to identify the blood vessels found at the local implant site, we used immunohistochemistry with anti-CD34 primary antibodies (rabbit monoclonal anti-CD34 IgG, Abcam ab81289). Results were quantified to determine the percentage of area corresponding to CD34-positive cells by using the Image J software. Results were normalized using control tissues as a reference.

Transmission Electron Microscopy (TEM)

For TEM, samples were fixed in 2.5% in cacodylate-buffered glutaraldehyde at 4°C for 4 h, rinsed in cacodylate buffer and then postfixed in 1% osmium tetroxide for 90 min. Then, samples were dehydrated and embedded in Epoxy resin (Carriel et al., 2012, 2017a; Chato-Astrain et al., 2018). Ultrathin sections were stained with aqueous uranyl acetate and lead citrate and examined with a transmission electron microscope (EM902; Carl Zeiss Meditec, Inc., Oberkochen, Germany).

Analysis of Hematological and Biochemical Parameters in Blood

For analytical studies, blood samples were collected from each animal ($n = 5$ for each group and period) with 5% heparin to prevent coagulation (Chato-Astrain et al., 2020). The hematological profile was determined by using a Sysmex KX-21N automatic analyzer counter (Florida, USA) and the concentration of hemoglobin (HGB), red blood cells (RBC), hematocrit (HCT), platelets (PLT), white blood cells (WBC), lymphocytes (LYM), neutrophils (NEUT), and monocytes-basophils-eosinophils (MXD) was analyzed. In addition, the biochemical profile was determined in plasma by using a Cobas c311 automatic analyzer (Roche Laboratories, Basel, Switzerland). For biochemical tests, blood was centrifuged at 3,500 rpm during 15 min and afterwards the plasma was collected for the analysis of alanine aminotransferase (ALT), aspartate aminotransferase (AST), total bilirubin (BILT), direct bilirubin (BILD), urea (URE), and creatinine (CRE). All parameters were evaluated by using RTU kits from Roche Laboratories.

Magnetic Resonance Imaging (MRI) Assessment

For MRI, animals were deeply anesthetized with isoflurane, placed in an MRI-compatible cradle, and scanned using a Biospec TM 70/20 USR instrument for laboratory animals (Bruker, Billerica, MA), equipped with 7 Tesla Ultrashield Refrigerated USR magnets. These analyses were performed at the animal facility of the Scientific Instrumentation Center of the University of Granada. First, a general scanning analysis was performed and high resolution axial T2-weighted datasets were acquired for the visualization of the whole animal. Second, we specifically analyzed the site of implantation and physiologically and immunologically important organs, such as satellite lymph nodes close to the grafting site, liver, kidneys and spleen ($n = 3$ in each time).

Statistical Analyses

First, each variable was analyzed using the Shapiro-Wilk test of normality. As all variables resulted to be non-normally distributed, non-parametric tests were used to compare the results obtained among different study groups. To identify statistical differences between two specific groups of samples, the Mann-Whitney *U*-test was used. In the case of the percentage of biodegraded biomaterial, the exact test of Fisher was used, since values were expressed as percentages. All tests were carried out two-tailed using SPSS 16.00 software. Statistical *p*-values below 0.05 were considered as statistically significant.

RESULTS

In vitro Rheological Characterization of FATLH

First, we obtained the viscoelastic moduli as a function of the amplitude of shear strain for a fixed frequency of 1 Hz. As observed in **Figure 2A**, the loss modulus, the storage modulus and the complex modulus showed approximately independent values of the shear strain amplitude at low values of this magnitude, corresponding to the linear viscoelastic region (LVR). As observed, within this region the storage modulus was much larger than the loss modulus (which is typical of crosslinked, gel-like systems) and, consequently, the complex modulus (which is defined as the root square of the sum of the squares of the loss modulus and the storage modulus) coincided approximately with the storage modulus. For larger values of the shear strain amplitude, the loss modulus begun to increase, whereas both the storage modulus and the complex modulus decreased. These changes marked the onset on the non-linear viscoelastic regime, for which the materials suffer irreversible changes at the microscopic level. As shown in **Figure 2**, the loss modulus exhibited a maximum around 0.1 of shear strain amplitude. This maximum is the so-called yield point, and corresponds to the onset of liquid-like flow of the material. Above the yield point, all moduli (loss, storage, and complex moduli) strongly decreased with shear strain amplitude. For larger values of the shear strain amplitude, we found a cross-over of the loss and storage moduli, for a shear strain amplitude value of ∼0.2. Above this value, the loss modulus became progressively larger than the storage modulus, indicating a predominantly liquid-like behavior, due to the strong, irreversible breakage of the internal structure of the material. At the highest values of the shear strain amplitude, the storage modulus was negligible and, consequently, the complex modulus coincided with the loss modulus.

Afterwards, we obtained the dynamic frequency spectrum of the materials, at constant value of the amplitude of the shear strain within the VLR (**Figure 2B**). As observed, all moduli (loss, storage, and complex moduli) showed a tendency to increase with the frequency of shear strain. This tendency was more accentuated for the loss moduli, which was almost negligible at the lowest values of the strain frequency as compared to the

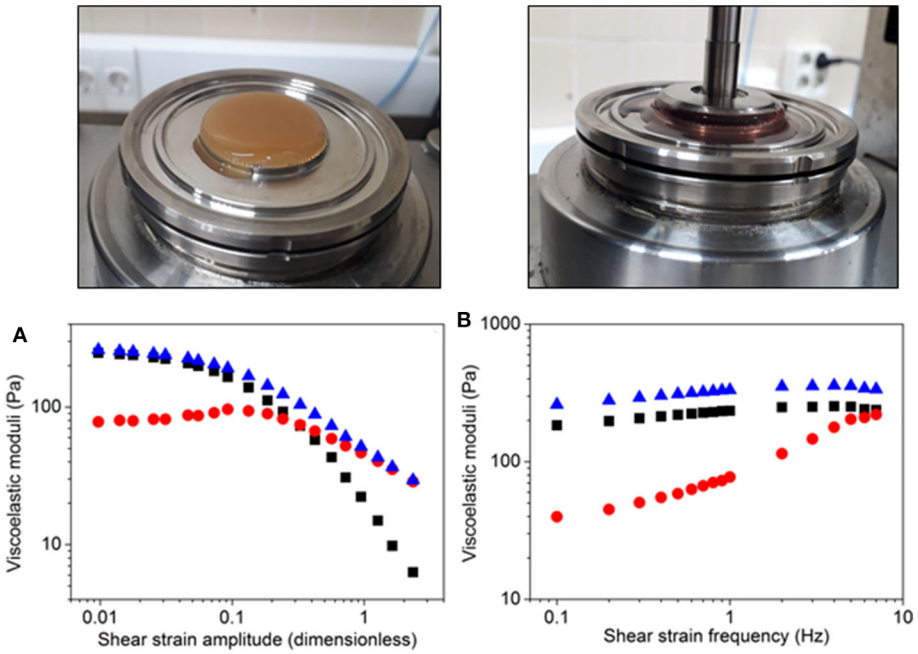

FIGURE 2 | Rheological characterization of FATLH. Representative FATLH images are shown above, before and during the rheological analysis. **(A)** Viscoelastic moduli as a function of shear strain amplitude for imposed oscillatory shear strain of fixed frequency (1 Hz). **(B)** Viscoelastic moduli as a function of shear strain frequency for imposed oscillatory shear strain of fixed amplitude (0.02). Squares (▪) represent the storage modulus, circles (●) the loss modulus, and triangles (▲), the complex modulus.

storage modulus. However, it reached values comparable to these of the storage modulus at the highest frequencies. For the whole range of frequencies under study, the complex modulus appeared as appreciably larger than the storage modulus, as an indication of the relevance of both, storage of energy and loss of energy due to friction forces, under the applied oscillatory shears.

In vivo Histological and Histochemical Analyses

Histological analysis of FATLH grafted subcutaneously showed that the biomaterials tended to integrate with time in the host tissue, and no signs of necrosis, infection, hemorrhage, tumorigenesis, or other pathological processes were detected (**Figure 3A**). In controls and in all the study times, we found that the most abundant cells in the host tissue were the native connective cells, which mainly consisted of fibroblasts, endothelial cells, and other cell types (**Figure 4**). Regarding the pro-inflammatory host cells recruited to the graft site, we found an initial population of neutrophils and lympho-plasmocytic cells in samples corresponding to 1 week of follow-up. In these samples, differences with controls were statistically significant. In contrast, pro-inflammatory cells significantly decreased at 5, 9, and 12 weeks, with non-significant differences with controls at these times and a complete regression of the inflammatory reaction at 12 weeks. For the pro-regenerative cells, we found an abundant macrophage cell population in the area surrounding the implanted hydrogels, which corresponded to ∼20% of the cells in the host tissue at 1, 5, and 9 weeks, and significantly decreased at 12 weeks, when values resembled those of controls. In the grafted biomaterial, we found that the most abundant cell population colonizing the graft were macrophages, especially after 5 and 9 weeks of follow-up. Host cells tended to form a capsule-like structure surrounding the biomaterial, with macrophages progressively driving the hydrogels biodegradation process from the surface inwards (**Figure 4B**).

Regarding the degradation rate of the grafted biomaterial, we found that the percentage of biomaterial that was removed from the implant site was 28.78% at 1 week, 77.62% at 5 weeks, and 90.48% at 9 weeks, with a complete biodegradation of the material at week 12 of the study (**Figure 3B**). Differences from each time of study vs. implanted graft at time 0 were statistically significant. Analysis of the grafted biomaterial revealed that FATLH were progressively colonized by host cells contributing to its biodegradation, mainly macrophages, although some fibroblasts were present especially at the first week (**Figure 4B**).

When the ECM of the host tissue was analyzed, we found an active process of *in situ* synthesis and deposition of fibrillar collagen fibers as determined by Masson and Picrosirius red histochemical staining. As shown in **Figures 4**, **5**, the synthesis of collagen fibers was progressive in the tissue surrounding the graft, resulting in a connective tissue similar to the control in 12-weeks samples. No signs of fibrotic response or other pathological processes were observed. Analysis using the PSR-POL method showed that control tissues were very rich in mature, thick collagen fibers stained in red that are compatible with type-I collagen (Zerbinati and Calligaro, 2018), with very few fibers

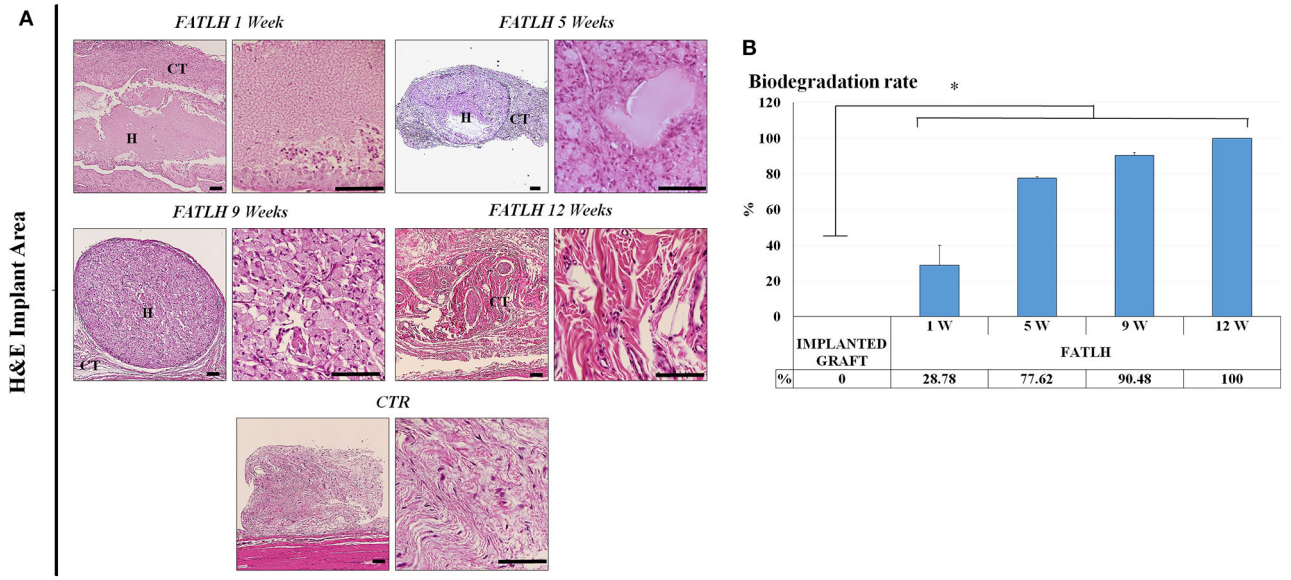

FIGURE 3 | Histological analysis of FATLH grafted *in vivo* using hematoxylin-eosin (H&E). **(A)** Representative images of control samples (CTR) and the implanting site of the experimental groups (FATLH) at different follow-up times. H = grafted FATLH biomaterials; CT = connective tissue. Scale bar = 100 μm. **(B)** Quantification of the percentage of FATLH biodegraded at each study time (1, 5, 9, and 12 weeks). Results are shown as percentage of the implant that were biodegraded regarding the size od the original implanted graft. *Differences between each study time and the original size of the implanted graft were statistically significant.

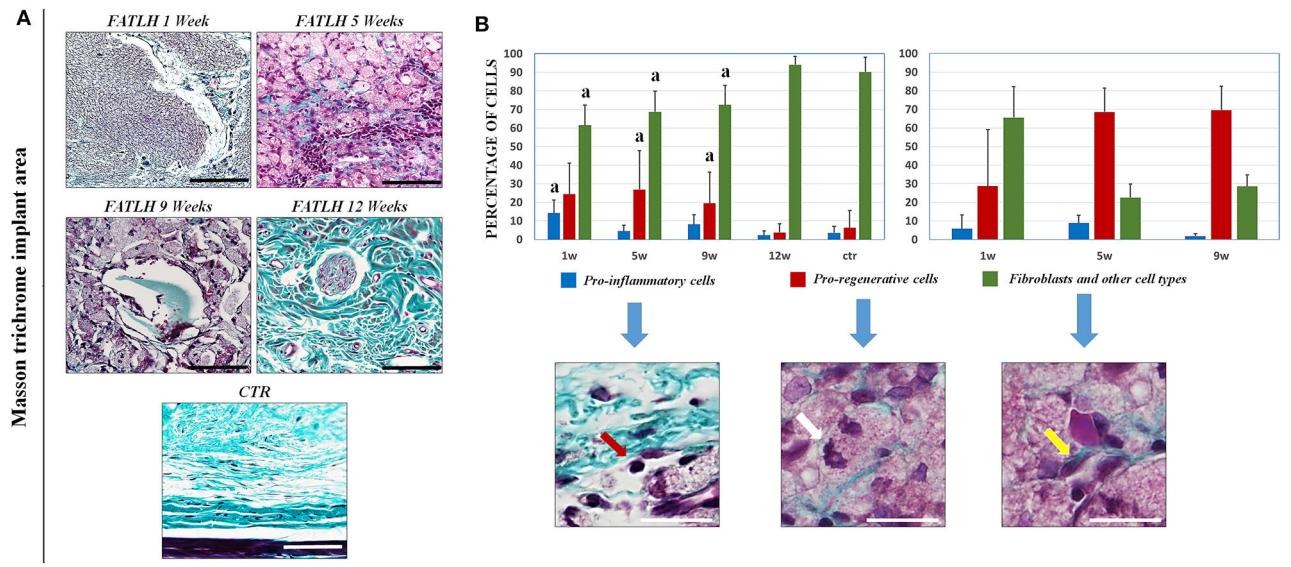

FIGURE 4 | Histochemical analysis of FATLH grafted *in vivo* using the masson trichrome staining. **(A)** Representative images of controls and implanted FATLH at different periods of time. Scale bar = 100 μm. **(B)** Analysis of the types of cells found at the implant site (left panel) and inside the biomaterial (right panel). For the implant site, results are shown at 1, 5, 9, and 12 weeks of follow-up, whereas 1, 5, and 9 weeks samples are shown for cells colonizing the biomaterial, since controls and 12-weeks samples did not contain any grafted material. Results are shown as percentage of each cell type in each histological sample. "a" = significant differences vs. controls. Illustrative examples of each type of cells are shown and labeled with red arrows (pro-inflamatory cells), white arrows (pro-regenerative cells), and fibroblast and other type of cells (yellow arrows). Scale bar = 30 μm.

stained in other colors. As shown in **Figure 5** the amount of collagen synthetized at the graft site at 1, 5, and 9 weeks was lower than control samples, and fibers mostly showed orange, yellow, and green birefringence for the PSR-POL method, which could be considered as recently-synthetized non-type I collagen fibers (Zerbinati and Calligaro, 2018). At 12 weeks, the amount of collagen was higher than other weeks, although lower than controls, and no signs of fibrosis were detected (**Figure 5**). At 12

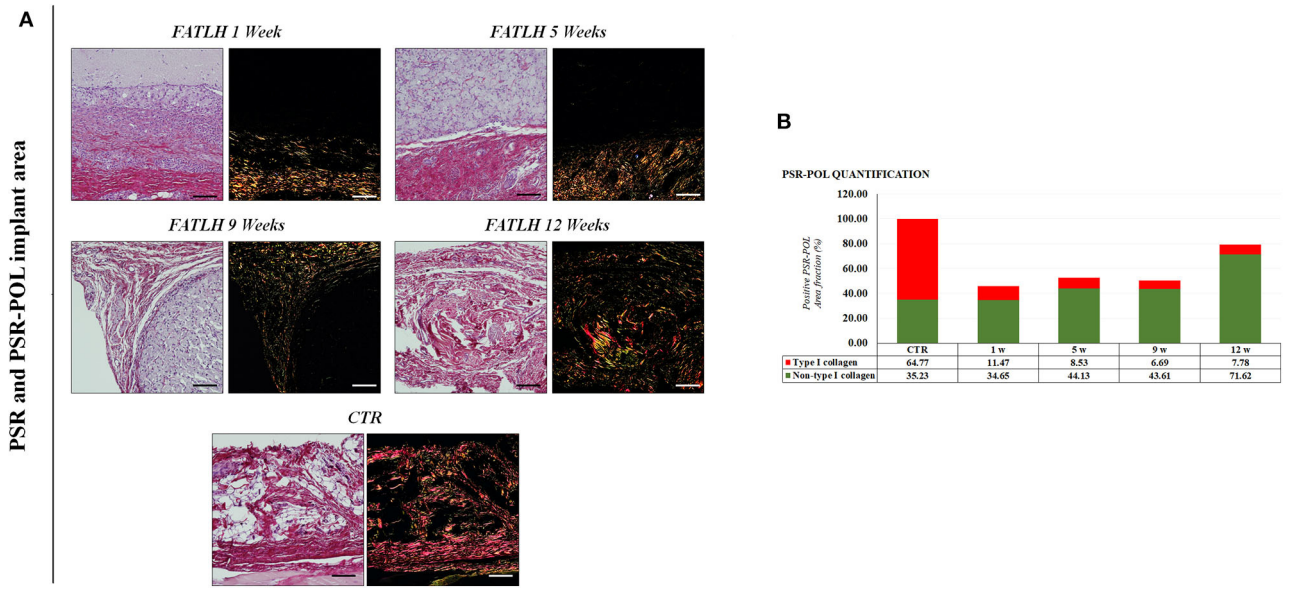

FIGURE 5 | Histochemical analysis of FATLH grafted *in vivo* using Picrosirius red staining method with white and polarized light. **(A)** Analysis of controls and animals grafted with FATLH at different periods of time. Scale bar = 100 μm. **(B)** Quantification of different types of collagen fibrers using the PSR-POL method. For each sample, the total percentage of area occupied by type-I collagen (in red) and other collagen types (in green) is shown. Values are normalized regarding the controls.

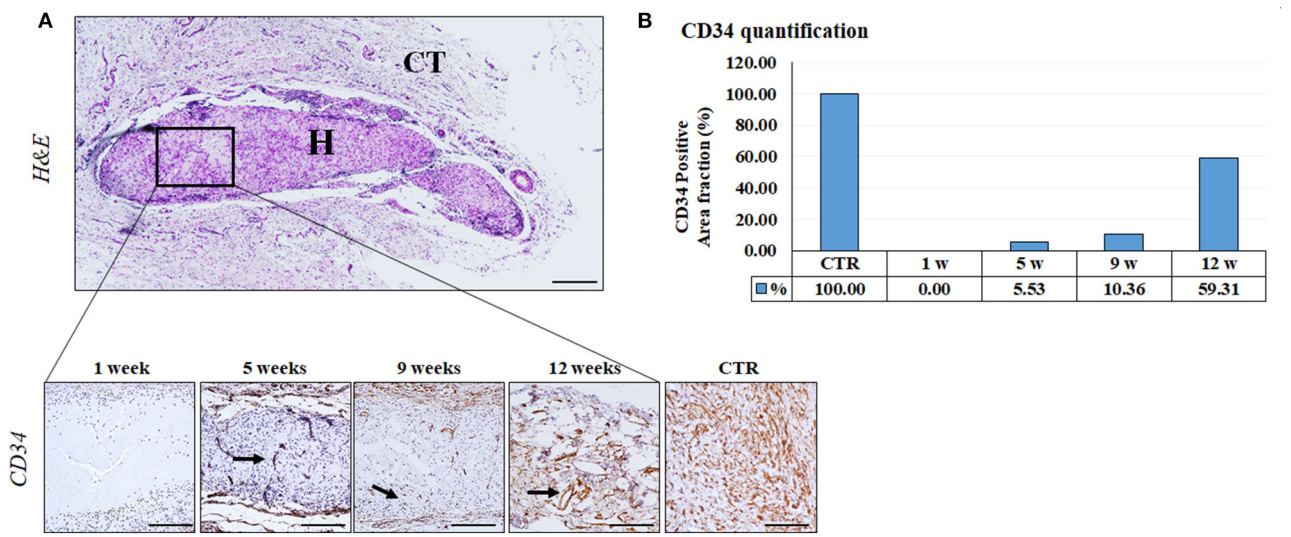

FIGURE 6 | CD34 Immunohistochemical analysis of implanted FATLH over the time. **(A)** Low magnification section of the grafted biomaterial stained with H&E (top panel). H: FATLH, CT: surrounding connective tissue. Lower panel: Positive immunohistochemical reaction for CD34 (black arrows). Scale bar = 200 μm (H&E) and 100 μm (CD34). **(B)** Percentage of tissue surface occupied by CD34- positive blood vessels, normalized regarding the controls.

weeks, most of the fibers were orange, yellow, and green, as in previous study times.

Furthermore, the immunohistochemical analysis and quantification of CD34 positive confirmed an active and progressive process of neovascularization inside the biomaterial, and newly-formed blood vessels were clearly identified within the grafted biomaterial from 5 weeks onwards (**Figure 6**). As shown in **Figure 6B**, the percentage of tissue occupied by blood vessels tended to increase with time.

The histological and histochemical analysis of the axillar regional lymph nodes did not revealed any pathologic signs of activation, edema or lymphadenopathy (**Figure 7**). Similarly, the histological evaluation of the spleen, liver, and kidney revealed a normal histological pattern and histochemical properties during the whole study as compare to the control (**Figure 7**).

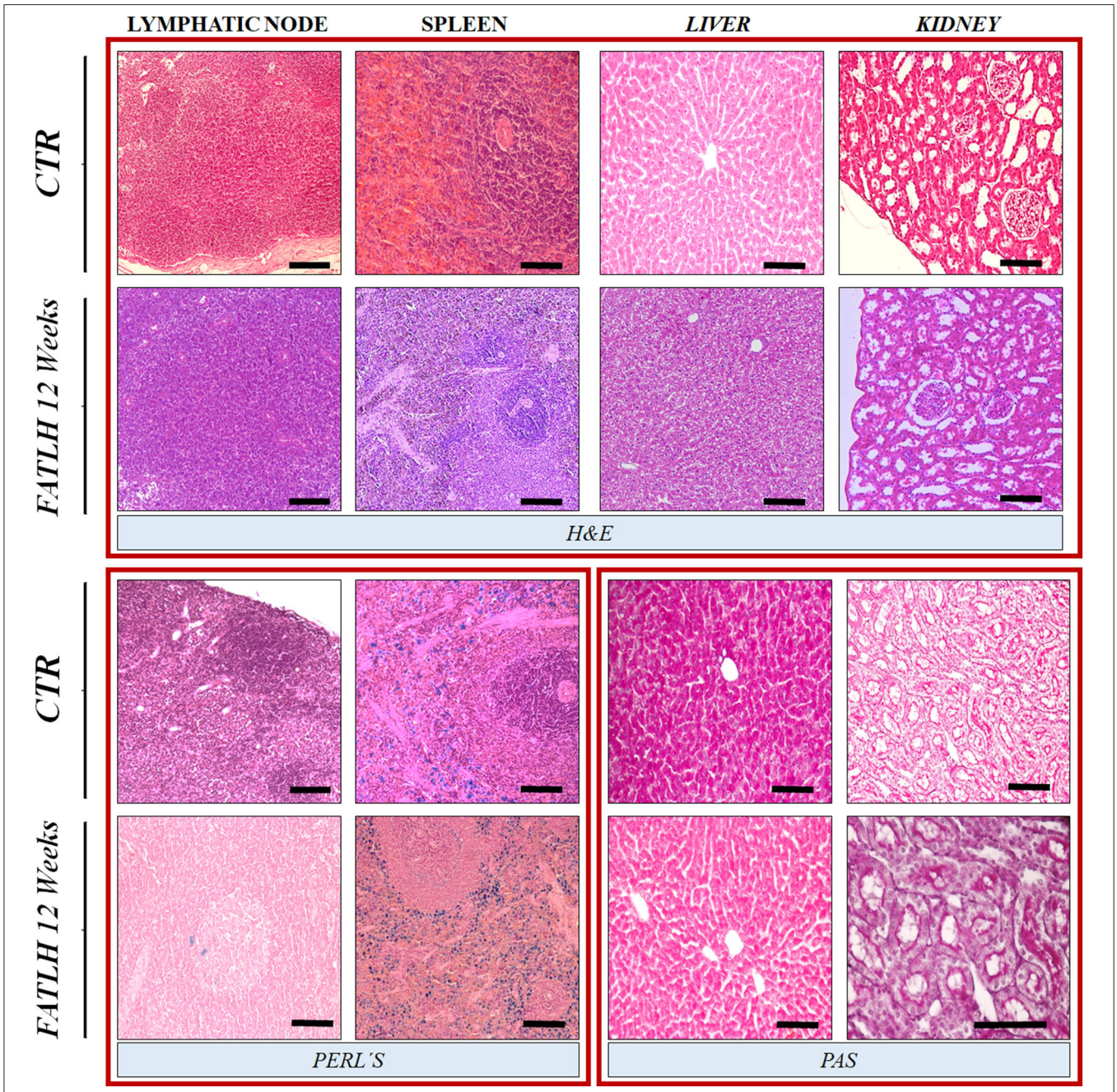

FIGURE 7 | Histological and histochemical analyses of vital organs in controls and FATLH groups at 12 weeks. Representative images of the host lymphatic node, spleen, liver, and kidney are shown using hematoxylin-eosin staining (H&E), Perl's histochemical method (Perl's) and periodic acid of Schiff (PAS) staining. Scale bar = 100 μm.

Ultrastructural Evaluation

Ultrastructural analyses were performed at the implantation site and distal organs. *In situ* analysis of the implantation site confirmed the presence of inflammatory cells, such as plasmocytes and lymphocytes, during the first week. In addition, a progressive decrease of these cells occurred over the time, and it was accompanied by an increase of macrophages tended at the grafting site. These macrophages showed clear signs of phagocytosis of the implanted FATLH until its complete biodegradation, which occurred between the ninth and twelfth week. Host fibroblasts also participated in tissue remodeling of the implanted area by generating collagen and elastic fibers that tended to surround the biomaterial. Interestingly, ultrastructural analysis revealed the presence of

some fibroblasts with signs of phagocytosis within the grafted hydrogels (**Figure 8**).

The ultrastructural analysis of the vital organs did not reveal any modification of the normal histological pattern and/or cellular structure (such as the presence of inflammatory reaction, fibrosis, edema, cell necrosis, or dysfunction, etc.) confirming the results observed by the histological and histochemical assessment described above. In fact, normal cell components were observed in lymph nodes (mainly, lymphocytes), spleen (abundant cells and blood vessels), liver (hepatocytes containing glycogen), and kidney (normal ultrastructural organization of the ductal epithelial cells and the glomerular filtration barrier). Representative images are shown in **Figure 8**.

Laboratory Testing and MRI

In general, blood determinations in animals grafted with the FATLH showed some slight variations followed by a clear normalization of the evaluated parameters over time (**Figure 9A**). In this sense, grafted animals showed a significant reduction of the RBC count and HCT values after 1 week with respect to the CTR ($p < 0.005$). However, both parameters displayed a slightly increase and normalization at 5 and 12 weeks while the HGB concentration remained within the physiological range during the whole study ($p > 0.05$). Concerning the PLT values, they were higher than in the CTR group, but differences were statistically significant only in 5 weeks animals. In relation to the profile of the leukocytes, the WBC values in operated animals were comparable to the CTR group ($p > 0.05$), although an increase was observed at 12 weeks. When leukocytes were evaluated separately, we observed a significant decrease in the percentage of lymphocytes (LYM) after 1 week with respect to CTR ($p = 0.02$) and these values were normalized over time. Interestingly, the MXD (monocytes, eosinophils, and basophils) values showed a significant increase after 1 week ($p = 0.02$) as compared to the CTR group, but these values were clearly normalized at 5 and 12 weeks ($p > 0.05$). Finally, the neutrophils (NEUT) showed some slight variations over time, but these differences were not statistically significant ($p > 0.05$) as compared to the CTR group (**Figure 9A**).

On the other hand, the biochemical analyses carried out on the plasma of each animal showed a significant increase of the AST transaminase values after 1, 5, and 12 weeks ($p < 0.05$), while the rest of the parameters evaluated resulted comparable to the values observed in the CTR group ($p > 0.05$). Specifically, we found virtually no variations in the liver parameters ALT, total, and direct bilirubin (BILT and BILD, respectively) nor in the kidney markers creatinine (CRE) and urea (URE), as compared to control animals (**Figure 9A**).

The images obtained by MRI analysis of the grafting site and distal organs suggest that all analyzed tissues and organs were morphologically normal, and no alterations were detected using this method (**Figure 9B**). At the implantation site, no signs of inflammatory response, hemorrhage, edema, or local affection of the surrounding connective tissues and muscles were observed. When distal organs were evaluated (lungs, satellite nodes, pericardium and heart in thorax and digestive tract, spleen, kidneys, liver, pancreas, and mesentery in abdomen), we did not observe any sign of inflammatory process, presence of interstitial liquids, or fibrotic response. Indeed, the anatomical structure and dimensions of the thoracic and abdominal organs were found within the normal physiological parameters just like the CTR group (**Figure 9B**).

DISCUSSION

FATLH are gaining interest as scaffolds for the generation of human bioartificial tissues for the clinical treatment of patients with severe tissue damage (Gonzalez-Andrades et al., 2017; Egea-Guerrero et al., 2019). In previous studies, we evaluated the local tissue response after grafting several types of bioartificial tissues generated by tissue engineering containing different cell types and fibrin-agarose biomaterials, including, among others, the oral mucosa, skin, sclera, peripheral nerve, and palate (Carriel et al., 2012; Fernandez-Valades-Gamez et al., 2016; Garcia-Martinez et al., 2017; Chato-Astrain et al., 2018). Although these studies demonstrated the high biocompatibility and regenerative properties of FATLH (Carriel et al., 2019), a time-course biodegradation analysis and the impact of the implantation of these biomaterials on the structure and function of distal organs, as well as the global blood profile have not yet been determined. In the present study, we investigated the local effects of FATLH implanted in laboratory animals, along with the long-term potential impact on distal organs in order to assess and characterize the local and systemic effects of the *in vivo* implantation of FATLH.

First, our biomechanical analyses allowed us to confirm that the biomechanical behavior of FATLH was compatible with a clinical use. Firstly, the FATLH biomaterials of the present work exhibited values of the mechanical moduli within the VLR of about 200 Pa for the storage and complex modulus, and 80 Pa for the loss modulus. These values are similar to those reported in the literature for native tissues (Scionti et al., 2014), where values for several tissues were reviewed. For example, for native cornea and oral mucosa values in the range 40–100 Pa for the storage modulus and 5–40 Pa for the loss modulus were reported. Slightly higher values, in the range 400–2,000 Pa for the storage modulus and 100–600 Pa for the loss modulus, were reported for brain tissue and liver. Secondly, with respect to the tendencies of the viscoelastic moduli to increase with the frequency of the oscillatory shear strain, it should be noted that (Chan and Titze, 1999) reported similar trends for the storage modulus and the damping factor of native oral mucosa for the same range of frequencies of the present work. It should be noted that even though the loss modulus and the damping factor are different quantities, they both are related to the energy loss associated to the viscous response of a material, and therefore can be safely compared. From the point of view of materials science, the biomechanical behavior of FATLH represent a typical initial elastic behavior, followed by an irreversible alteration of the inner

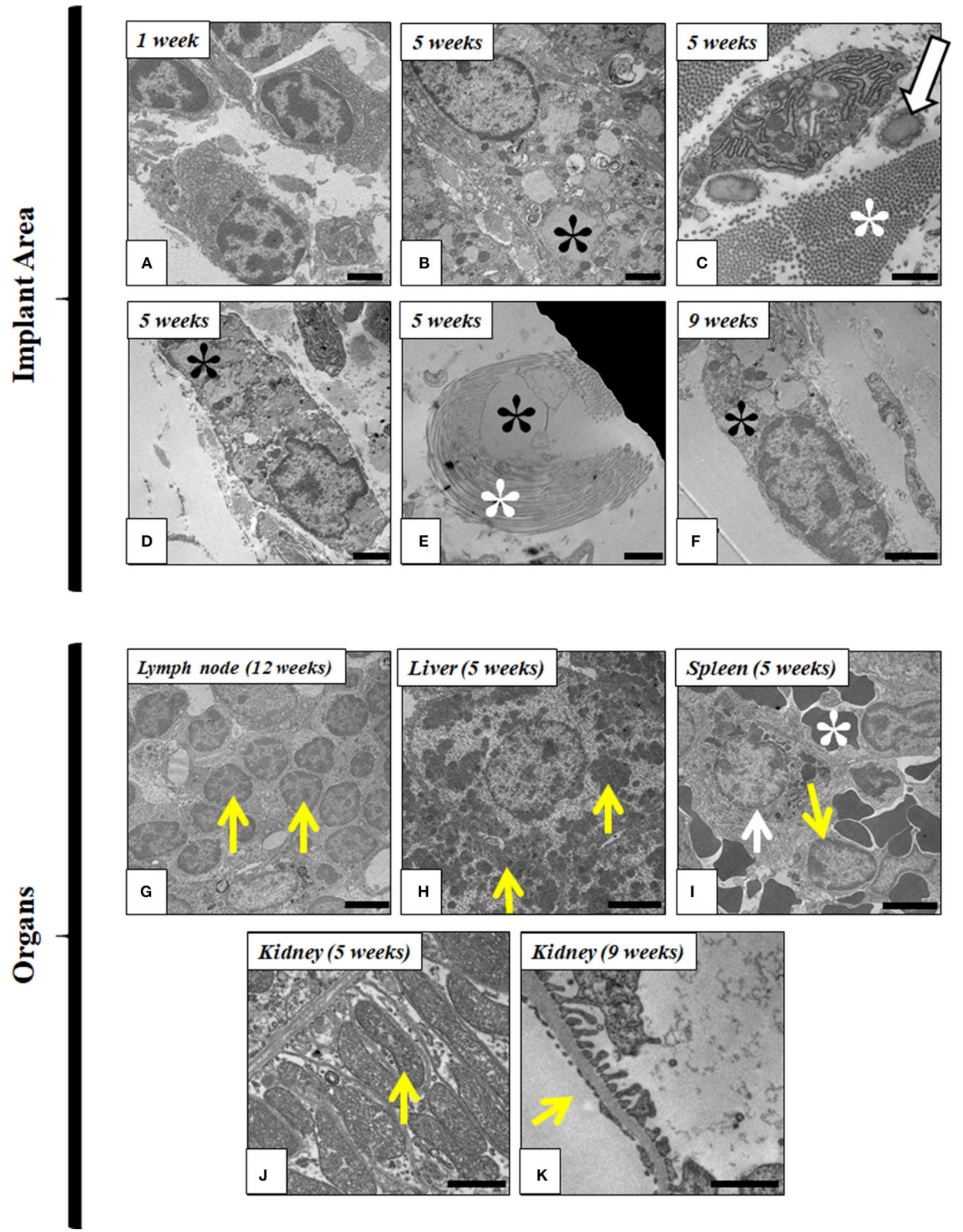

FIGURE 8 | Ultrastructural analysis of FATLH implanted in laboratory animals. Representative images of the local implant site are shown in **(A–F)**, while distal organs are shown in **(G–K)**. **(A)** Plasmocyte cells at the implant site (1 week); Scale bar = 2 μm. **(B)** Macrophage phagocytizing fibrin-agarose (black asterisk*) (5 weeks);

(Continued)

FIGURE 8 | Scale bar = 2 μm; **(C)** Fibroblast cell immersed in a rich extracellular matrix containing collagen (white asterisk*) and elastic fibers (arrow) (5 weeks); Scale bar = 1 μm. **(D)** Macrophage phagocytizing fibrin-agarose (black asterisk*) (5 weeks); Scale bar = 1 μm. **(E)** Fibrin-agarose (black asterisk*) surrounded by collagen fibers (white asterisk*) (5 weeks); Scale bar = 1 μm. **(F)** Fibroblast phagocytizing fibrin-agarose (black asterisk*) (9 weeks); Scale bar = 2 μm. **(G)** Lymphocyte in satellite lymph node (yellow arrows) (12 weeks); Scale bar = 2 μm. **(H)** Hepatocytes containing glycogen (yellow arrows) (5 weeks); Scale bar = 5 μm. **(I)** Spleen macrophage phagocytizing iron (white arrow), lymphocyte (yellow arrow), and erythrocytes (white asterisk*) (5 weeks); Scale bar = 5 μm. **(J)** Basal region of proximal convoluted tubules of the kidney showing abundant mitochondria (yellow arrow) (5 weeks); Scale bar = 1 μm. **(K)** Glomerular filtration barrier in kidney (yellow arrow) (9 weeks); Scale bar = 1 μm.

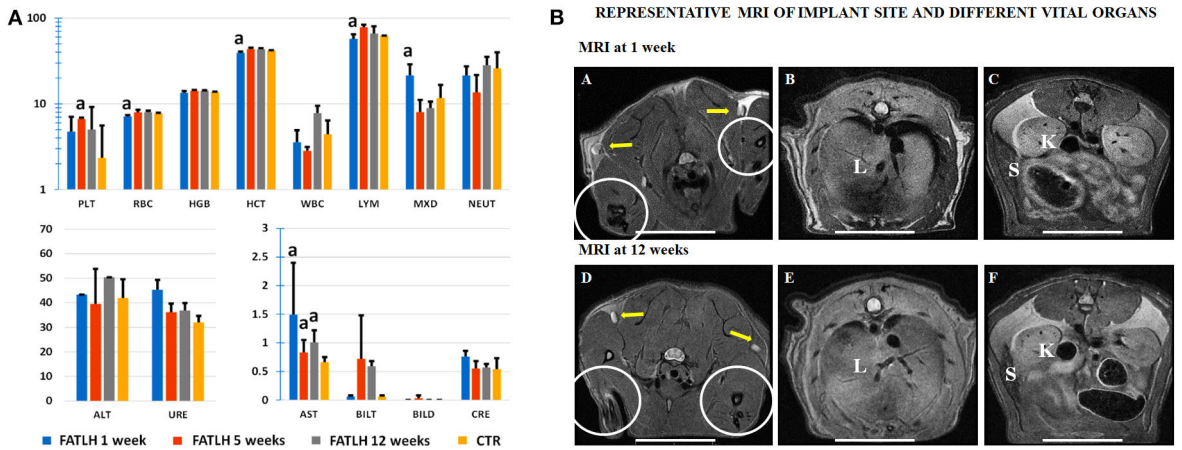

FIGURE 9 | Laboratory testing and magnetic resonance images (MRI) analysis of controls (CTR) and animals grafted with FATLH. **(A)** Hemogram and biochemistry analysis in blood of control and study animals at different times (1, 5, and 12 weeks). PLT: Platelets ($10^5/\mu L^{-1}$), RBC: Erythrocytes count ($10^6/\mu L^{-1}$), HGB: concentration of hemoglobin (g/dL), HCT: hematocrit count (%), WBC: white blood cells ($10^3/\mu L^{-1}$), LYM: lymphocytes (%), MXD: monocytes-basophils-eosinophils (%), NEUT: neutrophils (%), ALT: Alanine aminotransferase (U/L), URE: urea (mg/dL), AST: aspartate aminotransferase (10^2/U/L), BILT: total bilirubin (mg/dL), BILD: direct bilirubin (mg/dL), CRE: creatinine (mg/dL). Significant differences ($p < 0.05$) with the control group are highlighted with[a]. **(B)** MRI analysis of animals grafted with FATLH. Representative images of the implantation site and different vital organs are shown at 1 week and 12 weeks. The graft site is surrounded with circles; yellow arrows: satellite lymph nodes; L, liver; K, kidney; S, spleen. Scale bar: 2 cm.

structure of the biomaterial as it is strained beyond its elastic limit. As a whole, the frequency spectrum showed by FATLH was similar to that of crosslinked polymeric systems (Rodriguez et al., 2013), and significantly higher than hydrogels consisting of fibrin alone (Egea-Guerrero et al., 2019). Although new methods able to improve the biomechanical properties of FATLH are in need, these results suggest that these scaffolds may be able to support the usual shear forces to which an artificial tissue is subjected once grafted *in vivo*. All these biomechanical values are compatible with a biomaterial with a high volume-based swelling degree (Q), as demonstrated by previous works (Bonhome-Espinosa et al., 2017). The high porosity of FATLH allows the incorporation of a high amount of molecules of water to generate a biomaterial with ∼99.5% of water content (Scionti et al., 2014).

In the second place, we carried out a complete biocompatibility and biointegration analysis using a comprehensive approach including histological, hematological, biochemical, and imagenological approaches to support the clinical use of FATLH. The fact that all these methods coincided in the high degree of biocompatibility of the FATLH, they also confirm the safety of the *in vivo* use of these hydrogels in tissue engineering. In this regard, the use of highly-sensitive MRI image methods revealed that all animals were free from morphological alterations associated to the implant not only at the grafting site, but also in all major thoracic and abdominal organs. These results are in agreement with the histological and histochemical results obtained for distal organs, which were devoid of any alterations or modifications, suggesting that the subcutaneous implantation of FATLH is safe for the animals.

At the analytical level, we found that most parameters were normal in blood of the grafted animals, although some post-surgical changes were found. Thus, the transient decrease of RBC and HCT values and the transitory increase of the PLT count observed during this study could probably be related to the surgical procedure, which could generate this decrease that did not affect HGB concentration. The rapid recovering of all these values suggests that the FATLH is not able to generate any physiological alterations in the host animals at the hematopoiesis level. Similarly, some alterations were found for the percentage of LYM and MXD only during the first week, with a rapid normalization from the 5th week of the study. In general, this confirms the presence of a rapid, reversible post-surgical reaction in the host, which is likely associated to the surgical procedure rather than to the grafted material. The transient increase of the monocytes-basophils-eosinophils blood cell population may also be related to the subsequent increase of macrophages found at the grafting site, being these results supported by the well-known dynamics existing between circulating monocytes and

tissue macrophages (Yona et al., 2013). Moreover, our results are in line with the normalization of the hematological profile observed in Wistar rats in which acellular nerve allografts were used (Chato-Astrain et al., 2020). All these results coincide with the normal profile of biochemical parameters found in plasma of grafted animals, except for AST. It is well-known that blood and biochemical parameters are often affected in individuals with different kinds of diseases, traumatic injuries, cancer, or organ rejection (Kampfmann et al., 2012; Barone et al., 2018; Putzu et al., 2018; Dasgupta et al., 2019). In our case, the increase found for the AST liver marker could be associated to the anesthetic procedure, since certain reports found that AST might be altered by the use of ketamine anesthetics, especially in young mice (Cheung et al., 2017). Similarly, Fang and cols. demonstrated a transaminase increase in pediatric patients sedated with ketamine (Fang et al., 2019). Whether or not the grafted FATLH may play a role in AST increase should be determined in future works. Apart from this transaminase, our results suggest that the FATLH graft was safe for liver and kidney functions. One interesting unsolved question is whether or not the biodegradation process of a fibrin-based biomaterial could affect the blood coagulation system. Although we did not find any signs of hemorrhage or other pathologies in tissues corresponding to the study groups, future studies should shed light on this issue.

At the histological level, we found that the local and distal host tissue reaction to the implanted hydrogels was compatible with a normal response to a local surgical procedure, and no significant alterations were found at the grafting site or distal organs. Analysis of the implanted biomaterials revealed a local reaction related to an active process of ECM remodeling with the synthesis of fibrillar collagen and elastic fibers. The density, organization, blood supply, and cellularity of the newly-formed ECM was compatible with normal connective tissue without any signs of fibrotic response against the implanted hydrogels, although the number of vessels was higher in control tissues than in FATLH groups. In fact, the amount of collagen fibers found at the different times was lower or comparable to controls, suggesting that a fibrotic process was not ongoing. Interestingly, the types of collagen fibers present at all time were generally thin, immature fibers that could be related to recently synthetized non-type I collagen fibers (Zerbinati and Calligaro, 2018), confirming the lack of a strong fibrosis process, which typically contain thick type-I collagen fibers (Rittié, 2017). This phenomenon is common in biocompatible bioartificial tissues grafted *in vivo*, and suggests that this type of bioengineered tissues may induce a physiological process of ECM synthesis and remodeling (Carriel et al., 2012, 2013, 2019; Fernandez-Valades-Gamez et al., 2016; Chato-Astrain et al., 2018, 2020). Future studies using primary antibodies should be carried out to identify specific collagen types in the different samples.

Regarding the mechanisms of *in vivo* remodeling and biointegration of the FATLH, we found that these biomaterials were actively biodegraded by host macrophages, which is in agreement with previous reports suggesting that these cells are the main responsible for material reabsorption (Aderem and Underhill, 1999; Parkar et al., 2009; Ratnayake et al., 2017; Chato-Astrain et al., 2018). It has been previously demonstrated that biomaterials grafted *in vivo* may induce two types of reactions in the host tissues: a pro-inflammatory or a pro-regenerative reaction. The first one is characterized by the presence of an inflammatory infiltrate mainly consisting of neutrophils, lymphocytes, and pro-inflammatory M1 macrophages. In contrast, pro-regenerative reactions mostly contain anti-inflammatory alternatively activated M2 macrophages associated to an active process of angiogenesis, ECM remodeling and tissue repair (Anderson et al., 2008; Jones, 2008; Al-Maawi et al., 2017; Sok et al., 2017). In this milieu, our histological analysis allowed us to demonstrate that the initial local inflammatory reaction found at the implant site was very limited and mainly consisted of neutrophils and lymphoid cells surrounding the graft, and this reaction decreased over time until complete resolution at 12 weeks. Importantly, the combination of fibrin and agarose did not generate a chronic foreign body inflammatory reaction characterized by the infiltration of abundant lymphocytes, plasmocytes, and giant multinucleated cells (Kamata et al., 2019). Instead, our analysis revealed that the predominant recruited cell types at all times were the macrophages, and tissues corresponding to 5, 9, and 12 weeks of development had very few pro-inflammatory cells and numerous macrophage cells. Although future studies are in need to determine if these macrophages had a M1 or M2 phenotype using specific cell markers, the active angiogenesis and ECM remodeling processes and the scarce number of pro-inflammatory cells found at the host tissues, lead us to hypothesize that the cell reaction driven by fibrin-agarose is pro-regenerative rather than pro-inflammatory. This would be in agreement with the lack of Langhans-type giant cells at the graft site, which are related to active inflammatory processes requiring macrophage fusion to allow biomaterial phagocytosis. The size of the particles resulting from the biodegradation of the biomaterials to be phagocytosed becomes a determining factor (Champion et al., 2008; Milde et al., 2015). Furthermore, our results are comparable with the host response that we observed in previous *in vivo* studies conducted with FATLH in rabbit models of scleral (Carriel et al., 2019) and palate repair (Fernandez-Valades-Gamez et al., 2016) in which the inflammatory reaction was very mild and self-limited and results were compatible with an active process of tissue regeneration and biomaterial integration. In addition, our analysis revealed the presence of an important population of fibroblasts both in the host tissue and colonizing the biomaterial. We observed that host fibroblasts were able to actively interact with the graft, migrate to the biomaterial and produce the ECM molecules that we found in our histochemical analyses, especially including collagens, and elastic fibers. Furthermore, the TEM analysis revealed that fibroblasts were able to migrate into the grafted hydrogels and contributed to its biodegradation by phagocytosis. Interestingly, it was recently demonstrated that, under certain circumstances, fibroblasts can acquire an active phagocytic phenotype, regulate inflammation, or even mediate angiogenesis (Shinde and Frangogiannis, 2017; Le Fournis et al., 2019), which would explain the results found in our study.

On the other hand, our results showed that complete biointegration and biodegradation of implanted FATLH was achieved between the 9^{th} and 12^{th} week of

in vivo follow-up. Significant biodegradation coincided with a significant colonization of the biomaterial with macrophages and few lymphocytes and other pro-inflammatory cells. It is well-known that T lymphocytes may actively participate in the host response to grafted biomaterials (Anderson et al., 2008; Jones, 2008; Chato-Astrain et al., 2018) by mediating macrophage differentiation and the release of interleukins and interferons (Al-Maawi et al., 2017). As compared to previously published reports, the *in vivo* biodegradation process of FATLH was considerably faster than the 8 months observed for 1.5% agarose hydrogels implanted in Sprague-Dawley rats (Fernandez-Cossio et al., 2007), and slower than the ∼3 weeks of fibrin hydrogels (Kawase et al., 2015). Based on our results, it is clear that the combination of fibrin with a low concentration (0.1%) of type-VII agarose is an efficient alternative to delay the *in vivo* biodegradation process of our FATLH up to 9–12 weeks without any unwanted local effects or impact on host cell viability. The incorporation of a low concentration of agarose in the FATLH did not affect the biological properties of the fibrin, but improved its biomechanical properties without the adverse effects often observed in high concentrations of agarose (Fernandez-Cossio et al., 2007; Ahmed et al., 2008; Zarrintaj et al., 2018). In fact, the host tissue became very similar to control connective tissue after the FATLH was completely degraded.

Biointegration is strictly dependent on the presence of a well-defined vascular supply and a proper capillary network generated by the host tissue. It is well-known that fibrin is a natural reservoir of numerous growth factors (Sanchez-Munoz et al., 2015) and pro-angiogenic molecules able to induce proliferation of host endothelial cells to create new blood vessels (Morin and Tranquillo, 2013). In contrast, it was demonstrated that agarose can only support a slight neovascularization process, and this could occur in about 4 months of *in vivo* implantation (Fernandez-Cossio et al., 2007). In our case, we found that grafted FATLH were able to promote an active neovascularization process in around 5 weeks, which is closely related to the time required for FATLH remodeling. These findings can partially explain the high degree of integration, neovascularization, and active tissue regeneration observed with our FATLH-based models of skin, nerve, sclera, and palate (Carriel et al., 2012, 2013, 2019; Fernandez-Valades-Gamez et al., 2016; Chato-Astrain et al., 2018; Egea-Guerrero et al., 2019; Martin-Piedra et al., 2019). In all these studies, the neovascularization was essential for the success of the tissue regeneration.

In summary, the present study demonstrated that the implanted hydrogels were progressively biodegraded, and biomaterials remnants were observed for up to 9 weeks, until the total integration and reabsorption. All these results suggest that FATLH could be used for transitory replacement of tissues and organs requiring up to 2 months of *in vivo* stability, such as the human skin, oral mucosa, palate, and cornea. These superficial organs are frequently damaged, and a temporal substitution with a bioengineered organ based on FATLH would allow and promote the replacement of the grafts by native host structures during this time period. In this regard, we previously found that these organs are typically remodeled *in situ* and replaced by native structure in a very short time (Alaminos et al., 2006; Carriel et al., 2012, 2013, 2019; Fernandez-Valades-Gamez et al., 2016; Chato-Astrain et al., 2018). Interestingly, peripheral nerve repair also require the use of temporal biomaterials able to promote neural regeneration by means of a complex process including axonal sprouting, ECM synthesis, and neoangiogenesis. This process takes around 2 months, depending on the length of the gap (Carriel et al., 2013; Chato-Astrain et al., 2018). In consequence, development of novel ATMP based on the FATLH described in the present work could contribute to the clinical treatment of several conditions requiring tissue regeneration within this temporal frame. Specifically, FATLH could be used for a regenerative repair of damaged corneas and skin burns, but also for the clinical substitution of other human tissues and organs such as the peripheral nerve (Carriel et al., 2013, 2017a; Chato-Astrain et al., 2018), oral mucosa (Garzon et al., 2013; Fernandez-Valades-Gamez et al., 2016) and cartilage (Garcia-Martinez et al., 2017).

One of the limitations of the present study is the lack of a control group in which an inert biomaterial is grafted subcutaneously. Although we used a control with no grafted material showing the biological repair reaction driven by the surgical procedure, an inert material would rather inform us about the reaction driven by the incorporation of a biomaterial with no biological function. Although previous experiments published by our group showed that inert polypropylene biomaterials grafted subcutaneously in the Wistar rat are not associated to a strong inflammatory or fibrosis reaction, and results were very similar to the controls used in the present study (Martin-Piedra et al., 2017), future studies should confirm these findings. Another limitation is the need of performing specific molecular analysis able to characterize the cells found at the graft site. These analyses would complement the detailed histological studies carried out in the study.

CONCLUSIONS

In conclusion, this *in vivo* study confirm the high degree of biointegration and controlled biodegradability of FATLH, and suggests that these hydrogels could have potential clinical usefulness in engineering applications in terms of biosafety and biocompatibility.

DATA AVAILABILITY STATEMENT

The datasets generated for this study are available on request to the corresponding author.

ETHICS STATEMENT

The animal study was reviewed and approved by Ethics and Animal Experimentation Committee of the University of Granada and the Andalusian Directorate of Agricultural Production (CEEA).

AUTHOR CONTRIBUTIONS

IR, FC, and VC designed the study, wrote the article, performed surgical procedures, analyzed histological and MRI results, and analyzed quantitative results. ML-L and AB-E performed rheological characterization. FC carried out the fabrication of cell-free fibrin-agarose tissue-like hydrogel. FC, JC-A, DS-P, and VC performed and analyzed the hematological and biochemical studies. FC, ÓG-G, and VC, carried out histological and histochemical studies. RC, IR, and VC performed ultrastructural studies. IR, MA, and VC performed a critical review and contributed to manuscript writing. All authors contributed to the article and approved the submitted version.

FUNDING

This study was supported by the Spanish Plan Nacional de Investigación Científica, Desarrollo e Innovación Tecnológica (I+D+i) from the Spanish Ministerio de Ciencia, Innovación y Universidades (Instituto de Salud Carlos III), Grants FIS PI17/0391, PI17/0393, and PI18/332 (co-financed by ERDF-FEDER, European Union); Award no. AC17/00013 (NanoGSkin project) by ISCIII thorough AES 2017 and within the EuroNanoMed framework; IDI-20180052 (Agarmatriz), leaded by Hispanagar, SA, Burgos, Spain, through CDTI, Ministry of Economy and Competitiveness, Spain, Programa Operativo Pluriregional de Crecimiento Inteligente (CRIN) and ERDF-FEDER funds, EU; CS PI-0257-2017 and PE-0395-2019 from Consejería de Salud, Junta de Andalucía, Spain; FIS2017-85954-R (Ministerio de Economía, Industria y Competitividad, MINECO, and Agencia Estatal de Investigación, AEI, Spain, cofunded by Fondo Europeo de Desarrollo Regional, FEDER, European Union); Secyt 266, HCS 659/2018 (Secretary of Science and Technology of National Cordoba University, Argentina).

ACKNOWLEDGMENTS

The authors want to thank Ms. Amalia de la Rosa and Concepción Villegas for their collaboration in the animal experimentation and Fabiola Bermejo for technical assistance with histological analysis.

REFERENCES

Aderem, A., and Underhill, D. M. (1999). Mechanisms of phagocytosis in macrophages. *Annu. Rev. Immunol.* 17, 593–623. doi: 10.1146/annurev.immunol.17.1.593

Ahmed, T. A., Dare, E. V., and Hincke, M. (2008). Fibrin: a versatile scaffold for tissue engineering applications. *Tissue Eng. Part B Rev.* 14, 199–215. doi: 10.1089/ten.teb.2007.0435

Alaminos, M., Del Carmen Sanchez-Quevedo, M., Munoz-Avila, J. I., Serrano, D., Medialdea, S., Carreras, I., et al. (2006). Construction of a complete rabbit cornea substitute using a fibrin-agarose scaffold. *Invest. Ophthalmol. Vis. Sci.* 47, 3311–3317. doi: 10.1167/iovs.05-1647

Alaminos, M., Garzon, I., Sanchez-Quevedo, M. C., Moreu, G., Gonzalez-Andrades, M., Fernandez-Montoya, A., et al. (2007). Time-course study of histological and genetic patterns of differentiation in human engineered oral mucosa. *J. Tissue Eng. Regen. Med.* 1, 350–359. doi: 10.1002/term.38

Al-Maawi, S., Orlowska, A., Sader, R., James Kirkpatrick, C., and Ghanaati, S. (2017). *In vivo* cellular reactions to different biomaterials-physiological and pathological aspects and their consequences. *Semin. Immunol.* 29, 49–61. doi: 10.1016/j.smim.2017.06.001

Almeida, H. V., Eswaramoorthy, R., Cunniffe, G. M., Buckley, C. T., O'Brien, F. J., and Kelly, D. J. (2016). Fibrin hydrogels functionalized with cartilage extracellular matrix and incorporating freshly isolated stromal cells as an injectable for cartilage regeneration. *Acta Biomater.* 36, 55–62. doi: 10.1016/j.actbio.2016.03.008

Anderson, J. M., Rodriguez, A., and Chang, D. T. (2008). Foreign body reaction to biomaterials. *Semin. Immunol.* 20, 86–100. doi: 10.1016/j.smim.2007.11.004

Atala, A. (2012). Regenerative medicine strategies. *J. Pediatr. Surg.* 47, 17–28. doi: 10.1016/j.jpedsurg.2011.10.013

Banerjee, J., Seetharaman, S., Wrice, N. L., Christy, R. J., and Natesan, S. (2019). Delivery of silver sulfadiazine and adipose derived stem cells using fibrin hydrogel improves infected burn wound regeneration. *PLoS ONE* 14:e0217965. doi: 10.1371/journal.pone.0217965

Barone, F. C., Marcinkiewicz, C., Li, J., Sternberg, M., Lelkes, P. I., Dikin, D. A., et al. (2018). Pilot study on biocompatibility of fluorescent nanodiamond-(NV)-Z∼800 particles in rats: safety, pharmacokinetics, and bio-distribution (part III). *Int. J. Nanomed.* 13, 5449–5468. doi: 10.2147/IJN.S171117

Bonhome-Espinosa, A. B., Campos, F., Rodriguez, I. A., Carriel, V., Marins, J. A., Zubarev, A., et al. (2017). Effect of particle concentration on the microstructural and macromechanical properties of biocompatible magnetic hydrogels. *Soft Matter.* 13, 2928–2941. doi: 10.1039/C7SM00388A

Bruns, H., Kneser, U., Holzhuter, S., Roth, B., Kluth, J., Kaufmann, P. M., et al. (2005). Injectable liver: a novel approach using fibrin gel as a matrix for culture and intrahepatic transplantation of hepatocytes. *Tissue Eng.* 11, 1718–1726. doi: 10.1089/ten.2005.11.1718

Campos, F., Bonhome-Espinosa, A. B., Garcia-Martinez, L., Duran, J. D., Lopez-Lopez, M. T., Alaminos, M., et al. (2016). *Ex vivo* characterization of a novel tissue-like cross-linked fibrin-agarose hydrogel for tissue engineering applications. *Biomed. Mater.* 11:055004. doi: 10.1088/1748-6041/11/5/055004

Campos, F., Bonhome-Espinosa, A. B., Vizcaino, G., Rodriguez, I. A., Duran-Herrera, D., Lopez-Lopez, M. T., et al. (2018). Generation of genipin cross-linked fibrin-agarose hydrogel tissue-like models for tissue engineering applications. *Biomed. Mater.* 13:025021. doi: 10.1088/1748-605X/aa9ad2

Carriel, V., Alaminos, M., Garzon, I., Campos, A., and Cornelissen, M. (2014). Tissue engineering of the peripheral nervous system. *Expert Rev. Neurother.* 14, 301–318. doi: 10.1586/14737175.2014.887444

Carriel, V., Campos, F., Aneiros-Fernandez, J., and Kiernan, J. A. (2017b). Tissue fixation and processing for the histological identification of lipids. *Methods Mol. Biol.* 1560, 197–206. doi: 10.1007/978-1-4939-6788-9_14

Carriel, V., Garrido-Gomez, J., Hernandez-Cortes, P., Garzon, I., Garcia-Garcia, S., Saez-Moreno, J. A., et al. (2013). Combination of fibrin-agarose hydrogels and adipose-derived mesenchymal stem cells for peripheral nerve regeneration. *J. Neural Eng.* 10:026022. doi: 10.1088/1741-2560/10/2/026022

Carriel, V., Garzon, I., Jimenez, J. M., Oliveira, A. C., Arias-Santiago, S., Campos, A., et al. (2012). Epithelial and stromal developmental patterns in a novel substitute of the human skin generated with fibrin-agarose biomaterials. *Cells Tissues Organs.* 196, 1–12. doi: 10.1159/000330682

Carriel, V., Scionti, G., Campos, F., Roda, O., Castro, B., Cornelissen, M., et al. (2017a). *In vitro* characterization of a nanostructured fibrin agarose bio-artificial nerve substitute. *J. Tissue Eng. Regen. Med.* 11, 1412–1426. doi: 10.1002/term.2039

Carriel, V., Vizcaino-Lopez, G., Chato-Astrain, J., Durand-Herrera, D., Alaminos, M., Campos, A., et al. (2019). Scleral surgical repair through the use of nanostructured fibrin/agarose-based films in rabbits. *Exp. Eye Res.* 186:107717. doi: 10.1016/j.exer.2019.107717

Carriel, V. S., Aneiros-Fernandez, J., Arias-Santiago, S., Garzon, I. J., Alaminos, M., and Campos, A. (2011). A novel histochemical method for a simultaneous

staining of melanin and collagen fibers. *J. Histochem. Cytochem*. 59, 270–277. doi: 10.1369/0022155410398001

Champion, J. A., Walker, A., and Mitragotri, S. (2008). Role of particle size in phagocytosis of polymeric microspheres. *Pharm. Res*. 25, 1815–1821. doi: 10.1007/s11095-008-9562-y

Chan, R. W., and Titze, I. R. (1999). Viscoelastic shear properties of human vocal fold mucosa: measurement methodology and empirical results. *J. Acoust. Soc. Am*. 106, 2008–2021. doi: 10.1121/1.427947

Chato-Astrain, J., Campos, F., Roda, O., Miralles, E., Durand-Herrera, D., Saez-Moreno, J. A., et al. (2018). *In vivo* evaluation of nanostructured fibrin-agarose hydrogels with mesenchymal stem cells for peripheral nerve repair. *Front. Cell. Neurosci*. 12:501. doi: 10.3389/fncel.2018.00501

Chato-Astrain, J., Philips, C., Campos, F., Durand-Herrera, D., Garcia-Garcia, O. D., Roosens, A., et al. (2020). Detergent-based decellularized peripheral nerve allograft: an *in vivo* preclinical study in the rat sciatic injury model. *J. Tissue Eng. Regen. Med*. doi: 10.1002/term.3043. [Epub ahead of print].

Cheung, H. M. T., Chow, C. H., and Yew, D. T. W. (2017). How ketamine affects livers of pregnant mice and developing mice? *Int. J. Mol. Sci* 18:1098. doi: 10.3390/ijms18051098

Dasgupta, N., Ranjan, S., Ramalingam, C., and Gandhi, M. (2019). Silver nanoparticles engineered by thermal co-reduction approach induces liver damage in wistar rats: acute and sub-chronic toxicity analysis. *3 Biotech*. 9:125. doi: 10.1007/s13205-019-1651-6

Drifka, C. R., Loeffler, A. G., Mathewson, K., Mehta, G., Keikhosravi, A., Liu, Y., et al. (2016). Comparison of picrosirius red staining with second harmonic generation imaging for the quantification of clinically relevant collagen fiber features in histopathology samples. *J. Histochem. Cytochem*. 64, 519–529. doi: 10.1369/0022155416659249

Egea-Guerrero, J. J., Carmona, G., Correa, E., Mata, R., Arias-Santiago, S., Alaminos, M., et al. (2019). Transplant of tissue-engineered artificial autologous human skin in andalusia: an example of coordination and institutional collaboration. *Transplant. Proc*. 51, 3047–3050. doi: 10.1016/j.transproceed.2019.08.014

Eyrich, D., Brandl, F., Appel, B., Wiese, H., Maier, G., Wenzel, M., et al. (2007a). Long-term stable fibrin gels for cartilage engineering. *Biomaterials* 28, 55–65. doi: 10.1016/j.biomaterials.2006.08.027

Eyrich, D., Wiese, H., Maier, G., Skodacek, D., Appel, B., Sarhan, H., et al. (2007b). *In vitro* and *in vivo* cartilage engineering using a combination of chondrocyte-seeded long-term stable fibrin gels and polycaprolactone-based polyurethane scaffolds. *Tissue Eng*. 13, 2207–2218. doi: 10.1089/ten.2006.0358

Fang, H., Li, H. F., Yang, M., Zhang, F. X., Liao, R., Wang, R. R., et al. (2019). Effect of ketamine combined with lidocaine in pediatric anesthesia. *J Clin Lab Anal*. 34:e23115. doi: 10.1002/jcla.23115

Fernandez-Cossio, S., Leon-Mateos, A., Sampedro, F. G., and Oreja, M. T. (2007). Biocompatibility of agarose gel as a dermal filler: histologic evaluation of subcutaneous implants. *Plast. Reconstr. Surg*. 120, 1161–1169. doi: 10.1097/01.prs.0000279475.99934.71

Fernandez-Valades-Gamez, R., Garzon, I., Liceras-Liceras, E., Espana-Lopez, A., Carriel, V., Martin-Piedra, M. A., et al. (2016). Usefulness of a bioengineered oral mucosa model for preventing palate bone alterations in rabbits with a mucoperiostial defect. *Biomed. Mater.* 11:015015. doi: 10.1088/1748-6041/11/1/015015

Garcia-Martinez, L., Campos, F., Godoy-Guzman, C., Del Carmen Sanchez-Quevedo, M., Garzon, I., Alaminos, M., et al. (2017). Encapsulation of human elastic cartilage-derived chondrocytes in nanostructured fibrin-agarose hydrogels. *Histochem. Cell Biol*. 147, 83–95. doi: 10.1007/s00418-016-1485-9

Garzon, I., Miyake, J., Gonzalez-Andrades, M., Carmona, R., Carda, C., Sanchez-Quevedo Mdel, C., et al. (2013). Wharton's jelly stem cells: a novel cell source for oral mucosa and skin epithelia regeneration. *Stem Cells Transl. Med*. 2, 625–632. doi: 10.5966/sctm.2012-0157

Gonzalez-Andrades, M., Mata, R., Gonzalez-Gallardo, M. D. C., Medialdea, S., Arias-Santiago, S., Martinez-Atienza, J., et al. (2017). A study protocol for a multicentre randomised clinical trial evaluating the safety and feasibility of a bioengineered human allogeneic nanostructured anterior cornea in patients with advanced corneal trophic ulcers refractory to conventional treatment. *BMJ Open* 7:e016487. doi: 10.1136/bmjopen-2017-016487

Helmedag, M. J., Weinandy, S., Marquardt, Y., Baron, J. M., Pallua, N., Suschek, C. V., et al. (2015). The effects of constant flow bioreactor cultivation and keratinocyte seeding densities on prevascularized organotypic skin grafts based on a fibrin scaffold. *Tissue Eng. Part A* 21, 343–352. doi: 10.1089/ten.tea.2013.0640

Jockenhoevel, S., Zund, G., Hoerstrup, S. P., Chalabi, K., Sachweh, J. S., Demircan, L., et al. (2001). Fibrin gel – advantages of a new scaffold in cardiovascular tissue engineering. *Eur. J. Cardiothorac. Surg*. 19, 424–430. doi: 10.1016/S1010-7940(01)00624-8

Jones, K. S. (2008). Effects of biomaterial-induced inflammation on fibrosis and rejection. *Semin. Immunol*. 20, 130–136. doi: 10.1016/j.smim.2007.11.005

Kamata, M., Sakamoto, Y., and Kishi, K. (2019). Foreign-body reaction to bioabsorbable plate and screw in craniofacial surgery. *J. Craniofac. Surg*. 30, e34–e36. doi: 10.1097/SCS.0000000000004945

Kampfmann, I., Bauer, N., Johannes, S., and Moritz, A. (2012). Differences in hematologic variables in rats of the same strain but different origin. *Vet. Clin. Pathol*. 41, 228–234. doi: 10.1111/j.1939-165X.2012.00427.x

Kawase, T., Kamiya, M., Kobayashi, M., Tanaka, T., Okuda, K., Wolff, L. F., et al. (2015). The heat-compression technique for the conversion of platelet-rich fibrin preparation to a barrier membrane with a reduced rate of biodegradation. *J. Biomed. Mater. Res. Part B Appl. Biomater*. 103, 825–831. doi: 10.1002/jbm.b.33262

Keck, M., Gugerell, A., and Kober, J. (2019). Engineering a multilayered skin substitute with keratinocytes, fibroblasts, adipose-derived stem cells, and adipocytes. *Methods Mol. Biol.* 1993, 149–157. doi: 10.1007/978-1-4939-9473-1_12

Kiernan, J. A. (2008). *Histological and Histochemical Methods: Theory and Practice*. Oxford: Scion.

Le Fournis, C., Hadjichristou, C., Jeanneau, C., and About, I. (2019). Human pulp fibroblast implication in phagocytosis via complement activation. *J. Endod*. 45, 584–590. doi: 10.1016/j.joen.2018.10.023

Lee, C. R., Grad, S., Gorna, K., Gogolewski, S., Goessl, A., and Alini, M. (2005). Fibrin-polyurethane composites for articular cartilage tissue engineering: a preliminary analysis. *Tissue Eng*. 11, 1562–1573. doi: 10.1089/ten.2005.11.1562

Martin-Piedra, M. A., Alfonso-Rodriguez, C. A., Zapater, A., Durand-Herrera, D., Chato-Astrain, J., Campos, F., et al. (2019). Effective use of mesenchymal stem cells in human skin substitutes generated by tissue engineering. *Eur. Cell. Mater*. 37, 233–249. doi: 10.22203/eCM.v037a14

Martin-Piedra, M. A., Garzon, I., Gomez-Sotelo, A., Garcia-Abril, E., Jaimes-Parra, B. D., Lopez-Cantarero, M., et al. (2017). Generation and evaluation of novel stromal cell-containing tissue engineered artificial stromas for the surgical repair of abdominal defects. *Biotechnol. J*. 12:1700078. doi: 10.1002/biot.201700078

Meana, A., Iglesias, J., Del Rio, M., Larcher, F., Madrigal, B., Fresno, M. F., et al. (1998). Large surface of cultured human epithelium obtained on a dermal matrix based on live fibroblast-containing fibrin gels. *Burns* 24, 621–630. doi: 10.1016/S0305-4179(98)00107-7

Milde, R., Ritter, J., Tennent, G. A., Loesch, A., Martinez, F. O., Gordon, S., et al. (2015). Multinucleated giant cells are specialized for complement-mediated phagocytosis and large target destruction. *Cell Rep*. 13, 1937–1948. doi: 10.1016/j.celrep.2015.10.065

Mol, A., van Lieshout, M. I., Dam-de Veen, C. G., Neuenschwander, S., Hoerstrup, S. P., Baaijens, F. P., et al. (2005). Fibrin as a cell carrier in cardiovascular tissue engineering applications. *Biomaterials* 26, 3113–3121. doi: 10.1016/j.biomaterials.2004.08.007

Morin, K. T., and Tranquillo, R. T. (2013). *In vitro* models of angiogenesis and vasculogenesis in fibrin gel. *Exp. Cell Res*. 319, 2409–2417. doi: 10.1016/j.yexcr.2013.06.006

Myu Mai Ja, K. P., Lim, K. P., Chen, A., Ting, S., Li, S. Q., Tee, N., et al. (2018). Construction of a vascularized hydrogel for cardiac tissue formation in a porcine model. *J. Tissue Eng. Regen. Med*. 12, e2029–e2038. doi: 10.1002/term.2634

Noori, A., Ashrafi, S. J., Vaez-Ghaemi, R., Hatamian-Zaremi, A., and Webster, T. J. (2017). A review of fibrin and fibrin composites for bone tissue engineering. *Int. J. Nanomedicine*. 12, 4937–4961. doi: 10.2147/IJN.S124671

Parkar, N. S., Akpa, B. S., Nitsche, L. C., Wedgewood, L. E., Place, A. T., Sverdlov, M. S., et al. (2009). Vesicle formation and endocytosis: function, machinery, mechanisms, and modeling. *Antioxid. Redox Signal* 11, 1301–1312. doi: 10.1089/ars.2008.2397

Putzu, C., Cortinovis, D. L., Colonese, F., Canova, S., Carru, C., Zinellu, A., et al. (2018). Blood cell count indexes as predictors of outcomes in advanced non-small-cell lung cancer patients treated with nivolumab. *Cancer Immunol. Immunother*. 67, 1349–1353. doi: 10.1007/s00262-018-2182-4

Ratnayake, I., Ahrenkiel, S., Hoppe, A., and Thiex, N. (2017). Electron microscopy and tomography on endocytosis of macrophages. *Microsc. Microanal.* 23, 1268–1269. doi: 10.1017/S1431927617007000

Rico-Sanchez, L., Garzon, I., Gonzalez-Andrades, M., Ruiz-Garcia, A., Punzano, M., Lizana-Moreno, A., et al. (2019). Successful development and clinical translation of a novel anterior lamellar artificial cornea. *J. Tissue Eng. Regen. Med*. 13, 2142–2154. doi: 10.1002/term.2951

Rittié, L. (2017). *Fibrosis: Methods and Protocols*. New York, NY: Springer, doi: 10.1007/978-1-4939-7113-8

Rodriguez, M. A., Lopez-Lopez, M. T., Duran, J. D., Alaminos, M., Campos, A., and Rodriguez, I. A. (2013). Cryopreservation of an artificial human oral mucosa stroma. A viability and rheological study. *Cryobiology* 67, 355–362. doi: 10.1016/j.cryobiol.2013.10.003

Rodriguez-Arco, L., Rodriguez, I. A., Carriel, V., Bonhome-Espinosa, A. B., Campos, F., Kuzhir, P., et al. (2016). Biocompatible magnetic core-shell nanocomposites for engineered magnetic tissues. *Nanoscale* 8, 8138–8150. doi: 10.1039/C6NR00224B

Rosso, F., Marino, G., Giordano, A., Barbarisi, M., Parmeggiani, D., and Barbarisi, A. (2005). Smart materials as scaffolds for tissue engineering. *J. Cell. Physiol.* 203, 465–470. doi: 10.1002/jcp.20270

Sanchez-Munoz, I., Granados, R., Holguin Holgado, P., Garcia-Vela, J. A., Casares, C., and Casares, M. (2015). The use of adipose mesenchymal stem cells and human umbilical vascular endothelial cells on a fibrin matrix for endothelialized skin substitute. *Tissue Eng. Part A* 21, 214–223. doi: 10.1089/ten.tea.2013.0626

Scionti, G., Moral, M., Toledano, M., Osorio, R., Duran, J. D., Alaminos, M., et al. (2014). Effect of the hydration on the biomechanical properties in a fibrin-agarose tissue-like model. *J. Biomed. Mater. Res. A* 102, 2573–2582. doi: 10.1002/jbm.a.34929

Shinde, A. V., and Frangogiannis, N. G. (2017). Mechanisms of fibroblast activation in the remodeling myocardium. *Curr. Pathobiol. Rep*. 5, 145–152. doi: 10.1007/s40139-017-0132-z

Sok, M. C. P., Tria, M. C., Olingy, C. E., San Emeterio, C. L., and Botchwey, E. A. (2017). Aspirin-triggered resolvin D1-modified materials promote the accumulation of pro-regenerative immune cell subsets and enhance vascular remodeling. *Acta Biomater*. 53, 109–122. doi: 10.1016/j.actbio.2017.02.020

Swartz, D. D., Russell, J. A., and Andreadis, S. T. (2005). Engineering of fibrin-based functional and implantable small-diameter blood vessels. *Am. J. Physiol. Heart Circ. Physiol.* 288, H1451–H1460. doi: 10.1152/ajpheart.00479.2004

Van Lieshout, M., Peters, G., Rutten, M., and Baaijens, F. (2006). A knitted, fibrin-covered polycaprolactone scaffold for tissue engineering of the aortic valve. *Tissue Eng.* 12, 481–487. doi: 10.1089/ten.2006.12.481

Wang, X., and Liu, C. (2018). Fibrin hydrogels for endothelialized liver tissue engineering with a predesigned vascular network. *Polymers* 10:1048. doi: 10.3390/polym10101048

Wick, M. R. (2008). *Diagnostic Histochemistry*. Cambridge: Cambridge University Press.

Wittmann, K., Storck, K., Muhr, C., Mayer, H., Regn, S., Staudenmaier, R., et al. (2016). Development of volume-stable adipose tissue constructs using polycaprolactone-based polyurethane scaffolds and fibrin hydrogels. *J. Tissue Eng. Regen. Med*. 10, E409–E418. doi: 10.1002/term.1830

Yona, S., Kim, K. W., Wolf, Y., Mildner, A., Varol, D., Breker, M., et al. (2013). Fate mapping reveals origins and dynamics of monocytes and tissue macrophages under homeostasis. *Immunity* 38, 79–91. doi: 10.1016/j.immuni.2012.12.001

Zarrintaj, P., Manouchehri, S., Ahmadi, Z., Saeb, M. R., Urbanska, A. M., Kaplan, D. L., et al. (2018). Agarose-based biomaterials for tissue engineering. *Carbohydr. Polym*. 187, 66–84. doi: 10.1016/j.carbpol.2018.01.060

Zerbinati, N., and Calligaro, A. (2018). Calcium hydroxylapatite treatment of human skin: evidence of collagen turnover through picrosirius red staining and circularly polarized microscopy. *Clin. Cosmet. Investig. Dermatol*. 11, 29–35. doi: 10.2147/CCID.S143015

Conflict of Interest: The authors declare that the research was conducted in the absence of any commercial or financial relationships that could be construed as a potential conflict of interest.

frontiers in Bioengineering and Biotechnology

ORIGINAL RESEARCH
published: 17 June 2020
doi: 10.3389/fbioe.2020.00595

A New Non-invasive Technique for Measuring 3D-Oxygen Gradients in Wells During Mammalian Cell Culture

Carlos J. Peniche Silva[1], Gregor Liebsch[2], Robert J. Meier[2], Martin S. Gutbrod[2], Elizabeth R. Balmayor[3] and Martijn van Griensven[1]*

[1] cBITE, MERLN Institute for Technology-Inspired Regenerative Medicine, Maastricht University, Maastricht, Netherlands, [2] PreSens Precision Sensing GmbH, Regensburg, Germany, [3] IBE, MERLN Institute for Technology-Inspired Regenerative Medicine, Maastricht University, Maastricht, Netherlands

Oxygen tension plays an important role in overall cell function and fate, regulating gene expression, and cell differentiation. Although there is extensive literature available that supports the previous statement, little information is to be found about accurate O_2 measurements during culture. In fact, O_2 concentration at the cell layer during culture is commonly assumed to be equal to that of the incubator atmosphere. This assumption does not consider oxygen diffusion properties, cell type, cell density, media composition, time in culture nor height of the cell culture medium column. In this study, we developed a non-invasive, optical sensor foil-based technique suitable for measuring the 3D oxygen gradient that is formed during cell culture as a result of normal cell respiration. For this propose, we created a 3D printed ramp to which surface an oxygen optode sensor foil was attached. The ramps were positioned inside the culture wells of 24 well plate prior cell seeding. This set up in conjunction with the VisiSens TD camera system allows to investigate the oxygen gradient formation during culture. Cultivation was performed with three different initial cell densities of the cell line A549 that were seeded on the plate containing the ramps with the oxygen sensors. The O_2 gradient obtained after 96 h of culture showed significantly lower O_2 concentrations closer to the bottom of the well in high cell density cultures compared to that of lower cell density cultures. Furthermore, it was very interesting to observe that even with low cell density culture, oxygen concentration near the cell layer was lower than that of the incubator atmosphere. The obtained oxygen gradient after 96 h was used to calculate the oxygen consumption rate (OCR) of the A549 cells, and the obtained value of ∼100 fmol/h/cell matches the OCR value already reported in the literature for this cell line. Moreover, we found our set up to be unique in its ability to measure oxygen gradient formation in several wells of a cell culture plate simultaneously and in a non-invasive manner.

Keywords: oxygen, gradient, respiration rate, non-invasive, ramp, optical-based, sensor foil

OPEN ACCESS

Edited by:
Dimitrios I. Zeugolis, National University of Ireland Galway, Ireland

Reviewed by:
Hirotake Komatsu, Beckman Research Institute, United States
Martin James Stoddart, AO Research Institute, Switzerland
Marta Calatayud Arroyo, Institute of Agrochemistry and Food Technology, Spain

****Correspondence:***
Carlos J. Peniche Silva
c.penichesilva@maastrichtuniversity.nl

Specialty section:
This article was submitted to Tissue Engineering and Regenerative Medicine, a section of the journal Frontiers in Bioengineering and Biotechnology

Received: *24 January 2020*
Accepted: *15 May 2020*
Published: *17 June 2020*

Citation:
Peniche Silva CJ, Liebsch G, Meier RJ, Gutbrod MS, Balmayor ER and van Griensven M (2020) A New Non-invasive Technique for Measuring 3D-Oxygen Gradients in Wells During Mammalian Cell Culture. Front. Bioeng. Biotechnol. 8:595. doi: 10.3389/fbioe.2020.00595

INTRODUCTION

Oxygen tension plays an important role in regulating gene expression, cell differentiation and overall cell function and fate (Wenger, 2000; D'Ippolito et al., 2006; Hirao et al., 2007; Ivanovic, 2009; Vander Heiden et al., 2009; Rankin et al., 2011; Wagner et al., 2011; Nicolaije et al., 2012; Al-Ani et al., 2018). During bone formation, hypoxic gradients, that is an oxygen concentration

range from 5 to <1%, are established as the tissue grows. These gradients promote the formation of new blood vessels that deliver oxygen and nutrients to the growing tissue (Rankin et al., 2011). During cell culture *in vitro*, oxygen tension below 2–3% has been related to the inhibition of the osteogenic differentiation of human bone marrow-isolated multilineage inducible cells, while similar oxygenation conditions stimulated matrix mineralization and accelerated the transformation of osteoblasts to osteocytes in cultures of MC3T3 (an osteoblast precursor cell line) (D'Ippolito et al., 2006; Hirao et al., 2007). In immune cells, low oxygen tensions have been proven to affect the immune response by down-regulating T-cells function. For example, *in vitro* studies have shown that low O_2 concentration causes prolonged impairment of cytokine expression. Oxygen tension also affects the balance between T helper 1 cells and T helper 2 cells. For instance, low oxygen tension causes a shift toward T helper 2 responses and inhibits the T helper 1 responses (Sitkovsky and Lukashev, 2005). Furthermore, decreased oxygen tension ($\leq$5% oxygen concentration) also inhibits the capacity of mesenchymal stem cells to differentiate (Al-Ani et al., 2018) while higher oxygen tension values have been reported to promote differentiation (Ivanovic, 2009).

The previously mentioned facts illustrate the relevance of oxygen tension on how the cells react to their environment. In *in vivo* conditions, oxygen levels are finely tuned with respect to tissue and cell type by means of highly complex mechanisms that, until now, can't be replicated during *in vitro* cell/tissue culture. The oxygen concentration to which tissue is exposed in *in vivo* conditions are much lower than that of the atmosphere, even in those tissues in direct contact with air (Al-Ani et al., 2018). In contrast, culture of cells in incubators having ambient atmosphere, is often referred to as "normoxia," while cultures in incubators with lower levels of oxygenation are referred to as "hypoxia" (Saltzman et al., 2003; Wild et al., 2005; Wenger et al., 2015). In particular, "normoxic" incubators are erroneously assumed to deliver 20.9% of oxygenation to the cells in culture without considering other parameters, such as medium diffusion properties, height of the cell culture medium column, cell density and oxygen consumption rate (Wenger et al., 2015; Al-Ani et al., 2018). Another aspect to consider is that the oxygen concentration in the gas phase of a "normoxic" incubator at sea level is actually 18.6% (Wenger et al., 2015). The reason for this fact is that the gas mixture inside an incubator differs from that of the atmosphere in the content of N_2, O_2, H_2O, and CO_2 due to the extra content of CO_2 (38 mmHg for a 5% v/v concentration) and water vapor (47 mmHg) found inside an incubator, which is necessary for the maintenances of stable pH and the appropriate humidified conditions during cultivation, respectively. According to Dalton's law, the partial pressure of the gases inside a normobaric incubator will sum up to equal the atmospheric pressure outside the incubator, which at sea level is 760 mmHg. This means that the actual pO_2 inside an incubator at sea level, when considering the contribution of the partial pressure of the extra CO_2 and water vapor, is 141 mmHg, equivalent to 18.6% of the total atmosphere of the incubator.

Due to the essential role of oxygen in almost every biological process, inaccurate oxygen concentration measurements during cell culture could greatly affect the reproducibility of the experimental results. This also applies when the importance of monitoring the oxygen concentration during cell culture is underestimated (Karp, 2018).

Over the years, a broad spectrum of techniques has been explored for measuring oxygenation during cell culture. For instance, solid state electrodes, such as the Clark-type electrode, have been used for oxygen sensing during cultivation. These electrodes work by reducing oxygen electrochemically and recording the changes in current (Renger and Hanssum, 2009; Strovas et al., 2010). The main drawbacks of this system include oxygen consumption by the electrode itself. This effect is usually negligible in large volumes but it can limit Clark type electrodes applications in low volumes. This is why, in recent years many electrochemical oxygen sensors have been replaced by optical counterparts (Randers-Eichhorn et al., 1996; Strovas et al., 2010; Demuth et al., 2016). Alternatively, recent methods involving scanning electrochemical microscopy (SECM) and nanobead sensors attached to the outer membrane of cells have been employed (Saito et al., 2006; Kuang and Walt, 2007). Nonetheless, these techniques are only able to measure oxygen concentration near the cell membrane or near the oxygen sensor.

Techniques based in optical methods for measuring oxygen concentration quickly gained popularity because of their accessibility and their ability to indicate real time oxygen concentration in a non-invasive fashion (Randers-Eichhorn et al., 1996; Kellner et al., 2002; Strovas et al., 2010; Wang and Wolfbeis, 2014). The vast majority of optical sensors for oxygen are based in luminescent probes consisting of a transparent support and a sensing layer. This layer usually contains a quenchable probe and an unquenchable reference dye (Wang and Wolfbeis, 2014). Some techniques combine fluorescent sensor foils with 2D read-out technology to measure the pericellular oxygen concentration (Tschiersch et al., 2012; Wolff et al., 2019). With this system it is possible to gather real time information about the oxygen levels near the oxygen sensor. However, the amount of information that can be obtained using this system has been until now, limited to the oxygen concentration over a cross section of the cell culture and does not provide any data about the oxygen gradient inside the cell culture medium.

On the other hand, the use of an integrated needle-type micro sensor and recording system has allowed the measurement of the oxygen concentrations not only near the surface of the cells in culture but also the oxygen distribution inside the cell culture medium (Pettersen et al., 2005). With this technique it is possible to study the oxygen gradient formation that occurs during cell culture and its relation with cell density (Malda et al., 2004; Pettersen et al., 2005; Wenger et al., 2015). However, practical limitations for this technique restrict its use to a single culture well or T-Flask at a time. This greatly affects the applications of needle-type micro sensors in terms of simultaneous oxygen measurements due to the fact that any micro sensor multiplexing results in a quick rise of cable management complexity. In addition, the necessary set up for this technique involves the needle-type sensor moving inside the cell culture medium and near the cell surface. This means that the well plate or flask needs to be left open during the measurement. This endangers

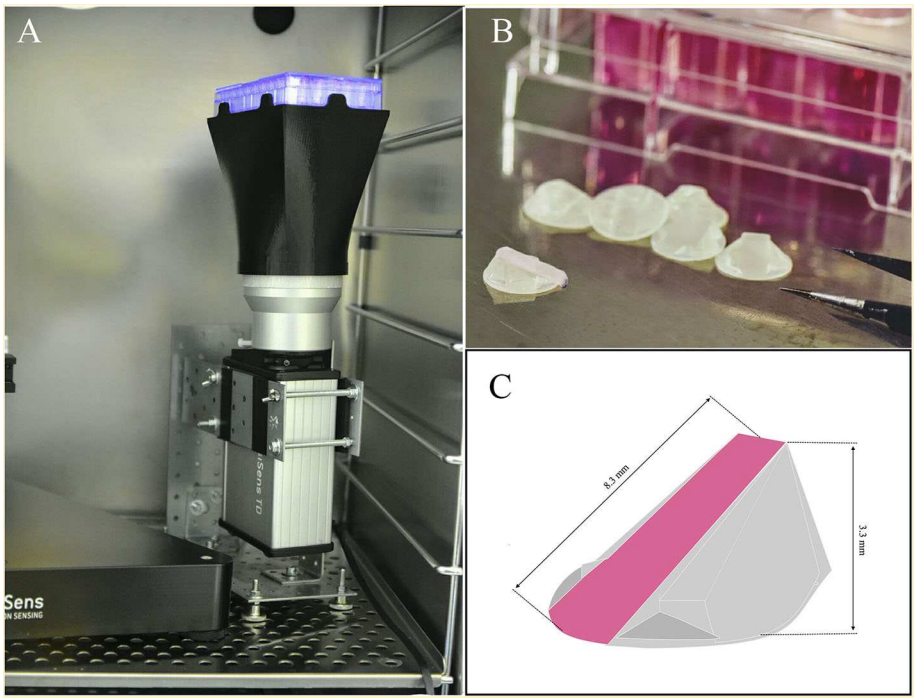

FIGURE 1 | (A) Set-up of the VisiSens TD camera system used during the measurements. A cell culture plate is mounted on the plate support/base on the camera system. A light source located around the camera lens illuminates the cell culture plate from below to excite the oxygen sensor foils inside the wells. The VisiSens TD camera collects the ratiometric signal from the dyes on the surface of the sensors as they interact with the dissolved oxygen inside the cell culture media. **(B)** Image of the ramps with the sensors attached on their surface. **(C)** Schematic representation of the 3 D printed ramp and geometric details. The SF-RPsSu4 sensor was attached to the rectangular surface of the ramp.

the sterility of the culture, especially when several sequential measurements are needed (Randers-Eichhorn et al., 1996).

Therefore, we aimed to develop a novel intrinsic system to measure oxygen gradients over time during cell culture. We have developed a simple and cost-effective technique that allows the non-invasive, real time study of the 3D oxygen gradient formation during cell culture. We based our technique on the use of the VisiSens TD camera system and the planar oxygen sensor foil SF-RPsSu4 (Maisch et al., 2019; Wolff et al., 2019). We created a 3D printable ramp to which the SF-RPsSu4 sensor can be attached on its diagonal surface (**Figure 1**) and can be incorporated inside cell culture wells. This configuration allows the sensor to measure the oxygen concentration at different heights from the bottom of the well to a maximum of 3.3 mm over the bottom without any moving parts involved in the set up. We also compared the oxygen profiles obtained with our developed technique to that obtained with the optical fiber-based needle type sensor PM-PSt7 mounted on a motorized and computer-aided micromanipulator. Our results show that with our set-up, oxygen gradient formation can be measured simultaneously in several wells of a cell culture plate in a non-invasive manner.

MATERIALS AND METHODS

Cells and Culture Conditions

Immortalized human lung epithelial cell line A549 (ATCC®-CCL-185™, ATCC, Manassas, VI, USA) were cultured in high glucose Dulbecco's Modified Eagle's Medium (D-MEM, Sigma-Aldrich, St. Louis, MO, USA) supplemented with fetal bovine serum (FBS, 10%) and a mixture of penicillin 100 U/ml and streptomycin 100 μm/ml (1%, Sigma-Aldrich, St. Louis, MO, USA).

Cultivation and oxygen concentration measurements were conducted under standard culture conditions in a humidified atmosphere containing 5% CO_2 and 18.6% O_2 at 37°C. No media exchange was conducted during the measurements.

Non-invasive Oxygen Concentration Measurement at Cell Monolayer

The VisiSens TD camera system (PreSens, Regensburg, Germany) was employed to monitor the oxygen concentration at the cell layer. The setup of the VisiSens TD camera system is presented in **Figure 1A**. Images were taken every hour for a period of 96 h. The VisiSens TD system works in conjunction with the commercially available, biocompatible, planar and self-adhesive oxygen-sensitive foil SF-RPsSu4 (PreSens, Regensburg, Germany).

This sensor exploits a fluorescence optical sensing scheme It contains an oxygen sensitive dye which reversibly interacts with the analyte via dynamic quenching (Wang and Wolfbeis, 2014; Wolff et al., 2019) and changes its phosphorescence intensity. Furthermore, the sensor foil includes an analyte insensitive reference dye. Both dyes are simultaneously excited via an LED lamp mounted on the VisiSens TD camera detector. The camera

detector records both emitted luminescence signals (red emission from the indicator and green emission from the reference dye) spectrally separated in its RGB color channels. Each recorded color pixel contains the local indicator and reference signal and thereby allows for ratiometric 2D RGB imaging (Tschiersch et al., 2012). The obtained set of images can be loaded into the software ScientifiCal (PreSens, Regensburg, Germany) and the color recorded to each pixel is converted to air saturation (%) by a two point calibration step (0% and 100% air saturation).

The calibration curve for this system follows an adapted Stern-Volmer (Klimant et al., 1995).

$$\frac{Io}{I} = \frac{Ro}{R} = \frac{\tau o}{\tau} = \left(\left(\frac{A}{1 + ksv^{*}pO2}\right) + (1 - A)\right)^{-1}$$

The written equation describes decay time (τ), intensity (I), intensity-ratio (R) in analogy, the index 0 describes the time, intensity or ratio at 0% O_2 (calibration point at 0% air saturation)

The sensor constants to mathematically describe the exact behavior of the oxygen dependent response curve are factory calibrated for the material. The non-linearity is a fixed material property of the sensing material (represented by parameter A). The value A for the used SF-RPSu4 oxygen sensor foil is give as 0.82. The two-point user calibration for 0 and 100% air saturation alongside with the factory calibrated sensor constants allow for precise and accurate determination of oxygen with these sensors.

For the measurement, the SF-RPSu4 sensors were cut manually to a diameter of 10 mm and glued to the bottom of the wells of a 48 well plate (Eppendorf AG, Hamburg, Germany). The SF-RPSu4 sensors are commercially available with biocompatible self–adhesive backside. The glue is a pressure sensitive adhesive that requires no curing time nor waiting time before the sensors are applied. One-time incubation for 30 min with 70% ethanol was conducted for disinfection of the sensors. Afterwards, ethanol was aspirated and the sensor foils were allowed to rest for 30 min to ensure the evaporation of the remaining ethanol. Subsequently, sensors were washed twice with PBS (Sigma-Aldrich, St. Louis, MO, USA). Conditioning of the sensor foils was performed by 1-h incubation with cell culture medium at 37°C to enhance cell adhesion as suggested by the manufacturer. A total of 7×10^4 A549 cells/cm^2 were seeded on the attached sensors in triplicate.

Triplicates of wells containing only the sensor foils and cell culture medium were included as negative controls. Two single wells equipped with SF-RPSu4 sensors were used for a two-point calibration (0 and 100% O_2). For the 0% O_2 calibration, a solution of 5% sodium sulfite (Na_2SO_3) was prepared. The oxygen dissolved in the cell culture medium is consumed by reacting with the sodium sulfite to form sodium sulfate (Na_2SO_4). Oxygen saturated cell culture medium was added in the second well to obtain the 100% air saturation calibration point (equivalent to 20.95% O_2).

The cell culture plate was mounted on the VisiSens immediately after cell seeding and images were taken every hour during 96 h. All the images taken from the same experiment were loaded to the software VisiSens ScientifiCal (PreSens, Regensburg, Germany) as one single series (stack) of images. Noise reduction was applied with the standard value of 20 simultaneously to all the images from the series and all times images were processed in the same way. The noise reduction function is a color threshold that discards all pixels from the measurement that show too low intensity values. These noise filtered pixels represent the areas where no sensor is present in the recorded field of view, so that no fake pixels were taken into account for calculation. Calibration was performed by assigning the 0% O_2 and 100% air saturation references values to the wells containing the respective calibration solutions. A Z-profile tool was employed to manually select the region of interest (ROI) directly on the wells containing the cells seeded on the SF-RPsSu4 sensor foils. This tool allows the determination of the average value of air saturation from each recorded pixel within the selected ROI per image. Values expressed as air saturation percentages were converted to oxygen saturation considering that 100% air saturation equals 20.95% oxygen saturation at 37°C.

Non-invasive Oxygen 3D Gradient Measurement

The resin YOE-Microflu 365 (Miicraft, Burms, Germany) was utilized for producing the 3D printed ramps with the use of the MiiCraft DLP 3D printer (Ray Optics, Taiwan). The ramps were designed to be 8.3 mm long reaching a maximum height of 3.3 mm above the bottom of the well (**Figures 1B,C**). With a surface area on the base of the ramp of 54 mm^2, the ramp occupies 27% of the surface area available for cell growth in a well from a 24 well plate.

The VisiSens TD camera system was employed to investigate the 3D oxygen gradient formation during 96 h of culture with a time interval of 1 h between two measurements. The SF-RPsSu4 sensor foils were cut by hand and attached to the rectangular-shaped surface of the ramp. The ramps were randomly positioned at the bottom of each well prior cell seeding. Sterilization was conducted as described above for the monolayer experiments.

A total of 5.0×10^4; 1.0×10^5 and 1.5×10^5 A549 cells were seeded per well in a 24 well plate (Eppendorf AG, Hamburg, Germany) in triplicate. This is, 0.35×10^5, 0.68×10^5, and 1.02×10^5 cells/cm^2, respectively considering the surface area occupied by the ramp inside the culture well. The final volume of cell culture medium in each well was 1 ml, leaving the ramps totally submerged.

The cell culture plate containing the ramps with the attached sensor foils, calibration solutions, and cells was mounted on the VisiSens immediately after seeding and images were taken every hour during 96 h.

Another three 24 well plates were prepared as described before and used for obtaining the cell count for three time points of interest; 48, 72, and 96 h. Manual cell count was performed by using a Neubauer chamber using the exclusion dye Trypan blue.

For the 3D oxygen gradient measurement, the images corresponding to the time points 48, 72, and 96 h were selected. A lineal profiling tool was employed to measure the oxygen concentration values across the length of the sensor foil per time point. For this, triplicates of a profiling line were drawn from the

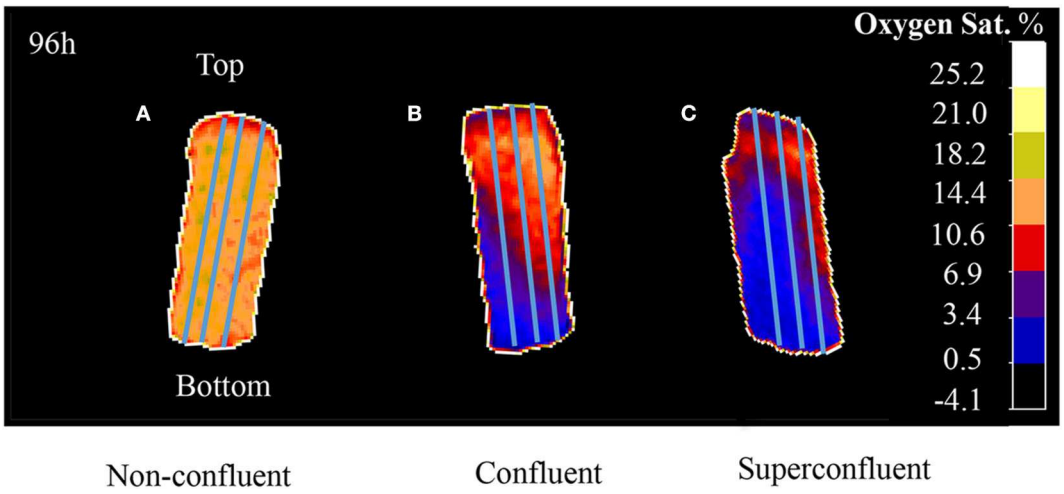

FIGURE 2 | A profiling tool was use to draw triplicates of a line across the entire length of the sensor (from the bottom to the top of the ramp). VisiSens ScientifiCal output for three different degrees of culture confluence: **(A)** subconfluent, **(B)** confluent, and **(C)** superconfluent after 96 h of culture. Initial cell densities used were 3.5 $\times$ 10^4 cells/cm^2 for subconfluent, 6.8 $\times$ 10^4 cells/cm^2 for confluent, and 1.02 $\times$ 10^5 cells/cm^2 for superconfluent cultures.

bottom to the top of each ramp (**Figure 2**) for each one of the selected time points.

Determination of the Oxygen Consumption Rate

Oxygen consumption rate (OCR) was determined after 96 h of culture for those wells where a theoretical linear oxygen gradient was observed to be formed. That is, where the measured oxygen gradient fits a straight line with $R^2 > 0.9$. According to Fick's first law of diffusion, a solute will move from high concentration zones to low concentration zones with a magnitude proportional to its concentration gradient. The mathematical equivalent to Fick's first law is the equation $J = -D\frac{\Delta C}{\Delta x}$ where "J" represents the flux of a solute, "D" the diffusion coefficient of the solute in the mixture and ($\frac{\Delta C}{\Delta x}$) the spatial concentration gradient of the solute determined experimentally.

During cell culture, normal cell respiration at the bottom of the wells creates a low oxygen concentration zone compared to the surface of the well. This results in a concentration gradient that, assuming steady state conditions, will be the only driving force for the flux of oxygen from the top to the bottom of the well (Pettersen et al., 2005).

In our experiments, the absence of movements or turbulences in the cell culture media and the constant atmospheric pressure inside the incubator implies a steady state-like condition, where the diffusion of oxygen to the cell layer is driven only by the oxygen consumption rate of the cells in culture Therefore, it is safe to assume that the flux of oxygen will be equal to the respiration rate of the cells in culture (Pettersen et al., 2005). The diffusion coefficient of oxygen (D) in cell culture medium (9% salinity and 37°C) is ~3.37 $\times$ 10^{-5} cm^2/s (Pettersen et al., 2005). Cell count after 96 h of culture was determined from one of the plates prepared for this propose as described before.

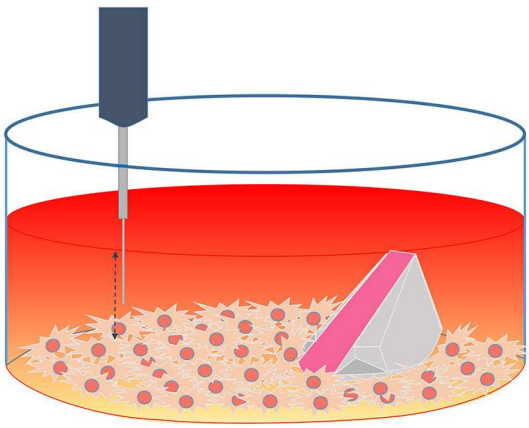

FIGURE 3 | Schematic representation of the experimental set up using both techniques (ramp and microsensor) inside a confluent cell culture well.

Oxygen Profiling With Fiber-Based Needle Type Microsensor

An optical fiber-based needle type sensor PM-PSt7 (PreSens, Regensburg, Germany) mounted on a motorized Automated Micromanipulator (AM, PreSens, Regensburg, Germany) was employed for measuring the oxygen concentration at different heights inside one of the confluent cell culture well after 96 h of measurements with the ramps and the VisiSens TD system (**Figure 3**).

Setting up the PM-PSt7 implies that the culture plate remains open during the measurements. To prevent contamination and media evaporation, the wells were covered with a plate seal foil Microseal "B" adhesive seal (Bio-Rad Laboratories, Germany) and perforated with the needle type sensor. The diameter of the

optical fiber of the PM-PSt-7 probe is <50 um and the diameter of the needle is 0.8 mm.

The micromanipulator was set to move the PM-PSt7 sensor through the cell culture medium along the z-axis with a step size of 500 μm. Sets of six measurements with an interval of 10 s between measurements were performed at six different altitudes. At each altitude, the micromanipulator stopped its movement and, after a resting time of 30 s, the set of measurement for that altitude was performed. The resting time of 30 s prior starting the measurement at each altitude was included to avoid measurements in the presence of turbulences created by the movement of the microsensor through the cell culture medium. Data were collected by means of the software PreSens Profiling Studio (PreSens, Regensburg, Germany).

The sterilization of the PM-Pst7 micro sensor was conducted by incubation in 70% ethanol for 30 min fallowed by washing steps with PBS.

Statistical Analysis

The statistical analysis was performed by means of the GraphPad Prism 8.3.0 software (GraphPad Software, Inc., La Jolla, USA). For comparison of the oxygen profiles, a minimum of $N = 3$ measurements were considered. Two-way ANOVA associated with Tukey's multiple comparison test was selected for evaluation of the oxygen profiles at different time points per cell density. Linear regression was performed for the oxygen gradients obtained after 96 h of culture for the three different cell densities.

RESULTS

Non-invasive Oxygen Concentration Measurement at Cell Monolayer

Oxygen depletion at the cell layer was monitored by means of the VisiSens system during 96 h, starting immediately after cell seeding. **Figure 4A** shows a preview from the VisiSens's output once noise reduction and calibration were applied for three different time points of interest; 48, 72, and 96 h. As shown in **Figure 4B**, oxygen concentration at the cell layer steadily decreased from 16 to 3% during the time in culture. The obtained data confirm that during cultivation, oxygen concentration at the cell layer decreases as a result of normal respiration.

Non-invasive Oxygen 3D Gradient Measurement

The 3D oxygen gradient in the cell culture medium column over the cell layer was effectively measured in a non-invasive manner by means of the ramps and the VisiSens TD camera system. **Figure 5** shows a preview of the output from the VisiSens TD system for two different time points, 24 and 96 h after seeding. The obtained oxygen profiles (the oxygen concentration as function of the height of the cell culture medium column above the cell layer) for each initial cell density and three time points after seeding are shown on **Figure 6**. The acquired profiles show clear differences in the oxygen distribution within the cell culture medium column between each cell density per time point. Significant differences ($p < 0.0001$) were observed between the oxygenation values

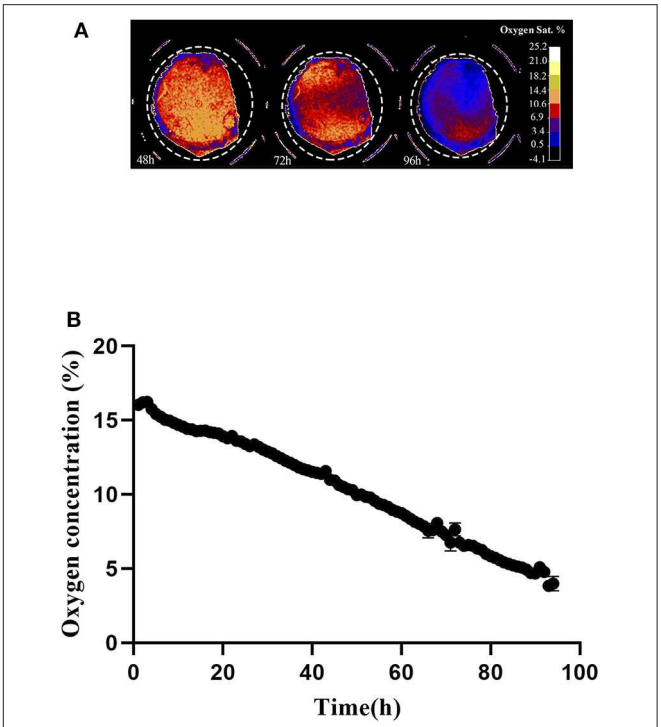

FIGURE 4 | (A) Output from the VisiSens ScientificCal software after calibration and noise reduction. 7×10^4 cells where seeded in a 48 well plate containing the SF-RPsSu4 sensors attached to the bottom of the wells. Images were taken every hour for a period of 96 h. Time points 48, 72, and 96 h are shown. Dashed circle indicate the selection of the ROI. **(B)** Z-Profile of the oxygen concentration measured at the cell layer by means of the VisiSens TD system and the SF-RPsSu4 sensor foils attached to the bottom of the well. Initial cell density 7×10^4 cells/cm^2.

measured at different heights in the cell culture medium column for each cell density at the three selected time points; 48, 72, and 96 h. An overview of the differences in the oxygen distribution at the top and the bottom of the ramps as well as the obtained OCR for the cells after 96 h in culture are summarized in **Table 1**. The OCR values obtained after 96 h of culture were 96.3 ± 12.53 and 107 ± 10.17 fmol/h/cell, respectively for the wells with higher cell density, where a theoretically linear oxygen gradient ($R^2 > 0.9$) was observed. The oxygen gradient measured for the wells with the lowest initial cell count after 96 h of culture rendered values of $R^2 < 0.7$ and therefore, accurate calculation of OCR was not possible for these wells.

After 48 h of culture, significant differences ($p < 0.0001$) were observed for the oxygen values measured, from the bottom to an approximated height of 2.2 mm over the cell layer between the wells seeded with 5×10^4 cells and those with higher cell densities. Meanwhile, only significant differences ($p < 0.0001$) were found for the measurements from the bottom to a height of 1.5 mm between the wells seeded with 1×10^5 and 1.5×10^5 cells (**Figure 6A**). For the next time point of 72 h, significant differences ($p < 0.0001$) were measured for the oxygenation values from the bottom to an approximate height of 1.7 mm

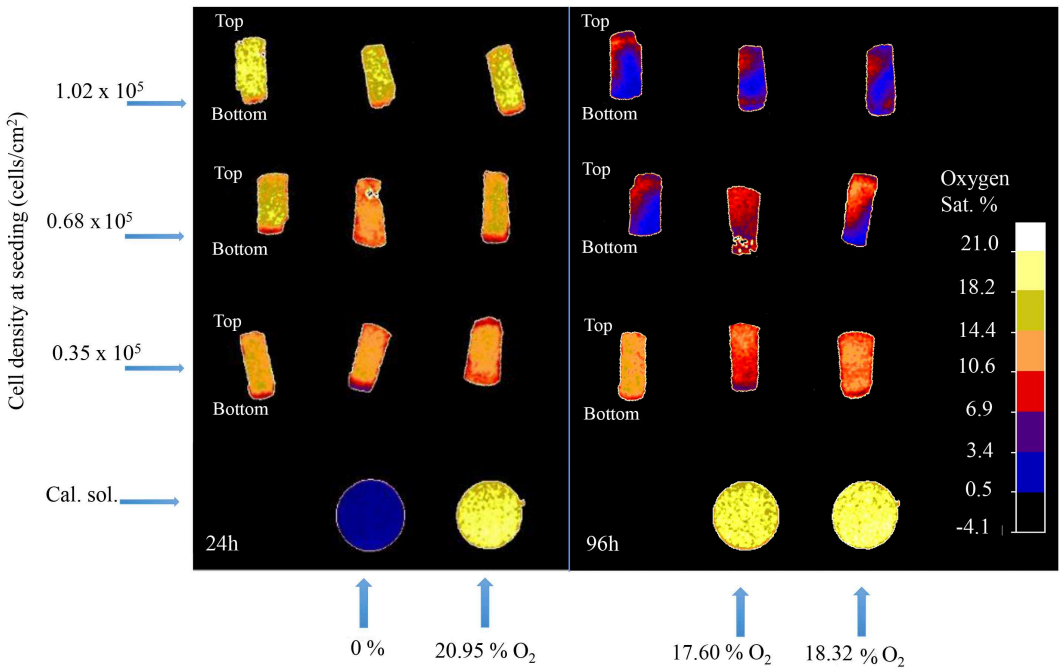

FIGURE 5 | Software output for two different time-points after seeding; 24 and 96 h. Rounded shaped signals corresponds to the calibration solutions. Rectangular shaped signals correspond to the sensors attached to the surface of the ramps.

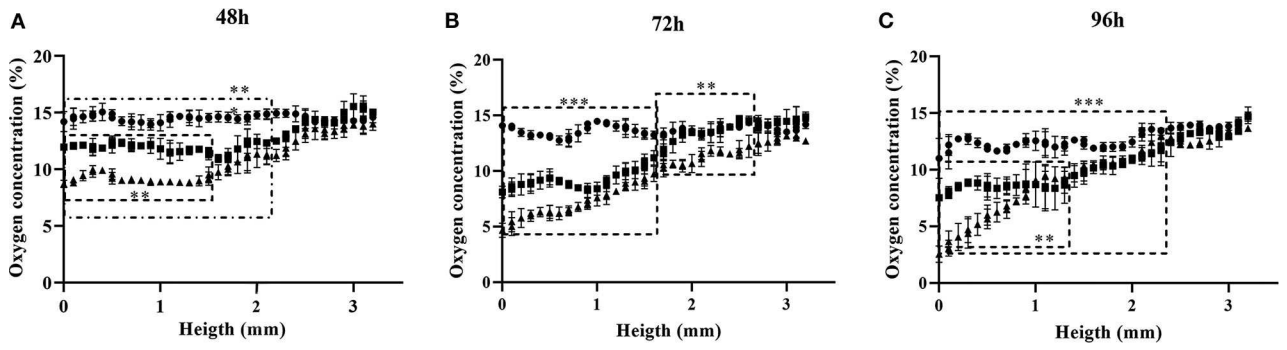

FIGURE 6 | Oxygen profiles obtained for three different cell densities at time points 48 **(A)**, 72 **(B)**, and 96 h **(C)** after seeding. Seeding densities are: • 3.5 × 10^4 cells/cm^2; ■ 6.8 × 10^4 cells/cm^2; ▲ 1.02 × 10^5 cells/cm^2. Significant differences ($p < 0.0001$) between profiles are delimited.

between the three different cell densities. From this height and to the top of the ramp, only significant differences were found between the wells seeded with the higher cell count of 1.5 × 10^5 cells and the other two cell densities (**Figure 6B**). Ninety-six hours after seeding, significant differences ($p < 0.0001$) for the oxygen values measured at each point below a height of 2.5 mm from the bottom of the well were found between the wells seeded with the lower cell count and the other two (higher) cell densities. At this point, the wells seeded with 1 × 10^5 and 1.5 × 10^5 cells, reported significant differences ($p < 0.0001$) from the bottom to a height of 1.2 mm over the cell layer. Above this height to the top of the ramp, the profiles obtained for both cell densities were indistinct (**Figure 6C**).

Oxygen Profiling With Fiber-Based Needle Type Microsensor

The PM-PSt7 sensor was employed to measure the oxygen profile after 96 h of measurement with the ramps and the VisiSens TD system. Oxygenation values at the top and the bottom of the well-obtained with the two techniques are summarized in the **Table 2**. No significant differences were found between the obtained profiles from the two techniques.

DISCUSSION

A complex system of organs and tissues work together *in vivo* to finely tune oxygen concentration and distribution across

TABLE 1 | Oxygen concentration (%) during time in culture.

Initial cell density ($\times 10^5$ cells/cm^2)		48 h	72 h	96 h	Cell density at 96 h ($\times 10^5$ cells/cm^2)	R^2 (top to bottom linearity)	OCR at 96 h of culture (fmol/h/cell)
0.35	Top	14.58 ± 0.49	14.18 ± 0.37	14.8 ± 0.74	1.57 ± 0.32	0.66	–
	Bottom	14.02 ± 0.88	13.28 ± 0.28	11.01 ± 1.21			
	Difference	0.56	0.9	3.79			
0.68	Top	15.04 ± 0.23	14.89 ± 0.42	14.69 ± 0.39	2.8 ± 0.49	0.91	96.3 ± 12.53
	Bottom	11.95 ± 0.22	8.10 ± 0.52	7.52 ± 0.12			
	Difference	3.09	6.79	7.17			
1.02	Top	14 ± 0.57	12.91 ± 0.25	13.66 ± 0.1	3.42 ± 0.67	0.93	107 ± 10.17
	Bottom	8.71 ± 0.32	4.67 ± 0.63	2.53 ± 0.71			
	Difference	5.29	8.24	11.13			

Comparison of the pericellular oxygen concentration (base of the ramp) and the concentration at the top of the ramp (3.3 mm from the base) for A549 cells cultured at 18.5% oxygen in 24 well plates. Three initial cell densities were seeded (n = 3). One plate was used for the oxygen measurements and one was used to determine the cell count at each time point. After 96 h of culture, linear regression was performed and oxygen consumption rates (OCR) was calculated from the obtained oxygen gradients with $R^2 > 0.9$.

TABLE 2 | Comparison of the oxygen gradient (%) obtained by two different techniques.

	VisiSens + 3D printed ramp	Microsensor PSt7
Top	12.9 ± 0.39	10.15 ± 0.49
Bottom	7.52 ± 0.17	6.2 ± 0.9
Difference	5.3	4.2

After 96 h of measurement with the VisiSens TD camera system, the micro sensor PM-PSt7 was employed to measure the oxygen gradient in one of the confluent wells previously studied by means of our ramp-based technique. n = 3.

temporal and spatial scales (Wittenberg and Wittenberg, 1989; Saltzman et al., 2003; Al-Ani et al., 2018). On the other hand, diffusive forces mainly driven by the oxygen consumption rate of the cells and the diffusion properties of cell culture media are the major regulatory mechanism for oxygenation during cell culture.

The limitation of oxygenation in cell culture stands as one of the most underappreciated problems of basic and translational research (Place et al., 2017; Ast and Mootha, 2019) potentially having a direct impact not only on the experimental results but in their reproducibility (Begley and Ellis, 2012; Begley and Ioannidis John, 2015; Karp, 2018). This is especially relevant in the fields of regenerative medicine and tissue engineering where so much effort is focused on the design of materials and scaffolds to provide with the adequate oxygen supply to the newly formed tissue (Fiedler et al., 2014).

The "conventional" technique for oxygen sensing involving the VisiSens TD camera system and the SF-RPSu4 sensor foils at the bottom of the wells proved during our studies, to be a suitable tool for non-invasive measurements of the variation in the oxygen concentration close to the surface of the cells. Nonetheless, no relevant information about 3D oxygen gradient formation in the cell culture medium column above the cell layer could be obtained with the conventional set up.

Similar limitations would be observed using other examples of the current commercially available technology for oxygen sensing. For instances, the RED eye patch oxygen sensor works in combination with the Neofox fluorometer and a fiber optic probe to measure the concentration of oxygen in gas, as well as dissolved oxygen in solutions. The output of this system provides a single oxygen concentration values per measurement. This feature makes this system suitable for pharmaceutical and medical application, such as blood bag analysis or bioprocess control. Nevertheless, it make it inadequate when it comes to measuring oxygen gradients in cell culture. Furthermore, multiplexing of RED eye patches for simultaneous measurements would be limited to low numbers of sensors due to the involvement of fiber optic probes per sensor foil necessary for the measurements (Molina et al., 2014; Gandolfo et al., 2016).

With our developed method, it was possible to assess how the oxygen tension at the cell layer decreases as a function of cell density and time in culture in a non-invasive fashion. The absence of moving parts in our set up ensures that the oxygen distribution inside the cell culture well is due only to the cellular respiration and the oxygen diffusion through the cell culture medium. Medium exchange was not conducted to avoid external disturbances to the oxygen distribution in the stagnant cell culture medium column. The cell line A549 was selected for this study because of its wide range of application as a model in cancer research and lung diseases (Schnitzer et al., 2009; Jeong et al., 2017; Camerlingo et al., 2019). Moreover, according to previous studies, the expansion and proliferation of this cell line does not appear to be significantly inhibited by cell contact when cultured in DMEM medium (Cooper et al., 2016). Thus, high cell density culture can be easily achieved in relatively short periods of time (Cooper et al., 2016).

Attaching the SF-RPSu4 sensor foil on the 3D printed ramp effectively allowed the interaction between the sensor and the oxygen molecules at different height at the cell culture medium column. The utilization of the VisiSens TD camera system permitted the non-invasive real-time oxygen monitoring from the moment of seeding to the end of the experiment 96 h later. Few differences in the oxygen distribution inside the wells with lower cell count after 96 h of culture were observed. For these wells, oxygen was found to range from 11 to 15% from the bottom to the top of the ramp at the latest time point. Nevertheless, it is worth noticing that the oxygen tension measured at the bottom of

the wells after 96 h of culture (11%) is considerably lower than the oxygen concentration in the gas phase of the incubator (18.5%).

For the wells seeded with 1×10^5 and 1.5×10^5 cells, respectively, significant differences ($p < 0.0001$) between the oxygen distributions within the cell culture medium column were also observed. These differences were especially noticeable during the first 72 h of culture when the biggest differences in cell density between the wells with different initial cell density are to be observed. However, by the end of the measurements, oxygen profiles for both cell densities were found to be very similar. Only significant differences were registered within a distance of 1 mm from the bottom of the well. This is expected to be related to the cell count at each time point. For instance, at 72 h of culture the wells seeded with 1.5×10^5 cells (superconfluent by time point 96 h) achieved 35% higher cell density than those seeded with 1×10^5 cells (confluent by time point 96 h). Meanwhile, after 96 h of culture, the difference between cell densities was only of 18%. This is to be expected as it is known that highly dense cultures tend to reduce expansion rate when nutrients in the culture media are depleted (Vander Heiden et al., 2009; Yuan et al., 2013)

The OCR for the A549 cell line calculated using the obtained oxygen gradients and cell count after 96 h of culture from the highly confluent and superconfluent wells show no significant differences and are very similar to the OCR values reported in the literature for this cell line, which is 97 fmol/h/cell (Wu et al., 2007; Wagner et al., 2011). OCR determined from the gradient measured in the subconfluent wells was not considered due to the lower R^2 values. This could be related to the fact that, during cultivation of low cell densities cultures, the oxygen consumption by the cell monolayer tends to occur just fast enough to barely surpass the oxygen ability to diffuse into the cell culture medium and to the bottom of the well (Place et al., 2017; Al-Ani et al., 2018). Based on this, we hypothesize that, even when the oxygen concentration at the bottom of the well was registered to be lower than the oxygen concentration of the gas phase, the oxygen consumption rate of the cell monolayer in low cell density culture was not sufficient to promote a clear tendency to the formation of a linear gradient of oxygen concentration, hence, rendering lower values of R^2.

The statistical analysis of the comparison between the oxygen gradient measured with the 3D printed ramps and the PM-PSt7 sensor after 96 h of culture showed no significant differences. Interestingly, oxygen concentration closer to the surface of the cell culture medium was measured to be 12.9% when employing the VisiSens technique with the 3D printed ramps. Meanwhile, a value of 10.15% was obtained with the PM-Pst7 microsensor (**Table 2**). Such a difference of 3 percentage units between the obtained oxygen concentration values from each technique was reduced to only 1 percentage unit at the bottom of the well and closer to the cell layer. The lower oxygen concentration at the surface of the cell culture medium measured with the PM-Pst7 microsensor could be related to the utilization of the plate seal foil Microseal "B" to cover the cell culture well during the oxygen measurement with the microsensor. This foil was used to prevent evaporation of the cell culture medium and minimize the risk of contamination during the measurements. Yet, the low permeability to oxygen declared by the manufacturer for the Microseal "B" could have created a "closed environment" during the measurements with the microsensor that modified the oxygen concentration in the gas phase and the surface of the cell culture medium. This possible change in the atmosphere of the cell culture well was not expected to affect the oxygen concentration closer to the cells in culture during the oxygen measurement with the microsensor due to the fact that the required time for performing the necessary measurements, does not exceed 30 min and the equilibration of oxygen in culture medium is known to be a slow process that requires significantly longer time periods (Allen et al., 2001; Place et al., 2017).

The obtained result validates the use of our 3D printed ramps as a suitable tool for measuring oxygen concentration at different heights at the cell culture medium column. Moreover, in contrast to the microsensor measurements, our ramps allowed the study of several culture wells simultaneously while keeping sterile conditions during the measurement. Furthermore, our non-invasive, optical sensor foil based technique for oxygen measurement during cell culture, does not involve any moving parts or cables and allowed the study of the complete gradient formation, from the bottom of the cell culture well to the surface of the well with micrometric resolution. The use of the SF-RPSu4 sensor foils has been validated since more than 10 years of research and reported in over a hundred scientific publications (Kellner et al., 2002; Faget et al., 2013; Hofmann et al., 2013; Maisch et al., 2019; Wolff et al., 2019). The self-adhesive sensor foils can be attached to the ramps very easily. The dye molecules inside the sensitive layer of the SF-RPSu4 sensor foil are incorporated in a polymer matrix and have no contact to the washing solutions, therefore cleaning of both, ramps and sensor foils can be conducted with ethanol 70% prior the beginning of the measurements. Furthermore, the sensor's response is fully reversible and shows no signal hysteresis, which means that these sensors can be used repeatedly. Nevertheless, a check of the calibration data is performed after ∼10,000 images.

Additionally, the sensor foils used on the ramps comprise a hydrophobic polymer surface material that hampers cell attachment without prior treatment. This way the growth of undesired biofilms on the sensor that could lead to biofouling is prevented. Besides, the ramp puts the sensor in an angle to the cell culture bottom of the well plate, which makes it more likely for biological material to sediment to the bottom and attach there and not to the foil on the ramp. Not to mention that adherent cells of a size of 10–15 μm (A549 cells) cannot grow up the ramps which has a size of several millimeters.

This makes our system a suitable tool as first solution to easily check a protocol over the whole time period of incubation with respect to sufficient/adequate oxygen supply. Moreover, due to the simplicity of our setup, oxygen gradient measurements are possible in any standard cell culture plate (96, 48, 24, 12, 6 well plate) allowing the study of oxygenation during cell culture in different conditions (e.g., difference in medium volume, height of column medium and cell concentration) while monitoring a number or even all wells of a cell culture plate simultaneously. This feature allows, not only to ensure that oxygenation conditions are replicated while scaling cell

culture/experiments from one plate to another of different size, but it also improves the reproducibility of the experiments by providing a tool to easily report the oxygenation condition at the moments of the performed assays.

During our study, we have used the ramps with the cell line A549 as proof of concept. Nevertheless, we expect our system to be reliable when applied to a different cell line. Of course, cell lines with lower growth rate and/or metabolic activity are expected to induce less steep gradients during culture in the same period than cell lines with higher growth rates (assuming same initial seeding density). Similarly, cell lines with low metabolic activity may need higher cell densities or longer time in culture to deplete the oxygen near the surface of the cells faster than the diffusion rate of the oxygen to the bottom of the well. Answering this kind of questions is one of the applications for the developed technique.

Furthermore, future applications for our technique could involve the adaptation of other types of sensor foils (e.g., pH and CO_2) that are compatible with the VisiSens TD camera system (Blossfeld et al., 2013; Keil et al., 2017) to the developed ramps together with the SF-RPSu4 sensor foil. The development of a multimodal sensor tool to study in a non-invasive manner the gradient and distribution of not only oxygen, but CO_2 and pH, could provide a higher throughput analysis of cell respiration and metabolic activity. Tracking of the CO_2 released per unit of O_2 consumed could allow the determination of the respiratory quotient while the monitoring of the pH allows the accurate quantification of the dissolved CO_2 (Keil et al., 2017),

Nonetheless, an inconvenience of utilizing the ramps for oxygen sensing during cell culture is the 54 mm^2 surface area occupied by the ramp inside the culture well. This means that, from the 200 mm^2 available for cell growth in a 24 well plates, only 146 mm^2 are open for the cells. This needs to be considered when calculating the cell density per cm^2. Optimization in terms of design of the ramp's geometry should be conducted to reduce the total area in contact with surface of the wells.

CONCLUSIONS

With the present study we aimed to the development of a simple, cost-effective technique for non-invasive 3D oxygen gradient measurement during mammalian cell culture. For this, we created a 3D printed ramp to use in conjunction with the optical sensor foil SF-RPSu4 and the VisiSens TD camera system. With our developed technique, it was possible to measure the oxygen gradient formation during cell culture of A549 cells at different cell densities simultaneously in a non-invasive way. The data gathered from the oxygen distribution inside the cell culture medium column was used to calculate the oxygen consumption rate of the cells in culture and the obtained value matches those reported in the literature. Thus, our optical sensor foil-based technique could be utilized for characterization of oxygen consumption rates of different cells types. Furthermore, the 3D oxygen gradient measured with the ramps was comparable to that measured with the needle type microsensor. Additionally, our technique was found to be unique in its ability to monitor simultaneously the 3D oxygen gradient formation in several wells of a culture plate. Future applications for our 3D printed ramps could as well involve testing other different sensor foils, such as pH or CO_2 optical sensor foils.

DATA AVAILABILITY STATEMENT

The raw data supporting the conclusions of this article will be made available by the authors, without undue reservation.

AUTHOR CONTRIBUTIONS

CP performed all the experiments, acquired the data, performed the data analysis, and wrote the first version of the manuscript. GL, RM, and MSG designed and produced the ramps, participated in the study design, and supported all the experiments performed. EB participated in the experimental design, data analysis, and statistics. MvG participated in the experimental design and statistical analysis, directed the study, and critically revised the manuscript. All authors contributed to the article and approved the submitted version.

FUNDING

The research presented in this manuscript was funded by the Bayerische Forschungsstiftung with the grant "HAPPIHYPO" (grant number−1163-15).

ACKNOWLEDGMENTS

CP is grateful to the German Academic Exchange Service (Deutscher Akademischer Austauschdienst DAAD) for providing him with a research scholarship number 57299294. The authors thank Jasia King (cBITE, MERLN Institute, Maastricht University) for her assistance with mathematical analysis and Sebastian Eggert (Queensland University of Technology) for his assistance with the microsensor setup.

REFERENCES

Al-Ani, A., Toms, D., Kondro, D., Thundathil, J., Yu, Y., and Ungrin, M. (2018). Oxygenation in cell culture: critical parameters for reproducibility are routinely not reported. *PLoS ONE* 13:e0204269. doi: 10.1371/journal.pone.0204269

Allen, C. B., Schneider, B. K., and White, C. W. (2001). Limitations to oxygen diffusion and equilibration in *in vitro* cell exposure systems in hyperoxia and hypoxia. *Am. J. Physiol. Lung Cell. Mol. Physiol.* 281, L1021–L1027. doi: 10.1152/ajplung.2001.281.4.L1021

Ast, T., and Mootha, V. K. (2019). Oxygen and mammalian cell culture: are we repeating the experiment of Dr. Ox? *Nat. Metabol.* 1, 858–860. doi: 10.1038/s42255-019-0105-0

Begley, C. G., and Ellis, L. M. (2012). Raise standards for preclinical cancer research. *Nature* 483, 531–533. doi: 10.1038/483531a

Begley, C. G., and Ioannidis John, P. A. (2015). Reproducibility in Science. *Circ. Res.* 116, 116–126. doi: 10.1161/CIRCRESAHA.114.303819

Blossfeld, S., Schreiber Cm Fau-Liebsch, G., Liebsch G Fau-Kuhn, A. J., Kuhn Aj Fau-Hinsinger, P., and Hinsinger, P. (2013). Quantitative imaging of rhizosphere pH and CO2 dynamics with planar *optodes*. *Ann. Bot.* 112, 267–276. doi: 10.1093/aob/mct047

Camerlingo, R., Miceli, R., Marra, L., Rea, G., D'agnano, I., Nardella, M., et al. (2019). Conditioned medium of primary lung cancer cells induces EMT in A549 lung cancer cell line by TGF-ß1 and miRNA21 cooperation. *PLoS ONE* 14:e0219597–e0219597. doi: 10.1371/journal.pone.0219597

Cooper, J. R., Abdullatif, M. B., Burnett, E. C., Kempsell, K. E., Conforti, F., Tolley, H., et al. (2016). Long Term culture of the A549 cancer cell line promotes multilamellar body formation and differentiation towards an alveolar type II pneumocyte phenotype. *PLoS ONE* 11:e0164438. doi: 10.1371/journal.pone.0164438

Demuth, C., Varonier, J., Jossen, V., Eibl, R., and Eibl, D. (2016). Novel probes for pH and dissolved oxygen measurements in cultivations from millilitre to benchtop scale. *Appl. Microbiol. Biotechnol.* 100, 3853–3863. doi: 10.1007/s00253-016-7412-0

D'Ippolito, G., Diabira, S., Howard, G. A., Roos, B. A., and Schiller, P. C. (2006). Low oxygen tension inhibits osteogenic differentiation and enhances stemness of human MIAMI cells. *Bone* 39, 513–522. doi: 10.1016/j.bone.2006.02.061

Faget, M., Blossfeld, S., Von Gillhaußen, P., Schurr, U., and Temperton, V. (2013). Disentangling who is who during rhizosphere acidification in root interactions: combining fluorescence with optode techniques. *Front. Plant Sci.* 4:392. doi: 10.3389/fpls.2013.00392

Fiedler, T., Belova, I. V., Murch, G. E., Poologasundarampillai, G., Jones, J. R., Roether, J. A., et al. (2014). A comparative study of oxygen diffusion in tissue engineering scaffolds. *J. Mater. Sci.* 25, 2573–2578. doi: 10.1007/s10856-014-5264-7

Gandolfo, M. J., Kyle, A. H., and Minchinton, A. I. (2016). "Tissue discs: a 3D model for assessing modulation of tissue oxygenation," in *Oxygen Transport to Tissue XXXVII*, eds. C. E. Elwell, T. S. Leung, and D. K. Harrison (New York, NY: Springer), 169–175. doi: 10.1007/978-1-4939-3023-4_21

Hirao, M., Hashimoto, J., Yamasaki, N., Ando, W., Tsuboi, H., Myoui, A., et al. (2007). Oxygen tension is an important mediator of the transformation of osteoblasts to osteocytes. *J. Bone Miner. Metab.* 25, 266–276. doi: 10.1007/s00774-007-0765-9

Hofmann, J., Meier, R. J. Mahnke, A., Schatz, V., Brackmann, F., Trollmann, R., et al. (2013). Ratiometric luminescence 2D *in vivo* imaging and monitoring of mouse skin *oxygenation*. *Methods Appl. Fluoresc.* 1:045002. doi: 10.1088/2050-6120/1/4/045002

Ivanovic, Z. (2009). Hypoxia or *in situ* normoxia: The stem cell paradigm. *J. Cell. Physiol.* 219, 271–275. doi: 10.1002/jcp.21690

Jeong, J. Y., Ryu, J., Yoon, N. A., Kang, S., Seong, H., Fudhaili, A., et al. (2017). Abstract 109: Effects of trifluoperazine analogue on A549 human lung cancer cells. *Cancer Res.* 77:109. doi: 10.1158/1538-7445.AM2017-109

Karp, N. A. (2018). Reproducible preclinical research—is embracing variability the answer? *PLoS Biol.* 16:e2005413. doi: 10.1371/journal.pbio.2005413

Keil, P., Liebsch, G., Borisjuk, L., and Rolletschek, H. (2017). "MultiSense: a multimodal sensor tool enabling the high-throughput analysis of respiration," in *Plant Respiration and Internal Oxygen: Methods and Protocols*, ed K. Jagadis Gupta (New York, NY: Springer), 47–56. doi: 10.1007/978-1-4939-7292-0_5

Kellner, K., Liebsch, G., Klimant, I., Wolfbeis, O. S., Blunk, T., Schulz, M. B., et al. (2002). Determination of oxygen gradients in engineered tissue using a fluorescent sensor. *Biotechnol. Bioeng.* 80, 73–83. doi: 10.1002/bit.10352

Klimant, I., Meyer, V., and Kühl, M. (1995). Fiber-optic oxygen microsensors, a new tool in aquatic biology. *Limnol. Oceanogr.* 40, 1159–1165. doi: 10.4319/lo.1995.40.6.1159

Kuang, Y., and Walt, D. R. (2007). Detecting oxygen consumption in the proximity of Saccharomyces cerevisiae cells using self-assembled fluorescent nanosensors. *Biotechnol. Bioeng.* 96, 318–325. doi: 10.1002/bit.21092

Maisch, M., Lueder, U., Kappler, A., and Schmidt, C. (2019). Iron lung: how rice roots induce iron redox changes in the rhizosphere and create niches for microaerophilic Fe(II)-oxidizing bacteria. *Environ. Sci. Technol. Lett.* 6, 600–605. doi: 10.1021/acs.estlett.9b00403

Malda, J., Rouwkema, J., Martens, D. E., Le Comte, E. P., Kooy, F. K., Tramper, J., et al. (2004). Oxygen gradients in tissue-engineered Pegt/Pbt cartilaginous constructs: Measurement and modeling. *Biotechnol. Bioeng* 86, 9–18. doi: 10.1002/bit.20038

Molina, L. Thomas, G., Twahir, U., and Moomaw, E. W. (2014). Real-time kinetic studies of bacillus subtilis oxalate decarboxylase and ceriporiopsis subvermispora oxalate oxidase using luminescent oxygen sensor. *J. Biochem. Technol* 5, 826–831.

Nicolaije, C., Koedam, M., and Van Leeuwen, J. P. (2012). Decreased oxygen tension lowers reactive oxygen species and apoptosis and inhibits osteoblast matrix mineralization through changes in early osteoblast differentiation. *J. Cell. Physiol.* 227, 1309–1318. doi: 10.1002/jcp.22841

Pettersen, E. O., Larsen, L. H., Ramsing, N. B., and Ebbesen, P. (2005). Pericelullar oxygen depletation during ordinary tissue culturing, measured with oxygen microsensors. *Cell Prolif.* 38, 257–267. doi: 10.1111/j.1365-2184.2005.00345.x

Place, T. L., Domann, F. E., and Case, A. J. (2017). Limitations of oxygen delivery to cells in culture: an underappreciated problem in basic and translational research. *Free Radical. Biol. Med.* 113, 311–322. doi: 10.1016/j.freeradbiomed.2017.10.003

Randers-Eichhorn, L., Bartlett, R. A., Frey, D. D., and Rao, G. (1996). Noninvasive oxygen measurements and mass transfer considerations in tissue culture flasks. *Biotechnol. Bioeng.* 51, 466–478. doi: 10.1002/(SICI)1097-0290(19960820)51:4<466::AID-BIT10>3.0.CO;2-G

Rankin, E. B., Giaccia, A. J., and Schipani, E. (2011). A central role for hypoxic signaling in cartilage, bone, and hematopoiesis. *Curr. Osteoporos. Rep.* 9, 46–52. doi: 10.1007/s11914-011-0047-2

Renger, G., and Hanssum, B. (2009). Oxygen detection in biological systems. *Photosyn. Res.* 102:487. doi: 10.1007/s11120-009-9434-2

Saito, T., Wu, C.-C., Shiku, H., Yasukawa, T., Yokoo, M., Ito-Sasaki, T., et al. (2006). Oxygen consumption of cell suspension in a poly(dimethylsiloxane) (PDMS) microchannel estimated by scanning electrochemical microscopy. *Analyst* 131, 1006–1011. doi: 10.1039/b600080k

Saltzman, D. J., Toth, A., Tsai, A. G., Intaglietta, M., and Johnson, P. C. (2003). Oxygen tension distribution in postcapillary venules in resting skeletal muscle. *Am. J. Physiol. Heart Circ. Physiol.* 285, H1980–H1985. doi: 10.1152/ajpheart.00322.2002

Schnitzer, S. E., Weigert, A., Zhou, J., and Brüne, B. (2009). Hypoxia enhances sphingosine kinase 2 activity and provokes sphingosine-1-phosphate-mediated chemoresistance in A549 lung cancer cells. *Mol. Cancer Res.* 7:393. doi: 10.1158/1541-7786.MCR-08-0156

Sitkovsky, M., and Lukashev, D. (2005). Regulation of immune cells by local-tissue oxygen tension: HIF1α and adenosine receptors. *Nat. Rev. Immunol.* 5, 712–721. doi: 10.1038/nri1685

Strovas, T. J., Mcquaide, S. C., Anderson, J. B., Nandakumar, V., Kalyuzhnaya, M. G., Burgess, L. W., et al. (2010). Direct measurement of oxygen consumption rates from attached and unattached cells in a reversibly sealed, diffusionally isolated sample chamber. *Adv. Biosci. Biotechnol.* 5, 398–408. doi: 10.4236/abb.2010.15053

Tschiersch, H., Liebsch, G., Borisjuk, L., Stangelmayer, A., Rolletschek, H., and Rolletschek, H. (2012). An imaging method for oxygen distribution, respiration and photosynthesis at a microscopic level of resolution. *New Phytol.* 196, 926–936. doi: 10.1111/j.1469-8137.2012.04295.x

Vander Heiden, M. G., Cantley, L. C., and Thompson, C. B. (2009). Understanding the warburg effect: the metabolic requirements of cell proliferation. *Science* 324:1029. doi: 10.1126/science.1160809

Wagner, B. A., Venkataraman, S., and Buettner, G. R. (2011). The rate of oxygen utilization by cells. *Free Radical. Biol. Med.* 51, 700–712. doi: 10.1016/j.freeradbiomed.2011.05.024

Wang, X.-D., and Wolfbeis, O. S. (2014). Optical methods for sensing and imaging oxygen: materials, spectroscopies and applications. *Chem. Soc. Rev.* 43, 3666–3761. doi: 10.1039/C4CS00039K

Wenger, R. H. (2000). Mammalian oxygen sensing, signalling and gene regulation. *J. Exp. Biol.* 203, 1253−1263.

Wenger, R. H., Kurtcuoglu, V., Scholz, C. C., Marti, H. H., and Hoogewijs, D. (2015). Frequently asked questions in hypoxia research. *Hypoxia* 3, 35–43. doi: 10.2147/HP.S92198

Wild, J. M., Fichele, S., Woodhouse, N., Paley, M. N. J., Kasuboski, L., and Van Beek, E. J. R. (2005). 3D volume-localized pO2 measurement in the human lung with 3He MRI. *Magn. Reson. Med.* 53, 1055–1064. doi: 10.1002/mrm.20423

Wittenberg, B. A., and Wittenberg, J. B. (1989). Transport of oxygen in muscle. *Annu. Rev. Physiol.* 51, 857–878. doi: 10.1146/annurev.ph.51.030189.004233

Wolff, P. E. A., Heimann, L., Liebsch, G., Meier, R. J., Gutbrod, M., van Griensven, M., and Balmayor, E. R. (2019). Oxygen-distribution within 3-D collagen I hydrogels for bone tissue engineering. *Mater. Sci. Eng. C.* 95, 422–427. doi: 10.1016/j.msec.2018.02.015

Wu, M., Neilson, A., Swift, A. L., Moran, R., Tamagnine, J., Parslow, D., et al. (2007). Multiparameter metabolic analysis reveals a close link between attenuated mitochondrial bioenergetic function and enhanced glycolysis dependency in human tumor cells. *Am. J. Physiol. Cell Physiol.* 292, C125–C136. doi: 10.1152/ajpcell.00247.2006

Yuan, H.-X., Xiong, Y., and Guan, K.-L. (2013). Nutrient sensing, metabolism, and cell growth control. *Mol. Cell* 49, 379–387. doi: 10.1016/j.molcel.2013.01.019

Conflict of Interest: GL, RM, and MSG are employees of PreSens Precision Sensing GmbH, Regensburg, Germany.

The remaining authors declare that the research was conducted in the absence of any commercial or financial relationships that could be construed as a potential conflict of interest.

frontiers in Bioengineering and Biotechnology

ORIGINAL RESEARCH
published: 19 June 2020
doi: 10.3389/fbioe.2020.00681

Long-Term *in vivo* Evaluation of Orthotypical and Heterotypical Bioengineered Human Corneas

Ingrid Garzón[1,2†], Jesus Chato-Astrain[1,2†], Carmen González-Gallardo[3], Ana Ionescu[4], Juan de la Cruz Cardona[4], Miguel Mateu[1,2], Carmen Carda[5], María del Mar Pérez[4], Miguel Ángel Martín-Piedra[1,2] and Miguel Alaminos[1,2]*

[1] Tissue Engineering Group, Department of Histology, University of Granada, Granada, Spain, [2] Instituto de Investigación Biosanitaria ibs.GRANADA, Granada, Spain, [3] Division of Ophthalmology, University Hospital San Cecilio, Granada, Spain, [4] Biomaterials Optics Group, Department of Optics, University of Granada, Granada, Spain, [5] Department of Histology and Pathology, University of Valencia, Valencia, Spain

OPEN ACCESS

Edited by:
Dimitrios I. Zeugolis, National University of Ireland Galway, Ireland

Reviewed by:
Alexander V. Ljubimov, Cedars-Sinai Medical Center, United States
Lisa Jane White, University of Nottingham, United Kingdom

***Correspondence:**
Miguel Ángel Martín-Piedra
mmartin@ugr.es

[†] These authors have contributed equally to this work

Specialty section:
This article was submitted to Tissue Engineering and Regenerative Medicine, a section of the journal Frontiers in Bioengineering and Biotechnology

Received: *17 January 2020*
Accepted: *02 June 2020*
Published: *19 June 2020*

Citation:
Garzón I, Chato-Astrain J, González-Gallardo C, Ionescu A, Cardona JC, Mateu M, Carda C, Pérez MM, Martín-Piedra MÁ and Alaminos M (2020) Long-Term in vivo Evaluation of Orthotypical and Heterotypical Bioengineered Human Corneas. Front. Bioeng. Biotechnol. 8:681. doi: 10.3389/fbioe.2020.00681

Purpose: Human cornea substitutes generated by tissue engineering currently require limbal stem cells for the generation of orthotypical epithelial cell cultures. We recently reported that bioengineered corneas can be fabricated *in vitro* from a heterotypical source obtained from Wharton's jelly in the human umbilical cord (HWJSC).

Methods: Here, we generated a partial thickness cornea model based on plastic compression nanostructured fibrin-agarose biomaterials with cornea epithelial cells on top, as an orthotypical model (HOC), or with HWJSC, as a heterotypical model (HHC), and determined their potential *in vivo* usefulness by implantation in an animal model.

Results: No major side effects were seen 3 and 12 months after implantation of either bioengineered partial cornea model in rabbit corneas. Clinical results determined by slit lamp and optical coherence tomography were positive after 12 months. Histological and immunohistochemical findings demonstrated that *in vitro* HOC and HHC had moderate levels of stromal and epithelial cell marker expression, whereas *in vivo* grafted corneas were more similar to control corneas.

Conclusion: These results suggest that both models are potentially useful to treat diseases requiring anterior cornea replacement, and that HHC may be an efficient alternative to the use of HOC which circumvents the need to generate cornea epithelial cell cultures.

Keywords: tissue engineering, bioengineered cornea, Wharton's jelly stem cells, heterotypical human cornea, artificial cornea

INTRODUCTION

Transplantation of a functional tissue-engineered cornea could contribute to the clinical treatment of patients with severe corneal defects (Garzon et al., 2014b; Gonzalez-Andrades et al., 2017). Several approaches have been described for the treatment of diseased corneas from a regenerative medicine standpoint (Oie and Nishida, 2016). On the one hand, tissue-engineered cell sheets or individual corneal layers can be efficiently generated in the laboratory using corneal epithelial cells (Sangwan and Sharp, 2017; Pellegrini et al., 2018; Le-Bel et al., 2019), stromal keratocytes

(Isaacson et al., 2018) or extra-corneal cells (Nishida et al., 2004) combined with different types of biomaterials or substrates. On the other hand, promising models of bioartificial corneas have been developed by tissue engineering (Ghezzi et al., 2015), including full-thickness corneas (Griffith et al., 1999; Alaminos et al., 2006) and anterior lamellar partial thickness corneas consisting of an epithelial layer with cornea epithelial cells and a subjacent stromal layer with biomaterials and keratocytes (Gonzalez-Andrades et al., 2009; Mi et al., 2010; Zaniolo et al., 2013; Couture et al., 2016; Rico-Sanchez et al., 2019).

However, the clinical translation potential of most of these strategies is still uncertain and highly dependent on the availability of adequate limbal stem cell sources for the generation of bioengineered cornea models with corneal cells. In this regard, human limbal stem cell cultures raised from limbal biopsies are difficult to obtain, and the procedure is subjected to the risk of causing limbal stem-cell deficiency in the healthy eye (Nishida et al., 2004).

In addition, patients suffering from bilateral limbal stem cell deficiency (LSD) may not be candidates for limbal biopsy and need alternative sources of corneal epithelial cells (Nguyen et al., 2017). For these reasons, the search for alternative cell sources to generate heterotypical bioartificial human corneas using extra-corneal cells is a current challenge in tissue engineering.

Previous reports have demonstrated that human mesenchymal stem cells (MSC) may have the potential to differentiate into cornea epithelial cells for the generation of partial human corneas *in vitro* (Liu et al., 2008; Gomes et al., 2010; Lin et al., 2013). Among the different types of MSC that could be potentially used in cornea tissue engineering, human umbilical cord Wharton's jelly stem cells (HWJSC) have several advantages, including accessibility, proliferation and differentiation potential, and immune-privileged status (Garzon et al., 2020). In fact, our research group was able to generate *in vitro* a biomimetic substitute of the human anterior cornea using HWJSC as an alternative cell source (Garzon et al., 2014b). Although promising results were obtained *in vitro*, the *in vivo* usefulness of these bioengineered corneas remains to be determined.

In the present study, we generated partial human orthotypical cornea (HOC) models with corneal cells, and human heterotypical cornea (HHC) models with HWJSC. We then characterized the main stromal and epithelial markers of these bioengineered cornea substitutes both *in vitro* and *in vivo* to determine the differentiation potential of HWJSC and the clinical translational potential of bioengineered corneal substitutes with this source of stem cells.

MATERIALS AND METHODS

Cell Isolation and Culture

To generate primary cultures of human cornea stromal and epithelial cells, we used limbal sclero-cornea rings that were discarded after cornea transplant surgery. First, cornea remnants attached to the limbus were isolated by surgical dissection and digested in *Clostridium histolyticum* type-I collagenase (Thermo Fisher Scientific, Waltham, MA, United States) for 6 h at 37°C. Isolated keratocytes were obtained by centrifugation and cultured in Dulbecco's modified Eagle's medium (DMEM) supplemented with 10% fetal calf serum, 4 mM L-glutamine and 1% antibiotic–antimycotic solution (Thermo Fisher Scientific). Then the limbal tissue was carefully dissected and small explants were cultured directly in Petri dishes with epithelial cell culture medium (Garzon et al., 2014b). HWJSC were isolated from five human umbilical cords obtained from cesarean deliveries using published protocols (Garzon et al., 2014a). First, arteries and veins were removed from the umbilical cord, and the Wharton's Jelly tissue was surgically dissected and digested with a mixture of type-I collagenase (Thermo Fisher Scientific) and a 0.5 g/L trypsin – 0.2 g/L EDTA solution (Sigma-Aldrich, St. Louis, MO, United States). Cells were harvested by centrifugation and cultured in 75 cm^2 culture flasks using Amniomax™ culture medium (Thermo Fisher Scientific). All cell cultures were kept in a cell incubator at 37°C with 5% CO_2 using standard cell culture conditions.

All methods and experimental protocols were performed in accordance with relevant guidelines and regulations according to the Association for Research in Vision and Ophthalmology (ARVO) Statement for the Use of Animals in Ophthalmic and Vision Research. For the use of human tissues, the project was approved by the local Human Research and Ethics Committee of the province of Granada -PEIBA- (numbers 9/2017 and 3/2016), and all tissue donors or their parents and/or legal guardians provided their informed consent.

Generation of HOC and HHC Cornea Models

Orthotypical models of the human cornea containing cornea cells (HOC) and heterotypical models containing non-corneal cells as the epithelial cell source (HHC) were generated with fibrin-agarose biomaterials with a final agarose concentration of 0.1% as previously reported by our research group (Gonzalez-Andrades et al., 2009; Garzon et al., 2014b). To do so, we first fabricated a biomaterial containing corneal stromal cells that will act as a biological substitute of the corneal stroma, and we then generated an epithelial layer (with corneal or extra-corneal cells) on top of this stroma substitute (Alaminos et al., 2006; Gonzalez-Andrades et al., 2009; Ionescu et al., 2015) to resemble the structure of the human native cornea. To generate the stromal substitute, we used the following protocol: per each ml of mixture, 760 μl of human plasma (obtained from healthy blood donors) were mixed with 15 μl of tranexamic acid (Amchafibrin, Fides-Ecofarma, Valencia, Spain), 75 μl of DMEM (Thermo Fisher Scientific) containing 100,000 cultured stromal cells (activated fibroblasts), 50 μl of melted 2% type-VII agarose in PBS (both, from Sigma-Aldrich) and 100 μl of 1% $CaCl_2$ (Sigma-Aldrich). This mixture was rapidly aliquoted in Transwell cell culture inserts with 0.4 μm porous membranes (Corning-Costar, Corning, NY, United States) and allowed to jellify at 37°C for at least 6 h. Then, HOC models were generated by subculturing the previously cultured cornea epithelial cells on top of the stroma substitutes, whilst HHC models were generated with HWJSC instead of epithelial cells. In both models, stratification and differentiation

of the epithelial-like cell layer were promoted with an air–liquid culture technique. This technique was performed by lowering the amount of culture medium in the porous inserts, so that only the stromal substitute remained submerged, whereas the developing epithelium was in direct contact with air and received nutrition from the stromal layer (Reichl and Muller-Goymann, 2003).

Finally, bioengineered corneas were subjected to plastic compression nanostructuration (Ionescu et al., 2011). This technique was previously used to induce the formation of irreversible covalent interactions and hydrogen bonding between the molecules of the biomaterial, resulting in a significant improvement of the biomechanical properties of these artificial tissues that allowed surgical handling (Ionescu et al., 2011; Campos et al., 2016). For this, bioengineered corneas were placed between a pair of sterile nylon filter membranes (Merck-Millipore, Darmstadt, Germany), and two pieces of Whatman 3 mm absorbent paper (Sigma-Aldrich) were set in contact with each filter membrane. Then, a flat glass surface weighing 500 g was used to apply a homogeneous pressure on the surface of the system for 3 min. Finally, human bioartificial corneas were carefully retired and kept in PBS to prevent them from excessive dehydration.

In vivo Evaluation of HOC and HHC Cornea Models in Laboratory Animals

Animal study design: in order to characterize both cornea models *in vivo*, samples were implanted on the anterior cornea surface of New Zealand laboratory rabbits using the DALK technique. A total of 20 rabbits were included in the study, which were randomly assigned to one of the following groups: (1) four animals were grafted with HOC and euthanatized after 3 months of follow-up, (2) four animals with HOC analyzed after 12 months, (3) four animals with HHC analyzed after 3 months, (4) four animals with HHC analyzed after 12 months, and (5) four non-operated rabbits used as controls.

Animals were deeply anesthetized by an intramuscular injection of xylazine (5 mg/kg) followed 10 min later by an intramuscular injection of ketamine (25 mg/kg), and local anesthetics drops were administered in the eye. Then the right eye was exposed, and the anterior layers of the cornea (approximately, two thirds of the stromal thickness) were surgically removed using a surgical microscope. To do that, a manual keratotome was first used to make a circular incision approximately 6 mm in diameter and 200 μm deep in the corneal thickness. Then an air bubble was injected into the central layer of the cornea stroma with a Hessburg-Barron vacuum trephine, and an ophthalmic crescent knife was used to horizontally dissect the most external stromal layers along with the superjacent epithelium. The limbus was preserved in all eyes. After careful debridement of the cornea surface, the bioengineered HOC or HHC was placed on this surface and sutured to the remaining cornea with 10/0 nylon suture stitches. Local antibiotics and anesthetics drops were administered after surgery. To protect the artificial tissue from mechanical damage, the eyelid of the treated eye was closed for 1 week. In all animals, the left eye was not treated and served as a control.

Ophthalmic evaluation was carried out every week, and slit-lamp bio-microscopy and anterior segment optical coherence tomography (OCT) was performed at the moment of the euthanasia of each animal (3 and 12 months of the surgical procedure). Both eyes were examined in each animal, and major side effects were registered, including tumorigenesis, hemorrhage, rejection or infection. The presence of inflammation was identified by the presence of hyperemia or neovascularization. Then, all eyes were surgically extracted and analyzed histologically as described below.

Animal experimentation was approved by the regional ethical committee (Ethics and Animal Experimentation Committee of the Andalusian Directorate of Agricultural Production – CEEA), ref. number 25/06/2018/099.

Histological and Immunohistochemical Evaluation of HOC and HHC Cornea Models

Histological methods were used to evaluate *in vitro* HOC and HHC samples corresponding to 1, 2, and 3 weeks of development and *in vivo* HOC and HHC samples grafted in laboratory animals for 3 and 12 months. Samples were fixed in 3.7–4.0% wt/vol buffered formaldehyde for 24 h at 4°C and dehydrated in ethanol series (1 h in 70% ethanol, two incubations of 1 h in 96% ethanol, two incubations of 1 h in 100% ethanol), cleared in xylene (two incubations of 1 h) and embedded in paraffin (two incubations of 1 h in paraffin melted at 60°C) using an automated Citadel Tissue Processor (Thermo Fisher Scientific). Tissue sections 5 μm thick were obtained and placed on glass slides, dried at room temperature, dewaxed with three incubations of 5 min in xylene and rehydrated with an ethanol series (three incubations of 5 min in 100%, two incubations of 5 min in 96%, 5 min in 70%, 5 min in 50% ethanol, and 5 min in distilled water).

For histological analysis, tissue sections were incubated for 3 min in hematoxylin (PanReac AppliChem, Barcelona, Spain), rinsed in tap water for 5 min, stained with eosin (PanReac AppliChem) for 1 min and dehydrated using an ethanol series (3 incubations of 5 min in 96% and 3 incubations of 5 min in 100% ethanol), xylene (3 incubations of 15 min) and cover-slipped using Permount (Fisher Scientific International, Pittsburgh, PA, United States). Tissue sections stained with H&E were used to quantify the number of cell layers in the corneal epithelium. In each sample, the epithelial layer was examined using 600× magnification, and the number of cell layers was determined by three expert histologists.

Immunofluorescence assays in tissue sections were performed using previous standardized protocols (Martin-Piedra et al., 2017). Samples were first treated for 25 min with 0.01 M citrate buffer (Dako, Glostrup, Denmark) at 95°C for antigen retrieval. After rising in PBS, samples were preincubated in prehybridization buffer containing 10% donkey serum, and primary antibodies were applied and incubated for 2 h at room temperature. Then, samples were washed three times in PBS and secondary FITC-conjugated anti-mouse or Cy3-anti-rabbit secondary antibodies (Sigma-Aldrich) were used at 1:500 dilution. Tissues were then counterstained using DAPI mounting

medium (Vector Laboratories, Burlingame, CA, United States) and cover-slipped. Analysis was performed using a Nikon Eclipse 90i fluorescence microscope. Primary antibodies used for immunofluorescence analysis were specific of the cornea epithelium: anti-cytokeratin 3/12 (Abcam ab68260), plakoglobin (Abcam ab12083), crystallins CRY-αA (Santa Cruz sc-28306), CRY-αB (Millipore ABN185), CRY-β (Santa Cruz sc-22745), CRY-λ1 (Sigma Prestige HPA040403), and CRY-Z (Abcam ab154842). As the manufacturers claims that anti-PKG and anti-CRY-λ1 antibodies are specific for human antigens, these were therefore used to specifically identify human cells. The immunofluorescence results were analyzed semiquantitatively by three independent histologists in a blinded manner to reduce potential biases. Each histologist scored the positive signal in each sample as strong (+++), moderate (++), slight (+), very slight (±) or negative (−), as previously described (Garzon et al., 2009).

For immunohistochemistry, tissue sections were treated with 3% H_2O_2 to quench endogenous peroxidase, and antigen retrieval and prehybridization were carried out as described for immunofluorescence. Then, samples were incubated overnight at 4°C in anti-type I collagen (Acris R1038) or anti-vimentin (Sigma V6630) primary antibodies and washed in PBS. Then, peroxidase-labeled secondary antibodies (Vector Laboratories) were used and the signal was detected using a diaminobenzidine (DAB) development kit (Vector Laboratories). In both cases (immunofluorescence and immunohistochemistry), isotype-specific immunoglobulins were used instead of the primary antibodies as negative controls.

For scanning electron microscopy (SEM), samples were fixed in cacodylate-buffered 2.5% glutaraldehyde, dehydrated in alcohol series (50, 70, 96, and 100% ethanol, 30 min in each concentration) and dried by the critical point method using a Critical Point Dryer (Bal-Tec, Los Angeles, CA, United States). This method consists in replacing all the ethanol embedding the tissue by liquid carbon dioxide at high pressure, which is then evaporated at low pressure, resulting in a critically dried sample. Then, tissues were sputter-coated with gold-palladium using a Mini Sputter Coater System (Quorum Technologies Ltd., Lewes, United Kingdom) and examined a Quanta 200 scanning electron microscope (FEI, Eindhoven, Netherlands).

For transmission electron microscopy (TEM), samples were fixed in cacodylate-buffered 2.5% glutaraldehyde for 8 h, washed three times in cacodylate duffer and postfixed in 1% osmium tetroxide for 90 min. After fixation, samples were dehydrated in increasing concentrations of acetone (30, 50, 70, 95, and 100%), embedded in Spurr's resin and cut into ultrathin sections with an ultramicrotome. For analysis, sections were stained with aqueous uranyl acetate and lead citrate and examined with an EM902 transmission electron microscope (Carl Zeiss Meditec, Inc., Oberkochen, Germany).

Optical Properties of the HOC and HHC Cornea Models

In order to characterize the different cornea models from an optical standpoint, we analyzed the transmittance of each sample and the reduced scattering and absorption coefficients. The inverse adding-doubling method was used to determine scattering and absorption using total reflection and total transmission measurements made with a single integrating sphere, as previously described (Ionescu et al., 2015, 2017). Total diffuse reflection and transmission measurements were made with a 158.2-mm-diameter integrating sphere (Oriel, model 70674. Newport Corp., Irvine, CA, United States) with a 11-mm-diameter detector port and a 4-mm-diameter sample port with a baffle between ports. The entrance port was 15 mm in diameter. All measurements were obtained for HOC and HHC corneas and native control corneas at 457.9, 488, and 514.5 nm with an argon ion laser (Stellar-Pro-L Model, Modu-Laser, Centerville, UT, United States) and at 632.8 nm with a He-Ne laser (30564 Model, Research Electro-Optics, Boulder, CO, United States). The maximum output power was 1000 mW ± 5% for the argon laser and 12 mW for the He-Ne laser. The diameter of both argon and He-Ne lasers beams was 2 mm. Three reflection measurements were made in each sample, and were referenced to a 98% Optopolymer reflectance standard (OPST3-C, Optopolymer, Munich, Germany) and a dark measurement (with the sample port empty). For transmission, three measurements were made in each corneal model and a control cornea, and were referenced to 100% with the lasers illuminating the open port (empty port) and a dark measurement with an open port but with no illumination from the lasers. Reflectance of the sphere wall, thickness, and refractive index of the cornea models and the control native cornea were also measured and used to calculate the absorption and reduced scattering coefficients, using the inverse adding-doubling method (Prahl et al., 1993; Sardar et al., 2005, 2009; Yust et al., 2012).

Statistical Analysis

Quantitative results obtained for the optical parameters (transmittance, absorption and reduced scattering) were analyzed statistically to identify differences among samples. First, a global comparison of all study samples (HOC, HHC, and controls) was carried out using the Kruskal–Wallis test. Then, *post hoc* comparisons between two specific types of corneas (HOC vs. controls, HHC vs. Controls, and HOC vs. HHC) was performed using the Mann–Whitney test. Non-parametric tests were used because the parameters analyzed here did not fulfill the criteria for parametric testing. A Bonferroni-adjusted *P*-value of 0.001 was considered as statistically significant for the double-tailed tests, since numerous statistical comparisons were carried out at the same time. *P*-values between 0.05 and 0.001 were considered as marginally significant, meaning that these values would have been considered as significant if the Bonferroni correction had not been applied.

RESULTS

Clinical Results

In vivo analyses of generated HOC and HHC models allowed us to evaluate the safety and biointegration of bioartificial corneas. In this regard, we found no signs of tumorigenesis, hemorrhage,

rejection, infection, or other major side effects in any of the animals. Macroscopic examination of the rabbit eyes revealed that HOC and HHC resulted in corneas with some inflammatory signs around the suture stitches, especially 3 months after *in vivo* implantation. However, inflammation tended to resolve after 12 months. In fact, ophthalmic evaluation of HOC revealed some inflammation around the stitches in 2 out of the 4 rabbits analyzed at 3 months, and 1 out of 4 rabbits at 12 months. For HHC, 2 of the 4 animals showed inflammation at 3 months, and none at 12 months (**Figure 1**). Slit lamp analyses showed no differences between the two types of cornea and the controls, with a well-defined linear structure of the cornea in all cases. OCT evaluation revealed a regular structure consisting of a corneal stroma with a normal overlying epithelium in control eyes. Cross-sectional images obtained by OCT on corneas undergoing surgery showed that the grafted tissue was tightly attached to the host cornea stroma in all cases. However, an interface between both tissues was clearly identifiable in all HOC and HHC eyes after 3 and 12 months (**Figure 1**).

Histological Analysis

Histological evaluation of different samples by H&E are shown in **Figure 2A**. Analyses of *in vitro* HOC samples showed a stratified epithelium consisting of polygonal and rounded cells. Quantification of the number of cell layers disclosed that the cell number tended to increase with time in culture: at 1 week, HOC had an average of 2 epithelial cell layers, at 2 weeks, we found an average of 4.5 layers, and an average of 6 layers were found at week 3. Analysis of *in vitro* HHC samples showed that these cells tended to be more flattened as compared to HOC, and showed an average of 1.5 cell layers at week 1, 6.5 layers at week 2, and 9 layers at week 3. Regarding the stromal cells, we found that these cells were scattered throughout the fibrin-agarose biomaterial in all sample types.

In vivo grafting resulted in higher levels of tissue differentiation in both types of cornea. In all *in vivo* samples, the epithelium consisted of an average of 6.5 epithelial cell layers showing a well-organized stratification pattern very similar to control corneas. Moreover, the stroma was formed by a dense, highly organized fibrillar mesh containing large numbers of stromal cells after 12 months of development, whereas the interface between the host tissue and the implant was detectable only in samples corresponding to 3 months after *in vivo* implantation.

Further characterization of the *in vivo* HOC and HHC samples with TEM (**Figure 2B**) confirmed the presence of a stratified corneal epithelium that showed polarity and signs of differentiation such as rounded cells in the basal layer and flattened cells on top, cell–cell cohesion, and a basement membrane underlying the corneal epithelium. In the stroma, abundant collagen fibers were found with different spatial orientation corresponding to different corneal stroma layers, and some stromal cells were detected between adjacent stromal layers.

Analyses with SEM (**Figure 2B**) showed that the surface of HOC and HHC was fully covered by an epithelial layer consisting of flat polygonal cells exhibiting evident signs of cell desquamation and cell renewal.

Corneal Stroma Differentiation Determined by Immunohistochemistry

Analyses of cells in the stroma of different samples showed that most cells were positive for the vimentin stromal marker both *in vitro* and *in vivo* (**Figure 3A**). In addition, collagen I immunohistochemistry (**Figure 3B**) showed that HOC

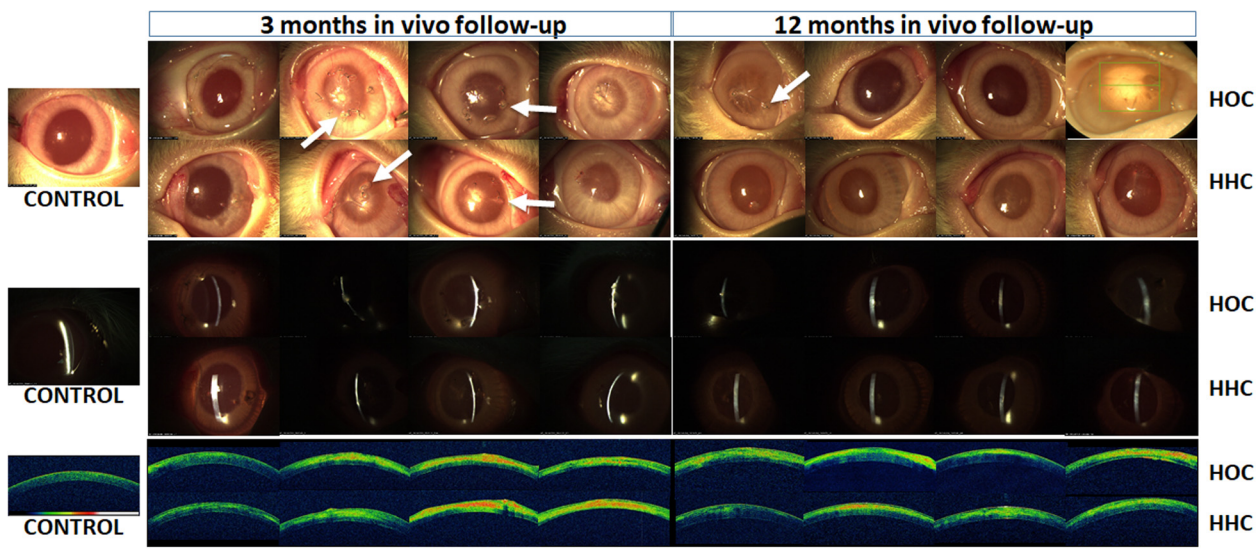

FIGURE 1 | Clinical results in HOC and HHC bioartificial corneas grafted on the surface of rabbit eyes after 3 and 12 months of follow-up. Top images show the macroscopic findings; central images show slit lamp observations; lower images illustrate OCT findings. Controls are non-grafted normal rabbit eyes. HOC, human orthotypical cornea; HHC, human heterotypical cornea; OCT, optical coherence tomography. Arrows correspond to the inflammatory signs around the suture stitches.

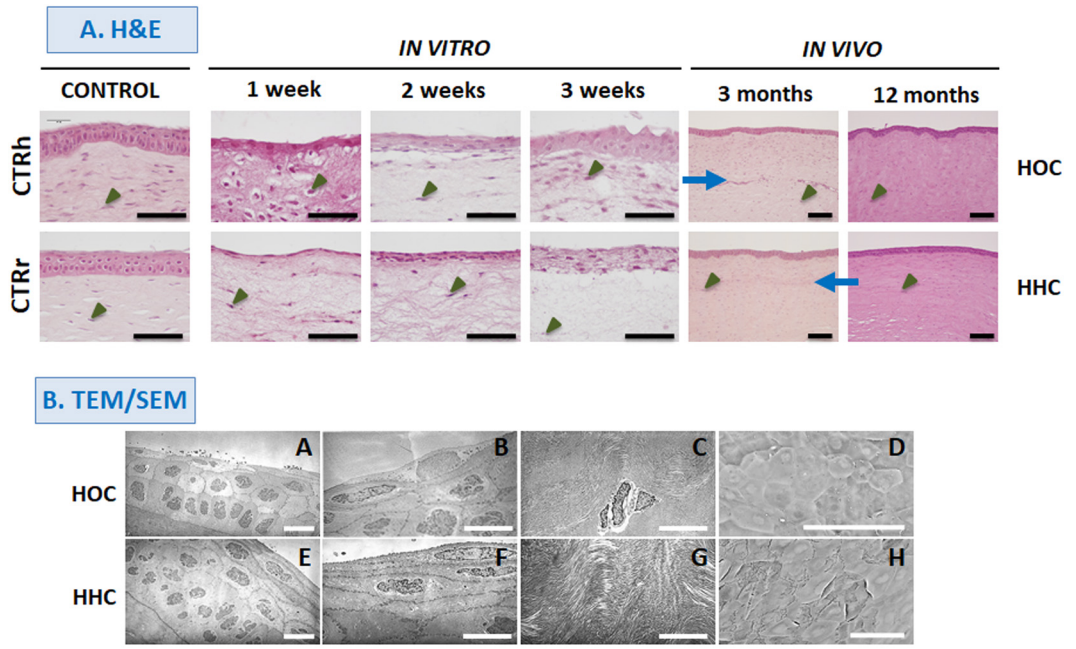

FIGURE 2 | Histological evaluation of different samples with hematoxylin and eosin (H&E) staining **(A)**, and electron microscopy **(B)**. HOC, human orthotypical cornea; HHC, human heterotypical cornea. A, B, E, and F show TEM images of HOC and HHC epithelium at different magnifications. C and G show TEM images of corneal stroma. D and H show SEM images of the corneal epithelial surface in HOC and HHC. Controls are normal human corneas (CTRh) and normal rabbit corneas (CTRr). Blue arrows correspond to the interface between the host tissue and the implant, and some illustrative stromal cells are highlighted with arrow heads. Scale bars: 100 μm for H&E and SEM, and 10 μm for TEM images.

maintained *in vitro* did not express this marker, but collagen was present in *in vivo* samples at 3 months and its expression was increased at 12 months. In contrast, HHC showed positive collagen expression after 2 weeks of *in vitro* development, and expression increased steadily thereafter. The highest levels of expression were seen *in vivo*, especially after 12 months being similar to control group (**Figure 3B**).

Corneal Epithelium Differentiation Determined by Immunofluorescence

To determine the epithelial phenotype of the epithelial layer in HOC and HHC cornea substitutes, we analyzed CK3/12 and PKG expression. Orthotypical epithelial cells produced positive signals for CK3/12 cytokeratin in all stages of *in vitro* development, especially in the most superficial layer (**Figure 4A** and **Table 1**). This expression increased and showed strong positivity *in vivo* and was seen in all epithelial layers, being comparable to controls. However, HHC were initially negative and turned moderately positive after 3 weeks of *in vitro* development. In our *in vivo* samples of HOC and HHC, expression levels were strong and similar to those in control human corneas.

Analysis of the cell–cell junction protein PKG (**Figure 4B** and **Table 1**), also showed positive expression in all HOC samples, especially at week 3 *in vitro* and in all *in vivo* samples, which showed strong expression. For the HHC samples, *in vitro* corneas were moderately positive for PKG from week 2 of development, and *in vivo* samples were strongly positive. Interestingly, PKG expression was very low in control rabbit corneas and strongly positive in control human tissues.

Crystallin Expression

Immunohistochemical assays for crystallins, key proteins in corneal transparency, showed that all proteins were highly expressed by the control human cornea epithelium, although control rabbit cornea showed slight or very slight expression levels of CRY-Z and CRY-λ1 (**Figures 5**, **6** and **Table 1**). In the bioengineered corneas, expression of all crystallins tended to increase with time in all corneas maintained *in vitro*, with highest levels in corneas with the highest number of epithelial cell layers except for CRY-λ1, which was moderately positive from week 1 (**Figure 6B** and **Table 1**). In general, the expression levels tended to be higher in *in vitro* HOC samples than in *in vitro* HHC samples, except for CRY-Z (**Figure 6C** and **Table 1**), which was expressed more strongly in HHC than HOC, and CRY-λ1, which was expressed at similar levels in both models. After 3 months of *in vivo* development, HOC and HHC samples were comparable to control human corneas for CRY-αA (**Figure 5A** and **Table 1**) and CRY-β (**Figure 6A** and **Table 1**), whereas lower expression was found for the rest of crystallins analyzed in this work. At 12 months of *in vivo* development, the levels of CRY-αA expression in both HOC and HHC were strong and similar to human control cornea, and this was also the case of CRY-αB (**Figure 5B** and **Table 1**) and CRY-Z for the HHC samples. Controls *in vivo* HOC samples at 12 months showed similar

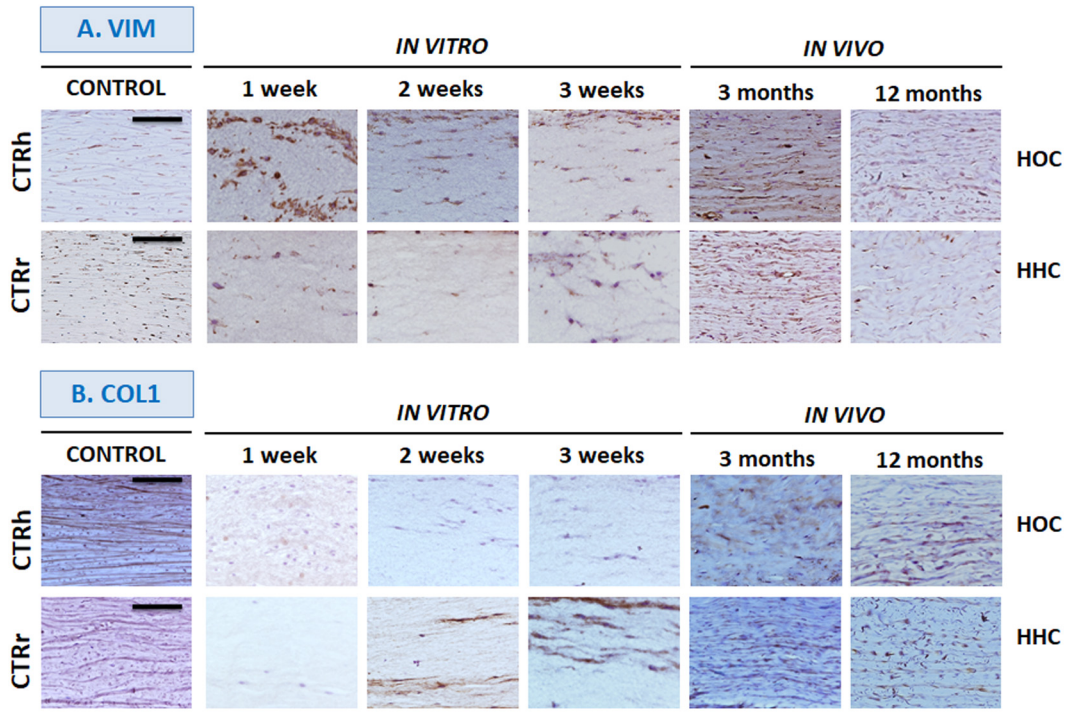

FIGURE 3 | *In vitro* and *in vivo* analyses of corneal stroma differentiation determined by immunohistochemistry for vimentin (VIM, **A**) and type I collagen (COL1, **B**). HOC, human orthotypical cornea; HHC, human heterotypical cornea. Controls are normal human corneas (CTRh) and normal rabbit corneas (CTRr). Scale bars: 100 μm for all images.

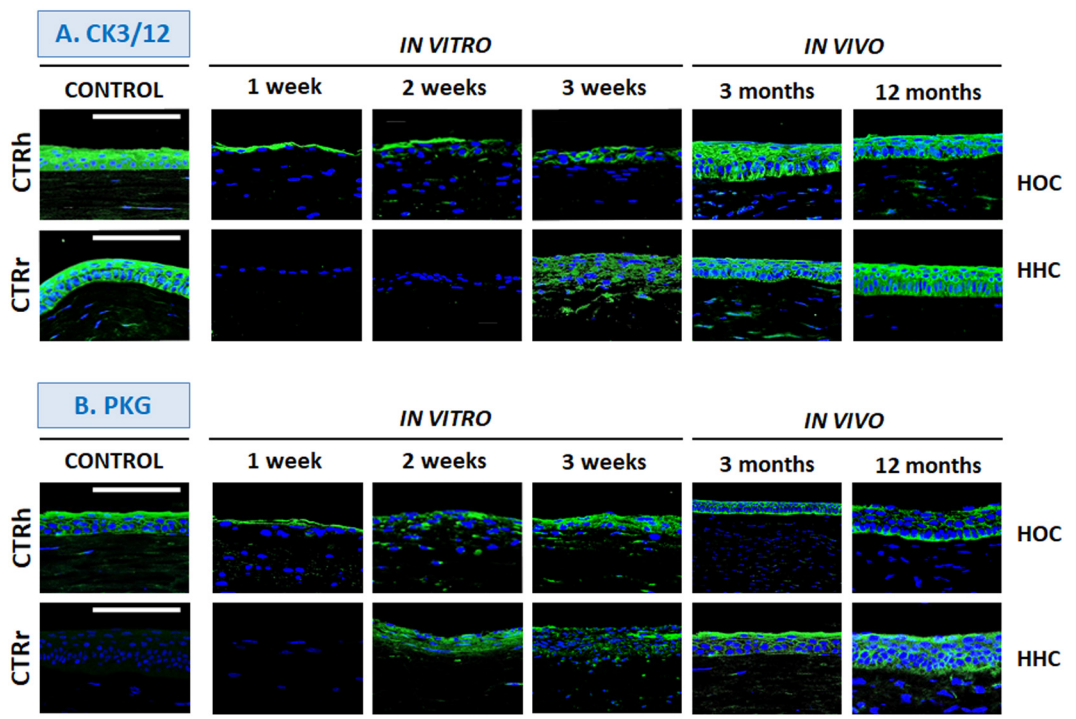

FIGURE 4 | Differentiation of corneal epithelium *in vitro* and *in vivo* determined by immunohistochemistry for cytokeratin 3/12 (CK3/12, **A**) and plakoglobin (PKG, **B**). HOC, human orthotypical cornea; HHC, human heterotypical cornea. Controls are normal human corneas (CTRh) and normal rabbit corneas (CTRr). Scale bars: 100 μm.

TABLE 1 | Semiquantitative analysis of expression of several epithelial markers as determined by immunofluorescence.

		In vitro 1 week	*In vitro* 2 weeks	*In vitro* 3 weeks	*In vivo* 3 months	*In vivo* 12 months	Control human cornea	Control rabbit cornea
CK3/12	HOC	+	+	++	+++	+++	+++	+++
	HHC	–	–	++	+++	+++		
PKG	HOC	+	+	+++	+++	+++	+++	±
	HHC	–	++	++	+++	+++		
CRY-αA	HOC	+	++	+++	+++	+++	+++	+++
	HHC	+	+	+++	+++	+++		
CRY-αB	HOC	–	±	+	±	++	+++	+++
	HHC	±	+	+	+	+++		
CRY-β	HOC	+	+	++	++	++	++	++
	HHC	–	+	+	++	+		
CRY-λ1	HOC	++	++	++	+	+	+++	±
	HHC	++	++	++	+	++		
CRY-Z	HOC	–	+	++	++	++	+++	+
	HHC	+	++	+++	++	+++		

HOC, human orthotypical cornea; HHC, human heterotypical cornea.

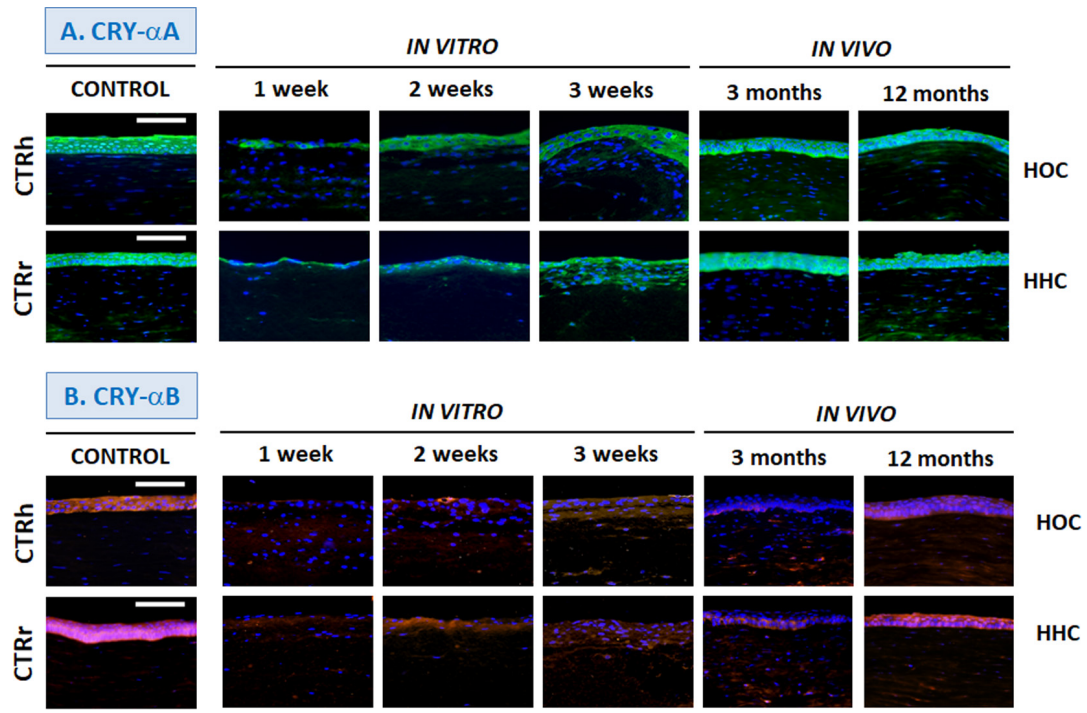

FIGURE 5 | Differentiation of corneal epithelium *in vitro* and *in vivo* determined by immunohistochemistry for crystallins CRY-αA **(A)** and CRY-αB **(B)**. HOC, human orthotypical cornea; HHC, human heterotypical cornea. Controls are normal human corneas (CTRh) and normal rabbit corneas (CTRr). Scale bars: 100 μm.

moderate expression. However, *in vivo* expression levels of CRY-αB, CRY-λ1, and CRY-Z were lower in HOC samples at 12 months as compared to human controls, and HHC samples at 12 months showed lower CRY-β and CRY-λ1 expression levels than human controls.

Optical Behavior

Tests of the optical behavior of controls and HOC and HHC bioengineered human corneas showed that light transmittance in all samples depended on the wavelength, and statistically significant differences were found among the different samples analyzed here. Globally, average values of bioengineered corneas represented approximately 60% of the transmittance in control corneas (approximately 80% for all HOC samples and 30% for al HHC samples) (**Figure 7A**). Interestingly, the duration of development in culture did not significantly influence the transmittance capacity of *in vitro* samples ($P > 0.05$). However, the type of sample was directly related with this parameter, and

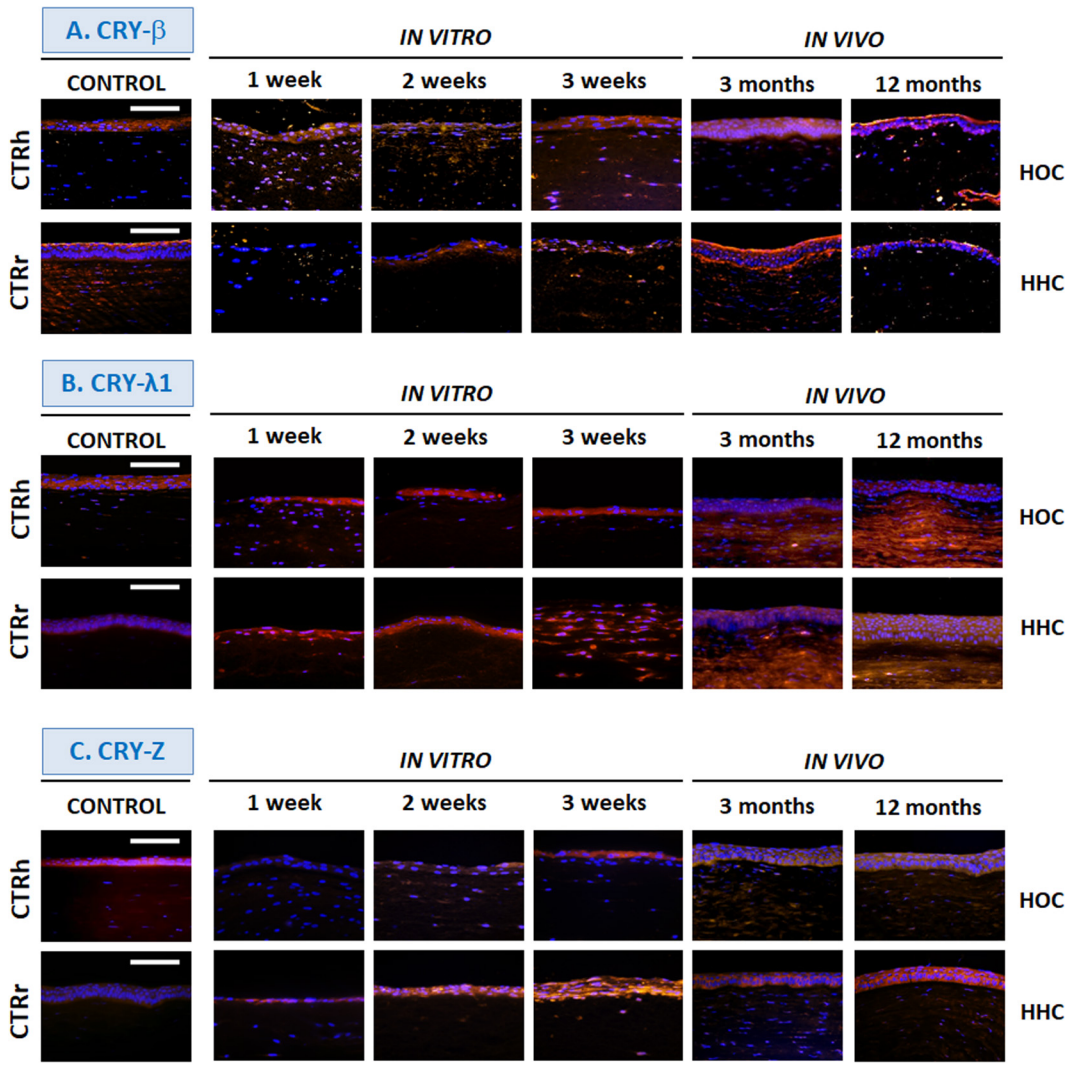

FIGURE 6 | Differentiation of corneal epithelium *in vitro* and *in vivo* determined by immunohistochemistry for crystallins CRY-β **(A)**, CRY-λ1 **(B)** and CRY-Z **(C)**. HOC, human orthotypical cornea; HHC, human heterotypical cornea. Controls are normal human corneas (CTRh) and normal rabbit corneas (CTRr). Scale bars: 100 μm.

HOC *in vitro* samples showed significantly higher transmittance than HHC *in vitro* samples ($P = 1.57 \times 10^{-272}$). The absorption and reduced scattering coefficients values of HOC *in vitro* samples were significantly higher than controls ($P = 2.31 \times 10^{-5}$ for absorption and $P = 1.81 \times 10^{-39}$ for scattering), and the same behavior was found for HHC *in vitro* samples ($P = 1.78 \times 10^{-122}$ for absorption and $P = 2.37 \times 10^{-199}$ for scattering). However, HOC showed significantly lower levels of absorption and reduced scattering than HHC *in vitro* samples ($P = 1.01 \times 10^{-204}$ for absorption and $P = 3.78 \times 10^{-285}$ for scattering) (**Figures 7B,C**).

When HOC and HHC were grafted *in vivo*, we found a substantial increase in transmittance values. In HOC and HHC *in vivo* models 3 months after implantation, global mean transmittance was approximately 55 and 63%, respectively, corresponding to approximately 66 and 76%, respectively of the transmittance in control corneas. Therefore, we found an increase of transmittance 12 months after implantation, with transmittance values of approximately 75% for both HOC and HHC, corresponding to 90% of control corneas. Differences between HOC and HHC were marginally significant at this time ($P = 0.00719$), but both cornea models were significantly lower than controls ($P = 1.82 \times 10^{-180}$ for HOC and $P = 2.96 \times 10^{-196}$ for HHC). Regarding the absorption coefficient, we found that both HOC and HHC had significantly higher absorption coefficients than controls after 3 months of follow-up ($P < 1.00 \times 10^{-100}$ for HOC and HHC), with HOC being higher than HHC ($P = 0.00001$). However, *in vivo* samples 12 months after implantation showed absorption coefficients that were lower than those in control corneas, with differences being statistically significant ($P < 1.00 \times 10^{-100}$). Finally, we found that the reduced scattering coefficients of HOC and HHC after 3 months were lower than *in vitro* samples, although did not reach the low levels of control corneas ($P < 1.00 \times 10^{-100}$ for HOC and $P = 4.84 \times 10^{-302}$ for HHC). After 12 months,

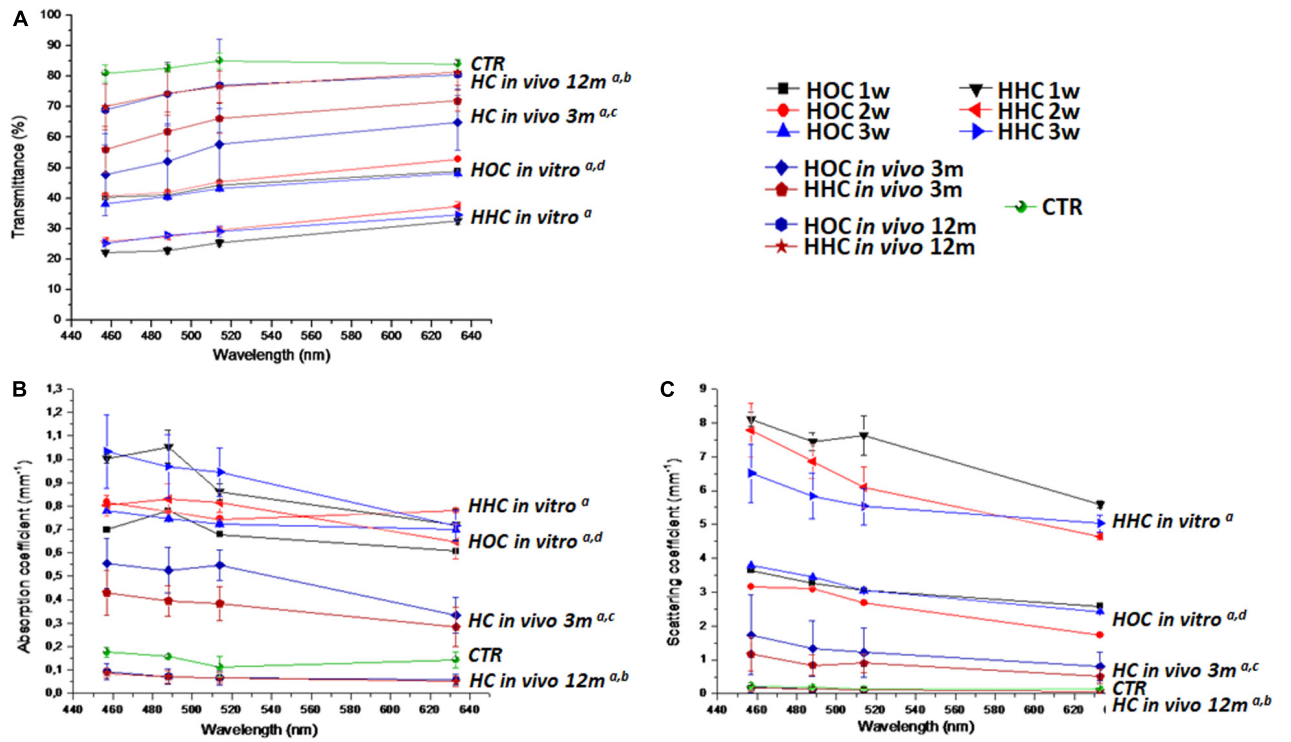

FIGURE 7 | Optical properties of cornea models *in vitro* and *in vivo* determined with the inverse adding-doubling method. **(A)** Transmittance of each type of cornea; **(B)** absorption coefficient; **(C)** reduced scattering coefficient. HOC, human orthotypical cornea; HHC, human heterotypical cornea; HC, human artificial corneas (HOC and HHC). Controls are normal rabbit corneas (CTR). a: differences with controls were statistically significant; b: differences with HC *in vivo* at 3 m were statistically significant; c: differences with HOC *in vitro* were statistically significant; d: differences with HHC *in vitro* were statistically significant.

reduced scattering values were very similar to control corneas, although statistical differences with controls were detected ($P = 1.58 \times 10^{-111}$ for HOC and $P = 2.36 \times 10^{-88}$ for HHC). At this time, differences between HOC and HHC were marginally significant ($P = 0.19009$) for the reduced scattering.

DISCUSSION

The potential usefulness of novel HHC models lies in their ability to support the *in vitro* construction of human bioartificial cornea substitutes without the drawbacks associated with the use of autologous limbal stem cells (Behaegel et al., 2017). For this reason, we evaluated the *in vitro* and *in vivo* behavior of novel HHC substitutes generated from HWJSC.

Our results showed that both HHC and HOC cornea substitutes may hold potential for clinical use, and *in vivo* outcomes obtained with both cornea types showed no significant side effects on the host eyes. The initial inflammatory process found at 3 months was self-limited, and most cases evaluated at 12 months were devoid of significant inflammation. This was especially evident in HHC, which did not show any case of inflammation after 12 months. Although the differences with HOC were not substantial at this time (one case vs. no cases), we might hypothesize that the use of MSC in HHC could exert a positive influence in terms of inflammation. Even though future works should be carried out with a larger sample size to confirm or not this hypothesis, the immunomodulatory effects of HWJSC have been previously demonstrated in different settings (El Omar et al., 2014; Garzon et al., 2020). Analyses with OCT disclosed adequate biointegration of the grafted tissue with host cornea demonstrated by a close attachment of both tissue layers, albeit with a detectable limit between the two structures after 12 months. In this regard, it is well known that complete integration of tissues implanted in the cornea, including human keratoplasty, may progress slowly due to the avascular nature of the human cornea (Amiri et al., 2017). In fact, it has been demonstrated that a transplanted cornea could be easily detached by mild trauma or physical activity several years after the transplantation procedure (Jafarinasab et al., 2012).

In addition, our histological analyses confirmed previous reports (Garzon et al., 2014b) showing that HWJSC were able to differentiate *in vitro* into an epithelial-like layer on top of the stromal substitutes, although the histological and morphological patterns of both cornea types showed some differences that suggest that the differentiation process is not complete *in vitro* (Garzon et al., 2014b). However, the epithelial layer in both HOC and HHC corneas became similar to the native human cornea epithelium once were grafted *in vivo*. This finding suggests that the *in vivo* environment and the local release of soluble paracrine factors may be necessary to induce and enhance terminal cell differentiation of HWJSC (Alfonso-Rodriguez et al., 2015).

Analyses of the corneal stroma showed that the grafted bioengineered stroma substitute was integrated into the host cornea, with no evidence of rejection or other side effects at the histological level. Our results confirmed that stromal cells expressed vimentin, which is essential for normal growth, differentiation, integrity and function in corneal cells as previously demonstrated (Kivela and Uusitalo, 1998). In addition, our analyses confirmed the presence of mature collagen fibers in corneas grafted *in vivo*, and also in *in vitro* samples with the HHC model. The early expression of collagen by HHC cells may be explained by the high biosynthetic activity of WHJSC, which derive from a mucous connective tissue that is committed to produce large amounts of fibrillar and non-fibrillar extracellular matrix components in the umbilical cord (Corrao et al., 2013). In summary, the presence of vimentin-positive stromal cells immersed within a collagen-rich matrix resembling the native corneal stroma suggests that the implanted substitute may be undergoing adequate stromal differentiation after *in vivo* grafting. Moreover, the *in vivo* formation of a basement membrane on top of the stroma may support epithelial cell development, which appears to be a critical factor in corneal healing and transparency (Torricelli et al., 2016).

Analysis of the epithelial layer in the bioartificial cornea models demonstrated that HHC were able to develop a stratified epithelial-like structure similar to that seen in the HOC model. Strikingly, both HHC and HOC grafted *in vivo* showed high levels of expression of the cornea epithelium markers CK3/12 and PKG and several crystallins, similar to the levels seen in native human corneas. However, HHC showed late *in vitro* expression of both markers compared to HOC. These findings are not unexpected, since the HOC model was constructed with corneal cells that are previously committed to cornea differentiation, whereas HWJSC would likely require a differentiation induction process driven by different factors (Garzon et al., 2020). In addition to CK3/12 and PKG, further analyses should be carried out to determine the expression of other markers of corneal epithelial cells and limbal stem cells, such as KRT15, KRT17, ΔNp63, and ABCG2 (Ebrahimi et al., 2009; Wright and Connon, 2013). In this regard, we previously demonstrated that HOC show positive expression of most of these markers by microarray (Rico-Sanchez et al., 2019), (data are accessible at https://www.ncbi.nlm.nih.gov/geo/query/acc.cgi?acc=GSE86584), and that native HWJSC express high amounts of MSC undifferentiation markers, which decrease upon epithelial differentiation coinciding with a positive expression of specific differentiation markers (Alaminos et al., 2010). Whether or not this also occurs in our HHC model remains unexplored, although the positive results found with H&E, TEM, and SEM analyses support the hypothesis that HWJSC may have been able to differentiate to corneal epithelium.

An important unsolved question is the adequate characterization of the xenograft that allow us to definitely identify the origin of the cells found in the rabbit cornea. Rabbit limbal epithelial stem cells show rapid self-renewal (Zheng et al., 2019), and grafted human cells may disappear after several months of *in vivo* follow-up. In this regard, we found that two primary antibodies (anti-PKG and anti-CRY-λ1) showed positive expression in corneas grafted in rabbits, and very low expression in rabbit controls. Although this supports the possibility that the cells found in corneas grafted *in vivo* were human, survival of the grafted epithelial cells should be confirmed in future studies using FISH analysis or other highly sensitive techniques (Catanese et al., 2011).

Apart from the role of crystallins as corneal epithelium marker, a crucial aspect in the analysis of bioengineered human corneas is transparency, which is directly dependent on many factors such as the presence of cornea crystallins (Cvekl and Zhang, 2017). Although crystallins are not well known, it has been demonstrated that their contribution to cornea transparency is directly related to their molecular weight and three-dimensional structure, and their spatial structure can control light scattering (Tardieu, 1998).Transparency is essentially controlled by α crystallins, which are the biggest of these proteins and have adequate structure determining corneal transparency (Tardieu, 1998). Other crystallins with lower molecular weights such as crystallin β, λ, and Z could influence corneal transparency to a lesser extent. Analysis of crystallin expression should be therefore considered in corneas developed by tissue engineering. In the present study, we confirmed that bioengineered corneas maintained *in vitro* showed low expression of most cornea crystallins compared to human controls, as previously reported by our group (Garzon et al., 2014b). The low expression of CRY-αA and CRY-αB shown by *in vitro* samples coincided with the lowest levels of transparency (as determined by light transmittance) and the highest levels of light absorption and reduced scattering, especially in the first weeks of development, and suggest that the corneal epithelium differentiation level of these samples was low. Remarkably, the expression levels of collagen type I also tended to be low in corneas maintained *in vitro*, suggesting that an appropriate organization of the stromal fibers is crucial for corneal transparency (Meek and Knupp, 2015). In contrast, bioengineered HHC and HOC corneas grafted *in vivo* showed improved transparency after follow-up for 12 months. This would be expected to correlate with the higher expression of crystallin epithelial markers in our *in vivo* samples. Indeed, the levels of CRY-αA, CRY-αB, and CRY-Z became similar to control corneas in HHC, and the levels of CRY-αA and CRY-β were similar to control corneas in HOC. The transparency of *in vivo* corneas determined by light transmittance did not reach the values in native corneas, but was approximately 90% of controls after 12 months, with no differences between both models. Together, these findings suggest that bioengineered corneas require prolonged *in vivo* periods to synthesize and release key proteins related to transparency, such as collagen type I and several types of crystallins.

One of the limitations of the present study is the need of analyzing additional limbal stem cell markers in HOC and HHC by immunohistochemistry, along with the previously mentioned need of confirming the human nature of the epithelial layer. In addition, the bioengineered corneas generated in this work are devoid of the cornea endothelial layer, and future studies should be focused on the generation of full-thickness bioartificial corneas including the epithelial, stromal and endothelial corneal layers (Giasson et al., 2014).

CONCLUSION

Altogether, our results suggest that bioartificial cornea models may show adequate *in vivo* biointegration levels, which may support their clinical use. HWJSC showed cornea epithelial differentiation potential and may be considered as a potential alternative epithelial cell source for the generation of human corneas by tissue engineering without the need of using epithelial cell cultures established from human cornea biopsies.

DATA AVAILABILITY STATEMENT

The datasets generated for this study are available on request to the corresponding author.

ETHICS STATEMENT

The studies involving human participants were reviewed and approved by the Human Research and Ethics Committee of the province of Granada (PEIBA). The patients/participants provided their written informed consent to participate in this study. The animal study was reviewed and approved by the Ethics and Animal Experimentation Committee of the University of Granada and the Andalusian Directorate of Agricultural Production (CEEA).

AUTHOR CONTRIBUTIONS

IG, JC-A, MM-P, and MA carried out the artificial tissue development, data analysis, and manuscript preparation. CG-G and JC-A carried out the animal studies and obtained the clinical results. AI, JC, and MP were responsible for the optical analyses. MM was involved in immunofluorescence analyses in all samples. CC was responsible for TEM microphotographs. All authors contributed to the article and approved the submitted version.

FUNDING

This work was supported by the Spanish Plan Nacional de Investigación Científica, Desarrollo e Innovación Tecnológica (I+D+i) from the Spanish Ministry of Science and Innovation: Grants FIS PI17/0391 and FIS PI14/0955 from Instituto de Salud Carlos III and Grant RTC-2017-6696-1 (all of them, cofinanced by FEDER funds, European Union) and PGC2018-101904-A-I00 from Ministry of Science, Innovation and Universities of Spain.

ACKNOWLEDGMENTS

The authors thank Amalia de la Rosa and Concha López, and the Experimental Unit of the Virgen de las Nieves University Hospital for their support with the surgical procedures and animal experimentation. The authors also express their thanks to K. Shashok for improving the use of English in the manuscript.

REFERENCES

Alaminos, M., Del Carmen, S.-Q. M., Munoz-Avila, J. I., Serrano, D., Medialdea, S., Carreras, I., et al. (2006). Construction of a complete rabbit cornea substitute using a fibrin-agarose scaffold. *Invest. Ophthalmol. Vis. Sci.* 47, 3311–3317. doi: 10.1167/iovs.05-1647

Alaminos, M., Perez-Kohler, B., Garzon, I., Garcia-Honduvilla, N., Romero, B., Campos, A., et al. (2010). Transdifferentiation potentiality of human Wharton's jelly stem cells towards vascular endothelial cells. *J. Cell Physiol.* 223, 640–647. doi: 10.1002/jcp.22062

Alfonso-Rodriguez, C. A., Gonzalez-Andrades, E., Jaimes-Parra, B. D., Fernandez-Valades, R., Campos, A., Sanchez-Quevedo, M. C., et al. (2015). Ex vivo and in vivo modulatory effects of umbilical cord Wharton's jelly stem cells on human oral mucosa stroma substitutes. *Histol Histopathol.* 30, 1321–1332. doi: 10.14670/HH-11-628

Amiri, F., Ghiyasvandian, S., Navab, E., and Zakerimoghadam, M. (2017). Corneal transplantation: a new view of life. *Electron Physician.* 9, 4055–4063. doi: 10.19082/4055

Behaegel, J., Ni Dhubhghaill, S., Koppen, C., and Zakaria, N. (2017). Safety of cultivated limbal epithelial stem cell transplantation for human corneal regeneration. *Stem Cells Int.* 2017:6978253. doi: 10.1155/2017/6978253

Campos, F., Bonhome-Espinosa, A. B., Garcia-Martinez, L., Duran, J. D., Lopez-Lopez, M. T., Alaminos, M., et al. (2016). Ex vivo characterization of a novel tissue-like cross-linked fibrin-agarose hydrogel for tissue engineering applications. *Biomed Mater.* 11:e055004. doi: 10.1088/1748-6041/11/5/055004

Catanese, M., Popovici, C., Proust, H., Hoffart, L., Matonti, F., Cochereau, I., et al. (2011). Fluorescent in situ hybridization (FISH) on corneal impression cytology specimens (CICS): study of epithelial cell survival after keratoplasty. *Invest Ophthalmol Vis Sci.* 52, 1009–1013. doi: 10.1167/iovs.10-5394

Corrao, S., La Rocca, G., Lo Iacono, M., Corsello, T., Farina, F., and Anzalone, R. (2013). Umbilical cord revisited: from Wharton's jelly myofibroblasts to mesenchymal stem cells. *Histol Histopathol.* 28, 1235–1244. doi: 10.14670/HH-28.1235

Couture, C., Zaniolo, K., Carrier, P., Lake, J., Patenaude, J., Germain, L., et al. (2016). The tissue-engineered human cornea as a model to study expression of matrix metalloproteinases during corneal wound healing. *Biomaterials* 78, 86–101. doi: 10.1016/j.biomaterials.2015.11.006

Cvekl, A., and Zhang, X. (2017). Signaling and gene regulatory networks in mammalian lens development. *Trends Genet.* 33, 677–702. doi: 10.1016/j.tig.2017.08.001

Ebrahimi, M., Taghi-Abadi, E., and Baharvand, H. (2009). Limbal stem cells in review. *J. Ophthalmic. Vis. Res.* 4, 40–58.

El Omar, R., Beroud, J., Stoltz, J. F., Menu, P., Velot, E., and Decot, V. (2014). Umbilical cord mesenchymal stem cells: the new gold standard for mesenchymal stem cell-based therapies? *Tissue Eng Part B Rev.* 20, 523–544. doi: 10.1089/ten.TEB.2013.0664

Garzon, I., Alfonso-Rodriguez, C. A., Martinez-Gomez, C., Carriel, V., Martin-Piedra, M. A., Fernandez-Valades, R., et al. (2014a). Expression of epithelial markers by human umbilical cord stem cells. A topographical analysis. *Placenta.* 35, 994–1000. doi: 10.1016/j.placenta.2014.09.007

Garzon, I., Martin-Piedra, M. A., Alfonso-Rodriguez, C., Gonzalez-Andrades, M., Carriel, V., Martinez-Gomez, C., et al. (2014b). Generation of a biomimetic human artificial cornea model using Wharton's jelly mesenchymal stem cells. *Invest. Ophthalmol. Vis. Sci.* 55, 4073–4083. doi: 10.1167/iovs.14-14304

Garzon, I., Chato-Astrain, J., Campos, F., Fernandez-Valades, R., Sanchez-Montesinos, I., Campos, A., et al. (2020). Expanded differentiation capability of human Wharton's jelly stem cells. A systematic review. *Tissue Eng. Part B Rev.* doi: 10.1089/ten.TEB.2019.0257 [Epub ahead of print].

Garzon, I., Sanchez-Quevedo, M. C., Moreu, G., Gonzalez-Jaranay, M., Gonzalez-Andrades, M., Montalvo, A., et al. (2009). In vitro and in vivo cytokeratin patterns of expression in bioengineered human periodontal mucosa. *J. Periodontal. Res.* 44, 588–597. doi: 10.1111/j.1600-0765.2008.01159.x

Ghezzi, C. E., Rnjak-Kovacina, J., and Kaplan, D. L. (2015). Corneal tissue engineering: recent advances and future perspectives. *Tissue Eng. Part B Rev.* 21, 278–287. doi: 10.1089/ten.TEB.2014.0397

Giasson, C. J., Deschambeault, A., Carrier, P., and Germain, L. (2014). Adherens junction proteins are expressed in collagen corneal equivalents produced in vitro with human cells. *Mol. Vis.* 20, 386–394.

Gomes, J. A., Geraldes Monteiro, B., Melo, G. B., Smith, R. L., Cavenaghi Pereira, Da Silva, M., et al. (2010). Corneal reconstruction with tissue-engineered cell sheets composed of human immature dental pulp stem cells. *Invest. Ophthalmol. Vis. Sci.* 51, 1408–1414. doi: 10.1167/iovs.09-4029

Gonzalez-Andrades, M., Garzon, I., Gascon, M. I., Munoz-Avila, J. I., Sanchez-Quevedo, M. C., Campos, A., et al. (2009). Sequential development of intercellular junctions in bioengineered human corneas. *J. Tissue Eng. Regen. Med.* 3, 442–449. doi: 10.1002/term.178

Gonzalez-Andrades, M., Mata, R., Gonzalez-Gallardo, M. D. C., Medialdea, S., Arias-Santiago, S., Martinez-Atienza, J., et al. (2017). A study protocol for a multicentre randomised clinical trial evaluating the safety and feasibility of a bioengineered human allogeneic nanostructured anterior cornea in patients with advanced corneal trophic ulcers refractory to conventional treatment. *BMJ Open* 7:e016487. doi: 10.1136/bmjopen-2017-016487

Griffith, M., Osborne, R., Munger, R., Xiong, X., Doillon, C. J., Laycock, N. L., et al. (1999). Functional human corneal equivalents constructed from cell lines. *Science* 286, 2169–2172. doi: 10.1126/science.286.5447.2169

Ionescu, A. M., Alaminos, M., De La Cruz, Cardona, J., De Dios Garcia-Lopez Duran, J., Gonzalez-Andrades, M., et al. (2011). Investigating a novel nanostructured fibrin-agarose biomaterial for human cornea tissue engineering: rheological properties. *J. Mech. Behav. Biomed. Mater.* 4, 1963–1973. doi: 10.1016/j.jmbbm.2011.06.013

Ionescu, A. M., Cardona, J. C., Garzon, I., Oliveira, A. C., Ghinea, R., Alaminos, M., et al. (2015). Integrating-sphere measurements for determining optical properties of tissue-engineered oral mucosa. *J. Eur. Opt. Soc. Rapid Pub.* 10:15012. doi: 10.2971/jeos.2015.15012

Ionescu, A. M., De La Cruz Cardona, J., Ghinea, R., Garzon, I., Gonzalez-Andrades, M., Alaminos, M., et al. (2017). "Optical properties of an anterior lamellar human cornea model based on fibrin-agarose," in *Proceedings of the Third International Conference on Applications of Optics and Photonics*, ed. M. F. M. Costa, Faro.

Isaacson, A., Swioklo, S., and Connon, C. J. (2018). 3D bioprinting of a corneal stroma equivalent. *Exp. Eye Res.* 173, 188–193. doi: 10.1016/j.exer.2018.05.010

Jafarinasab, M. R., Feizi, S., Esfandiari, H., Kheiri, B., and Feizi, M. (2012). Traumatic wound dehiscence following corneal transplantation. *J. Ophthalmic. Vis. Res.* 7, 214–218.

Kivela, T., and Uusitalo, M. (1998). Structure, development and function of cytoskeletal elements in non-neuronal cells of the human eye. *Prog. Retin. Eye Res.* 17, 385–428. doi: 10.1016/s1350-9462(98)00001-9

Le-Bel, G., Guerin, L. P., Carrier, P., Mouriaux, F., Germain, L., Guerin, S. L., et al. (2019). Grafting of an autologous tissue-engineered human corneal epithelium to a patient with limbal stem cell deficiency (LSCD). *Am. J. Ophthalmol. Case Rep.* 15:100532. doi: 10.1016/j.ajoc.2019.100532

Lin, H. F., Lai, Y. C., Tai, C. F., Tsai, J. L., Hsu, H. C., Hsu, R. F., et al. (2013). Effects of cultured human adipose-derived stem cells transplantation on rabbit cornea regeneration after alkaline chemical burn. *Kaohsiung J. Med. Sci.* 29, 14–18. doi: 10.1016/j.kjms.2012.08.002

Liu, Y., Wang, X., and Jin, Y. (2008). Can bone marrow cells give rise to cornea epithelial cells? *Med. Hypotheses* 71, 411–413. doi: 10.1016/j.mehy.2008.03.044

Martin-Piedra, M. A., Garzon, I., Gomez-Sotelo, A., Garcia-Abril, E., Jaimes-Parra, B. D., Lopez-Cantarero, M., et al. (2017). Generation and evaluation of novel stromal cell-containing tissue engineered artificial stromas for the surgical repair of abdominal defects. *Biotechnol. J.* 12:1700078. doi: 10.1002/biot.201700078

Meek, K. M., and Knupp, C. (2015). Corneal structure and transparency. *Prog. Retin. Eye Res.* 49, 1–16. doi: 10.1016/j.preteyeres.2015.07.001

Mi, S., Chen, B., Wright, B., and Connon, C. J. (2010). Ex vivo construction of an artificial ocular surface by combination of corneal limbal epithelial cells and a compressed collagen scaffold containing keratocytes. *Tissue Eng. Part A.* 16, 2091–2100. doi: 10.1089/ten.TEA.2009.0748

Nguyen, K. N., Bobba, S., Richardson, A., Park, M., Watson, S. L., Wakefield, D., et al. (2017). Native and synthetic scaffolds for limbal epithelial stem cell transplantation. *Acta Biomater.* 65, 21–35. doi: 10.1016/j.actbio.2017.10.037

Nishida, K., Yamato, M., Hayashida, Y., Watanabe, K., Yamamoto, K., Adachi, E., et al. (2004). Corneal reconstruction with tissue-engineered cell sheets composed of autologous oral mucosal epithelium. *N. Engl. J. Med.* 351, 1187–1196. doi: 10.1056/NEJMoa040455

Oie, Y., and Nishida, K. (2016). Corneal regenerative medicine. *Regen. Ther.* 5, 40–45. doi: 10.1016/j.reth.2016.06.002

Pellegrini, G., Ardigo, D., Milazzo, G., Iotti, G., Guatelli, P., Pelosi, D., et al. (2018). Navigating market authorization: the path holoclar took to become the first stem cell product approved in the european union. *Stem Cells Transl. Med.* 7, 146–154. doi: 10.1002/sctm.17-0003

Prahl, S. A., Van Gemert, M. J., and Welch, A. J. (1993). Determining the optical properties of turbid mediaby using the adding-doubling method. *Appl. Opt.* 32, 559–568. doi: 10.1364/AO.32.000559

Reichl, S., and Muller-Goymann, C. C. (2003). The use of a porcine organotypic cornea construct for permeation studies from formulations containing befunolol hydrochloride. *Int. J. Pharm.* 250, 191–201. doi: 10.1016/s0378-5173(02)00541-0

Rico-Sanchez, L., Garzon, I., Gonzalez-Andrades, M., Ruiz-Garcia, A., Punzano, M., Lizana-Moreno, A., et al. (2019). Successful development and clinical translation of a novel anterior lamellar artificial cornea. *J. Tissue Eng. Regen. Med.* 13, 2142–2154. doi: 10.1002/term.2951

Sangwan, V. S., and Sharp, J. A. H. (2017). Simple limbal epithelial transplantation. *Curr. Opin. Ophthalmol.* 28, 382–386. doi: 10.1097/ICU.0000000000000377

Sardar, D. K., Yow, R. M., Tsin, A. T., and Sardar, R. (2005). Optical scattering, absorption, and polarization of healthy and neovascularized human retinal tissues. *J. Biomed. Opt.* 10:51501. doi: 10.1117/1.2065867

Sardar, D. K., Yust, B. G., Barrera, F. J., Mimun, L. C., and Tsin, A. T. (2009). Optical absorption and scattering of bovine cornea, lens and retina in the visible region. *Lasers Med. Sci.* 24, 839–847. doi: 10.1007/s10103-009-0677-0

Tardieu, A. (1998). alpha-Crystallin quaternary structure and interactive properties control eye lens transparency. *Int. J. Biol. Macromol.* 22, 211–217. doi: 10.1016/s0141-8130(98)00018-x

Torricelli, A. A., Santhanam, A., Wu, J., Singh, V., and Wilson, S. E. (2016). The corneal fibrosis response to epithelial-stromal injury. *Exp. Eye Res.* 142, 110–118. doi: 10.1016/j.exer.2014.09.012

Wright, B., and Connon, C. J. (2013). Limbal epithelial stem cell identification using immunoblotting analysis. *Methods Mol. Biol.* 1014, 79–99. doi: 10.1007/978-1-62703-432-6_6

Yust, B. G., Mimun, L. C., and Sardar, D. K. (2012). Optical absorption and scattering of bovine cornea, lens, and retina in the near-infrared region. *Lasers Med. Sci.* 27, 413–422. doi: 10.1007/s10103-011-0927-9

Zaniolo, K., Carrier, P., Guerin, S. L., Auger, F. A., and Germain, L. (2013). A tissue-engineered corneal wound healing model for the characterization of reepithelialization. *Methods Mol. Biol.* 1037, 59–78. doi: 10.1007/978-1-62703-505-7_4

Zheng, M., Tian, C., Fan, T., and Xu, B. (2019). Fibronectin regulates the self-renewal of rabbit limbal epithelial stem cells by stimulating the Wnt11/Fzd7/ROCK non-canonical Wnt pathway. *Exp. Eye Res.* 185:107681. doi: 10.1016/j.exer.2019.05.021

Conflict of Interest: The authors declare that the research was conducted in the absence of any commercial or financial relationships that could be construed as a potential conflict of interest.

frontiers in Bioengineering and Biotechnology

ORIGINAL RESEARCH
published: 03 July 2020
doi: 10.3389/fbioe.2020.00755

VEGF Over-Expression by Engineered BMSC Accelerates Functional Perfusion, Improving Tissue Density and In-Growth in Clinical-Size Osteogenic Grafts

Rene' D. Largo[1,2†‡], Maximilian G. Burger[1,2‡], Oliver Harschnitz[1,2†], Conny F. Waschkies[3,4], Andrea Grosso[1,2], Celeste Scotti[5†], Alexandre Kaempfen[2], Sinan Gueven[5†], Gernot Jundt[6], Arnaud Scherberich[5], Dirk J. Schaefer[2], Andrea Banfi[1,2] and Nunzia Di Maggio[1]**

[1] Cell and Gene Therapy, Department of Biomedicine, Basel University Hospital and University of Basel, Basel, Switzerland, [2] Plastic and Reconstructive Surgery, Department of Surgery, Basel University Hospital and University of Basel, Basel, Switzerland, [3] Institute for Biomedical Engineering, ETH and University of Zurich, Zurich, Switzerland, [4] Department of Surgical Research, University Hospital Zurich, Zurich, Switzerland, [5] Tissue Engineering, Department of Biomedicine, University Hospital of Basel, University of Basel, Basel, Switzerland, [6] Institute of Pathology, University Hospital of Basel, Basel, Switzerland

The first choice for reconstruction of clinical-size bone defects consists of autologous bone flaps, which often lack the required mechanical strength and cause significant donor-site morbidity. We have previously developed biological substitutes in a rabbit model by combining bone tissue engineering and flap pre-fabrication. However, spontaneous vascularization was insufficient to ensure progenitor survival in the core of the constructs. Here, we hypothesized that increased angiogenic stimulation within constructs by exogenous VEGF can significantly accelerate early vascularization and tissue in-growth. Bone marrow stromal cells from NZW rabbits (rBMSC) were transduced with a retroviral vector to express rabbit VEGF linked to a truncated version of rabbit CD4 as a cell-surface marker. Autologous cells were seeded in clinical-size 5.5 cm^3 HA scaffolds wrapped in a panniculus carnosus flap to provide an ample vascular supply, and implanted ectopically. Constructs seeded with VEGF-expressing rBMSC showed significantly increased progenitor survivival, depth of tissue ingrowth and amount of mineralized tissue. Contrast-enhanced MRI after 1 week *in vivo* showed significantly improved tissue perfusion in the inner layer of the grafts compared to controls. Interestingly, grafts containing VEGF-expressing rBMSC displayed a hierarchically organized functional vascular tree, composed of dense capillary networks in the inner layers connected to large-caliber feeding vessels entering the constructs at the periphery. These data constitute proof of principle that providing sustained VEGF signaling, independently of cells experiencing hypoxia, is effective to drive rapid vascularization and increase early perfusion in clinical-size osteogenic grafts, leading to improved tissue formation deeper in the constructs.

Keywords: VEGF, bone marrow stromal cells, osteogenic grafts, vascularization, gene therapy

OPEN ACCESS

Edited by:
Dimitrios I. Zeugolis, National University of Ireland, Galway, Ireland

Reviewed by:
Moyo Kruyt, University Medical Center Utrecht, Netherlands
Xinluan Wang, Shenzhen Institutes of Advanced Technology (CAS), China

***Correspondence:**
Andrea Banfi
Andrea.Banfi@usb.ch
Nunzia Di Maggio
Nunzia.DiMaggio@usb.ch

†Present address:
Rene' D. Largo, Department of Plastic Surgery, The University of Texas MD Anderson Cancer Center, Houston, TX, United States
Oliver Harschnitz, The Center for Stem Cell Biology, Sloan-Kettering Institute for Cancer Research, New York, NY, United States
Celeste Scotti, Novartis Institutes for Biomedical Research, Basel, Switzerland
Sinan Gueven, İzmir Biomedicine and Genome Center, Dokuz Eylul University, İzmir, Turkey

‡*These authors have contributed equally to this work*

Specialty section:
This article was submitted to Tissue Engineering and Regenerative Medicine, a section of the journal Frontiers in Bioengineering and Biotechnology

Received: *02 February 2020*
Accepted: *12 June 2020*
Published: *03 July 2020*

INTRODUCTION

Bone grafts are crucial to treat bone tissue loss due to trauma, surgery or other clinical conditions where physiological bone repair is insufficient. Autografts are currently the gold standard for bone repair, but this approach is often associated with several limitations, including chronic pain at the harvest site, neurovascular injury, structural weakness and the limited amount of autologous bone available (Younger and Chapman, 1989; Giladi et al., 2018). Moreover, upon implantation *in vivo*, a major hurdle, especially for large defects, is osteonecrosis due to lack of an endogenous vascular network which can improve host integration (Rouwkema et al., 2008). Grafts consisting of bone tissue and an internal vascular network supplied by large caliber vessels, called bone flaps, have been applied for surgical reconstruction of large segmental defects (Sparks et al., 2017). However, bone flaps also suffer from complications, including insufficient mechanical strength, significant donor site morbidity, as well as complicated surgical procedures to generate grafts of a predefined shape (Bodde et al., 2003). Therefore, available surgical strategies are currently insufficient and there is an unmet clinical need to promote vascularized bone regeneration. Bone tissue-engineering holds promise for the generation of osteogenic grafts, combining osteogenic progenitors with biocompatible scaffolds. For this purpose, bone marrow stromal cells (BMSC) are a rich source of potent osteoprogenitors, able to produce bone tissue both ectopically and orthotopically when associated with ceramic biomaterials (Iaquinta et al., 2019). However, in general this strategy has yet to prove effective in humans for defects of clinically relevant size (i.e., a few cubic centimeters). One significant issue underlying these failures is the lack of rapid vascularization, which results in progenitor death and failure of bone formation inside the graft at depths greater than about 1 mm (Scheufler et al., 2008; Guven et al., 2011).

Several approaches to accelerate vascularization of tissue-engineered bone grafts are currently being investigated, such as surgical techniques (flap or arterio-venous loop fabrication), biomaterial-based methods (scaffold micro-fabrication designed to facilitate vascular in-growth) or co-culture of osteogenic and vasculogenic progenitors inside the grafts (Rao and Stegemann, 2013; Almubarak et al., 2016). We have previously developed biological substitutes of clinically relevant size in a rabbit model by combining bone tissue engineering and flap pre-fabrication (Scheufler et al., 2008). Autologous cell-based, large bone flaps in rabbits were prefabricated using porous ceramic scaffolds loaded with BMSC and wrapped by a panniculus carnosus flap, as an ample exogenous vessel source. This led to the formation of healthy bone tissue in the periphery of the graft, a fibrotic area in the middle and necrosis in the core, because of insufficient blood supply, despite the presence of a highly vascularized panniculus carnosus layer placed around the scaffolds.

Vascular Endothelial Growth Factor (VEGF) is the master regulator of blood vessel growth and the key molecular target of strategies to promote vascular network expansion in regenerative medicine (Gianni-Barrera et al., 2020). Here, we test the hypothesis that increased angiogenic stimulation from within the core of bone constructs by VEGF can significantly accelerate early vascular in-growth, improve graft perfusion and therefore ensure cell viability deeper in the construct.

MATERIALS AND METHODS

Bone Marrow Harvest and rBMSC Culture

The study was approved by the Animal Ethics Committee of the Swiss Federal Veterinary Office[1]. Bone marrow was harvested from 7 young adult New Zealand White (NZW) rabbits (Charles River Laboratories, Kisslegg, Germany) with an average body weight of 2.3 ± 0.2 kg. Animals were sedated by subcutaneous administration of 25 mg per kg of body weight ketamine hydrochloride (Ketaminol 5%®ad us. vet., Veterinaria AG, Zurich, Switzerland) and 2.5 mg per kg of body weight xylazine (Narcoxyl 2%® ad us. vet., Veterinaria AG, Zurich, Switzerland) before transfer to the operating room, where inhalation anesthesia was initiated with isoflurane (Forene®, Abbott AG, Baar, Switzerland). Transcutaneous arterial oxygen saturation and heart rate were monitored with a pulse oximeter (NPB 290, Nellcor Puritan Bennett, Pleasanton, CA, United States) fixed to a front limb. Before surgery, single shot antibiotic prophylaxis with 15 mg per kg of body weight sulfadoxin-trimethoprim (Borgal® 24% ad us. vet., Veterinaria AG, Zurich, Switzerland) and 0.05 mg per kg of body weight buprenorphine (Temgesic®, Essex Chemie AG, Luzern, Switzerland) for pain relief were administered subcutaneously. After the area over the iliac crests was shaved and prepped with povidone iodine solution (Betaseptic®, Mundipharma Medical Company, Basel, Switzerland), bone marrow was harvested by repeated puncture of both iliac bones (2–3 per side) using 20 gauge needles and 20 ml syringes filled with 1 ml of heparin sodium solution (Heparin-Na® 5′000 IU/ml, B. Braun Medical AG, Emmenbrücke, Switzerland), yielding average aspirate volumes of 18 ± 4 ml (range: 13–24 ml) per animal. Fresh aspirates were diluted with a double volume of phosphate buffered saline (PBS, Gibco, Invitrogen Corporation, Basel, Switzerland), and centrifuged, resulting in the elimination of supernatant fat, blood clots, and small tissue particles. Nucleated cells were then stained with crystal violet 2.3% (Sigma-Aldrich, Fluka Chemie AG, Buchs, Switzerland), counted and plated at a density of 1×10^5 cells/cm^2 on tissue culture flasks. *In vitro* culture was performed in α-minimum essential medium (Gibco, Grand Island, NY, United States) supplemented with 10% fetal bovine serum and FGF-2 (5 ng/ml; R&D Systems, Minneapolis, MN, United States). Before reaching cell confluency, rBMSC were detached with 0.05% trypsin/0.01% EDTA (Gibco), counted and replated at a density of 2×10^3 cells/cm^2 for cell *in vitro* expansion.

Cell Cycle Analysis

The proportion of actively cycling cells was determined by measuring their nuclear DNA content by flow cytometry after

[1]http://bvet.admin.ch

staining with propidium iodide as described before (Helmrich et al., 2012). The data were analyzed using the cell cycle analysis tool from FlowJo Software (Becton, Dickinson and Company) using the Watson model. BMSC from three different rabbits from duplicate dishes were analyzed at each time point.

Vector Construction

Total RNA was purified from 20 to 30 mg samples of rabbit kidney and spleen tissue with the RNeasy Mini Kit (Qiagen, Basel, Switzerland). cDNA was synthesized with Omniscript Reverse Transcription Kit (Qiagen, Basel, Switzerland) according to the manufacturer's instructions. Full rabbit VEGF sequence was not available. Watkins et al. described the complete CDS of rabbit VEGF, but they used primers based on human VEGF sequence for the amplification (Watkins et al., 1999). One of the two partial sequences of rbVEGF we found on NCBI matched with the 3′ end of Watkins' VEGF sequence. The forward primer was constructed based on the human sequence; however, being the leading sequence, it would not interfere with the final amino acid sequence. Full-length rbVEGF-165 was cloned from kidney-RNA by PCR using the following primers: forward: 5′- TTT GGA TCC ATG AAC TTT CTG CTG TCT T -3′; reverse: 5′- TTT CTC GAG TCA CCG CCT CGG CTT GT -3′. PCR conditions were as follows: 94°C × 2 min + (94°C × 30 s + 58°C × 30 s + 72°C × 60 s) × 40 cycles + 72°C × 5 min. A truncated version of rabbit CD4, comprising only the extracellular and transmembrane domains, was generated by inserting a stop codon after codon 424 (NCBI accession number NP_001075782). PCR was performed on spleen cDNA with the following primers: reverse: 5′- CAA TTG TCA TCA CCG GCA CTT GAC ACA G -3′; forward: 5′- GTT TAA ACA TGA ACC GGA GAA TCT ACT -3′. PCR conditions were: 94°C × 2 min + (94° × 40 s + 52° × 40 s + 72° × 60 s) × 5 cycles + (94°C for 40 s, 58°C for 40 s, and 72°C for 60 s) × 30 cycles + 72°C × 5 min.

BMSC Retroviral Transduction

The amphotropic retrovirus was produced by Phoenix helper-free packaging lines by transient transfection as previously described (Pear et al., 1993). Rabbit BMSCs were infected at high efficiency with the retroviral constructs according to a previously published protocol (Springer and Blau, 1997). In order to achieve the highest efficiency, transduction was carried out few days after plating, when the cells had their highest mitotic activity. rBMSC were cultured in 60-mm dishes and were incubated with retroviral vector supernatants supplemented with 8 μg/mL polybrene (Sigma-Aldrich) for 5 min at 37°C and centrifuged at 1100 *g* for 30 min at room temperature in the dishes, followed by fresh medium replacement. The infection rate of the rBMSC after each transduction round (0 to 6 rounds) was determined by FACS analysis with mouse anti rabbit CD4-FITC conjugated antibody (MCA799F, AbD Serotec).

Cell Sorting

Expression of truncated CD4 by individual cells was assessed by staining transduced rBMSC with a specific antibody to rabbit CD4 directly conjugated to fluorescein isothiocyanate (MCA799F, AbD Serotec). 3–5 × 10^5 cells were resuspended into 200 μl of 0.5% BSA and incubated with 5 μl of antibody for 20 min on ice. Data were acquired with a FACS Calibur flow cytometer (Becton, Dickinson and Company) and analyzed using FlowJo software (Becton, Dickinson and Company). Cell sorting was performed with a FACS Vantage SE cell sorter (Becton, Dickinson and Company).

Rabbit-VEGF ELISA Measurements

The production of rabbit-VEGF in cell culture supernatants was quantified using a Quantikine mouse VEGF immunoassay ELISA kit (R&D Systems Inc., Minneapolis, MN, United States). One ml of fresh medium was incubated on rBMSCs cultured in 60-mm dishes in duplicate for 4 h, filtered, and frozen. Results were normalized by the number of cells in each dish and the time of incubation.

3D Perfusion Seeding

Porous ceramic scaffolds (porosity: 80 ± 3%, pore size distribution: 22%, 100 μm; 32%, 100–200 μm; 40%, 200–500 μm; 6%, 500 μm) made of 100% hydroxyapatite, with a Ca/P ratio of 1.66 ± 0.5 (Engipore®, Fin-Ceramica, Faenza, Italy[2]), were fabricated in the shape of large tapered cylinders (30 mm height, 20 mm upper base diameter, 10 mm lower base diameter, 5.5 cm^3 volume). Autologous expanded rBMSC were seeded in tapered cylinders for each animal, using a previously described bioreactor system (Wendt et al., 2003), based on the principle of direct perfusion of a single cell suspension through the interconnected pores of 3D scaffolds. Briefly, scaffolds were pre-wetted in complete medium and press-fitted into custom-made polycarbonate chambers (one scaffold per chamber), positioned at the bottom of two vertical Teflon-columns and connected with each other at their base through a U-shaped tubing. rBMSC (naïve, control CD4 and VEGF-expressing) suspended in 10 ml of medium were introduced into the bioreactor and perfused through the ceramic pores in alternating directions at a flow rate of 1.2 ml/min for 18 h using a standard syringe pump (Programmable PHD 2000®, Harvard Apparatus, Holliston, MA, United States). A seeding density of 10 × 10^6 cells/cm^3 of ceramic was consistently used, corresponding to a total number of 55 × 10^6 rBMSC for tapered cylinders. All 3D perfusion cultures were incubated in humidified atmosphere at 37°C/5% CO_2.

Surgical Procedure

Cell-seeded ceramic scaffolds were retrieved from the bioreactor, rinsed in PBS, placed in sterile Falcon tubes pre-filled with PBS, and transferred to the operating room. After the surgical site on the dorsum of animals was shaved, disinfected and draped, a midline skin incision was made to expose the panniculus carnosus. Three anteriorly pedicled 6.5-cm wide and 8-cm long panniculus carnosus flap centered over an axial vascular pedicle were raised: two flaps were located cranially and one flap caudally. The cell-scaffold constructs (one with VEGF-transduced BMSC, one with CD4 BMSC and

[2]www.finceramica.it

one with naïve BMSC) were randomly assigned to one of the three flap sites, wrapped with a panniculus carnosus flap and covered by a semipermeable membrane (Biobrane®, UDL Laboratories Inc., Rockford, IL, United States). The membrane material is permeable to oxygen and nutrients, and allows drainage of exudate through small pores, thereby preventing the accumulation of wound fluid and seroma formation. After 8 weeks, rabbits were euthanized by intravenous injection of pentobarbital (Nembutal® , Sanofi, Basel, Switzerland) and constructs retrieved with the surrounding semipermeable membrane. The vascular pedicle was isolated at the flap base and inspected for patency. After division of the vascular pedicle, the constructs were exposed and assessed macroscopically for signs of infection and external vascularization.

Dynamic Contrast Enhanced MRI

Perfusion MRI was performed on a 3T clinical scanner (Siemens Magnetom Verio) with a 15-channel transmit/receive kneecoil with a dynamic 3D GE sequence (TE 1.38 ms, TR 3.8 s, flip angle 15°, spatial resolution 0.9 × 0.9 × 0.9 mm^3, dynamic scans sampled every 6 s, total 60 dynamic scans). MRI signal change upon contrast-enhancement was analyzed semi-quantitatively using the initial uprising slope of the signal time curve as a measure of tissue perfusion ("wash-in") and the initial area under the curve at 20 dynamic scans after contrast arrival (AUC20) as a measure for blood volume fraction after normalization to baseline. Slope and bolus arrival were computed (after manual selection of contrast arrival time on the signal time curves) using in-house MATLAB scripts (MATLAB R2018a, MathWorks®).

Microtomography

After explantation, constructs were fixed in 4% paraformaldehyde overnight and stored in PBS until micro-computed tomography (μ-CT) analysis. Data were acquired by using a phoenix nanotom m scanner (General Electric, Fairfield, CT) with 0.5-mm aluminum filtered x-rays (applied voltage 70 kV; current 260 μA). Transmission images were acquired during a 360° scan rotation with an incremental rotation step size of 0.25°. Reconstruction was made using a modified Feldkamp algorithm at an isotropic voxel size of 2.5 μm. Threshold-based segmentation and 3D measurement analyses (bone mineral density and volume) were performed using ImageJ software (Schneider et al., 2012) with the BoneJ (Doube et al., 2010) and 3D Shape (Sheets et al., 2013) extensions. The threshold employed for the segmentation was set at 325 mg/cm^3, as previously determined to clearly distinguish between ceramic and newly formed mineralized tissue (Scheufler et al., 2008). Three-dimensional rendering of the structures was performed using VGStudio MAX 2.2 software (Volume Graphics, Heidelberg, Germany).

Histology and Immunohistochemistry

After μ-CT analysis, constructs were decalcified by 7% EDTA and embedded in paraffin. The sections (7 μm thickness) were stained with Masson's trichrome staining (RAL Diagnostics, Martillac, France). For immunofluorescence staining, sections were first deparaffinized in Ultra-clear and then rehydrated in graded ethanol. For antigen retrieval, sections were incubated with 0.05% trypsin and 0.1% CaCl2 in water for 13 min at 37°C and 10 min at room temperature, then rinsed 3 × 10 min in 100 mM glycine and 2 × 2 min in PBS. Blocking was performed for 1 h at room temperature with 5% goat serum and 2% BSA in PBS/0.3% Triton. Sections were then incubated for 1 h at room temperature with anti-rabbit CD4 primary antibody (MCA799GA, Clone Ken-4, Bio-Rad, Hercules, CA, United States 1:100) and subsequently for 1 h with a fluorescently labeled secondary antibody (AlexaFluor 647, Invitrogen, Carlsbad, CA, United States 1:200). Fluorescence images were acquired with a Nikon Ti2 Eclipse epifluorescence microscope (Nikon, Tokyo, Japan). The number of $CD4^+$ cells was quantified automatically on 5 representative images from each of 3 concentric 1.5 mm-deep layers (outer, middle and inner) in each construct (n = 4 constructs/group) using FIJI software (ImageJ[3]) and normalized by the number of total cells (detected by DAPI staining) or by the tissue area (mm^2). To assess vascularization, immunohistochemical staining for CD31 with a rabbit specific antibody (SC1506, Santa Cruz, 1:100) was performed. After incubation with a biotinylated secondary antibody and subsequently with an ABC-alkaline phosphatase complex, the specific staining was revealed by using Fast Red (all reagents from Dako, Bollschweil, Germany). Matched IgG control antibody was used as a negative control.

Statistics

Data are presented as mean ± SEM. The normal distribution of all data sets was assessed by the Shapiro-Wilk test and the significance of differences was evaluated with analysis of variance (ANOVA) followed by the Bonferroni test (for multiple comparison), or with the Student's t-test (for single comparisons); $p < 0.05$ was considered statistically significant.

RESULTS

Optimization of rBMSC Transduction

VEGF expression throughout the osteogenic graft was ensured by genetically engineering the seeded progenitors with a retroviral vector (Helmrich et al., 2012), which integrates in the genome and therefore is not lost upon cell expansion. Since retroviral vectors efficiently transduce only dividing cells, we first determined the earliest time after isolation and plating when rabbit BMSC (rBMSC) enter the cell cycle and proliferation is at its peak. Cell cycle analysis was performed on samples from 3 independent donors starting from day 3 after the initial plating to the time of first confluence, which was reached consistently by day 10. rBMSC proliferation increased 5 days after isolation (41.7 ± 7.3% of cycling cells), reproducibly reached a peak by day 7 (58.5 ± 10.3%) and it was maintained until day 9

[3]http://fiji.sc/Fiji

(41.9 ± 7.9%), after which replication declined with increasing confluence (**Figure 1A**). Based on these results, we determined the optimal time to start transduction to be on day 6 after isolation. Cells were transduced twice per day up to six times with a retroviral vector expressing a truncated version of rabbit CD4 (trCD4), which was non-functional through removal of the intracellular domain and acted as a convenient cell-surface reporter gene (Misteli et al., 2010). The transduction efficiency was evaluated after each round by FACS quantification of the CD4-positive cells. More than half of the cells were transduced after two rounds (56.7% ± 1.2%) and the number of CD4-positive cells reached 70% after six rounds (70.1 ± 5.2%). Although a plateau was not reached, it was determined that six rounds of transduction would provide a suitable balance between maximizing transduction efficacy and minimizing cell manipulation and this protocol was used to generate all cell populations for further analysis described below.

Generation of FACS-Sortable VEGF-Expressing rBMSC

A bicistronic retroviral vector (**Figure 1B**) was constructed carrying the cDNA for rabbit $VEGF_{165}$ (VEGF) and the truncated version of rabbit CD4 (trCD4), joined through an internal ribosomal entry site (IRES) that allows the translation of both proteins from the same mRNA at a fixed ratio (Banfi et al., 2012). A retroviral vector expressing only trCD4 in the second cistron was used to generate control cells. Freshly isolated rBMSC from 4 individual animals were transduced according to the optimized protocol previously described (Helmrich et al., 2012). Using freshly produced viral vector supernatants, the average transduction efficiency was 63.4 ± 20.9% with the VEGF vector and 50.6 ± 16.2% for the control vector (n = 4). Upon reaching the first confluence, rBMSC were FACS purified in order to remove non-transduced cells and to yield pure CD4-positive populations (**Figure 1C**), which were replated for *in vitro* cell expansion. Removal of non-transduced cells was done to ensure a homogeneous distribution of the signal throughout the constructs, because VEGF binds tightly to extracellular matrix and therefore remains highly localized in the microenvironment around each producing cell *in vivo* and does not diffuse through tissue (Ozawa et al., 2004; Gianni-Barrera et al., 2020). Production of VEGF protein by VEGF-expressing rBMSC was confirmed by ELISA (609.5 ± 284.6 ng/10^6 cells/day of rabbit VEGF), whereas naïve and CD4-rBMSC secreted background amounts (23.5 ± 22.9 and 24.2 ± 25.9 ng/10^6 cells/day, respectively).

Generation of the Osteogenic Constructs

Clinical-size osteogenic constructs were generated as previously described (Scheufler et al., 2008) with tapered hydroxyapatite cylinders of 2-cm diameter at the base, 1-cm diameter at the top and 3.5-cm height (**Figure 2A**). Expanded rBMSC were seeded using a perfusion bioreactor system (**Figure 2B**), which is based on the principle of direct perfusion of a single cell suspension through the interconnected pores of 3D scaffolds and which has been shown previously to ensure a homogenous cell distribution within the pores of the scaffolds (Wendt et al., 2003). Naïve, VEGF-expressing and CD4-rBMSC were generated from each of the four independent rabbit donors (n = 4). Each rabbit received one construct for each condition generated with its own autologous cells. Scaffolds were first wrapped in a panniculus carnosus flap, which provided the vascularization source for new vessels to invade the construct from the outside toward the core, and further covered by a semipermeable membrane and then implanted under the skin of the dorsum of each rabbit donor for 8 weeks (**Figure 2C**). The membrane employed in this study was used to avoid uncontrolled sources of vascularization besides the panniculus carnosus, since it is permeable to oxygen and nutrients, but does not allow the invasion by surrounding blood vessels and cells. At the moment of harvesting, all constructs appeared viable, surrounded by a healthy panniculus carnosus layer, which was not removed in order to preserve the vascular connections with the scaffolds.

VEGF-Expressing rBMSC Increase the Amount of Mineralized Tissue Throughout the Construct *in vivo*

Constructs were harvested 8 weeks after implantation. Before undergoing decalcification for histological procedures, the constructs were analyzed by micro-computerized tomography (μ-CT). The analysis was performed mid-way on the long axis at a virtual cross-section of 1.5 cm and 3 concentric sections, each 1.5-mm deep, were designed in order to distinguish an outer, middle and inner layer (**Figure 3A**). Tissue density was calibrated according to Houndsfield units (HU) and color-coded (HU scale, **Figures 3B–D**). Constructs containing VEGF-expressing rBMSC were characterized by higher HU values reaching deeper in the construct (evidenced by the areas colored in red and orange in **Figure 3D**) compared to the Naïve (**Figure 3B**) and CD4 control (**Figure 3C**) conditions. These data were confirmed by quantification of the total tissue density (**Figure 3E**). As expected, a gradual decrease in tissue density could be observed at increasing depths from the construct surface. However, VEGF expression induced a consistently greater tissue density in all layers. Interestingly, VEGF enabled the inner layer to reach a tissue density similar or greater than the one of the more superficial layer in control conditions (VEGF inner = 497.4 ± 38.7 mg/cm^3 vs. Naïve outer = 486.1 ± 28.6 mg/cm^3 and CD4 outer = 477.0 ± 33.3 mg/cm^3). The increased tissue density in each layer of the constructs containing VEGF-expressing cells was due to a significant increase by about 25% in the amount of mineralized tissue compared to the control conditions (**Figure 3F**). On the other hand, the density of the mineralized tissue itself was not different among the three conditions (**Figure 3G**), showing that VEGF did not affect the quality of the mineralized matrix, but enabled a greater amount of it to be deposited.

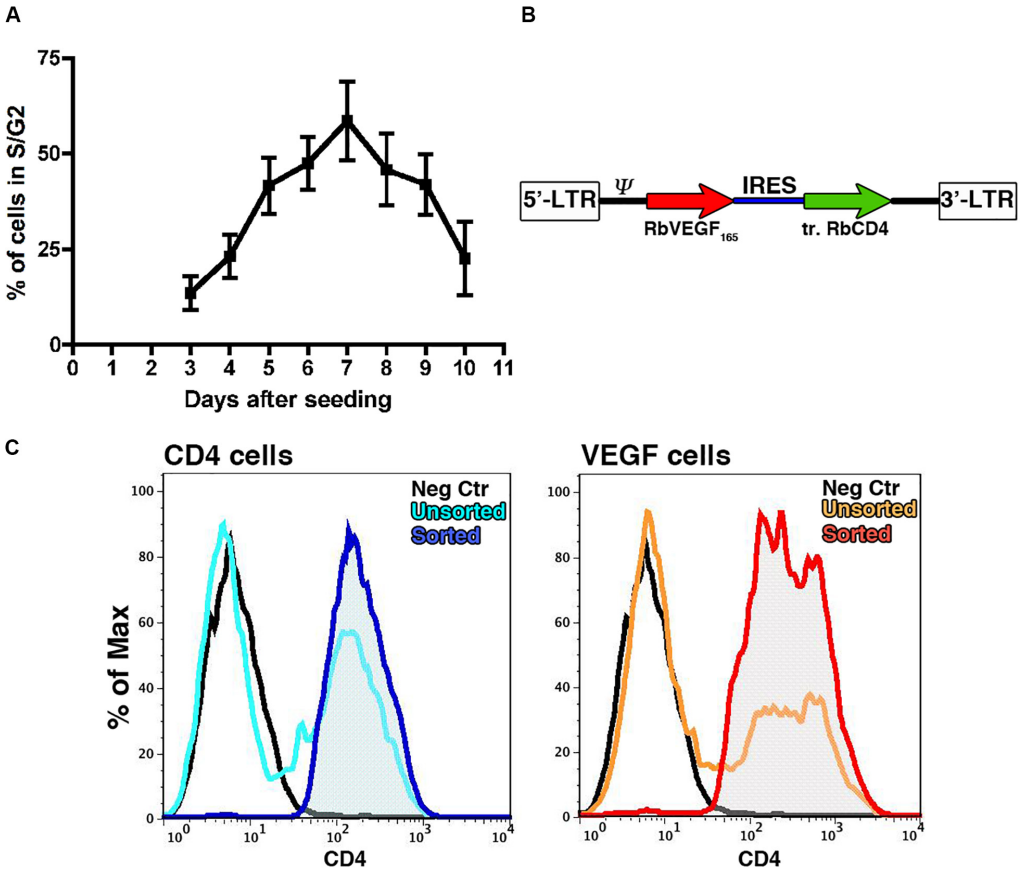

FIGURE 1 | (A) Assessment by flow cytometry of the proportion of cells in active proliferation (S/G2 phases) at different time points after initial plating (n = 3). **(B)** Map of the bicistronic retroviral vector carrying the coding sequences of rabbit $VEGF_{165}$ ($rVEGF_{165}$) and of a truncated version of rabbit CD4 (tr.rCD4) linked through an Internal Ribosomal Entry Sequence (IRES). **(C)** Representative FACS plots for transduced rBMSC (light blue and orange plots) and FACS purified populations (blue and red plots) stained for CD4 as a marker of transduction; Isotype controls = black plots.

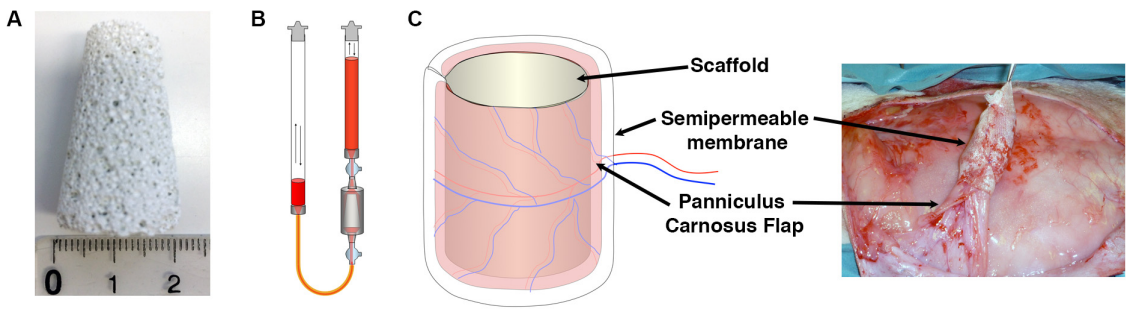

FIGURE 2 | (A) Porous ceramic scaffolds were fabricated in the shape of large tapered cylinders (30 mm height, 20 mm lower base diameter, 10 mm upper base diameter, 5.5 cm^3 volume). **(B)** Schematic representation of the perfusion bioreactor system used in the study, providing bidirectional alternating flow through the construct chamber during cell seeding and culture. **(C)** Constructs were covered with a panniculus carnosus vascularized flap, insulated with a semipermeable membrane and implanted subcutaneously *in vivo*.

VEGF Expression Increases Dense Tissue Ingrowth

Tissue ingrowth and bone formation were assessed histologically by Masson's trichrome staining. Constructs loaded with naïve, control CD4 and VEGF-expressing rBMSC were analyzed at three different positions along the main axis of the constructs in three independent rabbits and tissue invasion was quantified on transverse sections at five standardized points within each transverse section (red arrows in **Figure 4A**). Frank bone tissue could not be detected in any condition, but dense collagenous

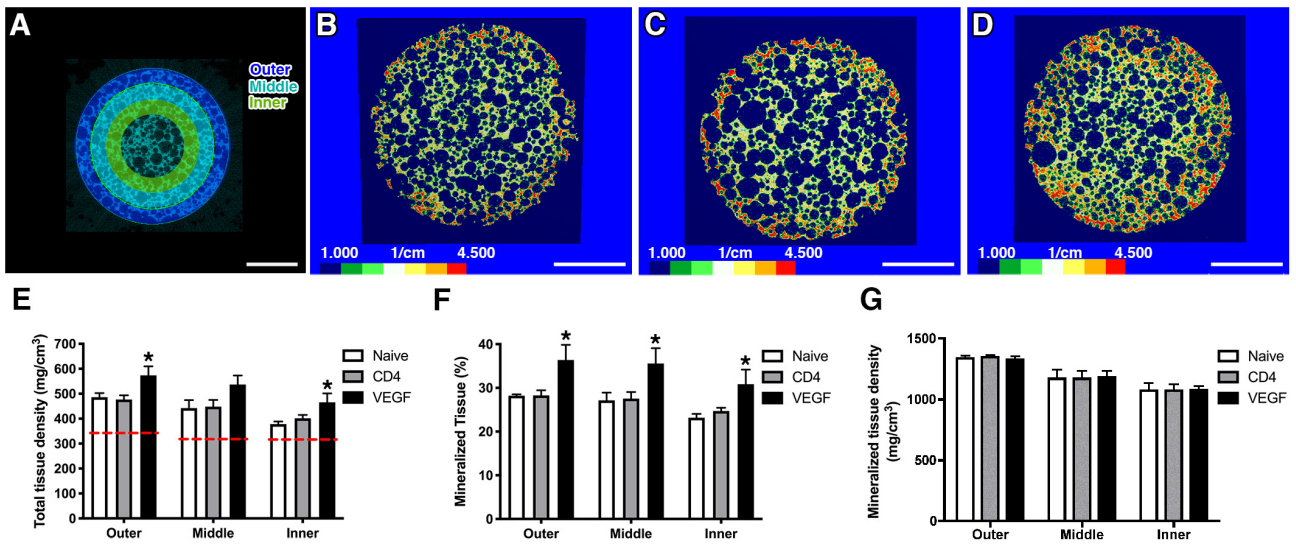

FIGURE 3 | (A) For μ-CT analysis, 3 concentric sections, each 1.5-mm deep, were designed in order to distinguish an outer, middle and inner layer (size bar = 5 mm). **(B–D)** Representative images of constructs containing naïve rBMSC **(B)**, CD4- **(C)** and VEGF-expressing rBMSC **(D)**, color-coded according to tissue density (Houndsfield units, HU) (size bar = 5 mm); **(E–G)** Quantification of total tissue density **(E)**, percentage of mineralized tissue **(F)** and density of mineralized tissue **(G)** in the three concentric layers defined in panel **(A)** ($n = 4$, $^*p < 0.05$). The red dashed lines in **(E)** represent the density values of empty scaffolds implanted without any cells.

matrix could be observed to fill the scaffold pores in all conditions, similar to pre-bone matrix not yet fully mineralized (**Figure 4B**). However, the depth of growth of this dense tissue was significantly different among conditions (**Figure 4C**). In fact, while both naïve and control CD4 cells similarly generated dense tissue in about the first 2.5 mm from the construct surface, VEGF-expressing rBMSC promoted a 35% increase in the depth of tissue invasion (3.52 ± 0.17 mm vs. naïve = 2.6 ± 0.25 mm and CD4 = 2.59 ± 0.20 mm; $p < 0.05$ and <0.01, respectively). A separate analysis of the data confirmed the reproducibility of this trend in the individual rabbits (**Figure 4D**).

VEGF Expression Improves the Survival of Seeded rBMSC

The survival of seeded progenitors was tracked by immunofluorescent staining of the truncated CD4 marker expressed from the retroviral vectors used to transduce both the control CD4 and VEGF populations, which had been used also for the FACS purification. The quantification of progenitor survival was performed separately in 3 concentric sections, each 1.5-mm deep, in order to distinguish an outer, middle and inner layer, similarly to the analysis of the μ-CT data above. As shown in **Figure 5A**, rBMSC could be detected within the scaffold pores in both groups 8 weeks after implantation. Quantification of CD4 + cells showed that VEGF expression significantly improved the survival of seeded progenitors by greater than 2-fold in the outer and middle layer, both in relation to the total amount of cells within the pores (**Figure 5B**) and as absolute amount of cells per mm^2 of pore tissue (**Figure 5C**). However, the most striking difference was observed in the inner layer, where progenitor survival dropped to virtually zero in the controls, but was maintained at levels similar to the middle layer by VEGF expression (**Figure 5C**; Outer: CD4 = 232.6 ± 21.2 cells/mm^2 vs. VEGF = 476.1 ± 56.7 cells/mm^2, $p < 0.01$; Middle: CD4 = 164.4 ± 73.7 cells/mm^2 vs. VEGF = 437.1 ± 64.7 cells/mm^2, $p < 0.05$; Inner: CD4 = 19.1 ± 19.1 cells/mm^2 vs. VEGF = 307.1 ± 23.9 cells/mm^2, $p < 0.05$).

VEGF-Expressing rBMSC Improve Vascularization to the Core and Promote Artery Formation in the Periphery

In order to determine whether better progenitor survival and tissue growth could be consequent to improved vascularization of the VEGF-expressing constructs, blood vessels were visualized histologically by CD31 staining (**Figure 6**). By the end of the experiment 8 weeks after implantation, some blood vessels were present in most of the pores of the scaffolds in all three conditions (red signal in **Figure 6A**). However, the VEGF-expressing scaffolds were invaded by much more abundant and denser vascular networks throughout the depth of the constructs. Moreover, VEGF overexpression promoted the formation of dense micro-vascular capillary networks in the deeper areas (**Figure 6B**), whereas both control conditions contained only rare small-caliber vessels within the deep pores. Interestingly, the outer shell of VEGF constructs was vascularized by large-caliber vessels, with homogenous diameters and filled with red blood cells, corresponding to arteries and veins, whereas the morphology and frequency of vessels in the naïve and CD4 constructs was similar between the outer and inner regions (**Figure 6C**).

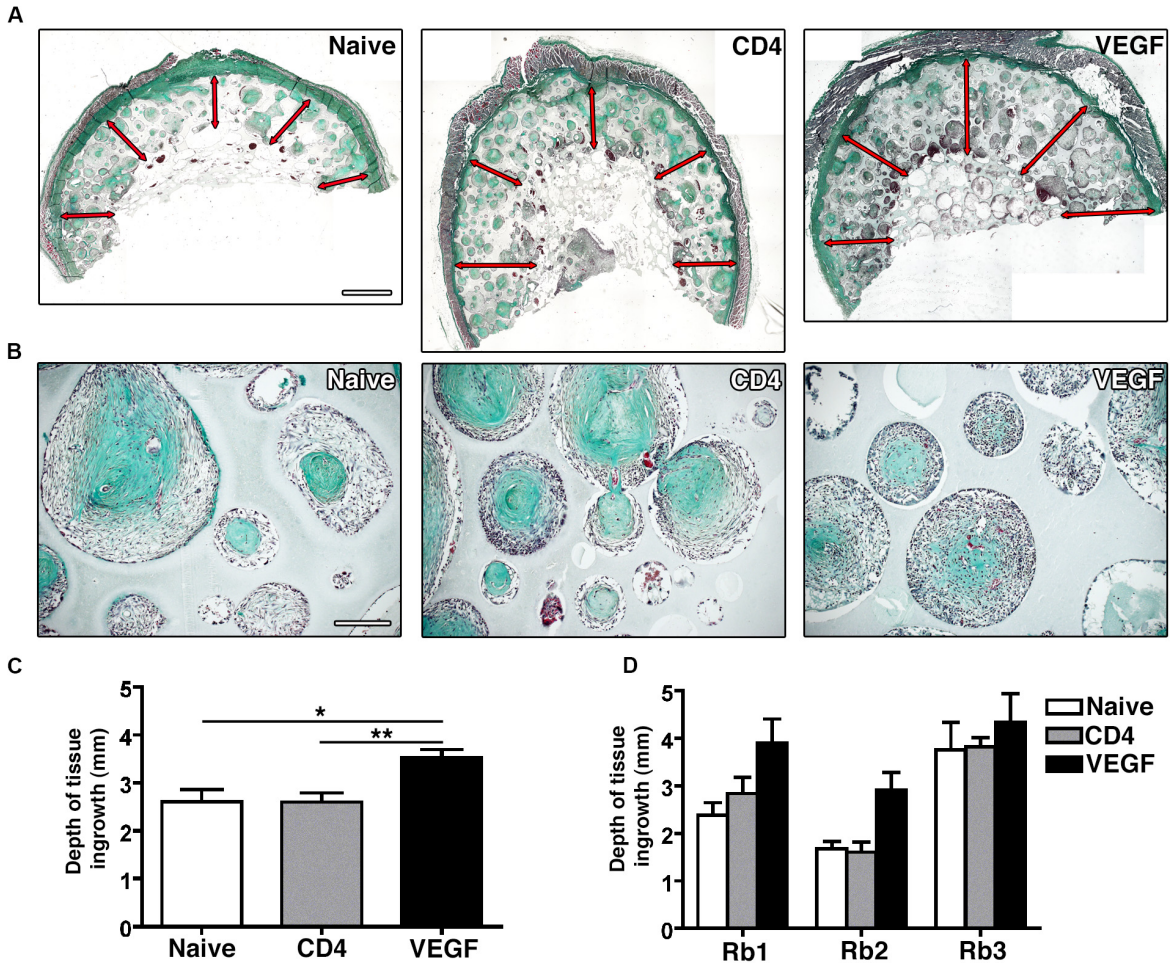

FIGURE 4 | (A) Representative macroscopic pictures of graft sections stained with Masson's Trichome. Red arrows indicate tissue invasion (size bar = 2 mm). **(B)** Representative pictures of scaffold pores containing collagenous dense matrix (Masson's trichrome staining, size bar = 100 μm). **(C)** Quantification of the average depth of tissue ingrowth for the 3 conditions ($n = 3$, $^{*}p < 0.05$, $^{**}p < 0.01$). **(D)** Quantification of the depth of tissue ingrowth for the three individual rabbits (Rb1-3) included in the overall analysis in panel **(C)**.

VEGF-Expressing rBMSC Improve the Depth of Functional Early Blood Perfusion

The histological data on tissue growth and blood vessel formation suggest that the beneficial effect of VEGF expression may take place by improving blood flow to critically under-perfused progenitors in the middle layer of the constructs, thereby enabling their survival and differentiation. To verify this hypothesis, early blood flow inside the constructs was measured non-invasively by dynamic contrast enhancement in the MRI at the crucial time of 1 week after implantation. The analysis was performed similarly to the μ-CT data. Tomographic images were selected mid-way on the long axis at a virtual cross-section of 1.5 cm and three concentric sections, each 1.5-mm deep, were designed in order to distinguish an outer, middle and inner layer. MRI signal intensity upon contrast agent injection was analyzed in each layer over time (60 dynamic scans, **Figure 7A**) and used to calculate tissue perfusion (**Figure 7B**) and the blood volume fraction (**Figure 7C**; Cuenod and Balvay, 2013). The results show that both tissue perfusion and blood volume fraction were significantly increased in the outer and middle layers of VEGF-expressing constructs compared to naïve and CD4 controls. Interestingly, VEGF expression improved blood flow in the middle layer to similar levels as in the outer layer of the controls. Tissue perfusion was improved also in the inner layer by VEGF, but it only reached levels similar to the middle layer of the controls.

DISCUSSION

In this study, we show that sustained VEGF over-expression in clinical-size osteogenic grafts by genetically modified rabbit BMSC was effective to significantly: (1) increase the depth of tissue ingrowth; (2) improve the long-term survival of seeded progenitors and the formation of mineralized tissue; (3) support the establishment of a hierarchical vascular

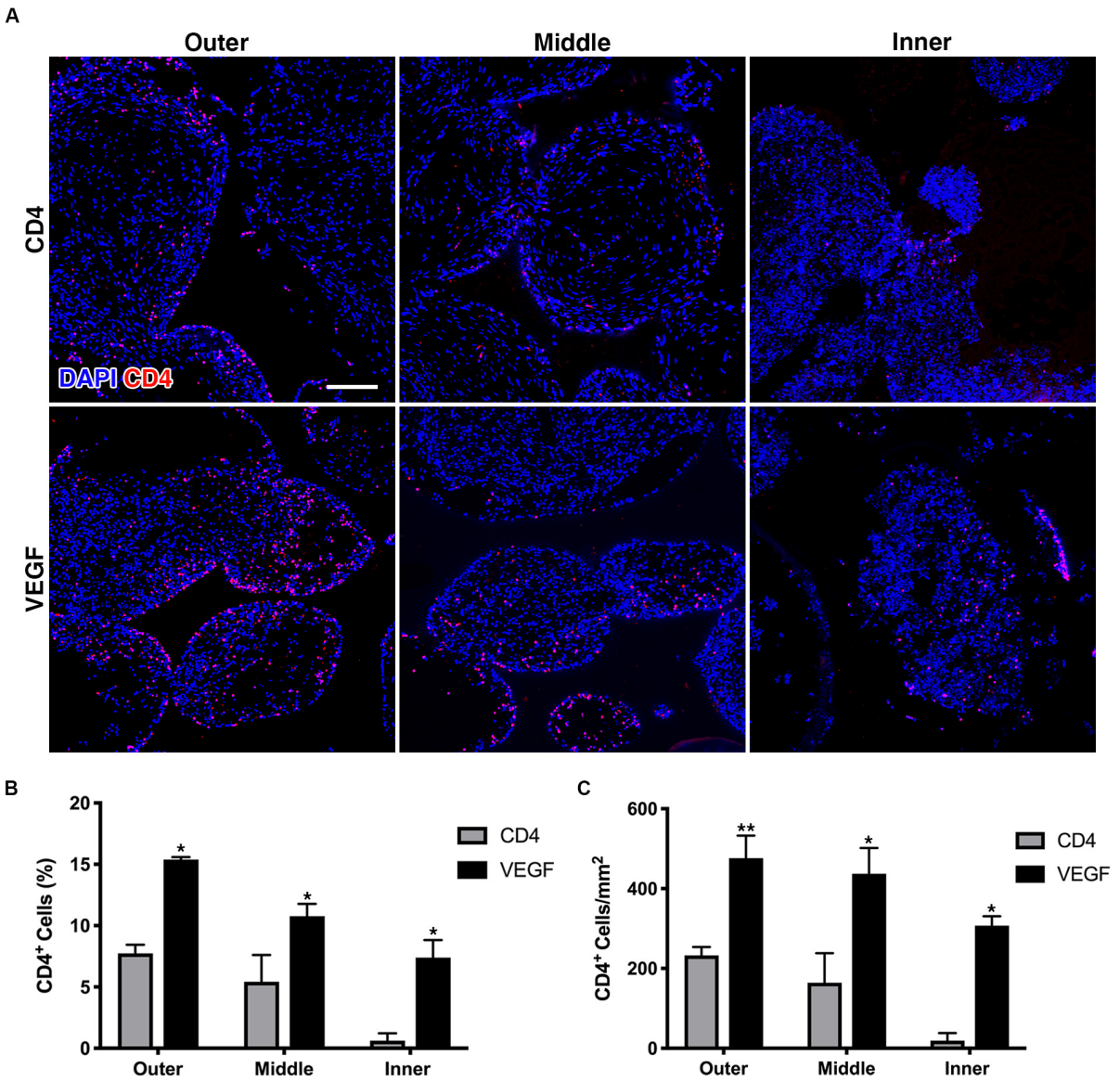

FIGURE 5 | (A) Representative immunofluorescence images from the outer, middle and inner layers of graft sections stained for rbCD4 (red) to detect the seeded progenitors and counterstained with DAPI (blue) to label nuclei (size bar = 100 μm); **(B,C)** quantification of the number of $CD4^+$ cells, expressed as percentage (%) of the total cell number **(B)** and as absolute number per mm^2 of tissue area **(C)** in each layer ($n = 4$, $^*p < 0.05$, $^{**}p < 0.01$).

network, and (4) improve early blood perfusion in clinical-size scaffolds.

Even though the initial growth of new vessels can be quite rapid, sustained VEGF signaling for about 4 weeks is required for their subsequent stabilization and ability to persist indefinitely. In fact, if delivery is too transient, newly induced vessels regress promptly upon cessation of the VEGF stimulus (Gianni-Barrera et al., 2020). Therefore, rapid passive release of recombinant factors from scaffolds is inadequate to ensure new vessel persistence and a large body of work has focused on different strategies to ensure controlled and sustained delivery of angiogenic molecules (Martino et al., 2015). VEGF over-expression in BMSC was previously shown to ensure sustained angiogenic signaling and to promote vascularization in non-clinical size osteogenic grafts implanted subcutaneously in nude rats (Helmrich et al., 2013). However, it is not clear whether such growth could be sufficiently fast and extensive to reach the tissue depths required in clinical-size constructs, where the rapid establishment of a vascular network is needed to ensure progenitor cell survival in the core of the scaffold. In fact, survival of the implanted cells in small constructs is supported by the availability of surrounding vasculature within a short distance. On the contrary, in constructs of clinically relevant size (i.e., a few cubic centimeters) the distance for diffusion of oxygen and nutrients is exceeded and vessel in-growth depends on physiological VEGF upregulation by ischemic conditions

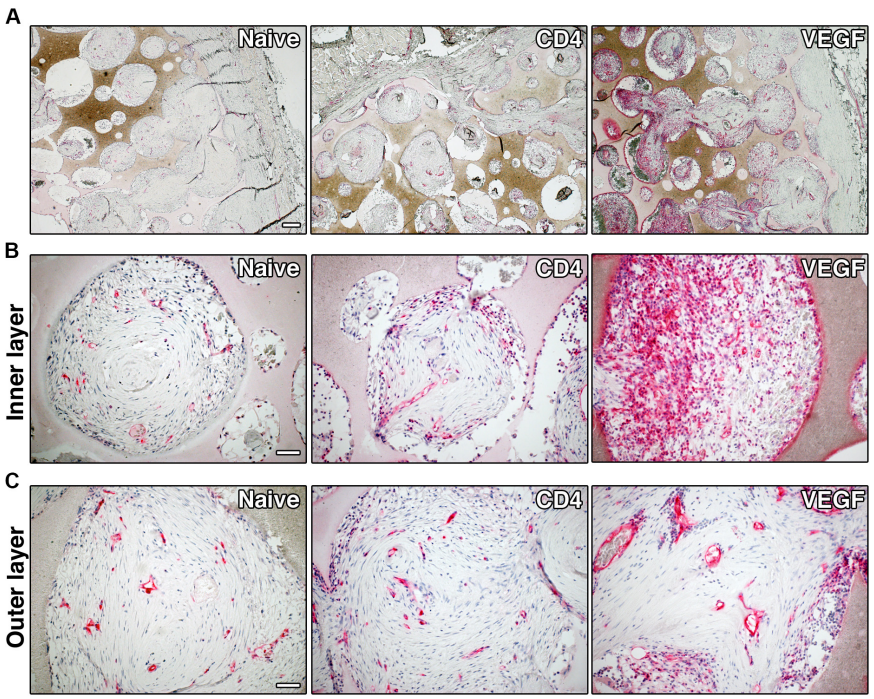

FIGURE 6 | Representative images of graft sections immuno-stained for CD31, showing blood vessels (in red), at low-magnification (**A**, size bar = 200 μm) and high-magnification (**B**, inner layer and **C**, outer layer, size bar = 50 μm).

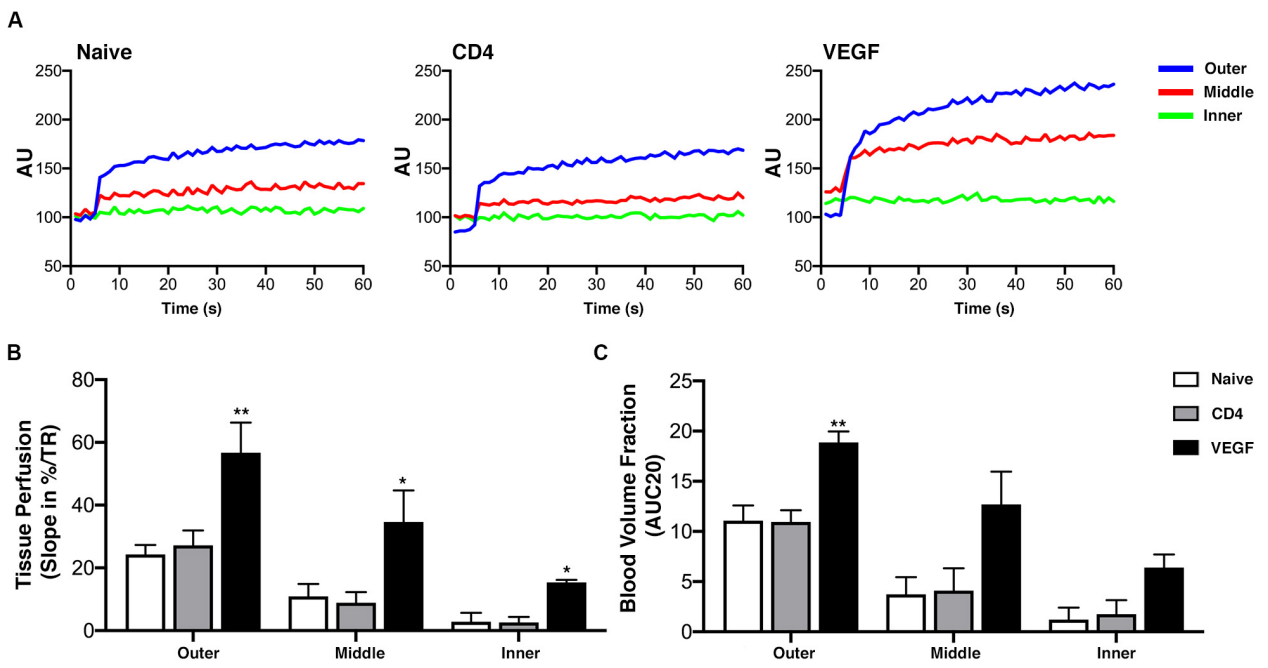

FIGURE 7 | Early blood flow inside the constructs assessed non-invasively by dynamic contrast-enhanced magnetic resonance imaging (DCE MRI) at 1 week after implantation (n = 4). **(A)** DCE-MRI signal time-course for each layer in naïve, CD4 and VEGF-expressing constructs, expressed in arbitrary units (AU). **(B)** Tissue perfusion computed from contrast "wash-in," i.e., the initial uprising slope of the signal-time curve, expressed as the percentage increase over repetition time (%/TR). **(C)** Blood volume fraction determined from the initial area under the normalized DCE curve at 20 dynamic scans after contrast arrival (AUC20) for each layer and construct (*$p < 0.05$, **$p < 0.01$).

generated inside the construct. However, this process is too slow to ensure timely vascularization to significant depths, causing cell death after transplantation and failure of tissue formation (Sharma et al., 2019). We previously investigated the potential of providing a highly vascularized tissue source around the constructs (Scheufler et al., 2008). However, the simple availability of abundant vascular networks around the graft still requires endogenous upregulation of angiogenic signals induced by ischemia to recruit new vessel growth inside the construct. Therefore, bone formation was still limited to the outer periphery and could not exceed about 1 mm of depth, while only fibrous tissue was formed more deeply. Here, we tested the strategy to combine a rich vascular supply around the implants (*panniculus carnosus*) with angiogenic signals directly produced by the osteogenic progenitors seeded throughout the scaffolds in constructs of clinically relevant size (5.5 cm^3). To this end, rabbit bone marrow mesenchymal progenitors were genetically modified with a retroviral vector to stably overexpress VEGF and ensure consistent long-term expression despite cell expansion (Helmrich et al., 2012). We have previously reported that *in vivo* delivery of retrovirally transduced progenitors producing therapeutic and functional levels of VEGF led to an increase in tissue VEGF protein at least 6-fold higher than that induced by ischemia alone (von Degenfeld et al., 2006). Indeed, our data show that providing a VEGF signal throughout the construct, independently of intervening hypoxia, promoted both the speed and efficacy of vascularization of clinical-size constructs.

Crucially, the functional perfusion of inner layers was significantly improved already by 1 week after implantation. In fact, given sufficient time, all constructs are eventually invaded by vessels to the inner layer (e.g., see **Figure 5** after 8 weeks), but perfusion within the first week determines whether seeded progenitors survive (Rouwkema and Khademhosseini, 2016) and recent data suggest that significant progenitor death may start as soon as 3 days after implantation (Moya et al., 2018). The fact that VEGF expression on one hand improved long-term progenitor survival up to 8 weeks, and on the other increased functional perfusion all the way to the inner layer several millimeters inside the constructs within the first 7 days (**Figure 7B**) suggests that vascular ingrowth can be a rather rapid process, given the appropriate stimulation.

The functional significance of this increase in perfusion can be understood by comparing its distribution within the constructs with that of tissue formation. Under control conditions (Naïve and CD4 cells) tissue formation took place to a depth of about 2.5 mm (**Figure 4C**), indicating that blood perfusion is required at a level between that of the outer and middle layers (depths of 0–1.5 and 1.5–3.0 mm, respectively), whereas the very little flow in the inner layer (3.0–4.5 mm depth) is incompatible with progenitor survival, which in fact were essentially absent in the inner layer of control grafts (**Figure 5**). VEGF expression increased perfusion in all three layers, leading the middle and inner layers to receive a similar blood flow as the outer and middle layers of the control conditions, respectively (**Figure 7**). Consistently with these changes, the survival of seeded progenitors was significantly improved by VEGF expression all the way through the inner layer and tissue formation was promoted throughout the middle layer and into the inner layer, to about 3.5 mm of depth. Although blood flow in the outer layer of controls was already sufficient to enable tissue formation, the increase due to VEGF expression appeared to be beneficial also in this location, as evidenced by the improvement in tissue density and mineralization (**Figures 3E,F**).

The accelerated kinetics of vessel growth afforded by VEGF over-expression is also reflected in the different structure of the definitive vascular networks visible after 8 weeks (**Figure 6**). The slow growth in the naïve and CD4 conditions yielded only a sparse microvascular network, with similar morphology throughout the constructs. On the other hand, the robust and rapid growth induced by sustained VEGF signaling led to a hierarchically organized functional vascular tree, composed of dense capillary networks in the inner layers, capable of ensuring a robust exchange of nutrients and respiratory gases, connected to large-caliber feeding vessels entering the constructs at the periphery, which are necessary to supply effective blood flow to the inner layers. In fact, the effective expansion of the microvascular capillary bed by VEGF (angiogenesis) has been shown to induce enlargement and recruitment of feeding arteries (arteriogenesis) (Springer et al., 2003) both through increased shear stress and gap junction-mediated retrograde signaling along the vessel walls (Pries et al., 2010; Annex, 2013).

One limitation emerging from this study is that osteogenic differentiation did not reach the stage of frank bone. In all groups the tissue that was formed displayed histological features typical of osteogenic commitment of progenitors and clearly distinct from fibrous tissue, namely the deposition of a dense and homogeneous collagenous matrix, within which sparse cells remained embedded (**Figure 4B**). Further, μ-CT analysis showed density values typical of a mineralized matrix (500–600 mg/cm^3 in the VEGF conditions; **Figure 3E**) and denser than both the HA scaffold measured as a reference (<325 mg/cm^3) and the same scaffolds implanted without any cells (red dashed lines in **Figure 3E**), thereby ruling out the possibility of pathological calcification. This incomplete osteogenic differentiation was not due to VEGF expression or the genetic modification of the progenitors, as both VEGF and CD4 cells behaved similarly to the naïve condition. Rather, the need to introduce a FACS-purification step after retroviral transduction reduced the amount of available rBMSC and required their expansion for >18 population doublings in order to obtain sufficient autologous cells for each rabbit to seed 3 clinical-size constructs. Although naïve cells did not require FACS purification, they underwent the same degree of *in vitro* expansion in order to maintain appropriate control conditions. In fact, it is well known that BMSC dramatically lose their *in vivo* bone-forming capacity during the first few passages of *in vitro* expansion (Banfi et al., 2000). The importance of limiting BMSC *in vitro* culture can be appreciated by comparing the results of previous experiments in which the same constructs were seeded with the same amount of naïve rBMSC expanded only until the first confluence (about 12 population doublings), where frank bone formation was observed in 9/12 constructs (75%), albeit only to a depth of <1 mm (Scheufler et al., 2008).

In conclusion, these data constitute proof of principle that providing sustained VEGF signaling, independently of cells experiencing hypoxia, is effective to drive rapid vascularization and increase early perfusion in clinical-size osteogenic grafts, leading to improved progenitor survival and tissue formation deeper in the constructs. However, when VEGF delivery is achieved by genetic modification of the osteoprogenitors, the necessary degree of *in vitro* expansion can reduce their *in vivo* bone-forming capacity. Therefore, it would be desirable to achieve sustained VEGF delivery in the constructs while limiting *in vitro* manipulation of the osteoprogenitors. One strategy could be to optimize further the genetic modification process to achieve greater transduction efficiencies and avoid the FACS purification step to eliminate non-transduced cells. In fact, retroviral vectors infect only dividing cells, with greater efficacy the faster the cell cycle (Springer and Blau, 1997), and rBMSC transduction was limited to 70% despite targeting the protocol to the proliferation kinetics. However, lentiviral vectors infect target cells regardless of cell cycle status and allow more efficient transduction rates (High and Roncarolo, 2019). Further, clinically compliant new generation vectors, such as self-inactivating lentiviruses with chromatin insulator elements providing a more attractive safety profile, as they ensure stable and sustained transgene expression without risks of insertional mutagenesis (De Ravin et al., 2016).

Another attractive strategy would be to avoid genetic modification of progenitors altogether and to provide angiogenic signaling by decorating the scaffold itself with recombinant VEGF protein. For example, a variety of protein engineering approaches have been developed to allow growth factor cross-linking into fibrin matrices or to endow them with super-affinity for extracellular matrix, effectively ensuring that morphogenic signals are both protected from proteolytic degradation and presented to their target cells in the physiological context of matrix association (Martino et al., 2015).

DATA AVAILABILITY STATEMENT

The datasets generated for this study are available on request to the corresponding author.

ETHICS STATEMENT

The animal study was reviewed and approved by the Animal Ethics Committee of the Swiss Federal Veterinary Office.

AUTHOR CONTRIBUTIONS

RL, AS, DS, AB, and ND designed the study. RL, MB, OH, CW, AG, CS, AK, SG, GJ, and ND performed the experiments, acquired, analyzed, and interpreted the data. RL, MB, OH, CW, AG, CS, AK, SG, GJ, AS, DS, AB, and ND wrote/revised the manuscript and gave final approval. All authors contributed to the article and approved the submitted version.

FUNDING

This work was supported by an Intramural Research Grant of the Department of Surgery of Basel University Hospital and the EU FP7 grant MAGISTER (214685) to AB.

ACKNOWLEDGMENTS

We gratefully acknowledge Dr. Marianna Trani, Dr. Silvia Reginato, and Dr. Uta Helmrich for help with the genetic modification of rBMSC.

REFERENCES

Almubarak, S., Nethercott, H., Freeberg, M., Beaudon, C., Jha, A., Jackson, W., et al. (2016). Tissue engineering strategies for promoting vascularized bone regeneration. *Bone* 83, 197–209. doi: 10.1016/j.bone.2015.11.011

Annex, B. H. (2013). Therapeutic angiogenesis for critical limb ischaemia. *Nat. Rev. Cardiol.* 10, 387–396. doi: 10.1038/nrcardio.2013.70

Banfi, A., Muraglia, A., Dozin, B., Mastrogiacomo, M., Cancedda, R., and Quarto, R. (2000). Proliferation kinetics and differentiation potential of ex vivo expanded human bone marrow stromal cells: implications for their use in cell therapy. *Exp. Hematol.* 28, 707–715. doi: 10.1016/s0301-472x(00)00160-0

Banfi, A., Von Degenfeld, G., Gianni-Barrera, R., Reginato, S., Merchant, M. J., Mcdonald, D. M., et al. (2012). Therapeutic angiogenesis due to balanced single-vector delivery of VEGF and PDGF-BB. *FASEB J.* 26, 2486–2497. doi: 10.1096/fj.11-197400

Bodde, E. W., De Visser, E., Duysens, J. E., and Hartman, E. H. (2003). Donor-site morbidity after free vascularized autogenous fibular transfer: subjective and quantitative analyses. *Plast. Reconstr. Surg.* 111, 2237–2242. doi: 10.1097/01.prs.0000060086.99242.f1

Cuenod, C. A., and Balvay, D. (2013). Perfusion and vascular permeability: basic concepts and measurement in DCE-CT and DCE-MRI. *Diagn. Interv. Imaging* 94, 1187–1204. doi: 10.1016/j.diii.2013.10.010

De Ravin, S. S., Wu, X., Moir, S., Anaya-O'brien, S., Kwatemaa, N., Littel, P., et al. (2016). Lentiviral hematopoietic stem cell gene therapy for X-linked severe combined immunodeficiency. *Sci. Transl. Med.* 8:335ra357.

Doube, M., Klosowski, M. M., Arganda-Carreras, I., Cordelieres, F. P., Dougherty, R. P., Jackson, J. S., et al. (2010). BoneJ: free and extensible bone image analysis in ImageJ. *Bone* 47, 1076–1079. doi: 10.1016/j.bone.2010.08.023

Gianni-Barrera, R., Di Maggio, N., Melly, L., Burger, M. G., Mujagic, E., Gurke, L., et al. (2020). Therapeutic vascularization in regenerative medicine. *Stem Cells Transl. Med.* 9, 433–444.

Giladi, A. M., Rinkinen, J. R., Higgins, J. P., and Iorio, M. L. (2018). Donor-site morbidity of vascularized bone flaps from the distal femur: a systematic review. *Plast. Reconstr. Surg.* 142, 363e–372e. doi: 10.1097/prs.0000000000004691

Guven, S., Mehrkens, A., Saxer, F., Schaefer, D. J., Martinetti, R., Martin, I., et al. (2011). Engineering of large osteogenic grafts with rapid engraftment capacity using mesenchymal and endothelial progenitors from human adipose tissue. *Biomaterials* 32, 5801–5809. doi: 10.1016/j.biomaterials.2011.04.064

Helmrich, U., Di Maggio, N., Guven, S., Groppa, E., Melly, L., Largo, R. D., et al. (2013). Osteogenic graft vascularization and bone resorption by VEGF-expressing human mesenchymal progenitors. *Biomaterials* 34, 5025–5035. doi: 10.1016/j.biomaterials.2013.03.040

Helmrich, U., Marsano, A., Melly, L., Wolff, T., Christ, L., Heberer, M., et al. (2012). Generation of human adult mesenchymal stromal/stem cells expressing defined xenogenic vascular endothelial growth factor levels by optimized transduction

and flow cytometry purification. *Tissue Eng. Part C Methods* 18, 283–292. doi: 10.1089/ten.tec.2011.0413

High, K. A., and Roncarolo, M. G. (2019). Gene therapy. *N. Engl. J. Med.* 381, 455–464.

Iaquinta, M. R., Mazzoni, E., Bononi, I., Rotondo, J. C., Mazziotta, C., Montesi, M., et al. (2019). Adult stem cells for bone regeneration and repair. *Front. Cell. Dev. Biol.* 7:268. doi: 10.3389/fcell.2019.00268

Martino, M. M., Brkic, S., Bovo, E., Burger, M., Schaefer, D. J., Wolff, T., et al. (2015). Extracellular matrix and growth factor engineering for controlled angiogenesis in regenerative medicine. *Front. Bioeng. Biotechnol.* 3:45. doi: 10.3389/fcell.2019.0045

Misteli, H., Wolff, T., Fuglistaler, P., Gianni-Barrera, R., Gurke, L., Heberer, M., et al. (2010). High-throughput flow cytometry purification of transduced progenitors expressing defined levels of vascular endothelial growth factor induces controlled angiogenesis in vivo. *Stem Cells* 28, 611–619. doi: 10.1002/stem.291

Moya, A., Paquet, J., Deschepper, M., Larochette, N., Oudina, K., Denoeud, C., et al. (2018). Human mesenchymal stem cell failure to adapt to glucose shortage and rapidly use intracellular energy reserves through glycolysis explains poor cell survival after implantation. *Stem Cells* 36, 363–376. doi: 10.1002/stem.2763

Ozawa, C. R., Banfi, A., Glazer, N. L., Thurston, G., Springer, M. L., Kraft, P. E., et al. (2004). Microenvironmental VEGF concentration, not total dose, determines a threshold between normal and aberrant angiogenesis. *J. Clin. Invest.* 113, 516–527. doi: 10.1172/jci18420

Pear, W. S., Nolan, G. P., Scott, M. L., and Baltimore, D. (1993). Production of high-titer helper-free retroviruses by transient transfection. *Proc. Natl. Acad. Sci. U.S.A.* 90, 8392–8396. doi: 10.1073/pnas.90.18.8392

Pries, A. R., Hopfner, M., Le Noble, F., Dewhirst, M. W., and Secomb, T. W. (2010). The shunt problem: control of functional shunting in normal and tumour vasculature. *Nat. Rev. Cancer* 10, 587–593. doi: 10.1038/nrc2895

Rao, R. R., and Stegemann, J. P. (2013). Cell-based approaches to the engineering of vascularized bone tissue. *Cytotherapy* 15, 1309–1322. doi: 10.1016/j.jcyt.2013.06.005

Rouwkema, J., and Khademhosseini, A. (2016). Vascularization and angiogenesis in tissue engineering: beyond creating static networks. *Trends Biotechnol.* 34, 733–745. doi: 10.1016/j.tibtech.2016.03.002

Rouwkema, J., Rivron, N. C., and Van Blitterswijk, C. A. (2008). Vascularization in tissue engineering. *Trends Biotechnol.* 26, 434–441.

Scheufler, O., Schaefer, D. J., Jaquiery, C., Braccini, A., Wendt, D. J., Gasser, J. A., et al. (2008). Spatial and temporal patterns of bone formation in ectopically pre-fabricated, autologous cell-based engineered bone flaps in rabbits. *J. Cell Mol. Med.* 12, 1238–1249. doi: 10.1111/j.1582-4934.2008.00137.x

Schneider, C. A., Rasband, W. S., and Eliceiri, K. W. (2012). NIH Image to ImageJ: 25 years of image analysis. *Nat. Methods* 9, 671–675. doi: 10.1038/nmeth.2089

Sharma, D., Ross, D., Wang, G., Jia, W., Kirkpatrick, S. J., and Zhao, F. (2019). Upgrading prevascularization in tissue engineering: a review of strategies for promoting highly organized microvascular network formation. *Acta Biomater.* 95, 112–130. doi: 10.1016/j.actbio.2019.03.016

Sheets, K. G., Jun, B., Zhou, Y., Zhu, M., Petasis, N. A., Gordon, W. C., et al. (2013). Microglial ramification and redistribution concomitant with the attenuation of choroidal neovascularization by neuroprotectin D1. *Mol. Vis.* 19, 1747–1759.

Sparks, D. S., Saleh, D. B., Rozen, W. M., Hutmacher, D. W., Schuetz, M. A., and Wagels, M. (2017). Vascularised bone transfer: history, blood supply and contemporary problems. *J. Plast. Reconstr. Aesthet. Surg.* 70, 1–11. doi: 10.1016/j.bjps.2016.07.012

Springer, M. L., and Blau, H. M. (1997). High-efficiency retroviral infection of primary myoblasts. *Somat. Cell Mol. Genet.* 23, 203–209. doi: 10.1007/bf02721371

Springer, M. L., Ozawa, C. R., Banfi, A., Kraft, P. E., Ip, T. K., Brazelton, T. R., et al. (2003). Localized arteriole formation directly adjacent to the site of VEGF-induced angiogenesis in muscle. *Mol. Ther.* 7, 441–449. doi: 10.1016/s1525-0016(03)00010-8

von Degenfeld, G., Banfi, A., Springer, M. L., Wagner, R. A., Jacobi, J., Ozawa, C. R., et al. (2006). Microenvironmental VEGF distribution is critical for stable and functional vessel growth in ischemia. *FASEB J.* 20, 2657–2659. doi: 10.1096/fj.06-6568fje

Watkins, R. H., D'angio, C. T., Ryan, R. M., Patel, A., and Maniscalco, W. M. (1999). Differential expression of VEGF mRNA splice variants in newborn and adult hyperoxic lung injury. *Am. J. Physiol.* 276, L858–L867.

Wendt, D., Marsano, A., Jakob, M., Heberer, M., and Martin, I. (2003). Oscillating perfusion of cell suspensions through three-dimensional scaffolds enhances cell seeding efficiency and uniformity. *Biotechnol. Bioeng.* 84, 205–214. doi: 10.1002/bit.10759

Younger, E. M., and Chapman, M. W. (1989). Morbidity at bone graft donor sites. *J. Orthop. Trauma* 3, 192–195. doi: 10.1097/00005131-198909000-00002

Conflict of Interest: CS is currently employed by the company Novartis.

The remaining authors declare that the research was conducted before such employment and in the absence of any commercial or financial relationships that could be construed as a potential conflict of interest.

Citation: Largo RD, Burger MG, Harschnitz O, Waschkies CF, Grosso A, Scotti C, Kaempfen A, Gueven S, Jundt G, Scherberich A, Schaefer DJ, Banfi A and Di Maggio N (2020) VEGF Over-Expression by Engineered BMSC Accelerates Functional Perfusion, Improving Tissue Density and In-Growth in Clinical-Size Osteogenic Grafts. Front. Bioeng. Biotechnol. 8:755. doi: 10.3389/fbioe.2020.00755

frontiers in Bioengineering and Biotechnology

ORIGINAL RESEARCH
published: 17 July 2020
doi: 10.3389/fbioe.2020.00708

Thermosensitive Micellar Hydrogels as Vehicles to Deliver Drugs With Different Wettability

*Rossella Laurano and Monica Boffito**

Department of Mechanical and Aerospace Engineering, Politecnico di Torino, Turin, Italy

The design of adaptable drug delivery systems able to encapsulate and release drugs with different wettability has been attracting widespread interest. Additionally, many attempts have been made to tune hydrophobic/hydrophilic drug release kinetics over time, avoiding the so-called *burst release*. In this scenario, hydrogels resulting from the assembly of micellar structures showing a hydrophobic core and a hydrophilic shell could represent a promising alternative to design versatile drug vehicles. In this regard, this work aimed at designing new thermosensitive micellar hydrogels starting from a custom-made amphiphilic poly(ether urethane) (PEU). Specifically, a commercial triblock copolymer (Poloxamer® 407), selected to ensure the temperature-driven chain arrangement into micelles, was reacted with 1,6-diisocyanatohexane and 1,4-cyclohexanedimethanol. The successful PEU synthesis was proved by size-exclusion chromatography ($\overline{M}_W$ 50000 Da) and infrared spectroscopy. Subsequently, the wettability-driven drug arrangement within the micelle network as well as the influence of drug-loading on the resultant formulation thermosensitivity was investigated by selecting ibuprofen (IBU) and ibuprofen sodium salt (IBUSS) as hydrophobic and hydrophilic drugs, respectively. Specifically, growing drug amounts were loaded into PEU solutions, and the average hydrodynamic micelle diameters and the critical micellar temperatures (CMT) were measured. Systems containing IBU at the highest tested concentration (i.e., 20 mg/mL) showed a significantly higher micelle average diameter (58.2 ± 4.7 nm) and a remarkably lower CMT (8.9°C) with respect to both the control (40.1 ± 1.4 nm and 21.6°C) and IBUSS-loaded formulations (37.3 ± 2.1 nm and 22.4°C). Then, the influence of drug encapsulation on the temperature at which micelles begin to aggregate was rheologically assessed, showing that IBU-loading induced a decrease in this parameter (14.6, 8.7, and 13.7°C for virgin, IBU-loaded, and IBUSS-loaded hydrogel, respectively). Finally, IBU and IBUSS releasing mechanism was analysed using the Korsmayer–Peppas model (*n* value of 0.63 ± 0.007 and 0.89 ± 0.003 for IBU- and IBUSS-loaded gels, respectively). Thanks to their micellar organisation, the here-developed hydrogel platform allowed the encapsulation of a high number of molecules with different wettability. Additionally, these systems exhibited tunable payload-releasing time without burst release and open the way toward the engineering of smart systems for the sustained co-delivery of multiple drugs in a target tissue/organ.

Keywords: polyurethanes, hydrogels, smart vehicles, thermo-sensitivity, drug delivery systems, micellar gels, drug wettability, tunable release

OPEN ACCESS

Edited by:
Dimitrios I. Zeugolis, National University of Ireland Galway, Ireland

Reviewed by:
Katrien Veerle Bernaerts, Maastricht University, Netherlands
Piera Di Martino, University of Camerino, Italy
Pablo Taboada, University of Santiago de Compostela, Spain

****Correspondence:***
Monica Boffito
monica.boffito@polito.it

Specialty section:
This article was submitted to Tissue Engineering and Regenerative Medicine, a section of the journal Frontiers in Bioengineering and Biotechnology

Received: *24 December 2019*
Accepted: *05 June 2020*
Published: *17 July 2020*

Citation:
Laurano R and Boffito M (2020) Thermosensitive Micellar Hydrogels as Vehicles to Deliver Drugs With Different Wettability. Front. Bioeng. Biotechnol. 8:708. doi: 10.3389/fbioe.2020.00708

INTRODUCTION

During the last years, the design of smart drug delivery systems has emerged as an ambitious challenge due to the need to (i) deliver drugs over time while reducing the administered dosage, (ii) reduce side effects associated to non-target tissues, and (iii) increase drug therapeutic efficacy in the pathological site. In this scenario, thermosensitive hydrogels are promising candidates as drug vehicles due to their ability to encapsulate therapeutic agents in the sol state, undergo a temperature-driven sol-to-gel transition entrapping drug molecules, and release their payload upon *in situ* injection (Gong et al., 2013; Dimatteo et al., 2018; Ghasemiyeh and Mohammadi-Samani, 2019). In addition, thermosensitive gels do not show cytotoxic effects associated with their gelation process, as they do not require neither chemical crosslinking agents nor potentially dangerous crosslinking reactions (e.g., photo-curing with UV light, in particular within the UVB and UVC range) to undergo gelation. However, two challenging issues are still attracting the attention of the research community working on this topic: (i) payload *burst release* upon hydrogel application and (ii) the difficulty in loading high amounts of hydrophobic drugs within hydrophilic networks (Hoare and Kohane, 2008; Larrañeta et al., 2018). With the aim to limit the *burst release* phenomenon, drug molecules have been bound to polymeric chains through covalent or non-covalent interactions. For instance, Andrade-Vivero et al. (2006) exploited the presence of the amino groups on 4-vinylpyridine or on *N*-(3-aminopropyl)methacrylamide monomers incorporated in poly(hydroxyethyl methacrylate) hydrogels to improve both the loading efficiency and the release kinetics of ibuprofen and diclofenac through electrostatic interactions occurring between the cationic functional groups of the polymer and the anionic drug molecules. In another work, Nuttelman et al. (2006) were able to tune dexamethasone release kinetics by covalently binding drug molecules to mono-acrylated poly(ethylene glycol) (PEG) chains, later incorporated into PEG-based hydrogels through photopolymerisation. Alternatively, the control over drug release can be carried out by tuning the crosslinking degree of interpenetrating polymer networks (IPNs) (Li et al., 2007), reducing the permeability of the external hydrogel surface (Matsusaki et al., 2007), or designing systems with an additional diffusive barrier for drugs (e.g., hydrogels containing drug-loaded particles). In this regard, Boffito et al. (2019b) recently reported a significant reduction of the initial drug burst release of approximately 85% through the design of hybrid sol-gel systems composed by an injectable thermosensitive hydrogel and ibuprofen-loaded mesoporous silica matrices. A similar approach was also reported by Chen et al. (2004), who designed injectable Poloxamer®-based hydrogels containing lidocaine-loaded microspheres. On the other hand, the approaches reported in literature to improve the loading efficiency of hydrophobic drugs usually consist of the introduction of hydrophobic domains within the hydrogel network or the addition to the gel solution of specific molecules (e.g., cyclodextrins) as drug *reservoir*. For example, Liu et al. (2007) reported an improvement in the loading efficiency and a reduction in diffusion-release rate of *p*-hydroxyanisole from hydrophobically modified poly(methacrylic acid) hydrogels. In another work, Zhang et al. (2005) were able to improve the release rate of hydrophobic drugs through their incorporation in acryolyl-β-cyclodextrins, later co-polymerised with *N*-isopropylacryl amide. However, in all the aforementioned studies the addition of specific polymeric segments to the hydrogel solution or further processing steps during hydrogel preparation were required to minimise drug burst release and/or to increase drug-loading efficiency.

In this scenario, the design of micellar hydrogels could simultaneously face both the previously discussed issues. Indeed, the presence of both hydrophilic and hydrophobic segments in the amphiphilic polymer chains allows the formation of micellar structures with a hydrophobic core and a hydrophilic shell upon temperature increase. As a consequence, this micellar organisation allows good interaction with both hydrophilic and hydrophobic drugs and a prolonged payload release over time. Among the different compositions of amphiphilic polymers reported in literature, poly(ethylene oxide)-poly(propylene oxide)-poly(ethylene oxide) (PEO-PPO-PEO) triblock copolymers are the most widely investigated for drug delivery applications (Bodratti and Alexandridis, 2018; Rey-Rico and Cucchiarini, 2018). These materials are FDA approved, commercially available (trademarks Poloxamer® or Pluronic®) in a variety of different compositions (i.e., molecular weight and PEO content), and highly cytocompatible with no irritation after topical or parenteral administration. However, hydrogels based on Poloxamers® usually suffer from poor residence time in aqueous environments (Boffito et al., 2016), negatively affecting drug release kinetics and leading to *burst release*. With the aim to overcome these drawbacks, in 2016 we reported the synthesis of a Poloxamer® 407-based poly(ether urethane) which aqueous solutions exhibited faster gelation, higher mechanical performances, and improved stability in aqueous environment compared to thermosensitive hydrogels based on native Poloxamer® 407 as such (Boffito et al., 2016). The capability of Poloxamer 407-based PEU gels to progressively release both hydrophilic and hydrophobic molecules as well as ionic species has been already reported (Boffito et al., 2019a,b). However, the literature lacks a thorough investigation of the interactions occurring between drugs and micellar structures. Thus, starting from the high promise of PEU-based hydrogels as drug delivery systems, in this work we characterised the interactions occurring between polyurethane micelles and drugs with different wettability at both the nano- and macro-scales. Furthermore, the effects of drug wettability on hydrogel thermosensitive behaviour and on drug release time were also studied. To this aim, a thermosensitive micellar hydrogel was designed starting from the synthesis of a custom-made amphiphilic poly(ether urethane) (PEU). Specifically, a poly(ethylene oxide)-poly(propylene oxide)-poly(ethylene oxide) triblock copolymer (Poloxamer 407) was selected as macrodiol to ensure polymer thermosensitivity, while 1,6-hexamethylene diisocyanate and 1,4-cyclohexanedimethanol were identified as diisocyanate and chain extender, respectively, to obtain a high molecular weight PEU (Pontremoli et al., 2018). Subsequently, drugs with different wettability (ibuprofen and ibuprofen sodium

salt as hydrophobic and hydrophilic drug, respectively) were first loaded in PEU solutions at different concentrations. Then, their interactions with the temperature-induced micelle formation and nucleation processes was studied through the measurement of the average hydrodynamic micelle diameters and the estimation of the critical micellar temperature (CMT). In addition, both drug-loaded and not-loaded hydrogels were qualitatively and quantitatively characterised through tube inverting and gelation time tests and rheological analyses, respectively, to investigate the effect of drug encapsulation on hydrogel thermosensitivity and gelation process. Lastly, the drug release mechanism from gels embedding ibuprofen or ibuprofen sodium salt was assessed by means of drug release tests and the estimation of the release exponent values that characterise the drug transport mechanism according to the Korsmeyer–Peppas model.

MATERIALS AND METHODS

Materials

Poloxamer 407 [P407, poly(ethylene oxide)-poly(propylene oxide)-poly(ethylene oxide) triblock copolymer, $\overline{M}_n$ 12600 Da, 70% w/w poly(ethylene oxide)], 1,4-cyclohexanedimethanol (CDM), 1,6-hexamethylene diisocyanate (HDI), and dibutyltin dilaurate were purchased from Sigma-Aldrich, Italy. Before use, reagents were treated according to the protocol proposed by Pontremoli et al. (2018) to remove residual water. Briefly, P407 was dried under reduced pressure (approximately 200 mbar) at 100°C for 8 h and then cooled down at room temperature under vacuum; HDI was distilled under reduced pressure; CDM was stored at room temperature (RT) in a desiccator; 1,2-dichloroethane (DCE) was poured over activated molecular sieves (3 Å, Sigma Aldrich, Italy) and maintained overnight under nitrogen atmosphere. All solvents were purchased from Carlo Erba Reagents (Italy) in analytical grade.

Methods

Synthesis of Amphiphilic P407-Based Poly(Ether Urethane)

The P407-based poly(ether urethane) used in this work was synthesised following the pre-polymerisation method recently described by Laurano et al. (2019) (**Supplementary Figure S1**). Specifically, P407 was first dissolved in DCE (20% w/V concentration) at 80°C under continuous nitrogen flow. Then, HDI was added at 2:1 molar ratio with respect to P407 and the pre-polymerisation reaction proceeded for 150 min after the addition of a catalytic amount of dibutyltin dilaurate (0.1% w/w). Subsequently, the mixture was cooled down at 60°C and CDM (3% w/V in DCE) was added to the isocyanate-terminated prepolymer solution at 1:1 molar ratio with respect to P407. This second step of the reaction was carried on for 90 min and finally terminated through the addition of anhydrous methanol. The polymer was finally collected by precipitation in petroleum ether (4:1 volume ratio with respect to DCE total volume). To remove the catalyst and residual by-products, the polymer was then dissolved in DCE (20% w/V) and purified through precipitation in a mixture of diethyl ether/methanol (98/2 V/V, 5:1 volume ratio with respect to DCE). Finally, PEU was collected through centrifugation (Hettik, MIKRO 220R) at 0°C and 6,000 rpm for 20 min, dried overnight under the fume hood, and stored at 4°C under nitrogen atmosphere until use.

Hereafter, the synthesised PEU will be named CHP407, where C, H, and P407 identify the chain extender, the diisocyanate and the macrodiol, respectively.

Attenuated Total Reflectance Fourier Transform Infrared Spectroscopy

Attenuated Total Reflectance Fourier Transform Infrared (ATR-FTIR) spectroscopy was conducted on CHP407 samples to verify the success of the synthesis. Analyses were performed at RT using a Perkin Elmer spectrum 100 equipped with an ATR accessory (UATR KRSS) with diamond crystal. Spectra resulted from 32 scans in the range of 4,000 to 600 cm^{-1} with a resolution of 4 cm^{-1}. Analyses were elaborated using the Perkin Elmer software and results are reported as average spectra of three different polymer batches.

Size Exclusion Chromatography

Size Exclusion Chromatography (SEC) analyses were performed through an Agilent Technologies 1200 Series (CA, United States) to estimate the molecular weight of the synthesised PEU. The instrument was equipped with a Refractive Index (RI) detector and two Waters Styragel columns (HR1 and HR4) conditioned at 55°C. *N,N*-dimethylformammide (DMF, CHROMASOLV Plus, inhibitor free, for HPLC, 99.9%, Carlo Erba Reagents, Italy), added with 0.1% w/V LiBr (Sigma Aldrich, Italy), was used as mobile phase. A calibration curve based on poly(ethylene glycol) standards was defined in the range of peak molecular weight M_p 4,000 – 200,000 Da. Before analyses, 2 mg of polymer were dissolved in 1 mL of mobile phase and filtered through a 0.45 μm syringe filter [poly(tetrafluoroethylene) membrane, Whatman]. Number Average Molecular Weight ($\overline{M}_n$), Weight Average Molecular Weight ($\overline{M}_w$) and dispersity index (D) were estimated using the Agilent ChemStation software.

Dynamic Light Scattering

To thoroughly investigate the relationship occurring between drug loading and changes in micelle hydrodynamic diameter, dynamic light scattering (DLS) measurements were performed on CHP407 samples loaded or not-loaded with drugs characterised by a different wettability. Specifically, CHP407 was first dissolved at 0.5% w/V in physiological saline solution (0.9% NaCl); then Ibuprofen (IBU, Sigma Aldrich, Italy) or Ibuprofen Sodium Salt (IBUSS, Sigma Aldrich, Italy), as hydrophobic or hydrophilic drug, respectively, was added to PEU solution at 2, 5, 10, or 20 mg/mL concentration. Analyses were performed at 25, 30, and 37°C, according to the protocol recently published by Laurano et al. (2020), using a Zetasizer Nano S90 (Malvern Instruments, Worcestershire, United Kingdom) instrument. Before starting, samples were equilibrated at the test temperature for 15 min and then analysed according to Pradal et al. (2013). The reported hydrodynamic diameters resulted from the average of three different analysed samples. Data are reported as mean ± standard deviation.

Hereafter, drug loaded-CHP407 aqueous solutions (0.5% w/V) will be referred to as CHP407_IBU_Xmg/mL and CHP407_IBUSS_Xmg/mL, where X stands for the amount of encapsulated drug.

Critical Micellar Temperature

To investigate the effect of drug loading on the temperature at which micelle nucleation begins, the CMT of CHP407-based aqueous solutions was estimated using a fluorescent dye (1,6-diphenyl-1,3,5-hexatriene, DPH, Sigma Aldrich, Italy) as micellization marker. Samples (1 mL) were prepared by dissolving the polymer at 0.5% w/V concentration in physiological saline solution. Regarding the preparation of drug-loaded systems, IBU and IBUSS were first solubilised in ethanol and double-distilled water, respectively, at 40 mg/mL and then added to CHP407 solution (previously dissolved at slightly higher concentration) in order to reach the final volume of 1 mL and different drug concentrations (i.e., 2, 5, 10, and 20 mg/mL). Lastly, DPH (previously dissolved in methanol at 0.4 mM) was added to each sample at 10 μL/mL. Analyses were conducted according to the method described by Alexandridis et al. (1994). Briefly, virgin and drug-loaded solutions were heated between 5 and 40°C at 1°C/step, each step consisting of 5 min equilibration followed by UV/Vis spectra recording in the 500 nm to 300 nm spectral range (PerkinElmer, Lambda 25). Then, for each sample, the recorded absorbance values at 356 nm were plotted as a function of temperature obtaining a sigmoidal curve. The CMT was defined as the temperature corresponding to the first inflexion of this sigmoidal curve.

Hereafter, samples will be referred to as defined in the section "Dynamic Light Scattering."

Preparation of Drug-Loaded Hydrogels

Virgin CHP407 hydrogels were prepared by dissolving the polymer at 15% w/V concentration in physiological saline solution overnight at 4°C according to the protocol published by Pontremoli et al. (2018). In order to prepare drug-loaded gels, an aliquot of IBU or IBUSS solution previously prepared in EtOH or double-distilled water respectively (40 mg/mL) was first added to physiological solution to reach a final drug concentration of 1 mg/mL and then, the resulting medium was used to solubilise CHP407 at 15% w/V concentration (**Supplementary Figure S2**).

Hereafter, IBU- and IBUSS-loaded gels will be referred to as CHP407_IBU and CHP407_IBUSS.

Tube Inverting Test

To qualitatively investigate the effect of drug encapsulation on hydrogel thermo-sensitivity, Tube Inverting Test was performed on all the formulated CHP407-based hydrogels. Specifically, samples were first prepared in bijou sample containers with an inner diameter of 17 mm (CarloErba reagents, Italy) as previously described (see paragraph "Preparation of drug-loaded hydrogels"); then, they were subjected to a controlled temperature increase from 4 to 40°C at 1 ± 0.1°C/step and 5 min equilibration time. At each step, samples were inverted to allow the visual inspection of the sol-to-gel transition. Sol and gel conditions were defined as "flow liquid sol" and "no flow solid gel," respectively, within 30 s of observation. In order to better evaluate result variability due to operator's perception of both sol and gel states, the test was performed by three different operators, each of them characterising a set of all formulated compositions. Results are reported as mean ± standard deviation.

Gelation Time at Physiological Temperature

Gelation time test at physiological temperature (i.e., 37°C) was performed to qualitatively evaluate the time required by loaded- and not-loaded hydrogels to undergo a sol-to-gel transition. Samples were prepared as previously described (see paragraph "Preparation of drug-loaded hydrogels") and incubated at 37°C (Memmert IF75). At predefined time points (1–10 min, 1 min/step), hydrogels were inverted for 30 s to allow the visual inspection of the sol and gel states (defined as in the Tube Inverting Test). At the end of each step, samples were kept in an ice bath for 8 min to ensure that all the systems were in the sol state prior to the following incubation at 37°C. Result variability deriving from the qualitative evaluation of sol and gel conditions was investigated by asking to three different operators to characterise three different sets of formulations. Results are reported as mean ± standard deviation.

Rheological Characterisation

To thoroughly investigate hydrogel gelation mechanism and kinetics in the presence of hydrophobic or hydrophilic drugs, CHP407_IBU and CHP407_IBUSS were characterised using a stress-controlled rheometer (MCR302, Anton Paar Gmbh, Graz, Austria). The instrument was equipped with a 50 mm parallel plate geometry and a Peltier system for temperature control. CHP407 hydrogels were also analysed as control condition. Sol-to-gel transition was studied through temperature ramp tests carried out in the range 0°C–40°C, 2°C/min, 0.1 s^{-1} frequency. On the other hand, strain sweep tests were conducted at 37°C (10 Hz, strain range 0.01–500%) to investigate gel resistance to applied deformation. Lastly, frequency sweep tests were performed within the linear viscoelastic region (frequency range 0.1–100 rad/s, strain 0.1%) at 25, 30, and 37°C to characterise gel viscoelastic properties. For each analysis the sample was poured on the lower plate in the sol state at 0°C, heated at the test temperature and equilibrated for 10 min to reach thermal stability and finally tested.

Drug Release

The relationship between drug wettability and their release mechanism and timing from micellar hydrogels was studied through drug release tests conducted up to 14 days at 37°C. Specifically, drug-loaded hydrogels (1 mL) were prepared as previously described in paragraph "Preparation of Drug-Loaded Hydrogels" and incubated at 37°C for 15 min to ensure a complete sol-to-gel transition. Subsequently, 1 mL of Trizma® (0.1 M, pH 7.4, Sigma Aldrich, Italy) previously equilibrated at the test temperature was added to each sample as release medium. Extracts were collected and completely refreshed at different time points (i.e., 15, 30, 45, 60, 90 min, 2, 3, 4, 5, 7 h, 1, 2, 5, 7, and 14 days). Released drugs were then quantified according to the method proposed by Alsirawan et al. (2013) using a High-Performance Liquid Chromatography (HPLC, Thermo Scientific,

Dionex Ultimate 3000) instrument equipped with a C18 column (5 μm, 120 Å). Acetonitrile (ACN, CarloErba Reagents, Italy, HPLC grade) and phosphoric acid solution at 0.03% w/V were mixed at 60/40 V/V and used as mobile phase by setting 1.7 mL/min as flow rate. According to the selected mobile phase, 400 μL of each extract were added to 600 μL of ACN, to obtain a final Trizma®/ACN volume ratio of 40/60. Samples were then filtered through a 0.45 μm syringe filter [Macherey-Nagel, poly(tetrafluoro ethylene) membrane] and analyses were carried out at RT and 214 nm for 5 min with an injection volume of 20 μL. Subsequently, drugs were quantified by referring to a calibration curve based on IBU or IBUSS standards with concentration in the range of 0–1 mg/mL. Lastly, to better understand whether different release mechanisms occurred in the presence of IBU or IBUSS, the Korsmeyer–Peppas model was applied to the release data and the drug transport mechanism was defined based on the estimated release exponent n value (Dash et al., 2010).

Statistical Analysis

Statistical analysis was performed using GraphPad Prism 8.0 for MacOsX (GraphPad Software, La Jolla, CA, United States[1]). Two-way ANOVA analysis followed by Bonferroni's multiple comparison test was used to compare results. The statistical significance of each comparison was assessed as reported in Boffito et al. (2016).

RESULTS

Poly(Ether Urethane) Chemical Characterisation

ATR-FTIR spectroscopy performed on both the macrodiol and the synthesised polyurethane reported the appearance of new bands in CHP407 spectrum if compared to P407 one (**Supplementary Figure S3**). In detail, the peak at 1,720 cm^{-1} and 1,630 cm^{-1} can be ascribed to the stretching vibration of carbonyl groups; the band at 3,350 cm^{-1} can be attributed to the stretching vibration of N-H bonds, while at 1540 cm^{-1} the spectrum showed the bending vibration of N-H bonds together with the stretching vibration of C-N bonds. In addition, CHP407 showed an increased $\overline{M}_n$ compared to P407 (30,000 Da versus 10,000 Da) further confirming the success of the synthesis and a dispersity index of 1.6.

Investigation of the Interactions Occurring Between PEU Micelles and Drugs With Different Wettability

Measurement of Micelle Average Hydrodynamic Diameter

To investigate the effect of drug loading on micelle nucleation and on their corresponding hydrodynamic diameter, DLS measurements were conducted at three different temperatures on samples loaded with different amounts of IBU or IBUSS. Virgin CHP407 solutions were also analysed as control condition. Specifically, **Figure 1** reports DLS volume patterns of systems encapsulating the drugs at 2 and 20 mg/mL concentration, while results concerning CHP407 solutions loaded with IBU or IBUSS at 5 and 10 mg/mL concentration are illustrated in **Supplementary Figure S4**.

As reported in **Figure 1** (left column), irrespective of the analysed temperature, no differences were observed between CHP407 and drug-encapsulating CHP407 profiles when systems were loaded at a low IBU or IBUSS concentration (i.e., 2 mg/mL). Upon an increase in drug content up to 5 mg/mL (see **Supplementary Figure S4** – left column) an evident shift toward higher hydrodynamic diameter values was registered for samples containing IBU (red line) at 37°C, while no differences were observed at lower temperatures (i.e., 25 and 30°C) when compared to the control (blue line) and IBUSS-loaded CHP407 (green line) profiles. On the other hand, at the same payload concentration, IBUSS-loaded systems reported similar profiles with respect to the control at each analysed temperature. By further increasing drug concentration at 10 mg/mL and 20 mg/mL (see **Supplementary Figure S4** and **Figure 1** right columns, respectively), CHP407 solutions encapsulating IBU reported significant shifts toward higher hydrodynamic diameters at each tested temperature, thus suggesting that the introduction of a high amount of a hydrophobic drug favours the nucleation of bigger micelles. Conversely, no significant differences were observed between CHP407 and IBUSS-loaded CHP407 solutions irrespective of drug concentration and temperature.

Figure 2 reports micelle average hydrodynamic diameter measured at 25, 30, and 37°C upon an increase in drug content from 2 mg/mL up to 20 mg/mL. As expected, no differences were observed between the analysed systems when IBU and IBUSS were loaded at 2 mg/mL, with an average diameter around approximately 30, 35, and 40 nm at 25, 30, and 37°C, respectively. On the other hand, despite results observed in the volume patterns at 37°C for CHP407_IBU_5mg/mL (see **Supplementary Figure S4C**), micelles turned out to show similar average dimensions to those of CHP407 and CHP407_IBUSS_5mg/mL. Indeed, the average hydrodynamic diameters were measured to be 39.1 ± 1.4 nm, 37.2 ± 1.8 nm, and 35.4 ± 1.3 nm for CHP407, CHP407_IBU_5mg/mL, and CHP407_IBUSS_5mg/mL, respectively. Conversely, slight differences were observed at 25°C (35 ± 1.4 nm versus 28.7 ± 4 nm and 28.8 ± 1.2 nm for CHP407_IBU_5mg/mL, CHP407, and CHP407_IBUSS_5 mg/mL, respectively), thus suggesting that the addition of a hydrophobic drug favours the organisation of bigger structures at lower temperatures. Similar trends were also registered when drugs were encapsulated at 10 mg/mL, with an average hydrodynamic diameter slightly higher only for CHP407_IBU_10mg/mL at 25°C. Lastly, at the highest tested drug concentration (i.e., 20 mg/mL), the average hydrodynamic diameters of systems loaded with IBU turned out to be significantly higher compared to CHP407 and IBUSS-containing CHP407 solutions at each analysed temperature (e.g., average hydrodynamic diameters at 37°C were measured to be 40.1 ± 1.4 nm, 58.2 ± 4.7 nm, and

[1]www.graphpad.com

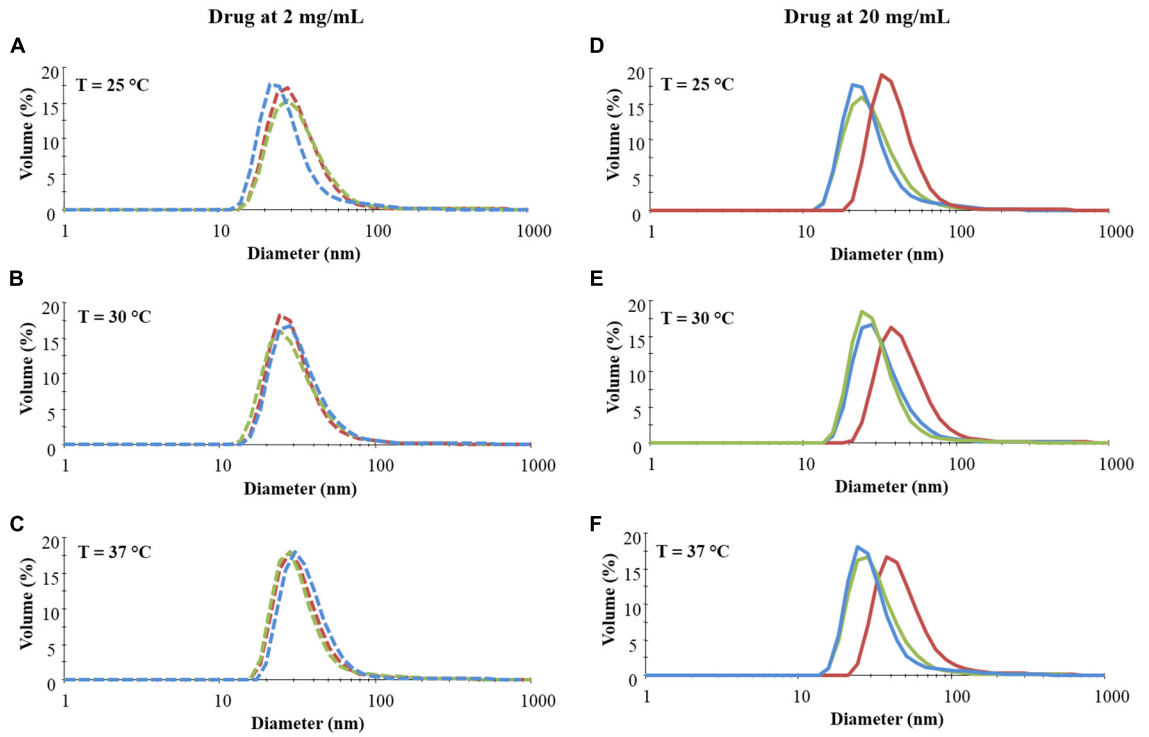

FIGURE 1 | Distribution patterns (by volume) of micelle hydrodynamic diameter measured in CHP407 solutions at 0.5% w/V concentration not loaded- (blue line) or loaded with 2 (dashed line) and 20 (continuous line) mg/mL of IBU (red line) or IBUSS (green line). Analyses were performed at 25°C **(A,D)**, 30°C **(B,E),** and 37°C **(C,F)**.

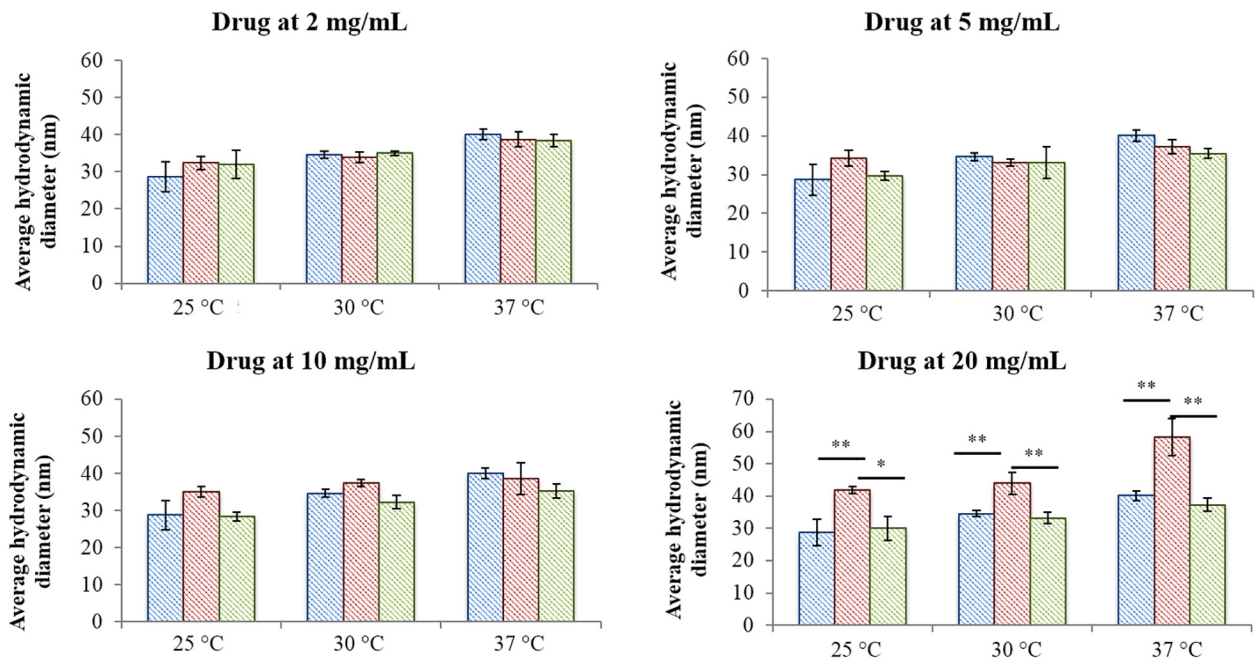

FIGURE 2 | Average hydrodynamic diameters of micelles formed in CHP407 (blue), IBU- (red) and IBUSS-loaded (green) solutions (at 2, 5, 10, and 20 mg/mL drug concentration) at different temperatures (25, 30, and 37°C) (*$p < 0.05$, **$p < 0.005$).

37.3 ± 2.1 nm for CHP407, CHP407_IBU_20mg/mL, and CHP407_IBUSS_20mg/mL, respectively).

Estimation of the Critical Micellar Temperature

The CMT was estimated for all considered formulations to investigate whether the presence of hydrophilic or hydrophobic drugs could affect the temperature at which micelles begin to nucleate. **Figure 3** reports the UV/Vis spectra recorded for CHP407-based solutions at 0.5% w/V concentration loaded or not loaded with IBU or IBUSS at 5 mg/mL (**Figures 3B,C**) and 20 mg/mL (**Figures 3D,E**) recorded at different temperatures (i.e., 15, 20, 25, and 30°C). Data concerning systems loaded with drugs at 2 and 10 mg/mL concentration are reported in **Supplementary Figure S5**.

At low drug concentration, i.e., 2 mg/mL, no differences were observed between CHP407_IBU_2mg/mL and CHP407_IBUSS_2mg/mL as the temperature at which the intensity of the peak at 356 nm begins to increase turned out to be 20°C for both analysed systems (see **Supplementary Figures S5B,C**). In addition, this result was in accordance with that of CHP407 control solution, thus suggesting that the introduction of a low amount of drug did not affect micelle nucleation mechanism, irrespective of its wettability.

Upon an increase in drug loading at 5 mg/mL concentration (**Figures 3B,C**), slight differences appeared in IBU-loaded samples as the intensity of DPH signal at 356 nm turned out to increase at a lower temperature with respect to the control and CHP407_IBUSS_5mg/mL (i.e., 15°C versus 20°C). By further increasing drug concentration up to 10 mg/mL and 20 mg/mL, spectra of IBU-containing samples (see **Supplementary Figure S5D** and **Figure 3D**, respectively) were almost overlapped at each reported temperature. This evidence suggested that DPH solubilisation into the micelle core began at a very low temperature and that at 10°C its complete encapsulation was almost achieved. On the other hand, CHP407 samples loaded with IBUSS (see **Supplementary Figure S5E** and **Figure 3E**) showed similar trends to those reported for lower drug concentrations.

Lastly, CMT values were estimated for all considered systems (see **Supplementary Figures S6**, **S7**) according to Boffito et al. (2016) and reported in **Table 1**. As expected, similar CMT values were observed for CHP407-based solutions not loaded or loaded with 2 mg/mL of IBU or IBUSS. However, upon drug content increase at 5, 10, or 20 mg/mL, the presence of IBU sharply lowered the CMT value of the system (i.e., CMT = 8.9°C for CHP407_IBU_20mg/mL), thus indicating that hydrophobic molecules enhanced micelle nucleation at lower temperatures. Conversely, irrespective of drug concentration, the introduction of IBUSS did not affect the process, with respect to the control.

Effect of Payload Encapsulation on Hydrogel Thermosensitivity

Tube Inverting and Gelation Time Tests

To qualitatively evaluate the influence of drug encapsulation on hydrogel thermo-sensitivity, tube inverting test and gelation time test at physiological temperature were performed on virgin hydrogels at 15% w/V concentration and on systems loaded with 1 mg/mL concentration of drug. Results are reported in **Figure 4**.

Regarding tube inverting test, drug loading seemed to slightly affect the gelation temperature of the hybrid systems irrespective of drug wettability. Indeed, gelation temperatures turned out to be 29.7 ± 0.6°C, 27.3 ± 0.6°C, and 28.0 ± 1°C for virgin CHP407, CHP407_IBU, and CHP407_IBUSS hydrogels, respectively. On the other hand, almost no differences were registered in their sol-to-gel transition time at 37°C.

Rheological Characterisation

In order to thoroughly understand the effect of drug encapsulation on sol-to-gel transition upon temperature increase, a complete rheological characterisation was performed on virgin CHP407 hydrogels and on systems loaded with IBU or IBUSS. **Figure 5** illustrates changes in solution viscosity recorded upon a controlled temperature ramp increase in the range 0–40°C.

In all analysed systems, viscosity initially decreased as a function of temperature according to the characteristic behaviour of sol systems subjected to a heating process. Then, a sharp viscosity increase was observed as a consequence of chain arrangement into an organised structure until complete sol-to-gel transition. In terms of trend of viscosity versus temperature, marked differences were observed among the investigated formulations, as the viscosity of CHP407_IBU (red line) started to increase at a lower temperature compared to the control and CHP407_IBUSS. Finally, the viscosity suddenly fell down at high temperatures (i.e., 35–36°C) due to gel melt fracture (Boffito et al., 2016), with no differences among the tested samples. The temperature at which the viscosity reaches the lowest value is defined as T_{onset}. This temperature is a crucial gelation parameter as it marks the beginning of the micelle nucleation process. The T_{onset} values estimated for the analysed systems are reported in **Table 2**.

The addition of IBUSS to CHP407 solutions did not significantly affect either the system minimum viscosity value or the T_{onset}, which was measured to be 14.6 and 13.7°C for CHP407 and CHP407_IBUSS, respectively. Concerning CHP407_IBU, consistent differences were registered with respect to the control in T_{onset} value, thus suggesting that the introduction of hydrophobic molecules could affect gelation mechanism.

Strain sweep tests conducted at 37°C (**Supplementary Figure S8**) measured storage and loss moduli (G' and G", respectively) values as a function of applied deformation. While similar storage and loss moduli values (approximately 7 and 1.6 kPa for G' and G", respectively) were registered within the linear viscoelastic region (i.e., strain range in which G' and G" are constant) for both unloaded- and drug-loaded gels, a significantly lower strain resistance was observed for CHP407_IBU (11.6% versus 18.6% strain at break for IBU-loaded and virgin/IBUSS-loaded gels, respectively), thus suggesting a different micelle organisation within the network in the presence of IBU.

Lastly, frequency sweep tests at 25, 30, and 37°C allowed the investigation of hydrogel gelation kinetics through the variation of G' and G" upon temperature increase (**Figure 6**). In general, G' values lower than G" ones characterise a system in the sol phase; conversely, G' values higher than G" ones are indicative

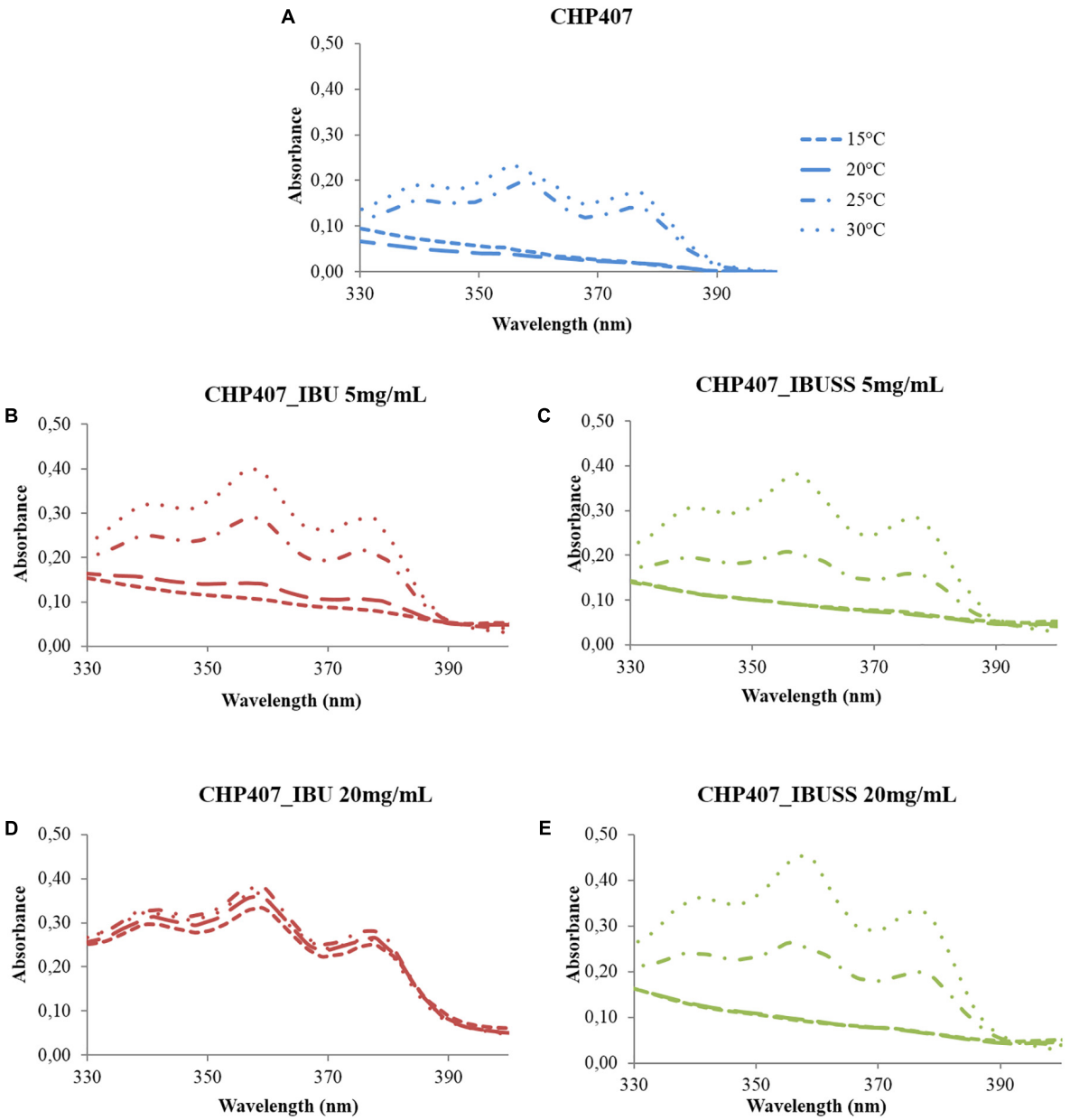

FIGURE 3 | UV/Vis spectra of virgin CHP407 solution (0.5% w/V concentration) **(A)** and IBU- and IBUSS-loaded formulations (red and green line, respectively) at 5 mg/mL **(B,C)** and 20 mg/mL **(D,E)** upon temperature increase in the range 5–40°C.

of a gel behaviour. The frequency at which G' becomes higher than G", i.e., the crossover frequency ($\omega_{G'/G''\,crossover}$), marks the transition from the typical behaviour of a sol toward that of a gel. Those samples that exhibit a G'/G" crossover within the investigated frequency range are defined as biphasic systems. The analysed systems turned out to be almost completely in the sol state at 25°C, in a biphasic phase at 30°C, and almost completely in the gel state at 37°C, although a complete gel development was not achieved because G' and G" were not frequency-independent. However, the crossover frequency values reported in **Table 3** suggested different gelation kinetics, with respect to the control sample, in the presence of both hydrophobic and hydrophilic drugs. Indeed, at 25°C the crossover frequencies of CHP407_IBU and CHP407_IBUSS hydrogels (i.e., 50 rad/s and 45 rad/s, respectively) were measured to be at lower frequencies if compared to CHP407 gels (i.e., 58 rad/s). Upon temperature increase up to 30°C, CHP407_IBU and CHP407 reached the G'/G" crossover at the same angular frequency (i.e., 4 rad/s), while CHP407_IBUSS exhibited the G'/G" crossover at 2.5 rad/s. Lastly, at 37°C all systems showed almost the same $\omega_{G'/G''\,crossover}$, suggesting that all the formulations achieved the same degree of network organisation.

Investigation of Payload Releasing Mechanism and Kinetics From Micellar Hydrogels

To study whether drug wettability could influence their release mechanism from micellar hydrogels, IBU and IBUSS, as hydrophobic and hydrophilic drug, respectively, were loaded in CHP407 gels at 1 mg/mL and their release kinetics was thoroughly investigated (**Figure 7**).

Irrespective of the nature of the encapsulated drugs, a sustained release over time was observed from CHP407-based hydrogels up to 14 days. In addition, starting from 7 h of incubation, IBUSS release (green line) was significantly higher than that of IBU (red line) at each analysed time point. However, considering the initial time steps up to 1 h, a delayed IBUSS release was registered followed by a sharp increase up to 7 h and finally by a sustained release which became complete on day 14. On the other hand, IBU-loaded hydrogels initially showed an increased payload release compared to IBUSS-loaded ones (8.5% versus 3.7% at 30 min of incubation) followed by a sustained release up to 14 days (approximately 95% released IBU). Thus, three and two different curve slopes could be identified in IBUSS and IBU profiles, respectively, which suggest the occurrence of different drug release mechanisms, and thus different release kinetics, as a consequence of drug wettability. In particular, 5 h incubation time marked a significant change in drug release kinetics as starting from this time point released IBUSS turned out to be always higher than IBU.

Lastly, to deeply investigate the mechanism underpinning the release of IBU or IBUSS within the first hours of incubation, the Korsmeyer–Peppas model was applied to drug-loaded CHP407 hydrogels (Dash et al., 2010). Specifically, the releasing exponent n was estimated for both CHP407_IBU and CHP407_IBUSS systems and they were measured to be 0.63 ± 0.007 and 0.89 ± 0.003, respectively. These results suggest the occurrence of two different release mechanisms of IBU and IBUSS from CHP407 gels, according to Dash et al. (2010).

TABLE 1 | Estimated critical micellar temperatures for virgin CHP407 solutions at 0.5% w/V concentration and drug-loaded formulations at 2, 5, 10, and 20 mg/mL concentration.

	Critical micellar temperature (°C)		
	CHP407 solutions	**CHP407_IBU solutions**	**CHP407_ IBUSS solutions**
0 mg/mL	21.6	–	–
2 mg/mL	–	21.8	22.7
5 mg/mL	–	19.2	22.5
10 mg/mL	–	10.7	22.6
20 mg/mL	–	8.9	22.4

DISCUSSION

Thermosensitive hydrogels are gaining increasing interest as drug delivery systems due to their capability to load high amounts of drugs. Moreover, the high water content of hydrogels perfectly mimics the extracellular matrix structure, thus reducing the probability of an adverse immune system response. However, the strong hydrophilic nature of these systems significantly limits the amount of hydrophobic drugs that can be encapsulated (Hoare and Kohane, 2008). To overcome this drawback, the introduction of hydrophobic blocks in the polymeric component can offer a higher number of binding sites to hydrophobic drugs, thus increasing the loading yield (Zha et al., 2002). However, this strategy generally requires a further functionalisation step. A promising alternative could be represented by micellar hydrogels, as their polymeric chains are composed by an alternation of hydrophobic and hydrophilic segments that upon temperature increase can arrange into organised structures with a hydrophobic core and a hydrophilic shell enhancing the interactions with drugs of different wettability.

In this work, the influence of drug nature on the temperature-driven micelle organisation and nucleation process has been thoroughly investigated at both the nano- and macro-scale. To this aim, an amphiphilic P407-based poly(ether urethane) was first synthesised and the success of its synthesis was assessed by ATR-FTIR spectroscopy. Indeed, the appearance of vibrational bands at 1,720 cm^{-1}, 3,350 cm^{-1}, and 1,540 cm^{-1} can be ascribed to the newly formed urethane bonds between isocyanate groups and hydroxyl terminal groups of the macrodiol and the chain extender in the first and second step of the synthesis, respectively. Furthermore, the absence of the peak attributed to unreacted isocyanates (i.e., 2,200 cm^{-1}) suggested that the reaction was complete and successfully carried out as reported by Boffito et al. (2016). In addition, the band at 1,630 cm^{-1} suggested the presence of a small amount of urea bonds as a consequence of side-reactions occurring during PEU synthesis in accordance with the work recently published by Laurano et al. (2020). However, these by-products did not affect the successful synthesis of a poly(ether urethane) characterised by a high molecular weight and a narrow molecular weight distribution as assessed through SEC analyses.

The effects of drug wettability on polymer chain arrangement and micelle organisation were first investigated at the nanoscale by analysing two characteristic micelle parameters, the CMT and the average hydrodynamic micelle diameter. The former was estimated using a fluorescent dye (Alexandridis et al., 1994), and the latter by adapting to micelle characterisation a conventional technique (i.e., DLS analyses) usually applied to solid spherical systems (e.g., nanoparticles) (Hoo et al., 2008; Lim et al., 2013). Indeed, the presence of the amphiphilic P407 building block in polyurethane backbone is responsible for chain organisation into spherical micellar structures upon system heating according to results published on similar PEUs differing for their chain extender (Boffito et al., 2016, 2019a; Laurano et al., 2020). Drug encapsulation into CHP407 solutions affected the average hydrodynamic diameter of the polymeric structures formed at 25, 30, and 37°C, with significant differences that can be correlated to molecule wettability. Specifically, the addition of the hydrophilic IBUSS did not alter the measured micelle hydrodynamic diameters irrespective of temperature and its concentration within the sample, thus

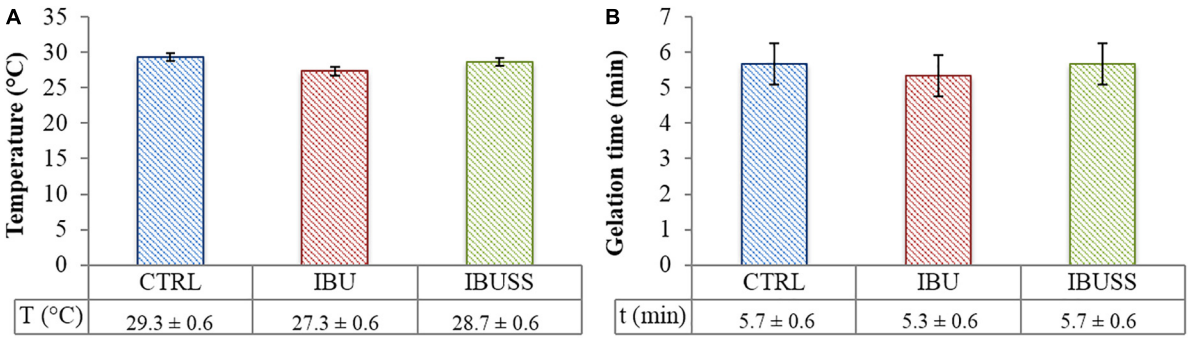

FIGURE 4 | Results of Tube Inverting test **(A)** and Gelation Time test at physiological temperature **(B)** performed on CHP407 (blue), CHP407_IBU (red), and CHP407_IBUSS (green) hydrogels at 15% w/V concentration and loaded with 1 mg/mL concentration of drugs to evaluate their effect on the sol-to-gel transition process. Results are reported as mean ± standard deviation of three independent analyses performed by three different operators. Systematic errors of tube inverting test and gelation time test are ± 0.5°C and ± 30 s, respectively.

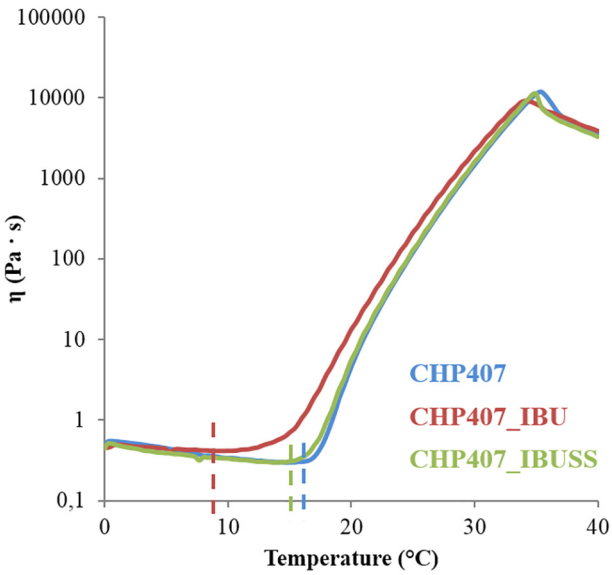

FIGURE 5 | Trend of viscosity as a function of temperature within the range 0–40°C for virgin CHP407 (blue line) at 15% w/V concentration and for hybrid systems (CHP407_IBU and CHP407_IBUSS, red and green line, respectively) loaded with 1 mg/mL concentration of drug.

TABLE 2 | T_{onset} and minimum value of measured viscosity (η_{min}) estimated for virgin and drug-loaded systems prepared at 15% w/V concentration and loaded with 1 mg/mL concentration of drug.

	Gelation parameters	
	η_{min} (Pa·s)	T_{onset} (°C)
CHP407	0.3	14.6
CHP407_IBU	0.42	8.7
CHP407_IBUSS	0.3	13.7

suggesting that no interactions occurred between IBUSS and micelle nucleation. Indeed, as a consequence of its hydrophilicity, IBUSS molecules preferentially interact with water molecules and/or chain hydrophilic segments. Conversely, IBU loading in CHP407 systems led to the formation of micelles characterised by higher hydrodynamic diameters with respect to the control (i.e., not-loaded CHP407 solutions). The formation of bigger polymeric structures as a consequence of IBU addition within the samples supported the hypothesis of the progressive hydrophobic drug arrangement into the hydrophobic micelle core upon temperature increase. Additionally, drug wettability also affected the temperature at which micelles began to aggregate (i.e., the CMT). Indeed, CMT is dependent on both polymer concentration, according to Boffito et al. (2016) and Laurano et al. (2020), and hydrophobic/hydrophilic balance (Okudan and Altay, 2019). In this work, being the polymeric content the same in all the analysed formulations, the progressive decrease of the estimated CMT values could be ascribed to the loading of increasing amounts of IBU. Indeed, the addition of hydrophobic drug molecules resulted in an increased system hydrophobic content, which led to the formation of stronger hydrophobic interactions and thus to the beginning of micelle aggregation phenomena at lower temperatures with respect to the control. On the other hand, the addition of IBUSS raised the hydrophilic content of the formulations, leading to a slight delay in polymeric chain arrangement into organised micelles with respect to the control. Additionally, this phenomenon was further worsened by the interactions occurring between drug molecules and chain hydrophilic blocks, which slightly hindered micelle formation. Therefore, based on these considerations and on the expected further decrease in CMT values moving from not-gelling solutions toward hydrogel formulations, in this work a new method was applied to prepare drug-loaded gels. Indeed, differently from the protocol we recently published (Boffito et al., 2019b), this new approach maximised IBU encapsulation within the hydrophobic micellar core during polymer solubilisation followed by its arrangement into micelles.

At the macro-scale the encapsulation of drugs in CHP407-based hydrogels, irrespective of their wettability, seemed to slightly interfere with the gelation temperatures as suggested by the Tube Inverting Test. This observation was further proved

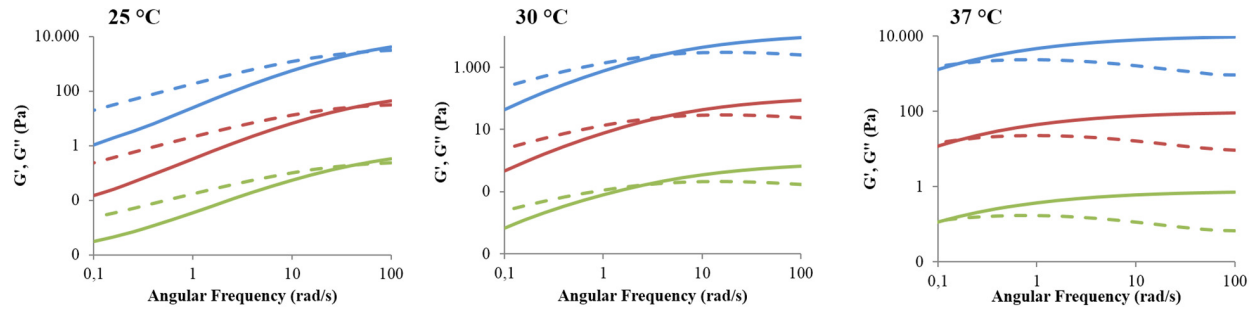

FIGURE 6 | Trends of storage and loss moduli versus angular frequency within the range 0.1–100 rad/s for CHP407 (blue), CHP407_IBU (red), and CHP407_IBUSS (green) hydrogels at 25, 30, and 37°C. The storage (G') and the loss moduli (G") are reported as continuous and dashed lines, respectively. For high graph clarity, G' and G" were shifted along the *Y* axis with respect to the control by a factor of 100 and 10,000 for CHP407_IBU and CHP407_IBUSS, respectively.

TABLE 3 | Crossover frequencies between storage and loss moduli ($\omega_{G'/G''crossover}$) measured at 25, 30, and 37°C for virgin and drug-loaded CHP407-based hydrogels (drug concentration 1 mg/mL).

	$\omega_{G'/G''crossover}$ (rad/s)		
	25°C	**30°C**	**37°C**
CHP407	58	4	0.15
CHP407_IBU	50	4	0.13
CHP407_IBUSS	45	2.5	0.12

by temperature ramp tests, which revealed a decreased T_{onset} for both drug-loaded gels with respect to the CHP407 one. However, the addition of IBUSS only mildly altered the T_{onset} of the system, further supporting our observations at the nanoscale and definitely proving that hydrophilic drug molecules do not affect the organisation capability of polymeric chains. On the other hand, the addition of IBU drastically decreased the temperature at which micelles begin to aggregate. Indeed, IBU molecules, being encapsulated into the micelle core, as suggested by DLS measurements, led to the formation of bigger micelles reaching the critical micellar volume required to trigger the sol-to-gel transition at lower temperatures (Boffito et al., 2016). Additionally, the introduction of hydrophobic molecules into the system brought to increased hydrophobic interactions. This hypothesis was further confirmed by the measured strain at break, which was significantly lower for IBU-loaded gels with respect to IBUSS-loaded and virgin gels. Therefore, the addition of a hydrophobic drug moves the beginning of the gelation transition toward lower temperatures and induces the formation of less mechanically resistant gels. Concerning gel development kinetics, both drug-loaded hybrid systems were characterised by faster transitions with respect to the control. Moreover, this phenomenon was particularly evident in CHP407_IBUSS hydrogels. Indeed, although micelle aggregation began at lower temperatures for IBU-loaded gels with respect to IBUSS-loaded ones, at 25°C the hydrogel encapsulating the hydrophilic drug showed a marked lower crossover frequency. These observations could be explained considering the different drug arrangement within the network (**Figure 8**). Specifically, IBU molecules were encapsulated into the hydrophobic micelle core, leading to the formation of bigger micellar structures (**Figure 8A**), meanwhile IBUSS molecules were entrapped in the interstitial spaces among micelles (**Figure 8B**). IBU organisation into micelle core initially favoured the gelation process lowering the T_{onset}, but then micelle nucleation and aggregation into the gel network turned out to be slightly hindered by their higher hydrodynamic diameters. On the other hand, hydrophilic drug arrangement with respect to the surrounding micelles did not alter T_{onset} value, but speeded up the sol-to-gel transition kinetics favouring micelle aggregation and packing into an organised network. However, at 37°C these differences between the analysed systems were levelled off as suggested by gelation time test results, $\omega_{G'/G''crossover}$ values, and temperature ramp test data. Indeed, although changes in the onset of gelation were observed, at temperatures higher than 30°C all the formulations tended to the same viscosity values. Thus, the here-developed micellar poly(ether urethane)-based hydrogels pave the way to the design of a drug delivery system able to encapsulate both hydrophilic and hydrophobic drugs without significantly altering the resultant hydrogel thermo-responsiveness.

In addition, the different wettability-driven drug arrangement into the gel network also affected their release kinetics from CHP407-based hydrogels. Specifically, the released amount of IBU turned out to be always lower than that of IBUSS from 7 h up to 14 days of incubation. Indeed, being encapsulated in the micelle core, drug molecules had a double diffusive barrier to pass through before reaching the external medium. However, this observation was not complied within the first 4 h of incubation as a consequence of the strong physical interactions occurring between IBUSS molecules and hydrophilic chain blocks, which led to a delayed release of the hydrophilic drug compared to the hydrophobic one (Hoare and Kohane, 2008). This different releasing mechanism of IBU and IBUSS from CHP407 gels was also supported by the estimated release exponent *n*. The Korsmeyer–Peppas model applied to CHP407_IBUSS gel release data within the first 7 h of incubation (being this model valid up to 60% release) evidenced an *n* value characteristic of case II transport. Indeed, IBUSS release was determined not only by diffusion and swelling/relaxation phenomena, but also by the occurrence of other processes influencing drug release, such as

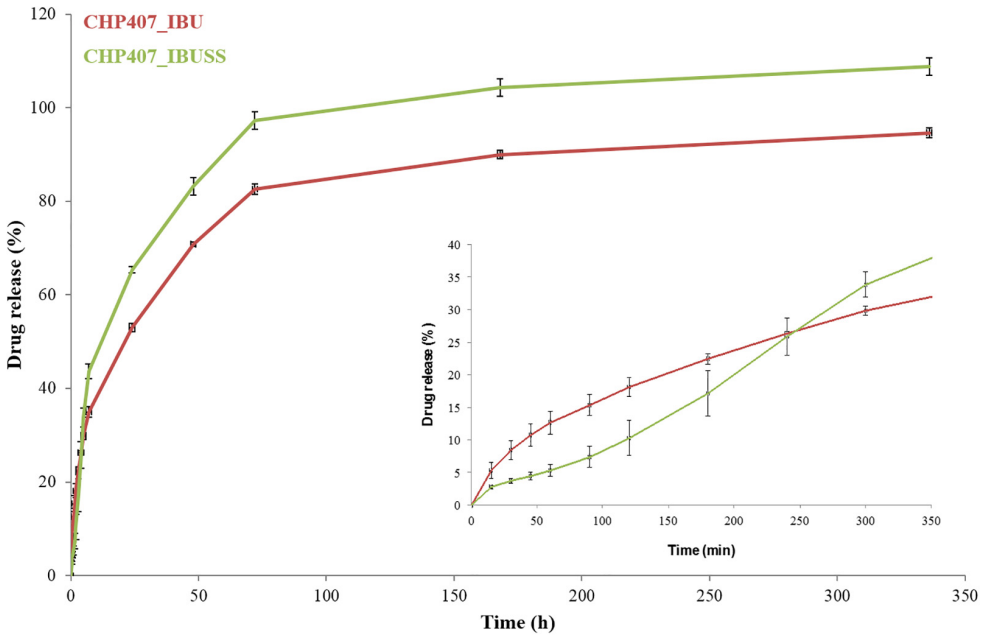

FIGURE 7 | Drug release profile of IBU (red line) and IBUSS (green line) loaded at 1 mg/mL in 15% w/V concentrated CHP407 hydrogels. The insert magnifies drug release profiles within the first 7 h of incubation.

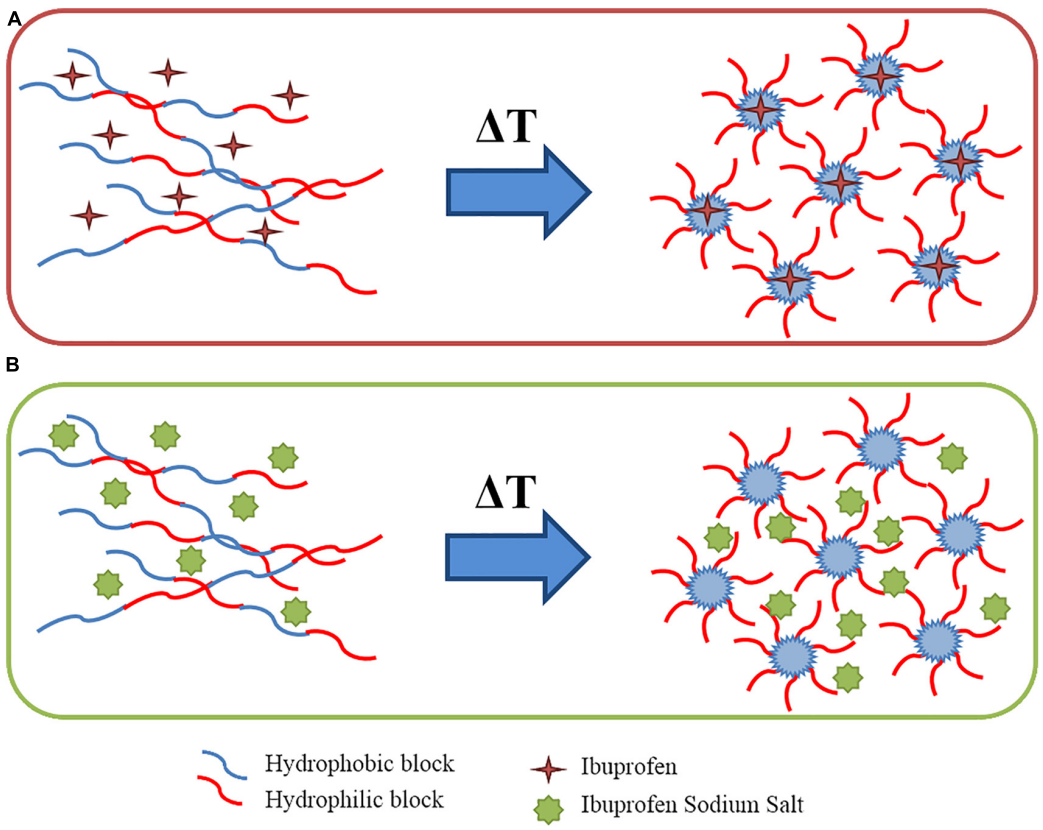

FIGURE 8 | Schematic representation of wettability-driven drug arrangement during chain organisation into micelles upon temperature increase: hydrophobic drugs loaded inside the micelle core **(A)** and hydrophilic drug entrapped in the interstitial spaces among micelles **(B)**.

the electrostatic interactions occurring between IBUSS molecules and the polymeric chains (Dash et al., 2010; Boffito et al., 2019b). On the other hand, the Korsmeyer–Peppas model applied to CHP407_IBU systems gave an *n* value characteristic of non-Fickian transport (Dash et al., 2010; Boffito et al., 2019b). Indeed, the drug first diffused from the micelles within the hydrogel interstitial spaces and then from the gel in the surrounding medium. This result is in contrast with our recently published work (Boffito et al., 2019b), in which we characterised IBU release as a purely diffusive process. However, this contrasting data can be correlated to the different adopted protocol for drug loading. In our previous work, the addition of IBU to already solubilised CHP407 hydrogels led to only a partially effective loading of the drug within micelle core, being a fraction of the polymer chains already aggregated into micelles at the hydrogel preparation temperature (i.e., 4°C). Hence, a part of the added IBU probably remained in the hydrophobic micelle inlets and was released via diffusion mechanism. In contrast, in the present work the addition of IBU during polymer solubilisation allowed its direct incorporation into the micelles, which progressively assembled, leading to an anomalous releasing mechanism characteristic of drug delivery carriers with a double diffusive barrier (Boffito et al., 2019b). Thus, working on the loading protocol, hydrophobic drugs could be portioned among the different hydrophobic domains present within the gels, i.e., micelle core and inlets, with a consequent fine modulation of the release mechanism. CHP407 chain organisation into micelles upon temperature increase could thus be successfully exploited to load high amounts of hydrophobic molecules within the gels and avoid their burst release. Other parameters potentially affecting the release profile and mechanism are hydrogel composition, the initial cargo concentration within the gels, and the releasing volume surrounding them, which all together govern gel residence time and the forces involved in the progressive delivery of the payload from the systems to the surrounding watery environment.

This study has thus reported for the first time a thorough investigation, at both the nano- and macro-scale, of the interactions occurring between amphiphilic polymers and drugs with different wettability, which in turn strongly influence polymer chain arrangement in aqueous environment as well as cargo localisation within the formed micelle network and its release. All these aspects finally merge in the definition of a new hydrogel platform with the huge potential of loading high concentrations of drugs with different wettability and being *ad hoc* customised to deliver selected payloads with a well-defined time schedule.

CONCLUSION

In this work, an amphiphilic poly(ether urethane)-based hydrogel was successfully developed, providing a step forward in the design of versatile drug delivery systems. According to the main goal of this investigation, IBU and IBUSS were selected as model drugs showing different wettability. In addition, they are widely employed in clinics as analgesic, anti-inflammatory, and antipyretic agents. Their loading within a vehicle phase opens the way to the possibility to locally release these drugs in target area, with the additional advantage of avoiding undesired side effects. The here-developed IBU- and IBUSS-loaded systems could thus find widespread application in the biomedical field in the treatment of many pathological states such as chronic wounds and musculoskeletal and rheumatic disorders. Our investigations evidenced that the characteristic PEU chain organisation into micelles in response to temperature increase could be exploited to encapsulate drugs with different wettability with no detrimental alterations of the thermo-sensitivity (i.e., all the resulting formulations retained the capability to gel in physiological conditions). In addition, the encapsulation of hydrophobic molecules within the micelles ensured prolonged drug release over time, thus avoiding their common burst release from hydrophilic networks. Furthermore, the different drug molecule arrangement within the gel network, as a consequence of their hydrophilic/hydrophobic nature and loading protocol, resulted in different drug releasing mechanism and timing. Thus, the here-developed platform could also open the possibility to design smart thermosensitive hydrogels able to simultaneously encapsulate and release high amounts of different therapeutic agents, thus eventually increasing the therapeutic efficacy through their co-current delivery into a target tissue/organ.

DATA AVAILABILITY STATEMENT

The datasets generated for this study are available on request to the corresponding author.

AUTHOR CONTRIBUTIONS

RL designed the experiments, analysed the data, and wrote the manuscript. MB designed the experiments, revised the manuscript, and supervised the whole work. Both authors contributed to the article and approved the submitted version.

FUNDING

This project has received funding from the European Union's Horizon 2020 Research and Innovation Program under grant agreement no. 685872-MOZART (www.mozartproject.eu).

ACKNOWLEDGMENTS

RL and MB acknowledge Prof. Gianluca Ciardelli (Politecnico di Torino) for financial support to this work. RL acknowledges Prof. Valeria Chiono (Politecnico di Torino) for supervision of her Ph.D.

SUPPLEMENTARY MATERIAL

The Supplementary Material for this article can be found online at: https://www.frontiersin.org/articles/10.3389/fbioe.2020.00708/full#supplementary-material

REFERENCES

Alexandridis, P., Holzwarth, J. F., and Hatton, T. A. (1994). Micellization of poly(ethylene oxide)-poly(propylene oxide)-poly(ethylene oxide) triblock copolymers in aqueous solutions: thermodynamics of copolymer association. *Macromolecules* 27, 2414–2425. doi: 10.1021/ma00087a009

Alsirawan, M. B., Mohammad, M. A., Alkasmi, B., Alhareth, K., and El-Hammadi, M. (2013). Development and validation of a simple HPLC method for the determination of ibuprofen sticking onto punch faces. *Int. J. Pharm. Pharm. Sci.* 5, 227–231.

Andrade-Vivero, P., Fernandez-Gabriel, E., Alvarez-Lorenzo, C., and Concheiro, A. (2006). Improving the loading and release of NSAIDs from pHEMA hydrogels by copolymerization with functionalized monomers. *J. Pharm. Sci.* 96, 802–814.

Bodratti, A. M., and Alexandridis, P. (2018). Formulation of Poloxamers for drug delivery. *J. Funct. Biomater.* 9, 11–35.

Boffito, M., Gioffredi, E., Chiono, V., Calzone, S., Ranzato, E., Martinotti, S., et al. (2016). Novel polyurethane-based thermosensitive hydrogels as drug release and tissue engineering platforms: design and in vitro characterization. *Polym. Int.* 65, 756–769. doi: 10.1002/pi.5080

Boffito, M., Grivet Brancot, A., Lima, O., Bronco, S., Sartori, S., and Ciardelli, G. (2019a). Injectable thermosensitive gels for the localized and controlled delivery of biomolecules in tissue engineering/rigenerative medicine. *Biomed. Sci. Eng.* 3, 67–76.

Boffito, M., Pontremoli, C., Fiorilli, S., Laurano, R., Ciardelli, G., and Vitale-Brovarone, C. (2019b). Injectable thermosensitive formulation based on polyurethane hydrogel/mesoporous glasses for sustained co-delivery of functional ions and drugs. *Pharmaceutics* 11, 501–521.

Chen, P. C., Kohane, D. S., Park, Y. J., Bartlett, R. H., Langer, R., and Yang, V. C. (2004). Injectable microparticle-gel system for prolonged and localized lidocaine release. II. In vivo anesthetic effects. *J. Biomed. Mater. Res. A* 70, 459–466. doi: 10.1002/jbm.a.30101

Dash, S., Murthy, P. N., Nath, L., and Chowdhury, P. (2010). Kinetic modeling on drug release from controlled drug delivery systems. *Act. Pol. Pharm.* 67, 217–223.

Dimatteo, R., Darling, N. J., and Segura, T. (2018). In situ forming injectable hydrogels for drug delivery and wound repair. *Adv. Drug. Deliv. Rev.* 127, 167–184. doi: 10.1016/j.addr.2018.03.007

Ghasemiyeh, P., and Mohammadi-Samani, S. (2019). Hydrogels as drug delivery systems; pros and cons. *Trend Pharm. Sci.* 5, 7–24.

Gong, C., Qi, T., Wei, X., Qu, Y., Wu, Q., Luo, F., et al. (2013). Thermosensitive polymeric hydrogels as drug delivery systems. *Curr. Med. Chem.* 20, 79–94. doi: 10.2174/0929867311302010009

Hoare, T. R., and Kohane, D. S. (2008). Hydrogels in drug delivery: progress and challenges. *Polymer* 49, 1993–2007. doi: 10.1016/j.polymer.2008.01.027

Hoo, C. M., Starostin, N., West, P., and Mecrtney, M. L. (2008). A comparison of atomic force microscopy (AFM) and dynamic light scattering (DLS) methods to characterize nanoparticle size distributions. *J. Nanopart. Res.* 10, 89–96. doi: 10.1007/s11051-008-9435-7

Larrañeta, E., Stewart, S., Ervine, M., Al-Kasasbeh, R., and Donnelly, R. E. (2018). Hydrogels for hydrophobic drug delivery. Classification, synthesis and applications. *J. Funct. Biomater.* 9, 13–33.

Laurano, R., Boffito, M., Torchio, A., Cassino, C., Chiono, V., and Ciardelli, G. (2019). Plasma treatment of polymer powders as an effective tool to functionalize polymers: case study application on an amphiphilic polyurethane. *Polymers* 11, 2109–2126.

Laurano, R., Cassino, C., Ciardelli, G., Chiono, V., and Boffito, M. (2020). Polyurethane-based thiomers: a new multifunctional copolymer platform for biomedical applications. *React. Funct. Polym.* 146: 104413. doi: 10.1016/j.reactfunctpolym.2019.104413

Li, S., Yang, Y., Yang, X., and Xu, H. (2007). In vitro degradation and protein release of semi-IPN hydrogels consisted of poly(acrylic acid-acrylamide-methacrylate) and amylose. *J. App. Polym. Sci.* 105, 3432–3438. doi: 10.1002/app.26389

Lim, J., Yeap, S. P., Che, H. X., and Low, S. C. (2013). Characterization of magnetic nanoparticle by dynamic light scattering. *Nanoscale Res. Lett.* 8, 381–395.

Liu, Y. Y., Liu, W. Q., Chen, W. X., Sun, L., and Zhang, G. B. (2007). Investigation of swelling and controlled-release behaviors of hydrophobically modified poly(methacrylic acid) hydrogels. *Polymer* 48, 2665–2671. doi: 10.1016/j.polymer.2007.03.010

Matsusaki, M., Sakaguchi, H., Serizawa, T., and Akashi, M. (2007). Controlled release of vascular endothelial growth factor from alginate hydrogels nano-coated with polyelectrolyte multilayer films. *J. Biomater. Sci.* 18, 775–783. doi: 10.1163/156856207781034160

Nuttelman, C. R., Tripodi, M. C., and Anseth, K. S. (2006). Dexamethasone-functionalized gels induce osteogenic differentiation of encapsulated hMSCs. *J. Biomed. Mater. Res. A* 76, 183–195. doi: 10.1002/jbm.a.30537

Okudan, A., and Altay, A. (2019). Investigation of the effects of different hydrophilic and hydrophobic comonomers on the volume phase transition temperatures and thermal properties of N-isopropylacrylamide-based hydrogels. *Int. J. Poly. Sci.* 1, 1–12. doi: 10.1155/2019/7324181

Pontremoli, C., Boffito, M., Fiorilli, S., Laurano, R., Torchio, A., Bari, A., et al. (2018). Hybrid injectable platforms for the in situ delivery of therapeutic ions from mesoporous glasses. *Chem. Eng. J.* 340, 103–113. doi: 10.1016/j.cej.2018.01.073

Pradal, C., Jack, K. S., Grondahl, L., and Cooper-White, J. J. (2013). Gelation kinetics and viscoelastic properties of pluronic and α-cyclodextrin-based pseudopolyrotaxane hydrogels. *Biomacromol* 14, 3780–3792. doi: 10.1021/bm401168h

Rey-Rico, A., and Cucchiarini, M. (2018). PEO-PPO-PEO trib-block copolymers for gene delivery applications in human regenerative medicine – an overview. *Int. J. Mol. Sci.* 19, 775–790.

Zha, L., Hu, J., Wang, C., Fu, S., Elaissari, A., and Zhang, Y. (2002). Preparation and characterization of poly(N-isopropylacrylamide-co-dimethylamino-ethyl methacrylate) microgel latexes. *Colloid Polym. Sci.* 280, 1–6. doi: 10.1007/s003960200000

Zhang, J. T., Huang, S. W., Liu, J., and Zhuo, R. X. (2005). Temperature sensitive poly[N-isopropylacrylamide-co-(acryloyl β-cyclodextrin)] for improved drug release. *Macromol. Biosci.* 5, 192–196. doi: 10.1002/mabi.200400167

Conflict of Interest: The authors declare that the research was conducted in the absence of any commercial or financial relationships that could be construed as a potential conflict of interest.

frontiers in Bioengineering and Biotechnology

REVIEW
published: 13 August 2020
doi: 10.3389/fbioe.2020.00972

Large Animal Models in Regenerative Medicine and Tissue Engineering: To Do or Not to Do

Iris Ribitsch[1], Pedro M. Baptista[2], Anna Lange-Consiglio[3], Luca Melotti[4], Marco Patruno[4], Florien Jenner[1], Eva Schnabl-Feichter[5], Luke C. Dutton[6], David J. Connolly[5], Frank G. van Steenbeek[7], Jayesh Dudhia[6] and Louis C. Penning[7]*

[1] Veterm, Department for Companion Animals and Horses, University Equine Hospital, University of Veterinary Medicine Vienna, Vienna, Austria, [2] Laboratory of Organ Bioengineering and Regenerative Medicine, Health Research Institute of Aragon (IIS Aragon), Zaragoza, Spain, [3] Department of Veterinary Medicine, Università degli Studi di Milano, Milan, Italy, [4] Department of Comparative Biomedicine and Food Science, University of Padua, Padua, Italy, [5] Clinical Unit of Small Animal Surgery, Department for Companion Animals and Horses, University of Veterinary Medicine Vienna, Vienna, Austria, [6] Department of Clinical Sciences and Services, Royal Veterinary College, Hertfordshire, United Kingdom, [7] Department of Clinical Sciences of Companion Animals, Faculty of Veterinary Medicine, Utrecht University, Utrecht, Netherlands

OPEN ACCESS

Edited by:
Dimitrios I. Zeugolis, National University of Ireland Galway, Ireland

Reviewed by:
Peter Pivonka, Queensland University of Technology, Australia
Janos Kanczler, University of Southampton, United Kingdom

***Correspondence:**
Iris Ribitsch
iris.ribitsch@vetmeduni.ac.at

Specialty section:
This article was submitted to Tissue Engineering and Regenerative Medicine, a section of the journal Frontiers in Bioengineering and Biotechnology

Received: *12 February 2020*
Accepted: *27 July 2020*
Published: *13 August 2020*

Citation:
Ribitsch I, Baptista PM, Lange-Consiglio A, Melotti L, Patruno M, Jenner F, Schnabl-Feichter E, Dutton LC, Connolly DJ, van Steenbeek FG, Dudhia J and Penning LC (2020) Large Animal Models in Regenerative Medicine and Tissue Engineering: To Do or Not to Do. Front. Bioeng. Biotechnol. 8:972. doi: 10.3389/fbioe.2020.00972

Rapid developments in Regenerative Medicine and Tissue Engineering has witnessed an increasing drive toward clinical translation of breakthrough technologies. However, the progression of promising preclinical data to achieve successful clinical market authorisation remains a bottleneck. One hurdle for progress to the clinic is the transition from small animal research to advanced preclinical studies in large animals to test safety and efficacy of products. Notwithstanding this, to draw meaningful and reliable conclusions from animal experiments it is critical that the species and disease model of choice is relevant to answer the research question as well as the clinical problem. Selecting the most appropriate animal model requires in-depth knowledge of specific species and breeds to ascertain the adequacy of the model and outcome measures that closely mirror the clinical situation. Traditional reductionist approaches in animal experiments, which often do not sufficiently reflect the studied disease, are still the norm and can result in a disconnect in outcomes observed between animal studies and clinical trials. To address these concerns a reconsideration in approach will be required. This should include a stepwise approach using *in vitro and ex vivo* experiments as well as *in silico* modeling to minimize the need for *in vivo* studies for screening and early development studies, followed by large animal models which more closely resemble human disease. Naturally occurring, or spontaneous diseases in large animals remain a largely untapped resource, and given the similarities in pathophysiology to humans they not only allow for studying new treatment strategies but also disease etiology and prevention. Naturally occurring disease models, particularly for longer lived large animal species, allow for studying disorders at an age when the disease is most prevalent. As these diseases are usually also a concern in the chosen veterinary species they would be beneficiaries of newly developed therapies. Improved awareness of the progress

in animal models is mutually beneficial for animals, researchers, human and veterinary patients. In this overview we describe advantages and disadvantages of various animal models including domesticated and companion animals used in regenerative medicine and tissue engineering to provide an informed choice of disease-relevant animal models.

Keywords: large animal models, sheep, pig, horse, dog, regenerative medicine, tissue engineering, naturally occurring disease

INTRODUCTION

The use of sentient animals for research purposes is a controversial topic, which has raised public and ethical concerns and is criticized by opponents claiming that animal models often do not generate appropriate benefit with regards to their potential risks and harm and as a consequence, are often ethically not permissible. The increasing status of pets as family members and corresponding high level of veterinary care for privately owned pets further amplifies the controversy over the use of animals for research purposes.

However, animal models are still an important and, at a regulatory level, a compulsory component of translational research, which cannot yet be replaced by *in vitro* experiments. Although *in vitro* models allow for systematic, standardized analysis of various cellular, biophysical and biochemical cues in a controlled environment, without the natural variability inherent to *in vivo* animal models, they can only offer an abstract insight into the pathophysiology of diseases and disorders. Therefore, while animal models cannot yet be replaced, the number of animals used should be reduced to a minimum and experiments involving animals should be optimized with regard to their translatability and the welfare of the animals.

However, to date a reductionist approach often using immature laboratory species is commonly employed (Jackson et al., 2017). Small rodent animals, specifically mouse and rat, are valuable for research into mechanisms of disease and fundamental biology, but findings from such small animal models often do not translate into human clinical applications (Prabhakar, 2012; Lorbach et al., 2015). Shanks et al. impressively illustrated the translational challenges, showing the difference in bioavailability of pharmaceuticals between humans, primates, dogs and rodents (Shanks et al., 2009). However, although awareness is increasing there is still a massive disproportion between rodent studies and large animal studies.

Therefore, the European Medicines Agency (EMA), the USA Federal Food and Drug Administration (FDA) and the International Society for Stem Cell Research (ISSCR) recommend the use of large animal models to evaluate efficacy, durability, dose response, degradation and safety of advanced therapeutic medicinal products (ATMPs)[1,2]. For successful and timely translation from animal models to regulatory approval and clinical application, a step-wise development using laboratory animals for screening and early development work, followed by a large animal model such as the pig, sheep or horse which offers a more realistic approach for late development and pivotal studies would be more appropriate (Hurtig et al., 2011).

Moreover, animals develop many naturally occurring (or spontaneous) diseases that are equivalent to human disease leading to the development of the "One Health One Medicine" concept which presumes that diseases in men and animals (mostly mammals) have similar aetiologies and pathophysiologies and require analogous therapeutic approaches. Hence, human and veterinary medicine can mutually benefit from research that applies a one health approach. Using large animal models with naturally occurring disease with a similar pathophysiology as in humans, allows study of not only new treatment strategies but also disease development and prevention at a relevant age. However, although using naturally occurring disease models best reflect disease complexity, standardization of disease grade and availability of sufficient clinical case numbers for recruitment into studies can be challenging.

In order to achieve the best output while following the three R's principle (to **r**educe, **r**efine and **r**eplace animal models) of using the smallest possible number of animals, animal models need to be optimized to the greatest possible extent (Madden et al., 2012). They require careful selection and design to ensure they are fit-for-purpose and address both optimal predictive validity, as well as ethical, animal-welfare and societal considerations. Species, anatomic, physiologic, biomechanical aspects and their clinical relevance need to be considered.

Furthermore, knowledge regarding the epidemiology and natural history of diseases in different animal species, disease similarities to humans, availability of diagnostics, treatment options, and outcome measures as well as criteria defining species specific quality of life and functional parameters is important but still scarce in the scientific community. Other important considerations in using large animal models include availability, handling and economic concerns.

To optimize scientific output and translational potential with animal welfare needs, tight cooperation between basic science, human and veterinary medicine is necessary. The veterinary academic environment offers unique expertise to make that goal attainable to the highest standards. This includes the veterinary knowledge required to make a rational decision for the choice of animal model rather than being based on in-house availability.

There are several research groups which have a track record of developing preclinical large animal models, some of which have managed to translate their research into clinical applications (Kang et al., 2010, 2013; Mcilwraith et al., 2011, 2012; Godwin et al., 2012; Smith et al., 2013; Bach et al., 2017; Whitehouse et al., 2017; Goldberg et al., 2018; Tellegen et al., 2018; Broeckx et al., 2019; Tellegen et al., 2019). This — by no means

[1]http://www.isscr.org/docs/guidelines/isscrglclinicaltrans.pdf

[2]https://www.fda.gov/vaccines-blood-biologics/biologics-guidances/cellular-gene-therapy-guidances

exhaustive — list clearly demonstrates the collective efforts of the veterinary community to provide large animal models to be used in translational projects.

However, yet it is still often argued, that translational studies using large animal models are rare because they are complex, time-consuming, technically demanding, slow, and usually not suitable for mechanistic investigations. Nevertheless, because large animals better reflect the human body conformation and pathophysiology of certain naturally occurring diseases than rodent models, these studies are essential justifying the challenges and costs. Unfortunately, the added value of the clinical relevance of large animal models is often not appreciated by reviewers of manuscripts and grant applications are assigned low scores on the basis of lack of mechanistic insights and insufficient conceptual novelty. However, for a successful translation of tissue engineering and regenerative medicine research into clinical therapies, it is critical that this misperception is corrected.

It is the authors' hope that this review, which introduces different large animal models, their naturally occurring diseases and their specificities, may stimulate biomedical researchers to look for the very best model possible for their specific research question and that it will encourage interdisciplinary cooperation to optimize the choice of disease-relevant animal models in the future. Deciding which animal model should be used in a particular study is first and foremost dependent on defining the specific question that needs to be answered. Only then can the pertinent benefits and drawbacks of individual models be considered and a decision made.

In this review, we focus on horses, sheep, dogs, cats and pigs as the most frequently used large animal models in research and do not include primates due to the ethical dimension and limited indications, which require their specific use. Using animals which are so similar to humans, raises serious ethical concerns. Therefore, the use of non-human primates is closely monitored and strictly regulated and much has been done to specifically safeguard these animals. The use of great apes has been completely prohibited. As long as non-human primates are used for medical research, the European Commission strongly advocates the "3Rs principle," now a legal obligation embedded in the EU legislation to: Replace non-human primates with viable alternatives whenever feasible, Reduce the use of non-human primates and Refine scientific procedures and the care and treatment of the animals. Even phasing-out the use of non-human primates in Europe is discussed[3].

WHY THE CHOICE OF ANIMAL MODELS IS CRUCIAL

The most obvious and demonstrative reason why the choice of animal models is crucial, are gross anatomic differences between the human and different animals and even between animals of different species (**Figure 1**). These differences imply that the same anatomic structures may have a different function and are subjected to different biomechanical strains. **Table 1**

[3]https://ec.europa.eu/health/sites/health/files/scientific_committees/scheer/docs/scheer_o_004.pdf

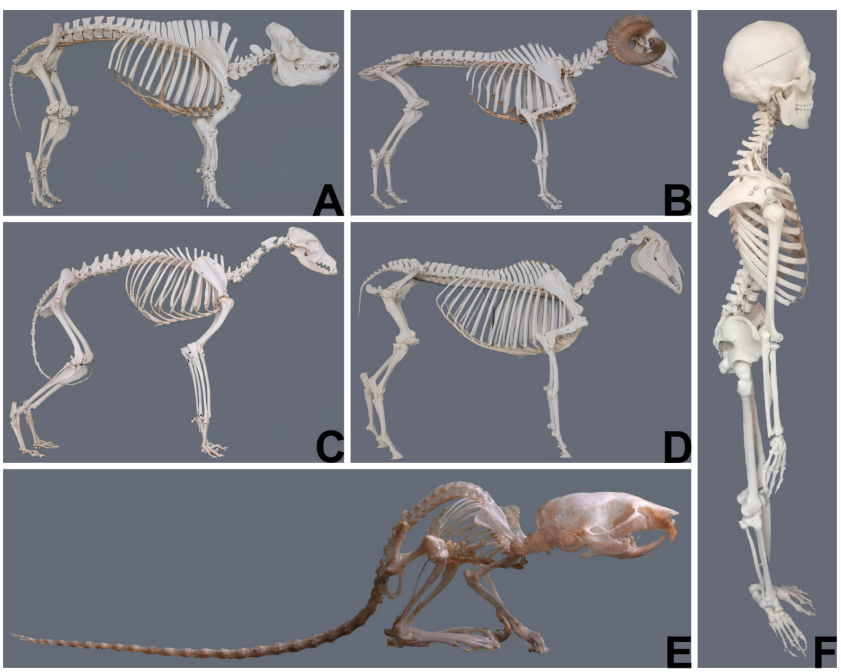

FIGURE 1 | Gross anatomical differences between animals of different species (courtesy of Niklas Dresen, Institute of veterinary anatomy, University Leipzig) and the human (courtesy of Elfriede Cremer, Bernhard Cremer and Elisabeth Schieder). **(A)** Pig; **(B)** Sheep; **(C)** Dog; **(D)** Horse; **(E)** Mouse; **(F)** Human.

TABLE 1 | Comparison of physiologic and biomechanical parameters of different model animals.

Species	Mouse (C57BL/6)	Rat	Rabbit	Canine	Mini-Pig	Sheep	Goat	Horse	Human
Body temperature (in °Celsius)	36.5–37.3°C	37.5–39.5	38.0–39.5	38.0–39	38.3–38.8	38.5–39.5	38.3–39.0	37.5–38.0	36.5–37.3
Heartrate (beats per minute)	491–626	250–450	150–300	60–160	68–72	60–80	60–80	28–40	60–80
Respiration rate per minute	272	70–120	35–100	15–30	14–18	16–30	10–30	10–14	12–20
Cartilage thickness medial femoral condyle (in mm)	0.1		0.3	0,6–1.3	1.5	0.7–1.7	0.7–1.5	1.75	2.35
Critical size cartilage defect (in mm)		1.4	3	4	6	7	7	9	10
Subchondral bone plate thickness medial femoral condyle (in mm)			0.4–0.5			0.7	0.3	0.7	0.2–0.5
Anterior cruciate ligament length (in mm)			10.6	21.2	37.0	31.77			37.78
Anterior cruciate ligament diameter (in mm)			4.84	5.45	10.86	9.27			12.73
Posterior cruciate ligament length (in mm)			10.0	22.8	39.68	37.03			40.30
Posterior cruciate ligament diameter (in mm)			4.34	5.33	8.2	6.67			14.23
Medial Meniscus length (in mm)			9.2	16.83	25.32	25.63			39.8
Lateral meniscus length (in mm)			10.0	16.3	25.60	26.03			33.28
Range of motion – knee joint extension (in °)			22	34	42	40	45		2.5
Range of motion – knee joint extension (in °)			161	160	144	146.7	145.5		137.5
Age of skeletal maturity (age until growths plates remain open)	3–6 months (growths plates remain open life–long)		16–39 weeks	12–24 weeks	42–52 weeks	36–48 months	36–48 months	60–72 months	18–22 years
Weight at skeletal maturity in kg	20–40 g	0.25–0.55	3–4	1–30	20–40	40–70	40–70	450–500	60–90
Life span in years	2	2.5–3.5		10–15	15	10–12	15–18	30	70–80

Table modified from Tankersley et al. (1994); Campen et al. (2005), Frisbie et al. (2006); Baumgartner et al. (2009), Chu et al. (2010); Proffen et al. (2012), Maher et al. (2015); Moran et al. (2016) and https://www.jax.org/news-and-insights/jax-blog/2017/november/when-are-mice-considered-old# and https://www.jax.org/jax-mice-and-services/strain-data-sheet-pages/body-weight-chart-000664.

illustrates differences of different animals to emphasize the importance of correct model selection with respect to species' physiologic aspects.

Age Matters

Age should be an important consideration in the choice of any animal model independent of the species used (Jackson et al., 2017). For practical and organizational reasons animal trials are often carried out in juvenile or neonatal animals. However, differences in the healing potential and therefore the healing response between juvenile and adult animals can bias the outcome of such trials (Namba et al., 1998; Beredjiklian et al., 2003; Conboy et al., 2005; Favata et al., 2006; Bos et al., 2008; Ansorge et al., 2012; Connizzo et al., 2013; Mienaltowski et al., 2016; Van Weeren and Back, 2016; Jackson et al., 2017). The use of skeletally mature animals of an appropriate age (**Table 1**) to mimic adult disease and healing potential is therefore a critical consideration for optimal study design. To truly reflect human age-related disease, the animals used should be of comparable age. Ideally old animals would be used to study age-related diseases as for instance senile osteoporosis. However, the use of elderly compared to immature or young adult animals requires specific considerations, as aged animals are more difficult to procure and may suffer from comorbidities. Hence, potential animal loss due to other diseases needs to be accounted for in the study design and financial planning. Furthermore, the predisposition for age-related diseases varies between species.

Naturally Occurring and Generated Models of Genetic Disease

Many naturally occurring genetic diseases have been identified in companion and farm animals which are often caused by a mutation in an orthologous gene and lead to a comparable clinical phenotype as observed in human patients, including the pathological alterations at the biochemical and cellular levels (Lairmore and Khanna, 2014; Kol et al., 2015). Most of these animal models are associated with congenital heart disease, lysosomal storage disease, hemophilia, muscular dystrophies, neurological disorders, immunodeficiencies and dwarfism (Lairmore and Khanna, 2014). Information about these naturally occurring genetic diseases in animals was compiled in a comprehensive database — Online Mendelian Inheritance in Animal — created by Prof. Frank Nicholas at The University of Sydney and Australian National Genomic Information Service[4].

Naturally Occurring and Generated Models of Musculoskeletal Disease

Osteoarthritis (OA) is a heterogeneous disease for which no single animal model perfectly recapitulates the complex etiology and clinical manifestations of the human disease (Aigner et al., 2010; Cohen-Solal et al., 2012; Little and Zaki, 2012; Mccoy, 2015). Currently available OA models are generally grouped into spontaneous, or surgically induced models. Spontaneous models include naturally occurring disease or genetically manipulated models, whereas surgically induced models employ (i) destabilization of the joint such as partial or total meniscectomy, meniscal tear, anterior cruciate ligament or posterior cruciate ligament transection, medial and/or lateral collateral ligament transection or osteotomy (ii) physical defects of the articular cartilage such as creation of articular grooves, (iii) impact trauma including transarticular impact, and intra-articular osteochondral fragmentation (iv) chemically induced lesions using intra-articular injection of monosodium iodoacetate, collagenase, carrageenan or Freund adjuvant (Bentley, 1975; Little and Zaki, 2012; Lampropoulou-Adamidou et al., 2014; Mccoy, 2015). Spontaneous models that develop progressive and chronic disease are likely to more closely mimic idiopathic OA. However, these models take longer to develop and tend to be more variable with respect to outcome measures (Vincent et al., 2012; Teeple et al., 2013; Lampropoulou-Adamidou et al., 2014; Mccoy, 2015).

Surgical models have the advantage of repeatability and reproducibility as well as rapid onset and progression (Lampropoulou-Adamidou et al., 2014), but for that reason are less ideal models of spontaneous OA and are often regarded as posttraumatic (secondary) OA (Bendele, 2001; Little and Hunter, 2013; Teeple et al., 2013; Mccoy, 2015).

The validity of chemically induced models for OA has been questioned (Poole et al., 2010; Teeple et al., 2013) due to the resulting widespread cell death and rapid joint destruction, which are not considered typical for either spontaneous or posttraumatic OA (Little and Zaki, 2012).

Animal models are further widely used in osteoporosis research. They include, among others, models for disuse induced osteoporosis, glucocorticoid-induced osteoporosis and postmenopausal osteoporosis. The most popular animal models of postmenopausal osteoporosis are those generated in the mouse, rat, sheep, and nonhuman primates by ovariectomy (Iwaniec, 2008).

The choice of the animal models differ markedly, depending on the objectives of the study. It has to be noted that rodents for example are of limited value for investigating intra−cortical bone remodeling, because they lack true Haversian cortical bone remodeling under physiological conditions due to their small weight (Baron et al., 1984; Lelovas et al., 2008; Iwaniec, 2008). Larger animals such as dogs are more appropriate for these studies because, similar to humans, dogs have well-developed Haversian remodeling (Iwaniec, 2008).

Challenges of Translating Results From Animal Models to Human Patients – An Example

To date, animal models of human asthma have included: Drosophila, rats, guinea pigs, cats, dogs, pigs, cattle, sheep, horses and primates, but the most widely used model is the mouse (Zosky and Sly, 2007; Kirschvink and Reinhold, 2008; Shapiro, 2008; Blume and Davies, 2013). The mouse is a useful model due to the availability of specific probes and reagents for studying allergic outcomes, such as cellular and humoral responses, and the good adaptability for genetic

[4]https://omia.org/home/

manipulation (Shapiro, 2008; Bonamichi-Santos et al., 2015). Nevertheless, this model has some limitations for translational medicine mainly related to the anatomical and physiological differences with respect to man. Obviously, the lung and bronchial tree, total lung capacity (6 liter for man vs. 1 ml for mouse), and the blood-gas barrier thickness (0.62 μm vs. 0.32 μm) are much smaller than in man and the bronchial artery supplies the entire lung in man but is absent in the pleura, septa and alveoli in mice. In addition, the respiratory rate, or beats per minute (10−14 vs. 250−350), is very different in people and mice. Moreover, the mouse lacks sub-mucosal glands and has limited airway smooth muscles compared to man (Lange-Consiglio et al., 2019). In view of these important differences, the pre-clinical results obtained when using a mouse model for asthma should be interpreted with care. Furthermore, the mouse does not have natural inflammatory or allergic pulmonary pathologies, so airway inflammation is usually induced by exposure to ovalbumin (OVA) or other aeroallergens. In contrast to naturally occurring human asthma, which is a chronic disease characterized by persistent inflammation and remodeling due to intermittent or continuous inhalation exposure to allergens resulting in chronic eosinophilic/neutrophilic inflammation (Aun et al., 2017; Bullone and Lavoie, 2019), the mouse model shows more acute (<3 months) inflammation and no remodeling. To circumvent this problem, systemic sensitization protocols and repeated exposures to allergens have been tried but the results obtained from different routes of systemic sensitization (subcutaneous injection, intraperitoneal injection or intranasal inhalation) and different allergens (OVA, fungi, *Ascaris* antigens, house dust mite, cockroach extracts), used alone or in combination, are difficult to compare and to interpret (Aun et al., 2017). For example, in the mouse the induced inflammation profile, although dependent on the antigen, is mainly Th2, mirroring disease in only a subsection of human asthmatics who are Th2 and/or Th1/Th17 (Douwes et al., 2002; Woodruff et al., 2009). Another criticism of the mouse model is that OVA does not induce asthma in human patients and the sensitization routes do not mimic the routes of exposure to allergens in human asthma (Aun et al., 2017). Hence, differences in the results may be due to the different types of allergens and sensitization routes.

An appropriate animal model for translational studies should mimic the pathological changes associated with human asthma and reflect the environmental factors that determine the evolution of human asthma.

HORSES AS ANIMAL MODELS

General Considerations

Horses (*equus caballus*) are a well-accepted, well-established and clinically relevant animal model particularly for musculoskeletal disease, which is of major interest in regenerative medicine.

An important aspect of clinical research is the precise demonstration of the initial injury, the disease progress, outcome and follow up. The validated applicability of advanced diagnostic methodologies in horses such as arthroscopy and MRI (together with scoring approaches) (Brittberg and Winalski, 2003; Marlovits et al., 2006), ultrasound, radiographs, CT and scintigraphy, has made the horse a popular model for which non-terminal studies with thorough evaluation and monitoring are possible. Also, second-look arthroscopy and serial sampling are feasible. Moreover, the large size of horses allows for the creation of critical size defects or multiple defects and offers a high amount of material that can be sampled for analysis. This enables large and comprehensive studies which may not be possible in smaller animals. Together with well-established histologic scoring (Mcilwraith et al., 2010) and pain scores (Price et al., 2003; Graubner et al., 2011; Dalla Costa et al., 2014; Gleerup et al., 2015) or assessment of other clinical parameters for horses these methods facilitate comparability of diagnosis, follow-up and results. Controlled postoperative exercise programs and rehabilitation protocols using e.g., treadmills and horse walkers further support standardization of the results. A broad offer of modern methods to further objectify outcome measures became available including gait kinematics (e.g., lameness locators) and/or kinetics using force plate/ground reaction force analysis.

Also the lack of traceability of cells injected for cell therapies could be overcome to a certain extent by using either super paramagnetic iron oxide particle (SPIO) for MRI (Delling et al., 2015a,b; Julke et al., 2015; Berner et al., 2016; Burk et al., 2016) or nuclear labeled (Technetium 99M, GFP, Indium 111) cells for scintigraphic tracing (Sole et al., 2012, 2013; Becerra et al., 2013; Trela et al., 2014; Dudhia et al., 2015; Spriet et al., 2015; Espinosa et al., 2016; Geburek et al., 2016; Scharf et al., 2016).

Some disadvantages of using the horse as a model include high costs of animal of animal purchase, maintenance/handling as well as ethical concerns and lower acceptance of the horse as an experimental animal compared to small animal studies by the lay public. In addition, some key parameters building the framework used in studies applying Omics approaches are not well enough researched in horses yet. A restrictive annotation status and availability of equine specific antibodies, molecular tools and markers are limiting factors. A major challenge when using horses is that their weight precludes non-weight-bearing investigations postoperatively. Significant limitations may arise regarding biomechanical strains, which far exceed those considered physiologic in humans and other animal models, which could render the stabilization of injured structures, transplants and/or sutures ineffective. Therefore, horses are a less amenable model for meniscus or bone repair. Nonetheless, these are major challenges in equine patients and several different attempts have been made or are envisaged to support healing of these structures by regenerative medicine approaches (Fox et al., 2010; Milner et al., 2011; Ferris et al., 2012; Kisiday et al., 2012; Mcduffee et al., 2012; Seo et al., 2014; Warnock et al., 2014; Govoni, 2015; Yu et al., 2015; Gonzalez-Fernandez et al., 2016) which may also hold valuable preclinical results for human medicine. For example, hyperextension of the stifle joint was found to lead to pathologic levels of forces and injury in the cranial horn of the equine medial meniscus, analogous to observations

in the human posterior medial horn upon hyperflexion (Drosos and Pozo, 2004).

Tendinopathy

Horses commonly suffer from naturally occurring tendon injuries (tendinopathy) and degenerative joint disease (osteoarthritis − OA) with similar pathophysiology to the human in terms of etiology and risk factors, which include over-exercise, age and genetic factors (Goodship et al., 1994; Patterson-Kane and Firth, 2009; Mcilwraith et al., 2012; Voleti et al., 2012; Smith et al., 2014; Andarawis-Puri et al., 2015). As athletic individuals, horses incur idiopathic primary or sports related injuries to tendon and joint related tissue.

An example is the equine superficial digital flexor tendon (SDFT) which performs a similar function to the human Achilles tendon during high-speed locomotion. In both species, their respective tendons are one of the most frequently injured (Jarvinen et al., 2005; Thorpe et al., 2010) with age and participation in sports as key risk factors. The SDFT supports the metacarpophalangeal (MCP) joint and functions as an energy storing elastic tissue to enable efficient locomotion. During high-speed locomotion the SDFT can experience strains of 16% as the MCP joint hyperextends. These strains are within the functional limit of the SDFT at which failure can occur (Richardson et al., 2007). The Achilles tendon can experience strains of up to 8% allowing as much as 34% of the total work performed by the calf muscles to be stored in the Achilles (Fukashiro et al., 1995).

Acute and chronic Achilles tendon pathology is estimated to be responsible for as many as 50% of all sports-related injuries in humans (Fukashiro et al., 1995; Maffulli, 1999; Jarvinen et al., 2005). The incidence of SDFT tendinitis in horses is reported to be as high as 8−43% (Dowling et al., 2000). Injuries in both often manifest within the body of the tendon as core lesions, which heal by the formation of fibrous scar tissue. This scar tissue is biomechanically inferior with significantly reduced elasticity which leads to a high risk of re-injury (Smith, 2008). It is therefore essential that repair strategies are aimed at restoring function by achieving scar-free healing for which regenerative medicine holds great potential. Studies in the horse to test and improve cell and cell free therapies for tendon regeneration (Smith et al., 2003; Pacini et al., 2007; Richardson et al., 2007; Schnabel et al., 2007; Fortier and Smith, 2008; Lacitignola et al., 2008; Smith, 2008; Godwin et al., 2012; Marfe et al., 2012; Carvalho Ade et al., 2013; Renzi et al., 2013; Smith et al., 2013; Van Loon et al., 2014; Geburek et al., 2015; Muttini et al., 2015) could serve as preclinical data for human medicine.

However, due to the challenges of standardization of disease grade and availability of sufficient clinical case numbers for recruitment of horses with naturally occurring disease, a number of induced equine models have been developed to investigate both tendon and joint disease.

Several surgically induced tendon injury models have been developed to try to achieve a standard lesion size, anatomical location and the ensuing inflammatory response as well as time to treatment (Guest et al., 2008; Schramme et al., 2010; Caniglia et al., 2012; Cadby et al., 2013). While most of these are aimed at partial or full transection of the tendon, the mechanically induced model described by Schramme et al. (2010) mimics a typical tendon core lesion of spontaneous disease with similarities in healing characteristics (Cadby et al., 2013). In contrast, collagenase induced tendon injury models which attempt to mimic core lesions (Williams et al., 1984; Nixon et al., 2008; Moraes et al., 2009; Schnabel et al., 2009; Crovace et al., 2010; Karlin et al., 2011; Watts et al., 2011, 2012; Carvalho Ade et al., 2013) lead to a strong inflammatory response and are difficult to standardize with respect to location, size, shape and volume due to leakage of collagenase through the injection sites and uncontrollable diffusion from the center of the tendon (Schramme et al., 2010).

Cartilage Injuries and Osteoarthritis

Another example to illustrate "what the horse can tell the human" is Osteoarthritis, a degenerative joint disease characterized by progressive loss of articular cartilage. Adult articular cartilage has limited capacity for repair and regeneration (Kim et al., 1991). Any disruption of the superficial zone, or injury to the chondrocytes that maintain the cartilage matrix and zonal architecture, affects the load-distribution of the viscoelastic hyaline cartilage and may ultimately culminate in degenerative joint disease (Rolauffs et al., 2010). OA of the knee and hip joints is one of the most commonly diagnosed diseases in human general practice with 52 million people (=22.7% of adults older than 18 years) in the United States and an estimated 30 – 40 million Europeans suffering from arthritis of one or more joints (Cheng et al., 2012; Johnson and Hunter, 2014). With age and obesity as key risk factors the prevalence of OA is expected to double by the year 2020 (Johnson and Hunter, 2014). As currently no proven disease-modifying therapy capable of restoring damaged articular cartilage and function of the joint is available, there is an increasing demand for novel, safe and effective treatments, which regenerative medical research could offer. In equids as for human patients, there is an unmet need for early diagnosis and effective treatments that allow return to full performance (Mccoy, 2015). In horses OA constitutes the main cause of chronic lameness with an incidence of chronic degenerative joint disease in elderly horses of up to 83.5%. Interestingly, not only is the pathophysiology of equine OA similar to the human but also the thickness of the knee cartilage is similar to the human (Frisbie et al., 2006; Malda et al., 2012). These similarities support the horse as relevant model for studies on naturally occurring OA.

A number of surgically induced equine models of articular cartilage degeneration and healing have been developed which were reviewed by Mcilwraith et al. (2011). As in humans, the major aims of OA research are to achieve resurfacing of the damaged cartilage with biomechanically resilience and acceptable pain control. However, for any studies on cartilage repair it is important that the duration should be at least 8 to 12 months, as failure at long-term follow-up is a common outcome in human and equine clinical trials even if short-term results look promising in animal models (Mcilwraith et al., 2011).

Asthma

Horses, analogous to humans, commonly suffer from asthma. Asthma is a chronic inflammatory disease characterized by airway hyper-responsiveness and airway remodeling due to increased mucus production, epithelial fibrosis, hypertrophy and hyperplasia of airways smooth muscles, and gland enlargement (Shinagawa and Kojima, 2003). This remodeling can induce irreversible obstruction of airways and may be a consequence of chronic tissue inflammation and altered repair processes. Since function and structure are closely related, the hypothesis is that remodeling leads to loss of airway and lung function (Bullone and Lavoie, 2019).

Around 300 million people worldwide (both adults and children) suffer from asthma and hence the societal impact is high[5]. The standard therapy is based on corticosteroid administration to reduce airway obstruction thus improving quality of life. However, about 20% of people are corticosteroid resistant and do not respond to therapy (Panettieri, 2016). Corticosteroid therapy is reparative and not regenerative and does not counteract remodeling. Better therapies may be derived from a regenerative approach to asthma-induced pathology.

The gold standard species for studies into human asthma would be human patients, but such studies are ethically impossible, because of the large number of patients requiring repeated biopsies to understand the causes of remodeling. Therefore, although requiring ethical authorizations, animal models are essential to advance understanding of the disease.

Severe equine asthma (SEA), which occurs spontaneously in horses (Herszberg et al., 2006; Williams and Roman, 2016), shares many features with human asthma. The horse has potential to be a good animal model with similar lung anatomy to man. SEA shares many features with human asthma: lower airway inflammation, completely reversible airflow obstruction, bronchial hyperresponsiveness, increased respiratory efforts at rest, coughing and exercise intolerance (Bullone and Lavoie, 2015; Couetil et al., 2007). This condition is spontaneously triggered by exposure to environmental antigens present in horse housing, similar to exposure in man and it can become incurable like chronic asthma in people. Up to 10–15% of adult horses suffer from SEA (Hotchkiss et al., 2007) with a Th-2 predominant cytokine profile (increase of IL-4), as described in human asthma (Lavoie et al., 2001; Klukowska-Rotzler et al., 2012), and decrease of Th-1 profile (decrease of interferon-γ). The predominant cell type in bronchoalveolar lavage fluid (BALF) found in horses may be different to humans depending on the severity of asthma: horses with severe and late-onset asthma have neutrophilic inflammation (Panettieri, 2016) as demonstrated in some people (Cosmi et al., 2016), while increased eosinophils are frequently detected in milder forms of equine asthma (Couetil et al., 2007). As in people with neutrophilic asthma, horses with SEA can show an increase in Th-17 expression (Debrue et al., 2005; Cosmi et al., 2016).

In a good animal model, homology of genes regulating immune function is essential and the horse shares higher homology with man for *IL2, IL23*, and *IL17*, compared to the mouse (Tompkins et al., 2010; Lange-Consiglio et al., 2019). However, the most interesting aspect of the horse as a model to study asthma is airway remodeling, although this is less marked and involves the bronchial tree more peripherally than in man (Bullone and Lavoie, 2019). The remodeling can be completely reversed by appropriate corticosteroid treatment in both human patients and horses (Bullone and Lavoie, 2019) and sequential biopsies can be collected from the same standing sedated horse without the imperative to sacrifice the animal as compared to the mouse (Leclere et al., 2011).

Additional Considerations Regarding Horses

In horses' wounds on the distal limbs show delayed healing compared to wounds located on the upper body.

Reasons for this are not fully understood. However, differences in the rate of epithelization and wound contraction, inefficient inflammatory response (resulting in chronic inflammation and hence impaired formation of healthy granulation tissue), imbalance in collagen homeostasis, profibrotic environment, tissue hypoxia and inappropriate cell apoptosis are discussed as contributing factors (Provost, 2019).

Interestingly ponies heal better and faster than horses, with ponies yielding a quicker and more intense inflammatory response and an improved resistance to infection as compared to horses (Provost, 2019). Some of the most important advantages and disadvantages of using horses as model animals are summarized in **Table 2**.

Another challenge of using horses as animal models, particularly for orthopedic disease, is so called supporting limb laminitis (SLL). Laminitis is a disorder of the tissue suspensory apparatus which suspends the distal phalanx to the inside of the

TABLE 2 | Advantages and disadvantages of the horse as a model.

Advantages	Disadvantages
Largest of the models: Multiple large (critical size) defects and serial sampling possible	Ethical concerns – companion animals
Functional correspondence of equine SDFT and human Achilles tendon	Different breeds, not usually purpose-bred for research
Thickness of the knee cartilage is similar to the human	Costs- Special facilities needed for housing, surgery, imaging, necropsy, etc.
Imaging plus validated scoring approaches	Non-weight-bearing postoperatively is not feasible
Arthroscopy (also second look) plus validated scoring approaches	Restrictive annotation status and availability of equine specific antibodies, molecular tools and markers
Controlled postoperative exercise programs and rehabilitation using treadmills and horse walkers to support standardization are well established	Weight – biomechanical strains, which far exceed those considered physiologic in humans
Well characterized temporal pattern of healing	
Equine aging well documented	
Clinical need – naturally occurring disease	

[5]https://goldcopd.org/wp-content/uploads/2016/04/GOLD-2018-WMS.pdf

horse's hoof wall. SLL of the contralateral or supporting limb occurs when horses are forced to bear weight predominantly unilaterally (with the supporting limb) for prolonged periods, due to a severe, unilateral lameness. Mechanical loading or overloading of the supporting limb is the primary factor in its pathogenesis (Baxter and Morrison, 2008; Orsini, 2012).

SHEEP AS ANIMAL MODELS

General Considerations

Domestic sheep (*Ovis aries*) provide unique opportunities in research as an experimental and pre-clinical animal model (Hems and Glasby, 1992; Glasby et al., 1993; Al Abri et al., 2014) because of their availability, low costs and acceptance by the society as a research animal (Diogo et al., 2017). Sheep are docile, easy to handle and relatively inexpensive with respect to housing and feeding. Their size (50−90 kgs) is more similar to humans than small animal models, lending themselves to repeated sampling from different anatomical structures over an extended period. Their size is ideal for clinical imaging modalities designed for humans such as MRI or CT (which are limited with other large animal models like the horse). At the same time, it allows for testing surgical procedures and medical devices in animals similar to human-size (e.g., bioengineered constructs, pacemakers, stents). On the other hand, sheep housing requires more space (barns for pens) which are not widely available. The commercial availability of molecular tools (e.g., antibodies) is also more limited than for rodents although these are increasing. Nonetheless, the practical disadvantages of the sheep as an experimental model do not make it inaccessible. Based on the aim of the study, the potential benefits may compensate its technical limitations. The publication and annotation of the sheep genome (Jiang et al., 2014) should improve the amount of commercially available reagents, thus facilitating the use of the ovine model in future studies. Concomitantly, the annotation of the sheep genome could support the development of useful biological tools for sheep as genetic models of human diseases (e.g., Huntington's Disease) (Pinnapureddy et al., 2015). Moreover, anesthesia and surgical equipment in sheep is more similar to humans than other large animals (like horses) and small rodents: Hence, using sheep does not require significant investment in large and specialized handling equipment, or surgical tables. At the same time, sheep can be sourced relatively easily and at low cost and they are considered as a socially acceptable animal model for research that raises fewer ethical issues than companion animals (Entrican et al., 2015; Rogers, 2016).

Sheep are used as models for a wide range of pathologies: cardiovascular diseases (Divincenti et al., 2014; Rabbani et al., 2017), orthopedics (Kon et al., 2000; Vandeweerd et al., 2013; Dias et al., 2018; Mcgovern et al., 2018; Music et al., 2018), respiratory function (Meeusen et al., 2009) and reproductive or pregnancy disorders (Andersen et al., 2018; Morrison et al., 2018). A major reason is that ruminants, as compared to rodents, share more anatomical and physiological characteristics (with exception of the digestive tract − testing efficacy of drugs may be complicated by the 4-stomach system and uptake dynamics which defer from human gastrointestinal tract characteristics) with humans (Scheerlinck et al., 2008). This makes the sheep a useful model for preclinical and translational studies in fields of Tissue Engineering and Regenerative Medicine.

Musculoskeletal Disorders

Sheep have anatomical and biomechanical features relatively similar to humans (bone composition, weight, joint structure and architecture) which allows for good simulation of healing and remodeling processes of bone or cartilage tissue (Newman et al., 1995; Taylor et al., 2006). In addition, arthroscopic evaluation is possible in the sheep due to the size of their stifle joints. Therefore, the ovine species is the most commonly used large animal model in orthopedic research including studies on: cartilage repair (Music et al., 2018), meniscal repair (Hurtig et al., 1998; Tytherleigh-Strong et al., 2005), osteochondral tissue engineering (Sanjurjo-Rodriguez et al., 2017), tendon defects (Crovace et al., 2008; Martinello et al., 2013), osteoarthritis (Oakley et al., 2004; Gugjoo et al., 2019), and osteoporosis (Dias et al., 2018) among the others.

Sheep have been involved in studies for treating critical-sized bone defects using scaffolds with or without Mesenchymal Stem cells (MSCs). These treatments were shown to enhance bone formation and improve mechanical properties if compared to gold standard reparative methodologies like bone grafts (Kon et al., 2000; Cipitria et al., 2013; Fernandes et al., 2014; Berner et al., 2015; Mcgovern et al., 2018; Pobloth et al., 2018).

Although the ovine knee cartilage differs in thickness to human cartilage (0.7−1.7 mm and 2.35 mm, respectively), it provides a close match regarding mechanical properties for preclinical studies (Frisbie et al., 2006; Chu et al., 2010; Mclure et al., 2012). Tissue engineering approaches including different cell sources (as MSCs or chondrocytes) have been widely tested in the sheep for chondral/osteochondral defects (Lo Monaco et al., 2018; Gugjoo et al., 2019). Cells can also be applied with scaffolds of different nature to improve and support regeneration (Chitosan, type I/III collagen, b-TCP, collagen hydrogels) (Bernstein et al., 2013; Sanz-Ramos et al., 2014; Dias et al., 2018). For example, Hopper et al. (2015) used a biphasic collagen-GAG scaffold loaded with MSCs in a full-thickness osteochondral defect boosting cartilage repair while Zorzi et al. (2015) used a 1:1 chitosan-collagen scaffold seeded with human MSCs for articular cartilage regeneration (Hopper et al., 2015; Zorzi et al., 2015). Recently, a bilayered scaffold to simulate the bone-cartilage interface (chondral and bone tissue components) has been developed and tested in sheep (Schagemann et al., 2009; Fan et al., 2013).

Furthermore, regenerative strategies for osteoarthritis (usually induced by meniscectomy) have been investigated in sheep (Song et al., 2014; Desando et al., 2016; Feng et al., 2018). Of particular interest are the studies on scaffolds for meniscal repair because of its shared characteristics with the human meniscus (cellularity, vascularity, biomechanics) (Chevrier et al., 2009; Brzezinski et al., 2017). Gruchenberg et al. (2015) tested a silk fibroin scaffold as a meniscal implant after meniscectomy in sheep showing its biocompatibility (Gruchenberg et al., 2015).

Spontaneous cartilage lesions (including osteoarthritis) have been observed in the sheep without experimental induction (Hurtig et al., 2011; Vandeweerd et al., 2013; Kuyinu et al., 2016). These are especially prevalent in aging sheep and might better recapitulate the human ailment than artificially created cartilage defects.

Sheep, like horses, are ideal candidates for tendinopathy modeling, but cheaper and easier to handle and house. Martinello et al. (2013) showed the treatment efficacy of MSCs, with or without PRP (platelet rich plasma), on collagenase-induced tendinitis in the superficial digital flexor tendon, with a better structural organization of the repaired tendon (Martinello et al., 2013). Deprés-Tremblay et al. (2018) tested the use of chitosan-PRP implants in an ovine acute defect model to mimic rotator cuff injuries. The implants led to an extensive bone remodeling and tissue ingrowth at the tendon-bone interface level (Deprés-Tremblay et al., 2018).

Nervous System

The ovine species also serves as an adequate and effective model to study peripheral nerve regeneration, because of the similar nerve size (Starritt et al., 2011) and similar regenerative behavior (Hems et al., 1994; Fullarton et al., 2001) compared to humans (Diogo et al., 2017).

Apart from conventional autografts and allografts for repairing peripheral nerve injuries in sheep (Frey et al., 1990; Matsuyama et al., 2000), tissue engineering techniques have also been applied. Casanas et al. (2014) applied a commercially available biodegradable scaffold with MSCs or PRP to reconstruct damaged radial and tibial nerves. The addition of MSCs, with or without PRP, led to the production of myelinated nerve fibers at the distal and proximal level with fiber regeneration and functional recovery after 6 months (Casanas et al., 2014). Radtke et al. (2011) compared the use of autologous nerve and acellularized vein grafts produced from spider silk. The outcomes obtained with the construct where similar to the nerve autograft results: axonal regeneration and myelination were achieved at 10 months (Radtke et al., 2011).

Using sheep models, MSCs were shown to play a reparative role in intervertebral disc regeneration. Injection of MSCs led to a reduction of degeneration of the discs compared to the control group (Freeman et al., 2016; Daly et al., 2018).

Heart Disease

Sheep have been frequently used as model for cardiovascular applications, especially for testing heart valves which have similar valve anatomy to the human and the sheep size permits access to the pulmonary and aortic valve. Kluin et al. (2017) developed an *in-situ* heart valve replacement for the pulmonary valve using a resorbable synthetic graft. 12 months post-implantation the tissue-engineered valve was shown to be colonized by host cells and replaced by newly formed tissue with a mature organization of the extracellular matrix without any sign of valve calcification (Kluin et al., 2017).

Cell therapies with MSCs have further been applied in acute myocardial infarction models to improve myocardial function. The inoculation of cells has been demonstrated to be safe, to increase vasculature, and to reduce fibrosis in the infarcted heart (Houtgraaf et al., 2013). Rabbani et al. (2017) showed that the injection of MSCs and endothelial cells (ECs) promoted angiogenesis and cardiac function, supposing that one of the mechanisms of action of the MSCs might lie in their differentiation potential toward the endothelial lineage (Rabbani et al., 2017).

Also, different tissue engineering approaches for the development of preclinical vascular grafts have been tested in the sheep model (Cummings et al., 2012; Aper et al., 2016; Fukunishi et al., 2016; Koobatian et al., 2016).

Tissue Engineering Applications in Other Systems

The ovine model has further been deployed to test regenerative approaches for treating respiratory disorders (similar airways structure and lung size to humans):

MSCs led to a reduction of inflammation and oedema and an improved oxygenation in sheep models of acute respiratory distress (Asmussen et al., 2014; Kocyildirim et al., 2017). In an induced emphysema model, the infusion of MSCs resulted in blood reperfusion of the damaged tissue and the formation of new extracellular matrix (Ingenito et al., 2012).

Recently, Kajbafzadeh et al. (2019) have tested the transplantation viability of decellularized kidneys in sheep.

The sheep model has also been described for wound healing studies because it allows for the creation of relatively large and deep wounds to mimic the typical scenario of traumatic injuries like burn injuries or decubitus ulcers. Martinello et al. (2018) used a sheep second intention wound healing model and showed how the intradermal and topical application of allogeneic MSCs led to a better re-epithelialization and dermal structure as compared to the control group at 42 days after wounding (Martinello et al., 2018). The identical model was recently used by Iacopetti et al. (2020) to compare secondary intention healing of wounds, treated with a topical application of commercially available hyaluronic acid, Manuka honey or Acemannan gel (Iacopetti et al., 2020).

In a similar ovine wound model, Liebsch et al. (2018) applied native spider silk as a wound dressing to test its biocompatibility and regenerative capacities (Liebsch et al., 2018). Mazzone et al. (2020) used bioengineered autologous skin substitutes to treat myelomeningocele in a spina bifida repair model. The skin substitute, made of hydrogel colonized by autologous fibroblasts and keratinocytes, was transplanted in utero. The skin substitutes showed a normal histology after 1 month (Mazzone et al., 2020).

Recently, Martines et al. (2020) evaluated the use of a low-temperature atmospheric pressure plasma (ionized gas) as a treatment for extensive wounds in a sheep model. The plasma stimulated cell proliferation, angiogenesis and the development of skin adnexa; concomitantly, it reduced bacterial infection and inflammation (Martines et al., 2020).

A different tissue engineering approach to treat myelomeningocele was used by Watanabe et al. to treat spina bifida wounds with a gelatin/collagen sponge hybrid scaffold (Watanabe et al., 2016).

Embryonic/Fetal Healing

True "scarless healing" is observed only in embryos and early fetus (Stramer et al., 2007). The restitutio ad integrum in embryos (Beredjiklian et al., 2003) is considered an ideal situation unmatched by any treatment regimen in adults. Therefore, an increasing amount of research studies is performed in embryos or fetal animals. To study the mechanism of fetal regeneration, relevant *in vivo* as well as *in vitro* models are required. Fetal sheep share many important physiological and developmental characteristics with humans and have hence proven themselves invaluable models for mammalian physiology (Almeida-Porada et al., 2004; Jeanblanc et al., 2014). Sheep frequently carry twins, which allows using one twin as uninjured control on a background of low genetic variation to enable differentiation between regular fetal development and fetal response injury.

Furthermore, their long gestational period (150 days) provides sufficient temporal resolution to translate findings obtained in sheep into human parameters (Almeida-Porada et al., 2004; Jeanblanc et al., 2014).

Fetal sheep have a fully functioning immune system by 75 days of gestation (gd) (Emmert et al., 2013). They produce leukocytes by 32 gd (Sawyer et al., 1978), TNF and Il-1 as early as 30−40 gd (Dziegielewska et al., 2000) and obtain the capability to form significant amounts of specific antibodies in response to antigenic stimulation as early as 70 gd (Silverstein et al., 1963). Fetal lambs reject orthotopic skin grafts and stem cell xenotransplants placed post 75−77 gd (Silverstein et al., 1964) and mount an inflammatory response to injury by gestational day 65 (Nitsos et al., 2006; Moss et al., 2008; Herdrich et al., 2010; Morris et al., 2014).

For all these reasons, results obtained in the fetal lamb have been directly applicable to the understanding of human fetal growth and development and are highly predictive of clinical outcome in a variety of applications including in utero stem cell transplantation (Liechty et al., 2000; Almeida-Porada et al., 2004, 2007; Porada et al., 2005; Kuypers et al., 2012; Kim et al., 2013; Jeanblanc et al., 2014).

Additional Considerations Regarding Sheep

Due to their special stomach system (4 stomachs: rumen, reticulum, omasum, and abomasum) bio-availability and efficacy of drugs administered orally is questionable for the human GI tract. Moreover, prolonged inappetence and application of non-steroidal anti-inflammatory drugs, antibiotics or both resulting in sustained high acidity in the abomasum may cause abomasal ulceration. Also stress, high dietary fiber and inadequate dietary fiber are believed to play a role (Ducharme, 2004; Fubini and Ducharme(eds), 2004).

Therefore, pain management and anti-microbial management have to be planned carefully and adapted to meet the special requirements of sheep (Lizarraga and Chambers, 2012; Varcoe et al., 2019). Sheep guidelines for pain assessment by facial expression are available (Hager et al., 2017) which may help managing pain.

Some of the most important advantages and disadvantages of using sheep as model animals are summarized in **Table 3**.

PIGS AS ANIMAL MODELS

General Considerations

Porcine models present the advantage of having similarities with the human in terms of gastrointestinal anatomy, metabolism and physiology (Court et al., 2004). When compared with other farm animals, pigs acquire early sexual maturity, sizeable litter size and have a quick reproduction time. They also breed year-round, which makes them highly suitable for biomedical research programs (Polejaeva et al., 2016). Due to these characteristics and the anatomical and physiological similarities, and also their size (young pigs have a size and body weight similar to human adults), pigs are widely used as models in organ transplantation and other surgical procedures (Kahn et al., 1988; Chari et al., 1994; Martin et al., 1999; He et al., 2013; Spetzler et al., 2015; Vogel et al., 2017), or as preclinical models in drug discovery (Swindle et al., 2012; Segatto et al., 2017), and numerous naturally occurring and generated genetic models of human disease (Swindle et al., 2012; Polejaeva et al., 2016). Hence, and similarly to the areas of medicine described above, the pig is gaining traction as the large animal model of choice for the study of tissue engineering and regenerative medicine products and applications, and of biomechanic studies. A good evidence of this is the steep rise in the number of publications in these broad areas in the past 30 years (Cone et al., 2017).

Drug Discovery and Toxicology

Traditionally, animal models used for preclinical testing of new drugs and toxicology studies have been rodents, mainly mice and rats, for the primary screening studies. Nonetheless, because translation from rodents into humans is often not fully

TABLE 3 | Advantages and disadvantages of the sheep as a model.

Advantages	Disadvantages
Multiple large (critical size) defects and serial sampling possible	Different breeds, not usually purpose-bred for research
Thickness of the knee cartilage is similar to the human	Special facilities needed for housing, surgery, imaging, necropsy, technical skills
Docile to handle	Non-weight-bearing postoperatively is not feasible but can modulate with location
Availability, and acceptance by the society as a research animal	Different stomach system than humans
Size is more similar to humans than small animal models or horses	Ethical concerns but minor compared to companion animals
Publication and annotation of the sheep genome	Costs
Imaging plus validated scoring approaches available (esp. for orthopedics)	
Arthroscopy (also second look) plus validated scoring approaches	

realized, regulatory agencies also demand the use of non-rodent models. Pigs are increasingly being used as an alternative to dogs or primates, the previous nonrodent species of choice (Swindle et al., 2012). However, due to growing pressure from the public, there has been a drive for new alternatives. The pig has been favored as a suitable alternative, since they have many anatomical and physiological features valuable for translational research and are already well accepted as one of the gold standard surgical models (Swindle et al., 2012). In particular, the cardiovascular system, skin and digestive tract closely mimic the human. Due to these similarities the metabolism and toxic effects of chemicals and drugs in pigs may more closely resemble the effects in man than some other laboratory animals. The minipig has been introduced recently as another alternative (Dalgaard, 2015) which is frequently used due to its smaller size and easier handling for drug discovery and toxicology applications (Mcanulty et al., 2011), boosted by the publication of the RETHINK project (Forster et al., 2010). Furthermore, the porcine CYP450 system has been studied and partially described, and their metabolic pathways have been found to be relatively analogous to humans, with substantial overlap in substrate specificity (Skaanild, 2006; Murayama et al., 2009).

Generated Genetic Models

With the advent of DNA recombination and gene editing technologies, modifying the pigs genome has enabled its use as a genetic model of numerous human diseases (Flisikowska et al., 2014; Yao et al., 2016). This is reflected in the multiple pig strains developed to study, amongst others, cancers, Duchenne muscular dystrophy, autosomal polycystic kidney disease, Huntington's disease, spinal muscular atrophy, cystic fibrosis, hemophilia A, X-linked severe combined immunodeficiency, retinitis pigmentosa, Stargardt's Disease, Alzheimer's disease, various forms of diabetes mellitus and cardiovascular diseases (Flisikowska et al., 2014; Rogers, 2016; Yao et al., 2016; Perleberg et al., 2018). From these, the RAG2 or RAG2/IL2RG KO pigs are particularly relevant for biomedical research, since they can accept xenografts and/or human bioengineered tissue/organs (Boettcher et al., 2018).

Transplantation Models

The pig has been used as a teaching and research animal model in surgery in the past decades. Starting in the 1990s, it became so prominent in academic and surgical training that it can be regarded as default model for non-survival surgical teaching classes, substituting the dog (Swindle, 2007). Its ubiquitous presence and use in academia, enabled also its widespread adoption in multiple models of liver, lung, heart, pancreas and kidney transplantation (Marubayashi et al., 1995; Martin et al., 1999; He et al., 2013; Fonouni et al., 2015; Mariscal et al., 2018). Furthermore, in transplantation medicine, the pig has also been proposed as xenograft donor, where porcine grafts have been transplanted into non-human primates with different degrees of success (Sachs et al., 2009; Griesemer et al., 2014). This has encouraged several research groups to target the porcine genome to eliminate the major xeno-antigen(s) recognized by human natural antibodies, in a so-called effort of humanizing the pig (Lai et al., 2002; Phelps et al., 2003; Petersen et al., 2011; Jeong et al., 2013). If ultimately realized, these procedures might enable the future xenotransplantation of porcine organs into humans as the main approach for transplantation medicine. Efforts are currently being taken to reduce the risk of viral zoonosis from porcine endogenous retrovirus (PERV), either by pharmacological treatment of PERV or by inactivating it with gene editing tools (Denner, 2017; Niu et al., 2017). Finally, other efforts have been concentrated on porcine uterus, urethra, kidney or liver bioengineering for transplantation (Baptista et al., 2011; Sullivan et al., 2012; Campo et al., 2017; Simoes et al., 2017). All these are an important testimony of the relevance of the pig as a vital translation research animal model.

Skin

The minipig has been used as a model in the development of dermatological products (Mitra et al., 2015; Yamamoto et al., 2017), and more recently, as a model for microbiome studies (Ericsson, 2019). As omnivores with an analogous gastrointestinal tract to humans, the well-characterized fecal microbiota of young and adult domestic pigs and other strains used in research also offers compositional resemblances to that of humans (Pedersen et al., 2013b; Zhao et al., 2015). Remarkably, many of these strains are used to investigate diet-induced obesity in genetically susceptible individuals and the same modifications (e.g., an increase in the ratio of Firmicutes to Bacteroidetes) observed between lean and obese humans are emulated in these pig models during the development of obesity (Pedersen et al., 2013a).

Musculoskeletal Disorders

In this particular area of biomedicine, the pig is experiencing a higher increase in adoption when compared to other large animal models (Cone et al., 2017) and several studies have been published assessing interspecies and interstrain differences in the anatomy and biomechanics of tissues and joints and their applicability in tissue engineering and regenerative medicine studies. Porcine models have a long history of use for studying the biomechanics of specific joints like the knee or the temporomandibular joint (TMJ), and specific tissues, including bone, cartilage, and ligaments (Xerogeanes et al., 1998; Sweigart et al., 2004; Proffen et al., 2012; Murphy et al., 2013; O'leary et al., 2017). Hence, the pig has been used with success to test the efficacy of bone substitute biomaterials (Li et al., 2015) and in osteochondral defect studies (Gotterbarm et al., 2008; Meng et al., 2020). Similarly, extensive research has been conducted with the pig in tendon and ligament repair as reviewed by others (Carpenter and Hankenson, 2004).

Pigs have also been used recently as a model of amyotrophic lateral sclerosis (ALS). This research has been based on the use of transgenic pigs with a mutated human copper/zinc superoxide dismutase 1 gene that mimics the human neurodegenerative disease in these pigs (Chieppa et al., 2014; Yang et al., 2014). Similarly, a pig model of Duchenne muscular dystrophy (DMD) has been created by Klymiuk et al. by deleting DMD exon 52 in male pig cells by gene targeting. The offspring generated by nuclear transfer exhibit absence of dystrophin

in skeletal muscles, progressive dystrophic changes of skeletal muscles with impaired mobility, muscle weakness and a maximum life span of 3 months due to respiratory impairment (Klymiuk et al., 2013).

Additional Considerations Regarding Pigs

Pigs suffer from porcine malignant hyperthermia also known as porcine stress syndrome which is characterized by hyperthermia triggered by stress, certain anesthetic agents or intense exercise and may lead to sudden death (Nelson, 1990). Some of the most important advantages and disadvantages of using pigs as model animals are summarized in **Table 4**.

COMPANION ANIMALS AS ANIMAL MODELS

General Considerations

The importance of companion animals to serve as models for human disease has received significant attention through the One Health initiative which aims to "break through the species barrier" in a drive toward a better link between medical and veterinary research for the benefit of both the human and veterinary patient (Christopher, 2015).

While the definition of companion animals covers a range of animals this article extends only to the dog and cat as models, as they share remarkable similarities with the human and provide unique opportunities for developing advanced therapeutics.

One of the main reasons why dogs returned as a focus of genetic research is related to the specific population structure that has been created over the past 150−200 years.

To fully appreciate and exploit the biomedical potential of dogs (both as pets and as experimental animals), some insight into the unique canine population structure is necessary. Domesticated dogs were subjected to rigorous breeding selection, for instance for behavioral traits and/or specific morphological features such as excessive muscle formation, short limbs or a specific coat color (Larson et al., 2012). Illustrative for this process is the extreme size variation, by far the largest of all mammals known, ranging from less than 1 kg for Chihuahua dogs to over 70 kg for Irish wolfhounds and Neapolitan Mastiffs. This selection process was intensified in the last two centuries and resulted in isolated genetic populations of dog breeds (Parker et al., 2010). Whereas the genetic variation over the various breeds remained intact, the reduced genetic variability within breeds worked as a genetic amplifier and offers "genetic dissection microscope" for research (Lindblad-Toh et al., 2005; Parker et al., 2010; Larson et al., 2012; Van Steenbeek et al., 2016). Together with the selection for unique traits, an increased risk for the development of specific inheritable disorders arose within breeds, providing physiologically relevant models corresponding to human conditions. To make the best out of the current situation may be to exploit the downside of inbreeding as a gene-discovery instrument for causative and modifier genes involved in complex diseases and/or rare diseases.

TABLE 4 | Advantages and disadvantages of the pig as a model.

Advantages	Disadvantages
Size of the pigs: Multiple and longitudinal measurements possible	Ethical concerns but minor compared to companion animals
Functional equivalence of various diseases in men and pigs	Special facilities needed for housing, surgery, imaging, necropsy
Genetic variation between breeds (cfr human population), moderate genetic variation within breeds (naturally occurring diseases)	Non-weight-bearing postoperatively is not feasible but can modulate with location
Imaging plus validated scoring approaches available (esp. for orthopedics)	Costs
Arthroscopy (also second look) plus validated scoring approaches	

Canine Inherited Copper Toxicosis

The trace element copper is indispensable for critical biochemical processes such as enzyme function, for instance cytochrome c oxidase (part of the respiratory enzyme complex) or superoxide dismutase (conversion of superoxide radicals into molecular oxygen or hydrogen peroxide) (Inesi, 2017). Since copper is a transition element (reduced as Cu+ and oxidized as Cu^2+) its Jekyll and Hyde character becomes evident in the involvement in chemical reactions leading to the production of reactive oxygen species. In a Fenton reaction, Cu^+ catalyzes the formation of the highly reactive hydroxyl radical ($OH^{\cdot}$). In the converse Haber-Weiss reaction Cu^{2+} inactivates the damaging superoxide radical O_2. Therefore, regulation of its intracellular free concentrations is of utmost importance and needs to be controlled within very narrow limits (Kim et al., 2008). Several inherited copper-related diseases are diagnosed in men such as Menke's Disease (copper deficiency disorder), Wilson Disease (WD, copper accumulation), and the very rare Indian childhood cirrhosis (Tanner, 1998), endemic Tyrolean infantile cirrhosis (Muller et al., 1996), and idiopathic copper toxicosis (Scheinberg and Sternlieb, 1996). These all are rare diseases posing specific obstacles for researchers aiming to dissect molecular pathways and for rational drug design. These obstacles include limited financial resources compared to diseases affecting large numbers of patients, smaller patient cohorts for clinical phase 1−3 studies, difficulties for properly matched case-control studies in genetics and molecular signaling studies.

Copper disorders also affect sheep and dogs (Twedt et al., 1979; Haywood et al., 2001; Fuentealba and Aburto, 2003). Deleteriously increased levels of hepatic copper are described in a number of dog breeds including Bedlington terriers, Skye terriers, West-Highland White terriers, Doberman, Dalmatians and Labrador retrievers (Twedt et al., 1979; Haywood et al., 1988; Thornburg et al., 1996; Thornburg, 1998; Webb et al., 2002; Hoffmann et al., 2006). In 1999 genetic mapping studies revealed that the copper toxicosis locus within Bedlington terriers was located on canine chromosome 10. 3 years after positional cloning a 13kB deletion covering exon-2 of

the murr1 gene was identified as the causative mutation for Bedlington terrier copper toxicosis (Van De Sluis et al., 1999, 2002). The causative role of murr1 mutations in WD is a matter of debate. Stuehler et al. found an association between murr1 mutations and WD, whereas two other papers did not detect a correlation between murr1 mutations and WD (Stuehler et al., 2004; Lovicu et al., 2006; Wu et al., 2006). This novel gene product, currently called COMMD1 (COpper Metabolism Murr1 Domain-containing protein 1) had no known function at the time it was discovered, and the mechanism of action related to hepatic copper accumulation remained enigmatic. The discovery that COMMD1 and ATP7B interact intracellularly revealed a mechanistic link between COMMD1 protein and copper toxicosis, later confirmed for the Menkes Disease protein ATP7A (De Bie et al., 2007; Vonk et al., 2012).

The discovery of the COMMD1 mutation and subsequent investigations into functions of COMMD1 is an intriguing example for a useful exploitation of inbred dog strains to reveal novel molecular and genetic pathways. Genetically speaking the big advantage of canine genetics to benefit human genetics is the ease to discover modifier genes. This is a needle-in-a-haystack technology in men even today, but the specific genetic population structure in inbred dogs clearly facilitates this approach.

Labrador retrievers are among the most popular breeds in the Western world.

It was already known for a long time that approximately one in every three first-line relatives of Labradors retrievers with copper toxicosis had elevated copper levels (Hoffmann et al., 2006). This pushed investigations into whether or not Labrador retrievers were new model animals for WD and as a consequence propelled genetic studies (Fieten et al., 2014). A SNP based genome-wide association study aiming to discover the genetic background of inherited copper toxicosis in Labrador retrievers included over 200 Labrador retrievers (154F, 81 M cases; 37F and 22 M as replication cohort) in the Netherlands that were genotyped on the 170k SNP Illumina Canine HD Bead Chip (Fieten et al., 2016). For details on the mechanism of action of these mutations the readers are referred elsewhere (Fieten et al., 2016). Approximately 12% of the phenotype can be explained by two mutations identified in Labrador retrievers. Since mutations in these genes were already described in copper-related disorders, it remains to be seen what other as-yet-unidentified genetic mutations will be discovered.

This genetic study clearly illustrates the power of the canine model. Explaining 12% of the phenotypic variation with an ample 250 dogs doesn't even remotely resemble the number of human patients used to explain similar percentage for age at menarche, Inflammatory Bowel Disease (IBD) and Rheumatoid arthritis (RA) for which over 100,000 individuals were included (Elks et al., 2010; Okada et al., 2014; Liu et al., 2015).

The examples prove that due to the specific population structure of inbred dog breeds, genetic studies can be successfully performed even for rare and/or complex genetic diseases.

In order to investigate COMMD1-deficient dogs as a preclinical model for liver stem cell transplantations, a breeding colony of five COMMD1 deficient dogs was created on a Beagle background and followed for over 4 years (Favier et al., 2011, 2012; Favier et al., 2015). This model for inherited copper toxicosis has some practical features specifically relevant for preclinical studies that aim to investigate surgical procedures. In contrast to mouse models, that are sacrificed for every liver measurement, the dogs' size allowed for a true longitudinal study permitting liver biopsy sampling twice a year.

Heart Disease

The most prevalent non ischaemic cardiomyopathies in humans are hypertrophic cardiomyopathy (HCM) and dilated cardiomyopathy (DCM), reported to affect 1 in 500 and 35 in 100,000 people, respectively (2017, Heron, 2016). Arrhythmogenic ventricular cardiomyoapthy (AVC) is also recognized as an important and distinct form of cardiomyopathy. Together they are associated with mechanical and/or electrical dysfunction and manifestations of the disease can range from microscopic alterations in cardiomyocytes and cardic fibroblasts to heart failure (which results in inadequate tissue perfusion and fluid retention) and arrhythmia which may cause sudden death. In veterinary species HCM is the most common feline cardiac disease affecting around 1 in 15 cats and DCM is the second most common cardiac disease in dogs and can affect a wide variety of breeds including the Doberman where its cumulative prevalance is as high as 44%. AVC has been comprehensively described in the Boxer breed at the molecular, cellular and clinical levels. All three cardiomyopathies share striking pathological and clinical similarities with the human disease. While there has been progress in the management of the symptoms associated with these cardiomyopathies in human patients, the actual disease processes remain a challenge to treat as there are few therapies that target the underlying pathology. There has therefore been an emphasis on the use of regenerative cellular therapies, although most studies have focused on ischaemic myocardial disease using mesenchymal stem cells (MSCs) derived mostly from bone marrow or adipose tissue. Stem cells derived from myocardial tissue have more recently been developed and have been tested in a number of induced disease models. A comparison of MSCs and cardiosphere derived cells (CDCs) suggests that CDCs are more efficacious in their ability to regenerate the myocardium (Li et al., 2012) and phase 1 clinical trials using autologous CDCs show encouraging results (Bolli et al., 2011; Makkar et al., 2012; Malliaras et al., 2014).

The development of cell-based approaches in the feline and canine clinic will have significant benefits for translation in human cardiomyopathy treatment.

Human and Feline Hypertrophic Cardiomyopathy

Hypertrophic cardiomyopathy is the most common cardiomyopathy in both humans and cats with a prevalence of approximately 0.1−0.2% and 16%, respectively (Maron et al., 1995; Payne et al., 2010; Semsarian et al., 2015; Husser et al., 2018). There is increasing literature that supports the cat as an animal model of human HCM and evidence suggests it is

essentially the same disease in both species (Maron and Fox, 2015). HCM is characterized by left ventricular hypertrophy in the absence of systemic causes and can result in heart failure and/or sudden death. In humans genetic mutations are identified in 60% of HCM cases, mainly in genes encoding sarcomeric proteins (Cahill et al., 2013). HCM in the cat is also considered to have a familial cause although only two causative mutations have so far been identified (Maron and Fox, 2015), in contrast several hundred have been identified in human patients. Both of the feline mutations occur in the cardiac myosin binding protein C (MYBPC3) gene, one of which occurs in the Maine Coon breed (A31P mutation) and the other in the Ragdoll breed (R820W mutation) (Meurs et al., 2005, 2007). It is of interest to note that one specific non-truncating mutation, MYBPC3/R820W, that occurs in Ragdolls has been identified in a human family with HCM (Ripoll Vera et al., 2010; Borgeat et al., 2014). The role sarcomeric mutations play in the development of HCM in non-pedigree cats requires further investigation.

The underlying molecular pathogenesis driving HCM remains to be elucidated although a common pathway is thought to exist in both humans and cats in which altered calcium handling within the myofilaments enhances calcium sensitivity, causing maximal force production and energy deficiency promoting mitochondrial dysfunction, cell death, fibrosis and cardiomyocyte hypertrophy (Huke and Knollmann, 2010; Marston, 2011; Song et al., 2013; Robinson et al., 2018).

Studies using myocardial tissue from a cat homozygous for the MYBPC3/R820W mutation suggest that increased myofilament calcium sensitivity can occur in the absence of haploinsufficiency, which is common feature in human MYBPC3 mutations (Messer et al., 2017). Increased myofilament calcium sensitivity was also seen in other HCM affected cats of unknown genotype but not in unaffected cats. An additional feature of the study was that the calcium sensitivity of the sarcomere is uncoupled from the phosphorylation status of troponin I, although it remains unclear how mutations outside the troponin complex cause this uncoupling phenomenon. The reasons clearly are complex but the similarities at the molecular level show the cat to be a highly relevant natural disease model for human HCM for deciphering the mechanisms. Targeting the disease with Epigallocatechin-3-gallate, for example can reverse troponin I phosphorylation uncoupling in cat HCM (Messer et al., 2017) which has been replicated in human HCM samples (Sheehan et al., 2018).

Such studies highlight the need to identify detailed molecular mechanisms for precise drug targeting. However, there are practical limitations with obtaining sufficient heart tissue and the survival of isolated primary cardiomyocytes is poor. Induced pluripotent stem cells (iPSC) or embryonic stem cells (ESCs) represent an alternative and robust source for preparing cardiomyocytes. The development and use of human ESCs represents an ethical dilemma and while less of an issue in veterinary species, there are only two reports of ES-like cells from cats, but these do not replicate indefinitely in culture unlike true ES cells. iPSCs on the other hand do not have the concerns associated with ESCs and can be relatively readily prepared from somatic cells.

Feline iPSCs have recently been reported for the first time by our group, the development of which represents a significant step in the generation of iPSC derived cardiomyocytes from a veterinary species (Dutton et al., 2019). It paves the way for generating further cell lines from feline patients carrying the HCM causing MYBPC3/R820W mutation to test novel therapeutics for modifying the disease. iPSCs can further be manipulated with technologies such as Clustered Regularly Interspaced Short Palindromic Repeats (CRISPR) to enable targeted genetic manipulation of both normal and diseased patient cell lines (Cai et al., 2018; Sasaki-Honda et al., 2018).

iPSCs derived from patients with HCM or iPSCs with a genetic mutation inserted using CRISPR to model HCM, display characteristics of hypertrophic cardiomyocytes in culture (Mosqueira et al., 2018) suggesting the suitability of the approach in establishing cell models of HCM. The availability of feline iPSC lines will enable dissecting out the molecular mechanisms of HCM enabling targeted drug screening where promising molecules can be rapidly assessed in the feline clinic with the potential of swift translation to human patients.

Human and Canine Dilated and Arrhythmogenic Ventricular Cardiomyopathy

DCM is the third most common inherited myocardial disease in humans with an estimated prevalance of 0.35% and some 2.5 million cases globally affected[6]. It is the second most common cardiac disease in dogs and accounts for 10% of canine cardiac diagnosis (Egenvall et al., 2006). As with feline HCM there are remarkable similarities in the pathophysiology of DCM between human and dog. Although it is a heterogenous disease it is characterized by progressive enlargement of the left ventricle that leads to reduced systolic function, congestive heart failure and a variety of arrhythmias. Underlying causes include systemic disorders such as hypertension and atherosclerosis in humans but is also now recognized as a primary genetic disorder that may manifest with or without accompanying predisposing factors. Giant dog breeds such as the Great Dane and Newfoundlands are at risk and a genetic basis has been proposed in some dog breeds including the Doberman Pinscher and Boxer in which the disease is both common and severe with a cumulative prevalence in European Dobermans >8 years of age of 44% (Mausberg et al., 2011; Simpson et al., 2015a,b). A genetic deletion in the Pyruvate Dehydrogenase Kinase 4 (PDK4) gene has been reported. PDK4 is critical in regulating mitochondrial energy metabolism as the genetic deletion predisposes affected individuals to developing DCM as it results in chronic energy attenuation (Meurs et al., 2012). More recently a missense variant in the titin gene has been reported in affected Doberman pinscher dogs negative for the PDK4 mutation. The Boxer breed has a distinct form of cardiomyopathy that closely

[6]https://www.bhf.org.uk/what-we-do/our-research/heart-statistics/heart-statistics-publications/cardiovascular-disease-statistics-2017

resembles AVC in humans (Vischer et al., 2017). A causative mutation in the striatin gene has been identified in Boxer dogs in the United States but this was not seen in the UK population (Meurs et al., 2010; Cattanach et al., 2015). The role of genetics in other dog breeds with DCM remain to be better described.

Histopathological observations of the myocardium show that canine cardiomyopathy displays either an attenuated wavy fiber type and fibro-fatty infiltration type (Tidholm and Jonsson, 2005) with the latter highly similar to AVC in humans. These findings emphasize the comparable pathological changes and clinical presentation between the two species (Basso et al., 2004; Meurs et al., 2014; Vila et al., 2017). The pathophysiologic mechanism underlying AVC is thought to involve mechanical and electrical decoupling and cardiomyocyte apoptosis (Wess et al., 2010) which with the fibro-fatty replacement of the myocardium are considered primary drivers for risk of arrhythmia and sudden cardiac death. Dogs that survive develop progressive ventricular dilation and systolic dysfunction leading to congestive heart failure (Wess et al., 2010; Meurs et al., 2014).

There have been efforts to use stem cells for the treatment of cardiac disease in humans spurred by observations that the adult heart processes regenerative ability (Condorelli et al., 2001; Nadal-Ginard et al., 2003). A number of clinical trials are under way or completed using adipose or bone marrow derived mesenchymal stem cells (MSC) although these are predominantly for ischaemic disease. One published study in Doberman pinchers with DCM administered allogeneic adipose derived MSCs that were virally transfected to overexpress stromal derived factor-1 to enhance homing and engrafting capabilities of endogenous MSCs to the myocardium (Pogue et al., 2013). Although no significant improvements in survival rates were found at 2-year follow up, the study demonstrated that the dog model of naturally occurring DCM can be utilized to overcome a number of challenges for regenerative therapies. There is increasing interest in CDCs as they appear to possess a superior ability to regenerate the myocardium (Li et al., 2012) compared to MSCs. CDCs are a heterogenous cardiac stem cell population which display features typical of stem cells such as forming clones, self-renewal and commitment to multiple lineages (Johnston et al., 2009; Chimenti et al., 2010; Cheng et al., 2014; Hensley et al., 2015). The use of CDCs clearly is not practical because of the need to sample from the patient and also because of expansion of cells from a diseased individual which adds to patient risk, time and treatment costs. Allogeneic cells offer an alternative off-the-shelf-product but risks include immunological complications that may lead to graft versus host disease. Work in a rodent model and other induced disease models suggests allogeneic CDCs are non-immunogenic (Malliaras et al., 2012). Allogeneic CDCs have been tested in a small clinical trial in dogs affected with DCM (Hensley et al., 2017) and no significant adverse effects were reported. Nevertheless, the process of cryofreezing of cell stocks may potentially alter intrinsic properties of the cells as has been shown for MSCs (Moezzi et al., 2005). Effects such as chromosome abnormalities resulting in abberrant cellular activity and risk of tumorigenesis may compromise their clinical use. However we have demonstrated that cryopreservation of dog CDCs does not alter their immunophenotype and cellular characteristics (Dutton et al., 2018a). Furthermore, we have shown at a molecular level that canine CDCs are also immune- privileged similar to the immunomodulatory function of MSCs (Dutton et al., 2018b) and cryopreservation retains this property suggesting they are safe to use *in vivo*.

Musculoskeletal Disorders in Companion Animals

Osteoarthritis

Dog models have long been used to study joint disorders particularly osteoarthritis. The canine model for osteoarthritis has been more commonly used than the horse, sheep or goat model (Mccoy, 2015). One of the reasons might be the easier post-operative management and follow up using various exercise regimes on e.g., treadmills (Mccoy, 2015). While there are some similarities in cartilage anatomy between humans and dogs, the standing angle in the hindlimb in dogs is much larger. This should be considered when biomechanical aspects are compared and evaluated (Mccoy, 2015). As stated previously the cartilage thickness in dogs is 0.6−1.3 mm and cartilage defects are considered to have a critical size at a minimum diameter of 4mm. Experimental OA is preferably induced in the stifle joint (Pond and Nuki, 1973; Marijnissen et al., 2002; Kuroki et al., 2011), whereas naturally occurring disease is also common in the elbow or hip joint with an estimation prevalence of OA affecting 20% of adult dogs (Mccoy, 2015).

With respect to osteoarthritis dogs are divided in two classes, non-chondordystrophic (NCD) and chondrodystrophic (CD) dogs. The last group presents with disproportionally short limbs, caused by aberrant endochondral ossification of long bones. Dachshunds are typical examples. The molecular mechanisms of this short limb phenotype is associated with a retrogene insertion of the FGF4 fibroblast growth factor 4 gene. This leads to elevated levels of FGF3 signaling. Interestingly, whereas CD dogs are more prone to intravertebral disc degeneration (IVDD), the insertion of the retrogene renders short-limb dogs less likely to develop OA in comparison with NC-dog (Tellegen et al., 2019). These examples emphasize the need to carefully select for a specific dog breed for musculoskeletal investigations.

Intervertebral Disc Degeneration

Despite walking on four legs in contrast to men walking on two only, both species develop intervertebral disc degeneration with great similarities and similar prevalence. Link-N is a protein involved in proteoglycan stabilization (beneficial) and is highly homologous between men and dogs. However, neither human link-N nor canine link-N can protect cultured canine intervertebral disc cells form degeneration, whereas human link-N improved glycosaminoglycn deposition

in human and bovine chondrocyte-like cell cultures (Bach et al., 2017).

In a classcial pre-clinical study a controlled release system for the COX-2 inhibitor celecoxib (cyclooxygenase-2) was tested in a dog model for IVDD (Tellegen et al., 2018). Since celecoxib prevented IVDD progression and reduced inflammation, follow-up studes will be conducted in a clincal study aiming to eliviate the chronic pain associated with low back pain.

Cranial Cruciate Disease and Meniscal Injury

Naturally occurring cranial cruciate disease has been studied extensively in veterinary medicine (Cook, 2010; Bergh et al., 2014). It can therefore be stated, that the pathophysiology differs between injuries in humans and canines, because dogs typically suffer from degenerative ruptures (Comerford et al., 2011) as compared to acute traumatic injuries seen in humans. To study new treatment approaches and validate their success, experimental models with artificially severed cruciate ligaments should be employed (Bozynski et al., 2016).

Dogs also suffer from naturally occurring meniscal pathologies and hence lend themselves as potential translational models to study mechanisms of degeneration or for testing new treatment strategies (Krupkova et al., 2018). The canine meniscus has comparable anatomic features (vascularization, cellularity, collagen structure) and similar permeability to the human (Sweigart et al., 2004; Deponti et al., 2015). However, some differences between canine and human menisci especially with regard to biomechanical properties such as the aggregate- and shear-modulus should be pointed out (Sweigart et al., 2004; Gupte et al., 2007).

Nervous System

Cats often serve as models to study spinal cord healing and comparative aspects in neurosurgery (Barbeau and Rossignol, 1987; Bélanger et al., 1996; Abelew et al., 2000; Bouyer and Rossignol, 2003). Biomechanical motion analyses using treadmills and force plates as well as electromyography (EMG) are performed to evaluate spine kinematics and muscular properties following experimentally induced spinal cord or cerebral lesions.

Additional Considerations Regarding Companion Animals

Dogs and cats are companion animals and pets and as such subject of unprecedented love and care in our society. Therefore, studies involving dogs and/or cats raise more ethical debate than other animal studies. However, most studies in these animals use clinical cases seen in veterinary hospitals and clinics, which highlights the importance of this underused resource for research. Some of the most important advantages and disadvantages of using dogs as model animals are summarized in **Table 5**.

TABLE 5 | (a) Advantages and disadvantages of canine research in general and hepatology in particular. (b) Advantages and disadvantages of companion animals as models.

Advantages	Disadvantages
Size of the dogs: Multiple and longitudinal measurements possible	Ethical concerns – companion animals – More of a concern if experimental use
Functional equivalence of various diseases in men and dogs/cats	No canine hepatitis virus causally correlated with canine hepatitis
Large genetic variation between breeds (cfr human population), limited genetic variation within breeds (genetic magnifier glass)	Specific drug intolerances for specific breeds
Imaging plus validated scoring approaches available (esp. for orthopedics)	
Dogs: Arthroscopy (also second look) plus validated scoring approaches	Costs
Dogs: Objective weight-bearing of legs possible (force plate analysis)	Special facilities needed for housing, surgery, imaging, necropsy
Dogs: Size variations cover new-born human-size until adult size	Size variation, so drug dosing needs special attention
Clinical need, large patient population (pets) available	

CONCLUSION

Companion animal and large animal models offer realistic naturally occuring disease models that more accurately evaluate safety and efficacy of new treatments as they share the heterogeniety of the human population including genetic and physiological variations and the complex interactions of these with the environment.

There are an increasing number of studies emerging from companion animals and large animal species that demonstrate they have much to offer to the human clinic in the quest for the next generation of drug or cell-based therapies and tissue engineering. The use of large animal models will enable greater attention to key questions. These include route of administration as it is not clear as yet which route(s) allow optimal engraftment of injected cells for different diseases. It also needs to be determined whether multiple injections will be more beneficial and if so the question arises whether there is an associated increase in risk of an adverse immune reaction. Cell therapies likely function via a paracrine mechanism and as such alternative approaches such as cell-free extracellular vesicle fractions or soluble factors, need to be explored that may reduce some risks posed by cell administration particularly of allogeneic cells.

For tissue engineered constructs implantation studies using animals with similar size and weight as human patients are crucial to test the implants under relevant biomechanical conditions.

To answer these questions pre-clinical trials with patient cohorts of sufficient size are required which need to be designed robustly to measure appropriate safety and efficacy readouts. Equivalent diseases in animals makes them not only relevant models which offer a more accurate evaluation of safety and efficacy of new treatments, but at the same time are potential beneficiaries of new treatment approaches. Hence, human and

veterinary medicine can mutually benefit if one appreciates the similarities.

AUTHOR CONTRIBUTIONS

IR contributed to conceptualization, writing the manuscript, merging the parts contributed by other authors, and revision and editing of the manuscript. PB, AL-C, LM, MP, ES-F, LD, DC, and FS wrote the manuscript. FJ revised and edited the manuscript. JD wrote, revised, and edited the manuscript. LP conceived the idea and wrote, revised, and edited the manuscript. All authors contributed to the article and approved the submitted version.

ACKNOWLEDGMENTS

We would like to thank Niklas Dresen, Institute of Veterinary Anatomy, University Leipzig as well as John Breteler, Elfriede Cremer, Bernhard Cremer, and Elisabeth Schieder for the provided graphical support and Michaela Hauser for formatting the references. PB acknowledges the funded projects PI15/00563 and PI18/00529 from ISCIII, Spain.

REFERENCES

Abelew, T. A., Miller, M. D., Cope, T. C., and Nichols, T. R. (2000). Local loss of proprioception results in disruption of interjoint coordination during locomotion in the cat. *J. Neurophysiol.* 84, 2709–2714. doi: 10.1152/jn.2000.84.5.2709

Aigner, T., Cook, J. L., Gerwin, N., Glasson, S. S., Laverty, S., Little, C. B., et al. (2010). Histopathology atlas of animal model systems - overview of guiding principles. *Osteoarthritis Cartilage* 18(Suppl. 3), S2–S6.

Al Abri, R., Kolethekkat, A. A., Kelleher, M. O., Myles, L. M., and Glasby, M. A. (2014). Effect of locally administered ciliary neurotrophic factor on the survival of transected and repaired adult sheep facial nerve. *Oman Med. J.* 29, 208–213. doi: 10.5001/omj.2014.51

Almeida-Porada, G., Porada, C., Gupta, N., Torabi, A., Thain, D., and Zanjani, E. D. (2007). The human-sheep chimeras as a model for human stem cell mobilization and evaluation of hematopoietic grafts' potential. *Exp. Hematol.* 35, 1594–1600. doi: 10.1016/j.exphem.2007.07.009

Almeida-Porada, G., Porada, C., and Zanjani, E. D. (2004). Plasticity of human stem cells in the fetal sheep model of human stem cell transplantation. *Int. J. Hematol.* 79, 1–6. doi: 10.1007/bf02983526

Andarawis-Puri, N., Flatow, E. L., and Soslowsky, L. J. (2015). Tendon basic science: development, repair, regeneration, and healing. *J. Orthop. Res.* 33, 780–784. doi: 10.1002/jor.22869

Andersen, M. D., Alstrup, A. K. O., Duvald, C. S., Mikkelsen, E. F. R., Vendelbo, M. H., and Ovesen, P. G. (2018). "Animal models of fetal medicine and obstetrics," in *Experimental Animal Models of Human Diseases - An Effective Therapeutic Strategy* ed. B. Ibeh (London: InTech).

Ansorge, H. L., Hsu, J. E., Edelstein, L., Adams, S., Birk, D. E., and Soslowsky, L. J. (2012). Recapitulation of the Achilles tendon mechanical properties during neonatal development: a study of differential healing during two stages of development in a mouse model. *J. Orthop. Res.* 30, 448–456. doi: 10.1002/jor.21542

Aper, T., Wilhelmi, M., Gebhardt, C., Hoeffler, K., Benecke, N., Hilfiker, A., et al. (2016). Novel method for the generation of tissue-engineered vascular grafts based on a highly compacted fibrin matrix. *Acta Biomater.* 29, 21–32. doi: 10.1016/j.actbio.2015.10.012

Asmussen, S., Ito, H., Traber, D. L., Lee, J. W., Cox, R. A., Hawkins, H. K., et al. (2014). Human mesenchymal stem cells reduce the severity of acute lung injury in a sheep model of bacterial pneumonia. *Thorax* 69, 819–825. doi: 10.1136/thoraxjnl-2013-204980

Aun, M. V., Bonamichi-Santos, R., Arantes-Costa, F. M., Kalil, J., and Giavina-Bianchi, P. (2017). Animal models of asthma: utility and limitations. *J. Asthma Allergy* 10, 293–301. doi: 10.2147/jaa.s121092

Bach, F. C., Laagland, L. T., Grant, M. P., Creemers, L. B., Ito, K., Meij, B. P., et al. (2017). Link-N: the missing link towards intervertebral disc repair is species-specific. *PLoS One* 12:e0187831. doi: 10.1371/journal.pone.0187831

Baptista, P. M., Siddiqui, M. M., Lozier, G., Rodriguez, S. R., Atala, A., and Soker, S. (2011). The use of whole organ decellularization for the generation of a vascularized liver organoid. *Hepatology* 53, 604–617. doi: 10.1002/hep.24067

Barbeau, H., and Rossignol, S. (1987). Recovery of locomotion after chronic spinalization in the adult cat. *Brain Res.* 412, 84–95. doi: 10.1016/0006-8993(87)91442-9

Baron, R., Tross, R., and Vignery, A. (1984). Evidence of sequential remodeling in rat trabecular bone: morphology, dynamic histomorphometry, and changes during skeletal maturation. *Anat. Rec.* 208, 137–145. doi: 10.1002/ar.1092080114

Basso, C., Fox, P. R., Meurs, K. M., Towbin, J. A., Spier, A. W., Calabrese, F., et al. (2004). Arrhythmogenic right ventricular cardiomyopathy causing sudden cardiac death in boxer dogs: a new animal model of human disease. *Circulation* 109, 1180–1185. doi: 10.1161/01.cir.0000118494.07530.65

Baumgartner, W., Gauly, M., Schuh, M., Hildebrandt, N., Moritz, A., Christen, C., et al. (2009). *Klinische Propädeutik der Haus-und Heimtiere*. Stuttgart: Enke Verlag.

Baxter, G. M., and Morrison, S. (2008). Complications of unilateral weight bearing. *Vet. Clin. North Am. Equine Pract.* 24, 621–642. ix, doi: 10.1016/j.cveq.2008.10.006

Becerra, P., Valdes Vazquez, M. A., Dudhia, J., Fiske-Jackson, A. R., Neves, F., Hartman, N. G., et al. (2013). Distribution of injected technetium(99m)-labeled mesenchymal stem cells in horses with naturally occurring tendinopathy. *J. Orthop. Res.* 31, 1096–1102. doi: 10.1002/jor.22338

Bélanger, M., Drew, T., Provencher, J., and Rossignol, S. (1996). A comparison of treadmill locomotion in adult cats before and after spinal transection. *J. Neurophysiol.* 76, 471–491. doi: 10.1152/jn.1996.76.1.471

Bendele, A. M. (2001). Animal models of osteoarthritis. *J. Musculoskelet. Neuronal Interact.* 1, 363–376.

Bentley, G. (1975). Articular cartilage studies and osteoarthrosis. *Ann. R. Coll. Surg. Engl.* 57, 86–100.

Beredjiklian, P. K., Favata, M., Cartmell, J. S., Flanagan, C. L., Crombleholme, T. M., and Soslowsky, L. J. (2003). Regenerative versus reparative healing in tendon: a study of biomechanical and histological properties in fetal sheep. *Ann. Biomed. Eng.* 31, 1143–1152. doi: 10.1114/1.1616931

Bergh, M. S., Sullivan, C., Ferrell, C. L., Troy, J., and Budsberg, S. C. (2014). Systematic review of surgical treatments for cranial cruciate ligament disease in dogs. *J. Am. Anim. Hosp. Assoc.* 50, 315–321. doi: 10.5326/jaaha-ms-6356

Berner, A., Henkel, J., Woodruff, M. A., Steck, R., Nerlich, M., Schuetz, M. A., et al. (2015). Delayed minimally invasive injection of allogenic bone marrow stromal cell sheets regenerates large bone defects in an ovine preclinical animal model. *Stem Cells Transl. Med.* 4, 503–512. doi: 10.5966/sctm.2014-0244

Berner, D., Brehm, W., Gerlach, K., Gittel, C., Offhaus, J., Paebst, F., et al. (2016). Longitudinal cell tracking and simultaneous monitoring of tissue regeneration after cell treatment of natural tendon disease by low-field magnetic resonance imaging. *Stem Cells Int.* 2016:1207190.

Bernstein, A., Niemeyer, P., Salzmann, G., Sudkamp, N. P., Hube, R., Klehm, J., et al. (2013). Microporous calcium phosphate ceramics as tissue engineering scaffolds for the repair of osteochondral defects: Histological results. *Acta Biomater.* 9, 7490–7505. doi: 10.1016/j.actbio.2013.03.021

Blume, C., and Davies, D. E. (2013). *In vitro* and *ex vivo* models of human asthma. *Eur. J. Pharm. Biopharm.* 84, 394–400.

Boettcher, A. N., Loving, C. L., Cunnick, J. E., and Tuggle, C. K. (2018). Development of Severe Combined Immunodeficient (Scid) pig models for translational cancer modeling: future insights on how humanized Scid Pigs can improve preclinical cancer research. *Front. Oncol.* 8:559. doi: 10.3389/fonc.2018.00559

Bolli, R., Chugh, A. R., D'amario, D., Loughran, J. H., Stoddard, M. F., Ikram, S., et al. (2011). Cardiac stem cells in patients with ischaemic cardiomyopathy (Scipio): initial results of a randomised phase 1 trial. *Lancet* 378, 1847–1857. doi: 10.1016/s0140-6736(11)61590-0

Bonamichi-Santos, R., Aun, M. V., Agondi, R. C., Kalil, J., and Giavina-Bianchi, P. (2015). Microbiome and Asthma: What have experimental models already taught us? *J. Immunol. Res.* 2015:614758.

Borgeat, K., Casamian-Sorrosal, D., Helps, C., Luis Fuentes, V., and Connolly, D. J. (2014). Association of the myosin binding protein C3 mutation (MYBPC3 R820W) with cardiac death in a survey of 236 Ragdoll cats. *J. Vet. Cardiol.* 16, 73–80. doi: 10.1016/j.jvc.2014.03.005

Bos, P. K., Kops, N., Verhaar, J. A., and Van Osch, G. J. (2008). Cellular origin of neocartilage formed at wound edges of articular cartilage in a tissue culture experiment. *Osteoarthritis Cartilage* 16, 204–211. doi: 10.1016/j.joca.2007.06.007

Bouyer, L. J., and Rossignol, S. (2003). Contribution of cutaneous inputs from the hindpaw to the control of locomotion. II. Spinal cats. *J. Neurophysiol.* 90, 3640–3653. doi: 10.1152/jn.00497.2003

Bozynski, C. C., Stannard, J. P., Smith, P., Hanypsiak, B. T., Kuroki, K., Stoker, A., et al. (2016). Acute management of anterior cruciate ligament injuries using novel canine models. *J. Knee Surg.* 29, 594–603. doi: 10.1055/s-0035-1570115

Brittberg, M., and Winalski, C. S. (2003). Evaluation of cartilage injuries and repair. *J. Bone Joint. Surg. Am.* 85-A, 58–69. doi: 10.2106/00004623-200300002-00008

Broeckx, S. Y., Martens, A. M., Bertone, A. L., Van Brantegem, L., Duchateau, L., Van Hecke, L., et al. (2019). The use of equine chondrogenic-induced mesenchymal stem cells as a treatment for osteoarthritis: a randomised, double-blinded, placebo-controlled proof-of-concept study. *Equine Vet. J.* 51, 787–794. doi: 10.1111/evj.13089

Brzezinski, A., Ghodbane, S. A., Patel, J. M., Perry, B. A., Gatt, C. J., and Dunn, M. G. (2017). (*) The ovine model for meniscus tissue engineering: considerations of anatomy, function, implantation, and evaluation. *Tissue Eng. Part C Methods* 23, 829–841. doi: 10.1089/ten.tec.2017.0192

Bullone, M., and Lavoie, J. P. (2015). Asthma "of horses and men"–how can equine heaves help us better understand human asthma immunopathology and its functional consequences? *Mol. Immunol.* 66, 97–105. doi: 10.1016/j.molimm.2014.12.005

Bullone, M., and Lavoie, J. P. (2019). The equine asthma model of airway remodeling: from a veterinary to a human perspective. *Cell Tissue Res.* 380, 223–236. doi: 10.1007/s00441-019-03117-4

Burk, J., Berner, D., Brehm, W., Hillmann, A., Horstmeier, C., Josten, C., et al. (2016). Long-term cell tracking following local injection of mesenchymal stromal cells in the equine model of induced tendon disease. *Cell Transplant.* 25, 2199–2211. doi: 10.3727/096368916x692104

Cadby, J. A., David, F., Van De Lest, C., Bosch, G., Van Weeren, P. R., Snedeker, J. G., et al. (2013). Further characterisation of an experimental model of tendinopathy in the horse. *Equine Vet. J.* 45, 642–648. doi: 10.1111/evj.12035

Cahill, T. J., Ashrafian, H., and Watkins, H. (2013). Genetic cardiomyopathies causing heart failure. *Circ. Res.* 113, 660–675. doi: 10.1161/circresaha.113.300282

Cai, B., Sun, S., Li, Z., Zhang, X., Ke, Y., Yang, J., et al. (2018). Application of CRISPR/Cas9 technologies combined with ipscs in the study and treatment of retinal degenerative diseases. *Hum. Genet.* 137, 679–688. doi: 10.1007/s00439-018-1933-9

Campen, M. J., Tagaito, Y., Jenkins, T. P., Balbir, A., and O'donnell, C. P. (2005). Heart rate variability responses to hypoxic and hypercapnic exposures in different mouse strains. *J. Appl. Physiol.* 99, 807–813. doi: 10.1152/japplphysiol.00039.2005

Campo, H., Baptista, P. M., Lopez-Perez, N., Faus, A., Cervello, I., and Simon, C. (2017). De- and recellularization of the pig uterus: a bioengineering pilot study. *Biol. Reprod.* 96, 34–45. doi: 10.1095/biolre/bio143396

Caniglia, C. J., Schramme, M. C., and Smith, R. K. (2012). The effect of intralesional injection of bone marrow derived mesenchymal stem cells and bone marrow supernatant on collagen fibril size in a surgical model of equine superficial digital flexor tendonitis. *Equine Vet. J.* 44, 587–593. doi: 10.1111/j.2042-3306.2011.00514.x

Carpenter, J. E., and Hankenson, K. D. (2004). Animal models of tendon and ligament injuries for tissue engineering applications. *Biomaterials* 25, 1715–1722. doi: 10.1016/s0142-9612(03)00507-6

Carvalho Ade, M., Badial, P. R., Alvarez, L. E., Yamada, A. L., Borges, A. S., Deffune, E., et al. (2013). Equine tendonitis therapy using mesenchymal stem cells and platelet concentrates: a randomized controlled trial. *Stem Cell Res. Ther.* 4:85. doi: 10.1186/scrt236

Casanas, J., De La Torre, J., Soler, F., Garcia, F., Rodellar, C., Pumarola, M., et al. (2014). Peripheral nerve regeneration after experimental section in ovine radial and tibial nerves using synthetic nerve grafts, including expanded bone marrow mesenchymal cells: morphological and neurophysiological results. *Injury* 45(Suppl. 4), S2–S6.

Cattanach, B. M., Dukes-Mcewan, J., Wotton, P. R., Stephenson, H. M., and Hamilton, R. M. (2015). A pedigree-based genetic appraisal of Boxer Arvc and the role of the Striatin mutation. *Vet. Rec.* 176:492. doi: 10.1136/vr.102821

Chari, R. S., Collins, B. H., Magee, J. C., Dimaio, J. M., Kirk, A. D., Harland, R. C., et al. (1994). Brief report: treatment of hepatic failure with ex vivo pig-liver perfusion followed by liver transplantation. *N. Engl. J. Med.* 331, 234–237. doi: 10.1056/nejm199407283310404

Cheng, K., Ibrahim, A., Hensley, M. T., Shen, D., Sun, B., Middleton, R., et al. (2014). Relative roles of Cd90 and c-kit to the regenerative efficacy of cardiosphere-derived cells in humans and in a mouse model of myocardial infarction. *J. Am. Heart Assoc.* 3:e001260.

Cheng, Y. J., Imperatore, G., Caspersen, C. J., Gregg, E. W., Albright, A. L., and Helmick, C. G. (2012). Prevalence of diagnosed arthritis and arthritis-attributable activity limitation among adults with and without diagnosed diabetes: United States, 2008-2010. *Diabetes Care* 35, 1686–1691. doi: 10.2337/dc12-0046

Chevrier, A., Nelea, M., Hurtig, M. B., Hoemann, C. D., and Buschmann, M. D. (2009). Meniscus structure in human, sheep, and rabbit for animal models of meniscus repair. *J. Orthop. Res.* 27, 1197–1203. doi: 10.1002/jor.20869

Chieppa, M. N., Perota, A., Corona, C., Grindatto, A., Lagutina, I., Vallino Costassa, E., et al. (2014). Modeling amyotrophic lateral sclerosis in hsod1 transgenic swine. *Neurodegener. Dis.* 13, 246–254.

Chimenti, I., Smith, R. R., Li, T. S., Gerstenblith, G., Messina, E., Giacomello, A., et al. (2010). Relative roles of direct regeneration versus paracrine effects of human cardiosphere-derived cells transplanted into infarcted mice. *Circ. Res.* 106, 971–980. doi: 10.1161/circresaha.109.210682

Christopher, M. M. (2015). One health, one literature: weaving together veterinary and medical research. *Sci. Transl. Med.* 7:303fs36.

Chu, C. R., Szczodry, M., and Bruno, S. (2010). Animal models for cartilage regeneration and repair. *Tissue Eng. Part B Rev.* 16, 105–115. doi: 10.1089/ten.teb.2009.0452

Cipitria, A., Reichert, J. C., Epari, D. R., Saifzadeh, S., Berner, A., Schell, H., et al. (2013). Polycaprolactone scaffold and reduced rhbmp-7 dose for the regeneration of critical-sized defects in sheep tibiae. *Biomaterials* 34, 9960–9968. doi: 10.1016/j.biomaterials.2013.09.011

Cohen-Solal, M., Hay, E., and Funck-Brentano, T. (2012). Animal models in OA: a means to explore bone. *Osteoporos. Int.* 23(Suppl. 8), S853–S856.

Comerford, E. J., Smith, K., and Hayashi, K. (2011). Update on the aetiopathogenesis of canine cranial cruciate ligament disease. *Vet. Comp. Orthop. Traumatol.* 24, 91–98. doi: 10.3415/vcot-10-04-0055

Conboy, I. M., Conboy, M. J., Wagers, A. J., Girma, E. R., Weissman, I. L., and Rando, T. A. (2005). Rejuvenation of aged progenitor cells by exposure to a young systemic environment. *Nature* 433, 760–764. doi: 10.1038/nature03260

Condorelli, G., Borello, U., De Angelis, L., Latronico, M., Sirabella, D., Coletta, M., et al. (2001). Cardiomyocytes induce endothelial cells to trans-differentiate into cardiac muscle: implications for myocardium regeneration. *Proc. Natl. Acad. Sci. U.S.A.* 98, 10733–10738. doi: 10.1073/pnas.191217898

Cone, S. G., Warren, P. B., and Fisher, M. B. (2017). Rise of the pigs: utilization of the porcine model to study musculoskeletal biomechanics and tissue engineering during skeletal growth. *Tissue Eng. Part C Methods* 23, 763–780. doi: 10.1089/ten.tec.2017.0227

Connizzo, B. K., Yannascoli, S. M., and Soslowsky, L. J. (2013). Structure-function relationships of postnatal tendon development: a parallel to healing. *Matrix Biol.* 32, 106–116. doi: 10.1016/j.matbio.2013.01.007

Cook, J. L. (2010). Cranial cruciate ligament disease in dogs: biology versus biomechanics. *Vet. Surg.* 39, 270–277. doi: 10.1111/j.1532-950x.2010.00653.x

Cosmi, L., Liotta, F., and Annunziato, F. (2016). Th17 regulating lower airway disease. *Curr. Opin. Allergy Clin. Immunol.* 16, 1–6. doi: 10.1097/aci.0000000000000227

Couetil, L. L., Hoffman, A. M., Hodgson, J., Buechner-Maxwell, V., Viel, L., Wood, J. L., et al. (2007). Inflammatory airway disease of horses. *J. Vet. Intern. Med.* 21, 356–361. doi: 10.1111/j.1939-1676.2007.tb02975.x

Court, F. G., Laws, P. E., Morrison, C. P., Teague, B. D., Metcalfe, M. S., Wemyss-Holden, S. A., et al. (2004). Subtotal hepatectomy: a porcine model for the study of liver regeneration. *J. Surg. Res.* 116, 181–186. doi: 10.1016/j.jss.2003.08.007

Crovace, A., Lacitignola, L., Francioso, E., and Rossi, G. (2008). Histology and immunohistochemistry study of ovine tendon grafted with cBMSCs and BMMNCs after collagenase-induced tendinitis. *Vet. Comp. Orthop. Traumatol.* 21, 329–336. doi: 10.3415/vcot-07-05-0050

Crovace, A., Lacitignola, L., Rossi, G., and Francioso, E. (2010). Histological and immunohistochemical evaluation of autologous cultured bone marrow mesenchymal stem cells and bone marrow mononucleated cells in collagenase-induced tendinitis of equine superficial digital flexor tendon. *Vet. Med. Int.* 2010:250978.

Cummings, I., George, S., Kelm, J., Schmidt, D., Emmert, M. Y., Weber, B., et al. (2012). Tissue-engineered vascular graft remodeling in a growing lamb model: expression of matrix metalloproteinases. *Eur. J. Cardiothorac. Surg.* 41, 167–172.

Dalgaard, L. (2015). Comparison of minipig, dog, monkey and human drug metabolism and disposition. *J. Pharmacol. Toxicol. Methods* 74, 80–92. doi: 10.1016/j.vascn.2014.12.005

Dalla Costa, E., Minero, M., Lebelt, D., Stucke, D., Canali, E., and Leach, M. C. (2014). Development of the Horse Grimace Scale (Hgs) as a pain assessment tool in horses undergoing routine castration. *PLoS One* 9:e92281. doi: 10.1371/journal.pone.0092281

Daly, C. D., Ghosh, P., Zannettino, A. C. W., Badal, T., Shimmon, R., Jenkin, G., et al. (2018). Mesenchymal progenitor cells primed with pentosan polysulfate promote lumbar intervertebral disc regeneration in an ovine model of microdiscectomy. *Spine J.* 18, 491–506. doi: 10.1016/j.spinee.2017.10.008

De Bie, P., Van De Sluis, B., Burstein, E., Van De Berghe, P. V., Muller, P., Berger, R., et al. (2007). Distinct Wilson's disease mutations in Atp7B are associated with enhanced binding to Commd1 and reduced stability of Atp7B. *Gastroenterology* 133, 1316–1326. doi: 10.1053/j.gastro.2007.07.020

Debrue, M., Hamilton, E., Joubert, P., Lajoie-Kadoch, S., and Lavoie, J. P. (2005). Chronic exacerbation of equine heaves is associated with an increased expression of interleukin-17 mRNA in bronchoalveolar lavage cells. *Vet. Immunol. Immunopathol.* 105, 25–31. doi: 10.1016/j.vetimm.2004.12.013

Delling, U., Brehm, W., Ludewig, E., Winter, K., and Julke, H. (2015a). Longitudinal evaluation of effects of intra-articular mesenchymal stromal cell administration for the treatment of osteoarthritis in an ovine model. *Cell Transplant.* 24, 2391–2407. doi: 10.3727/096368915x686193

Delling, U., Brehm, W., Metzger, M., Ludewig, E., Winter, K., and Julke, H. (2015b). *In vivo* tracking and fate of intra-articularly injected superparamagnetic iron oxide particle-labeled multipotent stromal cells in an ovine model of osteoarthritis. *Cell Transplant.* 24, 2379–2390. doi: 10.3727/096368914x685654

Denner, J. (2017). Can antiretroviral drugs be used to treat porcine endogenous retrovirus (PERV) Infection after Xenotransplantation? *Viruses* 9:213. doi: 10.3390/v9080213

Deponti, D., Di Giancamillo, A., Scotti, C., Peretti, G. M., and Martin, I. (2015). Animal models for meniscus repair and regeneration. *J. Tissue Eng. Regen. Med.* 9, 512–527. doi: 10.1002/term.1760

Deprés-Tremblay, G., Chevrier, A., Hurtig, M. B., Snow, M., Rodeo, S., and Buschmann, M. D. (2018). Freeze-dried chitosan-platelet-rich plasma implants for rotator cuff tear repair: pilot ovine studies. *ACS Biomater. Sci. Eng.* 4, 3737–3746. doi: 10.1021/acsbiomaterials.7b00354

Desando, G., Giavaresi, G., Cavallo, C., Bartolotti, I., Sartoni, F., Nicoli Aldini, N., et al. (2016). Autologous bone marrow concentrate in a sheep model of osteoarthritis: new perspectives for cartilage and meniscus repair. *Tissue Eng. Part C Methods* 22, 608–619. doi: 10.1089/ten.tec.2016.0033

Dias, I. R., Camassa, J. A., Bordelo, J. A., Babo, P. S., Viegas, C. A., Dourado, N., et al. (2018). Preclinical and translational studies in small ruminants (sheep and goat) as models for osteoporosis research. *Curr. Osteoporos. Rep.* 16, 182–197. doi: 10.1007/s11914-018-0431-2

Diogo, C. C., Camassa, J. A., Pereira, J. E., Costa, L. M. D., Filipe, V., Couto, P. A., et al. (2017). The use of sheep as a model for studying peripheral nerve regeneration following nerve injury: review of the literature. *Neurol. Res.* 39, 926–939. doi: 10.1080/01616412.2017.1331873

Divincenti, L. Jr., Westcott, R., and Lee, C. (2014). Sheep (*Ovis aries*) as a model for cardiovascular surgery and management before, during, and after cardiopulmonary bypass. *J. Am. Assoc. Lab. Anim. Sci.* 53, 439–448.

Douwes, J., Gibson, P., Pekkanen, J., and Pearce, N. (2002). Non-eosinophilic asthma: importance and possible mechanisms. *Thorax* 57, 643–648. doi: 10.1136/thorax.57.7.643

Dowling, B. A., Dart, A. J., Hodgson, D. R., and Smith, R. K. (2000). Superficial digital flexor tendonitis in the horse. *Equine Vet. J.* 32, 369–378. doi: 10.2746/042516400777591138

Drosos, G. I., and Pozo, J. L. (2004). The causes and mechanisms of meniscal injuries in the sporting and non-sporting environment in an unselected population. *Knee* 11, 143–149. doi: 10.1016/s0968-0160(03)00105-4

Ducharme, N. G. (2004). "Surgery of the bovine digestive system," in *Farm Animal Surgery*, 1st Edn, ed. S. L. Fubini, and N.G. Ducharme (Philadelphia, PA: Elsevier).

Dudhia, J., Becerra, P., Valdes, M. A., Neves, F., Hartman, N. G., and Smith, R. K. (2015). *In vivo* imaging and tracking of technetium-99m labeled bone marrow mesenchymal stem cells in equine tendinopathy. *J. Vis. Exp.* 106:e52748.

Dutton, L. C., Church, S. A. V., Hodgkiss-Geere, H., Catchpole, B., Huggins, A., Dudhia, J., et al. (2018a). Cryopreservation of canine cardiosphere-derived cells: implications for clinical application. *Cytometry A* 93, 115–124. doi: 10.1002/cyto.a.23186

Dutton, L. C., Dudhia, J., Catchpole, B., Hodgkiss-Geere, H., Werling, D., and Connolly, D. J. (2018b). Cardiosphere-derived cells suppress allogeneic lymphocytes by production of PGE2 acting via the EP4 receptor. *Sci. Rep.* 8:13351.

Dutton, L. C., Dudhia, J., Guest, D. J., and Connolly, D. J. (2019). Inducing pluripotency in the domestic cat (*Felis catus*). *Stem Cells Dev.* 28, 1299–1309. doi: 10.1089/scd.2019.0142

Dziegielewska, K. M., Moller, J. E., Potter, A. M., Ek, J., Lane, M. A., and Saunders, N. R. (2000). Acute-phase cytokines IL-1beta and TNF-alpha in brain development. *Cell Tissue Res.* 299, 335–345. doi: 10.1007/s004419900157

Egenvall, A., Bonnett, B. N., and Haggstrom, J. (2006). Heart disease as a cause of death in insured Swedish dogs younger than 10 years of age. *J. Vet. Intern. Med.* 20, 894–903. doi: 10.1111/j.1939-1676.2006.tb01803.x

Elks, C. E., Perry, J. R., Sulem, P., Chasman, D. I., Franceschini, N., He, C., et al. (2010). Thirty new loci for age at menarche identified by a meta-analysis of genome-wide association studies. *Nat. Genet.* 42, 1077–1085.

Emmert, M. Y., Weber, B., Wolint, P., Frauenfelder, T., Zeisberger, S. M., Behr, L., et al. (2013). Intramyocardial transplantation and tracking of human mesenchymal stem cells in a novel intra-uterine pre-immune fetal sheep myocardial infarction model: a proof of concept study. *PLoS One* 8:e57759. doi: 10.1371/journal.pone.0057759

Entrican, G., Wattegedera, S. R., and Griffiths, D. J. (2015). Exploiting ovine immunology to improve the relevance of biomedical models. *Mol. Immunol.* 66, 68–77. doi: 10.1016/j.molimm.2014.09.002

Ericsson, A. C. (2019). The use of non-rodent model species in microbiota studies. *Lab. Anim.* 53, 259–270. doi: 10.1177/0023677219834593

Espinosa, P., Spriet, M., Sole, A., Walker, N. J., Vaughan, B., and Galuppo, L. D. (2016). Scintigraphic tracking of allogeneic mesenchymal stem cells in the distal limb after intra-arterial injection in standing horses. *Vet. Surg.* 45, 619–624. doi: 10.1111/vsu.12485

Fan, W., Wu, C., Miao, X., Liu, G., Saifzadeh, S., Sugiyama, S., et al. (2013). Biomaterial scaffolds in cartilage-subchondral bone defects influencing the repair of autologous articular cartilage transplants. *J. Biomater. Appl.* 27, 979–989. doi: 10.1177/0885328211431310

Favata, M., Beredjiklian, P. K., Zgonis, M. H., Beason, D. P., Crombleholme, T. M., Jawad, A. F., et al. (2006). Regenerative properties of fetal sheep tendon are not adversely affected by transplantation into an adult environment. *J. Orthop. Res.* 24, 2124–2132. doi: 10.1002/jor.20271

Favier, R. P., Spee, B., Fieten, H., Van Den Ingh, T. S., Schotanus, B. A., Brinkhof, B., et al. (2015). Aberrant expression of copper associated genes after copper accumulation in Commd1-deficient dogs. *J. Trace Elem. Med. Biol.* 29, 347–353. doi: 10.1016/j.jtemb.2014.06.007

Favier, R. P., Spee, B., Penning, L. C., and Rothuizen, J. (2011). Copper-induced hepatitis: the Commd1 deficient dog as a translational animal model for human chronic hepatitis. *Vet. Q.* 31, 49–60. doi: 10.1080/01652176.2011.563146

Favier, R. P., Spee, B., Schotanus, B. A., Van Den Ingh, T. S., Fieten, H., Brinkhof, B., et al. (2012). Commd1-deficient dogs accumulate copper in hepatocytes and provide a good model for chronic hepatitis and fibrosis. *PLoS One* 7:e42158. doi: 10.1371/journal.pone.0042158

Feng, C., Luo, X., He, N., Xia, H., Lv, X., Zhang, X., et al. (2018). Efficacy and persistence of allogeneic adipose-derived mesenchymal stem cells combined with hyaluronic acid in osteoarthritis after intra-articular injection in a sheep model. *Tissue Eng. Part A* 24, 219–233. doi: 10.1089/ten.tea.2017.0039

Fernandes, M. B., Guimaraes, J. A., Casado, P. L., Cavalcanti Ados, S., Goncalves, N. N., Ambrosio, C. E., et al. (2014). The effect of bone allografts combined with bone marrow stromal cells on the healing of segmental bone defects in a sheep model. *BMC Vet. Res.* 10:36. doi: 10.1186/1746-6148-10-36

Ferris, D., Frisbie, D., Kisiday, J., and Mcilwraith, C. W. (2012). *In vivo* healing of meniscal lacerations using bone marrow-derived mesenchymal stem cells and fibrin glue. *Stem Cells Int.* 2012:691605.

Fieten, H., Gill, Y., Martin, A. J., Concilli, M., Dirksen, K., Van Steenbeek, F. G., et al. (2016). The Menkes and Wilson disease genes counteract in copper toxicosis in Labrador retrievers: a new canine model for copper-metabolism disorders. *Dis. Model. Mech.* 9, 25–38. doi: 10.1242/dmm.020263

Fieten, H., Penning, L. C., Leegwater, P. A., and Rothuizen, J. (2014). New canine models of copper toxicosis: diagnosis, treatment, and genetics. *Ann. N. Y. Acad. Sci.* 1314, 42–48. doi: 10.1111/nyas.12442

Flisikowska, T., Kind, A., and Schnieke, A. (2014). Genetically modified pigs to model human diseases. *J. Appl. Genet.* 55, 53–64. doi: 10.1007/s13353-013-0182-9

Fonouni, H., Tahmasbi Rad, M., Esmaeilzadeh, M., Golriz, M., Majlesara, A., and Mehrabi, A. (2015). A simplified technique of pancreas transplantation in a porcine model. *Eur. Surg. Res.* 54, 24–33. doi: 10.1159/000367844

Forster, R., Bode, G., Ellegaard, L., and Van Der Laan, J. W. (2010). The RETHINK project–minipigs as models for the toxicity testing of new medicines and chemicals: an impact assessment. *J. Pharmacol. Toxicol. Methods* 62, 158–159.

Fortier, L. A., and Smith, R. K. (2008). Regenerative medicine for tendinous and ligamentous injuries of sport horses. *Vet. Clin. North Am. Equine Pract.* 24, 191–201. doi: 10.1016/j.cveq.2007.11.002

Fox, D. B., Warnock, J. J., Stoker, A. M., Luther, J. K., and Cockrell, M. (2010). Effects of growth factors on equine synovial fibroblasts seeded on synthetic scaffolds for avascular meniscal tissue engineering. *Res. Vet. Sci.* 88, 326–332. doi: 10.1016/j.rvsc.2009.07.015

Freeman, B. J., Kuliwaba, J. S., Jones, C. F., Shu, C. C., Colloca, C. J., Zarrinkalam, M. R., et al. (2016). Allogeneic mesenchymal precursor cells promote healing in postero-lateral annular lesions and improve indices of lumbar intervertebral disc degeneration in an ovine model. *Spine* 41, 1331–1339. doi: 10.1097/brs.0000000000001528

Frey, M., Gruber, H., Happak, W., Girsch, W., Gruber, I., and Koller, R. (1990). Ipsilateral and cross-over elongation of the motor nerve by nerve grafting: an experimental study in sheep. *Plast. Reconstr. Surg.* 85, 77–89. doi: 10.1097/00006534-199001000-00014

Frisbie, D. D., Cross, M. W., and Mcilwraith, C. W. (2006). A comparative study of articular cartilage thickness in the stifle of animal species used in human pre-clinical studies compared to articular cartilage thickness in the human knee. *Vet. Comp. Orthop. Traumatol.* 19, 142–146. doi: 10.1055/s-0038-1632990

Fubini, S. L., and Ducharme, N. G. (eds) (2004). "Surgical considerations," in *Farm Animal Surgery*, 1st Edn (St. Louis, MO: Elsevier).

Fuentealba, I. C., and Aburto, E. M. (2003). Animal models of copper-associated liver disease. *Comp. Hepatol.* 2:5.

Fukashiro, S., Komi, P. V., Jarvinen, M., and Miyashita, M. (1995). *In vivo* Achilles tendon loading during jumping in humans. *Eur. J. Appl. Physiol. Occup. Physiol.* 71, 453–458. doi: 10.1007/bf00635880

Fukunishi, T., Best, C. A., Sugiura, T., Shoji, T., Yi, T., Udelsman, B., et al. (2016). Tissue-engineered small diameter arterial vascular grafts from cell-free Nanofiber PCL/chitosan scaffolds in a sheep model. *PLoS One* 11:e0158555. doi: 10.1371/journal.pone.0158555

Fullarton, A. C., Myles, L. M., Lenihan, D. V., Hems, T. E., and Glasby, M. A. (2001). Obstetric brachial plexus palsy: a comparison of the degree of recovery after repair of a C6 ventral root avulsion in newborn and adult sheep. *Br. J. Plast. Surg.* 54, 697–704. doi: 10.1054/bjps.2001.3700

Geburek, F., Lietzau, M., Beineke, A., Rohn, K., and Stadler, P. M. (2015). Effect of a single injection of autologous conditioned serum (Acs) on tendon healing in equine naturally occurring tendinopathies. *Stem Cell Res. Ther.* 6:126.

Geburek, F., Mundle, K., Conrad, S., Hellige, M., Walliser, U., Van Schie, H. T., et al. (2016). Tracking of autologous adipose tissue-derived mesenchymal stromal cells with *in vivo* magnetic resonance imaging and histology after intralesional treatment of artificial equine tendon lesions–a pilot study. *Stem Cell Res. Ther.* 7:21.

Glasby, M. A., Mountain, R. E., and Murray, J. A. (1993). Repair of the facial nerve using freeze-thawed muscle autografts. A surgical model in the sheep. *Arch. Otolaryngol. Head Neck Surg.* 119, 461–465. doi: 10.1001/archotol.1993.01880160109018

Gleerup, K. B., Forkman, B., Lindegaard, C., and Andersen, P. H. (2015). An equine pain face. *Vet. Anaesth. Analg.* 42, 103–114.

Godwin, E. E., Young, N. J., Dudhia, J., Beamish, I. C., and Smith, R. K. (2012). Implantation of bone marrow-derived mesenchymal stem cells demonstrates improved outcome in horses with overstrain injury of the superficial digital flexor tendon. *Equine Vet. J.* 44, 25–32. doi: 10.1111/j.2042-3306.2011.00363.x

Goldberg, A. J., Zaidi, R., Brooking, D., Kim, L., Korda, M., Masci, L., et al. (2018). Autologous Stem Cells in Achilles Tendinopathy (ASCAT): protocol for a phase IIA, single-centre, proof-of-concept study. *BMJ Open* 8:e021600.

Gonzalez-Fernandez, M. L., Perez-Castrillo, S., Sanchez-Lazaro, J. A., Prieto-Fernandez, J. G., Lopez-Gonzalez, M. E., Lobato-Perez, S., et al. (2016). Assessment of regeneration in meniscal lesions by use of mesenchymal stem cells derived from equine bone marrow and adipose tissue. *Am. J. Vet. Res.* 77, 779–788. doi: 10.2460/ajvr.77.7.779

Goodship, A. E., Birch, H. L., and Wilson, A. M. (1994). The pathobiology and repair of tendon and ligament injury. *Vet. Clin. North Am. Equine Pract.* 10, 323–349. doi: 10.1016/s0749-0739(17)30359-0

Gotterbarm, T., Breusch, S. J., Schneider, U., and Jung, M. (2008). The minipig model for experimental chondral and osteochondral defect repair in tissue engineering: retrospective analysis of 180 defects. *Lab. Anim.* 42, 71–82. doi: 10.1258/la.2007.06029e

Govoni, K. E. (2015). HORSE SPECIES SYMPOSIUM: use of mesenchymal stem cells in fracture repair in horses. *J. Anim. Sci.* 93, 871–878.

Graubner, C., Gerber, V., Doherr, M., and Spadavecchia, C. (2011). Clinical application and reliability of a post abdominal surgery pain assessment scale (PASPAS) in horses. *Vet. J.* 188, 178–183. doi: 10.1016/j.tvjl.2010.04.029

Griesemer, A., Yamada, K., and Sykes, M. (2014). Xenotransplantation: immunological hurdles and progress toward tolerance. *Immunol. Rev.* 258, 241–258. doi: 10.1111/imr.12152

Gruchenberg, K., Ignatius, A., Friemert, B., Von Lubken, F., Skaer, N., Gellynck, K., et al. (2015). *In vivo* performance of a novel silk fibroin scaffold for partial meniscal replacement in a sheep model. *Knee Surg. Sports Traumatol. Arthrosc.* 23, 2218–2229. doi: 10.1007/s00167-014-3009-2

Guest, D. J., Smith, M. R., and Allen, W. R. (2008). Monitoring the fate of autologous and allogeneic mesenchymal progenitor cells injected into the superficial digital flexor tendon of horses: preliminary study. *Equine Vet. J.* 40, 178–181. doi: 10.2746/042516408x276942

Gugjoo, M. B., Fazili, M. R., Gayas, M. A., Ahmad, R. A., and Dhama, K. (2019). Animal mesenchymal stem cell research in cartilage regenerative medicine - a review. *Vet. Q.* 39, 95–120. doi: 10.1080/01652176.2019.1643051

Gupte, C. M., Bull, A. M., Murray, R., and Amis, A. A. (2007). Comparative anatomy of the meniscofemoral ligament in humans and some domestic mammals. *Anat. Histol. Embryol.* 36, 47–52. doi: 10.1111/j.1439-0264.2006.00718.x

Hager, C., Biernot, S., Buettner, M., Glage, S., Keubler, L. M., Held, N., et al. (2017). The Sheep Grimace Scale as an indicator of post-operative distress and pain in laboratory sheep. *PLoS One* 12:e0175839. doi: 10.1371/journal.pone.0175839

Haywood, S., Muller, T., Muller, W., Heinz-Erian, P., Tanner, M. S., and Ross, G. (2001). Copper-associated liver disease in North Ronaldsay sheep: a possible animal model for non-Wilsonian hepatic copper toxicosis of infancy and childhood. *J. Pathol.* 195, 264–269. doi: 10.1002/path.930

Haywood, S., Rutgers, H. C., and Christian, M. K. (1988). Hepatitis and copper accumulation in Skye terriers. *Vet. Pathol.* 25, 408–414. doi: 10.1177/030098588802500602

He, B., Musk, G. C., Mou, L., De Boer, B., Delriviere, L., and Hamdorf, J. (2013). Laparoscopic surgery for orthotopic kidney transplant in the pig model. *J. Surg. Res.* 184, 1096–1101. doi: 10.1016/j.jss.2013.03.015

Hems, T. E., Clutton, R. E., and Glasby, M. A. (1994). Repair of avulsed cervical nerve roots. An experimental study in sheep. *J. Bone Joint Surg. Br.* 76, 818–823. doi: 10.1302/0301-620x.76b5.8083277

Hems, T. E., and Glasby, M. A. (1992). Repair of cervical nerve roots proximal to the root ganglia. An experimental study in sheep. *J. Bone Joint Surg. Br.* 74, 918–922. doi: 10.1302/0301-620x.74b6.1447258

Hensley, M. T., De Andrade, J., Keene, B., Meurs, K., Tang, J., Wang, Z., et al. (2015). Cardiac regenerative potential of cardiosphere-derived cells from adult dog hearts. *J. Cell Mol. Med.* 19, 1805–1813. doi: 10.1111/jcmm.12585

Hensley, M. T., Tang, J., Woodruff, K., Defrancesco, T., Tou, S., Williams, C. M., et al. (2017). Intracoronary allogeneic cardiosphere-derived stem cells are safe for use in dogs with dilated cardiomyopathy. *J. Cell. Mol. Med.* 21, 1503–1512. doi: 10.1111/jcmm.13077

Herdrich, B. J., Danzer, E., Davey, M. G., Bermudez, D. M., Radu, A., Zhang, L., et al. (2010). Fetal tendon wound size modulates wound gene expression and subsequent wound phenotype. *Wound Repair Regen.* 18, 543–549. doi: 10.1111/j.1524-475x.2010.00615.x

Heron, M. (2016). Deaths: leading causes for 2014. *Natl. Vital Stat. Rep.* 65, 1–96.

Herszberg, B., Ramos-Barbon, D., Tamaoka, M., Martin, J. G., and Lavoie, J. P. (2006). Heaves, an asthma-like equine disease, involves airway smooth muscle remodeling. *J. Allergy Clin. Immunol.* 118, 382–388. doi: 10.1016/j.jaci.2006.03.044

Hoffmann, G., Van Den Ingh, T. S., Bode, P., and Rothuizen, J. (2006). Copper-associated chronic hepatitis in Labrador Retrievers. *J. Vet. Intern. Med.* 20, 856–861. doi: 10.1111/j.1939-1676.2006.tb01798.x

Hopper, N., Wardale, J., Brooks, R., Power, J., Rushton, N., and Henson, F. (2015). Peripheral blood mononuclear cells enhance cartilage repair in *in vivo* osteochondral defect model. *PLoS One* 10:e0133937. doi: 10.1371/journal.pone.0133937

Hotchkiss, J. W., Reid, S. W., and Christley, R. M. (2007). A survey of horse owners in Great Britain regarding horses in their care. *Part* 2: Risk factors for recurrent airway obstruction. *Equine Vet. J.* 39, 301–308. doi: 10.2746/042516407x180129

Houtgraaf, J. H., De Jong, R., Kazemi, K., De Groot, D., Van Der Spoel, T. I., Arslan, F., et al. (2013). Intracoronary infusion of allogeneic mesenchymal precursor cells directly after experimental acute myocardial infarction reduces infarct size, abrogates adverse remodeling, and improves cardiac function. *Circ. Res.* 113, 153–166. doi: 10.1161/circresaha.112.300730

Huke, S., and Knollmann, B. C. (2010). Increased myofilament Ca2+-sensitivity and arrhythmia susceptibility. *J. Mol. Cell. Cardiol.* 48, 824–833. doi: 10.1016/j.yjmcc.2010.01.011

Hurtig, M. B., Buschmann, M. D., Fortier, L. A., Hoemann, C. D., Hunziker, E. B., Jurvelin, J. S., et al. (2011). Preclinical studies for cartilage repair: recommendations from the international cartilage repair society. *Cartilage* 2, 137–152. doi: 10.1177/1947603511401905

Hurtig, M. B., Novak, K., Mcpherson, R., Mcfadden, S., Mcgann, L. E., Mul Drew, K., et al. (1998). Osteochondral dowel transplantation for repair of focal defects in the knee: an outcome study using an ovine model. *Vet. Surg.* 27, 5–16. doi: 10.1111/j.1532-950x.1998.tb00092.x

Husser, D., Ueberham, L., Jacob, J., Heuer, D., Riedel-Heller, S., Walker, J., et al. (2018). Prevalence of clinically apparent hypertrophic cardiomyopathy in Germany-An analysis of over 5 million patients. *PLoS One* 13:e0196612. doi: 10.1371/journal.pone.0196612

Iacopetti, I., Perazzi, A., Martinello, T., Gemignani, F., and Patruno, M. (2020). Hyaluronic acid, Manuka honey and Acemannan gel: wound-specific applications for skin lesions. *Res. Vet. Sci.* 129, 82–89. doi: 10.1016/j.rvsc.2020.01.009

Inesi, G. (2017). Molecular features of copper binding proteins involved in copper homeostasis. *IUBMB Life* 69, 211–217. doi: 10.1002/iub.1590

Ingenito, E. P., Tsai, L., Murthy, S., Tyagi, S., Mazan, M., and Hoffman, A. (2012). Autologous lung-derived mesenchymal stem cell transplantation in experimental emphysema. *Cell Transplant.* 21, 175–189. doi: 10.3727/096368910x550233

Iwaniec, T. (2008). "Animal models for osteoporosis," in *Osteoporosis*, 3rd Edn, eds R. Marcus, D. Feldman, D. Nelson, and C. Rosen (Amsterdam: Elsevier).

Jackson, S. J., Andrews, N., Ball, D., Bellantuono, I., Gray, J., Hachoumi, L., et al. (2017). Does age matter? The impact of rodent age on study outcomes. *Lab. Anim.* 51, 160–169. doi: 10.1177/0023677216653984

Jarvinen, T. A., Kannus, P., Maffulli, N., and Khan, K. M. (2005). Achilles tendon disorders: etiology and epidemiology. *Foot Ankle Clin.* 10, 255–266. doi: 10.1016/j.fcl.2005.01.013

Jeanblanc, C., Goodrich, A. D., Colletti, E., Mokhtari, S., Porada, C. D., Zanjani, E. D., et al. (2014). Temporal definition of haematopoietic stem cell niches in a large animal model of in utero stem cell transplantation. *Br. J. Haematol.* 166, 268–278. doi: 10.1111/bjh.12870

Jeong, Y. H., Park, C. H., Jang, G. H., Jeong, Y. I., Hwang, I. S., Jeong, Y. W., et al. (2013). Production of multiple transgenic Yucatan miniature pigs expressing human complement regulatory factors, human CD55, CD59, and H-transferase genes. *PLoS One* 8:e63241. doi: 10.1371/journal.pone.0063241

Jiang, Y., Xie, M., Chen, W., Talbot, R., Maddox, J. F., Faraut, T., et al. (2014). The sheep genome illuminates biology of the rumen and lipid metabolism. *Science* 344, 1168–1173.

Johnson, V. L., and Hunter, D. J. (2014). The epidemiology of osteoarthritis. *Best Pract. Res. Clin. Rheumatol.* 28, 5–15.

Johnston, P. V., Sasano, T., Mills, K., Evers, R., Lee, S. T., Smith, R. R., et al. (2009). Engraftment, differentiation, and functional benefits of autologous cardiosphere-derived cells in porcine ischemic cardiomyopathy. *Circulation* 120, 1075–1083. doi: 10.1161/circulationaha.108.816058

Julke, H., Veit, C., Ribitsch, I., Brehm, W., Ludewig, E., and Delling, U. (2015). Comparative labeling of equine and ovine multipotent stromal cells with superparamagnetic iron oxide particles for magnetic resonance imaging *in vitro*. *Cell Transplant.* 24, 1111–1125. doi: 10.3727/096368913x675737

Kahn, D., Hickman, R., Terblanche, J., and Von Sommoggy, S. (1988). Partial hepatectomy and liver regeneration in pigs–the response to different resection sizes. *J. Surg. Res.* 45, 176–180. doi: 10.1016/0022-4804(88)90062-5

Kajbafzadeh, A. M., Khorramirouz, R., Nabavizadeh, B., Ladi Seyedian, S. S., Akbarzadeh, A., Heidari, R., et al. (2019). Whole organ sheep kidney tissue engineering and *in vivo* transplantation: effects of perfusion-based decellularization on vascular integrity. *Mater. Sci. Eng. C Mater. Biol. Appl.* 98, 392–400. doi: 10.1016/j.msec.2019.01.018

Kang, N. V., Morritt, D., Pendegrass, C., and Blunn, G. (2013). Use of ITAP implants for prosthetic reconstruction of extra-oral craniofacial defects. *J. Plast. Reconstr. Aesthet. Surg.* 66, 497–505. doi: 10.1016/j.bjps.2012.11.036

Kang, N. V., Pendegrass, C., Marks, L., and Blunn, G. (2010). Osseocutaneous integration of an intraosseous transcutaneous amputation prosthesis implant used for reconstruction of a transhumeral amputee: case report. *J. Hand Surg. Am.* 35, 1130–1134. doi: 10.1016/j.jhsa.2010.03.037

Karlin, W. M., Stewart, A. A., Durgam, S. S., Naughton, J. F., O'dell-Anderson, K. J., and Stewart, M. C. (2011). Evaluation of experimentally induced injury to the superficial digital flexor tendon in horses by use of low-field magnetic resonance imaging and ultrasonography. *Am. J. Vet. Res.* 72, 791–798. doi: 10.2460/ajvr.72.6.791

Kim, B. E., Nevitt, T., and Thiele, D. J. (2008). Mechanisms for copper acquisition, distribution and regulation. *Nat. Chem. Biol.* 4, 176–185. doi: 10.1038/nchembio.72

Kim, H. K., Moran, M. E., and Salter, R. B. (1991). The potential for regeneration of articular cartilage in defects created by chondral shaving and subchondral abrasion. An experimental investigation in rabbits. *J. Bone Joint Surg. Am.* 73, 1301–1315. doi: 10.2106/00004623-199173090-00004

Kim, J., Zanjani, E. D., Jeanblanc, C. M., Goodrich, A. D., and Hematti, P. (2013). Generation of CD34+ cells from human embryonic stem cells using a clinically applicable methodology and engraftment in the fetal sheep model. *Exp. Hematol.* 41, 749–758.e5. doi: 10.1016/j.exphem.2013.04.003

Kirschvink, N., and Reinhold, P. (2008). Use of alternative animals as asthma models. *Curr. Drug Targets* 9, 470–484. doi: 10.2174/138945008784533525

Kisiday, J. D., Mcilwraith, C. W., Rodkey, W. G., Frisbie, D. D., and Steadman, J. R. (2012). Effects of platelet-rich plasma composition on anabolic and catabolic activities in equine cartilage and meniscal explants. *Cartilage* 3, 245–254. doi: 10.1177/1947603511433181

Kluin, J., Talacua, H., Smits, A. I., Emmert, M. Y., Brugmans, M. C., Fioretta, E. S., et al. (2017). In situ heart valve tissue engineering using a bioresorbable elastomeric implant - From material design to 12 months follow-up in sheep. *Biomaterials* 125, 101–117. doi: 10.1016/j.biomaterials.2017.02.007

Klukowska-Rotzler, J., Swinburne, J. E., Drogemuller, C., Dolf, G., Janda, J., Leeb, T., et al. (2012). The interleukin 4 receptor gene and its role in recurrent airway obstruction in Swiss Warmblood horses. *Anim. Genet.* 43, 450–453. doi: 10.1111/j.1365-2052.2011.02277.x

Klymiuk, N., Blutke, A., Graf, A., Krause, S., Burkhardt, K., Wuensch, A., et al. (2013). Dystrophin-deficient pigs provide new insights into the hierarchy of physiological derangements of dystrophic muscle. *Hum. Mol. Genet.* 22, 4368–4382. doi: 10.1093/hmg/ddt287

Kocyildirim, E., Cardenes, N., Ting, A., Caceres, E., Bermudez, C., and Rojas, M. (2017). The use of GMP-produced bone marrow-derived stem cells in combination with extracorporeal membrane oxygenation in ARDS: an animal model. *ASAIO J.* 63, 324–332. doi: 10.1097/mat.0000000000000566

Kol, A., Arzi, B., Athanasiou, K. A., Farmer, D. L., Nolta, J. A., Rebhun, R. B., et al. (2015). Companion animals: translational scientist's new best friends. *Sci. Transl. Med.* 7:308s21.

Kon, E., Muraglia, A., Corsi, A., Bianco, P., Marcacci, M., Martin, I., et al. (2000). Autologous bone marrow stromal cells loaded onto porous hydroxyapatite ceramic accelerate bone repair in critical-size defects of sheep long bones. *J. Biomed. Mater. Res.* 49, 328–337. doi: 10.1002/(sici)1097-4636(20000305)49:3<328::aid-jbm5>3.0.co;2-q

Koobatian, M. T., Row, S., Smith, R. J. Jr., Koenigsknecht, C., Andreadis, S. T., and Swartz, D. D. (2016). Successful endothelialization and remodeling of a cell-free small-diameter arterial graft in a large animal model. *Biomaterials* 76, 344–358. doi: 10.1016/j.biomaterials.2015.10.020

Krupkova, O., Smolders, L., Wuertz-Kozak, K., Cook, J., and Pozzi, A. (2018). The pathobiology of the meniscus: a comparison between the human and dog. *Front. Vet. Sci.* 5:73. doi: 10.3389/fvets.2018.00073

Kuroki, K., Cook, C. R., and Cook, J. L. (2011). Subchondral bone changes in three different canine models of osteoarthritis. *Osteoarthritis Cartilage* 19, 1142–1149. doi: 10.1016/j.joca.2011.06.007

Kuyinu, E. L., Narayanan, G., Nair, L. S., and Laurencin, C. T. (2016). Animal models of osteoarthritis: classification, update, and measurement of outcomes. *J. Orthop. Surg. Res.* 11:19.

Kuypers, E., Ophelders, D., Jellema, R. K., Kunzmann, S., Gavilanes, A. W., and Kramer, B. W. (2012). White matter injury following fetal inflammatory response syndrome induced by chorioamnionitis and fetal sepsis: lessons from experimental ovine models. *Early Hum. Dev.* 88, 931–936. doi: 10.1016/j.earlhumdev.2012.09.011

Lacitignola, L., Crovace, A., Rossi, G., and Francioso, E. (2008). Cell therapy for tendinitis, experimental and clinical report. *Vet. Res. Commun.* 32(Suppl. 1), S33–S38.

Lai, L., Kolber-Simonds, D., Park, K. W., Cheong, H. T., Greenstein, J. L., Im, G. S., et al. (2002). Production of alpha-1,3-galactosyltransferase knockout pigs by nuclear transfer cloning. *Science* 295, 1089–1092. doi: 10.1126/science.1068228

Lairmore, M. D., and Khanna, C. (2014). Naturally occurring diseases in animals: contributions to translational medicine. *ILAR J.* 55, 1–3. doi: 10.1093/ilar/ilu022

Lampropoulou-Adamidou, K., Lelovas, P., Karadimas, E. V., Liakou, C., Triantafillopoulos, I. K., Dontas, I., et al. (2014). Useful animal models for the research of osteoarthritis. *Eur. J. Orthop. Surg. Traumatol.* 24, 263–271.

Lange-Consiglio, A., Stucchi, L., Zucca, E., Lavoie, J. P., Cremonesi, F., and Ferrucci, F. (2019). Insights into animal models for cell-based therapies in translational studies of lung diseases: Is the horse with naturally occurring asthma the right choice? *Cytotherapy* 21, 525–534. doi: 10.1016/j.jcyt.2019.02.010

Larson, G., Karlsson, E. K., Perri, A., Webster, M. T., Ho, S. Y., Peters, J., et al. (2012). Rethinking dog domestication by integrating genetics, archeology, and biogeography. *Proc. Natl. Acad. Sci. U.S.A.* 109, 8878–8883. doi: 10.1073/pnas.1203005109

Lavoie, J. P., Maghni, K., Desnoyers, M., Taha, R., Martin, J. G., and Hamid, Q. A. (2001). Neutrophilic airway inflammation in horses with heaves is characterized by a Th2-type cytokine profile. *Am. J. Respir. Crit. Care Med.* 164, 1410–1413. doi: 10.1164/ajrccm.164.8.2012091

Leclere, M., Lavoie-Lamoureux, A., Gelinas-Lymburner, E., David, F., Martin, J. G., and Lavoie, J. P. (2011). Effect of antigenic exposure on airway smooth muscle remodeling in an equine model of chronic asthma. *Am. J. Respir. Cell Mol. Biol.* 45, 181–187. doi: 10.1165/rcmb.2010-0300oc

Lelovas, P. P., Xanthos, T. T., Thoma, S. E., Lyritis, G. P., and Dontas, I. A. (2008). The laboratory rat as an animal model for osteoporosis research. *Comp. Med.* 58, 424–430.

Li, T. S., Cheng, K., Malliaras, K., Smith, R. R., Zhang, Y., Sun, B., et al. (2012). Direct comparison of different stem cell types and subpopulations reveals superior paracrine potency and myocardial repair efficacy with cardiosphere-derived cells. *J. Am. Coll. Cardiol.* 59, 942–953. doi: 10.1016/j.jacc.2011.11.029

Li, Y., Chen, S. K., Li, L., Qin, L., Wang, X. L., and Lai, Y. X. (2015). Bone defect animal models for testing efficacy of bone substitute biomaterials. *J. Orthop. Transl.* 3, 95–104. doi: 10.1016/j.jot.2015.05.002

Liebsch, C., Bucan, V., Menger, B., Kohne, F., Waldmann, K. H., Vaslaitis, D., et al. (2018). Preliminary investigations of spider silk in wounds *in vivo* - Implications for an innovative wound dressing. *Burns* 44, 1829–1838. doi: 10.1016/j.burns.2018.03.016

Liechty, K. W., Mackenzie, T. C., Shaaban, A. F., Radu, A., Moseley, A. M., Deans, R., et al. (2000). Human mesenchymal stem cells engraft and demonstrate site-specific differentiation after in utero transplantation in sheep. *Nat. Med.* 6, 1282–1286. doi: 10.1038/81395

Lindblad-Toh, K., Wade, C. M., Mikkelsen, T. S., Karlsson, E. K., Jaffe, D. B., Kamal, M., et al. (2005). Genome sequence, comparative analysis and haplotype structure of the domestic dog. *Nature* 438, 803–819.

Little, C. B., and Hunter, D. J. (2013). Post-traumatic osteoarthritis: from mouse models to clinical trials. *Nat. Rev. Rheumatol.* 9, 485–497. doi: 10.1038/nrrheum.2013.72

Little, C. B., and Zaki, S. (2012). What constitutes an "animal model of osteoarthritis"–the need for consensus? *Osteoarthritis Cartilage* 20, 261–267. doi: 10.1016/j.joca.2012.01.017

Liu, J. Z., Van Sommeren, S., Huang, H., Ng, S. C., Alberts, R., Takahashi, A., et al. (2015). Association analyses identify 38 susceptibility loci for inflammatory bowel disease and highlight shared genetic risk across populations. *Nat. Genet.* 47, 979–986. doi: 10.1038/ng.3359

Lizarraga, I., and Chambers, J. P. (2012). Use of analgesic drugs for pain management in sheep. *N. Z. Vet. J.* 60, 87–94. doi: 10.1080/00480169.2011.642772

Lo Monaco, M., Merckx, G., Ratajczak, J., Gervois, P., Hilkens, P., Clegg, P., et al. (2018). Stem cells for cartilage repair: preclinical studies and insights in translational animal models and outcome measures. *Stem Cells Int.* 2018:9079538.

Lorbach, O., Baums, M. H., Kostuj, T., Pauly, S., Scheibel, M., Carr, A., et al. (2015). Advances in biology and mechanics of rotator cuff repair. *Knee Surg. Sports Traumatol. Arthrosc.* 23, 530–541.

Lovicu, M., Dessi, V., Lepori, M. B., Zappu, A., Zancan, L., Giacchino, R., et al. (2006). The canine copper toxicosis gene Murr1 is not implicated in the pathogenesis of Wilson disease. *J. Gastroenterol.* 41, 582–587. doi: 10.1007/s00535-006-1807-0

Madden, J. C., Hewitt, M., Przybylak, K., Vandebriel, R. J., Piersma, A. H., and Cronin, M. T. (2012). Strategies for the optimisation of *in vivo* experiments in accordance with the 3Rs philosophy. *Regul. Toxicol. Pharmacol.* 63, 140–154. doi: 10.1016/j.yrtph.2012.03.010

Maffulli, N. (1999). Rupture of the Achilles tendon. *J. Bone Joint. Surg. Am.* 81, 1019–1036.

Maher, R. L., Barbash, S. M., Lynch, D. V., and Swoap, S. J. (2015). Group housing and nest building only slightly ameliorate the cold stress of typical housing in female C57bl/6J mice. *Am. J. Physiol. Regul. Integr. Comp. Physiol.* 308, R1070–R1079.

Makkar, R. R., Smith, R. R., Cheng, K., Malliaras, K., Thomson, L. E., Berman, D., et al. (2012). Intracoronary cardiosphere-derived cells for heart regeneration after myocardial infarction (CADUCEUS): a prospective, randomised phase 1 trial. *Lancet* 379, 895–904. doi: 10.1016/s0140-6736(12)60195-0

Malda, J., Benders, K. E., Klein, T. J., De Grauw, J. C., Kik, M. J., Hutmacher, D. W., et al. (2012). Comparative study of depth-dependent characteristics of equine and human osteochondral tissue from the medial and lateral femoral condyles. *Osteoarthritis Cartilage* 20, 1147–1151. doi: 10.1016/j.joca.2012.06.005

Malliaras, K., Li, T. S., Luthringer, D., Terrovitis, J., Cheng, K., Chakravarty, T., et al. (2012). Safety and efficacy of allogeneic cell therapy in infarcted rats transplanted with mismatched cardiosphere-derived cells. *Circulation* 125, 100–112. doi: 10.1161/circulationaha.111.042598

Malliaras, K., Makkar, R. R., Smith, R. R., Cheng, K., Wu, E., Bonow, R. O., et al. (2014). Intracoronary cardiosphere-derived cells after myocardial infarction: evidence of therapeutic regeneration in the final 1-year results of the CADUCEUS trial (CArdiosphere-Derived aUtologous stem CElls to reverse ventricUlar dySfunction). *J. Am. Coll. Cardiol.* 63, 110–122.

Marfe, G., Rotta, G., De Martino, L., Tafani, M., Fiorito, F., Di Stefano, C., et al. (2012). A new clinical approach: use of blood-derived stem cells (BDSCs) for superficial digital flexor tendon injuries in horses. *Life Sci.* 90, 825–830. doi: 10.1016/j.lfs.2012.03.004

Marijnissen, A. C., Van Roermund, P. M., Tekoppele, J. M., Bijlsma, J. W., and Lafeber, F. P. (2002). The canine 'groove' model, compared with the ACLT model of osteoarthritis. *Osteoarthritis Cartilage* 10, 145–155. doi: 10.1053/joca.2001.0491

Mariscal, A., Caldarone, L., Tikkanen, J., Nakajima, D., Chen, M., Yeung, J., et al. (2018). Pig lung transplant survival model. *Nat. Protoc.* 13, 1814–1828. doi: 10.1038/s41596-018-0019-4

Marlovits, S., Singer, P., Zeller, P., Mandl, I., Haller, J., and Trattnig, S. (2006). Magnetic resonance observation of cartilage repair tissue (MOCART) for the evaluation of autologous chondrocyte transplantation: determination of interobserver variability and correlation to clinical outcome after 2 years. *Eur. J. Radiol.* 57, 16–23. doi: 10.1016/j.ejrad.2005.08.007

Maron, B. J., and Fox, P. R. (2015). Hypertrophic cardiomyopathy in man and cats. *J. Vet. Cardiol.* 17(Suppl. 1), S6–S9.

Maron, B. J., Gardin, J. M., Flack, J. M., Gidding, S. S., Kurosaki, T. T., and Bild, D. E. (1995). Prevalence of hypertrophic cardiomyopathy in a general population of young adults. *Echocardiographic analysis of* 4111 subjects in the CARDIA Study. Coronary Artery Risk Development in (Young) Adults. *Circulation* 92, 785–789. doi: 10.1161/01.cir.92.4.785

Marston, S. B. (2011). How do mutations in contractile proteins cause the primary familial cardiomyopathies? *J. Cardiovasc. Transl. Res.* 4, 245–255. doi: 10.1007/s12265-011-9266-2

Martin, J., Sarai, K., Yoshitake, M., Haberstroh, J., Takahashi, N., Lutter, G., et al. (1999). Successful orthotopic pig heart transplantation from non-heart-beating donors. *J. Heart Lung Transplant.* 18, 597–606. doi: 10.1016/s1053-2498(98)00017-5

Martinello, T., Bronzini, I., Perazzi, A., Testoni, S., De Benedictis, G. M., Negro, A., et al. (2013). Effects of *in vivo* applications of peripheral blood-derived mesenchymal stromal cells (PB-MSCs) and platlet-rich plasma (PRP) on experimentally injured deep digital flexor tendons of sheep. *J. Orthop. Res.* 31, 306–314. doi: 10.1002/jor.22205

Martinello, T., Gomiero, C., Perazzi, A., Iacopetti, I., Gemignani, F., DeBenedictis, G. M., et al. (2018). Allogeneic mesenchymal stem cells improve the wound healing process of sheep skin. *BMC Vet. Res.* 14, 1–9. doi: 10.1186/s12917-018-1527-8

Martines, E., Brun, P., Cavazzana, R., Cordaro, L., Zuin, M., Martinello, T., et al. (2020). Wound healing improvement in large animals using an indirect helium plasma treatment. *Clin. Plasma Med.* 17-18:100095. doi: 10.1016/j.cpme.2020.100095

Marubayashi, S., Asahara, T., Ono, E., Tashiro, H., Okugawa, K., Okimoto, T., et al. (1995). Auxiliary heterotopic partial liver transplantation in pigs with acute liver failure. *Surg. Today* 25, 429–432. doi: 10.1007/bf00311820

Matsuyama, T., Midha, R., Mackinnon, S. E., Munro, C. A., Wong, P. Y., and Ang, L. C. (2000). Long nerve allografts in sheep with Cyclosporin A immunosuppression. *J. Reconstr. Microsurg.* 16, 219–225.

Mausberg, T. B., Wess, G., Simak, J., Keller, L., Drogemuller, M., Drogemuller, C., et al. (2011). A locus on chromosome 5 is associated with dilated cardiomyopathy in Doberman Pinschers. *PLoS One* 6:e20042. doi: 10.1371/journal.pone.0020042

Mazzone, L., Moehrlen, U., Ochsenbein-Kolble, N., Pontiggia, L., Biedermann, T., Reichmann, E., et al. (2020). Bioengineering and in utero transplantation of fetal skin in the sheep model: a crucial step towards clinical application in human fetal spina bifida repair. *J. Tissue Eng. Regen. Med.* 14, 58–65. doi: 10.1002/term.2963

Mcanulty, P., Dayan, A., Ganderup, N.-C., Hastings, K., Turk, J., and Laughlin, M. (2011). *The Minipig in Biomedical Research*. Boca Raton, FL: Taylor & Francis.

Mccoy, A. M. (2015). Animal models of osteoarthritis: comparisons and key considerations. *Vet. Pathol.* 52, 803–818. doi: 10.1177/0300985815588611

Mcduffee, L. A., Pack, L., Lores, M., Wright, G. M., Esparza-Gonzalez, B., and Masaoud, E. (2012). Osteoprogenitor cell therapy in an equine fracture model. *Vet. Surg.* 41, 773–783. doi: 10.1111/j.1532-950x.2012.01024.x

Mcgovern, J. A., Griffin, M., and Hutmacher, D. W. (2018). Animal models for bone tissue engineering and modelling disease. *Dis. Model. Mech.* 11:dmm033084. doi: 10.1242/dmm.033084

Mcilwraith, C. W., Fortier, L. A., Frisbie, D. D., and Nixon, A. J. (2011). Equine Models of Articular Cartilage Repair. *Cartilage* 2, 317–326. doi: 10.1177/1947603511406531

Mcilwraith, C. W., Frisbie, D. D., and Kawcak, C. E. (2012). The horse as a model of naturally occurring osteoarthritis. *Bone Joint Res.* 1, 297–309. doi: 10.1302/2046-3758.111.2000132

Mcilwraith, C. W., Frisbie, D. D., Kawcak, C. E., Fuller, C. J., Hurtig, M., and Cruz, A. (2010). The OARSI histopathology initiative - recommendations for histological assessments of osteoarthritis in the horse. *Osteoarthritis Cartilage* 18(Suppl. 3), S93–S105.

Mclure, S. W., Fisher, J., Conaghan, P. G., and Williams, S. (2012). Regional cartilage properties of three quadruped tibiofemoral joints used in musculoskeletal research studies. *Proc. Inst. Mech. Eng. H* 226, 652–656. doi: 10.1177/0954411912447158

Meeusen, E. N., Snibson, K. J., Hirst, S. J., and Bischof, R. J. (2009). Sheep as a model species for the study and treatment of human asthma and other respiratory diseases. *Drug Discov. Today Dis. Model.* 6, 101–106. doi: 10.1016/j.ddmod.2009.12.002

Meng, X., Ziadlou, R., Grad, S., Alini, M., Wen, C., Lai, Y., et al. (2020). Animal models of osteochondral defect for testing biomaterials. *Biochem Res. Int.* 2020:9659412.

Messer, A. E., Chan, J., Daley, A., Copeland, O., Marston, S. B., and Connolly, D. J. (2017). Investigations into the sarcomeric protein and Ca(2+)-regulation abnormalities underlying hypertrophic cardiomyopathy in cats (*Felix catus*). *Front. Physiol.* 8:348. doi: 10.3389/fphys.2017.00348

Meurs, K. M., Lahmers, S., Keene, B. W., White, S. N., Oyama, M. A., Mauceli, E., et al. (2012). A splice site mutation in a gene encoding for PDK4, a mitochondrial protein, is associated with the development of dilated cardiomyopathy in the Doberman pinscher. *Hum. Genet.* 131, 1319–1325. doi: 10.1007/s00439-012-1158-2

Meurs, K. M., Mauceli, E., Lahmers, S., Acland, G. M., White, S. N., and Lindblad-Toh, K. (2010). Genome-wide association identifies a deletion in the 3' untranslated region of striatin in a canine model of arrhythmogenic right ventricular cardiomyopathy. *Hum. Genet.* 128, 315–324. doi: 10.1007/s00439-010-0855-y

Meurs, K. M., Norgard, M. M., Ederer, M. M., Hendrix, K. P., and Kittleson, M. D. (2007). A substitution mutation in the myosin binding protein C gene in ragdoll hypertrophic cardiomyopathy. *Genomics* 90, 261–264. doi: 10.1016/j.ygeno.2007.04.007

Meurs, K. M., Sanchez, X., David, R. M., Bowles, N. E., Towbin, J. A., Reiser, P. J., et al. (2005). A cardiac myosin binding protein C mutation in the Maine Coon cat with familial hypertrophic cardiomyopathy. *Hum. Mol. Genet.* 14, 3587–3593. doi: 10.1093/hmg/ddi386

Meurs, K. M., Stern, J. A., Reina-Doreste, Y., Spier, A. W., Koplitz, S. L., and Baumwart, R. D. (2014). Natural history of arrhythmogenic right ventricular cardiomyopathy in the boxer dog: a prospective study. *J. Vet. Intern. Med.* 28, 1214–1220. doi: 10.1111/jvim.12385

Mienaltowski, M. J., Dunkman, A. A., Buckley, M. R., Beason, D. P., Adams, S. M., Birk, D. E., et al. (2016). Injury response of geriatric mouse patellar tendons. *J. Orthop. Res.* 34, 1256–1263. doi: 10.1002/jor.23144

Milner, P. I., Clegg, P. D., and Stewart, M. C. (2011). Stem cell-based therapies for bone repair. *Vet. Clin. North Am. Equine Pract.* 27, 299–314.

Mitra, A., Leyes, A., Manser, K., Roadcap, B., Mestre, C., Tatosian, D., et al. (2015). Use of minipig skin biopsy model as an innovative tool to design topical formulation to achieve desired pharmacokinetics in humans. *J. Pharm. Sci.* 104, 1701–1708. doi: 10.1002/jps.24383

Moezzi, L., Pourfathollah, A. A., Alimoghaddam, K., Soleimani, M., and Ardjmand, A. R. (2005). The effect of cryopreservation on clonogenic capacity and *in vitro* expansion potential of umbilical cord blood progenitor cells. *Transplant. Proc.* 37, 4500–4503. doi: 10.1016/j.transproceed.2005.10.107

Moraes, J. R., Facco, G. G., Moraes, F. R., Engracia Filho, J. R., Miyazato, L. G., and Beretta, D. C. (2009). Effects of glycosaminoglycan polysulphate on the

organisation of collagen fibres in experimentally induced tendonitis in horses. *Vet. Rec.* 165, 203–205. doi: 10.1136/vr.165.7.203

Moran, C. J., Ramesh, A., Brama, P. A., O'byrne, J. M., O'brien, F. J., and Levingstone, T. J. (2016). The benefits and limitations of animal models for translational research in cartilage repair. *J. Exp. Orthop.* 3:1.

Morris, M. W. Jr., Allukian, M. III, Herdrich, B. J., Caskey, R. C., Zgheib, C., Xu, J., et al. (2014). Modulation of the inflammatory response by increasing fetal wound size or interleukin-10 overexpression determines wound phenotype and scar formation. *Wound Repair Regen.* 22, 406–414. doi: 10.1111/wrr.12180

Morrison, J. L., Berry, M. J., Botting, K. J., Darby, J. R. T., Frasch, M. G., Gatford, K. L., et al. (2018). Improving pregnancy outcomes in humans through studies in sheep. *Am. J. Physiol. Regul. Integr. Comp. Physiol.* 315, R1123–R1153.

Mosqueira, D., Mannhardt, I., Bhagwan, J. R., Lis-Slimak, K., Katili, P., Scott, E., et al. (2018). CRISPR/Cas9 editing in human pluripotent stem cell-cardiomyocytes highlights arrhythmias, hypocontractility, and energy depletion as potential therapeutic targets for hypertrophic cardiomyopathy. *Eur. Heart J.* 39, 3879–3892. doi: 10.1093/eurheartj/ehy249

Moss, T. J., Knox, C. L., Kallapur, S. G., Nitsos, I., Theodoropoulos, C., Newnham, J. P., et al. (2008). Experimental amniotic fluid infection in sheep: effects of *Ureaplasma parvum* serovars 3 and 6 on preterm or term fetal sheep. *Am. J. Obstet. Gynecol.* 198, 122.e1–122.e8. doi: 10.1016/j.ajog.2007.06.065

Muller, T., Feichtinger, H., Berger, H., and Muller, W. (1996). Endemic Tyrolean infantile cirrhosis: an ecogenetic disorder. *Lancet* 347, 877–880. doi: 10.1016/s0140-6736(96)91351-3

Murayama, N., Kaneko, N., Horiuchi, K., Ohyama, K., Shimizu, M., Ito, K., et al. (2009). Cytochrome P450-dependent drug oxidation activity of liver microsomes from Microminipigs, a possible new animal model for humans in non-clinical studies. *Drug Metab. Pharmacokinet.* 24, 404–408. doi: 10.2133/dmpk.24.404

Murphy, M. K., Arzi, B., Hu, J. C., and Athanasiou, K. A. (2013). Tensile characterization of porcine temporomandibular joint disc attachments. *J. Dent. Res.* 92, 753–758. doi: 10.1177/0022034513494817

Music, E., Futrega, K., and Doran, M. R. (2018). Sheep as a model for evaluating mesenchymal stem/stromal cell (Msc)-based chondral defect repair. *Osteoarthritis Cartilage* 26, 730–740. doi: 10.1016/j.joca.2018.03.006

Muttini, A., Russo, V., Rossi, E., Mattioli, M., Barboni, B., Tosi, U., et al. (2015). Pilot experimental study on amniotic epithelial mesenchymal cell transplantation in natural occurring tendinopathy in horses. Ultrasonographic and histological comparison. *Muscles Ligaments Tendons J.* 5, 5–11.

Nadal-Ginard, B., Kajstura, J., Leri, A., and Anversa, P. (2003). Myocyte death, growth, and regeneration in cardiac hypertrophy and failure. *Circ. Res.* 92, 139–150. doi: 10.1161/01.res.0000053618.86362.df

Namba, R. S., Meuli, M., Sullivan, K. M., Le, A. X., and Adzick, N. S. (1998). Spontaneous repair of superficial defects in articular cartilage in a fetal lamb model. *J. Bone Joint Surg. Am.* 80, 4–10. doi: 10.2106/00004623-199801000-00003

Nelson, T. E. (1990). Porcine malignant hyperthermia: critical temperatures for *in vivo* and *in vitro* responses. *Anesthesiology* 73, 449–454. doi: 10.1097/00000542-199009000-00013

Newman, E., Turner, A. S., and Wark, J. D. (1995). The potential of sheep for the study of osteopenia: current status and comparison with other animal models. *Bone* 16, 277s–284s. doi: 10.1016/8756-3282(95)00026-a

Nitsos, I., Rees, S. M., Duncan, J., Kramer, B. W., Harding, R., Newnham, J. P., et al. (2006). Chronic exposure to intra-amniotic lipopolysaccharide affects the ovine fetal brain. *J. Soc. Gynecol. Investig.* 13, 239–247. doi: 10.1016/j.jsgi.2006.02.011

Niu, D., Wei, H. J., Lin, L., George, H., Wang, T., Lee, I. H., et al. (2017). Inactivation of porcine endogenous retrovirus in pigs using CRISPR-Cas9. *Science* 357, 1303–1307. doi: 10.1126/science.aan4187

Nixon, A. J., Dahlgren, L. A., Haupt, J. L., Yeager, A. E., and Ward, D. L. (2008). Effect of adipose-derived nucleated cell fractions on tendon repair in horses with collagenase-induced tendinitis. *Am. J. Vet. Res.* 69, 928–937. doi: 10.2460/ajvr.69.7.928

Oakley, S. P., Lassere, M. N., Portek, I., Szomor, Z., Ghosh, P., Kirkham, B. W., et al. (2004). Biomechanical, histologic and macroscopic assessment of articular cartilage in a sheep model of osteoarthritis. *Osteoarthritis Cartilage* 12, 667–679. doi: 10.1016/j.joca.2004.05.006

Okada, Y., Wu, D., Trynka, G., Raj, T., Terao, C., Ikari, K., et al. (2014). Genetics of rheumatoid arthritis contributes to biology and drug discovery. *Nature* 506, 376–381.

O'leary, S. A., Link, J. M., Klineberg, E. O., Hu, J. C., and Athanasiou, K. A. (2017). Characterization of facet joint cartilage properties in the human and interspecies comparisons. *Acta Biomater.* 54, 367–376. doi: 10.1016/j.actbio.2017.03.017

Orsini, J. A. (2012). Supporting limb laminitis: the four important 'whys'. *Equine Vet. J.* 44, 741–745. doi: 10.1111/j.2042-3306.2012.00662.x

Pacini, S., Spinabella, S., Trombi, L., Fazzi, R., Galimberti, S., Dini, F., et al. (2007). Suspension of bone marrow-derived undifferentiated mesenchymal stromal cells for repair of superficial digital flexor tendon in race horses. *Tissue Eng.* 13, 2949–2955. doi: 10.1089/ten.2007.0108

Panettieri, R. A. Jr. (2016). Neutrophilic and Pauci-immune Phenotypes in Severe Asthma. *Immunol. Allergy Clin. North Am.* 36, 569–579. doi: 10.1016/j.iac.2016.03.007

Parker, H. G., Shearin, A. L., and Ostrander, E. A. (2010). Man's best friend becomes biology's best in show: genome analyses in the domestic dog. *Annu. Rev. Genet.* 44, 309–336. doi: 10.1146/annurev-genet-102808-115200

Patterson-Kane, J. C., and Firth, E. C. (2009). The pathobiology of exercise-induced superficial digital flexor tendon injury in Thoroughbred racehorses. *Vet. J.* 181, 79–89. doi: 10.1016/j.tvjl.2008.02.009

Payne, J., Luis Fuentes, V., Boswood, A., Connolly, D., Koffas, H., and Brodbelt, D. (2010). Population characteristics and survival in 127 referred cats with hypertrophic cardiomyopathy (1997 to 2005). *J. Small Anim. Pract.* 51, 540–547. doi: 10.1111/j.1748-5827.2010.00989.x

Pearce, A. I., Richards, R. G., Milz, S., Schneider, E., and Pearce, S. G. (2007). Animal models for implant biomaterial research in bone: a review. *Eur. Cell Mater.* 13, 1–10. doi: 10.22203/ecm.v013a01

Pedersen, R., Andersen, A. D., Molbak, L., Stagsted, J., and Boye, M. (2013a). Changes in the gut microbiota of cloned and non-cloned control pigs during development of obesity: gut microbiota during development of obesity in cloned pigs. *BMC Microbiol.* 13:30. doi: 10.1186/1471-2180-13-30

Pedersen, R., Ingerslev, H. C., Sturek, M., Alloosh, M., Cirera, S., Christoffersen, B. O., et al. (2013b). Characterisation of gut microbiota in Ossabaw and Gottingen minipigs as models of obesity and metabolic syndrome. *PLoS One* 8:e56612. doi: 10.1371/journal.pone.0056612

Perleberg, C., Kind, A., and Schnieke, A. (2018). Genetically engineered pigs as models for human disease. *Dis. Model. Mech.* 11:dmm030783. doi: 10.1242/dmm.030783

Petersen, B., Ramackers, W., Lucas-Hahn, A., Lemme, E., Hassel, P., Queisser, A. L., et al. (2011). Transgenic expression of human heme oxygenase-1 in pigs confers resistance against xenograft rejection during *ex vivo* perfusion of porcine kidneys. *Xenotransplantation* 18, 355–368. doi: 10.1111/j.1399-3089.2011.00674.x

Phelps, C. J., Koike, C., Vaught, T. D., Boone, J., Wells, K. D., Chen, S. H., et al. (2003). Production of alpha 1,3-galactosyltransferase-deficient pigs. *Science* 299, 411–414. doi: 10.1126/science.1078942

Pinnapureddy, A. R., Stayner, C., Mcewan, J., Baddeley, O., Forman, J., and Eccles, M. R. (2015). Large animal models of rare genetic disorders: sheep as phenotypically relevant models of human genetic disease. *Orphanet J. Rare Dis.* 10:107.

Pobloth, A. M., Schell, H., Petersen, A., Beierlein, K., Kleber, C., Schmidt-Bleek, K., et al. (2018). Tubular open-porous beta-tricalcium phosphate polycaprolactone scaffolds as guiding structure for segmental bone defect regeneration in a novel sheep model. *J. Tissue Eng. Regen. Med.* 12, 897–911. doi: 10.1002/term.2446

Pogue, B., Estrada, A. H., Sosa-Samper, I., Maisenbacher, H. W., Lamb, K. E., Mincey, B. D., et al. (2013). Stem-cell therapy for dilated cardiomyopathy: a pilot study evaluating retrograde coronary venous delivery. *J. Small Anim. Pract.* 54, 361–366. doi: 10.1111/jsap.12098

Polejaeva, I. A., Rutigliano, H. M., and Wells, K. D. (2016). Livestock in biomedical research: history, current status and future prospective. *Reprod. Fertil. Dev.* 28, 112–124.

Pond, M. J., and Nuki, G. (1973). Experimentally-induced osteoarthritis in the dog. *Ann. Rheum. Dis.* 32, 387–388. doi: 10.1136/ard.32.4.387

Poole, R., Blake, S., Buschmann, M., Goldring, S., Laverty, S., Lockwood, S., et al. (2010). Recommendations for the use of preclinical models in the study and treatment of osteoarthritis. *Osteoarthritis Cartilage* 18(Suppl. 3), S10–S16.

Porada, C. D., Park, P. J., Almeida-Porada, G., Liu, W., Ozturk, F., Glimp, H. A., et al. (2005). Gestational age of recipient determines pattern and level of transgene expression following in utero retroviral gene transfer. *Mol. Ther.* 11, 284–293. doi: 10.1016/j.ymthe.2004.09.009

Prabhakar, S. (2012). Translational research challenges: finding the right animal models. *J. Investig. Med.* 60, 1141–1146. doi: 10.2310/jim.0b013e318271fb3b

Price, J., Catriona, S., Welsh, E. M., and Waran, N. K. (2003). Preliminary evaluation of a behaviour-based system for assessment of post-operative pain in horses following arthroscopic surgery. *Vet. Anaesth. Analg.* 30, 124–137. doi: 10.1046/j.1467-2995.2003.00139.x

Proffen, B. L., Mcelfresh, M., Fleming, B. C., and Murray, M. M. (2012). A comparative anatomical study of the human knee and six animal species. *Knee* 19, 493–499. doi: 10.1016/j.knee.2011.07.005

Provost, P. J. (2019). "Wound healing," in *Equine Surgery*, 5th Edn, eds J. A. Auer, J. A. Stick, J. M. Kümmerle, and T. Prang (Amsterdam: Elsevier).

Rabbani, S., Soleimani, M., Sahebjam, M., Imani, M., Nassiri, S. M., Atashi, A., et al. (2017). Effects of endothelial and mesenchymal stem cells on improving myocardial function in a sheep animal model. *J. Tehran Heart Cent.* 12, 65–71.

Radtke, C., Allmeling, C., Waldmann, K. H., Reimers, K., Thies, K., Schenk, H. C., et al. (2011). Spider silk constructs enhance axonal regeneration and remyelination in long nerve defects in sheep. *PLoS One* 6:e16990. doi: 10.1371/journal.pone.0016990

Renzi, S., Ricco, S., Dotti, S., Sesso, L., Grolli, S., Cornali, M., et al. (2013). Autologous bone marrow mesenchymal stromal cells for regeneration of injured equine ligaments and tendons: a clinical report. *Res. Vet. Sci.* 95, 272–277. doi: 10.1016/j.rvsc.2013.01.017

Richardson, L. E., Dudhia, J., Clegg, P. D., and Smith, R. (2007). Stem cells in veterinary medicine–attempts at regenerating equine tendon after injury. *Trends Biotechnol.* 25, 409–416. doi: 10.1016/j.tibtech.2007.07.009

Ripoll Vera, T., Monserrat Iglesias, L., Hermida Prieto, M., Ortiz, M., Rodriguez Garcia, I., and Govea Callizo, N. (2010). The R820W mutation in the MYBPC3 gene, associated with hypertrophic cardiomyopathy in cats, causes hypertrophic cardiomyopathy and left ventricular non-compaction in humans. *Int. J. Cardiol.* 145, 405–407. doi: 10.1016/j.ijcard.2010.04.032

Robinson, P., Liu, X., Sparrow, A., Patel, S., Zhang, Y. H., Casadei, B., et al. (2018). Hypertrophic cardiomyopathy mutations increase myofilament Ca(2+) buffering, alter intracellular Ca(2+) handling, and stimulate Ca(2+)-dependent signaling. *J. Biol. Chem.* 293, 10487–10499. doi: 10.1074/jbc.ra118.002081

Rogers, C. S. (2016). Genetically engineered livestock for biomedical models. *Transgenic Res.* 25, 345–359. doi: 10.1007/s11248-016-9928-6

Rolauffs, B., Williams, J. M., Aurich, M., Grodzinsky, A. J., Kuettner, K. E., and Cole, A. A. (2010). Proliferative remodeling of the spatial organization of human superficial chondrocytes distant from focal early osteoarthritis. *Arthritis Rheum.* 62, 489–498.

Sachs, D. H., Sykes, M., and Yamada, K. (2009). Achieving tolerance in pig-to-primate xenotransplantation: reality or fantasy. *Transpl. Immunol.* 21, 101–105. doi: 10.1016/j.trim.2008.11.005

Sanjurjo-Rodriguez, C., Castro-Vinuelas, R., Hermida-Gomez, T., Fernandez-Vazquez, T., Fuentes-Boquete, I. M., De Toro-Santos, F. J., et al. (2017). Ovine mesenchymal stromal cells: morphologic, phenotypic and functional characterization for osteochondral tissue engineering. *PLoS One* 12:e0171231. doi: 10.1371/journal.pone.0171231

Sanz-Ramos, P., Duart, J., Rodriguez-Goni, M. V., Vicente-Pascual, M., Dotor, J., Mora, G., et al. (2014). Improved chondrogenic capacity of collagen hydrogel-expanded chondrocytes: *in vitro* and *in vivo* analyses. *J. Bone Joint Surg. Am.* 96, 1109–1117. doi: 10.2106/jbjs.m.00271

Sasaki-Honda, M., Jonouchi, T., Arai, M., Hotta, A., Mitsuhashi, S., Nishino, I., et al. (2018). A patient-derived iPSC model revealed oxidative stress increases facioscapulohumeral muscular dystrophy-causative DUX4. *Hum. Mol. Genet.* 27, 4024–4035. doi: 10.1093/hmg/ddy293

Sawyer, M., Moe, J., and Osburn, B. I. (1978). Ontogeny of immunity and leukocytes in the ovine fetus and elevation of immunoglobulins related to congenital infection. *Am. J. Vet. Res.* 39, 643–648.

Schagemann, J. C., Erggelet, C., Chung, H. W., Lahm, A., Kurz, H., and Mrosek, E. H. (2009). Cell-laden and cell-free biopolymer hydrogel for the treatment of osteochondral defects in a sheep model. *Tissue Eng. Part A* 15, 75–82. doi: 10.1089/ten.tea.2008.0087

Scharf, A., Holmes, S. P., Thoresen, M., Mumaw, J., Stumpf, A., and Peroni, J. (2016). MRI-based assessment of intralesional delivery of bone marrow-derived mesenchymal stem cells in a model of equine tendonitis. *Stem Cells Int.* 2016:8610964.

Scheerlinck, J. P., Snibson, K. J., Bowles, V. M., and Sutton, P. (2008). Biomedical applications of sheep models: from asthma to vaccines. *Trends Biotechnol.* 26, 259–266. doi: 10.1016/j.tibtech.2008.02.002

Scheinberg, I. H., and Sternlieb, I. (1996). Wilson disease and idiopathic copper toxicosis. *Am. J. Clin. Nutr.* 63, 842s–845s.

Schnabel, L. V., Lynch, M. E., Van Der Meulen, M. C., Yeager, A. E., Kornatowski, M. A., and Nixon, A. J. (2009). Mesenchymal stem cells and insulin-like growth factor-I gene-enhanced mesenchymal stem cells improve structural aspects of healing in equine flexor digitorum superficialis tendons. *J. Orthop. Res.* 27, 1392–1398. doi: 10.1002/jor.20887

Schnabel, L. V., Mohammed, H. O., Miller, B. J., Mcdermott, W. G., Jacobson, M. S., Santangelo, K. S., et al. (2007). Platelet rich plasma (PRP) enhances anabolic gene expression patterns in flexor digitorum superficialis tendons. *J. Orthop. Res.* 25, 230–240. doi: 10.1002/jor.20278

Schramme, M., Hunter, S., Campbell, N., Blikslager, A., and Smith, R. (2010). A surgical tendonitis model in horses: technique, clinical, ultrasonographic and histological characterisation. *Vet. Comp. Orthop. Traumatol.* 23, 231–239.

Segatto, N. V., Remiao, M. H., Schachtschneider, K. M., Seixas, F. K., Schook, L. B., and Collares, T. (2017). The oncopig cancer model as a complementary tool for phenotypic drug discovery. *Front. Pharmacol.* 8:894. doi: 10.3389/fphar.2017.00894

Semsarian, C., Ingles, J., Maron, M. S., and Maron, B. J. (2015). New perspectives on the prevalence of hypertrophic cardiomyopathy. *J. Am. Coll. Cardiol.* 65, 1249–1254.

Seo, J. P., Tsuzuki, N., Haneda, S., Yamada, K., Furuoka, H., Tabata, Y., et al. (2014). Osteoinductivity of gelatin/beta-tricalcium phosphate sponges loaded with different concentrations of mesenchymal stem cells and bone morphogenetic protein-2 in an equine bone defect model. *Vet. Res. Commun.* 38, 73–80. doi: 10.1007/s11259-013-9587-5

Shanks, N., Greek, R., and Greek, J. (2009). Are animal models predictive for humans? *Philos. Ethics Humanit. Med.* 4:2.

Shapiro, S. D. (2008). The use of transgenic mice for modeling airways disease. *Pulm. Pharmacol. Ther.* 21, 699–701. doi: 10.1016/j.pupt.2008.01.006

Sheehan, A., Messer, A. E., Papadaki, M., Choudhry, A., Kren, V., Biedermann, D., et al. (2018). Molecular defects in cardiac Myofilament Ca(2+)-regulation due to cardiomyopathy-linked mutations can be reversed by small molecules binding to troponin. *Front. Physiol.* 9:243. doi: 10.3389/fphys.2018.00243

Shinagawa, K., and Kojima, M. (2003). Mouse model of airway remodeling: strain differences. *Am. J. Respir. Crit. Care Med.* 168, 959–967. doi: 10.1164/rccm.200210-1188oc

Silverstein, A. M., Prendergast, R. A., and Kraner, K. L. (1964). Fetal response to antigenic stimulus. IV. Rejection of skin homografts by the fetal lamb. *J. Exp. Med.* 119, 955–964. doi: 10.1084/jem.119.6.955

Silverstein, A. M., Uhr, J. W., Kraner, K. L., and Lukes, R. J. (1963). Fetal response to antigenic stimulus. Ii. Antibody production by the fetal lamb. *J. Exp. Med.* 117, 799–812. doi: 10.1084/jem.117.5.799

Simoes, I. N., Vale, P., Soker, S., Atala, A., Keller, D., Noiva, R., et al. (2017). Acellular urethra bioscaffold: decellularization of whole urethras for tissue engineering applications. *Sci. Rep.* 7:41934.

Simpson, S., Edwards, J., Emes, R. D., Cobb, M. A., Mongan, N. P., and Rutland, C. S. (2015a). A predictive model for canine dilated cardiomyopathy-a meta-analysis of Doberman Pinscher data. *PeerJ* 3:e842. doi: 10.7717/peerj.842

Simpson, S., Edwards, J., Ferguson-Mignan, T. F., Cobb, M., Mongan, N. P., and Rutland, C. S. (2015b). Genetics of human and canine dilated cardiomyopathy. *Int. J. Genomics* 2015:204823.

Skaanild, M. T. (2006). Porcine cytochrome P450 and metabolism. *Curr. Pharm. Des.* 12, 1421–1427. doi: 10.2174/138161206776361183

Smith, R., Mcilwraith, W., Schweitzer, R., Kadler, K., Cook, J., Caterson, B., et al. (2014). Advances in the understanding of tendinopathies: a report on the Second Havemeyer Workshop on equine tendon disease. *Equine Vet. J.* 46, 4–9. doi: 10.1111/evj.12128

Smith, R. K. (2008). Mesenchymal stem cell therapy for equine tendinopathy. *Disabil. Rehabil.* 30, 1752–1758. doi: 10.1080/09638280701788241

Smith, R. K., Korda, M., Blunn, G. W., and Goodship, A. E. (2003). Isolation and implantation of autologous equine mesenchymal stem cells from bone marrow into the superficial digital flexor tendon as a potential novel treatment. *Equine Vet. J.* 35, 99–102. doi: 10.2746/042516403775467388

Smith, R. K., Werling, N. J., Dakin, S. G., Alam, R., Goodship, A. E., and Dudhia, J. (2013). Beneficial effects of autologous bone marrow-derived mesenchymal stem cells in naturally occurring tendinopathy. *PLoS One* 8:e75697. doi: 10.1371/journal.pone.0075697

Sole, A., Spriet, M., Galuppo, L. D., Padgett, K. A., Borjesson, D. L., Wisner, E. R., et al. (2012). Scintigraphic evaluation of intra-arterial and intravenous regional limb perfusion of allogeneic bone marrow-derived mesenchymal stem cells in the normal equine distal limb using (99m) Tc-HMPAO. *Equine Vet. J.* 44, 594–599. doi: 10.1111/j.2042-3306.2011.00530.x

Sole, A., Spriet, M., Padgett, K. A., Vaughan, B., Galuppo, L. D., Borjesson, D. L., et al. (2013). Distribution and persistence of technetium-99 hexamethyl propylene amine oxime-labelled bone marrow-derived mesenchymal stem cells in experimentally induced tendon lesions after intratendinous injection and regional perfusion of the equine distal limb. *Equine Vet. J.* 45, 726–731. doi: 10.1111/evj.12063

Song, F., Tang, J., Geng, R., Hu, H., Zhu, C., Cui, W., et al. (2014). Comparison of the efficacy of bone marrow mononuclear cells and bone mesenchymal stem cells in the treatment of osteoarthritis in a sheep model. *Int. J. Clin. Exp. Pathol.* 7, 1415–1426.

Song, W., Vikhorev, P. G., Kashyap, M. N., Rowlands, C., Ferenczi, M. A., Woledge, R. C., et al. (2013). Mechanical and energetic properties of papillary muscle from ACTC E99K transgenic mouse models of hypertrophic cardiomyopathy. *Am. J. Physiol. Heart Circ. Physiol.* 304, H1513–H1524.

Spetzler, V. N., Goldaracena, N., Knaak, J. M., Louis, K. S., Selzner, N., and Selzner, M. (2015). Technique of porcine liver procurement and orthotopic transplantation using an active porto-caval shunt. *J. Vis. Exp.* 99:e52055.

Spriet, M., Buerchler, S., Trela, J. M., Hembrooke, T. A., Padgett, K. A., Rick, M. C., et al. (2015). Scintigraphic tracking of mesenchymal stem cells after intravenous regional limb perfusion and subcutaneous administration in the standing horse. *Vet. Surg.* 44, 273–280. doi: 10.1111/j.1532-950x.2014.12289.x

Starritt, N. E., Kettle, S. A., and Glasby, M. A. (2011). Sutureless repair of the facial nerve using biodegradable glass fabric. *Laryngoscope* 121, 1614–1619. doi: 10.1002/lary.21868

Stramer, B. M., Mori, R., and Martin, P. (2007). The inflammation-fibrosis link? A Jekyll and Hyde role for blood cells during wound repair. *J. Invest. Dermatol.* 127, 1009–1017. doi: 10.1038/sj.jid.5700811

Stuehler, B., Reichert, J., Stremmel, W., and Schaefer, M. (2004). Analysis of the human homologue of the canine copper toxicosis gene Murr1 in Wilson disease patients. *J. Mol. Med.* 82, 629–634.

Sullivan, D. C., Mirmalek-Sani, S. H., Deegan, D. B., Baptista, P. M., Aboushwareb, T., Atala, A., et al. (2012). Decellularization methods of porcine kidneys for whole organ engineering using a high-throughput system. *Biomaterials* 33, 7756–7764. doi: 10.1016/j.biomaterials.2012.07.023

Sweigart, M. A., Zhu, C. F., Burt, D. M., Deholl, P. D., Agrawal, C. M., Clanton, T. O., et al. (2004). Intraspecies and interspecies comparison of the compressive properties of the medial meniscus. *Ann. Biomed. Eng.* 32, 1569–1579. doi: 10.1114/b:abme.0000049040.70767.5c

Swindle, M. M. (2007). *Swine in the Laboratory: Surgery, Anesthesia, Imaging, and Experimental Techniques*, 2nd Edn. Boca Raton, FL: CRC Press.

Swindle, M. M., Makin, A., Herron, A. J., Clubb, F. J. Jr., and Frazier, K. S. (2012). Swine as models in biomedical research and toxicology testing. *Vet. Pathol.* 49, 344–356. doi: 10.1177/0300985811402846

Tankersley, C. G., Fitzgerald, R. S., and Kleeberger, S. R. (1994). Differential control of ventilation among inbred strains of mice. *Am. J. Physiol.* 267, R1371–R1377.

Tanner, M. S. (1998). Role of copper in Indian childhood cirrhosis. *Am. J. Clin. Nutr.* 67, 1074s–1081s. doi: 10.1093/ajcn/67.5.1074s

Taylor, W. R., Ehrig, R. M., Heller, M. O., Schell, H., Seebeck, P., and Duda, G. N. (2006). Tibio-femoral joint contact forces in sheep. *J. Biomech.* 39, 791–798. doi: 10.1016/j.jbiomech.2005.02.006

Teeple, E., Jay, G. D., Elsaid, K. A., and Fleming, B. C. (2013). Animal models of osteoarthritis: challenges of model selection and analysis. *AAPS J.* 15, 438–446. doi: 10.1208/s12248-013-9454-x

Tellegen, A. R., Dessing, A. J., Houben, K., Riemers, F. M., Creemers, L. B., Mastbergen, S. C., et al. (2019). Dog as a model for osteoarthritis: the fgf4 retrogene insertion may matter. *J. Orthop. Res.* 37, 2550–2560. doi: 10.1002/jor.24432

Tellegen, A. R., Rudnik-Jansen, I., Beukers, M., Miranda-Bedate, A., Bach, F. C., De Jong, W., et al. (2018). Intradiscal delivery of celecoxib-loaded microspheres restores intervertebral disc integrity in a preclinical canine model. *J. Control. Release* 286, 439–450. doi: 10.1016/j.jconrel.2018.08.019

Thornburg, L. P. (1998). Histomorphological and immunohistochemical studies of chronic active hepatitis in Doberman Pinschers. *Vet. Pathol.* 35, 380–385. doi: 10.1177/030098589803500507

Thornburg, L. P., Rottinghaus, G., Dennis, G., and Crawford, S. (1996). The relationship between hepatic copper content and morphologic changes in the liver of West Highland White Terriers. *Vet. Pathol.* 33, 656–661. doi: 10.1177/030098589603300604

Thorpe, C. T., Clegg, P. D., and Birch, H. L. (2010). A review of tendon injury: why is the equine superficial digital flexor tendon most at risk? *Equine Vet. J.* 42, 174–180. doi: 10.2746/042516409x480395

Tidholm, A., and Jonsson, L. (2005). Histologic characterization of canine dilated cardiomyopathy. *Vet. Pathol.* 42, 1–8. doi: 10.1354/vp.42-1-1

Tompkins, D., Hudgens, E., Horohov, D., and Baldwin, C. L. (2010). Expressed gene sequences of the equine cytokines interleukin-17 and interleukin-23. *Vet. Immunol. Immunopathol.* 133, 309–313. doi: 10.1016/j.vetimm.2009.08.008

Trela, J. M., Spriet, M., Padgett, K. A., Galuppo, L. D., Vaughan, B., and Vidal, M. A. (2014). Scintigraphic comparison of intra-arterial injection and distal intravenous regional limb perfusion for administration of mesenchymal stem cells to the equine foot. *Equine Vet. J.* 46, 479–483. doi: 10.1111/evj.12137

Twedt, D. C., Sternlieb, I., and Gilbertson, S. R. (1979). Clinical, morphologic, and chemical studies on copper toxicosis of Bedlington Terriers. *J. Am. Vet. Med. Assoc.* 175, 269–275.

Tytherleigh-Strong, G., Hurtig, M., and Miniaci, A. (2005). Intra-articular hyaluronan following autogenous osteochondral grafting of the knee. *Arthroscopy* 21, 999–1005. doi: 10.1016/j.arthro.2005.05.001

Van De Sluis, B., Rothuizen, J., Pearson, P. L., Van Oost, B. A., and Wijmenga, C. (2002). Identification of a new copper metabolism gene by positional cloning in a purebred dog population. *Hum. Mol. Genet.* 11, 165–173. doi: 10.1093/hmg/11.2.165

Van De Sluis, B. J., Breen, M., Nanji, M., Van Wolferen, M., De Jong, P., Binns, M. M., et al. (1999). Genetic mapping of the copper toxicosis locus in Bedlington terriers to dog chromosome 10, in a region syntenic to human chromosome region 2p13-p16. *Hum. Mol. Genet.* 8, 501–507. doi: 10.1093/hmg/8.3.501

Van Loon, V. J., Scheffer, C. J., Genn, H. J., Hoogendoorn, A. C., and Greve, J. W. (2014). Clinical follow-up of horses treated with allogeneic equine mesenchymal stem cells derived from umbilical cord blood for different tendon and ligament disorders. *Vet. Q.* 34, 92–97. doi: 10.1080/01652176.2014.949390

Van Steenbeek, F. G., Hytonen, M. K., Leegwater, P. A., and Lohi, H. (2016). The canine era: the rise of a biomedical model. *Anim. Genet.* 47, 519–527. doi: 10.1111/age.12460

Van Weeren, P. R., and Back, W. (2016). Musculoskeletal disease in aged horses and its management. *Vet. Clin. North Am. Equine Pract.* 32, 229–247. doi: 10.1016/j.cveq.2016.04.003

Vandeweerd, J. M., Hontoir, F., Kirschvink, N., Clegg, P., Nisolle, J. F., Antoine, N., et al. (2013). Prevalence of naturally occurring cartilage defects in the ovine knee. *Osteoarthritis Cartilage* 21, 1125–1131. doi: 10.1016/j.joca.2013.05.006

Varcoe, T. J., Gatfort, K. L., Holman, S. L., Cheung, P., Berry, M. J., Wiese, M. D., et al. (2019). Considerations in selecting postoperative analgesia for pregnant sheep following fetal instrumentation surgery. *Anim. Front.* 9, 60–67. doi: 10.1093/af/vfz019

Vila, J., Pariaut, R., Moise, N. S., Oxford, E. M., Fox, P. R., Reynolds, C. A., et al. (2017). Structural and molecular pathology of the atrium in boxer arrhythmogenic right ventricular cardiomyopathy. *J. Vet. Cardiol.* 19, 57–67. doi: 10.1016/j.jvc.2016.09.001

Vincent, T. L., Williams, R. O., Maciewicz, R., Silman, A., and Garside, P. (2012). Mapping pathogenesis of arthritis through small animal models. *Rheumatology* 51, 1931–1941. doi: 10.1093/rheumatology/kes035

Vischer, A. S., Connolly, D. J., Coats, C. J., Fuentes, V. L., Mckenna, W. J., Castelletti, S., et al. (2017). Arrhythmogenic right ventricular cardiomyopathy in Boxer dogs: the diagnosis as a link to the human disease. *Acta Myol.* 36, 135–150.

Vogel, T., Brockmann, J. G., Pigott, D., Neil, D. A. H., Muthusamy, A. S. R., Coussios, C. C., et al. (2017). Successful transplantation of porcine liver grafts following 48-hour normothermic preservation. *PLoS One* 12:e0188494. doi: 10.1371/journal.pone.0188494

Voleti, P. B., Buckley, M. R., and Soslowsky, L. J. (2012). Tendon healing: repair and regeneration. *Annu. Rev. Biomed. Eng.* 14, 47–71.

Vonk, W. I., De Bie, P., Wichers, C. G., Van Den Berghe, P. V., Van Der Plaats, R., Berger, R., et al. (2012). The copper-transporting capacity of ATP7A mutants associated with Menkes disease is ameliorated by COMMD1 as a result of improved protein expression. *Cell. Mol. Life Sci.* 69, 149–163. doi: 10.1007/s00018-011-0743-1

Warnock, J. J., Fox, D. B., Stoker, A. M., Beatty, M., Cockrell, M., Janicek, J. C., et al. (2014). Culture of equine fibroblast-like synoviocytes on synthetic tissue scaffolds towards meniscal tissue engineering: a preliminary cell-seeding study. *PeerJ* 2:e353. doi: 10.7717/peerj.353

Watanabe, M., Li, H., Kim, A. G., Weilerstein, A., Radu, A., Davey, M., et al. (2016). Complete tissue coverage achieved by scaffold-based tissue engineering in the fetal sheep model of Myelomeningocele. *Biomaterials* 76, 133–143. doi: 10.1016/j.biomaterials.2015.10.051

Watts, A. E., Nixon, A. J., Yeager, A. E., and Mohammed, H. O. (2012). A collagenase gel/physical defect model for controlled induction of superficial digital flexor tendonitis. *Equine Vet. J.* 44, 576–586. doi: 10.1111/j.2042-3306.2011.00471.x

Watts, A. E., Yeager, A. E., Kopyov, O. V., and Nixon, A. J. (2011). Fetal derived embryonic-like stem cells improve healing in a large animal flexor tendonitis model. *Stem Cell Res. Ther.* 2:4. doi: 10.1186/scrt45

Webb, C. B., Twedt, D. C., and Meyer, D. J. (2002). Copper-associated liver disease in Dalmatians: a review of 10 dogs (1998-2001). *J. Vet. Intern. Med.* 16, 665–668. doi: 10.1111/j.1939-1676.2002.tb02405.x

Wess, G., Schulze, A., Butz, V., Simak, J., Killich, M., Keller, L. J., et al. (2010). Prevalence of dilated cardiomyopathy in Doberman Pinschers in various age groups. *J. Vet. Intern. Med.* 24, 533–538. doi: 10.1111/j.1939-1676.2010.0479.x

Whitehouse, M. R., Howells, N. R., Parry, M. C., Austin, E., Kafienah, W., Brady, K., et al. (2017). Repair of torn avascular meniscal cartilage using undifferentiated autologous mesenchymal stem cells: from *in vitro* optimization to a first-in-human study. *Stem Cells Transl. Med.* 6, 1237–1248. doi: 10.1002/sctm.16-0199

Williams, I. F., Mccullagh, K. G., Goodship, A. E., and Silver, I. A. (1984). Studies on the pathogenesis of equine tendonitis following collagenase injury. *Res. Vet. Sci.* 36, 326–338. doi: 10.1016/s0034-5288(18)31954-4

Williams, K., and Roman, J. (2016). Studying human respiratory disease in animals–role of induced and naturally occurring models. *J. Pathol.* 238, 220–232. doi: 10.1002/path.4658

Woodruff, P. G., Modrek, B., Choy, D. F., Jia, G., Abbas, A. R., Ellwanger, A., et al. (2009). T-helper type 2-driven inflammation defines major subphenotypes of asthma. *Am. J. Respir. Crit. Care Med.* 180, 388–395. doi: 10.1164/rccm.200903-0392oc

Wu, Z. Y., Zhao, G. X., Chen, W. J., Wang, N., Wan, B., Lin, M. T., et al. (2006). Mutation analysis of 218 Chinese patients with Wilson disease revealed no correlation between the canine copper toxicosis gene Murr1 and Wilson disease. *J. Mol. Med.* 84, 438–442. doi: 10.1007/s00109-005-0036-y

Xerogeanes, J. W., Fox, R. J., Takeda, Y., Kim, H. S., Ishibashi, Y., Carlin, G. J., et al. (1998). A functional comparison of animal anterior cruciate ligament models to the human anterior cruciate ligament. *Ann. Biomed. Eng.* 26, 345–352.

Yamamoto, S., Karashima, M., Sano, N., Fukushi, C., Tohyama, K., Arai, Y., et al. (2017). Utility of gottingen minipigs for prediction of human pharmacokinetic profiles after dermal drug application. *Pharm. Res.* 34, 2415–2424. doi: 10.1007/s11095-017-2247-7

Yang, H., Wang, G., Sun, H., Shu, R., Liu, T., Wang, C. E., et al. (2014). Species-dependent neuropathology in transgenic SOD1 pigs. *Cell Res.* 24, 464–481. doi: 10.1038/cr.2014.25

Yao, J., Huang, J., and Zhao, J. (2016). Genome editing revolutionize the creation of genetically modified pigs for modeling human diseases. *Hum. Genet.* 135, 1093–1105. doi: 10.1007/s00439-016-1710-6

Yu, H., Adesida, A. B., and Jomha, N. M. (2015). Meniscus repair using mesenchymal stem cells - a comprehensive review. *Stem Cell Res. Ther.* 6:86.

Zhao, W., Wang, Y., Liu, S., Huang, J., Zhai, Z., He, C., et al. (2015). The dynamic distribution of porcine microbiota across different ages and gastrointestinal tract segments. *PLoS One* 10:e0117441. doi: 10.1371/journal.pone.0117441

Zorzi, A. R., Amstalden, E. M., Plepis, A. M., Martins, V. C., Ferretti, M., Antonioli, E., et al. (2015). Effect of human adipose tissue mesenchymal stem cells on the regeneration of ovine articular cartilage. *Int. J. Mol. Sci.* 16, 26813–26831. doi: 10.3390/ijms161125989

Zosky, G. R., and Sly, P. D. (2007). Animal models of asthma. *Clin. Exp. Allergy* 37, 973–988.

Conflict of Interest: The authors declare that the research was conducted in the absence of any commercial or financial relationships that could be construed as a potential conflict of interest.

frontiers in Bioengineering and Biotechnology

ORIGINAL RESEARCH
published: 26 August 2020
doi: 10.3389/fbioe.2020.00984

Combination of a Gellan Gum-Based Hydrogel With Cell Therapy for the Treatment of Cervical Spinal Cord Injury

Eduardo D. Gomes[1,2†], Biswarup Ghosh[3†], Rui Lima[1,2], Miguel Goulão[1,2,3], Tiago Moreira-Gomes[1,2], Joana Martins-Macedo[1,2], Mark W. Urban[3], Megan C. Wright[4], Jeffrey M. Gimble[5], Nuno Sousa[1,2], Nuno A. Silva[1,2], Angelo C. Lepore[3‡] and António J. Salgado[1,2*‡]*

[1] Life and Health Sciences Research Institute (ICVS), School of Medicine, University of Minho, Braga, Portugal, [2] ICVS/3B's – PT Government Associate Laboratory, Guimarães, Portugal, [3] Department of Neuroscience, Vickie and Jack Farber Institute for Neuroscience, Sidney Kimmel Medical College, Thomas Jefferson University, Philadelphia, PA, United States, [4] Department of Biology, Arcadia University, Glenside, PA, United States, [5] Center for Stem Cell Research and Regenerative Medicine, Tulane University, New Orleans, LA, United States

OPEN ACCESS

Edited by:
Dimitrios I. Zeugolis,
National University of Ireland Galway, Ireland

Reviewed by:
Lisa Jane White,
University of Nottingham, United Kingdom
Chiara Tonda-Turo,
Politecnico di Torino, Italy

***Correspondence:**
Angelo C. Lepore
Angelo.Lepore@jefferson.edu
António J. Salgado
asalgado@med.uminho.pt

[†] These authors share first authorship

[‡] These authors share senior authorship

Specialty section:
This article was submitted to Tissue Engineering and Regenerative Medicine, a section of the journal Frontiers in Bioengineering and Biotechnology

Received: 20 January 2020
Accepted: 28 July 2020
Published: 26 August 2020

Citation:
Gomes ED, Ghosh B, Lima R, Goulão M, Moreira-Gomes T, Martins-Macedo J, Urban MW, Wright MC, Gimble JM, Sousa N, Silva NA, Lepore AC and Salgado AJ (2020) Combination of a Gellan Gum-Based Hydrogel With Cell Therapy for the Treatment of Cervical Spinal Cord Injury. Front. Bioeng. Biotechnol. 8:984. doi: 10.3389/fbioe.2020.00984

Cervical spinal cord trauma represents more than half of the spinal cord injury (SCI) cases worldwide. Respiratory compromise, as well as severe limb motor deficits, are among the main consequences of cervical lesions. In the present work, a Gellan Gum (GG)-based hydrogel modified with GRGDS peptide, together with adipose tissue-derived stem/stromal cells (ASCs) and olfactory ensheathing cells (OECs), was used as a therapeutic strategy after a C2 hemisection SCI in rats. Hydrogel or cells alone, and a group without treatment, were also tested. Four weeks after injury, compound muscle action potentials (CMAPs) were performed to assess functional phrenic motor neuron (PhMN) innervation of the diaphragm; no differences were observed amongst groups, confirming that the PhMN pool located between C3 and C5 was not affected by the C2 injury or by the treatments. In the same line, the vast majority of diaphragmatic neuromuscular junctions remained intact. Five weeks post-injury, inspiratory bursting of the affected ipsilateral hemidiaphragm was evaluated through EMG recordings of dorsal, medial and ventral subregions of the muscle. All treatments significantly increased EMG amplitude at the ventral portion in comparison to untreated animals, but only the combinatorial group presented increased EMG amplitude at the medial portion of the hemidiaphragm. No differences were observed in forelimb motor function, neither in markers for axonal regrowth (neuronal tracers), astrogliosis (GFAP) and inflammatory cells (CD68). Moreover, using Von Frey testing of mechanical allodynia, it was possible to find a significant effect of the group combining hydrogel and cells on hypersensitivity; rats with a SCI displayed an increased response of the contralateral forelimb to a normally innocuous mechanical stimulus, but after treatment with the combinatorial therapy this behavior was reverted almost to the levels of uninjured controls. These results suggest that our therapeutic approach may have beneficial effects on both diaphragmatic recovery and sensory function.

Keywords: cervical spinal cord injury, respiratory compromise, adipose tissue-derived stem/stromal cells, olfactory ensheathing cells, modified gellan gum hydrogels

INTRODUCTION

Cervical spinal cord injuries (SCI) represent more than half of the SCI cases worldwide (Charsar et al., 2017). Traumatic lesions at cervical levels often result in respiratory compromise, due to damage to neural circuits controlling the diaphragm (Lane et al., 2008; Charsar et al., 2017). This circuitry is comprised of phrenic motor neurons (PhMN) located in the mid-cervical region of the spinal cord innervating the diaphragm, while in turn, this population is controlled by descending axonal input from rostral ventral respiratory group (rVRG) neurons located in the brainstem (Charsar et al., 2017). Despite the importance of this critical neural circuitry and the higher frequency of cervical lesions, a majority of pre-clinical studies have focused on thoracic lesions, which involve different affected circuitry and functions and eventually different responses to treatment.

Among the existing works in traumatic cervical SCI, cellular transplantation strategies have been designed to address the following purposes: replacing or inducing plasticity of neurons involved in respiratory circuits (Li et al., 2003; Alilain et al., 2011); replacing glial cell types (Li et al., 2015a) or local interneurons (Lee et al., 2014); providing trophic support (Gransee et al., 2015); and restoring neurotransmitter signaling (Li et al., 2015b).

Our group has developed a tissue engineering (TE) strategy for SCI repair, previously tested in a rat model of lumbar injuries (Gomes et al., 2016). This approach is based on the combination of adipose tissue-derived stem/stromal cells (ASCs) and olfactory ensheathing cells (OECs), together with a modified Gellan Gum (GG)-based hydrogel, which can be used both as a matrix for neural regrowth, and/or as a vehicle for cellular transplantation. ASCs and OECs represent two distinct cellular populations with complementary effects, as already demonstrated by our group (Silva et al., 2013a; Gomes et al., 2016, 2018). On one hand, OECs offer physical support and guidance for neurite outgrowth and elongation, mainly through direct cell–cell contact (Ramon-Cueto et al., 2000; Gomes et al., 2018). On the other hand, ASCs and their secreted factors are able to potentiate neurite formation and growth, promoting neuritogenesis, besides possessing immunomodulatory properties (Salgado et al., 2010; Lopez-Santalla et al., 2015; Gomes et al., 2018). Moreover, both cells can be obtained from autologous sources, increasing their potential application to the clinic. The GG hydrogel presents physical properties very similar to the spinal cord tissue and was previously modified with GRGDS motifs to increase cell adhesion (Silva et al., 2012a). This modification also led to improved morphology, viability and secretome properties of encapsulated cells (Silva et al., 2013b). In a lumbar SCI model, the combined therapy of hydrogel and cells led to significant locomotor improvements of the paralyzed hindlimbs, associated with a decreased inflammatory and astroglial response (Gomes et al., 2016).

Based on the abovementioned results, we determine whether the application of the same therapeutic strategy to a cervical hemisection injury could result in a beneficial outcome, modulating the local environment and possibly favoring neuronal preservation and/or inducing axon growth through the injury or in spared pathways. Toward this aim, following a C2 hemisection, ASCs and OECs encapsulated in the GG hydrogel were transplanted into the spinal cord lesion and functional and histological recovery was assessed.

MATERIALS AND METHODS

ASCs and OECs Cultures

Human ASCs were isolated according to Dubois et al. (2008) in collaboration with LaCell LLC. Briefly, ASCs were isolated from human lipoaspirates obtained from consenting donors under an institutional review board approved protocol at LaCell LLC. These cells were cultured and maintained in α-MEM (Invitrogen, United States), with 10% Fetal Bovine Serum (FBS, Biochrom AG, Germany) and 1% antibiotic solution – penicillin/streptomycin (pen/strep; Invitrogen) at 37°C and 5% CO_2 (v/v).

Olfactory ensheathing cells were isolated and cultured as previously described (Silva et al., 2012b). The animal care committees of the research institutes approved all the animal protocols in accordance with standardized animal care guidelines (Zutphen et al., 2001). Briefly, OECs were harvested from olfactory bulbs of neonatal (P5–P7) Wistar-Han rats. Upon dissection, the meninges and blood vessels were removed and the tissue was digested with collagenase type I (2.5 mg/ml, Sigma, United States) for 15 min at 37°C, with agitation. The digested tissue was mechanically dissociated with a 5 ml pipette and centrifuged at 175 G for 5 min. Then, the tissue was resuspended and subjected to a second mechanical dissociation using a P1000 micropipette. After a second centrifugation step, cells were resuspended and seeded on uncoated plates for two consecutive periods of 24 h. It is expected that most of the fibroblasts and astrocytes attach in the first and second periods, respectively. After this purification step, the remaining cells were seeded on fibronectin coated surfaces. Cells were cultured in DMEM/F12 (Invitrogen) with 10% FBS and 1% pen/strep solution at 37°C and 5% CO_2 (v/v). OECs were additionally enriched with Bovine Pituitary Extract (5.36 μg/ml, Invitrogen) and Forskolin (1.4 μg/ml, Sigma).

Hydrogel Preparation

The synthesis of GG-GRGDS hydrogel was performed according to the protocols described by Silva et al. (2012a). Briefly, GG (Sigma) was firstly dissolved in 2-(*N*-morpholino)ethanesulfonic acid (MES) buffer (100 mM, pH 5.5, Sigma) at 37°C. 4-(4,6-Dimethoxy-1,3,5-triazin-2-yl)-4-methylmorpholinium chloride (DMT-MM, Sigma) and furfurylamine (Acros Organics, Belgium) were then added in a 4:1 M ratio (of each reagent relative to the -COOH groups in GG) and stirred at 37°C for 48 h. The solution was then dialyzed (Mw cutoff 12–14 kDa, Spectrum Labs, United States) alternately against distilled water and phosphate buffered saline (PBS, 0.1M, pH 7.2) for 5 days. Finally, water was removed by lyophilization to obtain furan-modified GG (furan-GG) as a white powder. Immobilization of maleimide-modified GRGDS peptide (mal-GRGDS, Anaspec, United States) to furan-GG was performed via Diels-Alder chemistry between the maleimide functional group of the peptide with the furan group of the GG. Furan-GG was first

dissolved in MES buffer at 37°C (1.2 mg/ml). Mal-GRGDS was then added in a 5:1 maleimide:furan molar ratio and vigorously stirred for 48 h. The solution was then dialyzed (Mw cutoff 12–14 kDa) alternately against distilled water and PBS for 5 days. Finally, the water was removed by lyophilization to obtain GRGDS-modified GG (GG-GRGDS) as a white powder.

GG-GRGDS 3D Hydrogel Preparation

GG-GRGDS lyophilized powder was sterilized by exposure to UV lights for 15 min, a method previously used without affecting the material properties (Silva et al., 2013b). Then, GG-GRGDS was dissolved in ultrapure water, at 1% (w/v) concentration and heated at 40°C overnight, in order to obtain a homogenous solution. Before encapsulating the cells, $CaCl_2$ at 0.3% (w/v) was added [to obtain a final concentration of 0.03% (w/v) of $CaCl_2$ in solution] to enable the ionic crosslinking of the hydrogel.

C2 Hemisection Injuries

Animals

As previously mentioned, all experimental procedures were approved either by the ICVS research committee and by the Thomas Jefferson University IACUC, being conducted in compliance with ARRIVE (Animal Research: Reporting of *In Vivo* Experiments) guidelines.

Ten weeks old female Wistar-Han rats (forelimb motor studies, Charles River, France) or twelve weeks old Sprague-Dawley (functional diaphragm studies, Taconic, United States), housed in light and temperature-controlled rooms and fed with standard diet, were used in the *in vivo* studies. Handling was performed for 3 days before the surgeries. Two sets of experiments were designed: the first one to assess diaphragm function and the second one dedicated to motor and sensory evaluation (**Tables 1**, **2**).

Cervical SCI and Treatments

All animals were anesthetized by intraperitoneal injection of a mixture (1.5:1) of ketamine (100 mg/ml, Imalgene/Merial, France) and medetomidine hydrochloride (1 mg/ml, Domitor/Pfizer, United States). Once anesthetized, the dorsal surface of the skin was shaved and disinfected with a 70% ethanol solution and topical iodine (Dynarex, Orangeburg, New York). Using a sterile #11 surgical blade (Electron Microscopy Sciences, Hatfield, PA, United States), a three-cm midline incision was made on the dorsal surface of skin and muscle, starting from the caudal portion of the occipital bone. Retractors were then used to expose the dorsal surface of the C2 and C3 vertebrae. Using rongeurs (Fine Science Tools, Foster City, CA, United States), remaining tissue was removed from the vertebrae and a laminectomy was performed to expose the spinal cord. The C2 and C3 dorsal roots were located, and a hemisection was performed at a location just caudal to the C2 root with a dissecting knife (Fine Science Tools, Foster City, CA, United States). To ensure a complete hemisection, a 30-gauge needle (BD Biosciences, San Jose, CA, United States) was passed through the injury several times. Within each set, animals were divided into four different groups according to the treatment/procedure: (1) animals subjected to SCI (hemisection) with no treatment (HS); (2) SCI animals treated with GG-GRGDS (GG-GRGDS); (3) SCI animals transplanted with cells (ASCs/OECs); (4) SCI animals treated with ASCs and OECs encapsulated in GG-GRGDS (GG-GRGDS + ASCs/OECs). The total animals per set and group is described in **Table 3**. Treatments were applied immediately after injury using a 30-gauge Hamilton syringe. The injection was performed manually, directly to the gap created by the lesion, at the slowest rate possible (around 1 min per injection). A total of 10 μl of hydrogel, cells or hydrogel with cells were injected per animal in the various groups. DMEM/F12 culture medium (OECs basal medium) was used as a vehicle for transplanted cells and injected as a control in non-treated animals. Rats treated with cells received a total of 200,000 cells (1:1 ASCs-OECs), either encapsulated in GG-GRGDS or in culture media. Following treatment, the dorsal muscle layers were sutured with 4–0 silk sutures (Covidien, Minneapolis, MN, United States), and the skin was closed with surgical staples (Fine Science Tools, Germany). The surface of the skin was treated with a topical iodine solution.

Post-operative Care

Following SCI surgery and treatment, post-operative care was performed as previously described (Lima et al., 2017). Briefly, rats were kept under heat lamps and received subcutaneous injections of a solution containing vitamins (10 ml/Kg, Duphalyte/Pfizer, United States), 0.9% NaCl, the analgesic butorphanol (10 mg/ml, Butomidor/Richter Pharma AG, Austria), the antibiotic enrofloxacin (5 mg/ml, Baytril/Bayer, Germany), and atipamezole (5 mg/ml, Antisedan/Pfizer, United States) as a reversal agent. Bladder expression was checked to confirm that animals regained control. Then, for 5 days rats received daily subcutaneous injections of all the above-mentioned components except for atipamezole.

TABLE 1 | Experimental layout, with number of animals used per test, time points and rat breeds used in each set.

Set	Set A – Forelimb motor studies			Set B – Functional diaphragm studies		
Rat breed	Wistar Han			Sprague Dawley		
Analysis	Test	*n*	Time point	Test	*n*	Time point
	Staircase test	8–10/group	2 and 5 weeks	CMAPs	5–8/group	4 weeks
	Grooming test	8–9/group	3 weeks	NMJ morphology	3/group	5 weeks
	Von Frey test	7–10/group	4 weeks	EMGs	6–8/group	5 weeks
	GFAP and CD68	3/group	5 weeks	5-HT sprouting	4/group	5 weeks

TABLE 2 | Total number of animals used per test, for each experimental group.

Test	HS	GG-GRGDS	ASCs/OECs	GG-GRGDS + ASCs/OECs
Staircase test	8	8	9	10
Grooming test	8	8	8	9
Von Frey test	7	8	7	10
GFAP and CD68	3	3	3	3
CMAPs	6	8	7	5
NMJs morphology	3	3	3	3
EMGs	6	8	7	8
5-HT sprouting	4	4	4	4

TABLE 3 | Total number of animals used per group and in each experimental set.

	Set A	Set B	
HS	8	6	
GG-GRGDS	8	8	
ASCs/OECs	9	7	
GG-GRGDS + ASCs/OECs	10	8	
Total	35	29	64

Throughout the treatment and recovery period, animals were examined for symptoms of illness or potential reaction to the treatment. The diet was enriched and the food was presented to the rats on the cage floor.

rVRG Axon Tracing

Three weeks after injury, animals were anesthetized as described in cervical injuries and subjected to intra-brainstem injections of AAV2-mCherry, as described previously (Goulao et al., 2019). A midline incision was made at the base of the cranium using a sterile #11 blade. After deflection of the muscle and the C1/cranium ligament, the bone covering a portion of the brainstem was removed. Using a Hamilton Gastight Syringe (Hamilton, Reno, NV, United States) with a 33-gauge needle, 0.3 μl of virus was injected 2 mm lateral to the right (ipsilateral rVRG tracing), 1 mm rostral and 2.6 mm ventral to the brainstem obex, using a stereotaxic apparatus (Kopf Instruments, Tujunga, CA, United States) and an UltraMicroPump (World Precision Instruments, Sarasota, FL, United States). The needle was left in place for 5 min before careful retrieval from the medulla. Postoperative care was given as described for C2 hemisection injuries. Spinal cord sections were later analyzed for mCherry labeling using a Zeiss Imager M2 upright microscope with Metamorph Software.

Compound Muscle Action Potential (CMAP) Recordings

Four weeks post-surgery, rats were anesthetized with isoflurane (Piramal Healthcare, Bethlehem, PA, United States) at a concentration of 3.0–3.5% diluted in oxygen. Animals were placed supine and the region just below the rib cage was shaved and cleaned with 70% ethanol. Phrenic nerve conduction studies were performed with stimulation at the neck via near nerve needle electrodes placed along the phrenic nerve. A reference electrode was placed on the shaved surface of the right costal region. The phrenic nerve was stimulated with a single burst at 6 mV (amplitude) for a 0.5 ms duration. Each animal was stimulated between 10 and 20 times to ensure reproducibility, and recordings were averaged for analysis. Animals were daily followed for any signs of distress in response to this procedure. ADI Powerlab 8/30 stimulator and BioAMPamplifier (ADInstruments, Colorado Springs, CO, United States) were used for both stimulation and recording, and Scope 3.5.6 software (ADInstruments, Colorado Springs, CO, United States) was used for subsequent data analysis. An additional control animal without lesion (laminectomy only) was used as an example of a normal CMAP recording.

Electromyography (EMG) Recordings

Five weeks post-surgery and immediately before sacrifice, animals were anesthetized with isoflurane at a concentration of 3.0–3.5% diluted in oxygen. All animals had fully recovered from CMAP recordings, with no signs of distress. Once deeply anesthetized, a laparotomy was performed to expose the right hemi-diaphragm. Bipolar electrodes spaced 3 mm apart were placed for recording in three separate sub-regions of the hemi-diaphragm: dorsal, medial, and ventral. Electrodes were always placed at the endplate band at all recording locations. Two recordings were averaged over a 2-min time frame for each animal, and peak amplitude, burst duration and frequency were taken. Using LabChart 7 software (AD Instruments, Colorado Springs, CO, United States), the EMG signal was amplified and filtered through a band-pass filter (50–3000 Hz). Following recordings, animals were immediately euthanized with a triple-dose of ketamine/xylazine/acepromazine and the spinal cord and diaphragm were collected after transcardial perfusion with 4% paraformaldehyde. As in CMAP recordings, an additional control animal without lesion (laminectomy only) was used as an example of a normal EMG recording.

Limb Motor Assessment

Staircase Test

The staircase (also called skilled paw reaching test) was performed with double staircase boxes (Campden Instruments, Lafayette, IN, United States), as previously described (Campos et al., 2013). The shape and dimensions of the boxes were similar to the ones described by Montoya et al. (1991). The apparatus consists of a clear chamber with a hinged lid that was developed to assess independent forelimb use in skilled reaching and grasping tasks. A narrow compartment, with a central platform running along its length, is connected to this chamber. The removable double staircase with seven steps on each side can be inserted in the space between the platform and the box walls. Five pellets were placed into each well of the double staircase apparatus. On the first day, the rats were familiarized with the test and pellets were freely available at random positions for 10 min. During the test session, animals were kept inside the box and had 15 min to reach, retrieve, and eat food pellets present on the steps. All sessions were performed at the same time of day under food-restriction. After

each test interval, animals were removed from the staircase boxes and the uneaten pellets were counted. During the first five test days, rats were presented with pellets on both sides of the staircase, while in the sixth and seventh day, pellets were placed only on one side, alternating sides from 1 day to the other (forced choice paradigm). The staircase test was performed during the second- and fifth-weeks post-injury. As the main outputs, eating scores were calculated. It considers the ratio between the number of pellets eaten and the total number of pellets available.

Grooming Test

Three weeks after injury grooming behavior was evaluated for all rats. A soft gauze with fresh tap water was applied to the rats' back head to induce grooming. Then the rats were placed in a glass cylinder and their behavior was filmed. After two complete cycles of grooming (starting by licking the paws and ending by cleaning behind the ears) the rats were placed back in their cages. Later, both forelimbs were scored using a scale varying from 0 (unable to touch the nose) up to 5 (reach the back of their ears), adapting a protocol from Bertelli and Mira (1993).

Von Frey Analysis

The Von Frey test was performed at 4 weeks post-injury, as described in Guimaraes et al. (2019). Animals were placed in an elevated grid and left to acclimatize to the experimental conditions for 5 min. Mechanical allodynia was then assessed using the up-and-down method (Chaplan et al., 1994) as described previously (Sotiropoulos et al., 2014). Briefly, the sural dermatome of the contralateral limbs (fore- and hindimb) was probed with a series of von Frey calibrated monofilaments: 15.0, 8.0, 6.0, 4.0, 2.0, 1.0, 0.6, and 0.4 g (North Coast Medical Inc., United States). Starting with the 2.0 g filament, the test would advance upward if no response was elicited (=0) or downward if a brisk withdrawn of the limb was produced (=X) until 6 measurements were obtained around the threshold point according to the model developed by Dixon (Dixon, 1980). Paw movements, associated with locomotion or weight shifting, were not counted as a response. The 50% response threshold was then calculated using the following formula:

$$50\%g\_threshold = \frac{(10^{Xf+K.\delta})}{10000}$$

where X_f = value (in log units) of the final von Frey filament; k = tabular value corresponding to pattern of positive and negative responses [X and 0 sequence; consult (Chaplan et al., 1994)]; δ = mean difference (in log units) between stimuli (0.224). If no response was obtained up to maximal force (15.0 g) or conversely, if all filaments elicited a response down to the minimal force (0.4 g), the values 15 and 0.25 were assumed as the 50% withdrawal threshold, respectively. In this experiment, a total of three animals without injury were used as controls.

Histological Characterization

In both experimental sets, animals were sacrificed 5 weeks post-injury/treatment.

Neuromuscular Junction (NMJ) Analysis

Four animals per group were used for NMJ analysis. Rats were euthanized with a mixture of ketamine/xylazine/acepromazine. Animals were placed supine; two incisions were made into the skin and underlying muscle starting from the xyphoid process and extending laterally along the rib cage to expose the right hemidiaphragm. The right hemi-diaphragm was excised using spring scissors (Fine Science Tools, Foster City, CA, United States), stretched flat and pinned down on silicon-coated 10 cm dishes, and washed with PBS (Gibco, Pittsburgh, PA, United States). Next, a 20-min fixation in 4% paraformaldehyde (PFA, Electron Microscopy Sciences, Hatfield, PA, United States) was performed, followed by several washes in PBS. After washing, superficial fascia was carefully removed from the surface of the diaphragm with Dumont #5 Forceps (Fine Science Tools, Foster City, CA, United States).

Whole-mount immunohistochemistry was performed, as described previously (Wright and Son, 2007). Diaphragms were rinsed 3× in PBS and then incubated in 0.1M glycine for 30 min. Following glycine incubation, α-bungarotoxin conjugated to Alexa Fluor 555 at 1:200 (Life Technologies, Waltham, MA, United States) was used to label post-synaptic nicotinic acetylcholine receptors for 15 min and then washed 3× in PBS. Ice-cold methanol was then added to the diaphragms for 5 min and then washed 3× in PBS. Diaphragms were then blocked for 1 h at room temperature in a solution of 2% bovine serum albumin and 0.2% Triton X-100 diluted in PBS (this solution was used for both primary and secondary antibody dilutions). Primary antibodies were added overnight at 4°C: pre-synaptic vesicle marker anti-SV2 at 1:10 (Developmental Studies Hybridoma Bank, Iowa City, IA, United States), neurofilament marker anti-SMI-312 at 1:1000 (Covance, Greenfield, IN, United States). On the following morning, the diaphragms were washed 3 × in blocking solution, and secondary antibody solution was then added for 1 h at room temperature: FITC anti-mouse IgG secondary (Jackson ImmunoResearch Laboratories, West Grove, PA, United States; 1:100), followed by washing 3× in PBS. Diaphragms were mounted with Vectashield mounting medium (Vector Laboratories, Burlingame, CA, United States), coverslips were added, and slides were stored at −20°C.

We morphologically evaluated NMJ innervation by quantifying three phenotypes at individual synapses: intact NMJs, completely denervated NMJs, and partially denervated NMJs. We identified intact NMJs by complete overlap of the pre-synaptic axon labeling with the post-synaptic α-bungarotoxin labeling. We defined completely denervated NMJs by total absence of overlap between pre- and post-synaptic marker labeling. Partially denervated NMJs showed some overlap of pre- and post-synaptic labeling; however, this overlap was not complete as observed with intact NMJs. For each muscle/animal, we quantified 200–300 NMJs across the entire hemi-diaphragm, and we expressed the data for each phenotype as the percentage of total NMJs. Whole-mounted diaphragms were imaged on a FluoView FV1000 confocal microscope (Olympus, Center Valley, PA, United States). We conducted NMJ analysis on ipsilateral hemi-diaphragm because previous published work showed no

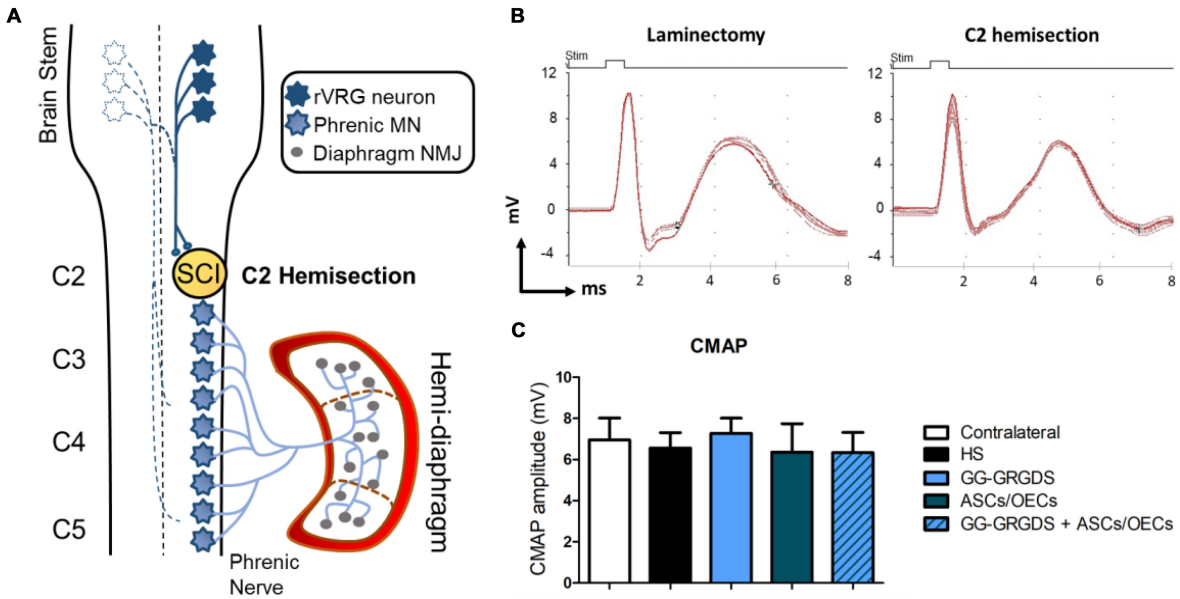

FIGURE 1 | Cervical hemisection injury at C2 level **(A)** does not affect CMAP amplitudes **(B,C)** analyzed at the ipsilateral hemi-diaphragm. **(A)** Schematic representation of the neuronal pathways controlling the hemi-diaphragm. Contralateral rVRG neurons are represented as white-filled stars. **(B)** Examples of the CMAP signals detected for a rat without SCI (laminectomy only) and a C2 hemisected rat. **(C)** Quantification of the average CMAP amplitude (mV) in the four treated groups and in the contralateral side of the injury. Data is presented as mean ± SD (n = 5–8 per group).

denervation or sprouting in contralateral hemi-diaphragm after cervical injury (Nicaise et al., 2012a,b).

Spinal Cord Tissue Processing

Five weeks post-injury, a rough dissection of the spine and spinal cord was performed in PFA perfused animals, centered on the site of hemisection and the tissues were additionally fixed in 4% PFA overnight. A more detailed dissection of the spinal cord was then conducted and the tissues were carefully placed on a solution of saccharose at 30% (w/v). After 24 h, 2.5–3 cm length of spinal cord tissues, centered on the lesion, were involved in frozen section medium (Neg-50, Thermo Scientific, United States), frozen with liquid nitrogen and stored at −20°C. Later on, longitudinal cross sections of 20 μm thickness were performed using a Leica CM1900 cryostat.

Immunohistochemistry

Frozen longitudinal sections of cervical spinal cord were air-dried and washed three times (5 min each) with PBS. Samples were then incubated in blocking solution (5% normal goat serum and 0.4% Triton X-100 diluted in PBS) for 1 h at room temperature. Sections were incubated overnight at 4°C with primary antibodies in blocking solution. The following primary antibodies were used: polyclonal rabbit 5-HT antibody (Immunostar, Hudson, WI, United States), polyclonal rabbit anti-Glial Fibrillary Acidic Protein (GFAP, Dako, Denmark) and monoclonal mouse anti-CD68 (Merck Millipore, MA, United States). Sections were then washed with PBS (three washes, 5 min each) and incubated with the following secondary antibodies conjugated to Alexa fluorophores (Invitrogen) in blocking solution for 1 h at room temperature: AF488 goat anti-rabbit (Jackson ImmunoResearch Laboratories, West Grove, PA, United States) for 5-HT, AF488 goat anti-rabbit (Invitrogen) for GFAP and AF594 goat anti-mouse (Invitrogen) for CD68. After washing with PBS (three washes, 5 min each), sections were coverslipped. For 5-HT staining, images were acquired with a Zeiss Imager M2 upright microscope, and MetaMorph software was used to quantify 5-HT immunostaining. For quantification of CD68+ reactive macrophages/monocytes, and GFAP+ cells, tissue sections were imaged on an Olympus IX81 inverted microscope. The total area of CD68 and GFAP expressing cells was quantified in 4–6 slices per animal.

Statistics

All statistical analyses were performed using GraphPad Prism version 5.00 for Windows (GraphPad Software, United States). Differences among groups were assessed by one-way ANOVA test or by the two-way ANOVA test followed by the Bonferroni *post hoc* test, in data with a normal distribution. Data without a normal distribution or with a small number of samples were analyzed with the non-parametric test Kruskal–Wallis followed by the Dunn's multiple comparison test. A p-value of $\leq$0.05 (95% confidence level) was set as the criteria for statistical significance, for all the analyses performed.

RESULTS

Functional and Morphological Innervation of the Ipsilateral Hemi-Diaphragm

Lesions at the C2 spinal cord level are not expected to directly affect the PhMN pool located between C3

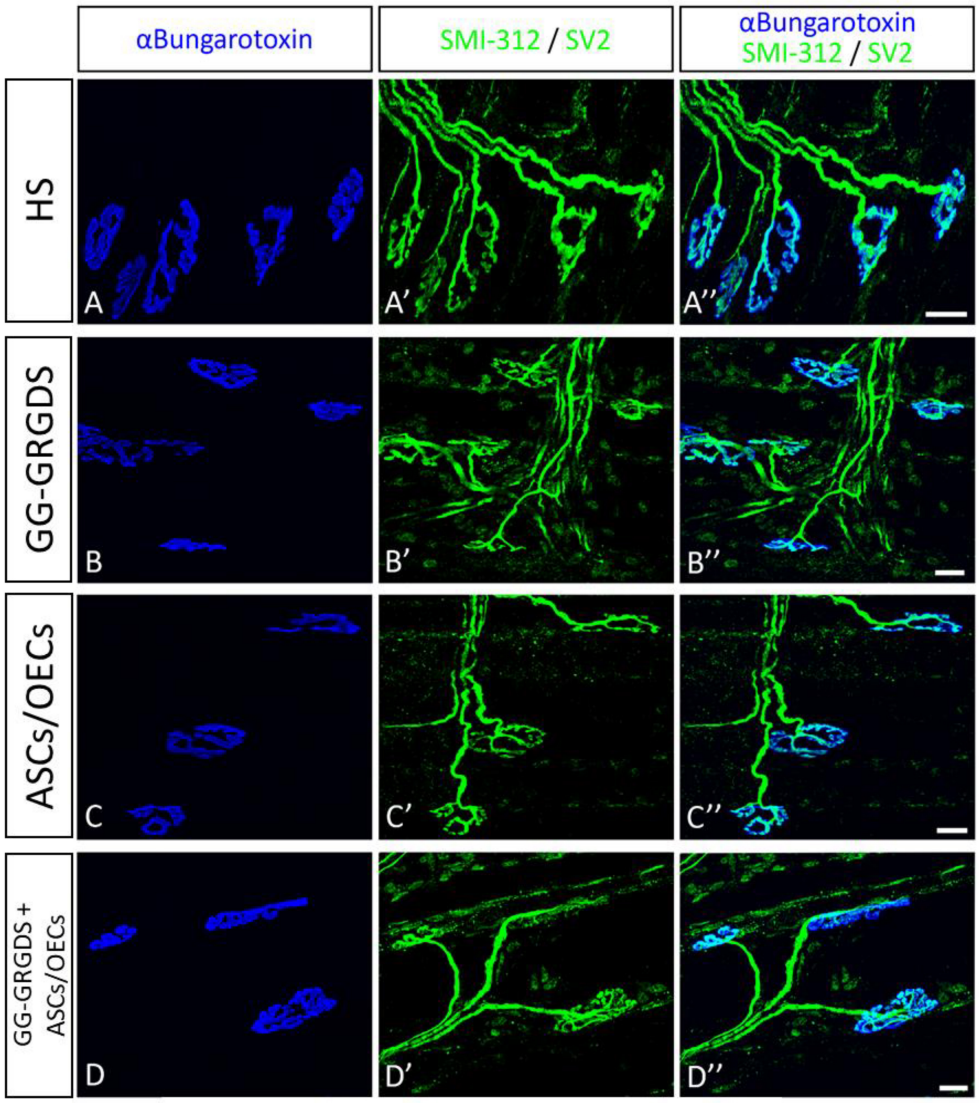

FIGURE 2 | NMJ morphology in the ipsilateral hemi-diaphragm. No significant alterations were seen among groups and most of the NMJs were intact. Nicotinic acetylcholine receptors stained with α-bungarotoxin (in blue, **A–D**) and pre-synaptic terminals stained with SMI-312 and SV2 (in green, **A'–D'**). **(A"–D")**: merged images. **(E)** Quantification of intact, partially-denervated and completely-denervated NMJs at the ipsilateral hemi-diaphragm. Data is presented as median ± IQR (n = 3 per group).

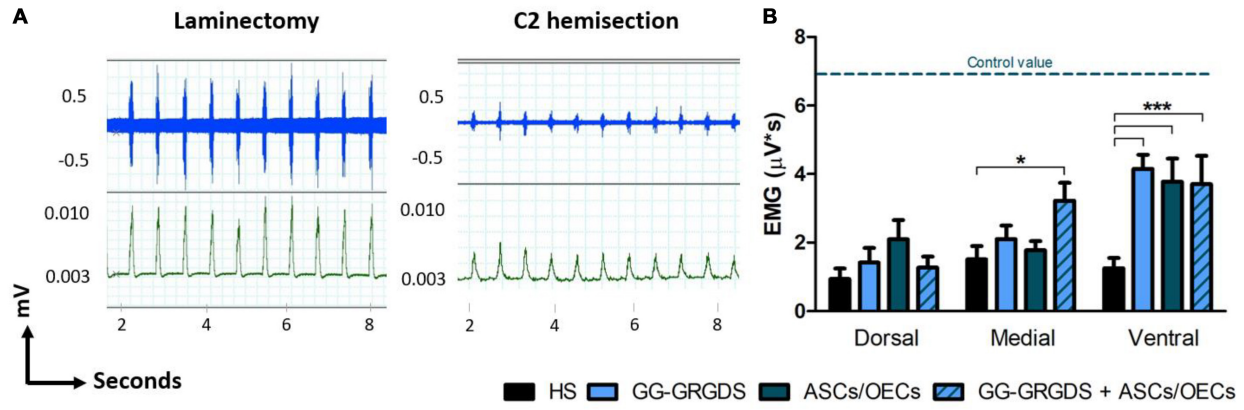

FIGURE 3 | EMG recovery in the ipsilateral hemi-diaphragm, 5 weeks after C2 cervical hemisection injury. **(A)** Non-treated rats (right graph) present a reduced EMG activity (dorsal recordings represented) in comparison to non-lesioned rats (only subjected to a laminectomy, left graph), revealing a normal pattern of EMG activity. Blue traces are the raw EMG signals (top) whereas green representative traces are the integrated EMG signals (bottom). **(B)** Treatments with hydrogel, cells or both led to significant recovery of integrated EMG amplitude at the ventral portion of the ipsilateral hemi-diaphragm, while in the medial portion only the combinatorial treatment provided significant improvement. No differences were seen among groups at the dorsal portion. Data is presented as mean ± SEM (n = 6–8 per group); $^{*}p < 0.05$, $^{***}p < 0.001$.

and C5. Therefore, in order to confirm the functional innervation of the ipsilateral hemi-diaphragm, CMAPs were recorded after supramaximal stimulation of the phrenic nerve. No significant alterations were observed among groups regarding CMAP amplitudes (**Figures 1A,B**), even in comparison to the non-lesioned contralateral hemi-diaphragm (**Figure 1B**). Moreover, after histological assessment of NMJ morphologies in the ipsilateral hemi-diaphragm, no differences were seen in the percentage of intact, partially denervated or completely denervated NMJs (**Figure 2**). The majority of NMJs analyzed were intact (almost 100%), demonstrating that the injury did not affect diaphragmatic morphological innervation. In both CMAP and NMJ assessments, the treatments did not influence the results obtained.

Ipsilateral Hemi-Diaphragm Function Assessment

Five weeks after injury, diaphragmatic function was assessed through EMG analysis. After recordings at three different subregions of the hemi-diaphragm ipsilateral to injury, it was observed a clear reduction in EMG amplitudes following SCI (**Figures 3A,B**). At the ventral portion of the hemi-diaphragm, all treatments induced a significant recovery of EMG amplitude. However, it should be highlighted that at the medial portion only the combination of hydrogel and cells was capable of promoting a significant improvement (**Figure 3B**). This result suggests a beneficial effect for the conjugation of hydrogel and cells.

Serotonergic Innervation of the Ipsilateral Cervical Spinal Cord

Serotonergic descending input plays an important role in the excitability of the spinal cord motor neurons, including PhMNs. Therefore, 5-HT axon sprouting was assessed at the ipsilateral lesioned side of the spinal cord specifically within the PhMN pool. Interestingly, all treatments induced an increase in the number and length of 5-HT fibers caudal to the lesion site in the ipsilateral C3-C5 ventral horn (**Figure 4**), with the cells-only and combined treatment inducing the highest levels of serotonergic fiber sprouting.

Forelimb Motor Evaluation

Motor impairment of the forelimbs is another significant consequence of cervical SCI. In the C2 hemisection, only the right forelimb was expected to be affected. In order to evaluate the recovery of motor function, two different motor behavior paradigms were performed. The first one was the staircase test, in which rats under food restriction are assessed for their fine motor skills, such as reaching and grasping abilities, to retrieve and eat a sugared pellet. At 2 and 5 weeks after injury, rats were subjected to the test, where during the first 5 days they could retrieve pellets from both right and left sides and in the last 2 days, pellets were only available on the left or on the right side (forced choice, **Figure 5**). In both modalities of the test, no significant differences were observed among groups for the eating score, either in the learning phase (**Figure 5**, top graphs) or in the forced choice paradigm (**Figure 5**, bottom graphs).

The second motor paradigm used was the grooming test. Grooming is a natural behavior in rodents that can be used to assess forelimb movement capacity. Using a pre-defined scale, where 1 means limited movements, while 5 represents a normal movement with complete grooming cycles, rats were evaluated at 3 weeks post-injury (**Figure 6**). The movement capacity of the right forelimb was significantly affected in all rats; however, there were no differences among groups. There were also no differences across treatment groups for the left, contralateral forelimb.

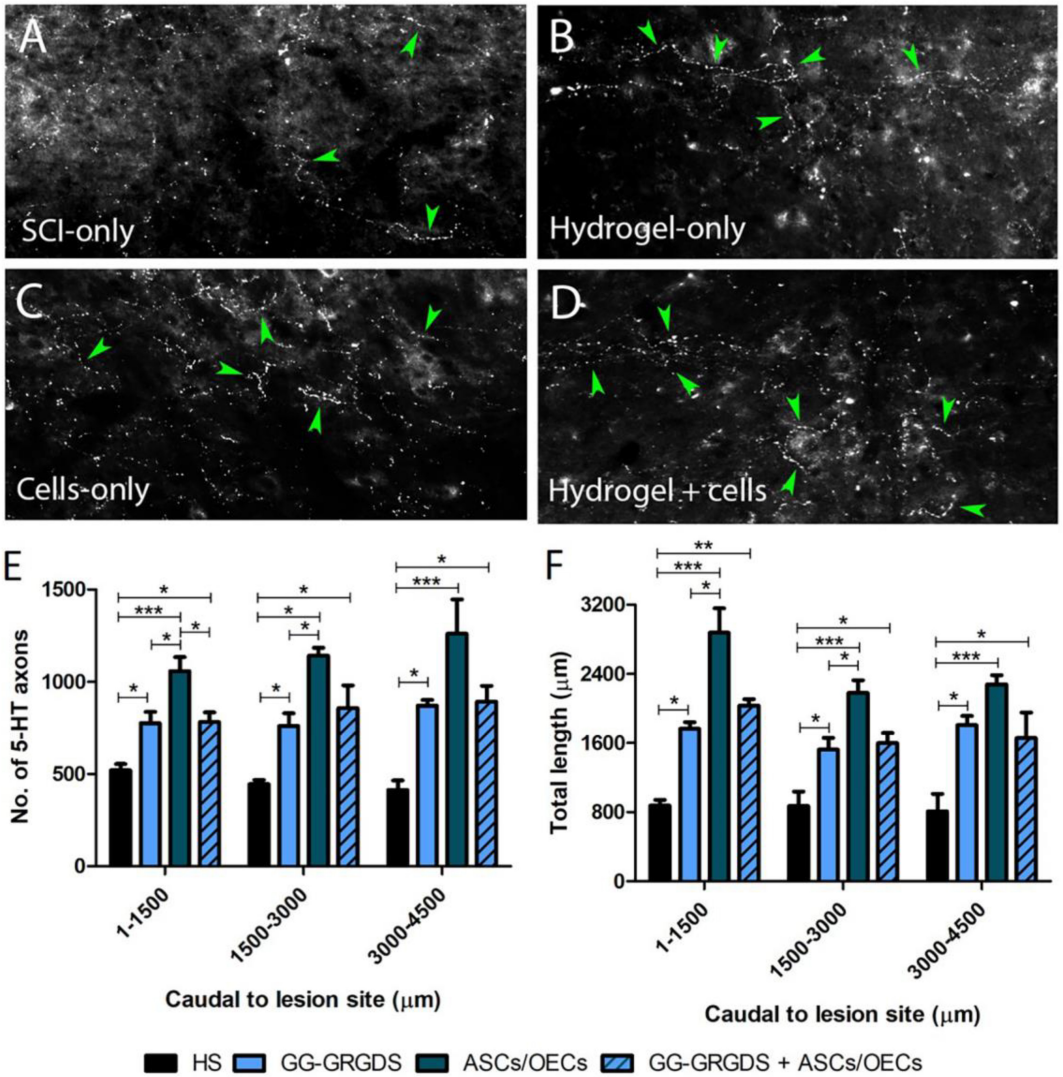

FIGURE 4 | Serotonergic axon sprouting caudal to the ipsilateral lesion site. **(A–D)** Representative confocal images of 5-HT fibers in the caudal cervical spinal cord. **(E,F)** 5-HT axon numbers and total length. Data is presented as mean ± SD (n = 4 per group).

Overall, these motor paradigms reinforce the idea that the injury was correctly performed, but treatments were unable to induce any motor recovery.

Sensory Function After Injury

A common outcome following SCI is sensory dysfunction. With the objective of evaluating the response to mechanical stimuli, rats were subjected to the Von Frey test 4 weeks post-lesion. Following C2 cervical injury, it was observed a marked increase in sensitivity of the contralateral limbs (**Figure 7**), responding to a stimulus usually innocuous to non-injured rats. However, after treatments, all treated groups demonstrated recovery from the hypersensitivity observed in the left hindpaw, while very interestingly, in the forepaw, only the combinatorial strategy induced significant recovery of sensory function to levels similar to uninjured controls (**Figure 7**).

DISCUSSION

Cervical SCI pre-clinical research is of great clinical relevance since lesions at this level account for more than half of SCI cases every year (Singh et al., 2014). TE approaches to cervical lesions have already been employed with some success (Liu et al., 2017; Geissler et al., 2018). For instance, Geissler et al. (2018) transplanted neural progenitor cells on a collagen-based hydrogel leading to functional recovery of rats with unilateral cervical contusion injuries. In another study, Liu et al. (2017) combined alginate hydrogels seeded with Schwann cells with BDNF viral delivery, in a C5 lateral hemisection model in rats. They showed that serotonergic and other descending axons could be traced throughout the scaffolds. Ghosh et al. (2018) have recently demonstrated that local BDNF delivery using an

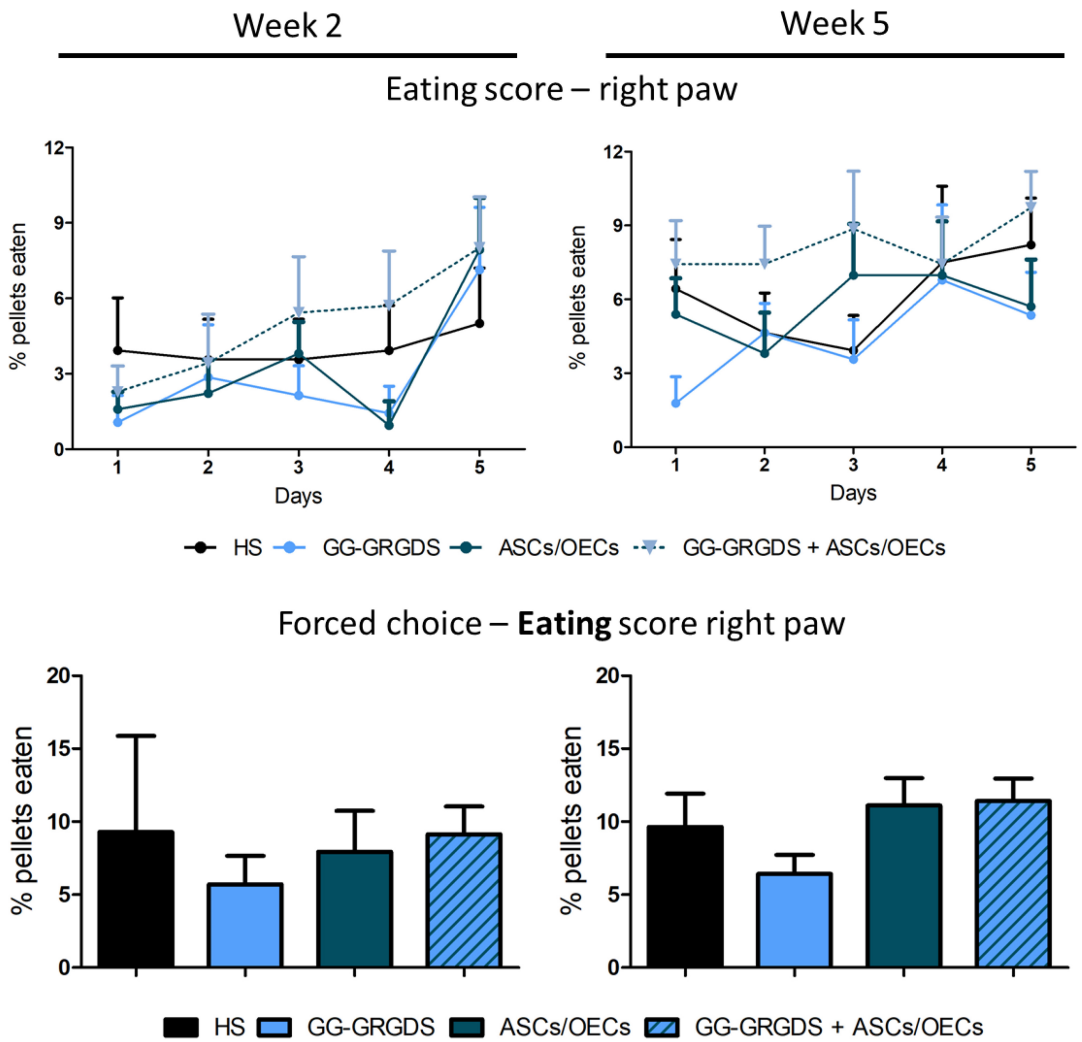

FIGURE 5 | Staircase test for the right paw, performed at **2** and **5** weeks after injury. There are no significant differences among groups in none of the time points evaluated, for both the staircase test **(upper graphs)** and the forced choice task of the test **(bottom graphs)**. Data is presented as mean ± SEM (*n* = 8–10 per group).

engineered hydrogel significantly enhanced diaphragmatic respiratory function.

In our case, the combination of ASCs and OECs with the peptide-grafted GG hydrogel has led to relevant functional and histological improvements in other models of SCI (Gomes et al., 2016). After a hemisection injury at the thoracic level, the administration of cellular transplants of ASCs/OECs was sufficient to induce a significant recovery of locomotor function, assessed by the BBB test, together with a marked decrease in inflammatory cells close to the lesion site (Gomes et al., 2018). On the other hand, in a more aggressive hemisection lumbar injury model, the combination of ASCs/OECs with GG-GRGDS hydrogel was the only treatment capable of promoting functional locomotor improvements, associated with similar decreases in inflammatory cells. In addition, the combined treatment reduced the levels of astrocytes close to the injury and preserved the levels of neurofilament-positive cells. Importantly, the number of ASCs that survived transplantation was higher when cells were transplanted within the hydrogel matrix (Gomes et al., 2016). Taking these results into account, the objective of this study was to ascertain if the same strategy could induce therapeutic efficacy in a cervical model of SCI.

While most clinical cases of SCI are contusive in nature, the C2 hemisection is a powerful model to investigate mechanisms of axon regeneration and sprouting as it creates a very precise and restricted injury, as well as complete ablation of defined axonal pathways. C2 hemisection interrupts the input of rVRG neurons from the brainstem, to PhMNs located around C3-C5 segments resulting in paralysis of the ipsilateral hemidiaphragm. In this sense, as a first experiment, the functionality and morphology of diaphragmatic innervation by PhMNs were analyzed (**Figures 1**, **2**). As expected, there were no alterations in CMAP amplitudes, and no significant morphological denervation of NMJs of the hemidiaphragm. This

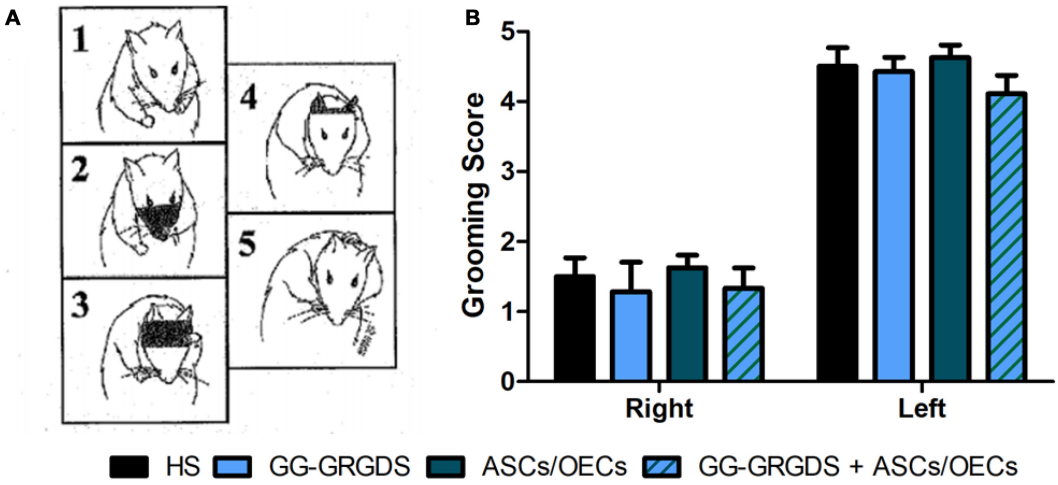

FIGURE 6 | Grooming test performed at 3 weeks after injury. **(A)** Representative images of the grooming scale behavior, with 1 meaning limited forepaw movement and 5 normal forepaw function. **(B)** No differences were seen in grooming capacity among groups, for both right and left forelimbs. As expected, the lesioned right paw presents deficits in grooming ability. Data is presented as mean ± SEM (n = 8 per group).

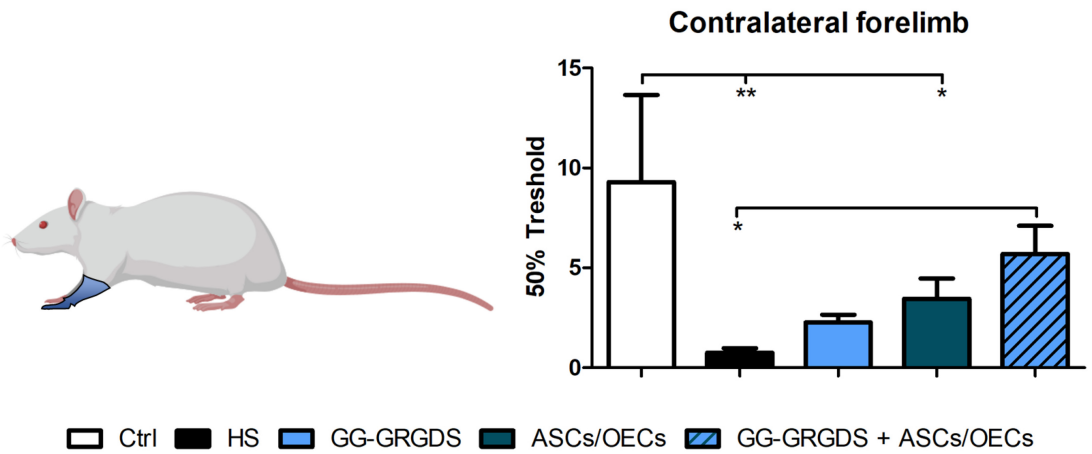

FIGURE 7 | Von Frey test performed at 4 weeks after injury. Forelimb sensory responses to Von Frey filaments were assessed and quantified. The combinatorial treatment led to a recovered sensory phenotype for the contralateral forelimb. Non-lesioned rats were used as a control. Data is presented as mean ± SEM (n = 8 per group); $^{*}p < 0.05$, $^{**}p < 0.01$.

was already seen in other recent works from the group using C2 cervical hemisections (Urban et al., 2018). This happens because the PhMN pool responsible for diaphragm innervation is not directly affected by the lesion, maintaining a response when activated and preserving overall NMJs structures. However, since they lose supraspinal input from the brainstem (rVRG neurons), they stop controlling diaphragmatic function. This loss of function is then reflected in the EMG recordings of the lesioned hemi-diaphragm (**Figure 3**). In the present work, different regions were analyzed independently, to dissect more closely the effects observed. Even though no differences were seen among groups at the dorsal portion of the diaphragm, medial and ventral portions registered significant improvements. In the ventral portion all treatments provided significant recovery of function, while in the medial portion, only the combinatorial treatment resulted in a significantly increased EMG signal. It is known that rostral spinal cord segments of the PhMN pool (C3) innervate the ventral region of the costal and crural areas of the diaphragm muscle, while more caudal segments innervate more dorsal portions (C5) (Fogarty et al., 2018). This anatomical characteristic might justify the higher improvement observed in ventral portions, as the treatments (hydrogel and/or cells) are applied at C2 level, possibly indicating a proximity-based effect. The combined treatment was effectively the only one capable of inducing partial recovery of EMG activity at the medial portion of the hemi-diaphragm, indicative of a more potent beneficial effect, in comparison to single treatment of hydrogel or cells. The hydrogel alone also induced partial recovery of function at the ventral portion. In this sense, the physical support provided by GG-GRGDS could also be in part responsible for

the recovery of function. As in the previous work (Gomes et al., 2016), the hydrogel was degraded with time, not being found at 5 weeks post-implantation. Yet, its confinement to the injury site was visually confirmed post-injection. Following the analysis of the spinal cord tissue, the most significant results were related with serotonergic innervation of the ipsilateral hemidiaphragm (**Figure 4**). Serotonin is synthesized in different populations of brainstem neurons and plays a crucial role in modulating motor function (Ghosh and Pearse, 2014). We observed a significant increase in all treatment groups, in the number and total length of 5-HT axons, in comparison to non-treated rats. This increased sprouting of 5-HT axons might partially account for the recovery observed in diaphragmatic function. The transplantation of OECs for instance, has been associated with increased regeneration of serotonergic fibers through different lesions, such as thoracic transection (Ramon-Cueto et al., 1998; Lu et al., 2001). The group transplanted with cells only presented the most significant recovery of 5-HT fibers, however this was not correlated with EMG signals. Therefore, other mechanisms might also be influencing diaphragmatic function, which could justify the improved EMG bursting in the combinatorial group.

Regarding limb motor function analysis, none of the therapeutic strategies employed impacted motor recovery. The motor behavior paradigms used address general forelimb movements (grooming test) but also skilled and fine detailed movements (staircase test). The specificity of the cervical neuronal circuitry might explain the different results observed between cervical and thoracic/lumbar studies. Forelimb motor function is highly dependent on supraspinal inputs, while thoracic and lumbar-derived movements rely significantly on local circuitries, such as central pattern generator (CPG) activity (Filli et al., 2011). Long-distance CST projections are difficult to regenerate, and we observed no regrowth of rVRG axons into and through the lesion site (**Supplementary Figure S1**). No differences were also observed in astrogliosis and inflammatory levels, as measured by the total area of GFAP and CD68 positive cells (**Supplementary Figure S2**).

Interestingly, sensorial perception of the contralateral forelimb was also normalized following the combined treatment (**Figure 7**). The sensorial fibers are also affected following SCI, with patients frequently developing chronic pain (Siddall et al., 1999). In this sense, the recovery observed is also very important, for the establishment of therapies that could improve a rescue of different systems, often considered more important than locomotion by the patients (Anderson, 2004). The explanation for this recovery is still elusive, although chronic pain and sensorial mechanisms have been associated with inflammation (Detloff et al., 2008), and our strategy has demonstrated immuno-modulatory properties in other two injury models (Gomes et al., 2016, 2018).

Cells from non-autologous sources were used in this study, both human ASCs and rat pup derived OECs. The use of autologous cells could have impacted differently the results observed, as it is expected that cell rejection rates are less significant. Still, we previously demonstrated that human ASCs can be integrated into the spinal cord tissue and survive for more than 8 weeks (Gomes et al., 2016, 2018), which favors the potential application of human ASCs to the clinics. In fact, both ASCs and OECs have already been tested independently in human clinical trials, demonstrating to be safe (Mackay-Sim et al., 2008; Hur et al., 2016). Hence, their conjugation might represent a valuable step in SCI management, as it can ameliorate the results obtained from each cell type individually.

CONCLUSION

Cervical SCI are the frequent in humans, therefore, there is a need for more studies focusing on traumatic lesions affecting this spinal cord region. TE approaches such as the one presented here are promising, as they can address multiple targets, increasing the chances for functional recovery following an injury. In our work, the combination of GG-GRGDS hydrogel with ASCs/OECs led to an increased diaphragmatic activity together with a partial reestablishment of sensory function compromised by the injury. This is of the utmost relevance, as respiratory compromise and chronic pain are two of the main concerns of SCI patients. The specific mechanism(s) by which this therapeutic strategy exerts its effects may be related – at least in part – to an increase in specific serotonergic fiber sprouting in the ipsilateral caudal spinal cord. This strategy opens a window for improvement of a critical condition such as cervical SCI.

DATA AVAILABILITY STATEMENT

The datasets generated for this study are available on request to the corresponding author.

ETHICS STATEMENT

Human lipoaspirates obtained from consenting donors under an institutional review board approved protocol at LaCell LLC.

AUTHOR CONTRIBUTIONS

EG and BG contributed to the experimental design, data collection, analysis and interpretation, and drafting of the manuscript. RL, MG, TM-G, JM-M, MU, and MW contributed to the data collection, analysis, and interpretation. JG and NS provided the technical knowledge and materials for the experiments. NAS, AL, and AS interpreted the data, supervised the work, and revised the manuscript. All the authors approved the final version of the manuscript.

FUNDING

The authors want to acknowledge the financial support from the Prémios Santa Casa Neurociências – Prize Melo e Castro for Spinal Cord Injury Research (MC-04/17) and Portuguese Foundation for Science and Technology (SFRH/BD/103075/2014 to EG; CEECIND/04794/2017 to

NS). This work was funded by the FEDER, through the Foundation for Science and Technology (FCT) and national funds, under the scope of the projects POCI-01-0145-FEDER-007038, TUBITAK/0007/2014, POCI-01-0145-FEDER-029206, PTDC/MED-NEU/31417/2017, POCI-01-0145-FEDER-032619, POCI-01-0145-FEDER-016739, and POCI-01-0145-FEDER-031395. This work has also been developed under the scope of the project NORTE-01-0145-FEDER-029968 and NORTE-01-0145-FEDER-000013, supported by the Northern Portugal Regional Operational Programme (NORTE 2020), under the Portugal 2020 Partnership Agreement, through the European Regional Development Fund (FEDER). This work was also performed under the Memorandum of Understanding on Academic Exchanges between the School of Medicine, University of Minho and the Luso-American Development Foundation. Support was also provided by: Craig H. Neilsen Foundation (Grant #476686 to AL) and the NINDS (Grant #1R01NS079702). ASCs were kindly provided by Prof. Jeff Gimble (LaCell Inc., United States).

SUPPLEMENTARY MATERIAL

The Supplementary Material for this article can be found online at: https://www.frontiersin.org/articles/10.3389/fbioe.2020.00984/full#supplementary-material

FIGURE S1 | mCherry-labeled rVrg axons detected at the intact rostral spinal cord tissue, 5 weeks post-injury. Only a limited number of axons entered the lesion site, not growing through the lesion. No differences were observed amongst groups. **(A)** Rats without treatment; **(B)** Gg-Grgds-only treated rats; **(C)** Ascs/Oecs-only treated rats; **(D)** Gg-Grgds + Ascs/Oecs treated animals.

FIGURE S2 | Quantification of the total area occupied by Gfap+ **(A)** and Cd68+ **(B)** cells. No differences were observed amongst groups. Data is presented as mean ± Sem (n = 3 per group).

REFERENCES

Alilain, W. J., Horn, K. P., Hu, H., Dick, T. E., and Silver, J. (2011). Functional regeneration of respiratory pathways after spinal cord injury. *Nature*475, 196–200.

Anderson, K. D. (2004). Targeting recovery: priorities of the spinal cord-injured population. *J. Neurotrauma* 21, 1371–1383.

Bertelli, J. A., and Mira, J. C. (1993). Behavioral evaluating methods in the objective clinical assessment of motor function after experimental brachial plexus reconstruction in the rat. *J. Neurosci. Methods* 46, 203–208.

Campos, F. L., Carvalho, M. M., Cristovao, A. C., Je, G., Baltazar, G., Salgado, A. J., et al. (2013). Rodent models of Parkinson's disease: beyond the motor symptomatology. *Front. Behav. Neurosci.* 7:175. doi: 10.3389/fnbeh.2013.00175

Chaplan, S. R., Bach, F. W., Pogrel, J. W., Chung, J. M., and Yaksh, T. L. (1994). Quantitative assessment of tactile allodynia in the rat paw. *J. Neurosci. Methods* 53, 55–63.

Charsar, B. A., Urban, M. W., and Lepore, A. C. (2017). Harnessing the power of cell transplantation to target respiratory dysfunction following spinal cord injury. *Exp. Neurol.* 287(Pt 2), 268–275.

Detloff, M. R., Fisher, L. C., McGaughy, V., Longbrake, E. E., Popovich, P. G., and Basso, D. M. (2008). Remote activation of microglia and pro-inflammatory cytokines predict the onset and severity of below-level neuropathic pain after spinal cord injury in rats. *Exp. Neurol.* 212, 337–347.

Dixon, W. J. (1980). Efficient analysis of experimental observations. *Annu. Rev. Pharmacol. Toxicol.* 20, 441–462.

Dubois, S. G., Floyd, E. Z., Zvonic, S., Kilroy, G., Wu, X., Carling, S., et al. (2008). Isolation of human adipose-derived stem cells from biopsies and liposuction specimens. *Methods Mol. Biol.* 449, 69–79.

Filli, L., Zorner, B., Weinmann, O., and Schwab, M. E. (2011). Motor deficits and recovery in rats with unilateral spinal cord hemisection mimic the Brown-Sequard syndrome. *Brain* 134(Pt 8), 2261–2273.

Fogarty, M. J., Mantilla, C. B., and Sieck, G. C. (2018). Breathing: motor control of diaphragm muscle. *Physiology* 33, 113–126.

Geissler, S. A., Sabin, A. L., Besser, R. R., Gooden, O. M., Shirk, B. D., Nguyen, Q. M., et al. (2018). Biomimetic hydrogels direct spinal progenitor cell differentiation and promote functional recovery after spinal cord injury. *J. Neural Eng.* 15:025004.

Ghosh, B., Wang, Z., Nong, J., Urban, M. W., Zhang, Z., Trovillion, V. A., et al. (2018). Local BDNF Delivery to the Injured Cervical Spinal Cord using an Engineered Hydrogel Enhances Diaphragmatic Respiratory Function. *J. Neurosci.* 38, 5982–5995.

Ghosh, M., and Pearse, D. D. (2014). The role of the serotonergic system in locomotor recovery after spinal cord injury. *Front. Neural Circuits* 8:151. doi: 10.3389/fncir.2014.00151

Gomes, E. D., Mendes, S. S., Assuncao-Silva, R. C., Teixeira, F. G., Pires, A. O., Anjo, S. I., et al. (2018). Co-Transplantation of adipose tissue-derived stromal cells and olfactory ensheathing cells for spinal cord injury repair. *Stem Cells* 36, 696–708.

Gomes, E. D., Mendes, S. S., Leite-Almeida, H., Gimble, J. M., Tam, R. Y., Shoichet, M. S., et al. (2016). Combination of a peptide-modified gellan gum hydrogel with cell therapy in a lumbar spinal cord injury animal model. *Biomaterials* 105, 38–51.

Goulao, M., Ghosh, B., Urban, M. W., Sahu, M., Mercogliano, C., Charsar, B. A., et al. (2019). Astrocyte progenitor transplantation promotes regeneration of bulbospinal respiratory axons, recovery of diaphragm function, and a reduced macrophage response following cervical spinal cord injury. *Glia* 67, 452–466.

Gransee, H. M., Zhan, W. Z., Sieck, G. C., and Mantilla, C. B. (2015). Localized delivery of brain-derived neurotrophic factor-expressing mesenchymal stem cells enhances functional recovery following cervical spinal cord injury. *J. Neurotrauma* 32, 185–193.

Guimaraes, M. R., Soares, A. R., Cunha, A. M., Esteves, M., Borges, S., Magalhaes, R., et al. (2019). Evidence for lack of direct causality between pain and affective disturbances in a rat peripheral neuropathy model. *Genes Brain Behav.* 18:e12542.

Hur, J. W., Cho, T. H., Park, D. H., Lee, J. B., Park, J. Y., and Chung, Y. G. (2016). Intrathecal transplantation of autologous adipose-derived mesenchymal stem cells for treating spinal cord injury: a human trial. *J. Spinal Cord Med.* 39, 655–664.

Lane, M. A., Fuller, D. D., White, T. E., and Reier, P. J. (2008). Respiratory neuroplasticity and cervical spinal cord injury: translational perspectives. *Trends Neurosci.* 31, 538–547.

Lee, K. Z., Lane, M. A., Dougherty, B. J., Mercier, L. M., Sandhu, M. S., Sanchez, J. C., et al. (2014). Intraspinal transplantation and modulation of donor neuron electrophysiological activity. *Exp. Neurol.* 251, 47–57.

Li, K., Javed, E., Hala, T. J., Sannie, D., Regan, K. A., Maragakis, N. J., et al. (2015a). Transplantation of glial progenitors that overexpress glutamate transporter GLT1 preserves diaphragm function following cervical SCI. *Mol. Ther.* 23, 533–548.

Li, K., Javed, E., Scura, D., Hala, T. J., Seetharam, S., Falnikar, A., et al. (2015b). Human iPS cell-derived astrocyte transplants preserve respiratory function after spinal cord injury. *Exp. Neurol.* 271, 479–492.

Li, Y., Decherchi, P., and Raisman, G. (2003). Transplantation of olfactory ensheathing cells into spinal cord lesions restores breathing and climbing. *J. Neurosci.* 23, 727–731.

Lima, R., Monteiro, S., Lopes, J. P., Barradas, P., Vasconcelos, N. L., Gomes, E. D., et al. (2017). Systemic interleukin-4 administration after spinal cord injury modulates inflammation and promotes neuroprotection. *Pharmaceuticals* 10:83.

Liu, S., Sandner, B., Schackel, T., Nicholson, L., Chtarto, A., Tenenbaum, L., et al. (2017). Regulated viral BDNF delivery in combination with Schwann cells promotes axonal regeneration through capillary alginate hydrogels after spinal cord injury. *Acta Biomater.* 60, 167–180.

Lopez-Santalla, M., Mancheno-Corvo, P., Menta, R., Lopez-Belmonte, J., DelaRosa, O., Bueren, J. A., et al. (2015). Human adipose-derived mesenchymal stem cells modulate experimental autoimmune arthritis by modifying early adaptive T cell responses. *Stem Cells* 33, 3493–3503.

Lu, J., Feron, F., Ho, S. H., Mackay-Sim, A., and Waite, P. M. E. (2001). Transplantation of nasal olfactory tissue promotes partial recovery in paraplegic adult rats. *Brain Res.* 889, 344–357.

Mackay-Sim, A., Feron, F., Cochrane, J., Bassingthwaighte, L., Bayliss, C., Davies, W., et al. (2008). Autologous olfactory ensheathing cell transplantation in human paraplegia: a 3-year clinical trial. *Brain* 131(Pt 9), 2376–2386.

Montoya, C. P., Campbell-Hope, L. J., Pemberton, K. D., and Dunnett, S. B. (1991). The "staircase test": a measure of independent forelimb reaching and grasping abilities in rats. *J. Neurosci. Methods* 36, 219–228.

Nicaise, C., Hala, T. J., Frank, D. M., Parker, J. L., Authelet, M., Leroy, K., et al. (2012a). Phrenic motor neuron degeneration compromises phrenic axonal circuitry and diaphragm activity in a unilateral cervical contusion model of spinal cord injury. *Exp. Neurol.* 235, 539–552.

Nicaise, C., Putatunda, R., Hala, T. J., Regan, K. A., Frank, D. M., Brion, J. P., et al. (2012b). Degeneration of phrenic motor neurons induces long-term diaphragm deficits following mid-cervical spinal contusion in mice. *J. Neurotrauma* 29, 2748–2760.

Ramon-Cueto, A., Cordero, M. I., Santos-Benito, F. F., and Avila, J. (2000). Functional recovery of paraplegic rats and motor axon regeneration in their spinal cords by olfactory ensheathing glia. *Neuron* 25, 425–435.

Ramon-Cueto, A., Plant, G. W., Avila, J., and Bunge, M. B. (1998). Long-distance axonal regeneration in the transected adult rat spinal cord is promoted by olfactory ensheathing glia transplants. *J. Neurosci.* 18, 3803–3815.

Salgado, A. J., Reis, R. L., Sousa, N. J., and Gimble, J. M. (2010). Adipose tissue derived stem cells secretome: soluble factors and their roles in regenerative medicine. *Curr. Stem Cell Res. Ther.* 5, 103–110.

Siddall, P. J., Taylor, D. A., McClelland, J. M., Rutkowski, S. B., and Cousins, M. J. (1999). Pain report and the relationship of pain to physical factors in the first 6 months following spinal cord injury. *Pain* 81, 187–197.

Silva, N. A., Cooke, M. J., Tam, R. Y., Sousa, N., Salgado, A. J., Reis, R. L., et al. (2012a). The effects of peptide modified gellan gum and olfactory ensheathing glia cells on neural stem/progenitor cell fate. *Biomaterials* 33, 6345–6354.

Silva, N. A., Sousa, R. A., Pires, A. O., Sousa, N., Salgado, A. J., and Reis, R. L. (2012b). Interactions between Schwann and olfactory ensheathing cells with a starch/polycaprolactone scaffold aimed at spinal cord injury repair. *J. Biomed. Mater. Res. A* 100, 470–476.

Silva, N. A., Gimble, J. M., Sousa, N., Reis, R. L., and Salgado, A. J. (2013a). Combining adult stem cells and olfactory ensheathing cells: the secretome effect. *Stem Cells Dev.* 22, 1232–1240.

Silva, N. A., Moreira, J., Ribeiro-Samy, S., Gomes, E. D., Tam, R. Y., Shoichet, M. S., et al. (2013b). Modulation of bone marrow mesenchymal stem cell secretome by ECM-like hydrogels. *Biochimie* 95, 2314–2319.

Singh, A., Tetreault, L., Kalsi-Ryan, S., Nouri, A., and Fehlings, M. G. (2014). Global prevalence and incidence of traumatic spinal cord injury. *Clin. Epidemiol.* 6, 309–331.

Sotiropoulos, I., Lopes, A. T., Pinto, V., Lopes, S., Carlos, S., Duarte-Silva, S., et al. (2014). Selective impact of Tau loss on nociceptive primary afferents and pain sensation. *Exp. Neurol.* 261, 486–493.

Urban, M. W., Ghosh, B., Strojny, L. R., Block, C. G., Blazejewski, S. M., Wright, M. C., et al. (2018). Cell-type specific expression of constitutively-active Rheb promotes regeneration of bulbospinal respiratory axons following cervical SCI. *Exp. Neurol.* 303, 108–119.

Wright, M. C., and Son, Y. J. (2007). Ciliary neurotrophic factor is not required for terminal sprouting and compensatory reinnervation of neuromuscular synapses: re-evaluation of CNTF null mice. *Exp. Neurol.* 205, 437–448.

Zutphen, L. F. M. V., Baumans, V., and Beynen, A. C. (2001). *Principles of Laboratory Animal Science : A Contribution To The Humane Use and Care of Animals and to the Quality of Experimental Results, Rev. edn*. Amsterdam: Elsevier.

Conflict of Interest: The authors declare that the research was conducted in the absence of any commercial or financial relationships that could be construed as a potential conflict of interest.

Advantages of publishing in Frontiers

OPEN ACCESS
Articles are free to read for greatest visibility and readership

FAST PUBLICATION
Around 90 days from submission to decision

HIGH QUALITY PEER-REVIEW
Rigorous, collaborative, and constructive peer-review

TRANSPARENT PEER-REVIEW
Editors and reviewers acknowledged by name on published articles

Frontiers
Avenue du Tribunal-Fédéral 34
1005 Lausanne | Switzerland

Visit us: www.frontiersin.org
Contact us: info@frontiersin.org | +41 21 510 17 00

REPRODUCIBILITY OF RESEARCH
Support open data and methods to enhance research reproducibility

DIGITAL PUBLISHING
Articles designed for optimal readership across devices

FOLLOW US
@frontiersin

IMPACT METRICS
Advanced article metrics track visibility across digital media

EXTENSIVE PROMOTION
Marketing and promotion of impactful research

LOOP RESEARCH NETWORK
Our network increases your article's readership